WOODHEAD PUBLISHING SERIES IN ELECTRONIC AND OPTICAL MATERIALS

Ultrasonic transducers

Materials and design for sensors, actuators and medical applications

Edited by K. Nakamura

WP
WOODHEAD
PUBLISHING

VISIT…

LANZAROTE
Caliente.COM

Ultrasonic transducers

Related titles:

Advanced piezoelectric materials: science and technology
(ISBN 978-1-84569-534-7)
Piezoelectric materials produce electric charges on their surfaces as a consequence of applying mechanical stress. They are used in the fabrication of a growing range of devices such as transducers, actuators, pressure sensor devices and increasingly as a way of producing energy. This book provides a comprehensive review of advanced piezoelectric materials, their properties, methods of manufacture and applications.

MEMS for automotive and aerospace applications
(ISBN 978-0-85709-118-5)
A Micro-Electro-Mechanical System (MEMS) is a miniature device or machine that integrates elements such as actuators, sensors and a processor to form a microsystem. The automotive sector is currently the biggest consumer of MEMS and this market is expected to grow, driven by safety legislation. Emerging applications in the aerospace field will face unique challenges related to harsh environmental conditions and reliability requirements. Part I covers MEMS in automotive applications, including safety systems, stability control and engine management. Part II describes MEMS in aircraft such as navigation systems, devices for health monitoring and drag reduction. MEMS thrusters for nano- and pico-satellites are also covered.

In situ characterization of thin film growth
(ISBN 978-1-84569-934-5)
Recent advances in techniques to characterize thin films *in situ* during deposition could lead to an improved understanding of deposition processes and to better, faster diagnosis of issues with the deposition process. *In situ characterization of thin film growth* provides a comprehensive review of this increasingly important topic. Part I reviews electron diffraction techniques. Part II covers photoemission techniques, principles and instrumentation. Part III contains alternative *in situ* characterization techniques and the trend for combining different techniques.

Details of these books and a complete list of titles from Woodhead Publishing can be obtained by:

- visiting our web site at www.woodheadpublishing.com
- contacting Customer Services (e-mail: sales@woodheadpublishing.com; fax: +44 (0) 1223 832819; tel.: +44 (0) 1223 499140 ext. 130; address: Woodhead Publishing Limited, 80 High Street, Sawston, Cambridge CB22 3HJ, UK)
- in North America, contacting our US office (e-mail: usmarketing@woodheadpublishing.com; tel.: (215) 928 9112; address: Woodhead Publishing, 1518 Walnut Street, Suite 1100, Philadelphia, PA 19102-3406, USA

If you would like e-versions of our content, please visit our online platform: www.woodheadpublishingonline.com. Please recommend it to your librarian so that everyone in your institution can benefit from the wealth of content on the site.

Woodhead Publishing Series in Electronic and Optical Materials:
Number 29

Ultrasonic transducers

Materials and design for sensors, actuators and medical applications

Edited by
K. Nakamura

WP
WOODHEAD
PUBLISHING

Oxford Cambridge Philadelphia New Delhi

Published by Woodhead Publishing Limited,
80 High Street, Sawston, Cambridge CB22 3HJ, UK
www.woodheadpublishing.com
www.woodheadpublishingonline.com

Woodhead Publishing, 1518 Walnut Street, Suite 1100, Philadelphia,
PA 19102-3406, USA

Woodhead Publishing India Private Limited, G-2, Vardaan House,
7/28 Ansari Road, Daryaganj, New Delhi – 110002, India
www.woodheadpublishingindia.com

First published 2012, Woodhead Publishing Limited
© Woodhead Publishing Limited, 2012; except Chapter 13 © Government of Canada, 2012
The authors have asserted their moral rights.

This book contains information obtained from authentic and highly regarded sources. Reprinted material is quoted with permission, and sources are indicated. Reasonable efforts have been made to publish reliable data and information, but the authors and the publisher cannot assume responsibility for the validity of all materials. Neither the authors nor the publisher, nor anyone else associated with this publication, shall be liable for any loss, damage or liability directly or indirectly caused or alleged to be caused by this book.

Neither this book nor any part may be reproduced or transmitted in any form or by any means, electronic or mechanical, including photocopying, microfilming and recording, or by any information storage or retrieval system, without permission in writing from Woodhead Publishing Limited.

The consent of Woodhead Publishing Limited does not extend to copying for general distribution, for promotion, for creating new works, or for resale. Specific permission must be obtained in writing from Woodhead Publishing Limited for such copying.

Trademark notice: Product or corporate names may be trademarks or registered trademarks, and are used only for identification and explanation, without intent to infringe.

British Library Cataloguing in Publication Data
A catalogue record for this book is available from the British Library.

Library of Congress Control Number: 2012944085

ISBN 978-1-84569-989-5 (print)
ISBN 978-0-85709-630-2 (online)
ISSN 2050-1501 Woodhead Publishing Series in Electronic and Optical Materials (print)
ISSN 2050-151X Woodhead Publishing Series in Electronic and Optical Materials (online)

The publisher's policy is to use permanent paper from mills that operate a sustainable forestry policy, and which has been manufactured from pulp which is processed using acid-free and elemental chlorine-free practices. Furthermore, the publisher ensures that the text paper and cover board used have met acceptable environmental accreditation standards.

Typeset by RefineCatch Limited, Bungay, Suffolk, UK
Printed by TJ International Limited, Padstow, Cornwall, UK

Contents

Contributor contact details xiii
Woodhead Publishing Series in Electronic and Optical Materials xvii
Preface xxi

Part I Materials and design of ultrasonic transducers 1

1 Piezoelectricity and basic configurations for piezoelectric ultrasonic transducers 3
S. COCHRAN, University of Dundee, UK

1.1 Introduction 3
1.2 The piezoelectric effect 4
1.3 Piezoelectric materials 13
1.4 Piezoelectric transducers 20
1.5 Summary, future trends and sources of further information 31
1.6 References 33

2 Electromagnetic acoustic transducers 36
G. HÜBSCHEN, Fraunhofer Institute for Non-Destructive Testing (IZFP), Germany

2.1 Introduction 36
2.2 Physical principles 36
2.3 Lorentz-force-type transducers 41
2.4 Magnetostriction-type transducers 60
2.5 Conclusion 66
2.6 References 66

3 Piezoelectric ceramics for transducers 70
K. UCHINO, The Pennsylvania State University, USA and Office of Naval Research – Global, Japan

3.1 The history of piezoelectrics 70
3.2 Piezoelectric materials: present status 88
3.3 References 114

4 Thin-film PZT-based transducers 117
M. K. KUROSAWA, Tokyo Institute of Technology, Japan

4.1 Introduction 117
4.2 PZT deposition using the hydrothermal process 118
4.3 Applications using the bending and longitudinal vibration of the d_{31} effect 127
4.4 Thickness-mode vibration, d_{33} 140
4.5 Epitaxial film 150
4.6 Conclusions 151
4.7 References 151

5 High-Curie-temperature piezoelectric single crystals of the $Pb(In_{1/2}Nb_{1/2})O_3$–$Pb(Mg_{1/3}Nb_{2/3})O_3$–$PbTiO_3$ ternary system 154
Y. YAMASHITA, Toshiba Research Consulting Corporation, Japan and Y. HOSONO, Toshiba Corporation, Japan

5.1 Introduction 154
5.2 PIMNT ceramics 157
5.3 PIMNT single crystals grown by the flux method 163
5.4 PIMNT single crystals grown by the Bridgman method 165
5. 5 Recent research into PIMNT single crystals and their applications 175
5.6 Future prospects and tasks 177
5.7 Conclusions 179
5.8 References 180

Part II Modelling and characterisation of ultrasonic transducers 185

6 Modelling ultrasonic-transducer performance: one-dimensional models 187
S. COCHRAN and C. E. M. DÉMORÉ, University of Dundee, UK and C. R. P. COURTNEY, University of Bristol, UK

6.1 Introduction 187
6.2 Transducer performance expressed through the wave equation 188
6.3 Equivalent electrical circuit models 195
6.4 The linear systems model 202
6.5 Examples 205
6.6 Summary, future trends and sources of further information 216
6.7 References 218

7 The boundary-element method applied to micro-acoustic devices: zooming into the near field 220
A. BAGHAI-WADJI, RMIT University, Australia

7.1 Introduction 220
7.2 The acoustic wave equation: shear horizontal vibrations 221
7.3 Construction of infinite-domain Green's functions 224
7.4 Near-field analysis 239
7.5 Normalization of the field variables 249
7.6 Determining the asymptotic expansion terms for $\eta \to 0$ 250
7.7 Future trends 258
7.8 Key references for further reading 260
7.9 Acknowledgements 261
7.10 References 261

8 Electrical evaluation of piezoelectric transducers 264
K. NAKAMURA, Tokyo Institute of Technology, Japan

8.1 Introduction 264
8.2 Equivalent electrical circuit 265
8.3 Electrical measurements 267
8.4 Characterization of piezoelectric transducers under high-power operation 271
8.5 Load test 274
8.6 Summary 275
8.7 References 276

9 Laser Doppler vibrometry for measuring vibration in ultrasonic transducers 277
M. JOHANSMANN and G. WIRTH, Polytec GmbH, Germany

9.1 Introduction 277
9.2 Laser Doppler vibrometry for non-contact vibration measurements 278
9.3 Characterization of ultrasonic transducers and optimization of ultrasonic tools 286
9.4 Enhanced LDV designs for special measurements 303
9.5 Conclusion and summary 312
9.6 References 312

10 Optical visualization of acoustic fields: the schlieren technique, the Fresnel method and the photoelastic method applied to ultrasonic transducers 314
K. YAMAMOTO, Kansai University, Japan

10.1 Introduction 314

10.2 Schlieren visualization technique 314
10.3 Fresnel visualization method 320
10.4 Photoelastic visualization method 323
10.5 References 327

Part III Applications of ultrasonic transducers 329

11 Surface acoustic wave (SAW) devices 331
K. Hashimoto, Chiba University, Japan

11.1 Introduction 331
11.2 Interdigital transducers (IDTs) 332
11.3 Transversal SAW filter 351
11.4 SAW resonators 362
11.5 Conclusions 371
11.6 References 371

12 Airborne ultrasound transducers 374
D. A. Hutchins, University of Warwick, UK and A. Neild, Monash University, Australia

12.1 Introduction 374
12.2 Basic design principles 375
12.3 Transducer designs for use in air 381
12.4 Radiated fields in air 385
12.5 Applications 392
12.6 Future trends 402
12.7 Sources of further information and advice 403
12.8 Acknowledgements 403
12.9 References 404

13 Transducers for non-destructive evaluation at high temperatures 408
M. Kobayashi and C.-K. Jen, Industrial Materials Institute, Canada

13.1 Transducers for non-destructive evaluation at high temperatures 408
13.2 Sol-gel composite ultrasonic transducers 411
13.3 Structural-health monitoring demonstration 422
13.4 Process-monitoring demonstration 433
13.5 Conclusions 440
13.6 Sources of further information 441
13.7 References 441

14 Analysis and synthesis of frequency-diverse ultrasonic flaw-detection systems using order statistics and neural network processors 444
J. Saniie and E. Oruklu, Illinois Institute of Technology, USA

14.1 Introduction 444
14.2 Ultrasonic flaw-detection techniques 445
14.3 Neural network detection processor 456
14.4 Flaw-detection performance evaluation 460
14.5 System-on-a-chip implementation – a case study 465
14.6 Future trends 472
14.7 Conclusions 473
14.8 Further information 474
14.9 References 474

15 Power ultrasonics: new technologies and applications for fluid processing 476
J. A. Gallego-Juárez, Spanish National Research Council (CSIC), Spain

15.1 Introduction 476
15.2 New power ultrasonic technologies for fluids and multiphase media 478
15.3 Application of the new power ultrasonic technology to processing 490
15.4 Conclusions 513
15.5 Acknowledgements 514
15.6 References 514

16 Nonlinear acoustics and its application to biomedical ultrasonics 517
P. A. Lewin, Drexel University, USA and A. Nowicki, Polish Academy of Sciences, Poland

16.1 Introduction 517
16.2 Basic aspects of nonlinear acoustic wave propagation and associated phenomena 518
16.3 Measurements of and advances in the determination of B/A 519
16.4 Advances in tissue harmonic imaging 523
16.5 Nonlinear acoustics in ultrasound metrology 531
16.6 Nonlinear wave propagation in hydrophone probe calibration 534
16.7 Nonlinear acoustics in therapeutic applications 538
16.8 Conclusions 539
16.9 Acknowledgements 540
16.10 References 540

17 Therapeutic ultrasound with an emphasis on applications to the brain 545

P. D. MOURAD, University of Washington, USA

17.1 Introduction and summary 545
17.2 Fundamentals of propagation and absorption of ultrasound 547
17.3 Acoustic attenuation as absorption plus scattering 548
17.4 Physical and chemical processes engendered by medical ultrasound 549
17.5 Bubble formation and growth 551
17.6 Inertial cavitation and associated material stresses 554
17.7 Mechanical index 554
17.8 Diagnostic ultrasound 555
17.9 Therapeutic ultrasound 560
17.10 Ultrasound-facilitated delivery of drugs and antibodies into the brain 563
17.11 Neuromodulation by ultrasound 566
17.12 Conclusion 567
17.13 References 568

18 Microscale ultrasonic sensors and actuators 572

A. RAMKUMAR and A. LAL, Cornell University, USA

18.1 Introduction: ultrasonic horn actuators 572
18.2 Advantages of silicon-based technology 574
18.3 Silicon ultrasonic horns 580
18.4 Sensor integration and fabrication of silicon horns 584
18.5 Planar electrode characterization 586
18.6 Piezoresistive strain gauges 592
18.7 Applications: tissue penetration force reduction 597
18.8 Applications: cardiac electrophysiological measurement 602
18.9 Applications: microscale tissue metrology in testicular sperm extraction (TESE) surgery 606
18.10 Conclusions 614
18.11 References 615

19 Piezoelectric and fibre-optic hydrophones 619

A. HURRELL, Precision Acoustics Ltd, UK and P. BEARD, University College London, UK

19.1 Introduction 619
19.2 General hydrophone considerations 620
19.3 Piezoelectric hydrophones 626
19.4 Fibre-optic hydrophones 641
19.5 Summary 671
19.6 References 673

20 Ultrasonic motors 677

K. Nakamura, Tokyo Institute of Technology, Japan

20.1 Introduction 677
20.2 Standing-wave ultrasonic motors 678
20.3 Traveling-wave ultrasonic motors 694
20.4 Ultrasonic motor performance 700
20.5 Summary and future trends 702
20.6 References 703

Index *705*

Contributor contact details

(* = main contact)

Editor, Preface, Chapters 8 and 20

Prof. Kentaro Nakamura
Precision and Intelligence Laboratory
Tokyo Institute of Technology
R2-26, 4259 Nagatsuta
Midori-ku
Yokohama 226-8503
Japan

Email: knakamur@sonic.pi.titech.ac.jp

Chapter 1

Prof. Sandy Cochran
Institute for Medical Science and Technology
University of Dundee
Dundee DD2 1FD
UK

Email: s.cochran@dundee.ac.uk

Chapter 2

Dr Gerhard Hübschen
Lorisgartenstrasse 11
D-66740 Saarlouis
Germany

Email: gerhard.huebschen@t-online.de

Chapter 3

Prof. Kenji Uchino
ONRG-Asia
Office of Naval Research
7-23-17 Roppongi
Minato-ku
Tokyo 106-0032
Japan

E-mail: Kenji.Uchino@onrg.navy.mil

and

Electrical Engineering
International Center for Actuators and Transducers
The Pennsylvania State University
University Park
PA 16802
USA

E-mail: KenjiUchino@psu.edu

Chapter 4

Minoru Kuribayashi Kurosawa
Department of Information Processing
Tokyo Institute of Technology
4259 Nagatsuta
Midori
Yokohama 226-8502
Japan

Email: mkur@ip.titech.ac.jp

Chapter 5

Yohachi (John) Yamashita*
Toshiba Research Consulting Corporation
1, Komukai Toshiba-cho
Saiwai-ku
Kawasaki 212-8582
Japan

Email: yohachi.yamashita@nifty.ne.jp

Yasuharu Hosono
Corporate Research & Development Center
Toshiba Corporation
1, Komukai Toshiba-cho
Saiwai-ku
Kawasaki 212-8582
Japan

Chapter 6

Prof. Sandy Cochran* and Dr Christine Démoré
Institute for Medical Science and Technology
University of Dundee
Dundee DD2 1FD
UK

Email: s.cochran@dundee.ac.uk; c.demore@dundee.ac.uk

Dr Charles Courtney
Department of Mechanical Engineering
University of Bristol
Bristol BS8 1TR
UK

Email c.r.p.courtney@bristol.ac.uk

Chapter 7

Alireza Baghai-Wadji
School of Electrical and Computer Engineering
RMIT University
Building 10, 376-392 Swanston Street
Melbourne GPO Box 2476V
Melbourne VIC 3001
Australia

Email: alireza.baghai-wadji@rmit.edu.au

Chapter 9

Martin Johansmann* and Dr Georg Wirth
Polytec GmbH
Polytec-Platz 1-7
76337 Waldbronn
Germany

Email: M.Johansmann@polytec.de; G.Wirth@polytec.de

Chapter 10

Ken Yamamoto
Department of Pure and Applied Physics
Faculty of Engineering Science
Kansai University
3-3-35 Yamate-cho
Suita-shi
Osaka 564-8680
Japan

Email: ken@kansai-u.ac.jp

Chapter 11

Prof. Ken-ya Hashimoto
Department of Electrical and Electronics Engineering
Graduate School of Engineering
Chiba University
1-33 Yayoi-cho, Inage-ku
Chiba 263-8522
Japan

Email: k.hashimoto@ieee.org

Chapter 12

Prof. D. A. Hutchins*
School of Engineering
University of Warwick
Coventry CV4 7AL
UK

Email: D.A.Hutchins@warwick.ac.uk

Dr A. Neild
Department of Mechanical and Aerospace Engineering
Monash University
Victoria 3800
Australia

Email: adrian.neild@monash.edu

Chapter 13

Dr M. Kobayashi* and Dr C.-K. Jen
Industrial Materials Institute
National Research Council of Canada
75, boul. de Mortagne
Boucherville
Québec, J4B 6Y4
Canada

Email: makiko.kobayashi@cnrc-nrc.gc.ca; kobayashi@cs.kumamoto-u.ac.jp

Chapter 14

Prof. J. Saniie* and Prof. E. Oruklu
Department of Electrical and Computer Engineering
Illinois Institute of Technology
Chicago, IL 60616
USA

Email: sansonic@ece.iit.edu

Chapter 15

Prof. J. A. Gallego-Juárez
Power Ultrasonics Group
Spanish National Research Council (CSIC)
Serrano 144
28006 Madrid
Spain

Email: jgallego@ia.cetef.csic.es; jgallego@pusonics.es

Chapter 16

Prof. Peter A. Lewin*
School of Biomedical Engineering, Science and Health Systems
Biomedical Ultrasound Research and Education Center
Drexel University, Bossone 701
3141 Chestnut Street
Philadelphia, PA 19104
USA

Email: plewin@coe.drexel.edu

Prof. Andrzej Nowicki
Institute of Fundamental Technological Research
Polish Academy of Sciences
Pawinskiego 5 b
Warsaw, 02-106
Poland

Email: anowicki@ippt.gov.pl

Chapter 17

Dr Pierre D. Mourad
Department of Neurological Surgery
Applied Physics Laboratory
Department of Bioengineering
University of Washington
Seattle, WA 98195
USA

Email: pierre@apl.washington.edu

Chapter 18

Dr Abhishek Ramkumar*
Department of Electrical and Computer Engineering
Cornell University
121 Phillips Hall
Ithaca, NY 14853
USA

Email: ar339@cornell.edu

Prof. Amit Lal
Department of Electrical and Computer Engineering
Cornell University
118 Phillips Hall
Ithaca, NY 14853
USA

Email: lal@ece.cornell.edu

Chapter 19

Dr Andrew Hurrell
Precision Acoustics Ltd
Hampton Farm Business Park
Dorset DT2 8QH
UK

Prof. Paul Beard*
Department of Medical Physics and Bioengineering
University College London
Malet Place Engineering Building
London WC1E 6BT
UK

Email: pbeard@medphys.ucl.ac.uk

Woodhead Publishing Series in Electronic and Optical Materials

1 **Circuit analysis**
J. E. Whitehouse
2 **Signal processing in electronic communications: For engineers and mathematicians**
M. J. Chapman, D. P. Goodall and N. C. Steele
3 **Pattern recognition and image processing**
D. Luo
4 **Digital filters and signal processing in electronic engineering: Theory, applications, architecture, code**
S. M. Bozic and R. J. Chance
5 **Cable engineering for local area networks**
B. J. Elliott
6 **Designing a structured cabling system to ISO 11801: Cross-referenced to European CENELEC and American Standards**
Second edition
B. J. Elliott
7 **Microscopy techniques for materials science**
A. Clarke and C. Eberhardt
8 **Materials for energy conversion devices**
Edited by C. C. Sorrell, J. Nowotny and S. Sugihara
9 **Digital image processing: Mathematical and computational methods**
Second edition
J. M. Blackledge
10 **Nanolithography and patterning techniques in microelectronics**
Edited by D. Bucknall
11 **Digital signal processing: Mathematical and computational methods, software development and applications**
Second edition
J. M. Blackledge
12 **Handbook of advanced dielectric, piezoelectric and ferroelectric materials: Synthesis, properties and applications**
Edited by Z.-G. Ye

13 **Materials for fuel cells**
Edited by M. Gasik
14 **Solid-state hydrogen storage: Materials and chemistry**
Edited by G. Walker
15 **Laser cooling of solids**
S. V. Petrushkin and V. V. Samartsev
16 **Polymer electrolytes: Fundamentals and applications**
Edited by C. A. C. Sequeira and D. A. F. Santos
17 **Advanced piezoelectric materials: Science and technology**
Edited by K. Uchino
18 **Optical switches: Materials and design**
Edited by S. J. Chua and B. Li
19 **Advanced adhesives in electronics: Materials, properties and applications**
Edited by M. O. Alam and C. Bailey
20 **Thin film growth: Physics, materials science and applications**
Edited by Z. Cao
21 **Electromigration in thin films and electronic devices: Materials and reliability**
Edited by C.-U. Kim
22 **In situ characterization of thin film growth**
Edited by G. Koster and G. Rijnders
23 **Silicon-germanium (SiGe) nanostructures: Production, properties and applications in electronics**
Edited by Y. Shiraki and N. Usami
24 **High-temperature superconductors**
Edited by X. G. Qiu
25 **Introduction to the physics of nanoelectronics**
S. G. Tan and M. B. A. Jalil
26 **Printed films: Materials science and applications in sensors, electronics and photonics**
Edited by M. Prudenziati and J. Hormadaly
27 **Laser growth and processing of photonic devices**
Edited by N. A. Vainos
28 **Quantum optics with semiconductor nanostructures**
Edited by F. Jahnke
29 **Ultrasonic transducers: Materials and design for sensors, actuators and medical applications**
Edited by K. Nakamura
30 **Waste electrical and electronic equipment (WEEE) handbook**
Edited by V. Goodship and A. Stevels
31 **Applications of ATILA FEM software to smart materials: Case studies in designing devices**
Edited by K. Uchino and J.-C. Debus

32 **MEMS for automotive and aerospace applications**
Edited by M. Kraft and N. M. White
33 **Semiconductor lasers: Fundamentals and applications**
Edited by A. Baranov and E. Tournie
34 **Handbook of terahertz technology for imaging, sensing, and communications**
Edited by D. Saeedkia
35 **Handbook of solid-state lasers: Materials, systems and applications**
Edited by B. Denker and E. Shklovsky
36 **Organic light-emitting diodes: Materials, devices and applications**
Edited by A. Buckley
37 **Lasers for medical applications: Diagnostics, therapy and surgery**
Edited by H. Jelínková
38 **Semiconductor gas sensors**
Edited by R. Jaaniso and O. K. Tan
39 **Handbook of organic materials for optical and optoelectronic devices: Properties and applications**
Edited by O. Ostroverkhova
40 **Metallic films for electronic, optical and magnetic applications: Structure, processing and properties**
Edited by K. Barmak and K. Coffey
41 **Handbook of laser welding technologies**
Edited by S. Katayama
42 **Nanolithography: The art of fabricating nanoelectronics, nanophotonics and nanobiology devices and systems**
Edited by M. Feldman
43 **Laser spectroscopy for sensing: Fundamentals, techniques and applications**
Edited by M. Baudelet
44 **Chalcogenide glasses: Preparation, properties and applications**
Edited by J.-L. Adam and X. Zhang
45 **Handbook of MEMS for wireless and mobile applications**
Edited by D. Uttamchandani
46 **Subsea optics and imaging**
Edited by J. Watson and O. Zielinski
47 **Carbon nanotubes and graphene for photonic applications**
Edited by S. Yamashita, Y. Saito and J. H. Choi
48 **Optical biomimetics**
Edited by M. Large

Preface

Ultrasonic waves are useful for detecting and evaluating objects in any kind of medium: gas, liquid or solid, except for a vacuum. Ultrasonic waves have been a practical and powerful tool for several decades, particularly for medical diagnostics in hospitals and nondestructive testing in industry, because electromagnetic waves attenuate rapidly in the human body and metal objects. The safety of ultrasonic waves is, in general, high in comparison with X-rays, and practical measurements and imaging can be carried out with less expensive devices than other methods. The low propagation speed of ultrasonic waves is also a useful feature for measurement and imaging, since the time of flight can be easily used to estimate the distance between the object and the ultrasonic transducer, which can be used to create two-dimensional or even three-dimensional pictures. The propagation speed of ultrasonic waves ranges from 300 m/s to 10 000 m/s, which is much lower than electromagnetic waves, by the order of 10^4 to 10^6. The speed of sound, for example, in air, in water and in iron is 340 m/s, 1500 m/s and 6000 m/s, respectively. This means that the frequency of an ultrasonic signal is lower than that of an electromagnetic one by the order of 10^4 to 10^6 for the same spatial resolution, and an ultrasonic waveform can be directly converted to digital code without frequency shifting. Consequently, sophisticated signal-processing techniques can be applied to enhance the sensitivity and resolution of ultrasonic systems. The phased-array technique and dynamic control of the focal point are commonly used in medical ultrasonic instruments. Another important issue regarding ultrasonic waves arises from the nature of the phenomena: an ultrasonic wave is an elastic deformation and a kinetic movement of the medium. The reflectivity of an ultrasonic wave is determined by the difference in acoustic impedance between the object and the medium. Consequently, mechanical properties including the elastic modulus are reflected in the ultrasonically measured data, and can be used for the characterization of the object in both medical and industrial applications. In addition to the linear responses of the object, many trials have been carried out on the nonlinearity of the object or medium. Imaging using the second-harmonic component has been implemented in a commercial ultrasonic echo system for medical use.

Ultrasonic waves convey mechanical energy in addition to information. The mechanical ultrasonic energy has been used for various kinds of processing in industry, and the technology is sometimes called ‘power ultrasonics.’ Ultrasonic cleaning is one of the most popular applications in power ultrasonics. Ultrasonic machine bonding of wires or chips in electronic devices is the second largest market for power ultrasonics. Mechanical machining with ultrasonic vibration and the enhancement of chemical reactions are also important uses of power ultrasonics in industry. Several high-power ultrasonic devices, such as ultrasonic motors and transformers, have been developed during the last three decades, and some of these are now used in consumer products. In the medical field, ultrasonic vibrations have been applied as a surgical knife in the treatment of disease and ultrasonic shock waves are used for destroying kidney stones. Recently, high-intensity focused ultrasound, called HIFU, has been studied by many researchers, and there have been tests on treating some kinds of cancer.

Ultrasonic waves are also useful for signal processing. Surface acoustic waves (SAWs), in particular, have played an important role as frequency filters and signal duplexers in communication systems from the dawn of color television to the recent explosive growth in digital wireless communication devices. Though signal processing has been carried out through digital calculation in many recent practical applications, it is thought that these elastic-wave-based devices will be used in the future as analog processing units in very high-frequency applications. Various sensor devices based on SAWs and bulk ultrasonic waves have been developed. The vibratory gyroscope is one of the successful examples, which is widely used in digital cameras and car navigation systems for detecting rotational velocity and acceleration. These devices have become much reduced in size with the use of MEMS (micro-electro-mechanical systems) technology.

A very wide range of frequencies is used in ultrasonic applications. Normally, an ultrasonic wave is defined as an acoustic wave beyond the audible frequency. However, in practice, frequencies lower than 20 kHz are in use for several applications. In some SONAR (SOund Navigation And Ranging) systems, the several kilohertz region is used to avoid attenuation. Waves at several hundred hertz are used in ocean acoustics for global-scale tomography. A 40-kHz ultrasound is typically used in air for detecting objects, as a trade-off between detection range, which is limited by attenuation, and spatial resolution, which is determined by the wavelength. For medical diagnostics, frequencies from 2 MHz to 20 MHz are chosen for the target application. Waves of several megahertz are used for industrial flaw detection in metal objects. Both longitudinal and transverse waves are used for nondestructive testing in solid materials. Ultrasonic microscopy is useful for the evaluation of microelectronics devices, where frequencies from 100 MHz to 1 GHz are used to give a spatial resolution close to that of optical microscopy. Higher frequencies, over 1 GHz, are sometimes required for material characterization and scientific research. Vibration systems from 15 kHz to 100 kHz are conventionally applied for power ultrasonics applications, such as machining, welding and cleaning. A megahertz ultrasonic cleaner has been developed for the precise cleaning of silicon wafers and electronic devices. Higher frequencies have also been explored for ultrasonic welding, both for wire bonding and plastic welding, to cope with the downsizing of the devices. Ultrasonic devices such as filters, sensors and actuators have been designed to operate at various frequencies, from 20 kHz to several gigahertz, depending on their construction and the application.

The signal strength of ultrasonic waves is also widely spread, from the very small signals reflected from tissues to giant amplitudes in power ultrasonic applications. The human hearing system is able to detect an acoustic power of only 1 $\mathrm{pW/m^2}$ in air at a frequency of 1–4 kHz, which is defined as 0 dB. Sound pressure at 0 dB is much lower than atmospheric pressure, by the order of 10^{-10}. We sometimes need to detect weaker signals in ultrasonic measurements. The human ear cannot hear sound over 120 dB, but it is not difficult to produce a hot spot of sound pressure around 160 dB or more in air at tens of kilohertz. In ultrasonic cleaners, sound pressure greater than atmospheric pressure is easily obtained in water. Cavitation, tiny bubbles oscillating under a high sound pressure field, induces an extremely high pressure and temperature, and various kinds of physical and chemical phenomena. If the design of a vibration system for an ultrasonic machining tool is poor, even if the tool is made of metal it may break because of material fatigue caused by the cyclic application of repeated large stresses at an ultrasonic frequency.

As stated above, ultrasonic technology is diverse in both applications and phenomena. It is difficult to cover all of these in a single book. This book focuses on ultrasonic transducers, particularly those used for medical and industrial applications. Though there are various kinds of transduction principles for converting electric signals to ultrasonic waves and vice versa, the piezoelectric effect is mainly dealt with in this book. Since Paul Langevin succeeded in transmitting and receiving ultrasonic signals in sea using a sandwich transducer with crystals in 1917 (see Chapter 3), the piezoelectric transducer has been a powerful method for ultrasonic generation and detection. Highly effective piezoelectric ceramics were invented after World War II, and the majority of ultrasonic transducers are now based on the piezoelectric effect. For high-resolution measurement, short pulses or modulated signals should be transmitted and received. This means that there is less internal reverberation and a wider frequency response is required, which is not necessarily compatible with higher sensitivity. The trade-off between bandwidth and sensitivity is key for designing ultrasonic transducers for measurement. On the other hand, for high-power applications and ultrasonic functional devices, transducers usually operate at their resonance modes, and the selection of modes and the tuning of resonance frequencies are important issues in design.

This book is in three parts. The basic concepts of piezoelectric transducers are described in Part I. The first chapter is an introduction to piezoelectric transducers, and is followed by chapters on piezoelectric ceramics (Chapter 3), thin-film transducers (Chapter 4) and single crystals (Chapter 5). We have chosen to include thin films and single crystals out of various recent research topics, since they are of increasing importance for high-performance medical transducers. The electromagnetic acoustic transducer, called an ‘EMAT,’ is introduced in Chapter 2. It is exceptional among piezoelectric transducers, as it is useful for industrial nondestructive evaluation of metal objects. Part II includes methods for predicting and evaluating transducer performance. Chapter 6 is a fundamental treatise on one-dimensional models for ultrasonic transducers, while an intensive and detailed discussion of the boundary-element method is presented in Chapter 7. One of the most frequently used ways to analyze ultrasonic transducers is the finite element method (FEM); it is not included in this book because there are already several popular commercial packages, many freeware and shareware programs as well as good books. Though commercial packages are well made, especially their user interfaces, and they are easy to use, a fundamental knowledge of wave motion is essential for finding the correct result. If the basic phenomena are under control, numerical methods are very powerful for designing the details. Similarly, finite-difference time domain (FDTD) analysis, which has become widely used in acoustics, is not dealt with in this book. Chapter 7 summarizes the state-of-the-art methodologies for describing near-field phenomena by considering the shear horizontally polarized waves in the boundary-element method applications. Experimental evaluation methods are introduced in the latter half of Part II. First, measurements using the electrical port of a transducer are briefly mentioned in Chapter 8, which includes evaluation at higher amplitudes and load tests. Second, it is important to know whether a designed vibration mode or vibration distribution has been obtained. The most reliable tool to measure ultrasonic vibration without contact is laser Doppler vibrometry, which is described in Chapter 9. It is also important to understand the ultrasonic field radiating from a vibrating surface. The distribution of an ultrasonic field is usually measured by scanning with a needle hydrophone. Hydrophones are covered in Part III. The optical principles for instantly visualizing sound fields without scanning sensors are introduced in Chapter 10. Part III is on applications of ultrasonic transducers. Surface acoustic wave (SAW) devices are reviewed in Chapter 11, where several important concepts for designing SAW devices are introduced. Nondestructive testing, noncontact measurements in air and measurements under severe conditions are presented in Chapters 12 and 13. Capacitive transducers are included in Chapter 12 as one of the promising airborne transducers. Signal processing is important for enhancing the signal-to-noise ratio and resolution in addition to the performance of a transducer. Of the various kinds of processing techniques, one example is described in Chapter 14. Power ultrasonic technology for industrial use is explained in Chapter 15. The finite amplitude approach to ultrasonic waves has practical applications, such as in the medical field. Chapter 16 is about nonlinear aspects of ultrasonic waves, including tissue harmonic imaging and an evaluation method using nonlinearity, while Chapter 17 describes ultrasonic therapeutic treatment, from basic theory to reviews of several practical applications. Ultrasonic transducers for functional devices are presented in Chapters 18, 19 and 20. Techniques for micro-sensors and actuators are given in Chapter 18. Hydrophones are essential devices for ultrasonic field evaluation, and are considered in Chapter 19, where the fiber-optic method is introduced in addition to conventional piezoelectric hydrophones. As an example of high-power devices based on piezoelectric transducers, ultrasonic motors are described in Chapter 20.

This is a multi-authored book, and every chapter is independently written to some extent, but the overlap between them is as small as possible. We have successfully chosen authors for the chapters, whose expertise is highly recognized in their fields. Thanks to the enthusiasm and the efforts of the authors, I believe that all the chapters are attractive and will be useful to the readers, and I hope that this book will inspire them to develop novel applications of ultrasonic waves. I am also grateful to the staff at Woodhead Publishing, in particular Cliff Ewell, Vicki Hart, Rachel Cox, Anneka Hess and Laura Pugh, for their continuous support in producing this book.

Kentaro Nakamura

1

Piezoelectricity and basic configurations for piezoelectric ultrasonic transducers

S. COCHRAN, University of Dundee, UK

Abstract: Piezoelectricity underpins a very large proportion of the ultrasonic transducers in use and in development today. This chapter first reviews ferroelectricity and piezoelectricity in an ultrasonic context, particularly focusing on the constitutive equations, then describes the configurations of basic piezoelectric transducers in the form of single- and dual-element devices, arrays and Langevin transducers. Ancillary components within these structures are outlined, along with mathematical analysis where appropriate.

Key words: piezoelectricity, ultrasound, transducers.

1.1 Introduction

Ultrasound can be generated and detected in different ways, including through the electromagnetic techniques described in Chapter 2 of this book, the optical techniques described in Chapters 9 and 19, and the capacitive techniques described in Chapter 12. However, the most common technique is to use piezoelectric materials. These convert electrical energy to mechanical energy and vice versa directly upon application of an electric field or pressure, respectively (Berlincourt *et al.*, 1964).

In this chapter, the associated phenomena of ferroelectricity and piezoelectricity are described. Piezoelectric materials are available in the form of crystals, ceramics and polymers. These are introduced with particular reference to important material parameters for use in ultrasonic transducers; further details on specific important types of material are provided in Chapters 3 and 5. Piezoelectric composite materials are also introduced. Piezoelectric transducers are then described, beginning with the example of a simple single-element transducer. The components and mode of operation of this device are outlined, including ancillary matching layers and backing material. The issue of external case design is considered briefly, as ultrasonic isolation is necessary in practical transducers, particularly for low-frequency applications, along with passive electrical components to adjust the electrical properties of the transducer. The main technical content of the chapter concludes with a description of multi-element piezoelectric transducers, beginning with the dual-element pitch-catch transducer, followed by one-dimensional (1D) ultrasonic arrays, and finally the Langevin structure. A summary is provided and an outline of future trends.

1.2 The piezoelectric effect

Known since 1880 (Graff, 1981), the piezoelectric effect allows the direct generation of electrical signals from the application of pressure and the direct generation of pressure from electrical signals. It is quite straightforward to achieve these effects at ultrasonic frequencies, making piezoelectricity the basis of most ultrasonic transducers.

1.2.1 Ferroelectricity

Piezoelectric materials are a subset of ferroelectric materials and it is therefore useful first to define ferroelectrics (Rosenberg, 1988). These materials are named for the types of properties they share with ferromagnetic materials, not because of an intrinsic link with iron. The key property of a ferroelectric material is that it has a finite electrical polarisation even when no external field is applied. The best example of a ferroelectric material is barium titanate, $BaTiO_3$ (Moulson and Herbert, 2003: 71–82); careful consideration of this material establishes a strong base for understanding other ferroelectric and piezoelectric materials.

As shown in Fig. 1.1(a), $BaTiO_3$ is a crystalline material with a cubic unit cell above approximately 130 °C. The Ba^{2+} ions occupy the corners, the Ti^{4+} ion the body centre and the O^{2-} ions the face centres of this unit cell, which has dimensions of approximately 0.4 nm. Below 130 °C, the unit cell becomes tetragonal, i.e. it is longer in the vertical direction, termed the c-axis, as shown in Fig. 1.1(b). The proportional change in dimension is very small, much less than 1%. In this condition, the Ti^{4+} and Ba^{2+} ions adopt positions upwards relative to the four O^{2-} ions originally

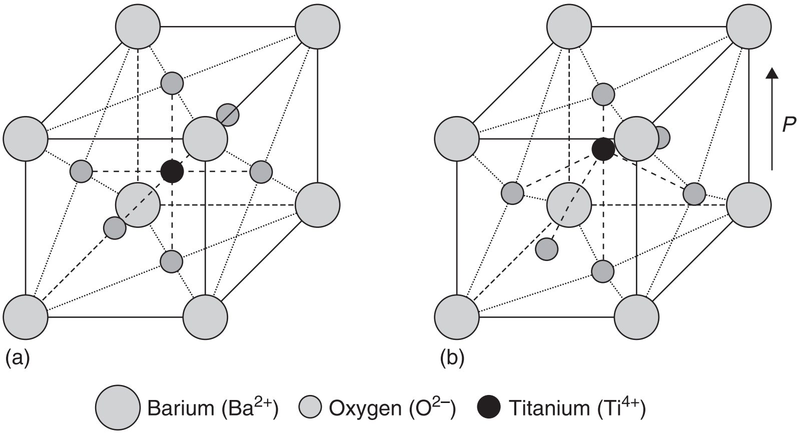

1.1 The crystalline unit cell of $BaTiO_3$. (a) Cubic above its Curie temperature and (b) tetragonal below the Curie temperature, with polarisation, *P*.

in the same horizontal plane, termed the a-b plane, as the Ti^{4+} ion, and the other O^{2-} ions adopt positions downwards. This results in a net electrical polarisation of the bulk material. The temperature below which this polarisation occurs is called the Curie temperature, T_c, in analogy with ferromagnetic materials.

$BaTiO_3$ is realised as a ceramic, originating as a mouldable paste, which is dried and sintered to form the final material. The properties of the paste result from the mixing of particles with a liquid and its basis in particles leads to a material comprising crystallites or grains tightly bound together, with properties differing between the individual grains and the collection of grains in the bulk ceramic because of the effects of the interfaces between the grains. Following the principle of minimisation of energy, and taking into account the resulting internal dynamics of the relative positions of the ions, $BaTiO_3$ divides itself into multiple domains within each grain, each domain having a common polarisation, but with the polarisation differing in direction from that of neighbouring domains by either 90° or 180°.

The natural polarisation of $BaTiO_3$ on manufacture is illustrated in Fig. 1.2(a) (Xu, 1991). If an external electrical field is applied subsequently, often with simultaneous heating above T_C then cooling, then the domains can be realigned by 90° or 180° in a process called poling, as shown in Fig. 1.2(b) and (c). The final realignment is imperfect as the domain orientations are constrained by the orientations of the unit cells within the crystallites, in turn constrained by the orientation of the grains within which the crystallites exist. Nevertheless, the outcome is substantially stronger polarisation than prior to the poling process. Because of the fundamental effect on the operating behaviour of ultrasonic transducers, it is particularly important to note that this polarisation is realised in the form of dipoles within the material but it is expressed as electrical charge on the surface of the material.

The poling process can be illustrated functionally by plots of polarisation, P, in units of Cm^{-2} against electric field, E_p, in units of $V.m^{-1}$. Fig. 1.3 shows such plots

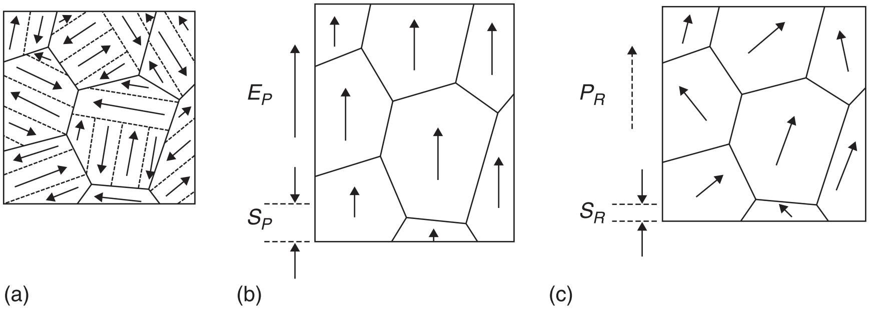

1.2 The polarisation of $BaTiO_3$ (a) in its natural condition (grain boundaries solid, domain walls broken), (b) during poling (poling field E_P, poling strain S_P) and (c) after poling (remanent polarisation P_R, remanent strain S_R).

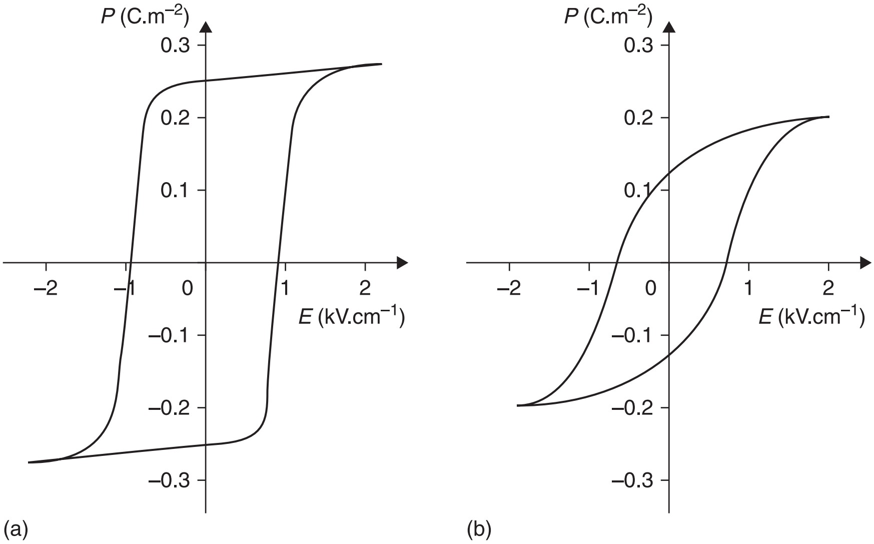

1.3 Polarisation loops for (a) single crystal $BaTiO_3$ and (b) $BaTiO_3$ ceramic.

for single crystal and ceramic $BaTiO_3$. Hysteresis is evident, and key features are the coercive field, E_c, at which previous polarisation becomes zero; the saturation polarisation, P_S, at which all possible domain realignment has occurred; and the remanent polarisation, P_R, remaining when the field required for saturation polarisation has been reduced to zero. The differences between the single crystal in Fig. 1.3(a) and the ceramic in Fig. 1.3(b) originate in the better dipole alignment possible in a single crystal than in a multicrystalline (granular) ceramic.

E_c, P_S and P_R are important for ultrasound applications requiring high-drive conditions as a bipolar electrical drive signal may be large enough to cause changes in polarisation. To make this less likely, materials with high coercive fields are desirable, termed hard materials. Poling then typically takes place at an elevated temperature, making it easier to realign domains, before cooling to ambient temperature with the poling field applied. A corollary is that if the transducer in which the material is used is heated then depoling is possible, total depoling occurring if T_c is exceeded, and a rule of thumb indicates that the long-term operating temperature should not exceed $T_c/2$.

1.2.2 Piezoelectricity

Piezoelectricity means electricity derived from pressure (Moulson and Herbert, 2003: 339–410). Thus, the direct piezoelectric effect, defined by the Curie brothers and illustrated in Fig. 1.4(a), is the generation of electricity from pressure, and the converse piezoelectric effect is the generation of pressure from electricity, shown

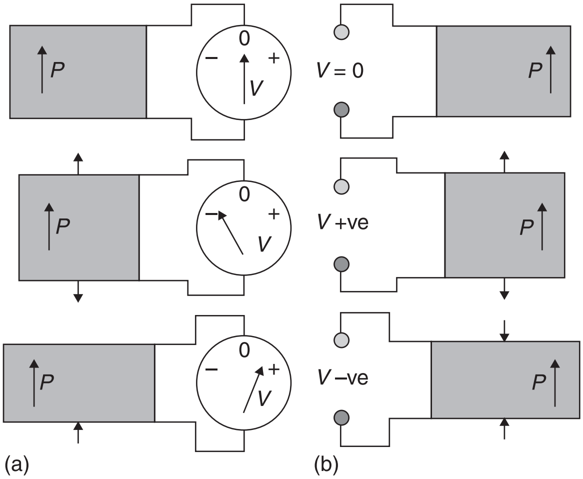

1.4 (a) The direct piezoelectric effect, with external pressure applied, and (b) the converse piezoelectric effect, with external voltage applied. The samples are shown wider upon compression because of the effects of Poisson's ratio.

in Fig. 1.4(b). For those working in ultrasound, used to first considering a source of ultrasound then a receiver, this is unintuitive as the converse effect applies to the source and the direct effect to the receiver. The piezoelectric effect occurs and was first demonstrated in natural materials such as quartz. However, the effect is weak in such materials and, although they formed the basis of viable ultrasonic transducers for underwater sonar, non-destructive evaluation (NDE) and early biomedical applications, the performance of many transducer designs increased significantly with the invention of ferroelectric materials in the 1950s (Graff, 1981).

Although $BaTiO_3$ is ferroelectric, with higher performance than natural piezoelectric materials, its performance is significantly exceeded by lead zirconate titanate, $Pb(Zr,Ti)O_3$ (PZT). The crystal structure of both materials is the same, termed perovskite, the name given to $CaTiO_3$. Systematically, perovskites have the composition ABO_3. Material science can thus be applied by considering the effects and positions particularly of the A- and B-site cations. Furthermore, adding small amounts of dopants to the basic perovskite can alter its properties significantly. For example, the domain walls can be made more resistant to movement under an applied electric field or pressure in a piezoelectrically hard material, typically with T_c increased but with a reduced performance in other respects. Conversely, the domain walls move more easily in a piezoelectrically soft material, having lower T_c but with improved values for other properties.

Piezoelectric materials couple electrical and mechanical effects and also thermal effects. They are thus inherently complicated, with a large number of parameters. This list is further increased by their very broad application range, the adoption of equivalent but distinct parameters in specific application-oriented communities and the use of different symbols to represent the same values in different scientific and engineering disciplines. However, a good starting point and fundamental reference to describe the behaviour of piezoelectric materials are the constitutive equations (Berlincourt *et al.*, 1964).

For a non-piezoelectric dielectric material, the electric displacement, D (C.m^{-2}), is defined as

$$D = \varepsilon E \tag{1.1}$$

where ε is the permittivity (F.m^{-1} = C.V^{-1}.m^{-1}) and E is the electric field (V.m^{-1}). In a 1D model of piezoelectric material, the electrical polarisation, P, caused by strain, S, i.e. a change in dimensions due to an applied stress, can be expressed as

$$P = eS \tag{1.2}$$

where e is the piezoelectric stress constant (C.m^{-2}). Combining Eqs 1.1 and 1.2

$$D=\varepsilon^S E + P=\varepsilon^S E + eS \tag{1.3}$$

where ε^S is the permittivity at constant strain.

For a conventional elastic solid, Hooke's law relates stress, T, linearly to strain, S

$$T = cS \tag{1.4}$$

where c is the stiffness. The stress due to the piezoelectric nature of a material is expressed as

$$T = -\, eE \tag{1.5}$$

Combining Eqs 1.4 and 1.5

$$T = c^E S - eE \tag{1.6}$$

where c^E is the stiffness at constant electric field.

Together, the expressions for D and T in Eqs 1.3 and 1.6 unambiguously relate the electrical and mechanical properties of piezoelectric materials. In combination with the wave equation, as explained in Chapter 6, they can be used as the basis of a mathematical analysis of ultrasonic transducers (Redwood, 1961; Lewis, 1978). Three other pairs of equations can also be used as constitutive relations for piezoelectric materials (Berlincourt *et al.*, 1964):

$$S = S^E T + dE \quad \text{and} \quad D = dT + \varepsilon^T E \tag{1.7}$$

$$E = -gT + \frac{D}{\varepsilon^T} \quad \text{and} \quad S = s^D T + gD \tag{1.8}$$

$$E = -hS + \frac{D}{\varepsilon^S} \quad \text{and} \quad T = c^D S - hD \tag{1.9}$$

Table 1.1 Variables and coefficients in the piezoelectric constitutive equations

	Name	Units
Variable		
D	Electric displacement	$\mathrm{C.m^{-2}}$
E	Electric field	$\mathrm{V.m^{-1}}$
S	Mechanical strain	–
T	Mechanical stress	$\mathrm{N.m^{-2}}$
Coefficient		
c^E, c^D	Elastic stiffness	$\mathrm{N.m^{-2}}$
d	Piezoelectric strain constant	$\mathrm{mV^{-1}}$
e	Piezoelectric stress constant	$\mathrm{C.m^{-1}}$
g	Piezoelectric voltage constant	$\mathrm{V.m.N^{-1}}$
ε^T, ε^S	Permittivity	$\mathrm{F.m^{-1}}$
h	Piezoelectric stiffness constant	$\mathrm{V.m^{-1}}$
s^E, s^D	Elastic compliance	$\mathrm{m^2.N^{-1}}$

The superscripts T and D indicate conditions of constant stress and constant electric displacement, respectively. The coefficients are important performance indicators for piezoelectric materials and reference is made to them in many places in this chapter; a summary is provided in Table 1.1.

The analysis presented so far has been implicitly 1D. However, piezoelectricity is a 3D phenomenon with a potentially very high degree of anisotropy in practical materials. Therefore, the constitutive equations can be taken further using the elasto-electric matrices, which explicitly express 3D piezoelectric effects (Cobbold, 2007: 336–44).

Considering Eqs 1.3 and 1.6, it is first necessary to redefine stress and strain as second-rank tensors (Nye, 1985):

$$\boldsymbol{T} = \begin{bmatrix} T_{11} & T_{12} & T_{13} \\ T_{21} & T_{22} & T_{23} \\ T_{31} & T_{32} & T_{33} \end{bmatrix} \quad \text{and} \quad \boldsymbol{S} = \begin{bmatrix} S_{11} & S_{12} & S_{13} \\ S_{21} & S_{22} & S_{23} \\ S_{31} & S_{32} & S_{33} \end{bmatrix} \qquad [1.10]$$

In these tensors, the first subscript refers to the face of a cube normal to the directions $1 = x$, $2 = y$ and $3 = z$ and the second subscript refers to the direction in which the stress or strain occurs, with the same relation between numbers and coordinate directions. Thus, T_{nn} and S_{nn}, $n = 1, 2, 3$, represent stress and strain for forces applied in direction n and the stress or strain occurring in the same direction whereas T_{mn} and S_{mn}, $m \neq n$, represent shear stresses and strains. As it is assumed that a piezoelectric material is in static equilibrium, i.e. that it does not rotate or move bodily,

$$T_{\mathrm{mn}} = T_{\mathrm{nm}} \quad \text{and} \quad S_{\mathrm{mn}} = S_{\mathrm{nm}}, \quad m, n = 1, 2, 3 \tag{1.11}$$

This means each of the second-rank tensors has only six independent components. Taking this into account, and the desirability of simplifying the notation, the stress, ***T***, can be re-expressed as

$$\boldsymbol{T} = [T_1\ T_2\ T_3\ T_4\ T_5\ T_6]^{\mathrm{T}} \tag{1.12}$$

where

$$T_1 = T_{11} \qquad T_2 = T_{22} \qquad T_3 = T_{33},$$

$$T_4 = T_{23} = T_{32} \qquad T_5 = T_{13} = T_{31} \qquad T_6 = T_{12} = T_{21}$$

and the superscript T represents transposition. The use of single subscript indices is often called engineering notation and the transposed form is adopted for compactness.

Exactly the same pattern is followed for

$$\boldsymbol{S} = [S_1\ S_2\ S_3\ S_4\ S_5\ S_6]^{\mathrm{T}} \tag{1.13}$$

The electric field, *E*, and electric displacement, *D*, are considered, more straightforwardly, as three-element vectors,

$$\boldsymbol{E} = [E_1\ E_2\ E_3]^{\mathrm{T}} \quad \text{and} \quad \boldsymbol{D} = [D_1\ D_2\ D_3]^{\mathrm{T}} \tag{1.14}$$

Again, the numerical subscript indices represent the coordinates *x*, *y* and *z*, respectively, and the transposed representation is used for compactness.

In full, Eqs 1.3 and 1.6 can then be represented by

$$\begin{bmatrix} T_1 \\ T_2 \\ T_3 \\ T_4 \\ T_5 \\ T_6 \\ D_1 \\ D_2 \\ D_3 \end{bmatrix} = \begin{bmatrix} c_{11}^E & c_{12}^E & c_{13}^E & c_{14}^E & c_{15}^E & c_{16}^E & -e_{11} & -e_{21} & -e_{31} \\ c_{21}^E & c_{22}^E & c_{23}^E & c_{24}^E & c_{25}^E & c_{26}^E & -e_{12} & -e_{22} & -e_{32} \\ c_{31}^E & c_{32}^E & c_{33}^E & c_{34}^E & c_{35}^E & c_{36}^E & -e_{13} & -e_{23} & -e_{33} \\ c_{41}^E & c_{42}^E & c_{43}^E & c_{44}^E & c_{45}^E & c_{46}^E & -e_{14} & -e_{24} & -e_{34} \\ c_{51}^E & c_{52}^E & c_{53}^E & c_{54}^E & c_{55}^E & c_{56}^E & -e_{15} & -e_{25} & -e_{35} \\ c_{61}^E & c_{62}^E & c_{63}^E & c_{64}^E & c_{65}^E & c_{66}^E & -e_{16} & -e_{26} & -e_{36} \\ e_{11} & e_{12} & e_{13} & e_{14} & e_{15} & e_{16} & \varepsilon_{11} & \varepsilon_{12} & \varepsilon_{13} \\ e_{21} & e_{22} & e_{23} & e_{24} & e_{25} & e_{26} & \varepsilon_{21} & \varepsilon_{22} & \varepsilon_{23} \\ e_{31} & e_{32} & e_{33} & e_{34} & e_{35} & e_{36} & \varepsilon_{31} & \varepsilon_{32} & \varepsilon_{33} \end{bmatrix} \begin{bmatrix} S_1 \\ S_2 \\ S_3 \\ S_4 \\ S_5 \\ S_6 \\ E_1 \\ E_2 \\ E_3 \end{bmatrix} \tag{1.15}$$

or

$$\begin{bmatrix} \boldsymbol{T} \\ \boldsymbol{D} \end{bmatrix} = \begin{bmatrix} \boldsymbol{c}^E & -\boldsymbol{e}^{\mathrm{T}} \\ \boldsymbol{e} & \boldsymbol{\varepsilon} \end{bmatrix} \begin{bmatrix} \boldsymbol{S} \\ \boldsymbol{E} \end{bmatrix} \tag{1.16}$$

where the square matrices are termed the elasto-electric matrices. Similar expressions can be developed for the other three pairs of constitutive equations, 1.7–1.9.

Equation 1.15 suggests that a constitutive relation requires 63 independent coefficients in the elasto-electric matrix: 36 for a general expression for stiffness, 18 for the piezoelectric stress constant and nine for permittivity. However, this number is reduced significantly when specific materials are considered, as discussed in Section 1.2.2.

The coefficients in the elasto-electric matrix provide a complete description of the behaviour of a piezoelectric material. However, in practice, reference is made more often to some properties than others, which are not represented directly by the matrix. Thus it is common to use alternative expressions for attenuation, the electromechanical coupling coefficient and other specific properties.

Attenuation (Sherrit and Mukherjee, 2007) can be included in the elasto-electric matrix through the use of complex coefficients, each dealing with a specific source of attenuation. Whilst this is conceptually simple, it does not take into account frequency dependence. Practical ultrasonic transducer design has therefore followed a different route, usually lumping attenuation into one or a small number of parameters to express the behaviour of a material or to allow the performance of a device to be predicted with computer software. One reason is that the desired outputs of a practical transducer resemble loss, either as radiated ultrasound or as the transfer of electrical energy to an external load. Furthermore, ancillary components in transducers, discussed in Section 1.3.1, may deliberately cause very high attenuation. However, there are some situations, for example in the design of high-power, narrowband transducers, where many of these loss mechanisms are minimised.

The simplest way to express attenuation is as a single coefficient, α, relating to mechanical wave propagation measured at a specific frequency, such as $f = 1$ MHz, and to assume that attenuation accrues with distance and increases linearly with frequency. This can provide reasonably accurate results in 1D modelling, although α may need adjustment to correspond with measurements. An alternative approach, with a better physical basis for piezoelectric materials, is to consider electrical and mechanical losses separately. Then electrical loss is expressed by the loss tangent, tan δ, where δ is the angle in the complex plane between the impedance vector of the piezoelectric sample at a non-resonant frequency, typically 1 kHz, and the negative reactance axis. Essentially, this defines the piezoelectric material, at a non-resonant frequency, as an ideal capacitor in series with a resistor where the resistor represents losses because of both finite conductance and the phenomena of bound charge and dipole relaxation (Moulson and Herbert, 2003). tanδ is the reciprocal of the electrical quality factor, Q_E, and is much more commonly quoted. Mechanical loss is most commonly quoted directly in terms of the mechanical quality factor, Q_m, which can be determined directly from electrical impedance spectroscopy using equations based on equivalent circuit representations of material samples.

It has been suggested that the electromechanical coupling coefficients, k, are the most important coefficients of a piezoelectric material (Berlincourt *et al.*, 1964). These coupling coefficients express the useful work done in a cycle involving application of stress under an electrical short circuit, opening of the circuit and the subsequent release of stress, then dissipation of the resulting stored energy, W_s, in an electrical load (Cobbold, 2007). k is the ratio of the stored energy dissipated in the load to the total energy, W_t, dissipated in the application of the stress and in the load:

$$k = \sqrt{\frac{W_s}{W_t}} \tag{1.17}$$

This indicates that k^2 represents the efficiency of intrinsic electromechanical energy conversion by a particular material. Various coupling coefficients are commonly cited, using the notation k_{mn}, where m represents the axis along which the load is connected, and n represents the excitation axis along which the stress is applied. For example, k_{31} is the coupling coefficient for a piezoelectric material with the electrical load connected to surfaces normal to the z-axis of the material, corresponding to the crystallographic c-axis and the numerical index 3, and the stress is applied transversely. There are many different coupling coefficients with varying amplitudes and degrees of complexity in relation to the transducer configuration required to exploit them. However, two coupling coefficients are particularly widely used. k_{33} is the coupling coefficient under a condition of finite 1D stress parallel to the z-axis, $T_3 \neq 0$, as realised in a tall, narrow bar, and k_t is the thickness-mode coupling coefficient under a condition in which strain is zero in the xy-plane, perpendicular to the z-axis, $S_1 = S_2 = 0$. k_{33} and k_t can be calculated as

$$k_{33} = \frac{d_{33}}{\sqrt{\varepsilon_{33}^T S_{33}^E}} \quad \text{and} \quad k_t = h_{33}\sqrt{\frac{\varepsilon_{33}^S}{c_{33}^D}} \tag{1.18}$$

In practice, k_t is often calculated most conveniently from the electrical impedance spectrum of a sample of material, as described in Chapter 6.

Three other parameters of piezoelectric materials are often used in transducer design: the characteristic acoustic impedance, Z; the speed of longitudinal or shear propagation, v, in whatever direction is of interest in the transducer; and the density of the material, ρ. These properties correspond directly with the basic theory for solids and elastic vibration (Cheeke, 2002: 77–90). Of particular note is Z, the characteristic acoustic impedance, often abbreviated as the acoustic impedance. Calculated as the product of ρ and v, it is measured in Rayl, or more commonly MRayl, 1 Rayl being $1\,\text{kg.m}^{-2}.\text{s}^{-1}$, and it is a fundamental property of a material.

1.3 Piezoelectric materials

In this section, piezoelectric materials are divided into four groups: piezoceramics, piezocrystals, piezopolymers and piezocomposites.

The first three groups are considered in detail elsewhere but are included here for practical illustration of the discussion of the previous section and as points of reference for the text on piezoelectric transducers in Section 1.4. To aid consideration, Table 1.2 gives a selection of the properties of examples of each group. Piezocomposites (Newnham *et al.*, 1978) differ from the other three groups in that they have more than one distinct physical phase within the material structure: typically, there is a piezoelectric material and a dissimilar passive material. They are not considered separately elsewhere in this book and are therefore covered in more detail here.

1.3.1 Piezoceramics

Piezoceramics are, presently, the most widely used piezoelectric materials. From developmental origins using $BaTiO_3$ in the 1950s, lead-based materials emerged with the highest performance for practical applications (Graff, 1981; Berlincourt *et al.*, 1964). The archetypal material is PZT. Crystallographically, PZT is a perovskite with hexagonal symmetry, class 6mm. This leads to significant simplification in the elasto-electric matrix. First, the matrix is symmetric about its leading diagonal, reducing the maximum number of coefficients from 81 to 45. Second, 24 of the coefficients are zero, reducing the number to 21. Third, many of these 21 coefficients share or have related values, reducing the number of independent coefficients to ten. This is illustrated in Fig. 1.5(a).

PZT is now available in many different forms. One simple classification is into piezoelectrically soft and hard types. As illustrated in Table 1.2, PZT-4 is hard and PZT-5H is soft. The piezoelectric coefficients, such as k_t and d_{33}, are therefore generally lower for PZT-4 than for PZT-5H. Permittivity is also much lower. However, Q_m is higher and tan δ is lower. In combination with its higher T_c, this makes it particularly appropriate for applications requiring high average output ultrasound intensities. PZT-5H is much less amenable to this requirement but its better piezoelectric performance can provide higher sensitivity as a source and in pulsed mode where the same transducer is used as both a source and a receiver.

Many applications now use standard ceramics such as PZT-4 and PZT-5H, but a wide range of ceramics is also available to suit particular applications. For example, lead metaniobate, $PbNbO_3$, shown in Table 1.2, has a particularly high $T_c \approx 400$ °C, a low acoustic impedance, $Z = 19$ MRayl, and low Q_m, making it suitable for operation at elevated temperatures and in situations where broad bandwidth operation is required.

Table 1.2 Properties of selected piezoelectric materials

Type of material			PZT-4	PZT-5H	$PbNbO_3$	PVDF	$LiNb0_3$	AIN	PMN-PT
			'Hard' ceramic	'Soft' ceramic	High-temperature ceramic	Polymer	Traditional single crystal	Crystalline thin film	New, high-performance single crystal
Thickness-mode coupling coefficient	k_t		0.47	0.52	0.33	0.19	0.16	0.24	0.57
Length-extensional coupling coefficient	k_{33}		0.69	0.75	0.33	0.13	0.16	0.31	0.90
Piezoelectric strain constant	d_{33}	$pm.V^{-1}$	290	590	85	25	5.9	5.5	1400
Piezoelectric voltage constant	g_{33}	$mV.m.N^{-1}$	26	20	32	230	22	52	30
Piezoelectric figure of merit	FOM = $d_{33}.g_{33}$	$pm.N^{-1}$	7.5	12	2.7	5.8	0.13	0.29	43
Stiffness	c_{33}^{D}	$GN.m^{-2}$	150	160	68	8.5	250	420	140
Density	ρ	$kg.m^{-3}$	7700	7500	6200	1800	4600	3300	8000
Longitudinal speed	v	ms^{-1}	4600	4600	3100	2200	7400	11 400	4040
Acoustic impedance	$Z = \rho v$	MRayl	35	34	19	3.9	34	37	32
Electrical loss tangent	$\tan \delta$		0.004	0.02	0.01	0.3	0.001	0.0005	0.01
Mechanical quality factor	Q_m		High	Medium	Low	Low	Very high	Very high	Low
Relative permittivity at constant stress	ε_{33}^{T}		1270	3430	300	8.4	29.8	12.0	3950
Relative permittivity at constant strain	ε_{33}^{S}		640	1470	270	10–12	29	10.7	818
Curie temperature (*usable temperature, **phase transition temperature)	T_c	°C	Medium / High (~350 °C)	Medium (~200 °C)	High (~400 °C)	Low (~150 °C)	Very high (~1200 °C)	Very high (~1150 °C*)	Low (~90 °C**)
Usual physical form			Bulk ceramic	Bulk ceramic	Bulk ceramic	Thin film	Bulk crystal	Thin crystal film	Bulk crystal

Note: Data in this table are drawn from various academic and commercial sources. All data are approximate and for guidance only.

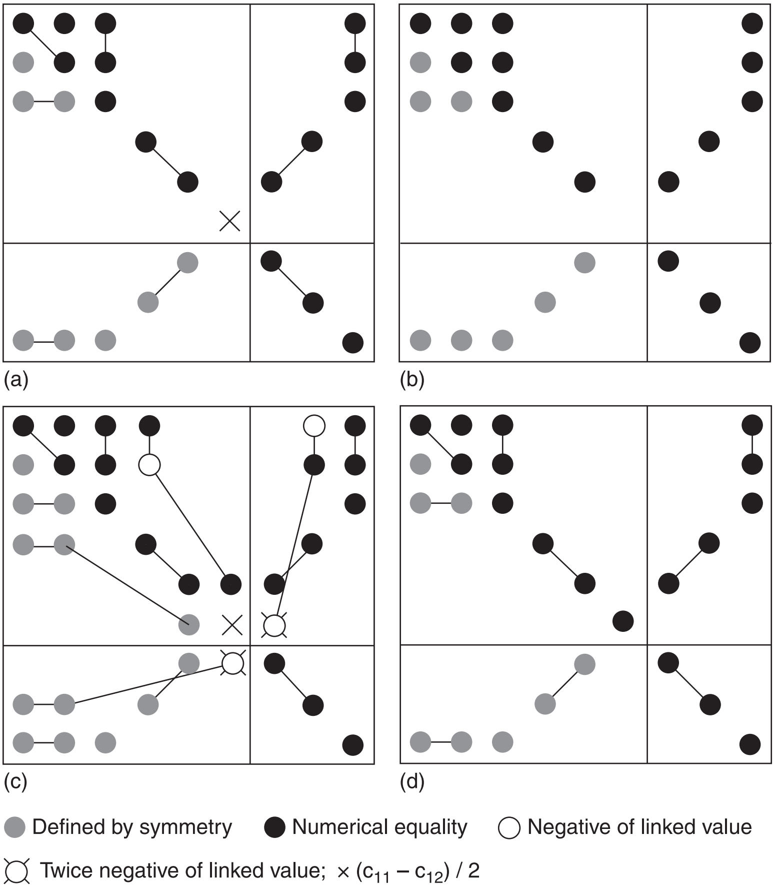
(a)
(b)
(c)
(d)
● Defined by symmetry
● Numerical equality
○ Negative of linked value
Twice negative of linked value; × $(c_{11} - c_{12})$ / 2

1.5 Coefficients in the elasto-electric matrices for (a) PZT (crystal class 6 mm), (b) PVDF (2 mm), (c) $LiNbO_3$ (3 m) and (d) PMN-PT (4 mm).

1.3.2 Piezopolymers

Polyvinylidene fluoride (PVDF) (Cobbold, 2007: 347–9) is the most widely reported piezoelectric polymer. Crystallographically, it has very low symmetry because poling is achieved by uniaxial or biaxial stretching rather than the application of an electric field. This leads to an orthorhombic structure, class 2 mm and it therefore has 17 independent coefficients, as shown in Fig. 1.5(b). The properties that make it attractive are its low acoustic impedance, Z = 3.9 MRayl, its low Q_m, and its high piezoelectric voltage constant, g_{33} = 0.23 V.m.N^{-1}. Together, these make it an excellent broadband receiver for underwater sonar and biomedical imaging applications, where the ultrasonic medium has an acoustic impedance, $Z \approx 1.5$ MRayl. Its physical form as a thin plastic film also finds it applications and assists with its use as a broadband receiver because this places its fundamental resonance at a high frequency, allowing spectrally flat operation at lower frequencies.

1.3.3 Piezocrystals

Piezocrystals were the first piezoelectric materials but they were largely superseded by piezoelectric ceramics. However, lithium niobate, $LiNbO_3$ (Wong, 2002), and aluminium nitride, AlN (Haussonne, 1995; Iriarte *et al.*, 2010), are two piezocrystals with properties that make them attractive for specific applications. In crystallographic terms, $LiNbO_3$ has lower symmetry than PZT but higher symmetry than PVDF, being trigonal, class 3m, with 12 independent elasto-electric coefficients as shown in Fig. 1.5(c). Its very low losses and very high longitudinal propagation speed make it particularly appropriate for high-frequency applications, the propagation speed leading to a relatively large thickness for a given operating frequency. $LiNbO_3$ has also been selected for applications with elevated temperatures because of its very high Curie temperature, $T_c \approx 1200$ °C. AlN has the same crystallographic symmetry as PZT and somewhat similar behavioural characteristics to $LiNbO_3$. However, it is distinguished by its realisation as a highly inert, crystalline thin film. This has led to its use in surface acoustic wave devices and in the exploration for applications where it can be integrated with test objects for NDE or with circuitry for minimally invasive sensing.

A much newer family of single-crystal piezoelectric materials is represented in Table 1.2 by lead magnesium niobate doped with lead titanate, $_{(x)}Pb(Mg_{1/3}Nb_{2/3})O_3 - {}_{(1-x)}PbTiO_3$ (PMN-PT) (Oakley and Zipparo, 2000). This family is classified as having tetragonal symmetry, class 4mm, with 11 independent elasto-electric coefficients, as illustrated in Fig. 1.5(d). Somewhat similar to PZT in many behavioural characteristics, its particularly attractive properties are its very high bar-mode coupling coefficient, $k_{33} \approx 0.9$, and piezoelectric strain coefficient, $d_{33} \approx 1400\,\text{pm.V}^{-1}$. Combined with a relatively high value for the piezoelectric voltage coefficient, $g_{33} \approx 30\,\text{mV.m.N}^{-1}$, it has a piezoelectric figure of merit, $d_{33}.g_{33}$, more than four times higher than the next highest figure, for PZT-5H. This has led to its widespread adoption in biomedical imaging (Chen and Panda, 2005).

As negative issues (Zhang and Shrout, 2010), PMN-PT has a very low Curie temperature, $T_c \approx 120$ °C (not quoted in Table 1.2) and an even lower temperature phase transition zone, usually characterised by the temperature of the rhombohedral to tetragonal phase transition, $T_{RT} \approx 90$ °C. With relatively high mechanical losses, this significantly limits its potential applications where elevated temperatures or high average output ultrasound intensities are required. To overcome this problem, research is under way to extend the binary PMN-PT material system to ternary systems and doped ternary systems (Zhang and Shrout, 2010). These properties lead to some loss in piezoelectric performance but better mechanical properties and thermal stability.

1.3.4 Piezocomposites

Piezocomposite materials increase the performance of ultrasonic transducers particularly in applications where there is a large acoustic impedance mismatch between the piezoceramic and the ultrasound propagation medium. Such applications include biomedical imaging, underwater sonar and NDE when the transducer is coupled to the test object through an intermediate component such as a perspex wedge (Krautkramer and Krautkramer, 1990: 196–202). Piezocomposites typically comprise pieces of a piezoelectric ceramic or single-crystal phase bound together with a polymer matrix. They are usually defined by their dimensional connectivity (Newnham *et al.*, 1978). For example, as shown in Fig. 1.6, a 1-3 connectivity composite comprises piezoelectric pillars in a polymer matrix, a 2-2 composite comprises alternate piezoelectric and polymer planks and a 0-3 composite comprises piezoelectric particles again in a polymer matrix. In general, an *m-n* connectivity composite has its piezoelectric phase connected in *m* dimensions and its polymer phase in *n* dimensions.

Initially, the best connectivity for the two phases was uncertain but it emerged that almost the simplest format, square pillars of piezoceramic in a polymer matrix, has straightforward fabrication as well as providing performance close to the theoretical ideal (Bennett and Hayward, 1997). Further work established that the minimum pillar height-to-width ratio should be around 1.8 to avoid unwanted modes within the pillars and three or more for the performance of the composite to approach the theoretical value (Hayward and Bennett, 1996).

A key step in the development of piezocomposites was the development of expressions for equivalent thickness-mode material parameters (Smith and Auld, 1991). There are three principal equations; first, for the equivalent piezoelectric stress constant:

$$e'_{33} = v_c \left(e_{33} - \frac{2e_{31}\left(c^E_{13} - c_{12}\right)}{c'} \right) \qquad [1.19]$$

second, for the equivalent relative permittivity at constant strain:

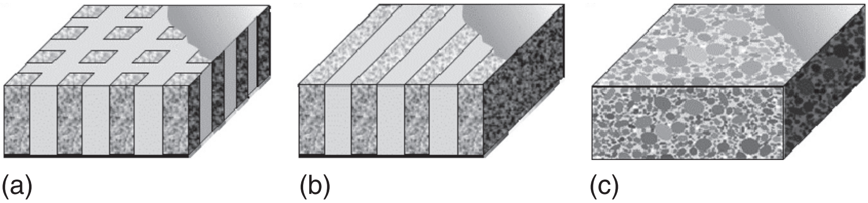

1.6 Piezocomposite material structures: (a) 1-3 connectivity, (b) 2-2 connectivity and (c) 0-3 connectivity. Polymer is shown as uniform grey, ceramic textured. The area in the top right indicates one of the surfaces to which the electrode is applied.

$$\varepsilon_{33}^{\prime S} = v_c\left(\varepsilon_{33}^{S} + \frac{2e_{31}^{2}}{c'}\right) + (1 - v_c)\varepsilon_{11} \qquad [1.20]$$

and, third, for the equivalent stiffness at constant electric field:

$$c_{33}^{\prime E} = v_c\left(c_{33}^{E} - \frac{2\left(c_{13}^{E} - c_{12}\right)^{2}}{c'}\right) + \left(c_{11}\left(1 - v_c\right)\right) \qquad [1.21]$$

where

$$c' = c_{11}^{E} + c_{12}^{E} + \frac{v_c\left(c_{11} + c_{12}\right)}{1 - v_c} \qquad [1.22]$$

The prime in these equations, ', indicates a quantity relating to the piezocomposite material specifically and v_c is the ceramic volume fraction in the composite material. In turn, these equations allow the calculation of other parameters in conventional formats, including the stiffness at constant electric displacement:

$$c_{33}^{\prime D} = c_{33}^{\prime E} + \frac{e_{33}^{\prime 2}}{\varepsilon_{33}^{\prime S}} \qquad [1.23]$$

and the piezoelectric stiffness constant:

$$h_{33}' = \frac{e_{33}'}{\varepsilon_{r}^{\prime S}} \qquad [1.24]$$

Calculating the density of the composite from:

$$\rho' = \rho_a v_c + \rho_p(1 - v_c) \qquad [1.25]$$

where ρ_a is the density of the active, piezoelectric phase and ρ_p the density of the passive phase, then allows the longitudinal-mode acoustic velocity in the thickness direction through the composite to be obtained:

$$v' = \sqrt{\frac{c_{33}^{\prime D}}{\rho'}} \qquad [1.26]$$

along with the acoustic impedance,

$$Z' = \rho' v' \qquad [1.27]$$

and the thickness-mode electromechanical coupling coefficient,

$$k_t' = h_{33}'\sqrt{\frac{\varepsilon_{r}^{\prime S}}{c_{33}^{\prime D}}} \qquad [1.28]$$

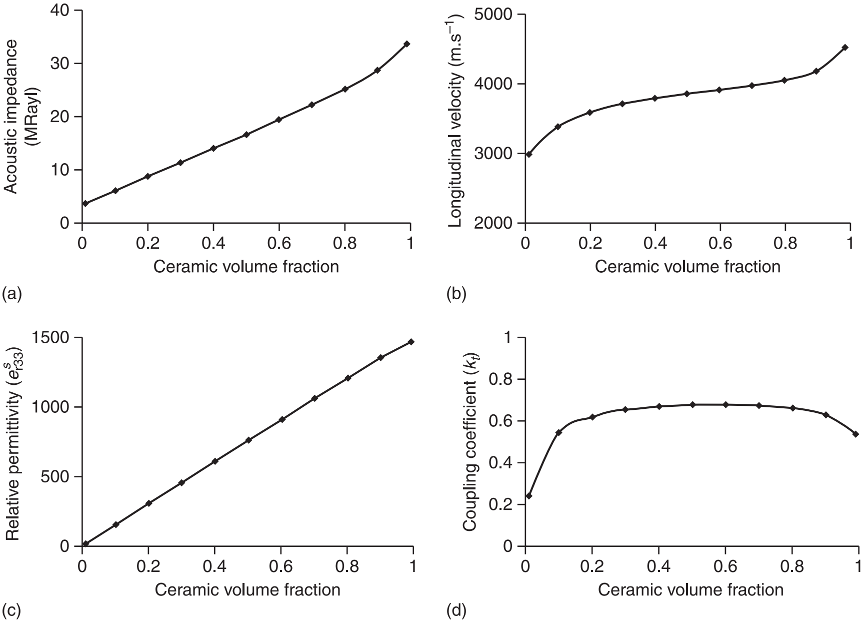

1.7 Coefficients and parameters of 1-3 connectivity piezoceramic-polymer composite: (a) acoustic impedance, (b) longitudinal velocity, (c) relative permittivity at constant strain and (d)thickness-mode coupling coefficient.

Piezocomposite behaviour (Smith, 1989) may be illustrated by graphs of Z, k_t, ε^S_{r33} and v, as shown in Fig. 1.7. The data in these graphs were calculated for a PZT-5H ceramic phase and a hard-setting epoxy polymer phase.

The acoustic impedance and thickness-mode coupling coefficient should be considered together. In Fig. 1.7(d), the value of k_t is almost constant and always above 0.6 for $0.2 < v_c < 0.9$, reaching a maximum $k_t \approx 0.68$. The equivalent value for the PZT-5H ceramic from Table 1.2 is $k_t = 0.52$. The reason k_t for the composite can exceed the value for the ceramic on which the composite is based is that the individual pillars in the composite are much less constrained by the polymer matrix than they would be by bulk ceramic. Thus, the piezoelectric phase in the composite operates with an effective coupling coefficient close to k_{33}. For PZT-5H, $k_{33} \approx 0.75$, leading to a higher coupling coefficient for the composite, in turn translating into better performance. A major attraction of new single-crystal materials, such as PMN-PT, is that they have very large values for k_{33}, for example, $k_{33} = 0.90$ for PMN-PT, allowing the manufacture of a very high-performance composite material.

Another reason to use a composite material is the possibility of achieving lower acoustic impedance when working with low acoustic impedance media. As shown in Fig. 1.7(a), the high plateau in k_t corresponds approximately to an acoustic impedance range $8.7 < Z < 28.7$ Mrayl. This is always lower than for PZT-5H, corresponding to an ultrasound intensity transmission coefficient range $0.50 > T_I > 0.19$, compared with PZT-5H for which $T_I \approx 0.16$ for a medium with $Z = 1.5$ MRayl. At the upper end of the range of Z, the gain is relatively small, whereas much better matching is achieved with $Z \approx 8.7$ MRayl. In turn, this leads to much better energy transfer out of and into a transducer made with the piezocomposite, increasing the transducer's bandwidth, sensitivity and efficiency.

A final reason to use a composite material is that it may significantly reduce the amplitude of ultrasound propagation in the lateral direction. The description of piezoelectric materials provided here has focused on their thickness-mode properties, such as k_t, c_{33}^E and d_{33}, as these are the properties that are usually relevant to the generation and detection of ultrasound. However, as should be clear from Eq. 1.15 and Fig. 1.5, non-zero off-diagonal coefficients exist in the elasto-electric matrices for all four crystal classes illustrated in Fig. 1.5. This means that electrical or mechanical stimulation in one direction, such as through the thickness, leads to a reaction in the other directions, which can be manifest as unwanted ultrasound excitation on transmission and interfering signals on reception. The solution for homogeneous bulk materials is usually to select an aspect ratio for the piezoelectric material that separates the desired thickness-mode operating frequency from the unwanted lateral modes. However, the inherent inhomogeneity of a piezocomposite is likely to diminish significantly the amplitude of lateral modes, provided care is taken to avoid the excitation of other ultrasound modes relating to the periodicity of 1-3 and 2-2 connectivity composites (Reynolds *et al.*, 2003).

Apart from performance advantages, piezocomposite materials also offer the possibility of increased customisation through the choice of the constituent material phases and ceramic volume fraction. However, there are some disadvantages. As shown in Fig. 1.7(c), the relative permittivity is lower than for PZT-5H, potentially making electrical impedance matching more difficult for some transducer configurations. The use of a polymer phase may also constrain the maximum operating temperature (Parr *et al.*, 2005) and viable processing during transducer manufacture (Bernassau *et al.*, 2009). Manufacturing is also more expensive than for ceramic, as the conversion of ceramic into composite is always an additional requirement. Finally, design is more complicated, requiring both material design and care in specifying geometry, for example because of the variation in longitudinal velocity, as shown in Fig. 1.7(b).

1.4 Piezoelectric transducers

Having covered the nature of piezoelectricity and its realisation in different materials, it is now possible to consider how these materials can be incorporated in useful transducers, beginning with the single-element transducer (Desilets *et al.*, 1978) then outlining other configurations. The transducers considered here are mainly for measurement and imaging; other structures are necessary for power ultrasonics (Astashev and Babitsky, 2007) and when measurement and imaging require high-power sources, for example for long-range or low-frequency underwater sonar (Stansfield, 1991). The most common form of device, termed the Langevin transducer, the sandwich transducer, or, in specialised form, the Tonpilz transducer, is introduced in Section 1.4.2.

1.4.1 The single-element transducer

A basic single-element transducer is shown schematically in Fig. 1.8 (Papadakis *et al.*, 1999).The important elements in this diagram are the ultrasound medium and couplant, the piezoelectric material, the mechanical damping material and matching layers, and remaining ancillary components – the transducer casing, wiring and electrical components. Sometimes the piezoelectric material, the mechanical damping material and the matching layers are called the transducer stack, these being the components that define the ultrasound performance of the device.

Ultrasound medium and couplant

For transducer design, ultrasound media may be classified according to their acoustic impedance and attenuation. In underwater sonar, biomedical applications (Hill *et al.*, 2004), and immersion testing for NDE (Krautkramer and Krautkramer,

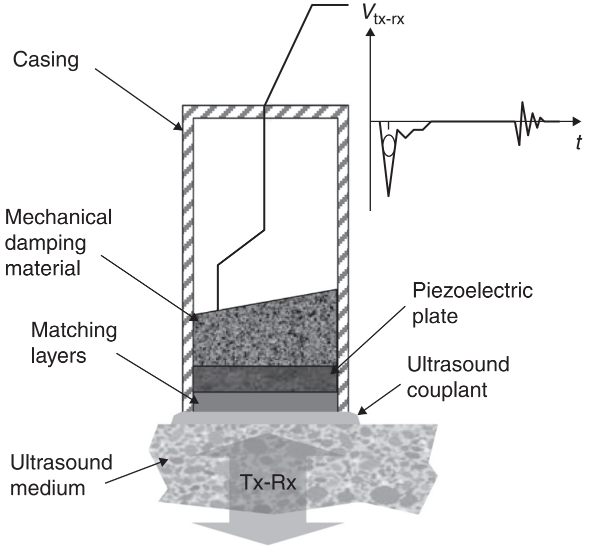

1.8 Single-element ultrasound transducer.

1990: 274–8), the acoustic impedance, $Z \approx 1.5$ Mrayl. Even with a piezocomposite, this is much lower than the impedance of the piezoelectric material, leading to the need for other components to enhance energy transfer between the piezoelectric material and the medium and to damp reverberation in the piezoelectric material. This problem is exacerbated if the ultrasound medium is air, $Z \approx 0.0004$ Mrayl, as discussed in Chapter 12.

In other applications of NDE, the transducer may be directly coupled to a plastic, composite, ceramic or metal specimen. In these cases, the acoustic impedance ranges upwards from $Z \approx 3$ MRayl. Better acoustic impedance matching and a large variation in the possible values of Z reduce the likelihood that matching layers will be present. However, as NDE transducers often require very high spatial resolution, the reverberation damping material is important. Further details on both medical and NDE transducers can be found elsewhere.

If the ultrasound medium is liquid or gas, a couplant to promote energy transfer between the transducer and the medium should not be required. However, a thin layer of surfactant may improve wetting of the front face of the transducer. For solid media, a couplant is almost always essential to fill the interstices caused by the roughness of the surfaces of the transducer and the medium, as ultrasound transmission is reduced if there is no couplant between even apparently very smooth surfaces. Typically, the couplant is in the form of a gel or other material with acoustic impedance similar to water but a higher viscosity to improve retention in the required location.

Piezoelectric material

The piezoelectric material in the transducer is used as the source or receiver of ultrasound. In many situations, the same transducer has both functions. This has the advantages that only a single device is needed, saving cost and complexity, and it can be guaranteed that the source and receiver positions are coincident. With an ultrasonic wavelength, for example, $\lambda \approx 150\,\mu\text{m}$, at an operating frequency, $f = 10\,\text{MHz}$, and the potential need for positional accuracy of a fraction of λ for measurement or imaging, it may otherwise be difficult to achieve such accuracy. The disadvantages are that the same device must be designed for both transmission and reception, resulting in suboptimal performance, and the electronic circuitry to which the device is connected must deal with both transmission and reception signals. These issues are considered further later.

The lateral dimensions of the piezoelectric material are chosen according to the purpose of the transducer. Very large dimensions relative to λ, for example $10\ \lambda$, lead to a highly directional device, and dimensions close to λ, for example $0.7\ \lambda$, lead to a wide transmitted beam and reception sensitivity with angle. Analytical expressions are available to calculate the beam width for simply shaped, co-phased transducer apertures (Bobber, 1988) and numerical calculation techniques are available for more complicated devices (Stepanishen, 1971).

The thickness of the piezoelectric material is usually defined according to the frequency of operation, f, and the longitudinal velocity, v, in the material. Except in unusual circumstances, the piezoelectric material acts approximately as a thickness-mode, half-wavelength resonator, with its surfaces effectively free to move, forming ultrasonic displacement antinodes. These are complemented by a static node in the central plane of the material, parallel to the front face of the transducer. The transducer may also be used at odd harmonics of the operating frequency; further details are provided in Chapter 6. Here, it is essential only to note that resonance is a fundamental aspect of the operation of most piezoelectric ultrasound transducers, substantially increasing their sensitivity.

As an example, the theoretical thicknesses, D, of various relevant piezoelectric materials in a transducer are given in Table 1.3 for f = 5 MHz, a frequency commonly encountered in biomedical imaging and NDE, calculated according to

$$D = \frac{v}{2f} \qquad [1.29]$$

In this table, the piezocomposite is made with 1-3 connectivity PZT-5H - hard-setting epoxy. It can be seen that the thicknesses are all well below 1 mm, leading to the need for highly accurate material fabrication and thinning in the ultrasound transducer industry.

Assuming a transducer in which reverberation in the piezoelectric material is heavily damped, the electrical impedance at the operating frequency can also be calculated approximately, corresponding to the reactance of a capacitor with dielectric permittivity $\varepsilon = \varepsilon_o \varepsilon^S_{r33}$, i.e.

$$|Z| = X_c = \frac{D}{2\pi f \varepsilon A} \qquad [1.30]$$

Table 1.3 Thickness of piezoelectric materials for f = 5 MHz transducer

Material	Longitudinal velocity, v (m.s^{-1})	Thickness, D (mm)	Relative permittivity, ε^S_{r33}	Electrical impedance $\|Z\|$		
				Large square device (Ω)	Long narrow device (Ω)	Small square device (kΩ)
PZT-4	4600	0.460	640	31.9	1370	58.7
PZT-5H	4600	0.460	1470	13.9	596	25.5
$LiNbO_3$	7400	0.740	29.0	1130	48 400	2070
PMN-PT	4040	0.404	818	21.9	939	40.2
Composite, v_c = 30%	3710	0.371	455	36.2	1550	66.4
Composite, v_c = 70%	3970	0.397	1060	16.6	711	30.4

where D is the piezoelectric material thickness and A is the area. To illustrate this, parameters for three transducer configurations are given in Table 1.3: a large square device with a square aperture of side 30 λ, area $A = 81\,\mathrm{mm}^2$; a long narrow device with length $30\,\lambda$ and width $0.7\,\lambda$, area $A = 1.89\,\mathrm{mm}^2$; and a small square device with a square aperture of side $0.7\,\lambda$, area $A = 0.044\,\mathrm{mm}^2$. Here, $\lambda = 0.3\,\mathrm{mm}$, assuming an ultrasonic medium with longitudinal velocity, $v = 1500\,\mathrm{ms}^{-1}$.

Table 1.3 indicates that, for most materials, the large square device is likely to have an electrical impedance lower than the conventional instrumentation impedance, $|Z| = 50\,\Omega$, and the long narrow device an electrical impedance that is much higher. However, both of these are in the range that may be amenable to electrical impedance matching. In contrast, the impedances for the small square device are all very high, in the tens of kiloohms range or more, indicating the likelihood of a difficulty in interfacing with conventional instrumentation to achieve a good signal-to-noise ratio (SNR).

From the indicative calculation of electrical impedance, it can be seen that there is more than one competing issue in the design of the piezoelectric element in a transducer. Typically, this has two consequences: the specialisation of commercial organisations in transducers with broad similarities, for example, for a particular application sector; and the use of computer-based design tools to explore the transducer parameter space and optimise a design prior to prototyping and production. Transducers for specific application sectors are covered in Part III of this book and the design tools are covered in Chapter 6 and elsewhere.

Mechanical damping material and matching layers

The mechanical damping material, often called the backing, and the matching layers both affect the theoretical impulse response of the piezoelectric material (Kossof, 1966; Gururaja and Panda, 1998). This theoretical response is a close match to the response of the material to a practical electrical pulse or a step function when the converse piezoelectric effect is used with the transducer as a source of ultrasound. The impulse response is also applicable to the situation in which ultrasound is incident on the transducer when it is acting as a receiver; however, it is more difficult in practice to generate an ultrasound waveform closely approximating an impulse than to generate such an electrical signal. Thus the theoretical ultrasound impulse response is more likely to be useful when dealing with reception when it is subject to convolution with a practical ultrasound waveform. The reason for shortening the impulse response of the transducer is to generate short signals in time to allow good spatial resolution in measurements and imaging (Papadakis *et al.*, 1999). When spatial resolution is less critical than other performance parameters such as range, the backing can be omitted to increase the transducer's sensitivity.

To provide good damping, the backing should be well matched in acoustic impedance to the piezoelectric material and should have high ultrasound attenuation to prevent reverberation within itself. Sometimes it is also shaped to prevent reverberation, e.g. with a sloping surface opposite the interface with the piezoelectric material to prevent coherent reflections. This is illustrated in Fig. 1.8. To achieve the required properties, a passive 0-3 connectivity composite is often used, comprising powder of a material with very high acoustic impedance in a polymer matrix. Tungsten powder and a soft-setting epoxy have particularly good properties; $Z \approx 98.5$ MRayl for tungsten and a soft-setting epoxy has been reported to have $\alpha \approx 16\,\mathrm{dB.cm^{-1}}$ at 1 MHz (O'Leary *et al.*, 2005). However, cost and the practicality of working with soft materials mean that substitutes for both phases are common.

As with many other aspects of ultrasound transducers, the design of the backing is amenable to numerical analysis and prediction. Scattering models exist for predicting the acoustic impedance and attenuation of a particular composite if the properties of its individual components are known (Webster, 2009) and these properties can be included within other computer models to predict the effect of the material on transducer performance, as outlined in Chapter 6.

A disadvantage of mechanical damping is that it is based on absorption of energy that would otherwise contribute positively to transducer performance. Matching layers, in contrast, do not have this disadvantage. Analogous to optical antireflective layers (Yeh, 1988), they promote energy transfer between two media, here the piezoelectric material in the transducer and the medium with which the transducer is in contact. For a matching layer of thickness, L, and acoustic impedance, Z_L, in which the wavelength at the frequency of interest is λ_L, the overall intensity transmission coefficient for propagation from the piezoelectric material into the ultrasonic medium at normal incidence (Cobbold, 2007) is

$$T_I = \frac{4Z_P Z_M}{(Z_P + Z_M)^2 \cos^2\theta + (Z_L + Z_P Z_M / Z_L)^2 \sin^2\theta} \qquad [1.31]$$

where Z_P is the acoustic impedance of the piezoelectric material, Z_M is the acoustic impedance of the ultrasonic medium, and

$$\theta = \frac{2\pi L}{\lambda_L} \qquad [1.32]$$

If the layer thickness, $L = \lambda_L/4$, then $\sin^2\theta = 1$, $\cos^2\theta = 0$, and

$$T_I = \frac{4Z_P Z_M}{(Z_L + Z_P Z_M / Z_L)^2} \qquad [1.33]$$

Equating $Z_L = \sqrt{(Z_P Z_M)}$ then gives $T_I = 1$, that is, perfect transmission. Z_P and Z_M can also be exchanged in this analysis. Thus a matching layer can work bidirectionally to achieve perfect transmission if its thickness is $\lambda_L/4$ and its acoustic impedance is the geometric mean of the impedances of the piezoelectric material and the ultrasonic medium. For the example of PZT-5H and a medium with Z = 1.5 Mrayl, the acoustic impedance of the matching layer, Z_L = 7.14 MRayl. Alternatively, for a piezocomposite material with the lower limit, Z = 8.7 MRayl, cited above, Z_L = 3.61 Mrayl, a much easier figure to achieve, e.g. with a polymer material.

Matching layers are very widely used, but they have some disadvantages. First, they work according to theory only at a single frequency; any change in frequency changes λ and thus departs from the optimum. They may thus reduce the effective bandwidth of the transducer. However, in practice it can also be found that the enhanced energy transmission from the piezoelectric material shortens reverberation and thus increases the bandwidth. Second, matching layers work only at normal incidence; a change in the angle of incidence will cause refraction at the surface of the matching layer and the path length off normal will not correspond to $\lambda/4$. This may encourage the use of physically curved transducers where normal incidence is easier to achieve. Third, matching layers inevitably attenuate ultrasound, reducing their effectiveness and also the transmitted ultrasound amplitude. For example, achieving the desired acoustic impedance, Z_L, may require filling a polymer with a higher acoustic impedance powder, leading to scattering and relatively high attenuation. Finally, it may be difficult in practice to maintain adhesion of a matching layer to a transducer operating at high average output intensities. Some of these problems are overcome in practical transducers by using more than one layer. The design methodology for this is described elsewhere (Inoue *et al.*, 1987).

Ancillary components

The ancillary components in an ultrasonic transducer comprise the casing, the cabling and any electronic circuitry, including electrical impedance matching.

Apart from its obvious function for physical protection and to prevent ingress of liquid media, the casing is also likely to need to provide electrical shielding. Sometimes this may be configured as a complete Faraday cage (Ott, 1988), involving electrical shielding in the ultrasonic path between the piezoelectric element and the ultrasound medium. This can be achieved in various ways, through the use of conductive foil, conductive mesh or a 0-3 composite comprising conductive particles in a polymer matrix (Gerold *et al.*, 2010). For safety and shielding, the electrode nearest the ultrasound medium should be connected as the ground electrode.

The cabling is almost always coaxial, though short lengths of twisted pair or even separate cables for signal and ground may be used in some situations. Generally, however, the cable must be compatible with very small received signals, of the order of microvolts or a few millivolts, and good shielding is essential. In the transducer arrays outlined in Section 1.4.2, it is usual to have a separate micro-coaxial cable for each transducer element, though the possibility of multiplexing to avoid the expense of multiple coaxial cables within one outer sheath is beginning to be exploited.

To avoid ringing in the cable and to promote good energy transfer in high-power transmission applications, electrical impedance matching (Gururaja and Panda, 1998) is often necessary, as indicated by the guideline figures for transducer electrical impedance in Table 1.3. As the piezoelectric element usually has resistive or capacitive electrical impedance itself, the simplest form of impedance matching is a series or parallel inductor. Transformer matching may be more effective in some situations and LC-ladder networks can also be used, providing the possibility of tailoring the frequency response of the combined network and transducer. The use of a specific cable length for electrical matching has also been reported (Ritter *et al.*, 2002).

The electronic circuitry in an ultrasound system is usually mainly located at the end of the cable remote from the transducer. However, for some transducers such as small PVDF hydrophones with very high electrical impedance, a preamplifier may be located in the same casing as the transducer. Multiplexing circuitry is also a well-known possibility, particularly for biomedical-imaging transducer arrays.

1.4.2 Other piezoelectric transducer configurations

The single-element transducer is a good workhorse, widely used, for example, in NDE, simple underwater sonar systems, remote sensing and a range of biomedical ultrasound applications such as transoesophageal cardiac measurements and some Doppler measurements. However, its design and the design of associated electronics involve compromises if it is used as both a source and receiver, not least because of the large disparity between electrical excitation signal amplitudes, which may be a few hundred volts, and received signal amplitudes, which may be a few millivolts or less. It also offers no control over the beam that can be produced, requiring physical manipulation to direct the beam appropriately.

Dual-element transducer

A first step in complexity beyond the single-element transducer is the dual-element configuration illustrated in Fig. 1.9 (Krautkramer and Krautkramer, 1990: 202–4). For NDE, this has two separate transducer stacks separated by an isolating material such as cork. The stacks are often identical, the system as a whole benefitting particularly from the possibility of achieving a much higher SNR because there is no need for the reception circuitry to deal with high-amplitude electrical excitation signals. Furthermore, the dead zone, close to the transducer, in which measurement is usually impossible, is reduced because the reception electronics do not need to allow for transmission ringdown. Disadvantages are the potential for the transmission and reception beam patterns to be displaced from one another and the additional cost and complexity.

From the point of view of transducer design, a dual-element device offers several possibilities, including the use of different piezoelectric materials for

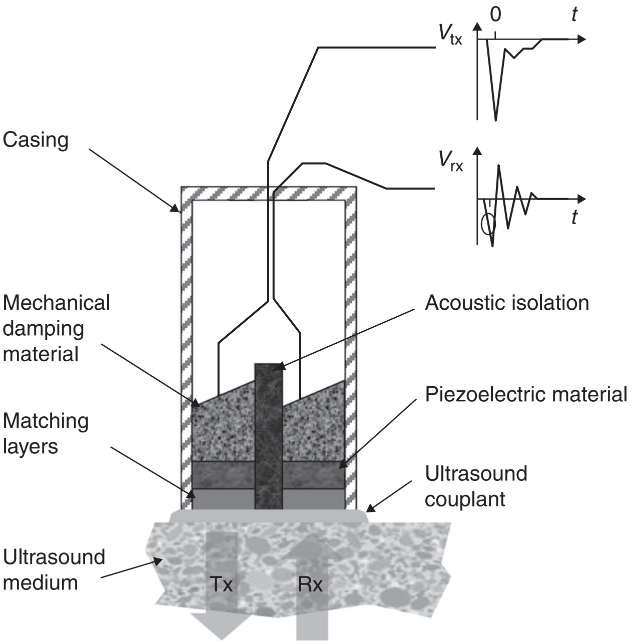
V_{tx}
0
t
Casing
V_{rx}
t
Mechanical damping material
Acoustic isolation
Piezoelectric material
Matching layers
Ultrasound couplant
Ultrasound medium
Tx
Rx

1.9 A dual-element pitch-catch transducer.

transmission and reception, and for the operating frequencies to be different to increase the overall bandwidth. For example, the use of a piezoelectrically hard material, such as PZT-4, for the transmitting stack will permit higher average drive intensities in combination with high reception sensitivity through the use of a piezoelectrically soft material, such as PZT-5H. It is also possible to use piezocomposites with different properties, such as a high ceramic volume fraction for the transmission stack and a low volume fraction for the reception stack.

One-dimensional arrays

A significant step-up in complexity from a dual-element transducer is a 1D transducer array (Gururaja and Panda, 1998), as outlined schematically in Fig. 1.10. It is mentioned, in particular, to highlight the similarity between the array elements and the basic transducer stack that has been outlined. The reason for using a transducer array is to permit electronic control of the ultrasound beam on transmission and the analysis of the received signals (Szabo, 2004: 171–212). It is particularly useful for imaging. The alternative is automated mechanical manipulation of a single-element transducer within a bath of couplant. This has practical disadvantages and also the fundamental drawbacks that it does not

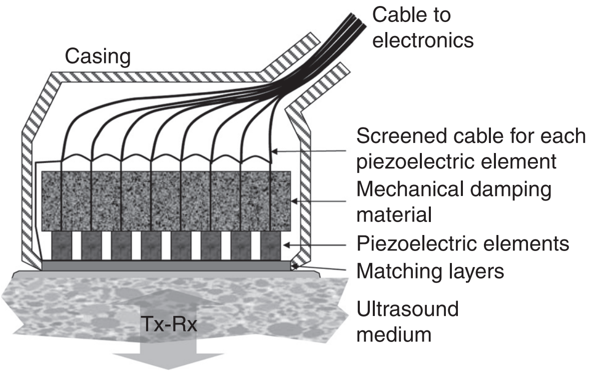

1.10 A piezoelectric transducer array.

permit Doppler imaging and the beam profile of the transducer is fixed, for example with a fixed focal depth and depth of field.

Some very large transducer arrays, operating at low frequency in underwater sonar, are manufactured from physically separate transducers housed within a common casing (Sherman and Butler, 2007: 213–319). However, the small dimensions of the arrays that are required to operate at the higher frequencies in biomedical imaging and NDE demand an integrated manufacturing process. Typically, this involves mounting multiconductor ribbon cables for electrical connections, the piezoelectric material and the matching layers on a backing block, then partially cutting through all these components into the backing to achieve good electrical and ultrasonic isolation between the array elements (De Silets *et al.*, 1975).

For beam forming, the elements are usually long and narrow, with the width typically at least a factor of ten smaller than the length. This generates a beam that is highly directional in the elevational plane, perpendicular to the length of the elements, and broad in the azimuthal plane, parallel to the length of the elements (Gururaja and Panda, 1998). As suggested in Table 1.3, element widths are typically of the same order as the ultrasound wavelength in the medium, with element lengths therefore a significant multiple of the wavelength. This raises two particular issues. First, each element is likely to have relatively high electrical impedance, requiring care in electrical system design and electrical impedance matching. Second, ultrasound propagation laterally in an element may occur at a resonant frequency close to the desired thickness-mode resonance at which the array operates. In that case, each element may be subdivided into narrower strips (Waller *et al.*, 1996) so that the resonant frequency of lateral propagation occurs at a much higher frequency.

High-power transducers

For applications requiring low frequency or high power, the structures that have been outlined would be unsatisfactory, as they would require piezoelectric components of unwieldy dimensions and would damage the backing and matching materials through the intensities they generate. Furthermore, the piezoelectric material might fracture because of the high tensile stresses generated. Instead, for such applications, the piezoelectric material generally operates in a structure in which multiple layers can function simultaneously, to keep the electrical impedance to a reasonable level whilst operating at a low frequency, with mechanisms that maintain the material in compression so that its lower strength in tension is not challenged, and without attenuative backing components.

Applications for high-power transducers include cutting, welding, drilling, cleaning and sonochemistry (Astashev and Babitsky, 2007), generating output intensities of many W.cm^{-2} and utilising ultrasound at frequencies of, at most, a few tens of kilohertz. These are similar to the frequencies and intensities required for high-power underwater sonar projectors (Wilson, 1988; Stansfield, 1991; Sherman and Butler, 2007), and the relevant devices bear many similarities. The archetype of such transducers is the Langevin, or sandwich, transducer. Some Langevin transducers are also called Tonpilz transducers, from the German for 'singing mushroom', because of their configuration with a long, narrow body and a head that tapers outwards to provide geometric acoustic impedance matching (Wilson, 1988: 111).

In a Langevin transducer, the piezoelectric material may form a rather small percentage of the total volume, as illustrated in Fig. 1.11. At the low frequencies at which these transducers are used, a conventional attenuative backing is

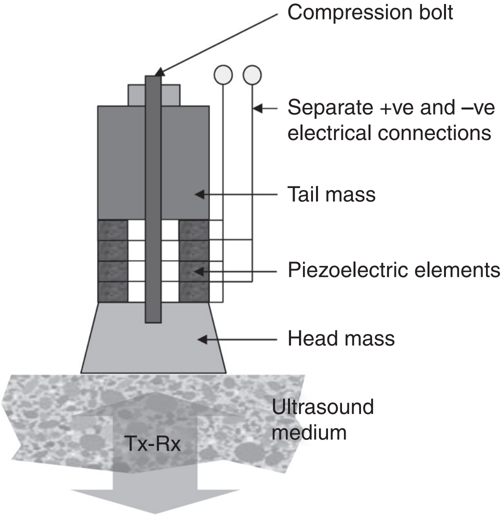

1.11 The Langevin transducer. Four piezoelectric rings are connected mechanically in series and electrically in parallel, sandwiched between a heavy inertial tail mass and a light head mass, achieving acoustic impedance matching geometrically. They are held in place by a high-tensile-strength compression bolt.

impossible because of the required size as well as the risk of damage from heating; furthermore, the specification of such a transducer often places a priority on the production of very high power over the imaging capabilities of broad bandwidth. This leads to a structure in which the operating frequency is set not just by resonance of the piezoelectric components but also by including the effects of the passive head and tail masses.

The piezoelectric ceramic components are often defined by the desired electrical impedance as well as by the ultrasonic performance of the device. Thus, a set of identical rings can be used, with alternating polarity and electrical connections so that they operate together rather than cancelling each other out (Lewis, 1978). These are coupled to the tail mass, which is an inertial component, usually steel, chosen so that most of the motion is that of the light head mass. The head mass may be made of aluminium or titanium, if the ultrasonic load is water, for example, for underwater sonar or ultrasonic cleaning, or it may be of steel, for example if the transducer is to be used in drilling or cutting.

The head and tail masses are held in contact with the piezoelectric components by a bolt of high tensile strength, but also with a cross-sectional area that is compatible with a large front surface velocity and displacement. Torque is applied to the bolt to precompress it so that the piezoelectric ceramic is maintained in compression rather than oscillating freely between tension and compression, as in the other transducers described here. This allows the ceramic to operate at much higher output intensities than would otherwise be possible. A hard ceramic is used (Wilson, 1988: 65–77) in order to withstand the high excitation voltages that are applied, to reduce the heat that is generated within it and to withstand the elevated temperatures that such transducers often reach. PZT-4 (called Navy Type I) and PZT-8 (called Navy Type III) are typical.

Langevin transducers can be used singly, for example for cutting and drilling, but can also be combined in arrays for underwater sonar. In the latter case, great care must be taken to ensure acoustic isolation between elements as the operating frequencies are so low. As there is little loss in the Langevin structure, any applications requiring more than narrowband operation are usually tackled with structures that generate resonances at more than one frequency, and potentially by utilising broadband electrical impedance matching. The excitation signals that are applied to these transducers are themselves usually narrowband, consisting of continuous wave or gated sinusoids.

1.5 Summary, future trends and sources of further information

1.5.1 Summary

Piezoelectricity is the basis for most contemporary ultrasonic transducers. Several forms of material can be used, including single crystals, ceramics, polymers and composites. A well-established framework exists to describe these materials, including their fundamental structure, basic behaviour and behaviour in transducers. Examination of the constitutive Eqs 1.3, 1.6 and 1.7–1.9 shows that many different properties are used in this framework. Specific sets of such properties are often adopted by application-oriented communities, as illustrated in Table 1.2, making the transducer designer's activities easier. However, understanding of the underlying general principles is repaid in development, particularly in broadening the range of options that are examined, and allows the adoption of innovative solutions.

Piezoelectric ultrasonic transducers have many different configurations, including single- and dual-element devices and transducer arrays. The basic structure of the majority can be described by a transducer stack. In this stack, piezoelectric materials are complemented by matching layers and backing material for mechanical damping. Additional components include wiring, electrical impedance matching and the physical casing. Detailed prediction of the behaviour of such transducers relies on computer-based tools for 1D analysis or full 3D analysis, as described elsewhere.

1.5.2 Future trends

Several future trends may be foreseen in piezoelectric materials and the ultrasonic transducers based on them.

In piezoelectric materials, new, high-performance single-crystal materials will be developed further, particularly to make them more practical. Increasing adoption is a self-reinforcing trend, with knowledge of the materials establishing a broader base and increased use driving innovation to reduce their price. The use of piezocomposites will also grow: after a period in which the manufacturers of the materials mainly controlled the manufacture of the transducers using them, piezocomposites are now becoming more widely available for other companies to incorporate in transducers. Finally, most piezoelectric materials are presently lead-based, with a consequent potential undesirable environmental effect. Further development of non-lead-based materials such as potassium sodium niobate (KNN) may allow their replacement in due course.

In transducers, two trends may be expected to dominate future development: the integration of electronics within the device and the viability of 2D arrays to allow electronic control of the transducer aperture and for real-time 3D imaging. Whilst some new opportunities remain in the design of the basic components of the transducer, the pace of innovation is slower than in electronics. Therefore, transducers whose performance is based on a combination of the transducer stack and integrated electronics may be expected to develop more rapidly than conventional devices (Bernassau, 2009). The viability of 2D arrays also depends on innovation in the electronics industry to a large extent, because of the need for high-density electrical interconnects and microfabrication. In fact, 2D arrays match very well with developments in microelectromechanical systems (MEMS) and are likely to develop quickly through innovations pioneered first in other types of MEMS.

1.5.3 Sources of further information

Piezoelectricity is a very well-established phenomenon and piezoelectric ultrasonic transducers have been in use for many decades, so there is a wealth of further information available in books and academic papers and on the Internet. For example, suppliers of piezoelectric material often have introductory text and material property databases available on their websites. Moreover, the references in this chapter have been selected to include additional information or as the basis for searching for citations. However, care must be taken to understand the sometimes wide difference in outlook between people working on the piezoelectric materials themselves – in the materials science community – and people working on their use – in the engineering communities for various applications. Sometimes sources of further information on piezoelectric materials deal well with the materials but superficially with applications. However, the piezoelectric effect is a necessary underpinning for all the applications communities, and thus serves as a link between them, when links at the applications level itself may be quite weak because of differences in the transducers these communities build, the jargon they use to describe them and the nature of the markets in which they are sold. Furthermore, survival, if not prosperity, in transducer engineering is possible with a relatively superficial understanding of piezoelectric materials, so sources on applications may have little or no worthwhile information on these materials.

1.6 References

Astashev V K and Babitsky V I (2007) *Ultrasonic Processes and Machines*, Springer-Verlag, Berlin, Germany, ISBN 9783540720607.

Bennett J and Hayward G (1997) Design of 1-3 piezocomposite hydrophones using finite element analysis, *IEEE Trans. Ultrason. Ferroelect. Freq. Contr.*, 44 (3), 565–74.

Berlincourt D A, Curran D R and Jaffe H (1964) Piezoelectric and piezomagnetic materials and their function in transducers, in Mason W P (ed.) *Physical Acoustics* Vol. IA, Academic Press, 169–270.

Bernassau A L, Hutson D, Démoré C E M, Flynn D, Amalou F *et al.* (2009) Progress towards wafer-scale fabrication of ultrasound arrays for real-time high-resolution biomedical imaging, *Sensor Review*, 29, 333–8.

Bobber R J (1988) *Underwater Electroacoustic Measurements*, Peninsula Publishing, CA, USA, ISBN 0932146198, 76–90.

Cheeke J D B (2002) *Fundamentals and Applications of Ultrasonic Waves*, CRC Press, FL, USA, ISBN 0849301300.

Chen J and Panda R (2005) Review: Commercialization of piezoelectric single crystals for medical imaging applications, *Proc. IEEE Ultrason. Symp.*, 235–40.

Cobbold R S C (2007) *Foundations of Biomedical Ultrasound*, Oxford University Press, NY, USA, ISBN 0195168313.

DeSilets C S, Fraser J and Kino G S (1975) Transducer arrays suitable for acoustic imaging, *Proc. IEEE Ultrason. Symp.*, 148–52.

DeSilets C S, Fraser J and Kino G S (1978) The design of efficient broadband piezoelectric transducers, *IEEE Trans. Son. Ultrason.*, SU-25, 115–25.

Gerold B, Reynolds S, Melzer A and Cochran S (2010) Early exploration of MRI-compatible diagnostic ultrasound transducers, *Proc. IEEE Int. Ultrason. Symp.*, in press.

Graff K F (1981) A history of ultrasonics, in Mason W P (ed.) *Physical Acoustics* Vol. XV, Academic Press, 2–97.

Gururaja T R and Panda R K (1998) Current status and future trends in ultrasonic transducers for medical imaging, *Proc. Int. Symp. Applications Ferroelectrics*, 223–8.

Haussonne F J M (1995) Review of the synthesis methods for AlN, *Mat. Manuf. Proc.* 10, 717–55.

Hayward G and Bennett J (1996) Assessing the influence of pillar aspect ratio on the behavior of 1-3 connectivity composite transducers, *IEEE Trans. Ultrason. Ferroelect. Freq. Contr.*, 43 (1), 98–108.

Hill C R, Bamber J C and ter Haar G R (2004) *Physical Principles of Medical Ultrasonics*, John Wiley and Sons Ltd, Chichester, England, ISBN 0471970026.

Inoue T, Ohta M and Takahashi S (1987) Design of ultrasonic transducers with multiple acoustic matching layers for medical applications, *IEEE Trans. Ultrason. Ferroelec. Freq. Contr.*, 34, 8–16.

Iriarte G F, Rodriguez J G and Calle F (2010) Synthesis of c-axis oriented AlN thin films on different substrates: A review, *Mat. Res. Bull.*, 45, 1039–45.

Kossof G (1966) The effects of backing and matching on the performance of piezoelectric ceramic transducers, *IEEE Trans. Son. Ultrason.*, SU-13, 20–30.

Krautkramer J and Krautkramer H (1990) *Ultrasonic Testing of Materials*, Springer-Verlag, New York, USA, ISBN 9783540512318.

Lewis G K (1978) A matrix technique for analyzing the performance of multilayered front matched and backed piezoelectric ceramic transducers, *Acoust. Imaging*, 8, 395–416.

Moulson A J and Herbert J M (2003) *Electroceramics*, John Wiley and Sons, Chichester, England, ISBN 9780471497486.

Newnham R E, Skinner D P and Cross L E (1978) Connectivity and piezoelectric-pyroelectric composites, *Mater. Res. Bull.*, 13, 525–36.

Nye J F (1985) *Physical Properties of Crystals*, Clarendon Press, Oxford, England, ISBN 9780198511656, 110–69.

O'Leary R, Hayward G, Smillie G and Parr A C S (2005) *CUE Materials Database*, www.strath.ac.uk/media/departments/eee/cue/downloads/cue_materials_database_ver1.2_aug_2005.pdf, downloaded 3 January 2011.

Oakley C G and Zipparo M J (2000) Single crystal piezoelectrics: A revolutionary development for transducers, *Proc. IEEE Ultrason. Symp.*, 1157–67.

Ott H W (1988) *Noise Reduction Techniques in Electronic Systems*, John Wiley and Sons, NY, USA, ISBN 0471850683, 159–202.

Papadakis E P, Oakley C G, Selfridge A R and Maxfield B (1999) Fabrication and characterization of transducers, in Papadakis E P (ed.) *Ultrasonic Instruments and Devices*, Academic Press, CA, USA, ISBN 0125319517, 472–563.

Parr A C S, O'Leary R and Hayward G (2005) Improving the thermal stability of 1-3 piezoelectric composite transducers, *IEEE Trans. Ultrason. Ferroelec. Freq. Contr.*, 52, 550–63.

Redwood (1961) Transient performance of a piezoelectric transducer, *J. Acoust. Soc. Am.,* 33, 527–36.

Reynolds P, Hyslop J and Hayward G (2003) Analysis of spurious resonances in single and multi-element piezocomposite ultrasonic transducers, *Proc. IEEE Ultrason. Symp.,* 1650–3.

Ritter T A, Shrout T R, Tutwiler R and Shung K K (2002) A 30-MHz piezo-composite ultrasound array for medical imaging applications, *IEEE Trans. Ultrason. Ferroelec. Freq. Contr.*, 49, 217–30.

Rosenberg H M (1988) *The Solid State*, Oxford University Press, Oxford, 215 *et seq*.

Sherman C H and Butler J L (2007) *Transducers and Arrays for Underwater Sound*, Springer, NY, USA.

Sherrit S and Mukherjee B K (2007) Characterisation of Piezoelectric Materials for Transducers, arXiv:0711.2657v1 [cond-mat.mtrl-sci].

Smith W A (1989) The role of piezocomposites in ultrasonic transducers, *Proc. IEEE Ultrason. Symp.,* 755–66.

Smith W A and Auld B A (1991) Modeling 1-3 composite piezoelectrics: Thickness-mode oscillations, *IEEE Trans. Ultrason. Ferroelect. Freq. Contr.*, 39 (1), 40–7.

Stansfield D (1991) *Underwater Electroacoustic Transducers*, Peninsula Publishing, California, USA, ISBN 0932146724.

Stepanishen P R (1971) Transient radiation from pistons in an infinite planar baffle, *J. Acoust. Soc. Am.*, 49, 1629–38.

Szabo T L (2004) *Diagnostic Ultrasound Imaging*, Academic Press, ISBN 0126801452.

Waller D, Chen J and Gururaja T R (1996) Requirements of piezoelectric materials for medical ultrasound transducers, *Proc. Int. Symp. Applied Ferroelectrics*, 565–8.

Webster R A (2009) *Passive Materials for High Frequency Piezocomposite Ultrasonic Transducers*, PhD Thesis, University of Birmingham, 30–7.

Wilson O B (1988) *Introduction to Theory and Design of Sonar Transducers*, Peninsula Publishing, ISBN 0-932146-22-8.

Wong K K (2002) *Lithium Niobate*, INSPEC, London, England, ISBN 0852967993.

Xu Y (1991) *Ferroelectric Materials and their Applications*, North-Holland, Amsterdam, ISBN 0444883541, 117–21.

Yeh P (1988) *Optical Waves in Layered Media*, John Wiley and Sons, NY, USA, 151–5.

Zhang S and Shrout T R (2010) Relaxor-PT single crystals: Observations and developments, *IEEE Trans. Ultrason. Ferroelec. Freq. Contr.*, 57, 2138–46.

2

Electromagnetic acoustic transducers

G. HÜBSCHEN, formerly Fraunhofer Institute for
Non-Destructive Testing (IZFP), Germany

Abstract: This chapter discusses electromagnetic acoustic transducers (EMATs), which produce ultrasonic waves without any coupling medium, in the surface of an electrically conductive material. In Section 2.1 the difference between piezoelectric and electromagnetic generation and reception of ultrasonic waves is described. Section 2.2 presents the mechanisms acting mainly during ultrasound excitation by EMATs, the Lorentz force and magnetostriction. Section 2.3 considers EMATs based on the Lorentz force and Section 2.4 looks at transducers using magnetostriction. Typical arrangements of RF coils and magnets are shown. Directivity patterns are presented. Methods for varying the beam angle are explained. Applications of EMATs are described.

Key words: electromagnetic acoustic transducer (EMAT), Lorentz force, magnetostriction, normal probe, linearly polarised shear wave, angle beam probe, SV wave, SH wave, directivity pattern.

2.1 Introduction

The classical method for generating ultrasound is based on the vibration of a crystal or a polarised ceramic excited by the piezoelectric effect and creating an ultrasonic source. By a buffer acoustically coupled to the crystal the ultrasonic wave is transferred through the probe and a coupling medium, e.g. water, oil or a gel, into the test object (see Fig. 2.1).

In contrast with the classical piezoelectric method of ultrasound generation, the electromagnetic excitation of ultrasound uses ultrasonic sources at the material surface induced by electromagnetic interactions in an electrically conductive material. From these sources the ultrasonic wave travels into the component. A detailed description of the electromagnetic interactions follows in Section 2.2. Since the ultrasonic wave is generated in the component itself, there is no need for a coupling medium and the electromagnetic acoustic transducer (EMAT) can be driven even with a small air gap.

2.2 Physical principles

The electromagnetic excitation of ultrasonic waves is based mainly on three different interaction mechanisms:

- The Lorentz force, produced by the interaction between induced eddy currents and static magnetic or quasi-static magnetic fields.

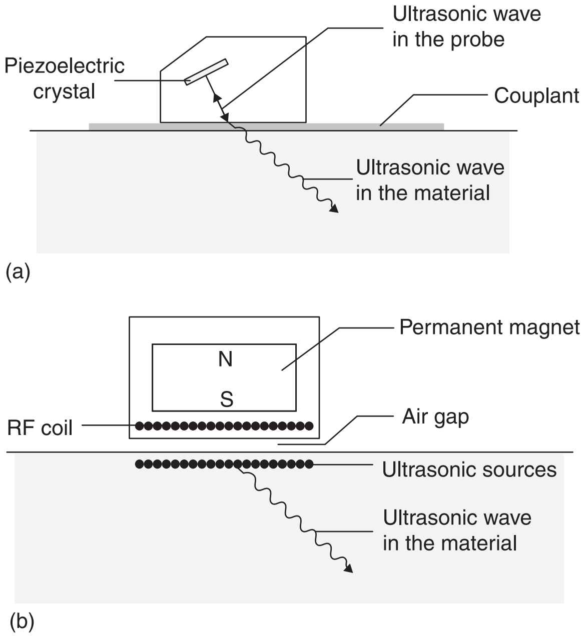
Piezoelectric crystal
Ultrasonic wave in the probe
Couplant
Ultrasonic wave in the material
(a)
Permanent magnet
N
S
RF coil
Air gap
Ultrasonic sources
Ultrasonic wave in the material
(b)

2.1 (a) Conventional ultrasonic transducer. (b) EMAT.

- The magnetic force, caused by the action of dynamic magnetic fields on the magnetising state
- Magnetostriction (analogous to the piezoelectric effect)

Coupling by Lorentz forces occurs in all electrically conductive materials. In ferromagnetic materials two other mechanisms additionally contribute to the generation of ultrasound. For non-ferromagnetic materials, Gaerttner *et al.* (1969) described the Lorentz force exactly. For ferromagnetic materials, the interaction mechanism is much more complicated. Wilbrand (1983, 1984, 1987) created a model with all three interaction mechanisms and verified it with ferromagnetic specimens. Besides these references, many other studies deal with the coupling mechanism and the energy transfer from electromagnetic to mechanic fields and vice versa (Thompson, 1973, 1978a, 1978b, 1990; Ilin and Kharitonov, 1980; Ogi, 1997; Hirao and Ogi, 2003; Dobbs, 1973). This short overview of the physical principles of the electromagnetic excitation of ultrasound follows to a large extent the above references and Niese (2010). During electromagnetic ultrasonic transduction in an electrically conductive or ferromagnetic material, electromagnetic field energy is transferred into elastic energy of an ultrasonic wave and vice versa.

Electromagnetically, the interaction is described by Maxwell's equations and in the solid the elasto-dynamic wave equation is valid. The resulting force on a lattice point in the solid is the sum of the Lorentz force, the magnetic force and the magnetostriction. Starting from a description of the electromagnetic and elastic fields, with the help of assumptions about the electromagnetic forces in magnetic elastic solids and about the electrodynamics of moving deformable media, as well as a phenomenological description of the magnetostriction, terms can be developed for the different force components. In ferromagnetic or electrically conductive materials Eq. 2.1 (Thompson, 1990; Wilbrand, 1987) is valid

$$\vec{F}_{res} = \vec{F}_L + \vec{F}_M + \vec{F}_{MS} \qquad [2.1]$$

with

$$\vec{F}_L = \vec{j}_e \times \vec{B}_0$$

$$\vec{F}_M = (\vec{\nabla}\vec{H}_{HF}) \cdot \vec{M}_0$$

$$\vec{F}_{MS} = \vec{\nabla} \cdot \overleftrightarrow{T}_{MS}$$

where $\vec{F}_L$ is the Lorentz force, $\vec{F}_M$ is the magnetic force, $\vec{F}_{MS}$ is the magnetostrictive force, $\vec{j}_e$ is the induced eddy current density, $\vec{B}_0$ is the magnetic flux density of the magnetisation, $\vec{M}_0$ is the magnetisation, $\vec{H}_{HF}$ is the dynamic magnetic field with $(\vec{\nabla}\vec{H}_{HF})$ the dyadic product, $\overleftrightarrow{T}_{MS}$ is the magnetostrictive stress tensor with $\overleftrightarrow{T}_{MS} = -\overleftrightarrow{e}\vec{H}$ and $\overleftrightarrow{e}$ is the tensor of the field-dependent magnetostrictive coefficients of the material.

Using Eq. 2.1, the forces acting on a test object can be deduced. These forces are generated by a current conductor in the presence of a magnetic field. Figures 2.2 to 2.4 show, for three basic configurations, the current direction in the RF coil and the direction of the magnetic bias field. The directions of the single

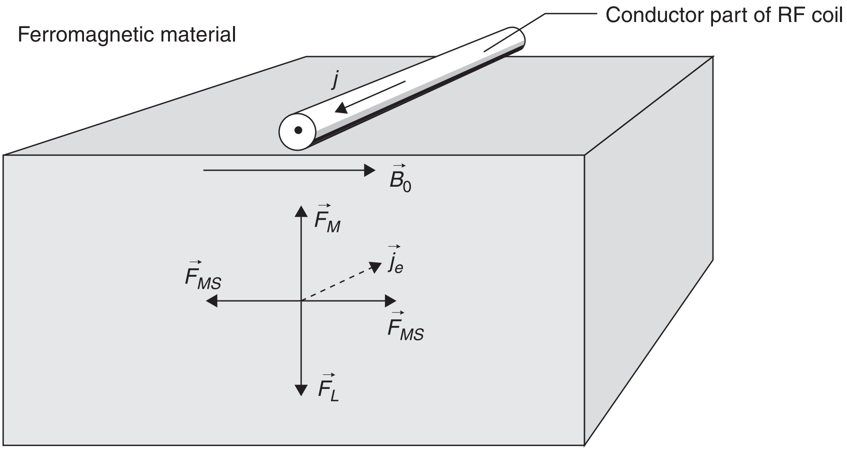

2.2 Electromagnetic ultrasonic conversion with horizontal magnetisation perpendicular to the current direction in a ferromagnetic material.

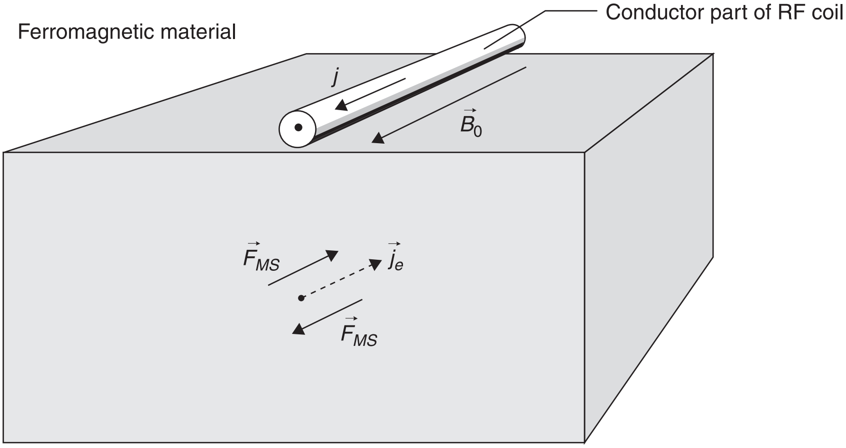
Ferromagnetic material
Conductor part of RF coil
j
$\vec{B}_0$
$\vec{F}_{MS}$
$\vec{j}_e$
$\vec{F}_{MS}$

2.3 Electromagnetic ultrasonic conversion with horizontal magnetisation parallel to the current direction in a ferromagnetic material.

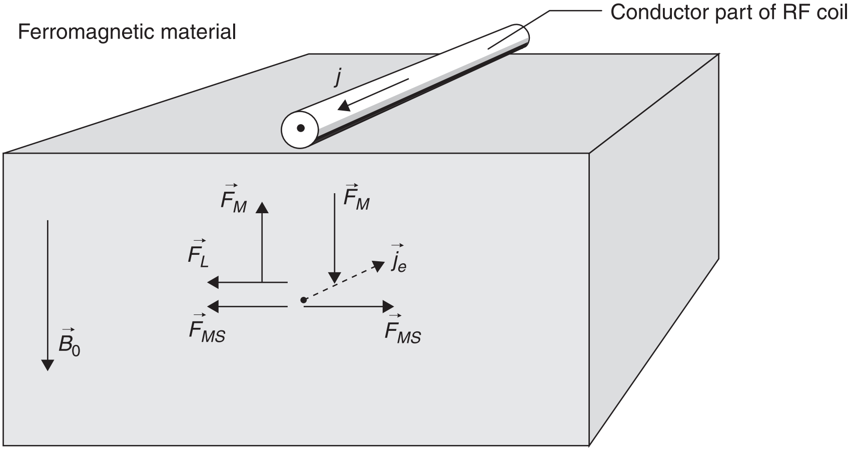
Ferromagnetic material
Conductor part of RF coil
j
$\vec{F}_M$
$\vec{F}_M$
$\vec{F}_L$
$\vec{j}_e$
$\vec{F}_{MS}$
$\vec{F}_{MS}$
$\vec{B}_0$

2.4 Electromagnetic ultrasonic conversion with perpendicular magnetisation in a ferromagnetic material.

force terms are shown for the horizontal and normal magnetic bias fields and for different RF-current directions according to Eq. 2.1. Three situations are considered:

- The magnetisation is horizontal (parallel to the test object’s surface) and perpendicular to the current direction in the RF coil (Fig. 2.2)
- The magnetisation is horizontal and parallel to the current direction in the RF coil (Fig. 2.3)

- The magnetisation is oriented normal to the test object's surface and perpendicular to the current direction in the RF coil (Fig. 2.4)

In the following, the three different mechanisms acting during the electromagnetic excitation of ultrasound are described in detail.

2.2.1 Excitation by Lorentz forces

Eddy currents are induced in the surface area of the test object lying directly under the transducer by a coil positioned in the transducer, which is driven, for a transmitter, mostly by an RF-burst signal. By superimposing a static or quasi-static magnetic field, the Lorentz force acts on the moving charge carrier and causes periodic lattice vibrations due to the oscillating eddy currents. The lattice vibrations of the solid act as ultrasonic sources. This mechanism is active in all electrically conductive, metallic materials. The excitation by Lorentz forces is proportional to the current in the RF coil and the static magnetic induction.

In a non-ferromagnetic material, the electromagnetic excitation of ultrasonic waves is based only on the Lorentz force. In the presence of a magnetic field with the magnetic flux density B_0 oriented perpendicular to the surface, the Lorentz force is oriented parallel to the surface (Fig. 2.5). For a magnetic bias field parallel to the surface, the Lorentz force is directed perpendicular to the surface.

2.2.2 Excitation by magnetic forces

When a ferromagnetic material is placed in a magnetic field, the solid is magnetised. Due to the gradient of the flux density at the surface and in the volume

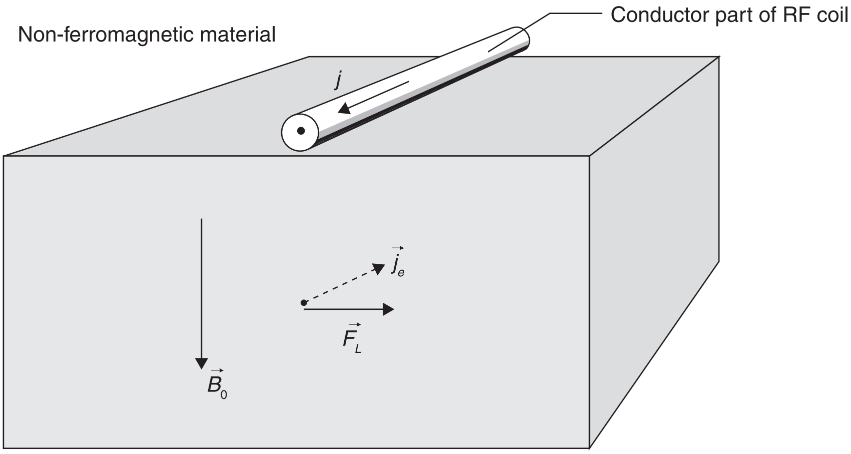

2.5 Electromagnetic ultrasonic conversion with perpendicular magnetisation in a non-ferromagnetic material.

of the specimen, magnetic forces exist. The geometry of the RF coil, as well as the skin effect, causes gradients of the flux density of the dynamic magnetic field. The gradients result in forces due to the magnetic moments. The magnetic force is proportional to the magnetising amplitude (Hübschen *et al.*, 1984).

In a horizontal magnetic field (a bias field), the magnetic force and the Lorentz force are antiparallel, perpendicular to the surface (see Fig. 2.2) and cancel each other completely or partially. Therefore the Lorentz force and the magnetic force are non-effective for the excitation of longitudinal waves in ferromagnetic materials. In the presence of a perpendicular magnetic bias field, the components of the magnetic force acting to the right and left of the current conductor are in opposite directions (Fig. 2.4) and cancel each other in the far field. So these magnetic forces play only a minor role in ultrasonic excitation by EMATs.

2.2.3 Excitation by magnetostriction

The change in the geometrical dimensions of a ferromagnetic solid exposed to an external magnetic field is called magnetostriction. It can be distinguished by a change in the volume and a change in length. The volume change is only a fraction of the change in the form of the magnetostrictive active material. If an oscillating magnetic field is applied by a RF coil to a ferromagnetic specimen, in the interaction area lattice displacements are generated, which create ultrasonic sources due to their periodic character. To achieve a favourable working point of magnetostriction in practice, the specimen is magnetised by a static or quasi-static magnetic bias field. Around this working point, the static magnetic field is modulated by the dynamic magnetic field of the RF coil. Without any magnetic bias field, lattice vibrations with double the frequency of the electrical driving signal of the RF coil are produced.

The following two sections describe different types of EMATs used as normal probes, angle beam probes and probes to generate ultrasonic guided waves in plates and tubes. We make a distinction between a transducer working mainly by the Lorentz force and one working mainly by magnetostriction.

2.3 Lorentz-force-type transducers

The following section describes EMATs working mainly by the Lorentz force. Section 2.3.1 deals with normal probes, Section 2.3.2 with angle beam probes and Section 2.3.3 with transducers for tube waves.

2.3.1 Normal probes

So far, we have described only the basic mechanisms of the electromagnetic excitation of ultrasonic waves. In the following, further explanation of how the magnetic fields and the eddy currents are produced in an electrically conductive (ferromagnetic) material will be given. Permanent magnets and electromagnets are used to generate magnetic fields parallel or perpendicular to the surface. Eddy currents are excited using RF coils with a rectangular, circular or meander-like shape. In the present section different EMATs with the ultrasonic waves normally incident are described.

Figure 2.6 shows the arrangement of the magnet and RF coil for the generation of linearly polarised shear waves under normal incidence in a ferromagnetic material. To produce shear forces tangential to the surface, two magnets are placed with alternating polarity side by side with a spacer between them. Below the poles of the magnets, there is a magnetic bias field with flux density B_0 inside the material, which is oriented perpendicular to the surface. Between the magnet poles and the material surface, an RF coil is positioned in such a way that for a fixed time under the south pole (S) the RF currents flow out of the drawing plane (marked with dots) and under the north pole (N) into the drawing plane (marked with crosses). The resulting direction of the vibration of the excited wave is oriented tangentially to the surface.

The RF coil is a flat rectangular coil where two sections of the coil are covered by the alternating magnet poles. In each of the coil sections the current direction is also oriented in the opposite direction. Therefore the resulting shear forces at the material surface acting at each moment are in the same direction. This leads to a polarisation parallel to the surface. The propagation of the ultrasonic shear wave is perpendicular to the material surface. Fig. 2.7(a) shows an EMAT normal probe for linearly polarised shear waves used for the measurement of residual stresses in the rim of railway wheels of freight wagons (Wilbrand, *et al.*, 1989; Schneider and Herzer, 1998). The probe is integrated into a scanning device allowing a

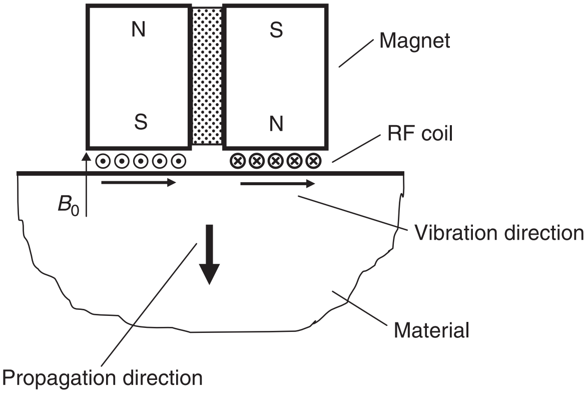

2.6 EMAT normal probe for linearly polarised shear waves (principle). The current direction in the RF coil is marked by dots (current flowing out of the drawing plane) and by crosses (current flowing into the drawing plane).

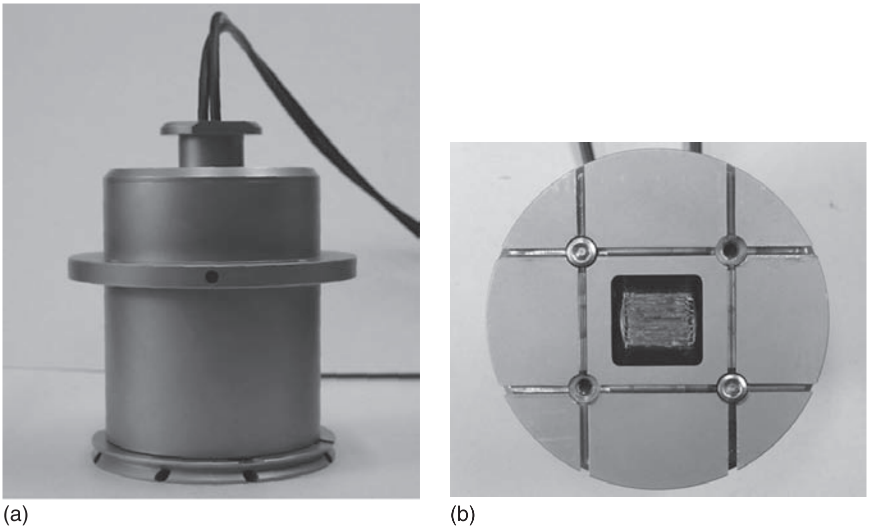
(a) (b)

2.7 (a) EMAT normal probe for linearly polarised shear waves. (b) Windings of the transmitter and receiver coils before the coils are covered with a protective sheet of ceramic substrate.

linear movement and a rotation to alter the polarisation direction by 90°. The top view of the bottom plate of the probe, Fig. 2.7(b), shows the windings of the transmitter and receiver coils before the coils are covered with a protective sheet of ceramic substrate. The area of the RF coil is surrounded by hard metal strips as additional wear protection.

Another standard EMAT for the normal insonification of shear waves is shown in Fig. 2.8. Here a single magnet is combined with an RF coil with a circular

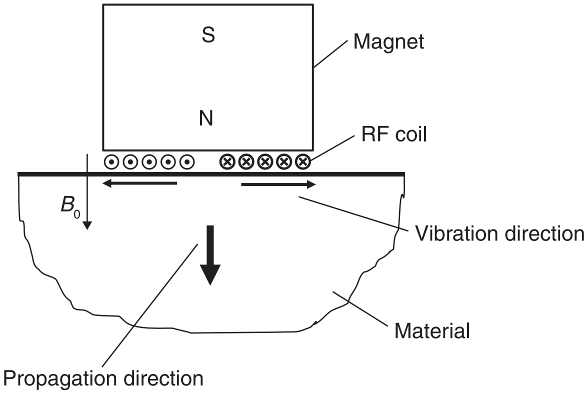

2.8 EMAT normal probe for radially polarised shear waves (principle).

shape. The magnet produces a magnetic field perpendicular to the material surface. In a slice through the magnet and coil, the instantaneous RF current direction in the coil is indicated. The superposition of the magnetic field and the eddy currents in the material leads to vibrations oriented parallel to the surface and with opposite elongations. This type of transducer consists of a magnet, a concentrator with special magnetic and electrical properties and an RF coil. The RF coil is a flat spiral coil, a so-called pancake coil. In practice, these transducers are, as for most EMATs, supplied with separate transmitter and receiver coils. The shear wave produced under normal incidence is radially polarised. An EMAT normal probe for radially polarised shear waves is shown in Fig. 2.9. In this view of the bottom side of the probe, we can see in the centre of the cylindrical housing an arrangement of spiral RF coils (pancake coils). Here the separate transmitter and receiver coils are superposed. The cylindrical ferromagnetic housing is a part of the magnet system used as a magnetic flux conducting element. In the centre of the housing there is a cylindrical permanent magnet and a flux concentrator is positioned between the magnet and the RF coils. The usual frequencies for such transducers are between 1 MHz and 10 MHz. A miniaturised version of such an EMAT probe (where the outer diameter of the probe was 6 mm) has been applied in a resonance technique at frequencies between 0.5 MHz and 1 MHz on aluminium airbag parts (Becker *et al.*, 1999). Further applications using resonance techniques at up to 200 MHz are described in Kawashima (1994). EMAT normal probes for linearly and radially polarised shear waves, as described above, can be used with electrically conductive ferromagnetic and non-ferromagnetic materials. The advantage of EMATs compared with piezoelectric (quartz crystal) transducers is their use without any coupling medium, which must be very highly viscous to transfer the shear movements of the transducer to the material surface. A scanning inspection is therefore nearly impossible using a piezoelectric method.

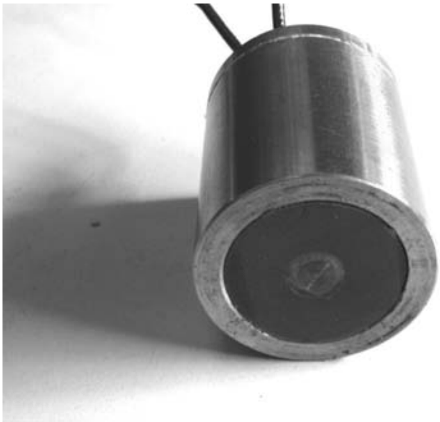

2.9 EMAT normal probe for radially polarised shear waves.

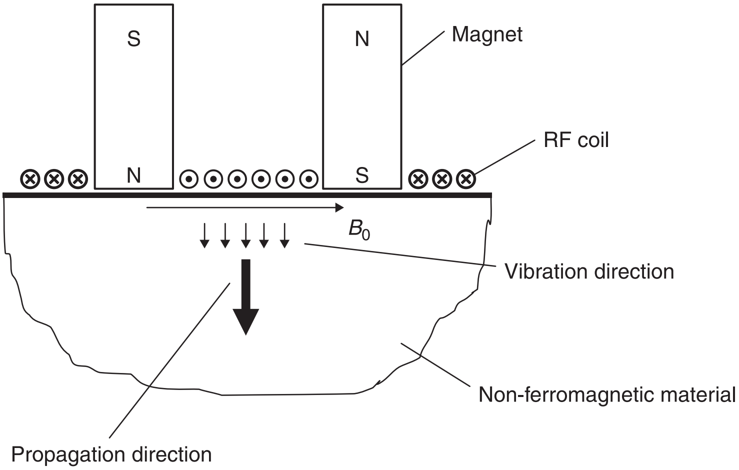

2.10 EMAT normal probe for longitudinal waves (principle).

In ferromagnetic materials it is not possible to generate longitudinal waves in an effective way and without any spurious shear waves due to the different excitation mechanisms (Lorentz force, magnetostriction and magnetic forces).

In non-ferromagnetic materials, it is possible to generate longitudinal waves purely using Lorentz forces by applying a magnetic bias field parallel to the surface using two magnets with alternating polarity [Fig. 2.10, see also Kawashima and McClung (1976)]. Between the two pole pieces a section of an RF coil is positioned where the currents flow in the same direction. In this case normal forces at the material surface lead to vibrations in the same direction. These create a longitudinal wave propagating perpendicular to the surface into the material. EMATs, where the longitudinal waves in non-ferromagnetic materials are normally incident, typically have a magnetic circuit built from a U-shaped permanent magnet or electromagnet. There is an RF coil designed as a double rectangular coil, where only the middle part, situated between the two poles of the magnet, contributes to the generation of longitudinal waves because of the excitation of eddy currents in the range of the horizontal magnetic bias field. The two outer parts of the RF coil are arranged on the outer side of each magnet pole piece and can be lifted off the material surface to reduce the excited eddy currents in the stray flux of the magnet system.

2.3.2 Angle beam probes

The EMATs described in the last chapter use RF coils with a spatially constant current direction within the transducer aperture. This is necessary for normal probes. For angle beam probes, the RF coils or the magnet systems used are built with alternating structures.

Non-segmented transducers

In this type of transducer, the RF coils have meander-like shapes, so that between two elements of the coil the current direction changes by 180°. Figure 2.11 shows a slice through the principal parts of an angle beam probe for SV waves (vertically polarised shear waves). Between the magnet, which generates a magnetic bias field perpendicular to the surface, and the surface of the material, elements of the coil are shown with the alternating current direction. By superposition of the magnetic field and the applied eddy currents in the material surface, alternating shear forces are created perpendicular to the eddy current and magnetic field direction. This leads to corresponding vibrations at the surface. The propagation direction of the excited ultrasonic wave, at the beam angle of the EMAT, can be varied by changing the frequency as shown later. Such angle beam probes for SV waves can be realised by most of the different EMAT types with permanent magnets or electromagnets. With pulsed electromagnets, there is better movement over ferromagnetic components. The basic probe parts are, for example, an M-shaped magnetic yoke made from transformer sheets (thickness typically 0.3 mm) with a magnetising coil and concentrator and an RF coil with a meander shape (Mohr and Repplinger, 1978). The RF coil is fixed beneath the middle pole with the flux concentrator and the material surface. The wavelength or the period of the transducer λ_s is defined as the distance between two neighbouring elements of the coil with the same current direction. Directivity patterns of an EMAT angle beam probe for SV waves are shown in Mohr and Repplinger (1978).

The formation of the beam angle for an EMAT angle beam probe for SV waves is shown in Fig. 2.12. The wires of a meander-like RF coil are arranged over the test object of electrically conductive material. In transmit mode, RF currents flow through them and the current direction alternates from wire to wire. There is a superposed static magnetic field in this arrangement. The RF currents lead to eddy currents in the material surface, within the skin depth of the applied frequency.

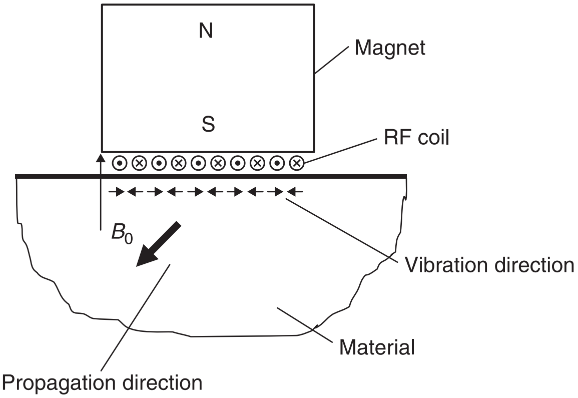

2.11 EMAT angle beam probe for SV waves (principle).

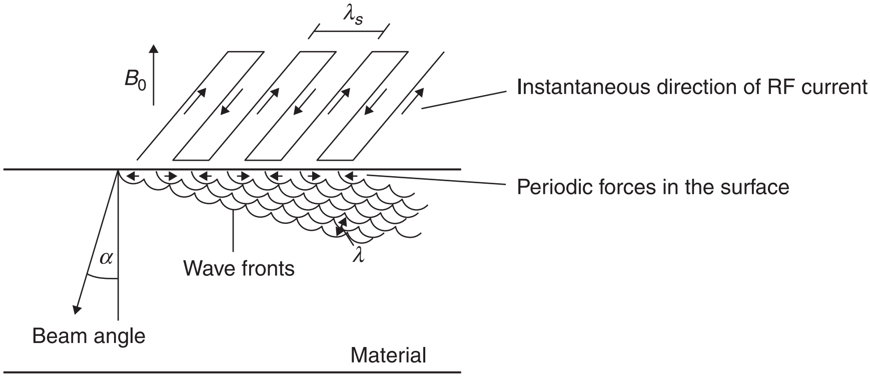
λ_s
B_0
Instantaneous direction of RF current
Periodic forces in the surface
α
Wave fronts
λ
Beam angle
Material

2.12 Superposition of elementary waves forming wave fronts and beam angle (SV wave).

Together with the magnetic field B_0, the eddy currents cause forces on the electrons in the material. These forces are perpendicular to the magnetic field and eddy currents are transferred to the metal lattice and create particle displacements, thus ultrasonic waves. The forces run parallel to the surface and alternate over a half period $\lambda_s/2$, i.e. if one wire radiates a wave trough then an adjacent wire radiates a wave crest. The Huygens elementary waves of all wires superpose and there is constructive interference. There two sound beams (the main lobes of the directivity patterns) are directed symmetrically around the surface normal at an angle of $+\alpha$ or $-\alpha$. The beam angle a is given by

$$\alpha = \arcsin (c/(\lambda_s f)) \qquad [2.2]$$

where c is the sound velocity, λ_s is the period of the transducer and f is the frequency.

Single radiators do not produce real Huygens elementary waves, but they have a special directivity pattern (Miller and Pursey, 1954). The functional relation of Eq. 2.2 is illustrated in Fig. 2.13, showing a series of curves for shear waves with the period of the transducer as a parameter. All curves show a lower cut-off frequency f_c, corresponding to the case of grazing incidence (beam angle 90°). With increasing frequency the beam angle becomes steeper and converges asymptotically for $f \to \infty$ to the value of 0°. Below the cut-off frequency f_c for SV waves there is a single frequency at which Rayleigh waves (surface waves) are generated. So an EMAT for SV waves can also be used for inspection with Rayleigh waves by choosing an appropriate frequency. Above the cut-off frequency, the beam angle can be varied by changing the frequency. This causes the axial resolution and the beam width of the directivity pattern to change also because of the change of ultrasonic wavelength $\lambda = c/f$ in the material.

So far, only the geometrical shape of the meander-like RF coil has been described. The technical realisation of such coils needs mechanical support in the

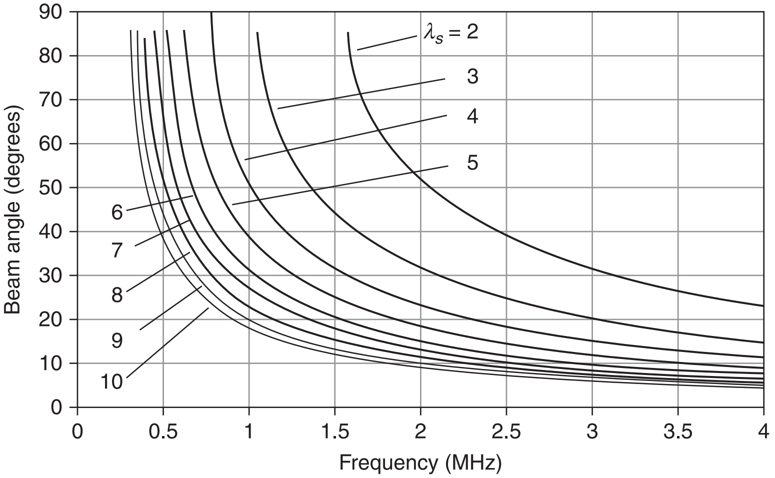

2.13 Beam angle as a function of the frequency of the transducer, λ_s (mm).

form of special machined plastic or ceramic parts, which are used to wind the wires of the coil (left side of Fig. 2.14). These plastic or ceramic bodies are machined in such a way that notches with depths of the order of 1 mm are made side by side. In these notches the wires of the coil are arranged as shown in the cross section on the left side of Fig. 2.14. If the wires are fed with RF currents, dynamic magnetic fields H_ω (H is the magnitude, ω the angular frequency) are generated with alternating directions due to the alternating current directions in adjacent notches. Printed circuit materials can also be used as RF coils. Instead of this classical design, it is also possible to use RF coils on transformers made of metallic materials (right side of Fig. 2.14). These materials have high saturation induction, high permeability and low electrical conductivity. The shape of this type of coil body is similar to the classical form. The main difference consists in

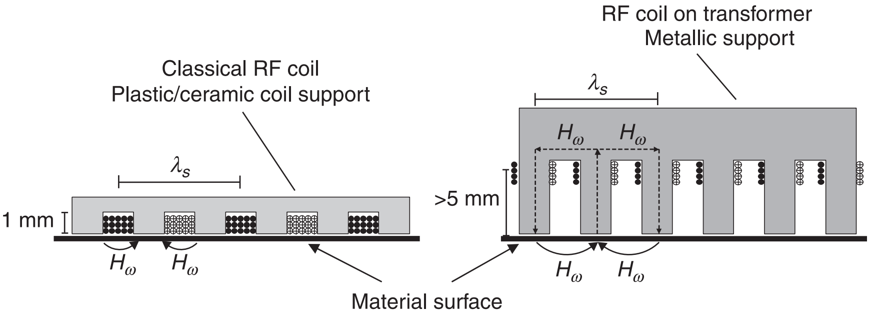
RF coil on transformer
Metallic support
Classical RF coil
Plastic/ceramic coil support
λ_s
λ_s
H_ω
H_ω
1 mm
>5 mm
H_ω
H_ω
H_ω
H_ω
Material surface

2.14 Variants of RF coils (Salzburger, 1988).

a larger notch depth of around 6 mm. The shape resembles a comb. Therefore the very thin wires are above the material surface by several millimetres, giving better wear protection of the RF coils than for the plastic coil bodies. Due to the highly permeable comb structure of the coil body, the dynamic magnetic fields H_ω are guided without any high loss into the material surface. Further details of this type of RF-coil variant can be found in Salzburger (1988). In general, separate transmitter and receiver coils are mostly used for EMAT probes. The number of turns of the RF coil of the transmitter is often chosen so that it is matched in the resistance to the generator output. For the receiver coil the number of turns is selected so that at the highest applied frequency the winding is in parallel resonance with its own winding capacitance.

Two examples of angle beam probes built with metallic coil bodies having comb structures are shown in Fig. 2.15. Both are applied to generate and receive Rayleigh waves. The EMAT probe on the left is built into a metallic device containing an electromagnet and a preamplifier with housing. The transmitter and receiver coil are arranged on the same coil body. The complete unit is integrated in a rail and used for the surface inspection of railroad wheels (especially high-speed trains) by Rayleigh waves. The probes work at a frequency of approximately 400 kHz (Salzburger and Repplinger, 1983; Salzburger *et al.*, 2008). The EMAT transmitter-receiver (TR) probe shown on the right is designed for scanning surface inspection with Rayleigh waves at a frequency of 1 MHz. The transmitter and receiver coil are located on two separate metallic coil bodies arranged side by side with a small skewing angle. The bottom plate of the probe has hard metal strips to enhance wear protection. Another application of SV wave angle beam EMATs is for the monitoring of the filling level of reactor pressure vessels in nuclear power plants as described in Hübschen *et al.* (1990).

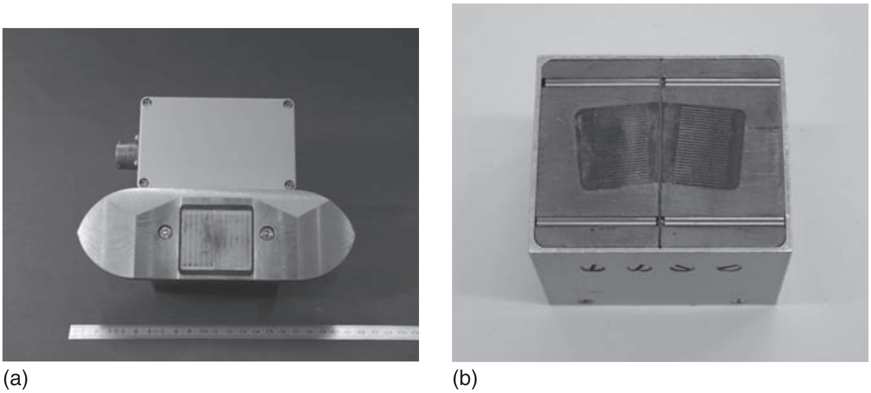
(a) (b)

2.15 EMAT angle beam probes with metallic coil bodies having comb structures. (a) The transmitter and receiver coil are on the same coil body. (b) The transmitter and receiver coil are on two separate metallic coil bodies.

Piezoelectric single-crystal angle beam probes for SV waves are widely used in non-destructive testing (NDT) mainly at fixed beam angles of 45° for the external volumetric inspection and inspection of the inner surface of components. The main application of EMAT angle beam probes for SV waves is surface inspection with Rayleigh waves.

Another wave type not usable for practical applications in NDT by piezoelectric transducers is the horizontally polarised shear wave (SH wave). In the following, different possibilities are presented for using this wave type using EMATs. Figure 2.16 shows the basic parts of an SH-wave EMAT. This type of transducer has two rows of small permanent magnets with alternating polarity (Thompson and Vasile, 1978). Between the magnets and the material surface, a rectangular flat coil is positioned so that the current flow under the first row of magnets is in the opposite direction to the current flow in the second row. Therefore the resulting Lorentz forces under each magnet pair perpendicular to the row direction are in the same direction. Between each pair of magnets the resulting Lorentz force is in opposite directions. Directivity patterns of this type of EMAT can be found in Maxfield and Fortunko (1983).

An EMAT angle beam probe for SH waves is shown in Fig. 2.17. In this side view the arrangement of permanent magnets with alternating magnetic fields from Fig. 2.16 is shown together with a conductor from the RF winding arranged between the magnets and the material surface. The period (wavelength) of the transducer λ_s is the distance between two magnets with the same polarity. If the

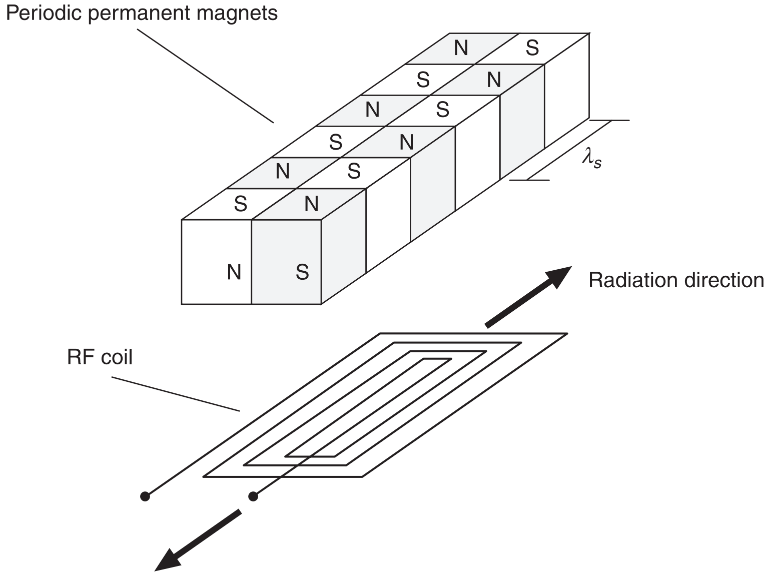

2.16 EMAT angle beam probe for SH waves (principle).

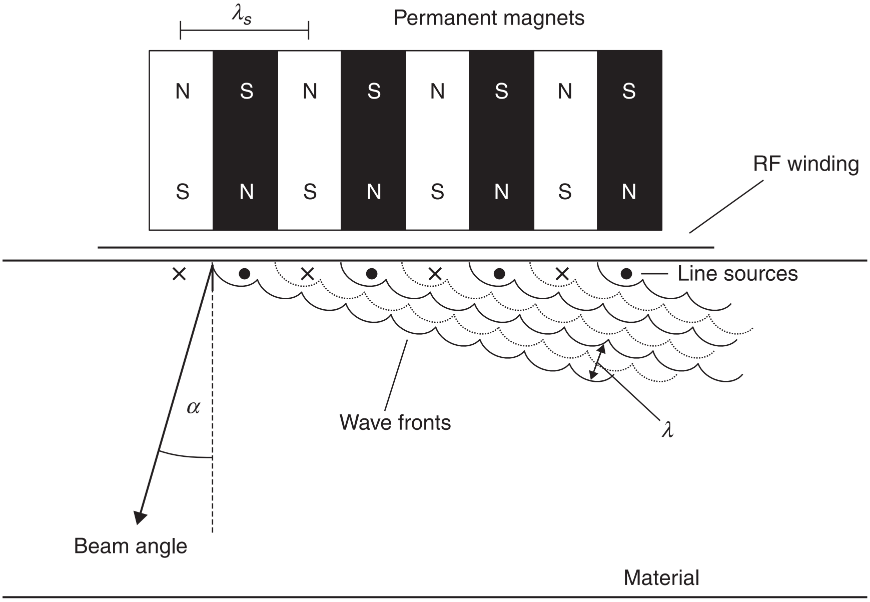

2.17 Superposition of elementary waves forming wave fronts and beam angle (SH wave).

RF coil is driven with an alternating current with a frequency in the ultrasonic range, then with the alternating magnetic fields the eddy currents induced in the surface generate transverse periodic forces because of the Lorentz force. The direction of the force is indicated by dots (force direction out of the drawing plane) and crosses (force direction into the drawing plane). These periodic forces act as ultrasonic line sources. The forces run parallel to the surface and alternate spatially over a half period $\lambda_s/2$ and temporally with the frequency of the alternating current in the RF coil. As for an SV-wave angle beam probe (see Fig. 2.12), the Huygens elementary waves generated by the single-line sources superpose and interfere constructively to form single wave fronts propagating at an angle α (the angle between the wave front normal and the surface normal). The beam angle α is given by Eq. 2.2. Compared with an SV-wave angle beam probe (Fig. 2.12) producing a shear wave polarised in the plane of incidence (given by the surface normal and the sound propagation direction), an SH-wave angle beam probe generates a shear wave polarised perpendicular to the plane of incidence. In Fig. 2.12 and Fig. 2.17 only one beam angle is shown, but, due to the symmetry of the radiation of the single ultrasonic line source, an EMAT for the angle incidence of bulk waves has two main lobes in the radiation pattern, as shown in Fig. 2.18. For monitoring from a fixed position or for the inspection of pipelines with guided waves in a circumferential (Hirao and Ogi, 1999) or axial direction, these two main lobes can be used to cover a larger area with only one transducer.

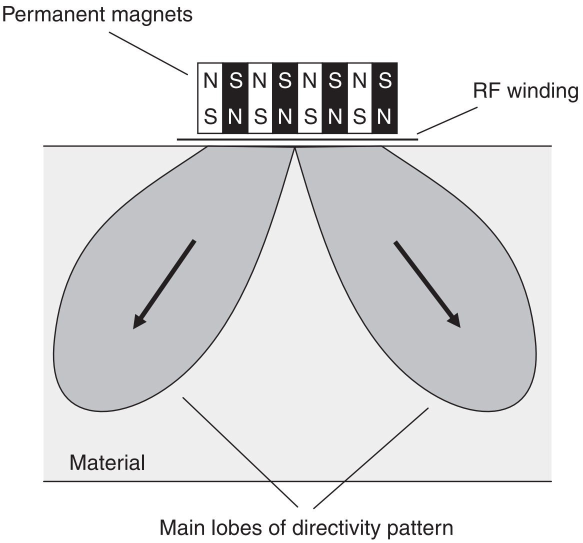

2.18 Characteristic directivity pattern of an EMAT angle beam probe for SH waves (non-segmented RF coil).

For most ultrasonic inspections it is necessary that the ultrasonic probes deliver a directed sound beam in one direction only.

Segmented transducers (phased-array transducers)

A sound beam mainly directed in one direction can be realized using the phased-array principle by dividing the RF coil into single RF coil segments (Fig. 2.19), which are driven on the transmitting side with separate power stages and on the receiving side also with separate electronic receiving channels and with a defined time delay (phase delay). This segmented coil arrangement has two main advantages compared with a non-segmented coil arrangement: the bandwidth of the generated ultrasonic signals is larger because the segmented coil segments consist of a smaller number of line elements and therefore the maximal signal amplitude is achieved for a smaller number of cycles in the driving tone burst signals. The larger bandwidth of the signals means a better axial resolution. Furthermore, a unidirectional radiation pattern is reached. The ratio of energy radiated in the forward and the backward direction increases with the number of segments.

Figure 2.20 schematically shows an example of an EMAT phased-array probe with a segmented RF coil. This is an EMAT angle beam probe for SV waves. The probe consists of an M-shaped electromagnet with a magnetising coil. The middle pole shoe has a flux concentrator. The RF coil is positioned between the concentrator and the material surface. The right side of Fig. 2.20 shows a top view of the segmented coil. This type of probe has been designed for the surface

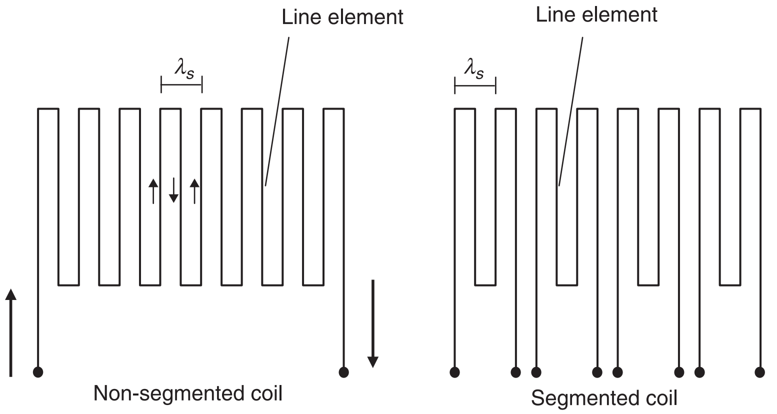
Line element
λ_s
Line element
λ_s
Non-segmented coil
Segmented coil

2.19 Shapes of RF coils.

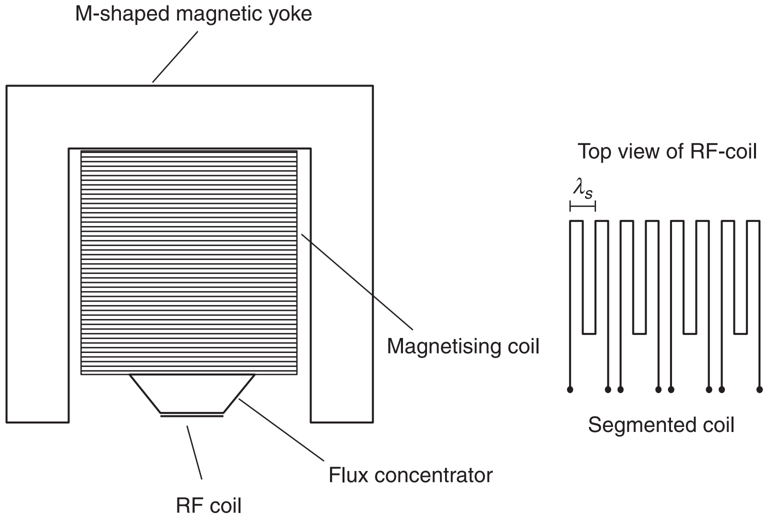
M-shaped magnetic yoke
Top view of RF-coil
λ_s
Magnetising coil
Segmented coil
Flux concentrator
RF coil

2.20 Angle beam probe for SV waves with segmented RF coil (phased-array probe).

inspection of large format pipes after production using Rayleigh surface waves and SV waves with a beam angel of 45° (Böttger *et al.*, 1987; Wilbrand *et al.*, 1987). The inspection frequency is 1 MHz.

We have discussed the possibility for EMATs that mainly use the Lorentz principle to generate and receive SV waves, by dividing a non-segmented RF coil (meander coil) into segmented coils. Such segmentation is also possible for EMATs that apply the Lorentz principle to excite and receive SH waves. Figure 2.21 shows a possible segmentation of the permanent magnet and RF-coil

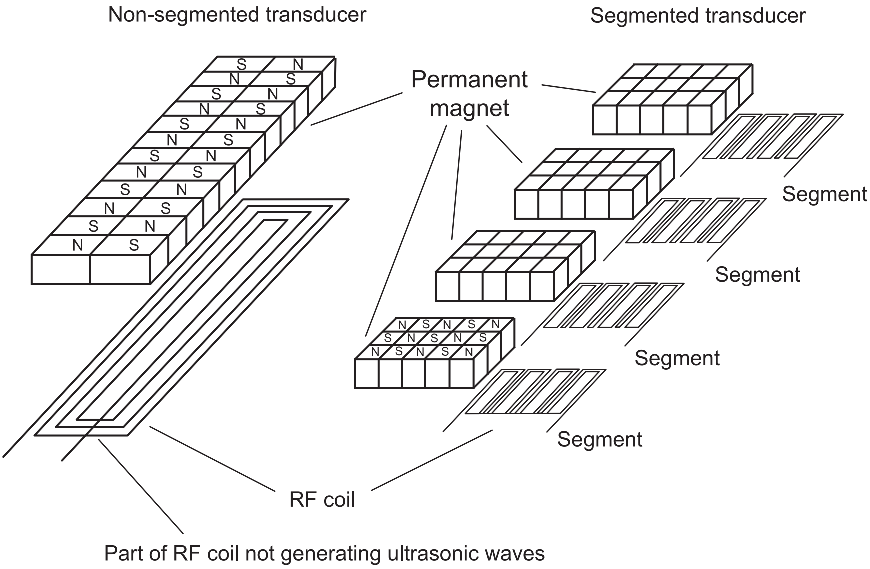

2.21 Segmentation of an EMAT SH-wave angle beam transducer.

arrangement for this type of transducer. The two rows of alternating permanent magnets and the rectangular RF coil found in a non-segmented transducer are divided into several magnet segments and RF-coil segments, which have a different structure compared with the non-segmented version. This magnet and RF-coil structure is chosen to optimise the efficiency of the coil. If the length of the magnet rows and the rectangular coil is reduced, as on the left side of Fig. 2.21, the ratio of the length of the active part of the coil to the non-active part decreases and therefore the efficiency of the RF coil is reduced. When dividing the magnet arrangement in the width direction into several small magnet pieces with alternating polarity (right side of Fig. 2.21) then the efficiency of the RF coil of each segment can be improved by positioning several small rectangular coils side by side in the width direction of a segment. Under each line of magnets in the width direction, a unidirectional shear force is generated due to the alternating direction of the magnetic field and alternating current.

A complete EMAT phased-array probe for SH waves is shown in Fig. 2.22. This type of probe has two parts. The upper part contains the cable connection with mechanical support and four preamplifiers with selected tuning capacitors. Lower parts can be plugged into this upper part via a special connector system. The lower parts contain the transmitter and receiver segments with alternating permanent magnets and RF coils and the high-voltage tuning capacitors for the transmitter segments. These lower sections are laid out for different surface shapes (flat or cylindrically curved). The bottom of this section is covered

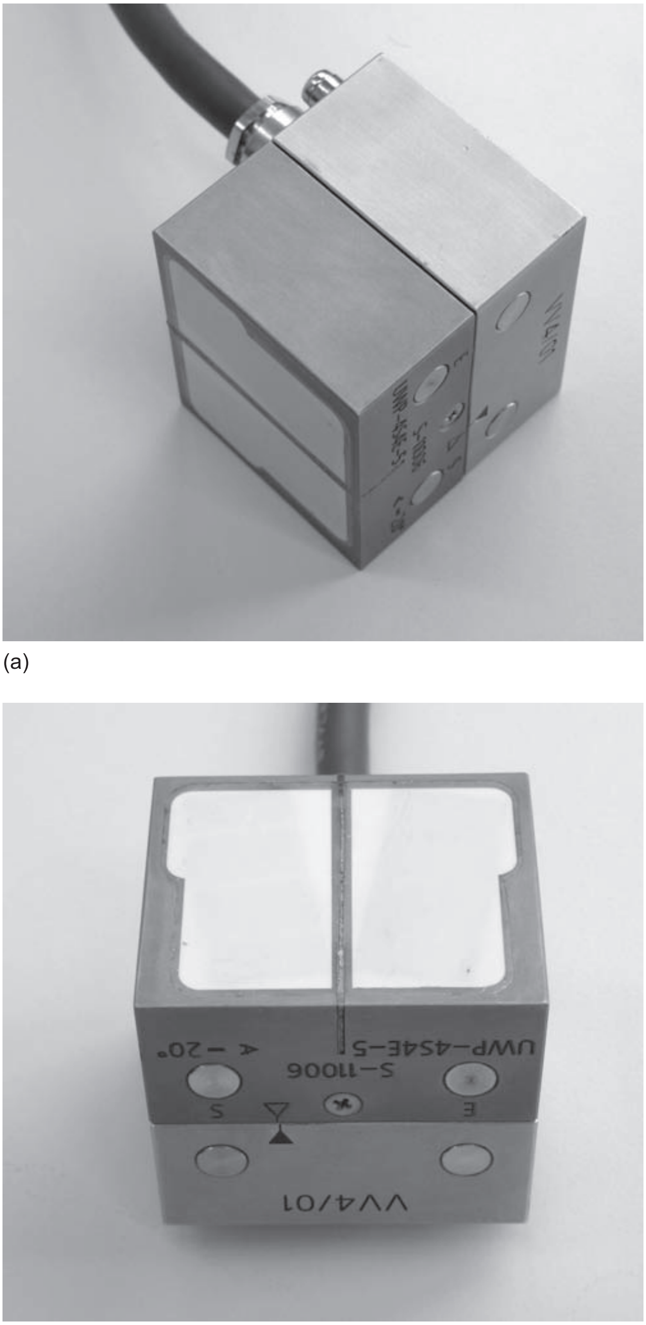
VV4/01
UWP-4S4E-5
S-11006
A −20°
S
E

(a)

(b)

2.22 EMAT phased-array probe for SH waves: (a) side view, (b) bottom view.

with a ceramic wear protection sheet. The permanent magnet arrangement of a complete EMAT phased-array probe (TR probe) for SH waves consists of two packages of segments arranged side by side under a certain squint angle. One is used as the transmitter and the other as the receiver. For a period λ_s of 5 mm, typical dimensions of the segments are 7.5 mm × 18 mm and 10 mm × 18 mm.

The beam angle of a non-segmented EMAT probe is varied by changing the frequency of the transmitter current. At different beam angles the basic sensitivity of the probe changes due to the variation of the ultrasonic wavelength in the material. Using segmented transducers (phased-array transducers) it is possible to change the beam angle by changing the time (phase) delay Δt between segments (Fig. 2.23) using the following relation:

$$\alpha = \arcsin (c_t \bullet \Delta t/D) \qquad [2.3]$$

where c_t is the sound velocity of the shear wave, Δt is the time delay between two adjacent segments and D is the distance between segments.

Non-segmented transducers generate ultrasonic signals with a small bandwidth due to excitation over a large aperture along the plane of sound incidence (given by the surface normal and the propagation direction). If the transducer is divided into several smaller segments, it is possible to excite with these segments ultrasonic signals with a larger bandwidth and therefore a better axial resolution. Applying the phased-array principle, it is furthermore possible to create a unidirectional radiation pattern.

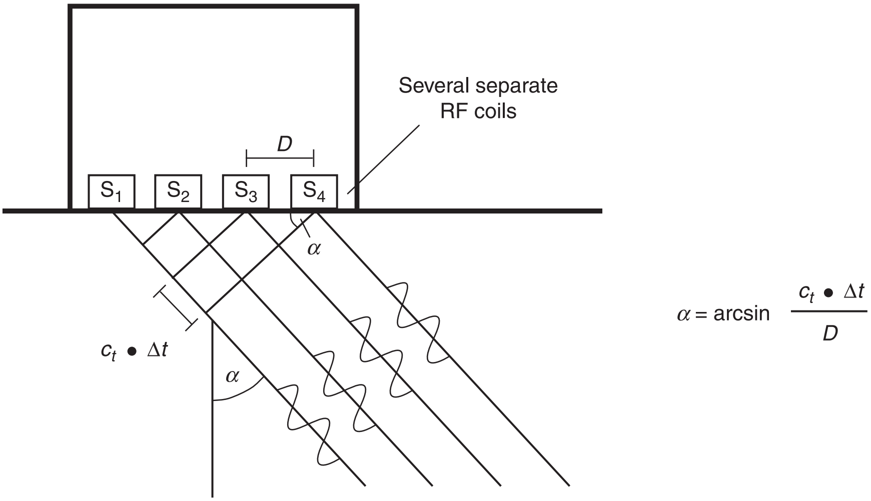
Several separate RF coils
D
S_1
S_2
S_3
S_4
α
$c_t \bullet \Delta t$
α
$\alpha = \arcsin \dfrac{c_t \bullet \Delta t}{D}$

2.23 Variation of beam angle for a segmented EMAT (array transducer).

Typical directivity patterns of an EMAT phased-array probe for SH waves (transmitter) with a period of 5 mm and four segments with three or four line elements are shown in Fig. 2.24. The probe was designed for an ambient temperature of 160 °C. The time delays between different segments are shown in Table 2.1. The directivity patterns were obtained on a half cylinder of ferritic steel and the probe transmitter was positioned at the centre of the flat side of the cylinder. With the help of an EMAT line receiver for SH waves, the radiated ultrasonic signal amplitude was recorded on the outer side of the curved part of the cylinder within a time gate and plotted as a function of the angle of incidence between 0° and 90°. In Fig. 2.24 the directivity patterns are shown for

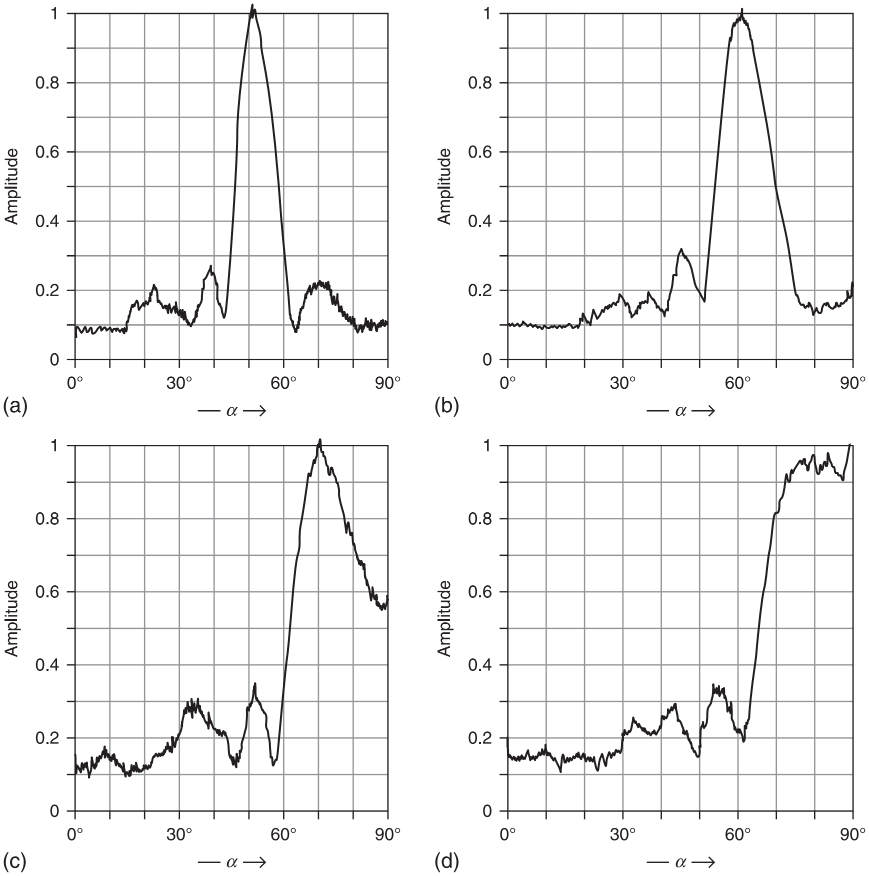

2.24 Directivity patterns of an SH-wave angle beam probe (phased-array) in the plane of incidence (transmitter with four segments and three or four line elements, period $\lambda_s = 5$ mm, $f = 680$ kHz). Beam angles: (a) 50°, (b) 60°, (c) 70° and (d) 80°.

Table 2.1 Beam angles and optimised time delays for an SH-wave phased-array EMAT

Beam angle (degree)	Time delay Δt_1(ns)	Time delay Δt_2(ns)	Time delay Δt_3(ns)
50	2858	5516	7462
60	3061	6048	8380
70	3347	6644	9212
80	3406	6788	9560

beam angles of 50°, 60°, 70° and 80° and a frequency of 680 kHz. The 6-dB beam width varies between 12° and 22°. Typical frequencies are in the range between 650 kHz and 1 MHz. Further details of SH-wave phased-array EMATs and their application for the inspection of austenitic and dissimilar metal welds are given in Hübschen and Salzburger (1989), Hübschen *et al.* (1993) and Sawaragi *et al.* (2000).

2.3.3 Transducers for tubes and rods

Using EMAT angle beam probes for SV or SH waves, it is possible to generate for in-plane products, such as steel or aluminium sheets, guided waves if the period of the transducer is of the order of the wall thickness or larger. The different modes can easily be selected by changing the frequency of the RF current in the transmitter coil. In tubes and rods, guided modes can be excited by EMATs, but, instead of plane transducers, specially designed transducers matched to the pipe or rod geometry have to be used. In Mohr and Hoeller (1976) methods are described to use different modes for the inspection of non-ferromagnetic heat-exchanger tubes. For the excitation and reception of so-called longitudinal modes (similar to Lamb modes in plates) in austenitic heat-exchanger tubes, an experimental set-up with an RF coil and magnet arrangement, shown in Fig. 2.25, has been applied. One end of a tube is positioned between the pole shoes of a laboratory magnet. At the outer and inner surface of the tube, the RF coils of the transmitter and receiver are arranged as sketched in the lower part of Fig. 2.25. The winding pattern of the coil (a meander coil) is shown in the upper left part of Fig. 2.25. A photograph of transmitter and receiver coils for tube waves is shown in Fig. 2.26. The coil support is a plastic material with machined notches. The copper wire is wound on the notches as shown. The period of the transducer is 15 mm. The support for the transmitter coil is a hollow cylinder placed around the outside of the pipe. The coil support for the receiver, placed inside the pipe, is a rod of plastic material with machined

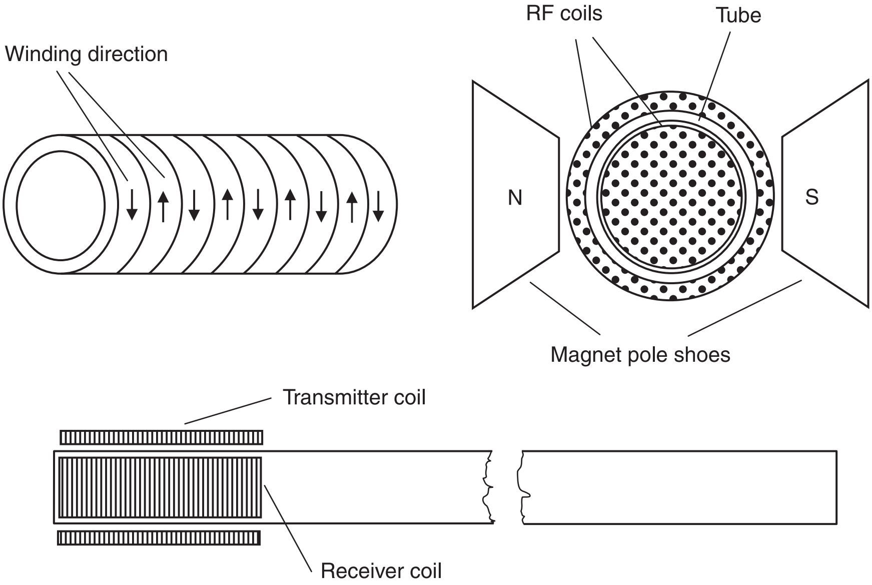
RF coils
Tube
Winding direction
N
S
Magnet pole shoes
Transmitter coil
Receiver coil

2.25 EMAT for tube waves, principal arrangement of RF coils and magnet after Mohr and Hoeller (1976).

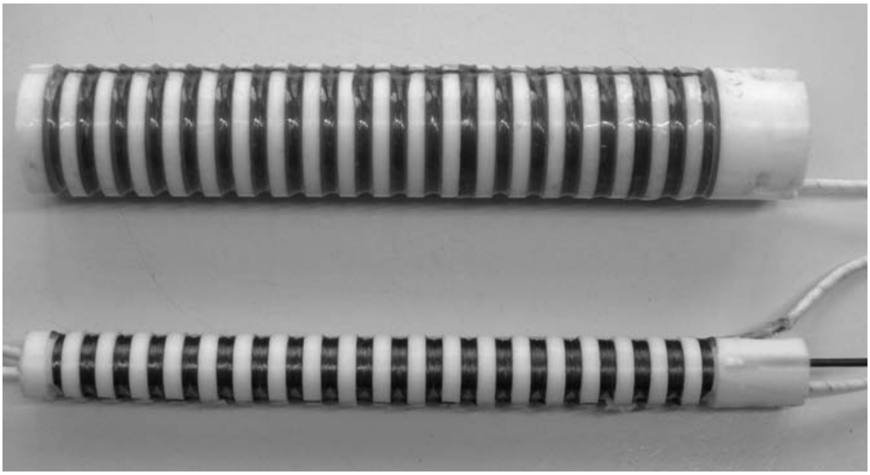

2.26 Transmitter coil (upper) and receiver coil (lower) for tube waves.

circumferential notches and copper wires. In Thompson *et al.* (1979) and Morimoto *et al.* (1984), EMATs with periodic permanent magnets are described for generating guided torsional waves in steam-generator and heat-exchanger tubes.

2.4 Magnetostriction-type transducers

In the sections above, EMAT probes using mainly the Lorentz force mechanism were described. In the following section, EMAT probes working mainly using magnetostriction will be considered. The section is also divided into subsections on normal probes and angle beam probes.

2.4.1 Normal probes

In Igarashi and Alers (1998), an EMAT normal probe for the excitation of bulk shear waves by magnetostrictive coupling is described. Here a static magnetic bias field oriented parallel to the surface is used in combination with flat rectangular RF coils. Figure 2.27 shows the magnetostrictive excitation of linearly polarised shear waves (Niese *et al.*, 2006; Niese, 2010). The magnetic bias field can be generated with a U-shaped magnetic yoke. This yoke can be laid out as an electromagnet or permanent magnet system. The figure is a cross section of a probe showing the two wires of the flat rectangular or circular coil. The current flows in opposite directions in the wires. This leads to dynamic magnetic field components directed parallel to the surface and also in the opposite direction. These dynamic magnetic fields modulate the static magnetic bias field and excite tangential shear forces, due to the magnetostriction effect. The resulting vibrations are parallel to the material surface. This type of EMAT normal probe for linearly polarised shear waves has been developed and used in combination with eddy current and magnetic flux leakage techniques for wall-thickness measurements in gas pipelines (Niese *et al.*, 2006).

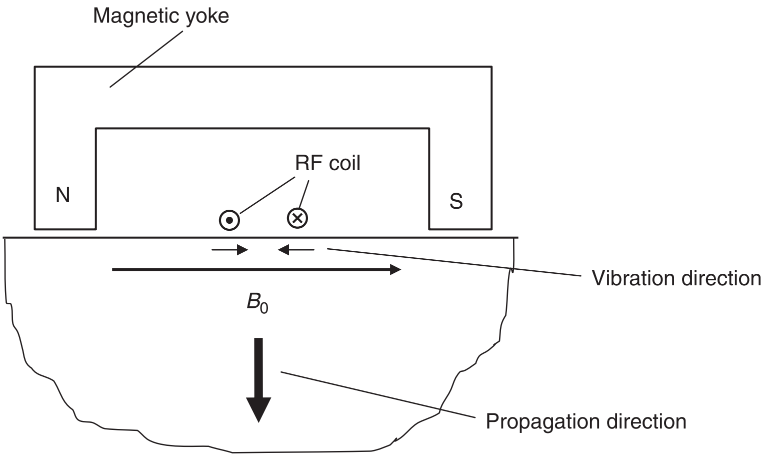

2.27 EMAT normal probe producing linearly polarised shear waves in a ferromagnetic material using magnetostriction.

2.4.2 Angle beam probes

In EMAT angle beam probes using the magnetostrictive principle, only U-shaped electromagnet systems are used for generating horizontal magnetic bias fields.

Non-segmented transducers

To generate and receive SV waves at an angle to the surface normal and for a beam angle of 90°, a Rayleigh surface wave meander-like RF coil is arranged between the pole shoes of an electromagnet in such a way that the line elements of the coil are arranged parallel to the pole shoes (Fig. 2.28). The driving RF currents in the coil, as well as the eddy currents in the material surface, create magnetic fields parallel to the material surface and parallel to the magnetic bias field. For adjacent elements, the directions of these dynamic magnetic fields are directed in opposite directions and show a phase shift of 180°. These dynamic magnetic fields modulate the static magnetic bias field and lead to alternating shear forces, producing tangential particle displacements and SV wave vibrations. A theoretical description of the transduction process can be found in Thompson (1973, 1978b). Separate RF coils are used for the transmitter and receiver, placed side by side or interleaved so that the transmitter and receiver coil are shifted by a quarter of a period (wavelength) of the transducer.

By turning a meander-like RF coil by 90° between the pole shoes of a U-shaped electromagnet, an angle beam EMAT probe for SH waves can be realised (Fig. 2.29). The line elements of the meander coil are parallel to the static magnetic bias field, which is tangential to the material surface. In this arrangement of the

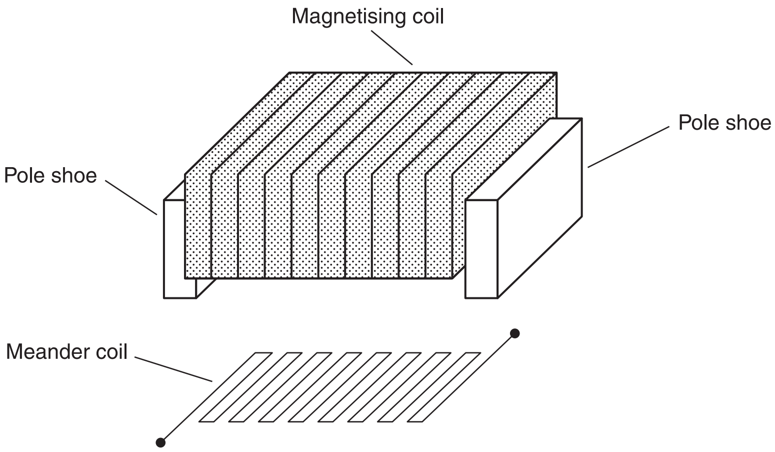

2.28 EMAT probe for SV and Rayleigh waves (magnetostrictive version), showing arrangement of RF coil and magnet.

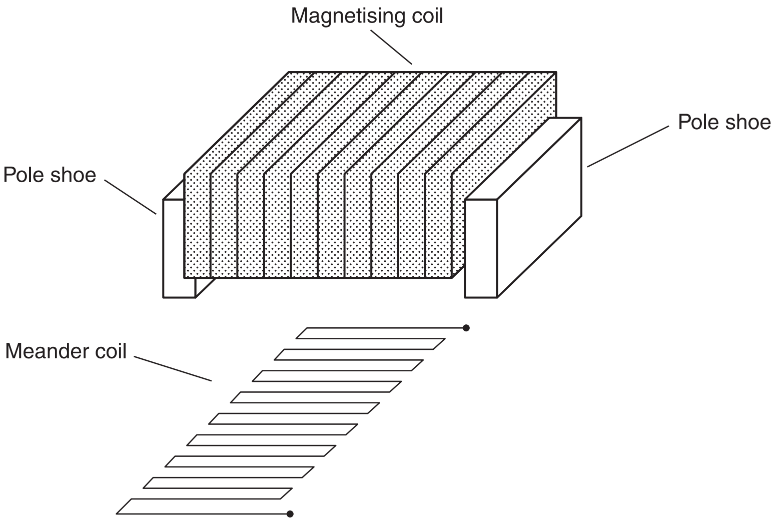

2.29 EMAT probe for SH waves (magnetostrictive version), showing arrangement of RF coil and magnet.

magnetic bias field and with the eddy currents induced by the line segments of the meander coil, there are no Lorentz forces because the magnetic bias field and the eddy currents are orientated in the same direction. The superposition of the dynamic magnetic fields with the static magnetic bias field creates alternating shear forces at the material surface, generating a deformation of the material, which leads to the particle displacements of an SH wave. Further details about this excitation mechanism can be found in Thompson (1978a, 1979).

This type of angle beam EMAT probe for SH waves consists of a U-shaped magnetic yoke with magnetising coils and an RF coil with a meander-like shape. The number of lines determines the directivity pattern in the plane of incidence. Typical directivity patterns (transmitter) of an angle beam probe for SH waves are given in Fig. 2.30 (Mohr *et al.*, 1980). As described above, the beam angle of such an EMAT probe can be changed by varying the frequency of the RF current in the coil.

These diagrams were produced using a ferritic half cylinder. The transmitter was placed at the centre of the flat surface of the cylinder. The radiated signal amplitude was measured using an EMAT line receiver at the cylindrical surface as a function of the angle of incidence from 0° to 90°. The period of the measured transmitter coil λ_s was 4 mm and the number of line elements in the meander coil was 12. The amplitude was tapered (Dolph–Tschebyscheff) by varying the number of windings of the elements to realise a low level of the side lobes. The frequency was varied between 804 kHz and 1.3 MHz. The corresponding beam angles were between 90° and 40°. The beam width decreases if the beam angle is reduced. Figure 2.31 shows an EMAT probe for SH waves, which is used in inspection

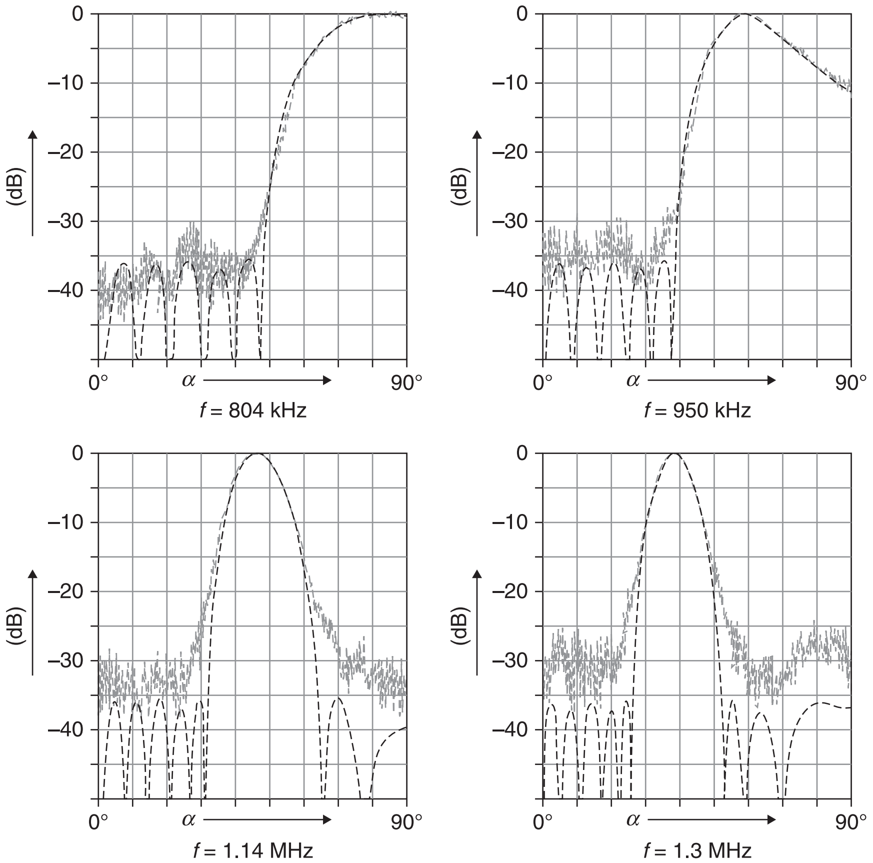

2.30 Directivity patterns in the plane of incidence of an SH-wave EMAT (transmitter, λ_s = 4 mm, 12 line elements, Dolph–Tschebyscheff tapering, measured on a ferritic half cylinder with a radius of 100 mm) (Mohr *et al.*, 1980).

systems to test laser weldments of thin steel sheets (wall thickness approximately 1 mm), so-called tailored blanks (Salzburger *et al.*, 1999). It is a TR probe and it generates guided SH waves at 1 MHz. In the top view of the probe housing, we can see, besides the cable and connection, two thin flexible tubes used for pressurised air. The bottom of the probe housing, Fig. 2.31(b), has holes so that the probe glides over the surface of the steel sheets on an air cushion. On the bottom, we can also see the two pole shoes of a U-shaped electromagnet. The RF coils of the transmitter and receiver are positioned above a ceramic protection sheet between the pole shoes.

To create guided SH waves in ferromagnetic tubes with small diameters (20 to 30 mm) the magnetostrictive EMAT of Fig. 2.29 can be modified by replacing the

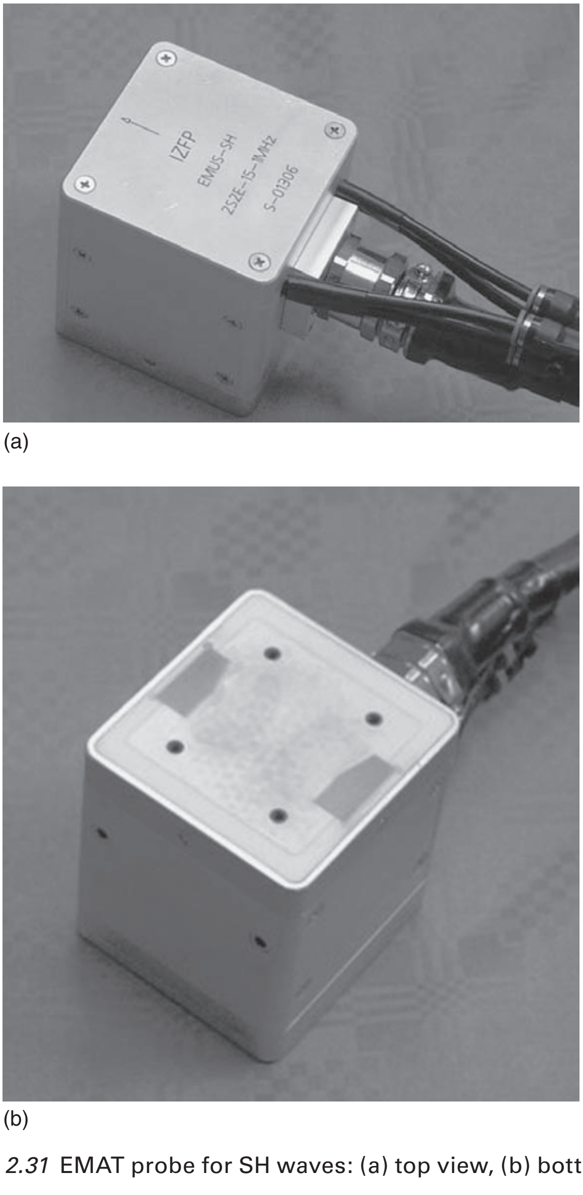

2.31 EMAT probe for SH waves: (a) top view, (b) bottom view.

electromagnet with a permanent magnet. The plane meander-like RF coil has a cylindrical form surrounding the magnet as shown on the left side of Fig. 2.32. Flux conductors are used to concentrate the magnetic flux in the tube wall. Figure 2.33 shows a laboratory prototype EMAT that will generate guided SH waves in the circumferential direction of a ferromagnetic tube for detecting longitudinal crack-like defects. We can see the curved RF coil, the magnet system

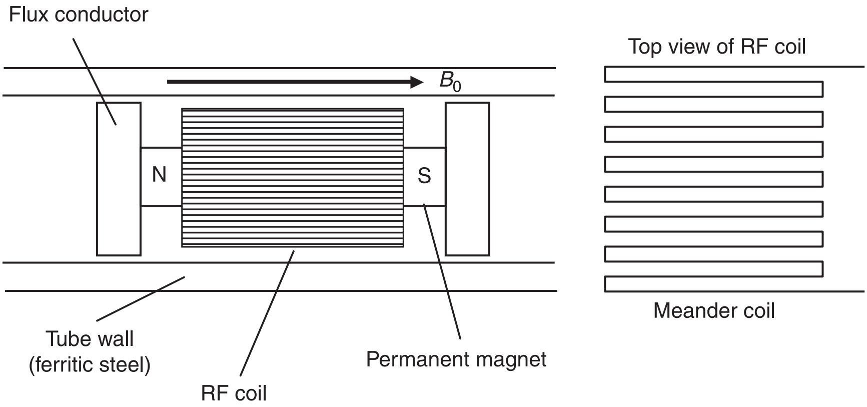
Flux conductor
B_0
N
S
Tube wall
(ferritic steel)
RF coil
Permanent magnet
Top view of RF coil
Meander coil

2.32 Arrangement of magnets and RF coil in an EMAT probe for guided SH waves in ferritic tubes (circumferential propagation).

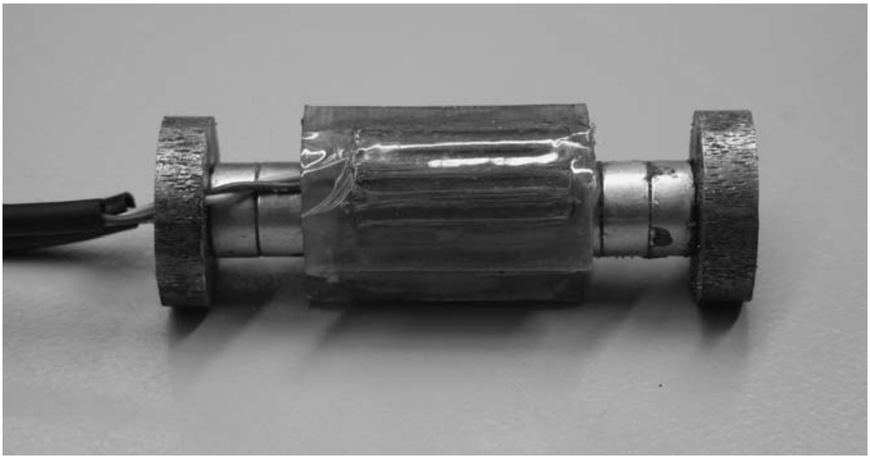

2.33 Laboratory prototype EMAT for circumferentially propagating guided waves in tubes.

and the flux conductor parts. The whole arrangement has to be moved through the inside of the tube.

Segmented transducers (phased-array transducers)

An EMAT angle beam probe for SV waves using the magnetostrictive principle, as shown in Fig. 2.28, can also be built as an EMAT phased-array probe. Only the non-segmented meander-like RF coil has to be segmented. This means the long coil with many line elements has to be divided into several shorter segments, e.g. with two or three line elements (see Fig. 2.19). As a transmitter, these segments are driven with separate power stages and, as shown earlier, with selected time (phase) delays between the electrical signals to produce a particular beam angle. When receiving, the ultrasonic signals picked up by the segments of the receiving coil are also electronically delayed in the separate receiving channels of the ultrasonic device. With this type of EMAT probe, using a beam angle of 90° it is possible to generate Rayleigh surface waves. The RF coil of an SH-wave EMAT can be made in the same way as the segmented meander-like RF coil of an SV-wave EMAT (Fig. 2.20). Results from using such SH-wave phased-array EMATs for the external detection of crack-like defects in the cladding of a reactor pressure-vessel component are given in Salzburger *et al.* (1996).

2.5 Conclusion

In this chapter, the physical principles of the electromagnetic excitation and reception of ultrasound are described. In electrically conductive material, the main mechanisms are the Lorentz force and magnetostriction. Furthermore, the design and technical realisation of EMATs for normal and angle incidence and applications were considered. EMATs have the following advantages: ultrasonic generation and reception is realised by EMATs without any coupling medium because transduction takes place at the surface of the component under test. Therefore such transducers are insensitive to environmental conditions and can be applied favourably at elevated temperatures and at high inspection speeds. EMATs can also generate a variety of ultrasonic wave types, which in practice cannot be generated by piezoelectric transducers. A disadvantage of EMATs is the lower transduction efficiency compared with piezoelectric transducers, which in most cases requires special electronic devices with high transmitter power and very low noise preamplifiers. In the past, one focus of application of EMATs has been flaw detection by guided waves (Salzburger, 2009). Another field of application using EMATs is the material characterisation by measuring residual stresses and texture.

In the future, EMATs will still be used for the inspection of components with guided waves, especially for the long-range inspection of pipes. Besides flaw detection, material characterisation using EMATs will be further developed in the future. For EMATs working magnetostrictively, ultrasonic parameters like time of flight, amplitude and phase of the ultrasonic signal can be used to determine material degradation due to neutron embrittlement and thermomechanical ageing (Altpeter *et al.*, 2010, 2011) and the stress and texture states of rolled metal products.

2.6 References

Altpeter, I., Dobmann, G., Hübschen, G., Kopp, M. and Tschuncky, R. (2010) Nondestructive characterization of neutron induced embrittlement in nuclear pressure vessel steel microstructures by using nondestructive electromagnetic testing, in *ENDE 2010 – The 15th International Workshop on Electromagnetic Nondestructive Evaluation*, West Pomeranian University of Technology, PS2/2 (93), Szczecin, 13–16 June 2010.

Altpeter, I., Tschuncky, R., Hällen, K., Dobmann, G., Boller, C. *et al.* (2011) Early detection of damage in thermo-cyclically loaded austenitic steels: Development of condition monitoring technology within the context of aging management, in *BIND 2011 – The 8th International Conference on Condition Monitoring and Machinery Failure Prevention Technologies*, Cardiff, Wales, 20–22 June 2011.

Becker, R., Dobmann, G. and Salzburger, H.-J. (1999) Process-integrated online monitoring of safety-relevant aluminum airbag pressure vessel components for a combined defect detection and material property determination by using contactless NDT (EMUS and EC) in Brusey, B. W., Bussiere, J. F., Dubois, M. and Moreau, A. (eds) *Canadian Institute of Mining, Metallurgy and Petroleum: Advanced Sensors for Metals Processing*, Quebec, Met. Soc., 151–7.

Böttger, W., Repplinger, W., Weingarten, W. and Wilbrand, A. (1987) EMA angle-probe prototype tests steel tubes on-line, *Steel Times*, 215, 8.

Dobbs, E. R. (1973) Electromagnetic generation of ultrasonic waves in Mason, W. and Thurston, R. N. (eds) *Physical Acoustics*, *Volume X*, New York, London, Academic Press, 127–91.

Gaertner, M. R., Wallace, W. D. and Maxfield, B. W. (1969) Experiments relating to the theory of magnetic direct generation of ultrasound in metals, *Phys. Rev.* 184, 702–4.

Hirao, M. and Ogi, H. (1999) An SH-wave EMAT technique for gas pipeline inspection, *NDT&E International* 32, 127–32.

Hirao, M. and Ogi, H. (2003) *EMATs for Science and Industry: Non Contacting Ultrasonic Measurements*, Boston, Kluwer Academic Publishers.

Hübschen, G., Löhr, E. and Wallerser, A. (1990) Monitoring the filling level of the RPV using stationary EMUS probes, *Nuclear Engineering and Design* 119, 459–66.

Hübschen, G., Repplinger, W. and Salzburger, H. J. (1984) Ultraschallprüfung mit elektromagnetischen Wandlern, *FhG-Berichet*, No. 1, 23–32, Lit. ISSN: 0342-1953.

Hübschen, G. and Salzburger, H. J. (1989) Inspection of dissimilar metal welds using horizontally polarized shear: SH-waves and electromagnetic ultrasonic EMUS probes, *International Journal of Pressure Vessel and Piping* 39, 331–44.

Hübschen, G., Salzburger, H. H. and Kröning, M. (1993) Progress in UT of austenitic and dissimilar metal welds using shear horizontal waves and electromagnetic US (EMUS) probes, *EPRI NDE Center: EPRI Pipe Inspection Workshop*, Charlotte, EPRI NDE Center, Sess. 2.

Igarashi, B. and Alers, G. A. (1998) Excitation of bulk shear waves in steel by magnetostrictive coupling, *1998 IEEE Ultrasonics Symposium*, 893–6.

Ilin, V. and Kharitonov, A. V. (1980) Theory of the EMA method of detecting Rayleigh waves for ferromagnetic and ferrimagnetic materials, *Sov. J. NDT* 16, 549–54.

Kawashima, K. (1994) Very high frequency EMAT for resonant measurement, *IEEE Ultrasonic Symposium Proceedings* 2, 1111–19.

Kawashima, K. and McClung, R. W. (1976) Electromagnetic ultrasonic transducer for generating and detecting longitudinal waves (with a small amount of radially polarized transverse wave), *Materials Evaluation* April, 81–90.

Maxfield, B. W. and Fortunko, C. M. (1983) The design and use of electromagnetic acoustic wave transducers, *Materials Evaluation* 41, November, 1399–408.

Miller, G. F. and Pursey, H. (1954) The field and radiation of mechanical radiators on the free surface of a semi-infinite isotropic solid, *Proc. R. Soc. Lond. A* 20, May, 223(1155), 521–4.

Mohr, W. and Hoeller, P. (1976) On inspection of thin-walled tubes for transverse and longitudinal flaws by guided ultrasonic waves, *IEEE Transactions on Sonics and Ultrasonics*, Vol. SU-23, Sept, 369–74.

Mohr, W., Huebschen, G. and Repplinger, W. (1980) Elektromagnetische Anregung senkrecht zur Einfallsebene polarisierter Ultraschalltransversalwellen und deren Anwendungspotential in der zfP, in *Deutsche Gesellschaft für Zerstörungsfreie Prüfung e. v. -DGZfP-, Berlin: Vortraege des Internationalen Symposiums "Neue Verfahren der zerstoerungsfreien Werkstoffprüfung und deren Anwendung insbesondere in der Kerntechnik"*, 17–19 September 1979.

Mohr, W. and Repplinger, W. (1978) EMA excitation of ultrasonic bulk waves with the purpose of application in NDE, *IEEE Group on Sonics and Ultrasonics: Ultrasonic Symposium 1978*, Pittsburgh, IEEE.

Morimoto, K., Arioka, N., Fukui, S. and Watanabe, Y. (1984) Development of electromagnetic acoustic transducer for heat exchanger tubes, *Non Destructive Testing Journal Japan* 2, 89–95.

Niese, F. (2010) EMUS Wanddickensensor für die Pipeline-Inspektion mit integrierter Wirbelstrom- und Streuflussprüfung, PhD Thesis, Naturwissenschaftlich-Technische Fakultät II der Universität des Saarlandes.

Niese, F., Yashnan, A. and Willems, H. (2006) Wall-thickness measurement sensor for pipeline inspection using EMAT technology in combination with pulsed eddy current and MFL, in *European Federation for Non-Destructive Testing (EFNDT): European Conference on Nondestructive Testing (9). DGZfP-Jahrestagung 2006. ZfP in Forschung, Entwicklung und Anwendung*, Berlin, Deutsche Gesellschaft für zerstörungsfreie Prüfung (DGZfP), 3.1.5.

Ogi, H. (1997) *Electromagnetic Acoustic Resonance and Noncontacting Materials*, Osaka University, Graduates School of Engineering Science, Department of Systems and Human Science, Division Mechanical Sciences, Osaka.

Salzburger, H.-J. (1988) A new design of the RF-part of electromagnetic-ultrasonic EMUS-Transducers, *4th European Conference on Non-Destructive Testing '87. Proceedings*, Vol. 4, Oxford, Pergamon Press, 2321–7.

Salzburger, H.-J. (2009) EMATs and its potential for modern NDE: State of the art and latest applications, *IEEE International Ultrasonic Symposium Proceedings*, 621–8.

Salzburger, H.-J., Dobmann, G. and Mohrbacher, H. (1999) Quality control of laser welds of tailored blanks using guided waves and EMATs in Brusey, B. W., Bussière, J. F., Dubois, M. and Moreau, A. (eds) *Canadian Institute of Mining, Metallurgy and Petroleum: Advanced Sensors for Metals Processing*, Quebec, Met. Soc., 173–83.

Salzburger, H.-J., Hübschen, G. and Kröning, M. (1996) Trockene Ultraschall-Prüfung von Reaktorkomponenten mittels EMUS – Potential, Nachweisempfindlichkeiten und Prüfkonzept, in *Staatliche Materialprüfungsanstalt Universität Stuttgart: MPA-Seminar (22). Band 2: Sicherheit und Verfügbarkeit in der Anlagentechnik mit dem Schwerpunkt Komponenten nuklearer und konventioneller Kraftwerke*, Stuttgart, 48.1–10.

Salzburger, H.-J. and Repplinger, W. (1983) Automatic in-motion inspection of the tread of railway wheels by e.m.a. excited Rayleigh waves, *Ultrasonic International 1983: Conference Proceedings*, Guildford, IPC Science and Technology Press.

Salzburger, H.-J., Wang, L. and Gao, X. (2008) In-motion ultrasonic testing of the tread of high-speed railway wheels using the inspection system AUROPA III, *17th World Conference on Nondestructive Testing*, Shanghai, China, 25–28 Oct.

Sawaragi, K., Salzburger, H. J., Hübschen, G., Enami, K., Kirihigashi, A. *et al.* (2000) Improvement of SH-wave EMAT phased array inspection by new 8-segment probes, *Nuclear Engineering and Design* 198(1–2), 153–63.

Schneider, E. and Herzer, R. (1998) Ultrasonic evaluation of stresses in the rims of railroad wheels, *Proceedings 7th European Conference on Non-destructive Testing*, Copenhagen, 26–29 May.

Thompson, R. B. (1973) A model for the electromagnetic generation and detection of Rayleigh and Lamb waves, *IEEE Transaction on Sonics and Ultrasonics*, SU-20, 340–6.

Thompson, R. B. (1978a) New configuration for the electromagnetic generation of SH waves in ferromagnetic materials, *IEEE Ultrasonic Symposium Proceedings*, 374–8.

Thompson, R. B. (1978b) A model for the electromagnetic generation of ultrasonic guided waves in ferromagnetic metal polycrystals, *IEEE Transaction on Sonics and Ultrasonics*, SU-25, 7–15.

Thompson, R. B. (1979) Generation of horizontal polarized shear waves in ferromagnetic materials using magnetostrictive coupled meander-coil electromagnetic transducers, *Appl. Phys. Lett.* 34, 175–7.

Thompson, R. B. (1990) Physical principles of measurements with EMAT transducers in Pierce, A. D. and Thruston, R. N. (eds) *Physical Acoustics, Volume XIX: Ultrasonic measurements: Measurements Methods*, Boston, Academic Press, 157–200.

Thompson, R. B., Elsley, R. K., Peterson, W. E. and Vasile, C. F. (1979) An EMAT system for detecting flaws in steam generator tubes, *1979 IEEE Ultrasonics Symposium*, 246–9.

Thompson, R. B. and Vasile, C. F. (1978) Excitation of horizontally polarized shear elastic waves by electromagnetic transducers with periodic permanent magnets, *J. Appl. Phys.* 50 (4), 2583–8.

Wilbrand, A. (1983) EMUS probes for bulk waves and Rayleigh waves, model for sound field and efficiency calculations in Höller P. (ed.) *New Procedures in Non-Destructive Testing*, Berlin, Heidelberg, New York, Springer, 71–80.

Wilbrand, A. (1984) Wechselwirkungsmechanismen bei der elektromagnetischen Ultraschallwandlung, *Materialprüfung*, 26(1/2), 7–11.

Wilbrand, A. (1987) Quantitative modeling and experimental analysis of the physical properties of electromagnetic-ultrasonic transducers in Chimenti, D. E. and Thompson, D. O. (eds) *Review of Progress in Quantitative Nondestructive Evaluation*, 7A, New York, London Plenum Press, 671–80.

Wilbrand, A., Repplinger, W., Böttger, W. and Weingarten, W. (1987) Fehlerprüfung mit elektrodynamisch angeregten freien Ultraschallwellen. Erste Erfahrungen im dynamischen Prüfbetrieb und Konzeption einer Prototypanlage Deutsche Gesellschaft für zerstörungsfreie Prüfung e.V. (DGZfP): Aktuelle Aufgaben der zfP: Bewährte Aufgaben-neue Wege, Teil 1, Berlin (DGZfP), (DGZfP- Berichtsbände 10).

Wilbrand, A., Repplinger, W., Hübschen, G. and Salzburger, H. J. (1989) EMUS systems for stress and texture evaluation by ultrasound in Dobmann, G., Green, R. E., Hauk, V., Höller, P. and Ruud, C. (eds) *Fraunhofer-Institut für zerstörungsfreie Prüfverfahren (IZfP): Nondestructive Characterization of Materials III*, Berlin, Heidelberg, New York, Springer.

3

Piezoelectric ceramics for transducers

K. UCHINO, The Pennsylvania State University, USA and
Office of Naval Research – Global, Japan

Abstract: This chapter reviews the history of piezoelectric materials in the following order: quartz, Rochelle salt, barium titanate, lead zirconate titanate, $Pb(Zr,Ti)O_3$ (PZT), lithium niobate/tantalate, relaxor ferroelectrics, PVDF, Pb-free piezoelectrics and composites. The detailed performance in conjunction with transducer applications is described.

Key words: piezoelectric material, quartz, Rochelle salt, barium titanate, lead zirconate titanate, relaxor ferroelectrics, Pb-free piezoelectrics, electromechanical coupling factor.

Note: Previously published in K. Uchino, *Advanced Piezoelectric Materials*, Woodhead Publishing, 2010.[1]

3.1 The history of piezoelectrics

The author hopes that the reader, in learning the history of piezoelectrics, will find a new perspective regarding the future of piezoelectric ceramics. Any material or product has a lifecycle determined by 'external' environmental forces, such as the four forces: social/cultural, technological, economic and political (STEP).[2] We will discuss first how these forces encouraged and discouraged the development of piezoelectric materials.

3.1.1 The dawn of piezoelectrics

The Curie brothers (Pierre and Jacques Curie) discovered the *direct piezoelectric effect* in single-crystal quartz in 1880. Under pressure, quartz and some other materials generate an electrical charge and voltage. The root of the word 'piezo' means 'pressure' in Greek; hence the original meaning of the word piezoelectricity implied 'pressure electricity'. Materials exhibiting this phenomenon also, conversely, produce a geometric strain proportional to an applied electric field. This is the *converse piezoelectric effect*, discovered by Gabriel Lippmann in 1881. Recognizing the connection between the two phenomena helped Pierre Curie to develop pioneering ideas about the fundamental role of symmetry in the laws of physics. Meanwhile, the Curie brothers put their discovery to practical use by devising the piezoelectric quartz electrometer, which could measure faint electric currents, and helped Pierre's wife, Marie Curie, 20 years later in her early research.

At 11:40 pm on 10 April 1912 the *Titanic* hit an iceberg, as the reader knows well. If the ultrasonic sonar system had been developed then, this disaster would not have happened. This tragic incident (a social force) inspired the development of ultrasonic technology using piezoelectricity.

3.1.2 World War I: underwater acoustic devices with quartz and Rochelle salt

With the start of World War I in 1914, more money was used to fund the accelerating development of ultrasonic technology in order to search for German U-boats at sea. This is the strongest force both socially and politically. Dr Paul Langevin, a professor at the Industrial College of Physics and Chemistry in Paris, who had many friends including Albert Einstein, Pierre Curie and Rutherford, started to experiment on ultrasonic signal transmission in seawater, in collaboration with the French Navy. Langevin succeeded in transmitting an ultrasonic pulse into the sea in the south of France in 1917. We can learn much about his practical development approaches from his original transducer design (Fig. 3.1). First, 40 kHz was chosen for the sound wave frequency. Increasing the frequency (shorter wavelength) gives a better resolution of the objective; however, it also leads to a rapid decrease in the reachable distance. Note that quartz and Rochelle salt single crystals were the only piezoelectric materials available in the early twentieth

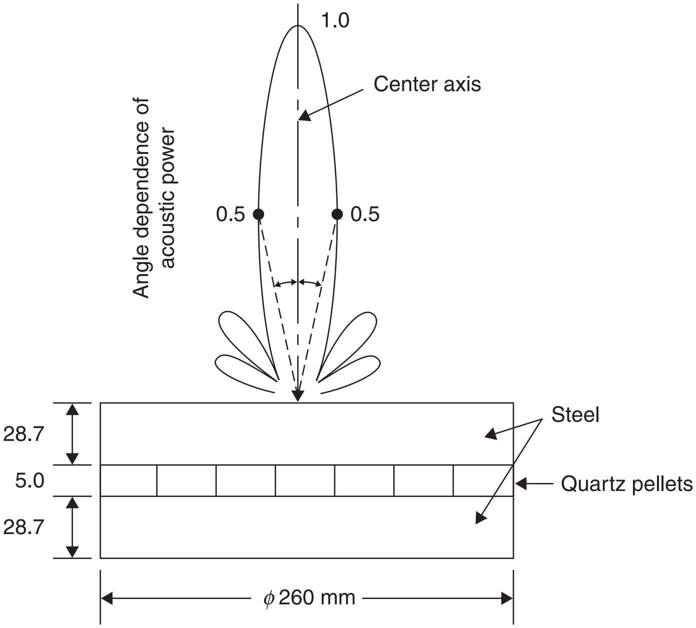

3.1 Langevin's transducer design.

century. Since the velocity of sound in quartz is about 5 km.s^{-1}, 40 kHz corresponds to a wavelength of 12.5 cm. If we use mechanical resonance in the piezoelectric material, a 12.5/2 = 6.25-cm-thick single crystal of quartz is required. However, at that time it was not possible to produce such a large high-quality single crystal.[3]

In order to overcome this dilemma, Langevin invented a new type of transducer: small quartz crystals were arranged in a mosaic sandwiched by two steel plates. Since the velocity of sound in steel is in a similar range to quartz, with a total thickness of 6.25 cm he succeeded in achieving a thickness resonance frequency around 40 kHz. This type of sandwich structure is called the *Langevin type* and is still commonly used. The quartz is located at the center, which corresponds to the nodal plane of the thickness vibration mode, where the maximum stress/strain (or the minimum displacement) is generated.

Further, in order to provide a sharp directivity for the sound wave, Langevin used a sound radiation surface with a diameter of 26 cm (more than double the wavelength). Since the half-maximum-power angle ϕ is

$$\phi = 30 \times (\lambda/2a) \text{ [degree]}, \tag{3.1}$$

where λ is the wavelength in the transmission medium (not in the steel) and a is the radiation surface radius, if we use $\lambda = 1500$ [m/s]/40 [kHz] = 3.75 cm and $a =$ 13 cm, we obtain $\phi = 4.3°$ for this original design. He succeeded in detecting a U-boat 3000 m away. Moreover, Langevin also observed many bubbles generated during his experiments, which seems to be the ‘cavitation’ effect. About 60 years later, this effect was used for ultrasonic cleaning systems. Though the mechanical quality factor is significantly high (i.e., low loss) in quartz, a major problem for this transducer application includes low electromechanical coupling k, resulting in (1) low mechanical underwater transmission power and receiving capability, and in (2) a narrow frequency bandwidth. In addition, only Brazil produced natural quartz crystals at that time. Thus, US researchers used Rochelle salt single crystals, which have a superior electromechanical coupling factor (k is close to 100% at 24 °C!) with a simple synthesizing process. Nicholson *et al.*[4] researched piezoelectric underwater transducers during World War I. The General Electric Laboratory (Moore[5]) and the Brush Company produced large quantities of crystals in the early 1920s. See Busch[6] for a detailed history of Rochelle salt.

Rochelle salt is sodium potassium tartrate [$NaKC_4H_4O_6 \cdot 4H_2O$], and has Curie temperatures at −18 °C and 24 °C with a narrow operating range of temperature for ferroelectricity, leading to high electromechanical coupling at 24 °C. On the other hand, its performance has a rather large temperature dependence. Worldwide, it was used for underwater transducer applications until barium titanate and PZT were discovered. Since this crystal is water soluble, it is inevitably degraded by humidity. However, the most delicate problem is its weakness to dryness. No suitable coating technology was developed for Rochelle salt devices to achieve a desired lifetime.

Much research effort was spent on discovering alternative piezoelectrics to Rochelle salt with better stability or reliability and continued after WWI.

Potassium di-hydrogen phosphate (KH_2PO_4 or KDP) was discovered by Georg Busch in 1935.[7] Knowing about the ferroelectricity of Rochelle salt and guessing that it was due to hydrogen bonds in the crystal, Busch searched hydrogen-bond crystals systematically and found KDP as a new ferroelectric/piezoelectric material. Though many piezoelectric materials (such as Rochelle salt, barium titanate and PVDF) were discovered accidentally through 'serendipity', KDP is an exceptional example of discovery through a perfectly planned systematic approach. Following KDP, other materials such as ammonium dihydrogen phosphate (ADP), ethylene diamine tartrate (EDT), dipotassium tartrate (DKT), etc., were discovered and tested. However, most of the water-soluble single-crystal materials have been forgotten because of the better performance and preparation for synthetic quartz and perovskite ceramics (BT, PZT).

3.1.3 World War II: the discovery of barium titanate

Barium titanate ($BaTiO_3$ or BT) ceramics were discovered independently during World War II in three countries: in the US by Wainer and Salomon[8] in 1942, in Japan by Ogawa[9] in 1944, and in Russia by Vul[10] in 1944. Compact radar systems required compact high-capacitance 'condensers' (at that time, the term 'condenser' rather than 'capacitor' was used). Based on the widely used 'tita-con' (titania condenser) composed of TiO_2-MgO, researchers doped various oxides to find higher permittivity materials. The noteworthy article by Ogawa and Waku[11] describes investigations on three dopants, CaO, SrO and BaO, for a wide fraction range. The maximum permittivity was found for $CaTiO_3$, $SrTiO_3$ and $BaTiO_3$ (all were identified as perovskite structures). In particular, the permittivity, over 1000 in $BaTiO_3$, was enormous (ten times higher than for tita-con) for that time, as illustrated in Fig. 3.2.

It should be pointed out that the original discovery of $BaTiO_3$ was not related to its piezoelectric properties. Equally important were the independent discoveries by Gray at Erie Resister (patent applied in 1946)[12] and by Shepard Roberts at MIT (published in 1947)[13] that the electrically poled BT exhibited 'piezoelectricity' due to domain re-alignment. At that time, researchers were arguing that a randomly oriented 'polycrystalline' sample should not exhibit 'piezoelectricity', but instead the secondary effect, 'electrostriction'. Because Gray was the first to verify that the polycrystalline BT exhibited piezoelectricity once it was electrically poled, he is considered to be the 'father of piezo-ceramics'.

The ease of mixture selection and manufacturability of BT ceramics prompted W. P. Mason[14] and others to study transducer applications with these electro-ceramics. Piezoelectric BT ceramics had a reasonably high coupling coefficient and were not water soluble, but the bottlenecks were (1) a large temperature coefficient for the electromechanical parameters because of the second phase transition (from tetragonal to rhombohedral) around room temperature or the operating temperature, and (2) an aging effect due to the low Curie temperature

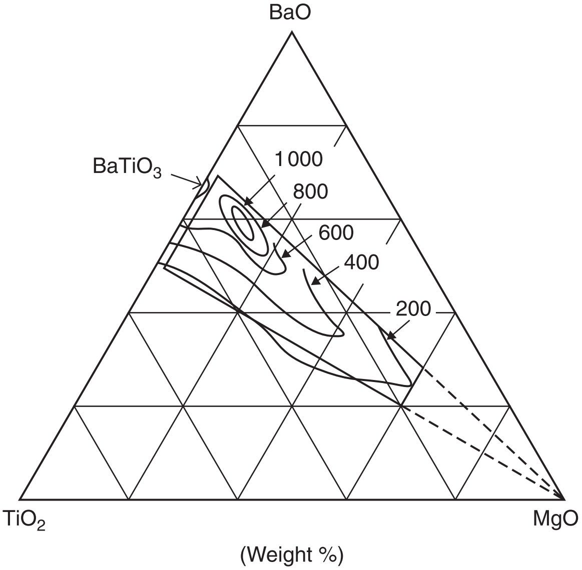

3.2 Permittivity of tita-con doped with BaO.

(the phase transition from cubic to tetragonal), which is around only 120 °C. In order to increase the Curie temperature above 120 °C, so as to decrease the second transition temperature below −20 °C, various ion replacements, such as Pb and Ca, were studied. From these trials, a new system PZT was discovered.

The first multilayer capacitor was invented by Sandia Research Laboratory engineers during the Manhattan Project using the coating/pasting method. The capacitor was used for the switch in the nuclear bomb dropped on Hiroshima (private communication with Dr Kikuo Wakino, Murata Manufacturing).

3.1.4 Discovery of PZT

PZT

Following the methodology used for the discovery of BT, the perovskite isomorphic oxides such as $PbTiO_3$, $PbZrO_3$ and $SrTiO_3$ and their solid solutions were intensively studied. In particular, the discovery of antiferroelectricity in lead zirconate[15] and the determination of the $Pb(Zr,Ti)O_3$ system phase diagram by the Japanese group Sawaguchi *et al.*[16] are noteworthy. Figure 3.3 shows the phase diagram of the $Pb(Zr,Ti)O_3$ solid-solution system reported by Sawaguchi *et al.*,[16] which was read and cited worldwide and triggered the PZT era.

The lead zirconate titanate system was discovered in a similar way to BT. This material was discovered by the Japanese research group, but its superior piezoelectricity was discovered by a US researcher Bernard Jaffe in 1954, then at

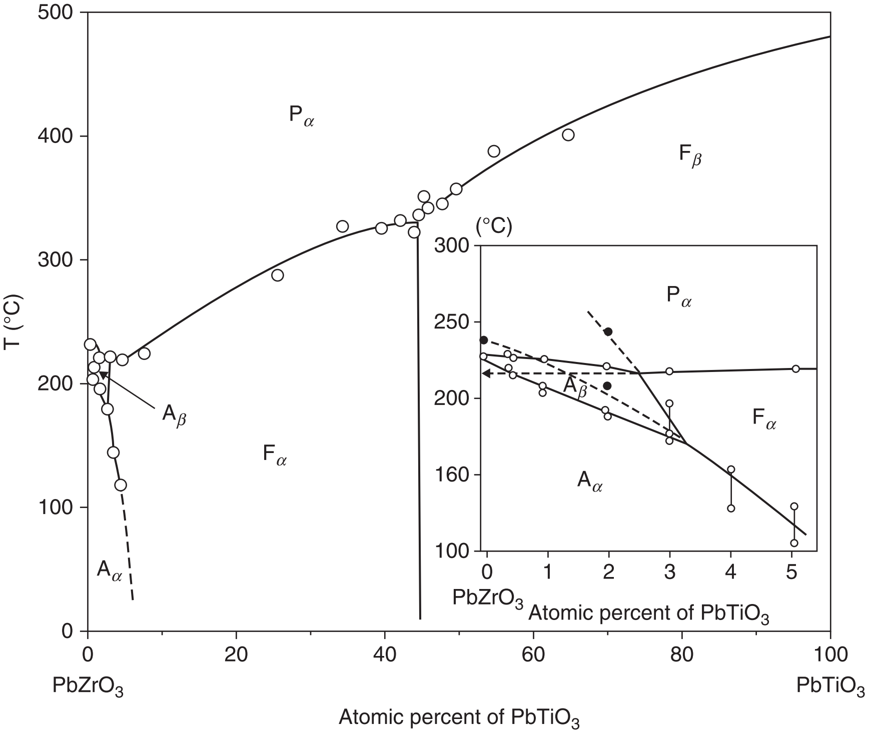

3.3 Phase diagram of the $Pb(Zr,Ti)O_3$ solid-solution system.

the National Bureau of Standards (NBS). He knew about the Japanese group's serial studies of the PZT system, and focused on the piezoelectric measurement around the so-called morphotropic phase boundary (MPB) between the tetragonal and rhombohedral phases. He found enormous electromechanical coupling around that mixture range.[17] His patent had a significant effect on the future development strategies of Japanese electro-ceramic industries. So, now there were two important classes of material with superior piezoelectricity: (1) Pb-included ceramics and (2) MBP mixtures.

Clevite Corporation

As mentioned in Section 3.1.2, the Brush Development Company manufactured Rochelle salt single crystals and their bimorph components for phonograph applications in the 1930s. In the 1940s they commercialized piezoelectric quartz crystals using a hydrothermal process. There was a large piezoelectric group in Brush led by Hans Jaffe. However, in 1952 the Clevite Corporation was formed by merging the Cleveland Graphite Bronze Corporation and Brush, and Hans Jaffe welcomed Bernard Jaffe from NBS to Clevite and they accelerated the development of PZT. Hans Jaffe and Bernard Jaffe were not related (just accidentally having the same last name). Their contribution to developing varieties of PZTs (i.e. hard and soft PZTs) by doping with acceptor (Mn) and donor (Nb) ions is noteworthy. 'PZT' was a trademark of Clevite, which prevented its use by other companies. These episodes are described in their famous Bible-like book, co-authored with Cook, *Piezoelectric Ceramics*.[18]

Clevite first concentrated on high-quality military and commercial piezoelectric filters. In the mid-1960s, they tried to develop consumer filters for AM radios, especially automobile radios, but the initial costs were too high. However, after 1967, they successfully started mass production of 10.7 MHz ceramic filters for FM automobile radios, and delivered them to Philco-Ford. Clevite was bought by Gould Inc. in 1969 and resold to Vernitron in 1970. These drastic business actions terminated the promising piezoelectric filter program initiated by Clevite.

Murata Manufacturing Company

The Murata Manufacturing Company Ltd was founded by Murata in 1944. He learned ceramic technology from his father, who was the chairman of the former Murata Pottery Manufacturing Company. Murata Manufacturing Company started with ten employees to produce electro-ceramic components. After World War II, under the guidance of Prof. Tetsuro Tanaka, who was one of the promoters of the Barium Titanate Study Committee during WWII, Murata started intensive studies on devices based on barium titanate ceramics. The first products with barium titanate ceramics were 50-kHz Langevin-type underwater transducers for fish-finders in Japan.[19] The second products were mechanical filters.[20]

In 1960, Murata decided to introduce PZT ceramics by paying a royalty to Clevite Corporation. As already mentioned, because of the disappearance of Clevite from the filter business, Murata increased their worldwide share of ceramic filter products.

Ternary system

Since PZT was protected by Clevite's patent, ternary solid solutions based on PZT with another perovskite phase were investigated intensively by Japanese ceramic companies in the 1960s. Examples of these ternary mixtures are PZTs in solid solution with $Pb(Mg_{1/3}Nb_{2/3})O_3$ (Matsushita-Panasonic), $Pb(Zn_{1/3}Nb_{2/3})O_3$ (Toshiba), $Pb(Mn_{1/3}Sb_{2/3})O_3$, $Pb(Co_{1/3}Nb_{2/3})O_3$, $Pb(Mn_{1/3}Nb_{2/3})O_3$, $Pb(Ni_{1/3}Nb_{2/3})O_3$ (NEC), $Pb(Sb_{1/2}Sn_{1/2})O_3$, $Pb(Co_{1/2}W_{1/2})O_3$ and $Pb(Mg_{1/2}W_{1/2})O_3$ (Du Pont), all of which were patented by different companies (almost all of these patents have now expired). The ternary systems have more flexibility when designing materials and so exhibit, in general, better performance than the binary PZT system, which created advantages for the Japanese manufacturers over Clevite and other US companies.

3.1.5 Lithium niobate/tantalate

Lithium niobate and lithium tantalate have the same type of chemical formula ABO_3 as $BaTiO_3$ and $Pb(Zr,Ti)O_3$. However, their crystal structure is not perovskite but ilmenite. Ferroelectricity in single crystals of $LiNbO_3$ (LN) and $LiTaO_3$ (LT) was discovered in 1949 by two researchers at Bell Telephone Laboratories, Matthias and Remeika.[21] Since the Curie temperatures in these materials are high (1140 °C and 600 °C for LN and LT, respectively), perfect linear characteristics can be observed in electro-optic, piezoelectric and other effects at room temperature. Though fundamental studies had been conducted, particularly in their electro-optic and piezoelectric properties, commercialization was slow initially because the figures of merit were not very attractive in comparison with perovskite ceramic competitors. Incidentally, the chemical element niobium was known as columbium (Cb) in the 1950s.

After Toshiba started mass production of LN single crystals in the 1980s, there was a drastic reduction in production costs. Murata commercialized filters, using the surface acoustic wave (SAW) mode on a LN single crystal, the so-called SAW filters. See Uchino[22] for recent developments of electro-optic light valves, switches and photorefractive memories, which are derived from optical communication technology.

3.1.6 Relaxor ferroelectrics: ceramics and single crystals

After the discovery of BT and PZT, in parallel to the PZT-based ternary solid solutions, complex perovskite-structured materials were intensively synthesized and investigated in the 1950s. In particular, the contribution by the Russian research group led by Smolenskii was enormous. They reported a huge dielectric permittivity in $Pb(Mg_{1/3}Nb_{2/3})O_3$ (PMN)[23] and $Pb(Zn_{1/3}Nb_{2/3})O_3$ (PZN).[24] PMN-based ceramics became major components of high-K (10 000 K) capacitors in the 1980s.

There were two epoch-making discoveries in the late 1970s and early 1980s, used in electromechanical couplings with relaxor ferroelectrics: electrostrictive actuator materials and high *k* (95%) piezoelectric single crystals.

Cross *et al.*[25] reported an extraordinarily large secondary electromechanical coupling, i.e. the 'electrostrictive' effect, with a strain level higher than 0.1% at room temperature, exhibiting negligible hysteresis with a rising and falling electric field, in a mix of 0.9 PMN and 0.1 $PbTiO_3$ (Fig. 3.4). Every phenomenon has primary and secondary effects, which are sometimes recognized as linear and quadratic phenomena, respectively. In actuator materials, these correspond to the piezoelectric and electrostrictive effects.

When the author started actuator research in the middle of the 1970s, precise 'displacement transducers' (we initially used this terminology) were required in the Space Shuttle program, particularly for deformable mirrors for controlling

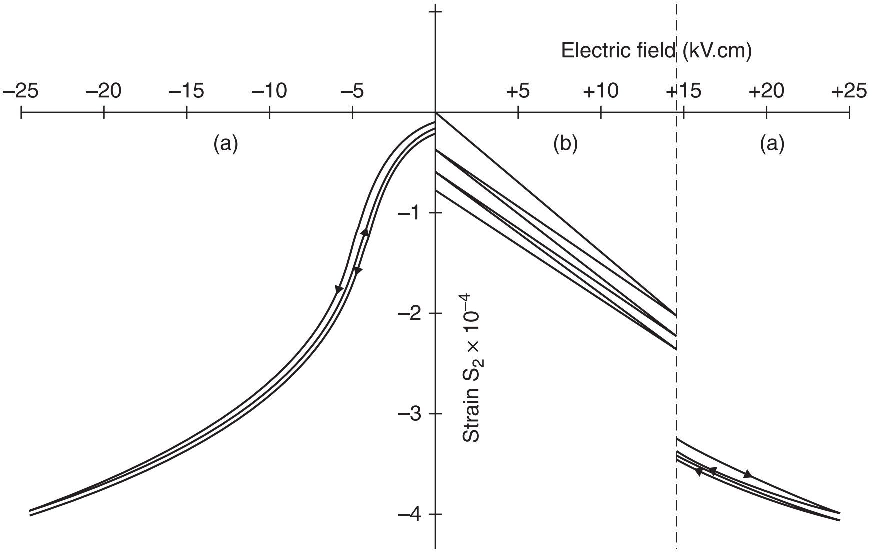

3.4 Strain level vs. electric field in a mix of 0.9 PMN and 0.1 $PbTiO_3$.

optical path lengths over several wavelengths (1 μm). Conventional piezoelectric PZT ceramics were plagued by hysteresis and aging effects under large electric fields; this was a serious problem for an optical positioner. Electrostriction, which is the secondary electromechanical coupling observed in centro-symmetric crystals, is not affected by hysteresis or aging.[22] Piezoelectricity is a primary (linear) effect, where the strain is generated in proportion to the applied electric field, while electrostriction is a secondary (quadratic) effect, where the strain is in proportion to the square of the electric field (with a parabolic strain curve). The electrostriction response should be much faster than the time required for domain reorientation in piezoelectrics and ferroelectrics. In addition, electric poling is not required. However, at that time, most researchers believed that the secondary effect would be minor, and could not provide a larger contribution than the primary effect. Of course, this may be true in most cases, but the author's group actually discovered that relaxor ferroelectrics, such as the lead magnesium niobate-based solid solutions, exhibit enormous electrostriction. This discovery, in conjunction with the invention of Uchino's multilayer actuator (1978), accelerated the development of piezoelectric actuators after the 1980s.

Prof. Nomura's group was interested in making single crystals of PZT in the 1970s, in order to clarify the crystal orientation dependence of piezoelectricity. However, it was difficult to prepare large single crystals around the MPBs (52/48). Thus, we focused on the $Pb(Zn_{1/3}Nb_{2/3})O_3$-$PbTiO_3$ solid-solution system, which has a phase diagram similar to the PZT system, but whose large single crystals are rather easily prepared. Refer to the MPB between the rhombohedral and tetragonal

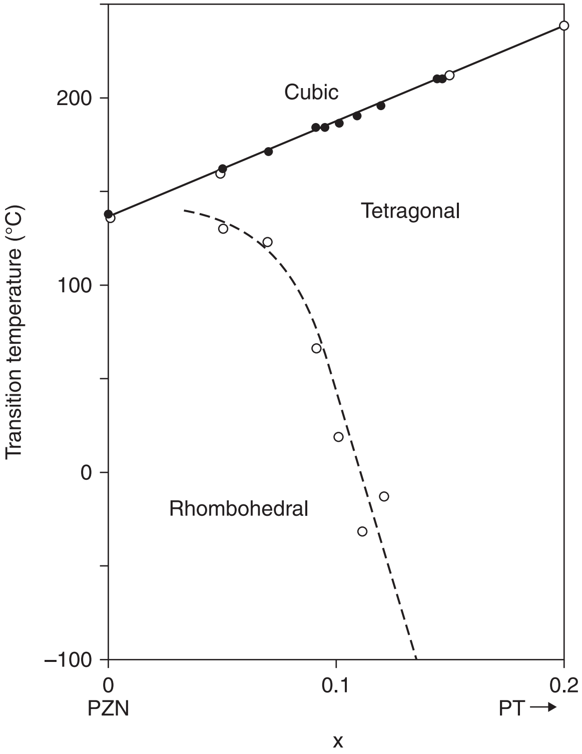

3.5 Phase diagram for PZN-PT.

phases in Fig. 3.5 compared with Fig. 3.3.[26] Figure 3.6 shows the changes of the electromechanical coupling factors with mole fraction of lead titanate ($PbTiO_3$ or PT) in the $Pb(Zn_{1/3}Nb_{2/3})O_3$-$PbTiO_3$ solid-solution system, reported by Kuwata *et al.* in 1982,[27] which was one of the most widely cited papers in the world in 1998. The MPB mix, 0.91 PZN–0.09 PT, exhibits a maximum for all parameters, as expected, and the highest values of the electromechanical coupling factor k_{33}^* and the piezoelectric constant d_{33}^* reached 95% and 1600 $pC.N^{-1}$, respectively. When a young PhD student, Kuwata, first reported these large numbers to the author, I did not believe them. We worked together to re-examine the experiments. When I saw the antiresonance frequency was almost twice the resonance frequency, I had to believe the incredibly high k value. The author still remembers that the first submission of our manuscript had been rejected because the referee did not 'believe this large value'. The maximum k_{33} in 1980 was about 72% in PZT-based ceramics. The paper was eventually published after communicating for one year by sending the raw admittance curves, etc. However, our original discovery was not believed or not required for applications until the middle of the 1990s.

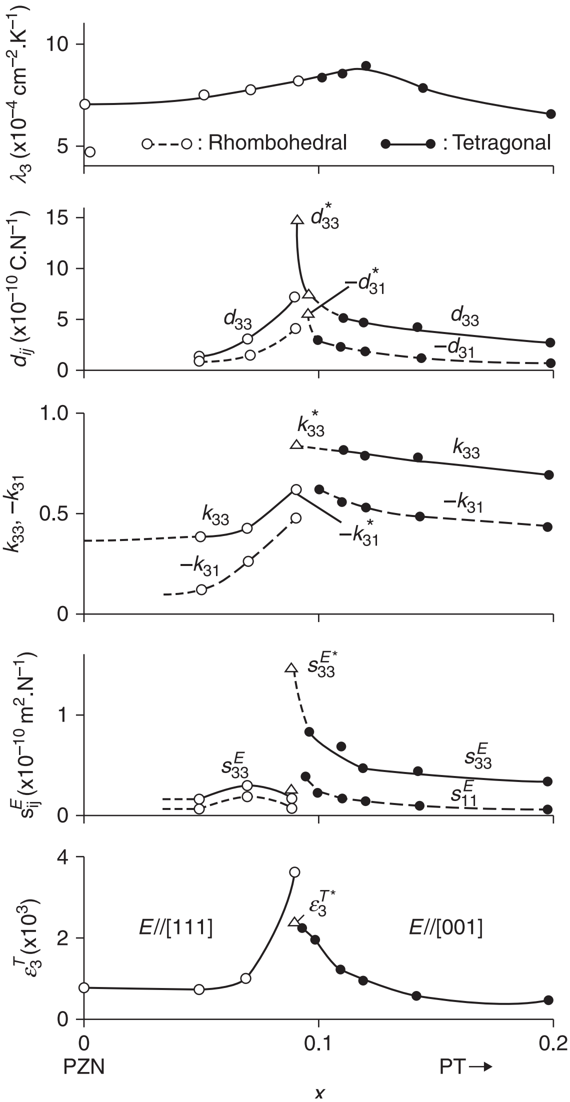

3.6 Changes of the electromechanical coupling factors with mole fraction of PT in the PZN-PT solid-solution system.

The economic recession and the aging population (the average life expectancy of Japanese women is now 86 years) in Japan have accelerated the development of medical technology, and high-*k* piezoelectric materials have been used for medical acoustics since the middle of the 1990s. Toshiba investigated PZN-PT single crystals in the 1980s aiming at medical acoustic applications, having a strong background in manufacturing the crystal lithium niobate. The data reported

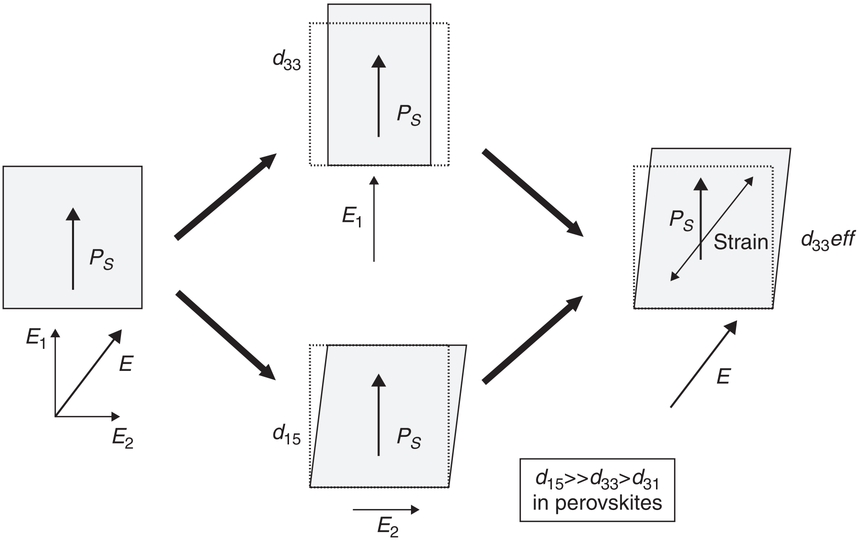

3.7 Intuitive model of piezoelectricity in relaxor ferroelectrics.

15 years prior were confirmed and improved data were obtained.[28] In parallel, Park and Shrout at Pennsylvania State University demonstrated strains as large as 1.7%, induced for the PZN-PT solid-solution single crystals.[29] The reader may be aware of the present fever regarding the application of these single crystals, sponsored by the US Navy. The single-crystal relaxor ferroelectric is one of those rare examples of a discovery being revived long after its original discovery, in this case 15 years later.

It is notable that the highest values are observed for a rhombohedral composition only when the single crystal is poled along the perovskite [001] axis, not along the [111] spontaneous polarization axis. Figure 3.7 is an intuitive model of the principles of this type of piezoelectricity, showing how the crystal orientation affects perovskite ferroelectrics. The largest electromechanical coupling is for the d_{15} shear mode in a perovskite structure because of the ease of rotation of the oxygen octahedron, in comparison with the squeeze deformation of the octahedron. See the theoretical paper by Du *et al.*,[30] which was one of the most widely cited papers in the world in 1998.

3.1.7 PVDF

In 1969, the piezoelectricity of polyvinylidene difluoride (PVDF) was discovered by Kawai at Kureha.[31] The piezoelectric coefficients of poled thin films of the material were reported to be as large as 6–7 $pC.N^{-1}$, ten times larger than that observed in any other polymer.

PVDF has a glass transition temperature (T_g) of about −35 °C and is typically 50–60% crystalline. To give the material its piezoelectric properties, it is mechanically stretched to orient the molecular chains and then poled under tension. Unlike other popular piezoelectric materials, such as PZT, PVDF has a negative d_{33} value. Physically, this means that PVDF will compress instead of expand or vice versa when exposed to an electric field. The PVDF-trifluoroethylene (PVDF-TrFE) copolymer is a well-known piezoelectric, which has been much used in sensor applications such as keyboards.

Bharti *et al.* reported that the field-induced strain level can be significantly enhanced by up to 5% with high-energy electron irradiation onto the PVDF films.[32]

3.1.8 Pb-free piezoelectrics

The twenty-first century has been called 'the century of environmental management'. We are facing serious global problems such as the accumulation of toxic wastes, the greenhouse effect, contamination of rivers and seas, lack of energy sources, oil, natural gas, etc. In 2006, the European Union issued a directive on the restriction of the use of certain hazardous substances in electrical and electronic equipment (RoHS), which explicitly limits the use of lead (Pb) in electronic equipment.

This means we may need to regulate the use of lead zirconate titanate (PZT), the most widely known piezoelectric ceramic, in the future. The Japanese and European industrial and research communities may see further governmental regulation on the use of PZT in the next 10 years. RoHS seems to be a significant threat to those piezoelectric companies that use only PZT piezo-ceramics. However, this is an opportunity for companies to consider alternative piezo-ceramics.

Pb (lead)-free piezo-ceramics began to be developed after 1999. Figure 3.8 shows statistics for various lead-free piezoelectric ceramics. The proportion of papers and patents for bismuth compounds [both the bismuth-layered type and the $(Bi,Na)TiO_3$ type] exceeds 61%. This is because bismuth compounds are easily fabricated in comparison with other compounds. Figure 3.9 shows the current best data reported by Toyota Central Research Lab, where strain curves for oriented and unoriented (K,Na,Li) $(Nb,Ta,Sb)O_3$ ceramics are shown.[33] Note that the maximum strain reaches up to 1500×10^{-6}, which is equivalent to the PZT strain.

3.1.9 Composites

Composite effects

Kitayama and Sugawara, Nippon Telegraph and Telephone, presented a paper on piezo-ceramic/polymer composites at the Japan IEEE Conference in 1972, which

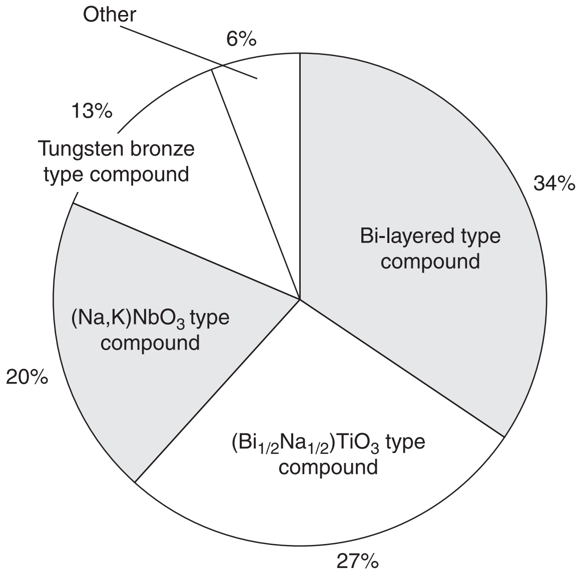

3.8 Percentages of papers and patents for lead-free piezoelectric compounds.

seems to be the first paper on piezoelectric-based composites.[34] Their paper discussed hot-rolled composites made from PZT powder and PVDF, and reported on the piezoelectric and pyroelectric characteristics. These composites are flexible, like PVDF, but have a higher piezoelectric performance than PVDF.

The contribution of Newnham *et al.* in establishing composite connectivity and in summarizing the sum, combination and product effects promoted the systematic study of piezo-composites.[35] In some cases, the averaged value of the output of a composite exceeds the outputs of both Phase 1 and Phase 2. Consider two different outputs, Y and Z, for two phases (i.e. Y_1, Z_1 and Y_2, Z_2). When a *figure of merit* (FOM) for an effect is given by the fraction (Y/Z), we may expect an extraordinary effect. Suppose that Y and Z follow the convex-type and concave-type sum effects, respectively, as illustrated in Fig. 3.10. The combination value Y/Z will exhibit a maximum at an intermediate ratio of phases; that is, the average FOM is higher than the FOMs for the pure phases (Y_1/Z_1 or Y_2/Z_2). This is called a *combination effect*. Newnham's group studied various connectivity piezo-ceramic/polymer composites that exhibited a combination property of g (the *piezoelectric voltage constant*) given by $d/\varepsilon_0\varepsilon$ (where d is the piezoelectric strain constant and ε is the relative permittivity), where d and ε follow the convex- and concave-type sum effects.

Magnetoelectric composites

When Phase 1 has an output Y for an input X, and Phase 2 has an output Z for an input Y, we would expect that a composite of them would have an output Z for

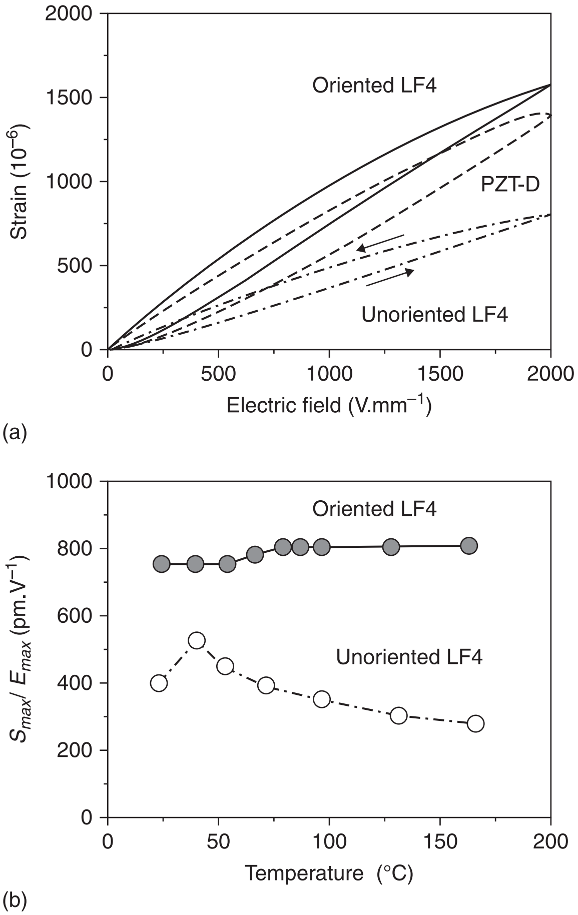

3.9 Strain curves for oriented and unoriented (K,Na,Li) (Nb,Ta,Sb)O_3 ceramics.

an input *X*. A completely new function is created for the composite structure, called the *product effect*.

Philips developed a magnetoelectric material based on the product effect,[36] which produces an electric voltage under a magnetic field, aiming to create a magnetic field sensor. This material was composed of magnetostrictive $CoFe_2O_4$ and piezoelectric $BaTiO_3$ mixed and sintered together. Figure 3.11(a) shows a micrograph of a transverse section of a unidirectionally solidified rod of the material with an excess of TiO_2. Four finned spinel dendrites of $CoFe_2O_4$ can be seen in the bulky whitish matrix of $BaTiO_3$. Figure 3.11(b) shows the magnetic field dependence of the magnetoelectric effect in an arbitrary unit measured at room temperature. When a magnetic field is applied to this composite, the cobalt ferrite exhibits magnetostriction, which is transferred to the barium titanate as

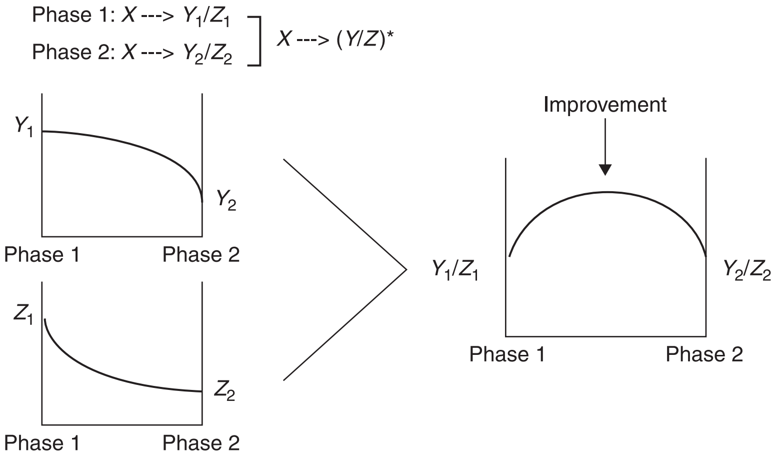
Phase 1: X ---> Y1/Z1
Phase 2: X ---> Y2/Z2
X ---> (Y/Z)*
Y1
Y2
Phase 1
Phase 2
Z1
Z2
Phase 1
Phase 2
Improvement
Y1/Z1
Y2/Z2
Phase 1
Phase 2

3.10 Output of a composite.

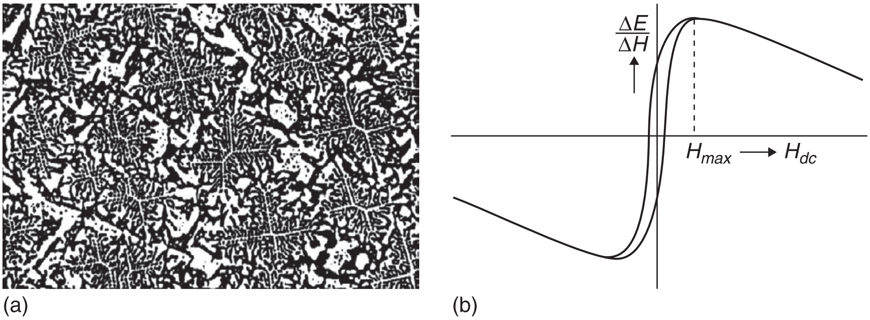
(a) (b)

3.11 (a) Micrograph of a transverse section of a unidirectionally solidified rod of a material with an excess of TiO_2. (b) Magnetic field dependence of the magnetoelectric effect.

stress, leading to the generation of a charge/voltage via the piezoelectric effect in the $BaTiO_3$.

Ryu *et al.* created a laminate structure from the magnetoelectric composite.[37] They used terfenol-D and high-*g* soft PZT layers, which have a much superior performance than cobalt ferrite and BT. However, due to the difficulty in co-firing these two materials, they used a laminated structure. This type of structure is now a standard for magnetoelectric sensor design as a microelectromechanical system (MEMS).

Piezoelectric dampers

An intriguing application of PZT composites is as passive mechanical dampers. Consider a piezoelectric material attached to an object whose vibration is to be

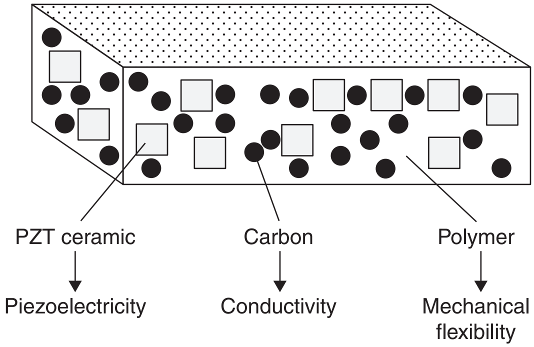

3.12 Composite of a polymer and a piezo-ceramic powder.

damped. When vibration is transmitted to the piezoelectric material, the vibration energy is converted into electrical energy by the piezoelectric effect, and an AC voltage is generated. If a resistor is added, however, the energy converted into electricity is consumed in Joule heating of the resistor, and the amount of energy converted back into mechanical energy is reduced, so that the vibration is rapidly damped. Taking the series resistance as R, the capacitance of the piezoelectric material as C and the vibration frequency as f, damping takes place most rapidly when the series resistor is selected in such a manner that the *impedance matching* condition, $R = 1/2\pi f\mathrm{C}$, is satisfied.[38]

Being brittle and hard, ceramics are difficult to assemble directly into a mechanical system. Hence, flexible composites can be useful in practice. When a composite of a polymer and a piezo-ceramic powder is fabricated (Fig. 3.12), the electrical conductivity of the composite is greatly enhanced by the addition of small amounts of carbon black.[39] By carefully selecting the electrical conductivity of the composite (i.e. electrical impedance matching), the ceramic powder effectively forms a series circuit with the carbon black, so that the vibration energy is dissipated effectively. The conductivity of the composite changes by more than ten orders of magnitude around a certain carbon fraction called the 'percolation threshold', where the carbon/powder link starts to be generated. This eliminates the use of external resistors. Note that the damper material exhibits a selective damping performance for a certain vibration frequency, depending on the selected resistivity of the composite, which can be derived from the electrical impedance matching between the permittivity and resistivity.

3.1.10 Other piezoelectric-related materials

Photostrictive materials

Photostriction was discovered by Dr P. S. Brody and the author independently almost at the same time in 1981.[40,41] In principle, the photostrictive effect arises from a superposition of the 'bulk' photovoltaic effect, i.e. the generation of a large

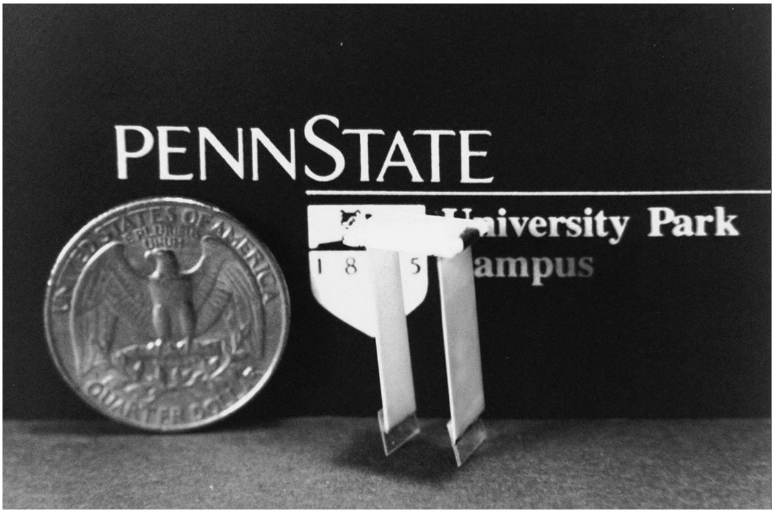

3.13 Two bimorph legs fixed to a plastic board.

voltage by the irradiation of light, and the converse piezoelectric effect, i.e. expansion or contraction under the voltage applied.[41] In certain ferroelectrics, a constant electromotive force is generated when they are exposed to light, and a photostrictive strain results from the coupling of this bulk photovoltaic effect to inverse piezoelectricity. A bimorph unit has been made from the ceramic PLZT 3/52/48 doped with slight amounts of tungsten.[42] The remnant polarization of one PLZT layer is parallel to the plate and in an opposite direction to the other plate. When violet light is irradiated on one side of the PLZT bimorph, a photovoltage of 1 kV.mm^{-1} is generated, causing a bending motion. The tip displacement of a 20-mm bimorph, 0.4 mm in thickness, was 150 μm, with a response time of 1 s.

A photo-driven micro-walking device, designed to move by light illumination, has been developed.[43] As shown in Fig. 3.13, it is a simple structure, having neither wires nor electric circuitry, with two bimorph legs fixed to a plastic board. When the legs are irradiated alternately with light, the device moves like an inchworm with a speed of 100 μm.min^{-1}.

In order to develop thick-film photostrictive actuators for space structure applications, in collaboration with the Jet Propulsion Laboratory, Penn State investigated the optimal range of sample thickness and surface roughness for photostriction. It was found that 30-μm-thick PLZT films exhibit the maximum photovoltaic phenomenon.[44]

Monomorphs

A 'monomorph' is defined as a single uniform material which can bend under an electric field. A semiconducting piezoelectric plate can generate this intriguing bending phenomenon, as discovered by Uchino's group.[45] When attending a conference of the Physical Society of Japan, the author learned about a surface layer on a ferroelectric single crystal due to the formation of a Schottky barrier. Polycrystalline piezoelectric samples were used by Uchino's group, with reduction processes to increase the thickness of the Schottky barrier. We succeeded in developing a monolithic bending actuator. A monomorph device has been developed to replace conventional bimorphs, with a simpler structure and manufacturing process. A monomorph plate 30 mm in length and 0.5 mm in thickness can generate a tip displacement of 200 µm, equal in magnitude to that of conventional bimorphs. The 'rainbow' actuator manufactured by Aura Ceramics[46] is a modification of these semiconducting piezoelectric monomorphs, where half of the piezoelectric plate is reduced to make a thick semiconducting electrode bend.

3.2 Piezoelectric materials: present status

In this section, the author discusses the fundamentals of piezoelectricity and gives the present status of the materials.

3.2.1 Piezoelectric figures of merit

There are five important figures of merit in piezoelectrics: the *piezoelectric strain constant d*, the *piezoelectric voltage constant g*, the *electromechanical coupling factor k*, the *mechanical quality factor Q_M* and the *acoustic impedance Z*.

Piezoelectric strain constant d

The magnitude of the induced strain x by an external electric field E is given by this figure of merit (an important figure of merit for actuator applications):

$$x = dE. \qquad [3.2]$$

Piezoelectric voltage constant g

The induced electric field E is related to an external stress X through the piezoelectric voltage constant g (an important figure of merit for sensor applications):

$$E = gX. \qquad [3.3]$$

Taking into account the relation, $P = dX$, we obtain an important relation between g and d:

$$g = d/\varepsilon_0\varepsilon \qquad [3.4]$$

where ε is the relative permittivity.

Electromechanical coupling factor k

The terms *electromechanical coupling factor*, *energy transmission coefficient* and *efficiency* are sometimes confused.[47] All are related to the conversion rate between electrical energy and mechanical energy, but their definitions are different.[48]

(a) *The electromechanical coupling factor k*

$$k^2 = (\text{Stored mechanical energy/input electrical energy}) \qquad [3.5]$$

or

$$k^2 = (\text{Stored electrical energy/input mechanical energy}). \qquad [3.6]$$

Consider Eq. 3.5 when an electric field E is applied to a piezoelectric material. See Fig. 3.14(a) left. Since the input electrical energy is $(1/2)\ \varepsilon_0\varepsilon\, E^2$ per unit volume and the stored mechanical energy per unit volume under zero external stress is given by $(1/2)\ x^2 / s = (1/2)\ (dE)^2 / s$, k^2 is

$$\begin{aligned} k^2 &= [(1/2)\ (dE)^2 / s] \,/\, [(1/2)\ \varepsilon_0\varepsilon\, E^2] \\ &= d^2 / \varepsilon_0\varepsilon\cdot s. \qquad [3.7] \end{aligned}$$

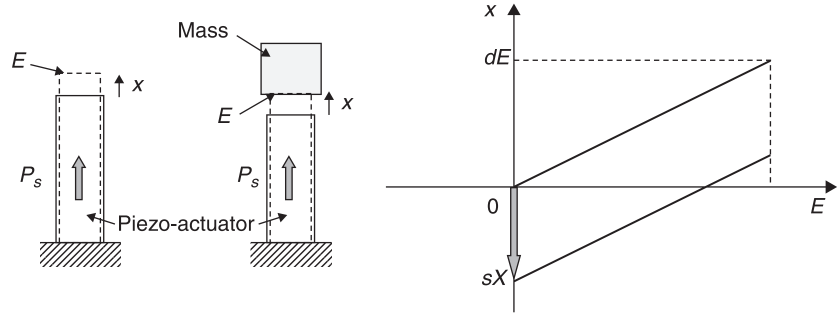

(a) Mass load model (b) Electric field vs. strain

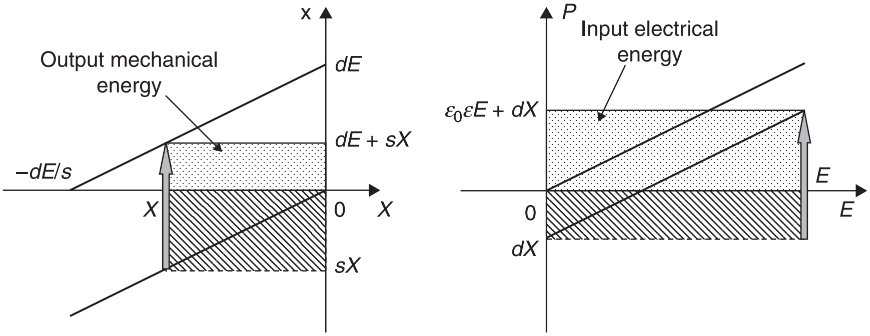

(c) Stress vs. strain (d) Electric field vs. polarization

3.14 Mass load model.

(b) *The energy transmission coefficient* λ_{max}

Not all the stored energy can actually be used, and the actual work done depends on the mechanical load. With zero mechanical load or a complete clamp (no strain), no output work is done. The energy transmission coefficient is defined by

$$\lambda_{\text{max}} = (\text{Output mechanical energy/input electrical energy})_{\text{max}} \qquad [3.8]$$

or equivalently,

$$\lambda_{\text{max}} = (\text{Output electrical energy/input mechanical energy})_{\text{max}}. \qquad [3.9]$$

These coefficients differ from those in Eqs 3.5 and 3.6 because the energy is 'spent' instead of 'stored'.

Consider the case where an electric field E is applied to a piezoelectric material under constant external stress X (< 0, because a compressive stress is necessary for external work). This corresponds to the situation where a mass is suddenly placed on an actuator, as shown in Fig. 3.14(a). Figure 3.14(b) shows two electric field versus induced strain curves, corresponding to two conditions: under a mass load and with no mass. Because the area under the electric field-strain domain is not the energy, we should use the stress-strain and electric field-polarization domains in order to find the mechanical energy and the electrical energy, respectively. Figure 3.14(c) shows how to calculate the mechanical energy. Note that the mass compresses the actuator initially by sX (s is the piezo-material's compliance and $X < 0$). This mechanical energy sX^2 is a sort of 'loan' of the actuator credited from the mass, which should be subtracted later. This energy corresponds to the hatched area in Fig. 3.14(c). By applying a step electric field, the actuator expands by the strain level dE under constant stress. This is the mechanical energy provided from the actuator to the mass, which corresponds to $|dEX|$. Like paying back the initial 'loan', the output work (from the actuator to the mass) can be calculated as the difference in the areas [shown by the dotted area in Fig. 3.14(c)]

$$\int (-X)dx = -(dE + sX)\,X. \qquad [3.10]$$

Figure 3.14(d) shows how to calculate the electrical energy. The mass load X generates the 'loan' electrical energy by inducing $P = dX$ [see the hatched area in Fig. 3.14(d)]. By applying a sudden electric field E, the actuator (like a capacitor) receives the electrical energy of $\varepsilon_0\varepsilon\, E^2$. Thus, the total energy is given by the difference in the areas [shown by the dotted area in Fig. 3.14(d)]

$$\int (E)dP = (\varepsilon_0\varepsilon\, E + dX)\,E. \qquad [3.11]$$

We need to choose the correct load to maximize the *energy transmission coefficient*. From the maximum condition of

$$\lambda = -(dE + sX)\,X\,/\,(\varepsilon_0\varepsilon\, E + dX)\,E, \qquad [3.12]$$

we obtain

$$\lambda_{\max} = \left[(1/k) - \sqrt{\left(\frac{1}{k^2}\right) - 1}\right]^2 = \left[(1/k) + \sqrt{\left(\frac{1}{k^2}\right) - 1}\right]^{-2}. \qquad [3.13]$$

See Uchino[47] for a detailed derivation. Notice that

$$k^2/4 < \lambda_{\max} < k^2/2, \qquad [3.14]$$

so that $\lambda_{\max}$ depends on k. For small k, $\lambda_{\max} = k^2/4$ and for large k, $\lambda_{\max} = k^2/2$.

This maximum does not agree with the condition for the maximum output mechanical energy. The maximum output energy is obtained when the dotted area in Fig. 3.14(c) is a maximum, that is, when the vertex of the rectangle lies on the line from dE on the vertical axis to $-dE/s$ on the horizontal axis. Therefore, the load should be half of the maximum generative stress and the mechanical energy: $-[dE - s(dE/2s)](-dE/2s) = (dE)^2/4\text{s}$. In this case, since the input electrical energy is given by $[\varepsilon_0\varepsilon E + d(-dE/2\text{s})]E$,

$$\lambda = 1/2[(2/k^2) - 1], \qquad [3.15]$$

which is close to the value $\lambda_{\max}$ when k is small, but when k is large it has a different value than predicted theoretically.

(c) *The efficiency* η

$$\eta = (\text{Output mechanical energy})/(\text{consumed electrical energy}) \qquad [3.16]$$

or

$$\eta = (\text{Output electrical energy})/(\text{consumed mechanical energy}). \qquad [3.17]$$

The efficiency differs from the coefficients in Eqs 3.8 and 3.9 because it uses ‘consumed’ energy instead of ‘input’ energy in the denominator. In a work cycle (e.g. an electric field cycle), the input electrical energy is transformed partially into mechanical energy and the rest of the energy is stored as electrical energy (electrostatic energy as in a capacitor) in the actuator. In this way, the ineffective electrostatic energy can be returned to the power source, leading to near 100% efficiency, if the loss is small. Typical values of dielectric loss in PZT are about 1–3%.

Mechanical quality factor Q_M

The mechanical quality factor, Q_M, is a parameter that characterizes the sharpness of the electromechanical resonance spectrum. When the motional admittance Y_m is plotted around the resonance frequency ω_0, the mechanical quality factor Q_M is defined with respect to the full width $[2\Delta\omega]$ at $Y_m/\sqrt{2}$ as

$$Q_M = \omega_0 / 2\Delta\omega. \qquad [3.18]$$

Also note that Q_M^{-1} is equal to the mechanical loss ($\tan\delta_m$). When we define a complex elastic compliance, $s^E = s^{E'} - js^{E'}$, the mechanical loss tangent is given by $\tan\delta_m = s^{E'}/s^{E'}$. The Q_M value is very important in evaluating the magnitude of the resonant displacement and strain. The vibration amplitude at an off-resonance frequency ($dE \cdot L$, where L is the length of the sample) is amplified by a factor proportional to Q_M at the resonance frequency. For example, a longitudinally vibrating rectangular plate generates a maximum displacement given by $(8/\pi^2) Q_M d_{31} EL$ through the transverse piezoelectric effect d_{31}. Refer to Uchino[47] for a detailed derivation.

It is important to note that Q_M^{-1} (= tan δ_m) generates heat in the piezo-sample when driven at its resonance mode.

Acoustic impedance Z

The acoustic impedance Z is a parameter used for evaluating the acoustic energy transfer between two materials. It is defined, in general, by

$$Z = (\text{pressure/volume velocity}). \tag{3.19}$$

In a solid material,

$$Z = \rho v = \sqrt{\rho c}, \tag{3.20}$$

where ρ is the density, v is the velocity of sound and c is the elastic stiffness of the material. Note $v = \sqrt{\dfrac{c}{\rho}}$.

In more advanced discussions, there are three kinds of impedance: specific acoustic impedance (pressure/particle speed), acoustic impedance (pressure/volume speed) and radiation impedance (force/speed). See Kinsler *et al.*[49] for details.

3.2.2 Piezoelectric resonance

The piezoelectric equations

When an electric field is applied to a piezoelectric material, deformation (ΔL) or strain ($\Delta L/L$) occurs. When the field is alternating, mechanical vibration is caused, and, if the driving frequency is adjusted to a mechanical resonance frequency of the device, a large resonating strain is generated. This phenomenon can be understood as a strain amplification due to accumulating input energy with time (amplification in terms of time), and is called *piezoelectric resonance*. The amplification factor is proportional to the mechanical quality factor Q_M. Piezoelectric resonance is very useful for realizing energy trap devices, actuators, etc. The theoretical treatment is as follows.[22]

If the applied electric field and the generated stress are not large, the stress X and the dielectric displacement D are given by:

$$x_i = s_{ij}^E X_j + d_{mi} E_m, \qquad (i, j = 1,2, \ldots, 6;\ m, k = 1,2,3) \tag{3.21}$$

$$D_m = d_{mi} X_i + \varepsilon_{mk}^X E_k. \tag{3.22}$$

These are called the *piezoelectric equations*. The number of independent parameters for the lowest symmetry trigonal crystal is 21 for s_{ij}^E, 18 for d_{mi} and 6 for ε_{mk}^X. The number of independent parameters decreases with increasing crystallographic symmetry. With polycrystalline ceramics, the poled axis is usually denoted the *z*-axis and the ceramic is isotropic with respect to this *z*-axis [Curie group $C_{\infty v}$ (∞m)]. The number of non-zero matrix elements in this case is ten (s_{11}^E, s_{12}^E, s_{13}^E, s_{33}^E, s_{44}^E, d_{31}, d_{33}, d_{15}, ε_{11}^X and ε_{33}^X).

Electromechanical coupling factor

The *electromechanical coupling factor k* is the rate of electromechanical transduction. The internal energy *U* of a piezoelectric vibrator is given by the sum of the mechanical energy U_M (= ∫x dX) and the electrical energy U_E (= ∫D dE). *U* is calculated as follows when the linear relations Eqs 3.21 and 3.22 are applicable:

$$\begin{aligned} U &= U_M + U_E \\ &= \left[(1/2)\sum_{i,j} s_{ij}^E X_j X_i + (1/2)\sum_{m,i} d_{mi} E_m X_i\right] \\ &\quad + \left[(1/2)\sum_{m,i} d_{mi} X_i E_m + (1/2)\sum_{k,m} \varepsilon_{mk}^X E_k E_m\right] \\ &= U_{MM} + 2U_{ME} + U_{EE} \\ &= (1/2)\sum_{i,j} s_{ij}^E X_j X_i + 2\cdot(1/2)\sum_{m,i} d_{mi} E_m X_i + (1/2)\sum_{k,m} \varepsilon_{mk}^X E_k E_m. \end{aligned} \qquad [3.23]$$

The *s* and *ε* terms are the purely mechanical and electrical energies (U_{MM} and U_{EE}), respectively, and the *d* term is the energy transduced from electrical to mechanical energy, or vice versa, through the piezoelectric effect (U_{ME}). The electromechanical coupling factor *k* is defined by

$$k = U_{ME} / \sqrt{U_{MM} \cdot U_{EE}}. \qquad [3.24]$$

Note that this definition is equivalent to the definition in Section 3.2.1:

$$k^2 = U_{ME}/U_E = \text{(Stored mechanical energy / input electrical energy)}$$

or

$$k^2 = U_{ME}/U_M = \text{(Stored electrical energy / input mechanical energy).}$$

The *k* value varies with the vibration mode (even in the same ceramic sample), and can have a positive or negative value (see Table 3.1). From Table 3.1, it can be seen that the k_{31}/k_{33} ratio around 0.47 originates from the d_{31}/d_{33} ratio around 0.43. The *k* value is primarily governed by the contributing piezoelectric constant *d* for that vibration mode.

Table 3.1 Piezoelectric resonators and their electromechanical coupling factors

	Coupling factor	Elastic boundary conditions	Resonator shape	Definition
a	k_{31}	$X_1 \neq 0,\ X_2 = X_3 = 0$ $x_1 \neq 0,\ x_2 \neq 0,\ x_3 \neq 0$	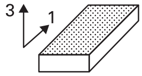	$\frac{d_{31}}{\sqrt{s_{11}^E \varepsilon_{33}^X}}$
b	k_{33}	$X_1 = X_2 = 0,\ X_3 \neq 0$ $x_1 = x_2 \neq 0,\ x_3 \neq 0$	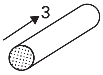 Fundamental mode	$\frac{d_{33}}{\sqrt{s_{33}^E \varepsilon_{33}^X}}$
c	k_p	$X_1 = X_2 \neq 0,\ X_3 = 0$ $x_1 = x_2 \neq 0,\ x_3 \neq 0$	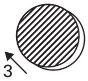 Fundamental mode	$k_{31}\sqrt{\frac{2}{1-\sigma}}$
d	k_t	$X_1 = X_2 \neq 0,\ X_3 \neq 0$ $x_1 = x_2 = 0,\ x_3 \neq 0$	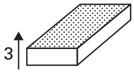 Thickness mode	$k_{33}\sqrt{\frac{\varepsilon_{33}^x}{c_{33}^D}}$
e	k_p'	$X_1 = X_2 \neq 0,\ X_3 \neq 0$ $x_1 = x_2 \neq 0,\ x_3 = 0$	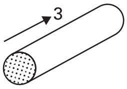 Radial mode	$\frac{k_p - Ak_{33}}{\sqrt{1-A^2}\sqrt{1-k_{33}^2}}$
f	k_{31}'	$X_1 \neq 0,\ X_2 \neq 0,\ X_3 = 0$ $x_1 \neq 0,\ x_2 = 0,\ x_3 \neq 0$	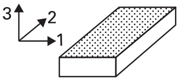 Width mode	$\frac{k_{31}}{\sqrt{1-k_{31}^2}}\sqrt{\frac{1+\sigma}{1-\sigma}}$
g	k_{31}''	$X_1 \neq 0,\ X_2 = 0,\ X_3 \neq 0$ $x_1 \neq 0,\ x_2 \neq 0,\ x_3 \neq 0$	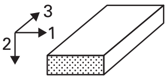 Width mode	$\frac{k_{31} - Bk_{33}}{\sqrt{1-k_{33}^2}}$
h	k_{33}'''	$X_1 \neq 0,\ X_2 \neq 0,\ X_3 \neq 0$ $x_1 \neq 0,\ x_2 = 0,\ x_3 = 0$	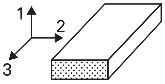 Thickness mode	$\frac{\sqrt{\frac{(k_p - Ak_{33})^2}{1-A^2} - (k_{31} - Bk_{33})^2}}{1 - k_{33}^2 - (k_{31} - Bk_{33})^2}$
i	k_{33}'	$X_1 \neq 0,\ X_2 = 0,\ X_3 \neq 0$ $x_1 = 0,\ x_2 \neq 0,\ x_3 \neq 0$	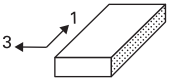 Width mode	$\frac{k_{33} - Bk_{31}}{\sqrt{(1-B^2)(1-k_{31}^2)}}$
j	$k_{24} = k_{15}$	$X_1 = X_2 = X_3 = 0,\ X_4 \neq 0$ $x_1 = x_2 = x_3 = 0,\ x_4 \neq 0$		$\frac{d_{15}}{\sqrt{\varepsilon_{11}^x s_{44}^E}}$

Note: $A = \frac{\sqrt{2}s_{13}^E}{\sqrt{s_{33}^E\left(s_{11}^E + s_{12}^E\right)}}$, $B = \frac{s_{13}^E}{\sqrt{s_{11}^E s_{33}^E}}$

Longitudinal vibration mode

Consider the longitudinal mechanical vibration of a piezo-ceramic plate through the transverse piezoelectric effect (d_{31}) as shown in Fig. 3.15. If the polarization is in the z direction and the x-plane and the y-plane are the planes of the electrodes, then the extensional vibration in the x direction is given by the following dynamic equation (if the length L is more than 4–6 times the width w or the thickness b, we can neglect the coupling modes with width or thickness vibrations):

$$(\partial^2 u/\partial t^2) = F = (\partial X_{11}/\partial x) + (\partial X_{12}/\partial y) + (\partial X_{13}/\partial z), \qquad [3.25]$$

where u is the displacement of the small volume element in the ceramic plate in the x direction. The relations between the stress, the electric field (only E_z exists) and the induced strain are

$$\begin{aligned}
x_1 &= s_{11}^E X_1 + s_{12}^E X_2 + s_{13}^E X_3 + d_{31} E_3,\\
x_2 &= s_{12}^E X_1 + s_{11}^E X_2 + s_{13}^E X_3 + d_{31} E_3,\\
x_3 &= s_{13}^E X_1 + s_{13}^E X_2 + s_{33}^E X_3 + d_{33} E_3,\\
x_4 &= s_{44}^E X_4,\\
x_5 &= s_{44}^E X_5,\\
x_6 &= 2(s_{11}^E - s_{12}^E)\, X_6.
\end{aligned} \qquad [3.26]$$

When the plate is very long and thin, X_2 and X_3 can be considered to be equal to zero through the plate. Since shear stress will not be generated by the electric field E_z ($= E_3$), Eq. 3.26 reduces to only one equation:

$$X_1 = x_1/s_{11}^E - (d_{31}/s_{11}^E)E_z. \qquad [3.27]$$

Introducing Eq. 3.27 into Eq. 3.25, and using $x_1 = \partial u/\partial x$ (non-suffix x corresponds to the Cartesian coordinate, and x_1 is the strain along the 1 or x direction) and $\partial E_z/\partial x = 0$ (because the potential is the same on each electrode), leads to a harmonic vibration equation:

$$-\,\omega^2 \rho\, s_{11}{}^E\, u = \partial^2 u/\partial x^2. \qquad [3.28]$$

Here, ω is the angular frequency of the drive field and ρ is the density. Substituting a general solution $u = u_1(x)e^{j\omega t} + u_2(x)e^{-j\omega t}$ into Eq. 3.27, and with the boundary

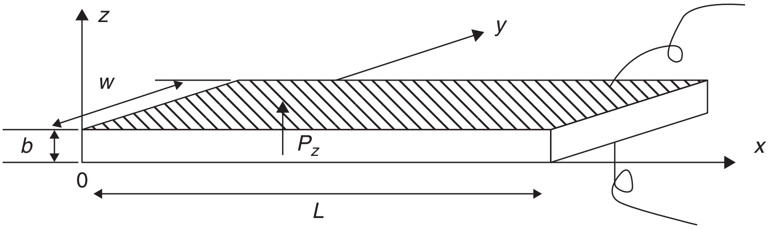

3.15 Longitudinal mechanical vibration of a piezo-ceramic plate.

conditions $X_1 = 0$ at $x = 0$ and $x = L$, where L is the sample length (due to the mechanically free condition at the plate end), the following solution can be obtained:

$$\partial u/\partial x = x_1 = d_{31}\, E_z\, [\sin \omega\, (L-x)/v + \sin(\omega x/v)]/\sin(\omega L/v)$$

$$= d_{31}E_Z \left(\frac{\cos\left[\dfrac{\omega(L-2x)}{2v}\right]}{\cos\left(\dfrac{\omega L}{2v}\right)} \right) \qquad [3.29]$$

Here, v is the *velocity of sound* in the piezo-ceramic, given by

$$v = 1/\sqrt{\rho s_{11}^{E}}. \qquad [3.30]$$

When the specimen is used as an electrical component such as a filter or a vibrator, the electrical impedance (applied voltage/induced current) is important. The current flow into the specimen is described by the surface charge increment, $\partial D_3/\partial t$, and the total current is given by:

$$i = j\omega w \int_0^L D_3\, dx = j\omega w \int_0^L (d_{31} X_1 + \varepsilon_{33}^{X} E_z)\, dx$$

$$= j\omega w \int_0^L \left[d_{31} \left\{ \frac{x_1}{s_{11}^{E}} - \left(\frac{d_{31}}{s_{11}^{E}} \right) E_z \right\} + \varepsilon_{33}^{X} E_z \right] dx. \qquad [3.31]$$

Using Eq. 3.29, the admittance for the mechanically free sample is

$(1/Z) = (i/V) = (i/E_z\, t)$

$$= (j\omega wL / E_z t) \int_0^L \left[\left(\frac{[d]_{31}^{2}}{s_{11}^{E}} \right) \left(\frac{\cos\left[\dfrac{\omega(L-2x)}{2v}\right]}{\cos\left(\dfrac{\omega L}{2v}\right)} \right) E_z + \left[\varepsilon_{33}^{X} \left[-\left(\frac{d_{31}^{2}}{s_{11}^{E}} \right) \right] E \right]_z \right] dx$$

$$= (j\omega wL/t)\, \varepsilon_{33}^{LC}\, [1 + (d_{31}^{2}/\varepsilon_{33}^{LC}\, s_{11}^{E})(\tan(\omega L/2v)/(\omega L/2v))], \qquad [3.32]$$

where w is the width, L the length, t the thickness of the rectangular piezo-sample, and V is the applied voltage. ε_{33}^{LC} is the permittivity in a longitudinally clamped sample, given by

$$\varepsilon_{33}^{LC} = \varepsilon_{33}^{X} - \left(\frac{d_{31}^{2}}{s_{11}^{E}} \right). \qquad [3.33]$$

The piezoelectric resonance is achieved where the admittance becomes infinite or the impedance is zero. The resonance frequency f_R is calculated from Eq. 3.32 (by putting $\omega L/2v = \pi/2$), and the fundamental frequency is given by

$$f_R = \omega_R / 2\pi = v / 2L = 1/\left(2L\sqrt{\rho s_{11}^{E}}\right). \qquad [3.34]$$

The antiresonance state is for zero admittance or infinite impedance:

$$(\omega_A L/2v)\cot(\omega_A L/2v) = -d_{31}^2/\varepsilon_{33}^{LC}\, s_{11}^E = -k_{31}^2/(1-k_{31}^2). \qquad [3.35]$$

The final transformation is provided by the definition,

$$k_{31} = d_{31}/\sqrt{s_{11}^E \cdot \varepsilon_{33}^X} \qquad [3.36]$$

The resonance and antiresonance states are mechanical resonance states with amplified strain/displacement states, but they are very different from the driving viewpoints. The mode difference is described by the following intuitive model.[22] In a high electromechanical coupling material with k almost equal to 1, the resonance or antiresonance states appear for tan ($\omega L/2v$) = ∞ or 0 [i.e., $\omega L/2v = (m-1/2)\pi$ or $m\pi$, where m is an integer], respectively. The strain amplitude x_1 distribution for each state (calculated using Eq. 3.29) is illustrated in Fig. 3.16. In the resonance state, large strain amplitudes and large capacitance changes (called *motional capacitance*) are induced, and the current can easily flow into the device. In contrast, for antiresonance, the strain induced in the device compensates completely, resulting in no capacitance change, and the current cannot flow easily into the sample. Thus, for a high-k material the first antiresonance frequency f_A should be twice as large as the first resonance frequency f_R.

It is notable that both the resonance and antiresonance states are for mechanical resonance, which can create a large strain in the sample under the minimum input electrical energy. The stress X_1 at the plate ends ($x = 0$ and $x = L$) is assumed to be zero in both cases. However, though the strain x_1 at the plate ends is zero for resonance, the strain x_1 is not zero (it is actually a maximum) for antiresonance. This means that there is only one vibration node at the plate center for resonance (top left in Fig. 3.16), and there are two additional nodes at both plate ends for antiresonance (top right in Fig. 3.16). The reason is due to the antiresonance drive, i.e. the high-voltage/low-current (minimum-power) drive due to the high impedance. The converse piezo-effect strain under E via d_{31} (uniform strain in the sample) superposes on the mechanical resonance strain distribution (distributed strain with nodes in the sample) two strains that have exactly the same level, theoretically, at antiresonance for $k_{31} = 1$.

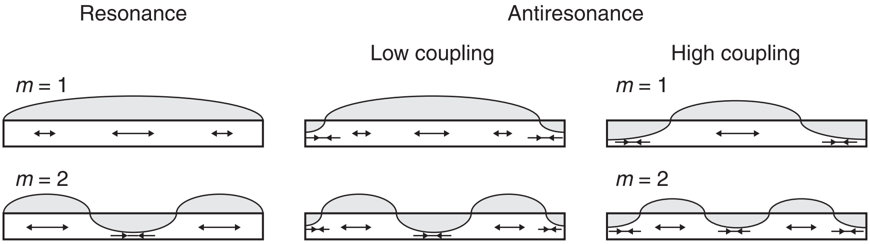

3.16 Strain amplitude for a piezo-ceramic plate.

In a typical case, where $k_{31} = 0.3$, the antiresonance state varies from the previously mentioned mode and becomes closer to the resonance mode (top center in Fig. 3.16). The low-coupling material exhibits an antiresonance mode where the capacitance change due to the size change (*motional capacitance*) is compensated completely by the current required to charge up the static capacitance (called *damped capacitance*). Thus, the antiresonance frequency f_A will approach the resonance frequency f_R.

The general procedure for calculating the electromechanical parameters (k_{31}, d_{31}, s_{11}^E and ε_{33}^X) from the impedance spectrum measurement is:

1. The velocity of sound v in the specimen is obtained from the resonance frequency f_R (Fig. 3.16), using Eq. 3.34: $f_R = v/2L$.
2. Knowing the density ρ, the elastic compliance s_{11}^E can be calculated from the velocity of sound, $v = 1/\sqrt{\rho s_{11}^E}$.
3. The electromechanical coupling factor k_{31} is calculated from v and the antiresonance frequency f_A through Eq. 3.35. In low-coupling piezoelectric materials, the following approximate equation is especially useful:

   $$k_{31}^2/(1 - k_{31}^2) = (\pi^2/4)(\Delta f/f_R) \quad [3.37]$$

   where $\Delta f = f_A - f_R$.
4. With the permittivity $\varepsilon_{33}{}^X$ from an independent measurement under an off-resonance condition, d_{31} is calculated from k_{31} through Eq. 3.36: $k_{31} = d_{31}/\sqrt{s_{11}^E \cdot \varepsilon_{33}^X}$.

Figures 3.17(a) and 3.17(b) compare observed impedance curves of rod-shaped samples for a typical k material (PZT-5H, $k_{33} = 0.70$) and a high-k material (PZN-PT single crystal, $k_{33} = 0.90$). Note the large separation between the resonance and antiresonance peaks in the high-k material, leading to the condition $f_A \approx 2f_R$. In contrast, a regular PZT sample has $f_A = 1.3\,f_R$. The bandwidth of the piezo-transducer is defined by $(\Delta f/f_R)$, leading to 100% for the PZN-PT sample and only 30% for PZT-5H.

3.2.3 Overview of piezoelectric materials

This section summarizes the current status of piezoelectric materials: single-crystal materials, piezo-ceramics, piezo-polymers, composites and piezo-films. Table 3.2 shows the piezoelectric material parameters.[50] Quartz, with the highest mechanical quality factor, is used for low loss transducers. The PZT family has high d and k and is suitable for high-power transducers. Sm-doped lead titanates have an extremely high mechanical coupling anisotropy k_t/k_p, suitable for medical transducers. The piezo-polymer PVDF has a low permittivity, hence the piezo-constant g is high, and in addition it has mechanical flexibility, and is suitable for pressure and stress sensor applications.[51]

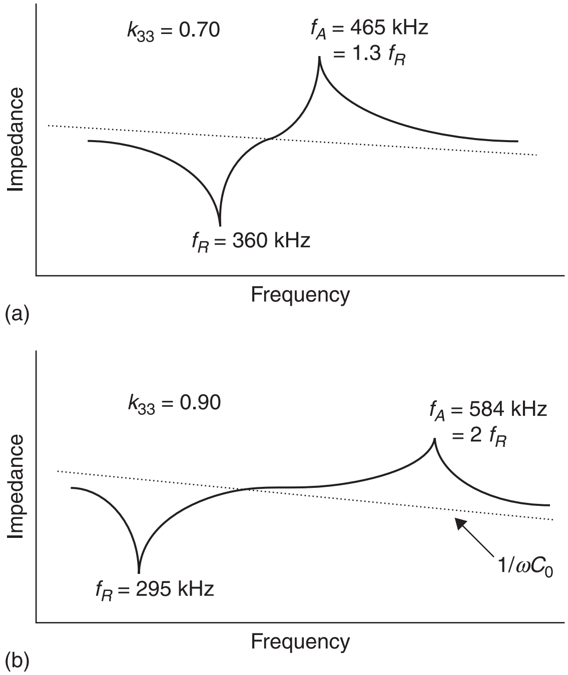

3.17 Impedance of rod-shaped samples for (a) PZT-5H ($k_{33} = 0.70$) and (b) PZN-PT ($k_{33} = 0.90$).

Table 3.2 Piezoelectric properties of representative piezoelectric materials[50,51]

Parameter	Quartz	$BaTiO_3$	PZT-4	PZT-5H	$(Pb,Sm)TiO_3$	PVDF-TrFE
g_{33} (10^{-3}V.m.N^{-1})	57.8	12.6	26.1	19.7	42	380
k_t	0.09	0.38	0.51	0.50	0.50	0.30
k_p		0.33	0.58	0.65	0.03	
$\varepsilon_3^X/\varepsilon_0$	5	1700	1300	340	175	6
Q_M	$> 10^5$		500	65	900	3–10
T_c(°C)		120	328	193	355	

Single crystals

Although piezoelectric ceramics are widely used for a large number of applications, single-crystal materials retain their utility, being essential for applications such as frequency-stabilized oscillators and surface acoustic devices. The most popular single-crystal piezoelectric materials are quartz, lithium niobate ($LiNbO_3$) and lithium tantalate ($LiTaO_3$). The single crystals are anisotropic, exhibiting different material properties depending on the cut of the materials and the direction of bulk or surface wave propagation.

Quartz is a well-known piezoelectric material. α-quartz belongs to the triclinic crystal system with point group 32 and has a phase transition at 537 °C to its β form, which is not piezoelectric. Quartz has a cut with a zero temperature coefficient. For instance, quartz oscillators, operating in the thickness shear mode of the AT-cut, are extensively used in clocks in computers and frequency-stabilized ones in TVs and VCRs. On the other hand, an ST-cut quartz substrate with X propagation has a zero temperature coefficient for surface acoustic wave, and so is used for SAW devices with high-stabilized frequencies. Another characteristic of quartz is its extremely high mechanical quality factor $Q_M > 10^5$.

Lithium niobate and lithium tantalate belong to an isomorphous crystal system with octahedra of oxygen. The Curie temperatures of $LiNbO_3$ and $LiTaO_3$ are 1210 °C and 660 °C, respectively. The crystal symmetry of the ferroelectric phase of these single crystals is 3 m, and the polarization direction is along *c*-axis. These materials have high electromechanical coupling coefficients for surface acoustic waves. In addition, large single crystals can easily be obtained from their melt using the conventional Czochralski technique. Thus, both materials are very important for manufacturing SAW devices.

Single crystals of $Pb(Mg_{1/3}Nb_{2/3})O_3$ (PMN), $Pb(Zn_{1/3}Nb_{2/3})O_3$ (PZN) and their binary systems with $PbTiO_3$ (PMN-PT and PZN-PT), having extremely large electromechanical coupling factors, are discussed in the following section.

Polycrystalline materials

Barium titanate, $BaTiO_3$, is one of the most thoroughly studied and most widely used ferroelectric materials. Just below the Curie temperature (130 °C), the vector of spontaneous polarization points in the [001] direction (the tetragonal phase), below 5 °C it reorients in the [011] direction (the orthorhombic phase) and below −90 °C in the [111] direction (the rhombohedral phase). The dielectric and piezoelectric properties of the ferroelectric ceramic $BaTiO_3$ are affected by its stoichiometry and microstructure and by dopants at the A or B site in the solid solution. Ceramic $BaTiO_3$ with dopants such as Pb or Ca ions has been used to stabilize the tetragonal phase over a wider temperature range and has been used as a commercial piezoelectric material. After the discovery of PZT, BT's role in piezoelectric devices reduced, and currently it is used primarily in capacitors. However, in the next 10 years, as the use of Pb becomes more strictly regulated, there may be a revival of BT-based piezo-ceramics.

The piezoelectric $Pb(Zr,Ti)O_3$ (PZT) solid-solution ceramics discovered in the 1950s are now widely used because of their superior piezoelectric properties. The phase diagram for the PZT system ($PbZr_xTi_{1-x}O_3$) is shown in Fig. 3.18. The crystalline symmetry of this solid-solution system is determined by the Zr content. Lead titanate also has a tetragonal ferroelectric phase with a perovskite structure. With increasing Zr content, *x*, the tetragonal distortion decreases and at $x > 0.52$ the structure changes from the tetragonal *4 mm* phase to another ferroelectric phase

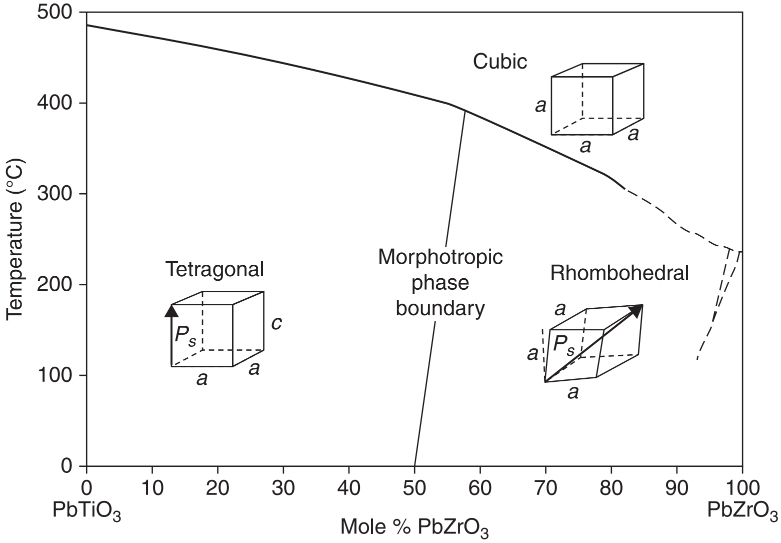

3.18 Phase diagram for the PZT system.

of rhombohedral $3m$ symmetry. The line dividing these two phases is called the *morphotropic phase boundary* (*MPB*). The boundary composition is considered to have both tetragonal and rhombohedral phases coexisting together. Figure 3.19 shows the dependence of several piezoelectric *d* constants on composition near the morphotropic phase boundary. The *d* constants have their highest values near the MPB. This enhancement of the piezoelectric effect is attributed to the increased ease of reorientation of polarization under an applied electric field.

Doping a PZT material with *donor* or *acceptor* ions changes its properties dramatically. Donor doping with ions such as Nb^{5+} or Ta^{5+} creates 'soft' PZTs, like PZT-5, because the Pb vacancies allow domain motion. On the other hand, acceptor doping with Fe^{3+} or Sc^{3+} leads to 'hard' PZTs, such as PZT-8, because the oxygen vacancies will restrict the motion of the domain wall.

PZT in ternary solid solutions with another perovskite phase has been investigated intensively by Japanese ceramic companies. Examples of these ternary compositions are: PZTs in solid solution with $Pb(Mg_{1/3}Nb_{2/3})O_3$ (Panasonic), $Pb(Zn_{1/3}Nb_{2/3})O_3$ (Toshiba), $Pb(Mn_{1/3}Sb_{2/3})O_3$, $Pb(Co_{1/3}Nb_{2/3})O_3$, $Pb(Mn_{1/3}Nb_{2/3})O_3$, $Pb(Ni_{1/3}Nb_{2/3})O_3$ (NEC), $Pb(Sb_{1/2}Sn_{1/2})O_3$, $Pb(Co_{1/2}W_{1/2})O_3$, $Pb(Mg_{1/2}W_{1/2})O_3$ (Du Pont), all of which were patented by different companies (almost all composition patents have already expired).

Table 3.3 summarizes the piezoelectric, dielectric and elastic properties of typical PZTs: soft PZT-5H, semi-hard PZT-4 and hard PZT-8. Soft PZTs have high *k*, high *d* and high ε in comparison with hard PZTs, while Q_M is quite high in hard PZTs. Thus, soft PZTs should be used for off-resonance applications while hard PZTs are suitable for resonance applications.

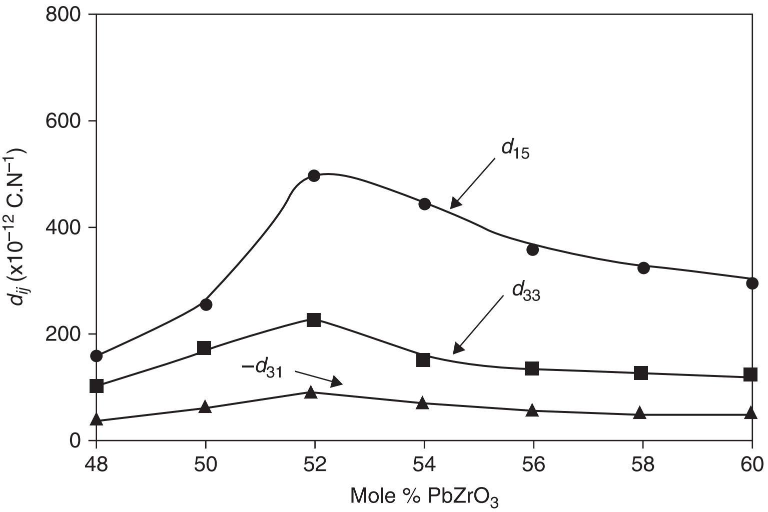

3.19 Composition vs. piezoelectric *d* constants near the morphotropic phase boundary.

The end member of PZT, lead titanate, has a large crystal distortion. $PbTiO_3$ has a tetragonal structure at room temperature with its tetragonality (lattice parameter deviation) $c/a = 1.063$ (Fig. 3.18). The Curie temperature is 490 °C. Densely sintered $PbTiO_3$ ceramics cannot be obtained easily, because they break up into a powder when cooled through the Curie temperature due to the large spontaneous strain. Lead titanate ceramics modified by adding a small amount of additives exhibit a high piezoelectric anisotropy. Both $(Pb,Sm)TiO_3$[52] and $(Pb,Ca)TiO_3$[53] exhibit extremely low planar coupling, that is, a large k_t/k_p ratio, where k_t and k_p are the thickness-extensional and planar electromechanical coupling factors, respectively. Since these transducers can generate purely longitudinal waves because of the k_t values, and no transverse waves because of the k_{31} values, clear ultrasonic imaging is expected without 'ghosts' caused by transverse waves. $(Pb,Nd)(Ti,Mn,In)O_3$ ceramics with a zero temperature coefficient for the surface acoustic wave delay have been developed as superior substrate materials for SAW device applications.[54]

Relaxor ferroelectrics

Relaxor ferroelectrics can be prepared either in polycrystalline form or as single crystals. They differ from the previously mentioned normal ferroelectrics in that they exhibit a broad phase transition from the paraelectric to the ferroelectric state, a strong frequency dependence of the dielectric constant (i.e. dielectric relaxation) and a weak remanent polarization. Lead-based relaxor materials have complex, disordered, perovskite structures.

Relaxor-type electrostrictive materials, such as those from a lead magnesium niobate–lead titanate, $Pb(Mg_{1/3}Nb_{2/3})O_3–PbTiO_3$ (PMN-PT), solid solution are

Table 3.3 Piezoelectric, dielectric and elastic properties of typical PZTs

	Soft PZT-5H	Semi-hard PZT-4	Hard PZT-8
EM coupling factor			
k_p	0.65	0.58	0.51
k_{31}	0.39	0.33	0.30
k_{33}	0.75	0.70	0.64
k_{15}	0.68	0.71	0.55
Piezoelectric coefficient			
d_{31} (10^{-12}m.V^{-1})	–274	–122	–97
d_{33}	593	285	225
d_{15}	741	495	330
g_{31} (10^{-3}Vm.N^{-1})	–9.1	–10.6	–11.0
g_{33}	19.7	24.9	25.4
g_{15}	26.8	38.0	28.9
Permittivity			
$\varepsilon_{33}{}^X/\varepsilon_0$	3400	1300	1000
$\varepsilon_{11}{}^X/\varepsilon_0$	3130	1475	1290
Dielectric loss (tan δ) (%)	2.00	0.40	0.40
Elastic compliances			
$s_{11}{}^E$ (10^{-12}m^2.N^{-1})	16.4	12.2	11.5
$s_{12}{}^E$	–4.7	–4.1	–3.7
$s_{13}{}^E$	–7.2	–5.3	–4.8
$s_{33}{}^E$	20.8	15.2	13.5
$s_{44}{}^E$	43.5	38.5	32.3
Mechanical Q_M	65	500	1000
Density ρ (10^3 kg.m^{-3})	7.5	7.5	7.6
Curie temperature (°C)	193	325	300

highly suitable for actuator applications. This relaxor ferroelectric also exhibits an induced piezoelectric effect. That is, the electromechanical coupling factor k_t varies with the applied DC bias field. As the DC bias field increases, the coupling increases and saturates. Since this behavior is reproducible (there is no hysteresis), these materials can be used as ultrasonic transducers tunable by the bias field.[55]

Single-crystal relaxor ferroelectrics with the MPB composition show tremendous promise as ultrasonic transducers and electromechanical actuators. Single crystals of $Pb(Mg_{1/3}Nb_{2/3})O_3$ (PMN), $Pb(Zn_{1/3}Nb_{2/3})O_3$ (PZN) and binary systems of these materials combined with $PbTiO_3$ (PMN-PT and PZN-PT) have extremely large electromechanical coupling factors.[27,56] Large coupling coefficients and large piezoelectric constants have been found for crystals from the morphotropic phase boundaries of these solid solutions. Single crystals of PZN-8%PT have a high k_{33} value of 0.94 for the (001) crystal cuts; this is very high compared with the k_{33} of conventional PZT ceramics of around 0.70–0.80.

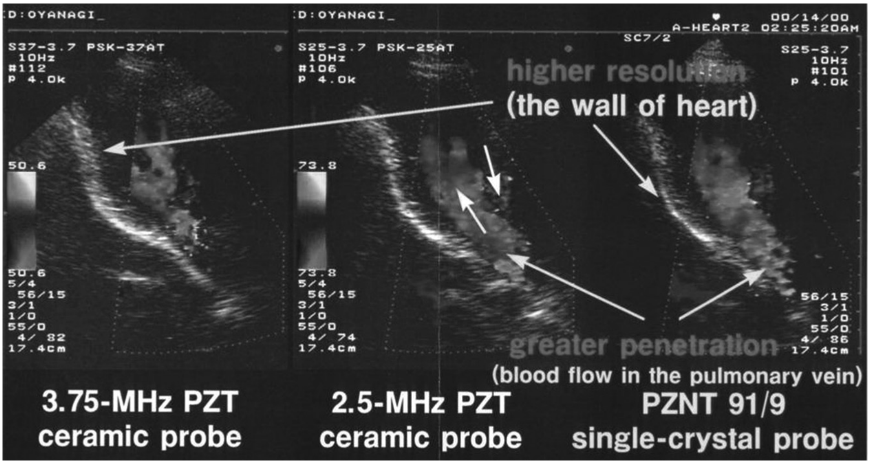
D:OYANAGI_
S37-3.7 PSK-37AT
D:OYANAGI_
S25-3.7 PSK-25AT
00/14/00
A-HEART2 02:25:20AM
higher resolution
(the wall of heart)
greater penetration
(blood flow in the pulmonary vein)
3.75-MHz PZT
ceramic probe
2.5-MHz PZT
ceramic probe
PZNT 91/9
single-crystal probe

3.20 Ultrasound images created with different probes.

Figure 3.20 demonstrates the superiority of the PZN-PT single crystal material compared with the PZT ceramic in a medical imaging transducer developed by Toshiba Corporation.[57] Conventionally, a physician needs to use two different PZT probes, one operating at a frequency of 2.5 MHz for checking wide and deep, and the other at 3.75 MHz for monitoring a particular area with a better resolution. A PZN-PT single-crystal (with very high k_{33} and k_t) probe has two additional advantages: wide bandwidth – without changing the probe, a physician can switch the drive frequency from 2.5 to 3.75 MHz; and a strong signal – because of the high electromechanical coupling, the received signal level is more than double that of a PZT probe.

Polymers

Polyvinylidene difluoride (see Fig. 3.21), PVDF or PVF2, becomes piezoelectric when stretched during fabrication. Thin sheets of the cast polymer are then drawn and stretched in the plane of the sheet, in at least one direction, and frequently also

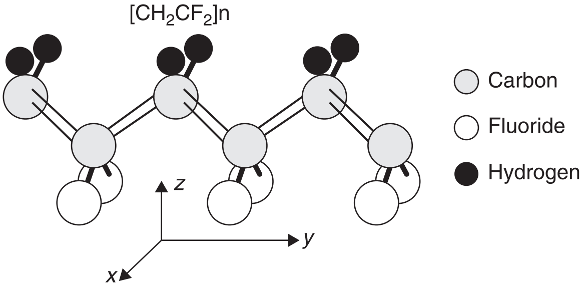
[CH2CF2]n
Carbon
Fluoride
Hydrogen
z
y
x

3.21 Polyvinylidene difluoride.

in a perpendicular direction, to transform the material to its microscopically polar phase. Crystallization during the melt forms the non-polar α phase, which can be converted into the polar β phase by a uniaxial or biaxial drawing operation; the resulting dipoles are then reoriented through electric poling.

Large sheets can be manufactured and thermally formed into complex shapes. The copolymerization of vinylidene difluoride with trifluoroethylene (TrFE) results in a random copolymer (PVDF-TrFE) with a stable, polar β phase. This polymer need not be stretched; it can be poled directly as formed. A thickness-mode coupling coefficient of 0.30 has been reported. Piezoelectric polymers have the following characteristics: (a) small piezoelectric d constants (for actuators) and large g constants (for sensors), due to their low permittivity, (b) light weight and soft elasticity, leading to good acoustic impedance matching with water or the human body, (c) a low mechanical quality factor Q_M, giving a broad resonance bandwidth. Such piezoelectric polymers are used for directional microphones and ultrasonic hydrophones.

Composites

Piezo-composites comprising piezoelectric ceramic and polymer phases are promising materials because of their excellent and readily tailored properties. The geometry for two-phase composites can be classified according to the dimensional connectivity of each phase into ten structures: 0–0, 0–1, 0–2, 0–3, 1–1, 1–2, 1–3, 2–2, 2–3 and 3–3.[58] A 1–3 piezo-composite, such as the PZT-rod/ polymer composite, is one of the most promising configurations. The advantages of this composite are its high coupling factors, low acoustic impedance, good matching to water or human tissue, mechanical flexibility, broad bandwidth in combination with a low mechanical quality factor and the possibility of making undivided arrays by structuring the electrodes. The thickness-mode electromechanical coupling of the composite can exceed the k_t (0.40–0.50) of the constituent ceramic, approaching almost the value of the rod-mode electromechanical coupling, k_{33} (0.70–0.80) of the ceramic.[59] The electromechanical coupling factors of these composites are much superior compared with polymer piezoelectrics. Acoustic impedance is the square root of the product of the density and elastic stiffness. The acoustic match to tissue or water (1.5 Mrayl) of a typical piezo-ceramic (20–30 Mrayl) is significantly improved by forming a composite structure, that is, by replacing some of the heavy, stiff ceramic with a light, soft polymer. Piezoelectric composite materials are especially useful for underwater sonar and medical diagnostic ultrasonic transducer applications.

3.2.4 Thin films

Both zinc oxide (ZnO) and aluminum nitride (AlN) are simple binary compounds with a Wurtzite-type structure, which can be sputter deposited as a c-axis-oriented thin film on a variety of substrates. Since ZnO has reasonable piezoelectric coupling, thin films of this material are widely used in bulk acoustic and surface acoustic wave devices. The fabrication of highly oriented (along the *c*-axis) ZnO films has been studied and developed extensively. However, the performance of ZnO devices is limited, due to their low piezoelectric coupling (20–30%). PZT thin films are expected to exhibit higher piezoelectric properties. At present, PZT thin films are used in micro-transducers and micro-actuators.

Thin-film preparation technique

Techniques for the fabrication of thin films of an oxide are classified into physical and chemical processes.

(a) Physical processes:
- electron beam evaporation
- RF sputtering, DC sputtering
- ion beam sputtering
- ion plating

(b) Chemical processes:
- sol-gel method (dipping, spin coating, etc.)
- chemical vapor deposition (CVD)
- metal-organic chemical vapor deposition (MOCVD)
- liquid phase epitaxy, melting epitaxy, capillary epitaxy, etc.

Sputtering is most commonly used for ferroelectric thin films of $LiNbO_3$, PLZT and $PbTiO_3$. Figure 3.22 illustrates magnetron sputtering. Heavy Ar plasma ions

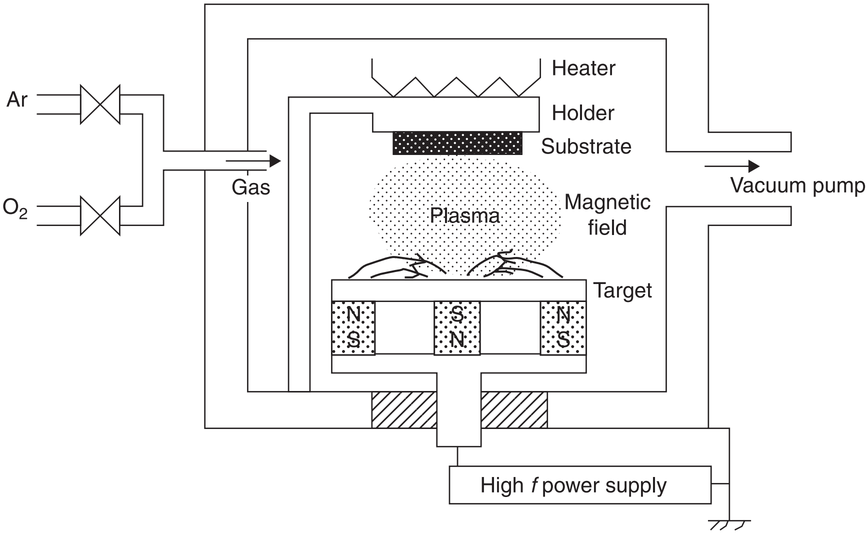

3.22 Magnetron sputtering.

bombard the cathode (target) and eject its atoms. These atoms are deposited uniformly on the substrate in an evacuated enclosure. By choosing a suitable substrate and deposition conditions, single crystal-like epitaxially deposited films can be obtained. The sol-gel technique has also been employed for producing PZT films. Applications of thin-film ferroelectrics include memory chips, surface acoustic wave devices, piezo-sensors and micro-mechatronic or MEMS devices.

As discussed in the previous section (see Fig 3.8), (001) epitaxially oriented PZT rhombohedral composition films are the most suitable for applications.[30] Kalpat *et al.* demonstrated (001) and (111) oriented films on the same Pt-coated Si substrate by changing the rapid thermal annealing profile.[60] Figure 3.23 shows results for PZT (70/30) films with (100), (111) and (222) orientations.

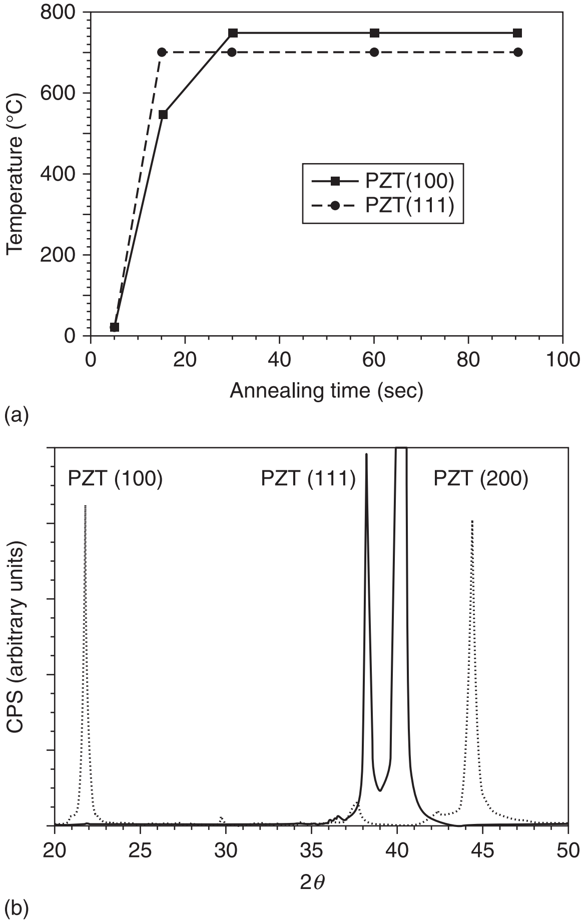

3.23 PZT (70/30) films. (a) Annealing time vs. temperature. (b) Counts per second vs. the X-ray tube setting angle.

MEMS applications

The micromachining process used to fabricate a PZT micropump is illustrated in Fig. 3.24. The etching process for the silicon/PZT unit is shown on the left-hand side of the figure and that for the glass plate on the right side. A schematic of the micropump used in testing blood is pictured in Fig. 3.25.[60] The blood sample and test chemicals enter the system through the two inlets, are mixed in the central cavity and pass through the outlet for analysis. The movement of the liquids through the system occurs through the bulk bending of the PZT diaphragm in response to a drive potential provided by the *interdigital surface electrodes*.

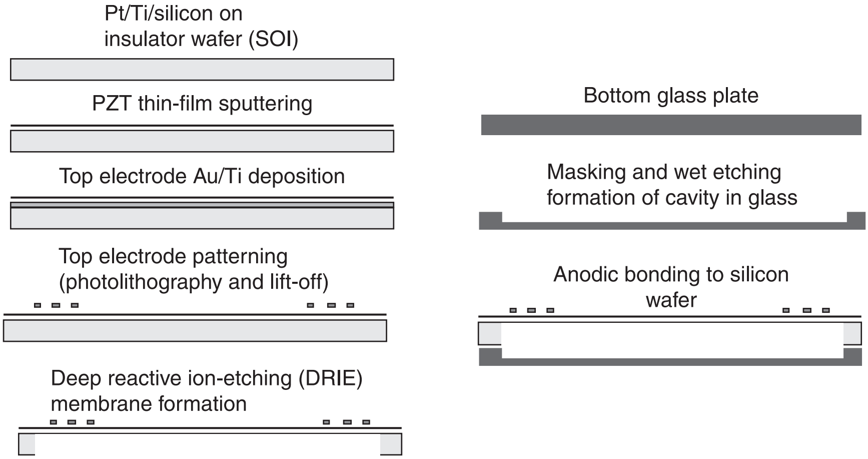
Pt/Ti/silicon on
insulator wafer (SOI)
PZT thin-film sputtering
Top electrode Au/Ti deposition
Top electrode patterning
(photolithography and lift-off)
Deep reactive ion-etching (DRIE)
membrane formation
Bottom glass plate
Masking and wet etching
formation of cavity in glass
Anodic bonding to silicon
wafer

3.24 Micromachining process used to fabricate a PZT micropump.

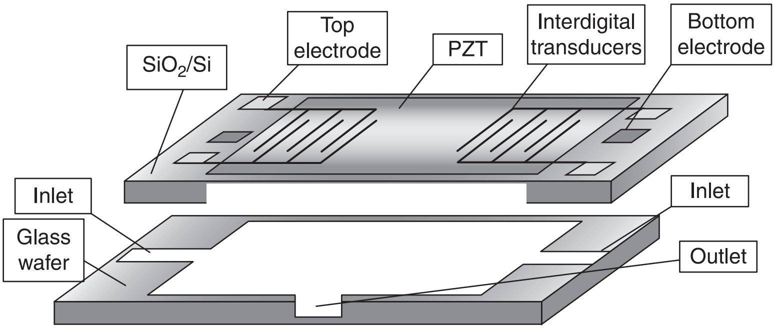
Top
electrode
PZT
Interdigital
transducers
Bottom
electrode
SiO$_2$/Si
Inlet
Glass
wafer
Inlet
Outlet

3.25 Micropump for testing blood.

Constraints in thin/thick films

A thin-film structure is inevitably affected by four significant types of parameter:

1. Size constraints: Similarly to a powder sample, there may exist a critical film thickness below which ferroelectricity disappears.[61]
2. Stress from the substrate: Tensile or compressive stress is generated due to the thermal expansion mismatch between the film and the substrate, sometimes leading to a higher coercive field for domain reorientation. The Curie temperature is also modified at a rate of 50 ° per 1 GPa.
3. Epitaxial growth: Crystal orientation dependence should also be considered, as for single crystals. An example is the rhombohedral composition, PZT, which exhibits maximum performance when the P_s direction is arranged at 57° cant to the film normal direction [i.e., the (001) crystallographic orientation].[30]
4. Preparation constraints: An Si substrate needs a low sintering temperature for a PZT film. Typically, 800 °C for a short period is the maximum for preparing PZT, which may limit the crystallization of the film, leading to a reduction in performance. A metal electrode, such as Pt, on an Si wafer also limits the crystallinity of a PZT film.

3.2.5 Surface acoustic wave materials

A *surface acoustic wave* (SAW), also called a *Rayleigh wave*, is essentially a coupling between longitudinal and shear waves. The energy carried by the SAW is confined near the surface. An associated electrostatic wave exists for a SAW on a piezoelectric substrate, which allows electro-acoustic coupling via a transducer. The advantages of SAW technology are:[62,63]

1. The wave can be electro-acoustically accessed and tapped at the substrate surface and its velocity is approximately 10^4 times slower than an electromagnetic wave.
2. The SAW wavelength is of the same order of magnitude as line dimensions produced by photolithography and the lengths for both short and long delays are achievable on reasonably sized substrates.

There is a very broad range of commercial system applications, which include front-end and IF (Intermediate Frequency) filters, CATV (Community Antenna Television) and VCR (Video Cassette Recorder) components, synthesizers, analyzers and navigators. In SAW transducers, finger (*interdigital*) electrodes can sample or tap the wave and the electrode gap gives the relative delay. A SAW filter is composed of a minimum of two transducers. A schematic of a simple SAW bi-directional filter is shown in Fig. 3.26. A bi-directional transducer radiates energy equally from each side of the transducer. Energy that is not associated with the received signal is absorbed to eliminate spurious reflections.

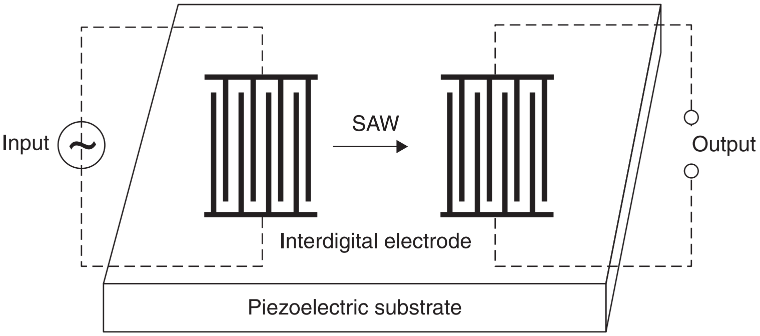

3.26 SAW bi-directional filter.

Various materials are currently used for SAW devices. The most popular single-crystal SAW materials are lithium niobate and lithium tantalate. These materials have different properties depending on the cut of the material and the direction of propagation. The fundamental parameters considered when choosing a material for a given device application are the SAW velocity, the temperature coefficients of delay (TCD), the electromechanical coupling factor and propagation loss. Surface acoustic waves can be generated and detected by spatially periodic, interdigital electrodes on the plane surface of a piezoelectric plate. A periodic electric field is produced when an RF source is connected to the electrode, thus permitting piezoelectric coupling to a traveling surface wave. If an RF source with a frequency, f, is applied to an electrode having periodicity, d, energy conversion from an electrical to a mechanical form will be a maximum when

$$f = f_0 = v_s / d \qquad [3.38]$$

where v_s is the *SAW velocity* and f_0 is the center frequency of the device. The SAW velocity is an important parameter determining the center frequency. Another important parameter for many applications is temperature sensitivity. For example, the temperature stability of the center frequency of SAW bandpass filters is a direct function of the temperature coefficient for the velocity and the delay for the material used. The first-order temperature coefficient of delay is given by

$$(1/\tau)\cdot(d\tau/dT) = (1/L)\cdot(dL/dT) - (1/v_s)\cdot(dv_s/dT), \qquad [3.39]$$

where $\tau = L/\mathrm{v}_s$ is the *delay time* and L is the SAW propagation length. The surface wave coupling factor, k_s^2, is defined in terms of the change in SAW velocity which occurs when the wave passes across a surface coated with a thin massless conductor, so that the piezoelectric field associated with the wave is effectively short-circuited. The coupling factor, k_s^2, is expressed by:

$$k_s^2 = 2\,(v_f - v_m)\,/\,v_f, \qquad [3.40]$$

where v_f is the free surface wave velocity and v_m the velocity on the metallized surface. In actual SAW applications, the value of k_s^2 relates to the maximum bandwidth obtainable and the amount of signal loss between input and output, which determines the fractional bandwidth as a function of minimum insertion loss for a given material and filter. Propagation loss is one of the major factors that determine the insertion loss of a device and is caused by wave scattering at crystalline defects and surface irregularities. Materials which show high electromechanical coupling factors combined with small temperature coefficients of delay are generally preferred. The free surface velocity, v_f, of the material is a function of the cut angle and propagation direction. The TCD is an indication of the frequency shift expected for a transducer due to a temperature change and is also a function of the cut angle and propagation direction. The substrate is chosen based on the device design specifications, which include operating temperature, fractional bandwidth and insertion loss.

Piezoelectric single crystals such as 128°Y-X (128°-rotated-Y-cut and X-propagation) – $LiNbO_3$ and X-112°Y (X-cut and 112°-rotated-Y-propagation) – $LiTaO_3$ have been extensively employed as SAW substrates for applications in Video Intermediate-Frequency (VIF) filters. A *c*-axis-oriented ZnO thin film deposited on a fused quartz, glass or sapphire substrate has also been commercialized for SAW devices. Table 3.4 summarizes some important material parameters for these SAW materials.

A delay line can be formed from a slice of glass such as PbO or K_2O doped SiO_2 glass in which the velocity of sound is nearly independent of temperature. PZT ceramic transducers are soldered onto two metallized edges of the slice of glass. The input transducer converts the electrical signal to a shear acoustic wave, which travels through the slice. At the output transducer the wave is reconverted into an electrical signal delayed by the length of time taken to travel around the slice. Such delay lines are used in color TV sets to introduce a delay of approximately 64 μs and are also employed in videotape recorders.

Table 3.4 SAW material properties

	Material	Cut-propagation direction	K^2 (%)	TCD ($ppm.C^{-1}$)	V_0 ($m.s^{-1}$)	ε_r
Single crystal	Quartz	ST-X	0.16	0	3158	4.5
	$LiNbO_3$	128°Y-X	5.5	–74	3960	35
	$LiTaO_3$	X112°-Y	0.75	–18	3290	42
	$Li_2B_4O_7$	(110)-<001>	0.8	0	3467	9.5
Ceramic	PZT-In$(Li_{3/5}W_{2/5})O_3$		1.0	10	2270	690
	$(Pb,Nd)(Tl,Mn,In)O_3$		26	<1	2554	225
Thin film	ZnO / glass		0.64	–15	3150	8.5
	ZnO / sapphire		1.0	–30	5000	8.5

There has been an interesting recent development of a SAW actuator application. A liquid transportation system was developed by using a standing-wave-type SAW device.[64] A liquid droplet can be transported by controlling the SAW wave.

3.2.6 Piezoelectric transducer designs

Piezoelectric actuators are a new field of research combining electronic and structural ceramics.[65–69] Two of the most popular actuator designs are the multilayer[70] and the bimorph (see Fig. 3.27). The multilayer, in which roughly 100 thin piezoelectric ceramic sheets are stacked together, has the advantages of a low driving voltage (100 V), quick response (10 μs), high generative force (1 kN) and high electromechanical coupling. But the displacement, of the order of 10 μm, is not sufficient for some applications. This contrasts with the characteristics of the bimorph, which consists of multiple piezoelectric and elastic plates bonded together to generate a large bending displacement of several hundred micrometers, but has a relatively low response time (1 ms) and generative force (1 N).

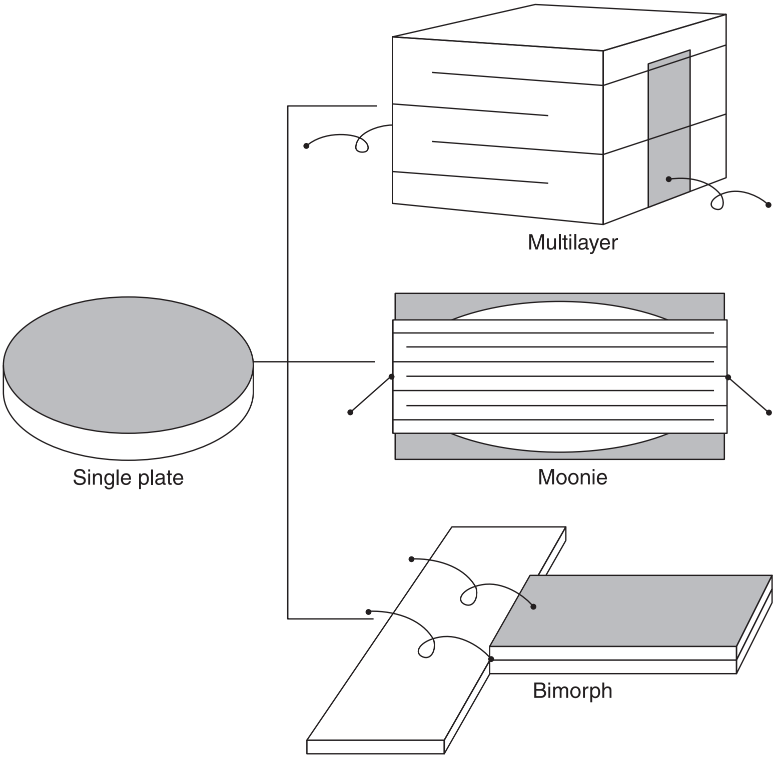

3.27 Piezoelectric actuators.

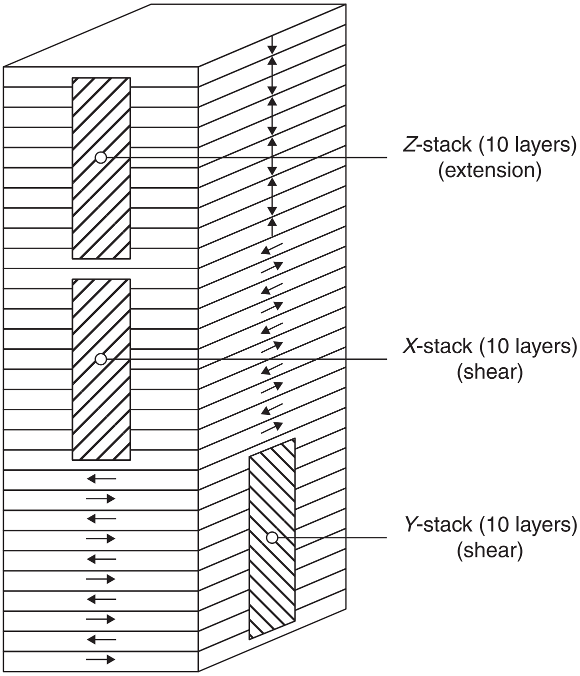

3.28 3D positioning actuator with a stacked structure.

A 3D positioning actuator with a stacked structure, as pictured in Fig. 3.28, was designed by a German company, where a shear strain was used to generate the x and y displacements.[71] Polymer-packed PZT bimorphs have been commercialized by ACX for vibration reduction/control applications in smart structures.[72]

Market research conducted in 1998 by the Japan Technology Transfer Association clarified that the actual demands for actuators are: 100 µm displacement, 100 N force and 100 µs response. Because neither the multilayer nor the bimorph can satisfy this actual demand, composite actuator structures called the ‘moonie’ and ‘cymbal’ were developed to provide characteristics intermediate between the multilayer and bimorph actuators; this type of transducer has a displacement an order of magnitude larger than the multilayer, and a much larger generative force with a quicker response than the bimorph.[73] The device consists of a thin multilayer piezoelectric element and two metal plates with a narrow moon-shaped or cymbal-shaped cavity bonded together as shown in Fig. 3.27. The moonie, with a size of $5 \times 5 \times 2.5\,\text{mm}^3$, can generate a 20 µm displacement under 60 V, eight times as large as the generative displacement produced by a multilayer of the same size.[74] This new compact actuator has been used in a miniaturized laser beam scanner.

3.3 References

1. K. Uchino: The development of piezoelectric materials and the new perspective. In *Advanced Piezoelectric Materials*, K. Uchino (Ed.), Woodhead Publishing Ltd (2010).
2. K. Uchino: *Entrepreneurship for Engineers*, CRC Press, New York, NY (2009).
3. K. Honda: *Ultrasonic World*, NHK books, No. 710, Tokyo, Japan (1994).
4. A. M. Nicholson: *Piezophony*, US Patent 1,495,429, filed 10 April 1918, patented 10 May 1924.
5. E. W. Moore: A method of growing large perfect crystals from solution, *J. Amer. Chem. Soc.*, **41**, 1060–6 (1919).
6. G. Busch: Early history of ferroelectricity, *Condensed Matter News*, **1**(2), 20–9 (1991).
7. G. Busch and P. Scherrer, *Naturwiss.*, **23**, 737 (1935).
8. E. Wainer and N. Salomon: High titania dielectrics, *Trans. Electrochem. Soc.*, **89** (1946).
9. T. Ogawa: On barium titanate ceramics [in Japanese], *Busseiron Kenkyu*, **6**, 1–27 (1947).
10. B. M. Vul: High and ultrahigh dielectric constant materials [in Russian], *Electrichestvo*, **3** (1946).
11. T. Ogawa and S. Waku: History of barium titanate discovery in Japan, *Splendid Tita-Bari* [in Japanese], Maruzen, Tokyo (1990).
12. B. Jaffe, W. Cook and H. Jaffe: *Piezoelectric Ceramics*, Academic Press, London (1971).
13. S. Roberts: Dielectric and piezoelectric properties of barium titanate, *Phys. Rev.*, **71**, 890–5 (1947).
14. W. P. Mason: Piezoelectric and electrostrictive effect in barium titanate ceramics, *Phys. Rev.*, **73**, 1398–9 (1948).
15. E. Sawaguchi, G. Shirane and Y. Takagi: Phase transition in lead zirconate, *J. Phys. Soc. Japan*, **6**, 333–9 (1951).
16. E. Sawaguchi: Ferroelectricity versus antiferroelectricity in the solid solutions of $PbZrO_3$ and $PbTiO_3$, *J. Phys. Soc. Japan*, **8**, 615–29 (1953).
17. B. Jaffe: *Piezoelectric Transducers Using Lead Titanate and Lead Zirconate*, US Patent 2,708,244, May (1955).
18. B. Jaffe, W. R. Cook Jr and H. Jaffe: *Piezoelectric Ceramics*, Academic Press, London (1971).
19. K. Abe, T. Tanaka, S. Miura and K. Okazaki: Study on Langevin type $BaTiO_3$ ceramic vibrator, *Bull. Inst. Chem. Res.*, Kyoto Univ., **31**, 295–304 (1953).
20. T. Tanaka: Barium titanate ceramics and their applications, *Bull. Inst. Chem. Res.*, Kyoto Univ., **32**, 43–53 (1954).
21. B. T. Matthias and J. P. Remeika: Ferroelectricity in the ilmenite structure, *Phys. Rev.*, **76**, 1886–7 (1949).
22. K. Uchino: *Ferroelectric Devices 2nd Edition*, CRC Press, New York, NY (2009).
23. G. A. Smolenskii and A. I. Agranovskaya: *Sov. Phys., Solid State*, **1**, 1429 (1960).
24. V. A. Bokov and I. E. Myl'nikova: *Sov. Phys., Solid State*, **2**, 2428 (1961).
25. L. E. Cross, S. J. Jang, R. E. Newnham, S. Nomura and K. Uchino: Large electrostrictive effects in relaxor ferroelectrics, *Ferroelectrics*, **23**(3), 187 (1980).
26. J. Kuwata, K. Uchino and S. Nomura: Phase transitions on the $Pb(Zn_{1/3}Nb_{2/3})O_3$–$PbTiO_3$ system, *Ferroelectrics*, **37**, 579 (1981).
27. J. Kuwata, K. Uchino and S. Nomura: Dielectric and piezoelectric properties of $0.91Pb(Zn_{1/3}Nb_{2/3})O_3 - 0.09PbTiO_3$ single crystals, *Jpn. J. Appl. Phys.*, **21**, 1298 (1982).

28. K. Yanagiwawa, H. Kanai and Y. Yamashita: *Jpn. J. Appl. Phys.*, **34**, 536 (1995).
29. S. E. Park and T. R. Shrout: *Mat. Res. Innovt.*, **1**, 20 (1997).
30. X. H. Du, U. Belegundu and K. Uchino: Crystal orientation dependence of piezoelectric properties in lead zirconate titanate: Theoretical expectation for thin films, *Jpn. J. Appl. Phys.*, **36**(9A), 5580–7 (1997).
31. H. Kawai: *Jpn. J. Appl. Phys.*, **8**, 975 (1969).
32. V. Bharti, H. S. Xu, G. Shanti, Q. M. Zhang and K. Liang: *J. Appl. Phys.*, **87**, 452 (2000).
33. Y. Saito: *Jpn. J. Appl. Phys.*, **35**, 5168–73 (1996).
34. T. Kitayama and S. Sugawara: *Proc. Study Comm. Electronic Circuit Components & Mater.*, Ref. No. CPM72-17 (1972-0) (1972).
35. R. E. Newnham, D. P. Skinner, L. E. Cross, *Mater. Res. Bull.*, **13**, 525 (1978).
36. J. Van Suchtelene: *Philips Res. Rep.*, **27**, 28 (1972).
37. J. Ryu, A. Vazquez Carazo, K. Uchino and H.-E. Kim: Magnetoelectric properties in piezoelectric and magnetostrictive laminate composites, *Jpn. J. Appl. Phys.*, **40**, 4948–51 (2001).
38. K. Uchino and T. Ishii: Mechanical damper using piezoelectric ceramics, *J. Ceram. Soc. Jpn.*, **96**, 863 (1988).
39. Y. Suzuki, K. Uchino, H. Gouda, M. Sumita, R. E. Newnham and A. R. Ramachandran: Mechanical dampers using piezoelectric composites, *J. Ceram. Soc. Jpn., Int'l Edition*, **99**, 1096 (1991).
40. P. S. Brody: *Ferroelectrics*, **50**, 27 (1983).
41. K. Uchino and M. Aizawa: Photostrictive actuators using PLZT ceramics, *Jpn. J. Appl. Phys. Suppl.*, **24**, 139–41 (1985).
42. M. Tanimura and K. Uchino: Effect of impurity doping on photo-strictive in ferroelectrics, *Sensors and Materials*, **1**, 47–56 (1988).
43. K. Uchino: Micro walking machine using piezoelectric actuators, *J. Rob. Mech.*, **124**, 44–7 (1989).
44. S. Thakoor, J. M. Morookian and J. A. Cutts: The role of piezoceramics microactuation for advanced mobility, *Conf. Proc. 10th IEEE Int'l Symp. on Appl. Ferroelectrics*, **1**, 205–11 (1996).
45. K. Uchino, M. Yoshizaki, K. Kasai, H. Yamamura, N. Sakai and H. Asakura: Monomorph actuators using semiconductive ferroelectrics, *Jpn. J. Appl. Phys.*, **26**(7), 1046 (1987).
46. Aura Ceramics, Inc., catalogue *Rainbow*.
47. K. Uchino: *Micromechatronics*, CRC/Dekker, New York, NY (2003).
48. T. Ikeda: *Fundamentals of Piezoelectric Materials Science*, Ohm Publishing Co., Tokyo (1984).
49. L. E. Kinsler, A. R. Frey, A. B. Coppens and J. V. Sanders: *Fundamentals of Acoustics*, John Wiley & Sons, New York, NY (1982).
50. W. A. Smith: *Proc. SPIE – The Int'l Society for Optical Engineering*, 1733 (1992).
51. Y. Ito and K. Uchino: Piezoelectricity, in *Wiley Encyclopedia of Electrical and Electronics Engineering*, Vol. **16**, p. 479, John Wiley & Sons, NY (1999).
52. H. Takeuchi, S. Jyomura, E. Yamamoto and Y. Ito: *J. Acoust. Soc. Am.*, **74**, 1114 (1982).
53. Y. Yamashita, K. Yokoyama, H. Honda and T. Takahashi: *Jpn. J. Appl. Phys.*, **20**, Suppl. 20–4, 183 (1981).
54. Y. Ito, H. Takeuchi, S. Jyomura, K. Nagatsuma and S. Ashida: *Appl. Phys. Lett.*, **35**, 595 (1979).

55. H. Takeuchi, H. Masuzawa, C. Nakaya and Y. Ito: *Proc. IEEE 1990 Ultrasonics Symposium*, 697 (1990).
56. T. R. Shrout, Z. P. Chang, N. Kim and S. Markgraf: *Ferroelectric Letters*, **12**, 63 (1990).
57. S. Saitoh, T. Takeuchi, T. Kobayashi, K. Harada, S. Shimanuki and Y. Yamashita: *Jpn. J. Appl. Phys.*, **38**(5B), 3380–4 (1999).
58. R. E. Newnham, D. P. Skinner and L. E. Cross: *Materials Research Bulletin*, **13**, 525 (1978).
59. W. A. Smith: *Proc. 1989 IEEE Ultrasonic Symposium*, 755 (1989).
60. S. Kalpat, X. Du, I. R. Abothu, A. Akiba, H. Goto and K. Uchino: Effect of crystal orientation on dielectric properties of lead zirconate titanate thin films prepared by reactive rf-sputtering, *Jpn. J. Appl. Phys.*, **40**, 713 (2001).
61. K. Uchino, E. Sadanaga and T. Hirose, Dependence of the crystal structure on particle size in barium titanate, *J. Amer. Ceram. Soc.*, **72** (8), 1555–8 (1989).
62. C. Campbell: *Surface Acoustic Wave Devices and Their Signal Processing Applications*, San Diego, Calif. Academic Press (1989).
63. H. Matthews: *Surface Wave Filters*, New York: Wiley Interscience (1977).
64. A. Yamamoto and T. Higuchi: Japan. Patent Disclosure, P2004-190537A (2004).
65. K. Uchino: Piezoelectric actuators 2006 – Expansion from IT/robotics to ecological/energy applications, *Proc. Actuator 2006*, p. 48, Bremen Messe, Bremen, Germany, 14–16 June (2006).
66. K. Uchino: Electrostrictive actuators: Materials and applications, *Bull. Am. Ceram. Soc.*, **65**(4), 647 (1986).
67. K. Uchino: Ceramic actuators: Principles and applications, *MRS Bull.*, **18**(4), 42 (1993).
68. K. Uchino (ed.): *Handbook on New Actuators for Precision Position Control*, Fuji Technosystem, Tokyo (1994).
69. K. Uchino: Recent developments in ceramic actuators, *Proc. Workshop on Microsystem Technologies in the USA and Canada*, Germany, mst news, special issue, VDI/VDE, 28–36 (1996).
70. S. Takahashi, A. Ochi, M. Yonezawa, T. Yano, T. Hamatsuki and I. Fujui: *Ferroelectrics*, **50**, 181 (1993).
71. A. Bauer and F. Moller: *Proc. 4th Int'l Conf. New Actuators*, Germany, 128 (1994).
72. Active Control Experts, Inc., catalogue *PZT Quick Pack* (1996).
73. Y. Sugawara, K. Onitsuka, S. Yoshikawa, Q. C. Xu, R. E. Newnham and K. Uchino: Metal-ceramic composite actuators, *J. Am. Ceram. Soc.*, **75**(4), 996 (1992).
74. H. Goto, K. Imanaka and K. Uchino: Piezoelectric actuators for light beam scanners, *Ultrasonic Techno.*, **5**, 48 (1992).

4

Thin-film PZT-based transducers

M. K. KUROSAWA, Tokyo Institute of Technology, Japan

Abstract: The miniaturization of ultrasonic actuators and sensors uses a deposition process for the fabrication of the piezoelectric film. The hydrothermal deposition process is suitable for the fabrication of these devices: it involves low reaction temperatures, is carried out in solution, self-polarization occurs and no annealing is required. Devices fabricated using hydrothermal PZT film deposition have high-intensity vibration capabilities, which is beneficial for actuator applications. The fabrication and analysis of an ultrasonic micro-motor, a touch-probe sensor and an ultrasonic micro-scalpel that operate using the transverse-mode d_{31} effect are described. The fabrication of a thickness-vibration-mode broadband hydrophone and a needle-type hydrophone, which use the longitudinal-mode d_{33} effect, are discussed.

Key words: hydrothermal process, lead zirconate titanate (PZT) film, microelectromechanical system (MEMS), micro-motor, micro-actuator, ultrasonic motor, touch-probe sensor, micro-scalpel, ultrasonic scalpel, hydrophone, ultrasonic probe.

4.1 Introduction

Several methods can be used to deposit a piezoelectric thin film. Of these, the hydrothermal method is commonly used because of the relatively thick films that can be deposited and the fact that the method can be used in the fabrication of complex shapes. The hydrothermal process is carried out in solutions at temperatures of around 200 °C and under high atmospheric pressure conditions, for the synthesis of minerals such as crystals. Recently, the hydrothermal process has been applied to deposit a film material during the fabrication of microelectromechanical devices. A series of experiments to deposit lead zirconate titanate (PZT) film on a titanium base material were carried out by Ohba and colleagues.[1–5] The hydrothermal PZT film was used to fabricate micro-actuators and sensors.

Ohba and co-workers fabricated a piezoelectric material by depositing a polycrystalline PZT film onto a titanium surface at temperatures below 200 °C. The process has the following advantages:

- low temperatures, i.e. below 200 °C
- no annealing is required
- complicated structures can be fabricated in solution
- films that are several microns to several tens of microns thick can be fabricated
- morphotropic phase boundary conditions can be achieved
- a transverse-mode d_{31} value of 93 $\mathrm{pC.N^{-1}}$ can be achieved.

Following the work by Ohba *et al.*, several other research groups carried out research into the practical application of devices fabricated using this technology: Morita *et al.*[6–9] described work on ultrasonic micro-motors, Kanda and co-workers investigated touch-probe micro-sensors,[10–13] Ishikawa *et al.*[14–16] studied broadband hydrophones and Hasegawa looked at needle micro-hydrophone applications.[17,18]

Recently, Morita *et al.*[19–21] demonstrated PZT and PT epitaxial film deposition using the hydrothermal method. The film had superior characteristics in remanent polarization. Funakubo and colleagues[22,23] succeeded in depositing epitaxial films of $KNbO_3$ and $(K,Na)NbO_3$. From the results of these published works, it is envisaged that epitaxial piezoelectric thick films will find many applications in the fabrication of advanced micro-transducers.

4.2 PZT deposition using the hydrothermal process

4.2.1 The hydrothermal process and the deposited film

The hydrothermal method has been investigated as a means of depositing PZT films on base materials in order to fabricate micro-actuators and sensors. The hydrothermal method utilizes a chemical reaction between the titanium base metal and the melted ions at a temperature that is slightly higher than the boiling point of water (i.e. 100 °C). The chemical reaction is carried out in solution, which enables three-dimensional base metals to be used. At the start of the deposition process, the titanium base material reacts with the metal ions in solution, and a strong adhesive film is deposited. With a titanium or a titanium alloy base material, a polycrystalline film is deposited (Fig. 4.1). The dimensions of the crystals depend on the process conditions; crystal sizes can range from several microns to more than 10 μm.

In addition to having a relatively low operating temperature and operating in solution, the hydrothermal process has other advantages. It is possible to deposit relatively thick films, of up to 100 microns; however, it takes a long time to deposit a thick film. The PZT film that is deposited is automatically polarized in the thickness direction during the hydrothermal process; hence there is no requirement for a subsequent poling process. Usually, when ferroelectric film materials are fabricated, an annealing process is necessary after the deposition process. However, for hydrothermal films, no annealing process is required; i.e. the PZT film deposited by the hydrothermal method has piezoelectric characteristics in the as-deposited condition. The hydrothermal process therefore allows complicated structures to be created and also permits the use of soft materials as the base material, for example resins.

The hydrothermal deposition process is carried out at temperatures higher than 100 °C and under high atmospheric pressure conditions; an autoclave (Fig. 4.2) is therefore used for the process. The autoclave shown in Fig. 4.2 has a capacity of

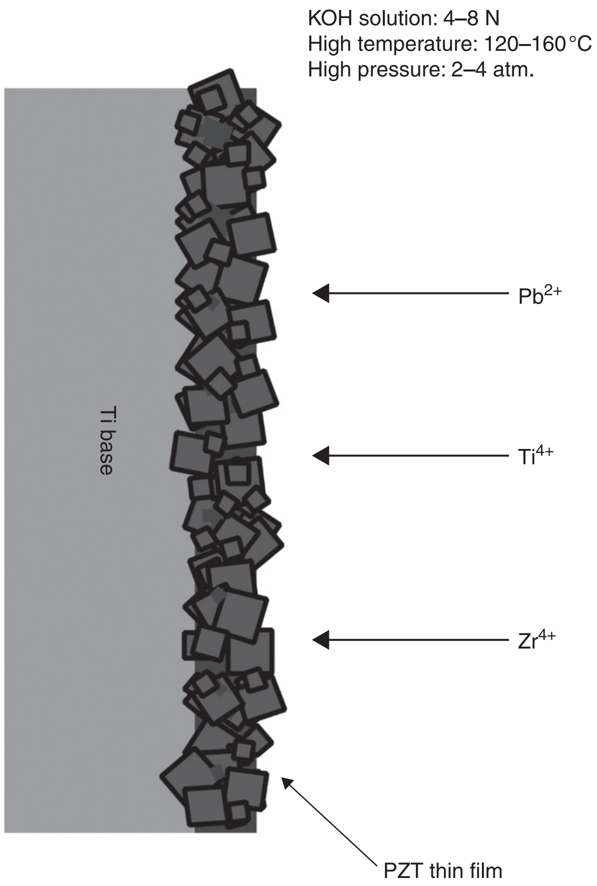

4.1 Polycrystalline film deposited on a titanium or a titanium alloy base.

50 ml, but a wide range of autoclave capacities are available on the market. These autoclaves have an inner vessel made of Teflon to provide high corrosion resistance, while the outer container is made of stainless steel or Hastelloy to provide resistance to both the high-pressure and high-corrosion conditions. The autoclave shown in Fig. 4.2 has a rotational cap to seal the system. The autoclave is maintained at an even temperature in an electric oven; it is rotated slowly at several turns per minute for a titanium base material.

The titanium base material and the reaction solution (described in more detail below) are put into the inner Teflon vessel. To avoid an explosion, the volume of the ingredients is restricted to less than 70% of the vessel capacity, so that space is left for expansion. While the autoclave rotates, it is essential to ensure that the base material is covered by the reaction solution. The base material therefore

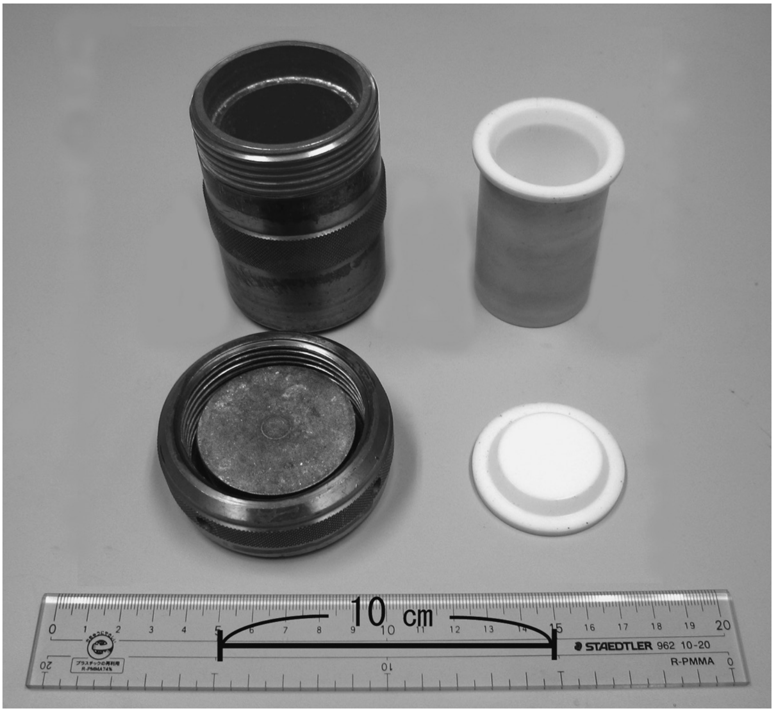

4.2 Autoclave for hydrothermal deposition.

needs to be fixed in a holder made of titanium wire or Teflon to prevent contact with the sides of the autoclave. After the thermal process, the autoclave is left to cool before opening.

The reaction process has two steps. Both processes are carried out in the autoclave at a high temperature and a high pressure. The first step is called the nucleation process. During the nucleation process, nuclear crystals of PZT are deposited on the titanium base. The process temperature is 140 °C or 160 °C. The autoclave is kept at this high temperature for 24 hours. The solution during the nucleation process contains a small number of titanium ions, as shown in Table 4.1. Titanium is also provided from the base material; therefore the overall titanium ion concentration of the first step is low. In the original process proposed by Ohba,[1–5] titanium ions were not added to the reaction solution at the nucleation step. Morita *et al.*[7,8] designed the 'improved nucleation process' described in this chapter. The reaction conditions for transducer fabrication are shown in Table 4.1. To ensure tight bonding of the film to the base material, this first step has a higher temperature than is used in the second step to increase the level of reaction.

The second step in the process is carried out at the slightly lower temperature of 120 °C, as shown in Table 4.1. The concentrations of each ion are adjusted to

Table 4.1 Reaction conditions for the hydrothermal method: the nucleation process and the crystal growth process

First process (nucleation)		
$ZrOCl_28H_2O$	0.532 g	Melted into 2 ml H_2O
$TiCl_4$	0.693 ml	1.95 mol.l^{-1} $TiCl_4$
$Pb(NO_3)_2$	1.20 g	Melted into 7 ml H_2O
KOH	2.69 g	Melted into 11 ml H_2O
At 140 °C for 24 hours		
Second and subsequent processes (crystal growth)		
$ZrOCl_28H_2O$	0.761 g	Melted into 2 ml H_2O
$TiCl_4$	1.10 ml	1.95 mol.l^{-1} $TiCl_4$
$Pb(NO_3)_2$	1.80 g	Melted into 7 ml H_2O
KOH	2.69 g	Melted into 11 ml H_2O
At 120 °C for 24 hours		

obtain the correct ingredient ratio for crystal growth. During the second stage, the PZT crystals grow. The thickness of the film is increased by repeating this crystal growth process. To obtain film thicknesses over 10 μm, it may be necessary to repeat the growth process more than ten times. After the crystal growth process has been repeated four times, there will be a 12-μm-thick film on both sides of the titanium base. Figure 4.3 shows an example of the weight and the thickness change of a bimorph element with film deposited on both sides.

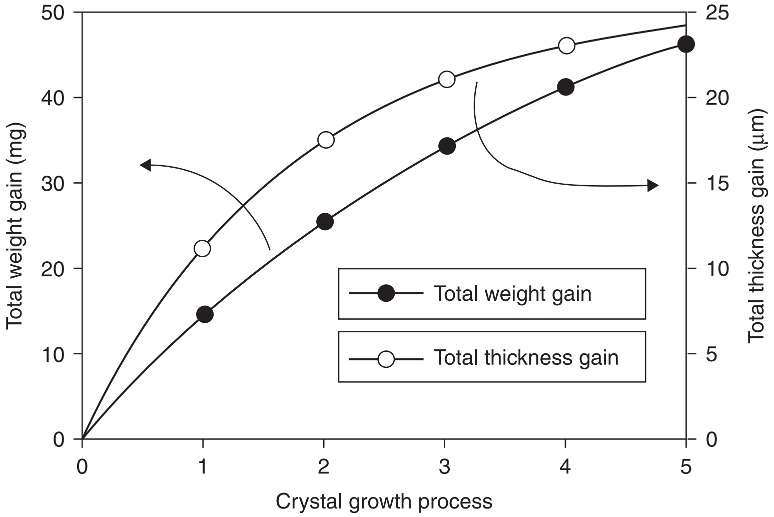

4.3 Weight and thickness change of a bimorph element for each crystal growth process.

Because annealing is not necessary with the hydrothermal method, repetition of the growth process results in thick films that do not contain cracks or other faults.

Solution preparation

Zirconyl chloride octahydrate, lead dinitrate and potassium hydroxide are used in powder or granulated form. These materials are weighed and dissolved in pure water in advance of the fabrication process. Titanium tetrachloride is a dense solution in its as-supplied form, and therefore the solution should be diluted before use. During the dilution of titanium tetrachloride with pure water, exothermic reactions take place and there is a risk that titanium dioxide will be precipitated. In order to avoid this precipitation, a slow dilution rate, with cooling, should be employed. After the dilution, the concentration is measured; this concentration will be different for each batch of diluted titanium tetrachloride solution that is used.

Film characteristics

Morita *et al.*[7] reported the results of X-ray diffraction (XRD) measurements of fabricated PZT films and these are shown in Fig. 4.4. It can be seen that a polycrystal PZT film was deposited on the titanium base. The surface of the film was observed using scanning electron microscopy (SEM) as shown in Fig. 4.5 (from Kanda *et al.*[11]). These three images show the results of the deposition when the crystal growth process was repeated twice, Fig. 4.5(a), five times, Fig. 4.5(b) and 15 times, Fig. 4.5(c). It is evident that when the growth process was repeated five times the resulting film has larger crystals than in the film produced when the growth process was only repeated twice. When the growth process is repeated 15 times, however, smaller crystals are seen due to new nucleation. The film has a

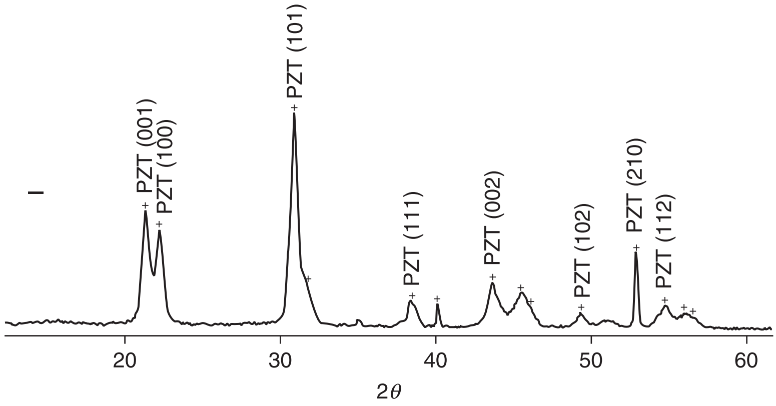

4.4 X-ray diffraction measurements of fabricated PZT films.

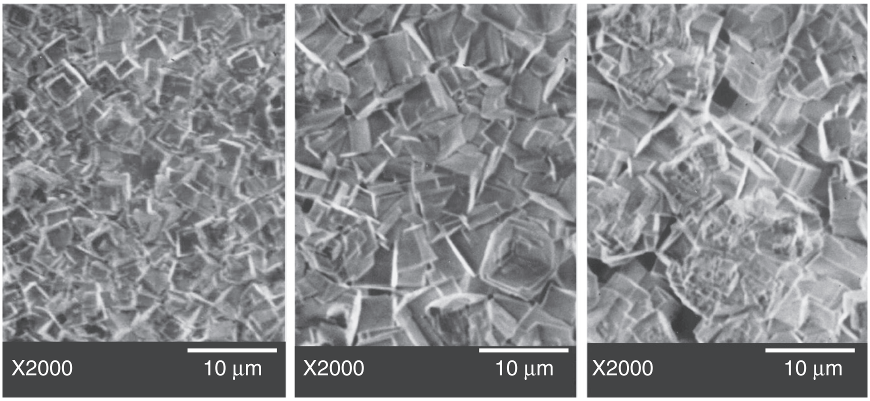

(a) (b) (c)

4.5 SEM images of film surface, with crystal growth process repeated (a) twice, (b) five times and (c) 15 times.

black appearance after five repetitions of the process; when the number of repetitions increases to 10 or 15, the surface becomes a light gray color. This color change occurs because PZT crystals are colorless and transparent by nature. Analysis of the relation between the number of repetitions of the growth process and the film thickness has demonstrated that the mean film thickness for one process repetition is from 2 to 4 µm. The deposited PZT film is firmly adhered to the titanium base, as shown in Fig. 4.6, which shows an SEM image of a cross section of the PZT film.[24]

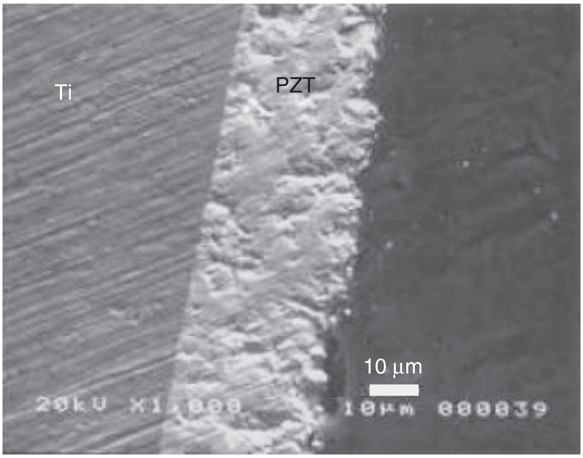

4.6 SEM image of a cross section of PZT film.

4.2.2 Material evaluation

The relative dielectric constant of the deposited PZT film was reported to be about 500.[8,12] The piezoelectric constant in the transverse mode, d_{31}, was measured by using a bimorph element as shown in Fig. 4.7.[3,8] The bimorph element is driven at a much lower frequency of bending resonance, and the bending displacement at the end is measured, for example, by laser displacement measurement. The displacement of the element is shown in Fig. 4.8. From the measurements, the piezoelectric factor d_{31} was estimated to be from −22 to −35 pC.N^{-1}.[8,11,12] The d_{31} value of the bulk material is three times higher than these values. In order to evaluate the piezoelectric factor e_{31}, a longitudinal vibrator was used (Fig. 4.9). From the vibration velocity and the *Q* factor at the resonance frequency, the e_{31} value was estimated to be −0.12 to −0.57 N.V^{-1}.[9–12] From the resonance frequency of the bending vibration, Young's modulus was estimated to be 1.3×10^{10} N.m^{-2}.[12]

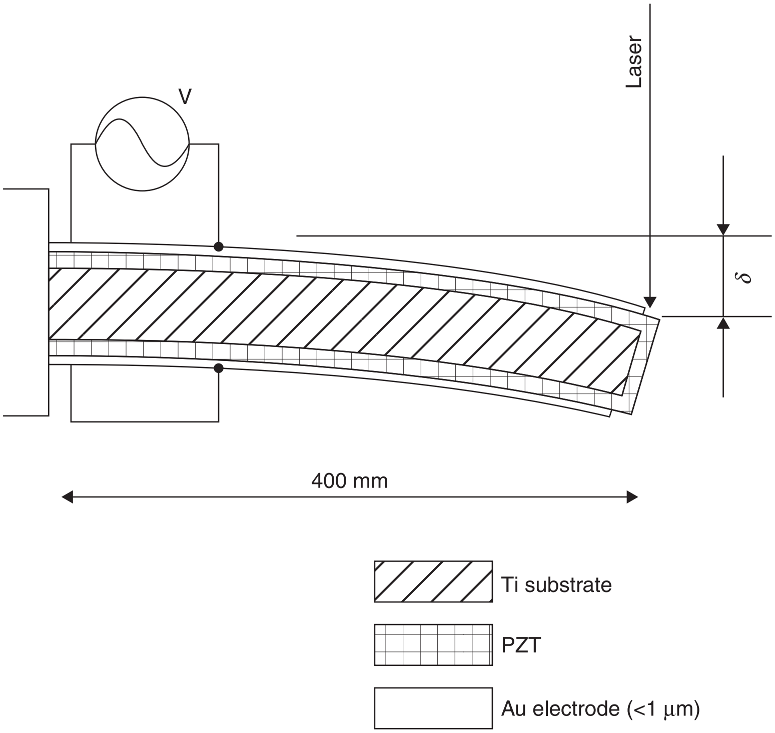

4.7 Bimorph element used to measure the piezoelectric constant in the transverse mode, d_{31}.

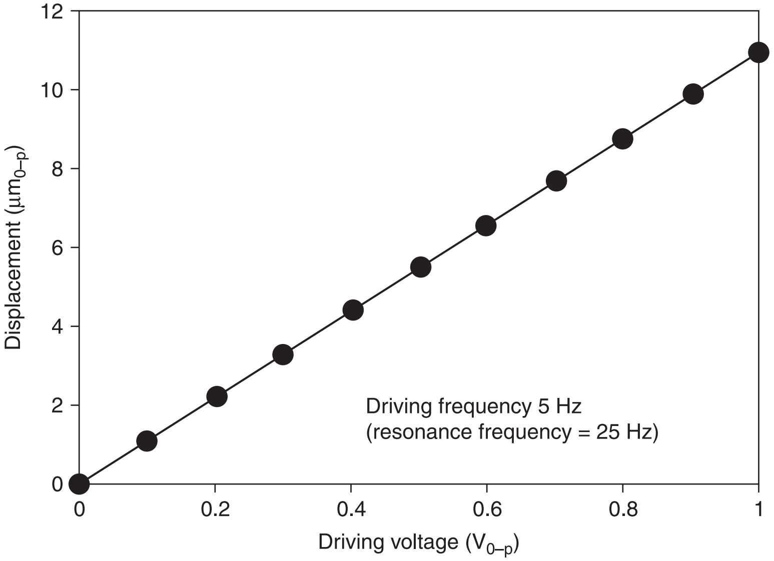

4.8 Displacement of the bimorph element.

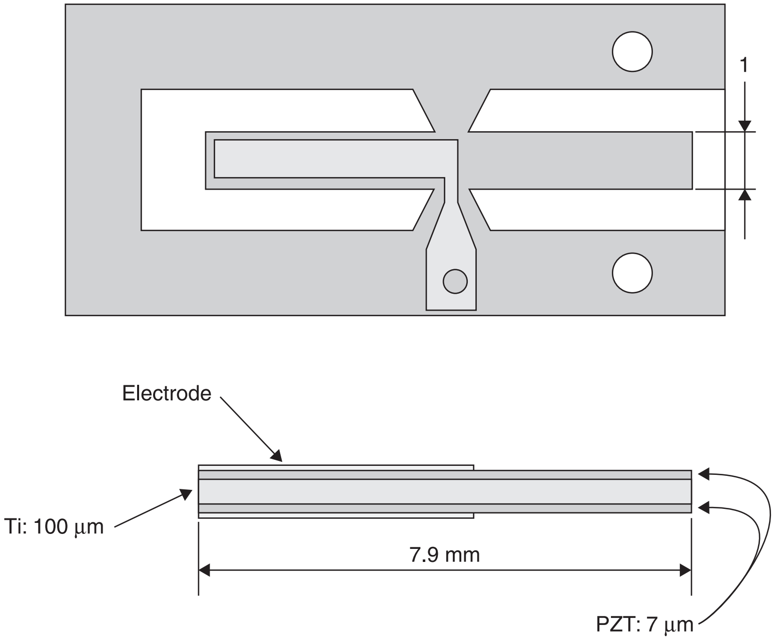
1
Electrode
Ti: 100 μm
7.9 mm
PZT: 7 μm

4.9 Longitudinal vibrator used to measure piezoelectric factor e_{31}.

4.2.3 Vibration velocity characteristics at resonance

At the resonance frequency, the dynamic characteristics of a piezoelectric film transducer are important. However, few investigations have reported on the high-intensity vibration conditions of film transducers.[11,24] For the hydrothermal PZT film transducer discussed here, the vibration velocity limit was tested using a sample vibrator as shown in Fig. 4.9. A 1-mm-wide and 7.9-mm-long rectangular half-wavelength longitudinal vibrator was fabricated from a 0.1-mm-thick titanium plate. The vibrator was fixed at its longitudinal vibration node, namely at the center, by the outer frame. The PZT film was deposited on both sides. For driving, a quarter-wavelength electrode was deposited and used to apply a voltage in the thickness direction to excite a thickness–longitudinal effect. Only one side of the vibrator was driven.

Three vibrators were used to measure the vibration velocity. They had different film thicknesses of 7, 17 and 38 μm – created by 2, 5 and 15 deposition process cycles, respectively. Each vibrator was driven at its resonance frequency of around 270 kHz, and the response of the vibration velocity at the end due to the driving voltage was measured in the length direction using a laser Doppler vibrometer. Because the vibrator was excited at its resonance mode, the pure longitudinal vibration mode was excited without any bending vibration.

The measured vibration velocity is shown in Fig. 4.10. The maximum vibration velocity was 2.2 m.s^{-1}, which is 3–5 times larger than the vibration velocities of

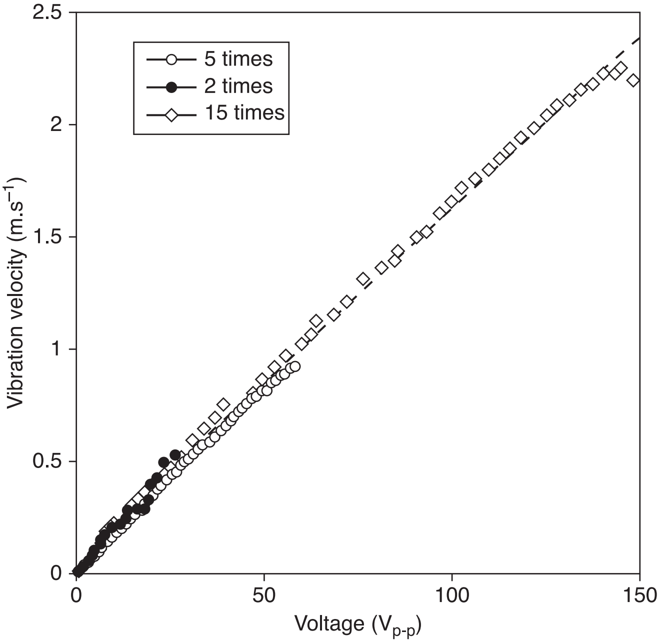

4.10 Vibration velocity vs. V$_{p-p}$.

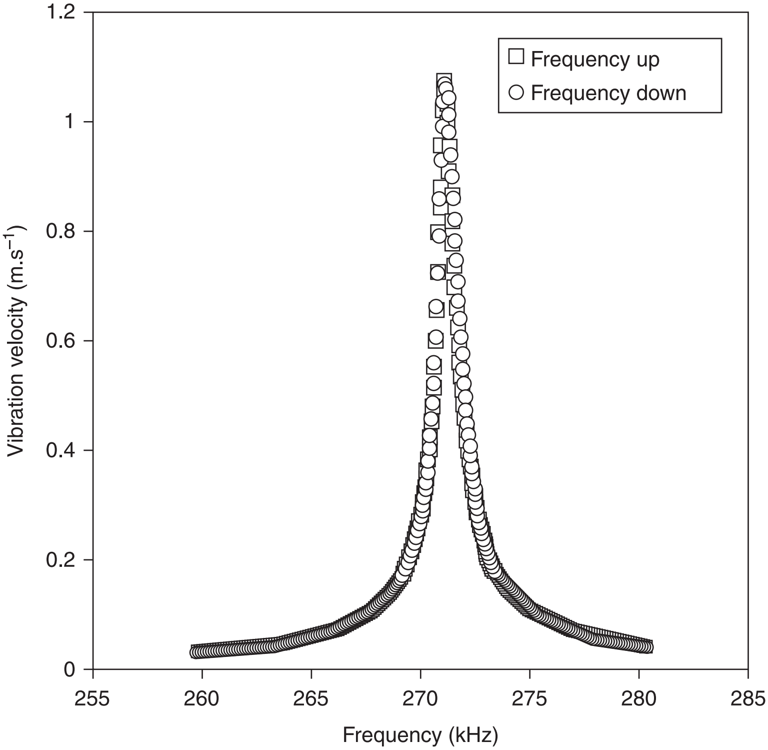

4.11 Vibration velocity vs. frequency.

the bulk ceramic PZT material. In addition, the linearity of the resonance is satisfactory, as shown in Fig. 4.11.[11] For the ceramic PZT vibrator, a jumping phenomenon is observed so that the symmetrical pattern shown in Fig. 4.11 is not maintained. It is supposed that the polycrystal structure of the hydrothermal PZT film causes this good linearity. The mechanical *Q* factor of Fig. 4.11 was 400. Other vibrators had even better *Q* factors of 1000. This difference in vibrator quality is caused by the uneven characteristics of the deposited film.

4.3 Applications using the bending and longitudinal vibration of the d_{31} effect

4.3.1 A cylindrical bending vibrator used for an ultrasonic micro-motor

Research into a cylindrical ultrasonic micro-motor has been reported previously.[6–9] The stator transducer had a diameter of 2.4 mm and a length of 10 mm, as shown in Fig. 4.12. A PZT film was deposited on the curved surface of a titanium tube

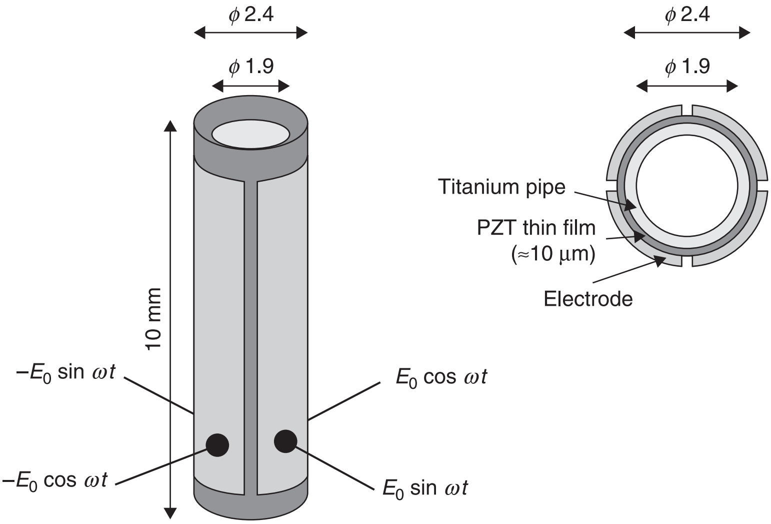

4.12 Ultrasonic micro-motor.

and four strips of electrode were then deposited on the tube element. The fundamental bending vibration mode was excited using a pair of facing electrodes. The deformations and rotation of the ultrasonic motor are illustrated in Fig. 4.13. A pair of degenerate bending vibration modes was generated at the resonance frequency. The phase relation in time is orthogonal, with a 90° phase difference. Therefore the rotation mode is excited.

A cross section of the ultrasonic micro-motor is shown in Fig. 4.14. The motor has two rotors to produce the output force. The pre-load to the rotor was adjusted by a coil spring. The maximum revolution speed was 430 rpm and the maximum output torque was 7.0 μN.m with an input voltage of 20 $V_{p\text{-}p}$ (peak-to-peak voltage).

In Kanda *et al.*,[11] the authors succeeded in operating an ultrasonic micro-motor with a cylindrical stator transducer of 1.4 mm outer diameter, 1.2 mm inner diameter and a length of 5.0 mm. The shape of the stator transducer is the same as that shown in Fig. 4.12. The PZT thin film was deposited on the curved surface of the titanium tube by the hydrothermal method and its thickness was about 12 μm. As shown in Fig. 4.15, the resonance frequency was about 227 kHz. From the frequency response, the mechanical Q factor was calculated to be 150. The piezoelectric factor e_{31} was estimated to be from 0.46 to 0.67 C.m^{-2}.

This motor may be one of the smallest ultrasonic motors developed to date. The starting torque was 0.67 μN.m with a preload of 5.3 mN and input voltage of 20 Vp-p. Under these conditions, the maximum revolution speed was 680 rpm.

Graphs of this motor's performance are shown in Fig. 4.16 and Fig. 4.17. As can be seen from Fig. 4.16, the output torque is proportional to the pre-load. When

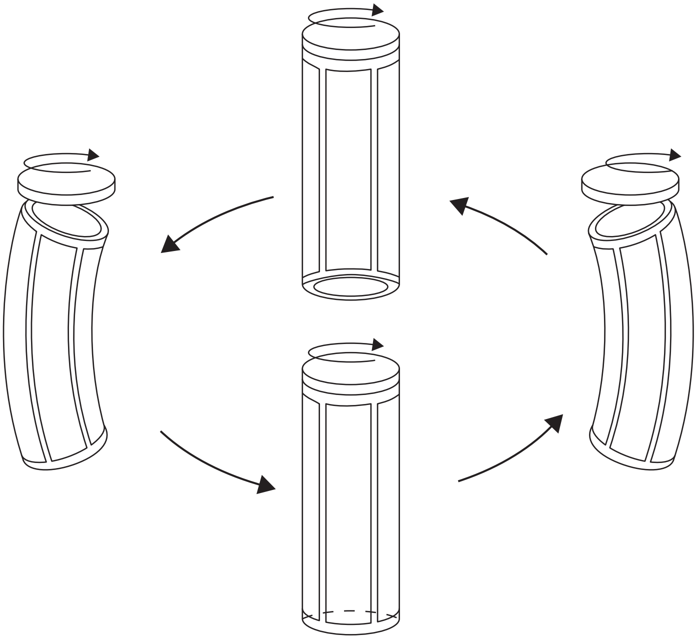

4.13 Deformation and rotation of the ultrasonic micro-motor.

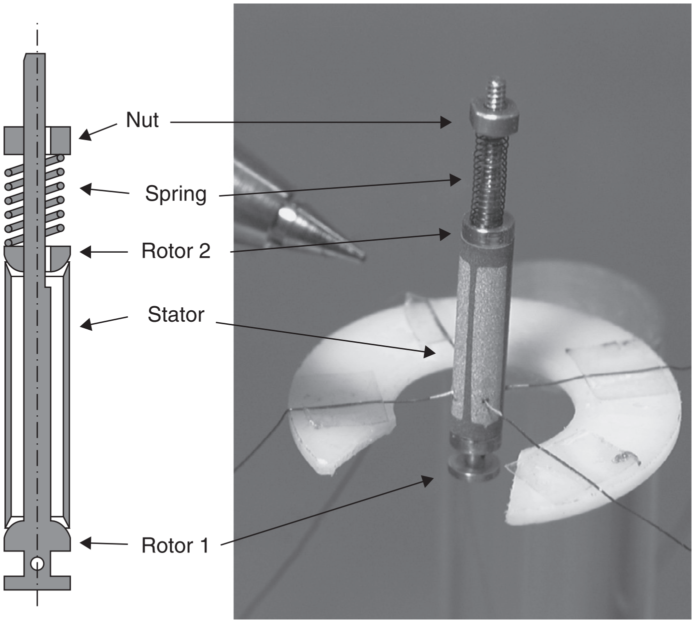
Nut
Spring
Rotor 2
Stator
Rotor 1

4.14 Cross section of the ultrasonic micro-motor.

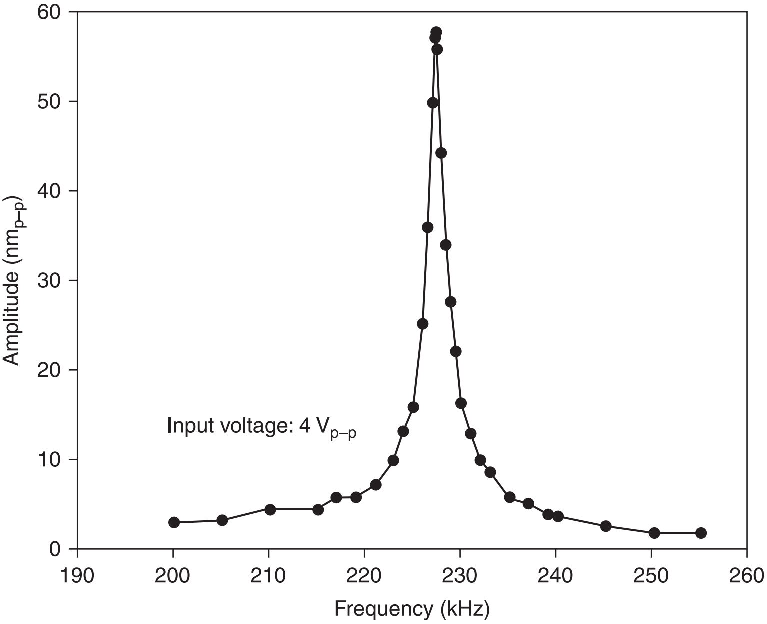

4.15 Amplitude vs. frequency for an ultrasonic micro-motor.

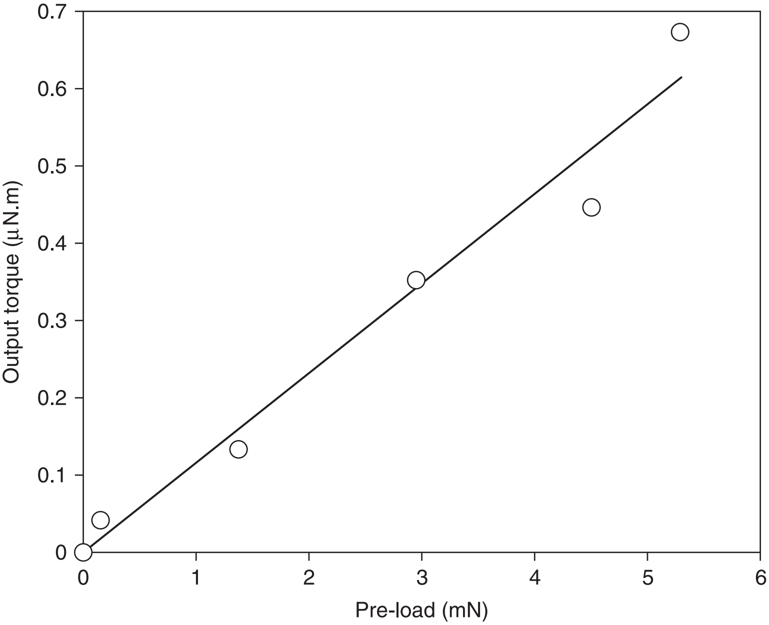

4.16 Output torque vs. pre-load for an ultrasonic micro-motor.

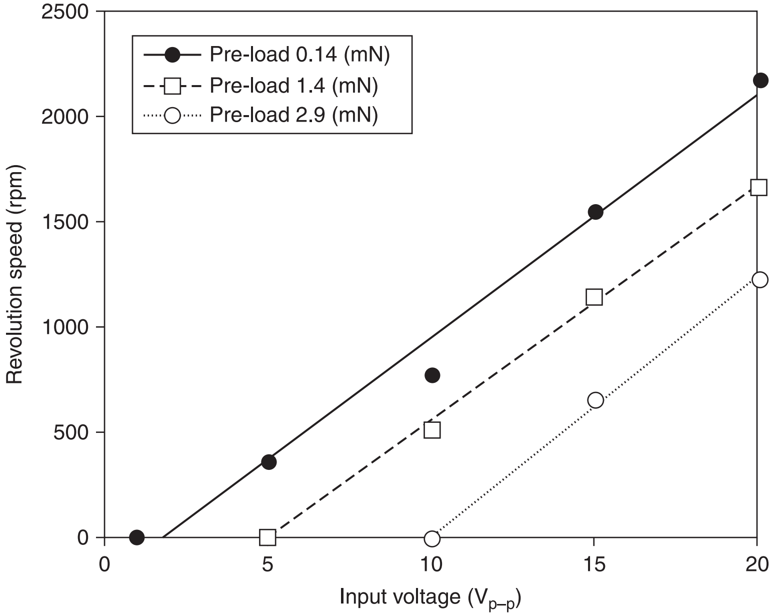

4.17 Revolution speed vs. input voltage for an ultrasonic micro-motor.

the pre-load is high, however, the no-load speed of the motor decreases, as shown in Fig. 4.17. For high-speed and light-load operation, the pre-load should be small and vice versa.

4.3.2 A touch-probe sensor for precise surface texture measurement

Vibro-touch sensors have been fabricated using PZT thin film.[10,13] The sensors were fabricated to measure material surface roughness and the surface microstructure of micro-devices – such as very-large-scale integration (VLSI) devices – at up to sub-nanometer resolution without causing any damage to the work pieces. The devices operate as a scanning probe sensor as shown in Fig. 4.18. The probe sensor can measure the surface profile using only a very small contact force.

The sensor element has a flat shape as shown in Fig. 4.19. The base material was a titanium thin plate with a thickness of 100 µm. A PZT film was deposited at a thickness of 10 µm on both sides of the titanium. Electrodes were deposited on both sides for the drive and pickup, respectively. The sensor element had a half-wavelength longitudinal vibration mode. At the nodal part of the vibration mode, the element was supported using a frame. A quarter-wavelength element was used for the drive and pickup. The other quarter wavelength was an exponential horn to enlarge the vibration amplitude to obtain high sensitivity.

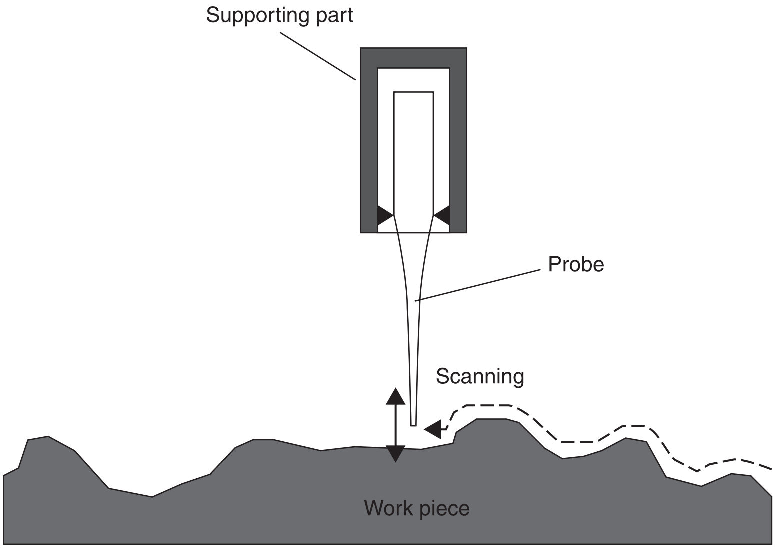
Supporting part
Probe
Scanning
Work piece

4.18 Surface texture measurement using a scanning probe sensor.

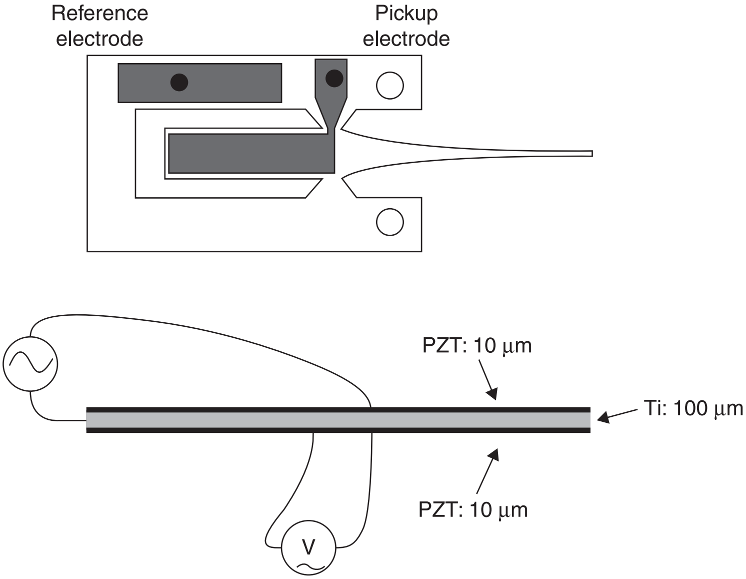
Reference electrode
Pickup electrode
PZT: 10 μm
Ti: 100 μm
PZT: 10 μm
V

4.19 Scanning probe sensor.

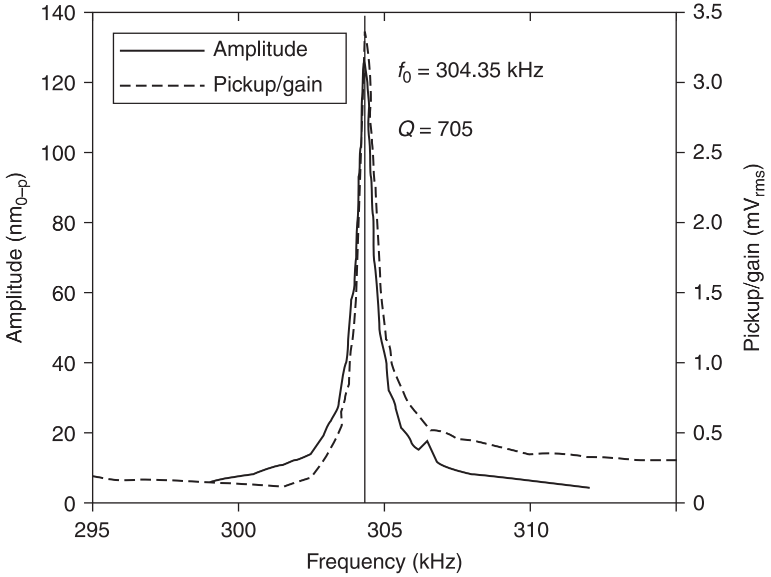

4.20 Amplitude vs. frequency for a scanning probe sensor.

The resonance frequency of the sensor was about 304 kHz, as indicated in Fig. 4.20. The vibration amplitude could be monitored using the pickup output voltage. In order to avoid electromagnetic coupling between the driving part and the sensing part, the sensor amplifier circuit had a balanced input stage as indicated in Fig. 4.21. The amplifier gain was about 20 dB. To balance the output of the sensor device, a reference electrode (similar to a dummy electrode) with the same capacitance as that of the pickup electrode was deposited on the frame. The equivalent noise level at the input terminal, including the sensor element, was 0.042 mV.

The change in output voltage from the pickup electrode was measured when the sensor approached the work piece. The sensor pickup voltage diminished when the sensor tip touched the work piece. The measurement results are shown in Fig. 4.22, with the sensor being driven at the resonance frequency. The cyclic contact with the work piece limited the vibration amplitude and so the pickup voltage decreased.

If the decrease in the vibration amplitude is kept constant by monitoring the pickup voltage, the cyclic contact condition of the sensor tip could be uniformly maintained. With this servomechanism, the sensor tip traces the surface of the work piece. The resolution of the sensor system is limited by the sensitivity of the element, and by the noise levels of the element and the sensing amplifier. The sensitivity of the device is the tangent of the pickup voltage decrease, as indicated in Fig. 4.22 by a solid line. In the case shown here, the tangent was 0.018 $mV.nm^{-1}$. From the sensitivity and the noise level, the resolution of the sensor was 2.4 nm.

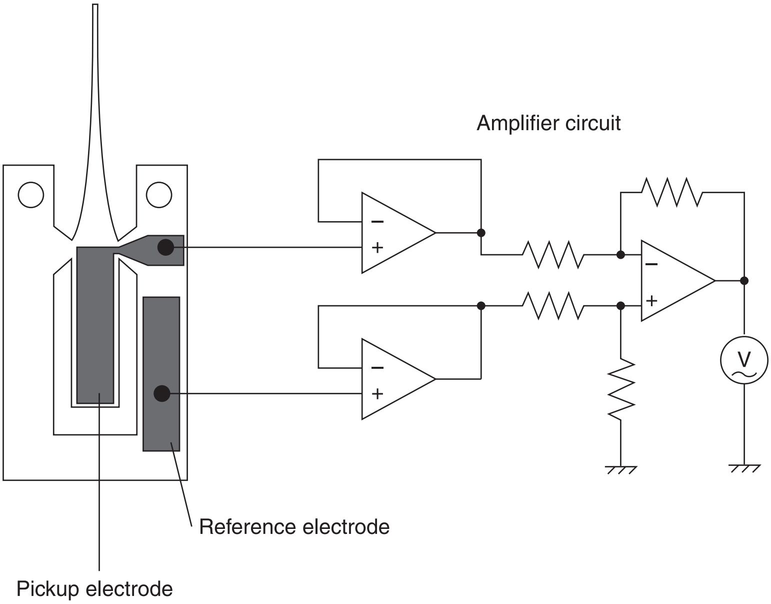
Amplifier circuit
Reference electrode
Pickup electrode
V

4.21 Amplifier circuit for a scanning probe sensor.

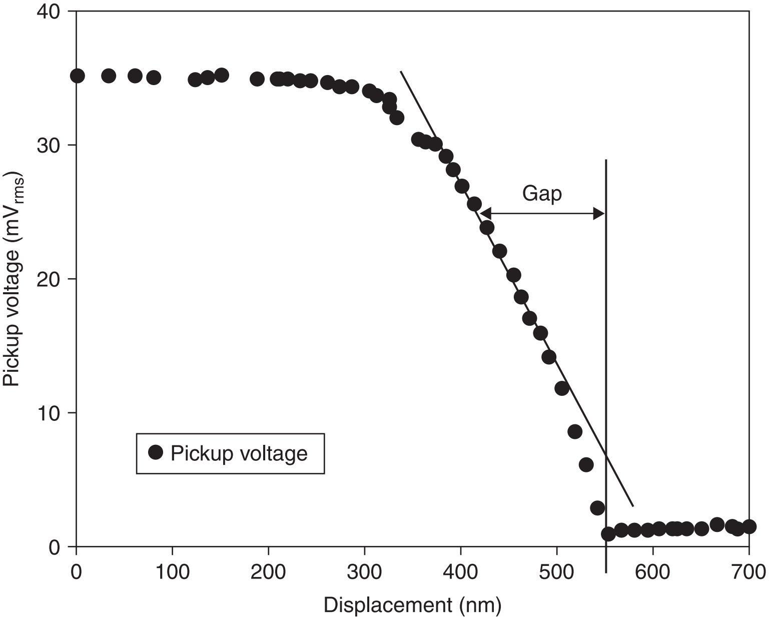

4.22 Pickup voltage vs. displacement for a scanning probe sensor.

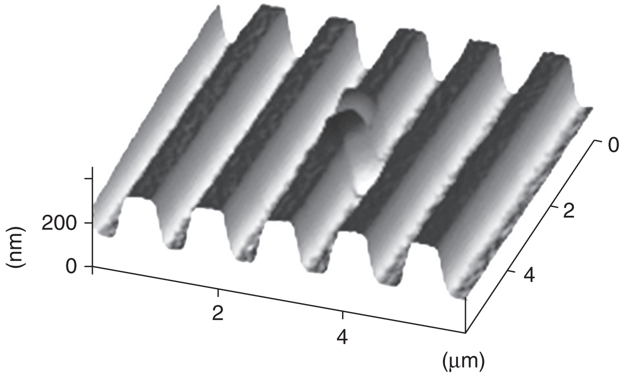

4.23 Surface of a glass grating measured using a scanning probe sensor.

To design an actual measuring system for a high-aspect-ratio minute surface structure, a sharp glass fiber with a radius of curvature of 300 nm was glued to the sensor tip. The sensor had a 284 kHz resonance frequency and a *Q* factor of 1500. The surface of a glass grating, shown in Fig. 4.23, was measured.[13] The driving voltage was maintained at 0.1 Vp-p, which gave a 60 nm vibration amplitude at the tip. The scanning speed was 2 $\mu m.s^{-1}$ and the vertical resolution was estimated to be 4 nm.

The resolution of the system depends on the quality of the piezoelectric film. In this case, the piezoelectric factor e_{31} was 0.13 $C.m^{-2}$. From an analytical approach, we know that the resolution is proportional to the piezoelectric factor. Hence, if the PZT film had as high a piezoelectric factor as the bulk material, namely $e_{31}= 3$ $C.m^{-2}$, the resolution would increase to 0.1 nm.

4.3.3 A high-intensity vibrator for an ultrasonic micro-scalpel

An ultrasonic micro-scalpel[25, 26] was designed in the form of a plate ultrasonic transducer with a support part, as shown in Fig. 4.24. The ultrasonic transducer was 9.8 mm long, 2.7 mm wide and 0.3 mm thick. The vibrator was a modified stepped horn to amplify the vibration velocity, with the tip of the horn being 0.6 mm wide. As shown in Fig. 4.24, the left-hand part of the transducer is a quarter-wavelength straight horn with a longitudinal vibration mode. The right-hand part of the transducer is basically also a straight horn but one that has been slightly modified. The basic design of the transducer is a stepped horn.

However, for a stepped horn, a significant stress concentration occurs at the stepped corners. Hence, as shown in Fig. 4.24, the stepped corner (namely, around the supporting part) was given a rounded shape instead of being sharp. The round shape was designed using the finite element method (FEM). If the stress

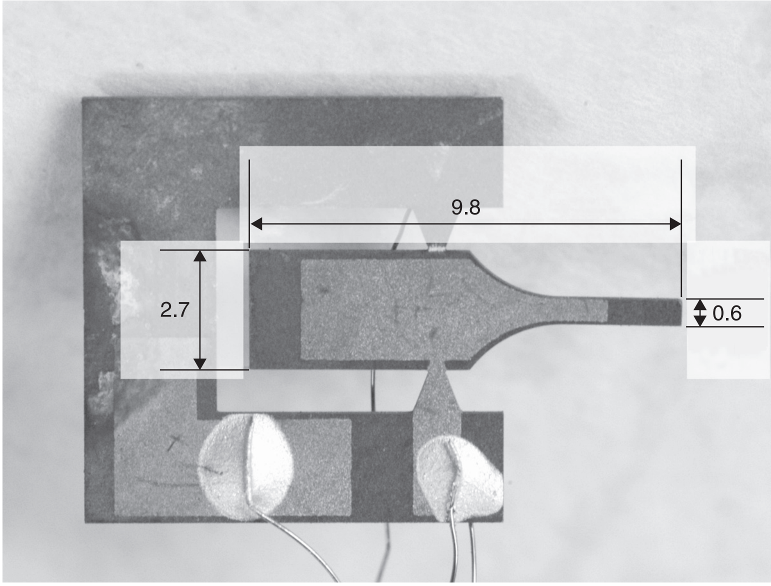

4.24 Ultrasonic micro-scalpel (units are mm).

concentration is large, i.e. there is a sharp corner, the step-up ratio becomes high and vice versa; there is a need to balance the reduction in the stress concentration and yet achieve the maximum gain factor of the horn. For a simple stepped horn manufactured from a uniform thick plate, the step-up ratio of the horn is calculated as (maximum width)/(minimum width); i.e. the step-up ratio is 2.7/0.6 = 4.5. Due to the round shape at the step, the gain factor of the horn decreased by about 20%; the gain factor of the vibration velocity was about 3.5.

The transducer materials were a 0.3-mm-thick titanium plate and the PZT film deposited on the titanium plate was about 20 μm thick, as shown in Fig. 4.25. The PZT film material was deposited using a hydrothermal method.[2] In order to obtain a 20-μm-thick PZT film, a total of five cycles of the reaction process were carried out; one cycle for the nucleation process and four cycles of the growth process, with each process taking 24 hours to complete as mentioned above. The relative dielectric constant and the piezoelectric constants d_{31} and e_{31} were 500, -34 pC.N^{-1} and -0.34 N.V^{-1}, respectively.[11]

In order to excite and monitor the vibration, gold electrodes were deposited on each side of the transducer by vacuum evaporation. As shown in Fig. 4.25, the electrode on one side was used for driving and that on the other side was used for detection. The driving voltage was applied between the electrode and the titanium base. The sensing voltage was measured between the pickup electrode and the reference electrode using a differential amplifier as shown in Fig. 4.25(b).

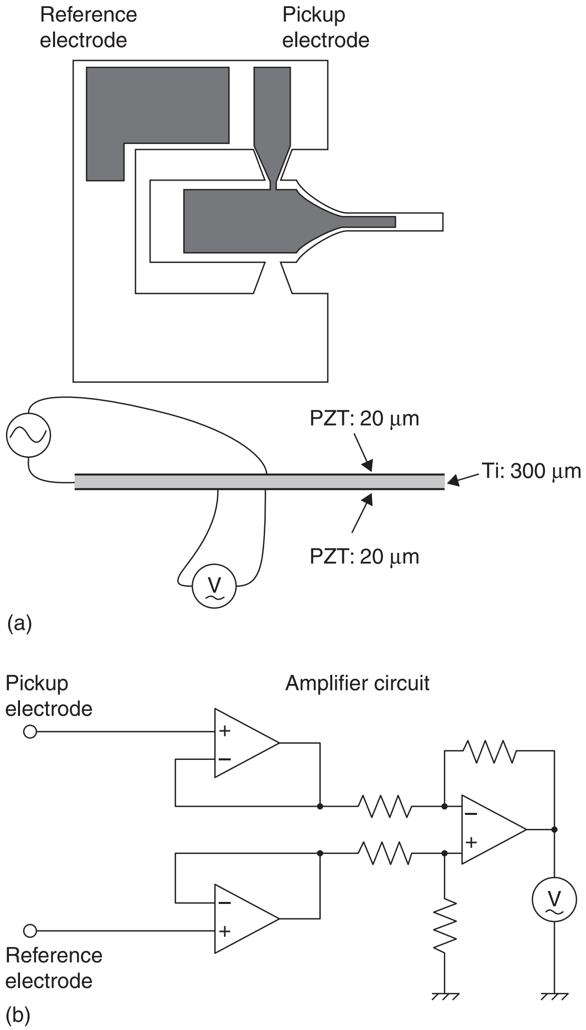
Reference electrode
Pickup electrode
PZT: 20 µm
Ti: 300 µm
PZT: 20 µm
V
(a)
Pickup electrode
Amplifier circuit
+
−
−
+
−
+
V
Reference electrode
(b)

4.25 Ultrasonic micro-scalpel: (a) diagram, (b) amplifier circuit.

The piezoelectric constants of the hydrothermal PZT film were lower than that of bulk PZT. For high-intensity ultrasonic vibration applications, however, the mechanical dynamic characteristics of the piezoelectric material are important if the higher vibration intensities that are necessary for the desired physical effect are to be achieved. For bulk PZT materials, the maximum vibration velocity obtainable is less than 1 $m.s^{-1}$. In contrast, a longitudinal ultrasonic vibrator using a hydrothermal PZT film generated a much higher vibration velocity: a maximum vibration velocity of 2.2 $m.s^{-1}$ was obtained.[4] With the material limitations of the PZT film and the transducer design with a step-up ratio of 3.5 mentioned above, the expected vibration velocity of the transducer was over 7 m.s^{-1}. This maximum vibration velocity is sufficient for a scalpel.

Vibration velocity and amplitude

The vibration velocity at the tip of the horn in the longitudinal direction was measured using a laser Doppler vibrometer (LDV). The relation between the vibration velocity and the driving frequency of the transducer with 1 Vp-p driving voltage is shown in Fig. 4.26. As shown in the graph, the resonance frequency of the longitudinal vibration mode was about 278.7 kHz. The mechanical Q factor of the transducer was about 910.

The relation between the vibration velocity and the driving voltage at the resonance frequency is shown in Fig. 4.27. The vibration velocity increased linearly with the driving voltage up to 35 Vp-p; the maximum vibration velocity was 2.3 m.s^{-1}. An attempt was made to increase the vibration velocity by using a higher driving voltage but the device broke under these conditions.

Pickup voltage

The pickup voltage of the sensing electrode is shown in Fig. 4.26. A differential input amplifier was used to measure the voltage between the sensing electrode and

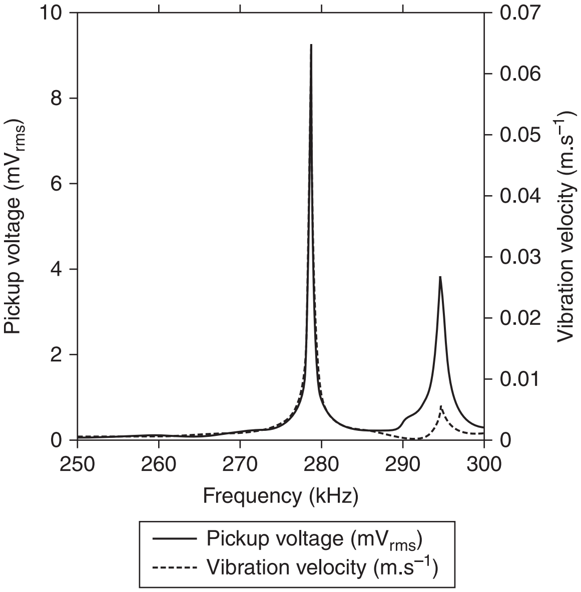

4.26 Pickup voltage and vibration velocity vs. frequency for an ultrasonic micro-scalpel.

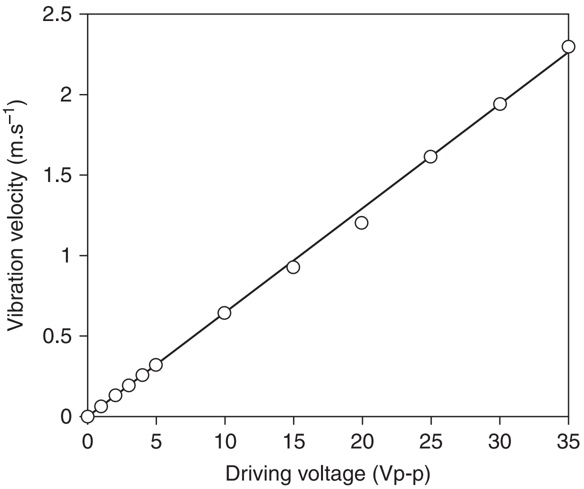

4.27 Vibration velocity vs. driving voltage at the resonance frequency for an ultrasonic micro-scalpel.

the reference electrode. From 250 to 290 kHz, in the frequency range around resonance, the pickup voltage was proportional to the vibration velocity without the influence of electromagnetic coupling.

Amplitude enhancement

In an attempt to achieve a higher intensity vibration velocity of the transducer, a design was implemented whereby the transducer was driven from both sides, as shown in Fig. 4.28. The relation between the vibration velocity and the driving voltage when the transducer is driven on both sides or on only one side is shown in Fig. 4.29. As indicated in the graph, the vibration velocity for both-sides driving was about 1.7 times that of one-side driving. The vibration velocity was 4.0 m.s^{-1} with 40 Vp-p driving voltage. When driven on only one side, the transducer could not vibrate at the 5 m.s^{-1} that is expected to be necessary for efficient cutting of tissues. However, when both sides were driven, the vibration velocity achieved was over 4 m.s^{-1}, i.e. a relatively high vibration velocity; although the ability to sense the vibration velocity was lost.

Cutting test

In order to demonstrate the operation of the scalpel, a cutting test was carried out in which the transducer was inserted into pork fat. When the scalpel was not vibrating, it could not be inserted into the pork fat. However, when vibrating at 4.0 m.s^{-1} at resonance frequency, the scalpel was smoothly inserted into

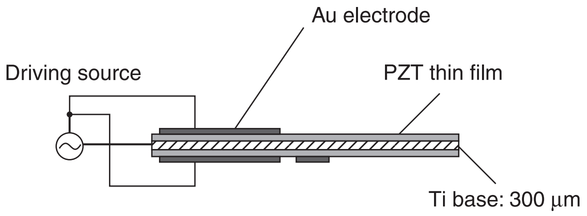

4.28 Driving an ultrasonic micro-scalpel from both sides.

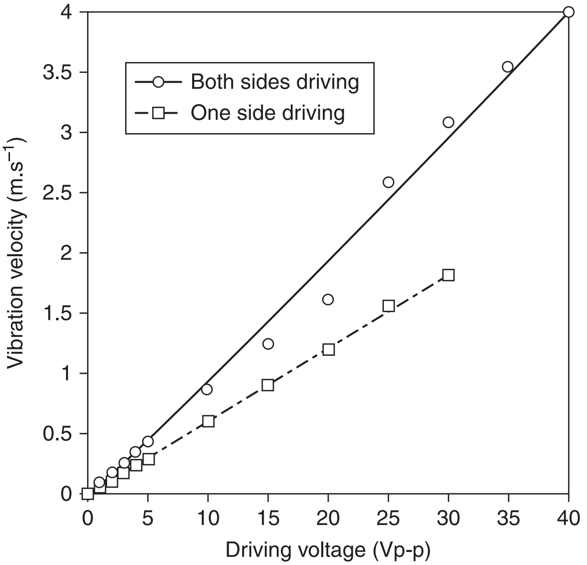

4.29 Vibration velocity vs. driving voltage for an ultrasonic micro-scalpel when driven on one side or both sides.

the pork fat and could be moved through the fat. It was not, however, possible to cut through lean meat. This might be a result of detuning of the resonance because of changes in the boundary conditions of the transducer. For this experiment, a tracking circuit for the resonance condition of the vibrator was not used.

4.4 Thickness-mode vibration, d_{33}

4.4.1 Hydrothermal PZT film using TiO_2 powder

As an alternative to a $TiCl_4$ solution, TiO_2 powder has been used in the hydrothermal process for the deposition of PZT film on a titanium base material. When TiO_2

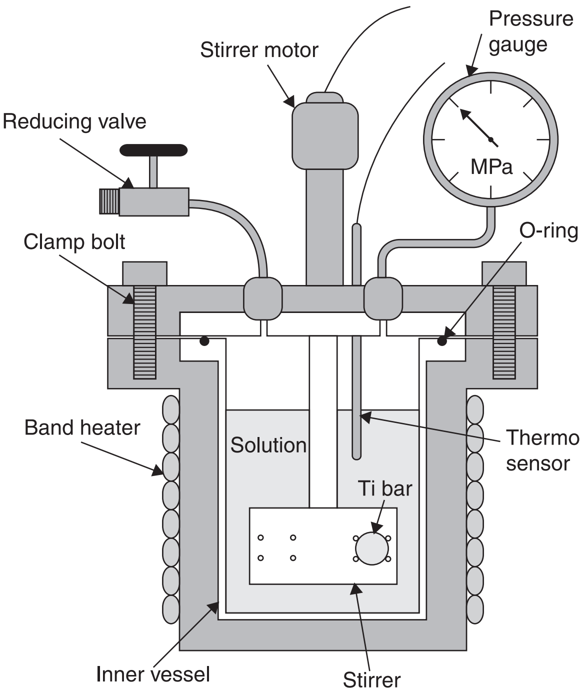

4.30 Diagram of a large autoclave.

powder is used, a larger autoclave (e.g. 500 ml capacity) is needed. The autoclave is shown in Fig. 4.30 and Fig 4.31. The larger autoclave has a heater external to the outer container. The heater is controlled using feedback from a thermometer in the autoclave to maintain the solution temperature at a constant level.

A stirrer is also installed in the autoclave to maintain a uniform temperature or to activate the reaction. The stirrer axis goes through the lid to a motor that controls the rotation speed. The rotation axis is sealed to avoid any pressure decrease inside the autoclave. The large autoclave is able to incorporate additional sensors and devices for specific functions if necessary. The solution can also be refreshed, through a plumbing system, so that the reaction process can be continuously maintained.[5]

4.4.2 Deposition process and film material

The use of TiO_2 powder in the deposition of a PZT film on a titanium metal base was reported by Ishikawa.[14–16] The raw materials used were lead nitrate, zirconyl chloride octahydrate, titanium dioxide and potassium hydroxide; the amounts for a 500 ml autoclave are listed in Table 4.2. Like the $TiCl_4$ solution process, this

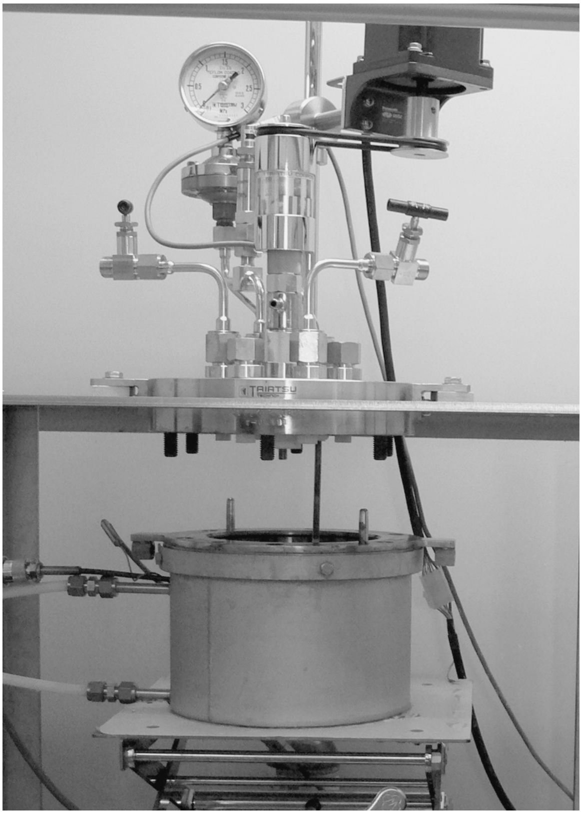

4.31 Large autoclave.

Table 4.2 Raw materials for the hydrothermal deposition of PZT with titanium dioxide powder

Material	Quantity
$ZrOCl_28H_2O$	52 ml (1 N)
TiO_2	1 g
$Pb(NO_3)_2$	87 ml (1 N)
KOH	200 ml (4 N)

process also has two steps. The material in the autoclave is also the same for both processes. Only the process temperatures are different; for the TiO_2 powder process the nucleation process is carried out at 160 °C and the crystal growth process at 140 °C. Each process lasts for 24 hours and the stirrer rotation speed is 245 rpm. By repeating the deposition process 20 times, a 50-μm-thick film was obtained. The Zr:Ti composition of the film was 80:20. Young's modulus, the density and d_{31} were 2.2×10^{10} $\mathrm{N.m^{-2}}$, 4.3 $\mathrm{kg.m^{-3}}$ and −26 $\mathrm{pC.N^{-1}}$, respectively. The thickness-vibration mode was observed at 18 MHz, and a vibration velocity of 0.8 $\mathrm{m.s^{-1}}$ was achieved with a 45 Vp-p driving voltage.[16]

The characteristics of the PZT film deposited depend on the TiO_2 powder material. Three kinds of TiO_2 material were investigated: anatase crystal 300-nm-diameter powder; anatase crystal 6-nm powder; and rutile crystal 300-nm-diameter powder. SEM images of the films are shown in Fig. 4.32. For the 6-nm-diameter rutile powder, the Zr:Ti composition was 59:41. For the other

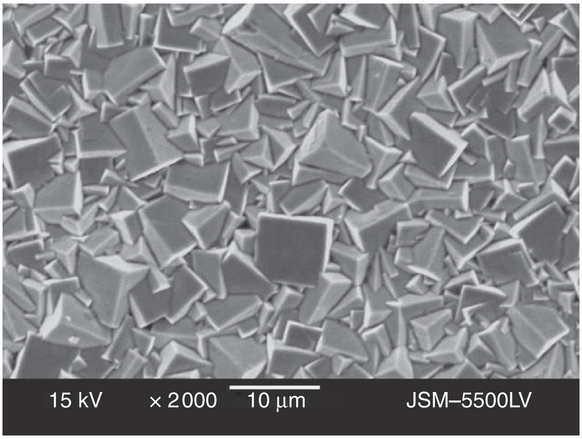

(a)

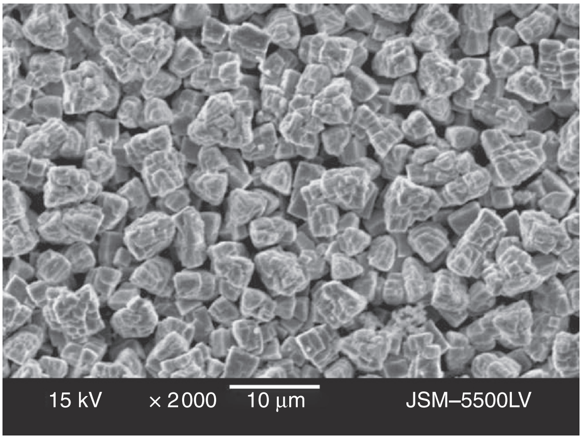

(b)

4.32 SEM images of PZT films deposited on different TiO_2 powder material: (a) anatase crystal 300-nm-diameter powder, (b) anatase crystal 6-nm powder. *(Continued)*

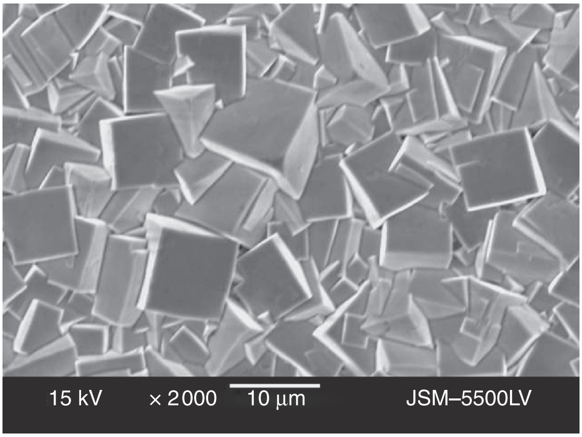

(c)

4.32 Continued. (c) Rutile crystal 300-nm-diameter powder.

powders the Zr level varied from 85% to 9%, with the titanium at a correspondingly lower ratio. The piezoelectric constant d_{33} ranged from 20 to 70 pC.N^{-1}.

4.4.3 Applications using the thickness-mode vibration

Thickness-mode vibration devices using thick polycrystal films have been reported in the literature. The transmitting characteristics of a broadband ultrasonic hydrophone have been described: the device used a 50-μm-thick PZT film on a 50-μm-thick titanium base foil with a frequency bandwidth from 1 to 20 MHz.[14,15] Transmitting characteristics with a frequency bandwidth from 1 to 50 MHz were reported. Due to the porous structure of the film, it seems that the mechanical impedance of the transducer was low. Even without a backing layer a good match with the water conditions was achieved, which suppressed the ringing vibration by adding a lossy component.

It has been demonstrated that high-intensity ultrasonic radiation in water is obtainable at 21 MHz up to 200 kPa using a 45 μm PZT film on 50 μm titanium. With continuous acoustic radiation, cavitation was observed.[16] An array probe device has also been reported.

4.4.4 A small-diameter ultrasonic probe

Two types of small-diameter (1 mm) thickness-mode vibration transducer were fabricated using hydrothermal PZT film.[17,18] Titanium wire or epoxy resin was used as the backing material for the transducers. These transducers were 1-mm-diameter, needle-type hydrophones, which are robust and have broadband measurement applications.

Titanium wire ultrasonic probe

A PZT film was deposited onto the tip of a titanium wire, which was 0.6 mm in diameter and 40 mm long. The PZT film was 20 μm thick and had a polycrystal structure as shown in Fig. 4.33. The transducer is shown in Fig. 4.34. The transducer was connected to a coaxial cable. The backing titanium wire was a hot electrode and was connected to the inner wire of the coaxial cable. An insulating layer covered the titanium wire. The bare surface of the PZT film was covered with a conductive layer and was connected to a metal pipe, which was shielded and was connected to the earthed coaxial cable. The outer diameter of the transducer was 1 mm and the effective diameter of the PZT film area was 0.6 mm.

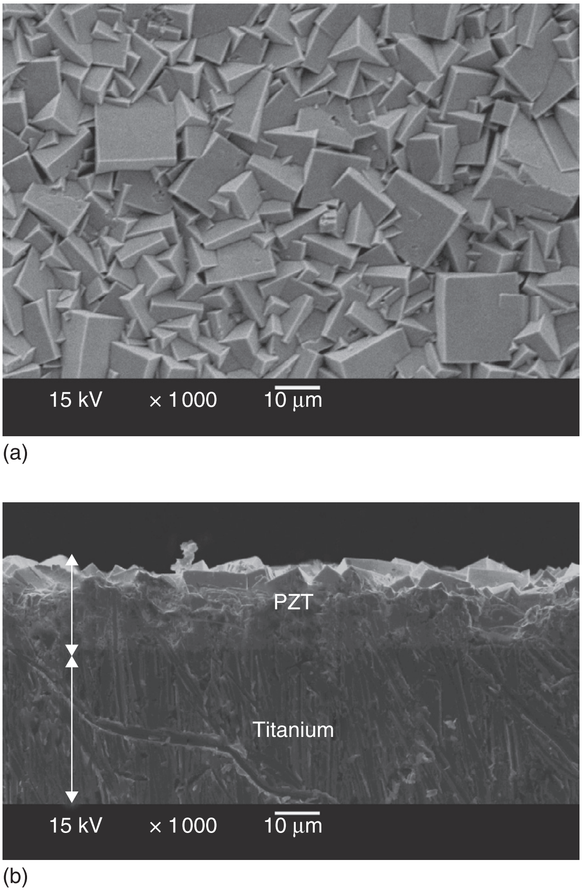

4.33 SEM images of PZT film deposited onto the tip of a titanium wire: (a) surface, (b) cross section.

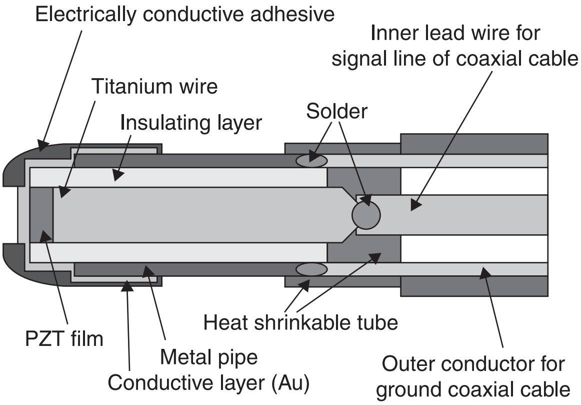
Electrically conductive adhesive
Inner lead wire for signal line of coaxial cable
Titanium wire
Insulating layer
Solder
Heat shrinkable tube
PZT film
Metal pipe
Conductive layer (Au)
Outer conductor for ground coaxial cable

4.34 Titanium wire ultrasonic probe.

The received waveform for the titanium wire-backed hydrophone is shown in Fig. 4.35. A pulse wave was radiated to a reflector 5 mm away, and was then received by the hydrophone. The frequency spectrum of the received signal is shown in Fig. 4.36. From the spectrum, it was found that the peak frequency and the center frequency were 36 MHz and 45 MHz, respectively. The upper and lower frequencies were 69 MHz and 21 MHz; the bandwidth was 47 MHz, namely 106% of the fractional bandwidth.

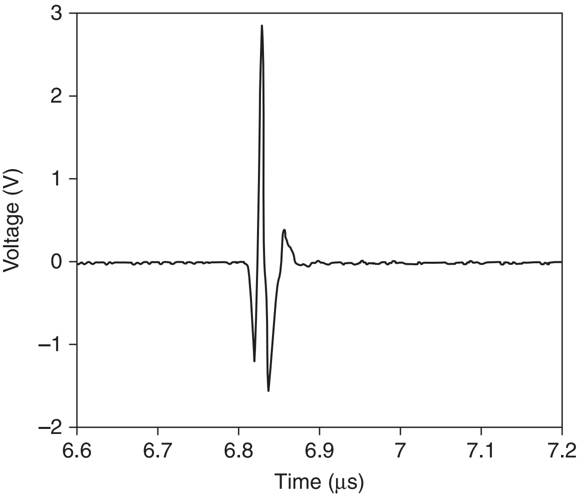

4.35 Received waveform for titanium wire-backed hydrophone.

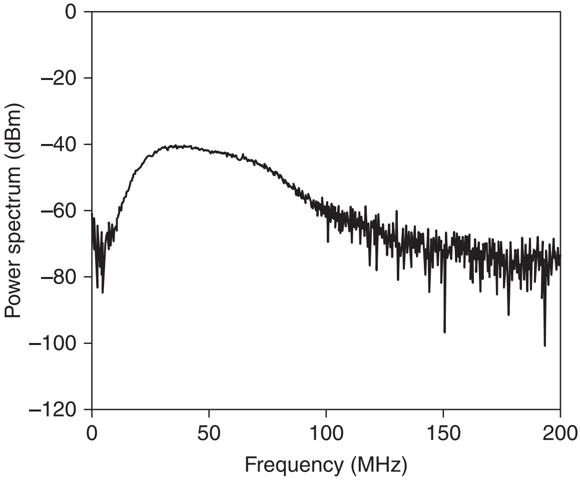

4.36 Frequency spectrum of the received signal for titanium wire-backed hydrophone.

Epoxy resin ultrasonic probe

In the second type of probe, a PZT film was deposited on a titanium substrate then exfoliated. The PZT film was 20 μm thick and had a polycrystal structure as shown in Fig. 4.37. The transducer is shown in Fig. 4.38. The transducer was connected to a coaxial cable. The backing epoxy resin is an electrically conductive adhesive and was connected to the inner wire of the coaxial cable. An insulating layer covered the hot wire. The bare surface of the PZT film was covered with a conductive layer and connected to a metal pipe, which was shielded and was connected to the earthed coaxial cable. The outer diameter of the transducer was 1 mm and the effective diameter of the PZT film area was 0.2 mm.

The signal received by the titanium wire-backed hydrophone is shown in Fig. 4.39. A pulse wave was radiated to a reflector 5 mm away and was then received by the hydrophone. The frequency spectrum of the received signal is shown in Fig. 4.40. From the spectrum, it was found that the peak frequency and the center frequency were 82 MHz and 69 MHz, respectively. The upper and lower frequencies were 98 MHz and 39 MHz; the bandwidth was 59 MHz, namely 86% of fractional bandwidth.

Both hydrophones were very tiny and solid in structure. The frequency range is several tens of megahertz, close to 100 MHz and broadband. A high space resolution of 20 μm in distance and 140 μm in a lateral direction was measured. A C-mode image of a coin was produced, as shown in Fig. 4.41.

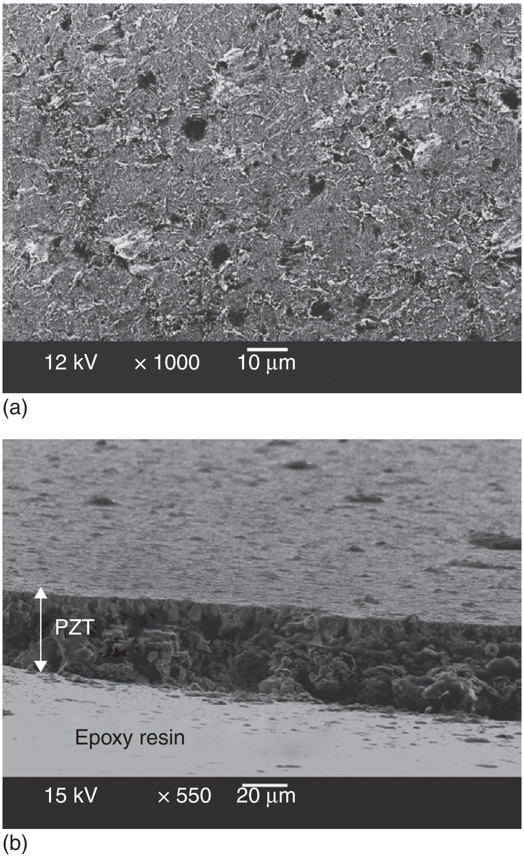
12 kV
× 1000
10 µm
(a)
PZT
Epoxy resin
15 kV
× 550
20 µm
(b)

4.37 SEM image of a PZT film deposited on a titanium substrate: (a) surface, (b) cross section.

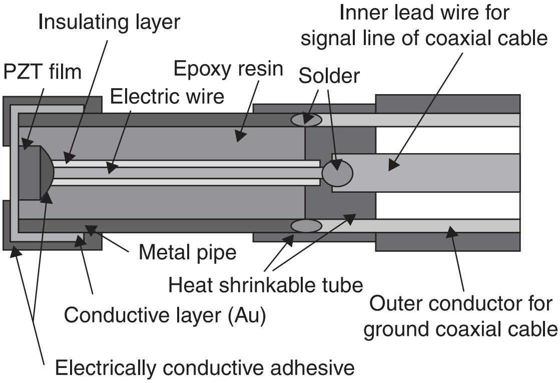
Insulating layer
Inner lead wire for signal line of coaxial cable
PZT film
Epoxy resin
Solder
Electric wire
Metal pipe
Heat shrinkable tube
Conductive layer (Au)
Outer conductor for ground coaxial cable
Electrically conductive adhesive

4.38 Epoxy resin ultrasonic probe.

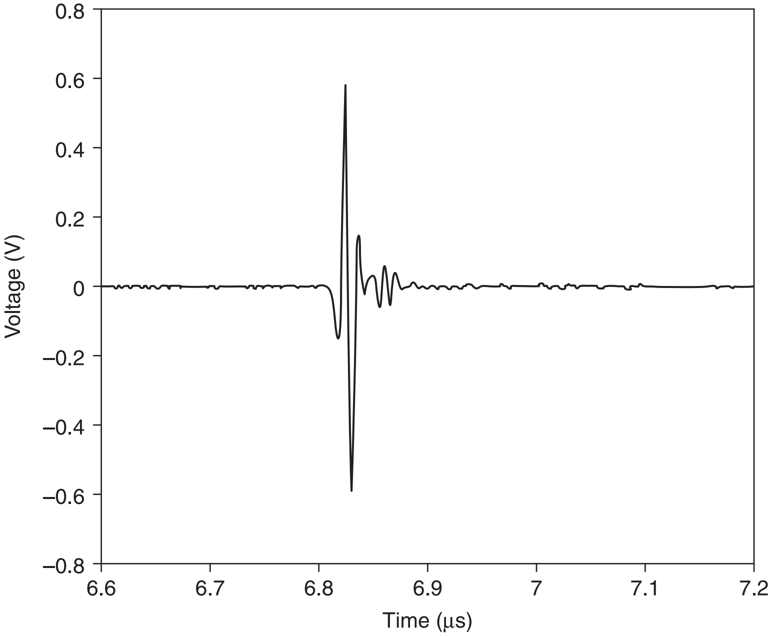

4.39 Signal received by titanium wire-backed hydrophone.

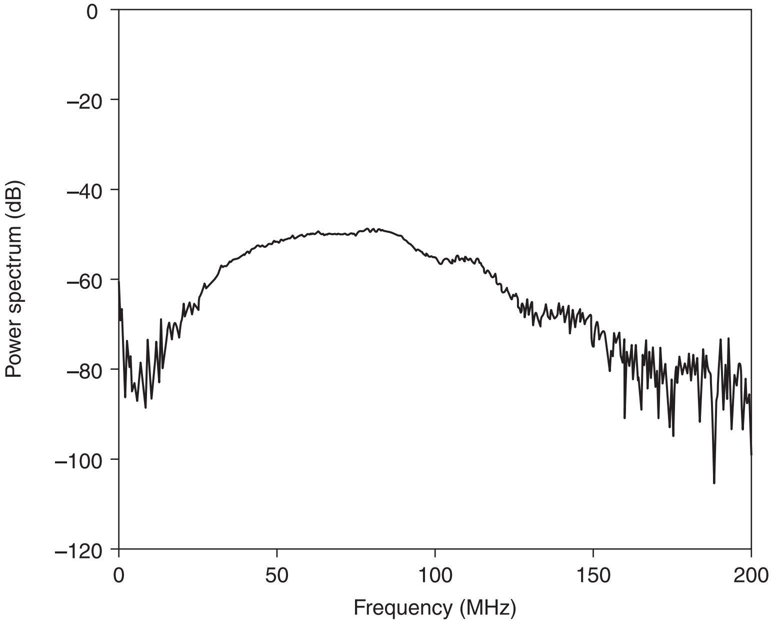

4.40 Frequency spectrum of the received signal for titanium wire-backed hydrophone.

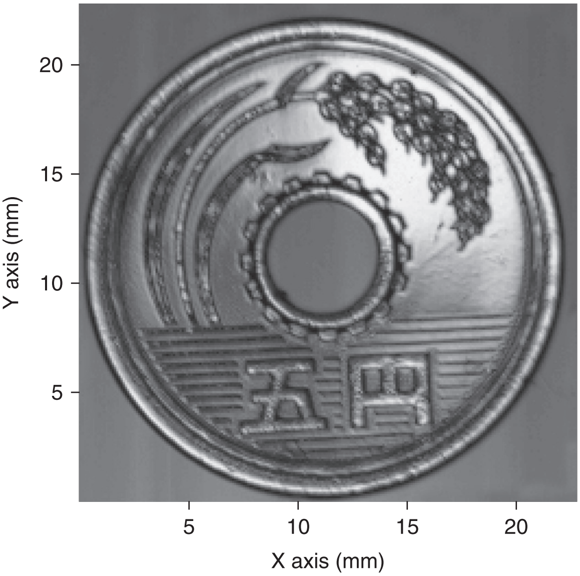

4.41 C-mode image of a coin produced by titanium wire-backed hydrophone.

4.5 Epitaxial film

For transducers with superior performance, a high-performance piezoelectric film material is desirable. Epitaxial piezoelectric films deposited using the hydrothermal process have been reported for single-crystal substrates or buffered layers. Morita *et al.* reported the successful deposition of PZT[19] and $PbTiO_3$[20] epitaxial films and evaluated their ferroelectric characteristics. For epitaxial film deposition, an $SrRuO_3$ (SRO)-oriented film deposited on an Nb-doped $SrTiO_3$ (STON) substrate was used. The substrate was placed in an autoclave for deposition.

An epitaxial PZT film was deposited at 150 °C, taking 9 hours to produce a 500-nm-thick film. Cross-sectional SEM images indicated a fine film material. The film was polarized during deposition with a residual polarization of 18.8 $\mu C.cm^{-2}$ and a coercive electric field of 59 $kV.cm^{-1}$. A $PbTiO_3$ film was also deposited in the same way at 150 °C, taking 24 hours to produce a 100-nm-thick film. A residual polarization of 96.5 $\mu C.cm^{-2}$ and coercive electric field of 290 kV/cm were reported. For a 430-nm-thick film, a d_{33} effect of 97 $pC.N^{-1}$ was measured.[21]

Epitaxial $KNbO_3$ and $(K,Na)NbO_3$ films were successfully deposited onto a $SrRrO_3/SrTiO_3$ substrate.[22,23] For the $KNbO_3$ film, a 3-hour hydrothermal process at 240°C resulted in a 16-µm-thick epitaxial film. The residual polarization of 20 $\mu C.cm^{-1}$ and the butterfly curve for strain were measured. High-frequency ultrasonic transmission and reception of over 90 MHz using the thickness-vibration mode in degassed water was demonstrated. Different orientations of

(K,Na)NbO_3 epitaxial films of up to 130 μm were deposited on the differently orientated substrates. The material constant of residual polarization, the coercive field and the piezoelectric constant d_{33} were measured to be 20 μC.cm^{-2}, 46 kV.cm^{-1} and 70 pm.V^{-1}, respectively.

4.6 Conclusions

The advantage of hydrothermal PZT films for the fabrication of ultrasonic transducers is that the film can be deposited on titanium or titanium alloy metal materials directly using a solution process. In addition, the deposited film is polarized so that an annealing process and poling process are not required in order to achieve a piezoelectric effect. As a result of these advantages, a wide variety of transducers can be fabricated for a wide range of applications.

The performance of hydrothermal PZT films is good, with high vibration velocities of more than 2 m.s^{-1} achievable, which is several times higher than that of the bulk PZT ceramic material. However, the density of the films is not as high, and the output force and the power[26] of the transducers are not as large. Low-density films, however, have merits for hydrophone applications due to the good matching that can be achieved with low impedance for water with broadband characteristics.

Recent trends in the development of hydrothermal films have been in the production of epitaxial and lead-free films. Epitaxial films of PT and PZT have been fabricated to obtain much higher performance materials for superior transducers. Lead-free films using KN and KNN are being investigated for future applications.

4.7 References

1. K. Simomura, T. Tsurumi, Y. Ohba and M. Daimon, Preparation of lead zirconate titanate thin film by hydrothermal method, *Jpn. J. Appl. Phys.*, **30**, No. 9B, 1991, pp. 2174–7.
2. T. Kikuchi, T. Tsurumi, Y. Ohba and M. Daimon, Bending actuator using lead zirconate titanate thin film fabricated by hydrothermal method, *Jpn. J. Appl. Phys.*, **31**, No. 9B, 1992, pp. 3090–3.
3. Y. Ohba, M. Miyauchi, T. Tsurumi and M. Daimon, Analysis of bending displacement of lead zirconate titanate thin film synthesized by hydrothermal method, *Jpn. J. Appl. Phys.*, **32**, No. 9B, 1993, pp. 4095–8.
4. Y. Ohba, K. Arita, T. Tsurumi and M. Daimon, Analysis of interfacial phase between substrate and lead zirconate titanate thin films synthesized by hydrothermal method, *Jpn. J. Appl. Phys.*, **33**, No. 9B, 1994, pp. 5305–8.
5. Y. Ohba, M. Miyauchi, E. Sakai and M. Daimon, Hydrothermal syntheses of lead zirconate titanate thin film fabricated by a continuous-supply autoclave, *Jpn. J. Appl. Phys.*, **34**, No. 9B, 1995, pp. 5216–19.
6. T. Morita, M. Kurosawa and T. Higuchi, An ultrasonic micro motor using bending cylindrical transducer base on PZT thin film, in *Proc. of Micro Electro Mechanical Systems*, pp. 49–54, 1995.

7. T. Morita, T. Kanda, Y. Yamagata, M. Kurosawa and T. Higuchi, Single process to deposit lead zirconate titanate (PZT) thin film by a hydrothermal method, *Jpn. J. Appl. Phys.*, **36**, No. 5B, 1997, pp. 2998–9.
8. T. Morita, M. K. Kurosawa and T. Higuchi, A cylindrical micro ultrasonic motor using PZT thin film deposited by single process hydrothermal method (ϕ=2.4 mm, L=10 mm stator transducer), *IEEE Trans. Ultrasonics, Ferroelectrics and Frequency Control*, **45**, No. 5, 1998, pp. 1178–87.
9. T. Morita, M. K. Kurosawa and T. Higuchi, A cylindrical shaped micro ultrasonic motor utilizing PZT thin film (1.4 mm in diameter and 5.0 mm long stator transducer), *Sensors and Actuators A*, **83**, 2000, pp. 225–30.
10. T. Kanda, T. Morita, M. K. Kurosawa and T. Higuchi, A flat type touch probe sensor using PZT thin film vibrator, *Sensors and Actuators A*, **83**, 2000, pp. 67–75.
11. T. Kanda, M. K. Kurosawa, H. Yasui and T. Higuchi, Performance of hydrothermal PZT film on high intensity operation, *Sensors and Actuators A*, **89**, 2001, pp.16–21.
12. T. Kanda, Y. Kobayashi, M. K. Kurosawa, H. Yasui and T. Higuchi, Estimation of hydrothermally deposited lead zirconate titanate (PZT) thin-film, *Jpn. J. Appl. Phys.*, **40**, Part 1, No. 9B, 2001, pp. 5543–6.
13. H. Tamura, M. K. Kurosawa and T. Kanda, Hydrothermally deposited PZT film probe sensor using a near-field optical fiber probe, IEICE, Technical Report US2005-2, pp. 7–12, 2005.
14. M. Ishikawa, M. Kurosawa, N. Katsura and S. Takeuchi, PZT thick film deposited by improved hydrothermal method for thickness mode ultrasonic transducer, *Mat. Res. Soc. Proc.*, **784**, 2004, pp. C11.27.1–5.
15. M. Ishikawa, M. K. Kurosawa, A. Endoh and S. Takeuchi, Lead zirconate titanate thick-film ultrasonic transducer for 1 to 20 MHz frequency bands fabricated by hydrothermal polycrystal growth, *Jpn. J. Appl. Phys.*, **44**, No. 6B, 2005, pp. 4342–6.
16. M. Ishikawa, M. K. Kurosawa, A. Endoh, T. Uchida, S. Takeuchi and N. Kawashima, Hydrothermal polycrystalline PZT thick film transducer for high intensity ultrasound radiation at over 20 MHz, *Proc. of 2006 IEEE Ultrason. Symp.*, 2006, pp. 2369–72.
17. T. Hasegawa, H. Kitsunai, N. Kawashima, S. Takeuchi, M. Ishikawa and M. K. Kurosawa, Development of small ultrasonic probe using lead zirconate titanate film deposited by hydrothermal method, *Jpn. J. Appl. Phys.*, Vol. 46, No. 7B, 2007, pp. 4801–4.
18. T. Hasegawa, M. Ishikawa, M. K. Kurosawa and S. Takeuchi, Evaluation of small ultrasonic probe using lead zirconate titanate poly-crystal film deposited by hydrothermal method, *Inst. Electrical Eng. Jpn, Trans. on Elec. Inf. Sys.*, Vol. 131, No. 6, pp. 1174–80, 2011 (in Japanese).
19. T. Morita, Y. Wagatsuma, H. Morioka, H. Funakubo, N. Setter and Y. Cho, Ferroelectric property of an epitaxial lead zirconate titanate thin film deposited by a hydrothermal method, *J. Mater. Res.*, **19**, No. 6, 2004, pp. 1862–8.
20. T. Morita and Y. Cho, Epitaxial $PbTiO_3$ thin films on $SrTiO_3$(100) and $SrRuO_3$/$SrTiO_3$(100) substrates deposited by a hydrothermal method, *Jpn. J. Appl. Phys.*, **43**, No. 9B, 2004, pp. 6535–8.
21. T. Morita and Y. Cho, Piezoelectric performance and domain structure of epitaxial $PbTiO_3$ thin film deposited by hydrothermal method, *Jpn. J. Appl. Phys.*, **45**, No. 5B, 2006, pp. 4489–92.
22. M. Ishikawa, K. Yazawa, T. Fujisawa, S. Yasui, T. Yamada, T. Hasegawa, T. Morita, M. Kurosawa and H. Funakubo, Growth of epitaxial $KNbO_3$ thick films by

hydrothermal method and their characterization, *Jpn. J. Appl. Phys.*, **48**, No. 9, pp. 09KA14, 1–4, 2009.

23. M. Ishikawa, H. Einishi, M. Nakajima, T. Hasegawa, T. Morita, Y. Saijo, M. Kurosawa and H. Funakubo, Effect of deposition time on film thickness and their properties for hydrothermally-grown epitaxial $KNbO_3$ thick films, *Jpn. J. Appl. Phys.*, **49**, No. 7, pp. 07HF01, 1–4, 2010.
24. T. Kanda, Y. Kobayashi, M. K. Kurosawa and T. Higuchi, Vibration velocity limitation of transducer using titanium-based hydrothermal lead zirconate titanate thick film, *Jpn. J. Appl. Phys.*, **42**, Part 1, No. 5B, 2003, pp. 3014–19.
25. Y. Umehara and M. K. Kurosawa, A micro ultrasonic scalpel using hydrothermal PZT thin film, in *Proc. the 2006 15th IEEE Int. Symp. on Applications of Ferroelectrics*, ISAF'06, pp. 340–3, Sunset Beach, North California, USA, 30 July–3 August 2006.
26. M. K. Kurosawa and Y. Umehara, A micro ultrasonic scalpel with modified stepped horn, *Inst. Electrical Eng. Jpn, Trans. on Elec. Inf. Sys.*, Vol. 131, No. 6, pp. 1144–9, 2011 (in Japanese).

5

High-Curie-temperature piezoelectric single crystals of the $Pb(In_{1/2}Nb_{1/2})O_3$–$Pb(Mg_{1/3}Nb_{2/3})O_3$–$PbTiO_3$ ternary system

Y. YAMASHITA, Toshiba Research Consulting Corporation, Japan and Y. HOSONO, Toshiba Corporation, Japan

Abstract: This chapter considers piezoelectric single crystals (PSCs) with a large piezoelectric constant (d_{33}), high Curie temperature (T_c), high phase-change temperature (T_{rt}) and high coercive field (E_c). Their piezoelectric properties are greatly superior to those of $Pb(Zr,Ti)O_3$ (PZT) ceramics so binary PSCs are used for transducer applications. PZNT and PMNT PSCs have shortcomings: low T_c, low T_{rt} and low E_c. Ternary systems are used to overcome the problems of PZT ceramics, binary PZNT and PMNT PSCs. Single crystals of a PIMNT ternary system, their manufacturing process and electrical properties are reviewed. The application of PIMNT materials with high d_{33}, T_c, T_{rt} and E_c for medical transducers is described.

Key words: relaxor, single crystal, transducer, piezoelectric constant, dielectric constant, electromechanical coupling factor, lead magnesium niobate, lead indium niobate, lead titanate.

5.1 Introduction

During the past 60 years barium titanate ($BaTiO_3$, BT) and lead zirconate titanate [$Pb(Zr,Ti)O_3$, PZT] ceramics have become established as the preferred ferroelectric materials for a wide variety of ferroelectric devices such as capacitors and many piezoelectric devices.

However, in the last three decades, relaxor materials with the general formula $Pb(B'B'')O_3$ where B' is a low-valence cation, e.g., Mg^{+2}, Ni^{+2}, Zn^{+2}, In^{+3} or Sc^{+3}, and B' is a high-valence cation, e.g. Nb^{+5}, Ta^{+5} or W^{+6}, have been investigated for applications such as multilayer ceramic capacitors and electrostrictive devices. In recent years, a new approach to the development of piezoelectric materials based on $PbZrO_3$-free, relaxor–lead titanate (PT) systems has attracted particular attention (Kuwata *et al.*, 1982; Shrout *et al.*, 1990; Yamashita, 1994). The morphotropic phase boundary (MPB) separates the ferroelectric rhombohedral and tetragonal phases of compositions. The advantage of relaxor–PT piezoelectric materials compared with conventional PZT ceramics, as shown in Table 5.1, is the ease with which piezoelectric single crystals (PSCs) near the MPB can be grown.

Table 5.1 Relaxor materials, high T_c materials and their MPBs with lead titanate

Relaxor materials	Abbreviation	T_c K (°C)	ε_{max}	Structure*	Ferroelectricity†	T_i at MPB (mol%)	T_c at MPB K (°C)
$Pb(B^{2+}{}_{1/3}B^{5+}{}_{2/3})O_3$							
$Pb(Cd_{1/3}Nb_{2/3})O_3$	PCdN	273 (0)	8 000	PC	F	28	653 (380)
$Pb(Zn_{1/3}Nb_{2/3})O_3$	PZN	413 (140)	22 000	R	F	9–10	448 (175)
$Pb(Mg_{1/3}Nb_{2/3})O_3$	PMN	263 (–10)	18 000	PC	F	30–33	428 (155)
$Pb(Ni_{1/3}Nb_{2/3})O_3$	PNN	153 (–120)	4 000	PC	F	28–33	403 (130)
$Pb(Mn_{1/3}Nb_{2/3})O_3$	PMnN	153 (–120)	4 000	PC	F	30–35	403 (130)
$Pb(Co_{1/3}Nb_{2/3})O_3$	PCoN	175 (–98)	6 000	M	F	33	523 (250)
$Pb(Mg_{1/3}Ta_{2/3})O_3$	PMgT	175 (–98)	7 000	PC	F	30?	373 (100)
$Pb(B^{3+}{}_{1/2}B^{5+}{}_{1/2})O_3$							
$Pb(Yb_{1/2}Nb_{1/2})O_3$	PYbN	553 (280)	150	M	AF	50	633 (360)
$Pb(In_{1/2}Nb_{1/2})O_3$	PIN	363 (90)	550	M	F	37	593 (320)
$Pb(Sc_{1/2}Nb_{1/2})O_3$	PSN	363 (90)	38 000	R	F	42	533 (260)
$Pb(Fe_{1/2}Nb_{1/2})O_3$	PFN	385 (112)	12 000	R	F	7?	413 (140)
$Pb(Sc_{1/2}Ta_{1/2})O_3$	PST	299 (26)	28 000	R	F	45	478 (205)
Others							
$PbZrO_3$	PZ	513 (240)	3 000	O	AF	47	633 (360)
$(Pb,La)(Zr,Ti)O_3$	PLZT	<623 (<350)	30 000	R, T	F, AF	35–47	<623 (<350)
$BiScO_3$	BS	>673 (>350)	<1 000	R	F	64	723 (450)
$BiInO_3$	BIn	>973 (>700)	<1 000	R	F?	70	843 (570)
$PbTiO_3$	PT	763 (490)	9 000	T	F		

Notes: * M: monoclinic, O: orthorhombic, PC: pseudocubic, R: rhombohedral, T: tetragonal. † AF: antiferroelectric, F: ferroelectric.

In particular, the binary system PSCs, $Pb[(Zn_{1/3}Nb_{2/3})_{0.91}Ti_{0.09}]O_3$ (PZNT 91/9) and $Pb[(Mg_{1/3}Nb_{2/3})_{0.68}Ti_{0.32})]O_3$ (PMNT 68/32), are well known because they have an extremely large electromechanical coupling factor in the longitudinal mode, $k_{33}> 90\%$, and a large piezoelectric constant, $d_{33} > 1500$ pC.N^{-1}, along the [001] axis. Various applications, such as in medical transducers, actuators and undersea sonars, exploit these excellent properties. The authors have already reported on the growth of large PSCs of PZNT 91/9 by the solution Bridgman method (Harada *et al.*, 1998) and the first fabrication of a 3.7-MHz phased-array probe using PSCs of PZNT 91/9 has been reported, as well as its pulse echo characteristics and the final imaging quality (Saitoh *et al.*, 1999a, 1999b).

However, these binary system PSCs have some disadvantages that must be overcome. Large PSCs of PZNT and PMNT near the MPB have been grown by the flux method (Kobayashi *et al.*, 1997; Hosono *et al.*, 2002b), the solution Bridgman method (Harada *et al.*, 1998) and the Bridgman method (Luo, 1999, 2000). Although they have diameters of more than 80 mm, and good dielectric and piezoelectric properties have been confirmed, they have a relatively low T_c of approximately 130–165 °C. In particular, the low T_c prevents their use in more general applications. Moreover, they have phase-transition temperatures from the rhombohedral to the tetragonal phase, T_{rt}, around 50–100 °C. Figure 5.1 shows schematic phase diagrams of solid solution systems of PZNT and PMNT. PZNT 91/9 and PMNT 70/30 PSC near the MPB consist mainly of rhombohedral phases at room temperature and have excellent dielectric and piezoelectric properties. The dielectric and piezoelectric properties of PSCs of PZNT and PMNT change at temperatures above T_{rt} because of the phase transformation (Yamashita *et al.*,

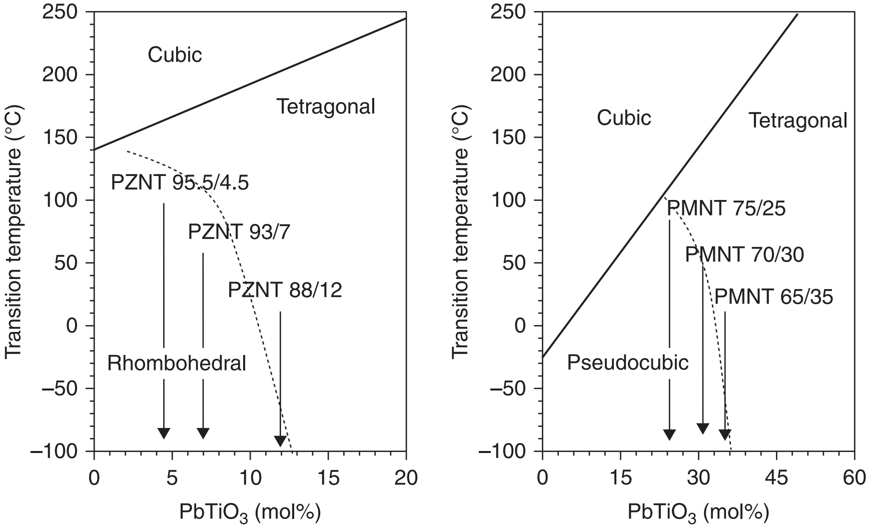

5.1 PZNT and PMNT phase diagrams near the MPB.

2004a; Feng *et al.*, 2004, 2006). The coupling factor of the rectangular bar mode, k'_{33}, decreases sharply at T_{rt} and then decreases gradually as the temperature moves toward T_c. Therefore, it is necessary to design the compositions of PSCs based on a consideration of the requirements of the specific application so as to achieve the optimum balance between the piezoelectric properties and thermal stability (Ye, 2008, 2009). However, it is difficult in binary systems of either PZNT or PMNT to raise T_{rt} and T_c simultaneously, as shown in Fig. 5.1. In general, when T_c increases, T_{rt} decreases. Therefore, designing crystal compositions with high T_{rt} and T_c is difficult with these binary PSCs (Yamashita *et al.*, 2004a).

On the other hand, the growth and electrical properties of some relaxor–PT PSCs with high $T_c > 250$ °C have been reported, such as PSCs of (1–x)$Pb(In_{1/2}Nb_{1/2})O_3$–x$PbTiO_3$ (PINT) (Yasuda *et al.*, 1999, 2001) and (1–x)$Pb(Yb_{1/2}Nb_{1/2})O_3$–x$PbTiO_3$ (PYNT) (Zhang *et al.*, 2002). Although the crystals have a high T_c, the crystal qualities are poor, the PSC sizes are small and the piezoelectric properties are inferior to those of PSCs of PZNT and PMNT. The present authors reported promising piezoelectric properties for $Pb(Sc_{1/2}Nb_{1/2})O_3$–$Pb(Mg_{1/3}Nb_{2/3})O_3$–$PbTiO_3$ (PSMNT) ceramics (Yamashita *et al.*, 1996) and single crystal growth and electrical properties for PSCs of $Pb(Sc_{1/2}Nb_{1/2})O_3$–$PbTiO_3$ (PSNT) (Yamashita and Shimanuki, 1996). PSNT has a relatively high T_c (> 200 °C); however, it has two major limitations: PSN has a high melting point (1420 °C) and there is a high raw-material cost for Sc_2O_3. Thus, the authors focused on PINT 63/37, which has a high Curie temperature, $T_c = 320$ °C, and a relatively low melting point of 1294 °C, as a candidate substitute material for PMNT 68/32 (melting point of 1271 °C) (Hosono *et al.*, 2000). Because the two melting points are similar, it should be possible to grow crystals of x$Pb(In_{1/2}Nb_{1/2})O_3$–y$Pb(Mg_{1/3}Nb_{2/3})$–z$PbTiO_3$ (PIMNT 100x/100y/100z). Moreover, it was assumed that the line connecting the MPB compositions of PMNT 68/32 and PINT 63/37 will be the MPB composition of the PIMNT ternary system. Therefore, the T_c of the PIMNT ternary system can be adjusted from 150 °C to 320 °C at MPB compositions, where the system is expected to exhibit good dielectric and piezoelectric properties (Hosono *et al.*, 2003a, 2003b).

In this chapter, the synthesis and evaluation of PIMNT ternary ceramics will be described. Next, crystal growth in a PIMNT ternary system by the flux and Bridgman methods will be discussed along with the compositional variation and the dielectric and piezoelectric properties.

5.2 PIMNT ceramics

This section describes the physical and electrical properties of PIMNT 100x/100y/100z ceramics near the MPB (Hosono *et al.*, 2003a). We focus on the compositions of the PIMNT ternary system, which are on the straight line connecting the MPBs of the PIMNT 0/68/32 (PMNT 68/32) and PIMNT 63/0/37 (PINT 63/37) binary systems. The purpose of this work was to study in detail the dielectric and piezoelectric properties of the PIMNT ceramic ternary system in the vicinity of the MPB, and to determine a ceramic material with good piezoelectric properties and a moderate T_c of around 200 °C.

Figure 5.2 shows the compositions of the samples synthesized in the PIMNT ternary system. Nine compositions along the MPB line and five compositions across the MPB line were prepared. Details of the procedure for preparing ceramic samples have been reported in previous papers (Hosono, 2003a). Figure 5.3 shows X-ray diffraction (XRD) patterns for PIMNT 100x/100y/100z ceramics. As shown in the figure, all of the ceramic samples had a single phase perovskite structure without any trace of pyrochlore. The results indicate that the perovskite structure is very stable in a PIMNT system. Fired PIMNT 25/43/32 indicated a rhombohedral (R) phase, whereas PIMNT 23/41/36 had a tetragonal (T) phase. However, compositions along the MPB, PIMNT 8/59/33 to PIMNT 56/8/36, showed three different peaks at around 45°, representing a mixture of the rhombohedral and tetragonal phases. Hence, the MPB is an almost linear, narrow region between the MPBs of the PIMNT 0/68/32 (PMNT 68/32) and PIMNT 63/0/37 (PINT 63/37) binary systems.

Figure 5.4 shows the dielectric properties of PIMNT 100x/100y/100z ceramics along the MPB measured at 100 kHz. The composition, PIMNT 0/68/32, showed a large dielectric constant with a maximum of 47 480. The dielectric constant maximum decreased as the PIN content increased. This is due to the low dielectric constant maximum of PIMNT 63/0/37. The dependence of T_c as a function of PIN (x) is shown in Fig. 5.5. T_c varied from 160 °C to 320 °C almost linearly as the PIN

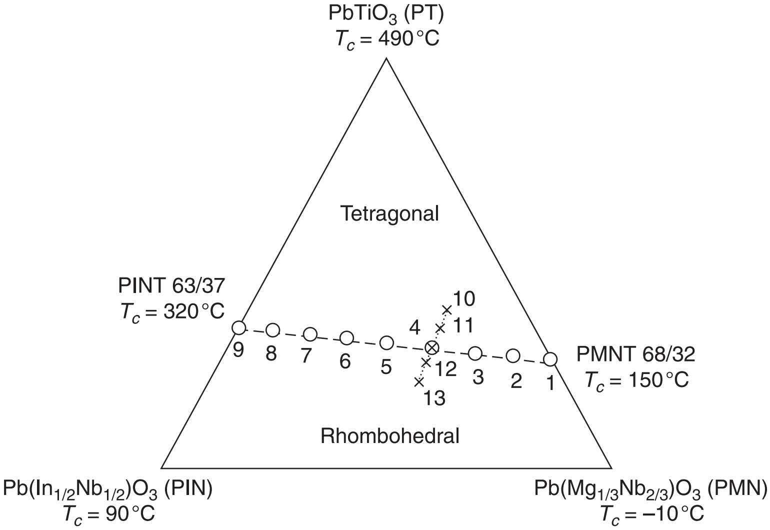

5.2 PIN-PMN-PT ternary system phase diagram.

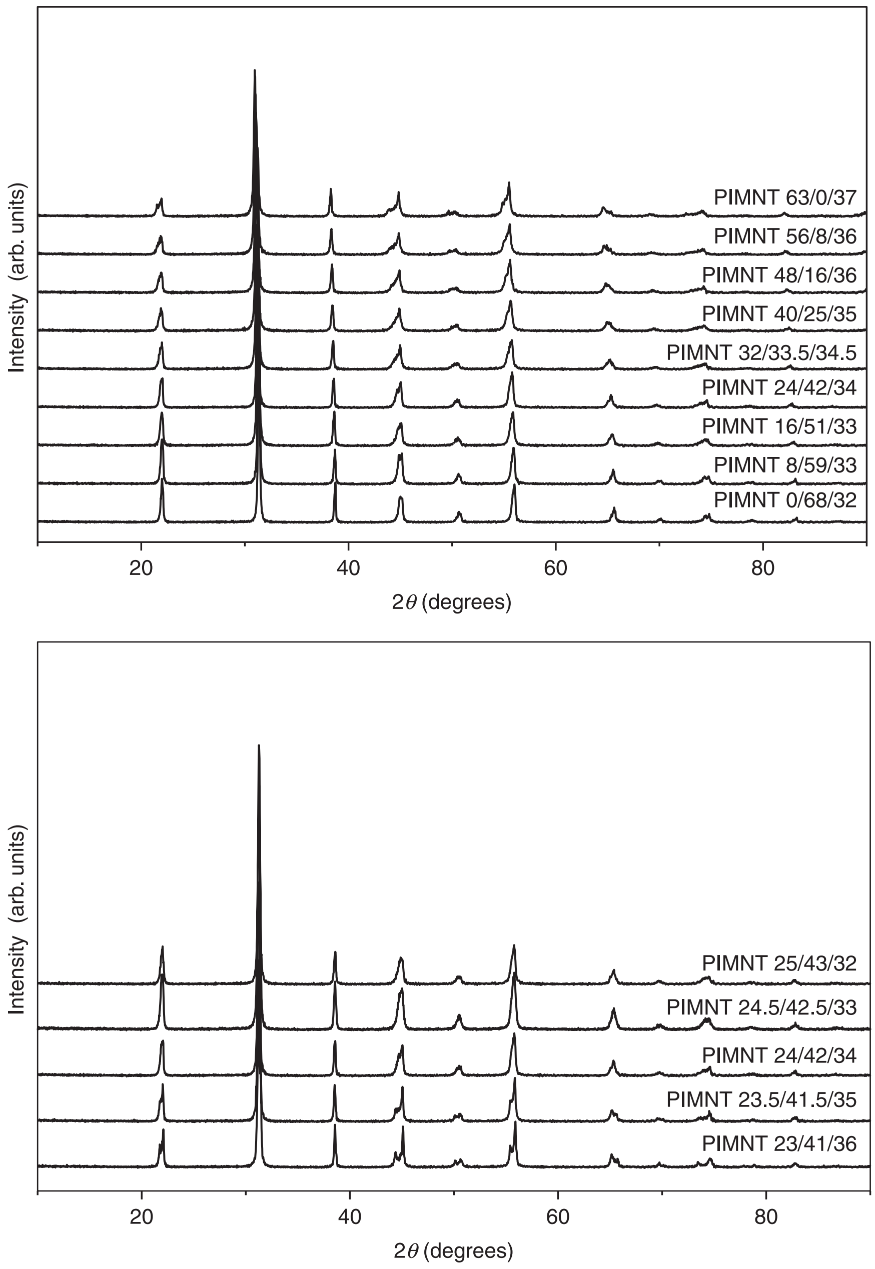

5.3 X-ray diffraction of the PIN-PMN-PT ternary ceramic system near the MPB.

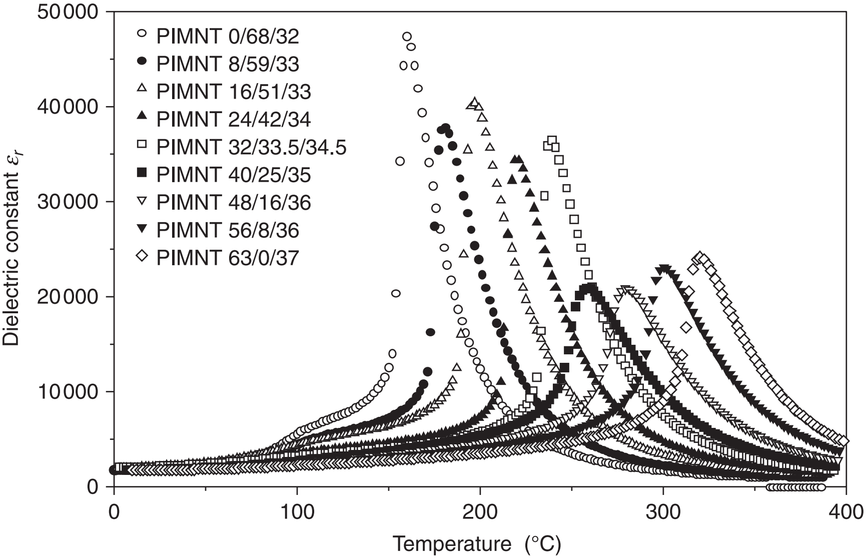

5.4 Dielectric constant vs. temperature measured at $f = 1.0$ kHz for the PIN-PMN-PT ternary ceramic system near the MPB.

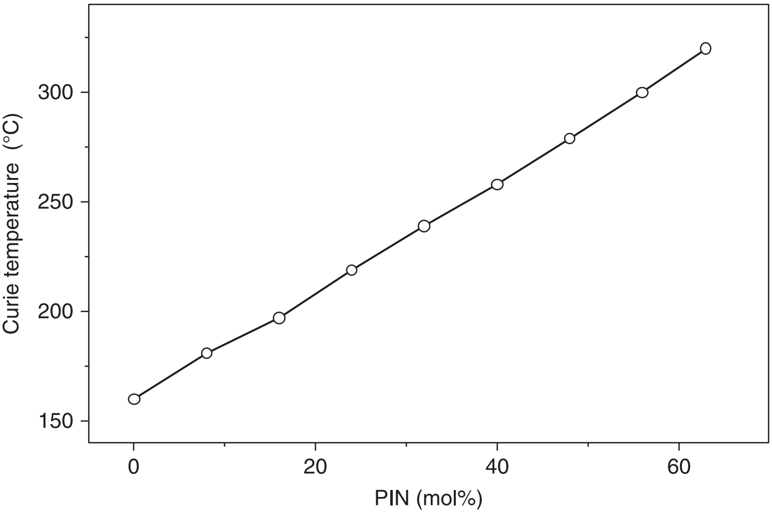

5.5 Curie temperature, T_c, of the PIN-PMN-PT ternary ceramic system near the MPB.

content increased. This result suggests that the T_c of the MPB composition in the PIMNT system can be controlled, leading to the realization of excellent piezoelectric properties.

Figure 5.6 shows the electromechanical coupling factor planar mode, k_p, for PIMNT ceramics along the MPB. The largest value of k_p = 67.6% was observed for PIMNT 24/42/34. The k_p values of the PIMNT ternary ceramics were slightly higher than those of the end member MPB compositions, PIMNT 0/68/32 and PIMNT 63/0/37. The compositions with high k_p showed low $\varepsilon_{33}{}^T/\varepsilon_0$. A high piezoelectric constant, d_{33} = 510 pC.N^{-1}, was found for PIMNT 0/68/32 and PIMNT 16/51/33. The high d_{33} values are attributable to their high dielectric constants and large coupling factors. Two compositions with a moderate T_c of around 200 °C were PIMNT 16/51/33 and PIMNT 24/42/34. The former composition, with T_c = 197 °C, showed $\varepsilon_{33}{}^T/\varepsilon_0$ = 2400, k_p = 67.1% and d_{33} = 510 pC.N^{-1} and the latter, with T_c = 219 °C, showed $\varepsilon_{33}{}^T/\varepsilon_0$ = 2120, k_p = 67.6% and d_{33} = 505 pC.N^{-1}. The electrical properties measured are excellent for high T_c piezoelectric materials. The high d_{33} values and reasonable T_c of PIMNT ceramic materials make them good candidates to replace conventional PZT ceramics in various piezoelectric applications. Tables 5.2 and 5.3 summarize the electrical properties of the PIMNT ceramics along and across the MPB. The ceramic samples across the MPB were used to confirm that the line connecting the MPBs of PIMNT 0/68/32 and PIMNT 63/0/37 is the MPB of the PIMNT ternary system. The peak post-poling dielectric constant at room temperature reached 3890 for PIMNT 23/41/36. This compound had a low coupling factor, k_p = 60.5%, and its

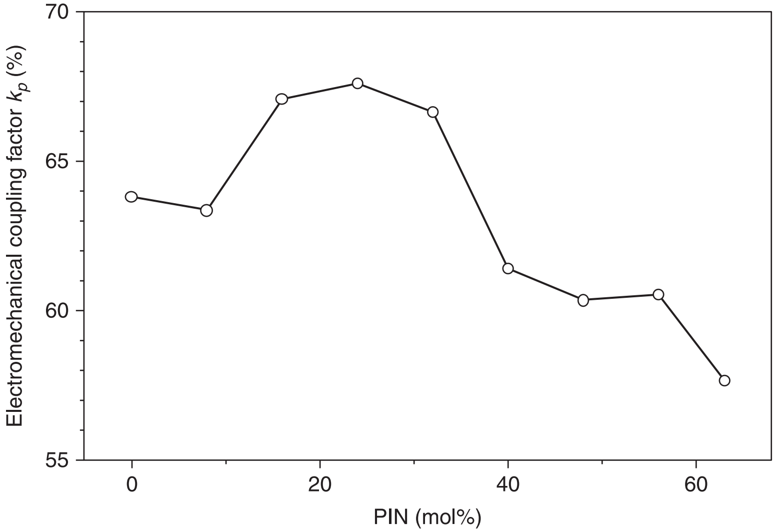

5.6 Electromechanical coupling factor planar mode k_p of the PIN-PMN-PT ternary ceramic system near the MPB.

Table 5.2 Dielectric and piezoelectric properties of PIMNT 100x/100y/100z ceramics along the MPB

Sample	Composition	T_c (°C)	$\varepsilon_r/\varepsilon_0$	$\varepsilon_{33}T/\varepsilon_0$	ε_{max}	k_p (%)	d_{33} (pC.N^{-1})
1	PIMNT 0/68/32	160	1830	2 320	47 480	63.8	510
2	PIMNT 8/59/33	181	1800	2 230	37 880	63.4	500
3	PIMNT 16/51/33	197	2080	2 400	40 460	67.1	510
4	PIMNT 24/42/34	219	2010	2 120	34 430	67.6	505
5	PIMNT 32/33.5/34.5	239	2140	2 160	36 520	66.7	495
6	PIMNT 40/25/35	258	1840	2 130	21 000	61.4	430
7	PIMNT 48/16/36	279	1840	2 120	20 890	60.3	430
8	PIMNT 56/8/36	300	1870	2 440	23 110	60.5	440
9	PIMNT 63/0/37	320	1800	2 450	24 190	57.7	435

Table 5.3 Dielectric and piezoelectric properties of PIMNT ceramics across the MPB

Sample	Composition	T_c (°C)	$\varepsilon_r/\varepsilon_0$	$\varepsilon_{33}T/\varepsilon_0$	ε_{max}	k_p (%)	d_{33} (pC.N^{-1})
10	PIMNT 23/41/36	231	2630	3890	32 860	60.5	550
11	PIMNT 23.5/41.5/35	223	2670	2560	35 710	62.1	515
4	PIMNT 24/42/34	219	2010	2120	34 430	67.6	505
12	PIMNT 24.5/42.5/33	211	1740	1910	35 250	65.3	465
13	PIMNT 25/43/32	213	1660	1850	35 720	66.8	465

phase was slightly tetragonal. On the other hand, compositions on the rhombohedral side had high coupling factors, $k_p > 65\%$, but low dielectric constants, $\varepsilon_{33}^T/\varepsilon_0 < 2000$. PIMNT 24/42/34 (on the line connecting the MPBs of PIMNT 0/68/32 and PIMNT 63/0/37) showed the highest coupling factor and a moderate dielectric constant as mentioned above. Therefore, the MPB of the PIMNT ternary system is an almost linear, narrow region between the MPBs of PIMNT 0/68/32 and PIMNT 63/0/37.

The PIMNT material system has a more stable perovskite structure than ceramics of PZNT or PMNT. The raw-material cost of In_2O_3 is lower than that of Sc_2O_3, which is used for PSNT. PIMNT materials have reasonably high k_p and d_{33}. A high T_c ranging from 180 to 240 °C is also attractive compared with that of PZNT 91/9 ($T_c = 170$ °C) or PMNT 70/30 ($T_c = 145$ °C). The material system may have a high coercive field E_c, which is closely related to T_c. PIMNT materials are suitable for use in high-T_c PSC applications if crystals of high quality and reasonable size are obtained.

5.3 PIMNT single crystals grown by the flux method

This section discusses PSCs of PIMNT grown by the conventional flux method and their dielectric and piezoelectric properties (Hosono *et al.*, 2003b). An excellent electromechanical coupling factor, $k_p = 67\%$, a relatively high Curie temperature, $T_c = 197$ °C, and good perovskite stability of PIMNT 16/51/33 and PIMNT 24/42/34 ceramics near the MPB have been confirmed (Hosono *et al.*, 2003a). Therefore, PIMNT ternary PSCs with MPB compositions are expected to have excellent piezoelectric properties as well as a high T_c (> 200 °C). However, to date there have been no reports on the synthesis of ternary PSCs that consist of six elements, Pb, In, Mg, Nb, Ti and O. The purpose of this work is to investigate the possibility of growing PIMNT ternary PSCs with good enough quality and size near the MPB and to characterize their properties.

High-purity chemicals (better than 99.9%), PbO, In_2O_3, MgO, Nb_2O_5 and TiO_2 (from Kojundo Chemical Lab. Co., Ltd, Saitama, Japan), were used as starting materials. A flux composition of 80 mol% PbO–20 mol% B_2O_3 was selected for PSC synthesis. The flux and the precalcined PIMNT powder were lightly mixed in a plastic bag without any solvent. The selected ratio was 50 PIMNT 16/51/33: 40 PbO: 10 B_2O_3 (mol%). The mixture (100 g) was placed in a 20 cm^3 platinum (Pt) crucible with a lid after twice premelting at 1000 °C for 1 hour. The Pt crucible was placed in 100 cm^3 and 300 cm^3 Al_2O_3 double crucibles with lids to prevent the evaporation of lead oxide and possible damage to the furnace. The crucible was placed in a computer-controlled electric furnace. The temperature was increased to 1230 °C and maintained for 5 hours before being slowly reduced to 850 °C at 1.2 $°C.h^{-1}$. After cooling to room temperature at a rate of 100 $°C.h^{-1}$, the crucibles were weighed to determine the weight loss of the contents during heat treatment. After crystal growth, the contents were rinsed in boiling 50% acetic acid for 24 hours to separate the PSCs from the residual flux. The PbO–B_2O_3 flux caused negligible damage to the Pt crucible and the weight losses due to PbO evaporation were less than 1.4% for the temperature profile described above. Crystals in the crucibles were visible to the naked eye. Figure 5.7 shows the top view of a PIMNT crystal obtained by the flux method. This large, yellowish-brown crystal was obtained from the top of the contents. The crystal structure was studied by XRD

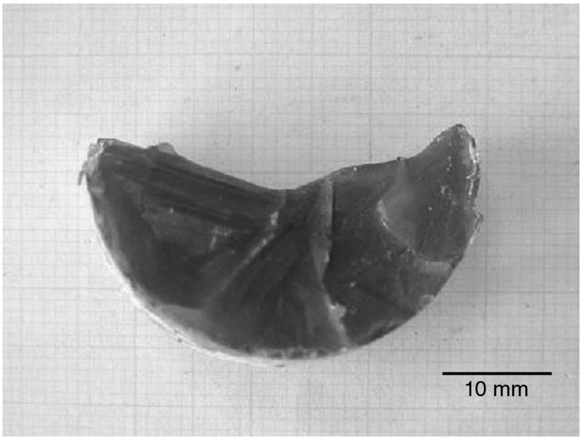

5.7 Top view of a PIMNT crystal obtained by the flux method.

after pulverizing some of the crystals. The crystals grown had a single-phase perovskite structure. PIMNT wafers with (001) faces were sliced from the crystals. The wafers have no serious inclusions, but consist of transparent and opaque areas.

A rectangular plate (9 mm × 7 mm × 0.4 mm) was used for electrical measurements. Au/Cr electrodes were sputtered on both sides of the test specimen. The specimen was poled by applying an electrical field of 1 kV.mm^{-1} for 10 min at room temperature. The electrical capacitance and dielectric loss were measured at 1 kHz using a computer-controlled impedance analyzer (HP4192A). The temperature dependence of the dielectric properties was measured at 1 kHz using the same measurement system, in a temperature range of 30 °C to 220 °C. The piezoelectric constant, d_{33}, was measured using a d_{33} meter (Institute of Acoustics Academia Sinica, Model ZJ-3D).

Figure 5.8 shows the dielectric properties of one of the PIMNT PSCs. It has a maximum dielectric constant at 187 °C, indicating a T_c about 40 °C higher than that of a PSC of PMNT 68/32. The broad peak of the dielectric constant around T_c is due to the scatter of the T_c resulting from the compositional variation in the crystal. A small peak of the dielectric constant is observed near 50 °C, which is considered to be the phase-transition temperature, T_{rt}, from the rhombohedral to the tetragonal phase. This indicates that the PSC is in the rhombohedral phase at room temperature. This result agrees with the XRD pattern without split peaks. The T_{rt} of the crystal was slightly lower than the value reported for the same ceramic in Section 5.2. In order to increase the T_{rt}, the composition should be shifted slightly toward that of the rhombohedral phase by reducing the Ti content or increasing the $Pb(In_{1/2}Nb_{1/2})O_3$ content. The room-temperature

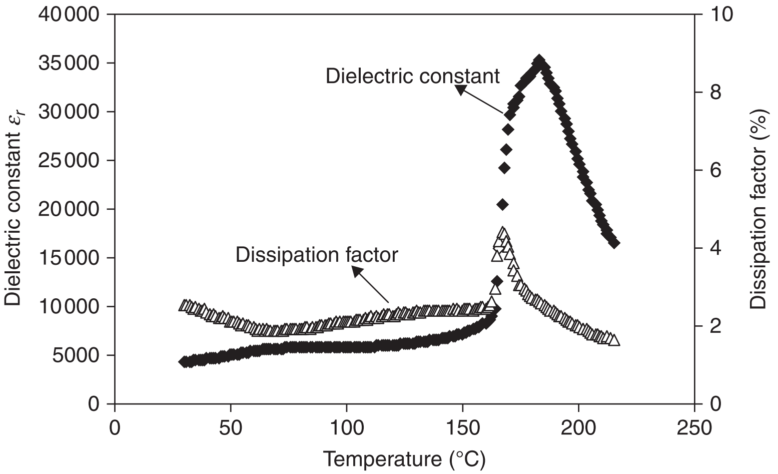

5.8 Dielectric constant and dissipation factor of a PSC of PIMNT 16/51/33 prepared by the flux method near the MPB.

dielectric constant, $\varepsilon_{33}{}^{T}/\varepsilon_0$, and dielectric loss factor after poling were 3100 and 0.8%, respectively. The piezoelectric constant, d_{33} = 2200 pC.N^{-1}, is extremely large and the value is comparable to those of PSCs of PZNT 91/9 and PMNT 70/30. The d_{33} value of a PSC of PINT 72/28 with a high Curie temperature, T_c >250 °C, is 700 pC.N^{-1}. Therefore, the d_{33} value of the PIMNT crystal is one of the highest values reported so far for any piezoelectric material with T_c > 180 °C.

In conclusion, PSCs of PIMNT 16/51/33 of high quality were synthesized by the flux method. The crystals show a large piezoelectric constant, d_{33} = 2200 pC. N^{-1}, with T_c = 187 °C.

5.4 PIMNT single crystals grown by the Bridgman method

5.4.1 Crystal growth of PIMNT 16/51/33

In this section, PSCs of PIMNT and $Pb(Sc_{1/2}Nb_{1/2})O_3$–$Pb(Mg_{1/3}Nb_{2/3})O_3$–$PbTiO_3$ (PSMNT) grown by the Bridgman method, and the dielectric and piezoelectric properties of these crystals, are discussed (Hosono *et al.*, 2003b, 2003c). As mentioned above, the present authors investigated the ceramics and PSCs of the PIMNT ternary system and reported that PSCs of PIMNT showed the highest piezoelectric constant among piezoelectric materials with a Curie temperature of higher than 185 °C (Hosono *et al.*, 2003a). Moreover, we reported that PSMNT ceramics, a ternary system similar to PIMNT, exhibited a large coupling factor, k_p = 70%, and piezoelectric constant, d_{33} = 680 pC.N^{-1}, with a high Curie temperature, $T_c = 207\,°C$, which is slightly superior to those of PIMNT ceramics (Yamashita *et al.*, 1996). Therefore, PSCs of PSMNT are also expected to show excellent piezoelectric properties if high-quality crystals are obtained. However, growing crystals of PSMNT ternary systems is very difficult because of the high melting point, 1420 °C, of $Pb(Sc_{1/2}Nb_{1/2})O_3$ (Yamashita and Shimanuki, 1996).

The purpose of this work was to grow large, high-quality PSCs of PIMNT and PSMNT using the solution Bridgman method and to investigate the compositional variation of the crystals in order to select a promising candidate piezoelectric material with high T_{rt} and T_c. Moreover, the electrical properties of PSCs of PIMNT grown by the Bridgman method are reported and compared with those of binary PSCs of PZNT and PMNT.

High-purity chemicals (better than 99.9%) were used as starting materials. PIMNT 16/51/33 and PSMNT 16/49/35 were selected as crystal compositions because they are on the MPB lines. In order to compare crystal growth, similar compositions were used. After wet-mixing the raw materials using a plastic ball mill with 5-mm-diameter ZrO_2 balls for 24 hours, the slurry was dried in an oven. Calcining was performed at 850 °C for 2 hours. The precalcined PIMNT (PSMNT) powders and flux were lightly mixed in a plastic bag without any solvent. The flux used for crystal growth was $PbO–B_2O_3$. The ratio selected was 50 PIMNT: 40 PbO: 10 B_2O_3 (mol%). A mixture weighing 245 g was placed in a 25-mm-diameter, 150-mm-long, 0.35-mm-thick Pt crucible after one premelt at 1000 °C. The Pt crucible was driven down through the hot zone at a speed of $0.4\,mm.h^{-1}$ after maintaining it at 1250 °C for 5 hours. After crystal growth, the crucibles were weighed to determine the weight loss of the contents during the heat treatment. The Pt crucibles were stripped off using a pair of nippers to observe the features of the solidified contents.

The Pt crucible suffered negligible damage and the weight losses due to PbO evaporation were less than 2% for the temperature profile described above. The $PbO–B_2O_3$ flux is very effective for preventing evaporation of PbO. A large PSC of PIMNT was found on the bottom of the crucible and many small crystals were observed on the sides of the crucible. The features of the solidified contents are very similar to those of the PZNT system. The solidified contents of the PIMNT were rinsed in boiling 80% acetic acid for 12 hours to separate the PSC from the residual flux. The crystal was 25 mm in diameter and 30 mm in length and its weight was 109 g, which is equal to approximately 44.4% of the raw materials. The morphology of the crystal indicates that a single nucleation event occurred on the bottom of the crucible and the crystal grew in the [111] direction. The crystal was sliced along the (001) plane after its orientation was determined from Laue X-ray diffraction patterns. Nineteen wafers, 0.5 mm in thickness, were obtained and lapped to about 0.36 mm in thickness. The PIMNT wafers were numbered from the part of the crystal grown near the bottom of the crucible upwards. Figure 5.9 shows one of the wafers obtained from a PSC of PIMNT prepared by

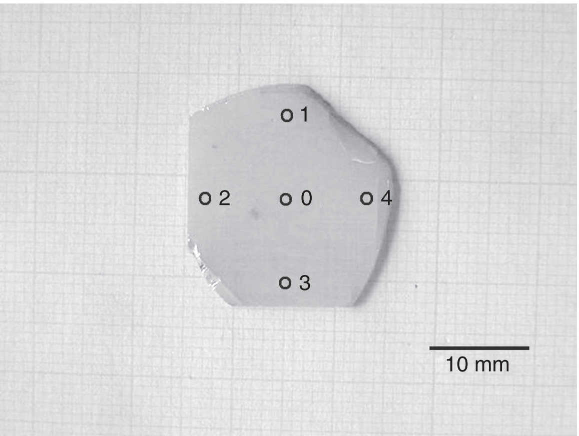

5.9 Wafer obtained from a PSC of PIMNT prepared by the Bridgman process.

the Bridgman process. Some wafers cut from the lower part of the crystal contained inclusions. The quality of the wafers improved from the lower to the upper part of the crystal. Six wafers were selected from the lower (1 and 2), middle (8 and 9) and upper parts (18 and 19) of the crystal for evaluation of their compositional variation and electrical properties.

The compositional variation of the PIMNT wafers was evaluated using an electron probe microanalyzer (EPMA, Shimadzu Corp., Model V6). Five measurement points in the form of a cross were set as shown in Fig. 5.9. The distance between neighboring points was 8 mm.

Three wafers were selected from the lower (2), middle (9) and upper (19) parts of the PSC of PIMNT for compositional analysis. Table 5.4 lists the average of the five points for the EPMA results and the theoretical values of the starting material: PIMNT 16/51/33. Figure 5.10 shows the EPMA results for the three wafers. The Ti content increased gradually from the lower part to the upper part. Luo reported the same behavior for PSCs of PMNT (Luo *et al.*, 2000). On the other hand, the In/Mg ratios of the three wafers were almost the same as the theoretical value. The PIMNT ternary system consists of four elements for the B-site (In, Mg, Nb and Ti) in the perovskite structure. Those elements have combinations such as $(In_{1/2}Nb_{1/2})^{4+}$, $(Mg_{1/3}Nb_{2/3})^{4+}$ and Ti^{4+} in the crystal in order to compensate for the charges. If the In/Mg ratio differs considerably in the crystal, obtaining a homogeneous crystal is very difficult. However, the In/Mg ratio is relatively constant in the PIMNT crystal. This is the key to obtaining a homogeneous PSC in the ternary system.

Table 5.4 EPMA results of three wafers cut from a PSC of PIMNT 16/51/33

Wafer number	PbO (wt%)	In_2O_3 (wt%)	MgO (wt%)	Nb_2O_5 (wt%)	TiO_2 (wt%)
2 (lower)	69.97	3.17	1.93	17.42	7.51
9 (middle)	68.99	3.23	2.37	17.65	7.76
19 (upper)	68.35	3.16	2.14	17.54	8.81
Theoretical value of PIMNT 16/51/33	69.04	3.43	2.12	17.26	8.15

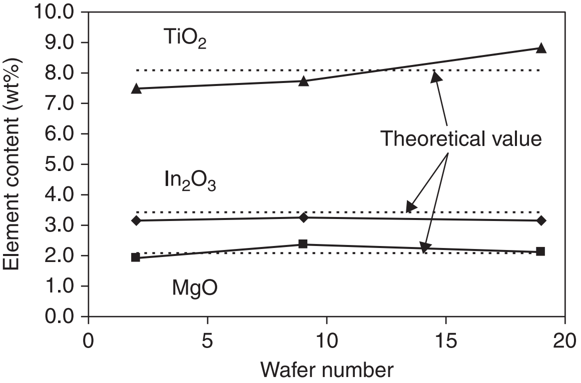

5.10 EPMA results for PSC wafers of PIMNT 16/51/33 prepared by the solution Bridgman method near the MPB.

5.4.2 Electrical properties of PSCs of PIMNT 16/51/33

Rectangular plates cut from three PIMNT wafers (1, 8 and 18) were used for electrical measurements. Au/Cr electrodes were sputtered on both sides of the test specimens. The dielectric constants and dielectric losses before and after poling were measured at 1 kHz using an impedance analyzer. A sliver transducer for the coupling factor, k'_{33}, measurement was obtained by dicing with a dicing saw (DISCO, Model DAD-2H/6T). The dicing pitch and wheel thickness were 0.22 mm and 0.05 mm, respectively. The sliver transducers were poled after dicing by applying an electric field of 1 kV.mm^{-1} at room temperature. The coupling factors k'_{33} were calculated using Eq. 5.1 after measuring the impedance curve using a network spectrum analyzer (HP4195A).

$$k_t, k'_{33} = \frac{\pi}{2} . \frac{f_s}{f_p} \tan\left(\frac{\pi}{2} . \frac{\left(f_p - f_s\right)}{f_p} \right) \qquad [5.1]$$

where f_p is the parallel resonance frequency and f_s is the series resonance frequency.

The temperature dependence of the dielectric properties of PSCs of PIMNT (wafers 1, 8 and 18) selected from the lower, middle and upper parts of the crystal were measured. The Curie temperature, T_c, varied from 181 °C to 196 °C with increasing wafer number. The T_c of the upper part is approximately 15 °C higher than that of the lower part of the crystal. The results of the EPMA tests indicate that the Ti content increases from the lower part to the upper part of the crystal. Therefore, this variation of T_c must be due to the increasing amount of $PbTiO_3$ (T_c = 490 °C) in the crystal. Peaks in the dielectric constant are observed below 100 °C in wafers 1 and 8, probably due to the phase transition from the rhombohedral phase to the tetragonal phase. This result indicates that the crystals are in the rhombohedral phase at room temperature. On the other hand, a small peak is observed for wafer 18 at approximately 30 °C. Therefore, the crystal must be near the MPB composition. In order to raise the T_{rt}, the composition needs to be shifted slightly into the rhombohedral phase by decreasing the Ti content in the crystal.

Table 5.5 lists the dielectric and piezoelectric properties of the PSCs of PIMNT for the lower, middle and upper parts. The dielectric constants of the plate transducers, $\varepsilon_{33}^T/\varepsilon_0$, ranged from 1480 to 4400 at room temperature. The upper part, wafer 18, showed a low $\varepsilon_{33}^T/\varepsilon_0$ because it belongs to the MPB composition near the tetragonal region at room temperature. Generally, the $\varepsilon_{33}^T/\varepsilon_0$ of a piezoelectric material in the tetragonal phase is small along the [001] direction. The piezoelectric constant, d_{33} = 1950 pC.N^{-1}, was a maximum for the middle part, wafer 8, which is almost the same as that of a crystal obtained by the flux method. The maximum coercive field, E_c = 8.9 kV.cm^{-1}, which is approximately twice that of PMNT 70/30, was observed in the upper part, for wafer 18. E_c

Table 5.5 Electrical properties of three wafers cut from PIMNT 24/42/34 PSC

	Wafer No. 1	Wafer No. 8	Wafer No. 18
Crystal part	Lower	Middle	Upper
Dielectric constant $\varepsilon_{33}^T/\varepsilon_0$	4400	3630	1480
Phase-transition temperature T_{rt} (°C)	91	55	–
Curie temperature T_c (°C)	181	191	196
Coupling factor k_t (%)	54.7	61.2	62.9
Piezoelectric constant d_{33} (pC.N^{-1})	1350	1950	1550
Remanent polarization P_r (μC.cm^{-2})	39.3	38.2	39.4
Coercive field E_c (kV.cm^{-1})	4.4	7.0	8.9
Coupling factor k_{33} (%)	64.7	80.3	83.6
Frequency const. $N'_{33}r$ (Hz.m)	1610	1110	1000

increases with increasing T_c. The remanent polarizations, P_r, of the three wafers show almost the same values. The upper part, wafer 18, also exhibits a large value because it belongs to the MPB composition very near the tetragonal region. The coupling factors sliver mode, k'_{33}, which are important for phased-array probes, were measured using sliver transducers obtained by dicing, as mentioned above. Observation by microscope revealed no serious cracking and chipping on the sides of the sliver transducers diced from wafers 8 and 18, but there were some cracks on the sides of the transducers diced from wafer 1. The reason for the cracking and chipping is thought to be that the crystal quality of wafer 1 was inferior to the others. Therefore, a very clear impedance behavior without any spurious modes or high k'_{33} values was observed for the sliver transducers of wafers 8 and 18. Moreover, they had high-frequency constants, N'_{33} =1000–1110 Hz.m. On the other hand, the k'_{33} values of the sliver transducers cut from wafer 1 were lower than for the other wafers. The low k'_{33} may be caused by poor crystal quality.

5.4.3 Crystal growth of PIMNT 24/42/34

After growing crystals of PIMNT 16/42/34, crystals of PIMNT 24/42/34 (Hosono *et al.*, 2005) were grown in order to increase T_{rt}.

Figure 5.11 shows a PSC of PIMNT 24/42/34 produced by the solution Bridgman process. A large size, 20 × 20 × 0.5 mm, and a good quality of wafer were obtained. The chemical composition of the pulverized powder of some PSCs is slightly different from that of the charged composition. The PbO ratio was a

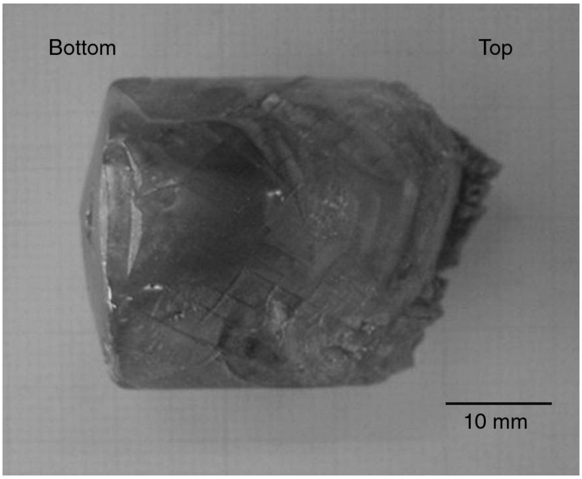

5.11 PSC of PIMNT 24/42/34 produced by the solution Bridgman process.

little higher than that of the charged composition because the PbO flux or a PbO inclusion might be included in the crystal samples. The PIMNT ternary system consists of four elements for the B-site (In, Mg, Nb and Ti) in the perovskite structure. Those B-site elements show three combinations, namely, $(In_{1/2}Nb_{1/2})^{4+}$, $(Mg_{1/3}Nb_{2/3})^{4+}$ and Ti^{4+}, in the crystal in order to compensate electrons. Therefore, $Pb(In_{1/2}Nb_{1/2})O_3$ and $Pb(Mg_{1/3}Nb_{2/3})O_3$ are in the rhombohedral phase but $PbTiO_3$ is in the tetragonal phase. The PIMNT ternary system changes phase as a function of its composition. The charged composition of PIMNT 24/42/34 is around the MPB. The ratio of $(In_2O_3$+MgO) to TiO_2 indicates the phase of the composition. The boundary between the rhombohedral phase and the tetragonal phase is 0.37 for the crystal composition and 0.35 for the charged composition. This means that the PSC of PIMNT obtained is a composition in the rhombohedral phase.

5.4.4 Electrical properties of PIMNT 24/42/34

Figure 5.12 shows the temperature dependence of the dielectric constants of poled plate transducers of PSCs of PIMNT 24/42/34 and PIMNT 16/51/33 measured at 1 kHz. Small peaks of the dielectric constant are observed at 50–90 °C, corresponding to the phase-transition temperature, T_{rt}. The T_{rt} and T_c of PSCs of PIMNT 24/42/34 and PIMNT 16/51/33 were 89 °C and 184 °C and 52 °C and 181 °C, respectively. The T_{rt} of PSCs of PIMNT 24/42/34 was about 40 °C higher than that of PSCs of PIMNT 16/51/33, whereas the T_c of PSCs of PIMNT 24/42/34 was almost the same as that of PSCs of PIMNT 16/51/33. The T_c of PSCs of PIMNT 24/42/34 was slightly lower than we expected because the $(In_2O_3$+MgO)/

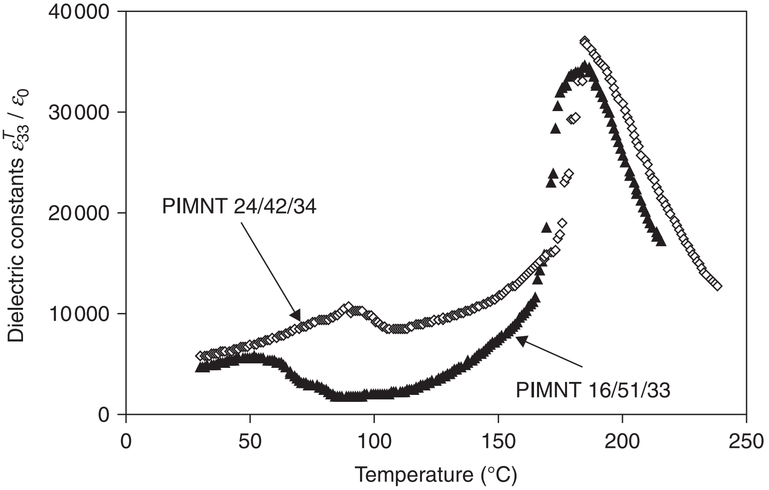

5.12 Dielectric properties of PSCs of PIMNT 24/42/34 and PIMNT 16/51/33.

TiO_2 ratio was lower than that of the charged composition for crystal growth. This means that the PSC of PIMNT has a low PT content, which shows a high T_c of 490 °C. The T_c (= 219 °C) of the PIMNT 24/42/34 ceramic has been confirmed in a previous report (Hosono *et al.*, 2003a).

Table 5.6 lists the dielectric and piezoelectric properties of PZNT 93/7, PMNT 70/30, PIMNT 24/42/34 and the ideal PSC for medical transducers. The dielectric constant after poling, $\varepsilon_{33}^T/\varepsilon_0$, of PIMNT 24/42/34 was 4900 at room temperature, which is almost the same value as that of PMNT 70/30. A high dielectric constant of the piezoelectric material is very important for ultrasonic medical array transducers. Recently, the capacitance of array transducers has been reduced, because the element size of array transducers is becoming smaller as the number of channels increases. In order to match the electrical impedance between a tiny piezoelectric element and a coaxial cable, a higher dielectric constant, which means larger capacitance, is required. A large piezoelectric constant, d_{33} = 2200 pC.N^{-1}, was observed for a PSC of PIMNT 24/42/34, which is almost the same as that of PSCs of PZNT 93/7 and PMNT 70/30. In ultrasonic applications, a few waveforms of the pulse voltage are applied to the transducer. Therefore, the stability of the piezoelectric properties when an inverse pulse voltage is applied to the transducer is important for a relaxor–PSC with relatively low T_c. The E_c of PSCs of PIMNT was 6.9 kV.cm^{-1}, which is around 1.5 times larger than that of PSCs of PMNT 67/33.

The coupling factors, k_{33}', which are important for phased-array probes, were measured using sliver transducers obtained by dicing. Observation by microscopy revealed no serious cracking and chipping on the sides of the sliver transducers diced from the plane transducer. The transducer showed a very clear impedance behavior, without any spurious and high k_{33}' values, of around 80%, which is

Table 5.6 Electrical properties of the obtained and the ideal PSCs for medical array transducers

	PZNT 93/07	PMNT 70/30	PIMNT 24/42/34	Ideal PSC
Free dielectric constant $\varepsilon_{33}^T/\varepsilon_0$	4000	7500	5000	>8000
Clamped dielectric constant ε_{33}^s	600	1200	1000	>1000
Phase-transition temperature T_{rt} (°C)	92	89	110	>100
Curie temperature T_c (°C)	165	145	184	>180
Coupling factor k_{31} (%)	58	50	70	<60
Coupling factor length mode k_{33} (%)	95	93	90	>95
Piezoelectric constant d_{33} (pC.N^{-1})	2400	2500	2200	>3000
Coercive field E_c (kV.mm^{-1})	0.5	0.3	0.7	>0.6
Coupling factor r. bar mode k_{33}' (%)	82	90	88	>90
Frequency constant N_{33r}' (Hz.m)	900	1180	1200	>1180
PSC size (mm)	50	70	75	>75

almost the same as those of PSCs of PZNT 91/9 and PMNT 70/30. Moreover, it had a high-frequency constant, N'_{33} = 1200 Hz.m, which is as high as that of PSCs of PMNT 70/30. The frequency constant, N'_{33}, is given by:

$$N'_{33} = 2 \times f_s \times d \tag{5.2}$$

where f_s is the series resonance frequency and d is the thickness of the transducer.

As indicated by the equation, a high-frequency constant means a thicker transducer can be vibrated at the same frequency. Therefore, a piezoelectric material with a high-frequency constant is promising for high-frequency applications.

Next, the temperature dependence of k'_{33} was measured using sliver transducers of PSCs of PIMNT 24/42/34 and PIMNT 16/51/33. The phase-transition temperatures, T_{rt}, the Curie temperatures, T_c, and the coupling factors, k'_{33}, at room temperature, for PSCs of PIMNT 24/42/34 and PIMNT 16/51/33 were 89 °C, 184 °C and 80%, and 52 °C, 181 °C and 82%, respectively. The T_{rt} and T_c values were measured using poled plate transducers before dicing to create sliver transducers. The k'_{33} values are almost the same as each other. Figure 5.13 shows the temperature dependence of k'_{33} of PSCs of PIMNT 24/42/34 and PIMNT 16/51/33. k'_{33} decreased in a step-like manner from 50 °C to 80 °C, which is similar to the behavior of PSCs of PZNT (Hosono *et al.*, 2002a). The authors think that k'_{33} exhibits a step-like decrease near the T_{rt} because a PSC of PIMNT starts to transform from the rhombohedral to the tetragonal phase at those temperatures, and the directions of spontaneous polarizations also change. Therefore, the degradation temperature of k'_{33} was in agreement with the T_{rt} measured using a poled PSC of PIMNT, as for PSCs of PZNT. Because a transducer may be heated to around

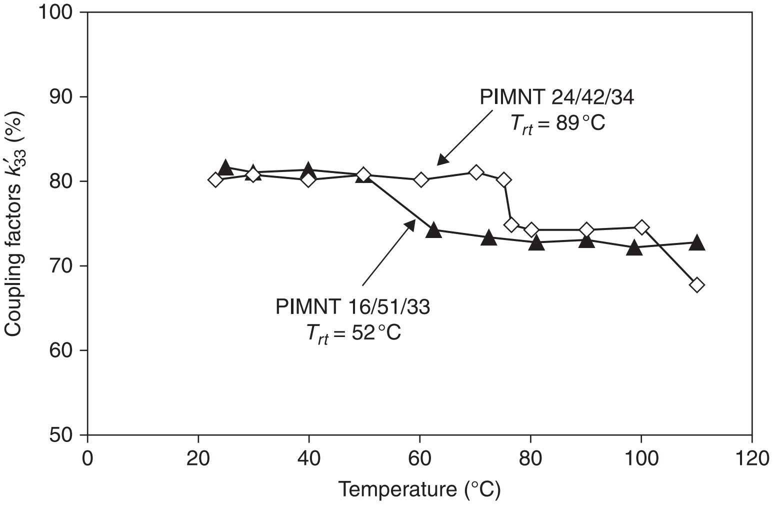

5.13 Temperature dependence of k'_{33} of PSCs of PIMNT 24/42/34 and PIMNT 16/51/33.

70 °C, the thermal stability of the piezoelectric properties is very important for medical transducers. Although k'_{33} for a PSC of PIMNT 16/51/33 decreased at about 50 °C, k'_{33} for a PSC of PIMNT 24/42/34 hardly changed until 70 °C. This result indicates not only that the PSC of PIMNT 24/42/34 had excellent piezoelectric properties but also that those properties had good thermal stability due to its high T_{rt}. Moreover, it had good voltage-proof properties due to its high T_c. Therefore, a PSC around the PIMNT 24/42/34 composition may be the best piezoelectric material for medical array transducers. In particular, the large coercive fields and high-frequency constants make PSCs of PIMNT useful for high-frequency transducer and multilayer transducer applications (Yamashita *et al.*, 2004b).

5.4.5 Summary for PSCs of PIMNT produced by the Bridgman process

In summary, the growth of crystals of PIMNT ternary systems was investigated by the solution Bridgman method using a PbO–B_2O_3 flux. The results obtained are as follows:

- A large PSC of PIMNT, 25 mm in diameter and 30 mm in length, was obtained by driving the crucible at a speed of 0.4 mm.h^{-1} from 1250 °C to 900 °C.
- The results of EPMA tests revealed that the Ti content gradually increased during the growth of PSCs of PIMNT. However, the In/Mg ratio was constant in PSCs of PIMNT.
- The Curie temperature, T_c, of a PIMNT crystal ranged from 181°C to 196 °C from the lower part to the upper part, which is in agreement with the EPMA results.
- Excellent dielectric and piezoelectric properties were confirmed in the crystal with T_{rt} = 89°C and T_c = 184 °C: the dielectric constant, $\varepsilon^T_{33}/\varepsilon_0 = 4900$, piezoelectric constant, d_{33} = 2200 pC.N^{-1}, coercive field E_c = 6.8 kV.cm^{-1}, coupling factor, k'_{33} = 80% and frequency constant, N'_{33} = 1200 Hz.m.

It was confirmed that growing crystals of the PIMNT system is as easy as growing PSCs of the PMNT system. However, the compositional variation of PSCs of PIMNT manufactured by the Bridgman process is similar to that of PSCs of PMNT. Finally, the PSC of PIMNT obtained exhibited good dielectric and piezoelectric properties as well as a high T_{rt} and T_c.

Figure 5.14 shows the relation between the Curie temperature, T_c, and piezoelectric constants, d_{33}, of relaxor–PT PSCs and PZT ceramics. The d_{33} values of relaxor–PT PSCs are larger than those of PZT ceramics, particularly PMNT 70/30, PZNT 91/9 and PIMNT 24/42/34. PINT 72/28, which has a high T_c of 260 °C, has a lower d_{33} than other PSCs. The low d_{33} may be caused by poor crystal quality and the high T_c. Because there is insufficient data on d_{33} for relaxor–PT PSCs with T_c over 200 °C, the relation between T_c and d_{33} is unclear.

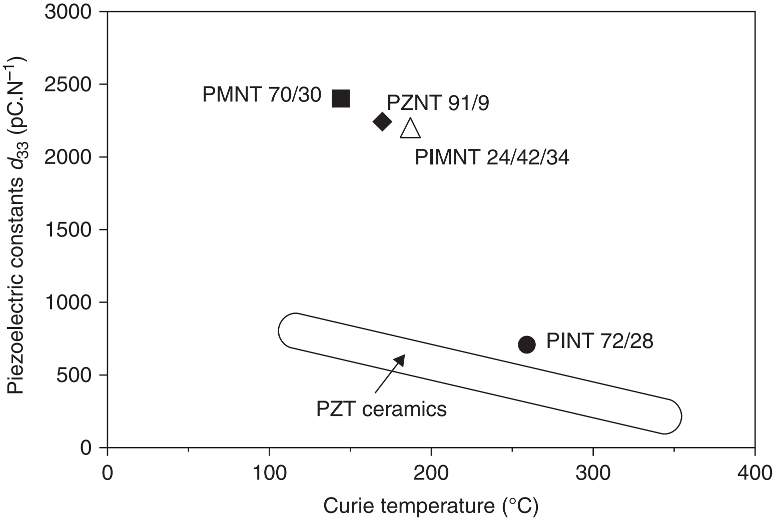

5.14 Piezoelectric constants as a function of Curie temperature of several relaxor–PT single crystals and PZT ceramics.

In this study, the starting material selected was PIMNT 16/51/33 and PIMNT 24/42/34, which lie on the compositional line connecting the MPB compositions of PMNT 68/32 (T_c = 150 °C) and PINT 63/37 (T_c = 320 °C). The T_c of PIMNT ternary systems with MPB compositions can be varied from 150 °C to 320 °C. Therefore, if the composition of PSCs of PIMNT is designed carefully with an optimum balance between the piezoelectric properties, high T_{rt} and high T_c, PSCs of PIMNT may become excellent candidates for applications such as medical imaging, non-destructive testing and actuators. Figure 5.15 shows a recent PSC of PIMNT produced by JFE Mineral Co., Chiba, Japan, using the Bridgman process. The crystal diameter is 80 mm, the length is 100 mm and the weight is 4 kg (see http://www.jfe-mineral.co.jp/seihin/seihin034.html). PSCs of almost the same size are also available from TRS Technologies, PA, USA (http://www.trstechnologies.com/Products/single_crystal.php), HC Materials, IL, USA (http://www.hcmat.com/) and Ibule Photonics Korea (http://www.ibule.com/en/products/sub_01.php).

5.5 Recent research into PIMNT single crystals and their applications

This section introduces research carried out between 2006 and 2012 into PIMNT materials and their applications. During this period, several important results for high-T_c PSCs of PIMNT, domain engineering and new electrode material effects were reported.

5.15 PSC of PIMNT produced using the Bridgman process.

Xu *et al.* (2007) reported the piezoelectric properties of PSCs of PIMNT 28/40/32 and found the dielectric constant was 5200, the piezoelectric constant, d_{33} = 1700–2200 pC.N^{-1}, the coercive field E_c = 10.9 kV.cm^{-1}, T_{rt} = 119 °C and T_c = 192 °C.

Tian *et al.* (2007) reported the piezoelectric property distribution of PSCs of PIMNT 24/44/32 prepared by the Bridgman process. They reported the dielectric constant as 5659, the piezoelectric constant d_{33} = 1924 pC.N^{-1}, the coercive field E_c = 5.8 kV.mm^{-1}, T_{rt} = 100 °C and T_c = 170 °C.

Yu *et al.* (2008) reported the growth and pyroelectric properties of PSCs of PIMNT 41/17/42 in the tetragonal phase. The material has a dielectric constant of 487 and a low dielectric loss of 0.3% at 50 Hz and room temperature. The pyroelectric properties with a pyroelectric coefficient of 5.7×10^{-4} C.m^{-2}.K and a detectivity of 6.34×10^{-5} Pa$^{-1/2}$ would satisfy the needs of operation as a high-T_c material. The results show that PSCs of PIMNT, having better temperature stability than pure PSCs of PMNT, are suitable for infrared detectors.

Zhang *et al.* (2008, 2009) reported the piezoelectric properties of PSCs of PIMNT 28–32/34–42/30–34 and found a dielectric constant of 4400, the piezoelectric constant d_{33} = 1510 pC.N^{-1}, E_c = 5.5 kV.cm^{-1}, T_{rt} = 124 °C and T_c = 164 °C. Zhang and Shrout (2010), Zhang *et al.* (2010) and Zhang (2012) are comprehensive and the best review papers of relaxor–PT materials for the last 13 years. These reviews introduce the PMNT and PIMNT material design, phase diagrams, crystal growth, dielectric constants, coercive field E_c, the temperature stability of the material constant and the importance of T_{rt} and T_c. The papers also introduced another high-T_c material system of PMN–PT–PZT crystals prepared by the solid state crystal growth (SSCG) process. The SSCG process has several advantages over the conventional modified Bridgman crystal growth process. Li *et al.* (2011) gave the electromechanical properties of PSCs of PIMNT [100] and [110]. These have piezoelectric constant d_{33} = 1600–2200 pC.N^{-1} and 830–1550 pC.N^{-1}, respectively.

Ye published a comprehensive handbook of single crystals (Ye, 2008) and a review paper (Ye, 2009), which are a good summary of recent progress of relaxor–PT PSC over the last ten years.

Liu *et al.* (2009) reported the complete set of material constants of PSCs of PIMNT at the MPB. Using combined resonance and ultrasonic methods, a full set of material constants has been measured for the MPB composition of PSCs of PIMNT poled along $[001]_c$. Compared with the MPB composition of PSCs of PMNT, PSCs of PIMNT have smaller anisotropy, higher $T_c \approx 197\,°\text{C}$ and higher $T_{rt} \approx 96\,°\text{C}$. The dielectric constant of this material is 7244. The electromechanical properties obtained are the best found so far for this ternary system with $d_{33} \approx$ 2742 pC.N^{-1}, $d_{31} \approx -1337$ pC.N^{-1}, $k_{33} \approx 95\%$ and $k_{31} \approx 65\%$.

Sun *et al.* (2009) reported on the design and fabrication of a high-frequency, 35 MHz to 60 MHz, ultrasonic transducer made from PSCs of PIMNT.

Yasuda *et al.* (2011) reported on the hierarchical domain structure of PSCs of 24PIN-46PMN-30PT. Lin *et al.* (2011a, 2011b) reported on domain size engineering in PSCs of tetragonal PIMNT and rhombohedral PMNT.

Lee *et al.* (2010) reported on the thickness dependence of the dielectric and piezoelectric properties of PMNT and PIMNT. PIMNT shows a high dielectric constant > 5500 at a thickness of 40 μm.

Yamamoto *et al.* (2011) reported effect of electrodes on dielectric and piezoelectric properties of lead magnesium niobate-lead titanate single crystal transducer. They showed a large change of the electrical properties have seen with different electrode.

Yamashita *et al.* (2011) reported manganese oxide and gold metal composite electrode for PMN-PT single crystal. They showed 140% larger dielectric constant and d33 compared to conventional electrode.

5.6 Future prospects and tasks

Ultrasonic array transducers are used in medical echo diagnostic ultrasound systems. Frequencies used for these applications are 2–20 MHz. A typical cardiac transducer operates at a center frequency of 2–4 MHz and uses a piezoelectric material plate of 15 × 25 mm. The key to achieving this is the performance of the piezoelectric material, which transmits the ultrasound and receives the echo. In recent decades, PZT5H ceramics with a high dielectric constant ($\varepsilon_{33}^T/\varepsilon_0 > 3500$) have been most commonly used for this purpose. However, recent research has focused on obtaining greater sensitivity and broader bandwidth, and new transducers such as piezoelectric composites have been studied.

PSCs of PZNT 91/9 and PMNT 70/30 have large d_{33} (> 2000 pC.N^{-1}), k_{33} (> 92%), k'_{33}(> 80%) and g_{33} (> 60 × 10^{-3} V.m.N^{-1}). These values are far larger than those obtained for any PZT ceramic specimens. This is one reason that intensive research on medical transducers has been conducted in various parts of the world during the last 20 years. After initial reports and presentations by Toshiba in the early 1990s, several organizations in the USA, South Korea and China entered the field. Saitoh *et al.* published the first B-mode and Doppler-mode images obtained by using PSCs of PZNT91/09 for cardiac transducers operating at 3.5 MHz with 96 channels (Saitoh *et al.*, 1999a). The echo amplitude of a PZNT probe is about 6 dB higher than for a PZT probe, and the frictional bandwidth is 30% wider. This means that both the penetration and the resolution of a PZNT probe are superior to those of conventional PZT probes. A large coupling factor k'_{33} (>82%), dielectric constant after poling ($\varepsilon_{33}^{T}/\varepsilon_0$> 3000) and low acoustic impedance Z_{33}< 24 (× 10^6 kg.m^{-2}.s^{-1}) make PSCs of PZNT 91/9 an excellent transducer material for medical diagnostic applications.

At present, the size of PSCs of PMNT and PIMNT is sufficient for various applications. However, the quality and uniformity of these crystals within and between wafers larger than 50 mm in diameter, from many manufacturers, are still insufficient (Yamashita *et al.*, 2004). Although it is usually easy to grow PSCs in the [111] or [110] directions, it is very difficult to grow them in the [001] direction; [001] wafers are used for medical transducers. There is always some inhomogeneous TiO_2 distribution within wafers. This is one of the causes of the large scatter of k_{33}, d_{33} and the dielectric constant within a wafer. In addition, the manufacture of high-frequency (i.e. more than 8 MHz) PSC transducers requires a thin thickness plate (less than 0.1 mm), which is very difficult because of the low-frequency constant and low mechanical strength of PSCs. The present cost of PSC wafers is more than five times that of PZT ceramics. Other drawbacks are temperature instability, mechanical properties, chipping by dicing, matching layers/electrode/PSC bonding strengths, low clamped dielectric constant, low E_c, de-poling, low production yield, etc. However, the PSCs of PIMNT, as introduced in this chapter, have gradually solved many of these shortcomings so far.

The Bridgman and solution Bridgman processes and the top-seeded solution growth (TSSG) process are well-established PSC growth processes. However, these processes have several shortcomings, such as Pt crucible cost and composition inhomogeneity. In order to resolve these shortcomings, a new approach has been studied. Solid state crystal growth (SSCG) (Lee *et al.*, 2000; Lee, 2004) and the templated crystal growth (TCG) processes have many advantages over conventional PSC processes and they are expected to reduce the cost of homogeneous relaxor PSCs for mass production in the near future. In addition, utilizing domain engineering (Wada *et al.*, 2005), as revealed through

PSC research, the piezoelectric properties of ceramic $BaTiO_3$ can also be drastically improved (Takahashi *et al.*, 2006a, 2006b). Xiang *et al.* (2010) described a high-temperature-poling process for PSCs of PZNT and obtained $d_{33} = 3425\,pC.N^{-1}$, which is the highest value found for relaxor–PT PSCs. Domain control using a special poling process is a promising future technology for improving piezoelectric properties.

Regarding piezoelectric material research, it is plausible that PIMNT materials may become the predominant materials for sophisticated, performance-oriented piezoelectric products in the near future. To that end, research on methods of evaluating PSC wafer quality and uniformity using non-destructive processes is an urgent task. Improvements in the uniformity of capacitance, the electromechanical coupling factor k_{33} and the piezoelectric constant d_{33} within and between wafers is also a major task for crystal growers. Detailed basic research to determine the mechanism accounting for the scatter of electrical properties should be conducted from the viewpoints of composition, domain structure and defect chemistry. Finally, research on new PSC, ceramic materials and technology to solve all of the present problems is essential. From the application aspect, a new dicing process to prevent cracking and the deterioration of PSCs is also necessary in order to make fine-pitch high-frequency array transducers. Because of the size dependency of the physical, dielectric and piezoelectric properties of small PSCs of less than $1.0\,mm^2$, a confirmation of scalability is required to design fine-sized piezoelectric medical array transducers.

5.7 Conclusions

Piezoelectric ceramics and PSCs in the $xPb(In_{1/2}Nb_{1/2})O_3–yPb(Mg_{1/3}Nb_{2/3})O_3–zPbTiO_3$ (PIMNT 100x/100y/100z) ternary system were investigated in order to develop new piezoelectric materials with a high piezoelectric constant, d_{33}, and high coercive field, E_c.

PSCs of PIMNT have been grown by the solution Bridgman method. The largest crystal obtained to date is 80 mm in diameter and 100 mm in length. Although the TiO_2 content gradually increased along the length of the crystal, the In/Mg ratio was almost constant, which is important for obtaining a uniform single crystal with the ternary system.

The PSCs of the PIMNT 20–30/35–50/30–35 ternary system show excellent electrical properties in the [001] plane, e.g. a dielectric constant $\varepsilon_{33}^T/\varepsilon_0 > 7000$, a piezoelectric constant $d_{33} > 2500\,pC.N^{-1}$ and a coupling factor sliver mode $k'_{33} >$ 85%, which are almost the same as or better than those of PSCs of the PZNT 91/9 and PMNT 68/32 binary systems. In addition, PIMNT has a high phase-transition temperature, $T_{rt} = 80–120\,°C$, and Curie temperature, $T_c = 160–195\,°C$. Moreover, it has a large coercive field $E_c = 4–8\,kV.cm^{-1}$ due to the high T_c. The high T_c, E_c and a frequency constant that is the same as single crystals of PMNT make PSCs of PIMNT the best transducer materials for medical applications and actuators that require stable temperature performance. Before piezoelectric crystals can be used for medical array transducers, a confirmation of the scalability of the physical, dielectric and piezoelectric properties with transducer structure (with backing and matching layers) is necessary.

5.8 References

Feng Z, Zao X and Luo H (2004), Composition and orientation dependence of phase configuration and dielectric constant tunability in poled $Pb(Mg_{1/3}Nb_{2/3})O_3$–$PbTiO_3$ crystals, *J. Phys. Condens. Matter*, **16**, 6771–8.

Feng Z, Zao X and Luo H (2006), Composition and orientation dependence of dielectric and piezoelectric properties in poled $Pb(Mg_{1/3}Nb_{2/3})O_3$–$PbTiO_3$ crystals, *J. Appl. Phys.*, **100**, 024104, 1–5.

Harada K, Shimanuki S, Kobayashi T, Saitoh S and Yamashita Y (1998), Crystal growth and electrical properties of $Pb[(Zn_{1/3}Nb_{2/3})_{0.91}Ti_{0.09}]O_3$ single crystals produced by solution Bridgman method, *J. Am. Ceram. Soc.*, **81**, 2785–8.

Hosono Y, Harada K, Yamashita Y, Dong M and Ye Z G (2000), Growth, electric and thermal properties of lead scandium niobate-lead magnesium niobate-lead titanate ternary single crystals, *Jpn. J. Appl. Phys.*, **39**, 5589–92.

Hosono Y, Harada K, Kobayashi T, Itsumi K, Izumi M, Yamashita Y and Ichinose N (2002a), Dielectric and piezoelectric properties of $0.93Pb(Zn_{1/3}Nb_{2/3})O_3$–$0.07PbTiO_3$ piezoelectric single crystals for medical array transducers, *Jpn. J. Appl. Phys.*, **41**, 7084–8.

Hosono Y, Yamashita Y, Sakamoto H and Ichinose N (2002b), Large piezoelectric constant of high-Curie-temperature $Pb(In_{1/2}Nb_{1/2})O_3$–$Pb(Mg_{1/3}Nb_{2/3})O_3$–$PbTiO_3$ ternary single crystal near morphotropic phase boundary, *Jpn. J. Appl. Phys.*, **41**, L1240–2.

Hosono Y, Yamashita Y, Sakamoto H and Ichinose N (2003a), Dielectric and piezoelectric properties of $Pb(In_{1/2}Nb_{1/2})O_3$–$Pb(Mg_{1/3}Nb_{2/3})O_3$–$PbTiO_3$ ternary ceramic materials near the morphotropic phase boundary, *Jpn. J. Appl. Phys.*, **42**, 535–8.

Hosono Y, Yamashita Y, Sakamoto H and Ichinose N (2003b), Growth of single crystals of high-Curie-temperature $Pb(In_{1/2}Nb_{1/2})O_3$–$Pb(Mg_{1/3}Nb_{2/3})O_3$–$PbTiO_3$ ternary systems near morphotropic phase boundary, *Jpn. J. Appl. Phys.*, **42**, 5681–6.

Hosono Y, Yamashita Y, Sakamoto H and Ichinose N (2003c), Crystal growth of $Pb(In_{1/2}Nb_{1/2})O_3$–$Pb(Mg_{1/3}Nb_{2/3})O_3$–$PbTiO_3$ and $Pb(Sc_{1/2}Nb_{1/2})O_3$–$Pb(Mg_{1/3}Nb_{2/3})O_3$–$PbTiO_3$ piezoelectric single crystals using the solution Bridgman method, *Jpn. J. Appl. Phys.*, **42**, 6062–7.

Hosono Y, Yamashita Y, Hirayama K and Ichinose N (2005), Dielectric and piezoelectric properties of $Pb[(In_{1/2}Nb_{1/2})_{0.24}(Mg_{1/3}Nb_{2/3})_{0.42}Ti_{0.34}]O_3$ single crystals, *Jpn. J. Appl. Phys.*, **44**, 7037–41.

Kobayashi T, Shimanuki S, Saitoh S and Yamashita Y (1997), Improved growth of large lead zinc niobate titanate piezoelectric single crystal for medical ultrasonic transducers, *Jpn. J. Appl. Phys.*, **36**, (9B), 6035–8.

Kuwata J, Uchino K and Nomura S (1982), Dielectric and piezoelectric properties of $0.91Pb(Zn_{1/3}Nb_{2/3})O_3$–$0.09PbTiO_3$ single crystals, *Jpn. J. Appl. Phys.*, **21**, 1298–301.

Lee H Y (2004), Solid state single crystal growth (SSCG) method: A cost-effective way of growing piezoelectric single crystals, in Trolier-McKenstry S, Cross L E and Yamashita Y, *Piezoelectric Single Crystals and Their Applications*, State College, Pennsylvania State University, 160–77.

Lee H Y, Kim J S and Kim D Y (2000), Fabrication of $BaTiO_3$ single crystals using secondary abnormal grain growth, *J. Eur. Ceram. Soc.*, **83**, (11), 1595–7.

Lee X J, Zhang S, Luo J, Li F and Shrout T R (2010), Thickness-dependent properties of relaxor–$PbTiO_3$ ferroelectric for ultrasonic transducers, *Adv. Func. Mater.*, **20**, 3154–62.

Li F, Zhang S, Lin D, Luo J, Xu Z, Wei X and Shrout T R (2011), Electromechanical properties of $Pb(In_{1/2}Nb_{1/2})O_3$-$Pb(Mg_{1/3}Nb_{2/3})O_3$-$PbTiO_3$ single crystals, *J. Appl. Phys.*, **109**, 014108.

Lin D, Zhang S, Li Z, Li F, Xu Z, Wada S, Luo J and Shrout T R (2011a), Domain size engineering in tetragonal $Pb(In_{1/2}Nb_{1/2})O_3$–$Pb(Mg_{1/3}Nb_{2/3})O_3$–$PbTiO_3$ crystals, *J. Appl. Phys.*, **110**, 084110.

Lin D, Lee H J, Zhang S, Li F, Li Z, Xu Z and Shrout T R (2011b), Influence of domain size on the scaling effects in $Pb(Mg_{1/3}Nb_{2/3})O_3$–$PbTiO_3$ ferroelectric crystals, *Scripta Mater.*, **64**, 1149–51.

Liu X, Zhang S, Luo J, Shrout T R and Cao W (2009), Complete set of material constants of $Pb(In_{1/2}Nb_{1/2})O_3$–$Pb(Mg_{1/3}Nb_{2/3})O_3$–$PbTiO_3$ single crystals with morphotropic phase boundary composition, *J. Appl. Phys.*, **106**, 074112.

Liu X, Zhang S, Luo J, Shrout T R and Cao W (2010), A complete set of material properties of single domain $0.26Pb(In_{1/2}Nb_{1/2})O_3$–$0.46Pb(Mg_{1/3}Nb_{2/3})O_3$–$0.28PbTiO_3$ single crystals, *Appl. Phys. Lett.*, **96**, 012907.

Luo H, Xu G, Xu G, Wang P and Yin Z (1999), Growth and characterization of relaxor ferroelectric PMNT single crystals, *Ferroelectrics*, **231**, 97–102.

Luo H, Xu G, Xu H, Wang P and Yin Z (2000), Compositional homogeneity and electrical properties of lead magnesium niobate titanate single crystals prepared by the modified Bridgman technique, *Jpn. J. Appl. Phys.*, **39**, 5581–5.

Saitoh S, Takeuchi T, Kobayashi T, Harada K, Shimanuki S and Yamashita Y (1999a), A 3.7 MHz phased array probe using $0.91Pb(Zn_{1/3}Nb_{2/3})O_3$–$0.09PbTiO_3$, *IEEE Trans. Ultrason. Ferroelect. Freq. Control*, **46**, 414–21.

Saitoh S, Takeuchi T, Kobayashi T, Harada K, Shimanuki S and Yamashita Y (1999b), An improved phased array ultrasonic probe using $0.91Pb(Zn_{1/3}Nb_{2/3})O_3$–$0.09PbTiO_3$ single crystal, *Jpn. J. Appl. Phys.*, **38**, 3380–4.

Shrout T R, Chang Z P, Kim N and Markgraf S (1990), Dielectric behavior of single crystals near the (1–x) $Pb(Mg_{1/3}Nb_{2/3})O_3$–(x)$PbTiO_3$ morphotropic phase boundary, *Ferroelectric Lett.*, **12**, 63–7.

Sun P, Zhou Q, Zhu B, Wu D, Hu C, Cannata J M, Tian Jin, Han P, Wang G and Shung K (2009), Design and fabrication of PIN–PMN–PT single crystal high-frequency ultrasonic transducers, *IEEE Trans. Ultrason., Ferroelect., Freq. Control*, **56**, 2760–3.

Takahashi H, Numamoto Y, Tani J, Matsuta K, Qiu J and Tsurekawa S (2006a), Lead-free barium titanate ceramics with large piezoelectric constant fabricated by microwave sintering, *Jpn. J. Appl. Phys.*, **45**, L30–3.

Takahashi H, Numamoto Y, Tani J, Matsuta K, Qiu J and Tsurekawa S (2006b), Piezoelectric properties of $BaTiO_3$ ceramics with high performance fabricated by microwave sintering, *Jpn. J. Appl. Phys.*, **45**, 7405–8.

Tian J, Han P, Huang X, Pan H, Carroll J F and Payne D (2007), Improved stability for piezoelectric crystals grown in the lead indium niobate–lead magnesium niobate-lead titanate system, *Appl. Phys. Lett.*, **91**, 222903.

Wada S, Yako K, Kanemoto H, Tsurumi T and Kiguchi T (2005), Enhanced piezoelectric properties of barium titanate single crystals with different engineered domain sizes, *J. Appl. Phys.*, **98**, 014109.

Xiang Y, Zhang R and Cao W (2010), Optimization of piezoelectric properties for [001]c poled $0.94Pb(Zn_{1/3}Nb_{2/3})O_3$–$0.06PbTiO_3$ single crystals, *Appl. Phys. Lett.*, **96**, 092902.

Xu G, Chen K, Yang D and Li J (2007), Growth and electrical properties of large size $Pb(In_{1/2}Nb_{1/2})O_3$–$Pb(Mg_{1/3}Nb_{2/3})O_3$–$PbTiO_3$ crystals prepared by the vertical Bridgman technique, *Appl. Phys. Lett.*, **90**, 032901.

Yamamoto N, Yamashita Y, Hosono Y and Itsumi K (2011), Effects of electrodes on dielectric and piezoelectric properties of lead magnesium niobate–lead titanate single-crystal transducer, *Jpn. J. Appl. Phys.*, **50**, NC04.

Yamashita Y (1994), Large electromechanical coupling factors in perovskite binary system, *Jpn. J. Appl. Phys.*, **33**, (9), 5328–31.

Yamashita Y and Shimanuki S (1996), Synthesis of lead scandium niobate–lead titanate binary system single crystals, *Mat. Res. Bull.*, **7**, 887–95.

Yamashita Y, Hosono Y and Ye Z G (2004a), Recent development trend of piezoelectric single crystals, A Review, *Trans. Mater. Resear. Soc. Jpn*, **29**, (4), 1059–66.

Yamashita Y, Harada K, Tao H and Ichinose N (1996), Piezoelectric properties of $Pb(Sc_{1/2}Nb_{1/2})O_3$–$Pb(Mg_{1/3}Nb_{2/3})O_3$–$PbTiO_3$ ternary ceramic materials near the morphotropic phase boundary, *Integrated Ferroelectrics*, **13**, 1–3.

Yamashita Y, Hosono Y and Ichinose N (2004b), Dielectric and piezoelectric properties of $Pb(In_{1/2}Nb_{1/2})O_3$–$Pb(Mg_{1/3}Nb_{2/3})O_3$–$PbTiO_3$ ternary materials with high Curie temperatures, in Trolier-McKenstry S, Cross L E and Yamashita Y, *Piezoelectric Single Crystals and Their Applications*, State College, Pennsylvania State University, 323–45.

Yamashita Y, Hosono Y, Harada K and Ye Z G (2004), Relaxor ferroelectric crystals: Recent development and application, in Setter N, *Piezoelectric Materials in Devices*, Lausanne, EPFL, 455–66.

Yamashita Y, Hosono Y, Yamamoto N and Itsumi K (2011), Effects of manganese oxides/gold composite electrode on piezoelectric properties of lead magnesium niobate titanate single crystal, *Jpn. J. Appl. Phys.*, **50**, NC05.

Yasuda N, Ohwa H, Ito K, Iwata M and Ishibashi Y (1999), Dielectric properties of the $Pb(In_{1/2}Nb_{1/2})O_3$–$PbTiO_3$ single crystal, *Ferroelectrics*, **230**, 115–20.

Yasuda N, Ohwa H, Kume M, Hayashi K, Hosono Y and Yamashita Y (2001), Crystal growth and electrical properties of lead indium niobate–lead titanate binary single crystal, *J. Cryst. Growth*, **229**, 299–304.

Yasuda N, Fuwa T, Ohwa H, Tachi Y, Yamashita Y, Fujita K, Iwata M, Terauchi H and Ishibashi Y (2011), Hierarchical domain structures in relaxor $24Pb(In_{1/2}Nb_{1/2})O_3$–$46Pb(Mg_{1/3}Nb_{2/3})O_3$–$30PbTiO_3$ near a morphotropic phase boundary composition grown by Bridgman method, *Jpn. J. Appl. Phys.*, **50**, NC01.

Ye Z G (2008), *Handbook of Advanced Dielectric, Piezoelectric and Ferroelectric Materials, Synthesis, Properties and Applications*, Woodhead Publishing.

Ye Z G (2009) High-performance piezoelectric single crystals of complex perovskite solid solutions, *Mater. Res. Soc. Bull.*, **34**, (4), 277–83.

Yu P, Wan F, Zhou D, Ge W X, Zhao X, Luo H, Sun J, Meng X and Chu J (2008), Growth and pyroelectric properties of high Curie temperature relaxor based ferroelectric $Pb(In_{1/2}Nb_{1/2})O_3$– $Pb(Mg_{1/3}Nb_{2/3})O_3$–$PbTiO_3$ ternary Single Crystals, *Appl. Phys. Lett.*, **92**, 252907.

Zhang S, Rhee S, Randall C A and Shrout T R (2002), Dielectric and piezoelectric properties of high Curie temperature single crystals in the $Pb(Yb_{1/2}Nb_{1/2})O_3$–$xPbTiO_3$ solid solution series, *Jpn. J. Appl. Phys.*, **41**, 722–6.

Zhang S, Luo J, Hackenberger W and Shrout T (2008), Characterization of $Pb(In_{1/2}Nb_{1/2})O_3$–$Pb(Mg_{1/3}Nb_{2/3})O_3$–$PbTiO_3$ ferroelectric crystal with enhanced phase transition temperature, *J. Appl. Phys.*, **104**, 064106.

Zhang S, Luo J, Hackenberger W, Sherlock N P, Meyer P J and Shrout T (2009), Electromechanical characterization of $Pb(In_{0.5}Nb_{0.5})O_3$–$Pb(Mg_{1/3}Nb_{2/3})O_3$–$PbTiO_3$ crystals as a function of crystallographic orientation and temperature, *J. Appl. Phys.*, **105**, 104506.

Zhang S and Shrout T R (2010), Relaxor–PT single crystals: Observation and development, *IEEE Trans. Ultrason. Ferroelect. Freq. Control*, **57**, 2138–46.

Zhang S, Liu G, Jiang W, Luo J, Cao W and Shrout T R (2010), Characterization of single domain $Pb(In_{0.5}Nb_{0.5})O_3$–$Pb(Mg_{1/3}Nb_{2/3})O_3$–$PbTiO_3$ crystals with monoclinic phase, *J. Appl. Phys.*, **110**, 064108. Available from: http://www.jfe-mineral.co.jp/seihin/seihin034.html. [Accessed 20 January 2012.]

Zhang S and Li F (2012), High performance ferroelectric relaxor–$PbTiO_3$ single crystals: Status and Perspective, *J. Appl. Phys.*, **111**, 031301. Available from: http://www.jfe-mineral.co.jp/seihin/seihin034.html. [Accessed 20 January 2012.]

6

Modelling ultrasonic-transducer performance: one-dimensional models

S. COCHRAN and C. E. M. DÉMORÉ,
University of Dundee, UK and
C. R. P. COURTNEY, University of
Bristol, UK

Abstract: One-dimensional models of piezoelectric transducers allow the rapid prediction of performance as well as assisting an understanding of transducer behaviour. This chapter initially describes the basis of transducer behaviour using wave equations. A description of Mason's model follows, and the KLM equivalent circuit and the linear systems model are also presented. Illustrative results are provided, with comparisons with results from finite element modelling, to demonstrate the capabilities and limitations of the one-dimensional approach to modelling.

Key words: one-dimensional modelling, piezoelectric devices, ultrasound transducers.

6.1 Introduction

The basic functions of ultrasound transducers are quite simple but understanding such transducers more than superficially and designing them accurately can be difficult. One way forward is through mathematical modelling. In this chapter, the models are one-dimensional (1D), incorporating only the thickness-mode behaviour of plates utilised in the majority of ultrasonic transducers. The behaviour in other modes can also be predicted with 1D models; for example, Mason (1948) first considered a bar and Meeker (1972) deals principally with a thickness-shear-mode transducer.

The first widely used 1D model was reported by Mason (1948) in the form of a passive electrical circuit mimicking the transducer's electrical behaviour around its fundamental resonant frequencies. A more fundamental way to express the behaviour of a transducer, based on the underlying physics, is through direct reference to wave propagation in the device, ultimately based on the constitutive equations. These two techniques are described in the next two sections of this chapter, including reference to piezocomposite materials (Smith and Auld, 1991). A more complex electrical analogy than Mason's was reported by Krimholtz, Leedom and Matthaei (Krimholtz *et al.*, 1970; Leedom *et al.*, 1971), which provided a clearer description of a transducer's behaviour and allowed understanding to be gained through links between the structure of the electrical circuit and the behaviour of the transducer. Subsequently, there have been many other contributions to the development of equivalent circuits. Some of these are noted in the references here. Another way to express this behaviour is through linear systems modelling in the Laplace and Fourier domains, as expressed by Hayward and his collaborators (for example, Hayward, 1984; Hayward and Jackson, 1986). This technique can provide useful functional insights, including, for example, for the secondary piezoelectric action, which is expressed as feedback within the model. A linear systems model is outlined here, along with its relation to other models.

The summary of this chapter emphasises the dependence of the choice of model on the device to be modelled, the resources available, the need for accuracy and the technical background of the person performing the modelling. It has been suggested that 1D modelling will become obsolete as computational resources expand; in the final section of this chapter, a rationale for continuing with 1D modelling is presented.

6.2 Transducer performance expressed through the wave equation

6.2.1 Transducer background

In most piezoelectric ultrasonic transducers, it is assumed that ultrasound will be generated or detected usefully by one particular surface in contact with the medium of interest. This surface may be an electrode placed directly on the piezoelectric material, or the piezoelectric material itself if the electrodes are off-axis such as in a 31-mode, but more commonly it will be a protective layer or a matching layer. The fact that only one surface is utilised suggests that 1D analysis of the transducer may be viable. This is the case when the aspect ratio of the piezoelectric material leads to operation in the thickness-extensional mode, typically with a width-to-thickness ratio of ten or more. This is common in many simple, single-element transducers for biomedical measurements (Cobbold, 2007), non-destructive testing (Krautkramer and Krautkramer, 1990), remote sensing and underwater sonar (Stansfield, 1991).

The behaviour of such transducers may be predicted from a mathematical analysis based on expressions defined in Chapter 1, along with other well-known results in physics and engineering. Many different analyses have been reported in the literature; here the approach taken is to base the analysis on the most fundamental results possible and to realise a solution suitable for multilayer structures, including both piezoelectric and non-piezoelectric materials. Such an approach is also viable with the equivalent circuit (transmission line) approach (Dion *et al.*, 1997) and expressed using the transfer-matrix approach (Sittig, 1967; Bloomfield, 2002). A basic physical configuration of a transducer is shown in Fig. 6.1; although this figure implies that all layers are piezoelectric, this need not be the case.

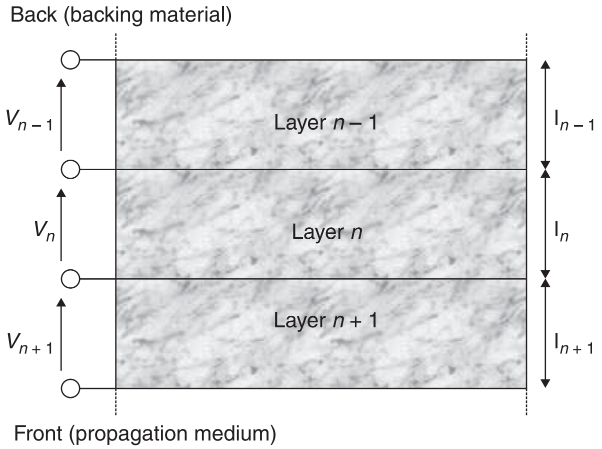

6.1 Basic physical configuration of a multilayer piezoelectric ultrasonic transducer.

6.2.2 Mathematical analysis

As noted in Chapter 1, Eq. 1.9, the constitutive equations for a piezoelectric material may be expressed in 1D as:

$$E = -hS + \frac{D}{\varepsilon^S} \qquad [6.1a]$$

and

$$T = c^D S - hD. \qquad [6.1b]$$

To relate these to the 1D wave equation in a piezoelectric transducer, it must first be noted that stress is defined as

$$T = \frac{F}{A}. \qquad [6.2]$$

Reference to Newton's second law, which defines force as the product of mass and acceleration, and utilising mass as the product of area, thickness and density, allows the stress to be expressed as

$$T = \rho l \frac{\partial^2 \xi}{\partial t^2}, \qquad [6.3]$$

where ρ is the density, l is the piezoelectric material thickness and ξ is the local acoustic particle displacement. Hence,

$$\frac{\partial T}{\partial z} = \rho \frac{\partial^2 \xi}{\partial t^2}. \qquad [6.4]$$

Expressing Hooke's law as

$$T = c\frac{\partial \xi}{\partial z} \tag{6.5}$$

then gives

$$c\frac{\partial^2 \xi}{\partial z^2} = \rho\frac{\partial^2 \xi}{\partial t^2}. \tag{6.6}$$

Hence

$$\frac{\partial^2 \xi}{\partial t^2} = v^2\frac{\partial^2 \xi}{\partial z^2} \tag{6.7}$$

where

$$v = \sqrt{\frac{c}{\rho}}. \tag{6.8}$$

Further, expressing the strain as

$$S = \frac{\partial \xi}{\partial z} \tag{6.9}$$

and differentiating with respect to the thickness, Eq. 6.1b can be rewritten as

$$\frac{\partial T}{\partial z} = c^D\frac{\partial^2 \xi}{\partial z^2} - h\frac{\partial D}{\partial z}. \tag{6.10}$$

From the differential form of Gauss's law for free charge,

$$\nabla \cdot D = 0 \Rightarrow \frac{\partial D}{\partial z} = 0. \tag{6.11}$$

Hence, Eq. 6.7 is valid for a piezoelectric material with wave propagation in the thickness dimension. It is convenient to solve this equation using Laplace transform methods, by first transforming Eq. 6.7 into

$$\bar{\xi} = \frac{v^2}{s^2}\frac{\partial^2 \bar{\xi}}{\partial z^2}, \tag{6.12}$$

where s is the Laplace operator and the bar indicates a term in the Laplace domain.

Solutions of Eq. 6.12 take the form

$$\overline{\xi_n} = \overline{\alpha_n} e^{-s\frac{l_n}{v_n}} + \overline{\beta_n} e^{s\frac{l_n}{v_n}} = \overline{\alpha_n} e^{-s\Delta t_n} + \overline{\beta_n} e^{s\Delta t_n} \tag{6.13}$$

with reference to layer n in a multilayer 1D transducer, where l_n is the layer thickness, α_n and β_n are the particle displacement amplitudes of the forward and backward propagating waves, respectively, at the back boundary of the layer, farthest from the propagation medium, and Δt_n is the transit time for wave propagation across layer n. Eq. 6.13 can now be applied to each of the constitutive equations in turn, to obtain the voltage across the layer and the forces acting upon it.

Voltage

To obtain the voltage across a layer in the transducer, Eq. 6.1a may be expressed as

$$\overline{E_n} = -h_n \frac{\partial \overline{\xi_n}}{\partial z} + \frac{\overline{D_n}}{\varepsilon_n^S} = -h_n \frac{\partial \overline{\xi_n}}{\partial z} + \frac{\overline{Q_n}}{A\varepsilon_n^S} \tag{6.14}$$

where

$$\overline{D_n} = \frac{\overline{Q_n}}{A}. \tag{6.15}$$

Hence,

$$\overline{V_n} = -h_n \int_{z=0}^{l_n} \frac{\partial \overline{\xi_n}}{\partial z} \partial z + \frac{\overline{Q_n}}{A\varepsilon_n^S} \int_{z=0}^{l_n} \partial z = -h_n \left(\overline{\xi_n}\Big|_{z=l_n} - \overline{\xi_n}\Big|_{z=0} \right) + \frac{\overline{Q_n}}{A\varepsilon_n^S} l_n. \tag{6.16}$$

Utilising Eq. 6.13 and rearranging then gives

$$\overline{V_n} = -h_n \left[\overline{\alpha_n} \left(e^{-s\Delta t_n} - 1 \right) + \overline{\beta_n} \left(e^{-s\Delta t_n} - 1 \right) \right] + \frac{\overline{Q_n}}{C_{0n}}, \tag{6.17}$$

where the static capacitance of the transducer layer,

$$C_{0n} = \frac{\varepsilon_n^S A}{l_n}. \tag{6.18}$$

Equation 6.16 provides an expression for $\overline{V_n}$ in terms of the acoustic particle displacement. To express it instead, more usefully, in terms of force, the relation between displacement and force can be used:

$$\overline{\alpha_n} = -\frac{\overline{F_{Fn}}}{sZ_{cn}} \text{ and } \overline{\beta_n} = \frac{\overline{F_{Bn}}}{sZ_{cn}} e^{-s\Delta t_n} \tag{6.19}$$

where Z_{cn} is the specific acoustic impedance,

$$Z_{cn} = \frac{c_n^D A}{v_n} \cdot \tag{6.20}$$

Then

$$\overline{V_n} = -\frac{h_n}{sZ_{cn}} (\overline{F_{Fn}} + \overline{F_{Bn}})(1 - e^{-s\Delta t_n}) + \frac{\overline{Q_n}}{C_{0n}}. \tag{6.21}$$

A general analysis of a multilayer structure may include multiple piezoelectric source or receiver layers, and electrically parallel and series layer connections. Whilst complicated configurations are of some interest, the focus here is on the most common configuration, a single layer or multiple layers connected electrically in parallel. Hence, two effects must be considered to take the voltage calculation further: the behaviour of the piezoelectric layers electrically in parallel and the behaviour of the external circuitry. Both of these can be simplified through the use of equivalent circuitry, as shown in Fig. 6.2.

Figure 6.2(a) shows that the total voltage is the same, $\overline{V_n} = \overline{V}$, across each layer, comprising contributions from the piezoelectric effect, $\overline{V_{pn}}$, and the stored charge. Thus, from Eq. 6.21,

$$\overline{Q_n} = C_{0n}\left[\overline{V} + \frac{h_n}{sZ_{cn}}(\overline{F_{Fn}} + \overline{F_{Bn}})\,(1 - e^{-s\Delta t_n})\right]. \qquad [6.22]$$

Furthermore, the multiple piezoelectric layers connected in parallel may be considered electrically as one equivalent voltage source in parallel with one equivalent capacitor. This capacitor has

$$C_\Sigma = \sum_{n=1}^{N} C_{0n} \qquad [6.23]$$

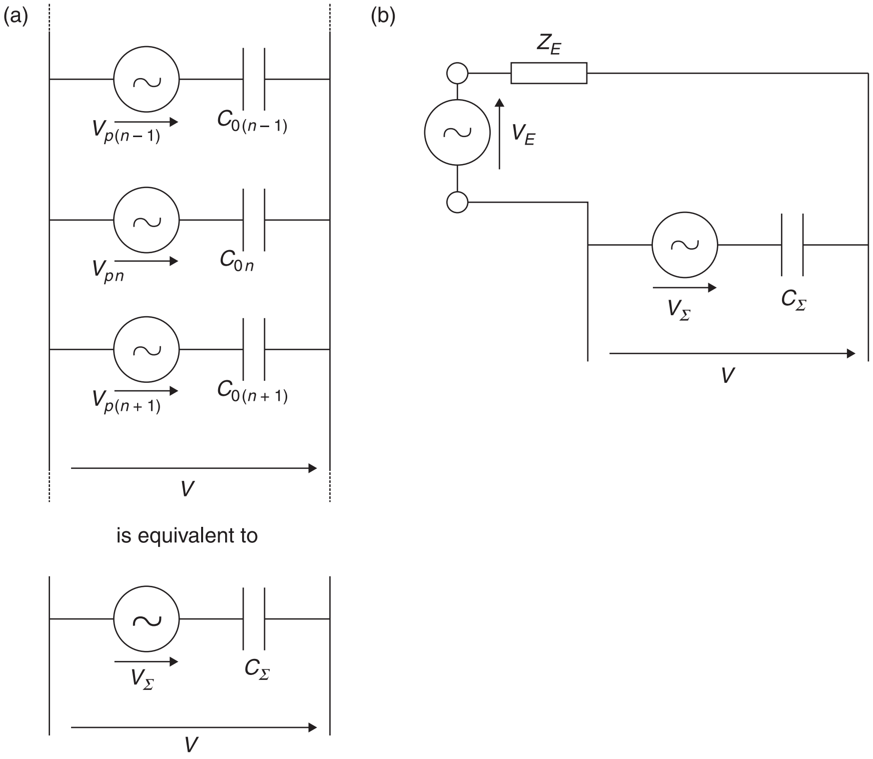

6.2 (a) Equivalence between multiple layers, as voltage sources with associated capacitance, and a single layer and (b) assumed simplified form of external circuitry.

and the equivalent voltage source has

$$\overline{V_\Sigma} = \sum_{n=1}^{N} \frac{C_{0n}}{C_\Sigma} \overline{V_n} = \sum_{n=1}^{N} -\frac{C_{0n}}{C_\Sigma} \frac{h_n}{sZ_{cn}} (\overline{F_{Fn}} + \overline{F_{Bn}})(1 - e^{-s\Delta t_n}) + \frac{\overline{Q_\Sigma}}{C_\Sigma}. \qquad [6.24]$$

The calculation of the total charge depends on the external electrical circuit. If this is assumed to have the simplified form shown in Fig. 6.2b then

$$\overline{Q_\Sigma} = \frac{\overline{V_E} - \overline{V_\Sigma}}{sZ_E}. \qquad [6.25]$$

Substituting this into Eq. 6.22 and rearranging then gives

$$\overline{V_\Sigma} = \frac{\overline{V_E}}{1 + sZ_E C_\Sigma} - \frac{sZ_E C_\Sigma}{1 + sZ_E C_\Sigma} \sum_{n=1}^{N} \frac{C_{0n}}{C_\Sigma} \frac{h_n}{sZ_{cn}} (\overline{F_{Fn}} + \overline{F_{Bn}})(1 - e^{-s\Delta t_n}). \qquad [6.26]$$

If the device has only one layer, $N = 1$, then this simplifies to

$$\overline{V} = \frac{1}{1 + sZ_E C_0} \left[\overline{V_E} - sZ_E C_0 \frac{h}{sZ_c} (\overline{F_{F1}} - \overline{F_{B1}})(1 - e^{-s\Delta t}) \right]. \qquad [6.27]$$

Forces

To obtain expressions for the forces, $\overline{\xi_n}$ can be replaced in Eq. 6.1b expressed in the Laplace domain:

$$\overline{T_n} = c_n^D \frac{s}{v_n} \left(\overline{\alpha_n} e^{-s\Delta t_n} + \overline{\beta_n} e^{s\Delta t_n} \right) - h_n \overline{D_n}, \qquad [6.28]$$

where Δt_n is the transit time for wave propagation across layer n. Following the approach taken for voltage, and using

$$\overline{T_n} = \frac{\overline{F_n}}{A}, \qquad [6.29]$$

this can be expressed as

$$\overline{F_n} = c_n^D A \frac{s}{v_n} \left(\frac{\overline{F_{Fn}}}{sZ_{cn}} e^{-s\Delta t_n} + \frac{\overline{F_{Bn}}}{sZ_{cn}} \right) - h_n \overline{Q_n}. \qquad [6.30]$$

Hence,

$$\overline{F_n} = \left(\overline{F_{Fn}} e^{-s\Delta t_n} + \overline{F_{Bn}} \right) - h_n \overline{Q_n} \qquad [6.31]$$

Equation 6.31 is an expression for the force at the interface between two layers in a transducer stack without reference to boundary conditions. These conditions may be expressed as the continuity of the acoustic particle displacement and the force:

$$\overline{\xi_n}\Big|_{z=l_n} = \overline{\xi_{n+1}}\Big|_{z=0} \quad \text{and} \quad \overline{F_n}\Big|_{z=l_n} = \overline{F_{n+1}}\Big|_{z=0} \qquad [6.32]$$

In dealing explicitly with the interfaces between layers, it is also necessary to define the transmission and reflection coefficients for the force travelling from layer m to layer n, respectively:

$$T^n_m = \frac{2Z_{cn}}{Z_{cm} + Z_{cn}} \quad \text{and} \quad R^n_m = \frac{Z_{cn} - Z_{cm}}{Z_{cm} + Z_{cn}}. \qquad [6.33]$$

From Eqs 6.30 and 6.32 it then follows that

$$\overline{F_{Fn}} = T^n_{n-1}\overline{F_{F(n-1)}}e^{-s\Delta t(n-1)} + R^{n-1}_n\overline{F_{Bn}}e^{-s\Delta tn} + T^n_{n-1}\frac{h_n\overline{Q_n}}{2} - T^n_{n-1}\frac{h_{n-1}\overline{Q_{n-1}}}{2} \qquad [6.34]$$

and

$$\overline{F_{Bn}} = T^n_{n+1}\overline{F_{B(n+1)}}e^{-s\Delta t(n+1)} + R^{n+1}_n\overline{F_{Fn}}e^{-s\Delta tn} + T^n_{n+1}\frac{h_n\overline{Q_n}}{2} - T^n_{n+1}\frac{h_{n+1}\overline{Q_{n+1}}}{2}. \qquad [6.35]$$

In these expressions, layer indices for the transmission and reflection coefficients less than one (i.e. $n - 1 = 0$, for $n = 1$) and greater than N (i.e. $n + 1 = N + 1$, for $n = N$) represent the media in contact with the back and front faces of the piezoelectric multilayer stack, that is, the propagation medium and the backing material.

To complete the mathematical analysis, substitutions can be made for the charge as defined in Eq. 6.22, leading to

$$\begin{aligned}\overline{F_{Fn}} = \left(\frac{1}{1 - T^n_{n-1}K_n}\right)\Bigg[&\overline{F_{F(n-1)}}T^n_{n-1}\left(e^{-s\Delta t(n-1)} - K_{n-1}\right)\\ &-\overline{F_{B(n-1)}}T^n_{n-1}K_{n-1} + \overline{F_{Bn}}\left(R^{n-1}_n e^{-s\Delta t_n} + T^n_{n-1}K_n\right)\\ &+\frac{T^n_{n-1}\overline{V}}{2}\left(h_nC_{0n} - h_{n-1}C_{0(n-1)}\right)\Bigg]\end{aligned} \qquad [6.36]$$

and

$$\begin{aligned}\overline{F_{Bn}} = \left(\frac{1}{1 - T^n_{n+1}K_n}\right)\Bigg[&\overline{F_{B(n+1)}}T^n_{n+1}\left(e^{-s\Delta t(n+1)} - K_{n+1}\right)\\ &-\overline{F_{F(n+1)}}T^n_{n+1}K_{n+1} + \overline{F_{Fn}}\left(R^{n+1}_n e^{-s\Delta t_n} + T^n_{n+1}K_n\right)\\ &+\frac{T^n_{n+1}\overline{V}}{2}\left(h_nC_{0n} - h_{n+1}C_{0(n+1)}\right)\Bigg]\end{aligned} \qquad [6.37]$$

where, for simplicity of expression,

$$K_n = h_n^2 C_{0n} \frac{1 - e^{-s\Delta t_n}}{2sZ_{cn}}. \qquad [6.38]$$

As with the voltage, if the device has only one layer then Eqs 6.36–6.38 can be simplified:

$$\overline{F_{F1}} = \left(\frac{1}{1 - T_0^1 K}\right)\left[\overline{F_{F0}}T_0^1 + \overline{F_{B1}}\left(R_1^0 e^{-s\Delta t} + T_0^1 K\right) + \frac{T_0^1 \overline{V}}{2} hC_0\right] \qquad [6.39]$$

and

$$\overline{F_{B1}} = \left(\frac{1}{1 - T_2^1 K}\right)\left[\overline{F_{B2}}T_2^1 + \overline{F_{F1}}\left(R_1^2 e^{-s\Delta t} + T_2^1 K\right) + \frac{T_2^1 \overline{V}}{2} hC_0\right], \qquad [6.40]$$

where

$$K = h^2 C_0 \frac{1 - e^{-s\Delta t}}{2sZ_c}. \qquad [6.41]$$

Here, $\overline{F_{F0}}$ and $\overline{F_{B2}}$ represent, respectively, the external forces incident on the back and front of the piezoelectric layer. These terms are also implicit in Eqs 6.36 and 6.37; if there are no external forces on the piezoelectric layer then they are zero. Furthermore, as noted in Chapter 1, layers in a transducer may be piezoelectric or non-piezoelectric, such as a matching layer. In the case of non-piezoelectric layers, $h_i = 0$ in the expressions that have been developed, producing results familiar from mechanical and electrical engineering.

6.2.3 Implementation

The three Eqs 6.28, 6.36 and 6.37 are important and they form a system of simultaneous equations for the electromechanical structure shown in Fig. 6.3. Solving this system produces numerical results representing the forces within each layer, forces radiated from the back and front faces of the device and the voltage across the device. With reference to the external electrical impedance and voltage, the latter also allows calculation of the electrical impedance of the device. If the Laplace operator, s, is replaced by the Fourier term, $j\omega$, then frequency domain results can be calculated by varying the frequency, f, implicit in $\omega = 2\pi f$, and assembling results over a range of frequencies. An inverse Fourier transform also allows time-domain results to be calculated.

6.3 Equivalent electrical circuit models

6.3.1 Historical background

Mason's model (Mason, 1948) has been the origin for a very large proportion of the 1D modelling described in the literature and executed for piezoelectric transducer design. It has two bases. First, piezoelectric transducers, and the other

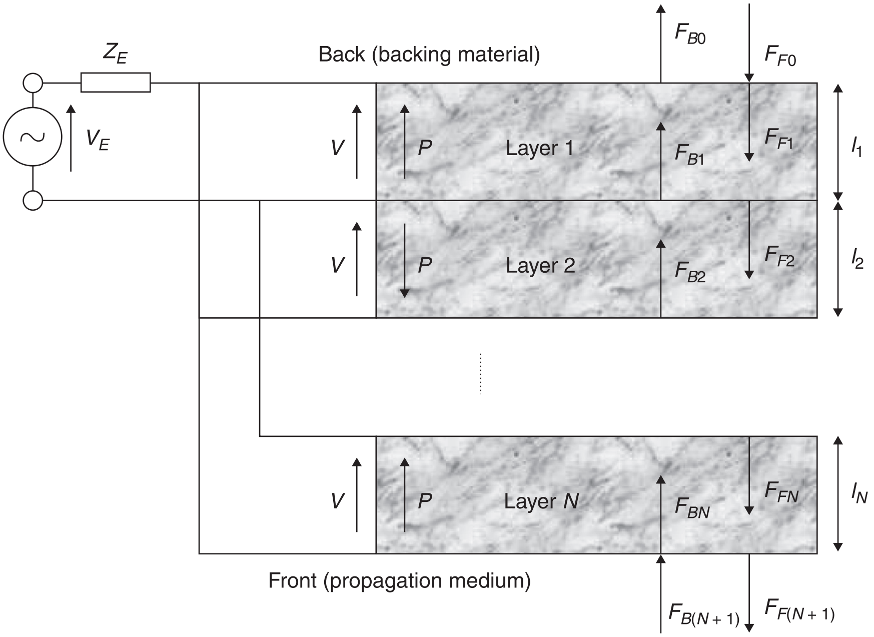

6.3 Electromechanical structure obtained by combining Fig. 6.1 and Fig. 6.2, showing polarisation directions (P) and forces propagating backward (F_B) and forward (F_F).

systems explored by Mason, are electromechanical systems and the use of knowledge from one component of this combination, i.e. electrical network theory, is helpful for many practitioners. Second, by the date of Mason's exposition, a very significant body of work existed in electrical network theory (Mason, 1948, p. 3) and this was a sound basis for the analysis of electrical circuit expressions of electromechanical systems.

These issues are important because piezoelectric devices are highly complex and lie at the nexus between the disciplines of electrical engineering, physics, materials science and mechanical engineering. Thus, their historical and future development has been and will be executed within this space and will inevitably require endeavour outside an individual's original discipline. To illustrate this further, the 1D model based on the wave equation described in Section 6.2 may be characterised as most familiar to physicists, whereas the finite element method (FEM), considered elsewhere, generally lies within the domain of mechanical engineering.

6.3.2 Mason's model

The Mason equivalent circuit is an analogue circuit mathematically equivalent to a piezoceramic crystal with electric fields and elastic wave propagation, each constrained to vary in only 1D. The wave propagation and the electric field do not have to be constrained to the same dimension; Mason's original formulation (Mason, 1948) considered a bar, which extended in the longitudinal direction, with an electric field perpendicular to its length. This section will describe the Mason equivalent circuit in terms of the thickness mode of a piezoceramic plate as described in Section 6.2.1.

Starting from the piezoelectric equations in 1D, Eqs 6.1a and 6.1b, and the equation of motion from Eq. 6.7, solutions relating the voltage and current across the plate and the force and velocity of each of the transducer surfaces are derived. An equivalent circuit, obeying the same equations, is given.

Starting with the solution to the equation for strain:

$$S = (\alpha \sin kz + \beta \cos kz)e^{i\omega t}, \qquad [6.42]$$

where the wave number $k = \omega/v^D$, the particle displacements can be written in terms of the complex amplitudes of the velocities of the front and back faces of the plate, v_F and v_B, respectively, which are assumed to be harmonic:

$$\left.\frac{\partial S}{\partial t}\right|_{z=l} = -v_F e^{i\omega t}. \qquad [6.43]$$

$$\left.\frac{\partial S}{\partial t}\right|_{z=0} = v_B e^{i\omega t}. \qquad [6.44]$$

Inserting Eq. 6.42 into Eqs 6.43 and 6.44 gives

$$\alpha = -\frac{1}{i\omega}\left(\frac{v_B}{\tan kl} + \frac{v_F}{\sin kl}\right) \qquad [6.45]$$

$$\beta = \frac{v_B}{i\omega}. \qquad [6.46]$$

Equations 6.42, 6.45 and 6.46 give the strain in the plate in terms of the velocities of the front and back faces. The next step is to relate the forces on each surface to their velocities. The forces on the front and back surfaces are given by

$$F_F = -AT\big|_{z=l} \qquad [6.47]$$

and

$$F_B = -AT\big|_{z=0} \qquad [6.48]$$

respectively. The stress, T, can be obtained using Eq. 6.1b and inserting the strain using Eq. 6.41 and current using

$$I = A\frac{\partial}{\partial t}D = i\omega AD, \qquad [6.49]$$

giving the force on the $z = 0$ face of the plate:

$$F_B = \frac{Z_0}{i\tan kl}v_B + \frac{Z_0}{i\sin kl}v_F + \frac{h}{i\omega}I \qquad [6.50]$$

and the $z = l$ face:

$$F_F = \frac{Z_0}{i\sin kl}v_B + \frac{Z_0}{i\tan kl}v_F + \frac{h}{i\omega}I. \qquad [6.51]$$

Here, $Z_0 = \rho A v^D$, the specific acoustic impedance, corresponding to Eq. 6.20. The voltage, V, can be written in terms of the face velocities and the current by substituting Eqs 6.49, 6.50 and 6.51 into Eq. 6.1a and integrating though the thickness of the plate:

$$V = \frac{h}{i\omega}v_B + \frac{h}{i\omega}v_F + \frac{I}{i\omega C_0}. \qquad [6.52]$$

Equations 6.50–6.52 are sufficient to describe the behaviour of the piezoceramic plate. However, in order to simplify calculations involving these mixed electromechanical systems it is often convenient to work with an equivalent circuit. As noted previously, Mason provided one such circuit suitable for a bar extending perpendicular to the applied electric field (Mason, 1948) and Berlincourt, Curran and Jaffe later clarified the intermediate steps taken to develop this circuit and applied it to other configurations, including the thickness modes of plates (Berlincourt *et al*., 1964; Rhyne, 1978).

Figure 6.4 shows the general form of the circuit; some of the impedances include a division by N^2 to aid later simplification. The voltages and currents generated in two branches of the circuit (V_1 and I_1 for the back face, and V_2 and I_2 for the front face) are converted to forces by ideal electromechanical transformers such that $F_B = NV_1$, $v_B = I_1/N$, $F_F = NV_2$ and $v_F = I_2/N$. Calculating the voltages

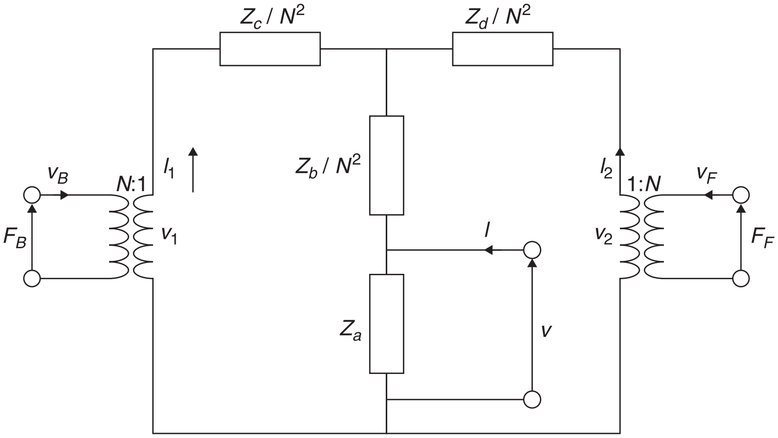

6.4 General form of Mason's equivalent circuit.

V_1, V_2 and V in terms of the currents I_1, I_2 and I for the circuit and then substituting the forces and face velocities using the above relations gives the following equations:

$$F_B = (N^2Z_a + Z_b + Z_c)v_B + (N^2Z_a + Z_b)v_F + NZ_aI \qquad [6.53]$$

$$F_F = (N^2Z_a + Z_b)v_B + (N^2Z_a + Z_b + Z_d)v_F + NZ_aI \qquad [6.54]$$

$$V = NZ_av_B + NZ_av_F + Z_aI. \qquad [6.55]$$

A comparison of Eqs 6.53–6.55 describing the equivalent circuit and Eqs 6.50–6.52 describing the piezoelectric plate indicates that they are identical if the values described below are used in the equivalent circuit.

From Eqs 6.52 and 6.55

$$Z_a = \frac{1}{i\omega C_0} \qquad [6.56]$$

$$N = hC_0. \qquad [6.57]$$

Comparing the v_B terms of Eqs 6.50 and 6.54 and substituting for Z_a gives

$$Z_b = \frac{Z_0}{i\sin kl} - N^2\frac{1}{i\omega C_0}. \qquad [6.58]$$

Similarly from the v_F term:

$$Z_d = iZ_0 \tan\frac{kl}{2}. \qquad [6.59]$$

Finally the v_B term of Eq. 6.52 compared with Eq. 6.50 gives

$$Z_c = iZ_0 \tan\frac{kl}{2}. \qquad [6.60]$$

Thus an equivalent circuit, as depicted in Fig. 6.4, with the parameter values given by Eqs 6.56–6.60, behaves in the same manner as the piezoelectric plate under consideration. The circuit can be further simplified by switching to a single ideal electromechanical transformer, and splitting the impedance Z_b into an inductance and a capacitance. The final Mason equivalent circuit is shown in Fig. 6.5, with the components marked with the appropriate values.

The process of deriving the equivalent circuit did not introduce any new assumptions or approximations beyond those used to develop the equations governing the piezoelectric plate, primarily that the electric and acoustic fields are uniform and perpendicular to the direction of polarisation and propagation, so the equivalent circuit should be interchangeable with the direct solution. The free or clamped behaviour of the plate can be obtained by setting the appropriate conditions on the acoustic ports, that is, $F_B = F_F = 0$ for free surfaces

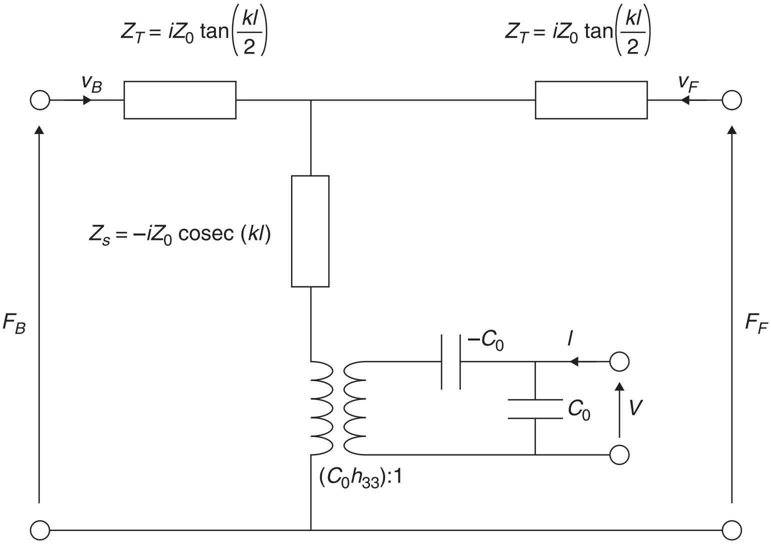
$Z_T = iZ_0 \tan\left(\frac{kl}{2}\right)$
$Z_T = iZ_0 \tan\left(\frac{kl}{2}\right)$
v_B
v_F
$Z_s = -iZ_0 \operatorname{cosec}(kl)$
F_B
F_F
$-C_0$
I
C_0
V
(C_0h_{33}):1

6.5 The final form of Mason's equivalent circuit for a piezoelectric plate.

and $v_B = v_F = 0$ for clamped surfaces, in the same manner as with the wave propagation equations.

An advantage of the equivalent circuit is that several such circuits, for both piezoelectric and passive materials, may be connected together to model complicated transducer configurations, such as stacks of plates or interdigital transducers, and network analysis may then be used to solve the systems (Sittig, 1967; Leedom *et al.*, 1971; Dion *et al.*, 1997; Bloomfield, 2002). Thus, rather than starting with a multilayer analysis and simplifying it for single layers as in Section 6.2, a single-layer solution is obtained and easily extended.

6.3.3 The KLM model

Krimholtz, Leedom and Matthaei proposed alternative equivalent circuits (Krimholtz *et al.*, 1970) with the aim of resolving three difficulties with the Mason equivalent circuit:

- the presence of a negative capacitance,
- the lack of a clear distinction between the electrical and acoustic parts of the system, and
- the complexity of circuits produced when multiple piezoelectric elements are combined.

Figure 6.6 shows the KLM equivalent circuit for a piezoceramic plate operating through its thickness. Note that the impedances of the two acoustic arms, Z_{TB} and Z_{TF},

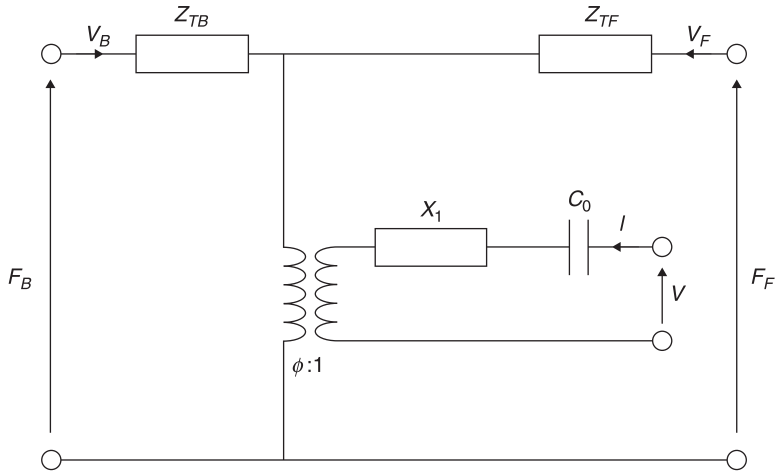

6.6 The KLM equivalent circuit.

are the impedances of lossless transmission lines of specific impedance Z_0 whose length is half the width of the plate, l, and which are terminated with impedances of Z_B and Z_F, respectively. Materials that do not exhibit piezoelectric properties, i.e. with $h = 0$, lead to a straightforward transmission line between the two acoustic ports.

The definitions for the transmission lines in this circuit are:

$$Z_{TB} = Z_0\left[\frac{Z_B\cos(kl/2) + iZ_0\sin(kl/2)}{Z_0\cos(kl/2) + iZ_B\sin(kl/2)}\right] \tag{6.61}$$

and

$$Z_{TF} = Z_0\left[\frac{Z_F\cos(kl/2) + iZ_0\sin(kl/2)}{Z_0\cos(kl/2) + iZ_F\sin(kl/2)}\right]. \tag{6.62}$$

The reactance,

$$X_1 = iZ_0\left(\frac{h_{33}}{Z_0}\right)^2\sin\left(\frac{kl}{2}\right) \tag{6.63}$$

and the transformer turns ratio, ϕ: 1, is defined by

$$\phi = \left(\frac{\omega Z_0}{2h_{33}}\right)\operatorname{cosec}\left(\frac{kl}{2}\right). \tag{6.64}$$

The parameters C_0 and Z_0 are the same as in the Mason circuit described in Section 6.3.2.

As with the Mason equivalent circuit, the behaviour of the KLM circuit exactly matches that predicted by the piezoelectric equations and the equation of motion for the 1D system, Eqs 6.1 and 6.3, and so the Mason and KLM equivalent circuits are also equivalent to each other (Sherrit *et al.*, 1999). In a further extension, Krimholtz, Leedom and Matthaei extended their analysis to allow transducers consisting of multiple layers to be reduced to a single equivalent circuit, provided that the variation of the electrical excitation was spatially either odd or even (Leedom *et al.*, 1971). This allows simplified models of stacked plate transducers and, using similar solutions for side-electroded piezoelectrics, interdigital electrodes.

6.4 The linear systems model

6.4.1 Brief background

The third approach to 1D modelling of the piezoelectric transducer outlined here is the linear systems model. If the model based upon the wave equation can be described as being based in physics, and the Mason equivalent circuit model in electrical network theory, the linear systems model has its basis in engineering systems theory, particularly as found within the broad remit of electronic engineering.

Defined by Hayward and co-workers in several papers (e.g. Hayward *et al.*, 1984), the linear systems model makes explicit the fact that the definitions of the piezoelectric device assume linearity. Furthermore, it comes closest to defining clearly and explicitly the presence of feedback in the piezoelectric transducer, through secondary piezoelectric action, and is thus a helpful aid to understanding the fundamental behaviour of such transducers. As such, it may be characterised as another representation of the same fundamental theory as the models described previously, with a particularly close relation with the transfer-matrix formalism (Sittig, 1967; Bloomfield, 2002). In addition, it has been usefully extended to include operations in both bar mode (Hayward *et al.*, 1990) and plank mode (Hayward and Gillies, 1989). Finally, its extension to multilayer structures is straightforward (Hayward and Jackson, 1986).

On the other hand, described elsewhere in its lattice form as ‘an elaborate model’ (Dion *et al.*, 1997), it has not attained the same popularity or widespread use as Mason’s model, the KLM model or their derivatives. As it has undoubted technical merits, this can be attributed to the lack of resonance between systems theory and practitioners in piezoelectric devices.

6.4.2 The model

The key components of the linear systems model are the use of the Laplace transform (Kreysig, 2005, pp. 220–70), with related expressions for impulse delays, and differentiation and integration with respect to time:

$$\delta(t-\tau) \rightarrow e^{-\tau s} \qquad [6.65a]$$

$$\frac{df(t)}{dt} \rightarrow sF(s) - f(0) \qquad [6.65b]$$

$$\int_0^t f(\tau)d\tau \rightarrow \frac{F(s)}{s}. \qquad [6.65c]$$

As with the other models, forces exerted by and on the two faces of the device are key parameters, as are the reflection coefficients at these faces, R_B^1 and R_1^F, utilising the terminology from Section 6.2, Eq. 6.33. The linear systems model can then be expressed as shown in Fig. 6.7 (Hayward and Jackson, 1986), with symbols drawn from this text, Section 6.2. As noted previously, the underlying mathematics is the same as for the wave equation solution and for the electrical circuit models. However, the linear systems model uniquely provides a route to increased fundamental understanding of the behaviour of the transducer. This can be described in terms of the performance for transmission and reception, with the knowledge that the transducer can act simultaneously as a transmitter and receiver provided the external electrical circuitry is arranged appropriately.

As with all the models discussed previously, the linear systems model has three ports. However, in common with the wave equation solution only, there is an explicit separation of inputs and outputs from each port, in terms of voltage, V_E and V, respectively; in terms of the front face of the piezoelectric layer, F_{F2} and F_{B2}, respectively; and in terms of the back face of the piezoelectric layer, F_{B0} and F_{F0}, respectively. Of these, the most important in a device with a single piezoelectric layer and a conventional lossy backing are: V_E, the voltage input for transmission; V, the voltage output, i.e. the net voltage on reception; F_{F2}, the front-face output on transmission; and F_{B2}, the front-face input for reception.

On transmission, V_E is the non-zero electrical input, transformed into the Laplace domain shown in Fig. 6.7 as $\overline{V}_E$, as are all time-dependent parameters. Via the upward branch from the V_E node, it contributes directly to the voltage observed across the transducer, V. Via the downward branch, it generates charge, which again contributes to the observed voltage, V, through its effect on the external equivalent electrical impedance Z_E, and this charge also generates force through the effect of the piezoelectric stiffness constant, h_{33}. These forces are transformed through factors of the relevant transmission coefficients, expressed in Fig. 6.7 in terms of reflection coefficients for simplicity. They then contribute directly to the force outputs from the front and back faces of the piezoelectric layer, F_{F2} and F_{B0}, respectively. They also contribute indirectly to further charge generation, occurring physically through secondary piezoelectric action, and thus to the voltage across the transducer, via positive feedback loops relating to action at the front and back of the piezoelectric layer.

On reception, F_{B2} is the non-zero front-face force input. This contributes directly, via the appropriate reflection coefficient, to F_{F2}, the front-face output, and the useful remainder is transmitted into the piezoelectric element. The lattice

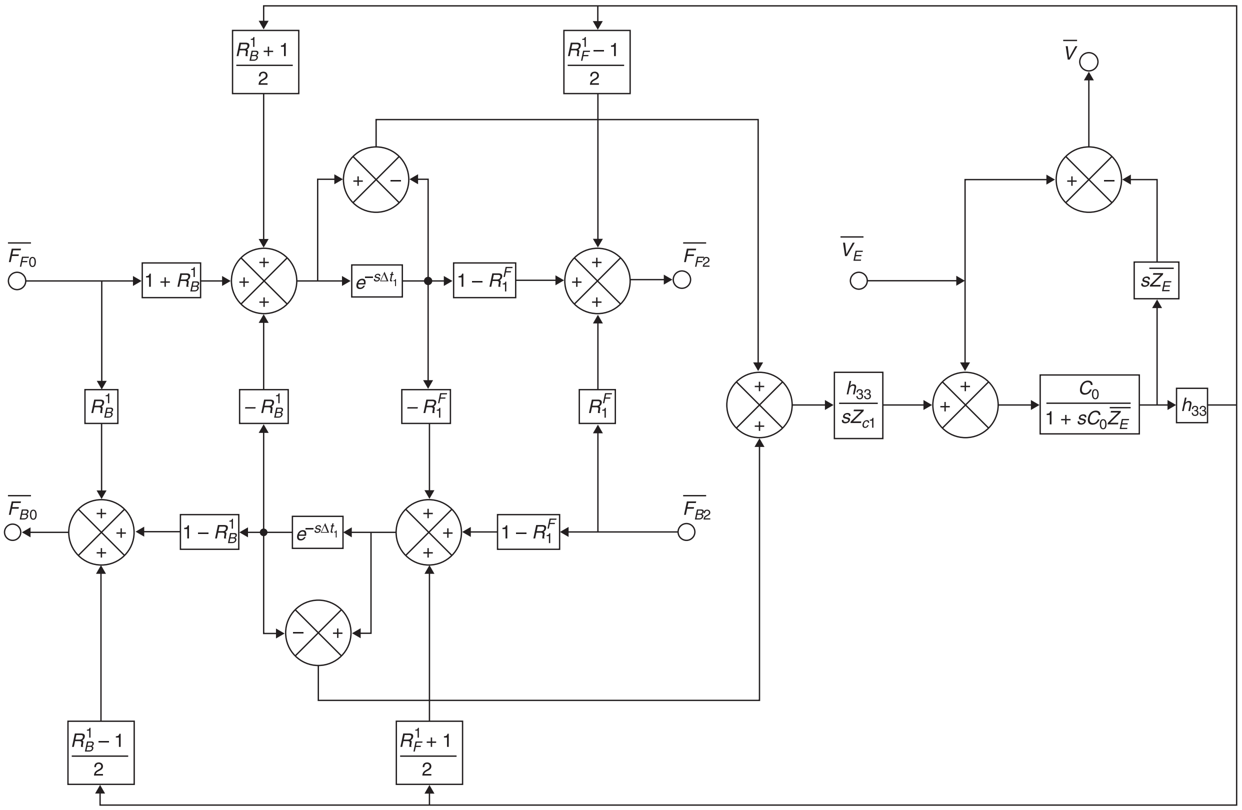
$\overline{F_{F0}}$
$1 + R_B^1$
$\frac{R_B^1 + 1}{2}$
$e^{-s\Delta t_1}$
$1 - R_1^F$
$\frac{R_F^1 - 1}{2}$
$\overline{F_{F2}}$
R_B^1
$-R_B^1$
$-R_1^F$
R_1^F
$\overline{F_{B0}}$
$1 - R_B^1$
$e^{-s\Delta t_1}$
$1 - R_1^F$
$\overline{F_{B2}}$
$\frac{R_B^1 - 1}{2}$
$\frac{R_F^1 + 1}{2}$
$\frac{h_{33}}{sZ_{c1}}$
$\overline{V_E}$
$\frac{C_0}{1 + sC_0\overline{Z_E}}$
h_{33}
$s\overline{Z_E}$
$\overline{V}$
+
−

6.7 Linear systems model of a piezoelectric plate (adapted from Hayward and Jackson, 1986).

structure of the model then indicates that this reverberates between the front and rear faces, suffering loss upon reflection from each face and thus decaying away. During this process, electrical charge is generated according to the differential displacement between the front and rear faces, represented in the model by the two feed-forward loops. This then generates a voltage output, $\overline{V}$, after modification related to the static capacitance of the device, C_0, and the external electrical impedance, $\overline{Z}_E$, and conversion from current, again relating to $\overline{Z}_E$. As before, the charge that is generated in turn generates forces that are fed back into the mechanical activity of the transducer as secondary piezoelectric action.

This illustrates the capability of the unidimensional linear systems modelling approach in aiding understanding of the behaviour of piezoelectric ultrasonic transducers. It is also possible to assess the effect of changes in key piezoelectric properties through this understanding, with specific reference to the structure of the model (Hayward and Jackson, 1986).

6.5 Examples

In an era of relatively accessible FEM, 1D modelling still has the capacity to fulfil useful roles: if FEM code cannot be afforded; as a way to evaluate multiple designs rapidly; and as the only design tool needed for routine design of simple piezoelectric ultrasonic transducers. Here, its capabilities and limitations are illustrated through a staged series of models. The results are presented mainly via electrical impedance spectroscopy, with some additional data representing pressure as functions of time and the related amplitude spectra. The geometries and other details relate to the outline transducer specifications presented in Section 1.4.1.

6.5.1 Piezoceramic and piezocomposite plate configurations

The first data reported here relate to a piezoelectric plate of the ‘soft’ ceramic PZT-5H, with the properties given in Table 6.1. The plate, and related 1–3 connectivity composites, have dimensions of $30\lambda \times 30\lambda$, that is, 9×9 mm, taking $\lambda = 0.3$ mm, corresponding to an operating frequency, $f = 5$ MHz and a propagation speed of $1500\,\text{m.s}^{-1}$, close to the value for water and biological soft tissue.

Figure 6.8 shows the electrical impedance of the plate calculated using a 1D model and the PZFlex FEM code (Weidlinger Associates, Inc., CA, USA), both with the plate air-loaded on both major surfaces. The 1D model is based on the solutions to the wave equation for the thickness-mode plate described in Section 6.2. There is obviously an excellent fit overall between the two models and also at the thickness-mode fundamental and third harmonic resonances. Discrepancies, evident as multiple harmonic resonances below 5 MHz in the FEM output and corresponding smaller features around the fundamental thickness-mode frequency, are caused by laterally propagating modes, which are explicitly

Table 6.1 Properties of selected piezoelectric materials

Type of material			PZT-4	PZT-5H	$PbNbO_3$	PVDF	$LiNbO_3$	AlN	PMN-PT
			'Hard' ceramic	'Soft' ceramic	High-temperature ceramic	Polymer	Traditional single crystal	Crystalline thin film	New, high-performance single crystal
Thickness-mode coupling coefficient	k_t		0.47	0.52	0.33	0.19	0.16	0.24	0.57
Length-extensional coupling coefficient	k_{33}		0.69	0.75	0.33	0.13	0.16	0.31	0.90
Piezoelectric strain constant	d_{33}	$pm.V^{-1}$	290	590	85	25	5.9	5.5	1400
Piezoelectric voltage constant	g_{33}	$mV.m.N^{-1}$	26	20	32	230	22	52	30
Piezoelectric figure of merit	$FOM = d_{33}.g_{33}$	$pm.N^{-1}$	7.5	12	2.7	5.8	0.13	0.29	43
Stiffness	c_{33}^D	$GN.m^{-2}$	150	160	68	8.5	250	420	140
Density	ρ	$kg.m^{-3}$	7700	7500	6200	1800	4600	3300	8000
Longitudinal speed	v	$m.s^{-1}$	4600	4600	3100	2200	7400	11400	4040
Acoustic impedance	$Z = \rho V$	Mrayl	35	34	19	3.9	34	37	32
Electrical loss tangent	$\tan \delta$		0.004	0.02	0.01	0.3	0.001	0.0005	0.01
Mechanical quality factor	Q_m		High	Medium	Low	Low	Very high	Very high	Low
Relative permittivity at constant stress	ε_{33}^T		1 270	3 430	300	8.4	29.8	12.0	3 950
Relative permittivity at constant strain	ε_{33}^S		640	1 470	270	10–12	29	10.7	818
Curie temperature (*Usable temperature / **Phase transition temperature)	T_c	°C	Medium/ high (~350 °C)	Medium (~200 °C)	High (~400 °C)	Low (~150 °C)	Very high (~1200 °C)	Very high (~1150 °C*)	Low (~90 °C**)
Usual physical form			Bulk ceramic	Bulk ceramic	Bulk ceramic	Thin film	Bulk crystal	Thin crystal film	Bulk crystal

Note: Data in this table are drawn from various academic and commercial sources. All data are approximate and for guidance only.

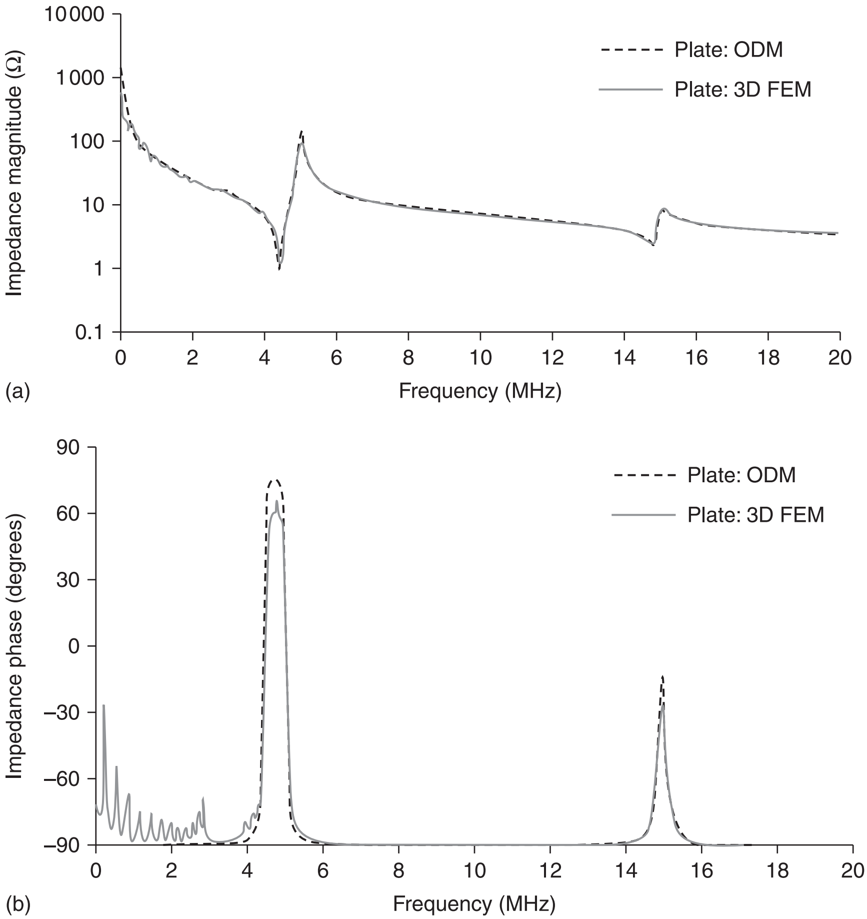

6.8 (a) Electrical impedance magnitude of a piezoceramic plate calculated with a 1D model and with FEM. (b) Electrical impedance phase for the plate.

absent from the 1D model. There is also evidence of a minor difference in attenuation, particularly in the smaller phase excursions predicted by FEM.

Figure 6.9 shows the front-face pressure output in the time and frequency domains. The time-domain waveform of the 1D model output corresponds very well with experimental data established in the literature (for example, Hayward and Jackson, 1986), with a decaying characteristic and evidence of high harmonics in the sharp peaks. The correspondence with FEM data is again generally excellent overall, though the effects of the band limit in the specific FEM model are evident in both the time and frequency domains. As before, lateral mode effects are

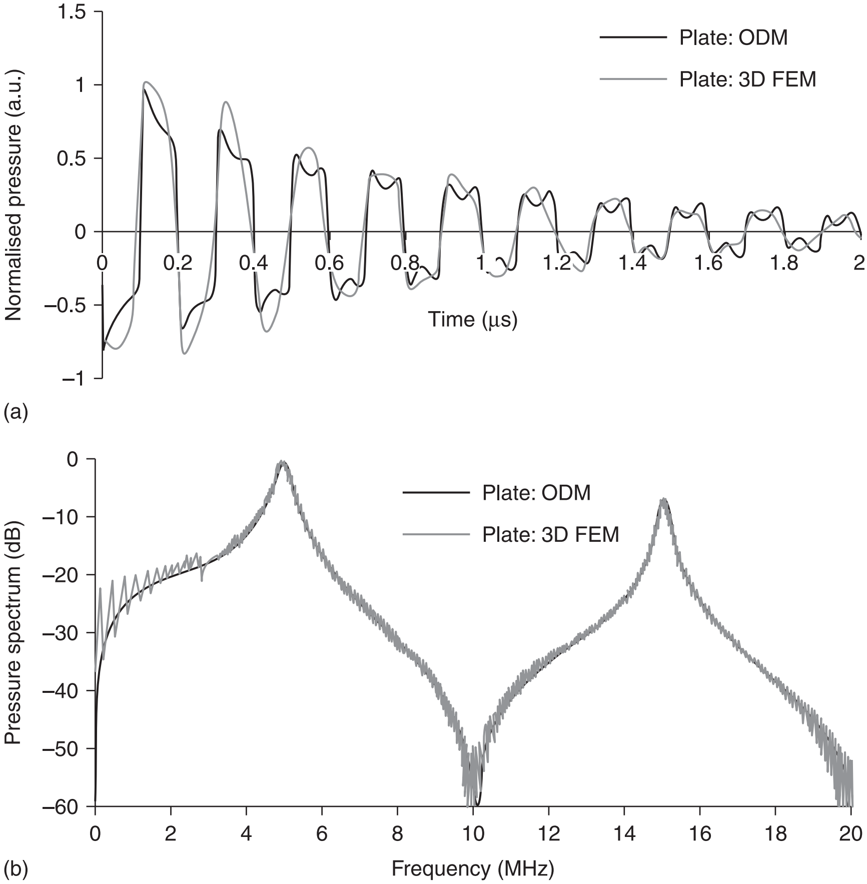

6.9 (a) Time-domain representation of the pressure output from the front face of a piezoceramic plate calculated with a 1D model and with FEM. (b) Frequency-domain representation of the pressure.

evident in the FEM data, particularly in the frequency domain, as is the small discrepancy in attenuation, in this case particularly in the time domain.

Although the 1D model cannot explicitly take into account the microstructure of piezocomposite materials (Section 1.3.4), the homogenisation model of Smith and Auld (1991) allows highly effective modelling through the use of equivalent material properties. Figures 6.10 and 6.11 compare the performance of the piezoceramic plate with composites with 30% and 70% piezoceramic volume fractions. The higher thickness-mode coupling coefficients of the composites are evident in the larger frequency separation between the minima and maxima in the electrical impedance magnitudes and the broader positive phase excursion in Fig. 6.10. Both composites have lower permittivity, leading to higher electrical

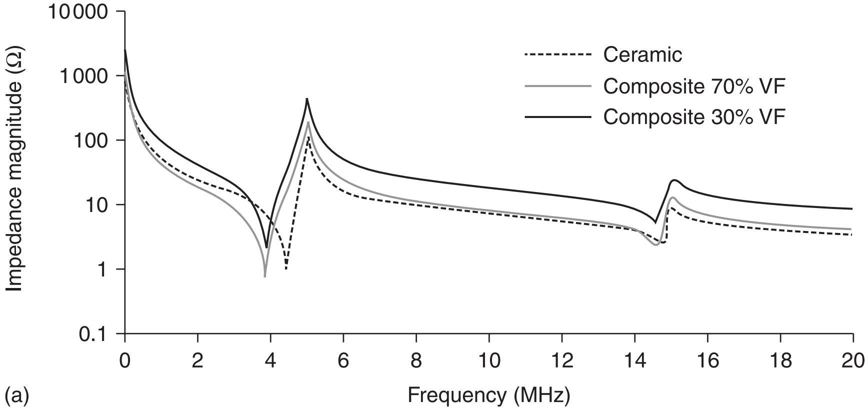

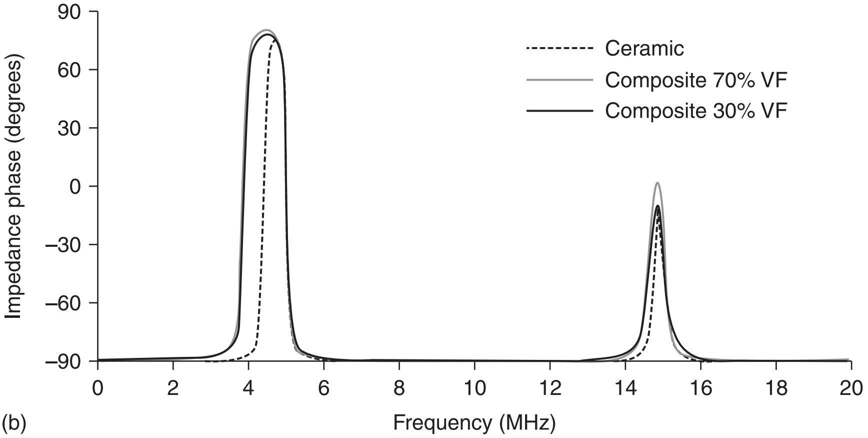

6.10 (a) Electrical impedance magnitudes calculated with a 1D model, comparing the piezoceramic plate of Fig. 6.9 with two piezocomposites with different volume fractions (VF). (b) Comparative electrical impedance phase characteristics.

impedance magnitudes, the 30% volume fraction clearly having a larger difference from the piezoceramic.

Functionally, a composite material should have higher attenuation than a ceramic. Often, this is evident as reduced variation in the electrical impedance characteristics but here the increased coupling coefficient compensates. However, the increased attenuation is clear in the front-face pressure outputs shown in Fig. 6.11, with more rapid decay in the time domain and broader bandwidth in the frequency domain, particularly for the 30% volume fraction. Although the 1D model predicts the output amplitude, this is not shown because of the normalisation used in Fig. 6.11 to make other effects clear.

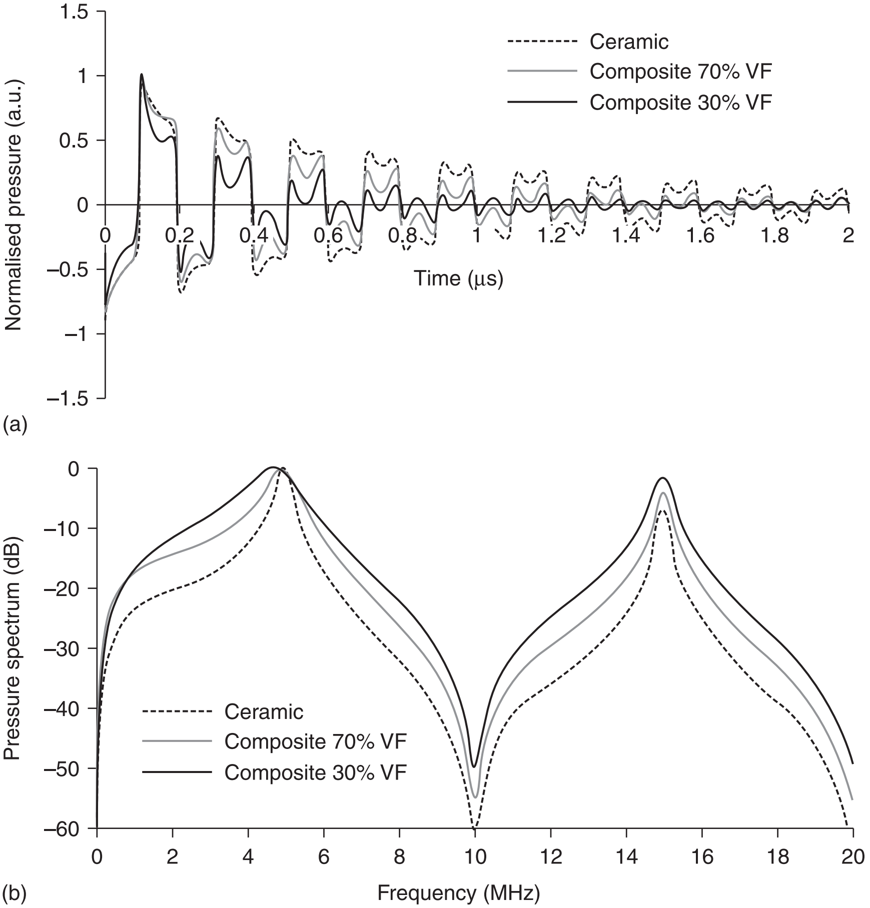

6.11 (a) Time-domain representation of the pressure output from the front face of the piezoceramic and piezocomposite plates calculated with a 1D model. (b) Frequency-domain representation of the pressure.

The 1D model can also predict the effects of other components within an overall transducer structure. Figures 6.12 and 6.13 show the plates detailed in Fig. 6.10 and Fig. 6.11 with the addition of mechanical damping materials and matching layers (Section 1.4.1). The data shown are for the front face of the transducer in air. The acoustic impedances of the mechanical damping materials are $Z = 17.5$ MRayl for the piezoceramic plate and composite with 70% volume fraction, and $Z = 7.5$ MRayl for the other composite. These are represented as mechanical loads on the back of the piezoelectric layers. The matching layer for the piezoceramic has an acoustic impedance $Z = 6.9$ MRayl and for the composites $Z = 3.7$ MRayl. The matching layers are represented as passive layers within the model.

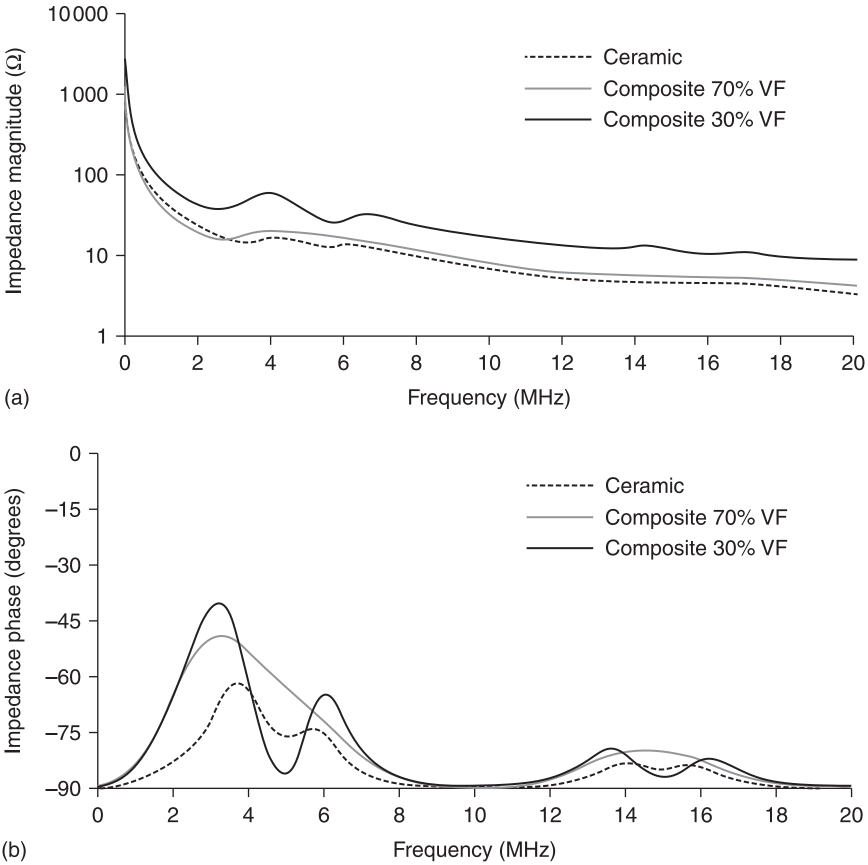

6.12 (a) Electrical impedance magnitudes calculated with a 1D model, comparing the piezoceramic plate of Fig. 6.9 with two piezocomposites with different volume fractions, when mechanical damping and a matching layer are added. (b) Comparative electrical impedance phase characteristics.

The two features close to the fundamental resonant frequencies in the electrical impedance of Fig. 6.12 are a result of the mismatch between the transducer and air; these would merge into a single feature if a water load was included in the model, effectively leading to an almost purely capacitive characteristic. The functional characteristics illustrated by the pressure output from the front face in Fig. 6.13(b) show the expected very much increased bandwidth for all three configurations, and much more rapid attenuation is evident in Fig. 6.13(a) than in Fig. 6.9(a) and Fig. 6.11(a). The short time delay before output in Fig. 6.13(a) is caused by the need for the pressure output of each piezoelectric plate to propagate through the matching layer before generating an output at the front face; the time scale is referenced to the front face of the piezoelectric plate.

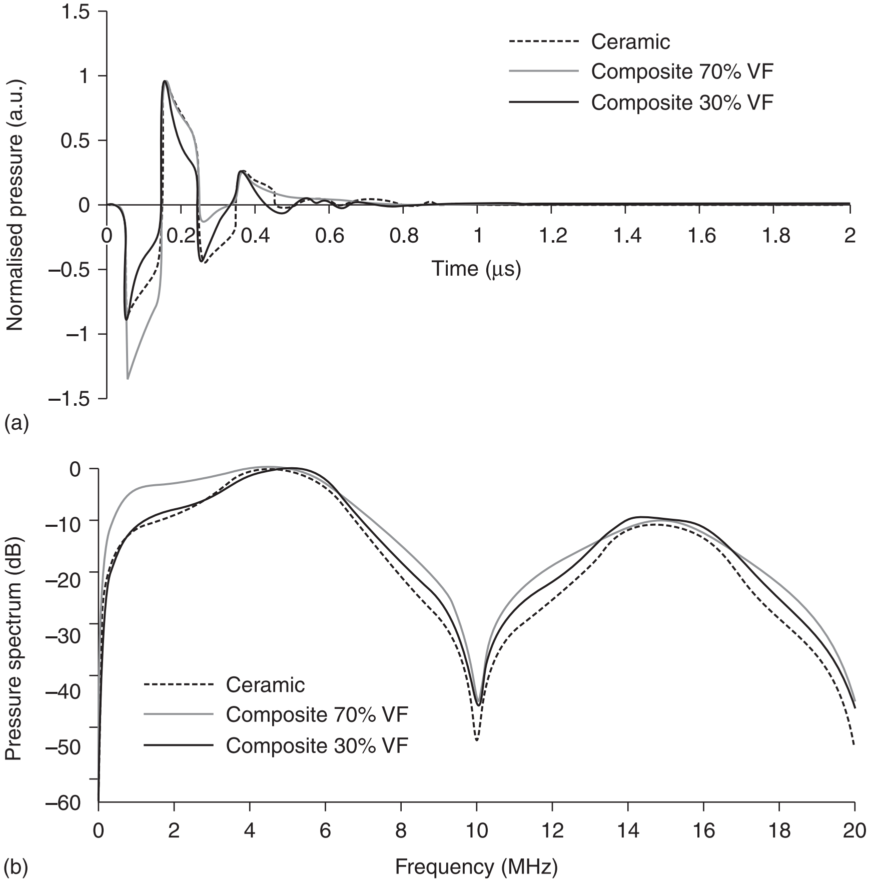

6.13 (a) Time-domain representation of the pressure output from the front face of the piezoceramic and piezocomposite plates calculated with a 1D model, when mechanical damping and a matching layer are added. (b) Frequency-domain representation of the pressure.

6.5.2 Other geometrical configurations

Berlincourt *et al.* (1964) note that an advantage of equivalent circuit modelling is that it can take advantage of both the existing body of work in electrical network theory and also circuits that have been developed for transducer geometries other than simple thickness-mode plates. It is also possible to achieve the same outcomes with other modelling techniques. For example, the linear systems approach has been extended in full to ‘tall, thin parallelepiped[s]’ (Hayward and Gillies, 1989), here referred to as planks, and, through the use of equivalent parameters, to bars (Hayward *et al.*, 1990). Planks are of particular interest in 1D imaging arrays, and bars in applications such as 2D arrays.

Figure 6.14 shows the outcome of modelling to calculate the electrical impedance of the piezoceramic plate modelled in Section 6.5.1, for reference, and the plank and bar defined in Section 1.4.1, the former having dimensions $30\lambda \times 0.7\lambda$ and the latter $0.7\lambda \times 0.7\lambda$. The external media are assumed to be air and there are no components other than the piezoelectric material.

The results of simple 1D modelling using the thickness-mode model are shown in Fig. 6.14. This approach correctly predicts a significant increase in electrical impedance because of the smaller areas of the plank and bar. However, the frequencies of the fundamental resonances and the third harmonics do not change. This is incorrect as, for non-plate configurations, the propagation velocity in the thickness direction is slower than for plates. Furthermore, there are no additional modes, as would be expected because of the 0.7λ lateral extent in either one (plank) or two (bar) dimensions.

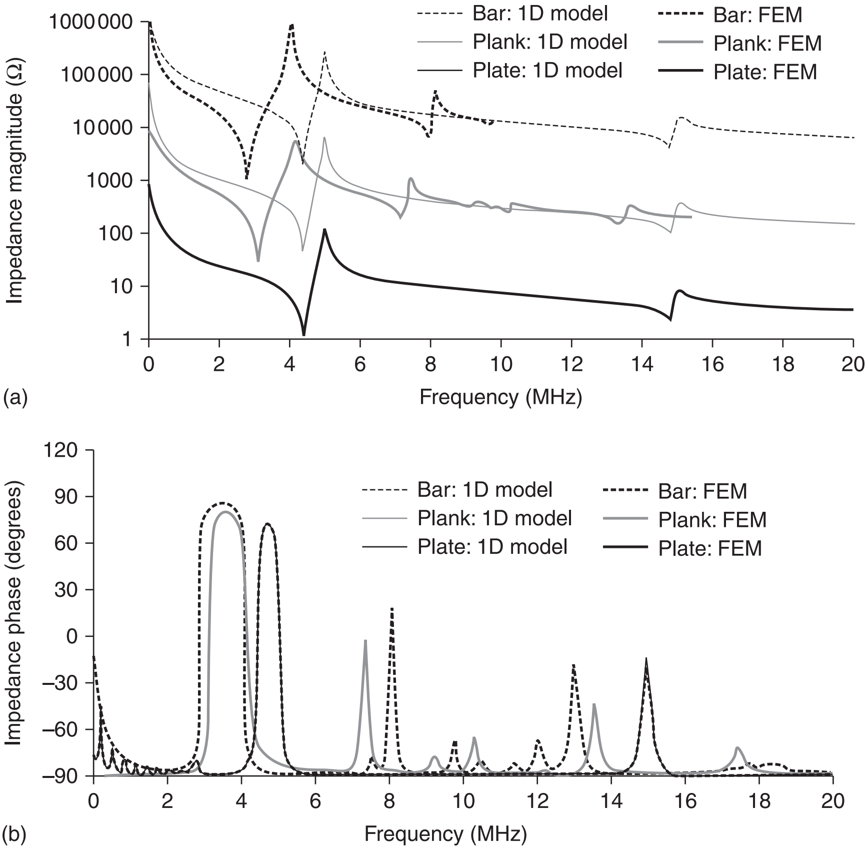

6.14 (a) Electrical impedance magnitudes comparing a piezoceramic plate, plank and bar, calculated with a 1D model and FEM. (b) Comparative electrical impedance phase characteristics.

The results of FEM are also shown in Fig. 6.14. Both the plank and the bar have been modelled using full 3D FEM models. The FEM results for the plate correspond exactly with the 1D model. The FEM results for both the plank and the bar show large downward shifts in the frequency of the fundamental thickness mode, and additional modes between the fundamental thickness mode and the third harmonic, caused by lateral propagation. These are absent from the 1D model, though they would be present in an adapted model (Hayward and Gillies, 1989). However, the 1D model has predicted the gross electrical impedance magnitude increases correctly.

The behaviour of the bar is illustrated in more detail in Fig. 6.15 and Fig. 6.16. The data from the bar in Fig. 6.14 are reproduced in Fig. 6.15, with the addition of the output of a 1D model based on equivalent material parameters. The excellent overall correspondence with the FEM data in magnitude and phase, except for the

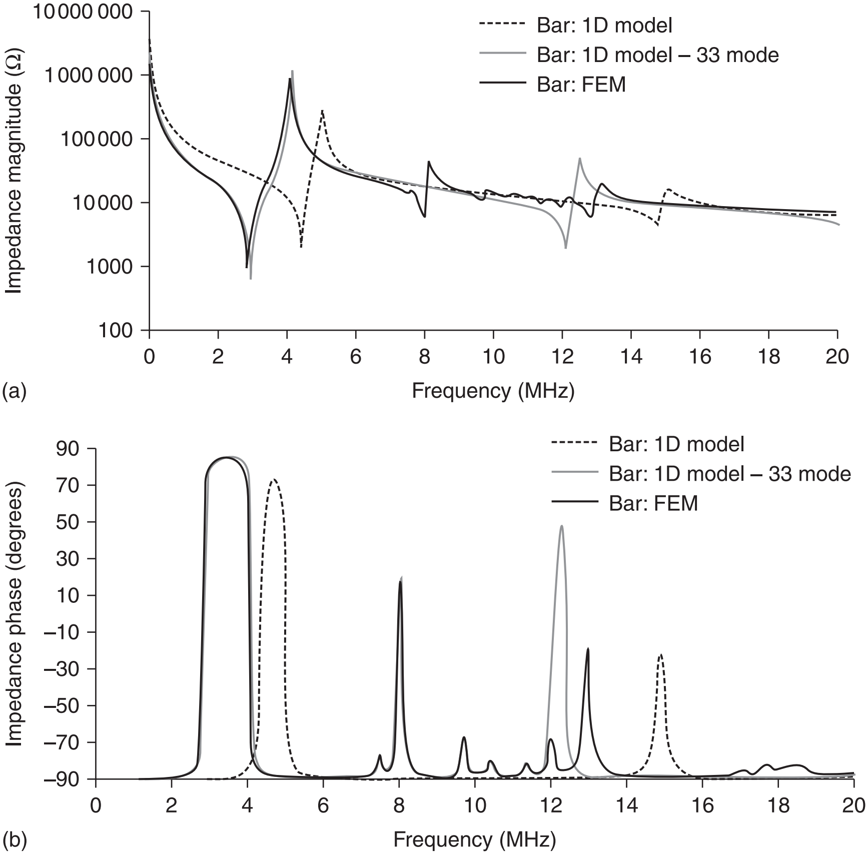

6.15 (a) Electrical impedance magnitudes of a piezoceramic bar, calculated with a 1D model in thickness and bar modes and FEM. (b) Comparative electrical impedance phase characteristics.

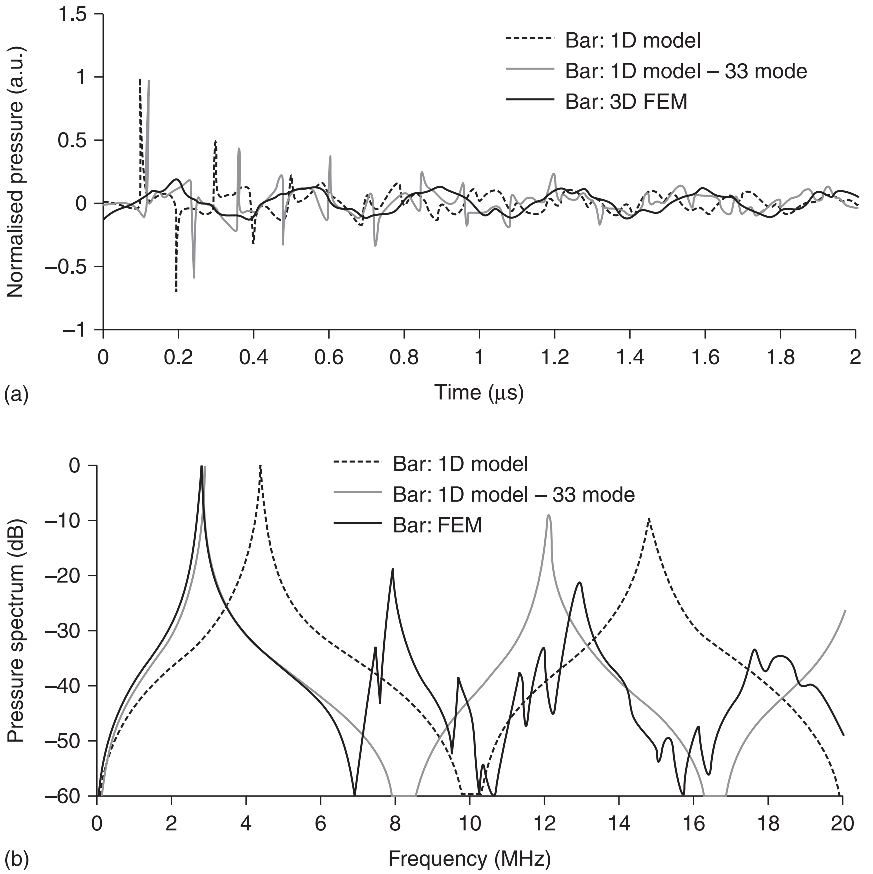

6.16 (a) Time-domain representation of the pressure output from the front face of a piezoceramic bar calculated with a 1D model in thickness and bar modes and with FEM. (b) Frequency-domain representation of the pressure.

additional high-frequency modes noted previously, offers additional evidence of the continuing utility of 1D modelling for convenience or if FEM is unavailable. The frequency domain representation of the pressure output from the front face in Fig. 6.16(b) shows large discrepancies between FEM and the simple 1D model based on plate properties at all frequencies. When the modified material properties are used, there is good correspondence around the fundamental resonance frequency, now shifted down significantly from 5 MHz, but the greater complexity of behaviour predicted by 3D FEM again results in discrepancies at higher frequencies. The characteristics of Fig. 6.16(a) show corresponding discrepancies, demonstrating that 1D modelling should be used only for bandlimited predictions, even with modified material properties.

6.6 Summary, future trends and sources of further information

6.6.1 Summary

The operation of piezoelectric ultrasonic transducers is sufficiently complex that computer-based models are now essential to realise designs with performance matched to users' expectations. Many such transducers operate in a way in which one ultrasonic mode is dominant, offering the possibility for significant simplification of the model. 1D modelling is thus now very well established.

All the 1D models are based ultimately on the same fundamental physics and mathematics, but there are three distinct approaches. The approach most closely associated with the underlying physics is a direct solution of the wave equation (Powell *et al.*, 1998). This can be derived from the basis of the constitutive equations and other fundamental results from electrical and mechanical theory. It is highly amenable to solutions with modern mathematical analysis software. The most common approach is based on the utilisation of techniques developed in electrical network theory (Mason, 1948). Reported further by Berlincourt *et al.* (1964) and with numerous further refinements, most notably by Krimholtz *et al.* (1970) in the KLM model, this offers solutions to several 1D configurations. However, the relation between the model and intuitive understanding is limited, though Redwood (1961, 1964) offers some useful discussion. The linear systems modelling approach reported by Hayward *et al.* (1984) is better in this respect, allowing fundamental behaviour such as secondary piezoelectric action to be considered. Realisation of the linear systems model relates most closely to transfer-matrix formulations (Sittig, 1967), which in turn relate to Mason's model.

In practice, excellent agreement can be obtained between the outcomes of 1D modelling and FEM, with 1D modelling generally more accessible, either through coding by an individual or group or through a relatively inexpensive commercial package. Furthermore, 1D models inevitably run more quickly than FEM, making them more appropriate for searching large parameter spaces, for example for transducer optimisation (Abrar and Cochran, 2007). Their flexibility can also be increased through additional analysis to extend them to piezocomposite materials and to modes other than the thickness mode dominant in a piezoelectric plate. Used with care, they can also achieve excellent results, directly comparable with FEM, in these situations.

6.6.2 Future trends

1D modelling is now a mature topic, offering researchers and practitioners in different communities a variety of approaches. It has been implemented in numerous places around the world and is likely to continue to provide an excellent grounding for those new to piezoelectric ultrasonic-transducer design for the foreseeable future.

If there are areas for further development, these are likely to relate to three situations. First, the fact that 1D modelling requires only a limited subset of material properties (Sherrit and Mukherjee, 2007) is very useful in situations in which designs must be executed with new materials and in situations in which externalities, such as temperature or pressure, limit the availability of full material properties (for example, Qiu *et al.*, 2011). Given its ability to model many practical transducer configurations, this is likely to keep it in use and to promote the continuing development of refinements and improvements. Second, losses associated with materials are subject to many different modelling approaches. However, it is relatively straightforward to develop code to utilise complex material parameters in 1D models (Whitworth, 2001), offering the most direct relation between material properties and modelling. Nevertheless, care must be taken as losses are highly dependent on frequency. Third, there are likely to be some situations in which transducer optimisation or the exploration of very large parameter spaces with 1D models is beneficial. Contemporary biomedical imaging arrays are very highly optimised (Gururaja and Panda, 1998) and 1D modelling is not appropriate in this situation, as it cannot take into account all of the many interacting geometrical effects. However, if a new transducer is to be developed from a basic specification then 1D modelling allows rapid examination of many different options. Furthermore, if additional parameters are introduced into transducer designs, such as in piezoelectric multilayer structures (Powell *et al.*, 1998; Abrar and Cochran, 2007) then the computational efficiency of 1D modelling is very helpful.

6.6.3 Sources of further information

The references supplied below provide many avenues into the literature on 1D piezoelectric ultrasonic-transducer modelling.

Whilst Mason's book (1948) may be seen as a key reference, the technical content provided by Berlincourt *et al.* (1964) is shorter and more accessible, providing more direct information on equivalent circuit models for different ultrasound propagation modes if Mason's model is to be used. Similarly, although Krimholtz *et al.* (1970) present the essential information on the KLM model, other sources such as Leedom *et al.* (1971) and much later publications such as that of Sherrit *et al.* (1999) may be more accessible. The same applies to the linear systems model, with the work by Hayward and Jackson (1986) presenting a full model and further analysis than that reported by Hayward *et al.* (1984). Outside the research literature, many books provide different presentations of 1D models, from the somewhat brief, such as Cheeke (2002, pp. 219–20), to the highly detailed and explanatory, such as Ristic (1983, pp. 117–63).

In summary, the interested reader will find a relatively small literature on 1D modelling, with clear distinctions between those contributions providing overarching guidance (for example, Berlincourt *et al.*, 1964), those clarifying this guidance (for example, Ristic, 1983), and those reporting new avenues, either of broad interest (for example, Hayward *et al.*, 1984) or of interest to the specialist, and those offering corrections to the existing literature (for example, Whitworth, 2001).

6.7 References

Abrar A and Cochran S (2007) Mathematical optimization of multilayer piezoelectric devices with nonuniform layers by simulated annealing, *IEEE Trans. Ultrason. Ferroelec. Freq. Contr.* 54 (10) 1920–9.

Berlincourt D A, Curran D R and Jaffe H (1964) Piezoelectric and piezomagnetic materials and their function in transducers, in Mason W P, *Physical Acoustics Vol. I Part A*, New York, Academic Press.

Bloomfield P E (2002) Multilayer transducer transfer matrix formalism, *IEEE Trans. Ultrason. Ferroelec. Freq. Contr.* 49 (9) 1300–11.

Cheeke J D N (2002) *Fundamentals and Applications of Ultrasonic Waves*, CRC Press ISBN 0-8493-0130-0.

Cobbold R S C (2007) *Foundations of Biomedical Ultrasound*, Oxford University Press ISBN 0-19-516831-3.

Dion J-L, Cornieles E, Galindo F and Agbossou K (1997) Exact one-dimensional computation of ultrasonic transducers with several piezoelectric elements and passive layers using the transmission line analogy, *IEEE Trans. Ultrason. Ferroelec. Freq. Contr.* 44 (5) 112031.

Gururaja T R and Panda K R (1998) Current status and future trends in ultrasonic transducers for medical imaging applications, in *Proc. IEEE Ultrason. Symp.* 223–8.

Hayward G (1984) A systems feedback representation of piezoelectric transducer operational impedance, *Ultrasonics* 22 (July) 153–62.

Hayward G and Gillies D (1989) Block diagram modeling of tall, thin parallelepiped piezoelectric structures, *J. Acoust. Soc. Am.* 86 (5) 1643–53.

Hayward G and Jackson M N (1986) A lattice model of the thickness-mode piezoelectric transducer, *IEEE Trans. Ultrason. Ferroelec. Freq. Contr.* 33 (1) 41–50.

Hayward G, MacLeod C J and Durrani T S (1984) A systems model of the thickness-mode piezoelectric transducer, *J. Acoust. Soc. Am.* 76 (2) 369–82.

Hayward G, Trench S and Gillies D (1990) Uni-dimensional modelling of piezoelectric cylindrical bar elements using modified material parameters, *Ultrasonics* 28 (1) 54–6.

Krautkramer J and Krautkramer H (1990) *Ultrasonic Testing of Materials*, Springer-Verlag, New York, USA, ISBN 9783540512318.

Kreysig E (2005) *Advanced Engineering Mathematics*, 9th ed., John Wiley and Sons, ISBN 978-0471728979.

Krimholtz R, Leedom D A and Matthaei G L (1970) New equivalent circuits for elementary piezoelectric transducers, *Electronic Letters* 6 (13) 398–9.

Leedom D, Krimholtz R and Matthaei G L (1971) Equivalent circuits for transducers having arbitrary even- or odd-symmetry piezoelectric excitation, *IEEE Trans. Son. Ultrason.* SU18 (3) 128–41.

Mason W P (1948) *Electromechanical Transducers and Wave Filters*, 2nd ed., New York, D Van Nostrand Company.

Meeker T R (1972) Thickness mode piezoelectric transducers, *Ultrasonics* 10 (1) 26–36.

Powell D J, Hayward G and Ting R Y (1998) Unidimensional modeling of multi-layered piezoelectric transducer structures, *IEEE Trans. Ultrason. Ferroelec. Freq. Contr.* 45 (3) 667–77.

Qiu Z, Sadiq M R, Démoré C E M, Parker M F, Marin P, Mayne K and Cochran S (2011) Characterisation of piezocrystals for practical configurations with temperature- and pressure-dependent electrical impedance spectroscopy, *IEEE Trans. Ultrason. Ferroelec. Freq. Contr.* 58 (9) 1793–803.

Redwood M (1961) Transient performance of a piezoelectric transducer, *J. Acoust. Soc. Am.* 33 (4) 527–36.

Redwood M (1964) Experiments with the electrical analog of a piezoelectric transducer, *J. Acoust. Soc. Am.* 36 (10) 1872–80.

Rhyne T L (1978) An improved interpretation of Mason's model for piezoelectric plate transducers, *IEEE Trans. Son. Ultrason.* SU25 (2) 98–103.

Ristic V M (1983) *Principles of Acoustic Devices*, Wiley Interscience ISBN 0-471-09153-7.

Sherrit S and Mukherjee B K (2007) Characterization of piezoelectric materials for transducers, arXiv:0711.2657v1 [cond-mat.mtrl-sci].

Sherrit S, Leary S P, Dolgin B P and Bar-Cohen Y (1999) Comparison of the Mason and KLM equivalent circuits for piezoelectric resonators in the thickness mode, in *Proc. IEEE Ultrason. Symp.* 921–6.

Sittig E K (1967) Transmission parameters of thickness-driven piezoelectric transducers arranged in multilayer configurations, *IEEE Trans. Son. Ultrason.* SU-14 167–74.

Smith W A and Auld B A (1991) Modeling 1–3 composite piezoelectrics: thickness-mode oscillations, *IEEE Trans. Ultrason. Ferroelect. Freq. Contr.* 39 (1) 40–7.

Stansfield D (1991) *Underwater Electroacoustic Transducers*, Peninsula Publishing, California, USA, ISBN 0932146724.

Whitworth G (2001) Discussion of one-D piezoelectric transducer models with loss, *IEEE Trans. Ultrason. Ferroelec. Freq. Contr.* 48 (4) 844–6.

7

The boundary-element method applied to micro-acoustic devices: zooming into the near field

A. BAGHAI-WADJI, RMIT University, Australia

Abstract: The effects of the near fields in micro-acoustic devices are pervasive and ubiquitous – they need to be understood profoundly, accounted for systematically and modelled accurately. This chapter summarizes the state-of-the-art methodologies for describing near-field phenomena by considering the simplest possible acoustic field; i.e., shear horizontally polarized waves. By referring to the cited works at the end of the chapter, and with some additional effort, the reader should be able to apply the presented theory to vector and more involved types of waves.

Key words: micro-acoustic device modelling and simulation, near-field phenomena, Green's functions, singularities, regularization techniques.

7.1 Introduction

In quasi-static approximation, boundary-value problems (BVPs) arising in micro-acoustic devices [1–3] can be formulated in terms of a system of eight coupled partial differential equations (PDEs), or, alternatively, an equivalent system of coupled integral equations. When taking full account of the electrodynamic–acoustic interaction, the number of governing differential (integral) equations rises to ten. In principle, the resulting system, subject to boundary conditions, can be solved numerically by applying the method of moments (MoM),[4] which is also known as the boundary-element method (BEM).[5] Due to the involvement of the Green's functions in the BEM, the method is notoriously known to require highly developed skills in the regularization of the arising singularities, to ensure the robustness and convergence of the results.[6–9] The appropriate tool to this end is the theory of generalized functions,[10] but, even so, much specialized knowledge and careful handling are needed to deal with the myriad of challenges that arise in practice.[11,12] In particular, the regularization task may become prohibitively complicated for problems where the Green's functions cannot be expressed in closed form – this is, as a rule, the case when the number of coupled equations exceeds two. The present author has been investigating these and related problems from various perspectives for nearly three decades, with a particular focus on the 'hard' near-field problem.[13–32] By considering the simplest problem in the theory of acoustics, i.e. shear horizontal wave (SHW) propagation, this chapter summarizes some of the highlights of this author's results.

The chapter is organized as follows. Section 7.2 discusses the equation of motion for a SHW in a form that is conventionally understood. The discussion is limited to two spatial dimensions (2D) and assumes time-harmonic oscillation of the fields. The governing equation, together with the constitutive equation, is cast in a form that can be interpreted as diagonalization with respect to time. Section 7.3 addresses the construction of infinite-domain Green's functions in two alternative but equivalent forms. Using a 2D Fourier transformation, i.e. expansions in terms of homogeneous plane waves, the time-diagonalized equation leads to an eigenvalue problem (a dispersion relation for slowness). The construction of Green's function in this formulation is straightforward, however, at a high cost: 2D Fourier-type integrals need to be solved. Frequency- and material-independent Green's functions are next introduced. 'Historically', this was the first step in this author's efforts to generate precalculated data sets and create a library. Then the significant concept of diagonalization with respect to a spatial coordinate is introduced. Using a 1D Fourier transformation, i.e. expansions in terms of inhomogeneous plane waves, the resulting diagonalized form is converted into an eigenvalue problem, and an alternative recipe for the construction of the Green's function is introduced. Section 7.4 opens the discussion of the all-important near-field calculations. Stated more precisely, expressions for the Green's functions in the proximity of the source are derived in several different, but, as shown, painstakingly accurate, equivalent forms. The exposition clearly demonstrates that the key steps involved in constructing Green's functions are commutative. This insight is then exploited to devise a tool for calculating the asymptotes of eigenpairs for the construction of Green's functions in the near field. Section 7.5 introduces a simple way of normalizing the governing equation of motion and the field variables. It also introduces an important variable η, which, in the limit $\eta \to 0$, describes the near field. Section 7.6, being the highlight of the chapter, compares two methods for investigating near fields. Section 7.7 gives a glimpse of this author's views of the future trends. Section 7.8, listing key references for further study, concludes the chapter.

Despite the fact that the chapter explains and contrasts a variety of powerful techniques for investigating the near field, it only scratches the surface of this fascinating field of research. Many significant details had to be omitted due to the space limitation. For example, in applying the method to sagittal waves, generalized eigenvectors need to be introduced to cope with degeneracies, an important topic, which is not discussed. Nonetheless, the reader, with the content given in this chapter, should be in a position to follow, apply and further develop most of the schemes and algorithms necessary for investigating near-field phenomena in micro-acoustics, and, thus, confidently apply the BEM.

7.2 The acoustic wave equation: shear horizontal vibrations

Consider the equation of motion describing shear horizontally polarized acoustic vibrations in an unbounded isotropic elastic medium. Assume a line force, in the form of a Dirac delta-function, positioned at the point (x',z') and oriented parallel to the y-axis:

$$\frac{\partial}{\partial x}\left[C_{44}\frac{\partial}{\partial x}u_2(x,z;t)\right]+\frac{\partial}{\partial z}\left[C_{44}\frac{\partial}{\partial z}u_2(x,z;t)\right]$$
$$+F_2(t)\delta(x-x')\delta(z-z')=\rho\frac{\partial^2}{\partial t^2}u_2(x,z;t) \qquad [7.1]$$

The x-axis is assumed to run horizontally to the right, the y-axis to be perpendicular to and pointing into this plane, and the z-axis to point vertically upwards. The time-dependent force magnitude $F_2(t)$ will be specified further below. Assume the elastic modulus C_{44} and the mass density ρ to be position independent. Then, Eq. 7.1 can be written in the form:

$$C_{44}\frac{\partial^2}{\partial x^2}u_2(x,z;t)+C_{44}\frac{\partial^2}{\partial z^2}u_2(x,z;t)+F_2(t)\delta(x-x')\delta(z-z')$$
$$=\rho\frac{\partial_2}{\partial t^2}u_2(x,z;t) \qquad [7.2]$$

Dividing the terms on both sides of this equation by C_{44}, introducing the material characteristic transversal velocity V_T, according to

$$V_T^2=C_{44}/\rho, \qquad [7.3]$$

and rearranging terms, leads to the inhomogeneous scalar wave equation for the displacement $u_2(x,z;t)$:

$$\left[\frac{\partial^2}{\partial x^2}+\frac{\partial^2}{\partial z^2}-\frac{1}{V_T^2}\frac{\partial^2}{\partial t^2}\right]u_2(x,z;t)=-\frac{1}{C_{44}}F_2(t)\delta(x-x')\delta(z-z') \qquad [7.4]$$

This equation, as it stands, is suitable for constructing the associated infinite-domain Green's function subject to the Sommerfeld radiation condition, ensuring retardation and L_2 integrability of the fields. Using a 2D Fourier transformation (the decomposition of the fields into homogeneous plane waves), the Green's function can be constructed straightforwardly in the spectral domain as shown below.

The following conventions simplify the treatment:

$$h(x,z;t)=\bar{h}(x,z;\omega)e^{-j\omega t} \qquad [7.5a]$$

$$\bar{h}(x,z;\omega)=\int_{-\infty}^{+\infty}\int_{-\infty}^{+\infty}\frac{dk_1}{2\pi}\frac{dk_3}{2\pi}\bar{\bar{h}}(k_1,k_2;\omega)e^{jk_1x}e^{jk_3z} \qquad [7.5b]$$

$$\bar{\bar{h}}(k_1,k_3;\omega)=\int_{-\infty}^{+\infty}\int_{-\infty}^{+\infty}dxdz\bar{h}(x,z;\omega)e^{-jk_1x}e^{-jk_3z} \qquad [7.5c]$$

Equation 7.5a expresses the fact that the field $h(x,z;t)$ varies time harmonically according to $e^{-j\omega t}$. $\overline{h}(x,z;\omega)$ is the complex amplitude of the field at the operating frequency ω; it is in general a complex-valued field distribution depending on the spatial variables x and z. Equation 7.5b expresses the spatial domain field distribution $\overline{h}(x,z;\omega)$ in terms of its associated spectral-domain Fourier components $\overline{\overline{h}}(k_1,k_2;\omega)$ at a given frequency. Equation 7.5c is the corresponding inverse Fourier transform expressing the spectral components $\overline{\overline{h}}(k_1,k_2;\omega)$ in terms of the spatial domain field distribution $\overline{h}(x,z;\omega)$ at a given frequency. For greater clarity, in addition to the spatio-temporal and wave-number-frequency independent variables, the list of independent variables may be augmented by including parameters such as the material characteristic velocity V_T. Parameters will follow the independent variables in the list and will be separated from them by a vertical line.

In source-free regions $[F_2(t) \equiv 0]$, Eq. 7.4 reduces to

$$\left[\frac{\partial^2}{\partial x^2}+\frac{\partial^2}{\partial z^2}\right]u_2(x,z;t)=\frac{1}{V_T^2}\frac{\partial^2}{\partial t^2}u_2(x,z;t). \qquad [7.6]$$

This equation will be referred to as the governing equation in diagonalized form with respect to time. To better illustrate the implications of diagonalization with respect to time and contrast it with diagonalization with respect to a spatial coordinate variable, as will be considered below, consider the following analysis. A solution ansatz of the form $\overline{\overline{u}}_2\,(k_1,k_3;\omega \mid V_T)\, e^{jk_1x}\, e^{jk_3z}\, e^{-j\omega t}$ for the displacement $u_2(x,z;t)$ results in an eigenvalue equation for the spectral displacement $\overline{\overline{u}}_2(k_1,k_3;\omega \mid V_T)$ and the corresponding eigenvalue $(\omega/V_T)^2$:

$$(k_1^2+k_3^2)\overline{\overline{u}}_2(k_1,k_3;\omega \mid V_T)=(\omega/V_T)^2\,\overline{\overline{u}}_2(k_1,k_3;\omega \mid V_T) \qquad [7.7]$$

In polar coordinates, $k_1 = k\cos\theta$ and $k_2 = k\sin\theta$, Eq. 7.7 reads

$$k^2\,\overline{\overline{u}}_2(k;\omega \mid V_T)=(\omega/V_T)^2\overline{\overline{u}}_2(k;\omega \mid V_T), \qquad [7.8]$$

which under the assumption $k \neq 0$ leads to

$$\overline{\overline{u}}_2(k;\omega \mid V_T)=\left(\frac{\omega}{kV_T}\right)^2\overline{\overline{u}}_2(k;\omega \mid V_T)=\left(\frac{1/V_T}{k/\omega}\right)^2\overline{\overline{u}}_2(k;\omega \mid V_T). \qquad [7.9]$$

Using the 'dynamic' slowness, $s = k/\omega$, the material specific slowness $S_T = 1/V_T$ and the non-dimensional slowness $\hat{s} = s/S_T$, Eq. 7.9 can be written in the form

$$\overline{\overline{u}}_2(s \mid S_T)=(S_T/s)^2\overline{\overline{u}}_2(s \mid S_T), \qquad [7.10]$$

leading to:

$$\overline{\overline{u}}_2(\hat{s}) = \frac{1}{\hat{s}^2}\overline{\overline{u}}_2(\hat{s}) \qquad [7.11]$$

For non-trivial solutions, $\overline{\overline{u}}_2(\hat{s}) \neq 0$, Eq. 7.11 results in the 'dispersion' equation $\hat{s}^2 = 1$ characterizing the wave propagation of a shear horizontally polarized field in an isotropic elastic medium specified by the parameters C_{44} and ρ. The significance of this will be seen with the governing equations for vector fields in anisotropic elastic materials.

7.3 Construction of infinite-domain Green's functions

7.3.1 Field analysis using a 2D Fourier transform

Assume a harmonic time dependence for the force, $F_2(t) = F_2 e^{-j\omega t}$, and a homogeneous plane-wave solution ansatz, as described in the preceding section:

$$u_2(x,z;t\,|\,V_T) = \int_{-\infty}^{+\infty}\int_{-\infty}^{+\infty} \frac{dk_1}{2\pi}\frac{dk_3}{2\pi}\bar{\bar{u}}_2(k_1,k_3;\omega\,|\,V_T)\,e^{jk_1x}e^{jk_3z}e^{-j\omega t} \qquad [7.12]$$

Because of the plane-wave expansion of the 2D Dirac delta function

$$\delta(x-x')\delta(z-z') = \int_{-\infty}^{+\infty}\int_{-\infty}^{+\infty} \frac{dk_1}{2\pi}\frac{dk_3}{2\pi}e^{jk_1(x-x')}e^{jk_3(z-z')} \qquad [7.13]$$

Eq. 7.4 transforms into

$$\bar{\bar{u}}_2(k_1,k_3\,|\,x',z';\omega\,|\,V_T) = \frac{F_2}{C_{44}}\frac{1}{k_1^2+k_3^2-(\omega/V_T)^2}e^{-jk_1x'}e^{-jk_3z'}. \qquad [7.14]$$

The primed variables x' and z' are the position coordinates of the line force, i.e. (x',z'). In order to signify that $\bar{\bar{u}}_2$ is associated with a line force, it will be denoted by $\bar{\bar{G}}_{22}(k_1,k_3\,|\,x',z';\omega|V_T)$. Furthermore, to account for the fact that $\bar{\bar{G}}_{22}$ is the response to a line force in the y direction, there is an additional subindex 2 to the right of the existing subindex 2, thus:

$$\bar{\bar{G}}_{22}(k_1,k_3\,|\,x',z';\omega\,|\,V_T) = \frac{1}{k_1^2+k_3^2-(\omega/V_T)^2}e^{-jk_1x'}e^{-jk_3z'}. \qquad [7.15]$$

For simplicity we will let the magnitude of the force be $F_2 = C_{44}$. The choice of the letter 'G' in Eq. 7.15 alludes to the Green's function, which is in the present case a scalar quantity. The Green's function G_{22} or its spectral-domain dual function $\bar{\bar{G}}_{22}$ is, by definition, the displacement response of the assumed infinite-domain isotropic elastic medium to a Dirac delta-function line-force excitation.

The inverse Fourier transform of $\bar{\bar{G}}_{22}(k_1,k_3\,|\,x',z';\omega|\,V_T)$ gives the frequency-dependent Green's function $\bar{G}_{22}$ in the spatial domain:

$$\bar{G}_{22}(x,z\,|\,x',z';\omega\,|\,V_T) = \int_{-\infty}^{+\infty}\int_{-\infty}^{+\infty} \frac{dk_1}{2\pi}\frac{dk_3}{2\pi}e^{jk_1x}e^{jk_3z}\bar{\bar{G}}_{22}(k_1,k_3\,|\,x',z';\omega\,|\,V_T)$$
$$= \int_{-\infty}^{+\infty}\int_{-\infty}^{+\infty} \frac{dk_1}{2\pi}\frac{dk_3}{2\pi}e^{jk_1(x-x')}e^{jk_3(z-z')}\frac{1}{k_1^2+k_3^2-(\omega/V_T)^2} \qquad [7.16]$$

The closed-form expression of the integrand in the second double integral allows the inference of several properties. Due to the harmonic exponential functions in the integral representation, differentiation and integration with respect to the spatial variables are immediate. However, this simplicity comes at the expense of carrying out integrations in two dimensions. The latter task may turn out to be a daunting undertaking in practice, because integration in the majority of cases can be carried out in numerical form only. To remedy this difficulty, we shall use 1D integral representations instead. However, before we delve into a deeper discussion of this and related issues, we will briefly explain the frequency-independent formulation of Green's functions and the universality in the context of numerical calculations.

Remark: From the above, it should be clear that the differences between the analytical and computational complexities become even more pronounced for 3D analyses where the inhomogeneous and homogeneous solution ansatzes lead correspondingly to 2D and 3D integrals. The techniques and concepts developed here, however, apply to 3D cases *mutatis mutandis*.

Frequency-independent formulation of the Green's function

The integral expression in Eq. 7.16 is a spectral-domain representation of the displacement response of an infinite elastic domain to a line-force excitation, oscillating time harmonically at the frequency ω. Since by definition an infinitely thin and infinitely extended line force does not induce any length scale, and furthermore, since the elastic medium under consideration is unbounded, and due to the fact that there are no objects of finite extension involved in the formulation of Eq. 7.16 (the total absence of any scatterer), the following conclusion can be inferred: the displacement field distribution considered at the operating frequencies ω must be related to the displacement field distribution at $\alpha\omega\,(\alpha \in R^+)$ by a simple scaling relation. To better appreciate this relation, manipulate Eq. 7.16 as follows.

$$
\begin{aligned}
&\bar{G}_{22}(x,z\,|\,x',z';\omega\,|\,V_T)\\
&=\int_{-\infty}^{+\infty}\int_{-\infty}^{+\infty}\frac{dk_1/\omega}{2\pi}\frac{dk_3/\omega}{2\pi}e^{j(k_1/\omega)(\omega x-\omega x')}e^{j(k_3/\omega)(\omega z-\omega z')}\frac{1}{(k_1/\omega)^2+(k_2/\omega)^2-1/V_T^2}\\
&=\int_{-\infty}^{+\infty}\int_{-\infty}^{+\infty}\frac{ds_1}{2\pi}\frac{ds_3}{2\pi}e^{js_1(\omega x-\omega x')}e^{js_3(\omega z-\omega z')}\frac{1}{s_1^2+s_3^2-S_T^2}\\
&=\int_{-\infty}^{+\infty}\int_{-\infty}^{+\infty}\frac{ds_1}{2\pi}\frac{ds_3}{2\pi}e^{js_1(X-X')}e^{js_3(Z-Z')}\frac{1}{s_1^2+s_3^2-S_T^2}\\
&=G_{22,\,FrequencyScaled}(X,Z\,|\,X',Z'\,|\,S_T)
\end{aligned}
\qquad [7.17]
$$

In the above transitions, the material-specific slowness, $S_T = 1/V_T$, has been used along with the slowness components, $s_1 = k_1/\omega$ and $s_3 = k_3/\omega$, which correspond to the x- and z-axes, respectively. Note also that by definition, slowness has the dimension of inverse velocity. Furthermore, the scaled variables (velocities) X

and Z have been introduced according to $X = \omega x$ and $Z = \omega z$, leading to the substitutions $k_1 x = (k_1/\omega)(\omega x) = s_1 X$ and $k_3 Z = (k_3/\omega)(\omega z) = s_3 Z$. Similarly, the scaled variables (velocities) $X' = \omega x'$ and $Z' = \omega z'$ have been introduced, resulting in the substitutions $k_1 x' = (k_1/\omega)(\omega x') = s_1 X'$ and $k_3 z' = (k_3/\omega)(\omega z') = s_3 Z'$. Consequently, this gives the non-dimensional variables $s_1 X$, $s_3 Z$, $s_1 X'$ and $s_3 Z'$. The introduction of the above normalized variables plays a significant role in carrying out numerical calculations and should be appreciated by experts, not only as good practice but also as a must in computational engineering.

Material-independent formulation of the Green's function

We will focus next on the implications of introducing a problem-specific slowness constant. Obviously, in the present case the transversal slowness, S_T, appears:

$$\begin{aligned}
&\overline{G}_{22}\left(x,z\,|\,x',z';\omega\,|\,V_T\right) = G_{22,FrequencyScaled}\left(X,Z\,|\,X',Z'\,|\,S_T\right) \\
&= \int_{-\infty}^{+\infty}\int_{-\infty}^{+\infty} \frac{ds_1/S_T}{2\pi}\frac{ds_3/S_T}{2\pi} e^{j(s_1/S_T)(S_T X - S_T X')} e^{j(s_3/S_T)(S_T Z - S_T Z')} \frac{1}{(s_1/S_T)^2 + (s_3/S_T)^2 - 1} \\
&= \int_{-\infty}^{+\infty}\int_{-\infty}^{+\infty} \frac{d\hat{s}_1}{2\pi}\frac{d\hat{s}_3}{2\pi} e^{j\hat{s}_1(\hat{X}-\hat{X}')} e^{j\hat{s}_3(\hat{Z}-\hat{Z}')} \frac{1}{\hat{s}_1^2 + \hat{s}_2^2 - 1} \\
&= G_{22,universal}\left(\hat{X}-\hat{X}',\hat{Z}-\hat{Z}'\right)
\end{aligned} \qquad [7.18]$$

In the above transitions, the scaled variables $\hat{s}_1 = s_1/S_T$, $\hat{s}_3 = s_3/S_T$, $\hat{X} = S_T\, X$, $\hat{Z} = S_T\, Z$, $\hat{X}' = S_T\, X'$ and $\hat{Z}' = S_T\, Z'$ and have been introduced, along with the 'universal' Green's function $G_{22,\, universal}(\hat{X} - \hat{X}', \hat{Z} - \hat{Z}')$:

$$G_{22,universal}\left(\hat{X}-\hat{X}',\hat{Z}-\hat{Z}'\right) = \int_{-\infty}^{+\infty}\int_{-\infty}^{+\infty} \frac{d\hat{s}_1}{2\pi}\frac{d\hat{s}_3}{2\pi} e^{j\hat{s}_1(\hat{X}-\hat{X}')} e^{j\hat{s}_3(\hat{Z}-\hat{Z}')} \frac{1}{\hat{s}_1^2 + \hat{s}_2^2 - 1} \qquad [7.19]$$

By writing $G_{22,\, universal}\,(\hat{X} - \hat{X}', \hat{Z} - \hat{Z}')$ rather than $G_{22,\, universal}\,(\hat{X}, \hat{Z}\,|\,\hat{X}', \hat{Z}')$, we have additionally made explicit that infinite-domain Green's functions are functions of the relative distance between the source and observation points (translational invariance). Furthermore, the introduction of non-dimensional variables $\hat{X} = S_T\, X = S_T\, \omega x$ and $\hat{Z} = S_T\, Z = S_T \omega z$ has resulted in frequency and material independence, emphasizing the attribute of 'universality' of the Green's function, and thus the notation $G_{22,\, universal}\,(\hat{X} - \hat{X}', \hat{Z} - \hat{Z}')$. The double integral in [7.19] has a closed-form representation

$$G_{22,universal}\left(\hat{X}-\hat{X}',\hat{Z}-\hat{Z}'\right) = \frac{j\pi}{2} H_0^{(1)}\left(\sqrt{\left(\hat{X}-\hat{X}'\right)^2 + \left(\hat{Z}-\hat{Z}'\right)^2}\right), \qquad [7.20]$$

explicitly showing that $G_{22,\, universal}(\hat{X} - \hat{X}', \hat{Z} - \hat{Z}')$ merely depends on the distance between the source and observation points.

Preliminary summary: The above result demonstrates the possibility of moulding Green's functions in a form that is material and frequency independent. The conditions necessary for the realization of this most favourable 'universality' property are:

- Consider a homogeneous infinitely extended elastic medium excited by a line force. Obviously, neither a line force nor an unbounded homogeneous medium introduces a characteristic length in the formulation – there is no geometry-induced characteristic length in the problem considered. The absence of topologically related metrics, however, does not necessarily imply the exclusion of other characteristic lengths. A closer examination of the problem shows that there is an implicit problem-specific length scale implied by the material-characterizing transversal velocity, V_T, and the operating frequency, ω, resulting in the 'length metric', V_T/ω, which can be interpreted as the wavelength at ω. However, as demonstrated above, ω and $V_T (= 1/S_T)$ can be absorbed into the coordinate variables and thus eliminated by introducing the slowness, $s = k/\omega$, and the normalized slowness, $\hat{s} = s/S_T$. Consequently, by introducing spatial variables scaled by (ω, S_T), i.e. $\hat{X}$ and $\hat{Z}$, the frequency- and material-independent formulation in Eq. 7.20 can be achieved.
- In Eq. 7.19, the occurrence of the unity in the denominator of the fraction at the far right is due to the length scale induced by V_T and ω.
- Note that in cases where two characteristic velocities, e.g. the longitudinal, V_L, and transversal, V_T, velocities with $\beta = V_T/V_L < 1$ exist, the occurrence of '1' and 'β' can be recognized in the spectral-domain representations of the corresponding dyadic Green's functions. Prominent examples are the dyadic Green's functions associated with sagittal polarized acoustic waves.
- In general anisotropic media, three characteristic velocities can be anticipated, i.e. one quasi-longitudinal (V_L) and two quasi-traversal (V_{T1}, V_{T2}) characteristic velocities. The triple constants (V_L, V_{T1}, V_{T2}) induce a '1', and $\beta_1 = V_{T1}/V_L < 1$, and $\beta_2 = V_{T2}/V_L < 1$ in the Fourier integral representations for the corresponding dyadic Green's functions. (The reason for the occurrence of dyadic Green's functions in the latter two types of media is the vector nature of the excited fields and the possibility of exciting the media with more than one independent localized source function.)
- Under simplifying yet physically permissible assumptions, certain anisotropic materials allow the construction of infinite-domain dyadic Green's functions in closed form. The resulting Green's functions involve Hankel-type functions, which are dependent on the distance R between observation ($\hat{X}$, $\hat{Z}$) and source ($\hat{X}'$, $\hat{Z}'$) points. In such cases, the operating frequency ω can still be scaled out by introducing slowness, based on the arguments outlined above. However, the procedure leads to integrals involving two parameters, β_1 and β_2. The Green's functions are, in such instances, referred to as the quasi-material-independent universal Green's functions. To obtain fully material-independent Green's functions in anisotropic media, more sophisticated

procedures need to be employed, details of which are outside the scope of this chapter.

- The Hankel function $H_0^{(1)}(R)$ in Eq. 7.20, while being compact and possessing well-established properties, is not suitable for large-scale numerical calculations. In particular, it should be mentioned that $H_0^{(1)}(R)$ cannot be factorized multiplicatively, a property which is essential in both fast and accelerated computing. More specifically, $G_{universal}(\cdot,\cdot)$ cannot be written in the form $f(\hat{X} - \hat{X}')h(\hat{X} - \hat{Z}')$ and there is no possibility for additionally factorizing $f(\hat{X} - \hat{X}')$ and $h(\hat{Z} - \hat{Z}')$ into $f_1(\hat{X})f_2(\hat{X}')$ and $h_1(\hat{Z})h_2(\hat{Z}')$, respectively. We can only expect to construct infinite series expansions, which involve eigenfunctions in real space, a procedure which is, as a rule, non-trivial. This limitation is particularly prohibitive when Green's functions are only available as numerical data sets, which is regrettably the case in the majority of practically relevant problems, rather than as exceptions. The prime reason for the absence of multiplicatively factorized forms is the complicated functional dependence of Green's functions on the distance $[(\hat{X}-\hat{X}')^2 + (\hat{Z}-\hat{Z}')^2]^{1/2}$ between the source and observation points. On the other hand, from a computational point of view, it is obviously advantageous to be able to factorize the contributions stemming from $\hat{X}-\hat{X}'$ and $\hat{Z}-\hat{Z}'$. This objective can be achieved by employing inhomogeneous rather than homogeneous plane-wave solution Ansatzes; i.e. by subjecting the field governing equations to a 1D rather than a 2D Fourier transform. As will be demonstrated, the use of inhomogeneous plane waves brings a plethora of novel and powerful tools for manipulating equations, and at the same time gives rise to a number of mathematically challenging questions. This author's attempts to systematically resolve the associated puzzles have revealed a number of far-reaching insights, some of which are presented in this manuscript for the first time.
- The above-mentioned limitations in regard to factorization become particularly prohibitive in the near-field calculations, where the distance between the observation and source points becomes negligibly small or even vanishes: $[(\hat{X} - \hat{X}')^2 + (\hat{Z} - \hat{Z}')^2]^{1/2} << \varepsilon \rightarrow 0^+$. The reason is that the regularization of singular or hyper-singular integrals would be greatly simplified if the Green's functions in the near-field zone could be factorized. The rest of this chapter discusses these shortcomings with suggestions for ways of overcoming them. This ambitious objective will be fulfilled by several easy-to-implement recipes. The final proposal, presented here in full detail for the first time, has a remarkably wide range of applications: it is applicable to general governing systems of coupled linear partial differential equations currently known in mathematical physics. Ongoing research work, alongside this author's recent publications,[24–29] can be regarded as a prelude for proving a series of conjectures related to the regularization of singular surface integrals.

7.3.2 Field analysis using a 1D Fourier transform

Preparatory considerations

The starting point is Eq. 7.1. In preparation for the discussion, the stress $T_4(x,z;t) = C_{44}\partial u_2(x,z;t)/\partial z$ associated with the spatial variation of $u_2(x,z;t)$ in the z-direction is:

$$T_4(x,z;t) = C_{44}\frac{\partial}{\partial z}u_2(x,z;t) \qquad [7.21a]$$

$$C_{44}\frac{\partial^2}{\partial z^2}u_2(x,z;t) + \frac{\partial}{\partial z}T_4(x,z;t) + F_2(t)\delta(x-x')\delta(z-z')$$
$$= \rho\frac{\partial^2}{\partial t^2}u_2(x,z;t) \qquad [7.21b]$$

The reason for distinguishing the z-axis will soon become clear. We will use a fictitious plane $z = z' = const$ and the Heaviside step function $H(\cdot)$, along with the 'less than' and 'greater than' signs, to write the field components $u_2(x,z;t)$ and $T_4(x,z;t)$, in the form:

$$u_2(x,z;t) = u_2^{<}(x,z;t)H(z'-z) + u_2^{>}(x,z;t)H(z-z') \qquad [7.22a]$$

$$T_4(x,z;t) = T_4^{<}(x,z;t)H(z'-z) + T_4^{>}(x,z;t)H(z-z') \qquad [7.22b]$$

Note that, in the present situation, the material coefficients C_{44} and ρ are position independent (constants) throughout space, so there is no need to introduce the pairs $[C_{44}^{<}, \rho^{<}]$ and $[C_{44}^{>}, \rho^{>}]$, respectively, characterizing the domains $z < z'$ and $z > z'$. Equations 7.16 ensure that the field solutions in the domains $z < z'$ and $z > z'$ are characterized by independent solution pairs $[u_2^{<}(x,z), T_4^{<}(x,z)]$ and $[u_2^{>}(x,z), T_4^{>}(x,z)]$, respectively. Equations 7.16 convey no information concerning the continuity or discontinuity conditions when crossing the fictitious 'interface' $z = z' = const$: no continuity conditions have been imposed. It will be shown next that these conditions arise automatically (naturally) from the formulation proposed in this section. To this end, substituting Eq. 7.16 into Eq. 7.21a results in:

$$T_4^{<}(x,z;t)H(z'-z) + T_4^{>}(x,z;t)H(z-z')$$
$$= C_{44}\left\{\left[\frac{\partial}{\partial z}u_2^{<}(x,z;t)\right]H(z'-z) + u_2^{<}(x,z;t)\left[\frac{\partial}{\partial z}H(z'-z)\right]\right\}$$
$$+C_{44}\left\{\left[\frac{\partial}{\partial z}u_2^{>}(x,z;t)\right]H(z-z') + u_2^{>}(x,z;t)\left[\frac{\partial}{\partial z}H(z-z')\right]\right\} \qquad [7.23]$$

Or, equivalently, by replacing the derivatives of the Heaviside function with Dirac delta functions:

$$T_4^<(x,z;t)H(z'-z)+T_4^>(x,z;t)H(z-z')$$
$$=C_{44}\left\{\left[\frac{\partial}{\partial z}u_2^<(x,z;t)\right]H(z'-z)-u_2^<(x,z;t)\delta(z'-z)\right\}$$
$$+C_{44}\left\{\left[\frac{\partial}{\partial z}u_2^>(x,z;t)\right]H(z-z')+u_2^>(x,z;t)\delta(z-z')\right\} \qquad [7.24]$$

Using the fact that the supports of the functions $H(z'-z)$, $H(z-z')$ and $\delta(z-z')$ are mutually exclusive and their union expands the entire z-axis, along with the fact that the Dirac delta function is symmetric, $\delta(z-z')=\delta(z'-z)$, we will proceed as follows. Multiply both sides of Eq. 7.24 first by $H(z'-z)$ and then by $H(z-z')$, respectively, to obtain:

$$T_4^<(x,z;t)H(z'-z)=C_{44}\left[\frac{\partial}{\partial z}u_2^<(x,z;t)\right]H(z'-z) \qquad [7.25a]$$

$$T_4^>(x,z;t)H(z-z')=C_{44}\left[\frac{\partial}{\partial z}u_2^>(x,z;t)\right]H(z-z') \qquad [7.25b]$$

Since the ‘less than’ and ‘greater than’ symbols unambiguously specify the validity ranges of Eqs 7.25a and 7.25b, i.e. $z<z'$ and $z>z'$, the Heaviside step functions $H(z'-z)$ and $H(z-z')$ will be omitted, leading to:

$$T_4^<(x,z;t)=C_{44}\frac{\partial}{\partial z}u_2^<(x,z;t) \qquad [7.26a]$$

$$T_4^>(x,z;t)=C_{44}\frac{\partial}{\partial z}u_2^>(x,z;t) \qquad [7.26b]$$

Because of Eq. 7.25, from Eq. 7.24 we can conclude that:

$$C_{44}\{-u_2^<(x,z;t)\delta(z'-z)\}+C_{44}\{+u_2^>(x,z;t)\delta(z-z')\}=0 \qquad [7.27]$$

Since C_{44} is finite, the terms on the left-hand side (LHS) can be divided by C_{44}. Integrating the resulting terms on the LHS with respect to z from $-\infty$ to ∞ leads to:

$$-\int_{-\infty}^{\infty}dz u_2^<(x,z;t)\delta(z'-z)+\int_{-\infty}^{\infty}dz u_2^>(x,z;t)\delta(z-z')=0 \qquad [7.28]$$

Or, equivalently,

$$-u_2^<(x,z'_-;t)+u_2^>(x,z'_+;t)=0, \qquad [7.29]$$

which is the interface condition for the displacement. Similarly, substituting Eq. 7.22 into Eq. 7.21b we arrive at

$$C_{44}\frac{\partial^2}{\partial x^2}\left[u_2^<(x,z;t)H(z'-z)+u_2^>(x,z;t)H(z-z')\right]$$
$$+\frac{\partial}{\partial z}\left[T_4^<(x,z;t)H(z'-z)+T_2^>(x,z;t)H(z-z')\right]$$
$$+F_2(t)\delta(x-x')\delta(z-z')=\rho\frac{\partial^2}{\partial t^2}\left[u_2^<(x,z;t)H(z'-z)+u_2^>(x,z;t)H(z-z')\right], \quad [7.30]$$

which can be expanded in the form:

$$\begin{aligned}&\left\{C_{44}\frac{\partial^2}{\partial x^2}u_2^<(x,z;t)\right\}H(z'-z)+\left\{C_{44}\frac{\partial^2}{\partial x^2}u_2^>(x,z;t)\right\}H(z-z')\\&+\left\{\frac{\partial}{\partial z}T_4^<(x,z;t)\right\}H(z'-z)-T_4^<(x,z;t)\delta(z'-z)\\&+\left\{\frac{\partial}{\partial z}T_4^>(x,z;t)\right\}H(z-z')-T_4^>(x,z;t)\delta(z-z')+\delta(x-x')\delta(z-z')\\&=\left\{\rho\frac{\partial^2}{\partial t^2}u_2^<(x,z;t)\right\}H(z'-z)+\left\{\rho\frac{\partial^2}{\partial t^2}u_2^>(x,z;t)\right\}H(z-z')\end{aligned} \quad [7.31]$$

Multiply both sides of Eq. 7.31 first by $H(z'-z)$ and then by $H(z-z')$ to obtain:

$$\begin{aligned}&\left\{C_{44}\frac{\partial^2}{\partial x^2}u_2^<(x,z;t)\right\}H(z'-z)+\left\{\frac{\partial}{\partial z}T_4^<(x,z;t)\right\}H(z'-z)\\&=\left\{\rho\frac{\partial^2}{\partial t^2}u_2^<(x,z;t)\right\}H(z'-z)\end{aligned} \quad [7.32a]$$

$$\begin{aligned}&\left\{C_{44}\frac{\partial^2}{\partial x^2}u_2^>(x,z;t)\right\}H(z-z')+\left\{\frac{\partial}{\partial z}T_4^>(x,z;t)\right\}H(z-z')\\&=\left\{\rho\frac{\partial^2}{\partial t^2}u_2^>(x,z;t)\right\}H(z-z')\end{aligned} \quad [7.32b]$$

As mentioned above, since the symbols $<$ and $>$ unambiguously specify the domains of validity of Eqs 7.32a and 7.32b; i.e. $z<z'$ and $z>z'$, the Heaviside step functions $H(z'-z)$ and $H(z-z')$ can be omitted, leading to:

$$C_{44}\frac{\partial^2}{\partial x^2}u_2^<(x,z;t)+\frac{\partial}{\partial z}T_4^<(x,z;t)=\rho\frac{\partial^2}{\partial t^2}u_2^<(x,z;t) \quad [7.33a]$$

$$C_{44}\frac{\partial^2}{\partial x^2}u_2^>(x,z;t)+\frac{\partial}{\partial z}T_4^>(x,z;t)=\rho\frac{\partial^2}{\partial t^2}u_2^>(x,z;t) \quad [7.33b]$$

From Eq. 7.32, Eq. 7.31 gives:

$$-T_4^<(x,z;t)\delta(z'-z)+T_4^>(x,z;t)\delta(z-z')+F_2(t\,0\delta(x-x')\delta(z-z')=0 \qquad [7.34]$$

Integrating the terms on the LHS with respect to z from $-\infty$ to ∞ leads to:

$$-\int_{-\infty}^{\infty} dzT_4^<(x,z;t)\delta(z'-z)+\int_{-\infty}^{\infty} dzT_4^>(x,z;t)\delta(z-z')$$

$$+\int_{-\infty}^{\infty} dzF_2(t)\delta(x-x')\delta(z-z')=0 \qquad [7.35]$$

Or, equivalently,

$$-T_4^<(x,z'_-;t)+T_4^>(x,z'_+;t)+F_2(t)\delta(x-x')=0, \qquad [7.36]$$

which is the interface condition for the stress. In summary, the results obtained so far:

$$T_4^<(x,z;t)=C_{44}\frac{\partial}{\partial z}u_2^<(x,z;t) \qquad [7.37a]$$

$$T_4^>(x,z;t)=C_{44}\frac{\partial}{\partial z}u_2^>(x,z;t) \qquad [7.37b]$$

$$-u_2^<(x,z'_-;t)+u_2^>(x,z'_+;t)=0 \qquad [7.38]$$

$$C_{44}\frac{\partial^2}{\partial x^2}u_2^<(x,z;t)+\frac{\partial}{\partial z}T_4^<(x,z;t)=\rho\frac{\partial^2}{\partial t^2}u_2^<(x,z;t) \qquad [7.39a]$$

$$C_{44}\frac{\partial^2}{\partial x^2}u_2^>(x,z;t)+\frac{\partial}{\partial z}T_4^>(x,z;t)=\rho\frac{\partial^2}{\partial t^2}u_2^>(x,z;t) \qquad [7.39b]$$

$$-T_4^<(x,z'_-;t)+T_4^>(x,z'_+;t)+F_2(t)\delta(x-x')=0 \qquad [7.40]$$

Organizing these equations into groups valid in the regions $z<z'$ and $z>z'$, along with the interface conditions we have:

$$T_4^<(x,z;t)=C_{44}\frac{\partial}{\partial x}u_2^<(x,z;t) \qquad [7.41a]$$

$$C_{44}\frac{\partial^2}{\partial x^2}u_2^<(x,z;t)+\frac{\partial}{\partial z}T_4^<(x,z;t)=\rho\frac{\partial^2}{\partial t^2}u_2^<(x,z;t) \qquad [7.41b]$$

$$T_4^>(x,z;t)=C_{44}\frac{\partial}{\partial z}u_2^>(x,z;t) \qquad [7.42a]$$

$$C_{44}\frac{\partial}{\partial z}u_2^>(x,z;t)+\frac{\partial}{\partial z}T_4^>(x,z;t)=\rho\frac{\partial^2}{\partial t^2}u_2^>(x,z;t) \qquad [7.42b]$$

$$-u_2^{<}(x,z'_-;t) + u_2^{>}(x,z'_+;t) = 0 \qquad [7.43a]$$

$$-T_4^{<}(x,z'_-;t) + T_4^{>}(x,z'_+;t) + F_2(t)\delta(x - x') = 0 \qquad [7.43b]$$

By (i) distinguishing the z direction in the governing and constitutive Eqs 7.21, (ii) introducing the fictitious plane $z = z' = const$, and finally (iii) substituting Eq. 7.22 into Eq. 7.21, the interface conditions on the interface plane $z = z' = const$ manifest themselves 'naturally'. This procedure is in contrast to the classical discussion, invariably described in textbooks on field theory as: (a) Assume a rectangular 'pillbox' centred at the point (x', z'). The edges of the pillbox run parallel to the x- and z-axes with lengths Δx and h, respectively. (b) Apply the Gauss integral theorem to the governing equations in the pillbox region. (c) Carry out the limiting process $h \rightarrow 0$.

The application of steps (a), (b) and (c) results in the same interface equation obtained above.

The following two remarks conclude this section.

Remark: In obtaining Eqs 7.24 and 7.29, the primary and derived fields on both sides of the equality signs in Eqs 7.21a and 7.21b were partitioned into terms proportional to $H^{<}(z' - z)$ and $H^{>}(z - z')$, respectively. Considering the Heaviside unit-jump functions $H^{<}(z' - z)$ and $H^{>}(z - z')$ as 'markers', and equating terms proportional to $H^{<}(z' - z)$ and $H^{>}(z - z')$ in each equation individually, we arrive at Eqs 7.41 and 7.42. However, since the formal structure of the sets of equations in 7.41 and 7.42 is the same, for the remaining part of our discussion we will omit the 'less than' and 'greater than' signs, and work instead with:

$$T_4(x,z;t) = C_{44}\frac{\partial}{\partial z}u_2(x,z;t) \qquad [7.44a]$$

$$C_{44}\frac{\partial}{\partial z}u_2(x,z;t) + \frac{\partial}{\partial z}T_4(x,z;t) = \rho\frac{\partial^2}{\partial t^2}u_2(x,z;t) \qquad [7.44b]$$

Remark: The introduction of the fictitious plane $z = z' = const$, the identification of the 'interface' conditions, Eq. 7.43, and obtaining the governing equations in the form of Eq. 7.44 are the initial steps for constructing the Green's function. The remaining steps are discussed in the next section. The pivot step is writing the governing equations, Eq. 7.44, in an equivalent diagonalized form. Diagonalized forms transform to eigenvalue equations in the spectral domain and are the foundation for the investigation presented in this chapter. Diagonalization will serve as an all-important tool for diagnosing and calculating near-field distributions, systematically and rigorously. The following sections can be seen as the testimony for the rich properties of eigensystems applied to the fundamental equations of acoustics.

Diagonalization of the acoustic equation for shear horizontally polarized waves

For shear horizontal vibrations, the relations are easy to transform into their equivalent diagonalized forms by inspection. Assuming a harmonic time dependence according to $e^{-j\omega t}$, it is easy to see that Eq. 7.44 can be written in the following 'diagonalized' form:

$$\begin{bmatrix} 0 & 1/C_{44} \\ -C_{44}\partial^2/\partial x^2 - \rho\omega^2 & 0 \end{bmatrix} \begin{bmatrix} \bar{u}_2(x,z;\omega) \\ \bar{T}_4(x,z;\omega) \end{bmatrix} = \frac{\partial}{\partial z} \begin{bmatrix} \bar{u}_2(x,z;\omega) \\ \bar{T}_4(x,z;\omega) \end{bmatrix} \quad [7.45]$$

This equation can be interpreted as follows: given $\bar{u}_2(x,z_0;\omega)$ and $\bar{T}_4(x,z_0;\omega)$ on the plane surface $z = z_0$, the application of the 2 × 2 matrix operator in Eq. 7.45 determines the rate of change of $\bar{u}_2(x,z_0;\omega)$ and $\bar{T}_4(x,z_0;\omega)$ in the direction normal to the surface $z = z_0$. It is immediate that by applying the matrix operator on $\bar{u}_2(x,z_0;\omega)$ and $\bar{T}_4(x,z_0;\omega)$, say, n times, the nth derivatives of $\bar{u}_2(x,z_0;\omega)$ and $\bar{T}_4(x,z_0;\omega)$ with respect to z at $z = z_0$ can be obtained. In this sense, Eq. 7.45 can be viewed as a potentially powerful tool for generating Taylor series expansions for vector fields.

Eigensystem describing shear horizontally polarized waves

We can factorize the field variables $u_2(x,y;t)$ and $T_4(x,y;t)$ by allowing them to vary harmonically in the x direction, and exponentially in the z direction:

$$\bar{\bar{u}}_2(x,z\,|\,k,\omega) = \bar{\bar{u}}_2(k,\omega)e^{jkx}e^{\lambda(k,\omega)z} \quad [7.46a]$$

$$\bar{\bar{T}}_4(x,z\,|\,k,\omega) = \bar{\bar{T}}_4(k,\omega)e^{jkx}e^{\lambda(k,\omega)z} \quad [7.46b]$$

Substitute these trial functions into Eq. 7.45 to obtain the algebraic system of equations:

$$\begin{bmatrix} 0 & 1/C_{44} \\ C_{44}k^2 - \rho\omega^2 & 0 \end{bmatrix} \begin{bmatrix} \bar{\bar{u}}_2(k,\omega) \\ \bar{\bar{T}}_4(k,\omega) \end{bmatrix} = \lambda(k,\omega) \begin{bmatrix} \bar{\bar{u}}_2(k,\omega) \\ \bar{\bar{T}}_4(k,\omega) \end{bmatrix} \quad [7.47]$$

This is an eigenvalue equation for the determination of the eigenvalue $\lambda(k,\omega)$ and the corresponding amplitude functions $\bar{\bar{u}}_2(k,\omega)$ and $\bar{\bar{T}}_4(k,\omega)$. The eigenvalues can be determined by setting the determinant of the resolvent to zero in Eq. 7.47:

$$\det\begin{bmatrix} -\lambda(k,\omega) & 1/C_{44} \\ C_{44}k^2 - \rho\omega^2 & -\lambda(k,\omega) \end{bmatrix} = 0 \Rightarrow \lambda^2(k,\omega) = k^2 - \frac{\rho}{C_{44}}\omega^2 = k^2 - (\omega/V_T)^2 \quad [7.48]$$

It is advantageous to define the complex valued $\lambda(k,\omega)$ according to:

$$\lambda(k,\omega) = \begin{cases} j\sqrt{(\omega/V_T)^2 - k^2} & |k| < \omega/V_T \\ -\sqrt{k^2 - (\omega/V_T)^2} & |k| > \omega/V_T \end{cases} \quad [7.49]$$

Using the fictitious plane $z = z' = const$, introduced earlier, subdivide the entire (x,z) space into mutually exclusive regions, $z > z'$ and $z < z'$. In the following, the symbols > and < will refer to the regions $z > z'$ and $z < z'$, respectively. Let $\lambda^{>} = \lambda$ and $\lambda^{<} = -\lambda$. Here $\lambda^{>}$ and $\lambda^{<}$, being by definition valid in the regions $z > z'$ and $z < z'$, respectively, ensure the finiteness of the fields in Eq. 7.46. More precisely, the fields decay sufficiently strongly to be L_2 integrable. The choice $\lambda^{>} = \lambda$ and $\lambda^{<} = -\lambda$ suffices to ensure the validity of the Sommerfeld radiation principle. In more general cases with anisotropic materials, $\lambda^{>}$ and $\lambda^{<}$ will be determined by explicitly imposing the Sommerfeld radiation condition and investigating the direction of the Poynting vector. From Eq. 7.48, the dispersion relation $C_{44}k^2 - \rho\omega^2 = C_{44}\lambda^2$ means the two equations in 7.47 are linearly dependent:

$$\begin{bmatrix} -\lambda(k,\omega) & 1/C_{44} \\ C_{44}\lambda^2(k,\omega) & -\lambda(\lambda,\omega) \end{bmatrix}\begin{bmatrix} \bar{\bar{u}}_2(k,\omega) \\ \bar{\bar{T}}_4(k,\omega) \end{bmatrix} = 0$$

$$\Rightarrow \left\{ \begin{matrix} \bar{\bar{T}}_4(k,\omega) = C_{44}\lambda(k,\omega)\bar{\bar{u}}_2(k,\omega) \\ C_{44}\lambda^2(k,\omega)\bar{\bar{u}}_2(k,\omega) = \lambda(k,\omega)\bar{\bar{T}}_4(k,\omega) \end{matrix} \right\} \qquad [7.50]$$

Therefore, it suffices to consider $\bar{\bar{T}}_4(k,\omega) = C_{44}\lambda(k,\omega)\bar{\bar{u}}_2(k,\omega)$. Setting $\bar{\bar{u}}_2(k,\omega) = 1$ yields an expression for the eigenvector:

$$\begin{bmatrix} \bar{\bar{u}}_2(k,\omega) \\ \bar{\bar{T}}_4(k,\omega) \end{bmatrix} = \begin{bmatrix} 1 \\ C_{44}\lambda(k,\omega) \end{bmatrix} \qquad [7.51]$$

In the following, if there is no danger of ambiguity, the arguments (k,ω) are omitted. Based on Eq. 7.51, we obtain the following eigenpairs for the regions $z > z'$ and $z < z'$, respectively:

$$\lambda^{>} = \lambda \Leftrightarrow \begin{bmatrix} \bar{\bar{u}}_2^{>} \\ \bar{\bar{T}}_4^{>} \end{bmatrix} = \begin{bmatrix} 1 \\ C_{44}\lambda^{>} \end{bmatrix} = \begin{bmatrix} 1 \\ C_{44}\lambda \end{bmatrix} \qquad [7.52a]$$

$$\lambda^{>} = -\lambda \Leftrightarrow \begin{bmatrix} \bar{\bar{u}}_2^{<} \\ \bar{\bar{T}}_4^{<} \end{bmatrix} = \begin{bmatrix} 1 \\ C_{44}\lambda^{<} \end{bmatrix} = \begin{bmatrix} 1 \\ -C_{44}\lambda \end{bmatrix} \qquad [7.52b]$$

More explicitly, from Eq. 7.46:

$$\begin{bmatrix} \bar{\bar{u}}_2^{>}\left(x,z\middle|z'\middle|k,\omega\right) \\ \bar{\bar{T}}_4^{>}\left(x,z\middle|z'\middle|k,\omega\right) \end{bmatrix} = \bar{\bar{A}}(k,\omega)\begin{bmatrix} 1 \\ C_{44}\lambda^{<} \end{bmatrix} e^{jkx}e^{\lambda(z-z')} \qquad [7.53a]$$

$$\begin{bmatrix} \bar{\bar{u}}_2^{<}\left(x,z\middle|z'\middle|k,\omega\right) \\ \bar{\bar{T}}_4^{<}\left(x,z\middle|z'\middle|k,\omega\right) \end{bmatrix} = \bar{\bar{B}}(k,\omega)\begin{bmatrix} 1 \\ -C_{44}\lambda \end{bmatrix} e^{jkx}e^{\lambda(z'-z)} \qquad [7.53b]$$

These equations hold for any continuously varying arbitrary value, $k \in R$. Thus, integrating with respect to k from $-\infty$ to ∞ leads to a complete solution of the fields in response to some force distribution on the fictitious plane $z = z' = const$. The next section elaborates the details.

Construction of the Green's function

The unknown coefficients $\bar{\bar{A}}(k,\omega)$ and $\bar{\bar{B}}(k,\omega)$ in Eq. 7.53 must be determined from the 'interface' conditions at $z = z' = const$. As described above, these conditions express the continuity of the displacement and the jump discontinuity of the stress components. Expressed in the k spectral domain:

$$\bar{\bar{u}}_2^{>}(x,z'_+\,|\,x',z'|k,\omega)=\bar{\bar{u}}_2^{<}(x,z'_-\,|\,x',z'|k,\omega) \qquad [7.54a]$$

$$\bar{\bar{T}}_4^{>}(x,z'_+\,|\,x',z'\,|\,k,\omega)-\bar{\bar{T}}_4^{<}(x,z'_-\,|\,x',z'|k,\omega)=-F_2e^{-jkx'} \qquad [7.54b]$$

Substituting the expressions for the displacements from Eq. 7.53 into Eq. 7.54a gives $\bar{\bar{A}}(k,\omega)=\bar{\bar{B}}(k,\omega)$. Using this result and submitting the expressions for the stress from Eq. 7.53 into Eq. 7.54b results in $\bar{\bar{A}}(k,\omega)=-e^{-jkx'}/(2C_{44}\lambda)$. Thus for the displacements in the regions $z > z'$ and $z < z'$, respectively:

$$\bar{\bar{u}}_2^{>}(x-x',z-z'\,|\,k,\omega)=-\frac{F_2}{2C_{44}\lambda}e^{jk(x-x')}e^{\lambda(z-z')} \qquad [7.55a]$$

$$\bar{\bar{u}}_2^{<}(x-x',z-z'\,|\,k,\omega)=-\frac{F_2}{2C_{44}\lambda}e^{jk(x-x')}e^{\lambda(z'-z)} \qquad [7.55b]$$

Using the absolute-value function $|\cdot|$, the expressions on the right-hand side (RHS) can be unified,

$$\bar{u}_2(x-x',z-z'\,|\,k,\omega)=-\frac{F_2}{2C_{44}\lambda}e^{jk(x-x')}e^{\lambda|z-z'|}, \qquad [7.56]$$

which is valid in the entire (x,z) space. Integrating over k from $-\infty$ to ∞ gives:

$$\bar{u}_2(x-x',z-z'\,|\,\omega)=\int_{-\infty}^{\infty}\frac{dk}{2\pi}\left[-\frac{F_2}{2C_{44}\lambda}\right]e^{jk(x-x')}e^{\lambda|z-z'|} \qquad [7.57]$$

Setting $F_2 = C_{44}$ (the unit line force), $\bar{u}_2(x-x', z-z'|\,\omega)$ can be replaced by the Green's function $\bar{G}_{22}(x-x', z-z'|\,\omega)$:

$$\bar{G}_{22}(x-x',z-z'\,|\,\omega)=-\frac{1}{4\pi}\int_{-\infty}^{\infty}dk\,\frac{1}{\lambda}e^{jk(x-x')}e^{\lambda|z-z'|} \qquad [7.58]$$

Remark: It is instructive to show that this integral representation for the Green's function is material, coordinate and frequency independent. The manipulations are self-explanatory.

$$
\begin{aligned}
\bar{G}_{22}(x-x',z-z'\,|\,\omega) &= -\frac{1}{4\pi}\int_{-\infty}^{\infty} dk\,\frac{1}{\lambda(k^2,\omega^2)}e^{jk(x-x)}e^{\lambda|z-z'|} \\
&= -\frac{1}{2\pi}\int_{0}^{\infty} dk\,\frac{1}{\lambda(k^2,\omega^2)}\cos k(x-x')e^{\lambda|z-z'|} \\
&= -\frac{1}{2\pi}\int_{0}^{\omega/V_T} dk\,\frac{1}{j\sqrt{(\omega/V_T)^2-k^2}}\cos k(x-x')e^{j\sqrt{(\omega/V_T)^2-k^2}|z-z'|} \\
&\quad -\frac{1}{2\pi}\int_{\omega/V}^{\infty} dk\,\frac{1}{-\sqrt{k^2-(\omega/V_T)^2}}\cos k(x-x')e^{-\sqrt{k^2-(\omega/V_T)^2}|z-z'|}
\end{aligned}
\tag{7.59}
$$

We will use the scaled variables $\hat{s}$, $\hat{X}$ and $\hat{Z}'$: $V_T k|\omega = V_T s = s/S_T = \hat{s}$, $\omega x|V_T = X/V_T = S_T X = \hat{X}$ and $\omega z/V_T = Z/V_T = S_T Z = \hat{Z}$. Similarly, we will use $\hat{X}'$ and $\hat{Z}'$. Then it is straightforward to see that Eq. 7.52 can be written in the form:

$$
\begin{aligned}
\bar{G}_{22}\left(x-x',z-z'\middle|\omega\right) &= -\frac{1}{2\pi}\int_{0}^{1} d\hat{s}\,\frac{1}{j\sqrt{1-\hat{s}}}\cos\hat{s}\left(\hat{X}-\hat{X}'\right)e^{j\sqrt{1-\hat{s}^2}|\hat{z}-\hat{z}'|} \\
&= -\frac{1}{2\pi}\int_{1}^{\infty} d\hat{s}\,\frac{1}{-\sqrt{\hat{s}^2-1}}\cos\hat{s}\left(\hat{X}-\hat{X}'\right)e^{-\sqrt{\hat{s}^2-1}|\hat{z}-\hat{z}'|} \\
&= \hat{G}_{22,Frequencyscaled}\left(\hat{X}-\hat{X}',\hat{Z}-\hat{Z}'\right)
\end{aligned}
\tag{7.60}
$$

This completes the derivation of the Green's function as the displacement response to a Dirac delta function line-force excitation of the elastic medium under consideration. It is a Fourier-type single-integral representation.

We will conclude this section by contrasting the procedures described in this and the preceding sections. (i) The one-dimensional Fourier-type integral representation in this section is oscillatory in the *x* direction. It is, depending on the 'critical' threshold value, $k_c = \omega/V_T$, oscillatory ($k < k_c$) or exponentially decaying ($k > k_c$). As will be demonstrated below, asymptotically large values of *k* are of particular significance when analysing the behaviour of acoustic, or, for that matter, any field, in the near-field zone – which is the major theme in this chapter. (ii) Normalized forms of the distances $x - x'$ and $z - z'$ appear in a symmetrical fashion in the integral representation in Eq. 7.19. However, the dependence of $\bar{G}_{22}(x - x',z - z'|\omega)$ on $x - x'$ and $z - z'$ is not symmetrical in Eq. 7.58. Despite this apparent difference, these integrals, however, are equivalent but alternative representations for the same Green's function $\bar{G}_{22}(x - x',z - z'|\omega)$. (iii) A further interesting observation, which has significant implications in computation, is the following. At the outset we could have partitioned the entire space into two semi-spaces by choosing an $x = x' = const$ plane, rather than the above (arbitrarily chosen) $z = z' = const$ plane. Simple symmetry arguments show that the resulting Fourier integral would be:

$$\bar{G}_{22}(z-z',x-x'\,|\,\omega)=-\frac{1}{4\pi}\int_{-\infty}^{\infty}dk\,\frac{1}{\lambda}e^{jk(z-z')}e^{\lambda|x-x'} \qquad [7.61]$$

This significant property has been overlooked in the literature dealing with Green's functions. As long as infinite-domain Green's functions are concerned, this property holds; i.e., irrespective of the isotropic or anisotropic nature of the problems. Thus scalar and dyadic infinite-domain Green's functions invariably possess the symmetry property $\bar{G}_{ij}(x - x', z - z', \omega) = \bar{G}_{ij}(z - z', x - x', \omega)$. Consequently, depending on computational requirements, the roles of the spatial coordinates x and z can be interchanged in the integral expressions. To elucidate the utility of this computationally significant flexibility, consider the integral in Eq. 7.58 under the condition $|z-z'|<<|x-x'|$ in an assumed xy-coordinate system, when keeping the source point (x',z') fixed. Then, obviously, the integrand oscillates quickly and decays slowly, both being unfavourable properties for numerical calculations. In particular, λ behaves according to $-|k|$ for asymptotically large values of k. In contrast to these 'ill-conditioned' properties, consider the alternative expression for the Green's function as given in Eq. 7.61. Obviously, under the same condition, $|z-z'|<<|x-x'|$, the slowly oscillating harmonic function is now tempered by a rapidly decaying exponential function – both of these properties are cherished by computational analysts. (iv) The next comment concerns the extraordinarily significant case of the near-field calculations – viewed as one of the major bottlenecks in applications of the BEM and at the same time the cornerstone of this chapter. The near-field zone is characterized by the condition that both $x-x'$ and $z-z'$ are simultaneously negligibly small; they both may even approach zero simultaneously. In this case, while k varies from $-\infty$ to $+\infty$, moderate values of k contribute insignificantly to $e^{jk(z-z')}e^{\lambda|x-x'|}$ and thus to the integral. (The relations are more involved in a rigorous analysis; here the focus is to communicate the essential ideas – and to this end the arguments are sufficiently sound. It should merely be added that the integrals behave according to $1/|k|^n$ ($n \geq 1$) for $k \rightarrow \pm\infty$. This property further strengthens our arguments.) Only asymptotically large values of k contribute appreciably to the integrand, and, consequently, to the resulting value of the associated integral. These preparatory considerations are to ensure a smooth transition to the next two sections, which exclusively consider the phenomena in the near-field zone (the distances $|x - x'|$ and $|z - z'|$ being simultaneously negligibly small, or even approaching zero). From the above, it is obvious that, in the near-field region, we only need to be concerned with the behaviour of the integrands at the limit $|k| \rightarrow \infty$. Since in the present situation the eigenpairs are functions of k^2, in the arguments which follow it suffices to consider $k \rightarrow \infty$ rather than $|k| \rightarrow \infty$. (v) For the sake of completeness, while the Green's function in the 2D Fourier representation possesses pole singularities, 1D Fourier representations possess branch point singularities. However, this property does not affect the proposed analysis of the phenomena in the near-field zone. (vi) Essentially similar statements can be made for semi-space isotropic and anisotropic media when excited by forces residing on the defining surface of the semi-space. In this case, we may expect the occurrence of surface guided modes (surface waves), which manifest themselves in the poles of the integrands in the corresponding Green's functions. Our arguments remain essentially valid.

7.4 Near-field analysis

7.4.1 Near-field asymptotic expansion of $\bar{G}_{22}(x - x', z - z'|\omega)$

We are interested in the near-field asymptotic expansion of $\bar{G}_{22}(x - x', z - z'|\omega)$; i.e., an expression which is valid for $x - x' \to 0$ and $z - z' \to 0$ ($x - x'$ and $z - z'$ simultaneously approaching zero). Our interest stems from the fact that computational difficulties in obtaining accurate expressions for the near field are the only serious bottleneck in the majority of BEM implementations. To this end we need to investigate the behaviour of the Green's function in the spectral domain in the limit $|k| \to \infty$, as argued above. To fully appreciate the significance of this point we need a few preparatory considerations. For k approaching infinity, it is certainly justified to say that the condition $|k| > \omega/V_t$ is satisfied. Consequently, the branch $\lambda = -\sqrt{k^2 - \omega^2 / V_T^2}$ needs to be chosen for the near-field calculations. Thus, because of Eq. 7.58, the integrand behaves asymptotically as follows:

$$\left\{\frac{1}{\lambda} e^{\lambda|z-z'|}\right\}_{k\to\infty} \approx \frac{1}{-\sqrt{k^2 - \omega^2 / V_T^2}} e^{-\sqrt{k^2-\omega^2/V_T^2}|z-z'|}$$

$$= \frac{1}{-|k|\sqrt{1-\omega^2/(kV_T)^2}} e^{-|k|\sqrt{1-\omega^2/(kV_T)^2}|z-z'|} = \frac{1}{-|k|\sqrt{1-\eta^2}} e^{-|k|\sqrt{1-\eta^2}|z-z'|} \qquad [7.62]$$

In the latter step the non-dimensional parameter $\eta = \omega/(V_t k)$ was introduced. From the $\eta \to 0$ ($k \to \infty$) asymptotic expansions

$$\sqrt{1-\eta^2} \approx 1 - \eta^2/2 + O(\eta^4) \qquad [7.63a]$$

$$1/\sqrt{1-\eta^2} \approx 1 + \eta^2/2 + O(\eta^4) \qquad [7.63b]$$

We use these relations in Eq. 7.62 to obtain

$$\frac{1}{\lambda} e^{\lambda|z-z'|} \approx -\frac{1}{|k|}(1+\eta^2/2) e^{-|k|(1-\eta^2/2)z-z'|} = -\frac{1}{|k|}(1+\eta^2/2) e^{-|k||z-z'|} e^{-\frac{1}{2}|k|\eta^2|z-z'|}. \qquad [7.64]$$

The occurrence of the non-reducible exponential term $e^{-|k||z-z'|}$ with an essential singularity at infinity ($k \to \infty$) alludes to a deep insight resulting from this analysis, which will be elaborated in the forthcoming sections. This singularity is of paramount significance for the analysis of the near fields. To better appreciate the importance, we will first focus on the exponent $-|k|\eta^2|z - z'|/2$ of the far-right exponential function in Eq. 7.64. Recall the definition of the parameter $\eta = \omega/(V_t k)$ where there is a hidden term $1/k$ in η. Thus substituting for η in $-|k|\eta^2|z - z'|/2$

leads to $-(\omega^2/2V_T^2)\,|z-z'|/|k|$. Alternatively, using the slowness and normalized slowness from the preceding section, η is $-(1/2V_T^2)\,|\hat{z}-\hat{z}'|/|s|$, or, equivalently, it is $-(1/2)\times|\hat{Z}-\hat{Z}'|/|\hat{s}|$. Thus, the two conditions in the near-field analysis, $|\hat{Z}-\hat{Z}'|\rightarrow 0$ and $|\hat{s}|\rightarrow\infty$, contribute to the asymptotic 'smallness' of the exponent $-(1/2)|\hat{Z}-\hat{Z}'|/|\hat{s}|$ of the exponential term $e^{-|k|\eta^2|z-z'|/2}$. The situation is fundamentally different for the exponential term $e^{-|k||z-z'|}$ in Eq. 7.64. With the slowness, it is easily seen that $e^{-|k||z-z'|}$ transforms to $e^{-|\hat{s}||\hat{Z}-\hat{Z}'|}$. In this case the limiting processes $|\hat{Z}-\hat{Z}'|\rightarrow 0$ and $|\hat{s}|\rightarrow\infty$ have an opposing influence on the magnitude of the exponent of $e^{-|\hat{s}||\hat{Z}-\hat{Z}'|}$: irrespective of how small the magnitude of $|\hat{Z}-\hat{Z}'|$ is, since $|\hat{s}|$ approaches infinity, the value of $|\hat{s}|$ can be chosen to be sufficiently larger than $1/|\hat{Z}-\hat{Z}'|$. Thus for $|\hat{s}|>>1/|\hat{Z}-\hat{Z}'|$ the magnitude of $|\hat{s}||\hat{Z}-\hat{Z}'|$ can be made arbitrarily large. This explains the essential singular nature of $e^{-|k||z-z'|}$ in the limit $k\rightarrow\infty$, which leads to a divergent series expansion for terms of the exponent $|k||z-z'|$.

This situation is fairly universal and is seen in various guises in more complicated cases of wave propagation in anisotropic media. A brief outline of this is given in the remaining sections.

With the above insight, expanding the far-right exponential function in Eq. 7.64 at the limit $\eta\rightarrow 0$ results in:

$$\frac{1}{\lambda}e^{\lambda|z-z'|}\approx-\frac{e^{-|k||z-z'|}}{|k|}\left(1+\frac{1}{2}\eta^2\right)\times\left(1+\frac{1}{2}|k|\,\eta^2\,|z-z'|\right) \qquad [7.65]$$

It is sufficient to include the dominant terms, so higher-order terms have been neglected. Multiplying out, rearranging terms and returning to the physical (dimensional) variables gives:

$$\frac{1}{\lambda}e^{\lambda|z-z'|}\approx-\frac{e^{-|k||z-z'|}}{|k|}$$
$$\times\left[1+\frac{(\omega/V_T)^2}{2}\frac{1}{|k|}|z-z'|+\frac{(\omega/V_T)^2}{2}\frac{1}{|k|^2}+\frac{(\omega/V_T)^4}{4}\frac{1}{|k|^3}|z-z'|\right] \qquad [7.66]$$

Substituting Eq. 7.66 into Eq. 7.58, the asymptotic limit of the Green's function $\bar{G}_{22}(x-x',z-z'|\omega)$ can be obtained in the near-field zone, which we will denote by $\bar{S}_{22}(x-x',z-z'|\omega)$ for greater clarity:

$$\bar{S}_{22}(x-x',z-z'\,|\,\omega)=\frac{1}{4\pi}\int_{-\infty}^{\infty}dk\frac{e^{jk(x-x')}e^{-|k||z-z'|}}{|k|}$$
$$\times\left[1+\frac{(\omega/V_T)^2}{2}\frac{1}{|k|}|z-z'|+\frac{(\omega/V_T)^2}{2}\frac{1}{|k|^2}+\frac{(\omega/V_T)^4}{4}\frac{1}{|k|^3}|z-z'|+O\left(\frac{1}{|k|^4}\right)\right] \qquad [7.67]$$

The O term is included to remind us of the asymptotic nature of $\bar{S}_{22}$; this term will be ignored below without causing any ambiguity. Because of the terms $e^{jk(x-x)}$ and $e^{\lambda|z-z'|}$ in Eq. 7.58, and the resulting exponential term $e^{-|k||z-z'|}$ in Eq. 7.67, and from the discussion above, we can now explain why the $k\rightarrow\infty$ asymptotic limit provides us with information for the near field. First, however, a few clarifying comments.

Remarks:

1. The above asymptotic expression can obviously be easily extended to include any number of terms. This innocent-sounding statement is much more difficult to prove when the ingredients of the integrand are only available in closed form: it is not at all trivial to show whether and how higher-order asymptotic terms can be obtained where the integrands of the associated Green's functions are only available numerically. Fortunately, as we will briefly describe, there are methods of finding asymptotic expansion terms, to any order desired, even if the integrands are only available numerically. The technique based on the diagonalized form (the eigenvalue formulation), which will be discussed at some length in this chapter, seems to provide the most efficient and physically interpretable procedure for obtaining an asymptotic expansion of Green's functions.
2. The exponential term $e^{-|k||z-z'|}$ has an essential singularity at $k \to \infty$ and thus cannot be represented in terms of a Laurent series expansion at infinity. This is fundamentally significant in the near-field analyses: the dominant term of the expansion is 'static', while the higher-order terms are quasi-static.
3. The integrand in Eq. 7.67 is an even function of k. Thus, ignoring the O term gives:

$$S_{22}(x-x',|z-z'|\omega) = \frac{1}{2\pi}\int_0^\infty dk\, \frac{\cos\left[k(x-x')\right]e^{-k|z-z'|}}{k}$$
$$\times\left[1+\frac{(\omega/V_T)^2}{2}\frac{1}{k}|z-z'|+\frac{(\omega/V_T)^2}{2}\frac{1}{k^2}+\frac{(\omega/V_T)^4}{4}\frac{1}{k^3}|z-z'|\right] \qquad [7.68]$$

In the limit $|z - z'| \to 0$, the integral $\frac{1}{\pi}\int_0^\infty dk\cos\left[k(x-x')\right]e^{-k|z-z'|}$ can be represented by a Dirac delta function $\delta(x - x')$. Using Eq. 7.58, we obtain:

$$\lim_{z\to z'_+}\frac{\partial \bar{G}_{22}^{>}}{\partial z} - \lim_{z\to z'_-}\frac{\partial \bar{G}_{22}^{<}}{\partial z}$$
$$= \lim_{z\to z'_+}\frac{\partial}{\partial z}\left\{-\frac{1}{4\pi}\int_{-\infty}^{\infty} dk\,\frac{1}{\lambda}e^{ik(x-x')}e^{\lambda(z-z')}\right\} - \lim_{z\to z'_-}\frac{\partial}{\partial z}\left\{-\frac{1}{4\pi}\int_{-\infty}^{\infty} dk\,\frac{1}{\lambda}e^{ik(x-x')}e^{-\lambda(z-z')}\right\}$$
$$= -\lim_{z\to z'}\frac{1}{2\pi}\int_{-\infty}^{\infty} dk e^{ik(x-x')}e^{\lambda(z-z')} = -\lim_{z\to z'}\frac{1}{\pi}\int_0^\infty dk\cos\left[k(x-x')\right]e^{\lambda|z-z'|} \qquad [7.69]$$

Comparing with

$$\lim_{z\to z'_+}\frac{\partial \bar{G}_{22}^{>}}{\partial z} - \lim_{z\to z'_-}\frac{\partial \bar{G}_{22}^{<}}{\partial z} = -\delta(x-x') \qquad [7.70]$$

gives:

$$\delta(x-x') = \lim_{z\to z'} \frac{1}{\pi} \int_0^{\infty} dk \cos\left[k(x-x')\right] e^{\lambda|z-z'|} \qquad [7.71]$$

This result has been examined more thoroughly elsewhere. The above derivation should satisfy the reader's curiosity. Using normalized slowness variables, introduced earlier, along with the relation $(V_T / \omega)\delta(x - x') = \delta(\hat{X} - \hat{X}')$ we find:

$$\delta\left(X' - \hat{X}'\right) = \lim_{\hat{Z}\to\hat{Z}'} \frac{1}{\pi} \int_0^{\infty} d\hat{s}' \cos\left[\hat{s}'\left(X' - \hat{X}'\right)\right] e^{\hat{\lambda}|\hat{Z}-\hat{Z}'|} \qquad [7.72]$$

with

$$\hat{\lambda} = \frac{V_T}{\omega}\lambda = \begin{cases} j\sqrt{1-\hat{s}'^2} & 1<\hat{s}'^2 \\ -\sqrt{\hat{s}'^2-1} & \hat{s}'^2>1 \end{cases} \qquad [7.73]$$

The finite part of the dominant term in Eq. 7.68 is equivalent to a logarithm function, which is the dominant term of a Hankel function. This result is gratifying since the expression in Eq. 7.58 is an integral representation of a Hankel function.

The above results are encouraging from a fundamental as well as a computational perspective. In particular, we showed that for determining the near-field expansion terms of Green's functions, which are needed in numerical computations, we can proceed as follows: (a) Construct the Green's function in the spectral domain, $\overline{\overline{G}}_{22}(x-x',z-z'|k,\omega)$. (For simplicity, we considered a 1D Fourier transform. The discussion can be extended straightforwardly to two dimensions *mutatis mutandis*.) (b) Transform the spectral-domain Green's function into the spatial domain to obtain $\overline{G}_{22}(x-x',z-z'\,|\,\omega)$ though in general this step cannot be carried out in closed form. (c) Find the near-field expression denoted by $\overline{\mathrm{S}}_{22}(x-x',z-z'|\omega)$, of the Green's function $\overline{G}_{22}(x-x',z-z'\,|\,\omega)$.

The details of this procedure are the bottleneck in most algorithms that deal with near-field calculations. Fortunately, the above analysis leads to an important insight. After carrying out step (a), we can proceed on a different path, rather than continuing with step (*b*): (*b*′) Find the asymptotic limit of the spectral-domain Green's function $\overline{\overline{G}}_{22}(x-x',z-z'\,|\,k,\omega)$ for $k \to \infty$, i.e. determine the function $\overline{\overline{S}}_{22}(x-x',z-z'\,|\,k,\omega)$. (*c*′) Transform $\overline{\overline{S}}_{22}(x-x',z-z'\,|\,k,\omega)$ into the spatial domain and obtain the near-field Green's function in the spatial domain, $\overline{S}_{22}(x-x',z-z'|\omega)$. This procedure uses the property that for the near-field distribution in the spatial domain only the far-field contribution to the Green's function is relevant.

The construction of Green's functions in the spectral domain requires the eigenpairs of the algebraic version of the underlying diagonalized governing equations. This insight raises further intriguing questions and at the same time suggests powerful answers.

The first question is whether it is possible (and admissible) to use the $k \to \infty$ limits of the eigenpairs associated with our problem to construct the $k \to \infty$ asymptotic limit $\bar{\bar{S}}_{22}(x-x',z-z'|k,\omega)$ of the Green's function $\bar{\bar{G}}_{22}(x-x',z-z'|k,\omega)$. This would mean that we have discovered a novel way for directly constructing $\bar{\bar{S}}_{22}(x-x',z-z'|k,\omega)$, over the $k \to \infty$ asymptotic limit of $\bar{\bar{G}}_{22}(x-x',z-z'|k,\omega)$. We will demonstrate that this question can be answered in the affirmative. Motivated by this insight and with an eye on more complex problems, a second question arises. Given the algebraic form of the system of governing partial differential equations, is it possible to develop a recipe to construct the spectral-domain far-field asymptote of the eigenpairs? If the answer to this question is yes, is our recipe still applicable, even when the solution is only numerical and no closed forms are available? The answer to the latter question defied this author's ability for more than two decades. However, we will show that a general recipe can be devised for the calculation of spectral-domain far-field asymptotic limits of eigenpairs for problems, not only in acoustics, but also those in classical mathematical physics.

We shall explain the steps involved by using the simplest possible problem, as introduced above. Extensions to more complex problems will be presented elsewhere.

Remark: It is much harder to establish relations between the remaining expansion terms in Eq. 7.68 and generalized functions in the limit $|z-z'| \to 0$. At the time of writing, only naïve interpretation can be provided. Much work needs to be done to provide a physically insightful interpretation of the higher-order terms in Eq. 7.68.

7.4.2 Construction of the near-field expansion of $\bar{G}_{22}(x-x',z-z'|\omega)$ based on the $k \to \infty$ asymptotic expansions of eigenpairs

The eigenpairs obtained in the previous section,

$$\lambda^{>} = \lambda \Leftrightarrow \begin{bmatrix} \bar{u}_2^{>} \\ \bar{T}_4^{>} \end{bmatrix} = \begin{bmatrix} 1 \\ C_{44}\lambda^{>} \end{bmatrix} = \begin{bmatrix} 1 \\ C_{44}\lambda \end{bmatrix} \tag{7.74a}$$

$$\lambda^{<} = -\lambda \Leftrightarrow \begin{bmatrix} \bar{u}_2^{<} \\ \bar{T}_4^{<} \end{bmatrix} = \begin{bmatrix} 1 \\ C_{44}\lambda^{<} \end{bmatrix} = \begin{bmatrix} 1 \\ -C_{44}\lambda \end{bmatrix} \tag{7.74b}$$

are our starting point. In the preceding section we used these eigenpairs to satisfy the interface conditions, construct the Green's function $\bar{\bar{G}}_{22}(x-x',z-z'|k,\omega)$ in the spectral domain, determine its $k \to \infty$ asymptotic limit, i.e. $\bar{\bar{S}}_{22}(x-x',z-z'|k,\omega)$, and calculate $\bar{S}_{22}(x-x',z-z'|\omega)$, the corresponding near-field distribution in the spatial domain. An important, perhaps intuitive, but by no means trivial result was the realization that $\bar{S}_{22}(x-x',z-z'|\omega)$ is equal to the real-space near-field asymptote of $\bar{G}_{22}(x-x',z-z'|\omega)$. In this section the calculation of $\bar{S}_{22}(x-x',z-z'|\omega)$ proceeds along a different path, which is conceptually and technically more direct. The method involves the following three steps:

1. Determine the asymptotic ($\eta \rightarrow 0$ as $k \rightarrow \infty$) limits of the above eigenpairs.
2. Using the resulting asymptotic eigenpairs, construct the asymptotic limit of the Green's function in the spectral domain, i.e. $\bar{\bar{S}}_{22}(x-x',z-z'|k,\omega)$.
3. Determine $\bar{S}_{22}(x-x',z-z'|\omega)$ from $\bar{\bar{S}}_{22}(x-x',z-z'|k,\omega)$, which is the same as in the foregoing section.

Using $\eta = \omega/(kV_T)$, introduced earlier, and selecting the $k \rightarrow \infty$ branch for the square roots, the correspondences in Eq. 7.74 can be written in the form:

$$-|k|\sqrt{1-\eta^2} \Leftrightarrow \left[\begin{array}{c} 1 \\ -C_{44}|k|\sqrt{1-\eta^2} \end{array}\right]^{>} \qquad [7.75a]$$

$$|k|\sqrt{1-\eta^2} \Leftrightarrow \left[\begin{array}{c} 1 \\ C_{44}|k|\sqrt{1-\eta^2} \end{array}\right]^{<} \qquad [7.75b]$$

Using the asymptotic expansion of the square root in the limit $\eta \rightarrow 0$ (or, equivalently, $k \rightarrow \infty$), and keeping two significant terms only, we obtain:

$$-|k|(1-\eta^2/2) \Leftrightarrow \left[\begin{array}{c} 1 \\ -C_{44}|k|(1-\eta^2/2) \end{array}\right]^{>} \qquad [7.76a]$$

$$|k|(1-\eta^2/2) \Leftrightarrow \left[\begin{array}{c} 1 \\ C_{44}|k|(1-\eta^2/2) \end{array}\right]^{<} \qquad [7.76b]$$

Substituting for η we find

$$-|k|+\frac{1}{2}\frac{\omega^2}{V_t^2}\frac{1}{|k|} \Leftrightarrow \left[\begin{array}{c} 1 \\ -C_{44}\left(|k|-\frac{1}{2}\frac{\omega^2}{V_T^2}\frac{1}{|k|}\right) \end{array}\right]^{>} \qquad [7.77a]$$

$$|k|-\frac{1}{2}\frac{\omega^2}{V_t^2}\frac{1}{|k|} \Leftrightarrow \left[\begin{array}{c} 1 \\ C_{44}\left(|k|-\frac{1}{2}\frac{\omega^2}{V_T^2}\frac{1}{|k|}\right) \end{array}\right]^{<} \qquad [7.77b]$$

Using the above asymptotic expansions for the eigenpairs, the asymptotic expressions for the displacement and stress distributions can be constructed, which are denoted here by a tilde above their respective symbols:

$$\tilde{\bar{\bar{u}}}_2^{>}(x,z\,|\,z'\,|\,k,\omega) = \bar{\bar{A}}(k,\omega)e^{jkx}e^{\left(-|k|+\frac{1}{2}\frac{\omega^2}{V_T^2}\frac{1}{|k|}\right)(z-z')} \qquad [7.78a]$$

$$\tilde{\bar{\bar{u}}}_2^{<}(x,z\,|\,z'\,|\,k,\omega) = \bar{\bar{A}}(k,\omega)e^{jkx}e^{\left(|k|-\frac{1}{2}\frac{\omega^2}{V_T^2}\frac{1}{|k|}\right)(z'-z)} \qquad [7.78b]$$

$$\tilde{\bar{\bar{T}}}_4^{>}(x,z\,|\,z'\,|\,k,\omega) = -\bar{\bar{A}}(k,\omega)C_{44}\left(|\,k\,|-\frac{1}{2}\frac{\omega^2}{V_T^2}\frac{1}{|\,k\,|}\right)e^{jkx}e^{\left(-|k|+\frac{1}{2}\frac{\omega^2}{V_T^2}\frac{1}{|k|}\right)(z-z')} \qquad [7.79a]$$

$$\tilde{\bar{\bar{T}}}_4^{<}(x,z\,|\,z'\,|\,k,\omega) = \bar{\bar{A}}(k,\omega)C_{44}\left(|\,k\,|-\frac{1}{2}\frac{\omega^2}{V_T^2}\frac{1}{|\,k\,|}\right)e^{jkx}e^{\left(|k|-\frac{1}{2}\frac{\omega^2}{V_T^2}\frac{1}{|k|}\right)(z'-z)} \qquad [7.79b]$$

Remark: For completeness, by introducing the absolute $|z - z'|$ and the signum function *sign* $(z - z')$, the above expressions can be written in a unified form:

$$\tilde{\bar{\bar{u}}}_2(x,z\,|\,z'\,|\,k) = \bar{\bar{A}}(k,\omega)e^{jkx}e^{\left(-|k|+\frac{1}{2}\frac{\omega^2}{V_T^2}\frac{1}{|k|}\right)|z-z'|} \qquad [7.80a]$$

$$\tilde{\bar{\bar{T}}}_4(x,z\,|\,z'\,|\,k,\omega) = -sign(z-z')\bar{\bar{A}}(k,\omega)C_{44}\left(|\,k\,|+\frac{1}{2}\frac{\omega^2}{V_T^2}\frac{1}{|\,k\,|}\right)e^{jkx}e^{\left(-|k|-\frac{1}{2}\frac{\omega^2}{V_T^2}\frac{1}{|k|}\right)|z-z'|} \qquad [7.80b]$$

Since these equations are valid in the entire z domain, the symbols > and < have been omitted.

In Eq. 7.78 we accounted for the continuity of the displacement at the fictitious ‘interface’ $z = z'$. The interface condition for the stress is:

$$\tilde{\bar{\bar{T}}}_4^{>}(x,z'_+\,|\,z'\,|\,k,\omega) - \tilde{\bar{\bar{T}}}_4^{<}(x,z'_-\,|\,z'\,|\,k,\omega) = -F_2e^{-jkx'} \qquad [7.81]$$

Here, $F_2e^{-jkx'}$ is the Fourier transform of a line force parallel to the y-axis and positioned at the point $x = x'$ on the fictitious interface $z = z'$. Substitute Eq. 7.79 into Eq. 7.81 and rearrange to obtain the expression:

$$\bar{\bar{A}}(k,\omega) = \frac{1}{2C_{44}}\frac{1}{|\,k\,|-\frac{1}{2}\frac{\omega^2}{V_T^2}\frac{1}{|\,k\,|}}F_2e^{-jkx'} \qquad [7.82]$$

To ensure consistency with the preceding calculations, assume $F_2 = C_{44}$. Then substituting Eq. 7.82 into the expressions for the asymptotes of the displacements directly leads to the $k \rightarrow \infty$ asymptote $\bar{\bar{S}}_{22}(x,z|x',z'|k,\omega)$ of the Green’s function, $\bar{\bar{G}}_{22}(x,z|x',z'|k,\omega)$:

$$\overline{\overline{S}}_{22}(x,z\,|\,x',z'\,|\,k,\omega)=\frac{1}{2}\frac{1}{|k|-\frac{1}{2}\frac{\omega^2}{V_T^2}\frac{1}{|k|}}e^{jk(x-x')}e^{\left(-|k|+\frac{1}{2}\frac{\omega^2}{V_T^2}\frac{1}{|k|}\right)|z-z'|}$$

$$=\frac{1}{2}\frac{1}{|k|-\frac{1}{2}\frac{\omega^2}{V_T^2}\frac{1}{|k|}}e^{jk(x-x')}e^{-|k||z-z'|}e^{\frac{1}{2}\frac{\omega^2}{V_T^2}\frac{1}{|k|}|z-z'|} \qquad [7.83]$$

Expanding the rightmost exponential function, and considering only the first two dominant terms, gives:

$$\overline{\overline{S}}_{22}(x-x',z-z'\,|\,k,\omega)=\frac{1}{2}\frac{e^{jk(x-x')}e^{-|k||z-z'|}}{|k|}\frac{1}{1-\frac{1}{2}\frac{\omega^2}{V_T^2}\frac{1}{|k|^2}}\left(1+\frac{1}{2}\frac{\omega^2}{V_T^2}\frac{1}{|k|}|z-z'|\right) \qquad [7.84]$$

Writing the fraction in front of the round bracket in terms of a series expansion of $1/|k|^2$, and simplifying, leads to:

$$\overline{\overline{S}}_{22}(x-x',z-z'\,|\,k,\omega)=\frac{1}{2}\frac{e^{jk(x-x')}e^{-|k||z-z'|}}{|k|}\times\left[1+\frac{(\omega/V_T)^2}{2}\frac{1}{|k|}|z-z'|\right.$$
$$\left.+\frac{(\omega/V_T)^2}{2}\frac{1}{|k|^2}+\frac{(\omega/V_T)^4}{4}\frac{1}{|k|^3}|z-z'|\right] \qquad [7.85]$$

Integrating over k from $-\infty$ to ∞ gives $\overline{S}_{22}(x-x',z-z'|\omega)$, which is the near-field asymptotic limit of the Green's function $\overline{G}_{22}(x,z,x',z'|\omega)$ in the spatial domain:

$$\overline{S}_{22}(x-x',z-z'\,|\,\omega)=\frac{1}{4\pi}\int_{-\infty}^{\infty}dk\,\frac{e^{jk(x-x')}e^{-|k||z-z'|}}{|k|}\times\left[1+\frac{(\omega/V_t)^2}{2}\frac{1}{|k|}|z-z'|\right.$$
$$\left.+\frac{(\omega/V_t)^2}{2}\frac{1}{|k|^2}+\frac{(\omega/V_t)^4}{4}\frac{1}{|k|^3}|z-z'|\right] \qquad [7.86]$$

Considering the fact that the integrand in Eq. 7.86 is an even function of k, it is immediately seen that Eqs 7.86 and 7.68 are equivalent.

Preliminary summary: It is instructive to emphasize the equivalence of the three procedures carried out in the previous sections. Essentially, they demonstrate the validity of commutativity properties, which are tacitly fulfilled in the near-field asymptotic calculations, among various operations. To be more precise, we showed that the outcomes of the following procedures are the same:

Recipe 1: Derive expressions for the eigenpairs ⇒ satisfy the boundary and interface conditions ⇒ construct the Green's function in the spectral domain, $\overline{\overline{G}}_{22}(x-x',z-z'|k,\omega)$ ⇒ transform $\overline{\overline{G}}_{22}(x-x',z-z'|k,\omega)$ to real space obtaining $\overline{G}_{22}(x-x',z-z'|\omega)$ ⇒ determine the near-field asymptotic limit of the Green's function in real space, $\overline{\mathrm{S}}_{22}(x-x',z-z'|\omega)$.

Recipe 2: Derive expressions for the eigenpairs ⇒ satisfy the boundary and interface conditions ⇒ construct $\bar{\bar{G}}_{22}(x-x',z-z'|k,\omega)$ ⇒ determine the limit $k\to\infty$ of $\bar{\bar{G}}_{22}(x-x',z-z'|k,\omega)$; i.e., determine $\bar{\bar{S}}_{22}(x,z|x',z'|k,\omega)$ ⇒ transform $\bar{\bar{S}}_{22}(x,z|x',z'|k,\omega)$ to real space, $\bar{S}_{22}(x-x',z-z'|\omega)$.

Recipe 3: Derive expressions for the eigenpairs ⇒ determine the $k\to\infty$ asymptotic limit of the eigenpairs ⇒ satisfy the boundary and interface conditions ⇒ construct $\bar{\bar{S}}_{22}(x,z|x',z'|k,\omega)$ ⇒ transform $\bar{\bar{S}}_{22}(x,z|x',z'|k,\omega)$ to real space, $\bar{S}_{22}(x-x',z-z'|\omega)$.

A comparison of the above recipes shows that proceeding to the limit, $k\to\infty$, at an early stage seems to considerably simplify the calculations. Thus, it is immediate to ask what is the earliest possible stage where we can proceed to the limit $k\to\infty$. An attempt to answer this question leads to the originating equation of the eigenvalues; i.e., to the underlying eigenvalue equation. At an even more fundamental level we realize that this eigenvalue equation is the result of the algebrization of the associated diagonalized form of the corresponding governing and constitutive equations. This leads to diagonalization and necessarily poses a deeper question concerning the existence and construction of diagonalized forms. The remaining sections will shed light on these ideas and relations. Extreme care has been taken to make the exposition in the following clear, self-consistent and rigorous. However, due to space limitations, thorough and in-depth formal proofs could not be included.

7.4.3 Asymptotic expressions for the eigenvector-eigenvalue hybridized vectors

Assume that the $\eta\to 0$ asymptotic expressions for the eigenpairs have been determined using any of the aforementioned methods, or employing techniques otherwise available. Furthermore, assume that the expansions have been determined such that the constant terms in the expressions of $\hat{u}_2=\sqrt{C_{44}}\,\tilde{\bar{\bar{u}}}_2$ and $\hat{T}_4=\tilde{\bar{\bar{T}}}_4/\left(\sqrt{C_{44}}\,|k|\right)$ constitute a normalized column vector. Then, upon defining $\hat{\lambda}=\lambda/|k|$, we have:

$$\begin{bmatrix}\hat{u}_2\\ \hat{T}_4\\ \hat{\lambda}\end{bmatrix}^{>}=\begin{bmatrix}\sqrt{2}/2\\ -\sqrt{2}/2\\ -1\end{bmatrix}+\begin{bmatrix}\sqrt{2}/8\\ \sqrt{2}/8\\ 1/2\end{bmatrix}\eta^2+O\left(\eta^4\right)\qquad[7.87\text{a}]$$

$$\begin{bmatrix}\hat{u}_2\\ \hat{T}_4\\ \hat{\lambda}\end{bmatrix}^{<}=\begin{bmatrix}\sqrt{2}/2\\ \sqrt{2}/2\\ 1\end{bmatrix}+\begin{bmatrix}\sqrt{2}/8\\ -\sqrt{2}/8\\ -1/2\end{bmatrix}\eta^2+O\left(\eta^4\right)\qquad[7.87\text{b}]$$

Note that, by construction, the norm of $([\hat{u}_2\ \hat{T}_4]^{>})^T$ evaluated at $\eta=0$ is one. The same statement holds for $([\hat{u}_2\ \hat{T}_4]^{<})^T$. Using the above expressions and omitting the O terms, we thus can write

$$\sqrt{C_{44}}\,\tilde{\bar{\bar{u}}}_2^{>}(x,z\,|\,z'\,|\,k,\omega)=\bar{\bar{A}}(k,\omega)\left(\frac{\sqrt{2}}{2}+\frac{\sqrt{2}}{8}\eta^2\right)e^{jkx}e^{|k|(-1+\frac{1}{2}\eta^2)(z-z')} \qquad [7.88a]$$

$$\frac{1}{\sqrt{C_{44}}}\frac{\tilde{\bar{\bar{T}}}_4^{>}(x,z\,|\,z'\,|\,k,\omega)}{|\,k\,|}=\bar{\bar{A}}(k,\omega)\left(-\frac{\sqrt{2}}{2}+\frac{\sqrt{2}}{8}\eta^2\right)e^{jkx}e^{|k|(-1+\frac{1}{2}\eta^2)(z-z')} \qquad [7.88b]$$

and

$$\sqrt{C_{44}}\,\tilde{\bar{\bar{u}}}_2^{<}(x,z\,|\,z'\,|\,k,\omega)=\bar{\bar{A}}(k,\omega)\left(\frac{\sqrt{2}}{2}-\frac{\sqrt{2}}{8}\eta^2\right)e^{jkx}e^{|k|(1-\frac{1}{2}\eta^2)(z'-z)} \qquad [7.89a]$$

$$\frac{1}{\sqrt{C_{44}}}\frac{\tilde{\bar{\bar{T}}}_4^{<}(x,z\,|\,z'\,|\,k,\omega)}{|\,k\,|}=\bar{\bar{A}}(k,\omega)\left(\frac{\sqrt{2}}{2}-\frac{\sqrt{2}}{8}\eta^2\right)e^{jkx}e^{|k|(1-\frac{1}{2}\eta^2)(z'-z)} \qquad [7.89b]$$

Remark: As in the previous section, the above expressions can be unified using absolute and signum functions:

$$\sqrt{C_{44}}\,\tilde{\bar{\bar{u}}}_2(x,z\,|\,z'\,|\,k,\omega)=\bar{\bar{A}}(k,\omega)\left(\frac{\sqrt{2}}{2}+\frac{\sqrt{2}}{8}\eta^2\right)e^{jkx}e^{-|k|(1-\frac{1}{2}\eta^2)|z-z'|} \qquad [7.90a]$$

$$\frac{1}{\sqrt{C_{44}}}\frac{\tilde{\bar{\bar{T}}}_4\,(x,z\,|\,z'\,|\,k,\omega)}{|\,k\,|}=-sign(z-z')\bar{\bar{A}}(k,\omega)\left(\frac{\sqrt{2}}{2}-\frac{\sqrt{2}}{8}\eta^2\right)e^{jkx}e^{-|k|(1-\frac{1}{2}\eta^2)|z-z'|} \qquad [7.90b]$$

In writing Eqs 7.88a and 7.89a the displacement continuity condition at $z=z'$ was taken into account. The interface condition for stress is:

$$\frac{1}{\sqrt{C_{44}}}\frac{\tilde{\bar{\bar{T}}}_4^{>}(x,z\,|\,z'\,|\,k,\omega)}{|\,k\,|}-\frac{1}{\sqrt{C_{44}}}\frac{\tilde{\bar{\bar{T}}}_4^{<}(x,z\,|\,z'\,|\,k,\omega)}{|\,k\,|}=-\frac{1}{\sqrt{C_{44}}}\frac{F_2}{|\,k\,|}e^{-jkx'} \qquad [7.91]$$

(Note that the original terms on both sides of this equation have been divided by $\sqrt{C_{44}}\,|\,k\,|$.) Substituting Eq. 7.88b and Eq. 7.89b into Eq. 7.91 results in:

$$\bar{\bar{A}}(k,\omega)=\frac{1}{\sqrt{C_{44}}}\frac{F_2e^{-jkx'}}{|\,k\,|}\frac{1}{\sqrt{2}-\frac{\sqrt{2}}{4}\eta^2} \qquad [7.92]$$

Substituting Eq. 7.92 into Eq. 7.90a leads to:

$$\tilde{\bar{\bar{u}}}_2(x-x',z-z'\,|\,k,\omega)=\frac{1}{2C_{44}}\frac{F_2}{|\,k\,|}\frac{\frac{\sqrt{2}}{2}+\frac{\sqrt{2}}{8}\eta^2}{\frac{\sqrt{2}}{2}-\frac{\sqrt{2}}{8}\eta^2}e^{jk(x-x')}e^{-|k||z-z'|}e^{\frac{1}{2}\eta^2|k||z-z'|} \qquad [7.93]$$

In this equation, consider the η fraction and the far-right exponential term. We will determine their $\eta \to 0$ asymptotic limits, and retain the first two dominant terms only, i.e. $1+\frac{1}{2}\eta^2$ and $1+\frac{1}{2}\eta^2\,|k\|z-z'|$, respectively. Set $F_2 = C_{44}$ and replace $\tilde{\bar{\bar{u}}}_2(x-x',z-z'|k,\omega)$ by $\tilde{\bar{\bar{S}}}_{22}(x-x',z-z'|k,\omega)$ to obtain:

$$\tilde{\bar{\bar{S}}}_{22}(x-x',z-z'\,|\,k,\omega)=\frac{1}{2}\frac{e^{jk(x-x')}e^{-|k\|z-z'|}}{|k|}\times\left[1+\frac{(\omega/V_T)^2}{2}\frac{1}{|k|}|z-z'|\right.$$
$$\left.+\frac{(\omega/V_T)^2}{2}\frac{1}{|k|^2}+\frac{(\omega/V_T)^4}{4}\frac{1}{|k|^3}|z-z'|\right] \qquad [7.94]$$

This is the expression we obtained by employing the alternative formulations in the preceding sections.

7.5 Normalization of the field variables

From a computational point of view it is advantageous to introduce the diagonal scaling matrix

$$S=\begin{bmatrix}\sqrt{C_{44}} & 0\\ 0 & 1/\sqrt{C_{44}}\end{bmatrix} \qquad [7.95]$$

and its inverse:

$$S^{-1}=\begin{bmatrix}1/\sqrt{C_{44}} & 0\\ 0 & \sqrt{C_{44}}\end{bmatrix} \qquad [7.96]$$

Consider Eq. 7.47. Inserting the 2 × 2 identity matrix in the form $S^{-1}S = I$ between the matrix and the vector, on the LHS, and multiplying both sides by S from the left result in:

$$S\begin{bmatrix}0 & 1/C_{44}\\ C_{44}k^2-\rho\omega^2 & 0\end{bmatrix}S^{-1}S\begin{bmatrix}\bar{\bar{u}}_2(k,\omega)\\ \bar{\bar{T}}_4(k,\omega)\end{bmatrix}=\lambda(k,\omega)S\begin{bmatrix}\bar{\bar{u}}_2(k,\omega)\\ \bar{\bar{T}}_4(k,\omega)\end{bmatrix} \qquad [7.97]$$

Then, with

$$S\begin{bmatrix}0 & 1/C_{44}\\ C_{44}k^2-\rho\omega^2 & 0\end{bmatrix}S^{-1}=\begin{bmatrix}0 & 1\\ k^2-\rho\omega^2/C_{44} & 0\end{bmatrix} \qquad [7.98]$$

and

$$S\begin{bmatrix}\bar{\bar{u}}_2(k,\omega)\\ \bar{\bar{T}}_4(k,\omega)\end{bmatrix}=\begin{bmatrix}\sqrt{C_{44}}\bar{\bar{u}}_2(k,\omega)\\ \bar{\bar{T}}_4(k,\omega)/\sqrt{C_{44}}\end{bmatrix} \qquad [7.99]$$

Eq. 7.89 reads:

$$\begin{bmatrix} 0 & 1 \\ k^2-\rho\omega^2/C_{44} & 0 \end{bmatrix}\begin{bmatrix} \sqrt{C_{44}}\,\bar{\bar{u}}_2(k,\omega) \\ \bar{\bar{T}}_4(k,\omega)/\sqrt{C_{44}} \end{bmatrix}=\lambda\begin{bmatrix} \sqrt{C_{44}}\,\bar{\bar{u}}_2(k,\omega) \\ \bar{\bar{T}}_4(k,\omega)/\sqrt{C_{44}} \end{bmatrix} \qquad [7.100]$$

It is an easy exercise to see that Eq. 7.100 can be transformed into:

$$\begin{bmatrix} 0 & 1 \\ 1-\dfrac{\rho}{C_{44}}\dfrac{\omega^2}{k^2} & 0 \end{bmatrix}\begin{bmatrix} \sqrt{C_{44}}\,\bar{\bar{u}}_2(k,\omega) \\ \left(1/\sqrt{C_{44}}\right)\left(\bar{\bar{T}}_4(k,\omega)/|k|\right) \end{bmatrix}=\frac{\lambda}{|k|}\begin{bmatrix} \sqrt{C_{44}}\,\bar{\bar{u}}_2(k,\omega) \\ \left(1/\sqrt{C_{44}}\right)\left(\bar{\bar{T}}_4(k,\omega)/|k|\right) \end{bmatrix} \qquad [7.101]$$

With $\eta^2=\dfrac{\rho}{C_{44}}\dfrac{\omega^2}{k^2}=\dfrac{\omega^2}{V_t^2k^2}$, $\hat{\lambda}(\eta)=\lambda/|k|$, $\hat{u}_2(\eta)=\sqrt{C_{44}}\,\bar{\bar{u}}_2(k,\omega)$ and $\hat{T}_4(\eta)=1/\sqrt{C_{44}}\times\bar{\bar{T}}_4(k,\omega)/|k|$, Eq. 7.93 takes on the following compact form:

$$\begin{bmatrix} 0 & 1 \\ 1-\eta^2 & 0 \end{bmatrix}\begin{bmatrix} \hat{u}_2 \\ \hat{T}_4 \end{bmatrix}=\hat{\lambda}\begin{bmatrix} \hat{u}_2 \\ \hat{T}_4 \end{bmatrix} \qquad [7.102]$$

This equation is the starting point for our discussion in the next section. We wish to devise a convenient recipe for determining the asymptotic expansions of the eigenpairs of Eq. 7.102 at the limit $\eta \to 0$ ($k \to \infty$) to arbitrary order. The manipulations can be carried out straightforwardly by first calculating the eigenpairs and then finding their expansion terms for $\eta \to 0$. This is exactly what we shall do next. However, the main thrust in this chapter is the presentation of a powerful novel method, which leads to the same result, but is more systematic in its conception and more general in its nature. And, more importantly, the method works in cases where no closed-form solutions are available.

7.6 Determining the asymptotic expansion terms for $\eta \to 0$

7.6.1 Direct approach

Step 1: Determine the eigenpairs associated with the 2 × 2 matrix in Eq. 7.102. In the present case, this is an easy task and has closed-form expressions:

$$\hat{\lambda}^{\pm}(\eta)=\pm(1-\eta^2)^{1/2} \Leftrightarrow \begin{bmatrix} \hat{u}_2(\eta) \\ \hat{T}_4(\eta) \end{bmatrix}^{\pm}=\begin{bmatrix} 1 \\ \pm\left(1-\eta^2\right)^{1/2} \end{bmatrix} \qquad [7.103]$$

Both eigenvectors have the common norm $(2-\eta^2)^{1/2}$. Dividing the components of the eigenvectors by $(2-\eta^2)^{1/2}$, we obtain the following eigenvalues with their corresponding normalized eigenvectors:

$$\hat{\lambda}^{\pm}(\eta) = \pm(1-\eta^2)^{1/2} \Leftrightarrow \begin{bmatrix} \hat{u}_2(\eta) \\ \hat{T}_4(\eta) \end{bmatrix}^{\pm} = \begin{bmatrix} \left(2-\eta^2\right)^{-1/2} \\ \pm\left(1-\eta^2\right)^{1/2}\left(2-\eta^2\right)^{-1/2} \end{bmatrix} \qquad [7.104]$$

Step 2: Formally arrange the displacement, $\hat{u}_2$, the stress, $\hat{T}_4$, and the decay constant, $\hat{\lambda}$, as a hybrid 3 × 1 'vector':

$$\begin{bmatrix} \hat{u}_2(\eta) \\ \hat{T}_4(\eta) \\ \hat{\lambda}(\eta) \end{bmatrix}^{\pm} = \begin{bmatrix} (2-\eta^2)^{-1/2} \\ \pm(1-\eta^2)^{1/2}(2-\eta^2)^{-1/2} \\ (1-\eta^2)^{1/2} \end{bmatrix} \qquad [7.105]$$

Step 3: In the limit $\eta \to 0$, individually determine the asymptotic expansions of $1/\sqrt{2-\eta^2}, \sqrt{1-\eta^2}/\sqrt{2-\eta^2}$ and $\sqrt{1-\eta^2}$, which constitute the components of the eigenvectors and their corresponding eigenvalues, respectively. Using powers of η ($\eta^0, \eta^1, \eta^2, \eta^3, \ldots$) as 'markers' and grouping terms, lead to:

$$\begin{bmatrix} \dfrac{1}{\sqrt{2-\eta^2}} \\ \pm\dfrac{\sqrt{1-\eta^2}}{\sqrt{2-\eta^2}} \\ \sqrt{1-\eta^2} \end{bmatrix} = \begin{bmatrix} \dfrac{\sqrt{2}}{2} \\ \pm\dfrac{\sqrt{2}}{2} \\ \pm 1 \end{bmatrix} + \begin{bmatrix} \dfrac{\sqrt{2}}{8} \\ \mp\dfrac{\sqrt{2}}{8} \\ \mp\dfrac{1}{2} \end{bmatrix}\eta^2 + \begin{bmatrix} \dfrac{3\sqrt{2}}{64} \\ \mp\dfrac{5\sqrt{2}}{64} \\ \mp\dfrac{1}{8} \end{bmatrix}\eta^4$$
$$+ \begin{bmatrix} \dfrac{5\sqrt{2}}{256} \\ \mp\dfrac{13\sqrt{2}}{256} \\ \mp\dfrac{1}{16} \end{bmatrix}\eta^6 + \begin{bmatrix} \dfrac{35\sqrt{2}}{4096} \\ \mp\dfrac{141\sqrt{2}}{4096} \\ \mp\dfrac{5}{128} \end{bmatrix}\eta^8 + O(\eta^{10}) \qquad [7.106]$$

Remark: Because the components of the hybrid vector on the left-hand side depend on the square of η, it is not surprising that only even powers of η appear on the right-hand side. Furthermore, by employing the O notation we conveniently group the terms proportional to η^{10} and higher in $O(\eta^{10})$.

Preliminary summary and comments: In the above, the eigenvalues $\lambda^{\pm}(\eta)$ were obtained by solving the characteristic determinant of the matrix in Eq. 7.102; i.e., the equation $\lambda^2 - (1-\eta^2) = 0$. In the present case, this is not easy. Sagittally polarized waves propagating in isotropic elastic media can still be tackled in closed form. However, in cases of practical interest (wave propagation in anisotropic media and coupled fields), the resulting characteristic determinants are generally of higher order. This fact renders the determination of the eigenvalues in closed form a difficult task, and, in many instances, even an impossible undertaking. Consequently, we need to resort to numerical techniques. However, by determining the eigenvalues and eigenvectors numerically we lose sight and explicit control of their functional structure, and thus their explicit η dependence. This problem has been the driving force for the development of the current work. By discussing the simplest possible problem, a powerful and at the same time an easy-to-apply method will be given for communicating the underlying ideas. The degree of complexity will be gradually increased to illuminate additional features of the method. It will be shown that, irrespective of the complexity of the problem, the proposed technique is a simple recipe for systematically determining the series expansions for the eigenvalues and their corresponding eigenvectors in terms of powers of η.

The reader might ask why it is so critically important to calculate series expansions of the eigenpairs in terms of powers of η. This issue was briefly addressed in the introduction. However, we are now in a position to have a better grasp of the underlying ideas.

7.6.2 The proposed method

The proposed method has the following four steps.

Step 1: Write the matrix in the governing equation, Eq. 7.102, in additive form:

$$\begin{bmatrix} 0 & 1 \\ 1-\eta^2 & 0 \end{bmatrix} = \begin{bmatrix} 0 & 1 \\ 1 & 0 \end{bmatrix} + \begin{bmatrix} 0 & 1 \\ -1 & 0 \end{bmatrix} \eta^2 = A^{(0)} + A^{(2)}\eta^2 \tag{7.107}$$

where we have introduced the matrices $A^{(0)}$ and $A^{(2)}$.

Step 2: Expand the eigenpairs in Eq. 7.102 in terms of integer powers of η:

$$\begin{bmatrix} \hat{u} \\ \hat{T} \end{bmatrix} = \sum_{i=0}^{\infty} \begin{bmatrix} \hat{u} \\ \hat{T} \end{bmatrix}^{(i)} \eta^i = \sum_{i=0}^{\infty} \phi^{(i)}\eta^i \tag{7.108a}$$

$$\hat{\lambda} = \sum_{i=0}^{\infty} \lambda^{(i)}\eta^i \tag{7.108b}$$

where we introduced the vectors $\phi^{(i)}$.

Step 3: Substitute the representation established in Eq. 7.107, along with the asymptotic expansions introduced in Eq. 7.108, into the governing equation, Eq. 7.102. Compare terms with equal powers of η on both sides of the resulting equation to obtain the following equations. The first five equations are:

$$\eta^0 : A^{(0)}\phi^{(0)} = \lambda^{(0)}\phi^{(0)} \tag{7.109a}$$

$$\eta^1 : A^{(0)}\phi^{(1)} = \lambda^{(0)}\phi^{(1)} + \lambda^{(1)}\phi^{(0)} \tag{7.109b}$$

$$\eta^2 : A^{(0)}\phi^{(2)} + A^{(2)}\phi^{(0)} = \lambda^{(0)}\phi^{(2)} + \lambda^{(1)}\phi^{(1)} + \lambda^{(2)}\phi^{(0)} \tag{7.109c}$$

$$\eta^3 : A^{(0)}\phi^{(3)} + A^{(2)}\phi^{(1)} = \lambda^{(0)}\phi^{(3)} + \lambda^{(1)}\phi^{(2)} + \lambda^{(2)}\phi^{(1)} + \lambda^{(3)}\phi^{(0)} \qquad [7.109d]$$

$$\eta^4 : A^{(0)}\phi^{(4)} + A^{(2)}\phi^{(2)} = \lambda^{(0)}\phi^{(4)} + \lambda^{(1)}\phi^{(3)} + \lambda^{(2)}\phi^{(2)} + \lambda^{(3)}\phi^{(1)} + \lambda^{(4)}\phi^{(0)} \qquad [7.109e]$$

Remark: In the above set of equations, while Eq. 7.109a is an eigenvalue problem, the remaining equations are inhomogeneous equations. We shall return to this property shortly. At this stage it should suffice to mention that Eq. 7.109a leads to two independent eigenpairs. Each eigenpair will serve as the genesis for an individual sequence of inhomogeneous equations starting with Eq. 7.109b. Thereby, asymptotic expansion terms for the eigenpairs can be obtained to any order desired.

Step 4: This step plays a pivotal role in the formulation; it consists of the normalization condition for the eigenvectors: $\phi^T \phi = 1$, where the superscript T signifies transposition. The normalization condition in terms of the series expansion for an eigenvector is

$$\left[\sum_{i=1}^{\infty}\left\{\phi^{(i)}\right\}^T \eta^i\right]\left[\sum_{i=1}^{\infty}\left\{\phi^{(i)}\right\}\eta^i\right] = 1. \qquad [7.110]$$

Equating the terms of equal powers of η on both sides of this equation, the following set of equations are obtained. The first five equations are:

$$\eta^0 : \{\phi^{(0)}\}^T\phi^{(0)} = 1 \qquad [7.111a]$$

$$\eta^1 : \{\phi^{(0)}\}^T\phi^{(1)} + \{\phi^{(1)}\}^T\phi^{(0)} = 0 \qquad [7.111b]$$

$$\eta^2 : \{\phi^{(0)}\}^T\phi^{(2)} + \{\phi^{(1)}\}^T\phi^{(1)} + \{\phi^{(2)}\}^T\phi^{(0)} = 0 \qquad [7.111c]$$

$$\eta^3 : \{\phi^{(0)}\}^T\phi^{(3)} + \{\phi^{(1)}\}^T\phi^{(2)} + \{\phi^{(2)}\}^T\phi^{(1)} + \{\phi^{(3)}\}^T\phi^{(0)} = 0 \qquad [7.111d]$$

$$\eta^4 : \{\phi^{(0)}\}^T\phi^{(4)} + \{\phi^{(1)}\}^T\phi^{(3)} + \{\phi^{(2)}\}^T\phi^{(2)} + \{\phi^{(3)}\}^T\phi^{(1)} + \{\phi^{(4)}\}^T\phi^{(0)} = 0 \qquad [7.111e]$$

Remark: The above results allow us to make an interesting observation. Consider Eqs 7.109a and 7.111a, which correspond to terms in η^0. As already mentioned, Eq. 7.109a is an eigenvalue equation for $\phi^{(0)}$ while Eq. 7.111a expresses the normalization condition for $\phi^{(0)}$. Next consider Eq. 7.109b and Eq. 7.111b corresponding to η^1. The occurrence of both $\phi^{(0)}$ and $\phi^{(1)}$ in these equations indicates that they can be written as a system of inhomogeneous equations for the determination of $\phi^{(1)}$ and $\lambda^{(1)}$, in terms of known values of $\phi^{(0)}$ and $\lambda^{(0)}$. Viewing the equations corresponding to higher powers of η, a similar conclusion can be made: the set of equations associated with each η^i $(i = 1,2,\ldots)$ constitutes a system of inhomogeneous equations, which can be solved successively to obtain $\phi^{(i)}$ and $\lambda^{(i)}$. So, the iterative process starts with an eigenvalue problem and continues with the solution of 3 × 3 inhomogeneous systems of equations. Note that the initial eigenvalue problem leads to two eigenpairs. Each eigenpair generates its own branch of solutions. It is this process that enables the construction of the two asymptotic expansions that were obtained by applying the standard method in the previous section. The next natural question is to ask how the results of the two methods compare.

Anticipating boundary-value problems with higher complexity, we will assume that there is a system of $2n$ rather than 2 partial differential equations. The direct method would, in general, lead to $2n$ eigenpairs. On the other hand, the proposed technique would lead to an initial eigenvalue system of order $2n$, resulting in $2n$ eigenpairs, each being the seed for the asymptotic expansion of an independent eigenvector.

To illustrate the method, we will continue with our 2 × 2 model problem by explicitly carrying out a few individual steps.

Equations corresponding to η^0:

$$A^{(0)}\phi^{(0)} = \hat{\lambda}^{(0)}\phi^{(0)} \tag{7.112a}$$

$$\{\phi^{(0)}\}^T\phi^{(0)} = 1 \tag{7.112b}$$

Obtaining the (η-independent) eigenpairs of Eq. 7.112a is straightforward:

$$\hat{\lambda}_{\pm}^{(0)} = \pm 1 \Leftrightarrow \begin{bmatrix} \hat{u}^{(0)} \\ \hat{T}^{(0)} \end{bmatrix}_{\pm} = \begin{bmatrix} 1 \\ \pm 1 \end{bmatrix} \tag{7.113}$$

Imposing the unitary condition Eq. 7.112b on the eigenvectors we obtain:

$$\hat{\lambda}_{\pm}^{(0)} = \pm 1 \Leftrightarrow \begin{bmatrix} \hat{u}^{(0)} \\ \hat{T}^{(0)} \end{bmatrix}_{\pm} = \begin{bmatrix} \sqrt{2}/2 \\ \pm\sqrt{2}/2 \end{bmatrix} \tag{7.114}$$

As in the previous section, we introduce the following 3 × 1 hybrid vectors:

$$\hat{\psi}_{\pm}^{(0)} = \begin{bmatrix} \hat{\phi}^{(0)} \\ \hat{\lambda}^{(0)} \end{bmatrix}_{\pm} = \begin{bmatrix} \hat{u}^{(0)} \\ \hat{T}^{(0)} \\ \hat{\lambda}^{(0)} \end{bmatrix}_{\pm} = \begin{bmatrix} \sqrt{2}/2 \\ \pm\sqrt{2}/2 \\ \pm 1 \end{bmatrix} \tag{7.115}$$

The information content in this pair of vectors is fully equivalent to the information in Eq. 7.112.

Equations corresponding to η^1:

$$A^{(0)}\phi^{(1)} = \hat{\lambda}^{(0)}\phi^{(1)} + \hat{\lambda}^{(1)}\phi^{(0)} \tag{7.116a}$$

$$\{\phi^{(0)}\}^T\phi^{(1)} + \{\phi^{(1)}\}^T\phi^{(0)} = 0 \tag{7.116b}$$

Substituting for $\phi^{(0)}$ and $\phi^{(1)}$ in terms of the corresponding $\hat{u}$ and $\hat{T}$, using the expression for $A^{(0)}$, and rearranging the unknowns $\hat{u}^{(1)}$, $\hat{T}^{(1)}$ and $\hat{\lambda}^{(1)}$ lead to:

$$\begin{bmatrix} -\hat{\lambda}^{(0)} & 1 & -\hat{u}^{(0)} \\ 1 & -\hat{\lambda}^{(0)} & -\hat{T}^{(0)} \\ \hat{u}^{(0)} & \hat{T}^{(0)} & 0 \end{bmatrix} \begin{bmatrix} \hat{u}^{(1)} \\ \hat{T}^{(1)} \\ \hat{\lambda}^{(1)} \end{bmatrix} = 0 \tag{7.117}$$

Substituting for $\hat{u}^{(0)}$, $\hat{T}^{(0)}$ and $\hat{\lambda}^{(0)}$ from Eq. 7.107, we can see that both solutions lead to $\hat{u}^{(1)} = 0$, $\hat{T}^{(1)} = 0$ and $\hat{\lambda}^{(1)} = 0$, hence

$$\begin{bmatrix} \hat{u}^{(1)} \\ \tilde{T}^{(1)} \\ \hat{\lambda}^{(1)} \end{bmatrix}_{\pm} = \begin{bmatrix} 0 \\ 0 \\ 0 \end{bmatrix}, \qquad [7.118]$$

in accordance with the result obtained by the 'standard' method discussed in the preceding section.

Equations corresponding to η^2:

$$A^{(0)}\phi^{(2)} + A^{(2)}\phi^{(0)} = \hat{\lambda}^{(0)}\phi^{(2)} + \hat{\lambda}^{(1)}\phi^{(1)} + \hat{\lambda}^{(2)}\phi^{(0)} \qquad [7.119a]$$

$$\{\phi^{(0)}\}^T\phi^{(2)} + \{\phi^{(1)}\}^T\phi^{(1)} + \{\phi^{(2)}\}^T\phi^{(0)} = 0 \qquad [7.119b]$$

Substituting for $\phi^{(i)}$ ($i = 0,1,2$), and $\lambda^{(0)}$, $\lambda^{(1)}$, and from the definitions for $A^{(0)}$ and $A^{(2)}$, results in:

$$\begin{bmatrix} -\hat{\lambda}^{(0)} & 1 & -\hat{u}^{(0)} \\ 1 & -\hat{\lambda}^{(0)} & -\hat{T}^{(0)} \\ \hat{u}^{(0)} & \hat{T}^{(0)} & 0 \end{bmatrix} \begin{bmatrix} \hat{u}^{(2)} \\ \hat{T}^{(2)} \\ \hat{\lambda}^{(2)} \end{bmatrix} = \begin{bmatrix} 0 \\ \hat{\lambda}^{(0)} \\ 0 \end{bmatrix} \qquad [7.120]$$

Remark: From an aesthetical as well as a methodological vantage point, it would have been instructive to introduce $\hat{\mu}^{(i)}$ as the negative of $\hat{\lambda}^{(i)}$:

$$\hat{\mu}^{(i)} = -\hat{\lambda}^{(i)}. \qquad [7.121]$$

Equation 7.120 would then transform into the following symmetric form:

$$\begin{bmatrix} \hat{\mu}^{(0)} & 1 & \hat{u}^{(0)} \\ 1 & \hat{\mu}^{(0)} & \hat{T}^{(0)} \\ \hat{u}^{(0)} & \hat{T}^{(0)} & 0 \end{bmatrix} \begin{bmatrix} \hat{u}^{(2)} \\ \hat{T}^{(2)} \\ \hat{\mu}^{(0)} \end{bmatrix} = \begin{bmatrix} 0 \\ -\hat{\mu}^{(0)} \\ 0 \end{bmatrix} \qquad [7.122]$$

However, so as not to unnecessarily obscure the flow of thought and the chain of arguments, the quantities $\hat{\mu}^{(i)}$ will not be introduced and the discussion will continue with Eq. 7.120.

As will be shown below, the matrix on the left-hand side of Eq. 7.120 appears in the calculation of asymptotic terms, irrespective of the order of terms associated with η^i. Denoting this matrix by Z,

$$Z = \begin{bmatrix} -\hat{\lambda}^{(0)} & 1 & -\hat{u}^{(0)} \\ 1 & -\hat{\lambda}^{(0)} & -\hat{T}^{(0)} \\ \hat{u}^{(0)} & \hat{T}^{(0)} & 0 \end{bmatrix} \qquad [7.123]$$

Equation 7.122 becomes:

$$Z\begin{bmatrix}\hat{u}^{(2)}\\ \hat{T}^{(2)}\\ \hat{\mu}^{(0)}\end{bmatrix}=\begin{bmatrix}0\\ \hat{\lambda}^{(0)}\\ 0\end{bmatrix} \qquad [7.124]$$

Using the results obtained in Eq. 7.115 leads to the matrices $Z_{\pm}$, which are used to successively build higher-order asymptotic terms:

$$Z_{\pm}=\begin{bmatrix}\mp 1 & 1 & -\sqrt{2}/2\\ 1 & \mp 1 & \mp\sqrt{2}/2\\ \sqrt{2}/2 & \pm\sqrt{2}/2 & 0\end{bmatrix} \qquad [7.125]$$

Using Eq. 7.124 a straightforward calculation results in:

$$\hat{\psi}_{\pm}^{(2)}=\begin{bmatrix}\hat{u}^{(2)}\\ \hat{T}^{(2)}\\ \hat{\lambda}^{(2)}\end{bmatrix}_{\pm}=\begin{bmatrix}\sqrt{2}/8\\ \mp\sqrt{2}/8\\ \mp 1/2\end{bmatrix}, \qquad [7.126]$$

which is in full accordance with the results obtained by the standard method.

Equations corresponding to η^{2i+1}, $i = 1,2,3,\ldots$:
Similar to the case of η^1, for odd exponents of η, i.e. η^{2i+1}, $i = 1,2,3,\ldots$, the equation

$$Z_{\pm}\hat{\psi}^{(2i+1)}=0 \qquad [7.127]$$

is valid, which is exactly equivalent to Eq. 7.117. Consequently, we have

$$\hat{\psi}_{\pm}^{(2i+1)}=0 \qquad [7.128]$$

as was the case for $\hat{\psi}^{(1)}$, again confirming the results from the standard technique.

Equations corresponding to η^4: In order to identify the pattern of the equations that arise, in particular to explain the occurrence of the matrix Z, the equations associated with η^4 will be explicitly written, taking into account the fact that the odd-numbered terms vanish:

$$\begin{bmatrix}0\,1\\ 1\,0\end{bmatrix}\phi^{(4)}+\begin{bmatrix}0\;\;0\\ -1\,0\end{bmatrix}\phi^{(2)}=\hat{\lambda}^{(0)}\phi^{(4)}+\hat{\lambda}^{(2)}\phi^{(2)}+\hat{\lambda}^{(4)}\phi^{(0)} \qquad [7.129a]$$

$$\{\phi^{(0)}\}^T\phi^{(4)}+\{\phi^{(2)}\}^T\phi^{(2)}+\{\phi^{(4)}\}^T\phi^{(0)}=0 \qquad [7.129b]$$

Observe that on the RHS of Eq. 7.129a as well as on the LHS of Eq. 7.129b the same sequence of $\phi^{(i)}$ terms occurs. It is instructive to write:

$$A^{(0)}\phi^{(4)}+A^{(2)}\phi^{(2)}=\sum_{i=0}^{2}\hat{\lambda}^{(2i)}\phi^{(4-2i)} \qquad [7.130a]$$

$$\sum_{i=0}^{2}\left\{\phi^{(2i)}\right\}^{T}\phi^{(4-2i)}=0 \qquad [7.130b]$$

Note that the sum of the superindices for both $A^{(0)}\phi^{(4)}$ and $A^{(2)}\phi^{(2)}$ is 4, which is the exponent of η^4, the term considered in the present case. From this discussion, followed by inductive reasoning, the general form of equations associated with an arbitrary even power of η should be clear.

From Eq. 7.129 proceed as follows: first consider Eq. 7.129a. The term $\hat{\lambda}^{(0)}\phi^{(4)}$ on the RHS involves the unknown $\phi^{(4)}$ multiplied by the known $\hat{\lambda}^{(0)}$. Transfer this term to the LHS. The term $\hat{\lambda}^{(2)}\phi^{(2)}$ on the RHS involves known values and thus remains on the RHS. The term $\hat{\lambda}^{(4)}\phi^{(0)}$ involves the unknown $\hat{\lambda}^{(4)}$ multiplied by the known $\phi^{(0)}$. This term should be transferred to the LHS as well. Next consider Eq. 7.129b. In the present case the eigenpairs are real valued. Thus $[\phi^{(0)}]^T\phi^{(4)} = [\phi^{(4)}]^T\phi^{(0)}$. These terms involving the unknown $\phi^{(4)}$ remain on the LHS. The term $[\phi^{(2)}]^T\phi^{(2)}$ involving the known term $\phi^{(2)}$ should be transferred to the RHS. Using the explicit forms for ϕ and $\hat{\lambda}$ results in

$$\begin{bmatrix} -\hat{\lambda}^{(0)} & 1 & -\hat{u}^{(0)} \\ 1 & -\hat{\lambda}^{(0)} & -\hat{T}^{(0)} \\ \hat{u}^{(0)} & \hat{T}^{(0)} & 0 \end{bmatrix}\begin{bmatrix} \hat{u}^{(4)} \\ \hat{T}^{(4)} \\ \hat{\lambda}^{(4)} \end{bmatrix}=\begin{bmatrix} \hat{\lambda}^{(2)}\hat{u}^{(2)} \\ \hat{u}^{(2)}+\hat{\lambda}^{(2)}\hat{T}^{(2)} \\ -\left\{\hat{u}^{(2)}\right\}^2/2-\left\{\hat{T}^{(2)}\right\}^2/2 \end{bmatrix} \qquad [7.131]$$

or, more compactly,

$$Z\phi^{(4)}=\begin{bmatrix} \hat{\lambda}^{(2)}\hat{u}^{(2)} \\ \hat{u}^{(2)}+\hat{\lambda}^{(2)}\hat{T}^{(2)} \\ -\left\{\hat{u}^{(2)}\right\}^2/2-\left\{\hat{T}^{(2)}\right\}^2/2 \end{bmatrix} \qquad [7.132]$$

Substituting the known values for $\hat{u}^{(0)}$, $\hat{T}^{(0)}$ and $\hat{\lambda}^{(0)}$, which constitute Z on the LHS, and the known values for $\hat{u}^{(2)}$, $\hat{T}^{(2)}$ and $\hat{\lambda}^{(2)}$, on the RHS, leads to:

$$\begin{bmatrix} \hat{u}^{(4)} \\ \hat{T}^{(4)} \\ \hat{\lambda}^{(4)} \end{bmatrix}_{\pm}=\begin{bmatrix} 3\sqrt{2}/64 \\ \mp 5\sqrt{2}/64 \\ \mp 1/8 \end{bmatrix} \qquad [7.133]$$

Equations corresponding to η^6: Following the discussion of η^4, it is an easy exercise to obtain:

$$A^{(0)}\phi^{(6)}+A^{(2)}\phi^{(4)}=\sum_{i=0}^{3}\hat{\lambda}^{(2i)}\phi^{(6-2i)} \qquad [7.134a]$$

$$\sum_{i=0}^{3}\left\{\phi^{(2i)}\right\}^{T}\phi^{(6-2i)}=0, \qquad [7.134b]$$

which can be transformed into:

$$Z\phi^{(6)} = \begin{bmatrix} \hat{\lambda}^{(2)}\hat{u}^{(4)} + \hat{\lambda}^{(4)}\hat{u}^{(2)} \\ \hat{u}^{(4)} + \hat{\lambda}^{(2)}\hat{T}^{(4)} + \hat{\lambda}^{(4)}\hat{T}^{(2)} \\ -\hat{\lambda}^{(2)}\hat{u}^{(4)} - \hat{T}^{(2)}\hat{T}^{(4)} \end{bmatrix} \qquad [7.135]$$

Substituting for the known quantities on the RHS gives:

$$\begin{bmatrix} \hat{u}^{(6)} \\ \hat{T}^{(6)} \\ \hat{\lambda}^{(6)} \end{bmatrix}_{\pm} = \begin{bmatrix} 5\sqrt{2}/256 \\ \mp 13\sqrt{2}/256 \\ \mp 1/16 \end{bmatrix} \qquad [7.136]$$

Equations corresponding to η^8: Based on the above discussion, it is easy to see that:

$$A^{(0)}\phi^{(8)} + A^{(2)}\phi^{(6)} = \sum_{i=0}^{4} \hat{\lambda}^{(2i)}\phi^{(8-2i)} \qquad [7.137a]$$

$$\sum_{i=0}^{4} \left\{\phi^{(2i)}\right\}^{T} \phi^{(8-2i)} = 0, \qquad [7.137b]$$

which written more explicitly gives:

$$Z\phi^{(8)} = \begin{bmatrix} \hat{\lambda}^{(2)}\hat{u}^{(6)} + \hat{\lambda}^{(4)}\hat{u}^{(4)} + \hat{\lambda}^{(6)}\hat{u}^{(2)} \\ \hat{u}^{(6)} + \hat{\lambda}^{(2)}\hat{T}^{(6)} + \hat{\lambda}^{(4)}\hat{T}^{(4)} + \hat{\lambda}^{(6)}\hat{T}^{(2)} \\ -\hat{\lambda}^{(2)}\hat{u}^{(6)} - \hat{T}^{(2)}\hat{T}^{(6)} - \left\{\hat{u}^{(4)}\right\}^{2}/2 - \left\{\hat{T}^{(4)}\right\}^{2}/2 \end{bmatrix} \qquad [7.138]$$

Substituting for the known quantities on the RHS results in:

$$\begin{bmatrix} \hat{u}^{(8)} \\ \hat{T}^{(8)} \\ \hat{\lambda}^{(8)} \end{bmatrix}_{\pm} = \begin{bmatrix} 35\sqrt{2}/4096 \\ \mp 141\sqrt{2}/4096 \\ \mp 5/128 \end{bmatrix} \qquad [7.139]$$

This completes the demonstration of the equivalence of the proposed method to the standard method. The benefit of the proposed method is that it only requires the eigenpairs of the (constant, η-independent) $A^{(0)}$ matrix followed by a sequence of matrix (Z^{-1}) vector multiplications, resulting in expansion terms for the eigenpairs to any order desired.

7.7 Future trends

The continuing miniaturization of micro-acoustic devices and advances in nanotechnology are expected to provide unique opportunities and flexibility for device and system designers. At the same time, it can easily be seen that fundamentally novel analysis and synthesis methodologies are required to tackle existing and emerging challenges in the modelling and simulation of micro-acoustic and phononic devices. Customization, physics-based, nature-inspired, problem-tailored tools and methodologies are no longer perceived as catch phrases to ensure grants and leverage academic promotion. It is this author's conviction that a departure from traditional methods seems inevitable to adequately respond to the demanding tasks ahead. This venture requires deep insight and expert-level foresight to grasp the complexity of the problems and to shorten the time for developing conceptually novel methodologies. The traditionally accepted categorization of the physical phenomena involved in micro-acoustic devices into quasistatic, electrodynamic, acoustic, piezoelectric and heat problems is no longer valid. Three-dimensional modelling, multi-scale analysis and homogenization techniques can no longer be seen as a luxury and a matter of choice: they are, rather, inevitable necessities. Based on this author's recent research results, the following ideas and speculation are relevant for the modelling and simulation of current and future small-scale micro-acoustic devices. Consider the governing partial differential equations describing piezo-electromagnetic coupled fields with complex-valued inhomogeneous, anisotropic, temperature-dependent material coefficients. The simultaneous excitation, propagation and scattering of a myriad of coupled acousto-thermal-electromagnetic fields in three dimensions involving several thousands of finite-aperture electrodes, busbars and the package need to be accurately and adequately taken into account. A rough back-of-the-envelope calculation reveals that traditional discretization techniques lead to matrices with ranks of several hundred millions to billions of unknowns. The storage, retrieval and processing of such an immense number of unknowns would severely exhaust available and near-future computational facilities – an exception may be quantum computing architectures, which are, however, out of reach in the foreseeable future. The accuracy and robustness of the algorithms also severely limit the choice and application of computational and simulation methods.

In the following a few ideas will be briefly outlined, which may serve as guidelines for future algorithm development for micro-acoustic devices:

1. The Universal Functions, touched upon in this chapter, have four favourable properties: a) the regularization of strong and hyperstrong singularities of dyadic Green's functions; b) the creation of astonishingly smooth geometry-independent and frequency-independent functions; c) they fully take into account near- and far-field phenomena; d) they use sophisticated quadratures in precalculating vital data sets, which need to be computed only once, thus allowing us to build libraries. The ability to create libraries offers more than just recycling a collection of modules for reuse in future applications. It also permits the addition of new modules and, whenever available, the replacement of an existing module with a new and more accurate one.
2. A series of horizontal and vertical hierarchies of auxiliary problems can be developed to solve an original (target) problem.[31] This technique enables the

construction of a lower-dimensional (vertical) hierarchy of auxiliary boundary-value problems, each leading to a further simplified (horizontal) hierarchy of auxiliary problems. The power of the hierarchical decomposition method relies on the property that lower-dimensional auxiliary problems share some of the significant features of the original problem, and that, by construction, they involve Hermitian operators. Consequently, the associated eigenfunctions are complete and orthonormal. The tensor product of lower-dimensional eigenfunctions allows the construction of problem-specific analysis and synthesis functions, which can easily be employed in Galerkin-type methods. A noteworthy feature of this method is that lower-dimensional auxiliary eigenvalue problems can be calculated with high accuracy and that typically only the first few solutions need to be retained for the analysis.

3. A further attractive method is the creation of *X*-based self-regularized distributed-elementary source dyadic Green's functions.[32] Here, *X* may be replaced by any traditional or non-standard analytical, semi-numerical or numerical simulation method. The method chops a piece out of the original structure, chooses a computational subspace in which the calculations have to be carried out, defines a stand-alone boundary-value problem, and solves the resulting enforced problem for a finite number of realizations of elementary excitation forces acting on the bounding surface of the boundary-value problem. It can be shown that the resulting Green's functions allow the analysis of any type of boundary (Dirichlet, Neumann) and interface conditions.
4. Powerful techniques such as model order reduction (MOR) and proper orthogonal decomposition (POD) can be employed to identify and retain the most energy-rich coherent vibrational structures (modes) in the solutions.

These concepts have been widely tested by this author and his research groups over the years and may build a sound platform for near-future algorithm development for modelling micro-acoustic devices.

7.8 Key references for further reading

Readers interested in digging more deeply into some of the issues discussed in this chapter might benefit from the following references. Baghai-Wadji[12] may be consulted for a host of general ideas that have been further developed in part in this chapter – it contains additional speculative ideas for future development. On the technical side, Baghai-Wadji,[11] Baghai-Wadji *et al.*[13] and Baghai-Wadji and Chehrehrazi[14] provide detailed instruction for the construction of Green's functions in closed form. Baghai-Wadji[15–18] and Baghai-Wadji and Penunuri[19] introduce the material-independent, geometry-independent and frequency-independent Universal Functions leading to the development of the fast MoM. Ramberger and Baghai-Wadji[20] is a systematic attempt to construct asymptotic tails of Green's functions in the spectral domain using numerical techniques.

Baghai-Wadji and Walter[21,22] and Baghai-Wadji[23] include original work on constructing Green's-function-based wavelets. Baghai-Wadji[24–29] summarize this author's more recent efforts to put the theory for calculating the near fields on a firm mathematical foundation. Muradoglu *et al.*[30] is a recipe for constructing localized basis functions. Finally, Smith and Baghai-Wadji[31] and Vagh and Baghai-Wadji[32] propose novel procedures for accelerating computations. This author is firmly convinced that these and similar methodologies will provide powerful tools for future computational challenges.

7.9 Acknowledgements

The author takes great pleasure in thanking the editor, Kentaro Nakamura, for his kind invitation to contribute to this book. Furthermore, he gratefully thanks Laura Pugh (commissioning editor), Anneka Hess (publications coordinator), Vicki Hart (publications coordinator) and Rachel Cox (project editor) of Woodhead Publishing for their patience, encouragement and guidance throughout the writing process of this chapter. Finally, the author thanks Jonathan Webley for his careful reading of the manuscript.

This project was carried out under an Australian Research Council (ARC) Linkage Grant: LP0775463. Generous support granted by EPCOS AG (Munich) and EPCOS Pty (Singapore) is gratefully appreciated.

7.10 References

1. B. A. Auld, *Acoustic Fields and Waves in Solids*, New York, John Willey & Sons, vols I and II, 1973.
2. C. K. Campbell, *Surface Acoustic Wave Devices for Mobile and Wireless Communications*, Florida, Academic Press, 1998.
3. K. Hashimoto, *Surface Acoustic Wave Devices in Telecommunications: Modelling and Simulation*, Berlin Heidelberg, Springer-Verlag, 2000.
4. R. F. Harrington, *Field Computation by Moment Methods*, Macmillan, New York, 1968.
5. C. A. Brebbia, J. C. F. Telles and L. C. Wrobel, *Boundary Element Techniques*, Springer Verlag, 1984.
6. G. F. Roach, *Green's Functions*, 2nd Ed., Cambridge University Press, 1967.
7. I. Stackgold, *Green's Functions and Boundary Value Problems*, A Wiley-Interscience Series of Texts, Monographs & Tracts, John Wiley & Sons, 1979.
8. N. I. Muskhelishvili, *Singular Integral Equations*, P. Noordhoff N. V., Groningen, Holland, 1953.
9. S. G. Mikhlin, *Multidimensional Singular Integrals and Integral Equations*, Pergamon Press, 1965.
10. R. P. Kanval, *Generalized Functions, Series on Mathematics in Science and Engineering*, vol. 171, Academic Press, 1983.
11. A. R. Baghai-Wadji, Theory and applications of Green's functions, *International Journal of High Speed Electronics and Systems*, Special Issue on Advances in Surface Acoustic Wave Technology, Systems and Applications 2, edited by C. C. W. Ruppel and T. A. Fjeldly, vol. 10, no. 4, pp. 949–1015, 2000.

12. A. R. Baghai-Wadji, Introduction to the special issue on modelling, optimization, and design of acoustic devices, *IEEE-UFFC, IEEE Transactions on Ultrasonics, Ferroelectrics and Frequency Control*, vol. 54, no. 10, pp. 1916–19.
13. A. R. Baghai-Wadji, S. Selberherr and F. Seifert, Two-dimensional Green’s function of a semi-infinite anisotropic dielectric in the wavenumber domain, *IEEE-UFFC Trans. Ultrasonics Ferroelectrics Frequency Control*, vol. UFFC-33, no. 3, pp. 315–17, 1986.
14. A. R. Baghai-Wadji and S. M. Chehrehrazi, Real-space Green’s function of an isolated point-charge in an anisotropic unbounded dielectric, *UFFC-IEEE, Ultrasonics, Ferroelectrics and Frequency Control Transactions*, vol. 44, no. 1, pp. 96–101, 1997.
15. A. R. Baghai-Wadji, Material, geometry, and frequency independent bivariate universal functions for the analysis of mechanical and electrical loading effects in acoustic devices: A fast-MoM approach, in *Proceedings IEEE-SU, Ultrasonics Symposium*, Lake Tahoe, Nevada, USA, October 1999.
16. A. R. Baghai-Wadji, Fast-MoM: A method-of-moments formulation for fast computations, ACES Journal, Special Issue of the *Applied Computational Electromagnetics Society Journal*, vol. 12, no. 2, pp. 75–80, 1997.
17. A. R. Baghai-Wadji, Universal functions for the analysis of electromagnetic interactions in SAW devices, in *Proceedings of 2004 International Ultrasonics, Ferroelectrics, and Frequency Control 50th Anniversary Joint Conference*, 4 pages, Montreal, Canada, 24–27 August 2004.
18. A. R. Baghai-Wadji, Universal functions in computational electromagnetics, in *Proceedings of ACES, Applied Computational Electromagnetics*, 8 pages, Monterey, USA, 24–28 March 2003.
19. A. R. Baghai-Wadji and D. Penunuri, Universal functions for 3D analysis of the massloading effect in SAW and BAW devices, in *Proceedings of IEEE-SU*, 4 pages, Munich, Germany, 8–11 October 2002.
20. S. Ramberger and A. R. Baghai-Wadji, Exact eigenvector and eigenvalue derivatives with application to asymptotic Green’s functions, in *Proceedings ACES 2002, Applied Computational Electromagnetics*, pp. 233–9, Monterey, CA, USA, 18–22 March 2002.
21. A. R. Baghai-Wadji and G. G. Walter, Green’s function induced wavelets- and wavelet-like orthogonal systems for EM applications, in *Proceedings ACES, Applied Computational Electromagnetics*, pp. 241–8, Monterey, USA, 18–22 March 2002.
22. A. R. Baghai-Wadji and G. G. Walter, Wavelets constructed from spectral domain asymptotic tails of Green’s functions, in *Proceedings of 2004 International Ultrasonics, Ferroelectrics, and Frequency Control 50th Anniversary Joint Conference*, 4 pages, Montreal, Canada, 24–27 August 2004.
23. A. R. Baghai-Wadji, B-spline wavelets constructed from spectral-domain asymptotic tails of Green’s functions, in *Proceedings of ACES, Applied Computational Electromagnetics*, 8 pages, Miami, Florida, USA, 12–16 March 2006.
24. A. R. Baghai-Wadji, On the genesis of differential operators in EMC applications, in *Proceedings of APEMC*, Jeju Island, Korea, 16–19 May 2011.
25. A. R. Baghai-Wadji, On the construction of physics-inspired integral representations for the Dirac delta function in EMC applications, in *Proceedings of APEMC*, Jeju Island, Korea, 16–19 May 2011.
26. A. R. Baghai-Wadji, Near-field phenomena in EMC applications, in *Proceedings of the Electromagnetic Compatibility Symposium*, Melbourne, Australia, September 2010.

27. A. R. Baghai-Wadji, Zooming into the near field: A novel formulation of the BEM as applied to EMC modelling and simulation problems, in *Proceedings of APEMC 2010*, Beijing, China, 2010 (invited).
28. A. R. Baghai-Wadji, Zooming into the near field: Shear-horizontal polarized acoustic waves, in *Proceedings of the 12th International Symposium on Integrated Circuits (ISIC)*, Singapore, 14–16 December 2009.
29. A. R. Baghai-Wadji, Zooming into the near fields: Erroneous assumption of superluminal speeds in Green's function theory as the origin of singularities, in *Proceedings of the IEEE International Ultrasonics Symposium and Short Courses*, Rome, Italy, 20–23 September 2009.
30. M. S. Muradoglu, A. R. Baghai-Wadji and T. W. Ng, Prospects of Wannier functions in investigating photonic crystal all-optical devices for signal processing, *Journal of The Optical Society of America A*, vol. 27, no. 4, pp. 757–65, 2010.
31. A. J. Smith and A. R. Baghai-Wadji, Ab-initio modeling of asymmetrical finite-barrier quantum wire structures, in *Proceedings of the IEEE Microwave Theory & Techniques Society (MTT-S) International Microwave Symposium for 2011 (IMS2011)*, Baltimore, USA, 5–10 June 2011.
32. H. Vagh and A. R. Baghai-Wadji, Distributed-elementary-source self-regularized dyadic Green's functions for modeling the massloading effect in acoustic devices, *Engineering Analysis with Boundary Elements Journal*, September 2011 (accepted).

8

Electrical evaluation of piezoelectric transducers

K. NAKAMURA, Tokyo Institute of Technology, Japan

Abstract: The characteristics of a piezoelectric transducer can be found by measuring the electrical impedance/admittance. The impedance of a transducer changes steeply around the mechanical resonance frequencies. The constants in an electrical equivalent model are estimated from electrical measurements. An electrical evaluation of a piezoelectric transducer is described. Constants in an equivalent circuit vary as the vibration amplitude and there is non-linearity due to high stress and high temperatures. It is difficult to measure the constants under high-vibration amplitudes. Transducer constants at a high-vibration amplitude using a transient state are evaluated. High-power characteristics of piezoelectric ceramics are demonstrated. A load test for high-power transducers is described.

Key words: piezoelectric transducer, admittance characteristics, electrical equivalent circuit, admittance loop, high-power characteristics, load test.

8.1 Introduction

The first thing we would want to find out after fabricating a transducer is its resonance frequency. The second would be the electro-mechanical coupling factor or the quality factor. These can be found through electrical measurements at the electrical port of the piezoelectric transducer. It is possible to determine the equivalent electrical circuit constants such as the equivalent mass, equivalent compliance and loss factor from the resonance curves of the impedance/admittance of the transducer. In order to understand a transducer in its entirety, of course, we need to measure the shape of the vibration mode as well as the absolute value of the vibration displacement amplitude. Measurements of vibration have been widely conducted using laser Doppler velocimetry in recent years, which is described in the next chapter in this book. The radiation pattern and waveform of the emitted sound field are also important for characterizing transducers for medical use and non-destructive testing. These are measured with a visualization technique such as the schlieren method or hydrophones. Optical methods for the evaluation of the radiated sound field are explained in Chapter 10. Hydrophones are described in detail in Chapter 19.

This chapter discusses the electrical evaluation of piezoelectric transducers. The relation between the electrical resonance curves and the equivalent electrical circuit is briefly explained. The circuit constants can be found from the electrical impedance/admittance characteristics near resonance. This electrical evaluation is usually carried out under low-voltage conditions. However, measurements at higher voltage are sometimes required, since the circuit constants, especially the loss factor, vary with the vibration amplitude due to high strain or temperature changes. We often encounter difficulties in the measurements in such a high-voltage region, because the resonance curve becomes asymmetric due to non-linearity. To overcome this problem, a method utilizing transient responses is introduced and typical high-power characteristics of actual piezoelectric ceramics are shown. For estimating output acoustic power and the efficiency of high-power transducers, a load test using an electrical power meter is demonstrated in the last section.

8.2 Equivalent electrical circuit

Figure 8.1 shows one of the simplest piezoelectric transducer configurations. A rectangular plate, with length L, width w and thickness b, vibrates in the fundamental longitudinal mode. The plate is polarized in the thickness direction, and both surfaces are metalized to act as electrodes. A sinusoidal voltage, with amplitude V, is applied between the electrodes, and the excitation electric field is in the thickness direction. The vibration direction is orthogonal to the electric field and the polarization, and its strength is given by the piezoelectric constant d_{31}. The angular frequency ω of the voltage source is chosen so that the length of the plate L is equal to the half the wavelength λ of the longitudinal wave. The longitudinal vibration velocity $v(x)$ is expressed as

$$v(x) = v \sin kx, \tag{8.1}$$

using the vibration amplitude v at the end of the plate and the wave number k.

$$k = \omega_0 \sqrt{\frac{\rho}{E}}. \tag{8.2}$$

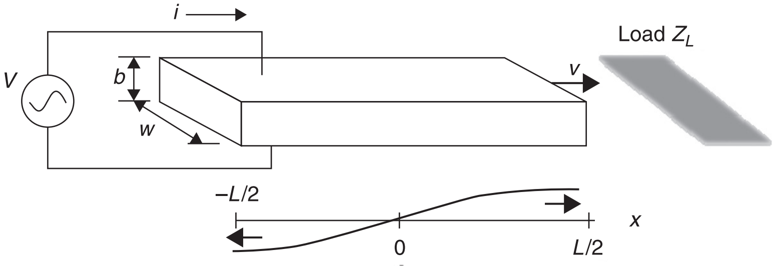

8.1 Longitudinal transducer composed of a piezoelectric ceramic plate.

Here, ω_0, ρ and E are the resonance angular frequency, the density and Young's modulus of the plate, respectively. The resonance condition is

$$L = \frac{\pi}{\omega_0}\sqrt{\frac{E}{\rho}}. \tag{8.3}$$

A mechanical load with an impedance z_L is assumed at the end of the plate.

The transducer working at or in the vicinity of the resonance can be modeled by an equivalent electrical circuit as shown in Fig. 8.2, where the mechanical resonance is denoted by a series connection of the equivalent mass l_m and the equivalent compliance c_m. The mechanical loss is represented by r_m. The mechanical resonance frequency is then determined as

$$\omega_0 = \frac{1}{\sqrt{l_m c_m}}. \tag{8.4}$$

The mechanical load z_L is connected in series to the resonance branch, and the current in the branch represents the vibration velocity v at the output end of the transducer. The kinetic energy in this circuit, $l_m v^2/2$, should be equal to the kinetic energy of the actual plate transducer. Then,

$$\frac{1}{2} l_m v^2 = \int_{-L/2}^{L/2} \frac{1}{2} \rho b w v^2(x)\, dx. \tag{8.5}$$

Evaluating the integral, the equivalent mass can be calculated as

$$l_m = \frac{\rho b w L}{2} \tag{8.6}$$

Equation 8.6 shows that the equivalent mass is equal to half the total mass of the transducer. The equivalent compliance can be derived from Eqs 8.3, 8.4 and 8.6, or by comparing the reactive energy stored in c_m with the total elastic energy in the transducer.

The mechanical branch is connected to the electrical one through the force factor A. The capacitance of the plate C_d, which is called 'damped capacitance' or 'blocked capacitance', is connected to the electrical terminal in parallel with the

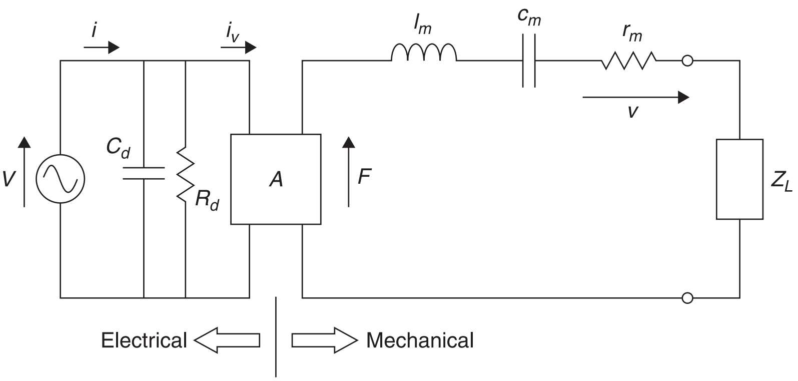

8.2 Equivalent electrical circuit with lumped constants.

dielectric loss R_d. For the vibration mode considered, the damped capacitance can be written simply as:

$$C_d = \frac{\varepsilon_{33}\varepsilon_0 Lw}{b}, \tag{8.7}$$

where ε_{33} and ε_0 are the permittivity of the material and the vacuum. The force factor is introduced as an analogy of an electrical transformer, relating the force F and the velocity v with the voltage V and the current i_v, respectively.

$$\begin{cases} Av = i_v \\ AV = F \end{cases} \tag{8.8}$$

The motional current i_v is a virtual current proportional to the vibration velocity. The total current i, measured at the electrical terminal of the transducer, is assumed to be the sum of the motional current and the reactive current flowing to the damped capacitance C_d.

Different equivalent circuits should be defined for different resonance modes, since the circuit is valid only around the specific resonance frequency.

8.3 Electrical measurements

Figure 8.3 illustrates the typical frequency responses of the admittance $Y = i/V$ measured across the electrodes of the transducer. The amplitude $|Y|$ and phase angle $\angle Y$ of the admittance are separately displayed on the same frequency axis f ($= \omega/2\pi$). The amplitude is usually shown in log scale. Two resonances appear in this figure: the first is the fundamental mode while the second is the third mode. Even-order modes cannot be excited using the uniform electrodes shown in Fig. 8.1, and only the responses for odd-order modes are observed. We will focus on the fundamental resonance.

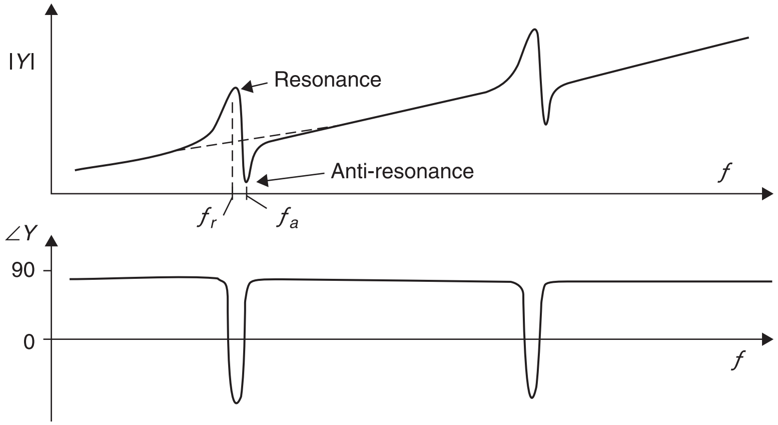

8.3 Typical frequency responses of the electrical admittance of a piezoelectric transducer.

The admittance shows a peak at the resonance frequency, f_r, then it drops rapidly and has a minimum value at the so-called 'anti-resonance frequency', f_a. The resonance frequency observed here, f_r, is slightly lower than the mechanical resonance frequency, f_0 (= $\omega_0/2\pi$), given by Eq. 8.4. If the admittance near resonance is re-plotted in the complex plane, the trajectory by frequency has a circular shape, as shown in Fig. 8.4. This is sometimes called an 'admittance loop'. We will analyze the loop by comparing it with the simplified equivalent circuit illustrated in Fig. 8.5.

The mechanical components l_m, c_m and r_m are moved to the electrical branch by multiplying or dividing by the factor of A^2:

$$\begin{cases} R_m = r_m / A^2 \\ L_m = l_m / A^2 \\ C_m = A^2 c_m \end{cases} \quad [8.9]$$

The dielectric loss is omitted for simplicity, while the mechanical load is removed ($z_L = 0$), assuming a free condition at the end of the transducer. The mechanical resonance frequency f_0 can be written as

$$f_0 = \frac{1}{2\pi\sqrt{L_m C_m}}. \quad [8.10]$$

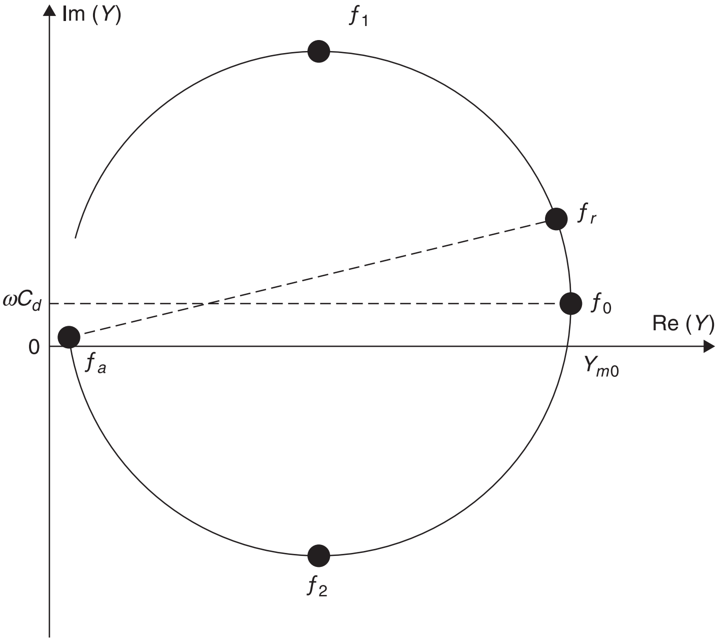

8.4 Admittance loop around the resonance frequency.

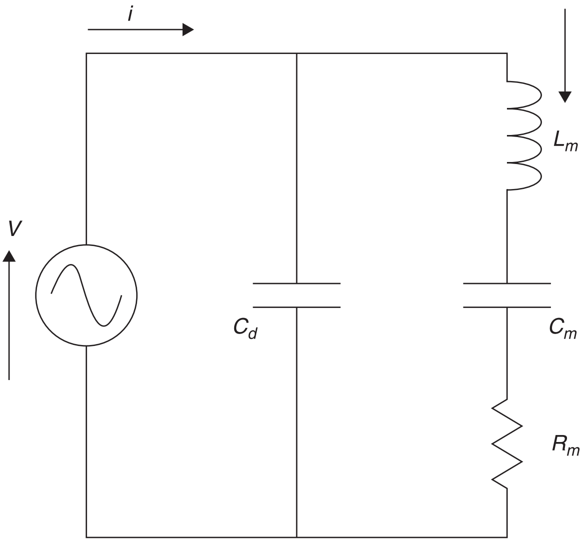

8.5 Simplified equivalent circuit model.

At this frequency, the real part of the admittance has a maximum as shown in Fig. 8.4. The diameter of the loop Y_{m0} is referred to as 'free motional admittance', and is equal to the inverse of the mechanical loss R_m. This means that we can find the value of R_m in the circuit from Y_{m0}:

$$R_m = 1/Y_{m0} \tag{8.11}$$

Then, the quality factor, Q, of the resonance can be estimated from f_0, f_1 and f_2 as

$$Q = \frac{f_0}{f_2 - f_1}. \tag{8.12}$$

Here, f_1 and f_2 are the frequencies where the imaginary part of the admittance is at the maximum and minimum values, respectively, and the amplitude of the admittance in the mechanical branch is $1/\sqrt{2}$ of that at the mechanical resonance frequency. Equation 8.12 is an approximate expression valid for large Q (>10). Most piezoelectric transducers have a high Q value ranging from 100 to over 1000, and Eq. 8.12 can be used in most cases. Using Q, the equivalent mass L_m is calculated as

$$L_m = \frac{QR_m}{2\pi f_0}. \tag{8.13}$$

The compliance C_m is found from Eq. 8.10. When a mechanical load is applied to the mechanical output of the transducer, the diameter of the admittance loop becomes smaller.

If the admittance is measured at frequencies far from the resonance, the damped capacitance, C_d, and its loss can be evaluated. The electro-mechanical coupling factor, k_v^2, is expressed as the ratio of the compliance C_m to the electrical capacitance C_d, and is usually measured from the resonance and anti-resonance frequencies using the approximation

$$k_V^2 \approx \frac{2(f_a - f_r)}{f_a}. \qquad [8.14]$$

To find the mechanical values for the resonant components l_m, c_m and r_m, we need to find the force factor A through vibration velocity measurements using laser Doppler velocimetry and the simple relations shown in Eqs 8.8 and 8.9.

It is easy to calculate the force factor for a simple transducer, such as the plate transducer described here. The motional current is an integral of the flux density, D, over the entire electrode

$$i_v = j\,\omega \int_s D dS, \qquad [8.15]$$

where $j^2 = -1$. D is the product of the piezoelectric constant k_{31} and the longitudinal stress T. The stress is calculated from the gradient of the longitudinal displacement u:

$$T(x) = E\frac{\partial u}{\partial x} = \frac{\pi E v}{j\omega L}\cos \pi \frac{x}{L}. \qquad [8.16]$$

From Eqs 8.15 and 8.16, the force factor A is calculated as

$$A = 2wEd_{31} = 2wd_{31}/s_{11}, \qquad [8.17]$$

where s_{11} is the compliance of the material. The electro-mechanical coupling factor of the transducer, k_v^2, which can be estimated from C_m and C_d, is expressed using the coupling factor of the material k_{31}^2 as

$$k_V^2 = \frac{8}{\pi^2} k_{31}^2 \qquad [8.18]$$

This relation is generally used to evaluate the coupling factor of materials from the resonance measurement of a plate-shaped specimen.

Constants in the equivalent electrical circuit are evaluated through measurements of electrical admittance as a function of frequency around resonance as described in this section. Commercial impedance analyzers are widely used to carry out admittance measurements of transducers. A combination of a PC-controlled function generator and an A/D converter board is also a practical set-up for the measurements. There are two ways to measure the admittance: under constant voltage or under constant current. The former means that the vibration velocity changes with frequency, while the latter is a measurement under constant vibration velocity. The two give the same results when the vibration strain is limited to be under a small value. But, for measurements in the high-vibration strain region, the two methods exhibit different results since the circuit constants vary with the vibration amplitude due to non-linear effects.

8.4 Characterization of piezoelectric transducers under high-power operation

In general, the loss factor increases in the high-vibration amplitude region, and the increase in the loss causes a temperature rise. The temperature rise reduces the resonance frequency. In addition, the material is softened due to a high level of vibration strain. This also has the effect of lowering the resonance frequency. We sometimes encounter difficulties in making stable measurements of a resonance curve as described in the previous section. A computerized system is a powerful tool for measuring the admittance characteristics in the high-amplitude region. However, it is difficult to avoid the effects of the temperature rise. A piezoelectric ceramic transducer can be broken, in some cases, because of heating beyond the Curie temperature of the material.

In order to eliminate the effect of the temperature rise, the measurements should be completed in a short time. In this section, a transient response method (Umeda *et al.*, 1998) for making rapid measurements will be introduced.

The set-up for the measurement is shown in Fig. 8.6. A specimen transducer is excited by a continuous wave voltage near the resonance frequency, ω. After the vibration velocity has reached the required level, the electrical terminal is short circuited at $t = 0$. The short-circuited current, which is identical to the motional current, i_v, is measured and recorded for $t > 0$. The current shows a decay oscillation at the resonance frequency, ω_0, as illustrated in Fig. 8.7, and is proportional to the vibration velocity. The vibration velocity should be measured simultaneously. The duration for applying the voltage should be as short as possible to avoid temperature changes, and is less than 0.1 s for ordinary transducers. However, we should try to raise the velocity amplitude as much as possible.

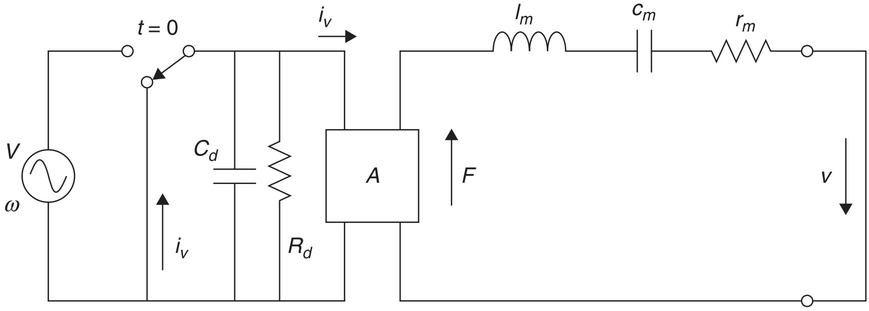

8.6 Transient method for measuring high-amplitude characteristics.

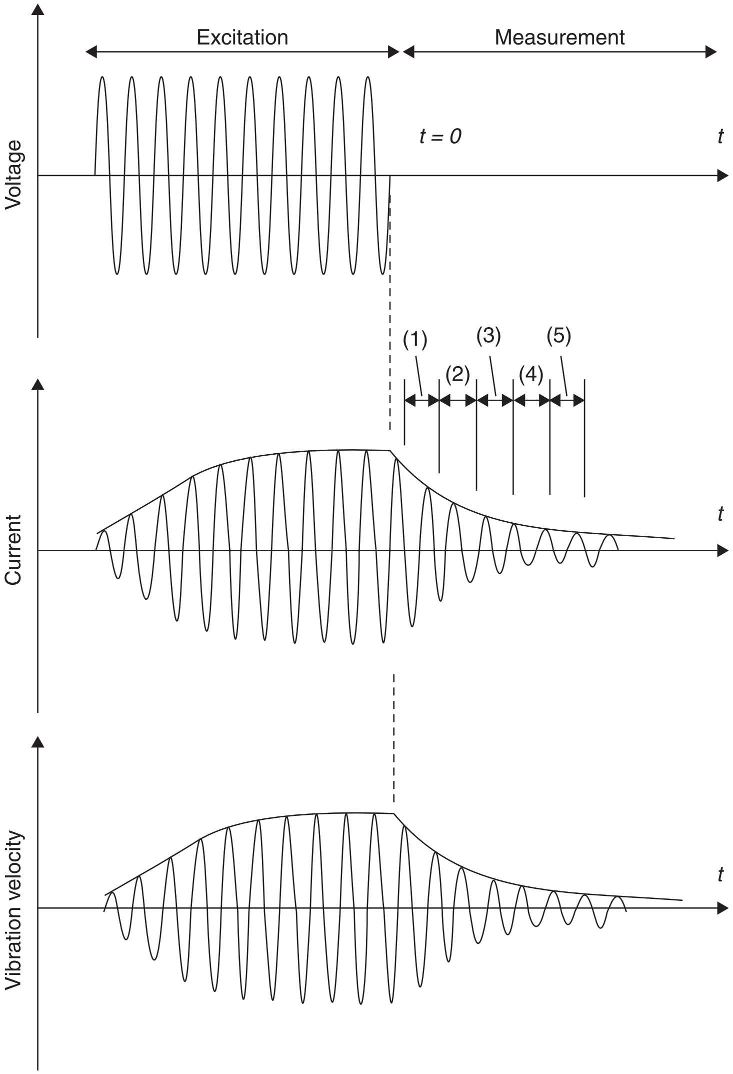

8.7 Waveforms observed in the transient method.

Carefully observe the decay oscillation of the current or the velocity by dividing it into many sections (1), (2), (3), etc., as indicated in Fig. 8.7, because the circuit constants vary with the vibration amplitude during the decay. For every section, the oscillation waveform is fitted by a curve $I_n \exp(-\alpha_n t)\sin(\omega_{0n} t + \phi_n)$. α_n and ω_{0n} are the attenuation constant and the angular resonance frequency for the nth section. The quality factor, Q_n, for the nth section can be determined as $Q_n = \omega_{0n}/(2\alpha_n)$. If we compare the current with the vibration velocity for every section, we can investigate the vibration amplitude dependence of the force factor, i.e. the piezoelectric constant. Figures 8.8 and 8.9 demonstrate the difference between various kinds of PZT materials measured through the transient method (Umeda *et al.*, 1999). The quality factor and the force factor are plotted as functions of the vibration velocity for different PZTs: #A, #B, #E, #N and #C. #A and #B are soft PZTs, while #E, #N and #C are hard ones. Though the soft PZTs have a higher force factor (higher piezoelectric constant), the quality factor is low and decreases

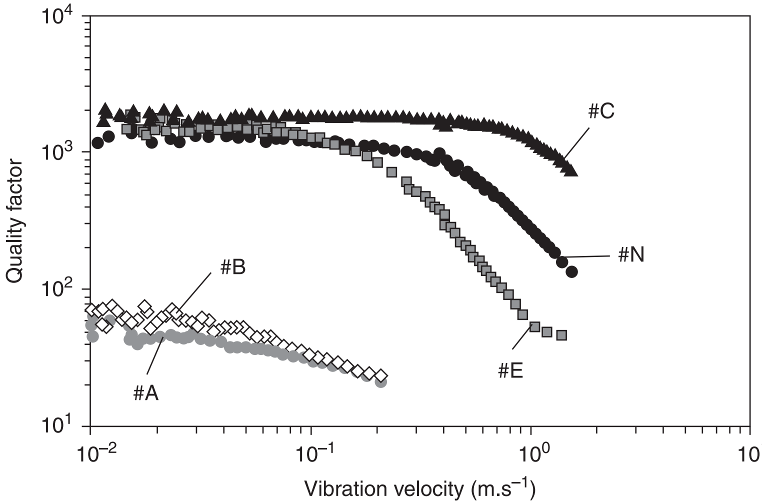

8.8 Quality factor vs. vibration velocity.

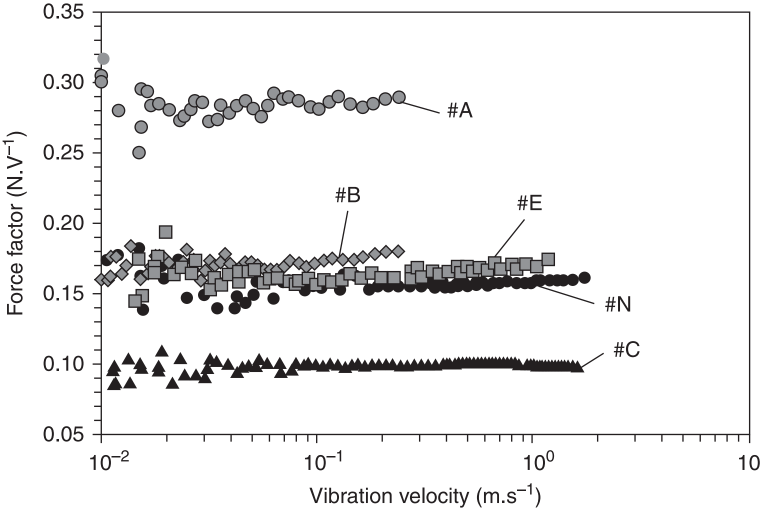

8.9 Force factor vs. vibration velocity.

rapidly with the vibration amplitude. On the other hand, the quality factor for the hard PZTs maintains a value of around 1000 even at 0.1 $m.s^{-1}$ or more. The hard PZT #C has a high quality factor in the high-vibration amplitude region up to 0.6 $m.s^{-1}$. This means that #C generates less heat in high-amplitude operation, and is suitable for high-power devices such as piezoelectric transformers, although its piezoelectric constant is rather low. An interesting point is the different behavior of the quality factors of #E and #N. The quality factor of #E has a higher value than #N at a low-vibration amplitude. However, #E drops more rapidly than #N, and #E shows worse characteristics at higher vibration velocity, over 0.2 $m.s^{-1}$. In general, the quality factor measured at low vibration velocities is indicated in the data sheets supplied by manufacturers. We should be careful when we choose PZT materials for high-power applications.

In the final part of this section, we will consider the maximum vibration velocity amplitude obtained at the end of a longitudinal transducer. The transducer will break mechanically at the center, if the vibration stress exceeds the fatigue limit. The maximum safety stress for extensional deformation ranges from 40 to 70 MPa for PZT ceramics. The vibration velocity at the end of the plate transducer is 1.7 $m.s^{-1}$ when the stress at the nodal point is 40 MPa. In practical continuous operation, the temperature increases quickly, even when the vibration amplitude is lower than this value, and thermal breakdown will occur faster than the mechanical breakdown. But we can conclude that the mechanical limit for the vibration velocity of a piezo-ceramic transducer is 1–2 $m.s^{-1}$. The kinetic energy stored in the transducer at these high amplitudes will reach a very high value. This high energy density of piezoelectric transducers attracted engineers, and was one of the motivating forces behind the development of high-power piezoelectric devices, such as ultrasonic motors and piezoelectric transformers.

8.5 Load test

The output acoustic power and efficiency of high-power transducers is measured by applying a mechanical load using an electrical power meter. Figure 8.10 illustrates a set-up for a load test. A large disk radiator is connected to the transducer under test via a transmission bar, and is immersed in water. Reflections from the water vessel's wall and bottom and the water surfaces should be minimized using an appropriate absorber. The radiator vibrates in an extensional mode, and both surfaces are loaded by the water. The input electrical power to the transducer, P_L, is measured and compared with the input power, P_0, under the no-load condition. The measurements should be carried out with the same vibration velocity under both the loaded and no-load conditions. The output acoustic power can be estimated from the difference $P_L - P_0$, since P_0 is wholly dissipated in the transducer under test. In general, a higher voltage is needed under the loaded condition to obtain the same vibration velocity as for the no-load case. The difference in the dielectric loss caused by the different voltages should

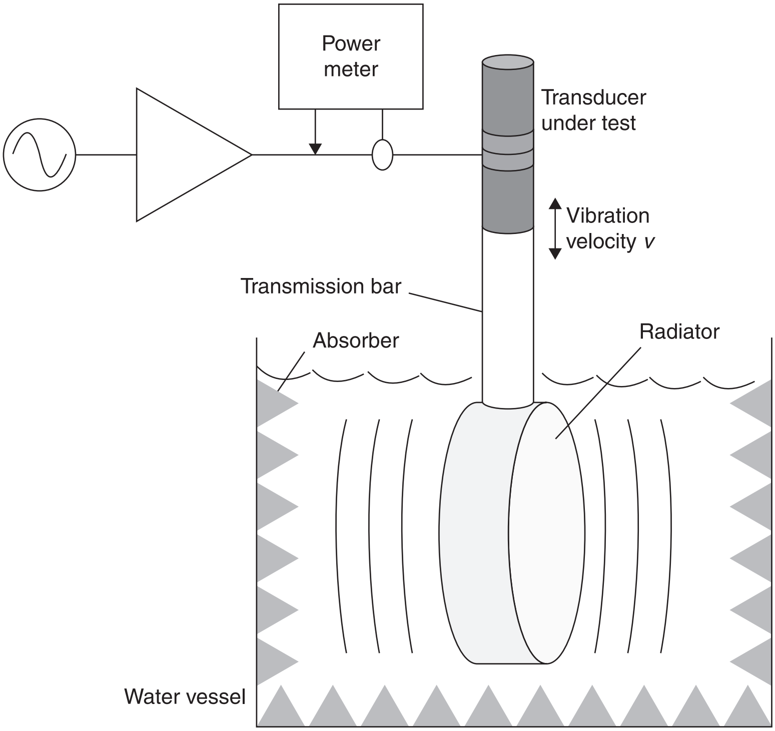

8.10 Transducer load test.

be compensated appropriately. The efficiency of the transducer is estimated from the ratio of the output acoustic power to the input electrical power, and reaches over 95% for the optimum load condition for Langevin transducers using PZT ceramics (Mori *et al.*, 1984).

This method can be used for different kinds of loads such as polymer specimens and other work pieces. Another transducer of the same type can be used as a dummy load, where the electrical port of the dummy transducer is terminated with an electrical resistor of the appropriate value. An inductor is often inserted in addition to the resistor in order to compensate the damped capacitance of the dummy load transducer.

8.6 Summary

The basic theory of the electrical evaluation of piezoelectric transducers has been explained in this chapter. The impedance/admittance measurements as functions of frequencies are easily carried out in the lower voltage region using a commercial impedance analyzer. The same measurements are possible with a combination of a computer-controlled signal generator and an A/D converter board. In the higher vibration amplitude region, both high strain and high temperature cause changes in the transducer characteristics; the loss factor especially increases rapidly as the vibration stress increases in ceramic transducers. The transient method is a powerful tool for high-power characterization of ultrasonic transducers. It should be noted that the quality factor given in the data sheets provided by manufacturers of piezo-ceramics is the value measured under low-vibration stress conditions. The loss factor increases dramatically in some piezoelectric ceramic materials at higher vibration stress. One should be careful when choosing piezoelectric materials for high-power applications.

A high-power load test is sometimes carried out using a water vessel or a dummy load transducer. The output acoustic power and the efficiency can be estimated by measuring the input electrical power.

8.7 References

Mori E, Ueha S, Tsuda Y, Kaneko S, Okada K, Masuda M and Ohoya K (1984) Load test of bolt-clamped Langevin type vibrator, *Jpn J Appl Phys*, 23, 209–11.

Umeda M, Nakamura K and Ueha S (1998) The measurement of high-power characteristics for a piezoelectric transducer based on the electrical transient response, *Jpn J Appl Phys*, 37, 5322–5.

Umeda M, Nakamura K and Ueha S (1999) Effects of vibration stress and temperature on the characteristics of piezoelectric ceramics under high vibration amplitude levels measured by electrical transient responses, *Jpn J Appl Phys*, 38, 5581–5.

9

Laser Doppler vibrometry for measuring vibration in ultrasonic transducers

M. JOHANSMANN and G. WIRTH, Polytec GmbH, Germany

Abstract: An experimental verification of an ultrasonic transducer or ultrasonic tool is an important design step. In this chapter we discuss laser Doppler vibrometry, which is an established experimental method for non-contact measurement of the transducer vibration amplitude and other properties. Basic measurements on a single test point are discussed as well as scanning entire surfaces and special technologies for ultra-high frequencies and for micro-structure devices.

Key words: laser Doppler vibrometry, scanning laser Doppler vibrometry, Mach–Zehnder interferometer, transducer characterization.

9.1 Introduction

To a certain extent numerical methods, such as finite element modelling (FEM), provide information about ultrasonic transducer performance and properties. Experimental verification and model updates of FEM data are frequently needed to achieve an accurate and reliable characterization of a transducer. Furthermore, an experiment allows a quick comparison of different transducer designs or materials.

Optical measurement methods are important because the testing of transducers and materials should be non-destructive and non-mass loading and should have a high spatial resolution. Laser Doppler vibrometry (LDV) is probably the most established optical method meeting these requirements.

Ultrasonic transducers and materials have an extremely wide range of designs and applications, ranging from conventional power transducers and ultrasonic wire-bonding machines to transducer designs for medical applications and surface wave transducers used in surface acoustic wave (SAW) devices. Because ultrasonic transducers cover such a wide field, some fundamental questions should be discussed before selecting the most appropriate measurement tool.

What is the frequency range of the transducer? Although many transducers start in the kilohertz range, medical applications require up to 100 MHz and the range of SAW filters may reach gigahertz.

Which velocity amplitudes are generated by the transducer? We will show later that any LDV has an upper velocity limit given by its optical design. For powerful transducers, especially at higher frequencies, these limits must be taken into account.

How is the vibration of the transducer composed? A Langevin transducer primarily generates a longitudinal out-of-plane (OOP) movement (displacement s_z, velocity v_z) but transversal in-plane (IP) components (s_x, s_y, v_x, v_y) may be present to a certain extent. Depending on the transducer's intended application, these transversal movements cannot be ignored and need to be qualified as well. There are LDV designs, which can simultaneously measure the OOP and IP vibrations to give the three spatial coordinates of the test sample; these are discussed below.

Can the transducer be characterized by a single-point measurement or is knowledge of the complete deflection shape necessary? At a given frequency a Langevin transducer will show a uniform longitudinal movement and one single measurement point may be sufficient for describing the displacement and velocity of the movement. Only at higher frequencies (modes) will the vibration shape become more complex and can no longer be described by a single point. The same is true for a tool attached to the transducer, such as a wire bonder assembly with ceramics capillary (Fig. 9.12). Along the axis of the capillary, there is a nodal line of zero displacement and the peak displacement is at the tip. The exact position of the nodal line as well as the maximum displacement of the tip depends on the mechanical design and the material of the capillary. For describing such a complex arrangement, a larger number of measurement points are needed. LDV technology can be used for both measuring a single point and sequentially measuring several points.

Other considerations are the size of the transducer and the desired diameter of the measuring laser spot (spatial resolution), etc. Based on these parameters (frequency, velocity, mode of vibration, OOP or IP, single or multiple points, large or micro-scale), the appropriate LDV design can be chosen.

In this chapter, we will provide an overview of the most frequently used LDV technologies for applications of out-of-plane and in-plane vibration, single point and sequential scanning, large structure as well as micro-structure and for ultra-high frequencies (UHFs). We limit the discussion to one popular design for each application but naturally there are other possible designs of LDV systems as well.

9.2 Laser Doppler vibrometry for non-contact vibration measurements

The major advantage of laser Doppler vibrometry is the availability of a real-time velocity or displacement signal. Together with a frequency analyser, an instantaneous spectrum of the vibration can be measured. Compared with conventional contact-type transducers, this technique covers an extremely wide frequency range and enables high-resolution velocity or displacement measurements even for very large displacements and velocities.

Basic single-point laser Doppler vibrometry is extendable by scanning the laser beam across a surface to obtain the geometric distribution of vibrational shapes, the so-called operational deflection shapes (ODS). Scanning laser Doppler vibrometry (SLDV) was first introduced in 1984 by the research group of the German car manufacturer Volkswagen AG (Stoffregen and Felske, 1985), who built a full-area scanning LDV (SLDV). Today, SLDVs are frequently applied for measuring the vibrational distribution on ultrasonic transducers and tools and even for visualizing ultrasonic sound fields (Littmann, 2010).

The laser Doppler technique measures the Doppler shift of light scattered in the direction of the light detector (the OOP vibration). An IP vibration measurement can be performed by using two inclined laser beams whereas a complete 3D vibration measurement (OOP plus both IP components) is possible by using three inclined LDV laser beams.

9.2.1 Theory and measurement principle

An interferometer illuminates a test object with a coherent light source (a laser) having a wavelength λ. The object scatters or reflects some of the laser light back to the LDV. When the measurement object is moving with a velocity, v, in the direction of the laser beam, the frequency, f, and phase of the back-scattered light are shifted. Based on the assumption that the velocity, v, is much smaller than the speed of light, the frequency change due to the Doppler effect is given by the simplified equation

$$f = \frac{2|v|}{\lambda} \qquad [9.1]$$

The light source, interferometer, detector and beam focusing optics are usually packaged in the vibrometer measurement head. Fibre optics may be incorporated to reduce the dimensions of the sensor head. By frequency or phase demodulation of the electrical signal from the photodetector, the velocity or displacement output signal is generated as an analogue or digital output signal. LDV signal processing (Johansmann, 2005) is not discussed in detail in this chapter, but one should be aware that standard LDV designs produce a displacement output derived from the signal phase and a simultaneous velocity output from demodulation of the Doppler frequency. An acceleration output can only be achieved by differentiation of the velocity or displacement signal but not directly from the detector signal.

9.2.2 Realization of a single-point laser Doppler vibrometer

The interferometer optical arrangement utilizes optical beating of a reference and the measurement beam. As a result of this interference, the photodetector will see the difference in frequency between the reference beam, f_R, and the measurement beam, f_M, which is equivalent to the Doppler frequency, f_D. The best-known interferometer arrangements for this purpose are the Michelson interferometer and the Mach–Zehnder interferometer.

The laser beam in a Mach–Zehnder interferometer (Fig 9.1) is usually divided by a polarizing beam splitter (PBS1). The measurement beam then passes through the second polarizing beam splitter (PBS2) to the test object. The quarter-wave plate (QWP) rotates the polarization of the back-reflected light about 90° and

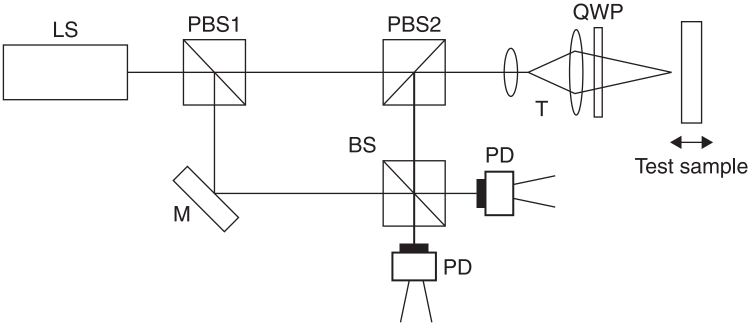

9.1 Mach–Zehnder interferometer.

the beam splitter PBS2 directs the light to the detector. At this detector, the reference and measurement beams have the same polarization but the beams are perpendicular to each other. Therefore, a non-polarizing beam splitter (BS) is used to combine the two beams. Two detectors (PD) are necessary to use the full power of the reference and measurement beams.

The laser (LS) is typically a red (632.8 nm) HeNe laser with low output power. To prevent eye damage, ideally no more than 1 mW should leave the interferometer. Other laser sources, such as a frequency-doubled Nd:YAG laser or a semiconductor laser diode, are possible as light sources and have certain advantages but also serious disadvantages in the standard LDV design.

Homodyne and heterodyne detection techniques

With the optical arrangement shown in Fig. 9.1, the reference-beam frequency, f_R, and the measurement-beam frequency, f_M, are the same if the object is not in motion and no optical beating occurs. The detector signal of the optical beat cannot be used directly to obtain information about the direction of the object's motion. For completeness it should be mentioned that information about the vibration direction can be obtained from a modified homodyne design. As most LDVs today are based on a heterodyne design, this is not discussed further.

In a heterodyne interferometer, a carrier frequency, f_c, is introduced by placing an acousto-optical modulator (a Bragg cell) in the path of either the reference or the measurement beam. Due to the Bragg cell, the photodetectors will receive a constant frequency offset, f_c, if the object is not in motion, a frequency offset $f_c + f_D$ if the object is moving towards the interferometer and $f_c - f_D$ if the object is moving away from the interferometer.

From Eq. 9.1 and assuming a red HeNe laser (632.8 nm) is used as the coherent light source (LS), a velocity of $v = 1\,\text{m.s}^{-1}$ will generate a Doppler frequency of $f_D = 3.16\,\text{MHz}$. Most ultrasonic transducers generate velocities below $10\,\text{m.s}^{-1}$, or 31.6 MHz when expressed in terms of the Doppler frequency.

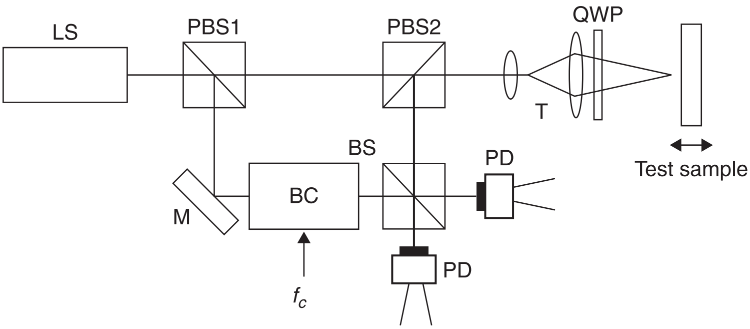

9.2 Heterodyne interferometer with an acousto-optical modulator, the Bragg cell (BC).

For harmonic vibration with frequency, f_{vib}, the bandwidth BW of the heterodyne signal can be practically estimated to be limited to

$$BW = 2(f_D + f_{vib}) \tag{9.2}$$

Consequently the carrier frequency, f_c, has to be chosen to be at least $f_D + f_{vib}$. With the popular centre frequency 40 MHz and a red HeNe laser, this condition is maintained up to a peak velocity of about 10 m.s^{-1} as long as the vibration frequency does not exceed a few megahertz. The maximum frequency of the transducer vibration, f_{vib}, should not exceed approximately half the carrier frequency. As a rule of thumb, vibration frequencies up to $0.5 f_c$ can be measured with negligible distortion, as long as the vibration amplitude does not exceed roughly 50 nm (for $\lambda = 632.8$ nm).

When measuring high-frequency vibrations, the required bandwidth and centre frequency are often dominated by the vibration frequency, f_{vib}, rather than by the Doppler frequency, f_D. The condition $f_{vib} \leq 0.5\, f_c$ is not relevant for ultra-high frequencies when the displacement amplitude is very small (nanometre or sub-nanometre). Refer to Rembe *et al.* (2006) for a detailed explanation of these relations. To summarize, with the frequently used Bragg cells operating at $f_c = 40$ MHz, the vibration velocity is limited to about ±10 m.s^{-1} and the vibration frequency to about 20 MHz. These parameters are listed in Table 9.1. For special ultrasonic transducers with higher frequencies or higher velocities, a different interferometer design with a much higher carrier frequency will be needed.

A Mach–Zehnder interferometer can be realized in many different designs: as a single package of laser and interferometer (Fig. 9.3), by using optical fibres to separate the laser from the interferometer or by using an optical fibre as part of the interferometer for guiding the measurement beam to the test object. Each design has its particular advantages but also limitations: for measuring a high-power large ultrasonic transducer, a bulk single package interferometer has the advantage of a large stand-off distance. Fibre-optic interferometers are more convenient to handle and provide a smaller laser spot, and are used to test miniature transducers, wire bonders or microelectromechanical system (MEMS) devices.

Table 9.1 Typical measurement parameters achievable with a Mach–Zehnder interferometer with 40 MHz carrier frequency and HeNe laser ($\lambda = 632.8$ nm)

Property	Ranging from
Velocity range	$< 0.1\,\mu m.s^{-1}$ to $\geq 10\,m.s^{-1}$
Displacement range	several picometres to > 1m
Frequency range	DC to ≥ 20 MHz
Measurement distance	~20 mm* to > 20 m
Laser spot diameter	< 1 µm* to > 50 µm

* In combination with a microscope objective.

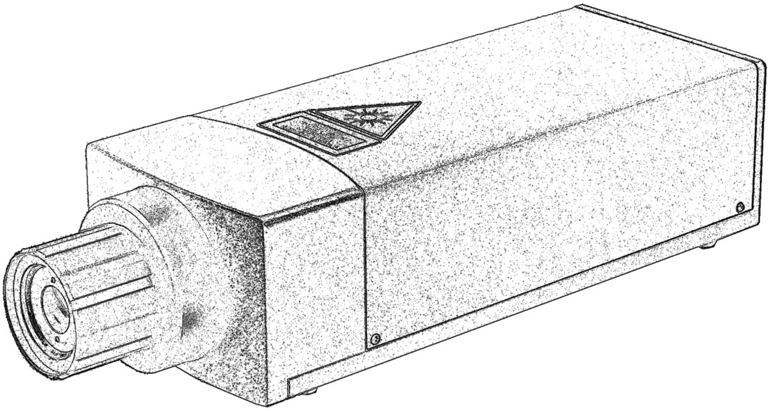

9.3 Compact Mach–Zehnder interferometer.

Various applications of ultrasonic transducers and devices require the measurement of the in-plane vibrations as well as the out-of-plane vibrations at the same location. In order to measure the in-plane vibrations and out-of-plane vibrations simultaneously, a special set-up consisting of three laser Doppler vibrometers has been developed. The device measures three vibration signals at different angles by positioning the three laser spots at exactly the same measurement location. Knowing the vector of each beam, the vibration data can be converted into the orthogonal coordinate system of the measured object. Thus, the vibration data in the direction of the three laser beams must be transferred into an orthogonal coordinate system by applying a coordinate transformation.

A simplified model of a 3D laser Doppler vibrometer is shown in Fig. 9.4. It has two laser vibrometers, one measuring one IP and the other the OOP component of vibration. Adding a third LDV would provide all three vibration components. A 3D LDV is shown in Fig. 9.5.

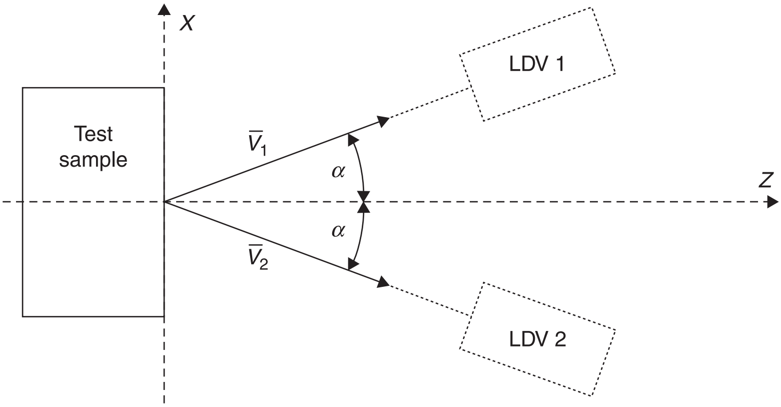
X
Test sample
LDV 1
LDV 2
$\overline{V}_1$
$\overline{V}_2$
α
α
Z

9.4 Simplified 2D model of a 3D LDV; two LDV beams point at the same spot; the angle to the *z*-axis is α, the *x*-axis is the in-plane axis.

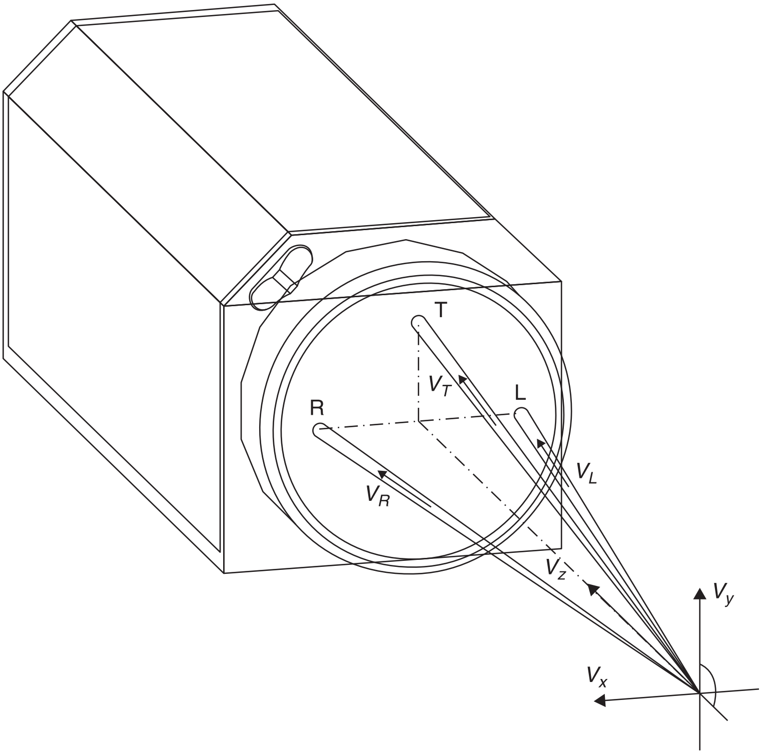
T
V_T
L
R
V_L
V_R
V_z
V_y
V_x

9.5 3D LDV in a single-point design. Three interferometers are built into one package using a common focusing lens.

In this model, the components of the velocity of the vibrations in the *x* and *z* directions, v_x and v_z, are calculated as:

$$v_x = \frac{v_1 - v_2}{2 \cdot \sin\alpha} \quad [9.3]$$

$$v_z = \frac{v_1 + v_2}{2 \cdot \cos\alpha} \quad [9.4]$$

Generally, the obtainable accuracy is different for the out-of-plane and the in-plane components of the vibration signal. This is due to the fact that the angles between the laser beams are less than 90° and, therefore, the sensitivity for in-plane vibrations is lower than for out-of-plane vibrations.

9.2.3 Principles of the scanning laser Doppler vibrometer

In general, an ODS is the excited motion for two or more degrees of freedom (point and direction) on a device or structure. An ODS can be shown either in the frequency domain or in the time domain. This definition of a 'shape' requires that all of the measured responses have the correct magnitude and phase relative to each other. In order to measure the ODS of an ultrasonic transducer or tool, measurements at several points are necessary, either by traversing a single-point LDV from point to point or, more efficiently, by using scanning laser Doppler vibrometry (SLDV). By scanning the laser beam over the object, a series of single-point measurements can be acquired sequentially with a very high spatial resolution. In the analysis of the data, all points are animated simultaneously and the ODS of the transducer can be visualized.

In SLDV, two servo-controlled galvanometer optical scanners (Fig. 9.6) steer the laser beam very accurately in the *x* and *y* directions over the structure. There is an initial teaching process using predefined scan points, after which it is possible

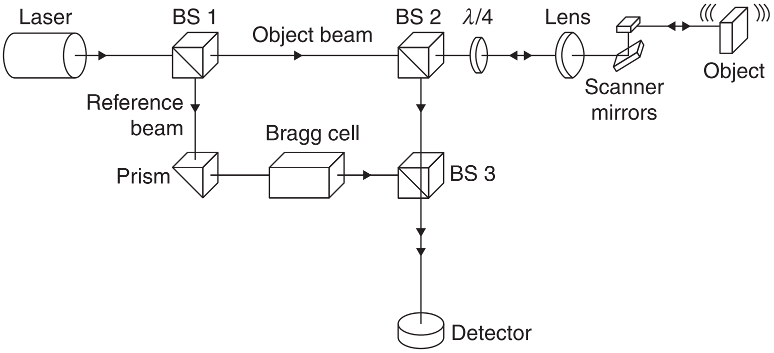

9.6 Simplified optical scheme of an SLDV measurement head.

to use an automated scan to measure the vibration behaviour of each point scanned. There are alternatives to galvanometer-type scanner motors but these are not yet commercially available.

Sequential point-by-point measurements can only be combined in one data set under the condition that the vibration is repeatable. For ultrasonic transducers this condition is fulfilled if the transducer is vibrating in a stationary state or if the vibration is repeatable, e.g. a repeatable transducer excitation with a burst signal or a wire-bonding tool, which repeatably touches the bond pad or substrate.

During the scanning process, stationary conditions are needed, which cannot always be maintained for long periods of time. Thus it is desirable to perform the entire scan as quickly as possible. The time needed to acquire the data for a single point is given by

$$W_t = \frac{k}{f_S} \tag{9.5}$$

where W_t is the time window, k is the number of samples and f_S is the sampling frequency. Further, the sampling theorem must be fulfilled

$$f_S > 2f_{vib} \tag{9.6}$$

where f_{vib} is the maximum vibration frequency.

In the example in Section 9.3.2, the wire-bonding transducer operates at 60 kHz. Thus a sampling frequency $f_s = 200$ kHz is appropriate. If the number of samples recorded is $k = 5$, then the time window $W_t = 25\,\mu\text{s}$ per point or theoretically 8.7 ms for all 350 scanning points. In practice, for $f_{vib} \geq 1$ kHz the data recording time can be mainly ignored and is not the limiting factor for the measurement duration. The time needed to move the x and y scanning mirrors from point to point and the time for the mirror vibrations to settle are in the order of several milliseconds depending on the mirror size (which is related to the maximum scan angle) and the galvanometer scanner motor response. With a good SLDV design, about 50 scan points per second (20 ms per point) can be achieved, resulting in approximately 7 seconds measurement time in this example.

In general, the frequency of a vibrating device can be measured at nearly every location (except at the nodes of standing waves), but the accuracy of the vibration amplitude depends on measuring at the correct location. In particular, for scanning measurements, where the deflection shapes have to be visualized, the density of the measurement grid is of importance. If the density is too high, the measurement time will increase without any additional benefits. If the density of the measurement grid is too low, the spatial resolution may be not sufficient to detect all antinodes due to spatial undersampling. The necessary grid density can be roughly estimated by the wavelength of the structural vibrations, λ_{min}, which depends on the expected maximum vibration frequency of the sample, f_{max}, and the acoustic velocity of the material c_{mat}:

$$\lambda_{min} = \frac{c_{mat}}{f_{max}} \tag{9.7}$$

In solid materials, the wave velocity has to be distinguished between the velocity, c_{long}, for longitudinal waves and the velocity, c_{trans}, for transversal waves. In general, the velocity for transversal waves is lower than the velocity for longitudinal waves in the same material. Thus the velocity for the transversal waves provides a suitable estimate for the required grid density.

Example: In steel the transversal wave velocity is about 3.255 $m.s^{-1}$. A vibration frequency of 50 kHz in steel will result in a transversal wavelength of about 60 mm. As a rule of thumb the scan point density should be a minimum of 5 to 10 times higher in order to achieve a smooth visualization of the deflection shape. One scan point every 5 to 10 mm might be a good choice. This estimate is valid for a bulk body, whereas in a plate the thickness of the material has to be considered as well. Although the above estimate is good for most measurement conditions, for a thin plate a higher scan point density may be necessary.

9.3 Characterization of ultrasonic transducers and optimization of ultrasonic tools

Many commercial products and tools today require ultrasonic transducers. Some examples are:

- Ultrasonic production tools such as wire bonders and sonotrodes (see below) for ultrasonic welding.
- Ultrasonic toothbrushes and dental scalers, ultrasonic cutting devices, e.g. for medical surgery and ultrasonic endovascular systems.
- Ultrasonic motors and actuators for digital cameras, ultrasonic inhalers, ultrasonic cleaning.
- Ultrasonic sensors and imaging systems for sonography, sonar systems, ultrasonic material testing and ultrasonic parking aids.
- Ultrasonic filters: electromechanical filters such as bulk acoustic wave (BAW) filters or SAW filters.
- PZT [$Pb(Zr,Ti)O_3$] transducers for hard disk drives (HDD), where they are used as secondary transducers for modern terabyte drives, and as piezo-exciters for head gimbal assembly (HGA) resonance tests in quality control.

Ultrasonic devices usually consist of different mechanical and electromechanical components, which need to be tuned and matched to each other to achieve high efficiency combined with low energy consumption.

In general, ultrasonic devices comprise an ultrasonic transducer to transform the electrical energy efficiently into mechanical vibration energy and a transmitter to distribute the mechanical energy and to achieve the required dynamical behaviour. For ultrasonic sensors and ultrasonic filters, there is an ultrasonic receiver to transform the transferred mechanical vibration energy back to electrical energy.

An example of an ultrasonic device is the sonotrode, which is a tool that applies the ultrasonic energy of the transducer to the material to be welded. Sonotrodes are available in many different shapes and sizes depending on the welding material and process.

Most ultrasonic devices are operated at one specific frequency. The optimum operational frequency of an ultrasonic transducer or receiver for a particular application has to be evaluated beforehand by theoretical considerations and may require validation by experiments. Once the best frequency for an application has been found, a suitable transducer must be selected or developed. The development of highly efficient transducers is the result of research into piezoelectric materials. As piezoelectric devices usually have different intrinsic dynamic characteristics, such as resonance frequency, in-plane and out-of-plane vibration amplitudes as well as combined modes, the specific vibration behaviour of each transducer has to be tested using laser Doppler vibrometer measurements. After a transducer has been characterized, the transmitter must be matched to the transducer to ensure the optimum performance of the complete assembly. In Section 9.3.2, the optimization of an ultrasonic tool is described using the example of a sonotrode for ultrasonic welding.

9.3.1 Applications of LDV for studies on ultrasonic transducers

In the previous sections we discussed how LDV allows non-contact measurements with high spatial resolution over a wide dynamic range. As a simple introduction to different LDV applications we start with a flat disk piezo-transducer, as it is widely used for consumer applications, such as buzzers. Using a single-point LDV, the basic properties of such a transducer can easily be revealed, such as resonance frequencies (the frequency response function), the displacement level at the resonance frequency or relations such as the displacement as a function of input power. The frequency response can be found either by sweeping a sinusoidal wave over a range of frequencies or, more efficiently, by applying a broadband signal, such as a frequency chirp or burst, to the transducer. With the latter method the entire frequency spectrum of a single point can be found with a single measurement within milliseconds. Figure 9.7 shows a transducer measured by this type of simple evaluation and Fig. 9.8 gives the frequency spectrum of the transducer. This simple transducer has a large number of resonance frequencies, ranging from 150 Hz to over 30 kHz.

In Fig. 9.8 we can see the frequency response of the transducer and the transducer displacement for one point for a given input signal. In order to visualize the displacement distribution across the transducer (ODS), we can either reposition the laser Doppler vibrometer and successively measure several points on the

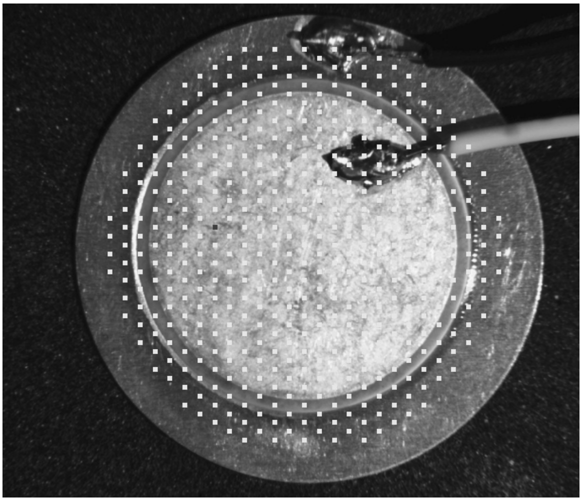

9.7 Simple buzzer-type transducer, 25 mm in diameter.

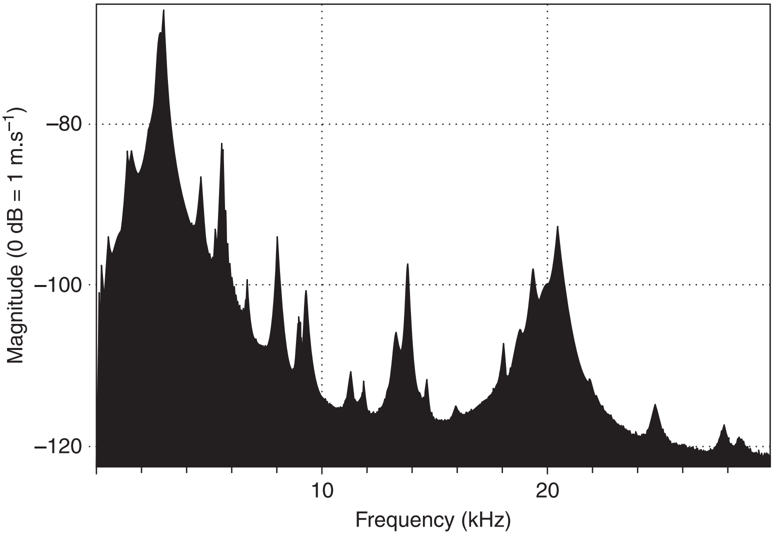

9.8 Frequency spectrum measured using a broadband chirp excitation with 1 V amplitude, start frequency 10 Hz, stop frequency 30 kHz. Peak displacement in the centre of the transducer is 40 nm at 2.856 kHz.

transducer or use a scanning LDV. In Fig. 9.7, the dots indicate the 479 test points measured by a SLDV, which applied a repetitive chirp signal to each test point. As discussed in Section 9.2.3, the repetitive excitation signal is the common phase reference for all measured points so that the transducer's deflection shapes for this

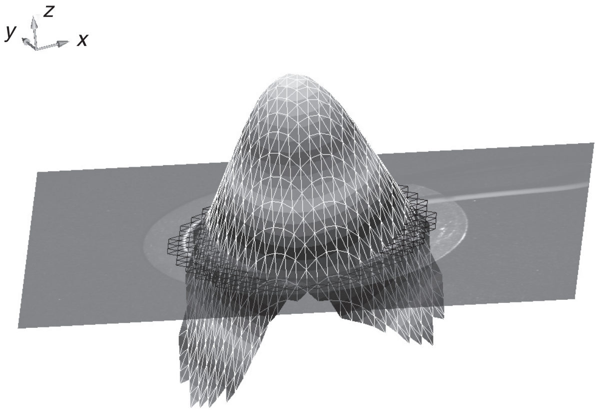

9.9 Transducer movement at 2.856 kHz.

reference can be plotted. In Fig. 9.9 the deflection shape at the resonance frequency of 2.856 kHz is given. As one would expect, the transducer performs an umbrella-like movement at this frequency.

At higher frequencies the complexity of the deflection shape increases. At 5.587 kHz there is a mode with two areas of opposite phase (Fig. 9.10).

Figure 9.10 shows why a common phase reference for all test points is needed: without such a reference we would get the magnitude of the two peaks but we would not realize that they are out of phase and moving in opposite directions. The result would look like Fig. 9.11 and our interpretation of the real movement at this frequency would be wrong.

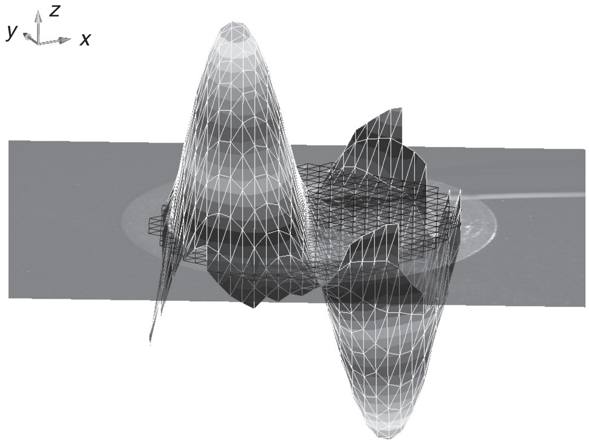

9.10 More complex mode at 5.587 kHz.

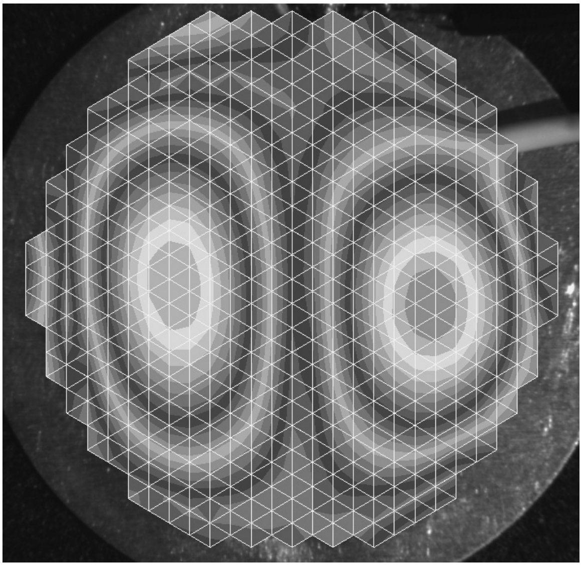

9.11 Same measurement as in Fig. 9.10 but without a phase reference. Only the magnitude of the displacement is shown and the real movement is not obvious.

In this section we described the LDV and SLDV measurement of a very simple transducer. The measurement procedures are the same for more complex transducers, piezoelectrical motors and other ultrasonic devices, as we will see next.

9.3.2 Verification and optimization of ultrasonic tools in industrial production

A large variety of ultrasonic devices are used within mass manufacturing processes, such as wire bonders in the semiconductor industry or sonotrodes for ultrasonic welding. Such devices are manufactured in relatively small quantities compared with consumer products, but they need to be tuned with a high degree of accuracy in order to guarantee high-quality manufacturing during their whole life cycle.

Some ultrasonic devices are manufactured in large quantities for use in consumer products, such as ultrasonic sensors for parking aids in cars, drives for ultrasonic toothbrushes, nebulizers for ultrasonic inhalers and actuators for computer hard disk drives.

For all these devices, the transmitter has to be matched as closely as possible to the ultrasonic transducer. The target of this optimization is the best energy distribution where the actuation is needed.

Due to tolerances in the manufacturing process of the transducer and the transmitter, the resonance behaviour of both components may deviate and not perfectly match each other. In many manufacturing processes, the efficiency of the devices needs to be verified by measurements after manufacture. During the manufacturing process, measurement data may be needed for tuning a device to a desired performance or to a certain resonance frequency.

There is a huge variety of actuation principles and designs for ultrasonic tools. In any particular manufacturing process, the specific design of the ultrasonic tool is a core technology and treated with a high level of confidentiality. For this reason many companies have their own development team for ultrasonic tool design. For experimental verification of transmitter performance and tool characteristics, laser Doppler vibrometry is a well-established technology.

The next three examples demonstrate the capability of LDV and SLDV technology for wire bonder design, a sonotrode with a Langevin transducer and a nebulizer for generating aerosols.

In semiconductor device fabrication, ultrasonic wire bonders of different types (ball bonding, capillary bonder, wedge bonder, etc.) are a standard technology.

A wire bonder using a ceramic capillary is shown in Fig. 9.12. The bonding wire is fed through the capillary. The ultrasonic transducer excites the capillary in

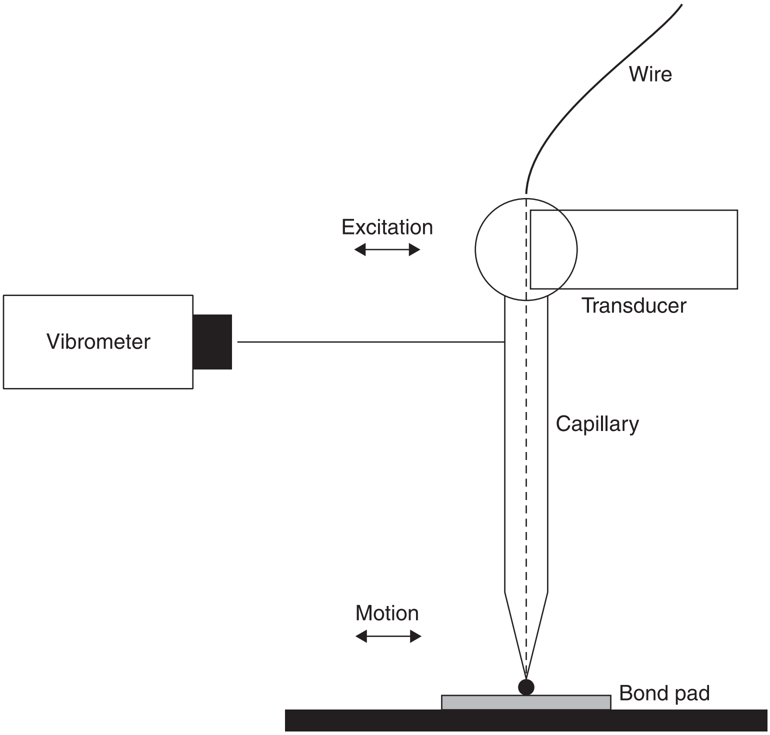

9.12 Capillary wire bonder.

a horizontal direction. The excited vibration mode of the capillary results in a horizontal motion of the capillary tip and the wire touching the bond pad. The combination of ultrasonic energy, heat and pressure welds the wire to the pad. The wire bonder assembly transfers the optimum amount of energy from the transducer to the capillary tip. This is achieved by exciting the second bending mode of the capillary. Furthermore, for a specific bonding process the best combination of capillary material and bonding wire has to be found.

The bending behaviour of the capillary can be evaluated by measuring the amplitude distribution along the capillary by a single-point vibrometer. The wire-bonding tool shown in Fig. 9.12 is measured point-by-point along a vertical line from the transducer side at the top to the tip of the capillary at the bottom. The measurement results are shown in Fig. 9.13. Two different transducer materials are compared in this chart and significant differences in the tip displacement are obvious. The measurements were made during a real bonding process and not in a 'free-air' (unloaded) condition. This test (Miller, 2003) is a perfect example of the use of a single-point LDV. This type of testing is quite time consuming because the sensor head has to be moved manually from point to point along the axis of the capillary and for each point a bond has to be performed. However, the measurements provide very accurate and high-resolution displacement data for the different capillary materials. The measurement of multiple points can be carried out more quickly and more effectively using SLDV as described in Section 9.2.3.

In Fig. 9.14(a), the measurement grid for the SLDV is shown superimposed on the capillary and transducer. The grid has about 350 measurement points, which were manually defined in the video image provided by a camera integrated into

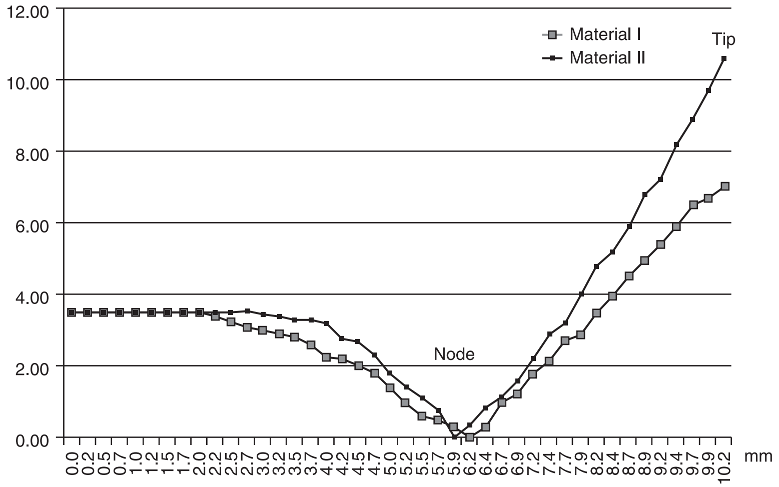

9.13 Displacement distribution of a wire-bonding capillary for two different materials. Bonding time was 5 ms. Measured point-by-point with LDV and manual traversing.

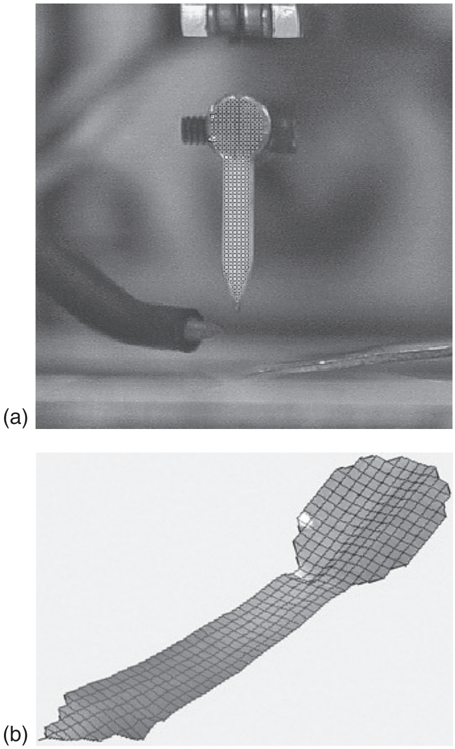

9.14 (a) Capillary-type ultrasonic wire bonder. About 350 scan points are defined on the capillary and the front of the transducer. (b) Deflection shape for the 'free-air' condition (not bonding) at 60 kHz.

the SLDV measurement head. During measurement, the laser beam moves from point to point and for each location the vibration data are stored (time history or complex fast Fourier transform of displacement or velocity). As the capillary is small, the measurement is made over a short distance (typically 300 mm) with a laser beam focused to a few micrometres in diameter. The resulting ODS of the capillary at the operational frequency of 60 kHz is shown in Fig. 9.14(b).

Another popular industrial ultrasonic device is the sonotrode, which is used in ultrasonic welding. It is typically used for welding plastics or plastic-coated packing materials in the food industry. Examples of such packing materials are chip bags, peanut packages, candy bags or milk packages.

The operating principle for ultrasonic welding in the food industry is shown in Fig. 9.15. Two sheets of plastic or plastic-coated paperboard are pinched between a static base, the anvil and the sonotrode. Because of the vertical ultrasonic vibrations of the sonotrode, the molecules of the plastic sheets are excited locally and the packing material is heated immediately in the local area of excitation. The heating causes welding of the thermoplastic material.

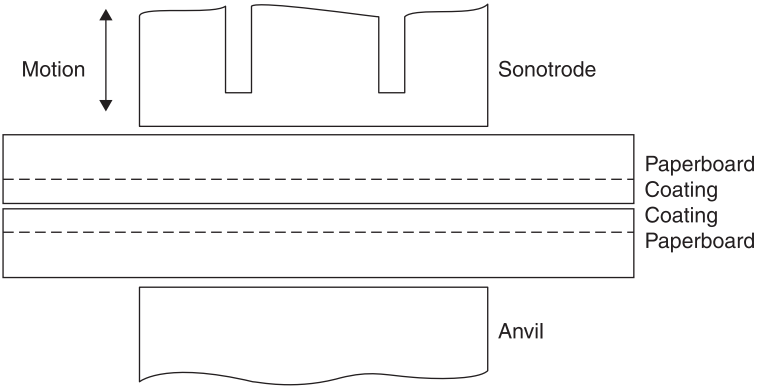
Motion
Sonotrode
Paperboard
Coating
Coating
Paperboard
Anvil

9.15 Ultrasonic welding.

The quality of the welded seam depends on a uniform vibration amplitude distribution at the welding surface of the sonotrode. Thus the vibrational behaviour of the sonotrode is of the utmost importance.

An ultrasonic welding device is shown in Fig. 9.16. It has a Langevin-type ultrasonic transducer, a transmitter, also called the booster, and the welding tool, the

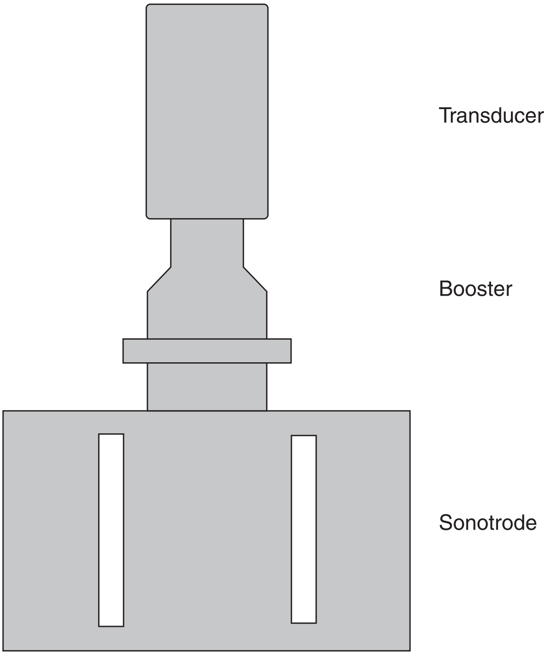
Transducer
Booster
Sonotrode

9.16 Ultrasonic welding device.

sonotrode. The transducer excites the sonotrode in the vertical direction via the booster. The booster is necessary for mechanical impedance matching between the sonotrode and the transducer, to optimize the amplitude of the sound wave. All three components need to be matched in terms of operational and resonance behaviour, which is achieved with the help of laser Doppler vibrometry measurements. Furthermore, the design of the sonotrode has to be tuned exactly to the excitation of the transformation piece in order to ensure a uniform amplitude distribution on the welding surface. As the amplitude distribution on the welding surface of the sonotrode is of the utmost importance, the measurement has to be performed on the lower surface of the sonotrode. Naturally, this is not possible during welding.

Figure 9.17 shows a standard industrial ultrasonic transducer with a sonotrode optimized for welding. Below the sonotrode welding surface there is a mirror, which makes measurement of the lower surface more convenient. The test identifies the resonance frequencies and the sonotrode deflection shape in the x, y and z directions (3D ODS). In order to measure the 3D ODS, a 3D SLDV is used

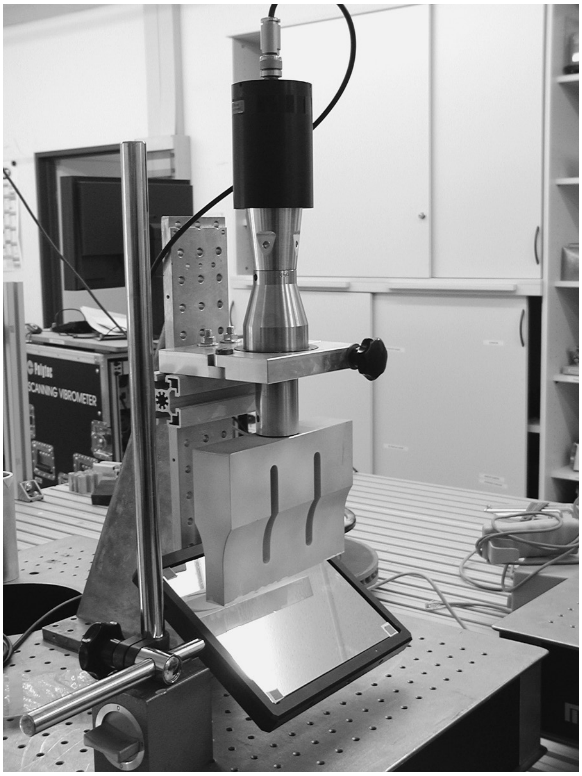

9.17 Measurement of a standard industrial ultrasonic transducer and sonotrode using a 3D SLDV. A mirror is used for easier access to all sides of the device.

(Schell *et al.*, 2005; Johansmann and Sauer, 2005). A 3D SLDV uses three scanning LDVs and a common data acquisition system. During the scanning process the three beams always target the same measurement point but from different positions at different angles.

In order to measure the entire sonotrode, four separate sets of scanning measurements were made and afterwards the different measurement data were combined into one data set by a stitching process. The 3D SLDV used for this test was equipped with an additional geometry laser to measure the distance from the SLDV sensor to the individual test points, which gives the geometry data of the sonotrode as shown in Fig. 9.18.

A total of 2600 points were measured with a frequency bandwidth of 100 kHz (256 kHz sampling frequency) and a frequency resolution of 62 Hz. In order to excite all frequencies simultaneously, a periodic burst signal was applied to the transducer. The resulting frequency spectrum averaged over all points looks very complex and shows a large number of resonances (Fig. 9.19). The design frequency of the sonotrode is 20 kHz, which is not easy to identify.

At most resonance frequencies the sonotrode has deflection shapes that are not suitable due to their non-uniform amplitude distribution on the welding surface, as shown in Fig. 9.20. At 9.94 kHz, most movement is along the centre line (longitudinally) but there is also a strong in-plane component in the transversal direction.

In contrast to Fig. 9.20, at the design frequency of 20 kHz the sonotrode front face shows a nice uniform longitudinal movement (Fig. 9.21). Existing in-plane components have a very low amplitude compared with the main longitudinal

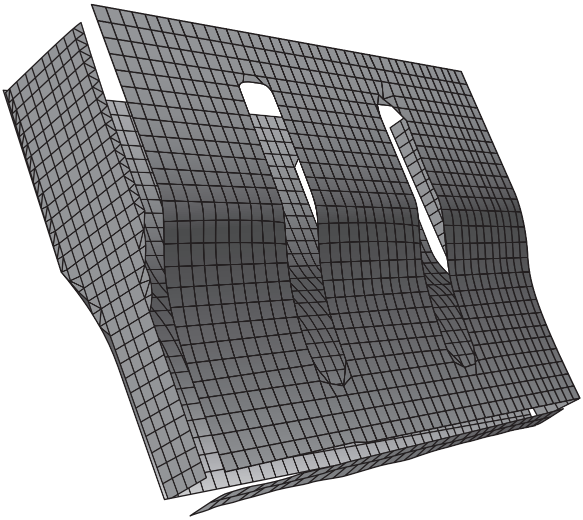

9.18 Geometry of the sonotrode.

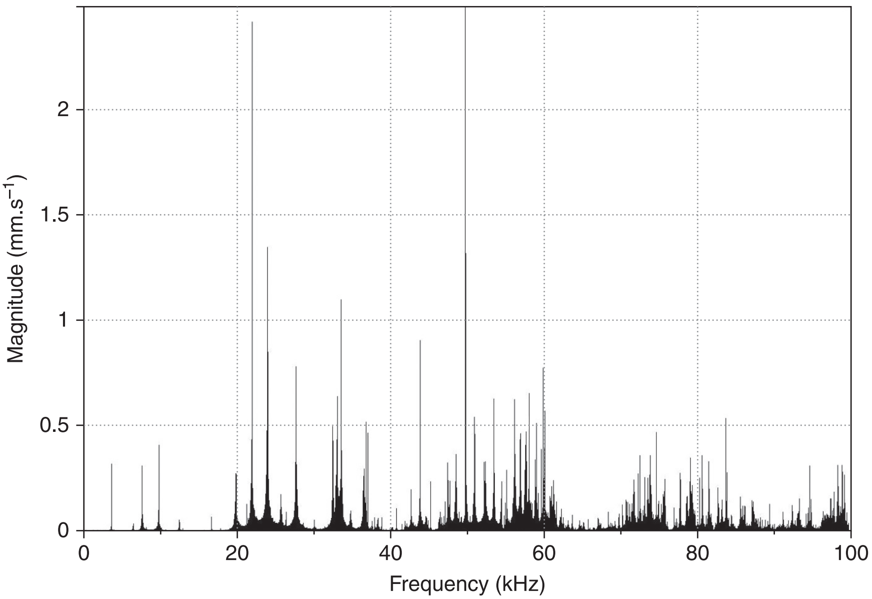

9.19 Frequency spectrum (longitudinal component) ranging from 0 Hz to 100 kHz averaged over all 2600 measurement points.

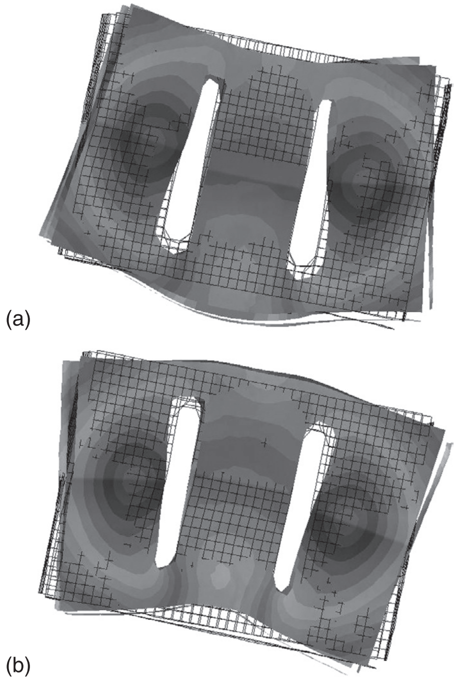

9.20 Deflection shapes for the sonotrode at 9.94 kHz: (a) and (b) have a phase difference of 180°.

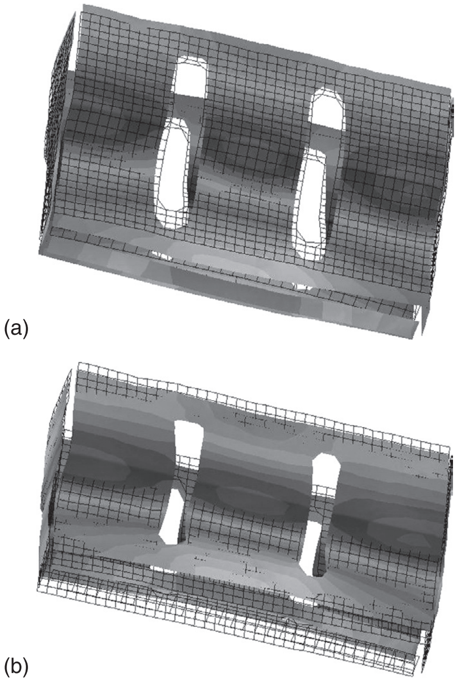

9.21 Uniform movement of the sonotrode front face at the design frequency of 20 kHz: (a) and (b) have a phase difference of 180°.

component. From the measured data a profile across the sonotrode welding surface was calculated, which is shown in Fig. 9.22. The movement of the sonotrode welding surface is not perfectly uniform and shows an increased amplitude in the centre of approximately 2.6 dB.

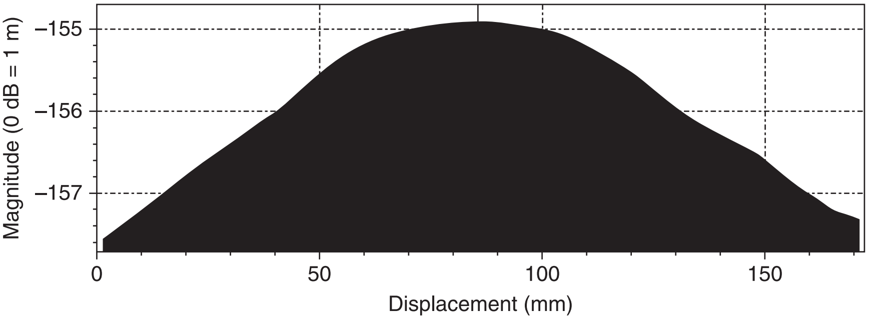

9.22 Profile across the sonotrode front face. The movement is not perfectly uniform but shows an increase in the centre of approximately 2.6 dB.

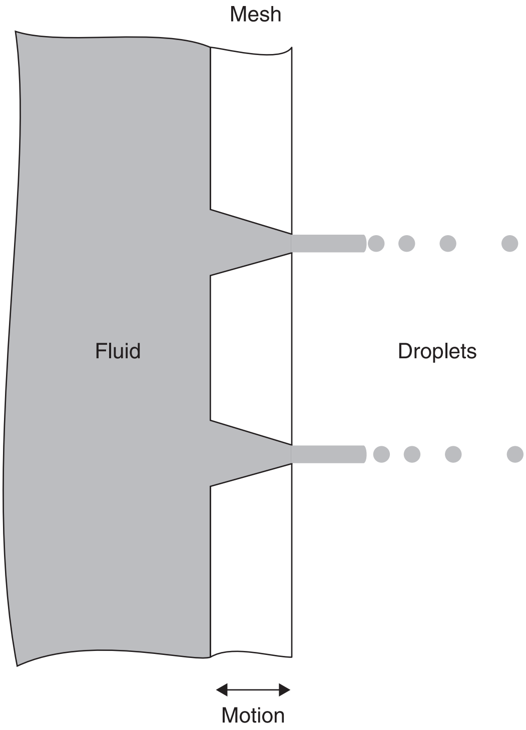

9.23 Droplet generation through ultrasonic mesh vibration.

Another example of a commercial ultrasonic device is the nebulizer in an ultrasonic inhaler. These medical inhalers are frequently used for treating respiratory illnesses. The nebulizer generates an aerosol of a fluid drug for inhalation. The nebulizer should be optimized for high therapeutic efficiency in terms of a short inhalation time and low drug consumption. This is achieved by optimizing the average droplet size and the droplet size distribution. Both parameters can be controlled by the frequency and design of the ultrasonic nebulizer mesh. Figure 9.23 shows droplet generation by a mesh vibrating at an ultrasonic frequency. The fluid on the left is atomized into droplets as it passes through the holes in the vibrating mesh.

The mesh is excited by a piezo-actuator ring as shown in Fig. 9.24. The piezo-actuator ring is fixed on a substrate disk with the mesh attached in the centre. Through the contraction and expansion of the piezo-ring, the substrate is forced into bending vibrations. The bending of the substrate excites the mesh vibrations perpendicular to the piezo-actuator vibration. In order to guarantee the appropriate vibrational behaviour of the mesh, the design of the actuator has to be optimized and the best vibration frequency must be chosen. Afterwards the shape of the mesh has to be matched and the operational deflection shape has to be verified. As

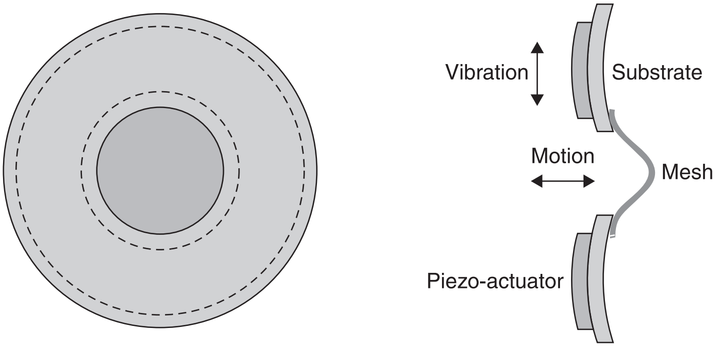

9.24 Excitation of an ultrasonic nebulizer mesh.

the amplitude distribution is important in this application, it is typically measured by scanning laser Doppler vibrometry.

Figure 9.25 shows an ultrasonic nebulizer with the defined measurement grid on top of a video image of the nebulizer, for performing a scanning laser Doppler vibrometer measurement. As significantly different vibration amplitudes of the actuator and the mesh are expected, two separate circular measurement grids were defined on the two components of interest. An outer measurement grid was defined on top of the actuator and an inner measurement grid was defined on the mesh.

Figure 9.26 shows the deflection shape of the actuator at the operational frequency for two different phase angles of the nebulizer. The rotation-symmetric bending mode for exciting a uniform mesh motion can be easily recognized.

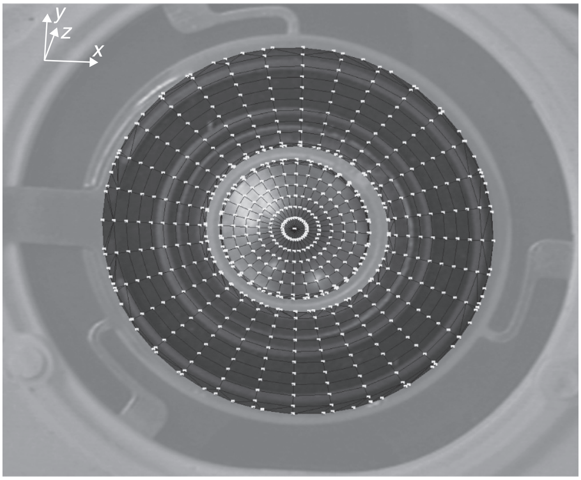

9.25 Ultrasonic nebulizer with measurement grid on the actuator (outer ring) and the mesh (centre) for SLDV measurement.

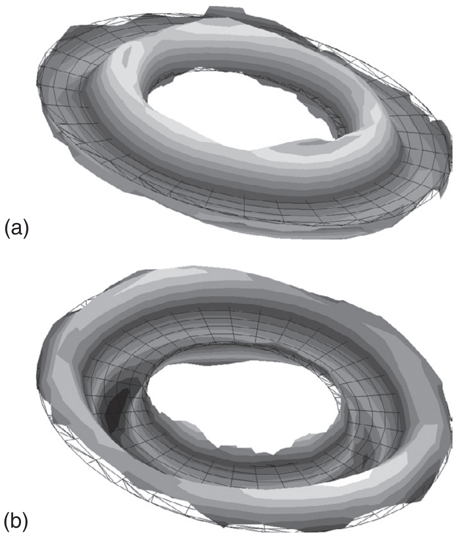

9.26 Two different phases of the rotation-symmetric bending mode of the actuator at the operational frequency.

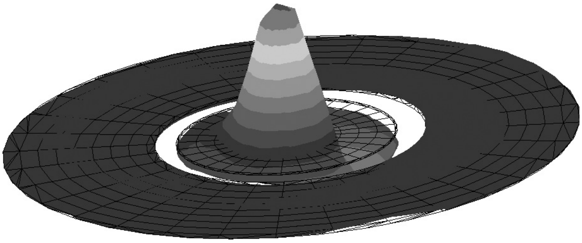

9.27 Rotation-symmetric deflection shape of the mesh at the operational frequency.

Figure 9.27 shows the deflection shape of the excited mesh at the same frequency. It is very uniform and rotation-symmetric. As expected, the amplitude of the mesh is much higher than the excitation amplitude of the actuator in the direction of the mesh vibration.

9.3.3 Visualization of the transducer sound pressure using an SLDV

In Section 9.3.2, an investigation of the ODS of a sonotrode was discussed. For many kinds of transducers the sound field distribution of the propagating waves is of interest. The classical method for measuring sound fields uses pressure probes or microphones but laser Doppler vibrometry can also be used to give a quantitative representation of the distribution of acoustic pressure (Nakamura *et al.*, 2002, 2006). This method is called refracto-vibrometry and makes use of the fact that a pressure change due to a sound wave results in a change of density of the medium and thus in a small change of the optical index of refraction, Δn. A laser beam passing through the medium will undergo an optical path length change and will have a virtual velocity, which is a function of the pressure change in the medium (Zipser and Lindner, 2002; Zipser *et al.*, 2002).

For refracto-interferometry measurements, the scanning LDV is of particular interest because an entire area of sound pressure distribution can be visualized. In 2003, Germany's Bosch Group used SLDV to visualize the sound field of parking and distance sensors for passenger cars (Bosch, 2003); see Fig. 9.28. At every measurement point, the sound distribution is integrated along the path of the laser beam through the medium to the reflector and back to the LDV ($2L$). Repositioning the LDV sensor and measuring from different directions allows a 'CT reconstruction' of the 3D sound field. This was demonstrated by Nakamura *et al.* (2006).

The method of refracto-vibrometry is not limited to measurements of conventional ultrasonic transducers in air but has also been successfully applied to measurements in liquids. Experiments are ongoing as well at much higher frequencies >> 1 MHz.

In order to demonstrate the capabilities of this method we visualized the sound pressure field of the sonotrode discussed in Section 9.3.2 (Fig. 9.29). The SLDV

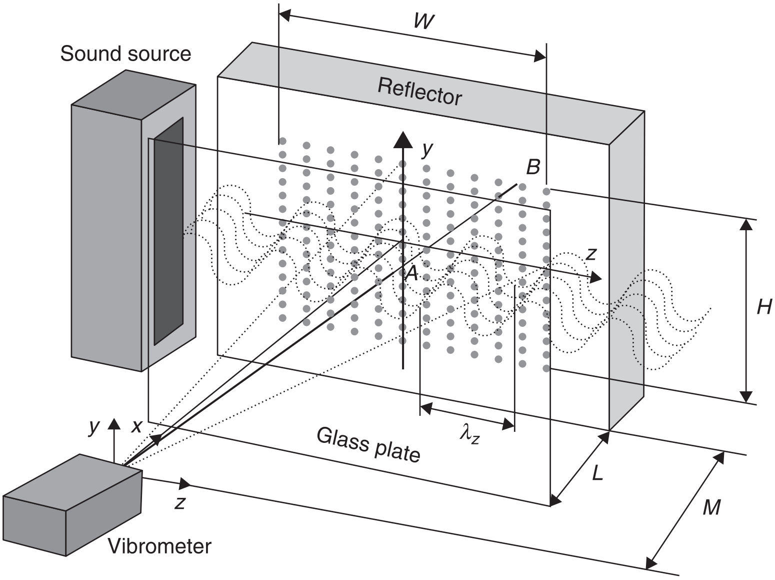

9.28 Arrangement proposed by Zipser and Franke (2008) to use an SLDV for sequential measurement of *N* scanning points within the area *W* in front of an ultrasonic sound source.

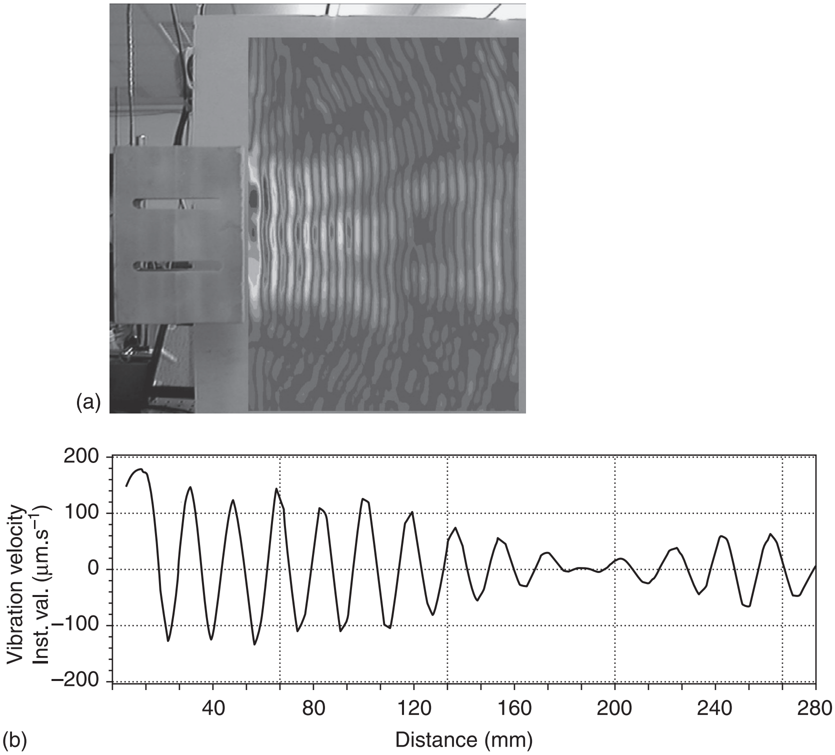

9.29 (a) The sound pressure distribution is visualized for a drive frequency of 20 kHz. (b) Velocity profile along the centre line of a sonotrode from the origin (sonotrode and scan mirror at 0°) to a distance of 270 mm (scan mirror at 20°). Towards the right, the wavelength seems to be increasing because of the increasing scan angle, which results in an error of the geometry of 6% at 20° scan angle.

sensor was placed perpendicular to the direction of the propagating wave. On the other side, a plate with a good scattering surface (painted white) was placed at a distance of about 0.18 m from the sonotrode axis. The measured peak-to-peak velocity was 320 µm.s^{-1}, which is quite a high level and about 10^3 times above the noise level of a typical LDV.

9.4 Enhanced LDV designs for special measurements

9.4.1 LDV design for measurement of high-frequency and high-velocity transducers

The majority of ultrasonic transducers can be characterized with an LDV design as described in Section 9.2.1. But there is an increasing number of new applications for high-frequency or high-velocity transducers in medicine, for specific industrial processes and for transducers used in radio communication (resonators, SAW filter, BAW filter, etc.). A standard LDV based on the popular 40-MHz Bragg cell is limited to a vibration velocity $< \pm 10\,\mathrm{m.s^{-1}}$ and a vibration frequency of about 20 MHz. For very high frequencies or velocities a different optical design is needed. High-frequency measurements require a laser source of higher laser intensity than the HeNe laser typically used in the Mach–Zehnder interferometer design described earlier (Rembe *et al.*, 2006). Different optical approaches have been discussed in scientific papers but most of these designs have never been made commercially available. As an acousto-optical frequency shifter (an AOM), a Bragg cell with sufficiently high frequency is the most obvious approach. But Bragg cells with high-frequency shifts (> 500 MHz) between the zero and first diffraction order beam are not efficient (less than 1%). In the design shown in Fig. 9.30, a specially designed Bragg cell is used combined with a very efficient Bragg cell material with an efficiency of over 90% in the visible region (Rembe *et al.*, 2008). As the maximum shift of this special Bragg cell in the visible region is below 350 MHz, higher shifts can only be achieved with higher diffraction orders and a Bragg-cell design optimized for the highest efficiency in the +1 and −1 orders, resulting in twice the frequency shift.

In order to fulfil the higher laser intensity requirement, a compact green diode-pumped, solid-state (DPSS) laser with frequency-doubled light from a

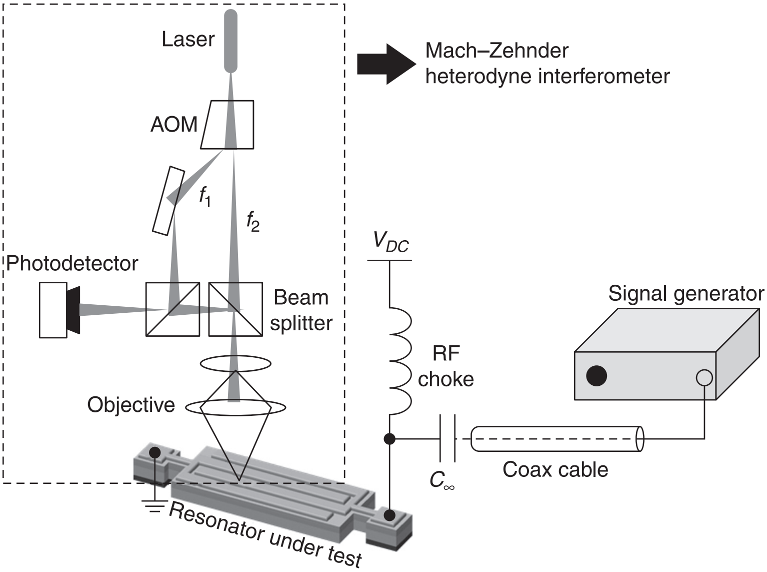

9.30 Optical arrangement of an ultra-high-frequency interferometer for a high-frequency resonator test.

Nd:YAG crystal is used ($\lambda = 532$ nm), providing an interferometer output intensity of about 5 mW. The laser beam is focused down to a spot size of 1 µm^2 resulting in an effective power density of a remarkable 5 GW.m^{-2}. To avoid damaging sensitive samples, the laser beam is triggered and turned on only for the short measurement period.

The AOM divides the laser beam into reference and measurement beams (Fig. 9.30). By using +1st and −1st orders, a frequency offset of 616 MHz is achieved. This allows measurements up to the 600 MHz frequency bandwidth and vibration velocities of 150 m.s^{-1} (at much lower frequencies < 40 MHz as $f_D + f_{vib}$ must not exceed f_c). A further extension of this method to 1.2 GHz is possible for small vibration displacements using a software bandwidth extension algorithm, which is not explained here. A microscope objective focuses the beam onto the device under test.

For a resonator, a single-point measurement at one location may be sufficient, but, in order to understand fully how waves propagate in a surface acoustic device filter or similar device (Fig. 9.31), we must collect data from many points successively. Referring all these measurements to a common phase reference such as the signal generator output, the amplitude and relative phase for each point can be found and the animated deflection shape of the wave motion can be calculated (Fig. 9.32 and Fig. 9.33).

Earlier we said that scanning many measurement points is possible by moving the LDV laser beam across the surface using a pair of galvanometer optical

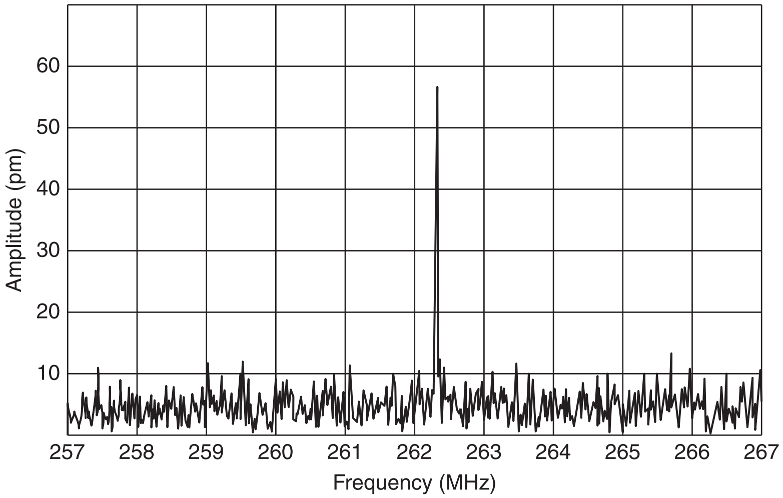

9.31 Spectrum of a SAW filter with a resonance at 262 MHz. An ultrasonic transducer generates a travelling wave, which is measured at one point. The displacement amplitude at 262.3 MHz is as small as 56 pm.

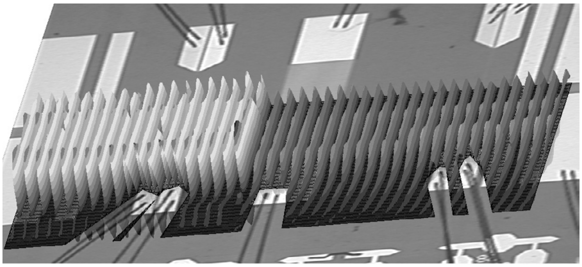

9.32 Photograph of a power SAW with a symmetrically excited transducer at 130 MHz. Superimposed on the image is the deflection shape: on the left there is a standing wave and on the right the wave is travelling from the centre to the right.

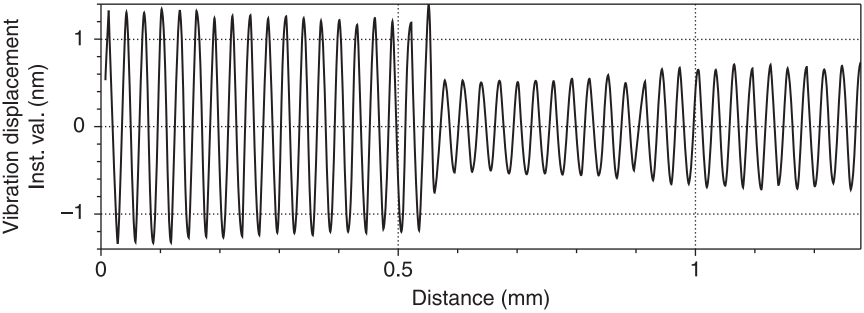

9.33 Displacement profile of the device shown in Fig. 9.32.

scanners. In this example, a different approach was used: the laser beam of the UHF LDV was stationary and the sample was moved by a high-precision X/Y traverse stage.

When measuring ultra-high frequencies, another important consideration must be taken into account: the wavelength of the vibration in the material (an acoustical wavelength) becomes rather short compared with conventional lower ultrasonic frequencies (refer to Section 9.2.3). Depending on the material properties at 500 MHz, the wavelength may only be 4 to 20 μm. Consequently the spatial resolution of the measurement must be high enough to ensure that the measurement is not integrated over an area of non-uniform vibration amplitude levels. This requires a small laser spot. By combing a UHF LDV with a standard microscope objective, a laser spot diameter of 1 μm is easily achieved. But also, the X/Y traversing system used for measuring the points must be carefully chosen as it must have a very high positional accuracy and resolution, to the same order as the laser spot diameter or better. The power SAW shown in Fig. 9.32 operates at 130 MHz, which is still relatively low. The wavelength measured from the profile shown in Fig. 9.33 is 29 µm and therefore much larger than the spatial resolution given by the laser spot.

9.4.2 Modified SLDV for micro-structures and small transducers

Measurement systems for the dynamic characterization of the smallest transducers and micro-structures (MEMS) require special properties. For micro-structures, the requirements are a non-contact measurement capability, high velocity or displacement resolution and high-frequency bandwidth. These requirements are fulfilled by laser Doppler vibrometry. Due to the small size of micro-structures, measurements on such devices also require a small laser spot size for achieving a high spatial resolution. This requirement can be fulfilled by combining LDV or SLDV with an optical microscope.

A special set-up features the optical resolution of a microscope combined with scanning laser Doppler vibrometry. Such a micro-system SLDV provides the best-to-date performance characteristics for out-of-plane vibration measurements, all the way down to the fundamental limitations of current technology.

A micro-system LDV uses a confocal microscope with superior optical resolution (Burdess *et al.*, 1997). The optical design minimizes aberrations and allows the laser beam to be focused down to a sub-micron spot size. Maximum laser transmissions and reflections are obtained by using optical coatings for IR and the HeNe laser wavelength (632.8 nm), which enables high optical sensitivity and thus low measurement noise.

A schematic diagram of the optical set-up is shown in Fig. 9.34. The measurement beam from the interferometer is coupled into an optical fibre with a core diameter of approximately 4 µm. The fibre end forms a pinhole for the emitted and returning laser light, and functions as a confocal beam path for the vibrometer laser beam. Lens L4 collimates the beam. By using a mirror system to deflect the laser beam in the *x* and *y* directions, the laser Doppler vibrometer becomes a scanning laser Doppler vibrometer with field-field measurement capability for visualization of deflection shapes. The mirror system M uses dual piezoelectrical actuated prisms. In conjunction with a collimating lens L4, this system allows scanning of small flat fields with parallel scanning beams. The laser beam is imaged onto the back focal plane of the microscope objective O by a pair of telescoping lenses L2 and L3. The microscope objective focuses the beam to a small spot at the focal point of the objective lens. The design is optimized for use with chromatic objective lenses with long stand-off distances up to 35 mm.

The laser beam is scattered back from the surface of the test object and is only sensitive to out-of-plane motions parallel to the optical axis. A digital camera is

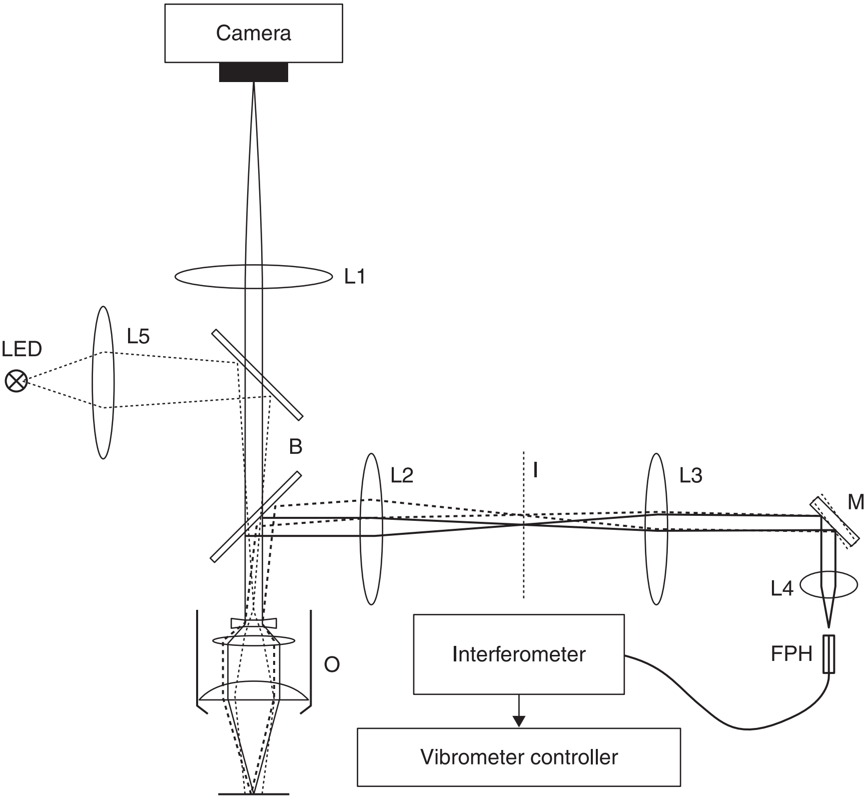

9.34 Schematic of a microscope laser scanning set-up.

used for beam alignment and superimposition of the image with the gathered vibration data.

Naturally the main application of such a micro-system LDV is for studying MEMS devices such as micro-accelerometers, pressure sensors, MEMS microphones, etc. Some ultrasonic transducers have shrunk to microscopic dimensions, such as the secondary thin-film PZT actuator used in modern computer hard disk drives in addition to the conventional voice coil motor (VCM). The stroke of such actuators is typically around 1 µm or less and laser Doppler vibrometry combined with a microscope is a perfect technology for studying the dynamical behaviour of a PZT–slider assembly (White *et al.*, 2004).

9.4.3 In-plane measurement of ultrasonic waves

The in-plane only laser Doppler vibrometer operates on the basis of the differential laser Doppler method. In contrast to the 3D single-point vibrometer introduced in

Section 9.2.2, where three laser Doppler vibrometers are combined, the in-plane vibrometer comprises just one interferometer. It is capable of measuring the in-plane vibrations in one direction, but without the need for an internal coordinate transform. Further, it is insensitive to the out-of-plane vibration component.

The design is shown in Fig. 9.35. The beam from a laser, LS, is split into two partial beams of equal intensity. In this design, a Bragg cell (AOM) is not only used for shifting the optical frequency of one of the two beams but also acts as a beam splitter. The zero-order diffraction beam does not undergo a frequency shift, whereas the first-order beam is typically shifted by 40 MHz. Using several prisms, the two laser beams are superposed within the specified stand-off distance on the test surface to be measured. Interference of the two beams results in a bright and dark interference fringe pattern where the fringes are spaced at a distance, Δs, as shown in Fig. 9.36.

The light scattered back from the measurement object is collected by the integrated receiving optics and focused on the photodetector. From there the detector signal is transferred to an electronics cabinet for demodulation and further processing.

The fringe spacing, Δs, is a system constant, which depends on the laser wavelength, λ, and the angle between the measurement beams, 2φ.

$$\Delta s = \frac{\lambda}{2\sin\varphi} \tag{9.8}$$

When a surface feature moves through the fringe pattern, the intensity of the light scattered back from it is modulated. The photodetector in the sensor head therefore generates an AC signal, with a frequency, f_D, which is directly proportional to the surface feature velocity component in the measurement direction, v_p, given by:

$$f_D = \frac{v_p}{\Delta s} \tag{9.9}$$

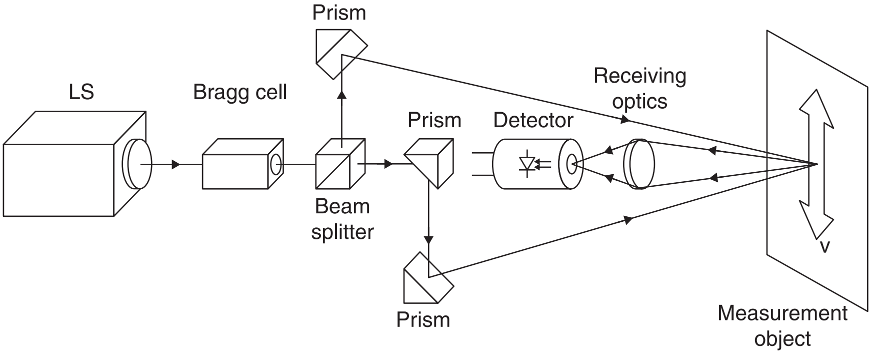

9.35 Optical design of an in-plane LDV.

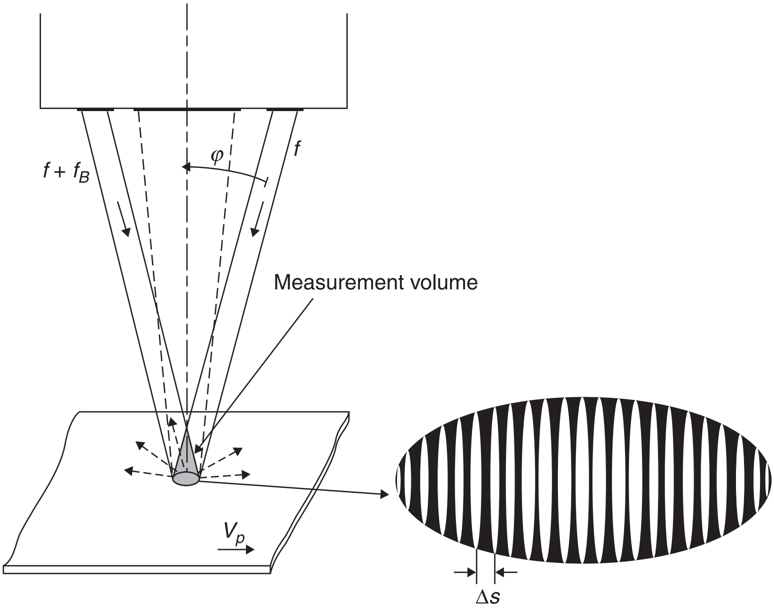

9.36 Measurement using an in-plane vibrometer.

The in-plane LDV operates in heterodyne mode. The frequency of one of the measurement beams is shifted by an offset of typically 40 MHz. Hence, the fringes in the measurement volume move with a constant velocity corresponding to the offset frequency, f_c. It is thus possible to detect the surface's direction of motion and to detect when the velocity is zero. The resulting modulation frequency, f_D, at the photodetector is in heterodyne mode:

$$f_D = f_c + \frac{v_p}{\Delta s} \quad [9.10]$$

In Section 9.2.2 we discussed in-plane and out-of-plane measurements using three separate LDV systems. Further, in Section 9.2.3 we showed that even 3D scanning measurements are possible using three SLDV systems with a common data acquisition. Thus it is a valid question regarding why another in-plane design, as discussed in this section, is needed: when using separate LDV sensors the in-plane and out-of-plane sensitivity strongly depends upon the angle, 2ϕ, between the laser beams. With a large angle the highest IP sensitivity is achieved but the OOP sensitivity is lost. One has to compromise between IP sensitivity, OOP sensitivity and the compactness of the optical arrangement. The IP LDV as shown in Fig. 9.35 and Fig. 9.36 is only sensitive to in-plane vibrations and not to out-of-plane vibrations. Furthermore, the optical design can be realized in a relatively small package. Thus such a design is typically used for applications where only in-plane measurements are needed and where space is limited.

Compared with the previously discussed OOP LDV and 3D SLDV designs, it should also be mentioned that the in-plane LDV must be designed for a certain fixed stand-off distance, where the two laser beams intersect. The intersection area of the two beams (and the measurement spot) is typically larger than for standard LDV designs, e.g. with a stand-off distance of 300 mm the spot diameter is about 0.15 × 0.3 mm^2.

Figure 9.37 shows the results of an in-plane LDV measurement: the outer ring of a compact piezo-motor (diameter 14 mm) performs a pure in-plane movement, which is internally transformed into a rotational movement of the motor shaft. The measurement shown was made with a 3D scanning laser Doppler vibrometer. The comprehensive data that can be measured with a 3D SLDV are not needed for the industrial production of these motors. A single-point measurement of the in-plane component amplitude is sufficient to qualify the motor's performance. For quality assurance, the measurement of one point using an in-plane laser Doppler vibrometer, as described in this chapter, can be the most efficient choice.

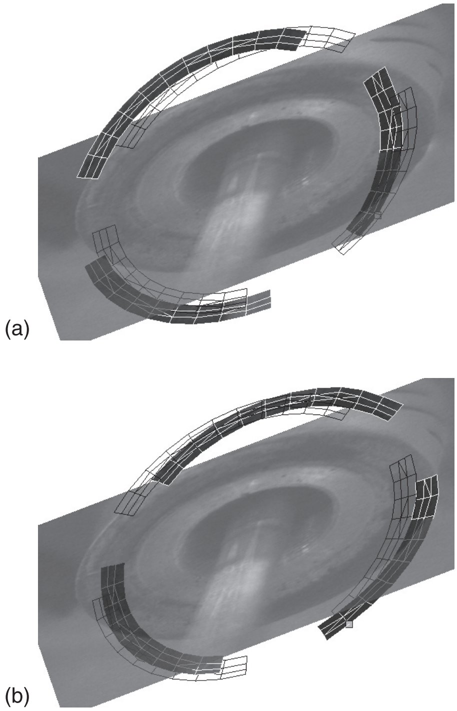

9.37 In-plane movement of a small piezo-motor at 60.2 kHz visualized with a 3D SLDV.

9.5 Conclusion and summary

We have discussed various optical methods all based on laser Doppler vibrometry for measuring the displacement, velocity and phase of transducers and ultrasonic tools. One single LDV optical design cannot address all the different needs of vibration measurements (in-plane vibration, out-of-plane vibration, high frequency, etc.). Thus we have briefly described several different interferometer designs capable of meeting many of the needs of measurement. Application examples have been given for the different types of LDVs, including measurements of single test points as well as the scanning of many points in one and three dimensions. Finally, special applications such as ultra-high-frequency measurements, very small test devices (micro-structures, MEMS) and a method for detecting only the in-plane vibration have been discussed.

9.6 References

Bosch (2003) Acoustic researchers are using lasers as microphones, *Bosch Research Info Issue 03/2003*, Bosch Corporate web site.

Burdess J. S., Harris A. J., Wood D., Pitcher R. J. and Glennie D. (1997) A system for the dynamic characterization of microstructures, *Journal of MEMS* Vol. 6.

Johansmann M. (2005) Targeting the limits of laser Doppler vibrometry, IDEMA Technical Paper, IDEMA, Tokyo.

Johansmann M. and Sauer J. (2005) A new tool for three-dimensional non-contact vibration measurements in automotive applications, SAE Paper No. 2005-26-052.

Littmann W. (2010) Refracto-vibrometry, *InFocus* Issue 1/2010, ISSN 1864-9203.

Miller A. (2003) *Advanced Diagnostic Technique for Wire Bonding Process Development*, Semicon Taiwan, Abstract.

Nakamura K., Hirayama M. and Ueha S. (2002) Measurements of air-borne ultrasound by detecting the modulation in optical refractive index of air, *Proc. 2002 IEEE International Ultrasonics Symp.*, pp. 609–12.

Nakamura K., Kambara H., Hirayama M. and Ueha S. (2006) Non-invasive measurement of sound field through the optical refractive index of air, *WESPAC IX*.

Rembe C., Siegmund G., Steger H. and Wörtge M. (2006) Measuring MEMS in motion by laser-Doppler vibrometry, in *Optical Inspection of Microsystems*, Optical Science and Engineering Series 109, edited by W. Osten, Boca Raton, Taylor and Francis Books, ISBN 0849336821.

Rembe C., Boedecker S., Dräbenstedt A., Pudewills F. and Siegmund G. (2008) Heterodyne laser-Doppler vibrometer with slow-shear-mode Bragg cell for vibration measurements up to 1.2 GHz, *Proc. of the 8th International Conference on Vibration Measurements by Laser Techniques, SPIE* 7098, 70980A.

Schell J., Johansmann M. and Schuessler M. (2005) *Three Dimensional Vibration Testing in Automotive Applications Utilizing a New Non-Contact Scanning Method*, SAE, USA.

Stoffregen B. and Felske A. (1985) Scanning laser Doppler analysis system, SAE Paper No. 850327.

White M. T., Hingwe P. and Hirano T. (2004) Comparison of a MEMS microactuator and a PZT milliactuator for high-bandwidth HDD servo, *American Control Conference*, Boston, Massachusetts.

Zipser L. and Franke H. (2008) Refracto-vibrometry – a novel method for visualizing sound waves in transparent media, *Acoustics '08 Congress*, Paris.

Zipser L. and Lindner S. (2002) German patent DE 10057924 A1, 22 November 2000, published 22 May 2002, Hochschule für Technik und Wirtschaft Dresden (FH).

Zipser L., Behrendt, R. and Lindner S. (2002) German patent DE 10057922 A1, 22 November 2000, published 22 May 2002, Hochschule für Technik und Wirtschaft Dresden (FH).

10

Optical visualization of acoustic fields: the schlieren technique, the Fresnel method and the photoelastic method applied to ultrasonic transducers

K. YAMAMOTO, Kansai University, Japan

Abstract: This chapter discusses three types of optical visualization techniques for evaluating the acoustic field transmitted from ultrasonic transducers: the schlieren technique, the Fresnel method and the photoelastic method. We begin with a review of the physical mechanism of the acousto-optic interaction used in visualization techniques, and then discuss the experimental apparatus and the observed images.

Key words: schlieren technique, Raman–Nath diffraction, Bragg reflection, Fresnel diffraction, photoelasticity.

10.1 Introduction

The optical visualization of ultrasonic waves is helpful for understanding wave propagation in transparent materials. Stroboscopic ultrasonic visualizations, such as the schlieren technique, the Fresnel method and the photoelastic method, have been used to find solutions to the problems encountered in ultrasonic non-destructive testing, as well as to evaluate probe design and performance. Video visualizations of vibrating materials and traveling ultrasonic pulses are also useful educational tools for studying wave behavior and properties.

In the first part of this chapter, the principles of Raman–Nath diffraction and Bragg reflection used in the schlieren visualization technique are described. The corresponding experimental system and observed images are also discussed. In the second part, Fresnel diffraction at low ultrasonic frequencies is explained. The Fresnel visualization method is also called a schlieren visualization technique in several reports. However, in this chapter, Fresnel and schlieren visualizations are described separately because of the difference in the ultrasonic frequencies used. Finally, the photoelastic visualization method, which is used to distinguish longitudinal and shear ultrasonic strains in a transparent material, is reviewed.

10.2 Schlieren visualization technique

Schlieren, meaning ‘streaks’ in German, are optical inhomogeneities in transparent materials that are not visible to the naked eye. Schlieren were first observed by Robert Hooke during an observation of candle light using lenses.[1] Most conventional schlieren systems, which are used to observe schlieren in air, water and glass, were developed by August Toepler.[2] The schlieren photograph of Mach waves created by Ernst Mach is a typical schlieren visualization result in fluid dynamics. Schlieren visualization shows index variations in transparent media. In acoustics, especially ultrasonic engineering, the schlieren technique is used to visualize the pressure field produced by an ultrasonic transducer, generally in water or in other tissue-mimicking media. The unique properties of the schlieren technique enable the investigation of specific features of the acoustic field, ultrasonic beam-profile irregularities and time-dependent phenomena.[3–8] Schlieren visualization is analogous to X-ray examination of the acoustic field.

10.2.1 Raman–Nath effect

Raman–Nath diffraction is an acousto-optic effect – an interaction between acoustic waves and light waves – especially the diffraction of laser light by ultrasonic waves. Raman–Nath diffraction is observed for relatively low ultrasonic frequencies, typically less than 10 MHz, and for a small acousto-optic interaction length, L, corresponding to the width of an ultrasonic wave, which is typically less than 10 mm. Light diffraction by the phase grating induced by the ultrasonic wave is commonly employed for the determination of the Raman–Nath parameter, v, describing the amplitude of the phase modulation,

$$v = \frac{2\pi \delta n L}{\lambda}, \qquad [10.1]$$

where δn and λ refer to the amplitude variation of the refractive index induced by the ultrasonic wave and the wavelength of the incident light. The pattern formed by the Raman–Nath diffracted light corresponds to that of conventional diffraction gratings at angles θ_m from the original direction. These angles are given by

$$\sin\theta_m = m\frac{\lambda}{\Lambda}, \qquad [10.2]$$

where Λ is the wavelength of the ultrasonic wave and m is the integer order maximum. If a helium–neon laser with a 633-nm wavelength is incident on the ultrasonic wave at 5 MHz in water, corresponding to a wavelength of approximately 0.3 mm, the first-order diffracted light angle is estimated to be 0.12°. The diffraction of light takes place for an arbitrary incidence angle (see Fig. 10.1). The Raman–Nath diffraction pattern can contain many diffraction orders with a symmetrical distribution of light intensity. The intensity of light diffracted by the diffraction grating is

$$I_m = J_m^2(v). \qquad [10.3]$$

Here, the incident light intensity is assumed to be 1 and $J_m(v)$ is the mth-order Bessel function of the first kind.

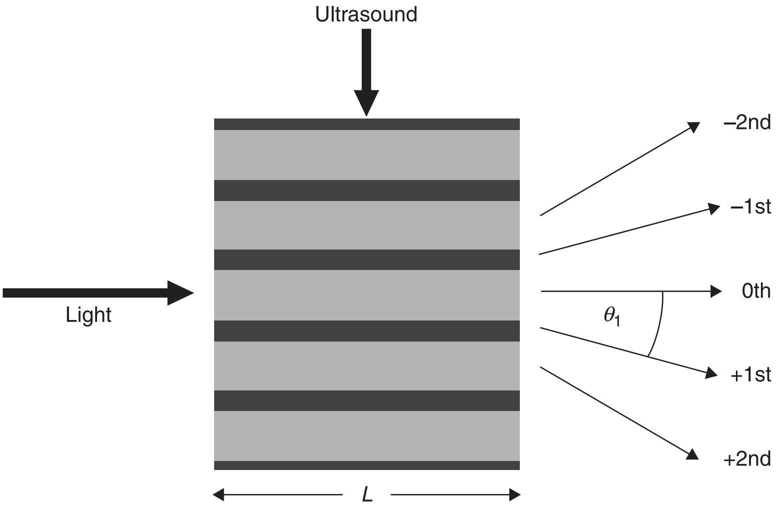

10.1 Raman–Nath diffraction.

10.2.2 Bragg reflection

In contrast with the Raman–Nath regime, Bragg reflection is observed at high ultrasonic frequencies, usually exceeding 10 MHz, and even at large v. Bragg reflection or diffraction occurs when light waves are incident on an ultrasonic wave with a comparable wavelength. The light is reflected in a specular fashion by the ultrasonic grating, and undergoes constructive interference in accordance with Bragg's law. Where the reflected waves interfere constructively, they remain in phase since the path length of each light wave is equal to an integer multiple of the acoustic wavelength, Λ. The path difference between two waves undergoing constructive interference is given by $2\Lambda\sin\theta$, where θ is the angle of reflection. With increasing ultrasonic frequency the angular selectivity increases and the number of observed peaks is gradually reduced. The reflection pattern consists of two reflection peaks of the zeroth and first orders. These peaks appear only at specific incidence angles near the Bragg angle (see Fig. 10.2), which are given by

$$\sin\theta = \frac{\lambda}{\Lambda}. \qquad [10.4]$$

θ is estimated to be 0.48° under conditions where the acoustic wavelength is 75 μm (20 MHz) in water and the incident light wavelength is 633 nm. When the acousto-optic interaction length is long enough, that is, when the ultrasonic wave is wide or its frequency is high, the intensities of the zeroth- and first-order Bragg reflection light are given by

$$I_0 = \cos^2\left(\frac{v}{2}\right), \qquad [10.5]$$

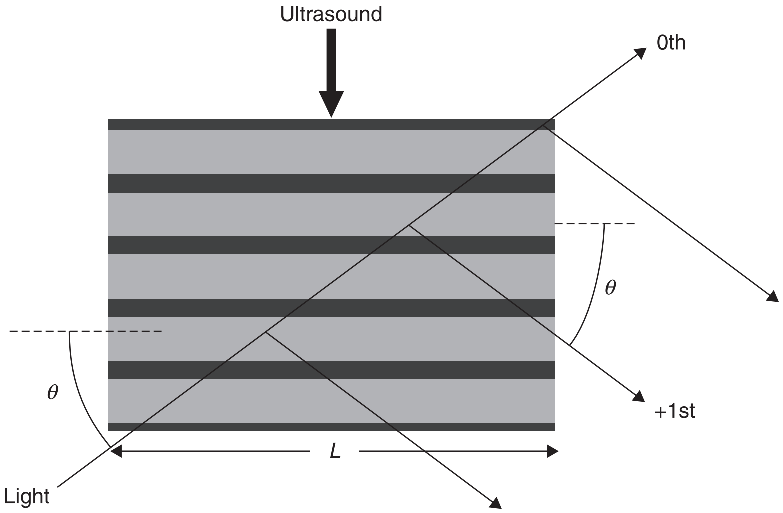

10.2 Bragg reflection.

$$I_{\pm 1} = \sin^2\left(\frac{v}{2}\right). \qquad [10.6]$$

10.2.3 Visualization system and images

A stroboscopic schlieren technique, which creates a slow-motion video of the ultrasonic pulses and burst wave propagation in water, is very useful to confirm both the temporal and spatial acoustic distributions for frequencies over several megahertz. A schematic diagram of a schlieren system is shown in Fig. 10.3. The two lenses, L2 and L3, have a diameter of 150 mm and a focal length of 500 mm. The point light source consists of a Xe lamp with a very sharp stroboscopic flash collimated by another lens, L1, with a spatial filter placed at the focal point of L2. An ultrasonic pulse is generated in water 60 times per second. The Xe flash lamp is designed to produce extremely intense, incoherent, full-spectrum white light for very short durations. The ultrasonic waves diffract the light into several orders through Raman–Nath diffraction or Bragg reflection. Only the first order passes through a slit placed at the focal plane of lens L3. The ultrasonic pulse can be seen by the naked eye or recorded with a video camera behind the slit. The stroboscope is triggered at a certain time after the pulse shot. If the delay is fixed, a still image is obtained. Because the light flash is as short as 180 ns and the ultrasonic pulse advances only 270 µm in water in that interval, a clean image is observed. A very slow and continuous increase of the delay time produces a slow-motion video. For 10 MHz ultrasonic waves, the wavefront cannot be seen because the wavelength is 150 µm in water. To visualize the wavefront of

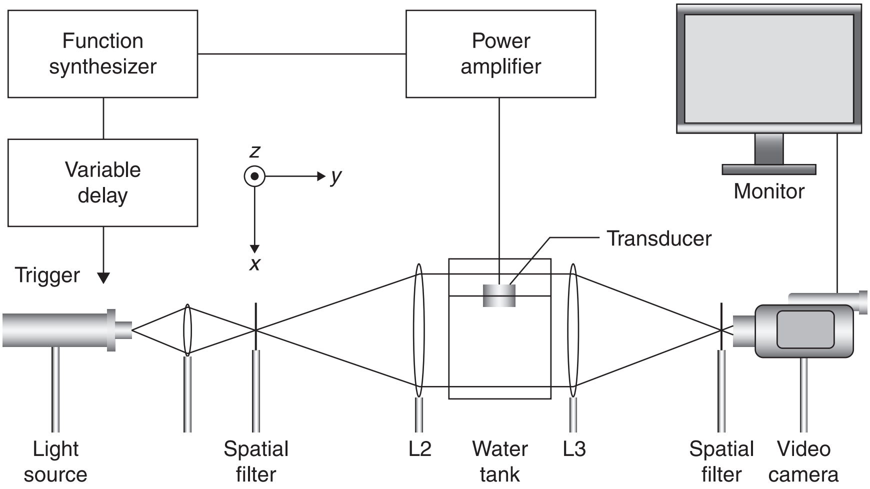
Function synthesizer
Power amplifier
Variable delay
z
y
x
Monitor
Transducer
Trigger
Light source
Spatial filter
L2
Water tank
L3
Spatial filter
Video camera

10.3 Schlieren system.

high-frequency ultrasonic waves, a pulsed laser emitting ultrashort pulses of light, generally of the order of femtoseconds to hundreds of femtoseconds, should be adopted as a light source.

The simplest case is shown in Fig. 10.4. A short pulse of plane waves is transmitted through water from a circular disk transducer with a diameter of 15 mm and resonance frequency of 10 MHz, which is driven by a short rectangular electric pulse of −200 V. The transducer, shown in the upper center area in Fig. 10.4, is a single-element longitudinal wave transducer with a quarter-wavelength layer acoustically matched to water. The transducer, made of lead zirconate titanate (PZT) ceramic, is designed for applications such as automated scanning, on-line thickness gauging and high-speed flaw detection. In Fig. 10.4(a),

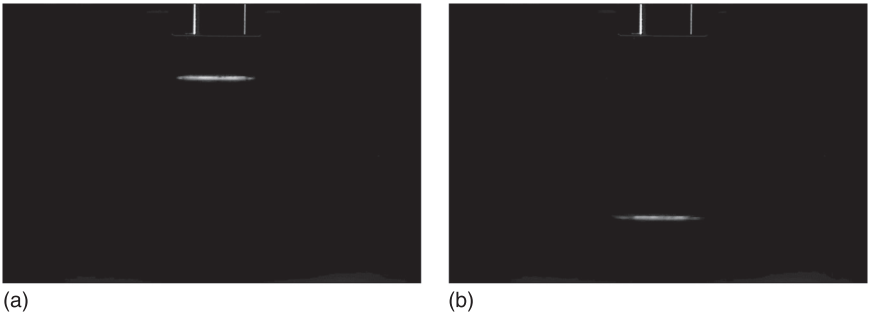
(a) (b)

10.4 Short pulse of plane waves transmitted downwards through water from a circular disk transducer, seen at the top. (a) The ultrasonic pulse 5 μs after applying the voltage. (b) The ultrasonic pulse 15 μs later.

the ultrasonic pulse traveling down from the upper transducer with a duration of less than 1 μs was visualized 5 μs after applying the voltage. Figure 10.4(b) is the image taken 15 μs after the image shown in (a).

Figure 10.5(a) shows a rectangular pulse of plane waves traveling in water with a duration of 20 μs and frequency of 10 MHz. In Fig. 10.5(b), which was taken 20 μs after the image in (a), the ultrasonic burst wave has passed through the water and the diffraction pattern cannot be seen.

To check the performance of an immersion-focused transducer, a transducer, 6 mm in diameter with frequency of 10 MHz, emitting a point-focus beam with a duration of 20 μs and a focal length of 20 mm, was used for the visualizations shown in Fig. 10.6. The image in Fig. 10.6(b) was taken 7 μs after the image in (a), and indicates that the beam diameter around the focal point and the focal zone are not restricted because the element diameter is too small compared with the focal length. It is not anticipated that such a high-resolution transducer will be necessary for non-destructive evaluations using ultrasonic imaging.

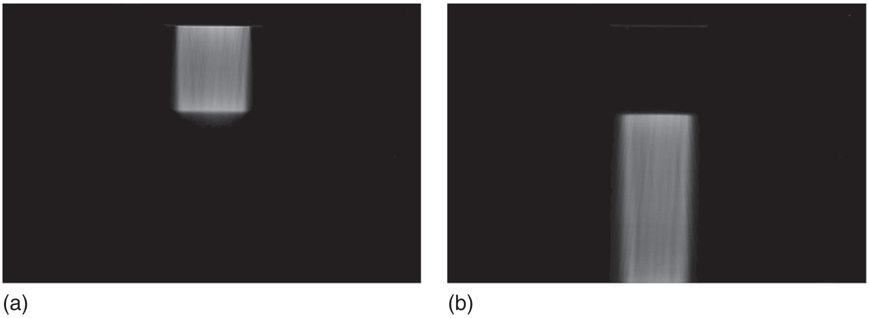
(a) (b)

10.5 Rectangular pulse of plane waves traveling in water: (a) initial image, (b) 20 μs later.

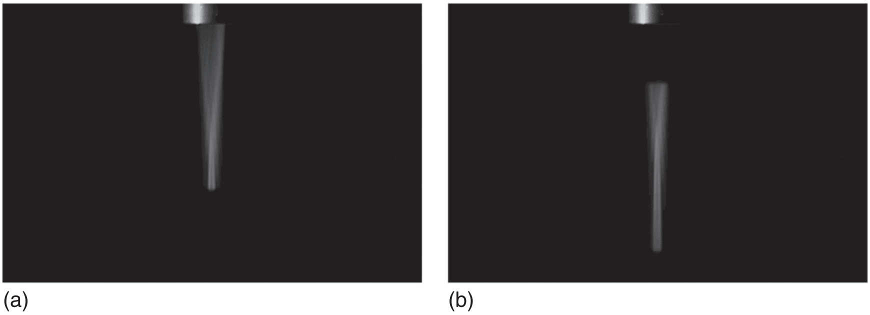
(a) (b)

10.6 Immersion-focused transducer emitting a point-focus beam: (a) initial image, (b) 7 μs later.

10.3 Fresnel visualization method

In this section Fresnel diffraction, which is observed at relatively low ultrasonic frequencies, is explained. The Fresnel visualization method is related to, but simpler than, the schlieren technique and performs a similar function. Fresnel and schlieren visualizations are described separately here because of the differences in the acousto-optical interaction. It is difficult to visualize an ultrasonic pulse and the burst wave clearly at frequencies less than several megahertz using the schlieren technique because of the small light diffraction angle. In images visualized by the Fresnel method, the wavefront of the ultrasonic wave can be seen.[9, 10] However, the contrast of the images created by the Fresnel method is not better than that of images created by the schlieren technique.

10.3.1 Fresnel diffraction

Generally Fresnel diffraction, also known as near-field diffraction, occurs when a wave passes through an aperture and diffracts in the near field, causing the diffraction pattern observed to differ in size and shape, depending on the distance between the aperture and the projector. In Fresnel diffraction, the intensity of the diffracted light, I, changes periodically depending on the distance, y, from the ultrasonic wave:

$$I(x,y) = 1 + 2\sum_{m=1}^{\infty} \cos mkx \cdot J_m\left(2v \sin\frac{m\pi\lambda}{\Lambda^2} y\right). \qquad [10.7]$$

Here, x and k are, respectively, the position along the direction of travel and the wave number of the ultrasonic wave. The optical configuration is shown in Fig. 10.7. The y axis corresponds to the focal point of the camera recording the ultrasonic waves. When the focal point of the camera changes continuously, the diffracted light pattern changes periodically. This is known as the Talbot effect, and it occurs because the phase and intensity gratings exist alternately.

10.3.2 Visualization system and images

The Fresnel visualization system is almost the same as the schlieren technique illustrated in Fig. 10.3. In this experiment, a slight defocusing of the camera lens makes it possible to visualize ultrasonic waves in water through Fresnel refraction and no slit or stopper is needed to cut the zeroth-order diffracted light.

Figure 10.8 shows visualized ultrasonic pulses at 1 MHz traveling in water from top to bottom. The immersed flat transducer, with diameter 15 mm and resonance frequency 1 MHz, applies a −400 V short rectangular pulse and then emits an approximately 2-cycle ultrasonic pulse. Figure 10.8(a) shows the

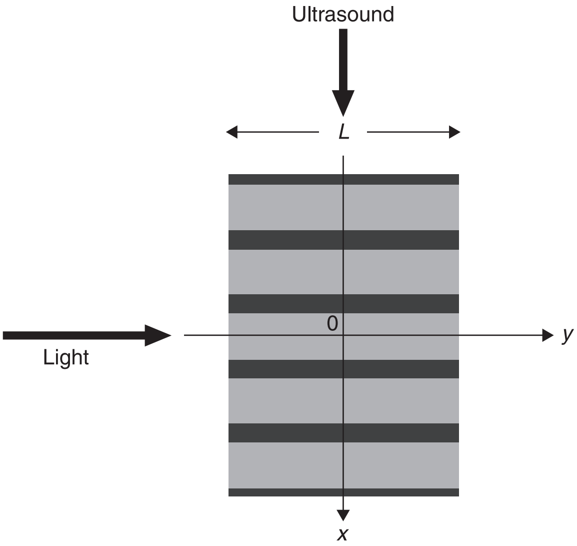

10.7 Fresnel diffraction.

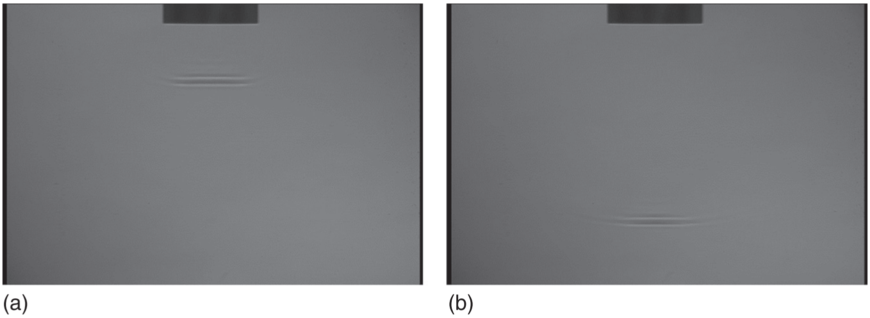
(a) (b)

10.8 Ultrasonic pulse traveling in water: (a) 7 µs after ultrasonic excitation, (b) 15 µs later.

ultrasonic pulse taken 7 µs after the ultrasonic excitation. Figure 10.8(b) is the propagating image taken 15 µs after the image in (a) and shows the ultrasonic diffraction effect as the ultrasonic pulse is wider than (a).

Ultrasonic tone-burst waves propagating in water with a duration of 15 µs and frequency of 1 MHz are shown in Fig. 10.9. Figure 10.9(a) shows the observation 15 µs after the ultrasonic excitation, and (b) shows the observation 15 µs after (a). These tone-burst ultrasonic wave images are better for understanding the ultrasonic diffraction effect than pulse images.

Figure 10.10 shows ultrasonic pulses excited by a −300 V rectangular short pulse. A PZT transducer with a cylindrical concave curvature and a resonance

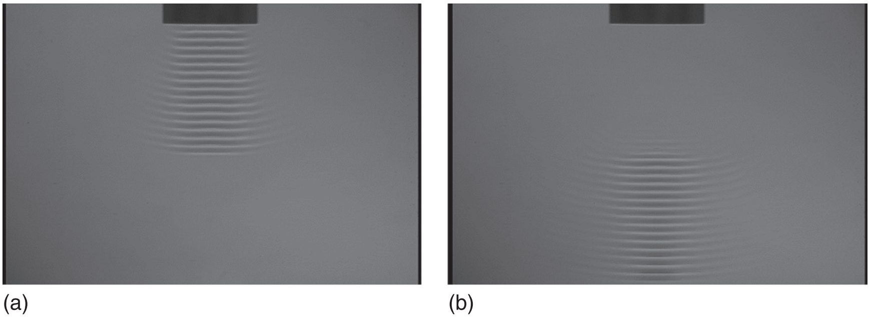

10.9 Ultrasonic tone-burst waves propagating in water: (a) 15 μs after ultrasonic excitation, (b) 15 μs later.

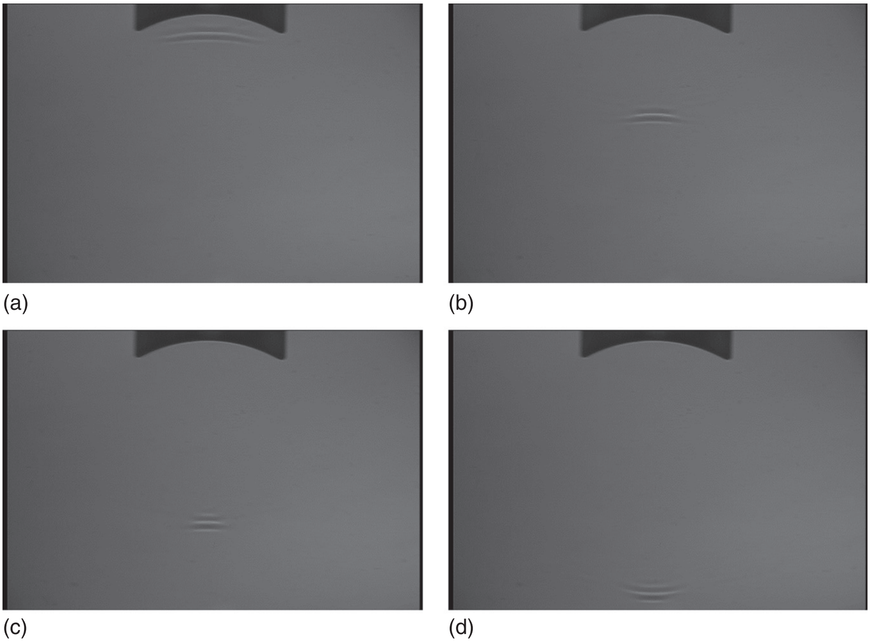

10.10 Sequence of ultrasonic pulses excited by a rectangular short pulse.

frequency of about 1 MHz was used to produce a line-focus beam with a focal length of 30 mm. This transducer is designed for the non-destructive inspection of cracks on the surface of a piece of metal immersed in water. In the Fresnel visualization method, experimental fields do not have a perfect sinusoidal pattern because the brightness of the visualized image is not completely proportional to the sound pressure in this technique.

10.4 Photoelastic visualization method

Unlike analytical methods of stress determination, photoelasticity gives a fairly accurate picture of a stress distribution, even around discontinuities in transparent materials such as glass and acrylic glass. The method serves as an important tool for determining the critical stress points in a material and is used for determining stress concentration factors. In ultrasonic engineering, the photoelastic visualization of an ultrasonic pulse has been used by several investigators seeking solutions to the problems encountered in the evaluation of probe design and performance.[11–15] In this section, photoelasticity based on the property of birefringence is explained, and the simultaneous visualization of an ultrasonic pulse in both a liquid and a solid is described.

10.4.1 Photoelasticity

Birefringence or double refraction, which is exhibited by many optical crystals, occurs when a ray of light passing through a material experiences two refractive indices. Photoelastic materials, however, exhibit the property of birefringence only with the application of stress, and the magnitude of the refractive indices at each point in the material is directly related to the state of the stress at that point. The normal stress difference, $\sigma_{xx} - \sigma_{zz}$, induced by a longitudinal ultrasonic wave traveling along the x axis in a transparent material can be visualized because the brightness of the image, I, is given by

$$I \propto \sin^2 \frac{\pi \beta d(\sigma_{xx} - \sigma_{zz})}{\lambda}, \tag{10.8}$$

where β is the photoelastic constant of the specimen and d is the width of the ultrasonic wave. In Fig. 10.11, ϕ indicates the angle between the direction of wave transmission, x, and the principal axis of the polarizer, P. When the longitudinal ultrasonic wave is traveling in the specimen along the x axis, the maximum visualization sensitivity condition is $\phi = \pi/4$ and only σ_{xx} exists. The brightness of the visualized image is then proportional to the wave pressure of the longitudinal wave. To visualize the shear stress, σ_{zx}, using a shear wave propagating along the x axis, the illumination condition $\phi = 0$ applies. In the photoelastic visualization method using a set of polarizer-analyzer systems, ϕ must be set to the maximum visualization sensitivity condition for the direction of the wave propagation and stress components. Longitudinal and shear waves propagating in the same direction cannot be visualized simultaneously under the maximum visualization condition. Similarly, waves traveling in different directions cannot be observed together. To resolve this problem, circularly polarized light is used in the visualization method. In this section all images are the result of photoelastic visualization with circularly polarized light.

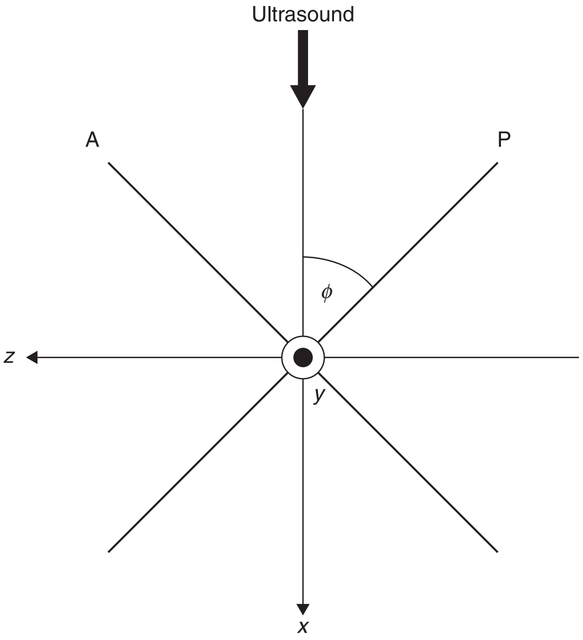

10.11 Photoelasticity.

10.4.2 Visualization system and image

Stroboscopic photoelastic visualization uses a piece of optical glass as the transparent specimen and is similar to the methods described above. In the circularly polarized light setup shown in Fig. 10.12, two quarter-wavelength ($\lambda/4$) plates have been added to the experimental setup for plane polarized light. The first quarter-wave plate is placed between the polarizer and the specimen and the second quarter-wave plate is placed between the specimen and the analyzer. Due to imperfections in the polarizer-analyzer system, there is light leakage even in the crossed Nicols condition.

Wave phenomena are induced by ultrasonic waves at liquid-solid and solid-solid boundaries, and these play an important role in acoustic microscopy and variable-angle transducer design. Simultaneous visualization of ultrasonic tone-burst waves and pulses in glass and water can be achieved by a technique that combines the stroboscopic photoelastic and Fresnel methods. Slightly deviating from the orthogonal condition to give a bias by leakage light, wavefronts separated by a distance of one wavelength and the distributions of ultrasonic waves in both water and glass can be visualized.

Figure 10.13(a) shows a 15-mm-wide tone-burst plane ultrasonic wave at 1 MHz incident on a lower glass block. The ultrasonic wave, emitted from a PZT transducer and visualized by the Fresnel technique, is incident perpendicular to

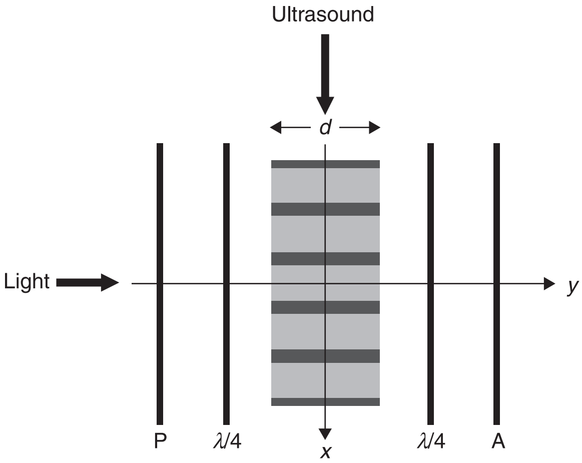

10.12 Stroboscopic photoelastic visualization.

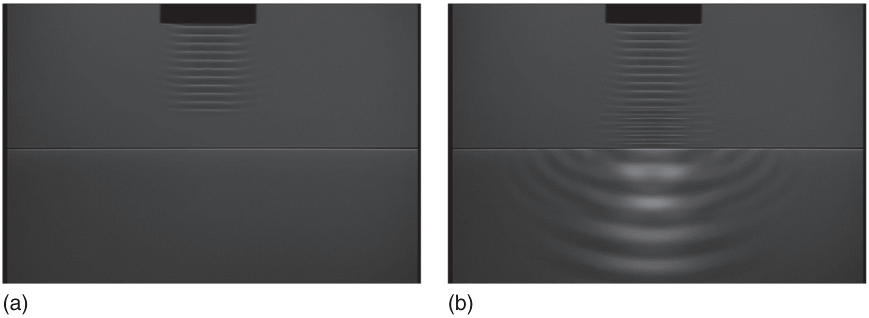

10.13 (a) Tone-burst plane ultrasonic wave incident on a glass block (bottom). (b) Reflection and transmission at the water–glass boundary.

the glass surface. Shortly after the wave is emitted, reflection and transmission occur at the water–glass boundary, as shown in Fig. 10.13(b). The perpendicular component is the longitudinal wave traveling vertically with a wavelength of about 6 mm corresponding to the longitudinal wave velocity in the glass (BK7). Waves are refracted at the water–glass boundary and propagate with the shear wave velocity in the glass, because incident wave diffraction components convert into shear waves at the boundary.

In Fig. 10.14(a) a tone-burst wave with a duration of 20 μs is incident on the water–glass boundary at an angle of 10° off the normal line of the surface. In Fig. 10.14(b) there are two refracting components in the glass. The brighter one corresponds to the shear wave propagating with a wavelength of about 3.7 mm. The right-hand portion in Fig. 10.14(b) shows that the longitudinal

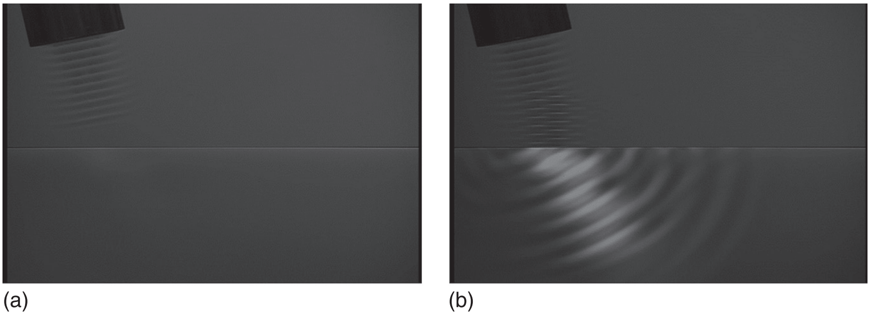
(a) (b)

10.14 (a) Tone-burst wave incident on water–glass boundary. (b) Two refracting components in the glass.

wave refracts at a larger angle than the shear wave and travels with a wavelength of about 6 mm.

Figure 10.15(b) shows the Rayleigh wave propagating near the glass surface; its displacement decays exponentially with distance from the free surface. In Fig. 10.15, the ultrasonic tone-burst wave at 1 MHz is incident at an angle greater than the critical incidence angles of both the longitudinal and shear waves.

Figure 10.16 shows the visualized distribution of the normal stress of the antisymmetric third mode (A3 mode) of a leaky Lamb wave propagating in 5-mm-thick optical glass (BK7). In Fig. 10.16(a), the leaky Lamb waves are excited by ultrasonic waves impinging at angle $\theta = \sin^{-1}(c_w/c)$, which is determined from the phase velocity, c, of the targeted mode of observation (A3) and the velocity of the longitudinal wave in water, c_w. We can see that the A3 mode has bright spots antisymmetrically located with the respect to the median plane of the glass plate with six bright spots per wavelength.

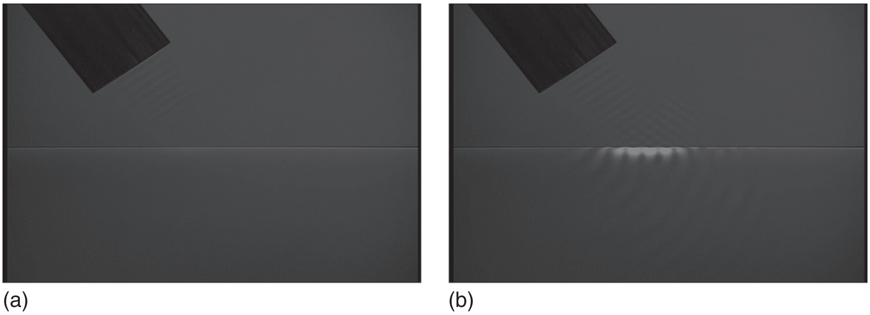
(a) (b)

10.15 (a) Ultrasonic tone-burst wave. (b) Rayleigh wave propagating near the glass surface.

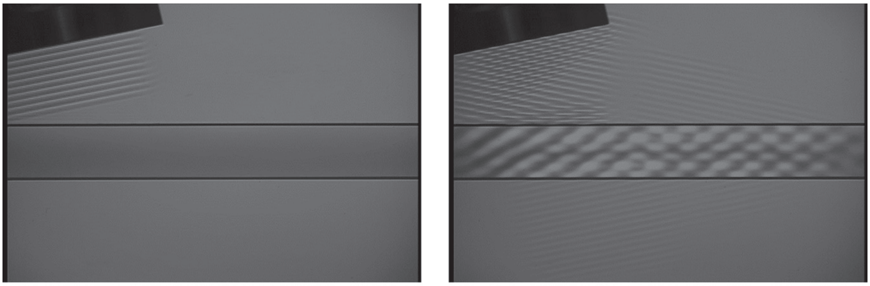

10.16 (a)Tone-burst wave incident on a glass pane. (b) Visualized distribution of normal stress of the A3 mode of a Lamb wave propagating in optical glass.

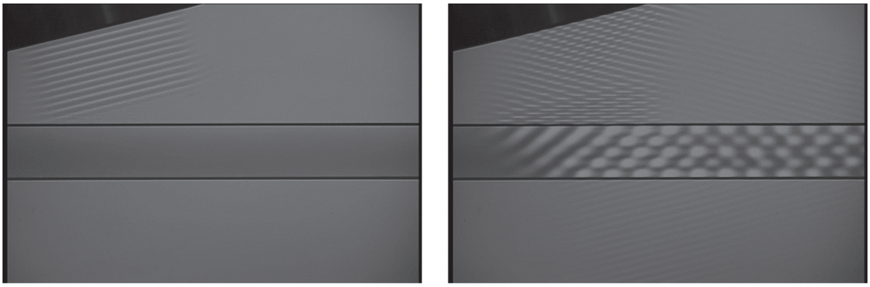

10.17 (a) Tone-burst incident wave. (b) The S2 mode of Lamb waves propagating in a glass plate.

Figure 10.17 shows the visualized distribution of the symmetric second mode (S2) of leaky Lamb waves propagating in the glass plate. The S2 mode has bright spots located symmetrically with respect to the median plane and five spots per wavelength.

10.5 References

1. Hooke R (1665), Of a New Property in the Air, *Micrographia*, Observation LVIII, 217–19.
2. Toepler A (1864), *Beobachtungen nach einer neuen optischen Methode*, Maximillan Cohen und Sohn.
3. Bronson N R (1969), An inexpensive schlieren apparatus, *Ultrasonics*, 7, 67–70.
4. Tsuruta T and Itoh Y (1969), Hologram schlieren and phase-contrast methods, *Jpn. J. Appl. Phys.*, 8, 96–103.
5. Kanda O, Sakai K, Yamamoto K and Takagi (2002), Observation of acoustic diffusion wave, *Jpn. J. Appl. Phys.*, 41, 232–6.

6. Yamamoto K, Pernod P and Preobrazhensky V (2004), Visualization of phase conjugate ultrasound waves passed through inhomogeneous layer, *Ultrasonics*, 42, 1049–52.
7. Neumann T and Ermert H (2006), Schlieren visualization of ultrasonic wave fields with high spatial resolution, *Ultrasonics*, 44, e1561–6.
8. Ohno M (2009), Observation of ultrasonic fields transmitted through bovine cortical or cancellous bones by the schlieren method, *Jpn. J. Appl. Phys.*, 48, 07GC10.
9. Patorski K (1981), Optical testing of ultrasonic phase gratings using a Fresnel diffraction method, *Ultrasonics*, 19, 169–72.
10. Yamamoto K (2005), Optical visualization of ultrasonic waves propagating in a fluid waveguide, *Acoust. Sci. & Tech.*, 26, 378–80.
11. Hall K G (1977), A qualitative evaluation of variable-angle ultrasonic transducers by the photoelastic visualization method, *Ultrasonics*, 15, 245–52.
12. Li H U and Negishi K (1993), Visualization of Lamb mode patterns in a glass plate, *Ultrasonics*, 32, 243–8.
13. Negishi K and Li H U (1996), Strobo-photoelastic visualization of Lamb waves with negative group velocity propagating on a glass plate, *Jpn. J. Appl. Phys.*, 35, 3175–6.
14. Nishimiya K, Mizutani K, Wakatsuki N, Ebihara T and Yamamoto K (2009), Visualization of mode conversion of Lamb-type waves in glass plates using pulsed light source, *Jpn. J. Appl. Phys.*, 48, 07GC06.
15. Yamamoto K, Nishimiya K, Wakatsuki N and Mizutani K (2010), Optical visualization of coupling modes of leaky Lamb waves with negative group velocity in the solid/fluid/solid trilayer, *Acoust. Sci. & Tech.*, 31, 185–7.

11

Surface acoustic wave (SAW) devices

K. HASHIMOTO, Chiba University, Japan

Abstract: This chapter aims to give the basics of surface acoustic wave (SAW) devices. First, the basic operation of interdigital transducers (IDTs) is discussed. The delta-function model is introduced, and the coupling-of-modes theory is adopted to allow for the influence of SAW reflection in the analysis. Next, SAW transversal filters are discussed. We explain their basic operation and design, and then their achievable performances are discussed. It is also shown that some of the difficulties caused in traditional SAW transversal filters can be overcome by the use of unidirectional IDTs. Finally, SAW resonators are discussed. After giving their basics, an overview of RF filters using SAW resonators is given.

Key words: surface acoustic wave (SAW), interdigital transducer (IDT), transversal filter, SAW resonator, SAW resonator filter.

11.1 Introduction

Although the existence of surface acoustic waves (SAWs) was first discussed in 1885 by Lord Rayleigh,[1] little interest was shown by engineers. In 1965, the situation changed dramatically. White and Voltmer showed that SAWs can be excited and detected efficiently by an interdigital transducer (IDT) placed on a piezoelectric substrate.[2] Since precise and fine IDT patterns can be generated by means of photolithography, the invention of the IDT stimulated worldwide research into the development of various SAW-based signal-processing devices in the VHF-UHF range.

Currently, SAW filters are widely used in the radio frequency (RF) stages as well as the intermediate frequency (IF) stages of modern telecommunication systems. With the successful research and development of SAW devices during the last forty years, there has been a high growth of the mobile phone market, which has in turn accelerated surprising advances in SAW device technology.

This chapter aim to give the basics of SAW devices. First, the basic operation of IDTs is discussed. The delta-function model is introduced to give an instinctive understanding of their behavior, and the coupling-of-modes (COM) theory is adopted to allow for the influence of internal reflection in IDTs.

Next, SAW transversal filters are discussed. Starting from a brief discussion of their fundamental properties, we describe achievable performances and the influence of a spurious signal called the triple transit echo (TTE) on filter performance. Low-loss SAW transversal filters using unidirectional transducers are also explained. Finally, SAW resonators and their use in RF filters are discussed. After giving the basics of SAW resonators, it is shown how RF filters are composed and designed using SAW resonators.

Of course, it is not possible to cover all SAW-related technology in this chapter. For example, discussions on the fabrication and characterization of SAW filters have been omitted, and applications to SAW sensors and actuators are not covered. There are many good information sources for further study.[3–23]

11.2 Interdigital transducers (IDTs)

11.2.1 Delta-function model

First of all, we will analyze the behavior of the IDT shown in Fig. 11.1. This type of IDT, composed of two electrodes per period, is called a single-electrode IDT, or simply a single IDT. In the figure, p_I is the IDT pitch (or period) and W is the finger overlap length, often called the aperture. For single-electrode IDTs, the number of IDT finger pairs is conventionally defined as half the number of electrode fingers. In this article, N_1 is defined as half the number of gaps between electrodes.

The basic operation of this device may be easily understood with the help of its impulse response. When an electrical impulse is applied between two electrodes, the substrate surface is deformed through piezoelectricity. Figure 11.2(a) shows the excited surface deformation at the surface. Although the deformation changes smoothly, here the variation is expressed as a spatial impulse (the delta function) to simplify the following discussion. Because of this simplification, this IDT model is called the delta-function model.[24] In this case, the horizontal axis gives the position in the IDT, and the periodicity is given by p_I. There is a sign inversion because the direction of the electric field changes alternately with x (see Fig. 11.1).

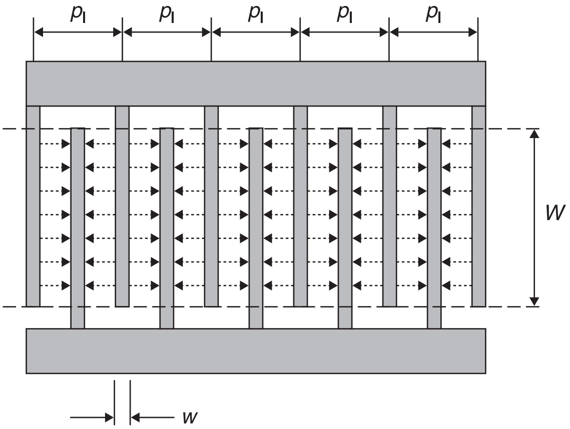

11.1 Interdigital transducer.

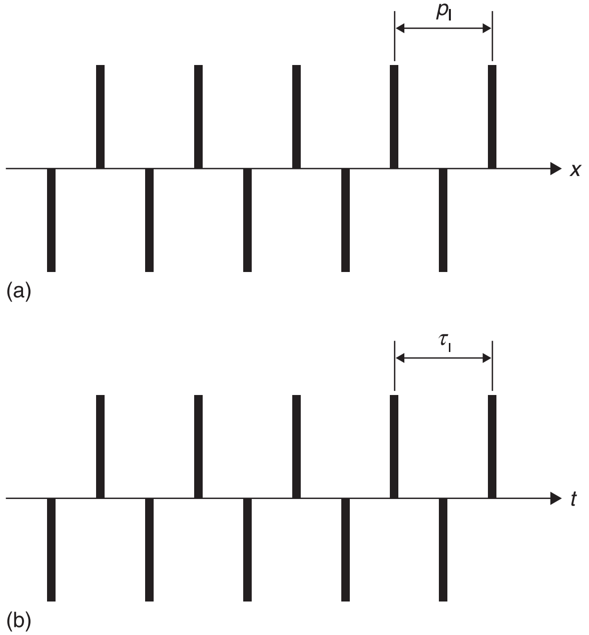

11.2 Impulse response of an IDT: (a) surface deformation, (b) SAW propagation.

The deformation propagates along the surface as a SAW. Figure 11.2(b) shows the waveform of the SAW pulse train at a fixed observation point outside the IDT. In this case, the horizontal axis is time, and the periodicity of the waveform is given by $\tau_I = p_I/V_S$, where V_S is the SAW velocity.

This implies that the acoustic impulse response $h_1{}^S(t)$ of the IDT detected at an observation point is given by

$$h_1^S(t) = \frac{c_S W}{2} \sum_{n=0}^{2N_1-1} (-1)^n \delta(t - L_n / V_S), \qquad [11.1]$$

where c_S is a proportional constant corresponding to the SAW excitation efficiency, $\delta(t)$ is the delta function, $L_n = (n{-}N_1 + 1/2)p_I/2 + x$, and x is the distance from the IDT center to the observation point.

The frequency response $H_1{}^S(f)$ of the IDT is simply given by replacing $\delta(t)$ in Eq. 11.1 with the sinusoidal voltage $\exp(2\pi jft)$ of unit amplitude, i.e.

$$\begin{aligned} H_1^S(f) &= \frac{c_S W}{2} \sum_{n=0}^{2N_1-1} (-1)^n \exp(-2j\pi f L_n / V_S) \\ &= jN_1 c_S W \exp(-2j\pi xf / V_S) \hat{H}_1^S(f) \end{aligned} \qquad [11.2]$$

where

$$\hat{H}_1^S(t) = \frac{\sin(N_I \pi f p_I / V_S)}{2N_I \cos(\pi f p_I / 2V_S)}. \qquad [11.3]$$

The final expression in Eq. 11.2 is equivalent to the situation where all the SAWs are excited at the middle of the IDT, and the frequency dependence of the excitation is given by $\hat{H}_I^S(f)$. The function has a maximum value of unity at the center frequency, f_c (= V_S/p_I), where the SAW wavelength is equal to the IDT pitch, p_I. In this situation, all the SAWs excited at each period are added synchronously, thus $|H_I^S(f_c)| = c_S WN$.

Figure 11.3 shows the relative amplitude in decibels, $20\log_{10}|\hat{H}_I^S(f)|$. It can be seen that the function is very similar to the function sinc x (= sin x/x). In fact, at $f \approx f_c$, the function can be approximated as

$$\hat{H}_I^S(t) = (-)^{N+1} \operatorname{sinc}\{N\pi(f/f_c - 1)\}. \qquad [11.4]$$

In the figure, this approximated function is also shown. It is seen that this approximation agrees well with the original function.

If a second IDT is placed in parallel with the first IDT, then, after the SAW excitation at the first IDT, a portion of the SAW energy arrives at the second IDT after a time delay, and is re-converted to an electrical signal through piezoelectricity. As shown in Fig. 11.4, the received pulse train is longer than the one in Fig. 11.2(a). The first pulse corresponds to the signal excited at the right end of the first IDT

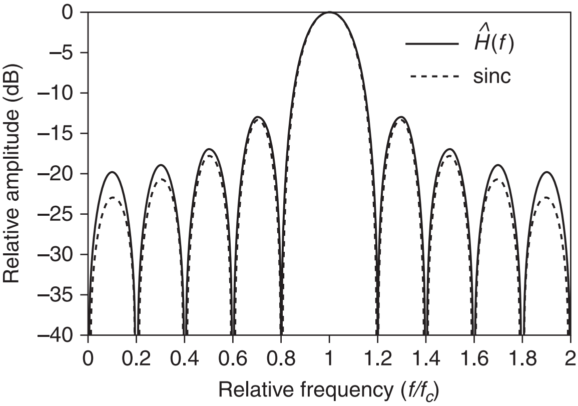

11.3 Frequency response of an IDT (N_I=5).

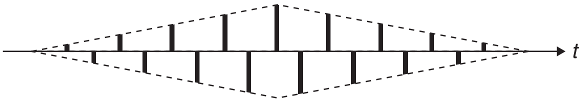

11.4 Impulse response of the transmission between two IDTs.

and detected at the left end of the second IDT, whereas the final one corresponds to the signal excited at the left end of the first IDT and detected at the right end of the second IDT. The amplitude has a maximum when the SAW pulse train just overlaps the second IDT.

This suggests that the electrical impulse response $h^{\mathrm{S}}_{21}(t)$ between two IDTs is given by

$$h^{\mathrm{S}}_{21}(t) = \frac{c_{\mathrm{S}}^2 W}{4} \sum_{m=0}^{2N_1-1} \sum_{n=0}^{2N_2-1} (-1)^{m+n} \delta(t - L_{mn}/V_{\mathrm{S}}), \qquad [11.5]$$

where $L_{mn} = (m + n - N_1 - N_2 + 1)p_{\mathrm{I}}/2 + L_{\mathrm{T}}$, L_{T} is the distance between the two IDTs (center to center), and N_2 is the number of finger pairs of the second IDT. For the derivation, we considered that the excitation efficiency of the IDTs is equal to the detection efficiency. This relation is called the reciprocity,[25] which may be understood because SAW detection is equivalent to the excitation of an anti-phase signal for the cancellation of the input signal.

Equation 11.5 gives the transfer function $H^{\mathrm{S}}_{21}(f)$ between two IDTs through application of the procedure used to derive Eq. 11.2:

$$H^{\mathrm{S}}_{21}(f) = N_1 N_2 c_{\mathrm{S}}^2 W \hat{H}_1(f) \hat{H}_2(f) \exp(-2j\pi f L_{\mathrm{T}}/V_{\mathrm{S}}), \qquad [11.6]$$

where $\hat{H}^{\mathrm{S}}_2(f)$ is the function defined in Eq. 11.3 for the second IDT. Equation 11.6 is equivalent to the situation where the SAW is excited at the middle of the first IDT and is detected at the middle of the second IDT, and the frequency dependence is given by the product of $\hat{H}^{\mathrm{S}}_1(f)$ and $\hat{H}^{\mathrm{S}}_2(f)$. SAWs excited by an IDT are also detected by it.

An analogy with Eq. 11.5 implies that the electrical impulse response, $h^{\mathrm{S}}_{11}(t)$, of the first IDT is given by

$$h^{\mathrm{s}}_{11} = \frac{c_{\mathrm{s}}^2 W}{4} \sum_{m=0}^{2N_1-1} \sum_{n=0}^{2N_1-1} (-1)^{m+n} \delta(t - |m-n| p_{\mathrm{I}}/V_{\mathrm{s}}), \qquad [11.7]$$

and its waveform is shown in Fig. 11.5.

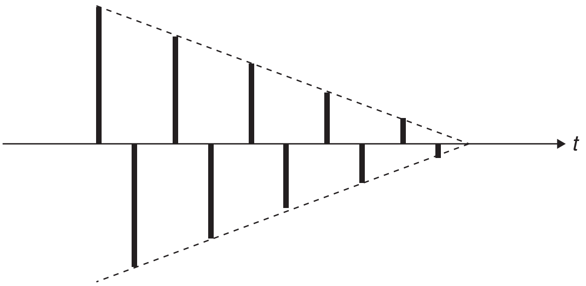

11.5 Impulse response of the regenerated signal at the first IDT.

The electrical frequency response, $H_{11}^{\mathrm{S}}(f)$, of the first IDT, IDT-1, is obtained in the following form after some mathematical manipulation:

$$\begin{aligned} H_{11}^{\mathrm{S}}(f) &= \frac{c_{\mathrm{S}}^2 W}{4}\sum_{m=0}^{2N_1-1}\sum_{n=0}^{2N_1-1}(-1)^{m+n}\exp(-2\pi jf|m-n|p_{\mathrm{I}}/V_{\mathrm{S}}) \\ &= c_{\mathrm{S}}^2 W N_1^2\left[\left|\hat{H}_1(f)\right|^2 + j\frac{(-1)^{2N_1}\sin(2\pi N_1 fp_{\mathrm{I}}/V_{\mathrm{S}})+2N_1\sin(\pi fp_{\mathrm{I}}/V_{\mathrm{S}})}{8N_1^2\cos^2(\pi fp_{\mathrm{I}}/2V_{\mathrm{S}})}\right]. \qquad [11.8] \end{aligned}$$

Figure 11.6 shows $H_{11}^{\mathrm{S}}(f)$ normalized by $H_{11}^{\mathrm{S}}(f_{\mathrm{c}}) = c_{\mathrm{S}}^2 W N_1{}^2$. In the calculation, N_1=5. It can be seen that the imaginary part changes rapidly near f_{c}, and it is zero at $f = f_{\mathrm{c}}$. The real part exhibits $\mathrm{sinc}^2 x$ dependence because it is proportional to $|\hat{H}_1{}^{\mathrm{S}}(f)|^2$ (see Eq. 11.8).

The behavior of two-port linear circuits, such as SAW devices, can be expressed in the form of an admittance matrix, [Y]:

$$\begin{pmatrix} i_1 \\ i_2 \end{pmatrix} = \begin{pmatrix} Y_{11} & Y_{12} \\ Y_{21} & Y_{22} \end{pmatrix}\begin{pmatrix} v_1 \\ v_2 \end{pmatrix}, \qquad [11.9]$$

where v_n and i_n are the voltage and the current at the port n, respectively. Note that, although $Y_{12} = Y_{21}$ due to the reciprocity[25] of the SAW devices, we will distinguish them for further discussion.

The admittance matrix elements are expressed as a sum of the contributions of (a) the electrostatic coupling, Y_{mn}^{e}, (b) the SAW propagation, Y_{mn}^{S}, and (c) other acoustic waves, called bulk acoustic waves or simply bulk waves, propagating in the substrate, Y_{mn}^{B}. That is,

$$Y_{mn} = Y_{mn}^{\mathrm{e}} + Y_{mn}^{\mathrm{S}} + Y_{mn}^{\mathrm{B}}. \qquad [11.10]$$

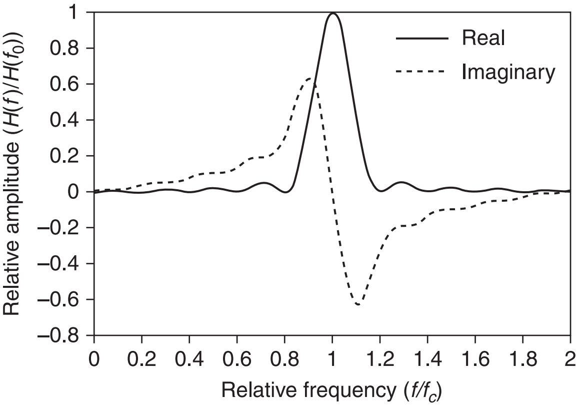

11.6 Frequency response of $H_{11}^{\mathrm{S}}(f)$.

In the following, we will ignore the influence of Y^{B}_{mn} for simplicity. First, let us derive Y^{e}_{mn}. Since the structure is periodic, a good approximation of the static capacitance C_{0i} of the ith IDT is

$$C_{0i} = N_i C_p, \qquad [11.11]$$

where C_{p} is the static capacitance per IDT period p_{I}. Although there also exists a static capacitance between IDTs, and its influence is sometimes significant, it is usually ignored in the analysis. Then, Y^{e}_{mn} is given by

$$\begin{pmatrix} Y^e_{11} & Y^e_{12} \\ Y^e_{21} & Y^e_{22} \end{pmatrix} = \begin{pmatrix} C_{01} & 0 \\ 0 & C_{02} \end{pmatrix}. \qquad [11.12]$$

For the single-electrode IDT, from pure electrostatic analysis, C_p is given by[26]

$$C_p = W\varepsilon(\infty)\frac{P_{-0.5}\left\{\cos\left(2\pi w / p_{\mathrm{I}}\right)\right\}}{P_{-0.5}\left\{-\cos\left(2\pi w / p_{\mathrm{I}}\right)\right\}}, \qquad [11.13]$$

where w is the finger width and $P_\nu(x)$ is the νth order Legendre function. This equation indicates $C_{\mathrm{p}} = W\varepsilon(\infty)$ when $w/p_{\mathrm{I}} = 0.25$. $\varepsilon(\infty)$ is a parameter determined by the substrate material, and is called the effective permittivity.[27] From electrostatic analysis[25]

$$\varepsilon(\infty) = \varepsilon_0 + \sqrt{\varepsilon^T_{11}\varepsilon^T_{33} - \varepsilon^{T2}_{13}}, \qquad [11.14]$$

where ε_0 is the permittivity in a vacuum and $\varepsilon^T_{\mathrm{ij}}$ is the permittivity of the piezoelectric substrate under zero stress.

The next step is to calculate Y^{S}_{mn}. In Eqs 11.6 and 11.8, we derived the transfer function $H^{\mathrm{S}}_{mn}(f)$ for the SAW transfer. It corresponds to Y^{S}_{mn} when the constant c_{S} is chosen appropriately. Namely,

$$\begin{pmatrix} Y^{\mathrm{s}}_{11} & Y^{\mathrm{s}}_{12} \\ Y^{\mathrm{s}}_{21} & Y^{\mathrm{s}}_{22} \end{pmatrix} = \begin{pmatrix} H^{\mathrm{s}}_{11} & H^{\mathrm{s}}_{12} \\ H^{\mathrm{s}}_{21} & H^{\mathrm{s}}_{22} \end{pmatrix}. \qquad [11.15]$$

Since the SAW is excited by the electric field generated by the charge on the IDT fingers, the excitation efficiency, c_{S}, should be proportional to the total charge. The relation can be written in the following form:[28]

$$c^2_{\mathrm{S}} W = 2\omega\eta^2 K^2 C_p, \qquad [11.16]$$

where K^2 is the electromechanical coupling factor for the SAW, corresponding to the strength of the piezoelectricity, and η is the element factor[29] expressing the influence of the charge distribution in an IDT period. For a given total charge, the highest excitation efficiency is achieved when the positive charges are concentrated at a point while the negative ones are concentrated at another point, and the distance between these points is $p_{\mathrm{I}}/2$. That is, η has a maximum value of unity when the IDT electrode widths are infinitesimal. A spatial distribution of charges always results in a reduction in the excitation efficiency due to interference among excited SAWs. Note that K^2 is basically only dependent upon the employed substrate whereas η is only dependent upon the finger arrangement.

For a single-electrode IDT, η is given by[28]

$$\eta = \frac{1}{P_{-0.5}\{-\cos(2\pi w/p_{\mathrm{I}})\}}, \qquad [11.17]$$

and $\eta = 0.84722$ when $w/p_{\mathrm{I}} = 0.25$.

It is interesting to note that K^2 can be estimated both theoretically and experimentally to high accuracy from the SAW velocities, V_{m} and V_{f}, when the top surface is fully covered by a conductive metal (metallized) or not (unmetallized), respectively, i.e.,[30]

$$K^2 = \frac{V_{\mathrm{f}}^2 - V_{\mathrm{m}}^2}{V_{\mathrm{f}}^2} \approx 2\frac{V_{\mathrm{f}} - V_{\mathrm{m}}}{V_{\mathrm{f}}}. \qquad [11.18]$$

Thus provided that V_{f}, K^2 (or V_{m}) and $\varepsilon(\infty)$ are given, we can simulate various IDT behaviors. Since these parameters are mostly determined by the piezoelectric substrate, selection of the substrate is one of the most important steps in device design.

Table 11.1 shows representative SAW substrate materials, which are used in practical devices and are commercially available. It is clear from the table that none of these substrates is perfect. In general, materials with large K^2 have a large temperature coefficient of velocity (TCV), which determines the temperature coefficient of frequency (TCF) since

$$\mathrm{TCF} = \mathrm{TCV} - \alpha, \qquad [11.19]$$

where α is the thermal expansion coefficient along the SAW propagation direction.

Figure 11.7 shows the IDT admittance Y_{11} calculated by the delta-function model with K^2 and $\varepsilon(\infty)$ values of 5.5% and $55.4\varepsilon_0$, respectively, which correspond

Table 11.1 SAW substrate materials in practical use

Material	K^2	TCF	Notes
YZ-$LiNbO_3$	Good	Bad	Weak diffraction
ST-cut quartz	Bad	Very good	
128°YX-$LiNbO_3$	Good	Bad	Weak spurious
X-112°Y-$LiTaO_3$	Marginal	Marginal	Weak spurious
45°XZ-$Li_2B_4O_7$	Marginal	Good	
64°(41°) YX-$LiNbO_3$	Very good	Bad	Leaky
42°(36°)YX-$LiTaO_3$	Good	Marginal	Leaky

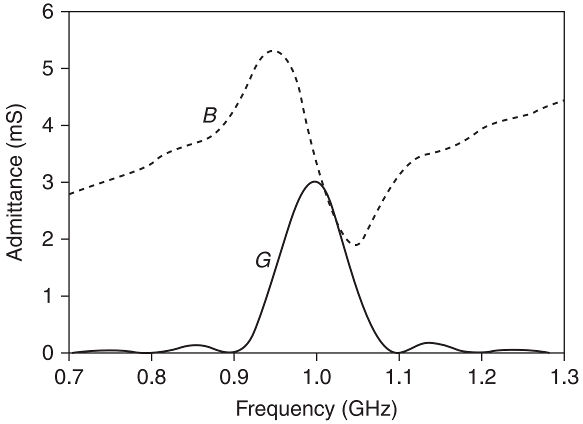

11.7 Frequency response of the input admittance Y_{11} for an IDT with N_1=10.

to those for 128°YX-LiNbO$_3$. In this calculation, $N = 10$ and $W = 30p_I$. As expected, G has sinc^2 x dependence.

11.2.2 Double-electrode IDTs

We sometimes use the double-electrode IDT shown in Fig. 11.8. In this case, one IDT period p_I has four electrodes. Since $p = p_I/4$, Bragg reflection does not occur at the center frequency, f_c (=V_S/p_I), for SAW excitation. Drawbacks of double-electrode IDTs are: (a) the necessity of fine-patterning techniques to fabricate narrower electrode widths, and (b) a smaller η.

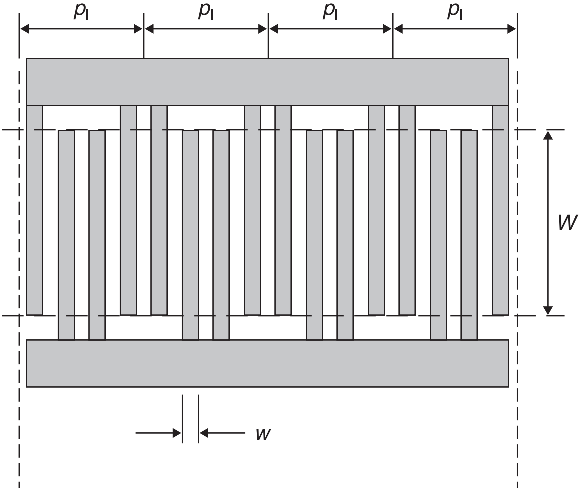

11.8 Double-electrode IDT.

11.2.3 Unidirectional transducers

The IDTs described above are symmetric with respect to the center of each period, and they excite SAWs toward both left and right directions with equal amplitude. We refer to this characteristic as bidirectionality. A unidirectional IDT (UDT) excites SAWs predominantly toward one of these directions.

Various UDTs have been proposed, and they are categorized into two types. The first type uses multi-phase electrical inputs. The UDT shown in Fig. 11.9(a) has a periodic finger geometry with an equal distance between fingers. Unidirectionality is realized by applying three-phase inputs whose phases are 120° out of phase with each other.[31] Unidirectionality is also achieved by applying two-phase inputs whose phases are 90° out of phase with each other, as in Fig. 11.9(b).[32]

A serious problem for these configurations is the interconnections between the fingers. All the fingers themselves can be realized by single-step photolithography. However, to interconnect third fingers requires a series connection or an air-gap structure.[31] The former results in an increased ohmic loss whereas the latter requires a complicated fabrication process.

To circumvent this problem, another type of two-phase UDT, shown in Fig. 11.10, was proposed, called a group-type UDT.[33] Several finger pairs with equal periodicity compose a group. Two different kinds of groups, whose periodicity is displaced by $p_I/4$, are placed alternately, and their common grounds are interconnected in series. This group structure reduces the ohmic loss.

In contrast, UDTs of the type shown in Fig. 11.11 and Fig. 11.12 have asymmetric geometries, and unidirectionality appears even though the conventional single-phase signal is applied. This type of UDT is called a single-phase unidirectional transducer (SPUDT).

First, consider the SPUDT structure shown in Fig. 11.11,[34] where thick and thin electrode fingers are aligned alternately. For electrical excitation, this structure is

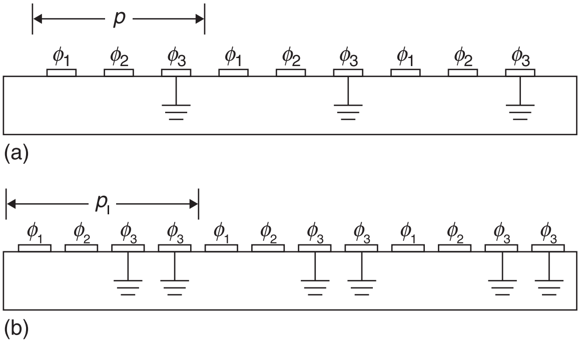

11.9 Multi-phase UDTs: (a) three-phase UDT, (b) two-phase UDT.

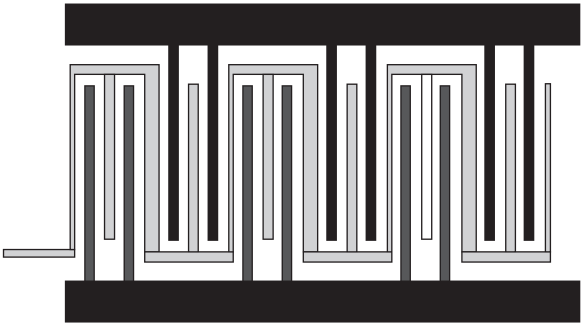

11.10 Group-type UDT.

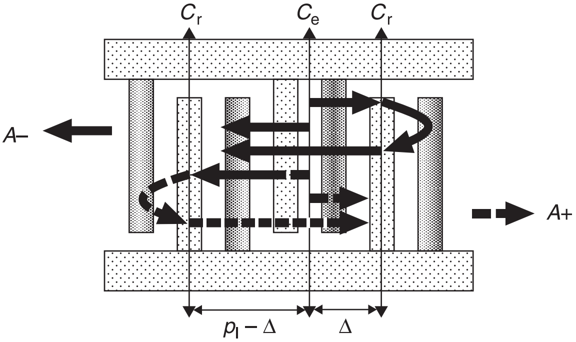
C_r
C_e
C_r
A–
A+
$p_I - \Delta$
Δ

11.11 Double-electrode-type IDT with two different finger thicknesses.

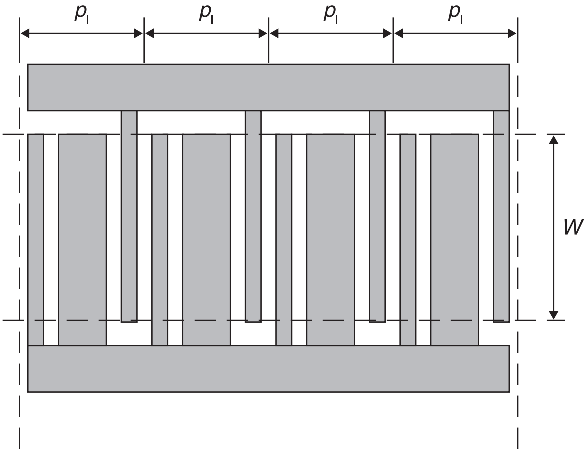

11.12 Distributed acoustic reflection transducer.

equivalent to a conventional double-electrode-type IDT, and the excitation center is at the point C_e in the figure. On the other hand, the thicker electrodes may mainly contribute to mechanical reflection and they are equivalent to a grating reflector with periodicity $p_I/2$. Thus the reflection center locates at the point C_r in the figure. It is clear that C_e is displaced by $p_I/8$ from C_r.

Let us denote the distance between the excitation and reflection centers as Δ. SAWs excited toward $+x$ and reflected at the reflection center return to the excitation center. Throughout propagation, they experience a phase shift of $\angle\Gamma\text{-}2\beta\Delta$, where Γ is the mechanical reflection coefficient, and they interfere with those excited directly toward $-x$. Similarly, SAWs excited toward $-x$ and reflected at the reflection center return to the excitation center. Their phase shift is given by $\angle\Gamma\text{-}2\beta(p_I\text{-}\Delta)$.

Because of the symmetrical electrode locations, the phase of Γ is $\pm\pi/2$ in general. Thus, if $\beta\Delta = \pm\pi/4$, two waves propagating toward $\pm x$ are in phase whereas those toward $\mp x$ are 180° out of phase. On the other hand, if $\beta\Delta = \pm 3\pi/4$, two waves propagating toward $\pm x$ are 180° out of phase whereas those toward $\mp x$ are in phase. Due to the periodicity of the structure, the effects of all reflected waves are summed. Thus, complete unidirectionality can be achieved when the condition $\Delta = \pm p_I(n/4 + 1/8)$ is satisfied. When this condition is not fulfilled, achievable performances are limited.

Figure 11.12 shows another type of SPUDT called the distributed acoustic reflection transducer (DART)[35] having three fingers per IDT period p_I. In this case, all the electrodes have the same thickness.

Due to the structural symmetry, the reflection center locates at the middle of the wide electrode. On the other hand, the excitation center may locate close to the middle of the narrow electrode connected to the upper busbar. Thus the distance Δ is expected to be close to $3p_I/8$, which is optimal for the UDT operation.

Even though a conventional single-electrode-type IDT has geometrical symmetry, unidirectionality may occur. That is, if the substrate material has crystallographic asymmetry, the reflection center will be displaced from the geometrical center of the electrode where the excitation center locates. This phenomenon is called natural unidirectionality.[36]

Note that unidirectionality can also be realized by placing one reflector at either side of a bidirectional IDT. Although the structure is very simple, the achievable bandwidth is much narrower than that of the IDT itself.

11.2.4 Coupling-of-modes theory

The delta-function model described above gives a good explanation of the behavior of IDTs, provided that SAW reflection is negligible. Since this assumption does not hold in general, the coupling-of-modes (COM),[37] *p* matrix[38] and equivalent circuit models[39] are widely used to simulate the behavior of IDTs, which all include the influence of reflection. The difference in these models is how one period of an IDT is expressed in a three-port black box, Fig. 11.13, where

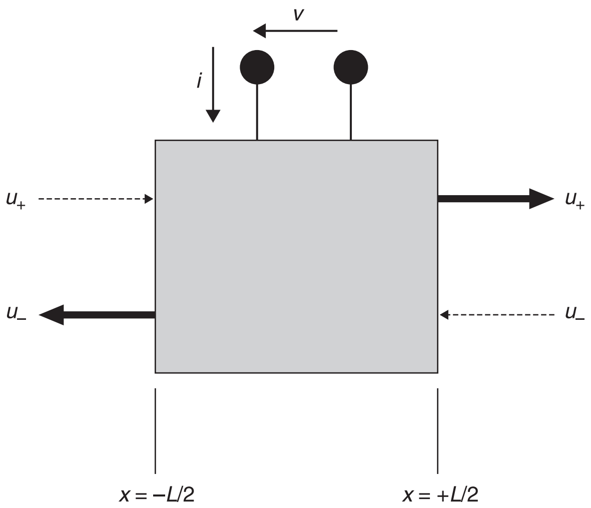

11.13 Three-port black box for an IDT.

$u_\pm(x)$ is the SAW amplitude propagating in the $\pm x$ direction, and v and i are the applied voltage and current, respectively.

Once each period is modeled, the whole IDT is expressed in the same three-port structure by the mutual connection. Short-circuited (SC) and open-circuited (OC) gratings are equivalent to IDTs where all electrodes are short-circuited or isolated electrically from the busbars, respectively.

We will discuss the COM model due to its simplicity and the number of references.

In the model, $U_\pm(x)$ [$= u_\pm(x)\exp(\pm j\pi x/p)$] and the current, $i(x)$, on the busbar are assumed to be governed by the following simultaneous linear equations:[40]

$$\frac{\partial U_+(x)}{\partial x} = -j\theta_u U_+(x) - j\kappa_{12} U_-(x) + j\zeta v, \qquad [11.20]$$

$$\frac{\partial U_-(x)}{\partial x} = +j\kappa_{12}^* U_+(x) + j\theta_u U_-(x) - j\zeta^* v, \qquad [11.21]$$

and

$$\frac{\partial i(x)}{\partial x} = -4j\zeta^* U_+(x) - 4j\zeta U_-(x) + j\omega C v, \qquad [11.22]$$

where C, κ_{12} and ζ are the static capacitance, and the reflection and the excitation coefficients per unit length, respectively. θ_u ($=\beta_u$-$2\pi/p_I$) is the detuning factor corresponding to the deviation of the wave number, β_u, of 'unperturbed' SAWs from the Bragg condition ($\beta_\mathrm{u} = 2\pi/p_\mathrm{I}$). Here 'unperturbed' is the artificial situation where the SAW reflection and excitation are ignored in the IDT.

It is expected that κ_{12}, ζ and C will be almost constant over a wide range of frequencies, while θ_u will change almost linearly with frequency. So θ_u is often expressed in the following form:

$$\theta_\mathrm{u} = 2\pi f / V_\mathrm{g} - 2\pi / p_\mathrm{I} + \kappa_{11}, \qquad [11.23]$$

where V_g is the SAW group velocity and κ_{11} is a constant called the self-coupling coefficient. When the Bragg frequency, f_B, is given for the IDT, κ_{11} is given by $\kappa_{11} = 2\pi (1 - f_\mathrm{B} p_\mathrm{I} / V_\mathrm{g})$.

The results of this analysis are accurate, especially for devices with conventional Rayleigh-type SAWs. Of course, the accuracy of the analysis is critically dependent on the parameters κ_{12}, ζ, C, V_g and κ_{11}. Numerical techniques for the determination of the parameters have been discussed in detail.[40]

When θ_u, κ_{12}, ζ and C are uniform (independent of x) throughout the IDT, the general solution of Eqs 11.20 and 11.21 is given by

$$U_+ (x) = a_+ e^{-j\theta^{\hat{\mathrm{p}}} x} + \Gamma_- a_- e^{+j\theta_\mathrm{p} x} + j\xi_+ v \qquad [11.24]$$

and

$$U_- (x) = \Gamma_+ a_+ e^{-j\theta_\mathrm{p} x} + a_- e^{+j\theta_\mathrm{p} x} + j\xi_- v \qquad [11.25]$$

where

$$\Gamma_+ = (\theta_\mathrm{u} \text{-} \theta_\mathrm{u})/\kappa_{12}$$

$$\Gamma_- = (\theta_\mathrm{u} \text{-} \theta_\mathrm{u})/\kappa_{12}{}^*$$

$$\xi_+ = (\zeta\theta_\mathrm{u} \text{-} \zeta^* \kappa_{12})/\theta_\mathrm{p}^2$$

$$\xi_+ = (\zeta^* \theta_\mathrm{u} \text{-} \zeta\kappa_{12}{}^*)/\theta_\mathrm{p}^2$$

and

$$\theta_\mathrm{p} = \beta_\mathrm{p} - 2\pi / p_\mathrm{I} = \sqrt{\theta_\mathrm{u}^2 - |\kappa_{12}|^2}\,. \qquad [11.26]$$

β_p is the SAW wave number in the IDT with $v = 0$, which is equivalent to a short-circuited (SC) grating.

Note that β_p for an open-circuited (OC) grating is given by

$$\beta_\mathrm{p} = 2\pi / p_\mathrm{I} + \sqrt{(\theta_\mathrm{u} - 4\left|\zeta\right|^2 / \omega C)^2 - \left|\kappa_{12} - 4\zeta^2 / \omega C\right|^2} \qquad [11.27]$$

from the condition $i(x) = 0$.

The total current, i, is calculated by substituting Eqs 11.24 and 11.25 into Eq. 11.22, i.e.,

$$i = \int_{-L/2}^{+L/2} \frac{\partial i(x)}{\partial x} dx = \int_{-L/2}^{+L/2} (-4j\zeta^* U_+ - 4j\zeta U_- + j\omega C v) dx. \qquad [11.28]$$

We can derive $a_\pm$ in terms of $U_+(-L/2)$, $U_-(+L/2)$ and v from Eqs 11.24 and 11.25. Then substitution of the result into Eqs 11.24, 11.25 and 11.28 gives the following expression, which is called the *p*-matrix form:[41]

$$\begin{pmatrix} U_+(+L/2) \\ U_-(-L/2) \\ i \end{pmatrix} = \begin{pmatrix} P_{11} & P_{12} & P_{13} \\ P_{12} & P_{22} & P_{23} \\ -4P_{13} & -4P_{23} & P_{33} \end{pmatrix} \begin{pmatrix} U_+(-L/2) \\ U_-(+L/2) \\ v \end{pmatrix}, \qquad [11.29]$$

where

$$P_{11} = \frac{\Gamma_+(1-E^2)}{1-\Gamma_+\Gamma_-E^2}, \qquad [11.30]$$

$$P_{12} = \frac{E(1-\Gamma_+\Gamma_-)}{1-\Gamma_+\Gamma_-E^2}, \qquad [11.31]$$

$$P_{22} = \frac{\Gamma_-(1-E^2)}{1-\Gamma_+\Gamma_-E^2}, \qquad [11.32]$$

$$P_{13} = \frac{(1-E)\{\xi_+(1+\Gamma_+\Gamma_-E)-\xi_+\Gamma_+(1+E)\}}{1-\Gamma_+\Gamma_-E^2}, \qquad [11.33]$$

$$P_{23} = \frac{(1-E)\{\xi_-(1+\Gamma_+\Gamma_-E)-\xi_-\Gamma_-(1+E)\}}{1-\Gamma_+\Gamma_-E^2}, \qquad [11.34]$$

and

$$P_{33} = \frac{4(1-E)\{(\xi_+-\Gamma_-\xi_-E)(\zeta^*+\Gamma_+\zeta)+(\xi_--\Gamma_+\xi_+E)(\zeta+\Gamma_-\zeta^*)\}}{\theta_p(1-\Gamma_+\Gamma_-E^2)}$$
$$-4jL(\zeta^*\xi_+ + \zeta\xi_-) + j\omega CL \qquad [11.35]$$

where $E = \exp(-j\theta_p L)$.

When the IDT is bidirectional and the x coordinate is chosen so that the excitation and reflection centers coincide with $x = np_I$, then κ_{12} and ζ are purely real.

Figure 11.14 shows the frequency response of the input admittance, Y ($=P_{33}$), of the IDT as a function of the normalized frequency $\theta_u p_I/2\pi$. The vertical axis is normalized by $2\pi f_c CL$ corresponding to the admittance of the IDT static capacitance at $f = f_c$. In the calculation, $\kappa_{12}p_I = 0$, $4\zeta^2 p_I/\omega C = 0.08$, and $L = 10p_I$. Comparison of this figure with Fig. 11.7 indicates that the COM analysis agrees well with the delta-function model when the influence of mechanical reflection is negligible.

Figure 11.15 shows the frequency response of $Y/2\pi f_c CL$ when $\kappa_{12}p_I = +\,0.04\pi$. Comparison of this figure with Fig. 11.14 indicates that, due to the non-zero κ_{12}, the frequency dependence of Re(Y) is deformed from the original $\mathrm{sinc}^2\, x$ shape and is peaky. This is due to the SAW resonance within the IDT.

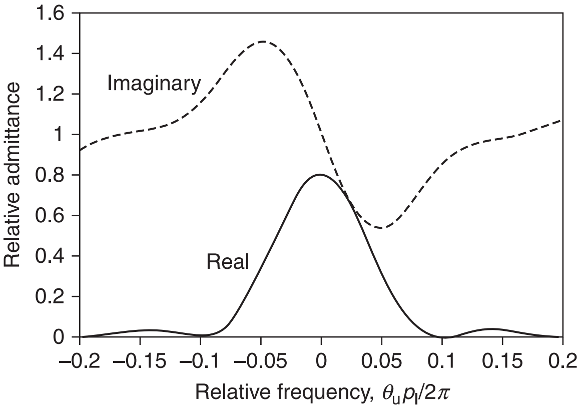

11.14 Frequency dependence of $Y/2\pi f_c CL$ when $\kappa_{12}p_I=0$.

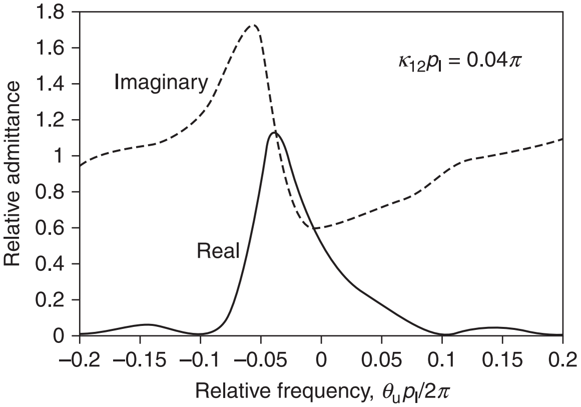

11.15 Frequency dependence of $Y/2\pi f_c CL$ when $\kappa_{12}p_I= + 0.04\pi$.

Figure 11.16 shows the frequency response of $Y/2\pi f_c CL$ when $\kappa_{12}p_I=-0.04\pi$. In this case, due to the negative $\kappa_{12}p_I$, the peak in Re(Y) is on the higher frequency side.

Figure 11.17 shows the change in the normalized radiation conductance, Re(Y)/4(ζL)^2, with $\kappa_{12}p_I$, in decibels, namely, 10 log{Re(Y)/4(ζL)^2} as a function of the normalized frequency. When $\kappa_{12}p_I$ is small, Re(Y) has typical sinc^2 x dependence. With an increase in $\kappa_{12}p_I$, the main lobe is peaky and the peak moves toward low frequencies. Although not shown, with an increase in L, the peak amplitude is steep and large while its position is scarcely changed.

When the IDT is not uniform and the simulation parameters are dependent on x, Eqs 11.20–11.22 should be solved numerically.

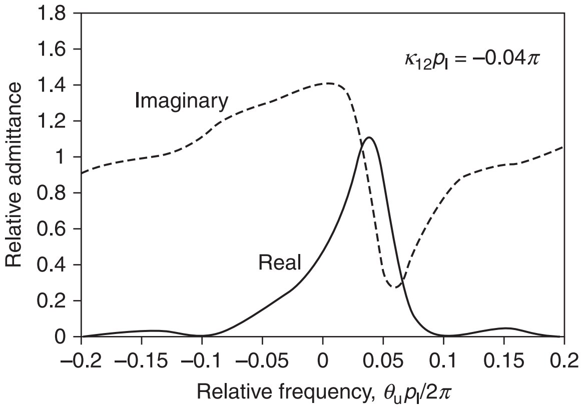

11.16 Frequency dependence of $Y/2\pi f_c CL$ when $\kappa_{12}p_I = -0.04\pi$.

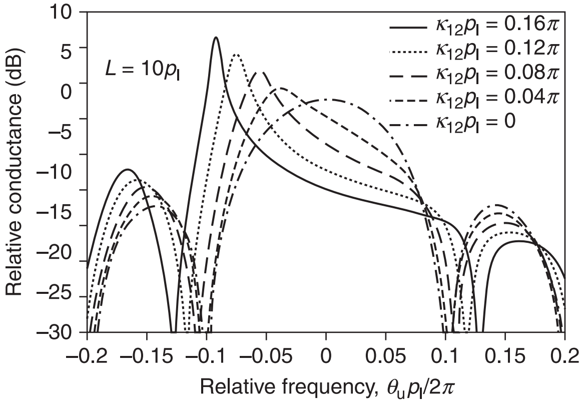

11.17 Change in frequency dependence of $\mathrm{Re}(Y)/4(\zeta L)^2$ with $\kappa_{12}p_I$.

Next, we will analyze the behavior of single-phase UDTs using the COM theory. We define $\mu = \angle(\kappa_{12}/\zeta^2)$. As described in Section 11.2.3, the directionality is due to the displacement, d, of the reflection center from the excitation center, where $d = \mu p_I/4\pi$.

Figure 11.18 shows the frequency response of $Y/2\pi f_c CL$ as a function of the normalized frequency $\theta_u p_I/2\pi$. The parameters are the same as those used for Fig. 11.15 except $\mu = 90°$. There are twin peaks. This is only typical for directional IDTs.

Figure 11.19 shows the change in the relative conductance, $\mathrm{Re}(Y)$, of the IDT with μ. The vertical axis is normalized by $4(|\zeta|L)^2$ corresponding to the peak amplitude of $\mathrm{Re}(Y)$ when $\kappa_{12}=0$. In the calculation, $|\kappa_{12}|p_I = 0.04\pi$. With an increase in μ, the height of the peak at lower frequencies decreases, and another peak

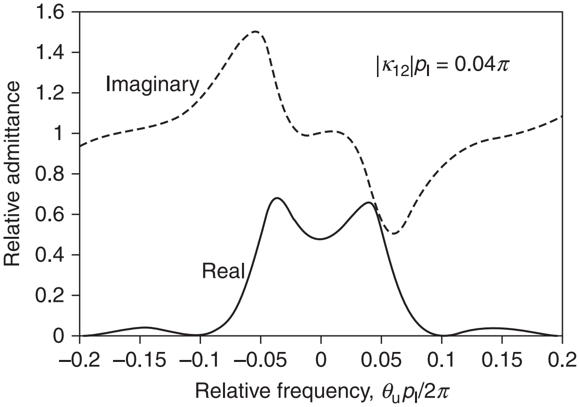

11.18 Frequency dependence of $Y/2\pi f_c CL$ when $\kappa_{12}p_I = j0.04\pi$.

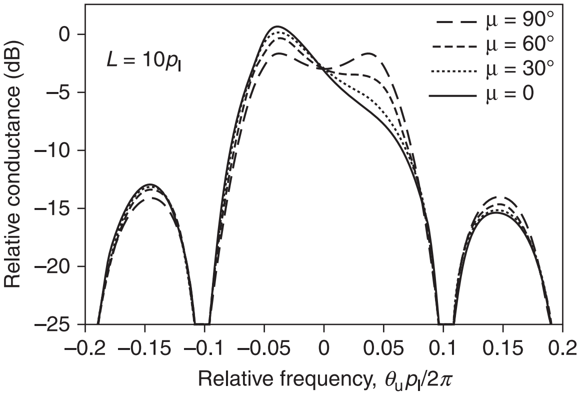

11.19 Variation of IDT conductance with μ.

appears at a higher frequency. When $\mu = 90°$, these two peaks have the same height, and $\mathrm{Re}(P_{33})$ is symmetric with respect to $\theta_u = 0$.

Figure 11.20 shows the directivity $D = |P_{13}/P_{23}|$. With an increase in μ, D becomes large and its maximum approaches $\theta_u = 0$. D has a maximum at $\theta_u = 0$ when $\mu = 90°$. The θ_u at the peak decreases with a further increase in μ; when $\mu > 90°$, the θ_u dependence of D is the mirror image of that for $180°\text{-}\mu$. The sign of μ does not affect the conductance characteristics, and the direction of the directivity is reversed.

Figures 11.21 and 11.22 show $|P_{13}|$ (forward) and $|P_{23}|$ (backward) for a unidirectional IDT with acoustic length $L = 20p_I$ and $\mu = 90°$, where the vertical axes are normalized by the values at the Bragg frequency, f_B, where $\theta_u = 0$. When $|\kappa_{12}|L$ is small, the typical frequency response with a sinc x shape can be seen, and the achievable directivity is limited. The directivity becomes large when $|\kappa_{12}|p_I$ is large. However, both $|P_{23}|$ and $|P_{13}|$ are considerably small near f_B due to the self-resonance of the IDT.

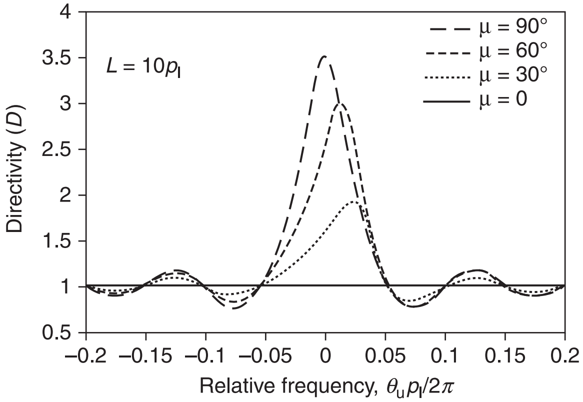

11.20 Variation of IDT directivity with μ.

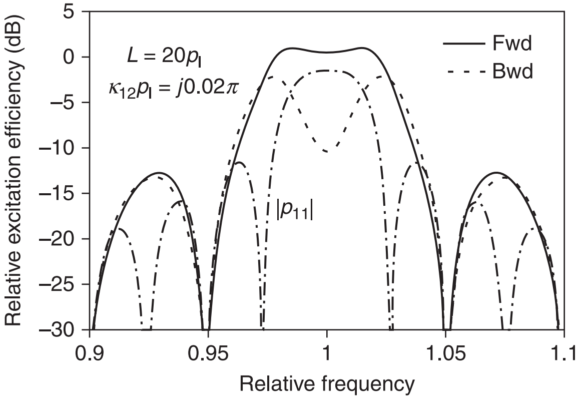

11.21 Frequency response of $|P_{13}|$ (forward) and $|P_{23}|$ (backward) of SPUDT ($\kappa_{12}p_l = j0.02\pi$, $L = 20p_l$). $|P_{11}|$ is also shown.

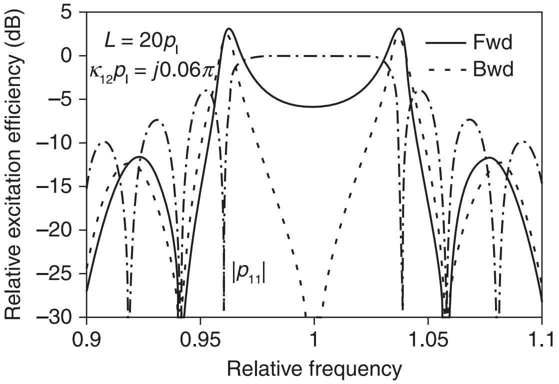

11.22 Frequency response of $|P_{13}|$ (forward) and $|P_{23}|$ (backward) of SPUDT ($\kappa_{12}p_l = j0.06\pi$, $L = 20p_l$). $|P_{11}|$ is also shown.

These figures also show $|P_{11}|$. Near f_B, $|P_{13}|$ and $|P_{23}|$ are very small because the SPUDT resonances and the SAW field hardly leak away to the outside. The response near f_B is small with an increase in $|\kappa_{12}|p_I$.

Figure 11.23 shows the change in $|P_{13}|$ and $|P_{23}|$ with L when $\kappa_{12}p_I = j0.02\pi$. Comparison of this figure with Fig. 11.21 and Fig. 11.22 suggests that the behavior of P_{13} and P_{23} is characterized by $|\kappa_{12}|L$. When $|\kappa_{12}|L<1$, the influence of the internal reflection is small and the device acts as a simple SAW transducer. On the other hand, when $|\kappa_{12}|L>1$, the influence is significant and the device behaves as a resonator. Thus $|\kappa_{12}|L\approx1$ is desired for standard SPUDT operation.

Figure 11.24 shows the change in $|P_{13}|$ and $|P_{23}|$ with μ when $|\kappa_{12}|p_I = 0.02\pi$ and $L = 20p_I$. The frequency for the maximum D and the shape of the passband change with μ. Although not shown, μ also limits the achievable maximum D for given $|\kappa_{12}|L$.

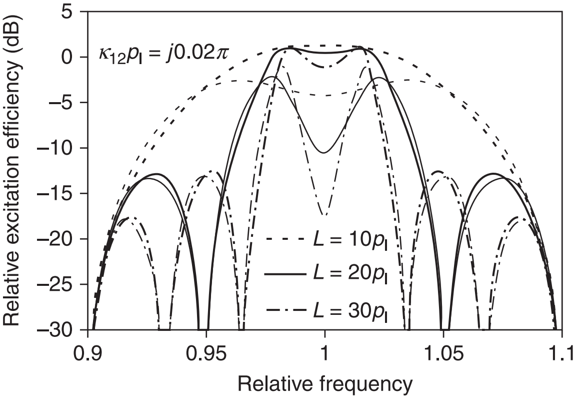

11.23 Change in $|P_{13}|$ (bold line) and $|P_{23}|$ (thin line) with L ($\kappa_{12}p_I=j0.02\pi$).

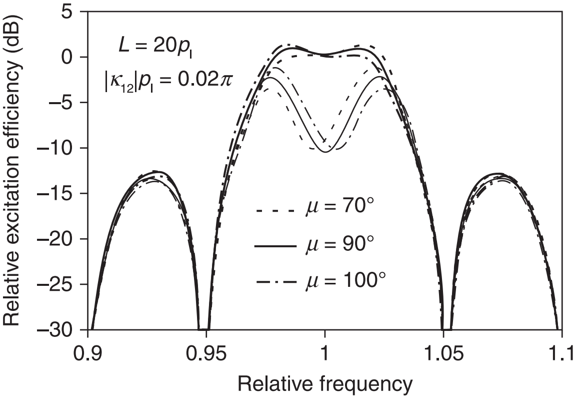

11.24 Change in $|P_{13}|$ (bold line) and $|P_{23}|$ (thin line) with μ ($|\kappa_{12}|p_I=0.02\pi$, $L=20p_I$).

11.3 Transversal SAW filter

11.3.1 Apodized IDTs

The delta-function model described in Section 11.2.1 indicates that the amplitude of a SAW pulse train can be made non-uniform by adjusting the overlap lengths, W_n, between adjacent IDT fingers, as shown in Fig. 11.25. This weighting technique is called apodization.

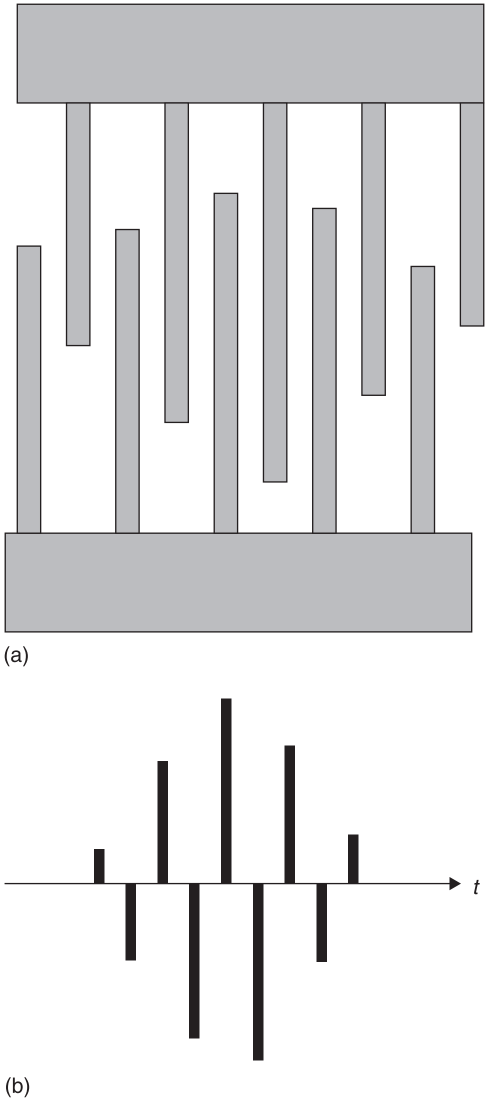

11.25 Apodized IDT: (a) electrode pattern, (b) SAW pulse train.

When we place this type of IDT with a conventional IDT in parallel, as shown in Fig. 11.26, we can flexibly synthesize the filter response. This type of device is called a SAW transversal filter.[42] In the device configuration shown in Fig. 11.26, there are dummy electrodes at both ends, which are cut obliquely to suppress the effect of reflection at the IDT ends. Acoustic absorbers are placed near the outer ends to suppress reflection from the substrate edges. A shield electrode is used to reduce electrostatic coupling between the two IDTs.

Half of the SAW power excited at the left IDT does not contribute to signal transfer. In addition, the right IDT can detect only half of the SAW power due to reciprocity.[43] Thus, the use of traditional bidirectional IDTs always causes an additional 3-dB loss at both transduction and detection. This loss is called the bidirectional loss.

When the delta-function model is applied, the transfer function $H^{S}_{21}(f)$ between the two apodized IDTs is given by

$$H^{s}_{21}(f)=\frac{c_s^2}{4}\sum_{m=0}^{2N_1-1}\sum_{n=0}^{2N_2-1}(-1)^{m+n}\mathrm{Min}(W_m^{(1)},W_n^{(2)})\exp(-2\pi jfL_{mn}/V_s), \qquad [11.36]$$

where the term $\mathrm{Min}(W_m^{(1)},W_n^{(2)})$ shows that a portion of the excited SAW energy can be detected by the second IDT when $W_n^{(2)}$ is smaller than $W_m^{(1)}$. The excited SAW energy itself becomes small when $W_m^{(1)}$ is smaller than $W_n^{(2)}$. When $W_n^{(2)}$ is constant and larger than or equal to $\mathrm{Min}(W_0^{(1)}, W_1^{(1)}, \ldots, W_{2N_1-1}^{(1)})$, Eq. 11.36 reduces to:

$$H^{S}_{21}(f)=N_2 c_S H_1(f)\hat{H}_2(f)\exp(-2\pi jfL_{\mathrm{T}}/V_S), \qquad [11.37]$$

where $\hat{H}^{S}_{2}(f)$ is the function defined in Eq. 11.3 for the second IDT, and

$$H^{s}_{1}(f)=\frac{c_s}{2}\sum_{n=0}^{2N_1-1}(-1)^n W_n\exp(-2\pi jfL_n/V_s). \qquad [11.38]$$

The desired frequency response can be synthesized by appropriate values of W_n.

The weighting, W_n, is often set to be symmetrical, i.e. $W_{2N-1-n}=W_n$, so that $\angle\{H^{S}_{21}(f)\}$ is proportional to f. This leads to a signal delay between the two IDTs

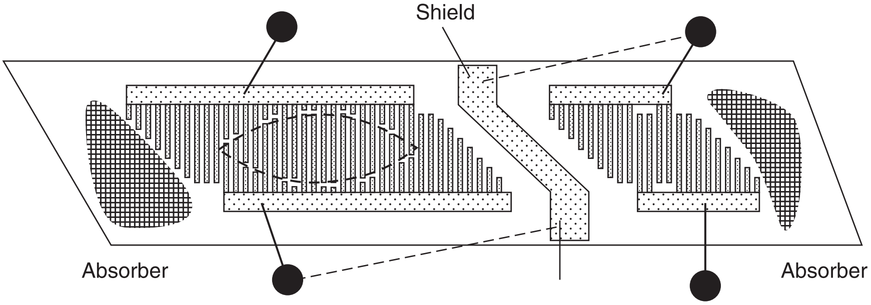

11.26 SAW transversal filter.

that is invariant with f (it is a constant group delay). This property is called the linear phase, which is desirable in signal processing.

It is interesting to note that W_n in Eq. 11.36 is equivalent to the Fourier expansion coefficients of $H_1^S(f)$. For example, we sometimes apply the following Hamming function for W_n:

$$W_n \approx 0.54 - 0.46\cos\varphi_n, \tag{11.39}$$

where $\varphi_n = \pi n/(2N_1 - 1)$. Figure 11.27 shows $H_1^S(f)$ for the weighting function. In the calculation, $N_1 = 80$. This weighting function has an out-of-rejection level of about 43 dB, which is much better than that of the unweighted IDT also shown in the figure (13 dB).

Figure 11.28 shows the calculated P_{13} of the Hamming weighted IDT ($L = 80p_I$, $N_1 = 80$) and the unweighted IDT with $N_2 = 20$. Since the total transfer function is given by their product, a further increase in N_2 of the unweighted IDT results in a reduced passband width, whereas a smaller N_2 results in increased insertion loss.

Figure 11.29 shows the calculated device response when these two IDTs are combined. A superior filter response with the out-of-band rejection better than 56 dB (≈43 + 13 dB) can be synthesized. The figure also shows the group delay, τ, estimated by $-\partial(\angle S_{21})/\partial\omega$. Although the IDTs are symmetrical, τ is not constant with respect to f. This is due to the TTE, which will be discussed in Section 11.3.2. In this design, the minimum insertion loss is about 15 dB. It includes the

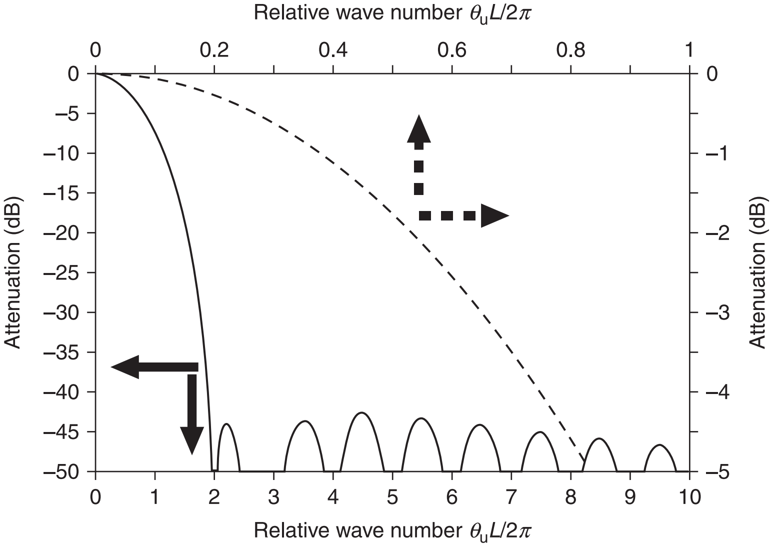

11.27 Fourier spectrum of the Hamming function where $r = 2\pi x/L$; the same data are shown at two resolutions. Arrows indicate the applicable scales.

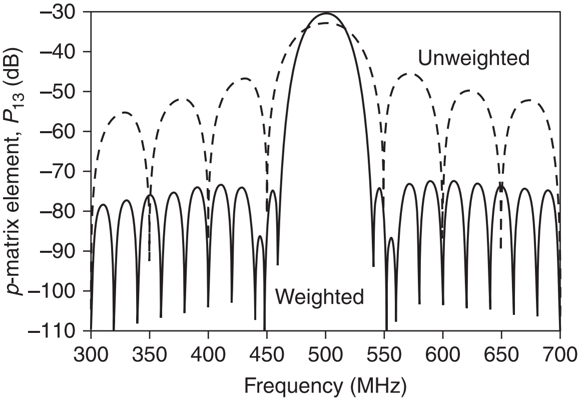

11.28 Frequency response of weighted and unweighted IDTs.

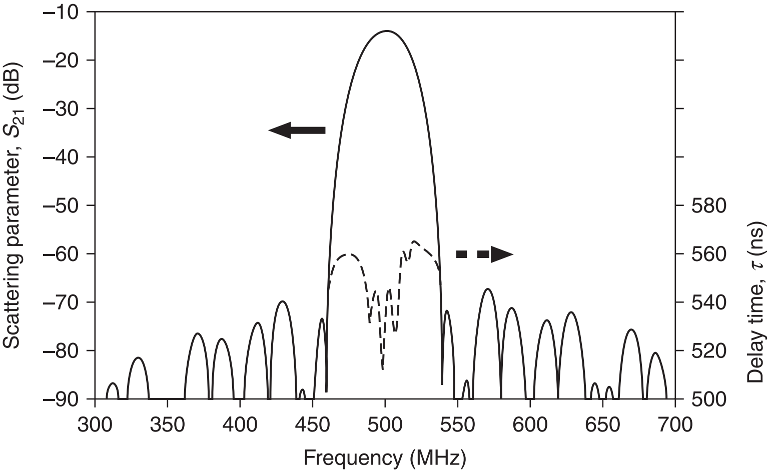

11.29 Frequency response of transversal SAW filter. Arrows indicate the applicable scales.

bidirectional loss of 6 dB; the remaining 9 dB is mainly caused by an impedance mismatch with peripheral circuitry, which will be discussed in Section 11.3.2. If we try to reduce the insertion loss, the influence of the TTE will be more apparent.

Theoretically, much better out-of-band rejection is realized by the use of appropriate weighting functions, such as

$$W_n \approx 0.42 - 0.50\cos\varphi_n + 0.08\cos(2\varphi_n) \qquad \text{(Blackman window)}$$

and

$$W_n \approx 0.35875 - 0.48829\cos\varphi_n + 0.14128\cos(2\varphi_n) - 0.01168\cos(3\varphi_n) \qquad \text{(Blackman–Harris window)}$$

The Blackman window gives an out-of-band rejection level of 60 dB, whereas the Blackman–Harris window gives 100 dB. However, the actually achievable out-of-band rejection is limited to about 45–60 dB by the diffraction effect, which will be discussed in Section 11.3.3. The Hamming function is advantageous as it is less sensitive to this effect because the minimum value of W_n is relatively large.

Next, we will design transversal SAW filters with wide bandwidth and a flat passband shape. Here, the IDT weighting pattern was designed using the Remez exchange algorithm.[44,45] The number of IDT finger pairs, N_1, can be estimated from the given specifications to high accuracy.

Figure 11.30 shows the weighting function given by the Remez exchange algorithm. Figure 11.31 shows P_{13} for the weighted and unweighted IDTs. It can

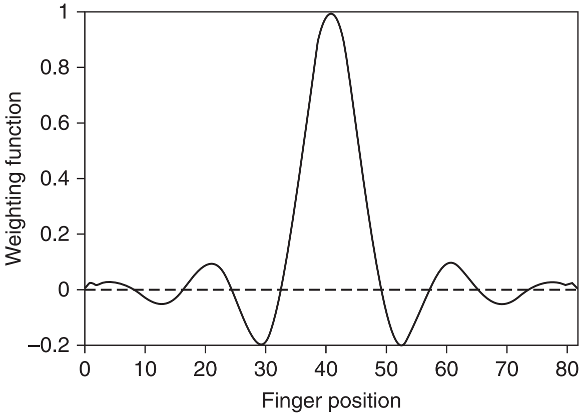

11.30 Designed weighting function.

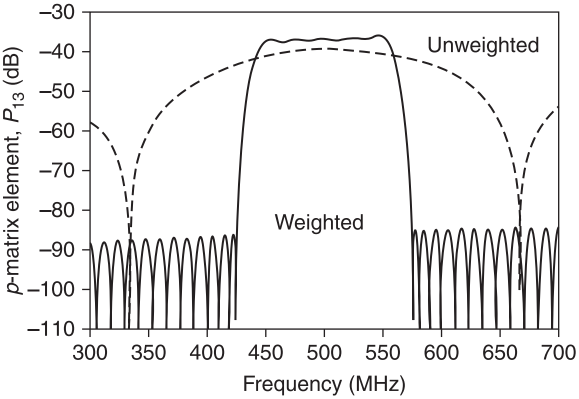

11.31 Frequency response of weighted and unweighted IDTs.

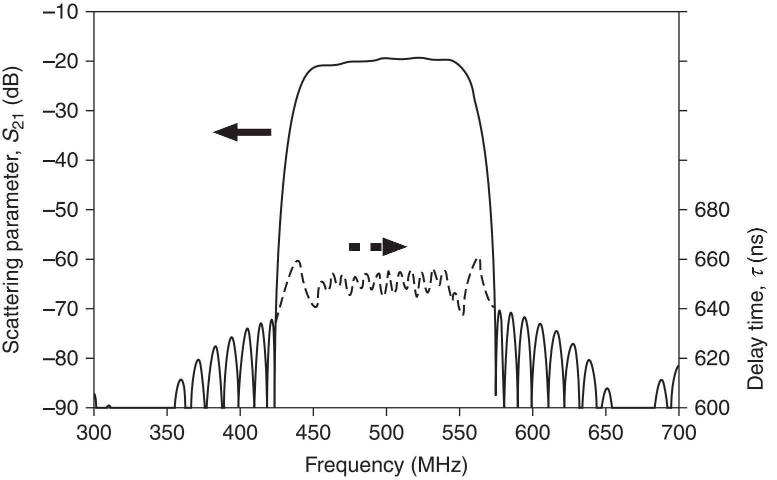

11.32 Frequency response of designed transversal filter. Arrows indicate the applicable scales.

be seen that flat passband and equi-ripple out-of-band characteristics are realized. In this case, N_2 is limited to 6 so as not to reduce the passband width.

Figure 11.32 shows the calculated device response. A flat passband and good out-of-band rejection are simultaneously achieved. The minimum insertion loss is 19.5 dB.

11.3.2 The influence of peripheral circuits

Figure 11.33 shows the whole circuit including peripheral circuits, where v_s is the open-circuit voltage (peak value) of the signal source, and R_0 is the circuit impedance, usually 50 Ω. In an RF-device simulation, we must take the influence of the peripheral circuits into account because they significantly affect the performance of the whole device.

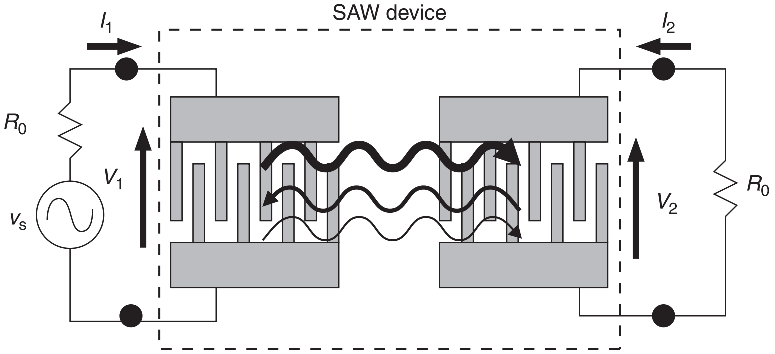

11.33 Transversal SAW filter with peripheral circuits.

In RF engineering, device performance is characterized by the scattering matrix elements, S_{mn}, which correspond to the output signal, b_m, at the port m relative to the input signal, a_n, at the port n. Note that a_m and b_m are normalized so that their square corresponds to the power.

a_m and b_m are related to the magnitude of the terminal voltage, v_m, and the current, i_m, at the port m by

$$a_m = \frac{v_m + R_0 i_m}{\sqrt{8R_0}}, \tag{11.40}$$

and

$$b_m = \frac{v_m - R_0 i_m}{\sqrt{8R_0}}. \tag{11.41}$$

A conversion formula from the admittance matrix, $[Y]$, to the scattering matrix, $[S]$, is

$$[S] = \{R_0[Y] + [I]\}^{-1}\{R_0[Y] - [I]\}, \tag{11.42}$$

where $[I]$ is the identity matrix. For example, S_{21} is given by

$$S_{21} = -\frac{2G_0 Y_{21}}{(Y_{11} + G_0)(Y_{22} + G_0) - Y_{12}Y_{21}} \tag{11.43}$$

where $G_0 = R_0^{-1}$.

Figure 11.34 shows S_{11} ($= S_{22}$) when the two IDTs used to calculate Fig. 11.7 are aligned. It can be seen that $|S_{11}| \approx 1$ at frequencies far from the center frequency (1 GHz). This is because SAWs are scarcely excited and most of the input electrical

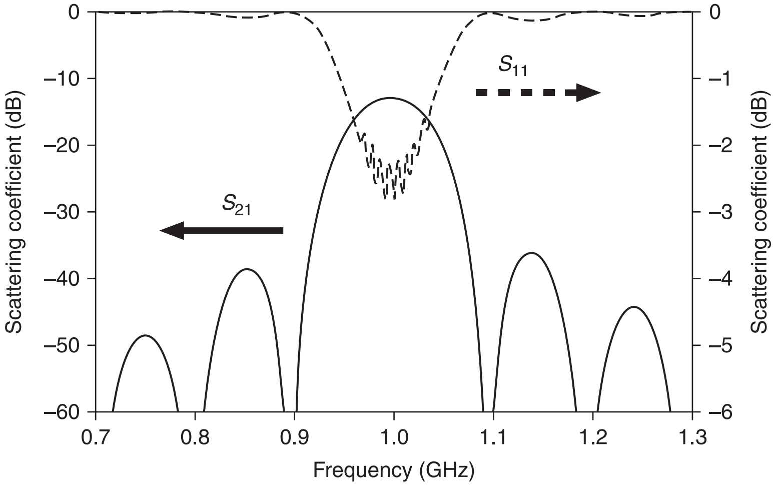

11.34 Frequency response of two-port SAW filter with $N = 10$. Arrows indicate the applicable scales.

power is reflected to the signal source. Near the center frequency, on the other hand, $|S_{11}|$ is small due to SAW excitation. Since IDTs are assumed to be ideal and lossless in this analysis, $1-|S_{11}|^2$ and $|S_{11}|^2$ give the excited SAW power and the electrically reflected power relative to the incident electrical power, respectively.

Figure 11.34 also shows the calculated S_{21}. It can be seen that there is a typical frequency response with a $\text{sinc}^2\, x$ dependency. Weak ripples are seen in both S_{11} and S_{21} near the center frequency. These are caused by electrical regeneration in the IDTs, which is equivalent to reflection.

We will now discuss electrical regeneration using the S_{21} given by Eq. 11.43. Recall that Y_{12} corresponds to the current induced in the first IDT by the voltage generated in the second IDT. This indicates that the term $Y_{12}Y_{21}$ in Eq. 11.43 is due to electrical regeneration by these IDTs. When the SAW arrives at the second IDT, a voltage is induced in the second IDT through the current flow to the peripheral circuit, and SAW regeneration equivalent to reflection occurs.

SAWs reflected by the second IDT are re-reflected by the first IDT, and are finally detected by the second IDT (Fig. 11.33). This response is called the triple transit echo (TTE); it interferes with the main response and causes ripples in the frequency response due to difference in the delay time. The impact of the TTE is significant only when $|Y_{12}|$ is comparable to G_0.

The TTE is not included in the basic operation of the SAW device described above. Thus the condition $|Y_{12}Y_{21}| << G_0^2$ should be satisfied. Equation 11.43 indicates that this condition is fulfilled only when $|Y_{12}Y_{21}| \approx \text{Re}(Y_{11})\text{Re}(Y_{22}) << G_0^2$. Under the condition, Eq. 11.43 can be approximated as

$$S_{21} \approx -\frac{2Y_{21}}{G_0}. \tag{11.44}$$

This result indicates that the TTE response can be suppressed only by reducing $|S_{21}|$, that is, by increasing the minimum insertion loss.

In addition to electrical regeneration, SAW reflection occurs due to structural discontinuities, for example, at IDT electrode edges. Since the electrodes are aligned periodically, strong SAW reflection (Bragg reflection) may occur at frequencies $f = 2nV_S/p$, where n is an integer and p is the periodicity of the IDT electrodes. Since $p = p_I/2$ for single-electrode IDTs, the Bragg reflection occurs at their center frequency f_c ($= V_S/p_I$).

11.3.3 Secondary effects

In the analyses above, SAWs excited by an IDT are assumed to be plane waves. However, a plane wave spreads with propagation due to diffraction, and finally forms a circular wave. The influence of diffraction is significant where W_n is small and the propagation distance is large. Since transversal filters sometimes include small W_n regions due to apodization, their characteristics are often significantly affected by diffraction.

The influence of diffracted SAWs is small in the passband where the SAW fields excited by each finger are added in phase. On the other hand, diffracted SAWs significantly influence device characteristics in the rejection band where the SAW fields cancel with each other and their strength is comparable to that of the diffracted ones. Then periodic nulls may disappear and out-of-band rejection may deteriorate. In addition, diffraction may widen the transition band. The effect of diffraction must be compensated for in the design of high-performance SAW transversal filters.

11.3.4 Single-phase unidirectional transducer (SPUDT) filters

The use of unidirectional transducers described in Section 11.2.3 allows us to realize low-loss SAW transversal filters without suffering the TTE problem. Even when the directivity is not perfect, acoustic reflection can be cancelled out with electrical regeneration, and thus the total SAW reflection coefficient, $\hat{S}_{11}$, can be suppressed by setting the peripheral circuit impedance appropriately.[46]

Figure 11.35 shows the frequency response of S_{21} for a SAW transversal filter composed of two identical unapodized SPUDTs with $L = 20p_I$, $|\kappa_{12}|p_I = 0.02\pi$ and $\mu = 90°$. In this calculation, we set the space length L_T between the IDTs to $50p_I$, and G_s and B_s are adjusted so that $\hat{S}_{11}$ is zero at the center frequency. In the figure, $\hat{S}_{11}$ for the SPUDT is also shown. Due to the suppressed $\hat{S}_{11}$ near the center frequency, a typical passband shape of the form of $\text{sinc}^2\, x$ is seen in spite of the small insertion loss.

In the figure, the group delay, τ, is also shown. τ is normalized by the τ_p for the propagation of the unit SPUDT period. A comparison of this figure with Fig. 11.29 and Fig. 11.32 indicates that the variation of τ with f is relatively large. This is mainly due to the variation of $\hat{S}_{11}$.

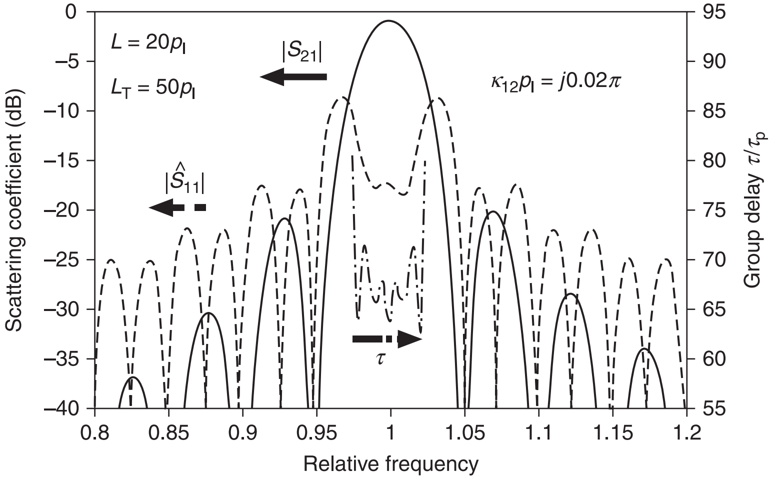

11.35 Frequency response of a SAW transversal filter composed of two unapodized SPUDTs. Arrows indicate the applicable scales.

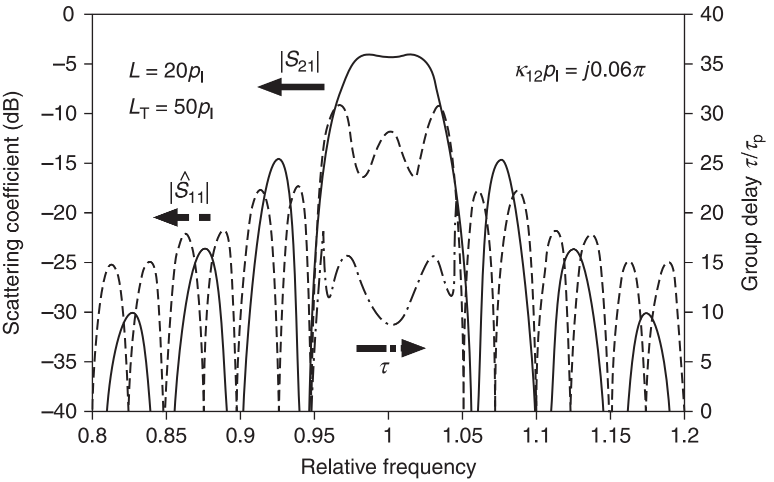

11.36 Frequency response of a SAW transversal filter composed of two SPUDTs. Arrows indicate the applicable scales.

Figure 11.36 shows the SPUDT filter when $|\kappa_{12}|p_I$ is increased to 0.06π. It can be seen that, although the passband shape of $\mathrm{sinc}^2\, x$ is not realizable due to strong internal reflection, the flat passband shape is realized. This is due to the extension of the impulse response length through the multiple echoes. As will be described in Section 11.3.5, low-loss and flat passband SAW transversal filters can be realized by the skillful use of this phenomenon. The design is called the resonant SPUDT.[47]

11.3.5 Resonant SPUDT filters

We will next discuss the design of weighting functions for the COM parameters, κ_{12} and ζ, for resonant SPUDT filters.

In the out-of-band region, $|p_{11}|$ for SPUDTs is small and the weighting function for ζ determines the frequency response. Thus, appropriate weighting is necessary to realize good out-of-band rejection. On the other hand, when κ_{12} is uniform, the frequency bandwidth giving large directivity is limited, as shown in Fig. 11.21 and Fig. 11.22. For wideband operation, weighting is needed also for κ_{12}.

Figure 11.37 shows the designed result when only the amplitude flatness was specified. It can be seen that a very flat passband and good out-of-band rejection are simultaneously realized. However, associated with very steep cut-off characteristics, the group delay deviation with the passband is large. Although a stronger resonance will result in steeper cut-off characteristics, it also results in the deterioration of the group delay deviation.

Figure 11.38 shows the designed result when the group delay flatness was also taken into account. Although the passband and out-of-band characteristics are somewhat worse, the group delay response is significantly improved.

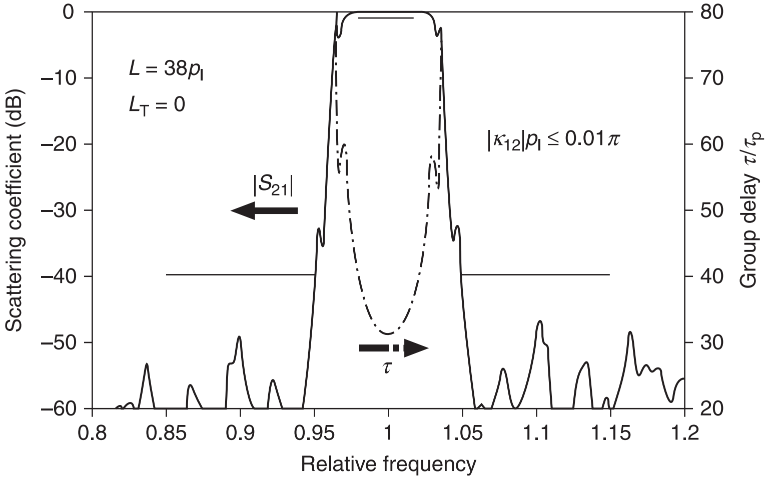

11.37 Result of optimization when the amplitude flatness is specified. Arrows indicate the applicable scales.

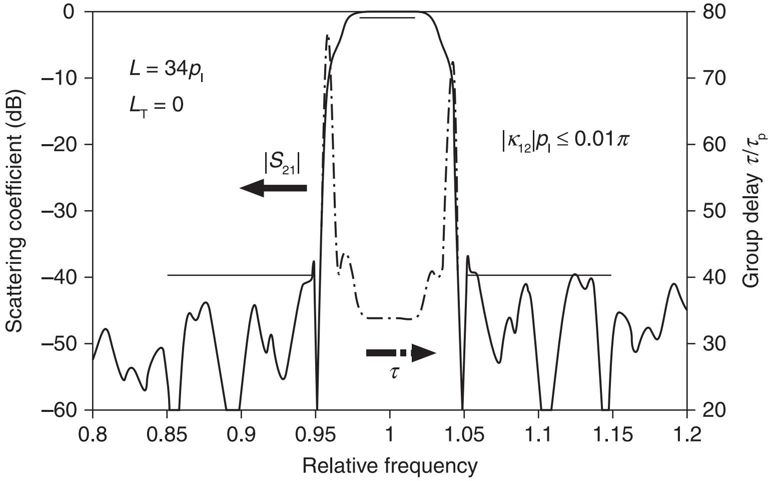

11.38 Result of optimization when flatness for both the amplitude and group delay is specified. Arrows indicate the applicable scales.

Figure 11.39 shows the weighting functions obtained by this optimization. In this case, the weighting for κ_{12} is gradual, and that for ζ changes rapidly. It can be seen that the regions with large ζ are sandwiched in regions where κ_{12} has the opposite sign. This results in an extension and delay of the main lobe in the impulse response, which are necessary for the realization of a symmetrical impulse response and are necessary for the group delay flatness.

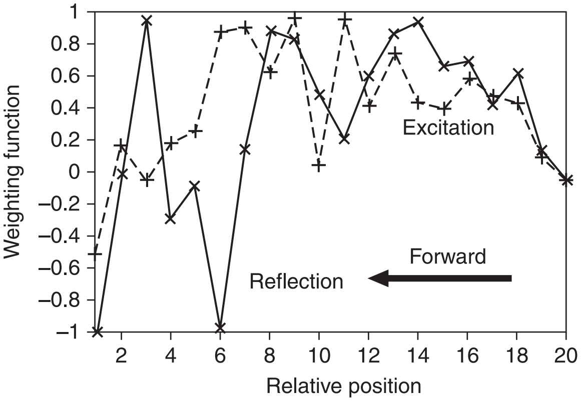

11.39 Designed weighting functions for excitation (ζ) and reflection (κ_{12}).

11.4 SAW resonators

11.4.1 One-port SAW resonators

Figure 11.40(a) shows a typical configuration for a one-port SAW resonator where two grating reflectors are placed at both ends of the IDT.[48] A very steep resonance can be detected by the IDT when the device is designed so that the resonance

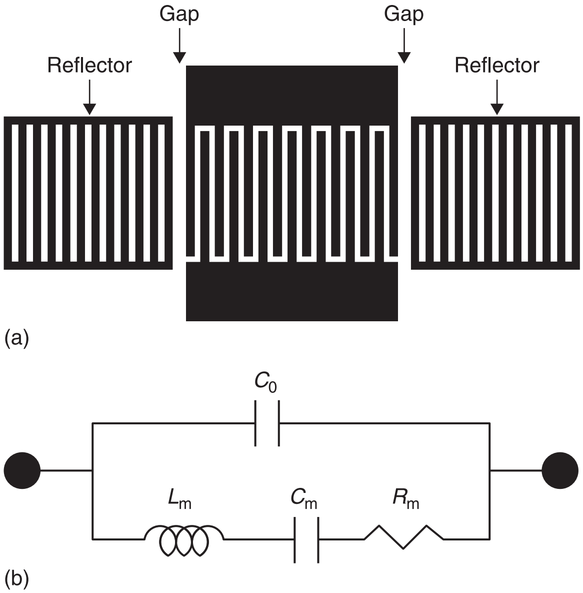

11.40 One-port SAW resonator: (a)structure, (b) equivalent electrical circuit.

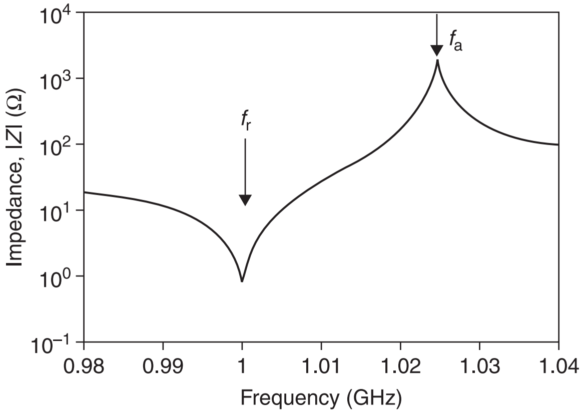

11.41 Typical electrical resonance characteristics of one-port SAW resonator.

frequencies of the IDT and reflectors coincide with each other. The length of the gaps between the IDT and the reflector are often adjusted to control the location of the resonance frequency within the reflector stopband.

Figure 11.40(b) shows its equivalent circuit near resonance, where C_m and L_m are the motional capacitance and inductance, respectively. C_0 is the static (clumped) capacitance of the IDT and R_m is the motional resistance.

Figure 11.41 shows typical electrical resonance characteristics for a one-port SAW resonator. Just above the resonance frequency, f_r, where the impedance $|Z|$ is a minimum, there is an anti-resonance frequency, f_a, where the impedance $|Z|$ is a maximum.

The equivalent circuit gives

$$f_r = \frac{1}{2\pi\sqrt{L_m C_m}} \tag{11.45}$$

and

$$f_a = \frac{1}{2\pi\sqrt{L_m (C_m^{-1} + C_0^{-1})^{-1}}}. \tag{11.46}$$

We can determine L_m and C_m from the measured C_0, f_r and f_a. R_m can be determined from G^{-1} at $f = f_r$.

The capacitance ratio, γ, is frequently used as a measure of the resonator performance:

$$\gamma = \frac{C_0}{C_m} = \frac{1}{(f_a / f_r)^2 - 1}, \tag{11.47}$$

which corresponds to the inverse of the effective electromechanical coupling factor. From the equivalent circuit, the quality factor, Q_r, at f_r is given by

$$Q_{\mathrm{r}} = 2\pi f_{\mathrm{r}} L_{\mathrm{m}} / R_{\mathrm{m}}. \qquad [11.48]$$

In the filter design, Q_{r} determines the minimum insertion loss and the steepness of the passband edges.[49]

Although the equivalent circuit shown in Fig. 11.40(b) implies that the Q factor Q_{a} at f_{a} is almost equal to Q_{r}, it is not true in general due to the existence of additional loss mechanisms, such as electrode resistance and energy leakage from the IDT region. Resistances are often added to an equivalent circuit to take these effects into account. For resonator characterization, the figure of merit is defined as

$$M_{\mathrm{r}} = Q_{\mathrm{r}} / \gamma, \qquad [11.49]$$

or

$$M_{\mathrm{a}} = Q_{\mathrm{a}} / \gamma. \qquad [11.49']$$

In the filter design, $M_r M_{\mathrm{a}}$ determines the achievable minimum insertion loss.[49]

The equivalent circuit also gives the following relations:

$$M_{\mathrm{r}} \cong \left| B_0 Z_{\mathrm{min}} \right|^{-1}, \qquad [11.50]$$

and

$$M_{\mathrm{a}} \cong \left| B_0 Z_{\mathrm{max}} \right|, \qquad [11.50']$$

where $B_0 = 2\pi f_{\mathrm{r}} C_0$, and Z_{max} and Z_{min} are the electrical impedances of the resonator at f_{a} and f_{r}, respectively. The impedance ratio, $|Z_{\mathrm{max}}/Z_{\mathrm{min}}|$ ($\approx M_{\mathrm{r}} M_{\mathrm{a}}$), is often used as the figure of merit.

For SAW resonators, frequency stability is very important and has been investigated extensively from various aspects. Previously, discussions were mainly about the mid-term and long-term stabilities. However, because modern communication systems use complicated signal-processing techniques or tight frequency allocations, short-term stability is also important. Detailed discussions on stabilities can be found in the literature.[9, 50]

11.4.2 Beam diffraction and transverse modes

The diffraction of the SAW excited by an IDT affects resonator performance. In high-Q SAW resonators, since SAWs propagate back and forth within the cavity many times, diffraction causes dissipation of the SAW energy from the cavity and results in a reduced Q_{r} (Fig. 11.42).

To circumvent this problem, total reflection at the boundary between the busbars and the grating reflector is used to guide the SAW energy in the transverse direction, as shown in Fig. 11.43.

When the effect is strong enough, higher-order resonances may appear. The higher-order modes resonate at a frequency that is a little higher than the main response. These are called higher-order transverse mode resonances.[50]

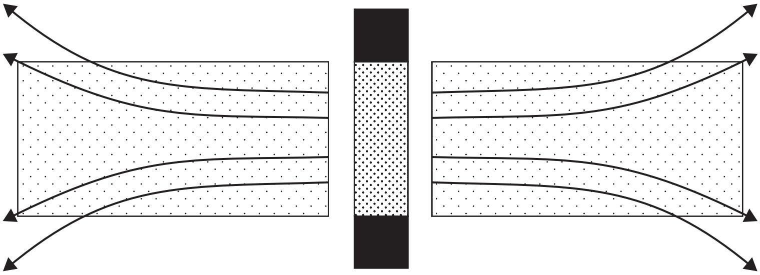

11.42 SAW beam spreading due to diffraction.

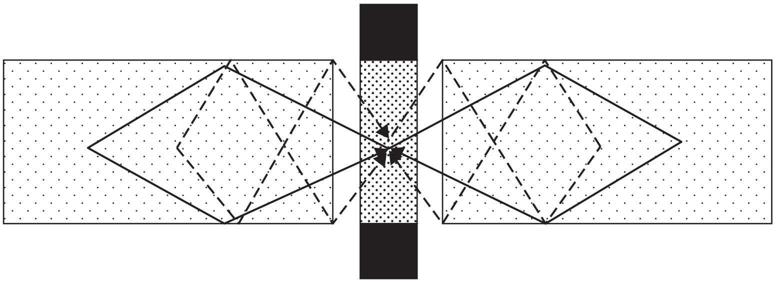

11.43 Trapping the energy in a waveguide structure.

In an oscillator, these inharmonic spurious resonances may cause an undesirable jump in the oscillation frequency, and may limit the adjustable frequency range. In a filter, on the other hand, they cause ripples in the passband or undesirable peaks in the rejection band.

Since the cut-off frequency of each transverse mode is dependent upon the aperture of the grating and the busbar width,[51] their adjustment makes suppression of the transverse modes possible. In addition, since the transverse modes have their own field distributions in the transverse direction, their excitation amplitudes can be controlled by an appropriate apodization of the IDT.[52]

11.4.3 Filters employing one-port resonators

The ladder-type configuration is historically well known for filter applications at low frequencies. However, recent advances have made it possible to use SAW resonators for ladder-type filters working above the gigahertz range.[53] Figure 11.44 shows an example of a ladder-type SAW filter. This type of filter has a low insertion loss and high-power durability compared with the acoustically coupled SAW resonator filters, which will be described in Sections 11.4.4 and 11.4.5.

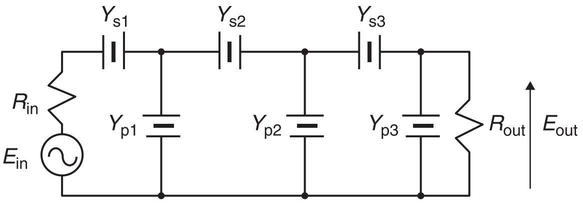

11.44 Basic configuration of ladder-type filter.

The basic aim is to make the resonance frequency, f_r^s, of Y_s at the series arms to be the same as the anti-resonance frequency, f_a^p, of Y_p at the parallel arms. Since $Y_s^{-1} \approx 0$ and $Y_p \approx 0$ near the resonance and anti-resonance frequencies, respectively, the input signal passes through the filter with little attenuation. On the other hand, at the anti-resonance frequency, f_a^s, of Y_s and the resonance frequency, f_r^p, of Y_p, respectively, the series arms are electrically open circuited and the parallel arms short circuited. This means there is no signal transmission to the output. Consequently, the type of frequency response shown in Fig. 11.45 is obtained. According to traditional electrical circuit theory, the out-of-band rejection improves with an increase in the number of resonators at the expense of increased insertion loss.

11.4.4 Two-port SAW resonators and filters

Figure 11.46(a) shows a two-port SAW resonator with grating reflectors on both sides of a conventional transversal filter. When the device is designed so that the reflectors resonate at the IDT resonance frequency, the transfer admittance is very large at resonance, and a very narrow but low-loss passband is realized.

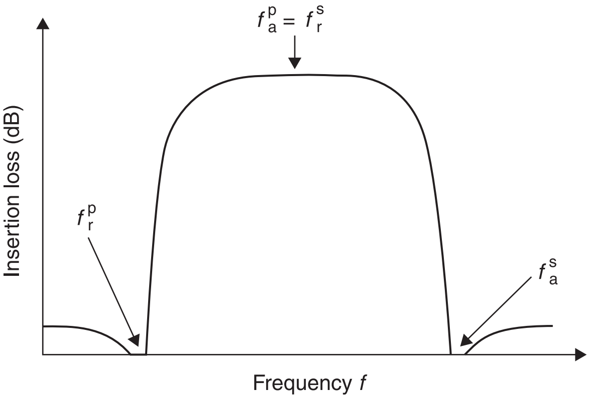

11.45 Frequency response of ladder-type filter.

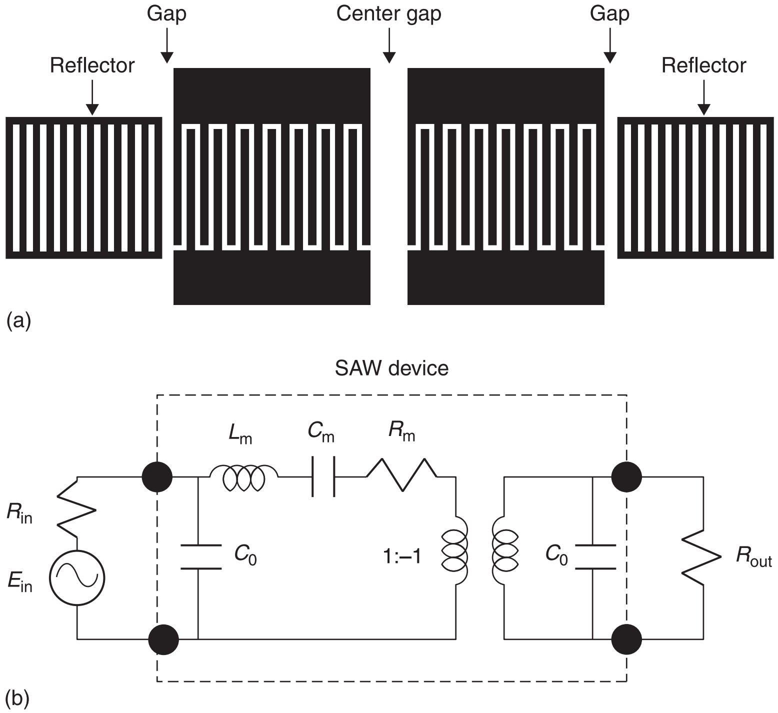

11.46 Two-port SAW resonator: (a) structure, (b) equivalent electrical circuit.

An oscillator can be constructed by using this device as a feedback element. This configuration is often used in the UHF range[49] because of its insensitivity to parasitic circuit elements.

Figure 11.47 shows the typical frequency response of a two-port SAW resonator. It can be seen that the steep resonance peak overlaps the conventional sinc x-type frequency response of a SAW transversal filter.

Figure 11.46(b) shows the equivalent circuit near the resonance frequency. Although the circuit is similar to that for the one-port SAW resonator shown in Fig. 11.40(b), the resonance circuit is involved as a shunt element between two IDTs. This is because the structure is equivalent to a one-port SAW resonator if the two IDTs are electrically connected in parallel.

11.4.5 Multi-mode resonator filter

Figure 11.48 shows the configuration of a transversely coupled SAW resonator filter,[54] where two identical one-port SAW resonators are in close proximity. Their lateral coupling raises two resonance modes. The field motions in the upper and lower resonators are in-phase for the first mode, whereas they are anti-phase for

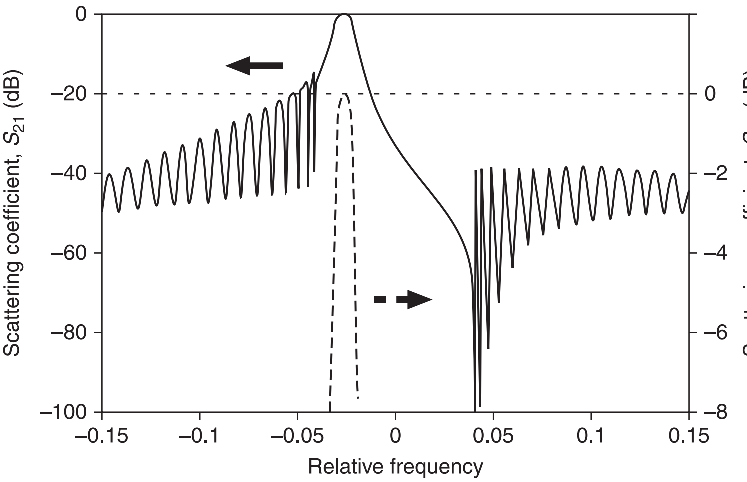

11.47 Typical frequency response of two-port SAW resonator; the same data are shown at two resolutions. Arrows indicate the applicable scales.

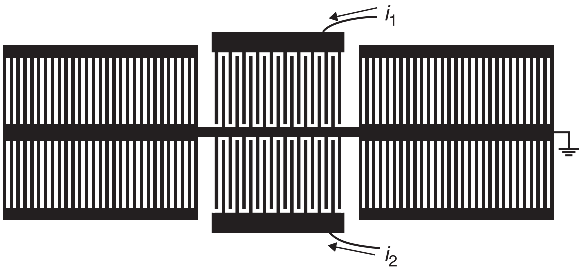

11.48 Transversely coupled SAW resonator filter.

the second one. The resonance frequencies for these two modes are slightly different from each other, the difference being determined by the strength of the lateral coupling.

Figure 11.49 shows the equivalent electrical circuit for a double-mode resonator filter, where Y_s and Y_a are the motional admittances for the symmetric and anti-symmetric modes, respectively, and ω_r^s and ω_r^a are their resonance frequencies. This configuration simultaneously has a flat passband shape, high out-of-band rejection and sharp skirt characteristics when the two resonance peaks are adjusted to partially overlap in the frequency domain. One important demerit is the fact that the bandwidth is intrinsically limited because of the weak lateral coupling of the two modes.

A longitudinally coupled double-mode resonator filter has exactly the same structure as the conventional two-port SAW resonator discussed previously, but it

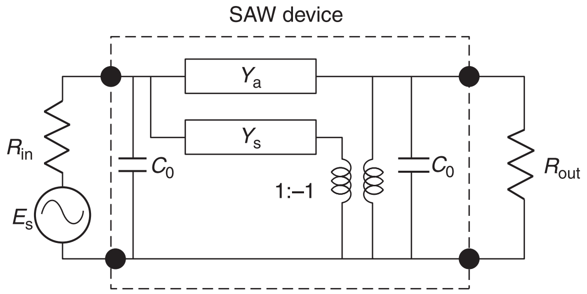

11.49 Equivalent circuit for double-mode resonator filter.

is designed to resonate at two different frequencies.[55] An appropriate adjustment of these two resonant frequencies gives a flat and wide passband as shown in Fig. 11.50.

By extending this principle, resonator filters with multiple modes can be synthesized. Figure 11.51 shows the filter characteristic when three resonances are employed. A comparison of this figure with Fig. 11.47 and Fig. 11.50 indicates that increasing the number of resonances gives: (a) a widened passband, (b) a sharp cut-off at the passband edges, and (c) the suppression of adjacent satellite peaks. Modulation of the IDT and reflector periodicities is effective for adjusting the location of the multiple resonance frequencies.[56]

One distinctive feature of multi-mode SAW filters is electrical isolation between the input and output ports. Since the input and output ports are only coupled

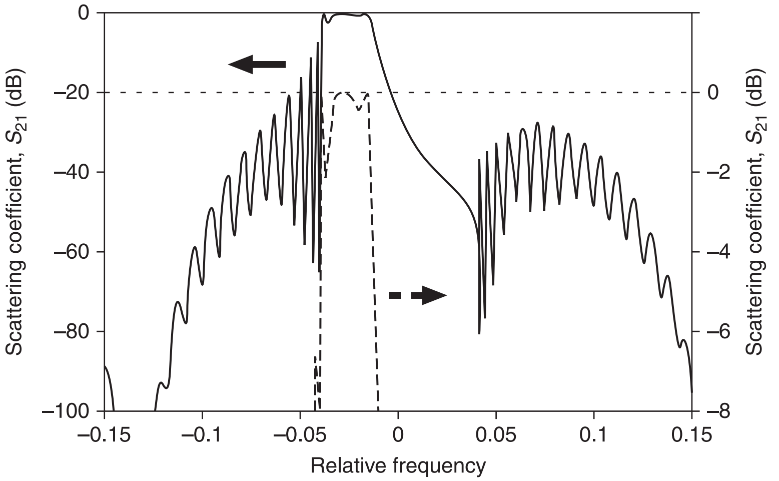

11.50 Frequency response of double-mode resonator filter; the same data are shown at two resolutions. Arrows indicate the applicable scales.

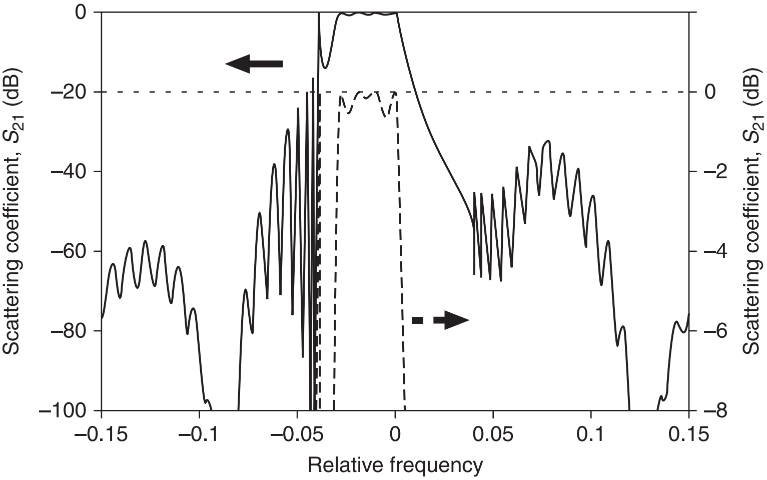

11.51 Frequency response of multi-mode resonator filter; the same data are shown at two resolutions. Arrows indicate the applicable scales.

acoustically, we can convert an unbalanced (single-end) signal to a balanced (differential) signal by connecting two identical resonators electrically, as shown in Fig. 11.52.[57] Theoretically, the filter performances are unchanged by the connection. There is also impedance conversion: the electrical connection shown in the figure has an input impedance four times smaller than the output impedance.

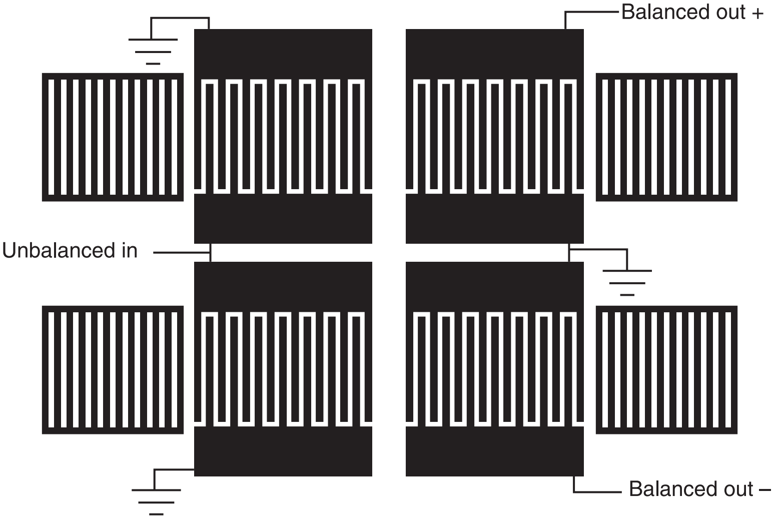

11.52 Multi-mode resonator filter with unbalanced-to-balanced and impedance conversion functions.

11.5 Conclusions

This chapter described the basics of SAW devices. First, the basic operation of IDTs was explained using the delta-function model and COM theory was introduced to allow for the influence of internal SAW reflection in IDTs. Next, SAW transversal filters were explained. In addition to their fundamental properties, the influence of the TTE on filter performance was detailed. Low-loss SAW transversal filters using unidirectional transducers were also described. Finally, SAW resonators were discussed. The basics of SAW resonators were given, and it was shown how RF filters are composed and designed using SAW resonators.

Although more than 45 years have passed since the first proposal for a SAW device, they are still being studied very intensively. Low-loss filters in the gigahertz range are mass-produced for mobile phones, and new device configurations, materials and applications are often proposed. Undoubtedly, necessity is the mother of invention.

11.6 References

1. Lord Rayleigh, On waves propagating along the plane surface of an elastic solid, *Proc. London Math. Soc.*, **7** (1885) pp. 4–11.
2. R.M. White and F.W. Voltmer, Direct piezoelectric coupling to surface elastic waves, *Appl. Phys. Lett.*, **17** (1965) pp. 314–16.
3. T.M. Reeder (ed.), Special issue on microwave acoustic signal processing, *IEEE Trans. Microwave Theory and Tech.*, **21**, 4 (1973).
4. L. Claiborne, G.S. Kino and E. Stern (eds), Special issue on surface acoustic wave devices and applications, *Proc. IEEE*, **64**, 5 (1976).
5. R.C. Williamson and T.W. Bristol (eds), Special issue on surface-acoustic-wave applications, *IEEE Trans. Sonics and Ultrason.*, **28**, 2 (1981).
6. R. Weigel and K. Hashimoto (eds), Special issue on microwave acoustic wave devices for wireless communication and sensing, *IEEE Trans. Microwave Theory and Tech.*, **49**, 4, Part II (2002).
7. H. Matthews (ed.), *Surface Wave Filters* (Wiley, New York, NY, USA, 1977).
8. E.A. Ash and E.G.S. Paige (eds), *Rayleigh-Wave Theory and Application* (Springer-Verlag, New York, NY, USA, 1985).
9. E.A. Gerber and A. Ballato (eds), *Precision Frequency Control*, Vol. I & II (Academic Press, Orlando, FL, USA, 1985).
10. S. Datta, *Surface Acoustic Wave Devices* (Prentice Hall, Englewood Cliffs, MA, USA, 1986).
11. G.S. Kino, *Acoustic Waves: Devices, Imaging, and Analog Signal Processing* (Prentice-Hall, Englewood Cliffs, MA, USA, 1987).
16. M. Feldmann and J. Henaff, *Surface Acoustic Waves for Signal Processing* (Altech House, Boston, MA, USA, 1989).
17. C.K. Campbell, *Surface Acoustic Wave Devices and Their Signal Processing Applications* (Academic Press, Boston, MA, USA, 1989).
18. C.K. Campbell, *Surface Acoustic Wave Devices for Mobile and Wireless Communication* (Academic Press, Boston, MA, USA, 1998).

19. K. Hashimoto, *Surface Acoustic Wave Devices in Telecommunications* (Springer-Verlag, Berlin, Germany, 2000).
20. C.C.W. Ruppel and T.A. Fjeldly (eds), *Advances in Surface Acoustic Wave Technology, Systems and Applications*, Vol. 1 (World Scientific, Singapore, 2000).
21. D.P. Morgan, *Surface Acoustic Wave Filters, Second Edition: With Applications to Electronic Communications and Signal Processing* (Studies in Electrical and Electronic Engineering) (Springer-Verlag, Berlin, Germany, 2007).
22. R.H. Tancrell and M.G. Holland, Acoustic surface wave filters, *Proc. IEEE*, **59**, (1971) pp. 393–409.
23. D.P. Morgan, *Surface Wave Devices for Signal Processing*, Chapter 3 (Elsevier, Amsterdam, the Netherlands, 1985) pp. 39–55.
24. H. Engan, Excitation of elastic surface waves by spatial harmonics of interdigital transducers, *IEEE Trans. Sonics and Ultrason.*, **24** (1977) pp. 147–66.
25. R.F. Milsom, N.H.C. Reilly and M. Redwood, Analysis of generation and detection of surface and bulk acoustic waves by interdigital transducers, *IEEE Trans. Sonics and Ultrason.*, **24** (1977) pp. 147–66.
26. K. Hashimoto, *Surface Acoustic Wave Devices in Telecommunications*, Chapter 3 (Springer-Verlag, Berlin, Germany, 2000) pp. 47–85.
27. S. Datta, B.J. Hunsinger and D.C. Malocha, A generalized model for periodic transducers with arbitrary voltages, *IEEE Trans. Sonics and Ultrason.*, **26**, 3 (1980) pp. 235–42.
28. K.A. Ingebrigtsen, Surface waves in piezoelectrics, *J. Appl. Phys.*, **40** (1969) pp. 2681–6.
29. R.C. Rosenfeld, R.B. Brown and C.S. Hartmann, Unidirectional acoustic surface wave filters with 2 dB insertion loss, *Proc. IEEE Ultrason. Symp.* (1974) pp. 425–8.
30. D.C. Malocha, Quadrature 3-phase unidirectional transducer, *IEEE Trans. Sonics and Ultrason.*, **26** (1979) pp. 313–15.
31. K. Yamanouchi, F. Nyfeller and K. Shibayama, Low insertion loss acoustic surface wave filter using group-type unidirectional interdigital transducers, *Proc. IEEE Ultrason. Symp.* (1975) pp. 317–21.
32. C.S. Hartmann, P.V. Wright, R.J. Kansy and E.M. Garber, Analysis of SAW interdigital transducer with internal reflections and the application to the design of single-phase unidirectional transducers, *Proc. IEEE Ultrason. Symp.* (1982) pp. 40–5.
33. T. Kodama, H. Kawabata, Y. Yasuhara and H. Sato, Design of low-loss SAW filters employing distributed acoustic reflection transducers, *Proc. IEEE Ultrason. Symp.* (1986) pp. 313–24.
34. P.V. Wright, Natural single-phase unidirectional transducer, *Proc. IEEE Ultrason. Symp.* (1985) pp. 58–63.
35. D.P. Chen and H.A. Haus, Analysis of metal-strip SAW grating and transducers, *IEEE Trans. Sonics and Ultrason.*, **26** (1985) pp. 395–408.
36. C.C.W. Ruppel, W. Ruile, G. Sholl, K.C. Wagner and O. Männer, Review of models for low-loss filter design and applications, *Proc. IEEE Ultrason. Symp.* (1994) pp. 313–24.
37. W.R. Smith, H.M. Gerard, J.H. Collins, T.M. Reeder and H.J. Show, Analysis of interdigital surface wave transducers by use of an equivalent circuit model, *IEEE Trans. Microwave Theory and Tech.*, **17** (1969) pp. 856–84.
38. K. Hashimoto, *Surface Acoustic Wave Devices in Telecommunications*, Chapter 7 (Springer-Verlag, Berlin, Germany, 2000) pp. 191–235.

39. G. Tobolka, Mixed matrix representation of SAW transducers, *IEEE Trans. Sonics and Ultrason.*, **26** (1979) pp. 426–8.
40. R.H. Tancrell and M.G. Holland, Acoustic surface wave filters, *Proc. IEEE*, **59** (1971) pp. 393–409.
41. D.P. Morgan, *Surface-Wave Devices for Signal Processing*, Chapter 3 (Amsterdam, the Netherlands, Elsevier, 1985) pp. 343–53.
42. J.H. McClellan, T.M. Parks and L.R. Rabiner, A computer program for designing optimum FIR linear phase digital filters, *IEEE Trans. Audio and Electroacoustics*, **AU-21** (1973) pp. 506–26.
43. C.K. Campbell, *Surface Acoustic Wave Devices and Their Signal Processing Applications* (Boston, MA, USA, Academic Press, 1989).
44. K. Hashimoto, *Surface Acoustic Wave Devices in Telecommunications*, Chapter 3 (Springer-Verlag, Berlin, Germany, 2000) pp. 47–85.
45. P. Ventura, M. Solal, P. Dufiliè, J.M. Hodè, and F. Roux, A new concept in SPUDT design, *Proc. IEEE Ultrason. Symp.* (1994) pp. 1–76.
46. E.A. Ash, Surface wave grating reflectors and resonators, *Proc. IEEE MTT Symp.* (1970) pp. 385–6.
47. K. Hashimoto, *Surface Acoustic Wave Devices in Telecommunications*, Chapter 5 (Springer-Verlag, Berlin, Germany, 2000) pp. 121–61.
48. G.K. Montress, T.E. Parker and D. Andres, Review of SAW oscillator performance, *Proc. IEEE Ultrason. Symp.* (1994) pp. 43–54.
49. E.J. Steples and R.C. Smythe, Surface acoustic wave resonators on ST-cut quartz, *Proc. IEEE Ultrason. Symp.* (1975) pp. 307–10.
50. W.H. Haydl, B. Dischler and P. Hiesinger, Multimode SAW resonators: A method to study the optimum resonator design, *Proc. IEEE Ultrason. Symp.* (1976) pp. 287–96.
51. O. Ikata, T. Miyashita, T. Matsuda, T. Nishikawa and Y. Satoh, Development of low-loss band-pass filters using SAW resonators for portable telephone, *Proc. IEEE Ultrason. Symp.* (1992) 112–15.
52. M. Tanaka, T. Morita, K. Ono and Y. Nakazawa, Narrowband bandpass filter using double-mode SAW resonators on quartz, *Proc. IEEE Freq. Contr. Symp.* (1984) pp. 286–93.
53. T. Morita, Y. Watanabe, M. Tanaka and Y. Nakazawa, Wideband low loss double mode SAW filters, *Proc. IEEE Ultrason. Symp.* (1992) pp. 95–104.
54. K. Hashimoto, T. Omori and M. Yamaguchi, Operation mechanism of double-mode surface acoustic wave filters with pitch-modulated IDTs and reflectors, *IEEE Trans. Ultrason., Ferroelec., and Freq. Contr.*, **54**, 10 (2007) pp. 2152–8.
55. H. Meier, Th. Baier and G. Riha, Miniaturization and advanced functionalities of SAW devices, *Proc. IEEE Ultrason. Symp.* (2000) pp. 395–401.

12

Airborne ultrasound transducers

D. A. HUTCHINS, University of Warwick, UK
and A. NEILD, Monash University, Australia

Abstract: A review of the technology and transduction methods behind airborne ultrasound is presented. This covers the main areas of transducer design and properties, but also the many applications to which ultrasound can be applied within gases. It will be shown that many of these applications require a wide bandwidth, so that signal processing can be applied. In addition, there are various ways of changing the directivity and achieving focussing, and these are also discussed.

Key words: air, ultrasound, attenuation, focussing.

12.1 Introduction

This chapter outlines the transducers and measurement techniques commonly used in air-coupled ultrasound and some of the applications of this field of study. Particular attention is paid to the development and construction of capacitive devices, as these are used to illustrate the applications covered. This chapter starts with a discussion of the basic design principles of the transducers used, governed mainly by the fact that air has a much lower acoustic impedance than most other media in which ultrasound is commonly used (such as solids, liquids and the human body). Thus, the properties of air are discussed in some detail in Section 12.2, before the problem of the acoustic impedance mismatch, and solutions to overcome this, are presented.

Section 12.3 continues with a description of the two main designs for airborne ultrasound, namely the use of either piezoelectric devices or those based on electrostatic principles (capacitive transducers). The latter are discussed in some detail, and this is followed in Section 12.4 by a discussion of the expected radiated fields in air from a planar device. This is then extended by looking at how the radiated fields in air can be focussed using curved geometries or mirrors.

The final section describes some of the many applications to which airborne ultrasonic methods have been applied. Air-coupled non-destructive evaluation (NDE) is one, where there are distinct advantages in removing the need for a liquid couplant. However, there are many more, including the imaging of thin materials using focussed airborne ultrasound, the use of gas jets to provide collimation, and the use of airborne ultrasound to measure gas flow velocity and temperature.

12.2 Basic design principles

12.2.1 The ultrasonic properties of air

Acoustic propagation in various gases has been the subject of much study. For instance, in the early 1900s, the absorption of sound in various gases, such as CO_2, N_2, H_2 and He, attracted some interest (Abello, 1928; Knudsen, 1933; Leonard, 1940; Peilemeier, 1945). Subsequent work investigated atmospheric sound absorption in air (Evans *et al.*, 1972; Bass and Shields, 1974; Bass *et al.*, 1984), and there have also been studies reporting the measurement of the acoustic velocity in various gas mixtures (Breazeale *et al.*, 1983; Smorenburg *et al.*, 1996; Zhang and Schouten, 1992; Vacek *et al.*, 2001). The sound velocity can, in fact, be used to determine the relative concentration of a gas in a mixture (Wilburn *et al.*, 1995; Wan *et al.*, 1996).

As an ultrasonic wave propagates through a homogeneous gas such as air, absorption and scattering combine to give the overall attenuation level. Absorption, which refers to the loss of amplitude accompanied by an increase of temperature in the propagating medium, is assumed to dominate. The sound pressure decays exponentially with sound propagation over a distance, s, due to conventional attenuation, and for a plane wave this can be written as

$$p = p_0 e^{-\alpha s}, \tag{12.1}$$

where p_0 is the initial pressure at $s = 0$ and the parameter α is defined as the sound attenuation coefficient, with units of $\mathrm{Np.m^{-1}}$. Attenuation is frequently expressed in *nepers* (Np), a natural logarithmic unit corresponding to a reduction in amplitude to $1/e$ of the initial or reference value. Correspondingly, the change in pressure level of the attenuated wave, expressed in decibels, is given by

$$\Delta\mathrm{PL} = 20\log\frac{p}{p_0} = 20\log e^{-\alpha s} = -8.686\alpha s. \tag{12.2}$$

Consequently, 8.686α is equivalent to an attenuation level expressed in $\mathrm{dB.m^{-1}}$.

In early work, only two mechanisms were assumed to be important in absorption: shear viscosity and thermal conductivity, which are known today as classical absorption. A comprehensive model has been developed for conversion between vibrational, rotational and translational energies of gas molecules, such as those found in the atmosphere. Many of the individual processes of conversion have been explored by calculation and by acoustic measurements on single gases and binary mixtures (Evans *et al.*, 1972).

Absorption has two basic forms: the classical loss associated with a change of the kinetic energy of molecules into heat, and the relaxation loss associated with a change of the kinetic translational energy of the molecules into internal energy within the molecules themselves. For the classical losses, the energy conversion under normal atmospheric conditions is caused mainly by viscous losses and heat conduction losses, which collectively are called the Stokes–Kirchhoff loss. This loss (α_{cl}) is a function of temperature, pressure and frequency, according to

$$\alpha_{cl} = 4.845 \times 10^{-8} \frac{T / T_0}{T + 110.4} f^2 / (P / P_0) \text{ in dB m}^{-1}, \qquad [12.3]$$

where T is the measured temperature, T_0 is a reference temperature (293.15 K or 20°C), f is the frequency, P is the measured pressure and P_0 is a reference pressure (101.325 kPa).

The two main forms of relaxation losses are due to rotationally excited and vibrationally excited molecules. Rotational absorption is also a function of temperature, pressure and frequency. Therefore, rotational absorption can be combined with the classical component as α_{cr}:

$$\alpha_{cr} = 15.895 \times 10^{-11} \frac{(T / T_0)^{1/2}}{P / P_0} f^2 \text{ in dB m}^{-1}. \qquad [12.4]$$

Vibrational absorption depends on the particular atmospheric constituent and the per cent mole fraction of water vapour as well as temperature, pressure and frequency. Air is considered to be a four-gas mixture, i.e., nitrogen (N_2), oxygen (O_2), carbon dioxide (CO_2) and water vapour (H_2O). The values quoted in Bass *et al.* (1984) on vibrational energy-transfer reactions for the molecular components of air showed that all the reactions involving CO_2 could be ignored. Therefore, vibrational absorption needs to take into account just N_2 and O_2, and their interaction with water vapour.

The total acoustic absorption coefficient due to atmospheric absorption, α, is expressed as the sum of components described above:

$$\alpha = \alpha_{cr} + \alpha_{vib,O} + \alpha_{vib,N}, \qquad [12.5]$$

where $\alpha_{vib,O}$ and $\alpha_{vib,N}$ are absorption caused by vibrational relaxation of O_2 and N_2, respectively.

$$\alpha_{vib,O} = 1.110 \times 10^{-1} \frac{e^{-2239.1/T}}{f_{r,O} + (f^2 / f_{r,O})} (T_0 / T)^{5/2} f^2 \qquad [12.6]$$

$$\alpha_{vib,N} = 9.480 \times 10^{-1} \frac{e^{-3352.0/T}}{f_{r,N} + (f^2 / f_{r,N})} f^2 \qquad [12.7]$$

in dB.m^{-1}, where $f_{r,O}$ and $f_{r,N}$ are the frequencies of maximum absorption for the gases. These are dependent on the water-vapour concentration, h (ANSI, 1989), according to

$$f_{r,O} = (P/P_0)\{24 + 4.41 \times 10^4 h[12.(0.05 + h)/(0.391 + h)]\} \text{ (Hz)} \qquad [12.8]$$

$$f_{r,N} = (P/P_0)(9 + 200\,h)\ \text{(Hz)} \qquad [12.9]$$

where h is the molar concentration of water vapour in per cent.

Assuming that absorption due to nitrogen, oxygen, and their interaction with water vapour from Eq. 12.5 dominates, the absorption coefficient, α, can be estimated for air as shown in Fig. 12.1. The contribution to α from each vibrational relaxation is proportional to the frequency squared for $f << f_r$, and is independent of frequency for $f >> f_r$. However, the absorption coefficient obtained by summing the classical and rotational components is proportional to the frequency squared for all frequencies. Therefore, for ultrasonic frequencies, only the classical and rotational absorption components are the major contributions to absorption. The main conclusion that can be drawn from this graph is that the absorption coefficient

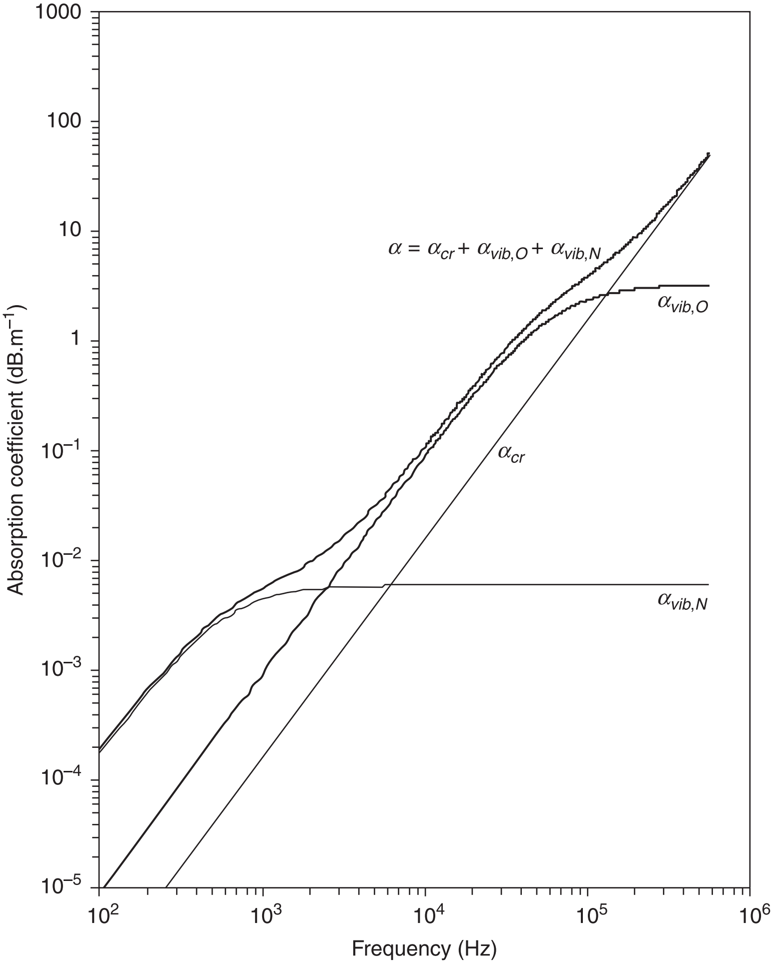

12.1 Absorption coefficient as a function of frequency for air.

increases with frequency, for a given value of *h*. This effectively limits the frequencies that can be used for most ultrasonic work in air to below 2 MHz or so, as further discussed by Wenmaekers *et al.* (2008).

Another factor of interest is the speed of sound in air. Assuming longitudinal wave propagation, various authors have estimated this under different conditions. For example, the local temperature (T) will affect the speed of sound (c) according to the following dependence (Hickling and Marin, 1986):

$$c = 331.31(T/273.16)^{1/2} \qquad \mathrm{m.s^{-1}} \qquad [12.10]$$

In addition, the value of c will be affected by air flow, namely by the component of the flow velocity in the direction of propagation. Hence, both temperature T and air flow changes can cause variations in the apparent value of the speed of sound. The former is a scalar effect, whereas flow is a vector quantity, and this can be used to distinguish their contributions (see discussion later in this chapter). Note that the speed of sound is also affected by moisture content, the relative concentrations of the different gases within it and other effects (Cramer, 1993). These effects have been studied in many gases, such as nitrogen, a major component of air (Wong and Wu, 1997). A paper has also been published on typical values for velocity and absorption (Bohn, 1988).

12.2.2 The acoustic mismatch problem

A common method used for ultrasonic transduction is to use a piezoelectric transducer together with some form of intermediate impedance matching layer or a viscous couplant (for a solid). The couplant layer need only have a thickness of one tenth of a wavelength to affect the acoustic properties (Silk, 1984), and it is therefore important to choose the couplant carefully, paying attention to such variables as the viscosity, the temperature and possible material contamination (Halmshaw, 1991). Another common method of coupling is to use water immersion, where impedance matching layers are commonly used. There are, however, many materials and industrial manufacturing processes where the presence of water will cause damage or inconvenience, and where air-coupled ultrasound may be useful (Grandia and Fortunko, 1995). In addition, many materials intended for the aerospace industry are not compatible with water (Buckley, 1998). Air-coupled ultrasound allows for rapid scanning without damage to the specimen material (Strycek *et al.*, 2000). The relatively short wavelengths in air provide the potential for high-resolution imaging, as the transducer is more directional (Schindel and Hutchins, 1995). It is a minimally invasive technique requiring no more contact than the natural environment.

Piezoelectric transducers are extensively used for the generation and detection of ultrasound in solids, but are inefficient when operating in air, due to the high impedance mismatch that occurs at the boundary between the transducer and air. The transmission coefficient (T) can be calculated from the acoustic impedance (Z) either side of the boundary using

$$T = \frac{4Z_1Z_2}{(Z_1 + Z_2)^2}. \qquad [12.11]$$

The values of T for transmission from various piezoelectric materials into water and air are given in Table 12.1. It can be seen that the transmission coefficient is much higher when the transducer is surrounded by water as opposed to air, and this is because the impedance of water is much higher than that of air, at 1.5×10^6 compared with 414 kg.m^{-3}.s^{-1}, respectively, at 20 °C. Even with the relatively low impedance of the polymer PVDF, the transmission coefficient into air is still very low.

12.2.3 Possible solutions to this problem

There are various solutions to the problem of acoustic mismatch. These may be summarised as follows:

- Reduce the acoustic impedance of the piezoelectric material.
- Use some form of impedance matching between the piezoelectric device and air.
- Use a highly resonant structure.
- Design a transducer with a thin membrane, which is inherently well-coupled to air.
- Use coded waveforms that allow signal processing, with the aim of enhancing the signal-to-noise ratio (SNR) of a particular measurement.

These features are covered in the next section; however, it is perhaps appropriate at this stage to outline the sort of processing steps that can be taken to enhance the signals where there are multiple boundaries exhibiting an acoustic impedance mismatch. The most common approach, provided the bandwidth is available, is to use a swept frequency signal in the form of a chirp (Schindel, 1999). A chirp signal is one in which the frequency is changed as a function of time. Figure 12.2 shows a chirp signal with a frequency range that sweeps between 250 and 750 kHz, with a duration of 50 μs, multiplied by a Hanning envelope (to smooth out any

Table 12.1 Acoustical properties of some piezoelectric materials (adapted from Bass *et al.*, 1984)

Material	Density ρ (kg.m^{-3})	Propagation velocity c_L (m.s^{-1})	Acoustic impedance Z (kg.m^{-3}.s^{-1})	T_{water}	T_{air}
Quartz SiO_2	2650	5760	15.3×10^6	0.325	10.8×10^{-5}
Zirconate piezoceramic PZT-5A	7750	3880	30×10^6	0.181	5.5×10^{-5}
Lead-niobate piezoceramic $PbNb_20_6$	5800	2800	16×10^6	0.313	10.3×10^{-5}
Piezopolymer PVDF	1780	2260	4.6×10^6	0.742	35.9×10^{-5}

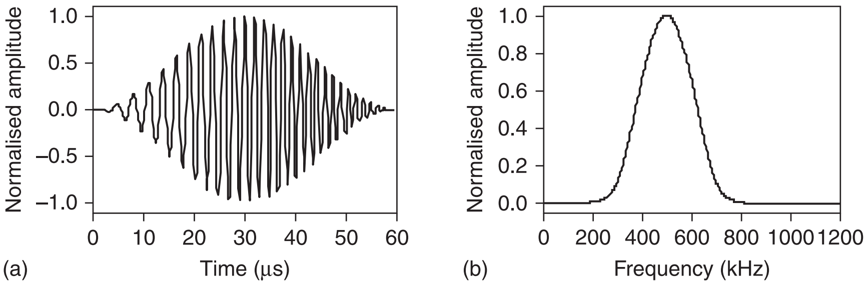

12.2 Chirp signal.

sudden changes in amplitude and to improve performance during signal processing). The waveform was numerically generated using

$$P(t) = \frac{1}{2}\left[1 - \cos\left(\frac{2\pi t}{T}\right)\right]\sin\left(2\pi f_s t + \frac{\pi B}{T}t^2\right) \qquad [12.12]$$

where f_s is the lowest frequency, B is the bandwidth and T is the signal duration.

By performing the post-processing technique of pulse compression, in which cross-correlation of the received signal is performed in the time domain, a large signal-to-noise enhancement is possible (Rao and Mehra, 1993; Rao, 1994). This has allowed the air-coupled testing of materials with a high acoustic impedance such as brass (Gan *et al.*, 2002) and steel (Blomme *et al.*, 2002). This is illustrated in Fig. 12.3, where a signal has been buried in noise. The pulse compression

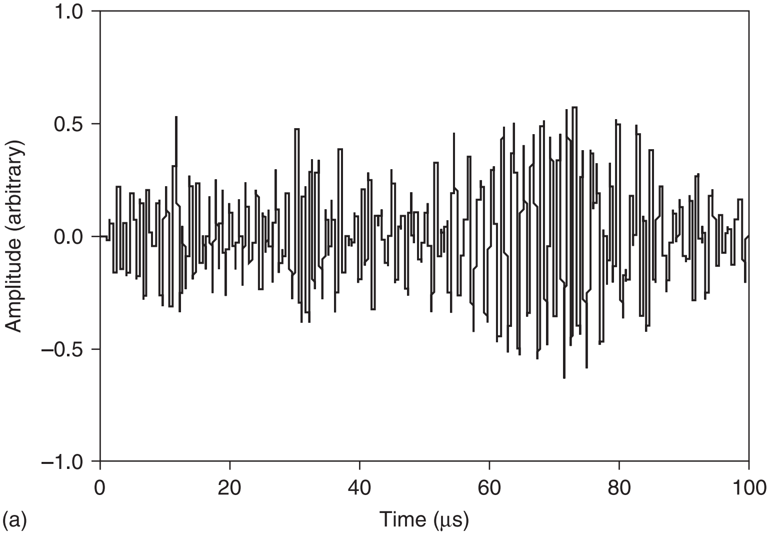

12.3 Signal buried in noise: (a) time waveform; (b) frequency spectrum. *(Continued)*

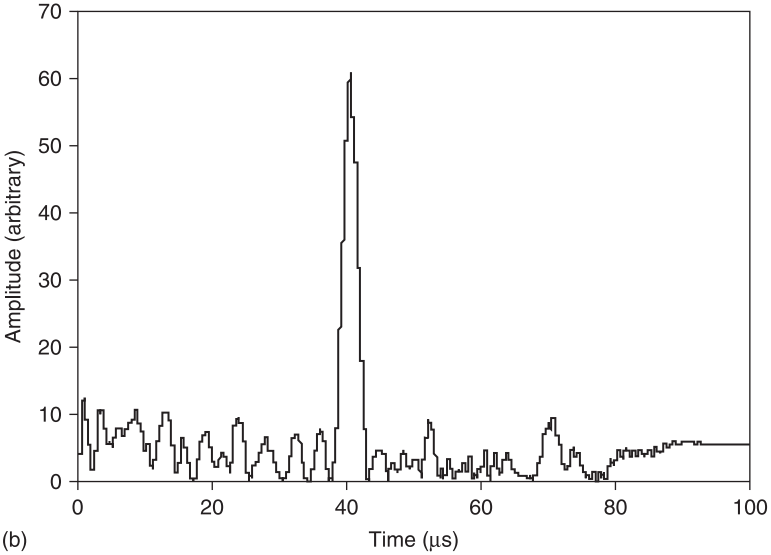

12.3 Continued

output, in the form of a cross-correlation with the original drive signal, shows the level of SNR enhancement that can be obtained. Note, however, that the use of a swept frequency chirp means that the transducers used in air must have a sufficiently wide bandwidth to allow such signals to be generated (Kažys *et al.*, 2007). Transducer designers should thus bear this in mind when designing systems for pulse compression operation.

12.3 Transducer designs for use in air

12.3.1 Piezoelectric transducers

The basic approach is to try and match the impedance of the device to that of air efficiently (Gómez Alvarez-Arenas, 2004). Some authors have taken different approaches to solve the acoustic impedance mismatch problem. Thus, for instance, there has been recent work on the use of piezoelectric polymers in the form of foams, and which hence have much lower impedances. Several different forms have been investigated, including cellular polypropylene foams (Bauer *et al.*, 2004) and foam-like electrets (Satyanarayan *et al.*, 2009). Attempts have also been made to improve this impedance mismatch by having an active piezoelectric element incorporated in a multilayer device, which results in a bending motion, using either a polymer or a metal membrane (Manthey *et al.*, 1992; Durris *et al.*, 1996). In another attempt to combine materials so that the matching problems are reduced, a conical shell was attached to a piezoelectric ring, which when driven causes flexural motion in the cone wall, and the resulting Lamb wave leaks energy into the air (Dabirikhah and Turner, 1994). However, these approaches tend to result in a narrow bandwidth.

A common approach has been to bond a matching layer to the front of the device. This layer must have an acoustical impedance between that of air and the piezoelectric; the optimum value, Z_L, is given by

$$Z_L = \sqrt{Z_1 Z_2}, \tag{12.13}$$

where Z_1 and Z_2 are the impedances of air and the piezoelectric material, respectively. Attempts to find a suitable material have been the source of much work (e.g. Schiller *et al.*, 1990; Krauss *et al.*, 1994). This approach, however, reduces the bandwidth of the device, since, for maximum energy transfer to occur, a matching layer of thickness equal to a quarter wavelength at the centre frequency of interest is required, and this dictates the frequency at which the transducer operates most effectively. Multiple matching layers, or a back-damping layer, have been proposed, and these can be used to broaden the bandwidth at the expense of signal intensity (Gudra and Opielinski, 2002; Vun *et al.*, 2006). Another approach to reducing the impedance mismatch between air and the transducer is to use a piezocomposite ceramic (Haller and Khuri-Yakub, 1994). A popular pattern for this application is 1-3 connectivity, which uses a series of piezoceramic pillars embedded in an epoxy filler covered on both sides with a thin metallic electrode. This can be used either with or without a matching layer (Gachagan and Hayward, 1998), although the use of a matching layer again reduces bandwidth, removing some of the inherent advantages of a piezocomposite. Indeed, one approach is deliberately to use a very narrow bandwidth to enhance sensitivity (Stoessel *et al.*, 2002).

12.3.2 Capacitive membrane devices

A capacitive transducer consists of two electrodes separated by a small distance, one being rigid and the other flexible. The use of a flexible metallised polymer membrane and a rigid backplate has allowed the frequency response of these transducers to be increased well into the ultrasonic region. The improved impedance matching to air of a capacitive transducer when compared with a piezoelectric transducer, and the high bandwidth, make this type of transducer highly suitable for air-coupled applications. The metal side of the membrane is the upper electrode, the backplate being the lower electrode. The polymeric membrane and any air gaps provide insulation between the two electrodes, as shown in Fig. 12.4. The membrane is typically 2–5 µm thick, and is usually of Mylar or a similar film, metallised on one side.

Some air tends to be trapped between the metallised polymer membrane and the backplate, and this trapped air acts as a natural spring. Consequently, the

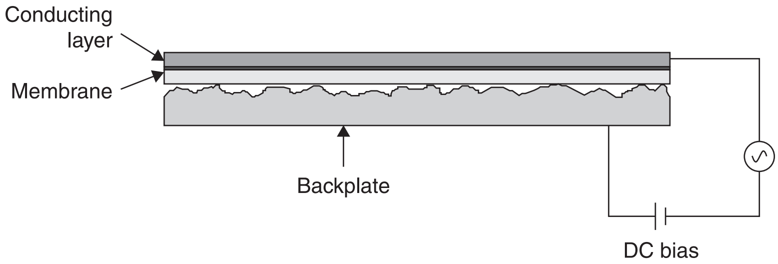

12.4 Membrane and backplate of a capacitive transducer.

device is intrinsically well suited to air-coupling. The conducting layer of the membrane is usually connected to a metal body surrounding the transducer, which is grounded to reduce noise.

The capacitance of two parallel plates separated by an air gap is given by

$$C = \frac{\varepsilon_o A}{d} \qquad [12.14]$$

where A is the surface area, d is the thickness of the air gap and ε_o is the permittivity of free space. During reception, the membrane will move due to fluctuations of the air pressure, which causes a change in the separation of the parallel plates, Δx, and consequently a change in the capacitance, ΔC, which can be found by differentiation to be

$$\Delta C = -\frac{\varepsilon_o A.\Delta x}{d^2} \qquad [12.15]$$

When a DC bias voltage (V_{DC}) is applied across the two plates then there is a charge change, which can be written as

$$\Delta Q = -\frac{\varepsilon_o A.\Delta x}{d^2}.V_{DC} \qquad [12.16]$$

Hence, the change in charge is proportional to the surface area and the DC bias, and is inversely proportional to the square of the initial electrode separation distance. During transmission, the application of a changing voltage causes the charge difference between the plates to alter, which in turn causes a change in the electrostatic forces and so induces membrane movement. It must be noted that this is a simplistic method of modelling the situation, which assumes ideal parallel plates.

The behaviour of a capacitance transducer, in terms of bandwidth, centre frequency and sensitivity, is critically dependent on the structure of the backplate (Carr and Wykes, 1993). There is also an effect caused by the DC bias voltage used, as this tends to decrease the air gap as the membrane is attracted to the backplate. The membrane thickness is another factor that affects the response, as the bandwidth and sensitivity both increase with decreasing membrane thickness.

The type of backplate used in the design of an air-coupled transducer can be broadly split into three groups: those using a roughened surface, grooves or a micromachined surface. When a roughened backplate is used, the frequency at which the peak amplitude occurs is increased as roughness is decreased, although V-grooved backplates have also been studied (Rafiq and Wykes, 1991; Hietanen, 1998). In general, then, the upper frequency of operation increases with smaller amounts of trapped air. Treating the membrane as a piston constrained by an air spring, the approximate resonant frequency can be calculated using

$$f_0 = \frac{1}{2\pi} \cdot \sqrt{\frac{\gamma P_a}{\rho d_m d_a}} \qquad [12.17]$$

where γ is the adiabatic constant of air, P_a is the atmospheric pressure, ρ is the membrane density, and d_m and d_a are the thicknesses of the membrane and air gap, respectively.

The use of V-grooved backplates has been extensively studied, because the grooved pattern provides many individual resonate elements, which can be modelled. If the wavelength is longer than all the different dimensions of the resonator, the Helmholtz model can be applied to predict the frequency of the peak amplitude, f_0, using

$$f_0 = \frac{c}{\pi} \sqrt{\frac{\rho_0}{2\sigma h}} \qquad [12.18]$$

where c is the speed of sound in air, ρ_0 is the density of air, σ is the mass per unit area of the membrane and h is the depth of the groove. This equation, which ignores the groove width, gives a good correlation with measured results and it has been confirmed experimentally that the membrane tension has little effect on the resonant frequency (Pizarro *et al.*, 1999; Hietanen *et al.*, 1993).

Micromachining has been used in an attempt to make the devices more reproducible, and with predictable responses. Backplates have been manufactured from polished silicon wafers, in which 40 μm diameter pits were etched to a depth of 35 μm on a pitch of 80 μm (Schindel *et al.*, 1995). A schematic diagram of this type of transducer is shown in Fig. 12.5. These pits trap air under the membrane; they act as air springs and so reduce the rigidity of the membrane. These devices have a wide bandwidth, which can be altered by applying different DC bias voltages (Hutchins *et al.*, 1998). This type of device will be used to illustrate various applications in later sections of this chapter.

Capacitive transducers can be fabricated completely using silicon micromachining, with the membrane being most commonly silicon nitride. These devices, known as capacitive micromachined ultrasonic transducers (CMUTs), have been investigated for use in air (Haller and Khuri-Yakub, 1996; Caronti *et al.*, 2002; McIntosh *et al.*, 2002; Noble *et al.*, 2001), and some have been developed for high-intensity applications using the collapse-snapback operation,

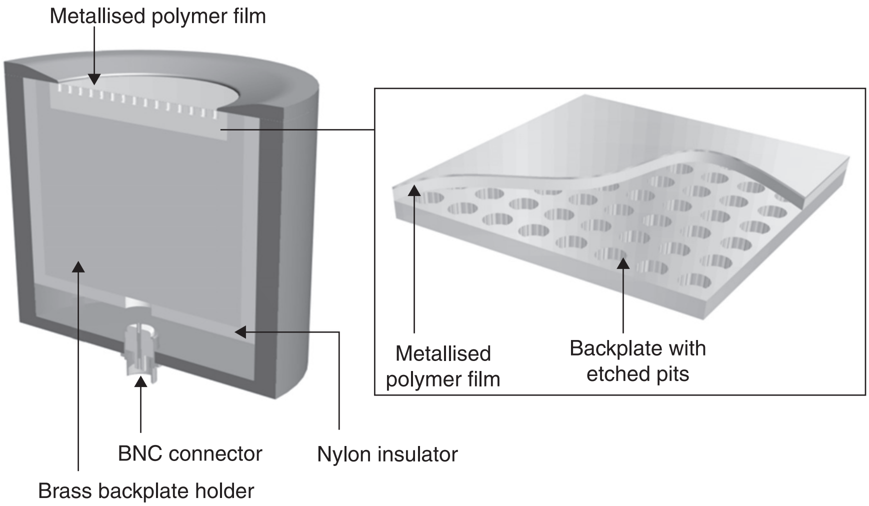

12.5 Capacitive transducer with etched pits in the backplate.

but they are most commonly used in medical imaging arrays. However, several papers have been published on the use of polymers for making CMUT devices (Chang *et al.*, 2006; Chiou *et al.*, 2007), for imaging and other applications, and this could gain popularity in the future because of the costs associated with silicon micromachining.

12.4 Radiated fields in air

12.4.1 Planar devices

The radiated field of a single air-coupled device has been investigated (Hutchins *et al.*, 2003), and the resulting output beam is very similar to that of a plane piston. This is evident in the plots shown in Fig. 12.6, which show the fields in a three-dimensional amplitude format, both (a) as measured in air with a miniature microphone and (b) as predicted theoretically, for an impulsive voltage drive on the transmitter. It can be seen that the side-lobe amplitudes are minimal, and that the main beam is relatively uniform, with a maximum at approximately 1.2 transducer diameters from the front face (assuming a centre frequency of approximately 250 kHz). There are small differences between theory and experiment, but to a first approximation the devices behave like plane pistons. This is further confirmed by Fig. 12.7, where the tone-burst operation at a frequency of 500 kHz is shown. Note now the more complicated near field caused by interference processes, and the more prominent side lobes, as would be expected for a plane piston.

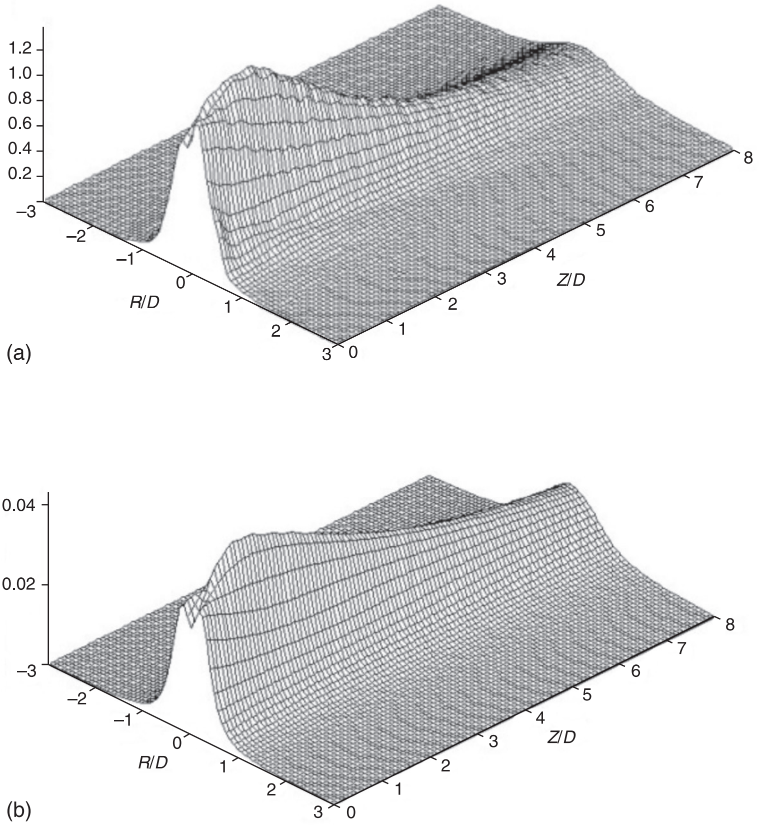

12.6 Radiated field amplitude for a single air-coupled device: (a) measured in air with a miniature microphone, (b) predicted theoretically.

12.4.2 Curved devices

It is possible to modify the field radiated from capacitive devices in air, either using a curved radiating surface or via an external mirror. Experiments have shown that curved surfaces can be used to achieve focussing, but that the chosen backplate curvature must be suitable for the easy attachment of a metallised polymer membrane. Two examples are shown in Fig. 12.8 (Robertson *et al.*, 2002). The first has a cylindrical surface, Fig. 12.8(a), which focusses in one linear dimension but not in the other; the focal region in the correct plane is akin to that from a spherical curvature, with a limited depth of field. With a conical surface, Fig. 12.8(b), the depth of field of the focal region tends to be much more extended along the axis, a phenomenon seen in other conventional medical devices for operation in water (Ju *et al.*, 2006).

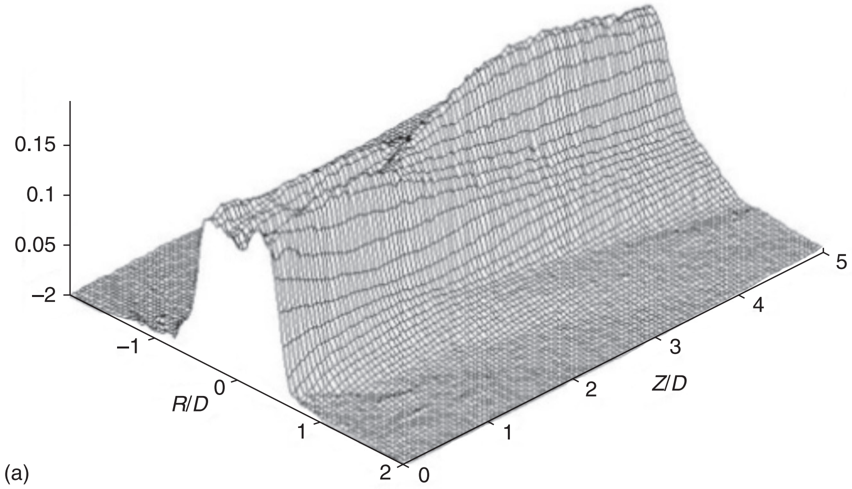

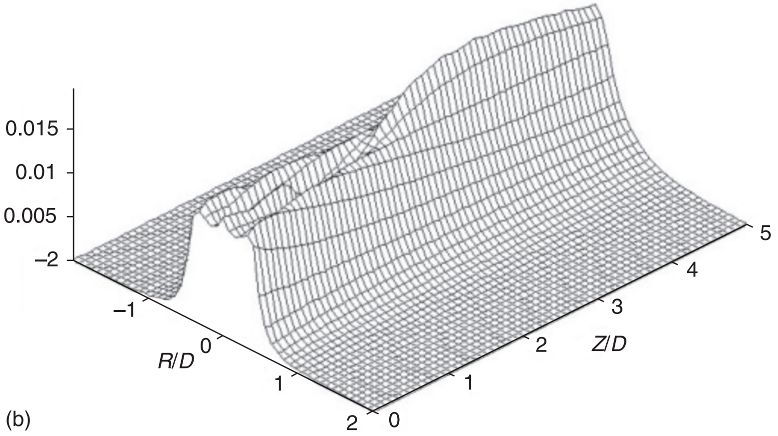

12.7 Radiated field amplitude for a single air-coupled device under tone-burst operation: (a) measured in air with a miniature microphone, (b) predicted theroetically.

12.4.3 Use of external mirrors

An alternative approach is to use an external mirror for focussing (Schindel, 1998). This type of device has been investigated, and the likely performance modelled for use in air (Neild *et al.*, 2004). Because capacitive devices are more easily manufactured with planar faces, it is convenient to bolt on an external mirror. The most effective way of doing this, especially with the near-field uniformity already demonstrated, is to use an off-axis parabolic mirror. Such a device is shown schematically in Fig. 12.9(a), with the field in the focal region as

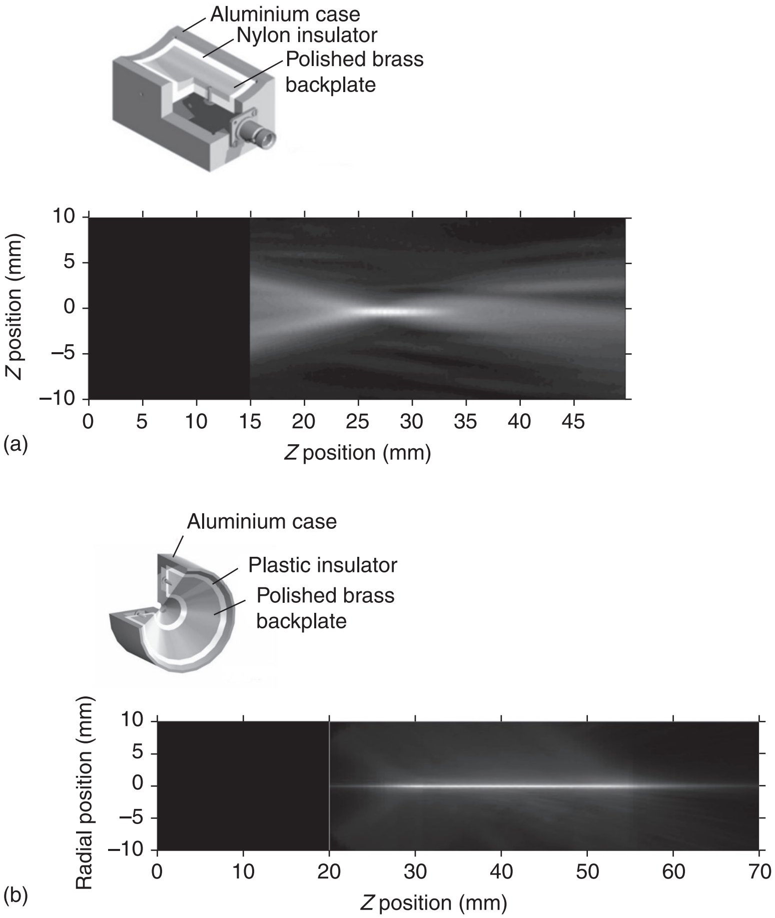

12.8 Curved capacitive transducers and their focal regions: (a) with a cylindrical surface, (b) with a conical surface.

measured experimentally in Fig. 12.9(b). The spot size, measured as the width of the focal point at half its maximum value, is about 0.4 mm, meaning that such devices can be used for high-resolution imaging in air.

An example of the type of measurement that can be performed is shown in Fig. 12.10. This shows the image formed by scanning a transducer such as that shown in Fig. 12.9(a) over the surface of a British ten-pence coin in air. The details of the coin surface have been reproduced reasonably well. This illustrates the fact that air-coupled ultrasound could be useful for material surface roughness and texture characterisation, especially if the features are in the 0.1–1 mm range, which is sometimes difficult to do optically.

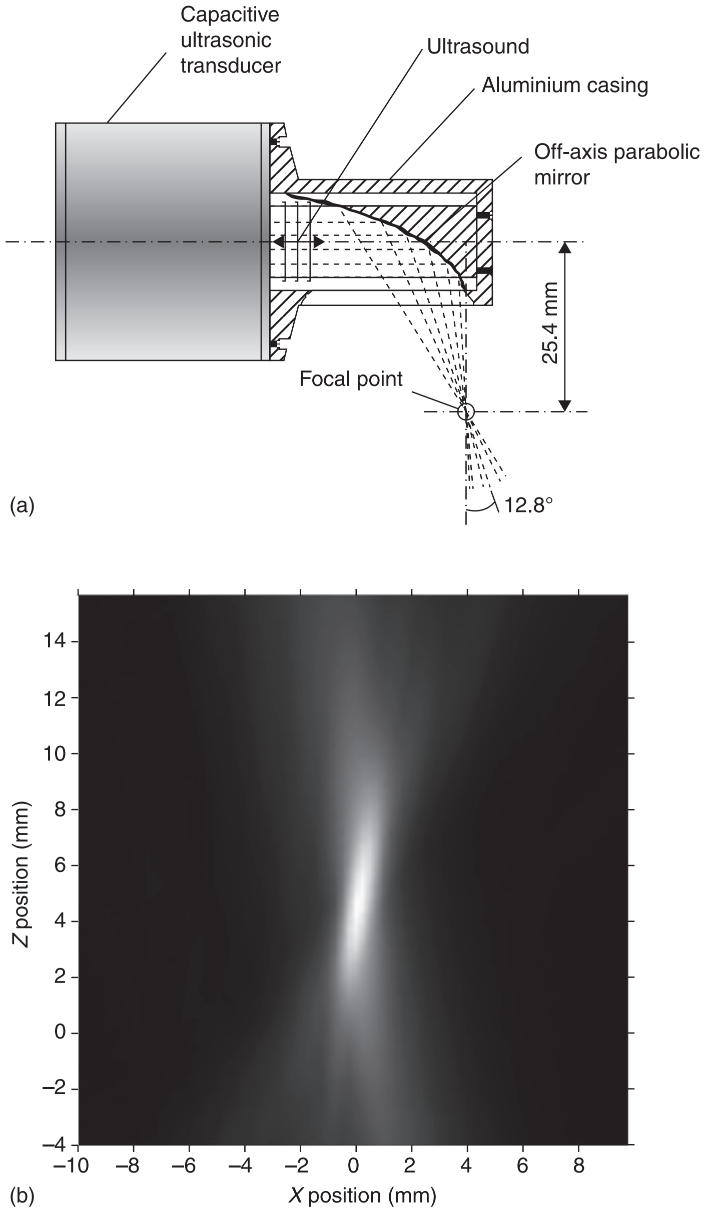
Capacitive ultrasonic transducer
Ultrasound
Aluminium casing
Off-axis parabolic mirror
25.4 mm
Focal point
12.8°
(a)
14
12
10
8
6
4
2
0
–2
–4
Z position (mm)
–10
–8
–6
–4
–2
0
2
4
6
8
X position (mm)
(b)

12.9 (a) Capacitive transducer with an external mirror. (b) Experimentally measured focal region.

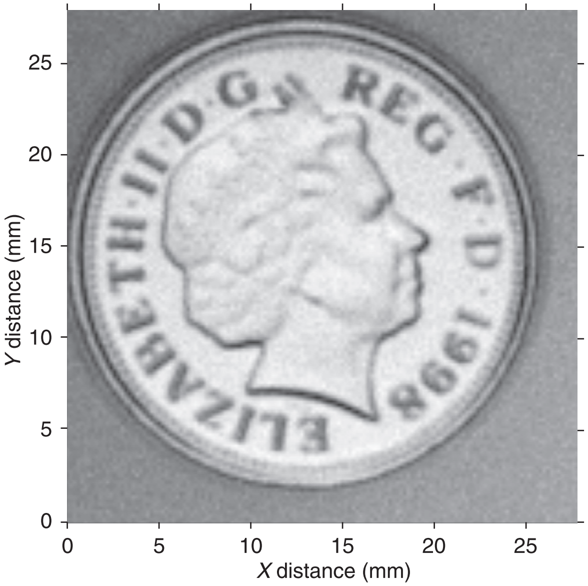

12.10 Image of the surface of a British ten-pence coin made by scanning in air using a capacitive transducer with an external mirror.

12.4.4 Airborne transducer arrays

It is possible to use multiple transducers in various geometries to form ultrasonic airborne arrays (Medina and Wykes, 2001). These operate in the same way as traditional arrays, as used for instance in medical imaging and non-destructive evaluation (NDE), using the periodicity of the array elements and the frequency of operation to dictate the radiated field patterns. As mentioned above, it is usual to design such arrays for operation at frequencies of < 1 MHz, because of excessive attenuation in air at higher frequencies. An example of the electrode geometry that could be adopted for a line array of capacitance devices for use in air is shown in Fig. 12.11 (Neild *et al.*, 2005). In air, these electrodes can be used to create a rigid backplate, using standard photolithography methods. Connections can then be made to each backplate element, so that phasing in either transmission or reception can be applied. This allows the radiated field to be controlled, in terms of beam steering, focussing or both.

Figure 12.12 shows both a theoretical simulation and an experimental scan in air for such an array. In this case, the phasing of the array is designed to focus on-axis, at a distance of 20 mm from the array. In the theoretical simulation, Fig. 12.12(a), the way in which contributions from the individual elements are visible close to the individual elements, but then combine to form the overall beam shape, is evident, as is the intended focussing. In the experimental scan, Fig. 12.12(b),

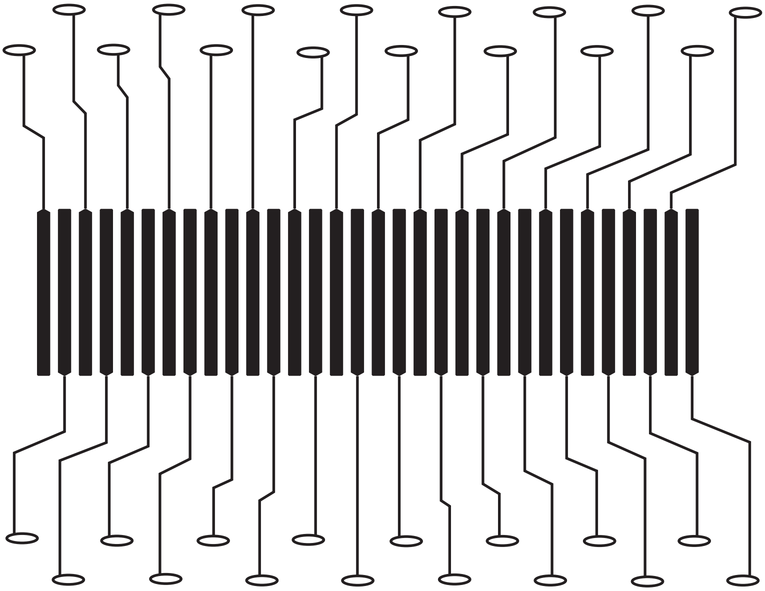

12.11 Possible electrode geometry for a line array of capacitance devices for use in air.

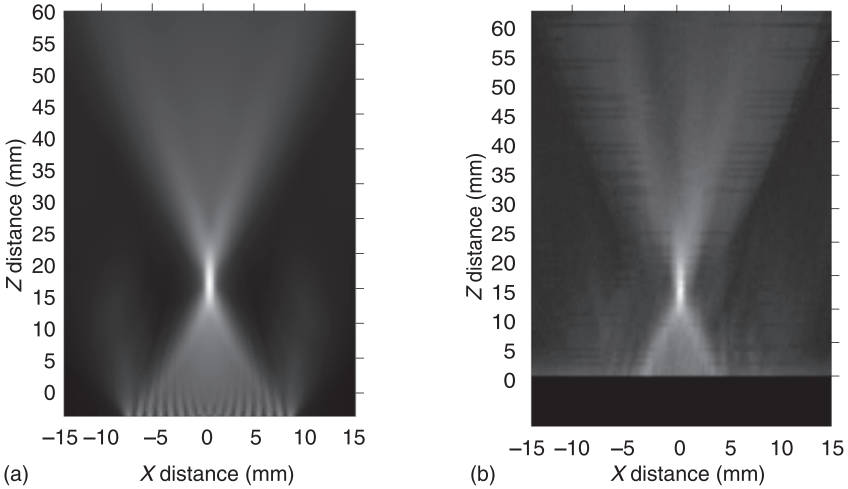

12.12 Results of a scan in air by a transducer array where the beam is focussed on-axis: (a) theoretical simulation, (b) experimental scan.

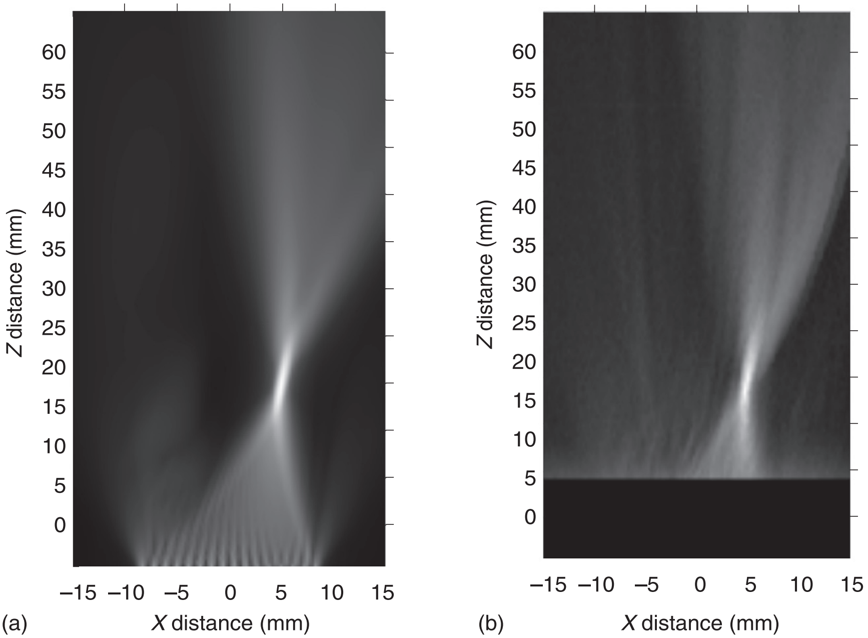

12.13 Results of a scan in air by a transducer array where the beam is focussed off-axis: (a) theoretical simulation, (b) experimental scan.

the contribution close to the transducer could not be recorded, because of feed-through from the tone-burst voltage signal used to drive the elements in transmission onto the received signal. However, it is clear that the expected focus did appear at the expected axial position of 20 mm from the front face of the array.

It is also possible to perform a similar experiment, but this time for a phasing scheme chosen so that the radiated beam is focussed off-axis (i.e. in the *x* direction). Here again, theory and experiment can be compared, as shown in Fig. 12.13. It can be seen again that the array has behaved as expected.

12.5 Applications

12.5.1 Air-coupled non-destructive evaluation (NDE)

There are many situations in which it is useful to be able to test a particular material or component without contact. For example, the material may be hot, moving on a production line or be of an absorbent material where a couplant cannot be used. Alternatively, it may be necessary to reduce the chances of contamination of biological or radioactive material. In such cases, non-contact methods of NDE are very important. There are many examples of such techniques, including laser ultrasound (Cielo *et al.*, 1985), electromagnetic acoustic transducers (EMATs) (Dixon *et al.*, 1999) and others, although each of these has its drawbacks – the laser technique can damage the surface and is often not eye-safe, and an EMAT needs an electrically conducting surface for efficient operation. Air-coupled ultrasound has none of these drawbacks. However, the technique does suffer because of the small signals, due to the impedance mismatch between the sample and air. However, this can be alleviated somewhat by the use of pulse compression and other techniques, as described earlier in Section 12.2.3.

A through-transmission arrangement is shown in Fig. 12.14. A pair of capacitive transducers of the type shown in Fig. 12.5 are placed either side of the sample, and a signal is passed from one to the other through the sample. The two transducers can be scanned as a pair over the sample, and data collected by the receiver. It is convenient to use an ultrasonic pulse compression (UPC) system to send chirp voltage drive signals to the source and to perform cross-correlations at the receiver.

An example of images formed in this way is shown in Fig. 12.15. These show images of an artificial square defect of 25.4-mm width, embedded within a carbon-fibre plate. A chirp signal and cross-correlation were used to produce these images, which show variations across the sample in terms of (a) changes in amplitude and (b) time of flight (phase). The defect has been clearly identified. Figure 12.16 shows another example of a carbon-fibre plate, but this time having impact damage. The photograph in Fig. 12.16(a) shows the impacted area, whereas the

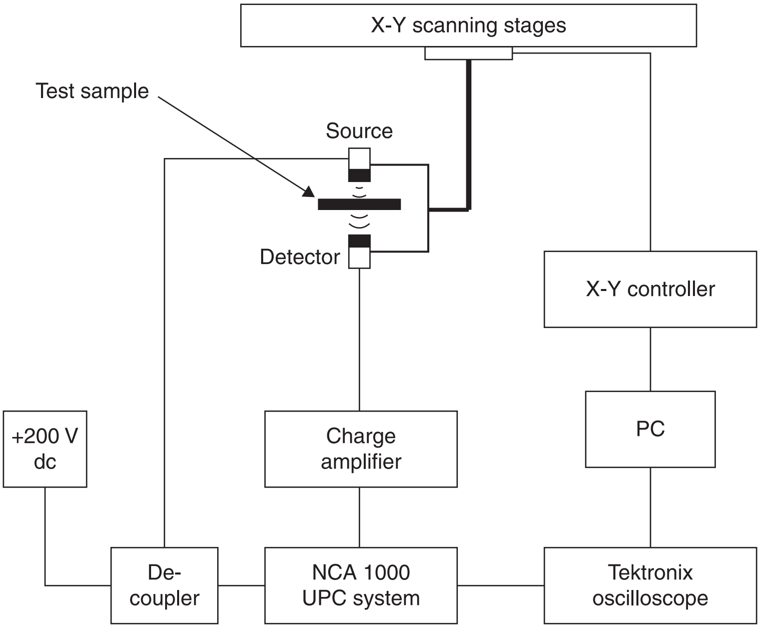

12.14 Through-transmission system for NDE.

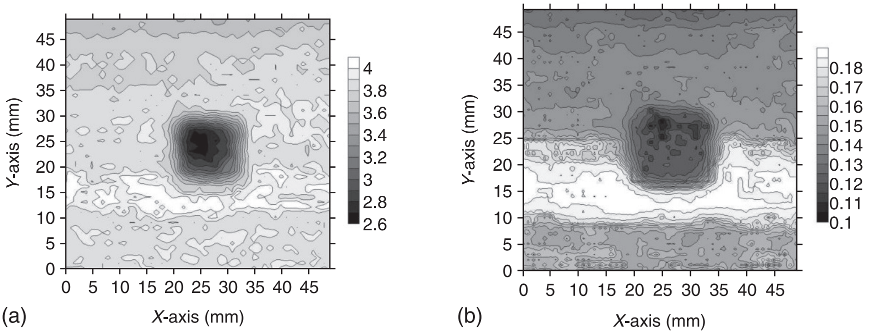

12.15 Images of a square defect in a carbon-fibre plate produced by a through-transmission system: (a) amplitude variation, (b) phase variation.

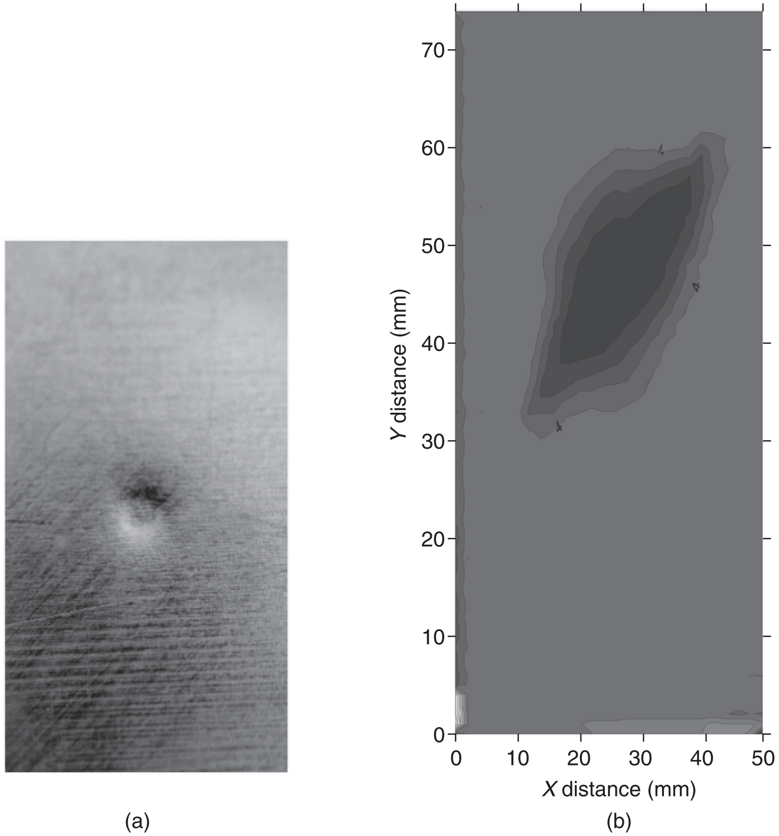

12.16 Carbon-fibre plate with impact damage: (a) photograph of the damaged plate, (b) image produced by a through-transmission system.

air-coupled ultrasonic image in Fig. 12.16(b) illustrates that the area of damage is much more extensive than is visible from the front surface.

There are many types of material that can be inspected using air-coupled ultrasound. An interesting example is the detection of contaminants in food materials. Ultrasound is sensitive to small changes in density or acoustic properties; hence, it can locate contaminants that are not detectable in some food materials using conventional X-ray and other imaging methods (Brosnan and Sun, 2004) or metal detector techniques (Graves *et al.*, 1998). Contaminants include unwanted pieces of glass, polymers and wood, which are not electrically conducting and which do not easily show up under X-ray illumination. The detection of contaminants is simple using ultrasound if the food material itself is fairly homogeneous. In addition to such measurements, it is also possible to measure the consistency of food, and whether any deliberate additives are present (Pallav *et al.*, 2009). Chocolate is a homogeneous material and is a good transmitter of ultrasound at frequencies below 1 MHz. A scanning rig can be used for the air-coupled imaging of chocolate, using two 10-mm-diameter capacitive transducers. These are scanned over a block of chocolate, and the internal structure can be revealed. The results obtained for two different samples are shown in Fig. 12.17, for (a) a solid chocolate sample and (b) one containing nuts. In the uniform chocolate sample, the imaging system has been able to identify the individual squares of chocolate. In addition, while the resolution of these images is somewhat limited by the 10-mm aperture of the imaging system, it is clear that the added nuts have been successfully detected as the darker areas (indicating a lower transmission amplitude). This allows the spatial distribution of the nuts to be estimated – a valuable tool for process control.

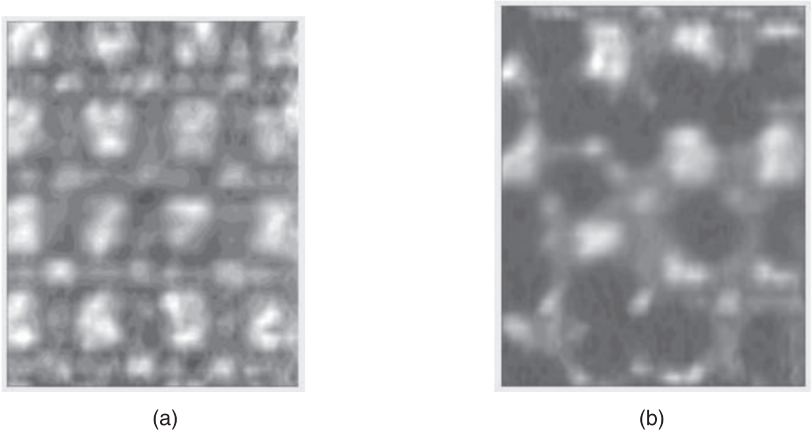
(a) (b)

12.17 Ultrasound images: (a) solid chocolate sample, (b) chocolate sample containing nuts.

12.5.2 Imaging of thin materials

The use of the focussing device shown earlier in Fig. 12.9 allows thin materials to be inspected. This is because, in through transmission, the amplitude of the signal can be detected at closely spaced intervals. In effect, the amplitude of transmission measures the local properties of the sample, so that scanning a pair of transducers over a surface allows these variations to be mapped over a finite area (Gan *et al.*, 2003a). An example of this technique is shown in Fig. 12.18. A similar apparatus to that shown in Fig. 12.11 can be used to image thin paper samples, but with the source replaced by a focussing device. Fig. 12.18 shows how the watermark of a banknote can be imaged using focussed air-coupled ultrasound, to produce a good facsimile of the optical image seen under natural illumination. In effect, the ultrasound measures changes in the density of the paper. This technology has many applications in security (e.g. by detecting watermarks under ink layers).

12.5.3 Gas-jet transducers

It is also possible to change the directivity of an ultrasonic signal in air by using an air-coupled transducer that operates within a gas jet (Choi *et al.*, 2002). The ultrasonic velocity within the gas jet is different from that in the surrounding air, so that the gas jet acts as a waveguide. The technique is thus analogous to the well-known water-jet devices, but with the water replaced by a gas to make it truly non-contact. The acoustic velocity within the jet can be changed by:

- using an air jet and adjusting the gas velocity along the beam axis
- heating or cooling the gas jet
- using a different gas or gas mixture within the jet

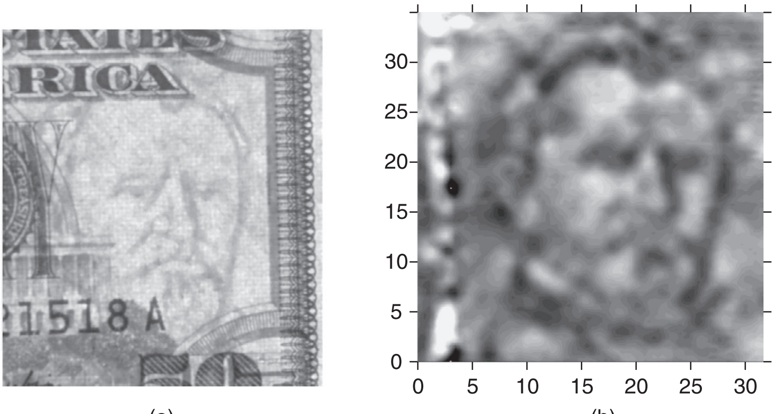

(a) (b)

12.18 (a) A watermark on a banknote. (b) Image of the banknote produced using focussed air-coupled ultrasound.

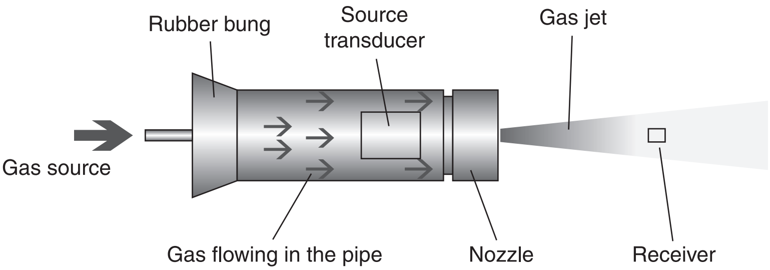

12.19 Gas-jet transducer.

This possibility has been investigated, using a wide range of temperatures and gas mixtures. The type of transducer device that can be used is shown schematically in Fig. 12.19. An air-coupled transducer is placed within a tube, through which the chosen gas passes at the required flow rate. The gas passes around the transducer, and is then emitted from a nozzle assembled to form the gas jet. Particular care has to be taken in the design of the internal wall curvature and nozzle parameters, so that as close to laminar flow as possible is produced for a particular gas and nozzle diameter, while causing as little disruption as possible to the emitted beam from the transducer. However, with careful consideration, this is possible for a wide range of gases and flow rates.

A waveguide is formed when the acoustic velocity is lower in the gas jet than in the surrounding air volume. This is different from water jets, where the velocity is higher in the jet; this is because the waveguide is formed from the large impedance mismatch at the waveguide boundaries. For air, the velocity will vary smoothly with distance from the beam axis at the edges of the jet, as there will inevitably be mixing of the jet and the surrounding air at the edges. Thus, to confine the ultrasonic beam, a lower acoustic velocity is required. Conversely, divergence can be enhanced using a higher acoustic velocity within the gas jet than that of still air. Investigations have shown that cooling the air within an air jet does indeed cause collimation of an ultrasonic beam. However, collimation can also be achieved by mixing some CO_2 with the air in the waveguide jet. Note, however, that the attenuation of ultrasound in CO_2 is much higher than in air; hence, there is an optimum concentration in any mixture, depending on the ultrasonic frequency used.

An illustration of the effects that can be achieved is shown in Fig. 12.20. The emitted beam was measured experimentally using a scanned miniature receiver. Three conditions were studied: no gas flow, with air at room temperature and with the addition of CO_2 to the gas mixture. It can be seen that the beam emitted from the nozzle was reasonably uniform in the absence of gas flow. When the air jet was operating, the beam diverged, with the energy radiating in a distinct conical pattern. Conversely, when CO_2 was added to the gas jet, there was a high degree of collimation, showing that indeed a waveguide had been formed.

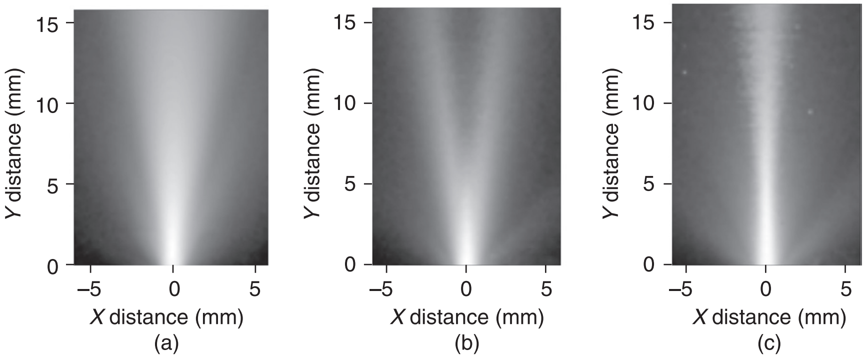

12.20 Beam emitted from a gas-jet transducer: (a) with no gas flow, (b) with a jet of air at room temperature, (c) with a jet containing additional CO_2.

12.5.4 Measurement of flow and temperature in gases

The use of ultrasound to measure flow is a well-known application, and is used in applications as varied as flow measurement in pipes, gas flow metering and blood flow studies. It is also used to measure the wind velocity outdoors, especially at locations such as airports. As stated above, the speed of sound, c, in a medium depends on the velocity component of the medium in the direction of travel. There is also a temperature (T) effect, given by Eq. 12.10.

Air-coupled ultrasound can be used in various ways to measure either the flow velocity of a given gas or its temperature. The standard approach is to measure the time of travel along a given path, but to do so in opposite directions. Adding the times of travel gives an estimate of the temperature (Huang *et al.*, 2007), whereas subtracting them gives a measure of the flow (by removing the temperature dependence, which is present in both values). One interesting additional approach is to use tomography, where measurements are taken in more than one direction, along selected ray paths, and a cross section of the spatial variations in flow velocity or temperature can be reconstructed (Gan *et al.*, 2003b; Ohyama *et al.*, 2009). Figure 12.21 shows the results of such an experiment using air-coupled transducers to study a hot gas jet, in this case produced by a heat gun. Figure 12.21(a) shows the reconstructed cross section of the flow velocity in $m.s^{-1}$, obtained from ultrasonic time-of-flight data. This can be compared with that measured experimentally via a standard hot-wire anemometer, scanned through the gas jet in a point-to-point measurement, as shown in Fig. 12.21(b). As can be seen, the two cross sections are very similar in form.

By treating the same data differently, it is possible via Eq. 12.18 to obtain values for the temperature variation across the gas jet. The equivalent results at the same location through the gas jet in terms of temperature are shown

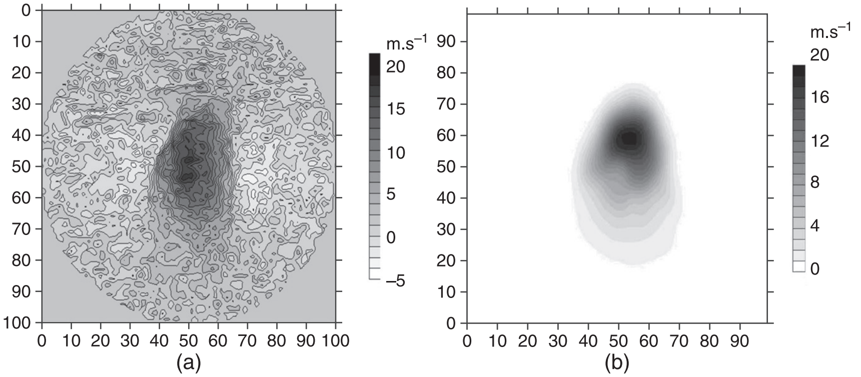

12.21 Cross section of the flow velocity of a hot gas jet measured experimentally by (a) air-coupled transducers and(b) a standard hot-wire anemometer.

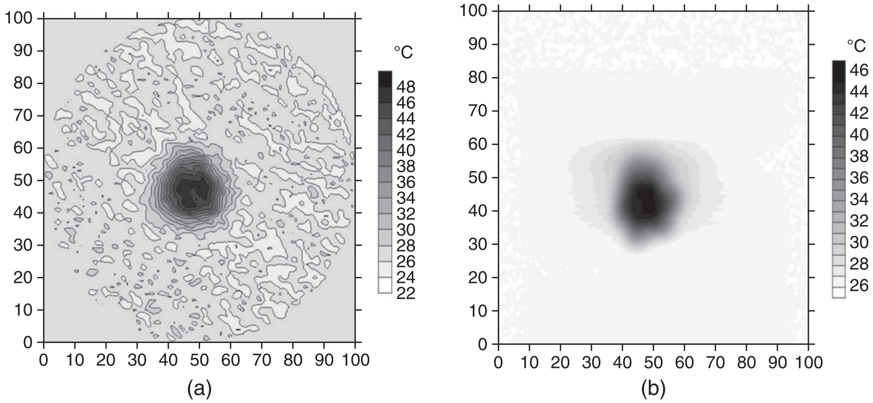

12.22 Cross section of the temperature of a hot gas jet measured experimentally by (a) air-coupled transducers and(b) a scanned miniature thermocouple.

in Fig. 12.22. Now the comparison of the ultrasonically derived variations is made with temperature data from a scanned miniature thermocouple. As can be seen, the two sets of reconstructed temperature profiles have very similar features.

The above measurements were for reasonably low temperatures. However, because of the non-contact nature of the measurement, it is possible to use the technique to estimate much higher temperatures, such as that found in flames. In the same way as for the gas jet, an ultrasonic signal can be transmitted through a flame, and the amplitude and travel time of the signal recorded as a function of position. Care must be taken in such a measurement because of the large temperature gradients that can exist at the edges of flames, where ultrasonic propagation can be affected by refraction effects. Despite this, it is possible to transmit useful signals through flames, as illustrated in Fig. 12.23(a). Here, the actual transmitted transient signals from a pair of air-coupled transducers are shown, when passing horizontally through the flame produced by a Bunsen

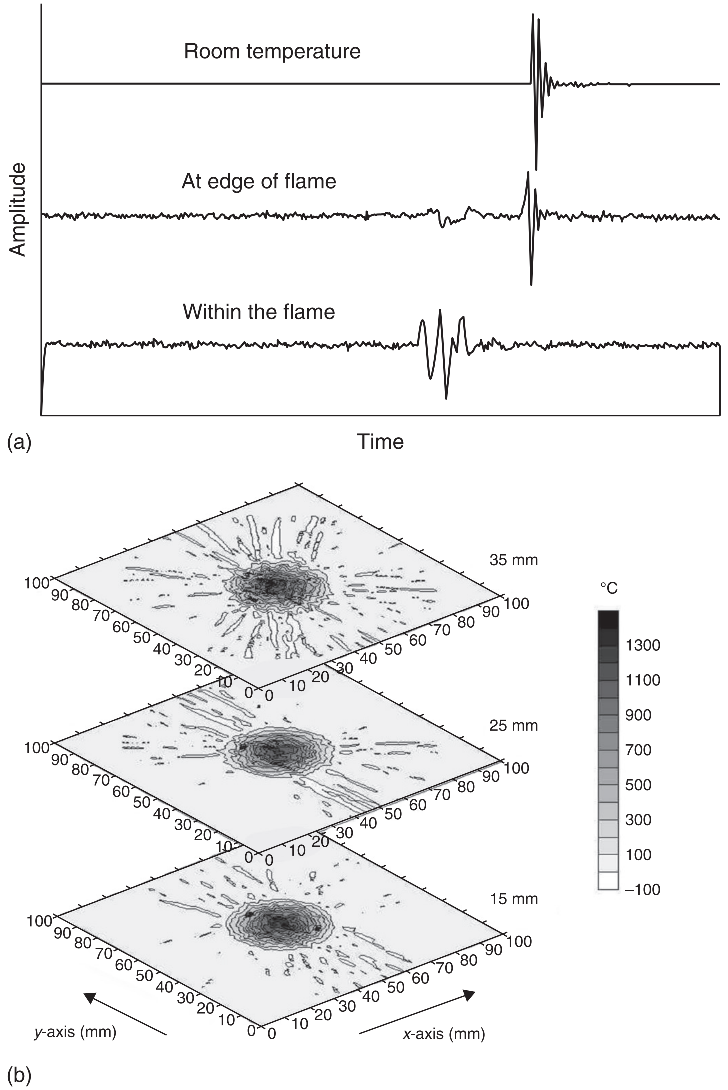

12.23 (a) Amplitude of an ultrasound beam passing through a flame measured by a pair of air-coupled transducers. (b) Temperature cross sections of the flame reconstructed at three heights above the burner exit orifice.

burner. When the beam is at room temperature (i.e. not passing through the flame), the transient signal is evident as in the top trace, with a reasonable SNR. If the beam intercepts the side of the flame, however, a very different behaviour is evident. There is a slight increase in the speed of the main signal, but an additional feature appears at an earlier time – this is the signal that has refracted into the flame, whose velocity is considerably higher within the heated gas region. When the beam is passed totally through the flame, only the higher velocity signal is present.

This type of signal can also be used for tomography, provided the transducers can be scanned around the flame and multiple paths sampled through it (Gan and Hutchins, 2003). The result of such an experiment is shown in Fig. 12.23(b), where the temperature cross section of the flame has been reconstructed at three heights above the burner exit orifice. As can be seen, some very high temperatures were measured using this technique. The data were taken in planes normal to the flame axis. This ensures maximum sensitivity to the temperature data, with a minimal contribution from the gas flow.

A final application of such transducers is the measurement of gas flow at very high or very low gas pressures. High gas pressures occur, for instance, within gas pipelines, where there is a need to inspect the inner wall for pitting or corrosion. With a capacitive transducer, as the pressure increases there is an initial improvement in the response in terms of bandwidth and sensitivity, up to pressures of 2 atmospheres or so. Beyond that, the sensitivity gradually drops. However, the converse is true for piezoelectric devices, where the impedance mismatch to the air improves as the density of the gas increases. Thus, for high-pressure pipeline inspections, piezoelectric devices are preferred. However, at low gas pressures, membrane-type capacitive transducers are better, because now the impedance of the air reduces as the pressure decreases; hence they are naturally more suited to such conditions.

An example of an application where such conditions exist is on the surface of Mars. There is a requirement to measure the wind speed on the Martian surface, to see what might be encountered by a Mars lander (Williams, 2001; Lenoir *et al.*, 2010). For the design of these vehicles, the wind speed must be measured accurately over a wide range of temperature conditions, and over a wide wind-speed range. The main problem is that the atmosphere is mainly CO_2 and at very low pressure of 60 mbar. Capacitive devices are able to operate under such conditions (Davis *et al.*, 2007). Figure 12.24 shows an example of the ultrasonic frequency spectra that arise from such a measurement, made in the laboratory using simulated Martian atmospheric conditions. These are spectra of ultrasonic waveforms, transmitted across a short distance within a low-pressure chamber. It can be seen that, as the pressure decreases, the frequency of operation of the transducers decreases and the sensitivity of the measurement also goes down. This is as expected – the density (ρ) of the gas is now much lower, and the expected resonant frequency, f_0, due partly to the nature of the 'gas spring' behind

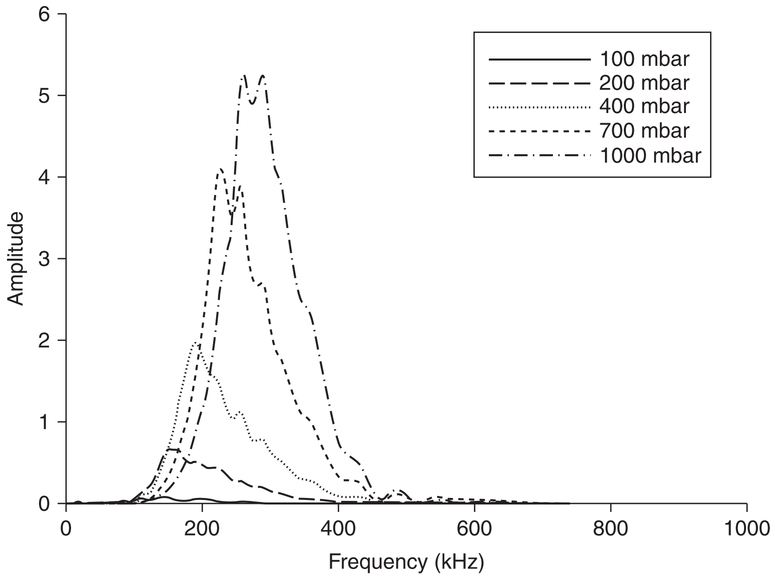

12.24 Ultrasonic frequency spectra measured in the laboratory using a simulated Martian atmosphere.

the membrane, decreases, as seen from Eq. 12.16. However, it is interesting to see that the transducer can still operate at such low pressures in gases. For these reasons, it is the main design being considered as part of an ultrasonic wind speed instrument for a future ESA mission to Mars.

12.6 Future trends

Both the piezoelectric and capacitive designs for airborne ultrasound have applications to different industrial sectors. However, both have their drawbacks – the impedance issue for piezoelectrics, and the need to apply polymer films manually during the construction of capacitive devices.

There is now a trend to try and address these problems using new microfabrication techniques. Using these techniques, it is possible to base transducers on many different materials. The techniques allow the use of forms of materials that give the required properties, rather than taking, say, a standard piezoelectric material and trying to match it to air. It has been recognised, for instance, that CMUTs could have wide-ranging application to ultrasonic measurement. They are used in air-coupled measurements and their use has been proposed for many different ultrasonic measurements, especially for medical imaging. In addition, microfabrication techniques have been developed for polymer materials. One of these, micro-stereolithography (MSL), is a type of rapid prototyping technology that can be used to form complicated shapes at high resolution (Tse *et al.*, 2003). This technique has the potential for the creation of CMUTs and other transducer types that can be used in gases, liquids and solids.

There has been recent interest in the use of airborne ultrasound for digital communications. This emerging technology can make use of some of the wide bandwidth designs mentioned in this chapter to transmit digital communication signals across a room (Li *et al.*, 2008). While this is unlikely to be used for high-capacity applications, such as wireless internet access, the useable bandwidth of up to 500 kHz allows many short-range communication signals to be transmitted. One aspect of particular interest is the high security features that are present – for instance, the signals are unlikely to pass from one room to another in a building, and would be very difficult to intercept if line-of-sight communication is used. This is anticipated to be a growth area in the use of airborne ultrasound in modern everyday use.

12.7 Sources of further information and advice

There are various good texts that give the background to acoustics in general and ultrasound at higher frequencies. The book by Finch (2004) has a good description of the fundamental background, including vibrations and waves. It is also a good source of knowledge on the various types of instrumentation and signal-processing techniques that are useful for ultrasound in air, including the FFT (fast Fourier transform) and how cross-correlation operates.

While not described in detail in this chapter, it is possible to produce shock waves and non-linear behaviour at ultrasonic frequencies in air. These effects, seen in air at high amplitudes, are able to produce various interesting phenomena, including enhanced directivity at low frequencies. These so-called acoustic searchlights have various applications (Haupt, 2009), where there is a need to send information to specific locations from a source. They hold much promise in military communications and high-amplitude acoustic targeting.

The use of air-coupled ultrasonic technologies is currently not that common; most ultrasound uses involve contact with either an inanimate object (NDE) or the human body (medical ultrasound). However, the necessary techniques, such as cross-correlation signal processing, are starting to become mainstream methods in conventional medical imaging, for example. Thus, knowledge of standard ultrasound techniques, as outlined in detail in this book and others, is a good guide to the future development of airborne ultrasound.

12.8 Acknowledgements

The authors would like to thank Duncan Billson, Doo-Won Choi, Lee Davis, Tat-Hean Gan, Prakash Pallav and Toby Robertson for scientific input into this chapter.

12.9 References

Abello T P (1928), Absorption of ultrasonic waves by various gases, *Physical Review*, 31, 1083–91.

ANSI (1989), S2.26-1978 ASA 23-78, Method for the calculation of the absorption of sound by the atmosphere, American National Standards Institute, New York.

Bass H E and Shields F D (1974), Vibrational relaxation and sound absorption in O_2/H_2O mixture, *J. Acoust. Soc. Am.*, 56, 856 (1974).

Bass H E, Sutherland L C, Piercy J and Evans L (1984), Absorption of sound by the atmosphere in *Physical Acoustics Vol. XVII* (edited by W P Mason), New York, Academic Press, 145–232.

Bauer S, Gerhard-Multhaupt R, Sessler G M (2004), Ferroelectrets: Soft electroactive foams for transducers, *Physics Today*, 57, 37–43.

Blomme E, Bulcaen D and Declercq N F (2002), Air-coupled ultrasonic NDE: experiments in the frequency range 750 kHz–2 MHz, *NDT&E International*, 35, 417–26.

Bohn, D (1988), Environmental effects on the speed of sound, *J. Audio Eng. Soc.*, 36, 223–31.

Breazeale M A, Cantrell J H and Heyman J S (1983), Ultrasonic wave velocity and attenuation measurements in *Methods of Experimental Physics 19* (edited by P D Edmonds), New York, Academic Press, 67–135.

Brosnan T and Sun D W (2004), Improving quality inspection of food products by computer vision: a review, *Journal of Food Engineering* 61, 3–16.

Buckley J (1998), Principles and application of air-coupled ultrasonics, *Insight*, 40, 755–9.

Caronti A, Caliano G, Iula A and Pappalardo M (2002), An accurate model for capacitive micromachined ultrasonic transducers, *IEEE Trans. Ultrason. Ferroelectr. and Freq. Control*, 49, 159–68.

Carr H and Wykes C (1993), Diagnostic measurements in capacitive transducers, *Ultrasonics*, 31, 13–20.

Chang M M, Deng M T, Gwol J T, Mail J D and Hsu E (2006), Polymer-based capacitive micromachined ultrasonic transducers (CMUTs) for micro surgical imaging applications, in *Proceedings of the 1st IEEE International Conference on Nano/Micro Engineered and Molecular Systems*, Zhuhai, China, 61–5.

Chiou D, Chen M, Chang M and Deng H (2007), Characterization and optimization design of the polymer-based capacitive micro-arrayed ultrasonic transducer, *Japan. J. Appl. Phys.*, 46, 7496–503.

Choi D W, Hutchins D A and Billson D R (2002), Gas jet as a waveguide for air-coupled ultrasonics, *Ultrasonics*, 40, 145–51.

Cielo P, Nadeau F and Lamontagne M (1985), Laser generation of convergent acoustic waves for materials inspection, *Ultrasonics*, 23, 55–62.

Cramer O (1993), The variation of the specific heat ratio and the speed of sound in air with temperature, pressure, humidity, and CO_2 concentration, *J. Acoust. Soc. Am.,* 93, 2510–16.

Dabirikhah H and Turner C W (1994), Leaky plate wave airborne ultrasonic transducer, *Electronics Letters*, 30, 1549–50.

Davis L A J, Hutchins D A and Noble R A (2007), Characterisation of cMUTs in rarefied gases, *IEEE Trans. Ultrasonics, Ferr. Freq. Control*, 54, 1065–71.

Dixon S M, Edwards C and Palmer S B (1999), A laser–EMAT system for ultrasonic weld inspection, *Ultrasonics*, 37, 273–81.

Durris L, Goujon L, Pelourson A, Gonnard P, Brissaud M and Richard C (1996), Airborne ultrasonic transducer, *Ultrasonics*, 34, 153–8.

Evans L B, Bass H E and Sutherland L C (1972), Atmospheric absorption of sound: theoretical predictions, *J. Acoust. Soc. Am.*, 51, 1565–75.

Finch R D (2004), *Introduction to Acoustics*, Prentice Hall, ISBN 978-0023375705.

Gachagan A and Hayward G (1998), Improving the bandwidth of 1-3 connectivity composite receivers using mode coupling, *J. Acoust. Soc. Am.*, 103, 3344–52.

Gan T H and Hutchins D A (2003), Air-coupled ultrasonic tomographic imaging of high temperature flames, *IEEE Trans. Ultras. Ferr. Freq. Contr.*, 50, 1184–90.

Gan T H, Hutchins D A and Billson D R (2002), Preliminary studies of a novel air-coupled ultrasonic inspection system for food containers, *Journal of Food Engineering*, 53, 315–23.

Gan T H, Hutchins D A, Billson D R and Schindel D W (2003a), High resolution air-coupled imaging of thin materials, *IEEE Trans. Ultras. Ferr. Freq. Contr.*, 50, 1516–24.

Gan T H, Hutchins D A, Carpenter P W and Wright W M D (2003b), Simultaneous reconstruction of flow and temperature cross-sections in gas jets using acoustic tomography, *J. Acoust. Soc. Am.*, 114, 759–66.

Gómez Alvarez-Arenas T E (2004), Acoustic impedance matching of piezoelectric transducers to the air, *IEEE Trans. Ultrason. Ferroelectr. Freq. Control*, 51, 624–33.

Grandia W A and Fortunko C M (1995), NDE applications of air-coupled ultrasonic transducers, *Proc. 1995 IEEE Ultrasonics Symposium* (Seattle, USA), 697–704.

Graves M, Smith A and Batchelor B (1998), Approaches to foreign body detection in foods, *Trends in Food Science and Techn.*, 9, 21–7.

Gudra T and Opielinski K J (2002), Influence of acoustic impedance of multilayer acoustic systems on the transfer function of ultrasonic airborne transducers, *Ultrasonics*, 40, 457–63.

Haller M I and Khuri-Yakub B T (1994), Micromachined 1-3 composites for ultrasonic air transducers, *Review Scientific Instruments*, 65, 2095–8.

Haller M I and Khuri-Yakub B T (1996), A surface micromachined electrostatic ultrasonic air transducer, *IEEE Trans. Ultrason. Ferroelectr. Freq. Control*, 43, 1–6.

Halmshaw R (1991), *Non-Destructive Testing*, 2nd ed. London: Arnold.

Haupt R W (2009), High-powered parametric acoustic array in air, *J. Acoust. Soc. Am.*, 125, 2688.

Hietanen J (1998) Closed-form formulation for sensitivity of capacitive ultrasonic transducers using V-grooved backplates, *Sensors and Actuators A: Physical*, 69, 139–42.

Hietanen J, Stor-Pellinen J and Luukkala M (1993), A Helmholtz resonator model for an electrostatic ultrasonic air transducer with V-grooved backplate, *Sensors and Actuators A: Physical*, 39, 129–32.

Hickling R and Marin SP (1986), The use of ultrasonics for gauging and proximity sensing in air, *J. Acoust. Soc. Am.*, 79, 1151–60.

Huang Y S, Huang Y P, Huang K N and Young M S (2007), An accurate air temperature measurement system based on an envelope pulsed ultrasonic time-of-flight technique, *Rev. Sci. Instrum.*, 78, 115102 (*9 pages*).

Hutchins D A, McIntosh J S, Neild A, Billson D R and Noble R A (2003), Radiated fields of capacitive micromachined ultrasonic transducers in air, *J. Acoust. Soc. Am.*, 114, 1435–49.

Hutchins D A, Schindel D W, Bashford A G and Wright W M D (1998), Advances in ultrasonic electrostatic transduction, *Ultrasonics*, 36, 1–6.

Ju K C, Tseng L T, Chen Y Y and Lin W L (2006), Investigation of a scanned cylindrical ultrasound system for breast hyperthermia, *Phys. Med. Biol.*, 51, 539–55.

Kažys R, Demčenko A, Mažeika L, Šliteris R and Žukauskas E (2007), Air-coupled ultrasonic non-destructive testing of aerospace components, *Insight*, 49, 195–9.

Knudsen V O (1933), The absorption of sound in gases, *J. Acoust. Soc. Am.*, 5, 112–21.

Krauss O, Gerlach R and Fricke J (1994), Experimental and theoretical investigations of SiO_2-aerogel matched piezo-transducers, *Ultrasonics*, 32, 217–22.

Lenoir B, Banfield D and Caughey D A (2010), Accommodation study for an anemometer on a Martian lander, *J. Atmospheric and Oceanic Technology*, e-View doi: 10.1175/2010JTECHA1490.1.

Leonard R W (1940), The absorption of sound in carbon dioxide, *J. Acoust. Soc. Am.*, 12, 241–4.

Li C, Hutchins D A and Green R J (2008), Short-range ultrasonic digital communications in air, *IEEE Trans. Ultras. Ferr. Freq. Contr.*, 55, 908–18.

Manthey W, Kroemer N and Mágori V (1992), Ultrasonic transducers and transducer arrays for applications in air, *Measurement Science and Technology*, 3, 249–61.

McIntosh J S, Hutchins D A, Billson D R, Robertson T J, Noble R A and Jones A D R (2002), The characterization of capacitive micromachined ultrasonic transducers in air, *Ultrasonics*, 40, 477–83.

Medina L and Wykes C (2001), Multiple target 3D location airborne ultrasonic system, *Ultrasonics*, 39, 19–25.

Neild A, Hutchins D A, Robertson T J and Schindel D W (2004), A model for the radiated field of a plane piston after reflection from a curved surface, *J. Acoust. Soc. Am.*, 116, 2793–801.

Neild A, Hutchins D A, Robertson T J, Davis L A J and Billson D R (2005), The radiated fields of focussing air-coupled ultrasonic phased arrays, *Ultrasonics*, 43, 183–95.

Noble R A, Jones A D R, Robertson T J, Hutchins D A and Billson D R (2001), Novel, wide bandwidth, micromachined ultrasonic transducers, *IEEE Trans. Ultrason. Ferroelectr. Freq. Control*, 48, 1495–507.

Ohyama S, Takayama J, Watanabe Y, Takahoshi T and Oshima K (2009), Temperature distribution and wind vector measurement using ultrasonic CT based on the time of flight detection, *Sensors and Actuators A: Physical*, 151, 159–67.

Pallav P, Hutchins D A and Gan T H (2009), Air-coupled ultrasonic evaluation of food materials, *Ultrasonics*, 49, 244–53.

Peilemeier W H (1945), Observed classical sound absorption in air, *J. Acoust. Soc. Am.*, 17, 24–7.

Pizarro L, Certon D, Lethiecq M and Hosten B (1999), Airborne ultrasonic electrostatic transducers with conductive grooved backplates: tailoring their centre frequency, sensitivity and bandwidth, *Ultrasonics*, 37, 493–503.

Rafiq M and Wykes C (1991), The performance of capacitive ultrasonic transducers using v-grooved backplates, *Meas. Sci. Technol.*, 2, 168–74.

Rao N (1994), Investigation of a pulse-compression technique for medical ultrasound: a simulation study, *Medical & Biological Engineering & Computing*, 32, 181–8.

Rao N and Mehra S (1993), Medical ultrasound imaging using pulse-compression, *Electronics Letters*, 29, 649–51.

Robertson T J, Hutchins D A and Billson D R (2002), Capacitive air-coupled cylindrical transducers for ultrasonic imaging applications, *Measurement Science and Technology*, 13, 758–69.

Satyanarayan L, Vander Weide J M, Declercq N F and Berthelot Y (2009), Investigation of a novel polymer foam material for air coupled ultrasonic transducer applications, in *Ultrasonic Wave Propagation in Non Homogeneous Media*, Springer; *Proceedings in Physics*, 128 (Springer, Berlin), p. 329. ISBN 978-3-540-89104-8.

Schiller S, Hsieh C K, Chou C H and Khuri-Yakub B T (1990), Novel high frequency air transducers, *Rev. Prog. Quant. Nondestr. Eval.*, 9, 795–8.

Schindel D W (1998), Ultrasonic imaging of solid surfaces using a focussed air-coupled capacitance transducer, *Ultrasonics*, 35, 587–94.

Schindel D W (1999), Air-coupled ultrasonic measurements of adhesively-bonded multilayer structures, *Ultrasonics*, 37, 185–200.

Schindel D W and Hutchins D A (1995), Applications of micromachined capacitance transducers in air-coupled ultrasonics and nondestructive evaluation, *IEEE Trans. Ultrason. Ferroelectr. Freq. Control*, 42, 51–7.

Schindel D W, Hutchins D A, Zou L and Sayer M (1995), The design and characterization of micromachined air-coupled capacitance transducers, *IEEE Trans. Ultrason. Ferroelectr. Freq. Control*, 42, 42–50.

Silk M G (1984), *Ultrasonic Transducers for Nondestructive Testing*, 1st ed. Bristol: Adam Hilger Ltd.

Smorenburg H E, Crevecoeur R M and de Schepper I M (1996), Fast sound in a dense helium argon gas mixture, *Physics Letters A*, 211, 118–24.

Stoessel R, Krohn N, Pfleiderer K and Busse G (2002), Air-coupled ultrasound inspection of various materials, *Ultrasonics*, 40, 159–63.

Strycek J O, Loertscher H P and Starman, S (2000), High speed large area scanning using air-coupled ultrasound, presented at *15th World Conf. on Nondestructive Testing*, Rome, Italy (published by ndt.net, http://www.ndt.net/article/wcndt00/papers/idn209/idn209.htm).

Tse L A, Hesketh P J, Rosen D W and Gole J L (2003), Stereolithography on silicon for microfluidics and microsensor packaging, *Microsystem Technologies*, 9, 319–23.

Vacek V, Hallewell G and Lindsay S (2001), Velocity of sound measurements in gaseous perfluorocarbons and their mixtures, *Fluid Phase Equilibria*, 185, 305–14.

Vun RY, Eischeid T, Bhardwaj M C (2006), Quantitative non-contact ultrasound testing and analysis of materials for process and quality control, *Proc Europ. Conf. on NDT* (Berlin, Germany), paper Th.3.7.2.

Wan J K S, Loffe M S and Depew M C (1996), A novel acoustic sensing system for on-line hydrogen measurements, *Sensors and Actuators B: Chemical*, 32, 233–7.

Wenmaekers R H C, Hak C C J M, Martin H J and Van Luxemburg L C J (2008), Air absorption error in room acoustical modeling, *Proceedings of Acoustics 08 Conference, Paris*, 3128–34.

Wilburn W S, Gould C R, Haase D G, Hoffenberg R S, Mioduszewski S and Roberson N R (1995), Determination of the concentration of SF_6 in an accelerator gas mixture by measuring the velocity of sound, *Nuclear Instruments and Methods in Physics Research Section A: Accelerators, Spectrometers, Detectors and Associated Equipment*, 355, 195–8.

Williams J P (2001), Acoustic environment of the Martian surface, *J. Geophy. Res.*, 106, 5033–41.

Wong G S K and Wu L (1997), Variation of measured nitrogen sound speed with temperature and pressure, *J. Acoust. Soc. Am.*, 102, 650–1.

Zhang W and Schouten J A (1992), The sound velocity of a mixture of He and N_2 up to 10 kbar and from 157 K to 298 K, *Fluid Phase Equilibria*, 79, 211–20.

13

Transducers for non-destructive evaluation at high temperatures

M. KOBAYASHI and C.-K. JEN,
Industrial Materials Institute, Canada

Abstract: Transducers fabricated from sol-gel composites are used in high-temperature non-destructive evaluation because of their suitable frequency range, high-temperature stability, thermal-cycle durability, high signal-to-noise ratio, broadband frequency characteristics, good acoustic bonding and curved-surface conformability.

The chapter introduces sol-gel composites and transducers made from them, such as the integrated ultrasonic transducer (IUT), buffer-rod IUT, wedge IUT and flexible ultrasonic transducer (FUT). There are applications for structural-health monitoring, including barrel and screw wear monitoring of micro-moulding machines, ultrasonic imaging of silicone oil, line defect detection and pipe thickness measurement. There are possibilities for process monitoring, such as filling monitoring and process optimisation of injection moulding.

Key words: high temperature, sol-gel composite, flexible ultrasonic transducer, structural-health monitoring, process monitoring.

13.1 Transducers for non-destructive evaluation at high temperatures

High-temperature sensors for non-destructive evaluation (NDE) are required by industry, especially for structural-health monitoring and for process monitoring. Continuous inspection of structures in harsh environments could optimise maintenance at nuclear and fossil fuel power plants (Fothergill *et al.*, 1989; Karasawa *et al.*, 2000), chemical and petroleum plants (Moore *et al.*, 2007), the aerospace industry (Dalton *et al.*, 2001), etc. Real-time process monitoring is also preferable because it could shorten process optimisation times. And, if there are continuous errors, it will be possible to stop manufacturing before producing too many substandard products. Online feedback from monitoring sensors to control systems allows efficient quality control of the final products and process optimisation; therefore, the development of high-temperature sensors for real-time monitoring is of great interest (Agrawal *et al.*, 1987; Piché *et al.*, 1994). Applications operating at elevated temperatures often have thermal cycles, for example, the operating temperature of coolant pipes in nuclear power plants is 290–330 °C (Kwon *et al.*, 1999), and in the aerospace industry the temperature range is −80 to 100 °C. Manufacturing processes are often carried out at elevated temperatures, for example, the nominal temperature at an external mould surface for a polymer injection moulding process is around 50 °C (Kobayashi *et al.*, 2002)

Published by Woodhead Publishing Limited, 2012

and the nominal temperature of a die for aluminium and magnesium die casting could be 200–350 °C (França *et al.*, 2000). Some applications require much higher temperatures; for example, the temperature of superheated steam used in aircraft engine manufacturing and operation is 565 °C (McNab *et al.*, 1998). Ultrasonic transducers (UTs) are widely used for NDE applications such as structural-health monitoring and process monitoring because of their sub-surface inspection capability, elastic property characterisation ability, fast inspection speeds, simplicity and ease of operation. However, the development of high-temperature ultrasonic transducers is still a challenging issue.

One of the major problems of high-temperature ultrasonic transducers is the piezoelectricity deterioration at elevated temperatures in ferroelectric ceramics. Piezoelectric materials are used in typical ultrasonic transducers to generate and receive ultrasound. Piezoelectricity is the result of the anti-symmetric structure within a unit crystal of a piezoelectric material. In piezoelectric ceramics, a high electrical field is applied at an elevated temperature to produce piezoelectricity, in an operation called poling. At the Curie temperature, the unit crystal structure transforms to a symmetric, cubic structure, which does not exhibit piezoelectricity. When this happens, the material will not recover its piezoelectric properties when the temperature decreases below the Curie temperature, unless the piezoelectric material is again subjected to a high electrical field. In addition, when a piezoelectric material is heated, the internal kinetic energies increase. This means that above a particular energy (i.e. temperature), which depends on the crystal structure, the dipoles, which were oriented during poling, will return to a random orientation. Therefore, the functional temperature of an ultrasonic transducer is determined by its Curie temperature and its crystal structure. Common piezoelectric materials for room temperature use may not operate at high temperatures. Single crystals of lithium niobate ($LiNbO_3$) showed reasonable performance up to 1000 °C (Baba *et al.*, 2010), though the ceramic form is preferable because single crystals often have low thermal and physical shock resistance (Patel *et al.*, 1990). Therefore, it is important to develop piezoelectric materials for high-temperature continuous NDE.

Besides high-temperature stability, there are several characteristics necessary for high-temperature ultrasonic transducers in structural-health monitoring and process monitoring, and these make the development of high-temperature ultrasonic transducers more challenging. High spatial resolution is also required to detect critical defects, which means that sensors should have a high signal-to-noise ratio (SNR), 2–20 MHz operating frequency and a broadband frequency characteristic. SNR is defined in this chapter as the ratio of the amplitude of the first echo and the noise between the first echo and the second echo:

$$SNR = 20\log_{10}\left(\frac{Amplitude_{echo}}{Amplitude_{noise}}\right) \quad \text{(dB)} \qquad [13.1]$$

High SNR and broadband frequency characteristics are also desirable for process monitoring. Generally speaking, higher frequencies have higher spatial resolution; however, this is not true at high temperatures because hot materials often have higher attenuation coefficients so that the high-frequency components are significantly decreased, which results in SNR deterioration. In order to maintain a high SNR, a relatively low operating frequency and a broad bandwidth are required for high-temperature NDE applications. In real situations, ultrasonic transducers often need to make contact with structures that have surfaces with different curvatures; however, conventional ultrasonic transducers, with rigid flat end surfaces, often show poor SNR for curved structures at elevated temperatures. The poor SNR is in part due to the fact that the area of contact is a narrow line, allowing only a small portion of the available ultrasonic energy to be transmitted into the structure. A thicker amount of gel couplant, present in the gap between the flat end surface of the ultrasonic transducer and the curved surface of the structure to be inspected, will cause an area other than this narrow contact line to induce a spatial spread of ultrasonic excitation, resulting in unwanted noise.

Backing materials are widely used with conventional ultrasonic transducers to achieve broadband frequency characteristics. A tungsten/epoxy composite is commonly used as a backing material because of its high ultrasound absorbance and good acoustic impedance matching with piezoelectric ceramics (Nguyen *et al.*, 1995). However, most organic materials cannot withstand temperatures above 300 °C. Furthermore, a difference in the thermal expansion of the backing material and the piezoelectric ceramic causes a characteristic deterioration in the broadband frequency after thermal cycling. Therefore, in order to have sufficient SNR and good broadband frequency characteristics for high-temperature NDE applications, it is desirable that curved-surface conformability and the problems caused by the backing materials are solved.

The couplant is another major source of problems for ultrasonic transducers at high temperatures. A gel couplant is often placed between the ultrasonic transducer and the inspection target to enable efficient ultrasonic transmission. However, a gel couplant evaporates at elevated temperatures and it is difficult to guarantee continuous performance for more than five minutes. A dry ceramic powder or refractory adhesive cement could be used as an alternative high-temperature couplant above 300 °C, though the signal strength and SNR are significantly reduced because of the porous microstructure of those couplants after drying (Kirk *et al.*, 1999). Thin metal foils such as gold or aluminium foil, which are another type of solid couplant, could replace gel-type couplants. In this case, in order to obtain acceptable ultrasonic transmission, a pressure of $> 10\,\text{MPa}$ must be applied between the ultrasonic transducer and the object (Mrasek *et al.*, 1996), which affects the durability of the ultrasonic transducers, especially if the objects have curved surfaces. Better couplant materials or acoustic bonding methods are required for stable high-temperature ultrasonic performance.

It is difficult to find commercial transducers that can cope with all of these problems, even though high-temperature ultrasonic transducers are available from various manufacturers, e.g. IHI Inspection & Instrumentation (Tokyo, Japan), Olympus NDT (Waltham, USA), Piezo Technologies (Indianapolis, USA) and Sigma Transducer (Richland, USA). A couplant is necessary for all of these transducers, so that a suitable acoustic bonding method is a concern for continuous high-temperature measurement. Every transducer has a rigid contact end, so that it is difficult to achieve a high SNR from curved surfaces (Jen *et al.*, 2004). According to Olympus NDT, pipe thickness measurement is possible using a special contour delay line, though the manufacture of a special contour delay line is not cost effective and is not suitable for more complex geometry. Furthermore, high-temperature ultrasonic transducers from Olympus NDT operate for only 10 s at 425 °C. Transducers from IHI Inspection & Instrumentation can operate continuously in a temperature range from −196 °C to 550 °C. However, IHI transducers also require a delay line. Therefore, further development of stand-alone high-temperature ultrasonic transducers is required for continuous NDE applications.

A buffer rod (or delay line) is often used for high-temperature applications. A measurement system with a buffer rod, a room-temperature broadband ultrasonic transducer and a cooling system can be used to monitor at elevated temperatures, such as the 960 °C of molten aluminium. This system has a high signal strength, high SNR and broadband frequency characteristics (Jen *et al.*, 1999). It was attempted for real-time monitoring of die casting (Jen *et al.*, 1997) and semi-solid metal casting (Jen *et al.*, 2000) and gave promising results. However, there are still a few points to be considered. First, the buffer rod and cooling system are relatively bulky. The size of any measurement system must be taken into account when placing sensors. Second, a suitable couplant must be used between the commercial ultrasonic transducer and the buffer rod. It is not cost-effective if the buffer rod requires special machining for installation into the inspection target. The use of a buffer rod is still valid for continuous NDE application at high temperatures regardless of these concerns.

13.2 Sol-gel composite ultrasonic transducers

13.2.1 Sol-gel composite material

Ultrasonic transducers made from a sol-gel composite material are suitable for continuous NDE at high temperatures. Sol-gel composite materials were invented by Barrow *et al.* (1996). The sol-gel technique is a thin-film fabrication method: organometallic precursors of the desired oxide material are mixed and dissolved in an appropriate solvent, then the solution is coated onto a substrate. Following thermal processes, the organometallic materials pyrolyse, oxidise and then crystallise. The coating and thermal processes are repeated until the film reaches the desired thickness. The sol-gel process is useful for electro-materials because of lower processing temperatures and the ease of large area fabrication. However, the maximum thickness of each coating is in the sub-micron range due to internal stresses during the thermal processes (Sayer *et al.*, 1999) and it is time consuming for applications that require a thickness of more than 10 μm. Barrow *et al.* (1996) added selected ferroelectric powders to the sol-gel solution before the coating process in order to reduce internal stresses during the thermal processes. The remainder of their fabrication process is almost the same as that for pure sol-gel film. A schematic of the general fabrication process for a sol-gel composite ultrasonic transducer is shown in Fig. 13.1. Using this method, films more than 200 μm thick, with a suitable frequency range for high-temperature NDE applications, were successfully manufactured. In addition, ultrasonic transducers made from sol-gel composites have several desirable characteristics for continuous NDE at high temperatures, such as high-temperature stability, thermal-cycle durability, high SNR, broadband frequency characteristics without a backing material, good acoustic bonding without a couplant and curved-surface conformability (Zou *et al.*, 1997; Kobayashi *et al.*, 2002, 2009).

Currently, three sol-gel composites are in use after investigation of various materials. A lead zirconate titanate (PZT) sol-gel solution is used for these sol-gel composites, because of its high dielectric constant, reasonable temperature stability and high adhesive strength between the powder and the substrate. Because of the high dielectric constant of PZT made using a PZT sol-gel solution, the applied electrical field is efficiently transmitted into the ferroelectric powder during poling and measurement. Three kinds of ferroelectric powder, PZT,

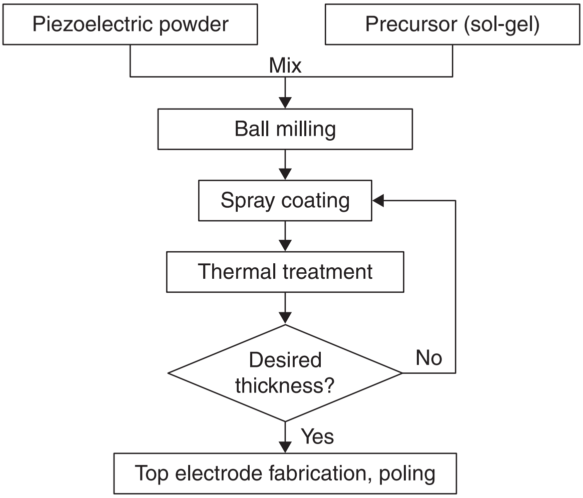

13.1 General fabrication process for a sol-gel composite ultrasonic transducer.

bismuth titanate (BIT) and lithium niobate, are used depending on the required temperature. Sol-gel composites are classified as: Phase 1 (powder derived), Phase 2 (sol-gel derived) and based on Newnham's definition (Newnham *et al.*, 1978). PZT/PZT exhibits the highest piezoelectricity up to 220 °C among those three types of material and for it the measured values of the relative dielectric constant, ε_r, the piezoelectric constant, d_{33}, and the thickness-mode electromechanical coupling coefficient, k_t, are 140–320, around 30×10^{-12} m.V^{-1} and around 0.24, respectively, and the signal strength at room temperature is comparable with that of commercial room-temperature ultrasonic transducers (Kobayashi *et al.*, 2006; Jen and Kobayashi, 2007). The variance in the dielectric constant was mainly caused by different fabrication conditions. Typical ultrasonic performance of PZT/PZT at 150 °C in pulse-echo mode is shown in Fig. 13.2. In pulse-echo mode, one transducer transmits a pulse and receives the echo reflected from the opposite side, whereas in transmission mode, two transducers serve as transmitter and receiver, respectively. L^n indicates the *n*th round-trip longitudinal echo through the substrate. PZT/PZT is used if the operating temperature is below 200 °C and the signal strength is more important than temperature stability.

BIT/PZT has medium piezoelectricity of these three materials and very stable ultrasonic performance up to 540 °C. The measured values of the relative dielectric constant, ε_r, and the piezoelectric constant, d_{33}, are around 80 and around 10×10^{-12} m.V^{-1}, respectively (Jen and Kobayashi, 2007). Typical ultrasonic performance of BIT/PZT at 400 °C in pulse-echo mode is given in Fig. 13.3. BIT/PZT is used if the maximum operating temperature is 200–500 °C

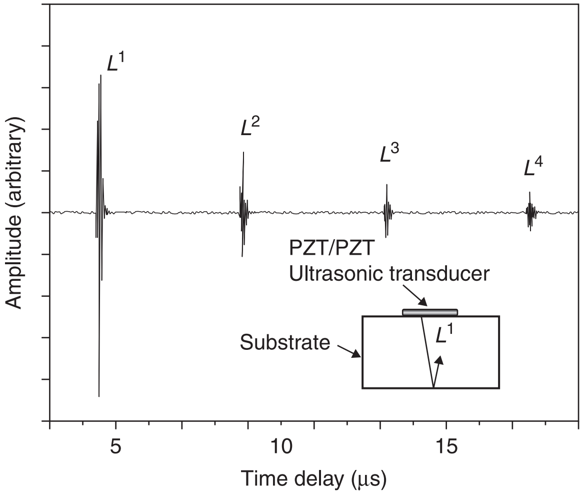

13.2 Typical ultrasonic performance of PZT/PZT at 150 °C in pulse-echo mode.

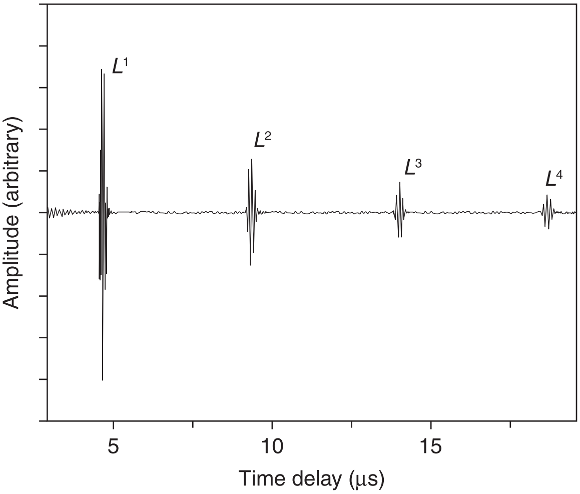

13.3 Typical ultrasonic performance of BIT/PZT at 400 °C in pulse-echo mode.

or if the signal stability is very important. The SNR shown in Fig. 13.3 seems to be slightly lower than that in Fig. 13.2, and there are two possible reasons. First, there is a difference in the piezoelectric strength between PZT/PZT and BIT/PZT. PZT/PZT can generate echoes with a higher signal strength than BIT/PZT, so that the amplitude ratio between the echo and noise could also be higher. Second, there is a temperature difference. Generally speaking, the ultrasound attenuation ratio and the scattering ratio are higher when the temperature of the metal substrate increases (Kobayashi *et al.*, 2007).

Lithium niobate/PZT has been developed for extremely high-temperature applications of more than 600 °C. It will function even at 800 °C with reasonable SNR. Its ultrasonic performance at 800 °C is shown in Fig. 13.4. Comparisons of the signal strength and SNR for these three materials at various temperatures are shown in Fig. 13.5 and Fig. 13.6, respectively. A titanium substrate was used for lithium niobate/PZT because of its high-temperature durability, whereas carbon steel substrates were used for PZT/PZT and BIT/PZT. The three materials, PZT/PZT, BIT/PZT and lithium niobate/PZT, demonstrated sufficiently high signal strengths and SNR for high-temperature continuous NDE applications at all temperatures shown in Fig. 13.5 and Fig. 13.6.

13.2.2 Ultrasonic transducers made with sol-gel composites

Ultrasonic transducers made with sol-gel composites are classified by the type of substrate on which they are deposited: integrated ultrasonic transducer (IUT), buffer-rod IUT, wedge IUT and flexible ultrasonic transducer (FUT).

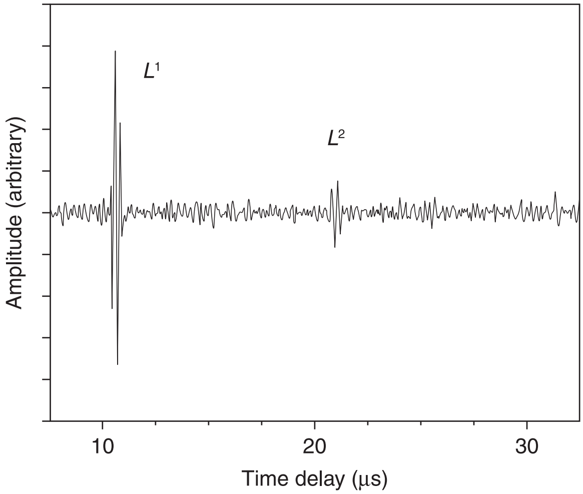

13.4 Ultrasonic performance of lithium niobate/PZT at 800 °C.

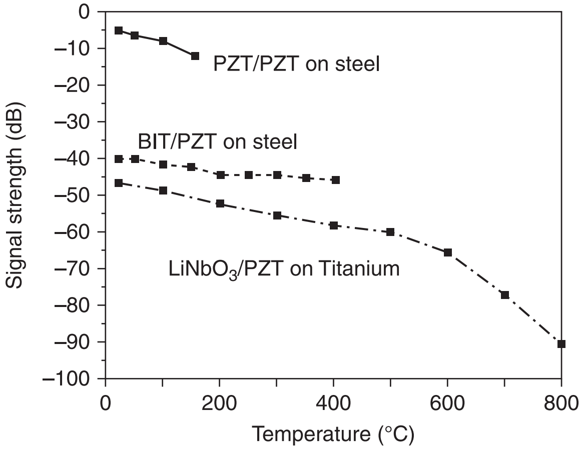

13.5 Signal strengths vs. temperature.

Integrated ultrasonic transducer (IUT)

In an IUT, the sol-gel composite is directly coated onto the monitoring structure or a part of the processing machine. It is the simplest type of transducer and it has all the useful sol-gel composite material characteristics mentioned in the previous section, i.e. suitable frequency range, high-temperature stability, thermal-cycle durability, high SNR, broadband frequency characteristics without a backing material, good acoustic bonding without a couplant and curved-surface

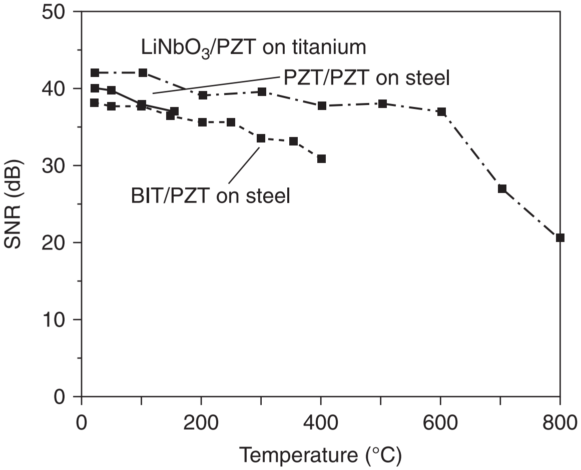

13.6 SNR vs. temperature.

conformability. In particular, IUTs can easily be integrated into complex geometry, such as spherically concave and convex and cylindrically concave and convex surfaces (Kobayashi and Jen, 2004). Moreover, on-site fabrication is possible by fabrication process modifications, though there are a few disadvantages, such as a relatively long installation time and the possibility of thermal damage to the structure during IUT integration. IUT fabrication at 150 °C to reduce thermal damage is possible (Kobayashi *et al.*, 2005); however, it sacrifices piezoelectric strength due to a reduction of the dielectric constant of the sol-gel-derived PZT phase. IUTs are the best choice if they can be installed onto a removable part with high-temperature durability or if the substrate has very complex geometry.

Buffer-rod IUT

In a buffer-rod IUT, the IUT is fabricated onto one end of a long ultrasonic delay line (or buffer rod). As already mentioned, a buffer rod is often used for high-temperature applications, but the necessity of a cooling system and couplant reduces usability. If an IUT is used instead of a commercial room-temperature ultrasonic transducer, there is no need for a cooling system or a couplant between the IUT and the buffer rod, which improves usability. Glass is often used as an ultrasonic delay-line material; however, steel is mainly used for buffer-rod IUT because of the ease of fabrication and cost effectiveness. Clad buffer rods consist of a tapered or uniform core and a cladding chosen to increase SNR (Jen and Legoux, 1998). The core is made of a low-ultrasonic-loss steel and the cladding has a higher ultrasonic velocity than the core.

An example of the ultrasonic performance of a PZT/PZT IUT fabricated onto a clad buffer rod of length 102 mm and core diameter 12.7 mm is shown in Fig. 13.7.

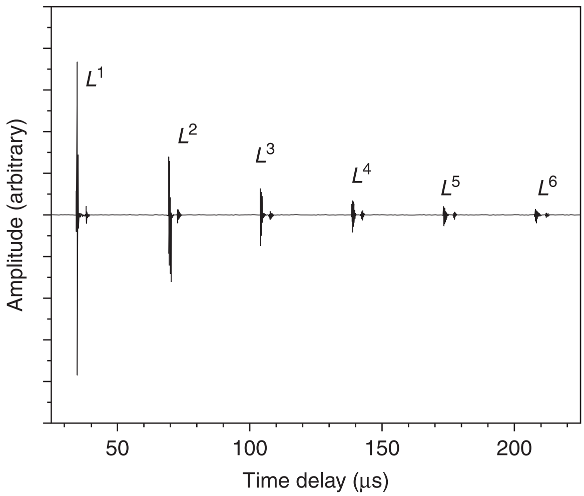

13.7 Ultrasonic performance of a PZT/PZT IUT fabricated onto a clad buffer rod of length 102 mm and core diameter 12.7 mm.

Due to wave diffraction effects and the finite diameter of the buffer rod, there were trailing echoes after the reflected longitudinal echoes, though the trailing echoes were suppressed due to the cladding layer of the buffer rod. If the clad buffer rod is assumed to have a constant temperature of 150 °C, Eq. 13.2 (Walker and Trahey, 1995) can be used to estimate the measurement accuracy:

$$\sigma(\Delta t - \Delta t') \geq \sqrt{\frac{3}{2 f_0^3 \pi^2 T (B^3 + 12B)} \left[\frac{1}{\rho^2} \left(1 + \frac{1}{SNR_1^2} \right) \left(1 + \frac{1}{SNR_2^2} \right) - 1 \right]} \quad [13.2]$$

where f_0 is the centre frequency, T is the time window for the selection, e.g. echoes L^1 and L^2 for the cross-correlation, B is the fractional bandwidth of the signal, i.e. the ratio of the 6dB bandwidth over f_0, ρ is the correlation coefficient used in the cross-correlation, SNR_1 and SNR_2 are the SNR of the first echo and the second echo, respectively, and $\sigma(\Delta t - \Delta t')$ is the standard deviation of the measured time delay (Δt is the true time delay and $\Delta t'$ is the estimated time delay). Since a sampling rate of 100 MHz was used in the experiment, using the cross-correlation method with interpolation (Ausel and Monchalin, 1989), the time measurement error was estimated to be 2 ns. The estimated accuracy of thickness measurements at 150 °C was 32 μm, mainly due to the broad bandwidth and high SNR, which could be useful for accurate thickness measurement in high-temperature liquids (Kobayashi *et al.*, 2009). This calculated accuracy is based on the assumption that the temperature is constant, or that the temperature is measured precisely and any change in the ultrasonic velocity due to temperature changes is well calibrated. Since the ultrasonic velocity is dependent on many parameters, such as temperature, pressure, etc., the calibration should be made for a precise thickness measurement; however, any measurement error of the temperature will cause further deterioration of the measurement accuracy (Jen *et al.*, 2005).

Wedge IUT

In a wedge IUT, the IUT is fabricated onto a wedge in order to generate shear waves (Jen *et al.*, 2006; Wu *et al.*, 2009, 2010). Since shear waves are totally reflected at solid/liquid interfaces, they are useful in some applications because it is expected that they will have a higher sensitivity to cracks or gaps filled with liquid. Additionally, shear waves have higher spatial resolution because they have a shorter wavelength at the same frequency (Kuttruff, 1991). Furthermore, shear waves are used to determine material properties such as the shear modulus and viscoelastic properties. Longitudinal waves and shear waves are needed to find Young's modulus. A longitudinal wave and two shear waves are used for the crystallographic orientation distribution (Moreau *et al.*, 2002). Therefore, a wedge IUT is designed to generate a longitudinal wave and a shear wave, as shown in Fig. 13.8, by mode conversion at a solid/air interface (Auld, 1973). A longitudinal

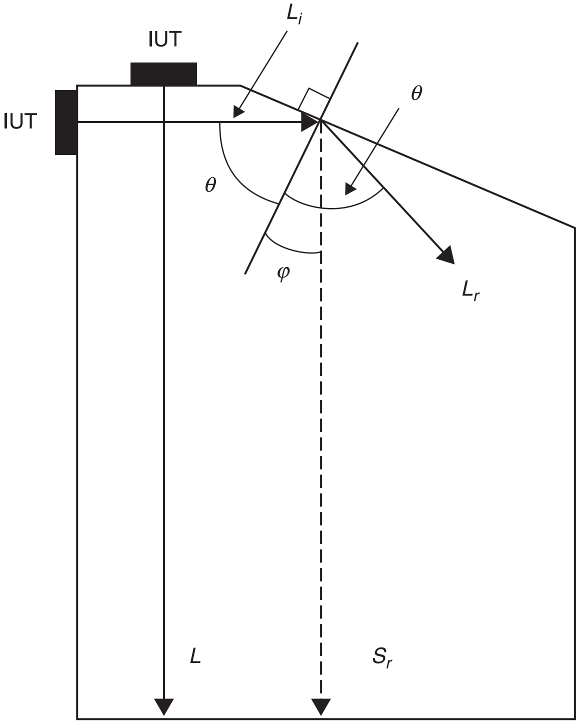

13.8 Generation of a longitudinal wave and a shear wave by mode conversion.

wave, L_i, generated by a longitudinal wave ultrasonic transducer is incident at the solid/air interface and is reflected as a longitudinal wave, L_r, and a shear wave, S_r. The equations governing the reflection and mode conversion with respect to the angle of incidence, θ, for L_i are:

$$\frac{V_l}{\sin\theta} = \frac{V_s}{\sin\varphi} \qquad [13.3]$$

$$R_{sl} = \frac{4(V_s/V_l)^2 \cos^2 2\varphi \sin 2\theta \cos 2\varphi}{\left[\cos^2 2\varphi + (V_s/V_l)^2 \sin\varphi \sin 2\theta\right]^2} \qquad [13.4]$$

where V_l and V_s are the longitudinal and shear-wave velocities in the wedge and R_{sl} is the energy reflection coefficient of the shear wave. The only criterion is that $\cot\theta$ is equal to V_s/V_l in the wedge, so that the shear waves due to mode conversion will propagate in the axial direction. In the wedge IUT, a PZT/PZT IUT to generate a longitudinal wave was fabricated at the top flat surface, and two PZT/PZT IUTs to generate two shear waves, polarised in the horizontal plane (SH wave) and the vertical plane (SV wave), respectively, were fabricated in planes parallel to the axial direction of the wedge, as shown in Fig. 13.9. Steel and brass were chosen as the wedge materials because of their high-temperature durability. The reflected echoes of the generated longitudinal wave and the SH wave from the end of the wedge, at 150 °C, are clearly shown in Fig. 13.10 and Fig. 13.11, respectively.

Structural-health monitoring using a fundamental-mode SH plate acoustic wave is attractive because one sensor can monitor a large area; the location of a defect can easily be obtained due to the non-dispersive characteristic of velocity in the plate regardless of the plate thickness and frequency. In this case, mode conversion at the wedge/plate interface needs to be considered. According to Snell's law, $\sin\phi_i = V_s/V_{SH0}$, where ϕ_i, V_s and V_{SH0} are the angle of the wedge, the shear-wave velocity in the wedge and the fundamental SH plate acoustic wave

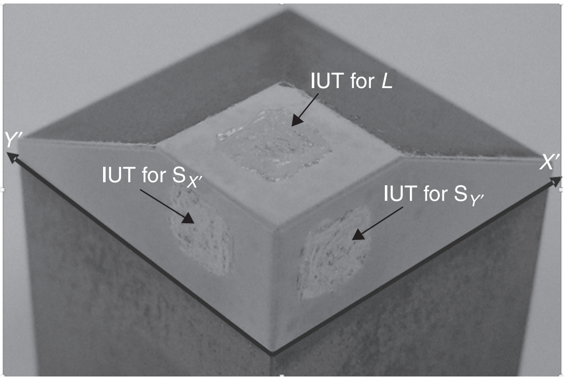

13.9 Wedge IUT.

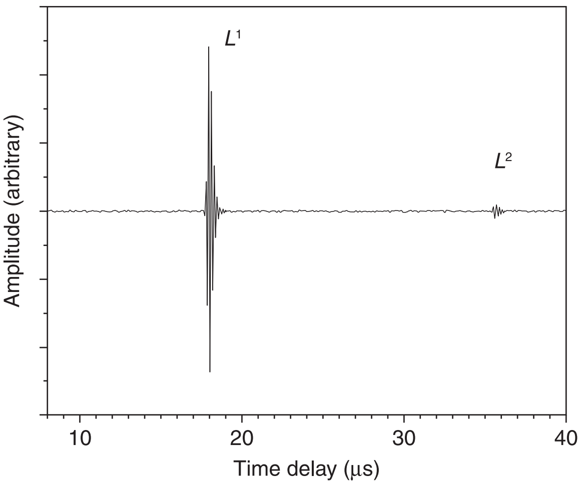

13.10 Reflected echo of the longitudinal wave for a wedge IUT.

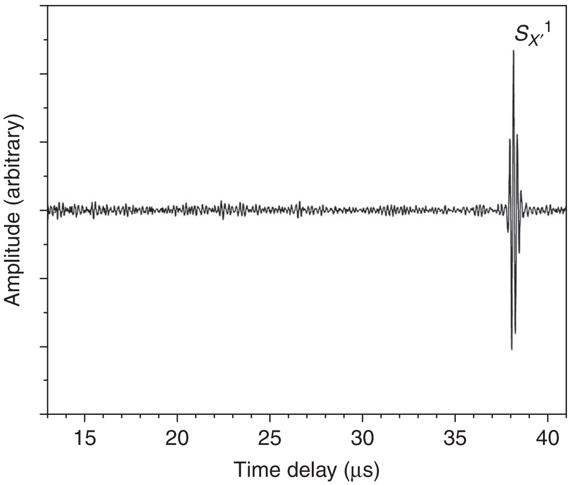

13.11 Reflected echo of the SH wave from the end of a wedge IUT.

phase velocity in the plate, which is equal to the shear-wave velocity in the plate, respectively. This means that the shear-wave velocity in the wedge must be lower than the shear-wave velocity in the plate. Poly(methyl methacrylate) (PMMA) is often used as a wedge material due to its low ultrasonic velocity. However, the operating temperature of PMMA is limited to temperatures under 100 °C. Therefore, for high temperatures, brass is used as a wedge material due to its low ultrasonic velocity compared with other metals. A PZT/PZT wedge IUT of the type shown in Fig. 13.8 was cut at an angle ϕ_i to monitor a stainless steel plate by

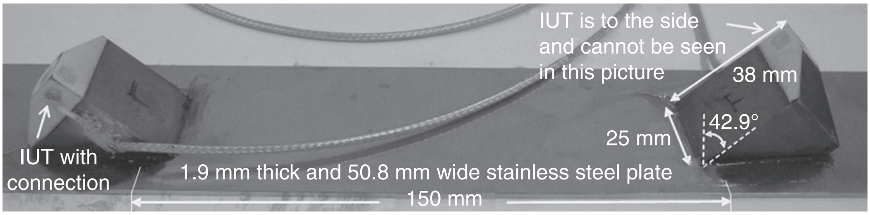
IUT is to the side
and cannot be seen
in this picture
38 mm
42.9°
25 mm
IUT with
connection
1.9 mm thick and 50.8 mm wide stainless steel plate
150 mm

13.12 Two PZT/PZT wedge IUTs set onto a stainless steel plate.

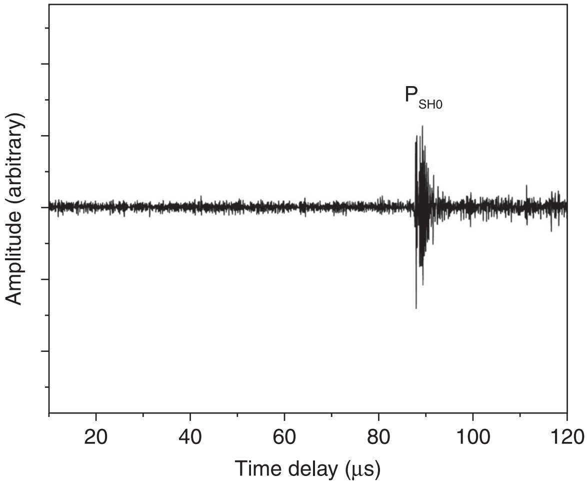

13.13 Measurements of the transmission mode at 200 °C for the system shown in Fig. 13.12.

the IUT which excites the SH wave. Two PZT/PZT wedge IUTs were set onto the stainless steel plate, 406.4 mm long, 50.8 mm wide and 1.9 mm thick, as shown in Fig. 13.12. The separation distance between the centres of the two wedge IUTs was 150 mm. A commercial adhesive was used as a couplant. Figure 13.13 shows the results of measurements of the transmission mode at 200 °C. The measured time delay was a reasonable match with the calculation.

Flexible ultrasonic transducer (FUT)

A high-temperature FUT can be realised by fabricating a sol-gel composite film onto a flexible substrate (Kobayashi *et al.*, 2006). Titanium foil, stainless steel foil and metalised polyimide foil with a thickness less than 75 μm are mainly used as the substrate material for FUTs because of their high-temperature durability, chemical durability and flexibility. FUTs have the advantage of the ease of on-site installation over IUTs, and also the advantages of IUTs, such as a suitable frequency range, high-temperature stability, thermal-cycle durability, high SNR, broadband frequency characteristics without a backing material and curved-surface conformability, except for good acoustic bonding without a couplant. In order to fabricate an IUT, the coating and thermal processes must be repeated, which may require a few hours, depending on the desired transducer thickness and the heating process used, whereas a FUT requires just a bonding process. A FUT can be installed without causing thermal damage, which is especially attractive for some aluminium alloys that cannot be exposed to high temperatures of more than 200 °C, and for some substrates with a paint coating. A FUT is very robust and can sustain the pressure and thermal shock during the bonding process, and even brazing (Shih *et al.*, 2010). For example, a BIT/PZT FUT was brazed onto a steel pipe, which had an outer diameter of 25 mm and a wall thickness of 3.5 mm. Pulse-echo measurements at various temperatures up to 490 °C are shown in Fig. 13.14. A FUT is the best choice if a number of sensors need to be installed, though the bonding method must be appropriate for the application.

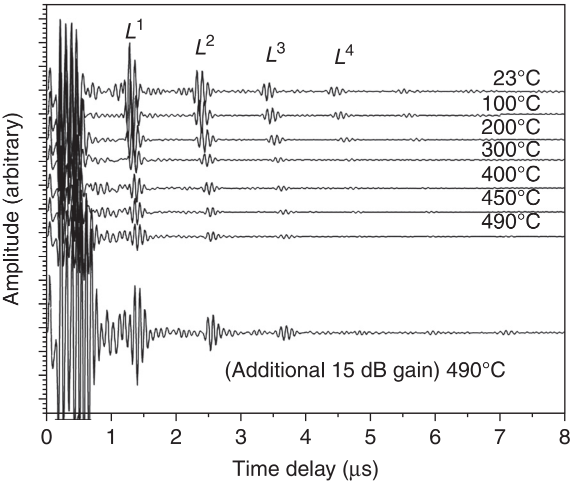

13.14 Pulse-echo measurements for a BIT/PZT FUT brazed onto a steel pipe.

13.3 Structural-health monitoring demonstration

13.3.1 Barrel wear and screw wear monitoring of micro-moulding machine by IUT

This section describes an attempt at ultrasonic real-time monitoring of barrel wear and screw wear using BIT/PZT IUTs to demonstrate their capability (Ono *et al.*, 2007). In a micro-moulding machine, the condition of the barrel and screw is important because, once screw or barrel wear occurs, the clearance between the threads of the screw and the barrel increases; as a result, the production rate and quality decrease because melt in the barrel cannot be transported properly. Figure 13.15 shows seven IUTs fabricated onto the barrel. UTs 1–3 and 5–7 were located in the feeding and heating zones, respectively, and UT4 was between these zones. The length of the barrel was 265 mm. The internal diameter was 14 mm, and the external diameter in the region of UTs 1–3, 5–7 and UT4 was 40 mm and 30 mm, respectively. All of the IUTs had almost the same ultrasonic performance. The centre frequency and the 6 dB bandwidth were around 8.6 MHz and around 4.4 MHz, respectively. Real-time monitoring of the micro-moulding process was performed. First, polyethylene (PE) pellets were fed into the barrel and melted. The screw was rotated at 110 rpm. A schematic diagram of ultrasonic wave propagation in pulse-echo mode is shown in Fig. 13.16. The IUT mounted on the external surface of the barrel generates ultrasonic waves, which propagate through the barrel to its inner wall, reaching the PE melt. The ultrasonic energy is partly reflected at the barrel inner wall/PE melt interface, and partly transmitted to the PE melt, then reflected either by the flight or the root of the screw. These echoes are denoted by L^1, L_{2F} and L_{2R} in Fig. 13.16, respectively. Echoes L^2, L_{4F}, and L_{6F} represent further round trip echoes in the corresponding media. Figure 13.17 shows the resulting signals acquired from UT6 in the heating zone of the barrel, as shown in Fig. 13.15. The reflected signals from the flight and the root of the screw and the reflected signals from the barrel are clearly visible in Fig. 13.17, with a SNR of more than 10 dB.

Therefore the potential for real-time monitoring of barrel wear and screw wear by an IUT without requiring system shutdown was successfully demonstrated.

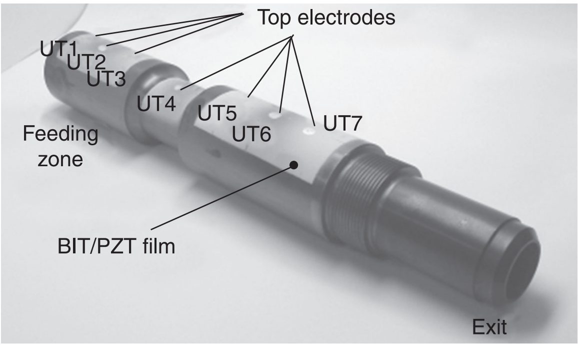

13.15 Seven IUTs fabricated onto the barrel of a micro-moulding machine.

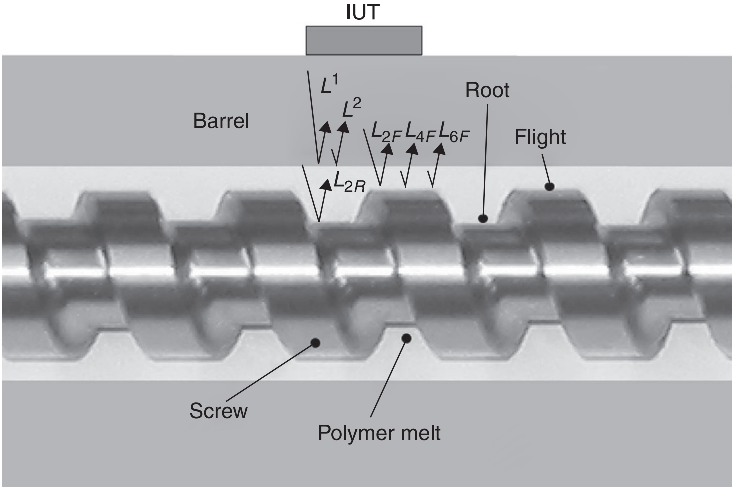
IUT
L^1
L^2
Barrel
L_{2F} L_{4F} L_{6F}
Root
Flight
L_{2R}
Screw
Polymer melt

13.16 Ultrasonic wave propagation in pulse-echo mode.

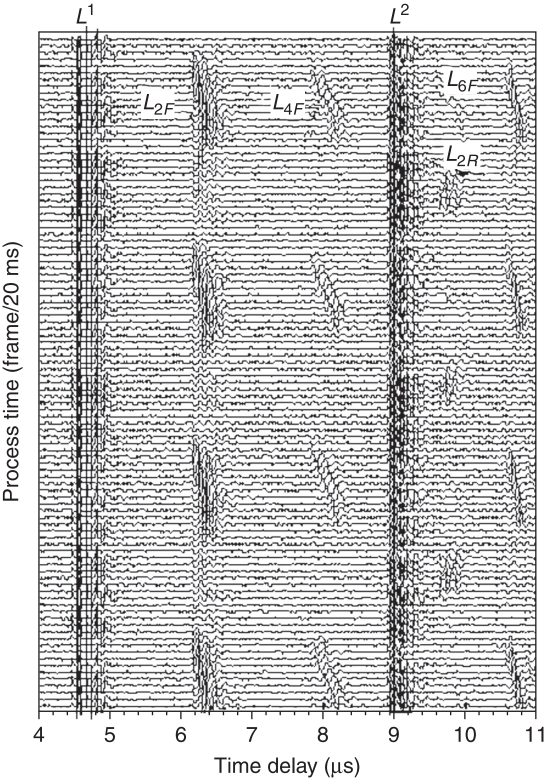

13.17 Signals acquired from UT6 in the heating zone of the barrel.

13.3.2 Ultrasonic imaging in 200 °C silicone oil by focussed buffer-rod IUT

Imaging at elevated temperatures demonstrates the high spatial resolution of an immersion high-temperature ultrasonic probe with a focusing lens at the probing end (Ono *et al.*, 2006). A compact immersion high-temperature probe was developed. An 8-MHz BIT/PZT buffer-rod IUT was fabricated as shown in Fig. 13.18; the length of the steel buffer rod was 50 mm. The diameters at the IUT and probing end were 32 mm and 30 mm, respectively. The periphery of the rod had a 2° taper angle from the UT to the probing end, to expedite assembly of the rod in a holder. The probing end of the buffer-rod IUT was machined into a semi-spherical surface as an ultrasonic lens, as shown in Fig. 13.19. The radius of

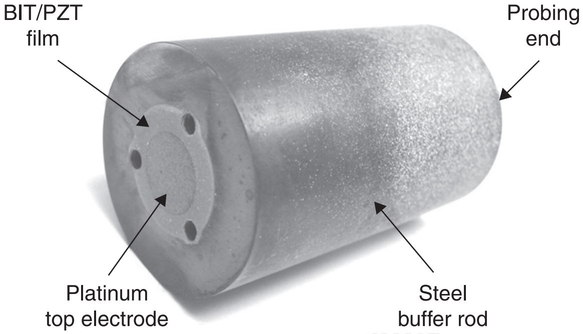
BIT/PZT film
Probing end
Platinum top electrode
Steel buffer rod

13.18 BIT/PZT buffer-rod IUT.

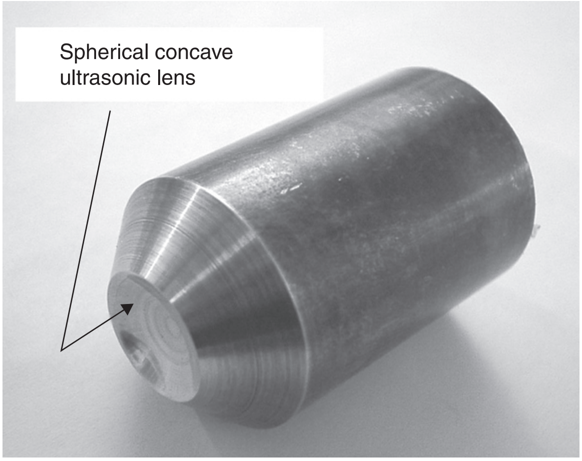
Spherical concave ultrasonic lens

13.19 Probing end of the buffer-rod IUT.

curvature and the aperture diameter of the lens were 11 mm and 15 mm, respectively. The buffer-rod IUT with its focussing lens was mounted in a stainless steel holder to seal the IUT from the liquid. This immersion high-temperature probe has the advantage that it can easily scan inside silicone oil, which acts as a liquid couplant between the probing end and the imaging target.

The experimental set-up is shown in Fig. 13.20. The high-temperature focussing probe was mounted on a manual Z-stage to adjust the distance between the probing end and the sample, and manipulated horizontally using an XY-stage driven by stepping motors. A crucible furnace heated the silicone oil in a stainless steel crucible. The reverse side of a US one cent coin was polished, to serve as a sample for surface and sub-surface imaging, and fixed on the sample holder. Figure 13.21 is a photograph of the sample. The line thickness of the smallest characters on the coin was about 0.2 mm. The temperature of the silicone oil was controlled and maintained at 200 ± 1 °C using a temperature controller with a thermocouple.

The first experiment was front-surface imaging. In the following imaging results, the data after subtraction are shown due to poor SNR because of reflected echoes inside the buffer rod. Figures 13.22 and 13.23 show the ultrasonic images. For the XY raster scan, the scan step was 100 µm. Those figures were constructed from the amplitude or time delay of the echoes from the sample surface; a darker colour indicates a larger amplitude or a longer time delay. The coin details, including the characters of 0.2 mm thickness, were clearly observed.

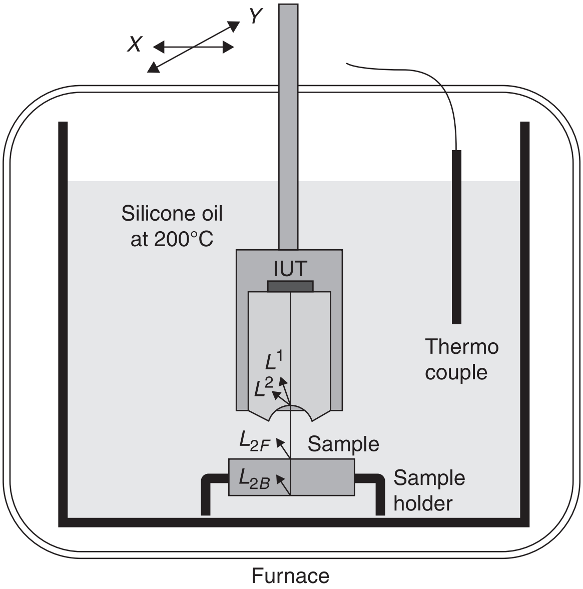

13.20 Experimental set-up for imaging hot silicone oil.

UNITED STATES OF AMERICA
E·PLURIBUS
·UNUM·
ONE CENT

13.21 Photograph of a US one cent coin used as a sample.

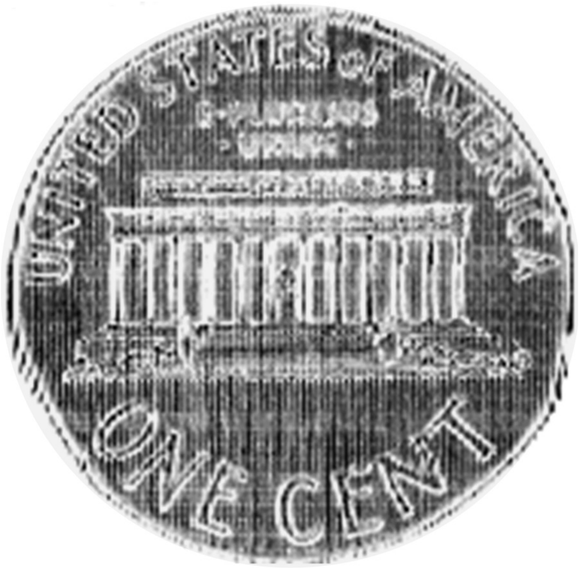
UNITED STATES OF AMERICA
ONE CENT

13.22 Ultrasonic front-surface image of a US one cent coin.

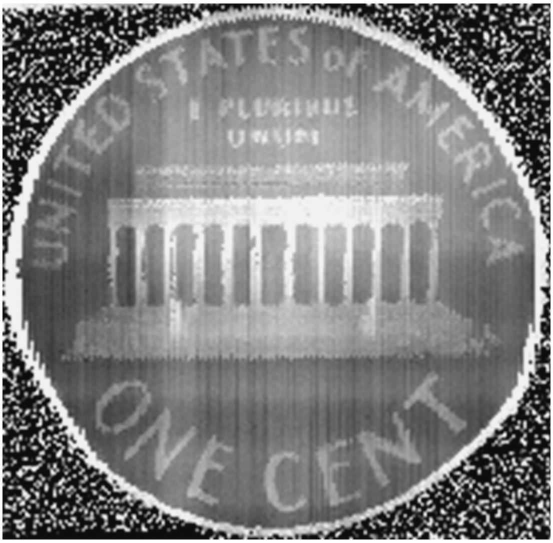

13.23 Ultrasonic front-surface image of a US one cent coin.

In order to investigate the performance of the immersion probe for precise thickness measurement inside a hot liquid, an experiment on sub-surface imaging was also carried out. The same sample and experimental set-up as in Fig. 13.20 and Fig. 13.21 were used again, except that the sample was placed face-down. Figures 13.24 and 13.25 show the ultrasonic sub-surface images measured in

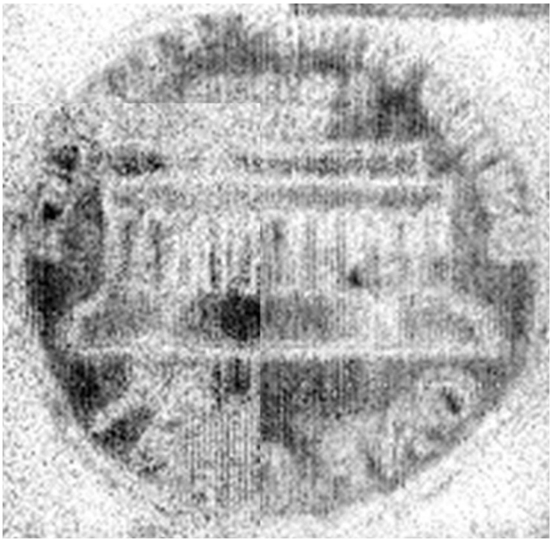

13.24 Ultrasonic sub-surface image of a US one cent coin.

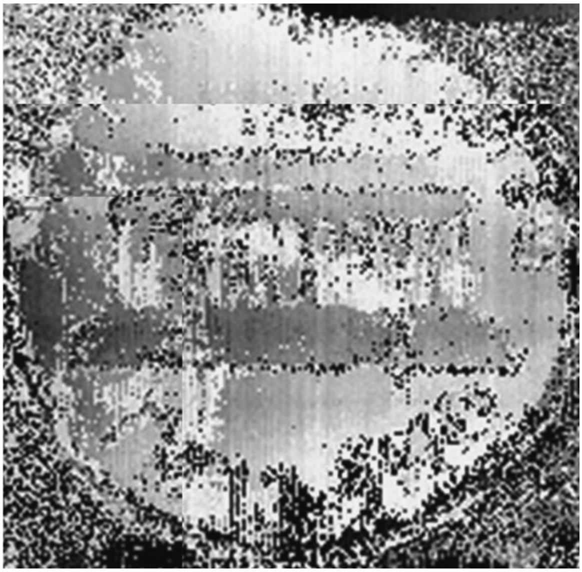

13.25 Ultrasonic sub-surface image of a US one cent coin.

silicone oil at 200 °C and constructed from the amplitude and time delay of the echoes, respectively. The images are poor quality due to insufficient SNR.

The possibility of precise thickness measurement inside a liquid at elevated temperature was demonstrated, though further investigation is required to improve SNR.

13.3.3 Line-defect detection on a stainless steel plate by wedge IUT

A wedge IUT on a stainless steel plate in pulse-echo mode was used to demonstrate the potential for defect detection (Wu *et al.*, 2010). An artificial line defect of depth 1 mm, width 1 mm and length 50.8 mm was created on a stainless steel plate, 1.9 mm thick and 50.8 mm width. The PZT/PZT brass wedge IUT shown in Fig. 13.9 was placed onto the stainless steel plate with a couplant, at a distance of around 30 mm from the line defect as shown in Fig. 13.26. Pulse-echo measurements at room temperature were made on the bare stainless steel plate and on the plate after applying a paint coating to the surface, and the results are shown in Fig. 13.27 and Fig. 13.28, respectively. From the time delays, it was confirmed that SH waves propagated in the stainless steel plate and were reflected by the line defect. The signal was not affected by the paint. A surface acoustic wave would be significantly affected because most of the energy of a Rayleigh wave is concentrated at $1\lambda_R$ to $2\lambda_R$ depth from the surface, where λ_R is the wavelength.

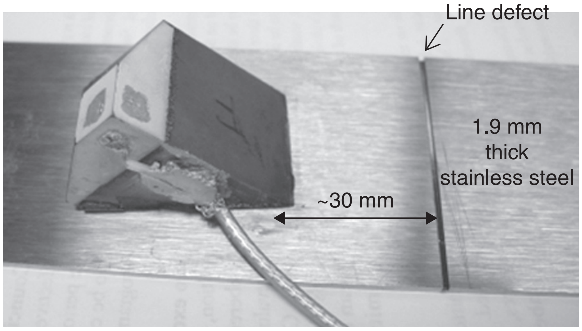

13.26 Stainless steel plate with line defect and the wedge IUT.

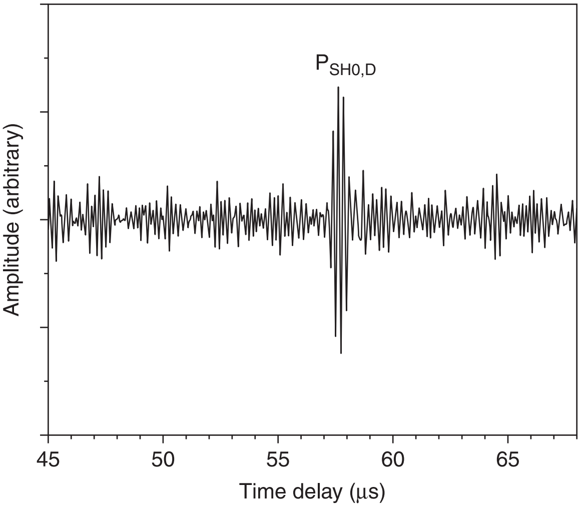

13.27 Pulse-echo measurements for the bare stainless steel plate.

Rayleigh waves are affected by surface finishes of a metal substrate, such as paint (Viktorov, 1967). The line defect was detected with acceptable SNR despite the paint, and the PZT wedge IUT showed the potential for surface crack detection.

13.3.4 Precise pipe thickness measurement at 200 °C by FUT

A PZT/PZT FUT with a 75-μm-thick titanium substrate was glued onto a steel pipe, as shown in Fig. 13.29, to demonstrate measurement accuracy (Kobayashi *et al.*, 2010). The dimensions of the PZT/PZT film and the top silver electrode were 14 mm by 15 mm and 2 mm by 4 mm, respectively. The glue was cured at

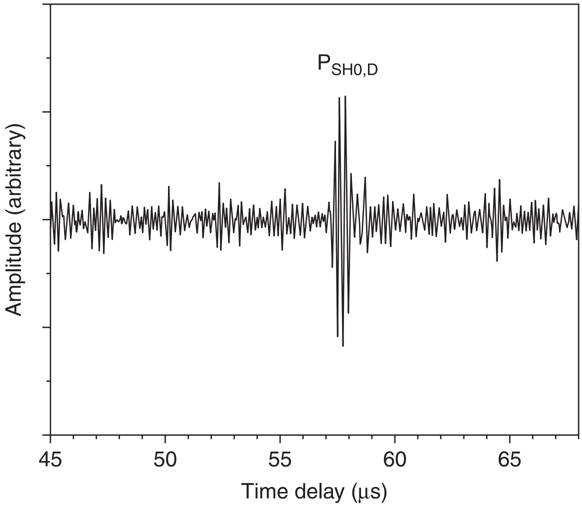

13.28 Pulse-echo measurements for the painted stainless steel plate.

80 °C for 90 minutes. The outer diameter and the wall thickness of the steel pipe were 101 mm and 4.5 mm, respectively. Pulse-echo measurement at 200 °C was successfully taken by a portable device (EPOCH LT) without using a signal averaging and filtering function. The pulse energy was 100 V, which was the lowest value for the EPOCH LT, and the gain was 16 dB out of an available 100 dB, which indicates a comparable signal strength with commercial room-temperature

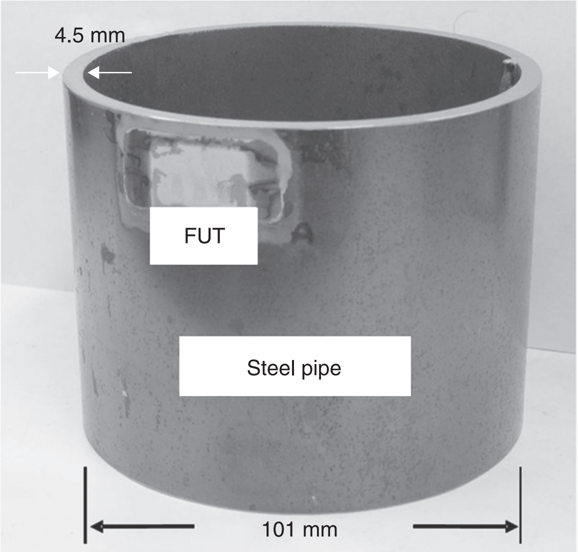

13.29 PZT/PZT FUT glued onto a steel pipe.

transducers. Figures 13.30 and 13.31 show the measured ultrasonic signals in the time and frequency domains, where L^n is the nth round trip of the longitudinal echo through the thickness of the pipe wall. The centre frequency and the 6 dB bandwidth of the L^1 echo were 9.8 MHz and 8.1 MHz, respectively. The accuracy calculated using Eq. 13.2 for this measurement was 13.3 µm. Such a high accuracy was achieved because of the high SNR and the high ratio of the signal bandwidth over the centre frequency (Kobayashi *et al.*, 2010).

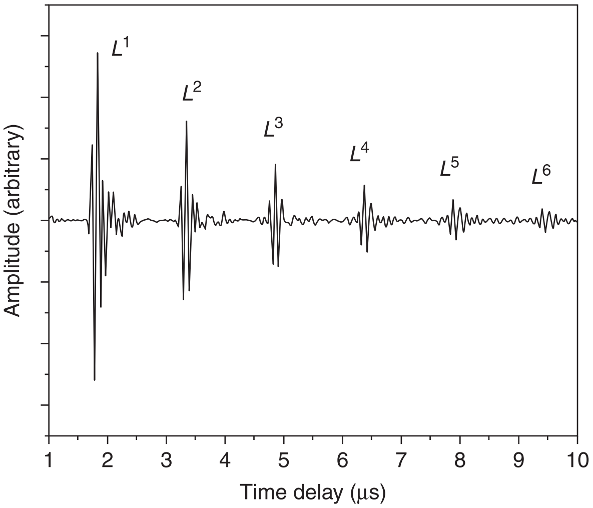

13.30 Ultrasonic signals in the time domain.

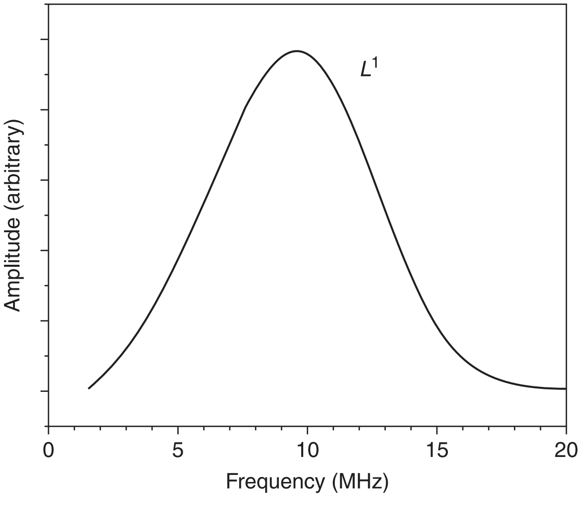

13.31 Ultrasonic signals in the frequency domain.

13.4 Process-monitoring demonstration

13.4.1 Monitoring of complete filling in injection moulding

Injection moulding is the process of forcing a melted polymer into a mould cavity with a particular shape. In this process, complete filling of the mould with the material is the most critical requirement, since an incomplete part must be rejected. Figures 13.32 and 13.33 show the IUTs and the inner surface of the mould, respectively, of a 150-ton injection-moulding machine (Engel). An array configuration of four IUTs (UT1–4) is embedded into a mould insert (Ono *et al.*, 2004). An IUT with and without its electrical connection is shown in Fig. 13.34. The mould cavity was 76 mm wide, 165 mm long and 1 mm thick. The probing ends of the IUT were flush with the mould cavity surface as seen in Fig. 13.33. Mould inserts are commonly used in injection moulding. IUTs could be directly fabricated onto a large mould if required.

Figure 13.35 shows a cross section of the mould (mobile and immobile parts). The figure shows the large mould insert with four HTUT sensor inserts (UTs 1–4), the moulded part (or polymer melt) and the paths of the ultrasonic echoes. For comparison, a temperature and pressure sensor (6190A, Kistler Instrument AG, Winterthur, Switzerland) was attached to the immobile mould. The end of this commercial temperature and pressure sensor was opposite UT1, as shown in the figure.

Ultrasonic waves propagate into the mould insert and reflect from the far surface of the mould cavity; when the polymer fills the mould cavity, the ultrasonic energy is partly transmitted to the molten polymer, and is then reflected by the immobile mould. In Fig. 13.35, the first round-trip echo in the mould insert is denoted by L^1 and in the polymer melt it is denoted by L_2 and the echoes

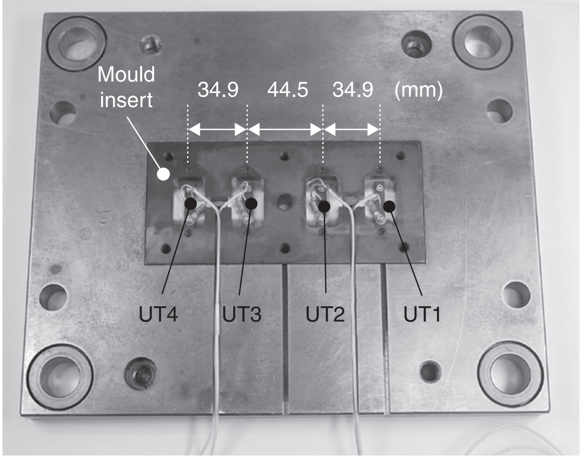

13.32 Outer surface of the mould showing the four IUTs.

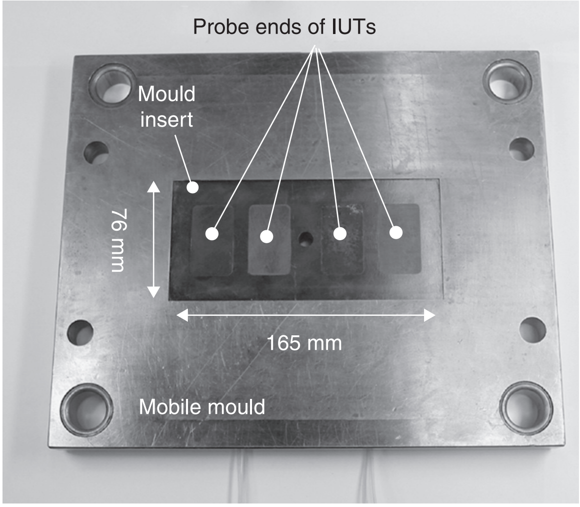
Probe ends of IUTs
Mould insert
76 mm
165 mm
Mobile mould

13.33 Inner surface of the mould showing the probe ends.

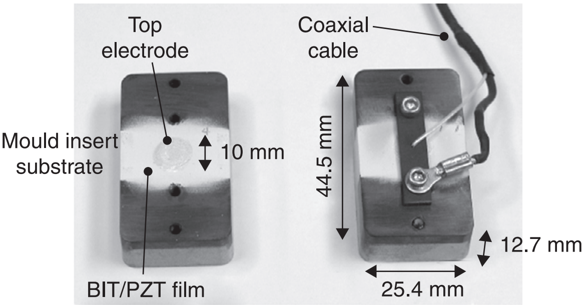
Top electrode
Coaxial cable
Mould insert substrate
10 mm
44.5 mm
12.7 mm
25.4 mm
BIT/PZT film

13.34 IUT with and without electrical connection.

L^2, L^3, . . . and L_4, L_6, . . . represent further round-trip echoes in the corresponding media.

Figure 13.36 shows one incomplete (#1) and three complete (#2–4) parts moulded successively under the same moulding conditions. The material employed was a polycarbonate. The corresponding locations of the probing ends of the IUTs on the parts are indicated by UT1–4. By chance, part #1 had defects on both lower corners, as indicated by the arrows in Fig. 13.36. The volume-filling percentage for part #1 was calculated to be 99%.

Figure 13.37 shows the variation in amplitude of the ultrasonic signals propagating through the parts, obtained with UT1–4 in ultrasonic pulse-echo mode, during the moulding cycles of the parts. At time A, as the polymer melt arrived at the probing ends of the IUT in the mould cavity, the signals started to

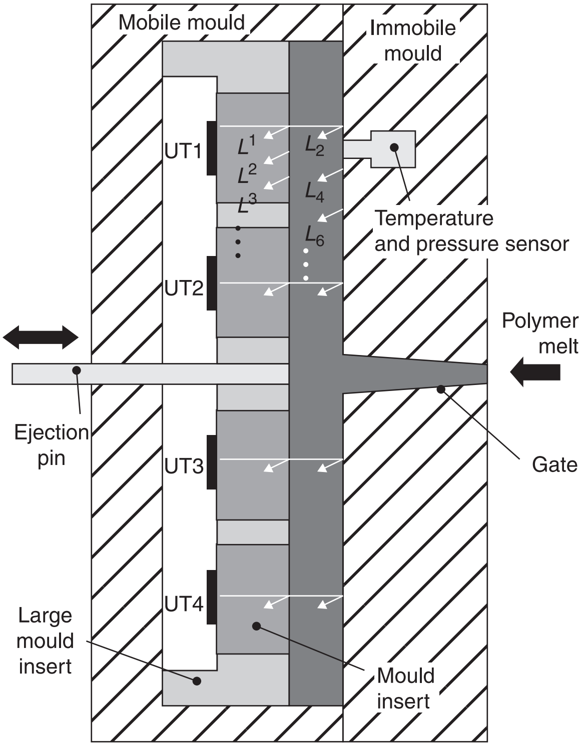
Mobile mould
Immobile mould
UT1
L^1
L^2
L^3
L_2
L_4
L_6
UT2
Temperature and pressure sensor
Polymer melt
Ejection pin
UT3
Gate
UT4
Large mould insert
Mould insert

13.35 Cross section of a mould with IUTs.

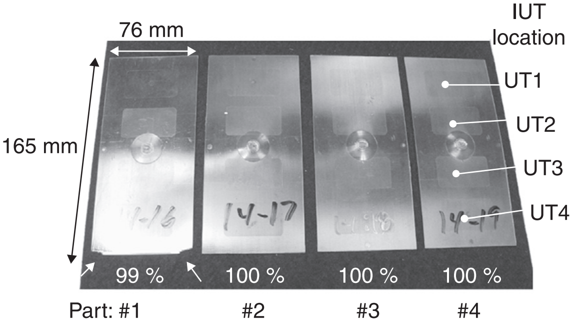
76 mm
165 mm
IUT location
UT1
UT2
UT3
UT4
14-16
14-17
14-18
14-19
99 %
100 %
100 %
100 %
Part: #1
#2
#3
#4

13.36 Moulded parts.

appear. Even though the mould cavity was filled at the UT3 and UT4 locations for part #1, the signal measured with UT4 appeared for a few seconds only at the beginning of the cycle. In addition, the signals measured with UT3 for part #1 gradually decreased to noise level before the mould was opened at time B. This is because the moulded part detached from the UT3 and UT4 locations before the

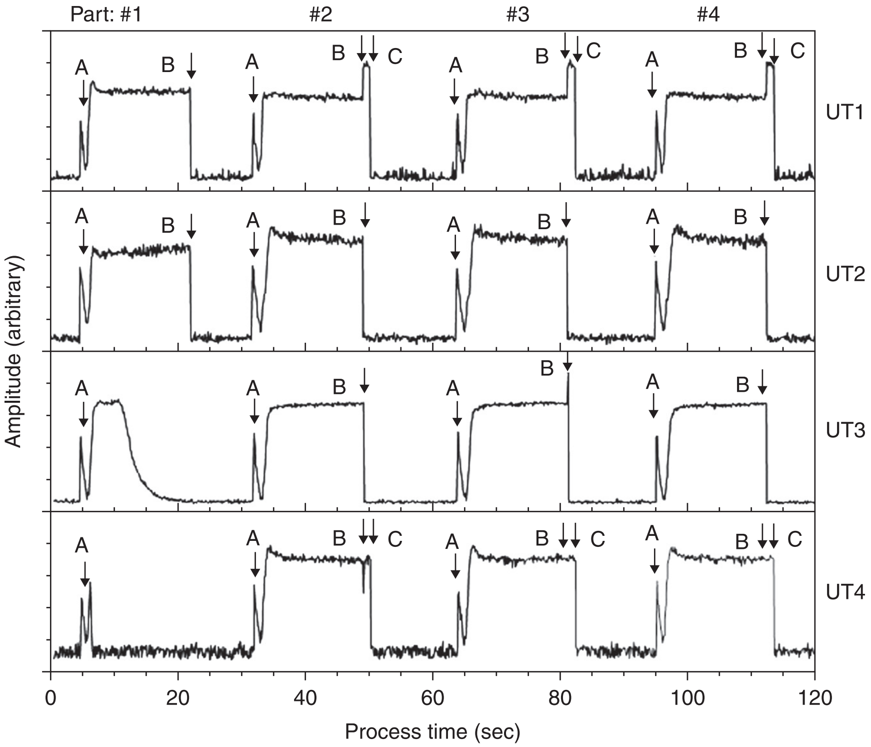

13.37 Amplitude of the ultrasonic signals propagating through the parts during moulding.

mould was opened due to shrinkage of the part caused by insufficient injection pressure. For parts #2–4, the signals disappear when the mould is opened at time B for UT2 and UT3 or when the part is ejected from the cavity at time C for UT1 and UT4.

In conclusion, this ultrasonic technique has the ability to monitor sensitively the incomplete filling for parts, even with an incomplete filling rate of 1%.

13.4.2 Process optimisation of injection moulding for micro-fluidic device

Miniature ultrasonic probes have been developed for process diagnostics of injection moulding for producing micro-fluidic devices (Ono *et al.*, 2005). A micro-fluidic device, consisting of one or more channels with at least one dimension less than 1 mm, has attractive features such as small sample requirement and low power consumption, realising a lab-on-a chip device. Injection moulding is a promising candidate for fabricating disposable micro-fluidic devices at low cost and in mass production. However, fine micro features need to be fabricated onto polymeric substrates precisely. A PZT/PZT IUT was fabricated onto one end of a 4 mm diameter and 12 mm long steel buffer rod. Figures 13.38 and 13.39 show pictures of the steel buffer-rod IUT and an ultrasonic probe with a holder and an electric cable, respectively. The top electrode was 2 mm in diameter. The ultrasonic frequency and 6 dB bandwidth of this probe were 17 MHz and 14 MHz, respectively. The probe has similar external dimensions to conventional temperature and cavity pressure sensors, so that it can be installed into injection moulding machines without modification of existing moulds. It also means that the temperature, pressure and ultrasonic sensors are interchangeable.

Two probes (UT1 and UT2) of the type shown in Fig. 13.39 were installed into the mobile mould of an injection moulding machine. To produce a micro-fluidic device, a replaceable mould insert with micro features, which are to be printed onto the surface of the moulded parts, was attached to an immobile mould. The mould cavity was 96 mm long, 16 mm wide and 1.1 mm deep. The mould insert used in the experiments had test patterns of 22 lines and 57 holes. The probing end

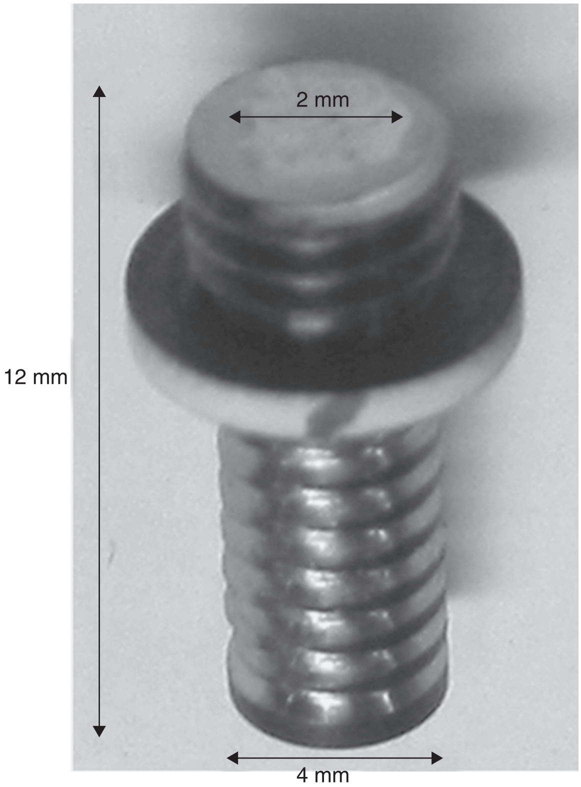

13.38 Steel buffer-rod IUT.

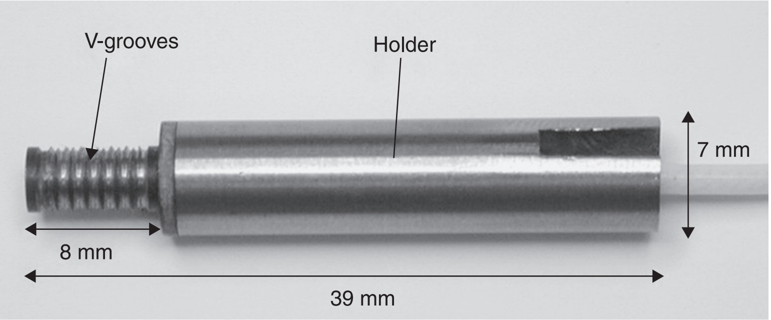

13.39 Ultrasonic probe with holder and electric cable.

of UT1 was located above a hole with a diameter of 770 µm and a height of 500 µm. The probing end of UT2 was placed over two lines with a width of 1 mm and depths of 300 µm and 500 µm. The material employed was PMMA. Figure 13.40 is a picture of a moulded part, showing the line and dot patterns printed onto its surface. The white circles in Fig. 13.40 indicate the areas corresponding to the probing ends of UT1 and UT2.

In order to investigate the effects of the holding pressure during moulding on process stability and product quality, parts were moulded with different holding pressures from 2.5 to 15 MPa. We measured the surface profile on the line pattern at the right side of the moulded parts using optical interferometry. The measurement results are given in Table 13.1. When the holding pressure was higher than 7.5 MPa, the surfaces were almost flat with a maximum variation of 5 µm or less. However, the maximum variation was much larger when the holding pressure was lower than 6 MPa. The maximum variation was 24 µm at 2.5 MPa.

The ultrasonic velocity was used to evaluate process stability and product quality of the surface flatness. A static ultrasonic velocity measurement (Piche *et al.*, 1988) showed that the ultrasonic velocity in this PMMA part increased during cooling from the liquid to the solid state and was 2300 m.s^{-1} at the glass transition temperature of 86°C. Therefore, it was expected that the polymer would

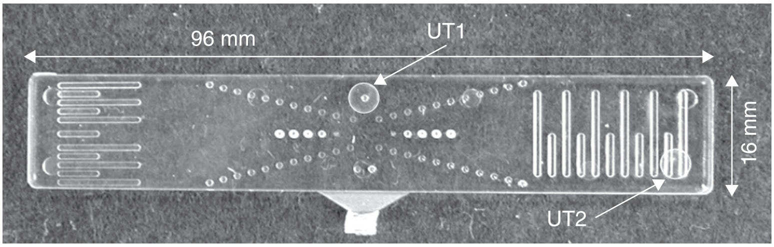

13.40 Test moulded part.

Table 13.1 Maximum variation of the surface profile of the line pattern of moulded parts of the type shown in Fig. 13.40 with different holding pressures

Holding pressure (MPa)	2.5	5.0	6.0	7.5	10.0	15.0
Maximum variation (μm)	24	15	8	5	5	4

be in the liquid or solid state at a velocity lower or higher than 2300 m.s^{-1}, respectively. Figure 13.41 shows the ultrasonic velocity obtained with UT1 during one cycle of moulding with respect to the process time. At 2.5–6 MPa, the parts detached from the probing end (at the mould cavity surface) before the velocity reached 2300 m.s^{-1} due to shrinkage caused by insufficient holding pressure, suggesting that the parts were still in the (viscous or rubbery) liquid state when

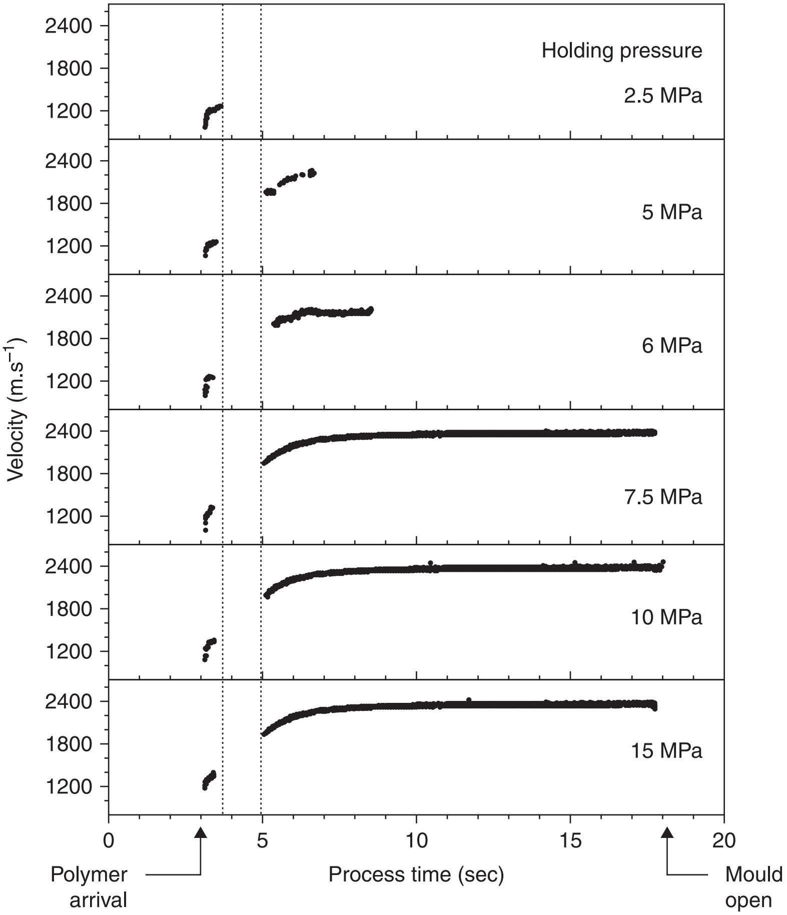

13.41 Ultrasonic velocity during one cycle of moulding.

they detached. This is why the surface roughness increases as the holding pressure decreases, particularly for a pressure lower than 6 MPa. At 7.5–15 MPa, the velocity is almost constant with a maximum of 2400 m.s^{-1} at 10 seconds, indicating that the polymer has already solidified. Therefore, the holding pressure must be higher than 7.5 MPa for stable moulding and to produce good parts under our experimental conditions and the material employed.

It can be concluded that it is possible to optimise the holding pressure and cooling time to improve the process efficiency of part manufacturing with good quality by using buffer-rod IUT real-time monitoring.

13.5 Conclusions

High-temperature sensors for NDE, especially for structural-health monitoring and process monitoring, are required in industries such as power plants, chemical plants, aerospace, polymer manufacture, etc. Continuous inspection of objects in harsh environments is highly desirable for efficient maintenance. Real-time process monitoring is also preferred for efficient quality control of final products and process optimisation. Therefore, the development of high-temperature sensors for real-time monitoring is of great interest. Ultrasonic transducers are widely used for NDE applications, such as structural-health monitoring and process monitoring, because of their sub-surface inspection capability, elastic property characterisation ability, fast inspection speeds, simplicity and ease of operation. However, the development of high-temperature ultrasonic transducers for these types of application is still challenging mainly due to thermal aging of the piezoelectric material and the temperature limitations of the backing material and couplant.

Ultrasonic transducers fabricated from sol-gel composites have the potential for high-temperature NDE because of their suitable frequency range, high-temperature stability, thermal-cycle durability, excellent SNR, broadband frequency characteristics without a backing material, good acoustic bonding without a couplant and curved-surface conformability. Three kinds of sol-gel composites, PZT/PZT for temperatures up to 200 °C, BIT/PZT for temperatures up to 500 °C, and lithium niobate/PZT for temperatures up to at least 800 °C, have been developed. The sol-gel composite material should be chosen according to the application. Four types of high-temperature ultrasonic transducers have been developed with sol-gel composite films. An IUT is simple and has superior integration ability for complex geometry. A buffer-rod IUT has superior temperature durability and is suitable for immersion inspection. A wedge IUT can generate shear horizontal waves. A FUT has the advantage of ease of installation.

The application of these transducers to structural-health monitoring and process monitoring at high temperatures was demonstrated. Reflected echoes from a barrel, screw flight and screw root were successfully obtained using a BIT/PZT IUT fabricated onto the external surface of the barrel of a micro-moulding machine. This IUT could be useful for barrel wear and screw wear monitoring.

Ultrasonic imaging of a sample with a surface height difference of about 0.2 mm was successfully obtained from inside 200 °C silicone oil using a focussed buffer-rod BIT/PZT IUT. A line defect on a stainless steel plate was detected in pulse-echo mode using SH waves generated by a wedge IUT, with or without paint. A PZT/PZT FUT precisely measured the thickness of a pipe at 200 °C with an accuracy as high as 13.3 µm. Complete filling monitoring of injection moulding using a BIT/PZT IUT and process optimisation of injection moulding for producing a micro-fluidic device using a buffer-rod PZT/PZT IUT were also demonstrated. A BIT/PZT IUT fabricated onto a mould insert was able to detect even 1% incomplete filling. A miniature PZT/PZT buffer-rod IUT showed its potential for pressure and cooling time optimisation.

Further investigations into reliability, whole sensor system design, etc. should be carried out for use in real applications.

13.6 Sources of further information

High-temperature ultrasonic transducers for short-term non-destructive testing are commercially available from the following companies:

- IHI Inspection & Instrumentation Co., Ltd.
- Olympus NDT Inc.
- Piezotech, LLC.
- Sigma Transducers, Inc.

Permanently bonded high-temperature transducers for structural-health monitoring and process monitoring are not widely available commercially. The technology for sol-gel composite high-temperature ultrasonic transducers is being licensed and is expected to be commercially available within a few years. For further information, contact Ngoc Huynh at the Industrial Materials Institute, the National Research Council (Canada): Ngoc.huynh@imi.cnrc-nrc.gc.ca

13.7 References

Agrawal A R, Pandelidis I O and Pecht M (1987), Injection-molding process control – a review, *Polym Eng Sci*, 27, 1345–57.

Auld B A (1973), *Acoustic Fields and Waves in Solids*, New York, Wiley.

Ausel J-D and Monchalin J-P (1989), Precision laser-ultrasonic velocity measurement and elastic constant determination, *Ultrasonics*, 27, 165–77.

Baba A, Searfass C T and Tittmann B R (2010), High temperature ultrasonic transducer up to 1000 °C using lithium niobate single crystal, *Appl Phys Lett*, 97, 232901.

Barrow D A, Petroff T E and Sayer M (1996), *Method for producing thick ceramic films by a sol gel coating process*. US patent 5585136. 1996-Dec-17.

Using, *Insight*, 37, 368–70.

Dalton R P, Cawley P and Lowe M J S (2001), The potential of guided waves for monitoring large areas of metallic aircraft structure, *J Nondestr Eval*, 20, 29–46.

Fothergill J R, Willis P and Waywell S (1989), Development of high-temperature ultrasonic transducers for under-sodium viewing applications, *British J NDT*, 31, 259–264.

França D R, Jen C-K, Nguyen K T and Gendron R (2000), Ultrasonic in-line monitoring of polymer extrusion, *Proc Eng Sci*, 40, 82–94.

Jen C-K and Kobayashi M (2007), Integrated and flexible high temperature piezoelectric ultrasonic transducers, in Chen C H, *Ultrasonic and Advanced Methods for Nondestructive Testing and Material Characterization*, World Scientific Publishing, 33–56.

Jen C-K and Legoux J-G (1998), *Clad ultrasonic waveguides with reduced trailing echoes*. US patent 5828274. 1998-Oct-27.

Jen C-K, Cao B, Nguyen K T, Loong C A and Legoux J-G (1997), On-line ultrasonic monitoring of a die-casting process using buffer rods, *Ultrasonics*, 35, 335–44.

Jen C-K, Nguyen K T, Cao B, Wang H and Loong C A (1999), *Ultrasonic sensors for on-line monitoring of castings and molding processes at elevated temperatures*. US patent 5951163. 1999-Sep-14.

Jen C-K, Liaw J-W, Chen T-F, Moreau A, Monchalin J-P and Yang C-C (2000), Ultrasonic evaluation of semi-solid metals during processing, *Meas Sci Technol*, 11, 1–6.

Jen C-K, Sun Z and Kobayashi M (2005), Real-time monitoring of barrel thickness and barrel/screw separation using ultrasound, *Meas Sci Technol*, 16, 1–9.

Jen C-K, Ono Y and Kobayashi M (2006), High temperature integrated ultrasonic shear wave probes, *Appl Phys Lett*, 89, 183506.

Karasawa H, Izumi M, Suzuki T, Nagai M and Fujimori S (2000), Development of under-sodium three-dimensional visual inspection technique using matrix-arrayed ultrasonic transducer, *J Nucl Sci Technol*, 37, 769–79.

Kirk K J, McNab A, Cochran A, Hall I and Hayward G (1999), Ultrasonic arrays for monitoring cracks in an industrial plant at high temperature, *IEEE Trans Ultrason, Ferroelect, Freq Contr*, 46, 311–19.

Kobayashi M and Jen C-K (2004), Piezoelectric thick bismuth titanate/lead zirconate titanate composite film transducers for smart NDE of metals, *Smart Mater Struct*, 13, 951–6.

Kobayashi M, Olding T R, Sayer M and Jen C-K (2002), Piezoelectric thick film ultrasonic transducers fabricated by a sol-gel spray technique, *Ultrasonics*, 39, 675–80.

Kobayashi M, Jen C-K, Ono Y and Moison J-F (2005), Integratable high temperature ultrasonic transducers for NDT of metals and industrial process monitoring, *Canadian Institute for NDE J*, 5–10.

Kobayashi M, Jen C-K and Lévesque D (2006), Flexible ultrasonic transducers, *IEEE Trans Ultrason, Ferroelectr, Freq Contr*, 53, 1478–86.

Kobayashi M, Nagata H, Hiruma Y, Tokutsu T, Takenaka T and Jen C-K (2007), Integrated ultrasonic transducers above 500 °C, *Proc IEEE Ultrasonics Symp*, 953–6.

Kobayashi M, Jen C-K, Bussiere J-F and Wu K-T (2009), High-temperature integrated and flexible ultrasonic transducers for nondestructive testing, *NDT&E Inter*, 42, 157–61.

Kobayashi M, Wu K-T, Shih J-L, Jen C-K and Kruger S E (2010), Flexible ultrasonic transducers for structural health monitoring of metals and composites, *Proc of SPIE*, 7648, 76480W1-10.

Kuttruff H (1991), *Ultrasonics: Fundamentals and Applications*, London, Elsevier Applied Science.

Kwon J-D, Park J-C, Lee Y-S, Lee W-H and Park Y-W (1999), The effects of thermal aging on material behavior and strength of CF8M in nuclear reactor coolant system, *Trans 15th Inter Conf Struct Mechan Reactor Technol*, 189–96.

McNab A, Kirk K J and Cochran (1998), Ultrasonic transducers for high temperature applications, *IEE Proc Sci Meas Technol*, 145, 229–36.

Moore P O, Workman G L and Kishoni D (2007), in *Nondestructive Testing Handbook, 3rd ed.* 7, ASNT, 424–74.

Moreau A, Lévesque D, Lord M, Dubois M, Monchalin J-P, Padioleau C and Bussière J F (2002), On-line measurement of texture, thickness and plastic strain ratio using laser-ultrasound resonance spectroscopy, *Ultrasonics*, 40, 1047–56.

Mrasek H, Gohlke D, Matthies K and Neumann E (1996), High temperature ultrasonic transducers, *NDT Net*, 1, (web journal).

Newnham R E, Skinner D P and Cross L E (1978), Connectivity and piezoelectric-pyroelectric composites, *Mater Res Bull*, 13, 525–36.

Nguyen K T, Lethiecq M, Karlsson B and Patat F (1995), Development of a broadband ultrasonic transducer for high temperature applications, *Acta Acustica*, 3, 331–8.

Ono Y, Kobayashi M, Jen C-K, Cheng C-C, Derdouri A and Simard Y (2004), *SPE ANTEC*, 556–60.

Ono Y, Cheng C-C, Kobayashi M and Jen C-K (2005), Real-time monitoring of injection molding for microfluidic devices using ultrasound, *Polym Eng Sci*, 45, 606–12.

Ono Y, Kobayashi M, Moison J-F and Jen C-K (2006), High temperature and broadband immersion ultrasonic probes, *IEEE Sensors J*, 6, 580–7.

Ono Y, Whiteside B R, Brown E C, Kobayashi M, Cheng C-C, Jen C-K and Coates P D (2007), Real-time process monitoring of micromolding using integrated ultrasonic sensors, *Trans Inst Measur Contr*, 29, 383–401.

Patel N D, Fulford S X and Nicholson P S (1990), High frequency-high temperature ultrasonic transducers, *Review of Progress in Quantitative Nondestr Eval*, 9, 823–8.

Piche L, Massines F, Hamel A and Neron C (1988), *Ultrasonic characterization of polymers under simulated processing conditions*. US patent 4754645. 1988-Jul-5.

Piché L, Lévesque D, Gendron R and Tatibouët J (1994), On-line ultrasonic characterization of polymer flows, *Proc VIth Symp Nondestr Character Mater*, 37–44.

Shih J-L, Kobayashi M and Jen C-K (2010), Flexible metallic ultrasonic transducers for structural health monitoring of pipes at high temperatures, *IEEE Trans Ultrason, Ferroelectr, Freq Contr*, 57, 2103–10.

Viktorov I A (1967), *Rayleigh and Lamb Waves*, translated and foreword by Mason W P, New York, Plenum Press.

Walker W F and Trahey G E (1995), A fundamental limit on delay estimation using partially correlated speckle signals, *IEEE Trans Ultrason, Ferroelectr, Freq Contr*, 42, 301–8.

Wu K-T, Jen C-K, Murayama R and Oliveira J E B (2009), Generation and detection of guided acoustic waves for NDT high temperature wedges, *Proc Cansmart Inter Workshop*, 103–13.

Wu K-T, Oliveira J E B and Jen C-K (2010), High temperature nondestructive testing of plates and pipes using mode selective wedges, to be published in *Proc IEEE Ultrason Symp*.

Zou L, Sayer M and Jen C-K (1997), Sol-gel fabricated thick piezoelectric ultrasonic transducers for potential applications in industrial material processes, *Proc IEEE Ultrason Symp*, 1007–11.

14

Analysis and synthesis of frequency-diverse ultrasonic flaw-detection systems using order statistics and neural network processors

J. SANIIE and E. ORUKLU,
Illinois Institute of Technology, USA

Abstract: Ultrasonic imaging is used for nondestructive evaluation of materials and flaw detection. Flaw detection in the presence of microstructure scattering noise is a challenging problem. Frequency-diverse ultrasonic detection algorithms decorrelate the microstructure scattering noise and enhance the visibility of echoes associated with defects. The performance of ranked order-statistic processors is examined using both theory and ultrasonic experiments. Split-spectrum processing combined with neural networks as post-processors can improve flaw detection. Neural networks have robust performance and are capable of outperforming conventional detection techniques. A field-programmable gate array (FPGA)-based case study demonstrates the real-time operation of ultrasonic flaw-detection algorithms. Architecture details and implementation results with various hardware/software partitioning schemes are discussed.

Key words: ultrasound, nondestructive evaluation, split-spectrum processing, neural networks, order statistics, flaw detection.

14.1 Introduction

In ultrasonic nondestructive evaluation (NDE) applications, such as flaw detection, the presence of high levels of scattering noise poses a significant and challenging problem. This chapter presents techniques based on frequency-diverse ultrasonic imaging, which induces a significant statistical variation in scattering noise or speckles. In particular, the split-spectrum processing (SSP) technique, which uses subband decomposition and post-processing detection methods including order statistics (OS) and neural networks (NN), is discussed in detail. The adaptive learning capability of neural networks facilitates robust detection. Experimental results are presented for comparison of the flaw-to-clutter visibility improvement with the proposed techniques. Finally, a field-programmable gate array (FPGA)-based hardware platform is described for the system-on-a-chip (SoC) realization of a real-time ultrasonic imaging system. This platform supports multiple embedded architectures including software-only, hardware/software co-design and hardware-only designs illustrating the possible trade-offs between hardware resources and system throughput. This chapter concludes with a discussion of recent and future trends in real-time ultrasonic imaging.

14.2 Ultrasonic flaw-detection techniques

In ultrasonic imaging, coherent noise resulting from the microstructure of materials consisting of a large number of complex and randomly distributed scatterers often masks the target echo to the extent that misdetection is the norm rather than the exception. Scattering noise, known as clutter, is a common problem that affects a wide range of detection and imaging applications including radar, optics and sonar. When scatterers are stationary, as is the case in ultrasonic imaging, clutter suppression cannot be achieved by signal averaging. Furthermore, clutter and target echoes span the same frequency range and signal filtering is also ineffective. Nevertheless, it is feasible to decorrelate clutter and improve target visibility by shifting the frequency band of the transmitter/receiver (using multi-channels) and to obtain a set of frequency-diverse signals. Clutter decorrelation using frequency diversity (also known as frequency agility when the frequency shifts from pulse to pulse using a single channel) for radar target detection dates back to the 1960s (Beasley and Ward, 1968; Lind, 1970; Barton, 1977). Averaging the decorrelated received clutter signals results in signal-to-clutter ratio enhancement. In the 1980s and 1990s, frequency-diverse detection for both ultrasonic imaging and radar target detection was explored (Bilgutay *et al.*, 1979; Newhouse *et al.*, 1982; Saniie *et al.*, 1990, 1991; Saniie and Nagle, 1992). These investigations resulted in the development of the theory and applications of signal subband decomposition followed by the Bayesian (Saniie *et al.*, 1992) and order statistics (Saniie *et al.*, 1990; Nagle and Saniie, 1995) post-detection processors.

A typical ultrasonic pulse-echo measurement setup for flaw detection using a 5-MHz transducer is shown in Fig. 14.1. An experimental ultrasonic signal consisting of grain scattering and a flaw echo from a hole inside a steel block is shown in Fig. 14.2(a). Figure 14.2(b) shows the improved visibility of the flaw

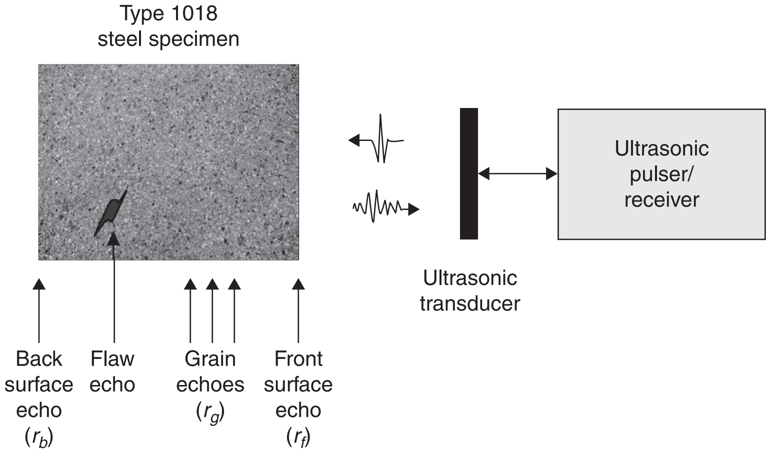

14.1 Typical ultrasonic pulse-echo measurement setup for flaw detection using a 5-MHz transducer.

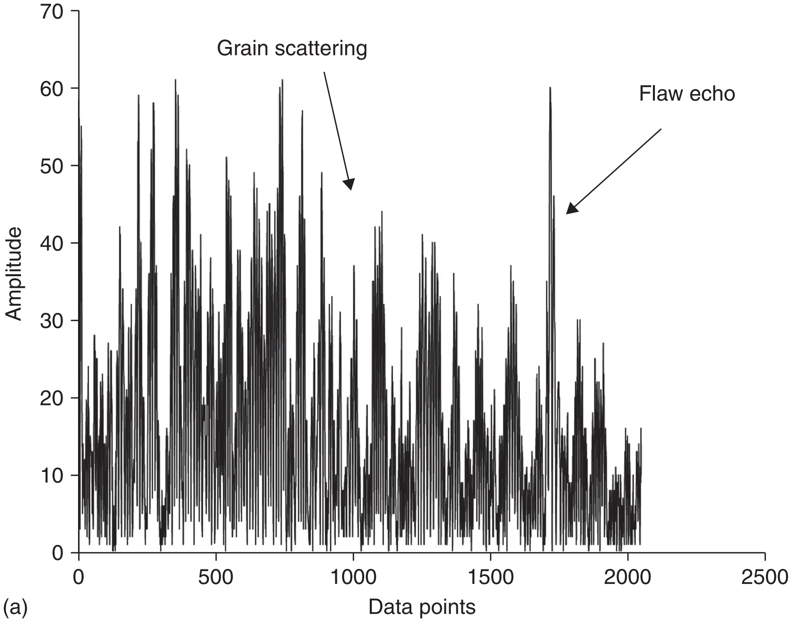

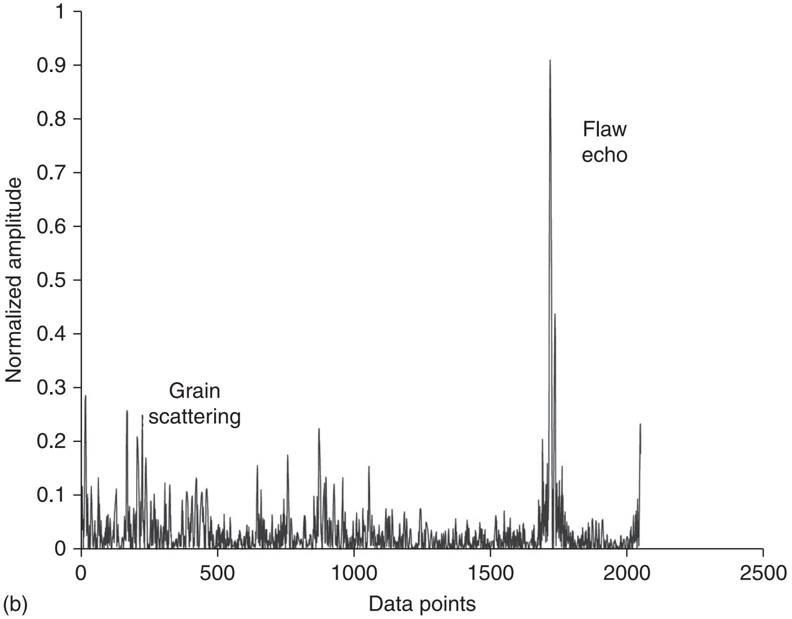

14.2 (a) Ultrasonic signal from a steel block with a hole (flaw). (b) Signal after frequency-diverse order statistic processing using a minimum detector.

echo after using a frequency-diverse order-statistic (i.e. minimum) processor, which will be discussed throughout this chapter.

14.2.1 Split-spectrum processing

In the ultrasonic imaging of materials, an effective method of obtaining frequency-diverse information is through split-spectrum processing of the broadband echoes (Bilgutay *et al.*, 1979; Newhouse *et al.*, 1982). The SSP procedure has five steps as shown in Fig. 14.3. The first step is data acquisition. In the second step, a fast Fourier transform (FFT) gives the frequency spectrum of the received echo signal. In the third step, several bandpass filters split the spectrum into different frequency bands as shown in Fig. 14.4. In the next step, an

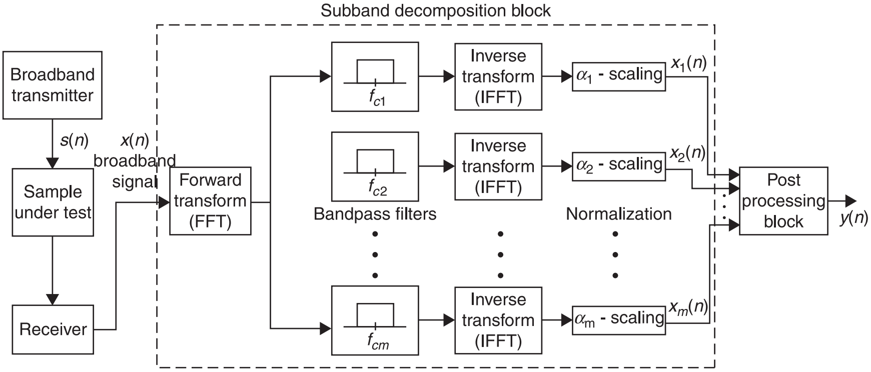
Subband decomposition block
Broadband transmitter
$s(n)$
$x(n)$ broadband signal
Sample under test
Receiver
Forward transform (FFT)
f_{c1}
f_{c2}
f_{cm}
Bandpass filters
Inverse transform (IFFT)
α_1 - scaling
α_2 - scaling
α_m - scaling
Normalization
$x_1(n)$
$x_2(n)$
$x_m(n)$
Post processing block
$y(n)$

14.3 Flaw detection system using split-spectrum processing.

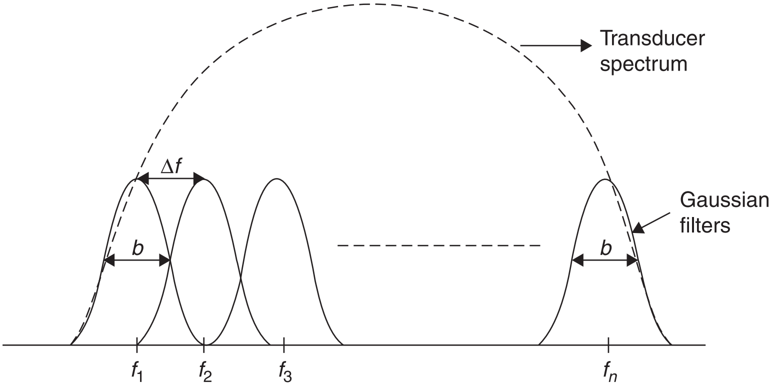
Transducer spectrum
Gaussian filters
Δf
b
b
f_1
f_2
f_3
f_n

14.4 Frequency bands in split-spectrum processing, where b is the filter bandwidth, Δf is the frequency step within the bands, and $f_1 \ldots f_n$ are the center frequencies of the subbands.

inverse FFT gives the time-domain signal of each individual frequency band. The signals from each individual frequency band are normalized and then passed to a post-processing block for detection. This detection processor can employ different techniques such as averaging, minimization, order-statistic filters or Bayesian classifiers (Saniie *et al.*, 1988, 1991; Saniie and Nagle, 1992; Saniie *et al.*, 1992).

SSP performance is greatly influenced by the number of bandpass filtering channels (or observations) across the signal spectrum, the correlation between the observations and the statistical information in each channel. Increasing the number of channels increases the likelihood of separating the flaw and grain echo information. However, there are only a limited number of information-bearing frequency bands. This means that increasing the number of channels results in many observations that only contribute to the grain (clutter) echo information. Another trade-off is between the bandwidth of the channels and the degree of overlap between channels. If the channel bandwidth is too small, flaw-echo information is concealed due to resolution loss. Excessive overlap between channels, on the other hand, results in disproportionate correlation among the channels. Correlation is not as critical for ultrasonic flaw-detection performance as choosing the proper frequency range containing significant flaw-echo information.

In order to enhance the visibility of the flaw echo masked by clutter, SSP utilizes a post-processor for combining all the incoming information from the subbands. This post-processor reconstructs the time-domain signal to maximize the flaw-to-clutter ratio (FCR). Several types of processors can be used to extract the flaw-echo information. Minimization, in particular, is very effective in suppressing the clutter echoes when flaw-echo information exists in all the observation channels (Saniie *et al.*, 1991). If there are too many null-observation channels (frequency bands where there is no flaw-echo information due to the frequency-dependent attenuation), then a minimization processor may not achieve the desired FCR improvement. Figure 14.5 shows channels that do not contain flaw-echo information. Under these circumstances, other post-processing methods such as median or maximization may offer more robust detection performance. Similar to minimization, median and maximization methods are called order-statistic filters and they will be discussed in more detail in Section 14.2.3. Order statistics were developed by statisticians and have been successfully employed in ultrasonic target detection (David, 1981; Saniie *et al.*, 1991; Saniie and Nagle, 1992).

In the following section, the frequency analysis of the ultrasonic signals is described and the frequency diversity between the clutter (i.e. grain scattering echoes) and the flaw echoes is highlighted. This difference in frequency response can be exploited by robust flaw-detection algorithms.

14.2.2 Frequency analysis of ultrasonic signals

In the Rayleigh scattering region, grain (i.e. microstructure) scattering results in an upward shift in the expected frequency of the broadband ultrasonic signal. This

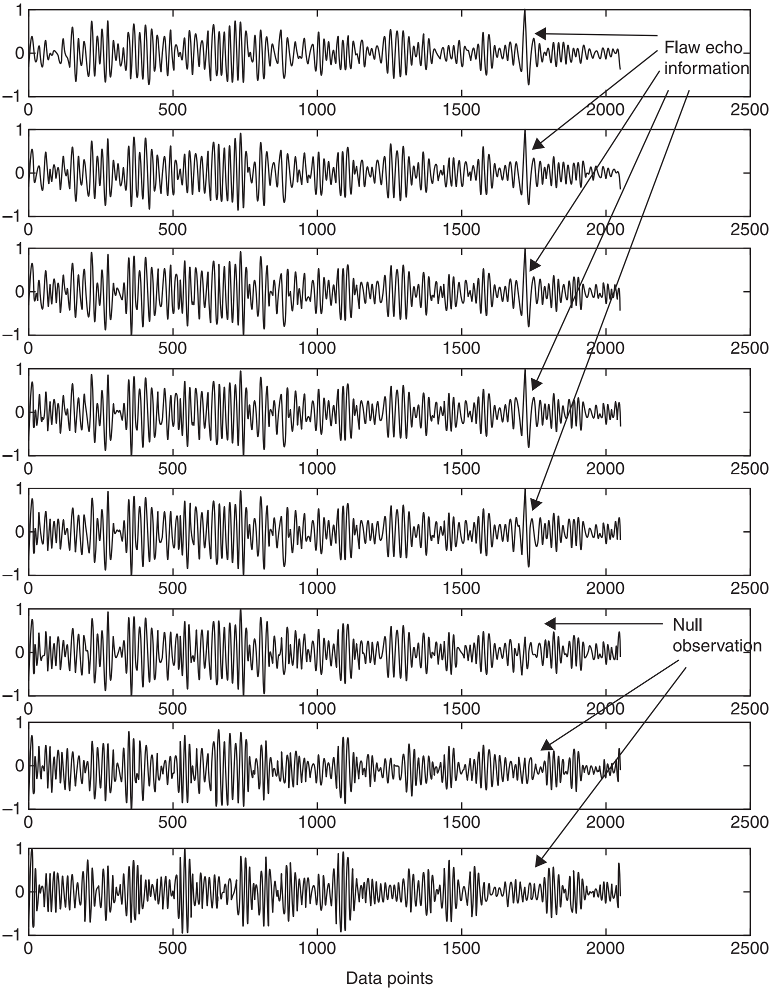

14.5 Channels with flaw-echo information and null-observation channels.

is not the case for flaw echoes, since flaws are generally larger in size than the grains and behave like geometrical reflectors. In fact, flaw echoes often display a downward shift in their expected frequency caused by the overall effect of attenuation. This downward frequency shift due to a flaw is a productive attribute, since the grain noise and flaw echoes are concurrently received and pre-processing methods can improve the flaw-to-clutter ratio. If the information-bearing frequency bands that are dependent on the specific characteristics of the materials are known *a priori*, optimal bandpass filtering can be employed (Saniie and Nagle, 1992).

The exploration of the frequency content of ultrasonic backscattered signals can give spectral energy profiles corresponding to the grains and the larger geometric reflectors (i.e. defects). The energy loss and attenuation of ultrasonic signals are caused by the microstructure of the propagating media through which scattering and absorption occurs. The intensity of scattering is a non-explicit function of the average grain diameter, the ultrasonic wavelength, the inherent anisotropic character of the individual grains and the random orientation of the crystallites. In the Rayleigh region (i.e. when the wavelength is larger than the size of the grains), the scattering coefficient varies with the average volume of the grain and the fourth power of the wave frequency, while the absorption coefficient increases linearly with frequency (Papadakis, 1965; Saniie *et al.*, 1988). Therefore, the attenuation coefficient can be modeled as:

$$\alpha(f) = a_1 f + a_2 \bar{D}^3 f^4 \qquad [14.1]$$

where a_1 is the absorption constant, a_2 is the scattering constant, $\bar{D}$ is the expected value of the grain diameter and f is the transmitted frequency.

The composite effects of scattering and attenuation due to grains can be characterized in terms of transfer functions derived from the spectra of measured signals obtained in the ultrasonic pulse/echo measurement mode as shown in Fig. 14.1. The front-surface echo, $r_f(t)$, represents the combined effect of the far-field transfer function of the transducer impulse response, $U(f)$, the ultrasonic pulser, receiver amplifier and the water propagation path. In RF frequencies (1–15 MHz range), the characteristics of the pulser/receiver and the water propagation path are frequency independent. Therefore, the transfer function of the received front-surface echo signal is proportional to the transfer function of the transducer impulse response (Saniie and Nagle, 1992):

$$R_f(f) \propto U(f) \qquad [14.2]$$

The spectrum of the received backscattered signal from the back wall of the specimen (see Fig. 14.1), $R_b(f)$, can be modeled as

$$R_b(f) \propto A(f)U(f) \qquad [14.3]$$

where $A(f)$ is the transfer function corresponding to the attenuation characteristics of the signal propagation path within the specimen. In Fig. 14.6(a), a heuristic evaluation of $A(f)$ is given by the ratio of the spectra of the above measured signals, $\frac{|R_b(f)|}{|R_f(f)|}$, using a steel block with an average grain size of 50 μm and a 5-MHz ultrasonic transducer. This figure clearly shows that there is a definite shift or emphasis of the lower frequencies. This indicates that echoes associated with flaws significantly greater in size than the echo wavelength have the dominant energy in the lower frequencies.

The microstructure scattering transfer function, $S(f)$, is the ratio of the expected spectrum of the grain echoes, $r_g(t)$, and the spectrum of the back-surface echo, $r_b(t)$, $|R_g(f)|/|R_b(f)|$, which is displayed in Fig. 14.6(b). These results

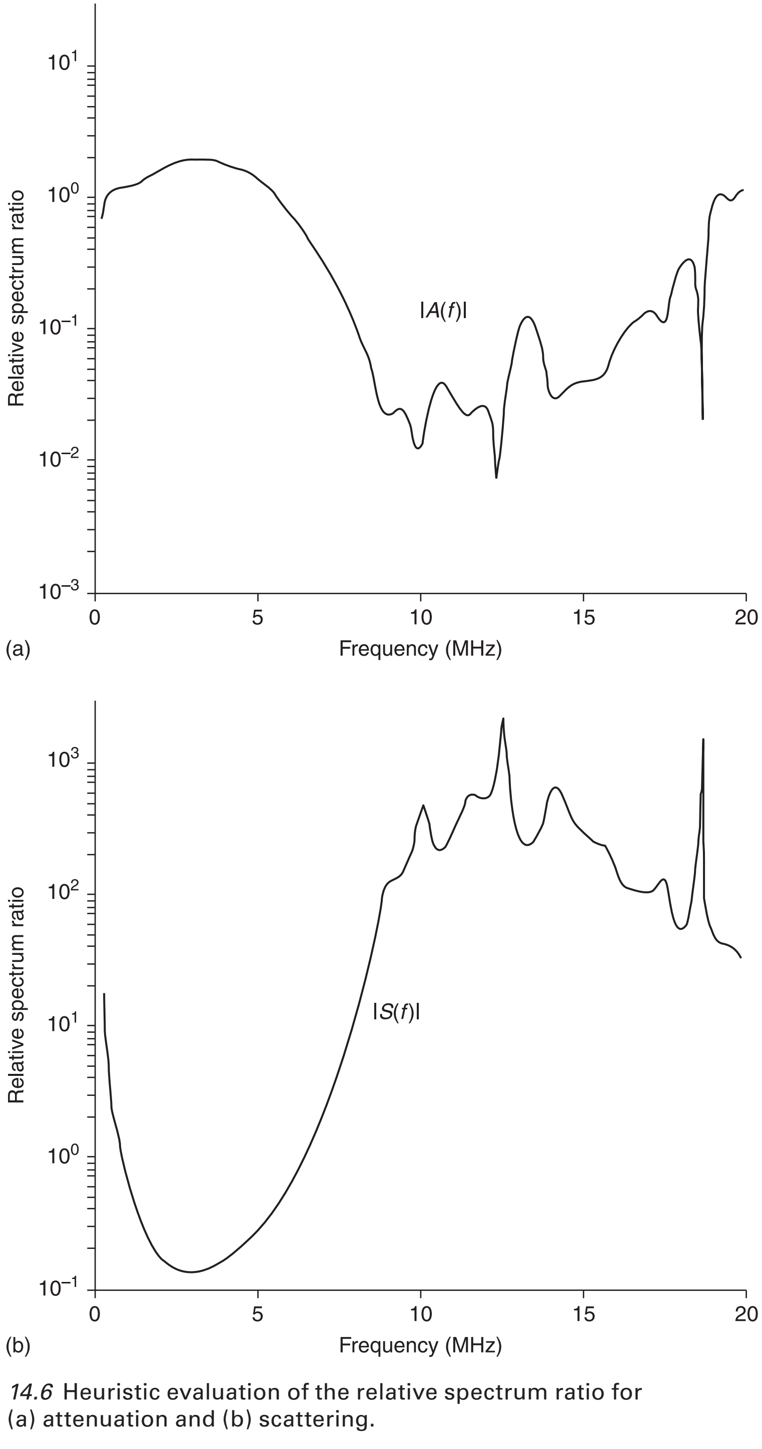

14.6 Heuristic evaluation of the relative spectrum ratio for (a) attenuation and (b) scattering.

indicate that grain scattering causes waves at lower frequencies to become poorly backscattered (i.e. attenuated), resulting in an upward shift in the expected frequency of the grain spectrum. In order to take advantage of this property for flaw detection, frequencies where the grain scattering is minimal should be emphasized in order to maximize the flaw-to-clutter ratio (Saniie and Nagle, 1992).

In summary, both flaw and grain echoes display predictable frequency dynamics associated with the physical properties of the materials. Experimental results (Fig. 14.6) also indicate the frequencies where high flaw-to-clutter ratios exist and this information can be utilized in the pre-processing stage (see the block diagram in Fig. 14.3). These characteristics are advantageous and lead to an optimal frequency range, containing high flaw-to-clutter ratios, for SSP during the pre-processing stage. In the next section, the order-statistic method is discussed in detail. It can utilize the frequency diversity of ultrasonic signals to improve flaw detection.

14.2.3 Order-statistic (OS) processors

As shown in the preceding section, the disparity in the energy at lower frequencies for echoes from the grains and flaws allows bandpass filtering techniques to extract flaw information in the pre-processing stage (Fig. 14.3). However, additional improvements in flaw-to-clutter ratio and resolution can be obtained through SSP techniques that focus on the statistical information in the frequency region of high flaw-to-clutter ratios.

In SSP, after subband decomposition, the next step is to use the partially uncorrelated observations and make use of statistical differences in the channels (i.e. that corresponding to random phase information in the received grain echoes) to improve the flaw-to-clutter ratio and resolution of the flaw echoes. The order-statistic filter is a quantile estimator (Saniie *et al.*, 1990) of the input density function that describes a specific point on the probability distribution function. The performance of the detector can be improved by choosing the position of the estimate where there are large statistical differences between the two hypotheses (flaw present, H_1, or not present, H_0).

The order-statistic (David, 1981) filter ranks a set of n input values corresponding to simultaneously sampled values of the n channels of the SSP output, $(x_1, x_2, x_3, \ldots, x_n)$,

$$x_{(1)} \leq x_{(2)} \leq x_{(3)} \ldots \leq x_{(n)} \qquad [14.4]$$

where a given order or rank, r, is chosen and $x_{(r)}$ is passed to the output. This processor is the median filter when $r = (n + 1)/2$ (for odd n), the maximum filter when $r = n$ and the minimum filter when $r = 1$.

An important step in optimizing the OS filter involves finding the relation between the statistical behavior of the input and output data. Assuming the input observations, x, are independent and identically distributed with distribution $F_X(x)$, the order statistic is known to be a consistent and asymptotically unbiased estimator of the quantile (Saniie *et al.*, 1990):

$$\lim_{\substack{n\to\infty \\ r\to\infty}} E\left[X_{(r)}\right] = F_X^{-1}(u_r) \qquad [14.5]$$

where $u_r = (r - 1)/(n - 1)$ is a constant (i.e. normalized rank) bounded between zero and one, and $E[X_{(r)}]$ is the expected value for the output of the OS filter. In the aforementioned limit, both r and n approach infinity but u_r is always finite. For infinite n, the OS filter is an unbiased quantile estimator. With a finite number of observations, n, the estimate will have some dispersion about the quantile value, u_r, which allows the values of neighboring quantiles to influence the output. The performance of an OS filter will generally improve with an increasing number of observations, n, since the variance will decrease (i.e., the effect of the random nature of the grain echoes will be reduced). The lower-ranked order statistics have been shown in the past to improve the resolution of echoes and the flaw-to-clutter ratio (Bilgutay and Saniie, 1984), provided all channels contain significant flaw information.

The parameters r and n can be used so that the OS filter emphasizes particular regions in the distributions of the input signals. The OS filtering operation censors the signal values outside this quantile region from the decision rule. This property is useful when the classes of signals exhibit a distinctive statistical difference over a limited range of quantiles, such as may occur with specular reflective targets.

The optimal rank is dependent on the input distributions and this is illustrated by the following two examples (Saniie *et al.*, 1991). In the first example, we assume that the number of observations is 25, and the target-plus-clutter observations (i.e. flaw echoes) are chi distributed with skewness equal to 0.566, within a Weibull clutter (i.e. grain echoes) with a skewness equal to 1.05. Their respective inverse distribution functions are shown in Fig. 14.7. The performance of the OS filter can be seen in Fig. 14.8, where the probability of detection for all possible rank values ($r = 1, 2, 3, \ldots, 25$) is plotted for 0 dB and 2 dB signal-to-clutter ratios (SCR). The lower ranks perform significantly better, since there is greater separation in smaller quantile regions where $u < 0.6$, as shown in Fig. 14.7. Here, u is the normalized rank with respect to the total number of observation channels and it is always less than or equal to 1. The optimal rank occurs at $r = 2$ for the lower SCR and $r = 4$ for the higher SCR. For the higher SCR, the optimal choice is less critical, since for any r value from 1 to 10 the OS filter shows good performance.

In the second example, both target-plus-clutter and clutter are Rayleigh distributed with skewness equal to 0.63. The inverse distributions are as shown in Fig. 14.9. In Fig. 14.10, the optimal r is 19 for the lower SCR (3 dB) and 20 for the higher SCR (6 dB). For the high SCR, the robustness of the upper ranks is

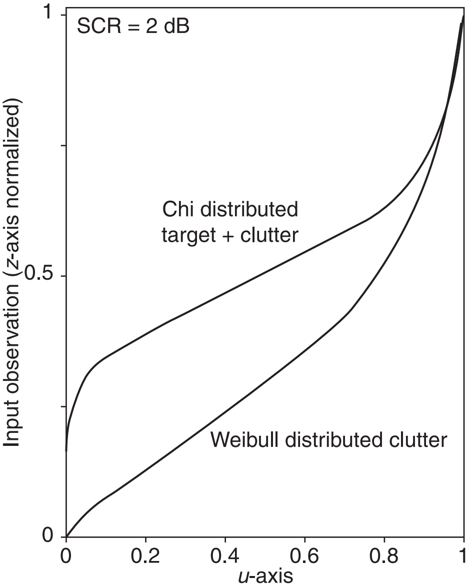

14.7 Inverse distribution functions of chi-distributed target-plus-clutter and Weibull-distributed clutter.

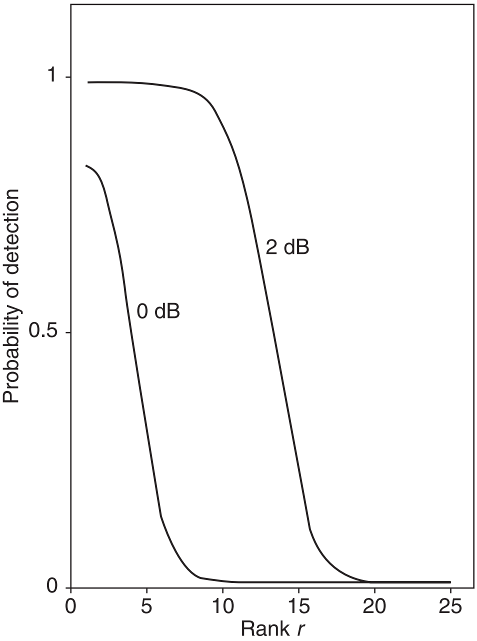

14.8 Probability of detection of chi-distributed target-plus-clutter in Weibull-distributed clutter for various ranks of OS filters with $n = 25$ and with the probability of false positives set at 0.001.

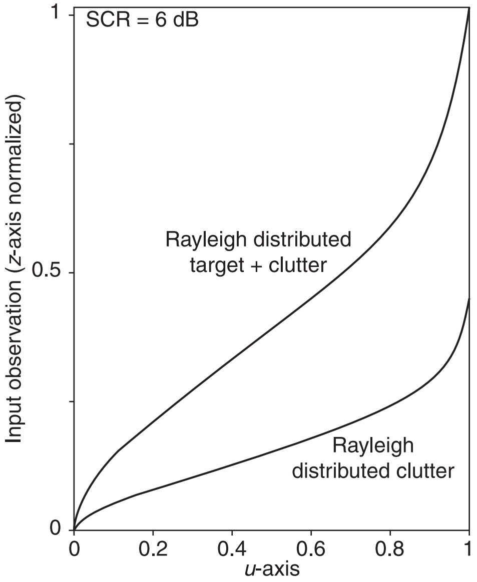

14.9 Inverse distribution functions of Rayleigh-distributed target-plus-clutter and Rayleigh-distributed clutter.

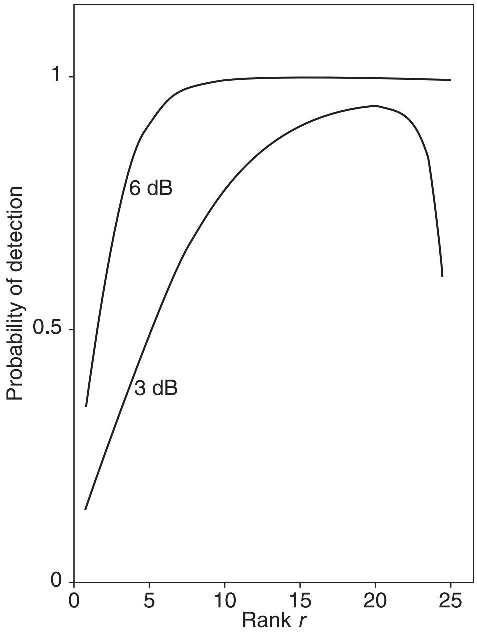

14.10 Probability of detection of a Rayleigh-distributed target in Rayleigh-distributed clutter for various ranks of OS filters with $n = 25$ and the probability of false positives set at 0.001.

self-evident from a visual examination of the inverse distributions of Fig. 14.9, and will increase as the input SCR increases.

In the next section, we will describe an alternative post-processing technique based on neural networks, which offers superior and more robust flaw-detection performance.

14.3 Neural network detection processor

Neural networks are nonlinear mapping processes that can be trained and adapted for signal classification applications (for example, Cichocki and Unbehauen, 1993; Gurney, 1997; Haykin, 2008). The learning process enables a neural network to recognize a target pattern without having a mathematical model of the target signals, which often are unknown. There are several key advantages of neural networks:

- Neural networks are trained for the required result. This means that no mathematical model is necessary.
- Neural networks approximate unknown systems, which include nonlinear models. Nonlinearity is an important property because it enhances network classification or approximation capabilities without needing to estimate any statistical parameter.
- Neural networks have a parallel structure, and thus fast performance for real-time detection applications.

In this study, a three-layer feedforward neural network (Hornik, 1989) is used as the post-processor of the ultrasonic flaw detector. Neural networks provide superior flaw-to-clutter ratio performance when compared with other post-detection processors. Furthermore, hardware realization of neural networks for real-time ultrasonic target-detection systems is feasible (Yoon *et al.*, 2006).

14.3.1 Neural network architecture

A neural network contains many nodes, which are connected to each other. Each node has a basic computation function and an activation function. A computation unit processes input signals and communicates with the activation function. The activation function unit produces the output of the node, which can be the final output of the neural network or the input of another neural node. A neural network can be classified as a feedforward neural network or a recurrent neural network. The former has a feedforward structure, where neural nodes receive input data and pass data to adjacent neural nodes without any feedback. In this study, a three-layer feedforward neural network was designed as the post-processor of an ultrasonic target-detection system.

An objective function is used when training a neural network. The squared-error function, which is computed as the difference between the output of the neural network and the desired output, is used as the objective function. The goal of neural network learning is to find weight coefficients to minimize the objective function. In this research, the back-propagation algorithm was used to train the neural network.

14.3.2 Neural network model for SSP post-processing

A three-layer feedforward neural network for SSP is shown in Fig. 14.11. The nodes in the first layer send SSP data to the second layer. The neural nodes in the second layer, the hidden-layer nodes, receive weighted inputs from the first layer and calculate a nonlinear mapping using the activation function. The output neural nodes in the third layer sum the weighted inputs from the second layer. A model of the neural nodes is shown in Fig. 14.12. The subscripts, *ij*, on the weight coefficients, w_{ji}, indicate the *i*th input and *j*th node.

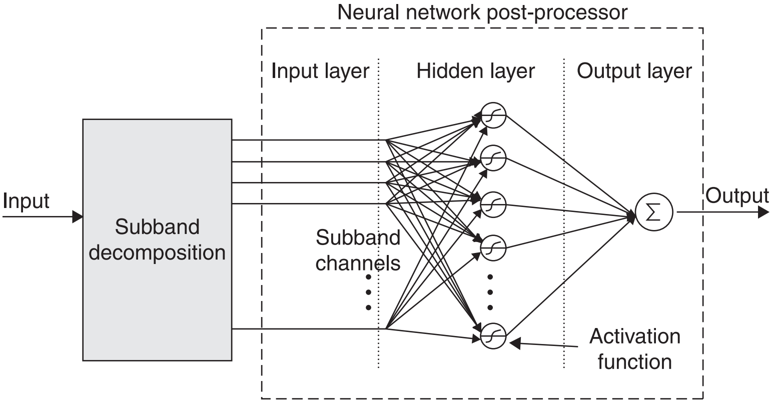
Neural network post-processor
Input layer
Hidden layer
Output layer
Input
Subband decomposition
Subband channels
Σ
Output
Activation function

14.11 Three-layer feedforward neural network for SSP.

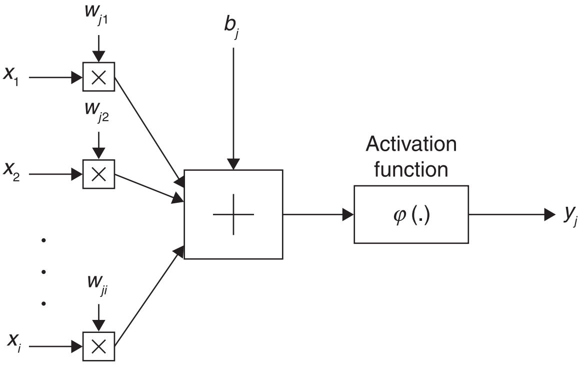
w_{j1}
b_j
x_1
w_{j2}
x_2
Activation function
φ (.)
y_j
w_{ji}
x_i

14.12 Model of the neural nodes.

The general neural node model can be expressed by

$$y_j = \varphi\left(\sum_i w_{ji} x_i + b_j\right) \tag{14.6}$$

where x_i is the set of inputs for each neuron, y_j is the set of outputs for each neuron and b_j is the bias set for each neuron. Each input is multiplied by a weight coefficient, w_{ji}. The subscript *ji* refers to the input *i* in neuron *j*. The term φ is the activation function.

There are several required properties for the activation function. First, the activation function of the hidden layer in a three-layer neural network needs to be nonlinear. Second, the weights and activations are bounded, which is called saturation. The third property is continuity and smoothness. The back-propagation algorithm needs the derivative of the activation function for its learning process. In this research, the activation function used in the hidden layer is the sigmoid function, which can be expressed by

$$\varphi(x) = (1 + e^{-x})^{-1} \tag{14.7}$$

14.3.3 Back-propagation learning process

The learning process allows a neural network to adapt to the environment of a particular application. Learning occurs through an iterative process of adjusting the weight values. We adapted the back-propagation algorithm (Masters, 1993) to train the neural network for the ultrasonic target-detection system. During learning, it is important to select the initial weights randomly since the training result can be limited to a local minimum based on the initial values. After training, the weight coefficients are fixed and used for the remaining input sets. Additional training of a neural network is only necessary when the environment of the application changes.

The activation function of the hidden nodes has an important role in the nonlinear mapping process. The output of the sigmoid function is one or zero when the input approaches positive or negative infinity, respectively. This means that the output will be one or zero when the input is very large, which may cause the nonlinear mapping process of the neural network to fail. To avoid this undesirable condition, the input data are normalized between −1 and 1.

To train the neural network for ultrasonic flaw detection, we used experimental ultrasonic data which have a flaw in an *a priori* known location. The desired output data comprise all *zero* values and a *one* value at the known flaw location. The initial values of the weights and bias were randomly selected. The number of input nodes is the same as the number of SSP channels and only one output node was used. It is important to note that the number of hidden nodes affects the performance of a neural network. In this research, we used five hidden nodes for the neural network after several trials. An objective function, such as the sum of the squared-error function, is necessary for achieving the minimization criterion to complete the learning process. If the minimization criterion of the objective function is not met, we can increase the number of epochs corresponding to a single presentation of all patterns in the training set. If the criterion is still not met with a large number of epochs, increasing the number of hidden nodes can solve the problem. However, increasing the number of epochs or hidden nodes increases the learning time.

14.3.4 Software implementation of the neural network

The neural network-based SSP post-processor was implemented in MATLAB for performance evaluation. The experimental data are used for both training and detection test. Figure 14.13 shows the data for training and the desired output data. The back-propagation learning algorithm computes the mean-squared error of the difference between the desired output and the real output value and adjusts the weight and bias coefficients until the mean-squared error function reaches a predetermined minimum value. After training, the neural network is expected to respond to flaw echoes if the input has flaw signals. The neural network outputs a large pulse for a flaw echo and a small value for the clutter echoes, since one was assigned to a flaw and zero was assigned to clutter echoes during learning. An 8-channel SSP and five hidden nodes were used for the neural network. Results from using the trained neural network as a flaw detector are shown in Fig. 14.14, and show an enhancement in the visibility of the flaw echo. If there are major changes in the experimental setup (such as a different

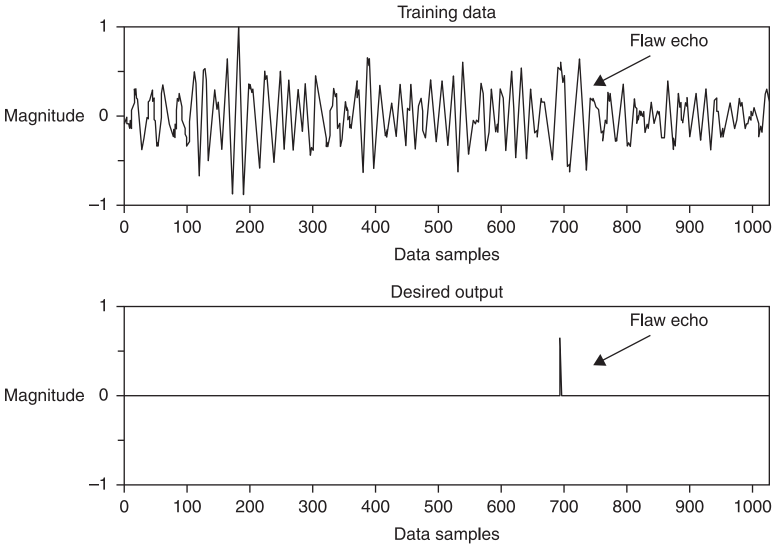

14.13 Training data and desired output data.

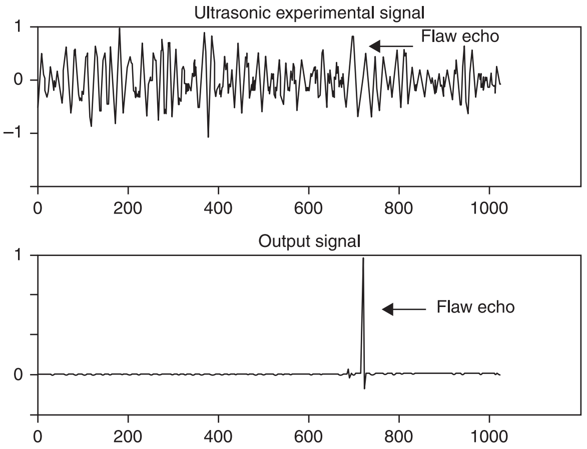

14.14 Detection results using neural network-based SSP.

type of transducer, a different frequency of interrogation or a change in the type of material), it may be necessary to re-train the neural network to derive new weight coefficients.

14.4 Flaw-detection performance evaluation

In this section, the neural network is compared with other conventional post-processing flaw-detection methods such as order statistics (minimum, median, averaging), geometric mean (Xin *et al.*, 1991) and polarity detectors (Bilgutay *et al.*, 1989). The mathematical expressions of these techniques are given as the following:

Average detector:

$$\phi_{av}(n) = \frac{1}{k}\sum_{j=1}^{k}\left|z_j(n)\right| \qquad [14.8]$$

Median detector:

$$\phi_{med}(n) = median[\left|z_j(n)\right|, j = 1,2,\ldots, k] \qquad [14.9]$$

Minimum detector:

$$\phi_{\min}(n) = \min[\left|z_j(n)\right|, j = 1,2,\ldots, k] \qquad [14.10]$$

Geometric-mean detector:

$$\phi_{gm}(n) = \sqrt[k]{\prod_{j=1}^{k}\left|z_j(n)\right|} \qquad [14.11]$$

Polarity detector:

$$\phi_p(n) = \begin{cases} & \textit{if } z_j(n) > 0 \textit{ or } z_j(n) < 0 \\ z(n) & \textit{for all } j = 1,2,\ldots,k \\ 0 & \textit{otherwise} \end{cases} \qquad [14.12]$$

where *z(n)* is the measured broadband signal, $z_j(n)$ is the SSP output of channel *j* and *k* is the total number of SSP channels.

The neural network and the other detection methods were implemented and compared with experimental ultrasonic data. For performance analysis and testing, experimental A-scan data from a steel block (type 1018, grain size 50 μm) were acquired and analyzed. A Panametrics (type 5052) pulser/receiver was used to drive the ultrasonic transducers and to receive the ultrasonic backscattered echoes. The received echo signals were converted into digital data for split-spectrum processing. The A-scan measurements were conducted using a broadband unfocused ultrasonic transducer of diameter 0.5 inch with a 5-MHz center frequency. Data were acquired at a sampling rate of 100 MHz and each sample had 8 bits. So, 1024 data points for each A-scan represents approximately a depth of 2.5 cm. The steel block has several holes (1.5 mm diameter) at known, separate locations. All the A-scan measurements probe the hole positions within the steel block. For performance analysis, the flaw-to-clutter ratio was evaluated by finding the maximum flaw-echo amplitude after the post-processing step. This value was compared with the largest amplitude of the clutter echoes. Therefore, the FCR can be defined as

$$\mathrm{FCR} = 20\log_{10}(F/C) \qquad [14.13]$$

where *F* is the maximum flaw-echo amplitude and *C* is the maximum clutter echo amplitude.

Figure 14.15 shows the experimental data in the time domain, Fig. 14.15(a), and frequency domain, Fig. 14.15(b), as well as the frequency spectrum of the 8-channel SSP bandpass filters, Fig. 14.15(c) and Fig. 14.15(d). Figure 14.15(c) shows the frequency range where the flaw echo exists in all subbands (no null observations). Figure 14.15(d) shows the frequency spectrum of the eight subband filters that cover the full-frequency spectrum of the original measured signal. In this case, some subband filter outputs (for higher frequency bands) may have a very low FCR and are considered to be null observations. Therefore, a robust flaw-detection method, which offers minimal sensitivity to the frequency coverage of the filters, is desirable (Yoon *et al.*, 2007). A comparison of the results from the various detectors applied to the SSP channels covering the low-frequency region (ranging from 1.5 MHz to 6 MHz) are shown in Fig. 14.16. In this frequency region, there are no null observations. With the neural network (NN) detector, the flaw echo is sharply detected without visible clutter. The other detectors also detect the flaw.

Table 14.1 shows the FCRs of the original input data and the six different post-processors. It also confirms that the neural network outperforms the other

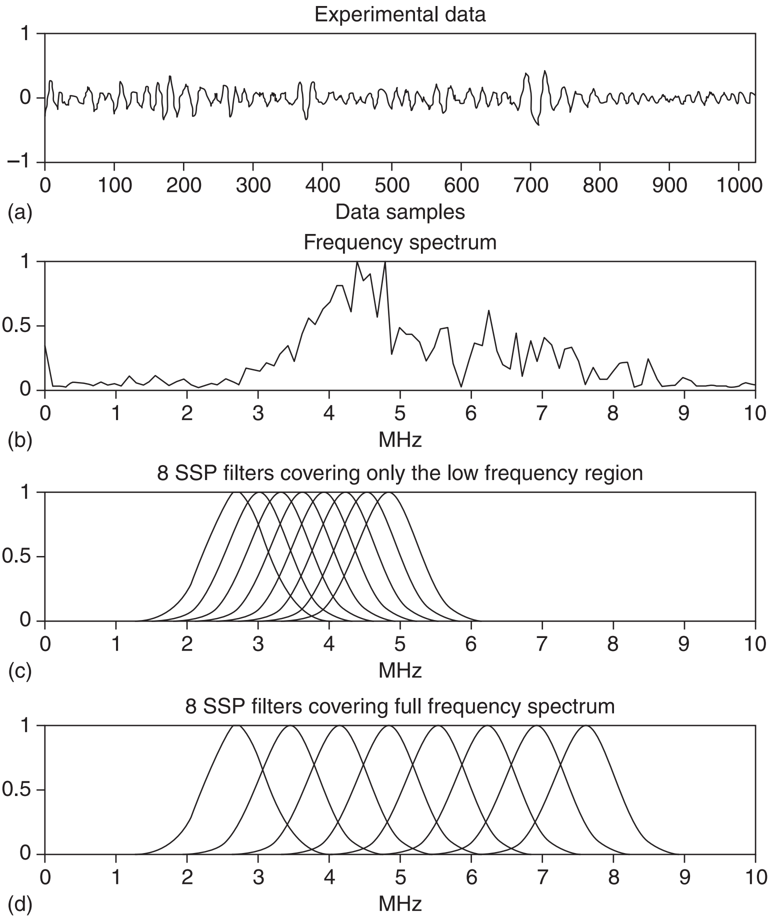

14.15 Experimental data in (a) the time domain, (b) the frequency domain and (c, d) frequency bands of SSP filters.

Table 14.1 FCR enhancement of various ultrasonic target detectors (average of multiple measurements)

Input FCR	Neural network detector	Minimum detector	Median detector	Average detector	Geometric-mean detector	Polarity-threshold detector
	SSP filters covering only the low-frequency range of the signal					
1.1 dB	46.8 dB	7.9 dB	7.1 dB	5.0 dB	7.0 dB	0 dB
	SSP filters covering the full-frequency range of the signal					
1.1 dB	23.7 dB	1.7 dB	1.0 dB	1.4 dB	1.5 dB	0.3 dB

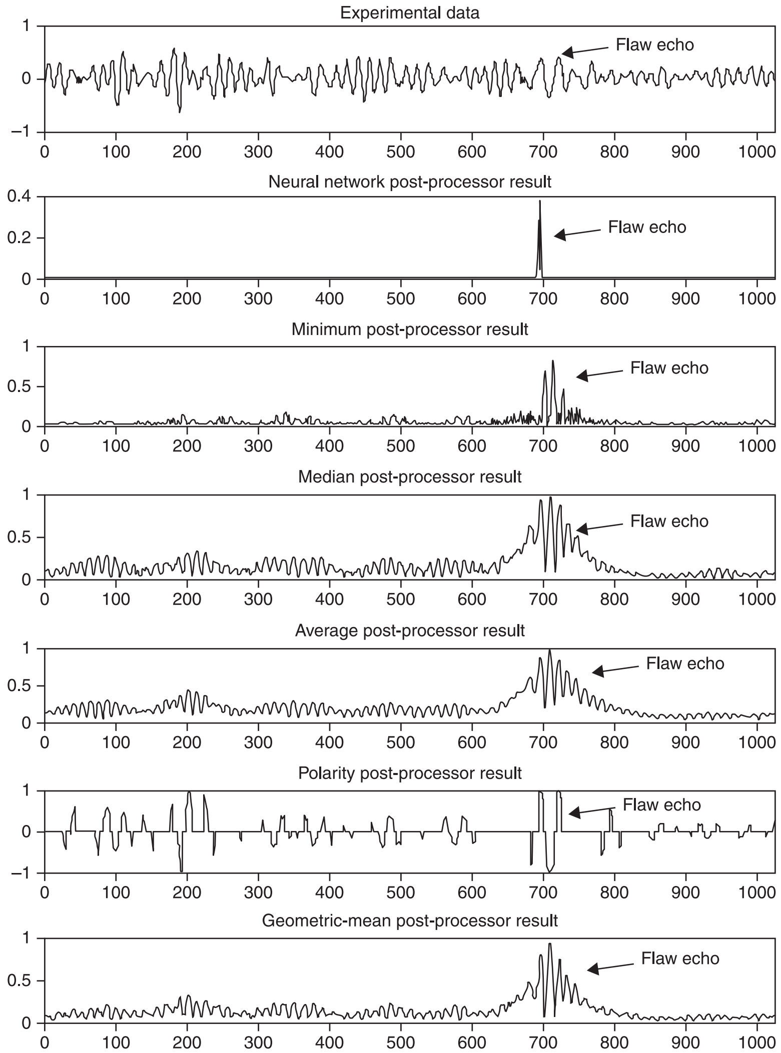

14.16 Comparison of the results from the various detectors applied to the SSP channels covering the low-frequency region.

techniques. The average FCR of the neural network detector is 46.8 dB; however, the average FCR of the minimum detector is 7.9 dB, when only the low-frequency region is covered. The FCRs of the other detectors are significantly lower than the minimum detector.

Figure 14.17 shows a comparison of the results from the various detectors applied to SSP channels covering the full-frequency spectrum (ranging from 1.5 MHz to 9 MHz) of the ultrasonic data. It is important to point out that null observations exist in this frequency range. The neural network can still detect the flaw signal, whereas the other detectors barely detect or fail to differentiate the presence of the flaw echo. In Fig. 14.16 and 14.17, the NN output values are very close to 0 for clutter echoes and significantly higher for target echoes. For the other detectors, the output values are normalized to −1 and 1, or 0 and 1 for presentation purposes.

These results confirm that the NN detector not only outperforms the conventional flaw-detection methods but also shows less vulnerability to null observations (third row in Table 14.1).

In the next section, we describe an FPGA-based hardware platform for real-time ultrasonic flaw-detection applications. Details of the architecture and implementation results are discussed.

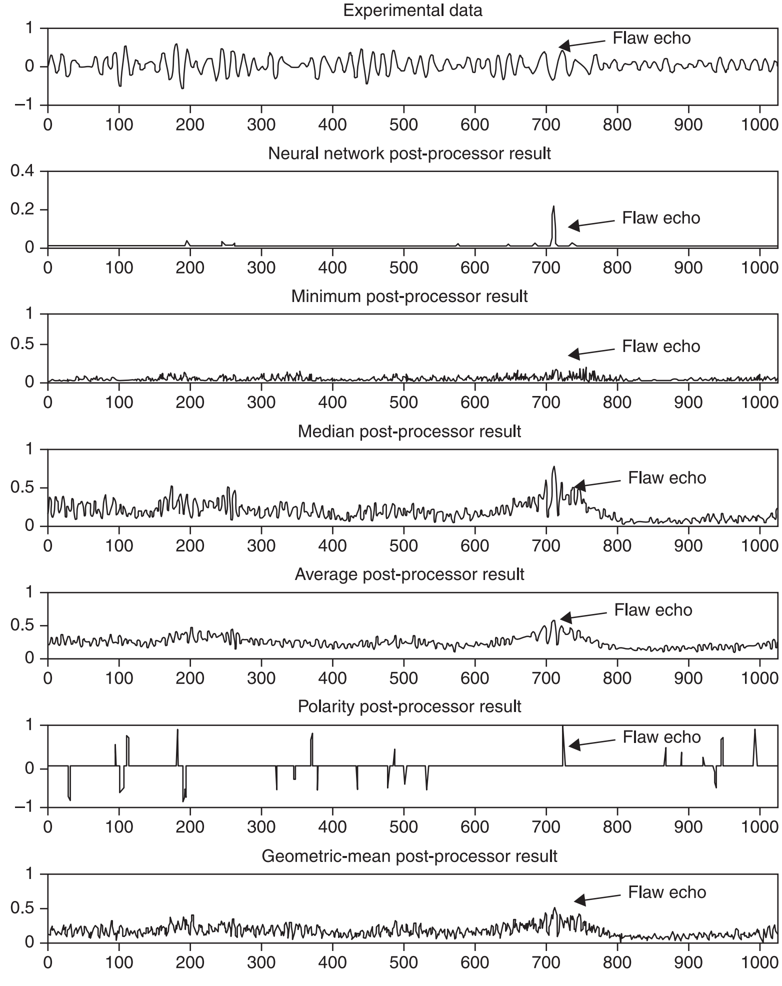
Experimental data

Neural network post-processor result

Minimum post-processor result

Median post-processor result

Average post-processor result

Polarity post-processor result

Geometric-mean post-processor result

14.17 Comparison of the results from the various detectors applied to the SSP channels covering the full-frequency spectrum.

14.5 System-on-a-chip implementation – a case study

A test system was designed and built to process real-time ultrasonic data using the SSP algorithm. An overview of the test system is shown in Fig. 14.18 (Weber *et al.*, 2011). The system has three major components. The first is the host computer, which allows a user to control the system and see all data and results. The application software runs on the host computer; it communicates with the hardware components implemented in an XtremeDSP unit produced by Nallatech (2005). This XtremeDSP unit combines a Xilinx Virtex-4 FPGA with dedicated analog-to-digital converter (ADC) and digital-to-analog converter (DAC) chips in a convenient package. The final component is the transducer and pulse generator. The pulse generator takes in a low-voltage transistor-transistor-logic signal and generates a high-voltage pulse to excite the transducer. In addition, it acquires the reflected echo.

14.5.1 Hardware realization

For real-time ultrasonic detection, a system requires three modules: communications, signal processing and signal capture. All three modules were packaged in a Xilinx Virtex-4 FPGA (Xilinx, 2008), which is supplied with the Nallatech XtremeDSP development kit. This board also provides other components used in the system: the dedicated ADC and DAC chips, fixed and programmable oscillators, a dedicated Virtex-II FPGA for clock management and a dedicated Spartan-II FPGA for PCI/USB communications control.

The *signal-capture* module controls the firing of the transducer and the capture of all echo data received by the dedicated ADC chips. It also provides a level of pre-processing of the incoming data with a configurable amplifier. It is important to note that the clock domain in this module is separate from the data-processing

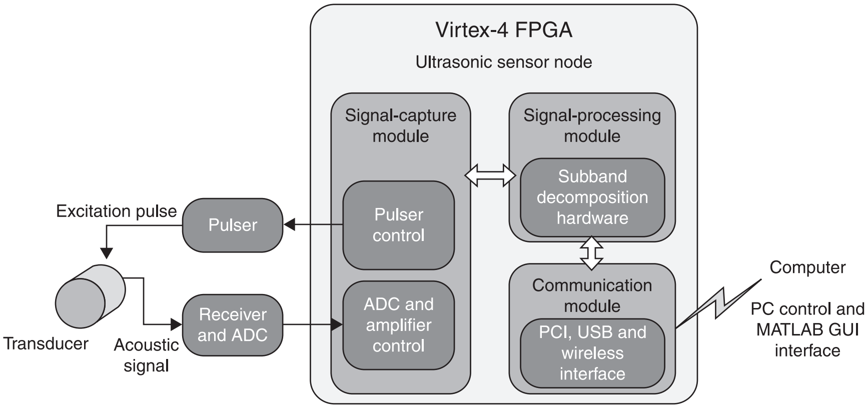
Virtex-4 FPGA
Ultrasonic sensor node
Signal-capture module
Signal-processing module
Subband decomposition hardware
Excitation pulse
Pulser
Pulser control
Communication module
Computer
Receiver and ADC
ADC and amplifier control
PCI, USB and wireless interface
PC control and MATLAB GUI interface
Transducer
Acoustic signal

14.18 Test system for processing real-time ultrasonic data using the SSP algorithm.

element. Hence, the sampling rate of the device is independent of the clock rate of the processing unit. This enables independent optimization of the clock rate and the sample rate for maximum performance.

The *communication module* provides an interface to the host PC and oversees all communications. It provides two primary services. It creates a register file and has the ability to access the registers through a memory-mapped interface and a direct memory access (DMA) interface that can easily be connected to internal block RAMs (BRAMs). It accomplishes this using a separate dedicated FPGA, which provides all the PCI or USB interfacing requirements, simplifying the design and making it more manageable. The system also has 16 separate channels for DMA access. These 16 channels can be connected to any internal BRAM within the FPGA. This is very useful for debugging and for verification of the system.

The *signal-processing module* implements the SSP algorithm. It performs all the transformations and computations to produce the final output data. It gathers input data from the signal-capture module and obtains parameter values from the communication module. As data flow into the module, they are transformed to the frequency domain through an FFT module. The FFT module used is a Radix-2-based IP core provided by Xilinx (Xilinx, 2010). This module is highly optimized by Xilinx to take full advantage of the dedicated digital-signal-processing blocks within the Virtex-4 device. Controlled by a design configuration parameter, the FFT is implemented with an 8-bit input precision. The data dynamically grow to a 19-bit output, which is then truncated to 16 bits before being passed on to the rest of the system. The output of the FFT module is decomposed by bandpass filters. The filters have dynamic set points. Both the center frequency and bandwidth of the filters are controlled by user-writable registers in the communication module. This allows the user to change the bandpass filter parameters without reconfiguring the FPGA. The filter parameters are chosen to optimize the subbands and are selected to cover the entire bandwidth of the echo response.

The subband channels are transformed by the inverse FFT (IFFT) modules. Since all subbands are independent, parallel IFFT modules are used to increase performance. The IFFT modules, like the FFT module, are highly optimized Xilinx IP cores. They take the 16-bit input and grow it to 27 bits. The resulting data are then processed without further truncation. By eliminating truncation, a very high dynamic range is achieved, which helps the hardware to perform very closely to the ideal software representation.

14.5.2 Application software

In order to maintain modularity and reusability, a software package was designed in a layered manner (Fig. 14.19). At the most basic level is the PCI/USB communication driver, controlled by the PC operating system. Above that is the communication application programming interface (API) developed by Nallatech. This provides support for basic communication between the host PC and the

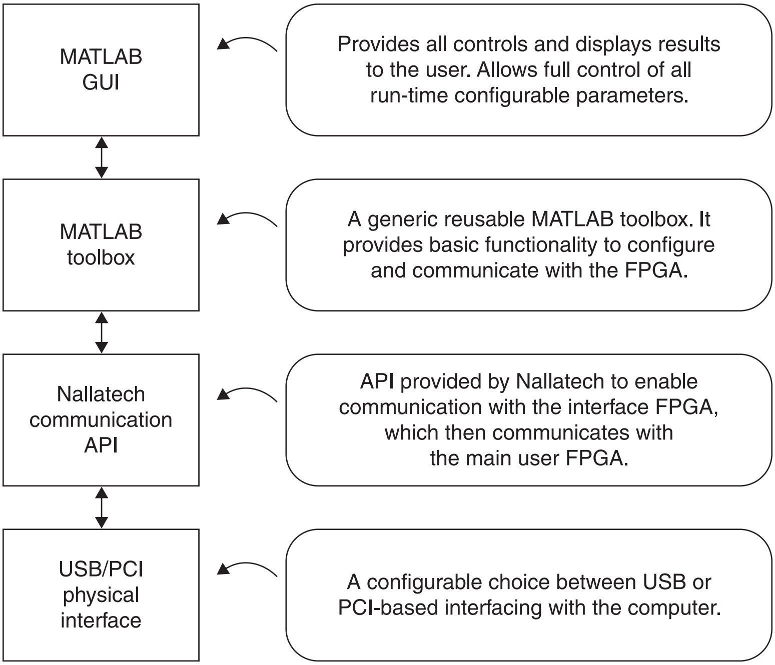
MATLAB GUI
Provides all controls and displays results to the user. Allows full control of all run-time configurable parameters.
MATLAB toolbox
A generic reusable MATLAB toolbox. It provides basic functionality to configure and communicate with the FPGA.
Nallatech communication API
API provided by Nallatech to enable communication with the interface FPGA, which then communicates with the main user FPGA.
USB/PCI physical interface
A configurable choice between USB or PCI-based interfacing with the computer.

14.19 Software interface for the ultrasonic flaw-detection system.

hardware components. It provides memory map register access and 16 DMA channel access to the internal memory blocks. Furthermore, in order to enable a simple interface to the hardware, a new MATLAB toolbox was developed. This toolbox acts as a wrapper around the Nallatech-developed API, providing a more convenient design for the most common communications between the host PC and the hardware.

In the following sections, a full hardware implementation is compared with various hardware/software (HW/SW) partitioning schemes.

14.5.3 Hardware/software co-design

A hardware/software co-design approach (Micheli and Gupta, 1997) enables a more robust design, which can comfortably meet the system requirements. The hardware/software design was developed with the Xilinx Embedded Development Kit (EDK) and targeted at an FPGA device with an embedded softcore MicroBlaze processor.

Initially all processing was executed by software running on a MicroBlaze processor. In order to improve performance, the FFT transform was realized in hardware through the addition of an FFT-accelerator co-processor. The FFT-accelerator co-processor was implemented as a custom VHDL-based design.

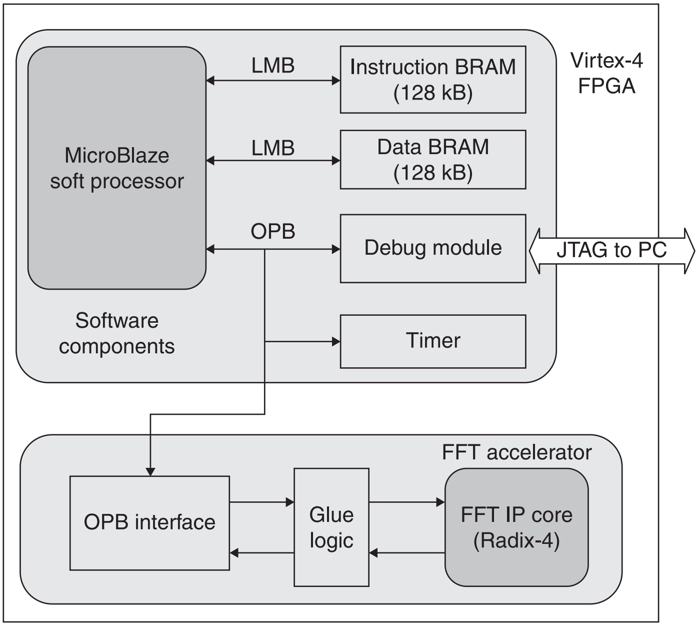
LMB
Instruction BRAM (128 kB)
Virtex-4 FPGA
MicroBlaze soft processor
LMB
Data BRAM (128 kB)
OPB
Debug module
JTAG to PC
Software components
Timer
FFT accelerator
OPB interface
Glue logic
FFT IP core (Radix-4)

14.20 Hardware/software co-design. The local memory bus is labeled LMB.

This accelerator was interfaced to the MicroBlaze processor through the on-chip peripheral bus (OPB) as shown in Fig. 14.20. Keeping the accelerator, processor and bus all within the same FPGA device gives very high performance. A software driver was created and the software design was updated to pass data to the accelerator and receive the FFT results. This accelerator demonstrates the integration of hardware design techniques with software design.

14.5.4 Software and hardware performance evaluation for SSP

The SSP detection performance of the software architecture (C code running on an embedded MicroBlaze processor) had identical performance to the theoretical MATLAB implementation. This performance result was expected. The software implementation used the same floating-point representation of the data as MATLAB. Therefore, there was no change in performance for the software implementation.

On the other hand, both the hardware architecture and the hardware/software co-design with the FFT accelerator used fixed-point hardware-based FFT processing units. Due to the fixed-point representation and the limited word length, there was some inherent data imprecision when calculating the FFT transforms. The final effect of this result is a decrease in overall system performance. For ten different data sets, the performance of the hardware architectures is given in Table 14.2.

Table 14.2 Comparison of FCR improvement using different hardware and software (HW/SW) co-design techniques using minimum detector

Data set	Input FCR (dB)	Software implementation 4-channel (dB)	Software implementation 8-channel (dB)	HW/SW co-design 4-channel (dB)	Hardware Radix-2 4-channel (dB)	Hardware Radix-2 8-channel (dB)
1	3.69	6.50	8.91	8.96	3.02	11.90
2	–2.33	15.80	17.12	15.46	12.31	13.20
3	2.24	12.67	11.96	9.67	8.73	8.90
4	–3.74	16.36	17.44	14.00	10.11	13.30
5	0.00	10.39	12.18	10.53	7.31	9.95
6	1.54	10.22	9.89	7.24	7.43	8.78
7	2.69	11.10	13.77	9.08	8.49	10.29
8	4.14	7.21	12.31	9.99	5.50	10.78
9	4.25	8.38	7.35	4.44	0.87	7.44
10	–1.70	10.27	10.42	11.43	10.48	12.39
Average	1.07	10.89	12.14	10.08	7.43	10.69

It is also important to notice that the 8-channel implementation is able to achieve results much closer to the theoretical ideal. In addition to the overall performance, the 8-channel implementation has a standard deviation of 1.98 compared with a standard deviation of 3.48 for the 4-channel approach. Hence, the 8-channel implementation provides a much more robust performance. The reason for this more robust performance is the placement of the window filters. The 8-channel result is able to use smaller filters with a similar overlap, and is still able to cover a larger portion of the frequency spectrum.

14.5.5 Execution time

For ultrasonic imaging, a real-time rate is considered to be a processing rate exceeding 1 kHz. This gives only a short 1-ms time window to perform all capture and processing of data. The execution times for the architectures are shown in Table 14.3. This table breaks down the execution time for each algorithmic processing step.

The pure software approaches fail to reach the real-time requirement. The basic software implementation with only a simple processor without a floating-point unit (FPU) struggles to perform all the computations. With a more complicated microprocessor, incorporating an FPU, the execution time of the design improves to 37.7 ms, although still well below the required rate. Both of these designs demonstrate that a software-only solution is not reasonable for this application.

Table 14.3 also shows the execution time for both Radix-2 and Radix-4 pure hardware architectures. These implementations aim for high performance using fast hardware processing elements and a highly parallel implementation, with multiple FFT cores for faster processing. Correspondingly, the designs easily exceed the processing rates required and provide orders of magnitude improvement in execution time compared with the software implementations, being 370 times faster.

As expected, the hardware/software co-design architecture has the middle-ground performance between the two pure designs. The hardware/software co-design is able to achieve a performance rate of 3.05 ms. While the design currently does not meet the real-time requirements, it is close enough to be optimized to achieve the needed performance. With a final optimization of the clock rate and code optimization it would be reasonable to expect performance gains to meet the requirements.

14.5.6 Resource usage

Resource usage is characterized with the three major resources provided within the Xilinx Virtex-4 FPGA device: logic slices, block RAMs and DSP48s. Logic slices are the fundamental configurable logical resources in an FPGA. They perform all logic, arithmetic and ROM storage and have elements to enable

Table 14.3 Processing time of the SSP algorithms

Algorithm stage	Software without FPU (cycles)	Software with FPU (cycles)	HW/SW co-design with FFT accelerator (cycles)	Hardware only (Radix-2 FFT IP-core) (cycles)	Hardware only (Radix-4 FFT IP core) (cycles)
FFT	28 764 300	599 026	3 456	5 190	1 322
Bandpass filtering	98 884	99 153	91 456	1 024	1 024
Inverse FFT	109 978 539	2 396 039	13 824	5 190	1 322
Post-processing	1 086 792	66 169	196 661	1 024	1 024
Total cycles	140 540 767	3 772 536	305 397	12 428	4 692
Total execution time	1 405.5 ms	37.7 ms	3.05 ms	108 μs	40.8 μs

Table 14.4 FPGA resource usage (number of components) for implementing SSP

	Software architecture without FPU	Software architecture with FPU	HW/SW co-design	Hardware architecture (4-channel)	Hardware architecture (8-channel)
Slices	1 307	1 886	5 836	8 378	14 505
DSP48	3	7	25	30	54
RAM16	35	35	39	28	48

distributed RAM storage. The particular device used provides support for up to 30 720 slices. For larger RAM storage needs, the device also provides 192 distributed dual port 18-kbit RAM blocks. The final important resource items provided are 192 DSP48 elements (Xilinx, 2007).

The evaluation of these three resources is a good representation of the cost of the implementation. The resource consumption for the designs is shown in Table 14.4. The resource usage tends to follow the trend in execution time. As the designs become more complex, they are able to achieve better performance.

14.6 Future trends

A common challenge today for ultrasonic imaging is the synergetic integration of sensor devices, signal-processing units and miniaturization. There has been an increasing demand for portable, handheld sensor devices, which can operate not only in controlled environments such as laboratories or clinics but also in the field. These devices could have a major impact on the ease of use and simplification of the diagnosis processes for medical practitioners or test engineers. However, there are major design challenges for the development of compact sensor devices:

Low-power consumption: Portable and handheld devices use battery power. Consequently, power consumption should be kept to a minimum in order to obtain a truly field-operable device.

Compact size: Besides power consumption, portable devices have a very limited space for the hardware components. An ideal solution would be tighter integration of the components with a system-on-a-chip (SoC) design. SoC is a single chip solution for complete system implementation, with built-in embedded input/output interfaces, control units, processors and data-processing elements.

High computation rate: Real-time operation with instantaneous results is a critical requirement for ultrasonic systems. Therefore, the hardware and software components should be designed primarily to cope with the very complex computational requirements of real-time systems.

Adaptability: Evolving standards or the introduction of new testing, imaging or diagnostic techniques can cause a sensor device to become outdated in a very short time. An ideal system should be designed in such a manner that the hardware kernel can be updated in order to make it future-proof. It is also important to have a feature-proof system in which more functionality can be added.

Network connectivity: The sensor device should be capable of transmitting and receiving data over the internet.

Integration with MEMS sensors: A complete system-on-a-chip solution necessitates using MEMS sensor arrays for imaging, target detection and classification.

In order to meet the design criteria, optimization is required of both the architecture and the algorithms. The following technology and signal-processing trends are promising for the next generation of ultrasonic imaging devices:

- The development of time-frequency (T/F) algorithms for robust target (flaw) detection and estimation. The backscattered signal information in ultrasonic nondestructive testing is nonstationary due to frequency-dependent scattering, attenuation and dispersion. Standard spectral analysis cannot determine the time of arrival of different frequency components in the signal. Joint T/F representations of such signals are more revealing. Therefore, T/F distributions such as the Gabor transform (GT), the Wigner–Ville distribution (WVD), the Choi–Williams (CW) distribution and the wavelet transform (WT) should be analyzed to see if they can be used for optimal ultrasonic flaw detection (Oruklu *et al.*, 2009).
- The design and synthesis of adaptive system-on-a-chip architectures that can support dynamic reconfiguration of on-chip processing engines through internal switches or partial programming of FPGA devices.
- Recently, similar multi-core and multiple processing element (PE) designs have been proposed in International Technology Roadmap for Semiconductors (ITRS) executive reports and conference proceedings: 'A possible ultimate evolution of on-chip architectures is asynchronous heterogeneous multi-core with hierarchical processors organization' (Hutchby, 2007). Reconfigurable ultrasonic imaging architectures that conform to the *more than Moore* domain definitions of the ITRS should be designed for sustaining high computational capability and adaptability (Oruklu and Saniie, 2009).
- Sensor development and integration for system-in-a-package (SiP) devices.
- ITRS long-term projections also indicate the need for SiP devices (ITRS, 2009). SiP devices focus on full integration with sensors and actuators, based on a wide range of new technologies such as MEMS sensors. Correspondingly, MEMS actuators can be integrated with digital signal-processing engines for a single chip solution in ultrasound imaging applications.

14.7 Conclusions

This chapter presented the theory and application of split-spectrum processing in ultrasonic flaw-detection problems. The frequency diversity of grain and flaw echoes suggests that order statistics and neural network post-processors can be used for enhancing flaw-echo visibility. When statistical information in observations deteriorates (e.g. null observations) and *a priori* information is not available, neural network post-processors perform more robustly. Furthermore, a case study demonstrated that reconfigurable embedded systems are capable of the real-time realization of ultrasonic imaging.

14.8 Further information

More information on this topic can be found in the journals: *IEEE Transactions on Ultrasonics*, *Ferroelectrics and Frequency Control*, *Journal of the Acoustical Society of America*, *Ultrasonics* (Elsevier) and in the *Proceedings of the IEEE Ultrasonics Symposium*, *International Congress on Ultrasonics* and meetings of the *Acoustical Society of America*.

14.9 References

Barton D K (1977), *Frequency Agility and Diversity (Radars, Volume 6)*, Artech.

Beasley E and Ward E (1968), A quantitative analysis of the sea clutter decorrelation system with frequency agility, *IEEE Transactions on Aerospace and Electronic Systems*, 4, 468–73.

Bilgutay N M and Saniie J (1984), The effect of grain size on flaw visibility enhancement using split-spectrum processing, *Materials Evaluation*, 42, 808–14.

Bilgutay N M, Saniie J, Newhouse V, and Furgason E S (1979), Flaw-to-grain echo enhancement, *Proceedings of Ultrasound International Conference*, 152–7.

Bilgutay N M, Bencharit U and Saniie J (1989), Enhanced ultrasonic imaging with split-spectrum processing and polarity thresholding, *IEEE Transactions on Acoustics, Speech, and Signal Processing*, 1722–32.

Cichocki A and Unbehauen R (1993), *Neural Networks for Optimization and Signal Processing*, Wiley.

David H A (1981), *Order Statistics, 2nd edition*, Wiley-Interscience.

Gurney K (1997), *An Introduction to Neural Networks*, CRC Press.

Haykin S (2008), *Neural Networks and Learning Machines, 3rd Edition*, Pearson.

Hornik K (1989), Multilayer feedforward networks as universal approximators, *Neural Networks*, 2, 359–66.

Hutchby J (2007), Emerging research devices, Japan, ITRS Conference. Available from: http://www.itrs.net/Links/2007Winter/2007_Winter_Presentations/06_ERD_2007_JP.pdf [Accessed 18 January 2011].

ITRS (2009), Executive summary, International Technology Roadmap for Semiconductors (ITRS), Available from: http://www.itrs.net/Links/2009ITRS/2009Chapters_2009Tables/2009_ExecSum.pdf [Accessed 18 January 2011].

Lind G (1970), Measurement of sea clutter correlation with frequency radar, *Philips Telecommunications Review*.

Masters T (1993), *Practical Neural Network Recipes in C++*, Academic Press Inc.

Micheli G D and Gupta R K (1997), Hardware/software co-design, *Proceedings of IEEE*, 85, 349–65.

Nagle D and Saniie J (1995), Performance analysis of linearly combined order statistic CFAR detectors, *IEEE Transactions on Aerospace and Electronic Systems*, 31, 522–32.

Nallatech (2005), Virtex-4 XtremeDSP, Development Kit User Guide, Lanarkshire, UK. Available from: http://www.xilinx.com/support/documentation/boards_and_kits/ug_xtremedsp_devkitIV.pdf [Accessed 18 January 2011].

Newhouse V, Bilgutay N, Saniie J and Furgason E (1982), Flaw-to-grain echo enhancement by split-spectrum processing, *Ultrasonics*, 59–68.

Oruklu E and Saniie J (2009), Dynamically reconfigurable architecture design for ultrasonic imaging, *IEEE Transactions on Instrumentation and Measurement*, 58, 2856–66.

Oruklu E, Aslan S and Saniie J (2009), Applications of time-frequency distributions for ultrasonic flaw detection, *IEEE Ultrasonics Symposium*, 2000–3.

Papadakis E P (1965), Ultrasonic attenuation caused by scattering in polycrystalline metals, *Journal of the Acoustical Society of America*, 37, 703–10.

Saniie J and Nagle D (1992), Analysis of order statistic CFAR threshold estimators for improved ultrasonic flaw detection, *IEEE Transactions on Ultrasonics, Ferroelectrics and Frequency Control*, 39, 618–30.

Saniie J, Wang T, and Bilgutay N M (1988), Statistical evaluation of backscattered ultrasonic grain signals, *Journal of the Acoustical Society of America*, 84, 400–8.

Saniie J, Donohue K and Bilgutay N M (1990), Order statistic filters as postdetection processors, *IEEE Transactions on Acoustics, Speech, and Signal Processing*, 38, 1722–32.

Saniie J, Nagle D and Donohue K (1991), Analysis of order statistic filters applied to ultrasonic flaw detection using split spectrum processing, *IEEE Transactions on Ultrasonics, Ferroelectrics and Frequency Control*, 38, 133–40.

Saniie J, Wang T and Jin X (1992), Performance evaluation of frequency diverse Bayesian ultrasonic detection, *Journal of Acoustical Society of America*, 91, 2034–41.

Weber J, Oruklu E and Saniie J (2011), FPGA-based configurable frequency-diverse ultrasonic target detection system, *IEEE Transactions on Industrial Electronics*, 58, 871–9.

Xilinx (2007), XtremeDSP for Virtex-4 FPGAs user guide, San Jose, CA, Xilinx, Inc. Available from: http://www.xilinx.com/support/documentation/user_guides/ug073.pdf [Accessed 18 January 2011].

Xilinx (2008), Virtex-4 User Guide, San Jose, CA, Xilinx, Inc. Available from: http://www.xilinx.com/support/documentation/user_guides/ug070.pdf [Accessed 18 January 2011].

Xilinx (2010), LogiCORE IP Fast Fourier Transform v8.0, San Jose, CA, Xilinx, Inc. Available from: http://www.xilinx.com/support/documentation/ip_documentation/ds808_xfft.pdf [Accessed 18 January 2011].

Xin J, Donohue K D, Bilgutay N M and Li X (1991), Frequency diverse geometric mean filtering for ultrasonic flaw detection, *Materials Evaluation*, 987–92.

Yoon S, Oruklu E and Saniie J (2006), Dynamically reconfigurable neural network hardware design for ultrasonic target detection, *IEEE Ultrasonics Symposium*, 1377–80.

Yoon S, Oruklu E and Saniie J (2007), Performance evaluation of neural network based ultrasonic flaw detection, *IEEE Ultrasonics Symposium*, 1579–82.

15

Power ultrasonics: new technologies and applications for fluid processing

J. A. GALLEGO-JUÁREZ, Spanish National Research
Council (CSIC), Spain

Abstract: The industrial interest in ultrasonic processing has revived during recent years particularly because ultrasonic technology may represent a flexible 'green' alternative for energy efficient processes. The major challenge in the application of high-intensity ultrasound to industrial processing is the design and development of specific power ultrasonic systems for large-scale operation. For ultrasonic processing in fluid and multiphase media, the development of a new family of power generators with extensive radiating surfaces has significantly contributed to the implementation, at semi-industrial and industrial scales, of several applications in sectors such as the food industry, the environment and manufacturing. This chapter presents these new technologies and the implemented applications.

Key words: high-power ultrasound, ultrasonic processing.

15.1 Introduction

Power ultrasonics is the high-intensity application of ultrasonic energy. High-intensity applications are those where the ultrasonic energy is used to produce permanent changes in the treated medium. The boundary between low and high intensity is very difficult to fix, but it can be approximately established for intensity values which, depending on the medium, vary between 0.1 W/cm^2 and 1 W/cm^2.

Although the initial theoretical studies of high-intensity acoustic waves were conducted by Earnshaw, Rayleigh and others in the late nineteenth and early twentieth century, the starting point for the modern field of power ultrasonics was in 1917 when Paul Langevin first noticed the physical effects of intense ultrasonic waves. Langevin, a brilliant professor at the School of Physics and Chemistry in Paris, designed and constructed piezoelectric ultrasonic transducers with high-power capacity for underwater applications. He realized that small fishes in the acoustic beam in the neighbourhood of the source were killed. Following Langevin's work, during the 1920s Wood and Loomis conducted interesting experiments with high-intensity ultrasonic waves (200–500 kHz), such as the formation of emulsions, flocculation of particles suspended in a liquid, levitation of matter, etc. (Wood and Loomis, 1927). In the 1950s, the development of new transducer materials as well as rapid advances in electronics made possible the production of commercial power ultrasonic systems for practical applications.

During the last 60 years, the uses of power ultrasound, particularly in solid and liquid media, have been thoroughly investigated and a number of applications have been developed. Typical recent industrial applications of power ultrasonics include plastic and metal welding, machining, and metal forming in solids and cleaning, atomisation, emulsification and dispersion, degassing and sonochemical reactions in liquids. In recent years, there has been a renewed interest in ultrasonic processing, particularly in those sectors where the ultrasonic energy may represent a clean and efficient tool, for example in the food industry, the environment, pharmaceuticals, chemicals manufacture, etc. At present, the implementation of new environmentally friendly and energy-saving technologies is one of the main objectives in the improvement of the quality of life. Power ultrasound can be considered to belong to this class of technologies and its successful use in medical therapy has underlined its innovative character.

The potential of power ultrasound involves physical and chemical processes. The physical processes are mainly due to the mechanical effects of the high-intensity waves in a medium while the chemical processes are the chemical effects induced by ultrasonic cavitation in liquids. The latter processes are within the field of sonochemistry while the general term for the whole area is sonoprocessing or power ultrasonic processing.

The application of high-intensity ultrasonic waves is based on the adequate exploitation of the non-linear effects associated with high amplitudes, such as the radiation pressure, streaming, cavitation, dislocation in solids, etc. As a consequence of these effects, a series of mechanisms are activated by the ultrasonic energy, such as heat, agitation, diffusion, interface instabilities, friction, mechanical rupture, chemical reactions, etc. These mechanisms can be employed to produce or to enhance a wide range of processes that very much depend on the irradiated medium. In fact, a typical characteristic of high-intensity ultrasonic waves is their ability to produce different processes in different media in such a way that they seem to have opposite effects at times. For example, power ultrasound is used in liquid suspensions for particle dispersion and in gas suspensions for particle agglomeration. Such apparently contradictory behaviour is clearly due to the different mechanisms activated by the ultrasonic energy, which mainly depend on the specific medium.

Another characteristic of high-intensity ultrasonic waves is their capacity to work synergistically with other forms of energy. This is the reason why many practical applications of power ultrasound are not exclusively ultrasonic processes but ultrasonically assisted processes.

A major problem in the application of high-intensity ultrasound to industrial processing is the design and development of efficient power ultrasonic technology capable of large-scale successful operation specifically adapted to a particular process.

Most ultrasonic processes have been investigated in solid and liquid media and, for a number of these, specific technologies have been developed that are currently used in conventional commercial systems. However, there is a third important medium, gas, where the application of ultrasonic energy has been notoriously lacking. The reason lies in the difficulty of efficiently generating and propagating ultrasound through gases. Fluid media, and gases in general, have low specific acoustic impedance and high acoustic absorption, which hinder acoustic energy transmission.

Regarding ultrasonic processing in fluid media, and more specifically in gases, the development of a new family of power generators with extensive radiators has strongly contributed to the semi-industrial and industrial implementation of several commercial applications, in sectors such as the food industry, the environment and manufacturing.

The goal of this chapter is to show the present status and the potential of power ultrasonics as an innovative and clean tool for processing in fluids (gases and liquids) and multiphase media (i.e. fluids with suspended particles, drops or bubbles and porous solids with internal fluids). Therefore, new technologies for high-intensity ultrasonic generation will be presented as well as their application in several industrial sectors.

15.2 New power ultrasonic technologies for fluids and multiphase media

The extension of the application of power ultrasonics requires the development of adequate systems fulfilling the requirements for each specific problem. This is particularly necessary for industrial applications where the solutions have to be technically and economically effective.

At present, the main difficulty for the industrial extension of power ultrasonic processing originates in the generation devices. Most existing power ultrasonic transducers are still based on the classical piezoelectric sandwich transducer, which was originally designed by Langevin (1918), and, even when improved (Neppiras, 1973), it has many limitations for industrial use. First of all, these transducers are limited in power capacity and in dimension. This type of transducer vibrates along its length in extensional mode, and, to avoid coupling with radial vibration modes, the cross-sectional diameter has to be smaller than ¼ of the wavelength of the operating vibration mode. As a consequence their use in industry requires the development of multi-element assemblies, which have many practical difficulties, such as tuning the operating frequency and in achieving production quality standards. Moreover, the design of power ultrasonic transducers requires extensive knowledge about the non-linear behaviour of such devices at high driving voltages. Tuned systems, when driven at high power, exhibit a whole range of non-linear phenomena, such as frequency shifts, modal interactions, etc., which affect performance (Nayfeh and Nayfeh, 1994). Therefore, in the design of power ultrasonic devices, guidelines for eliminating or reducing their non-linear behaviour at high power are needed (Cardoni and Lucas, 2002).

Hence, there is a need to develop transducer technology with high-power capacity and efficiency, an extensive radiating area to cover a large volume, and sufficient control of the acoustic field to distribute it according to the needs of the specific application. The non-linear behaviour of transducers when operating at high excitation must be understood and there must be suitable designs to avoid or palliate modal interactions and other unwanted effects.

To meet these objectives, a new family of power ultrasonic transducers with extensive radiators having high-power capacity, high efficiency and radiation pattern control has been developed. They are called extensive radiating area transducers, and there are several versions depending on the shape or profile of the radiator, which is adapted for a specific application.

15.2.1 Characteristics of the new family of power transducers with extensive radiators

Fluids, and especially gases, have low specific acoustic impedance and high acoustic absorption. Therefore, in order to obtain an efficient transmission of energy, it is necessary to achieve a good impedance match between the ultrasonic radiation source and the medium, a large amplitude of vibration, and high-directional or focused beams for energy concentration. In addition, for large-scale industrial applications, high-power capacity and extensive radiating areas are required. The new family of power transducers has been designed and developed to meet all these requirements in one device (Gallego-Juárez *et al.*, 2010).

The basic structure of such transducers is schematically shown in Fig. 15.1. There is a piezoelectrically activated vibrator, which drives an extensive radiator. The vibrator itself has a piezoelectric element of transduction in a sandwich

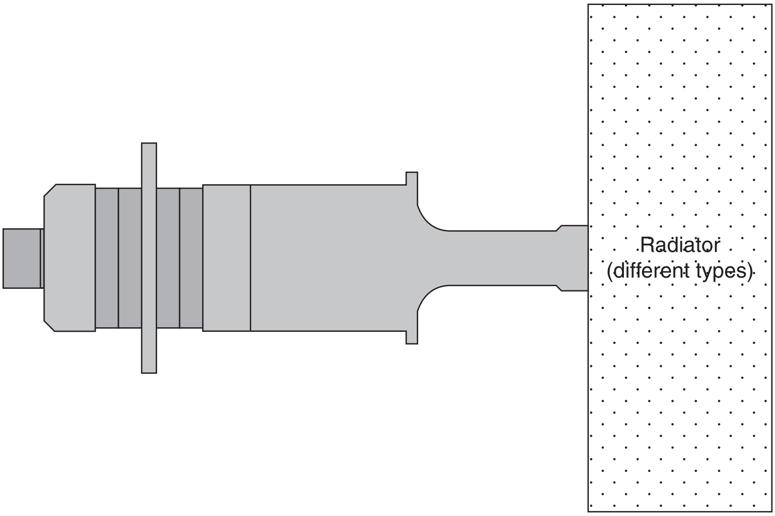

15.1 Basic structure of a transducer with an extensive radiator.

configuration and a solid horn, which acts as a vibration amplifier. The extensional vibration generated by the transducer element and amplified by the mechanical amplifier drives the radiator, which vibrates in one of its flexural modes. The extensive surface area of the radiator increases the radiation resistance and gives the vibrating system good impedance matching with the medium. The radiator is generally a circular or rectangular vibrating plate with a stepped, grooved or stepped-grooved profile. However, the radiator could be any shape adapted to a specific problem, such as a cylinder, a shell or anything else. The shape and profile of a radiator are designed to control the vibration distribution and the radiation pattern.

A transducer within the new family is characterized by the specific radiator and the main types developed are: the stepped-plate, the grooved-plate, the stepped-grooved-plate, the flat-plate with reflectors and the cylindrical radiator.

The basic characteristics and performance of each of these types of transducers will be described in the following sections.

The stepped-plate transducer

The stepped-plate transducer has the basic structure previously described. The radiator is an extensive circular or rectangular plate with a stepped profile vibrating in one of its natural flexural modes. The stepped profile of the plate allows the control of the radiation in such a way that the pattern can be tailored as needed. As a concentration of energy is generally required, high-directional and focusing radiators have been designed and developed in order to produce high-intensity acoustic levels.

The directional stepped profile: An extensive flat-plate radiator driven at ultrasonic frequencies will vibrate in one of its flexural modes and, as a consequence, will show a poor directivity pattern due to phase cancellation. Nevertheless, if the surface elements vibrating out of phase on the two sides of the nodal lines are alternately shifted along the acoustic axis by half a wavelength of the sound in the propagation medium, the radiation produced will be in phase across the whole beam (Fig. 15.2) and a directivity pattern equivalent to that of a theoretical piston will be obtained. The effect is clearly observed by comparing the measured directivity diagrams of a flat-plate radiator and a stepped-plate radiator with the same diameter and frequency (Fig. 15.3). The latter coincides with the computed diagram for a theoretical piston having the same diameter. In this way, we are able to design and construct piston-like radiators of any surface area and for any frequency.

The focusing stepped profile: Following a similar procedure it is possible, with adequate displacements of the different plate zones, to achieve any acoustic field configuration. Figure 15.4 shows the procedure used in designing focusing radiators. Because the plate zones separated by a nodal line vibrate out of phase, the radiated energy can be focused on a zone around a point, *P*, by modifying the

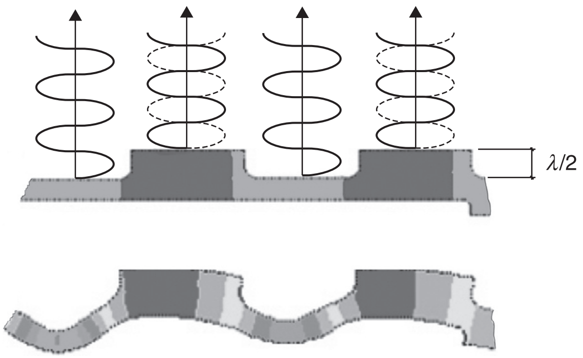

15.2 Phase matching effect of the radiated wave by the stepped-plate radiator.

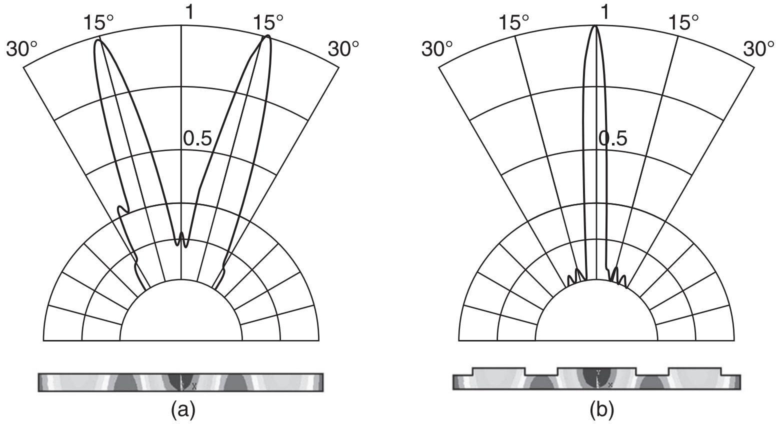

15.3 Directivity diagrams for a flat-plate radiator (a) and a stepped-plate radiator (b) with the same diameter and frequency.

profile of the plate in such a way that the plate zones between two nodal lines are shifted of a height h_i with respect to the maximal thickness of the plate, which is determined according to the following rule:

$$d_o = z_o \quad [15.1]$$

$$d_i = \left[(z_o + h_i)^2 + r_i^2\right]^{\frac{1}{2}} \quad [15.2]$$

$$d_i - d_{i-1} = \lambda/2 \quad [15.3]$$

where λ is the wavelength of the radiation in the medium and the subscript $i = 1, 2, 3, n$, indicates the different internodal zones.

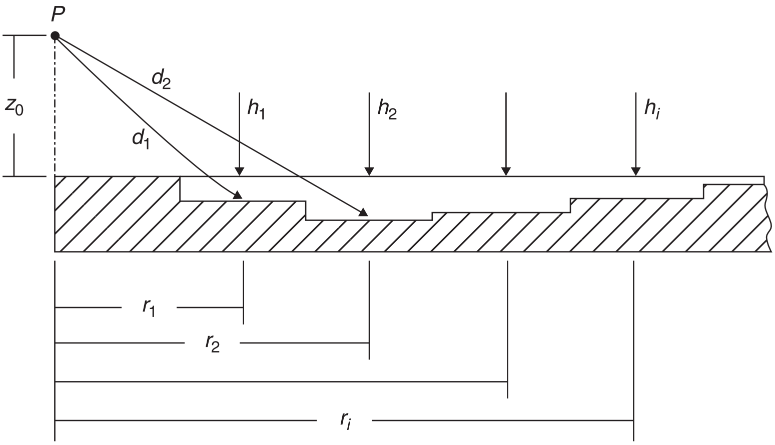

15.4 Procedure used to design focusing radiators.

As already mentioned, circular and rectangular stepped-plate transducers have been developed. In the first type of transducer, the plate radiator vibrates in one selected axisymmetric flexural mode while in the other the plate radiator vibrates in one flexural mode with nodal lines parallel to one of the sides of the plate. In both types of transducer, the plate radiator is driven at its centre by a length expander vibrator. Different prototypes of circular stepped-plate directional and focusing transducers have been developed for the frequency range 10–40 kHz and power capacities up to about 1 kW (Fig. 15.5). The design of these transducers,

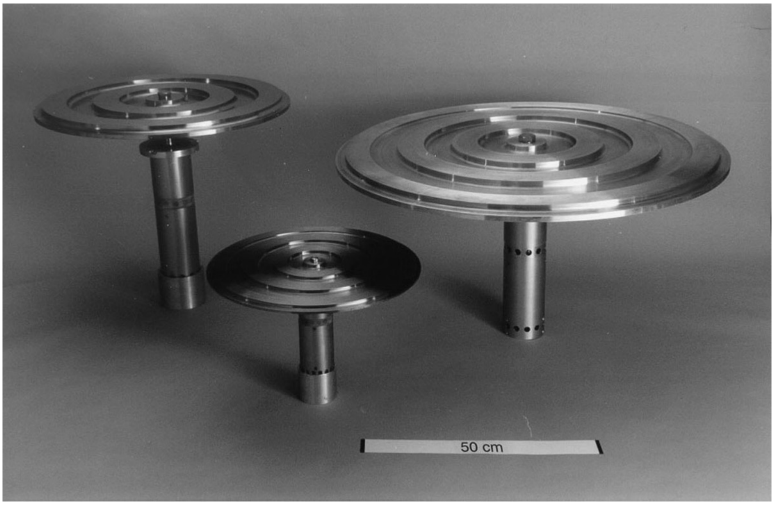

15.5 Prototypes of circular stepped-plate directional and focusing transducers.

Table 15.1 Main characteristics of directional circular stepped-plate transducers

Electroacoustic efficiency	75–80%
Directivity (3 dB beamwidth)	<2°
Maximum power capacity	1 kW
Frequency range	10–40 kHz
Maximum intensity levels	175 dB

initially using analytical methods, was further improved by finite element (FE) modelling. The main characteristics of directional circular stepped-plate transducers are summarized in Table 15.1.

The radiation pattern of one of these transducers, with a plate radiator of diameter 480 mm, is shown in Fig. 15.6. Figure 15.7 shows the acoustic field of a

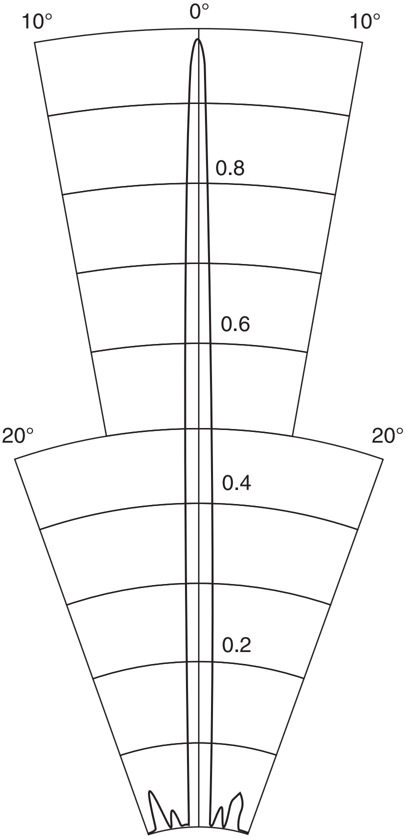

15.6 Radiation pattern of a directional circular stepped-plate transducer, with a plate radiator of diameter 480 mm and an operating frequency of 21 kHz.

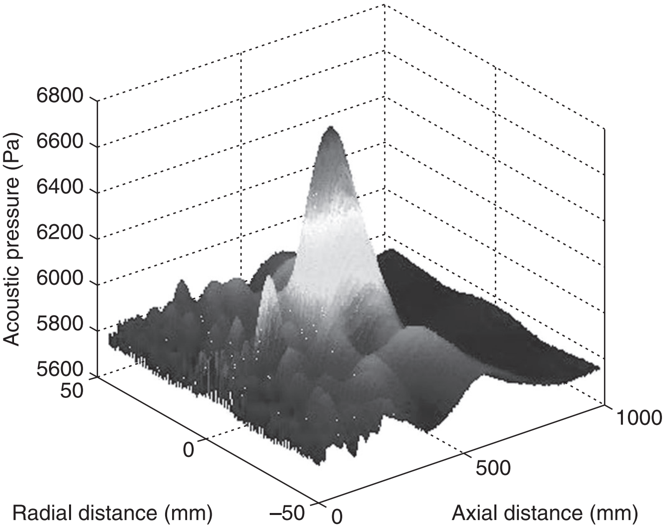

15.7 Acoustic field of a focusing circular-plate transducer with a plate radiator of diameter 390 mm and an operating frequency of 25.8 kHz.

focusing circular-plate transducer with a plate radiator of diameter 390 mm and an operating frequency of 25.8 kHz. The ultrasonic energy is concentrated in a focal volume of about 20 mm in diameter and 170 mm in length (dimensions taken at 3 dB of the maximum value), located at a distance of about 400 mm from the plate. Intensities of the order of 170 dB were obtained in the focus where the power applied to the transducer was 200 W. The acoustic field was measured as a continuous wave in an anechoic chamber 7.4 long, 5.6 wide and 5.5 m high using an 1/8 inch condenser microphone (B&K 4138).

For specific industrial applications, stepped-plate transducers with rectangular radiating surfaces have technical and practical advantages over transducers with circular radiators. Rectangular stepped-plate transducers have been designed and constructed with radiators operating in a resonant mode with 14 nodal lines parallel to the smaller side. Prototypes for 7 and 20 kHz have been developed with power capacities up to 2.7 kW (Fig. 15.8). The main characteristics are shown in Table 15.2. The directivity patterns are shown in Fig. 15.9.

The grooved-plate transducer

The performance of industrial transducers very much depends on their behaviour under high strain levels. There are power limitations on the industrial use of power ultrasonic devices; one of the more important ones is the difficulty of attaining very high power levels without non-linear disturbances and the other is the distribution and location of the stresses in order to maximize power capacity.

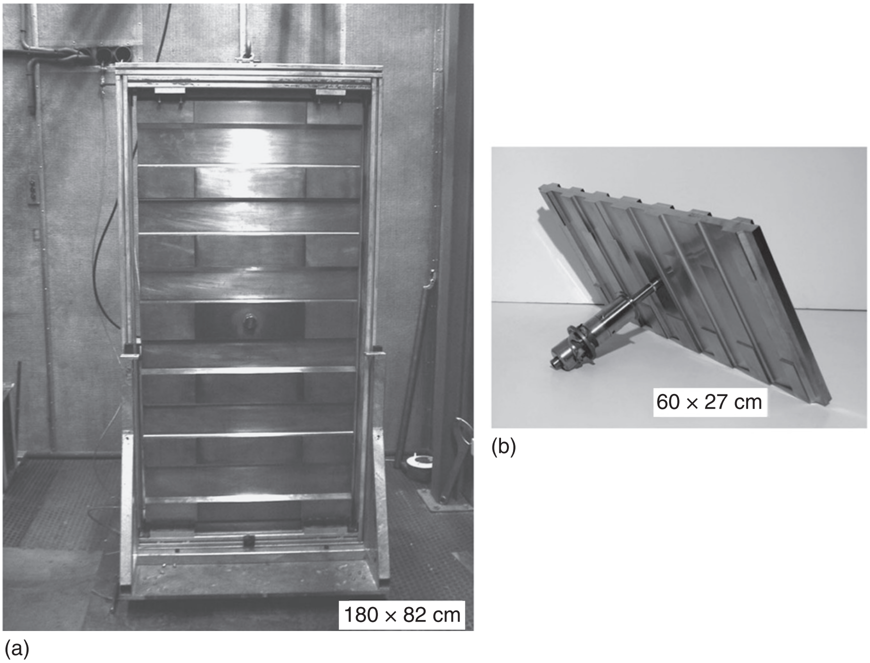

15.8 Prototypes of rectangular stepped-plate transducers for 7 kHz (a) and 20 kHz (b).

Table 15.2 Main characteristics of directional rectangular stepped-plate transducers

Radiating plate (m^2)	Frequency (kHz)	Bandwidth (Hz)	Directivity (3 dB beamwidth)		Efficiency (%)
			xz plane	*yz* plane	
1.8 × 0.8	7.6	1	About 2°		67
0.6 × 0.3	19.5	2.5	About 2°		75

The complexity of the structure of plate transducers, which are high modal density systems and combine longitudinal and flexural vibrations at the required tuned frequency, makes it difficult to avoid modal interactions at high power. Plate transducers frequently have, for some value of applied power, unwanted modes, giving rise to modal interactions, the energy being channelled from the excitation into other large-amplitude vibrations impeding power operation (Gallego-Juárez *et al.*, 2008).

Therefore, the design and development of reliable high-power ultrasonic transducers require identifying the possible modal interactions and implementing the design modifications needed to avoid or to palliate them.

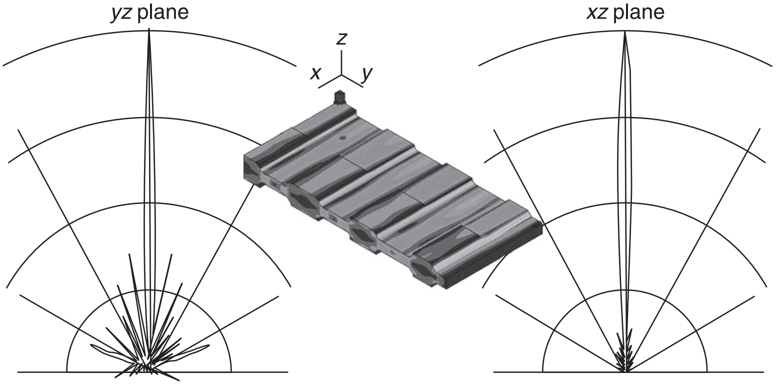

15.9 Directivity patterns of rectangular stepped-plate transducers.

The design procedure starts with an experimental investigation of the vibrational behaviour of a tuned transducer under high-power excitation and the study of design modifications to reduce or eliminate the effects of modal participation other than of the tuned mode. One of the main causes of modal interactions is the close proximity of an untuned mode to the operating driving frequency. The design strategy to mitigate this modal interaction is to separate the operating mode from undesired neighbouring modes by modifying the plate radiator. The methodology uses fine adjustments of the balance between the masses of the different zones of the plate radiator in order to magnify as much as possible the response of the operating tuned mode and, at the same time, to weaken or to move away the undesired neighbouring mode. One practical procedure is to create grooves in the back face of the plate radiator in appropriate zones. Using finite element modelling, it is possible to increase the separation between neighbouring modes for the cases considered. Such grooved-plate transducers can operate at higher power excitation without modal interactions (Gallego-Juárez *et al.*, 2008).

The other important requirement for the reliable and safe industrial operation of plate transducers is the distribution and location of the stresses in the plate radiator. These affect the power capacity, which directly depends on the maximum stress that the plate is able to withstand without failure of the material. Therefore, as a first condition, the plate must be made of a highly fatigue-resistant material, generally a titanium alloy. In addition, the stresses at the vibrating surface should be, as much as possible, uniformly distributed. In a flexural vibrating plate the objective should be to smooth out as much as possible the stress differences to give a balanced stress distribution. For that reason, the profile of the back face of the plate can be modified with slight grooves, which remove mass from particular plate zones. Such modifications are guided by FE modelling and depend on the vibration mode of the plate radiator.

The stepped-grooved-plate transducer

A stepped profile controls and selects the radiation pattern, while a grooved profile separates out untuned vibration modes to avoid or to mitigate modal interactions, as well as to produce a more uniform distribution of the stresses to increase power capacity. These two profiles are not opposite but complementary. Transducers with stepped-grooved-plate radiators have been designed by incorporating the two different profiles on the two faces of the plate. In addition, it has been possible, with some approximations, to combine a grooved profile with the focusing design. In this way, prototypes of circular-plate transducers with a stepped face for directional radiation and a grooved face for focusing the radiation have been designed and developed. In their practical realization, the theoretical stepped profiles for directing and focusing the radiation were slightly modified to improve the behaviour of the radiator with respect to modal interactions and stress distribution. Hence, plate transducers with high-power capacity and two different radiation patterns were constructed. Figure 15.10 shows two pictures of one of these transducers with an operating frequency of 41.3 kHz.

The flat-plate transducer with reflector

For directional stepped-plate radiators, the height of the steps has to be equal to half a wavelength of the radiation in the propagation medium. For ultrasonic radiation in air, the wavelength is shorter than 2 cm, but in water the wavelength is five times longer. Therefore, it is not practical to design directional stepped-plate transducers for water at low ultrasonic frequencies due to the required height of the steps. To obtain directional radiation in liquids (or in air at sonic frequencies) without using steps, a new type of vibrating-plate transducer was designed and constructed. The objective is to obtain highly directional radiation with a feasible

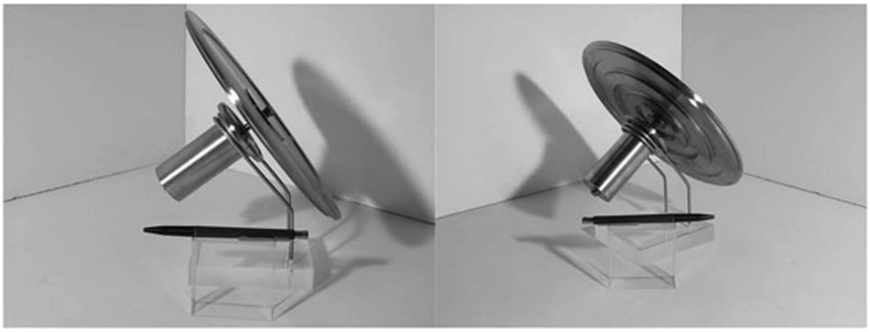

15.10 Prototype of a stepped-groove-plate transducer with an operating frequency of 41.3 kHz.

and easily repeatable construction. In addition, the new transducers use radiation from both faces of the vibrating plate. This is very important because it effectively doubles the efficiency of the transducer.

This design changes the phase of the radiation emitted by plate zones vibrating out of phase to make them in phase. However, using radiation from both plate faces means that the emissions from one specific plate sector will be out of phase on both sides of the plate.

The procedure consists of separating the radiation from each internodal sector using parallel walls perpendicular to the plate surface and exactly located in the nodal lines, without touching the plate. These walls are made of an aluminium alloy and are placed at 45° to the radiating surface. They form channels, which are closed by a reflector (Fig. 15.11). The distance from the reflector to the surface of the radiating plate differs for the sectors vibrating in and out of phase by half a wavelength ($\lambda/2$). Radiation generated by the flexural vibrating plate and reflected by the reflector, located alternately at distances of l and l+$\lambda/2$, emerges wholly in phase perpendicular to the plate (Rodríguez *et al.*, 2001). Figure 15.12 is a photograph of a prototype of a transducer for operating in air at a sonic frequency of 9.7 kHz. The highly directional radiation obtained (Fig. 15.13) confirms the good performance of this transducer configuration.

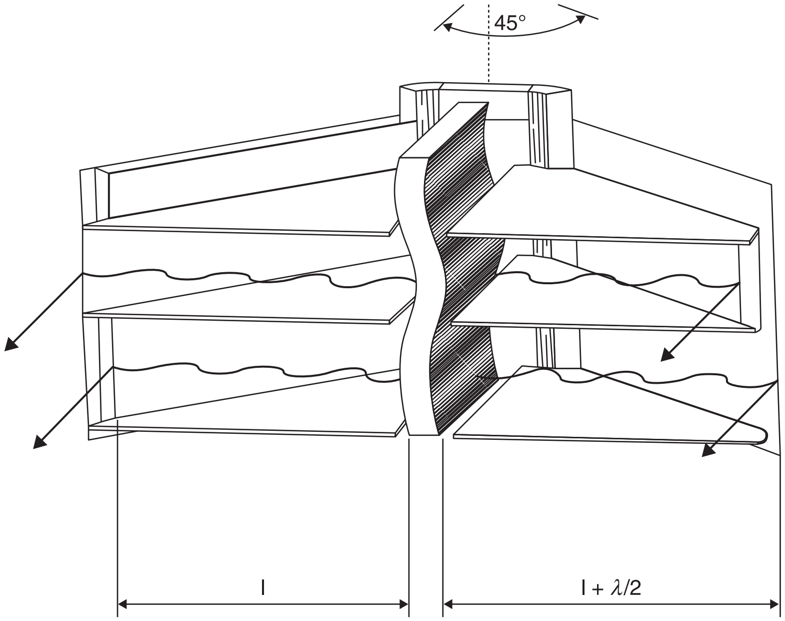

15.11 Flat-plate transducer with reflectors.

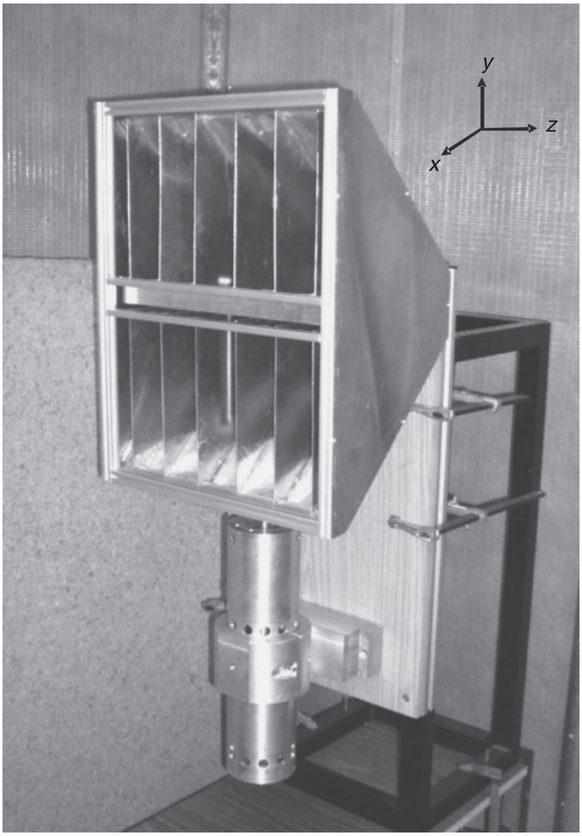

15.12 Prototype of a flat-plate transducer with reflector for operating in air at a sonic frequency of 9.7 kHz.

The transducer with cylindrical radiator

For applications where an intense ultrasonic field is required inside a treatment chamber, the chamber itself can be used as an ultrasonic radiator. A transducer with a cylindrical radiator has been conceived and developed, having the same general structure as shown in Fig. 15.1, but where the radiator is a cylinder instead of a plate. The cylinder is driven in one of its flexural modes.

In the prototype shown in Fig. 15.14, the cylindrical radiator vibrates with 12 nodal lines at a frequency of 21 kHz. The acoustic field inside the tube was computed and experimentally validated. When the power applied to the transducer was about 75 W, an average sound pressure level of about 153 dB was obtained inside the cylindrical chamber. Therefore, a high acoustic field was generated for relatively low power (Riera *et al.*, 2004b).

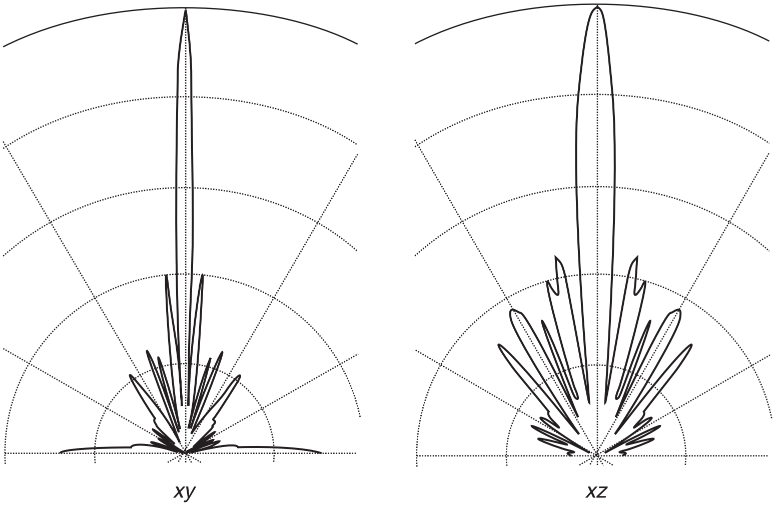

15.13 Directivity diagrams for a flat-plate transducer with reflector.

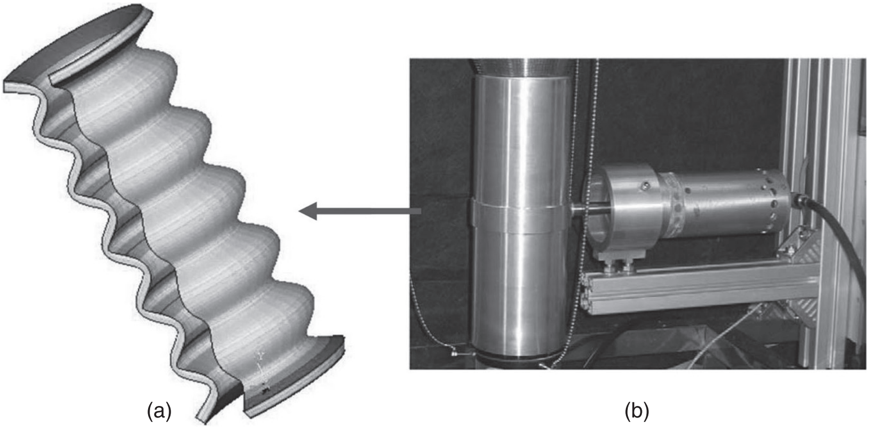

15.14 (a) Simulation of the vibration of a cylindrical radiator using finite element analysis. (b) Prototype of a transducer with a cylindrical radiator.

15.3 Application of the new power ultrasonic technology to processing

The new family of transducers with extensive radiators and the corresponding electronics for driving the single transducer units and controlling their resonance has significantly contributed to the semi-industrial and industrial implementation of a number of ultrasonic processes in the food industry, the environment and manufacturing. Each type of transducer was conceived and designed for a specific application.

15.3.1 Ultrasonics in food processing

The application of power ultrasound to food processing is one of the most promising fields for the future of ultrasound. The clean action of ultrasonic energy as mechanical non-contaminating non-ionizing radiation is important in the ongoing search for safer and higher quality production methods.

Despite the broad range of potential uses of power ultrasound in food processing, only a few processes have been established industrially. Recently, however, new processes have been developed and are starting or close to commercial introduction, such as defoaming, dehydration and supercritical fluid extraction assisted by ultrasound.

Ultrasonic defoaming

Foam is the dispersion of gas bubbles in liquid separated by a thin liquid film. It is generally an unwanted by-product in industrial processes because it causes difficulties in process control and in equipment operation. A typical example is in fermentation, where foam is one of the biggest problems; it is the cause of many adverse effects such as the loss of culture fluid and cells, contamination of the atmosphere, blocking oxygen transfer, corrupting fermentation data, etc. (Ghildyal *et al.*, 1980). Conventional defoaming methods employ thermal, chemical and mechanical effects. Thermal methods involve heating or cooling the foam, which is generally difficult and expensive. Chemical defoaming uses antifoam agents to reduce surface tension, which is, generally, very effective but may cause contamination. Mechanical methods rupture the bubbles by mechanical shocks, using rotating devices, air or liquid jets, vacuum systems, etc. In general, mechanical methods are effective only for coarse foams.

High-intensity ultrasonic waves are a clean and efficient way to break foam bubbles. The first application of ultrasound for foam breaking used acoustic defoamers based on aerodynamic acoustic sources (Dorsey, 1959; Boucher and Weiner, 1963). However, these devices, besides having high energy consumption, had practical difficulties such as a need for a large volume of air and in the control and sterilization of the air flow.

A new type of ultrasonic defoamer system (UDS) has been developed, which uses a stepped-grooved-plate transducer to focus airborne ultrasound (Gallego-Juárez *et al.*, 2005). This type of system has one or more piezoelectric power transducers, with specially designed stepped-grooved-plate radiators, and the electronics to drive and control the tuned assembly (Fig. 15.15). The electronics generate, control and monitor the correct electrical excitation of the transducers, tuning and maintaining an adequate level of acoustic energy to ensure the correct

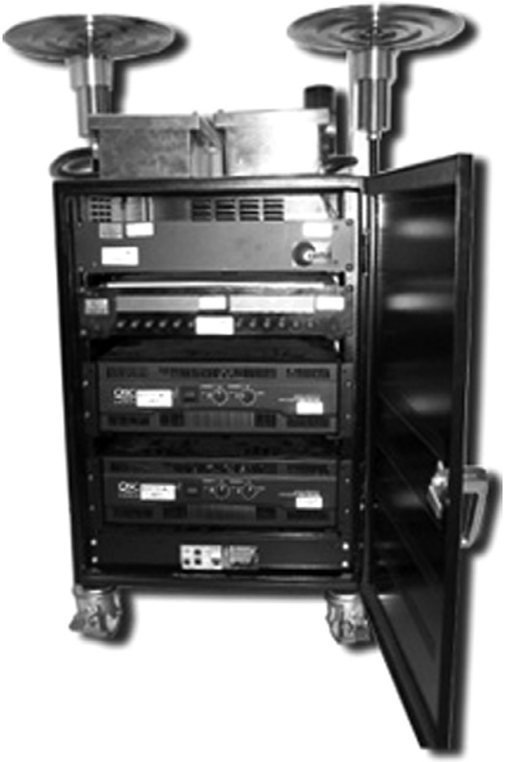

15.15 Ultrasonic defoamer system, which uses two stepped-grooved-plate transducers to focus airborne ultrasound.

amount of sound pressure. The control algorithms and the preconfigured parameters in the non-volatile memory have a fully automatic operation, requiring only electric power. UDS units have been constructed for operating frequencies of about 21 and 26 kHz. A UDS produces highly focused radiation in such a way that levels of acoustic pressure higher than 170 dB may be achieved at the focal area. It is a powerful and compact device, which does not interfere in the process, can be easily sterilized and fulfils industrial requirements. It can be static or mounted on a rotary device. A static UDS (Fig. 15.16) is generally used to control excess foam in high-speed bottling and canning lines for carbonic beverages. Lines of 20 cans/second can be processed with an applied power of about 300 W.

A rotary UDS (Fig. 15.17) is used to dissipate foam in reactors. This type of UDS uses an electronically controlled system to rotate the transducers.

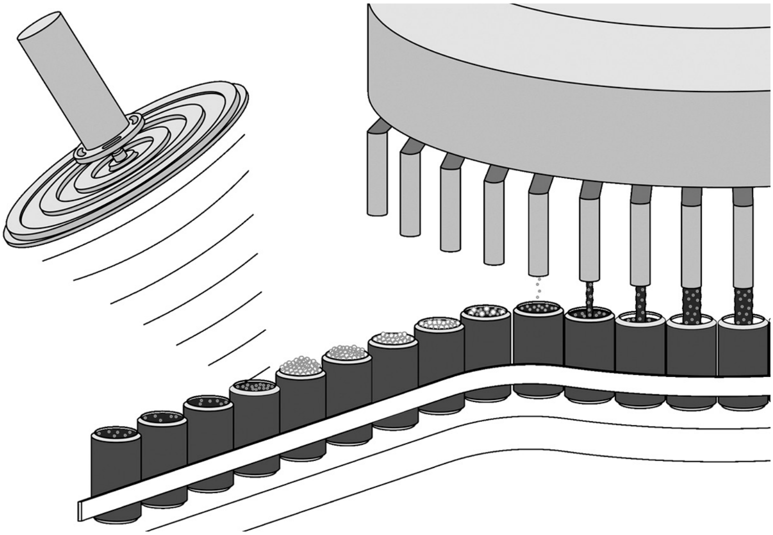

15.16 Static ultrasonic defoamer in canning line.

The ultrasonic transducers can rotate at different speeds and at different angles with respect to the axis of rotation in such a way that they perform complex trajectories to treat large areas of foam inhomogeneously distributed throughout the bulk. The rate of defoaming for a plate transducer, operating at a power in the range 200–300 W, varies from 10 to 40 m^3/h in reactors with diameters of 6 to 12 m. This means an energy consumption lower than 30 Wh/m^3 for each transducer of a UDS unit.

UDS is a clean, fast, safe and efficient system and has been successfully applied to control excess foam in fermentation vessels and in other large reactors as well as on high-speed canning and bottling lines during filling. UDS units are manufactured by the spin-off Spanish company PUSONICS and sold worldwide (www.pusonics.es).

Ultrasonic dehydration

Dehydration is a method for preserving food. For food dehydration, the two basic conventional procedures use mechanical or thermal energy. Mechanical dehydration compresses or centrifuges the material. In thermal dehydration or drying, the addition of energy in the form of heat is used to evaporate the liquid. Mechanical dehydration is useful for removing moisture that is weakly attached, while thermal drying provides a more complete removal of any kind of moisture from a product.

The dehydration method suitable for a specific application depends on the attachment of the liquid to the solid material. In general, there are three types of

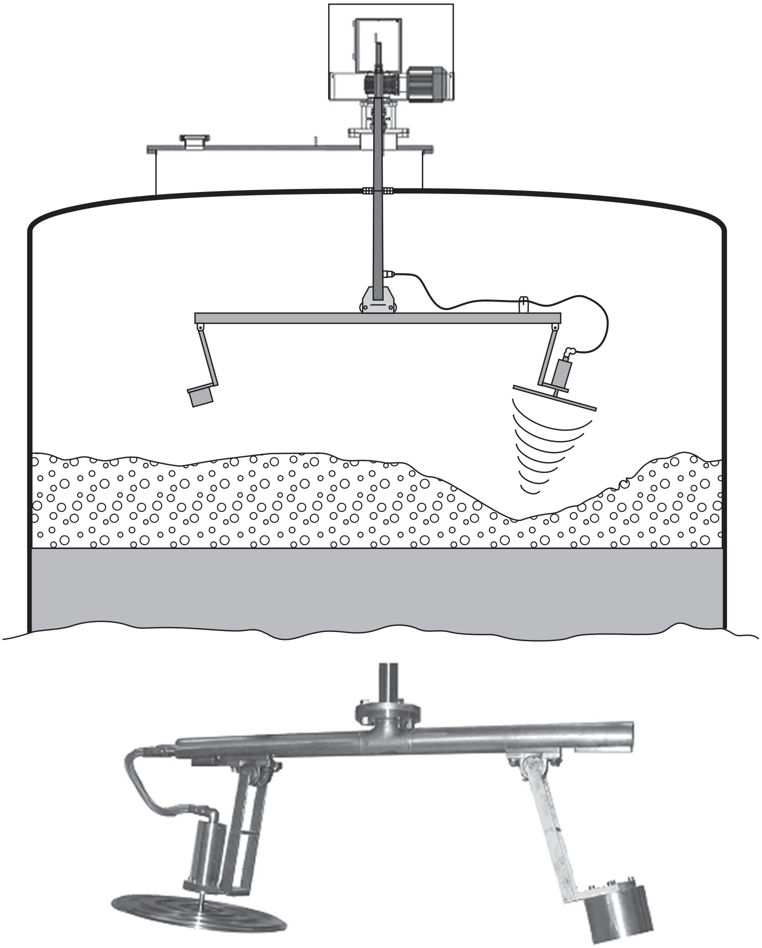

15.17 Rotary ultrasonic defoamer in a reactor.

attachment: chemical, mechanical and physicochemical. For food dehydration, conventional systems employ two main procedures: hot-air drying and freeze-drying. Hot-air drying is a widely used method but it can produce deteriorative changes in the food. In freeze-drying, food pieces are frozen and the ice sublimates; product deterioration is negligible but the process is expensive.

Today the food industry is adapting to new consumer requirements, such as high quality, safety, health benefits, etc. Therefore novel technologies at different stages of development are being introduced. In particular, special attention is being paid to non-thermal processes. Ultrasonic processing is one of these, and it is developing fast due to its flexibility and the availability of new equipment.

High-intensity airborne sonic and ultrasonic waves have been used to increase the drying rate of materials. Acoustically assisted hot-air drying uses lower temperatures and may be useful for drying heat-sensitive materials (Fairbank, 1975; Seya, 1970). High-intensity airborne ultrasound causes pressure variations at gas/liquid interfaces, and therefore increases the evaporation rate of moisture. Moreover, in a forced-air drying system, the air velocity influences heat and mass transfer. The acoustic energy produces an oscillating-velocity effect, which can increase the drying rate for a stable air velocity. In addition, high-intensity airborne ultrasound causes microstreaming at the interfaces, which reduces the diffusion boundary layer, increases mass transfer and accelerates diffusion (Borisov and Gynkina, 1973). Therefore, the application of airborne acoustic energy can positively contribute to the drying process. Nevertheless, the use of this technique has been very limited, probably because of insufficient improvements in drying rates or practical difficulties in the efficient generation of high-intensity ultrasound in air.

With the new family of power ultrasonic generators, new methods for food dehydration have been developed using two experimental procedures (Gallego-Juárez *et al.*, 2007):

- forced-air drying assisted by airborne ultrasound
- ultrasonic dehydration, where ultrasound is applied directly to the material.

The drying procedure using airborne ultrasound and forced air has been implemented in two different ways: (a) using a stepped-plate ultrasonic generator, as an airborne radiator, in combination with forced air, and (b) using a cylindrical-radiator transducer as a fluidized-bed dryer.

The system designed and constructed with the stepped-plate generator in combination with forced air is schematically shown in Fig. 15.18. A stepped-plate power ultrasonic transducer generates a high-intensity standing wave and the sample holder acts as a reflector. Figure 15.19 shows the results of drying vegetables (pieces of carrots of section 12 × 12 mm^2 and 2 mm in thickness) with forced air at 60 °C, 90 °C and 115 °C, without and with ultrasound at an acoustic pressure level of 155 dB. The effect of the ultrasonic radiation is significant at low air temperatures and diminishes as temperature increases. In general, the application of airborne ultrasound is useful in increasing the efficiency of forced-air drying, but the improvement seems to be relatively limited.

A fluidized-bed dryer with a cylindrical-radiator transducer is shown in Fig. 15.20. The conventional fluidized-bed drying chamber is replaced by a vibrating cylinder, which is the radiator of the transducer and generates a high-intensity ultrasonic field in its inside. The operating resonant frequency of the transducer is 21.8 kHz and the average sound-pressure level inside the chamber is about 155 dB. The results of drying carrot samples are shown in Fig. 15.21.

Ultrasonic dehydration using high-intensity ultrasonic vibration in direct contact with the food material is schematically shown in Fig. 15.22 (Gallego-Juárez *et al.*,

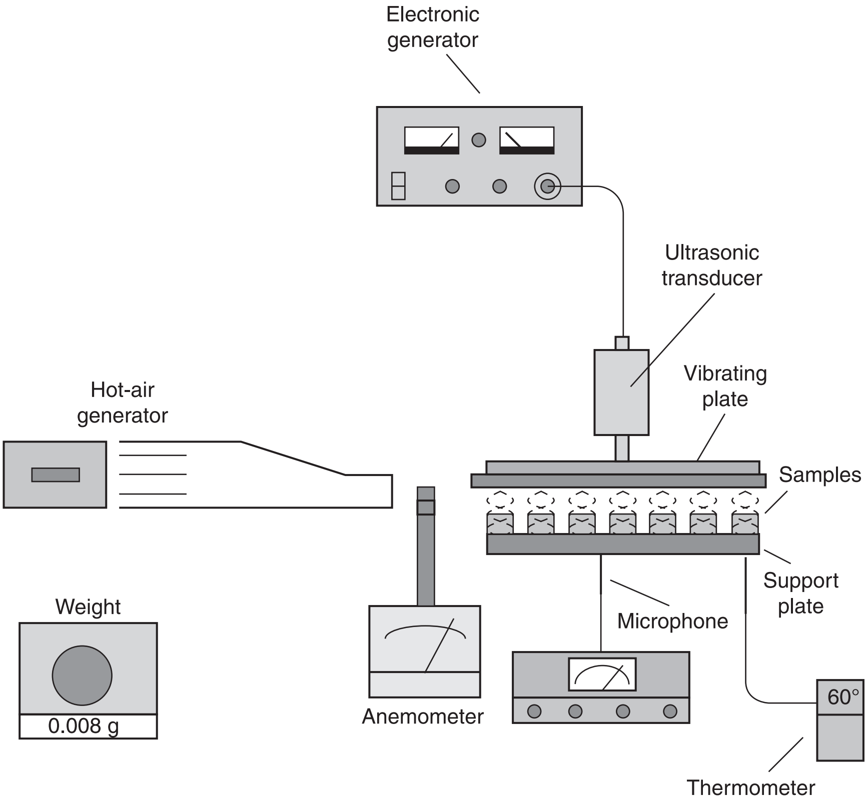
Electronic generator
Ultrasonic transducer
Vibrating plate
Hot-air generator
Samples
Support plate
Weight
0.008 g
Microphone
Anemometer
60°
Thermometer

15.18 System for food dehydration using a stepped-plate ultrasonic generator and forced air.

2001a). This system aims to increase the effectiveness of energy transfer. The type of generator used is the grooved-plate transducer with a rectangular shape. Good acoustic impedance matching between the vibrating plate of the transducer and the food material favours deep penetration of acoustic energy. The food material is subjected to high ultrasonic stresses, which produce a kind of 'sponge effect' and the quick migration of moisture through natural channels. In addition, ultrasonic cavitation inside the liquid may help separate strongly attached moisture. As an example of the application of this procedure, Fig. 15.23 shows the results of the kinetics of the dehydration process for a set of carrot samples at different powers (0 W, 25 W, 50 W, 75 W and 100 W). The procedure is commercially interesting both for its high efficiency and because of the good preservation of food quality (Soria *et al.*, 2010). It has been implemented in a full drying system currently at a semi-industrial stage.

These new experimental systems, designed and developed with different drying procedures, are basic models that can be scaled up for industrial application.

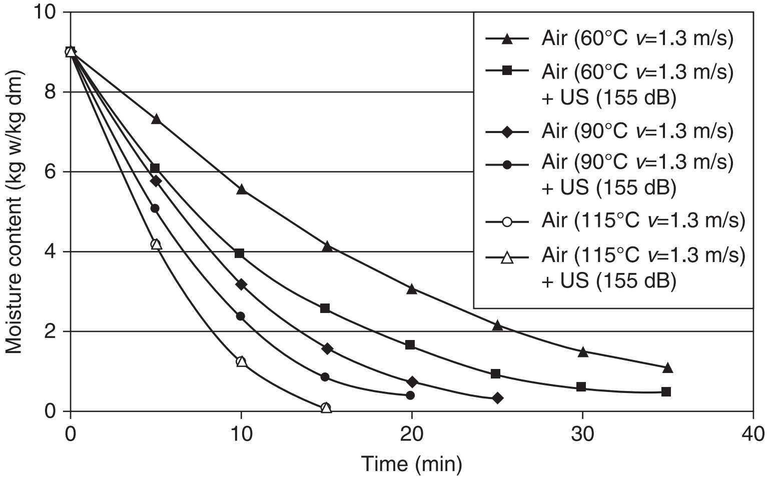

15.19 Moisture content of vegetables (pieces of carrots of section 12 × 12 mm^2 and 2 mm in thickness) dried with forced air at 60 °C, 90 °C and 115 °C, without and with ultrasound (US) at an acoustic pressure level of 155 dB.

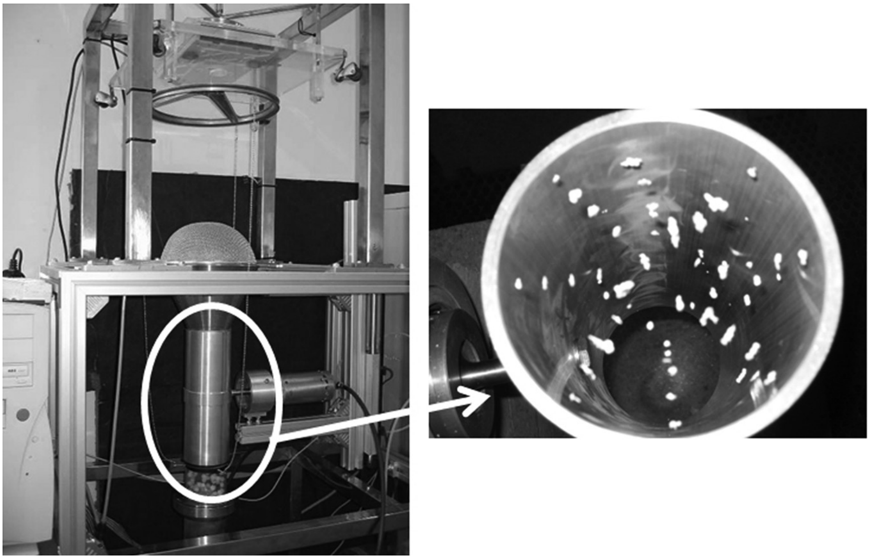

15.20 Fluidized-bed dryer with a cylindrical-radiator transducer.

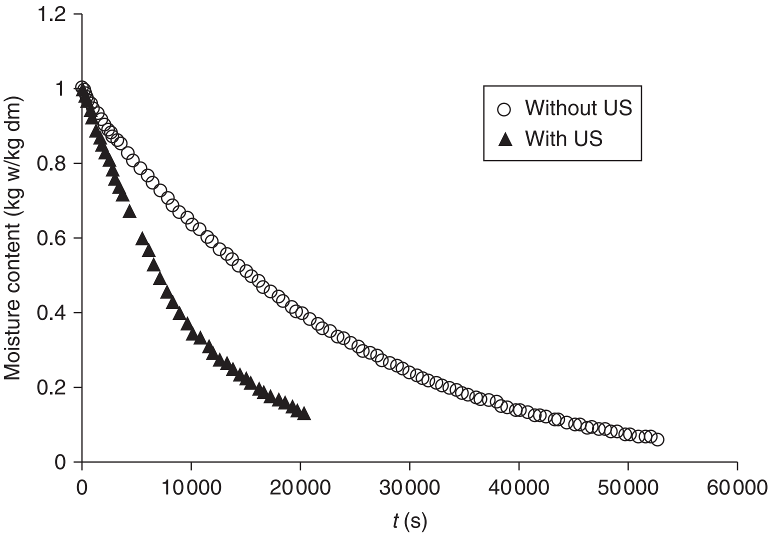

15.21 Moisture content of vegetables (pieces of carrots of section $12 \times 12\,\text{mm}^2$ and 2 mm in thickness) dried with a cylindrical-radiator transducer, without and with ultrasound (US) at an acoustic pressure level of 155 dB.

Supercritical fluid extraction assisted by ultrasound

The use of supercritical fluids as extracting agents has attracted much interest for years and, in particular, supercritical carbon dioxide is considered to be a very useful solvent in extraction because it is non-toxic, recyclable, cheap, relatively inert and non-flammable. Nevertheless, the process is slow.

Supercritical fluid extraction (SFE) is a separation process where a product containing the extractable compound is in contact with a supercritical solvent. The advantage of ultrasound in SFE is due to its mechanical effects on the process: it increases the penetration of the solvent into the product, thus enhancing mass transfer by radiation pressure, microstreaming and agitation (Vinatoru, 2001).

A supercritical fluid is a substance at a temperature and pressure above its thermodynamic critical point. It can diffuse through solids like a gas and dissolve materials like a liquid (Kordikowski *et al.*, 1996). Supercritical fluids have an enhanced dissolving power and have transport properties that favour high extraction capabilities. Of the fluids studied, CO_2 is nowadays the most commonly used for SFE applications because its critical constants are low compared with other solvents and it is available in high purity at low cost. In particular, supercritical CO_2 is widely used in the extraction of essential oil from vegetable substrates.

The application of ultrasound in SFE has been proposed for both kinetic acceleration and yield improvement (Riera *et al.*, 2003). A new procedure was

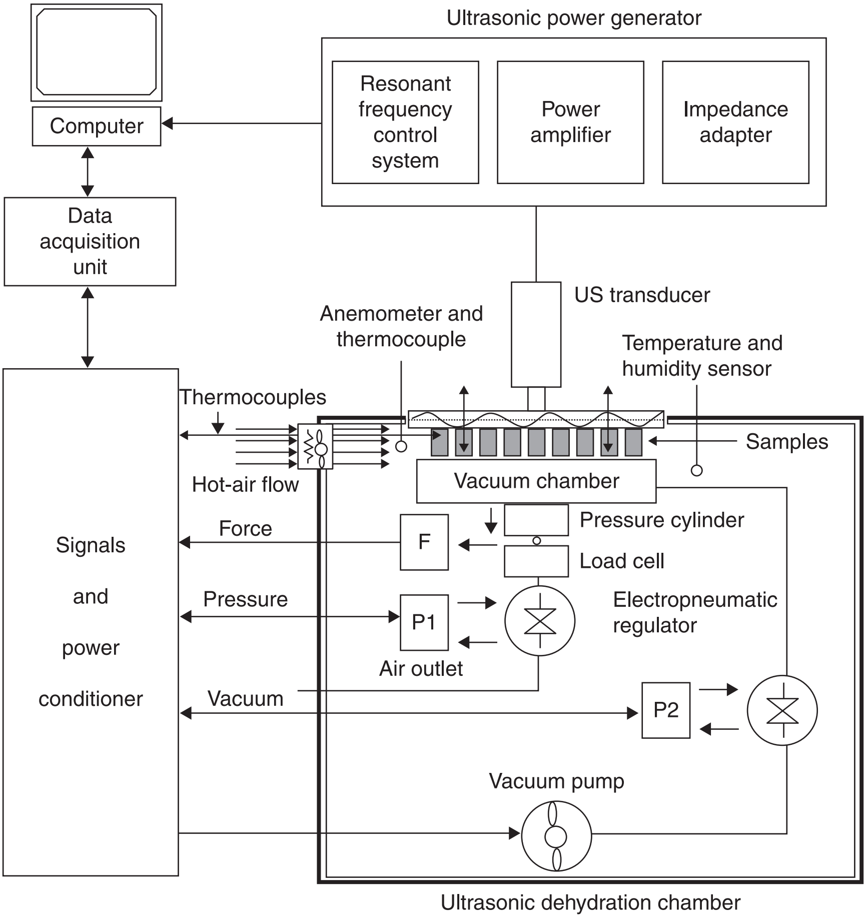
Ultrasonic power generator
Resonant frequency control system
Power amplifier
Impedance adapter
Computer
Data acquisition unit
US transducer
Anemometer and thermocouple
Temperature and humidity sensor
Thermocouples
Samples
Hot-air flow
Vacuum chamber
Pressure cylinder
Force
F
Load cell
Signals and power conditioner
Pressure
P1
Electropneumatic regulator
Air outlet
Vacuum
P2
Vacuum pump
Ultrasonic dehydration chamber

15.22 System for ultrasonic dehydration using high-intensity ultrasonic vibration in direct contact with the food material.

successfully tested in the extraction of almond oil in a pilot plant with four high-pressure extraction vessels, each having a capacity of 5 L (Fig. 15.24). The fluid used as a solvent in the extractor was supercritical CO_2 of 99% purity at 280 bar and 55 °C. The ultrasonic transducer, a simple piezoelectric sandwich with an enlarged radiating surface, was installed in the upper part of the extractor vessel and the power applied was about 50 W. A basket containing 1500 g of almonds was placed inside the supercritical fluid extractor and the solvent was introduced at a flow rate of 20 kg/h.

The results obtained (Fig. 15.25) showed that the kinetics and the extraction yield were enhanced by 30% and 20%, respectively (Riera *et al.*, 2004a). It was experimentally shown that the initial stage of extraction, which is controlled by solute solubility, was less affected by ultrasound than subsequent extraction,

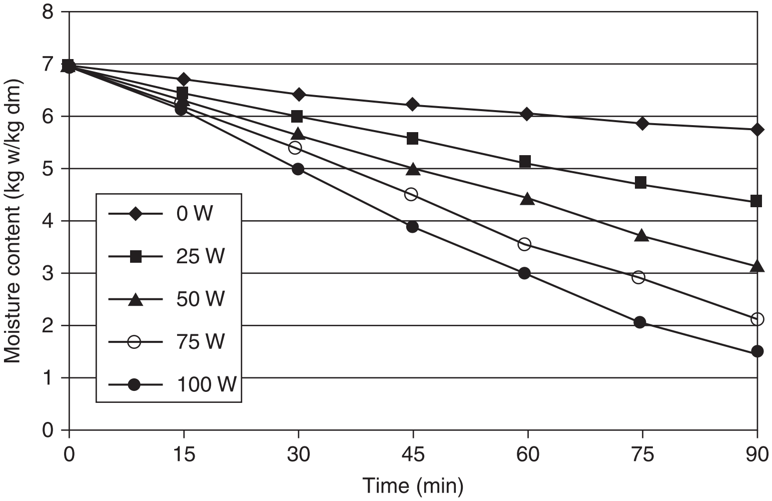

15.23 Moisture content of vegetables (pieces of carrots of section $12 \times 12\,\text{mm}^2$ and 2 mm in thickness) where the high-intensity ultrasonic vibration is in direct contact with the food material.

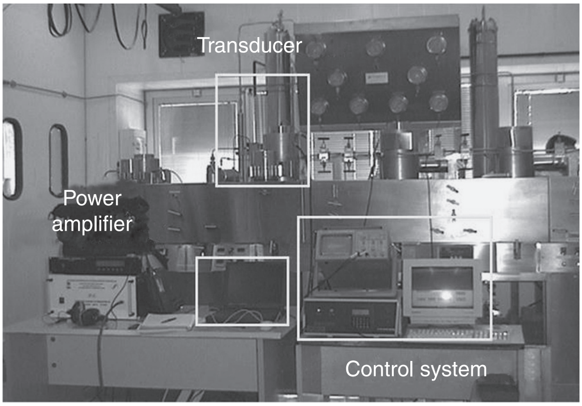

15.24 Pilot plant for extracting almond oil with SFE assisted by ultrasound.

which is controlled by internal mass transfer. Moreover, the results showed that almond particulate size influences the extraction rate, with small particles responding better to the ultrasonic action. Other trials for cocoa cake-oil extraction showed that the application of ultrasonic energy increased the extracted yield by about 43% (Riera *et al.*, 2010).

Following a similar procedure, Balachandran *et al.* (2006) studied the effect of power ultrasound during the extraction of pungent compounds from ginger. A power ultrasonic transducer operating at 20 kHz was used with a laboratory-scale

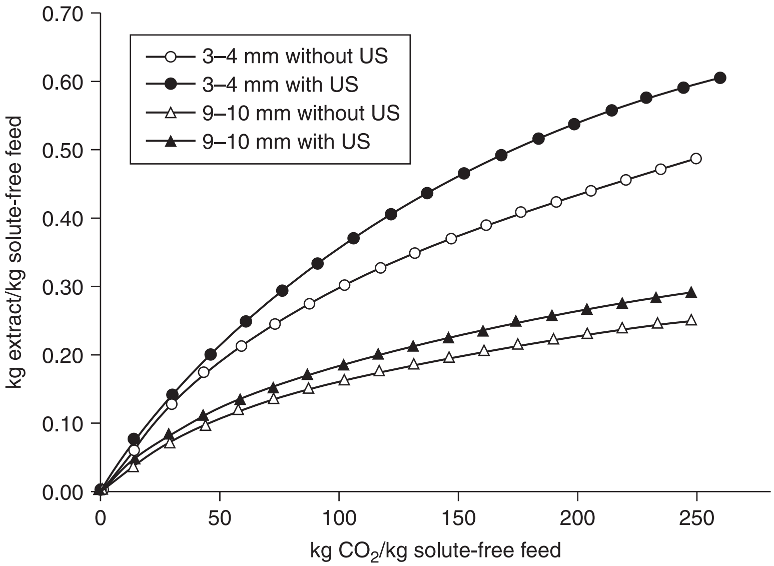

15.25 Results of extracting almond oil with SFE assisted by ultrasound (US), for samples 3–4 mm and 9–10 mm in diameter.

extraction vessel and the extraction of gingerol from freeze-dried ginger particles (4–8 mm) was monitored. The transducer was fitted externally to the wall of the extraction vessel and 300 W was applied during the trials. To maintain the temperature at 40 °C, the ultrasonic system and the extraction vessel were cooled in a water bath. They found that the application of ultrasonic energy increased both the extraction rate and the yield by up to about 30% at 160×10^5 Pa. The higher extraction rate was attributed to disruption of cell structures and to an increase in the accessibility of the solvent to the internal structure of the particles, which enhanced the intra-particle diffusivity. Hu *et al.* (2007) investigated the extraction of oil and coixenolide from adlay seeds using a solvent with a similar experimental system to that developed by Riera *et al.* (2004a). An increase of 14% in the extracted yield was obtained with ultrasound.

Important work is currently being carried out to scale the process up to an industrial level. Stepped-plate ultrasonic transducers for supercritical extraction in the frequency range from 18 kHz up to 50 kHz are under development.

15.3.2 Power ultrasound in environmental processes

Power ultrasound can be used in several different ways as an important and efficient tool in preventing or removing pollution. In recent years, there has been a strong development of applications in air cleaning, water purification, treatment of sludge, soil remediation and new sonochemical ‘green’ processes.

In this section, we will discuss air cleaning and sludge filtration, two processes in which ultrasonic energy plays an important role.

Air cleaning: fine-particle removal

The presence of suspended airborne particles, especially very fine particles, in the environment is generally undesirable and dangerous. Such tiny particles (smaller than about 2 microns) are a major health hazard because of their ability to penetrate deeply into the respiratory tissues, and the long time they remain in suspension. In addition, these particles are generally dangerous due to their origin (the condensation of chemically active elements produced during combustion processes) and their capability to act as a vehicle for noxious agents (e.g. viruses, bacteria and dioxin). Fine particles make up a significant percentage of the particulate emission from coal and fuel-oil burning processes such as in power plants, in the steel-melting industry (open-hearth and converter) and in the cement industry. Therefore it is necessary to deal with them by stopping their dispersal. The retention efficiency of conventional filters used in industry, such as electrostatic precipitators (ESPs), drops off steeply for particles under 2 or 3 μm (Riehle, 1997). Other filters that are effective for fine particles, such as bag filters, require significant maintenance that hinders their industrial use. As a consequence, improved technology is needed for fine-particle retention. Lately, there has been renewed interest in the control of emissions of fine particles from industrial combustion plants, in order to comply with US and European environmental policy. Legislation to reduce pollution is becoming progressively more stringent (Commission Directive 2008/50/EC).

Acoustic vibration agglomeration processes might have an important role to play in cutting down the concentration of small particles in smoke, mist and exhaust gases in general. High-intensity acoustic fields applied to an aerosol may induce interaction effects among suspended particles, giving rise to collisions and agglomerations. The principle of acoustic agglomeration is primarily based on the relative motion between suspended particles of different sizes, which promotes particle collisions, and is called the orthokinetic effect (Mednikov, 1965). However, particles may also agglomerate due to the action of hydrodynamic forces resulting from mutual distortions of the flow fields around particles, which is called the hydrodynamic effect (Dianov *et al.*, 1968; Tiwary and Reethof, 1986; Hoffmann and Koopmann, 1994; González *et al.*, 2002).

The study of such mechanisms, as well as the development of practical systems for their industrial application, has been the object of long-term research work. Using stepped-plate generators, a multifrequency acoustic agglomerator (Fig. 15.26) was developed and tested at a semi-industrial scale as a preconditioning system to be placed upstream of a conventional electrostatic filter (Gallego-Juárez *et al.*, 1998a).

The acoustic agglomeration chamber, with a length of about 4 m and a rectangular cross section of about 0.5 m^2, has four specially designed stepped-plate, high-intensity transducers mounted along its bottom wall. These achieve a

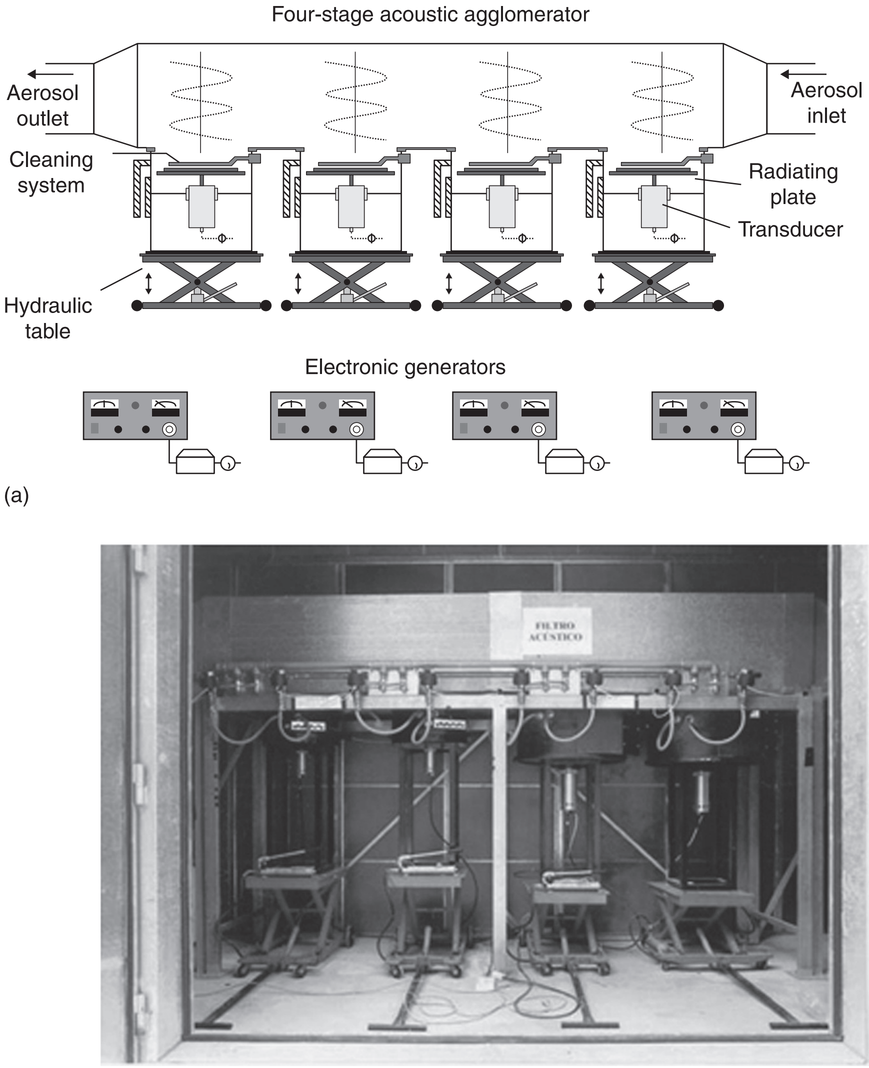
Four-stage acoustic agglomerator
Aerosol outlet
Aerosol inlet
Cleaning system
Radiating plate
Transducer
Hydraulic table
Electronic generators
(a)
FILTRO ACÚSTICO
(b)

15.26 Multifrequency acoustic agglomerator with stepped-plate generators.

homogeneous distribution of the sound field. The stepped-plate transducers, which generate coherent radiation, have their radiating surfaces aligned parallel to the opposite wall, which serves as a reflector in the construction of standing waves in a direction perpendicular to the gas flow (Gallego-Juárez *et al.*, 1999a). The chamber was operated with transducers of two different frequencies (10 and 20 kHz) in combined and separate experiments. The transducer support has an adjustment device to vary the radiator–reflector distance to achieve an optimum standing wave field.

The acoustic filter was used in combination with an electrostatic precipitator (ESP) (Fig. 15.27) in a pilot installation where the smoke, with a mean particle

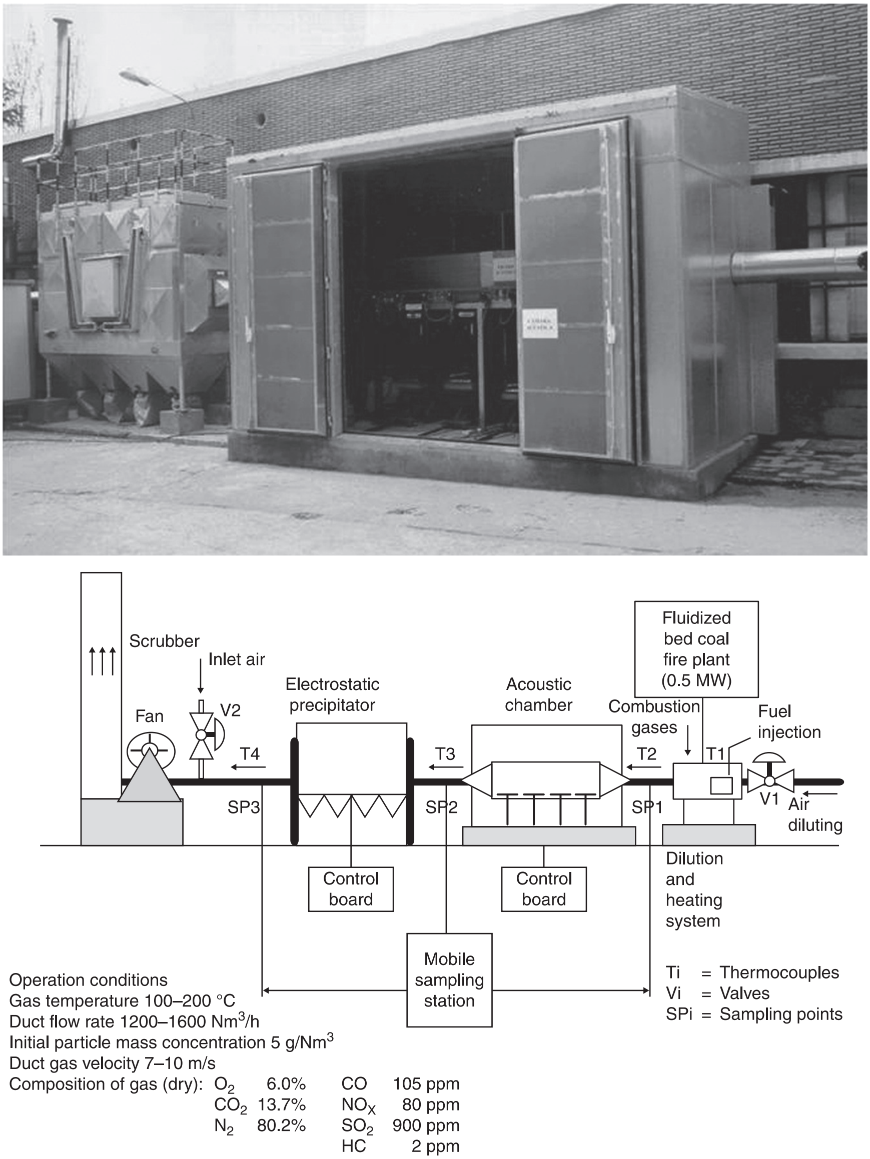
Scrubber
Inlet air
Fan
V2
T4
SP3
Electrostatic precipitator
T3
SP2
Control board
Acoustic chamber
Control board
Fluidized bed coal fire plant (0.5 MW)
Combustion gases
T2
T1
SP1
Fuel injection
V1
Air diluting
Dilution and heating system
Mobile sampling station
Ti = Thermocouples
Vi = Valves
SPi = Sampling points
Operation conditions
Gas temperature 100–200 °C
Duct flow rate 1200–1600 Nm^3/h
Initial particle mass concentration 5 g/Nm^3
Duct gas velocity 7–10 m/s
Composition of gas (dry): O_2 6.0% CO 105 ppm
CO_2 13.7% NO_X 80 ppm
N_2 80.2% SO_2 900 ppm
HC 2 ppm

15.27 Acousto-electrostatic filter.

diameter of 0.8 μm, was generated by a fluidized-bed coal combustion plant. The acousto-electrostatic filter showed a reduction of about 40% in the number of submicron-sized particles (Fig. 15.28) compared with the electrostatic filter alone. This is a significant improvement, particularly because of the very small size of the particles, the narrow gain margin left by the electrostatic filter, the low level of energy applied and the very short treatment time.

This system can be applied to any industrial process where agglomeration and precipitation of airborne particles are required.

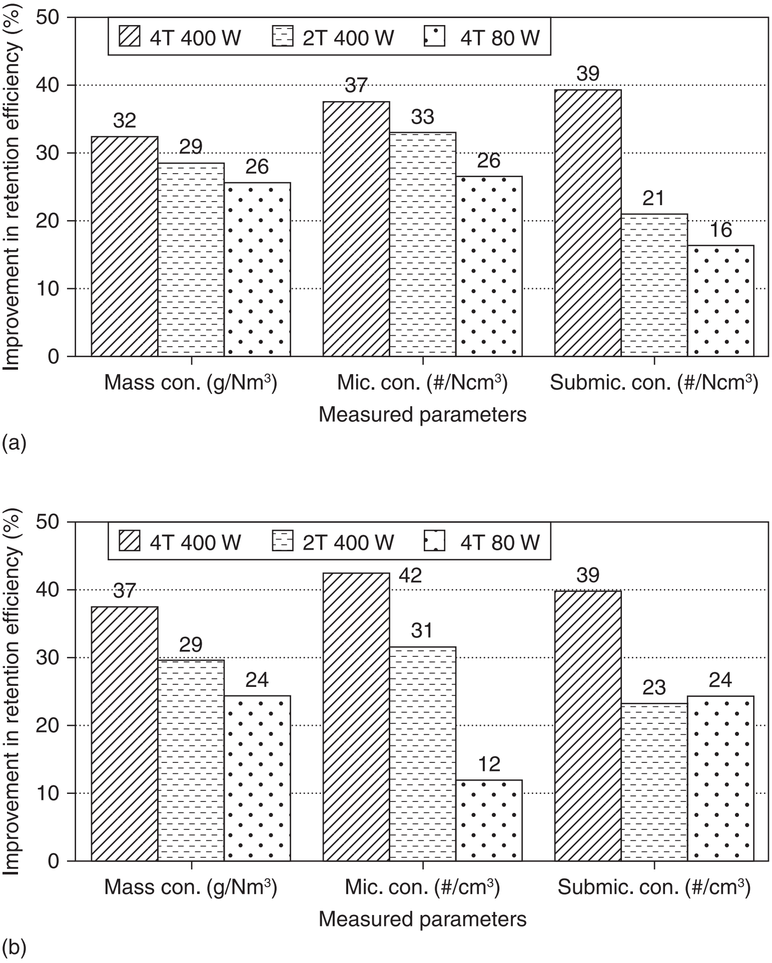

15.28 Reduction in particle emissions for two different frequencies: (a) 10 kHz, (b) 20 kHz. Results are for four transducers of 400 W (4T 400 W), two transducers of 400 W (2T 400 W) and four transducers of 80 W (4T 80 W).

Sludge filtration

One of the present requirements in sewage treatment is dewatering of the sludge. Conventional methods for solid–liquid separation are generally physical devices such as membranes, sieves, filtration beds, etc., and force-driven methods such as settling, flotation, centrifugation, etc. Other procedures involve the assistance of external fields such as electrical or magnetic fields. Acoustic fields are also a potential way to improve the efficiency of conventional separation processes.

For highly concentrated suspensions of fine particles, such as sludge, conventional filtration techniques are not satisfactory because of frequent fouling or blocking of the pores, resulting in slow processing rates or in flux decline. As a consequence, the residual moisture in the filter cake is too high, and it is very difficult to remove. Power ultrasonic processing may be effective in removing the residual moisture. Alternating stresses produced by the ultrasonic energy directly coupled to the sludge cause effective deliquoring by creating channels for moisture migration and driving out the liquor, in a similar way to a sponge when it is squeezed and repeatedly released (the sponge effect). In addition, high-intensity ultrasound may produce cavitation, which aids the removal of strongly attached moisture.

The filtration of finely dispersed sludge generally uses a porous filtration medium with a driving force to achieve flow through it. The solid particles are retained on the surface or within the filtration medium while the liquid passes through it. A vacuum, pressure or centrifugation can be used to force the fluid.

Typical filtration equipment is a rotary vacuum disk filter. The disk rotates about its axis and is partially submerged in a sludge container. Filtration takes place as each section of the disk is submerged in the sludge. The vacuum draws liquid through the disk into the filtrate lines and solid particles settle on the external surface, forming a cake.

Power ultrasonics can be used to improve conventional rotary vacuum filtration. The ultrasonic energy is applied using one (or several) rectangular grooved-plate transducer with its grooved surface directly coupled to the cake which formed on the filter surface during the first stage of the process (Fig. 15.29). The alternating stresses generated by the ultrasonic vibration improve the effect of the vacuum (static) pressure. While a static pressure alone may block pores and channels, the alternating compressions and decompressions produced by the acoustic wave in the cake may open them and facilitate migration of the liquid (Gallego-Juárez *et al.*, 1998b, 1999b).

The ultrasonic technique has been tested with different highly concentrated suspensions of fine particulate materials (in the range 30–60% mass concentration), applying different acoustic powers to determine performance. With the application of ultrasonic energy (Fig. 15.30), dewatering higher than 80% can be obtained with very short treatment times (2 seconds) and a relatively low acoustic intensity (about 800 W/m^2). This result is a substantial improvement over conventional ceramic filters actuated by a vacuum because about 50% of the remaining interstitial moisture was removed (Gallego-Juárez *et al.*, 2003).

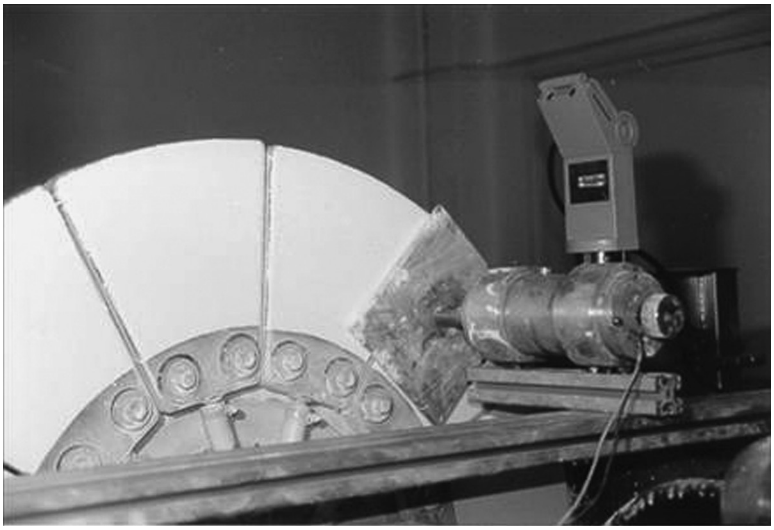

15.29 Rotary vacuum filtration aided by a rectangular grooved-plate transducer.

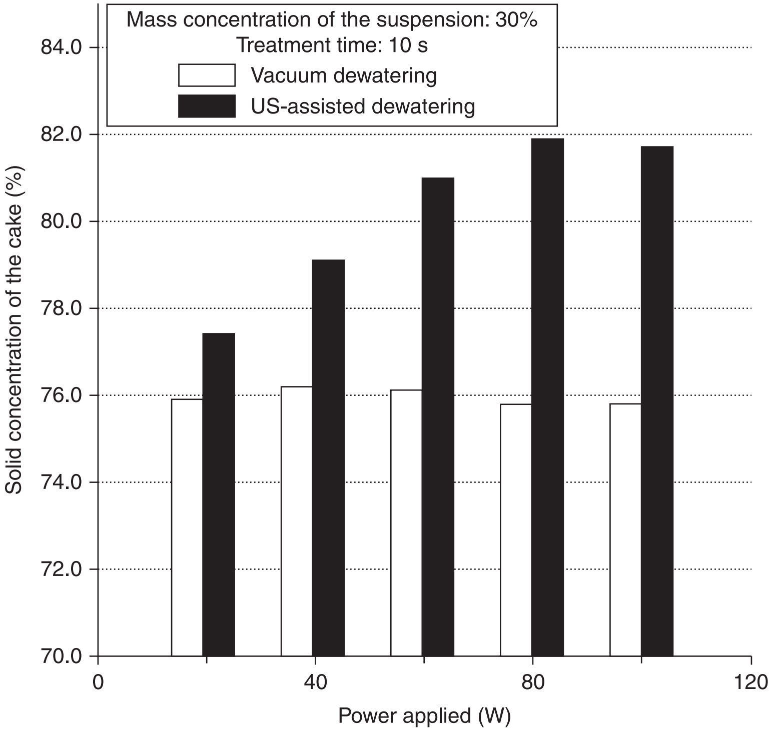

15.30 Comparison of rotary vacuum filtration with and without ultrasound.

15.3.3 Power ultrasound in manufacturing

The versatility of ultrasonic energy means it can be used in many different manufacturing processes, usually as an additional tool to improve either the manufactured product or the process. This section describes three recently developed manufacturing processes.

Ultrasonic washing in textile manufacturing

In textile manufacturing, fabric processing uses wet processes to improve the appearance and serviceability of the fabric. There may be several operations that require washing the fabric. The use of ultrasonic energy in such operations may help to speed up the process and improve the quality of the final product.

The cleaning of solid rigid materials is one of the more popular applications of power ultrasound. However, the use of ultrasonic energy for washing textiles has been explored for several years without achieving commercial development. The cleaning action of ultrasonic energy is mainly due to cavitation. The strategies for ultrasonic cleaning or washing have been generally directed towards the production of cavitation in the entire volume of the bath containing the fabrics to be washed. Such systems have significant problems: it is practically impossible to achieve a homogeneous distribution of the acoustic field in the entire washing volume. In areas of low acoustic energy, the cavitation threshold is not reached and this causes the washing to be uneven. Other general difficulties are due to the softness as well as the reticulate structure of the fabric materials. The softness of the fabric causes the cavitation to have a small erosive effect while the reticulate structure of the fabric favours the formation of layers of large bubbles that obstruct wave penetration.

To overcome these difficulties, a new procedure was developed and patented in which the textile is flat and passes through a thin layer of liquid using a roller-type system. Whilst in the liquid, it is exposed to an ultrasonic field generated by grooved-plate transducers in such a way that the plate radiator is in direct contact or very close to it (Fig. 15.31). The plate radiator is designed to vibrate with one of its simpler flexural vibration modes (where the nodal lines are parallel to the longest side of the plate) to avoid as much as possible differences in vibration amplitudes (Gallego-Juárez *et al.*, 2001b).

The new procedure has several notable characteristics. The cleaning effect is produced by the intense cavitation field generated by the plate radiator within the thin layer of liquid, which is very favourable for producing a high degree of cavitation (Moussatov *et al.*, 2005). From a practical point of view, a thin liquid layer is very convenient because of the low consumption of washing liquid. Homogeneity of the washing is achieved because the fabric passes along the plate surface in such a way that all of the fabric is exposed for the same amount of time to an intense acoustic field. Finally, the radiation force produced by the high-intensity ultrasonic beam directed over the surface of the textile helps to remove

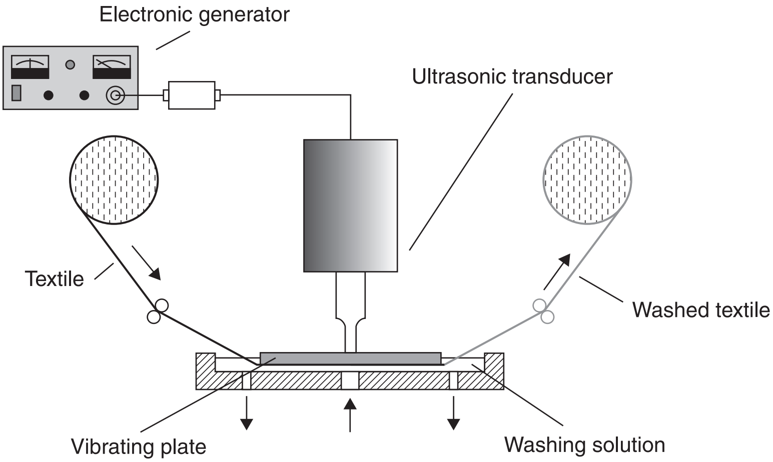
Electronic generator
Ultrasonic transducer
Textile
Washed textile
Vibrating plate
Washing solution

15.31 Washing of textiles assisted by ultrasonic energy.

the big bubbles formed within the reticulate structure of the fabric, which hinder penetration of the ultrasonic energy.

Washing tests carried out with typical textile samples (EMPA 101, AS9 and WFK 30D), showed that the washing performance, even at relatively moderate acoustic intensities, is clearly much higher than that obtained with a conventional washing machine (Fig. 15.32) while the energy consumption is very low (of the order of 0.1 kWh/kg of textile). This process has been implemented at a semi-industrial level (Gallego-Juárez *et al.*, 2010), as shown in Fig. 15.33.

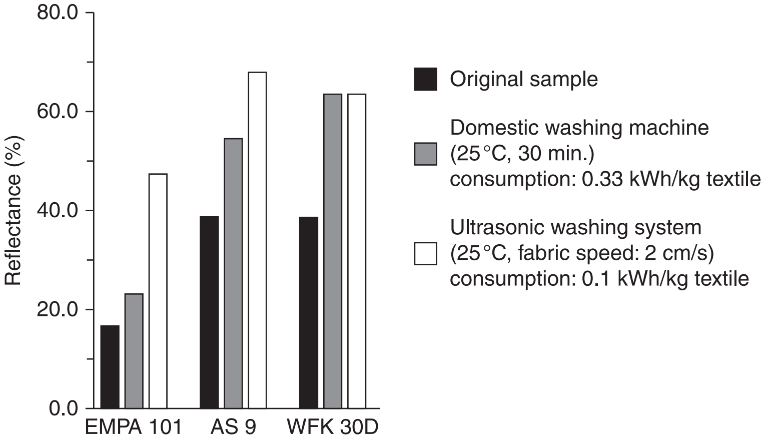

15.32 Comparison of ultrasonic washing and conventional domestic washing. EMPA 101: cotton with particles and some fat. AS 9: cotton with fatty material. WFK 30D: polyester with skin fat and particles.

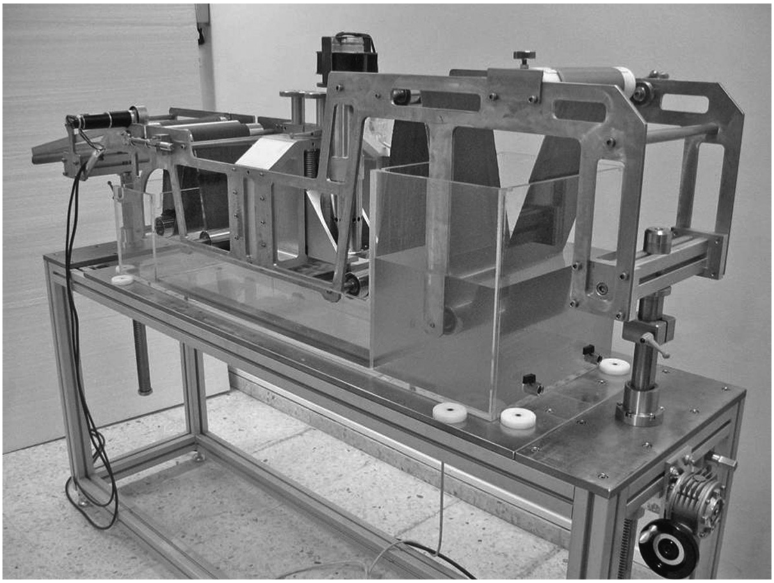

15.33 Semi-industrial implementation of ultrasonic textile washing.

Ultrasonic debubbling of liquid coating layers

Industrial coatings applied at high speed often contain bubbles of air trapped during the operation. Such bubbles will produce permanent surface defects after drying and, consequently, piece rejections in the production line. Chemical additives are generally used to alleviate the problem, but they are difficult to dose and, if not properly handled, can create problems that may be even worse than the air retention.

High-intensity airborne ultrasound is an adequate contactless method of rupturing the bubbles. A new process (Gallego-Juárez *et al.*, 2006) uses the direct application of airborne ultrasound to rupture the bubbles, which are semi-submerged within the coating layer (Fig. 15.34). The system developed has a stepped-plate high-directional transducer, working at 21 kHz, and a visualization system to film and analyse the debubbling effect acoustically induced in a coating layer deposited on a wood surface. The transducer is placed with its radiating plate parallel to the coated surface (Fig. 15.35).

Debubbling tests on a semi-industrial scale were carried out in a pilot coating curtain machine by coating oak, sapelly and melamine samples with industrial water-based and solvent-based coating liquids. High debubbling efficiency was obtained for all sizes of bubble for the water-based coating (Fig. 15.36), while the effect was more selective for the solvent-based coating, where a strong dependence on the bubble size was observed (Fig. 15.37). The results suggest that resonance of the semi-submerged bubbles is an important effect in the debubbling mechanism, and therefore it should be maximized to overcome the difficulties of rupturing

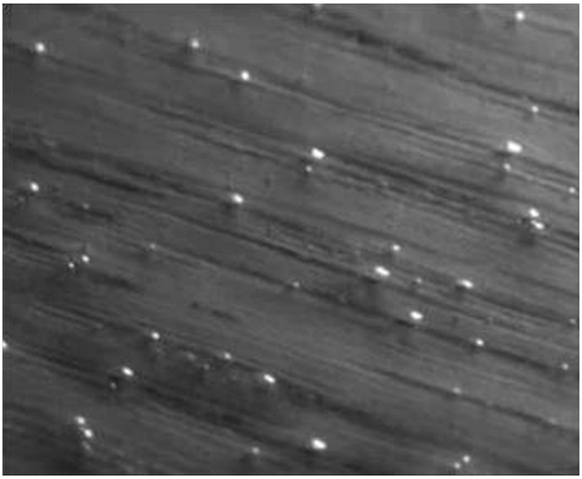

15.34 Semi-submerged bubbles within a coating layer.

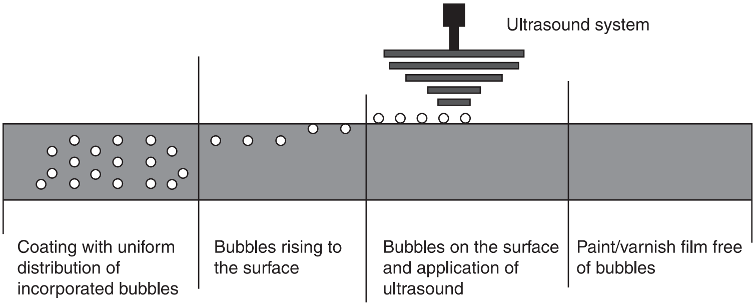
Ultrasound system
Coating with uniform distribution of incorporated bubbles
Bubbles rising to the surface
Bubbles on the surface and application of ultrasound
Paint/varnish film free of bubbles

15.35 Ultrasonic debubbling.

bubbles produced in high-viscosity coating liquids (Gonzalez-Gomez *et al.*, 2006). The new procedure is a promising approach for the quick debubbling of thin coating layers.

Ultrasonic enhancement of pigment dispersion in paint manufacture

Paint is a dispersion of small, coloured, insoluble particles (pigments) in a liquid medium composed of solvent and binder. Pigments are very fine powders, which provide colour and the ability to hide an underlying surface.

Pigment dispersion is a critical factor in the manufacture of paint, which is a complicated and cost-intensive operation. Most of the properties of a paint are enhanced when the pigment particles are as small as possible. The degree of pigment dispersion determines most of the essential properties of a paint. The

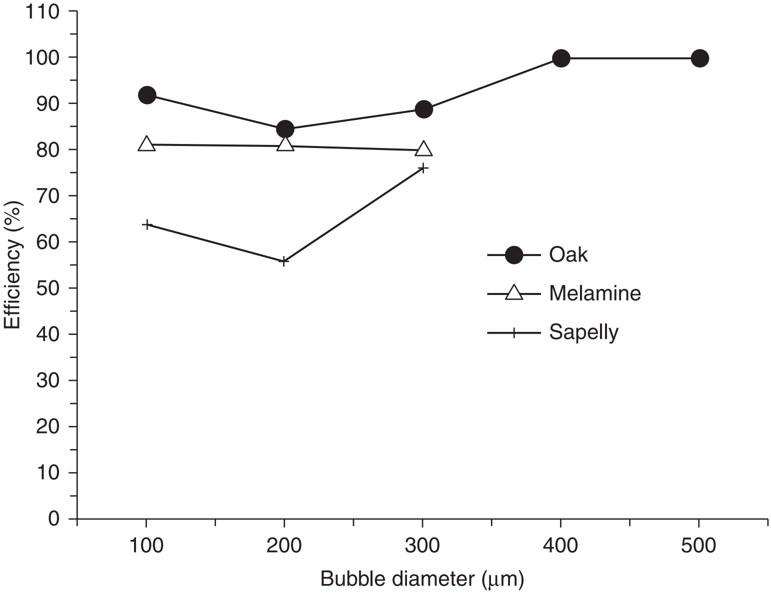

15.36 Debubbling efficiency for a water-based coating liquid (WAA2).

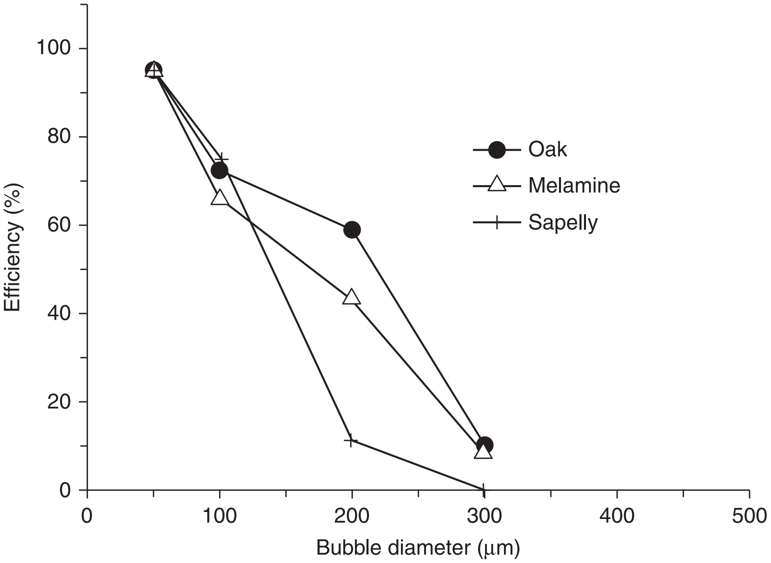

15.37 Debubbling efficiency for a solvent-based coating liquid (FUVA2).

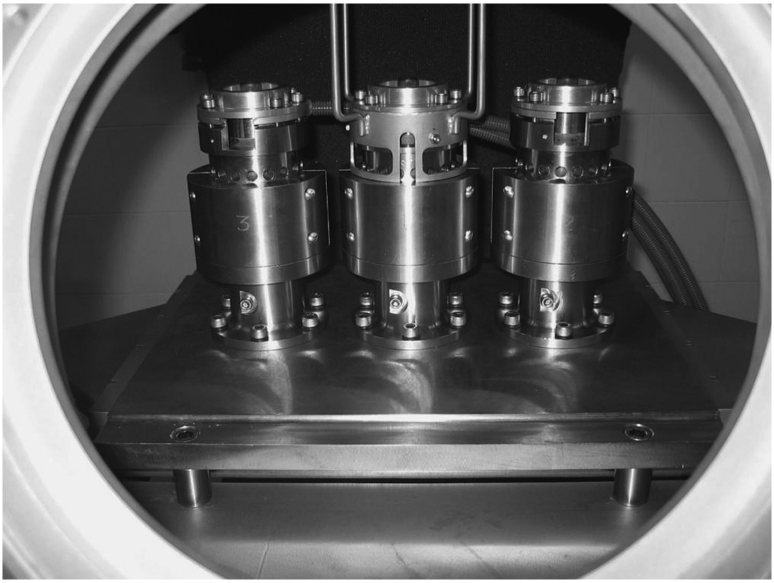

15.38 Semi-industrial reactor using rectangular grooved-plate power ultrasonic transducers for pigment dispersal in paints, pastes and inks.

objective of dispersion is to homogeneously incorporate particles into a liquid system, to deagglomerate the pigment powder, to stabilize this dispersion and to ensure that it remains stable during drying.

Power ultrasound is a potentially useful innovation for the paint industry. An ultrasound reactor to enhance pigment dispersion in paints, pastes and inks on a semi-industrial scale was developed within a European project (UE GROWTH-CRAFT-G1STCF-2002-50309). It used rectangular grooved-plate power ultrasonic transducers (Fig. 15.38). In this reactor, the ultrasound was generated by three transducers, mounted in a line within a closed chamber. The transducers produced strong cavitation in a volume around the plate radiators placed inside the chamber where the paint flows. Trials performed with a prototype, sonicating with power applied to the transducers in the range 400–600 W and treating paint flows of 50 to 100 kg/h, proved the pigment deagglomeration effect and that better pigment dispersion can be obtained than with classical grinding machines.

Industrial equipment for paint manufacture will require further development using transducers with higher power.

15.4 Conclusions

The applications included in this chapter are new processes in fluids and multiphase media. They represent only a few of the new sonoprocesses developed in recent years. There are other ultrasonic processes, mainly in the sonochemical area, in which relevant results on a laboratory and even industrial scale have been obtained. These include processes such as water treatment, decontamination of soil, crystallization, etc. The use of power ultrasound in processing is an expanding highly diverse field with a broad and varied range of applications.

In order to consolidate the future growth of ultrasonic technology, it is essential to have a good knowledge of each specific industrial problem prior to investigation and the development of optimal ultrasonic solutions.

15.5 Acknowledgements

The author wishes to thank all his co-workers at the Power Ultrasonics Group, CSIC, for their continual effort and valuable collaboration over the years. Their contribution has been essential for the development of the new technologies and processes presented in this chapter.

15.6 References

Balachandran, S., Kentish, S. E., Mawson, R. and Ashokkumar, M. 2006. Ultrasonic enhancement of the supercritical extraction from ginger. *Ultrasonics Sonochemistry*, 13, 471–9.

Borisov, Y. Y. and Gynkina, N. M. 1973. Acoustic drying. In: Rozenberg, L. D. (ed.) *Physical Principles of Ultrasonic Technology*. New York: Plenum Press.

Boucher, R. M. G. and Weiner, A. L. 1963. Foam control by acoustic and aerodynamics means. *British Chemical Engineering*, 8, 808–12.

Cardoni, A. and Lucas, M. 2002. Enhanced vibration performance of ultrasonic block horns. *Ultrasonics*, 40, 365–9.

Commission Directive 2008/50/EC. Relating to ambient air quality and cleaner air for Europe. *Official Journal of the European Union*.

Dianov, D. B., Podolskii, A. A. and Turubarov, V. I. 1968. Calculation of the hydrodynamic interaction of aerosol particles in a sound field under Oseen flow conditions. *Soviet Physics-Acoustics*, 13, 314–19.

Dorsey, A. E. 1959. Control of foam during fermentation by the application of ultrasonic energy. *Journal of Biochemical and Microbiological Technology and Engineering*, 1, 289–95.

Fairbank, H. V. 1975. Applying ultrasound to continuous drying process. *Ultrasonic International 1975 Conference Proceedings*. Guildford, UK: IPC Science and Technology Press Ltd, pp. 43–5.

Gallego-Juárez, J. A., Riera, E. and Rodriguez-Corral, G. 1998a. *Multifrequency acoustic chamber for the agglomeration and separation of suspended particles in gas effluents*. US patent 5,769,913.

Gallego-Juárez, J. A., Rodríguez-Corra, G. and Elvira-Segura, L. 1998b. *Dispositivo ultrasónico para la mejora de procesos de separación sólido-líquido en suspensions (Ultrasonic device for the improvement of solid-liquid separation process in suspensions)*. International patent W9800304ES.

Gallego-Juárez, J. A., Riera-Franco de Sarabia, E., Rodríguez-Corral, G., Hoffmann, T. L., Gálvez-Moraleda, J. C., Rodríguez-Maroto, J. J., Gómez-Moreno, F. J., Bahillo-Ruiz, A., Martín-Espigares, M. and Acha, M. 1999a. Application of acoustic agglomeration to reduce fine particle emissions from coal combustion plants. *Environmental Science and Technology*, 33, 3843–9.

Gallego-Juárez, J. A., Rodríguez-Corral, G., Elvira-Segura, L., Ekberg, B. and Norrgard, G. 1999b. *Method for making drying more effective*. European Patent 99110798.8-2113.

Gallego-Juárez, J. A., Yang, T., Vazquez-Martinez, F., Galvez-Moraleda, G. and Rodriguez-Corral, G. 2001a. *Dehydration method and device*, US Patent 6233844BV1.

Gallego-Juárez, J. A., Nájera, G., Rodriguez-Corral, G., Vazquez-Martinez, F. and Van-Der-Vlist, P. 2001b. *Process and device for continuous ultrasonic washing of textiles*. US Patent 6,266,836 B1.

Gallego-Juárez, J. A., Elvira-Segura, L. and Rodriguez, G. 2003. A power ultrasonic technology for deliquoring. *Ultrasonics*, 41, 255–9.

Gallego-Juárez, J. A., Rodríguez-Corral, G., Vitini, F. M., Acosta-Aparicio, V. M., Riera, E. and Blanco, A. 2005. *Macrosonic generator for industrial defoaming of liquids by air-borne radiation*. International patent PCT/ES2005/070113.

Gallego-Juárez, J. A., Gonzalez-Gomez, I., Rodriguez-Corral, G., Riera, E. and Garmendia-Barrena, M. I. 2006. *Procedure and ultrasonic device for the elimination of occluded bubbles in paint and varnish coating applied at high-speed*. Spanish Patent 200600619.

Gallego-Juárez, J. A., Riera, E., Blanco, S. D. L. F., Rodríguez-Corral, G., Acosta-Aparicio, V. M. and Blanco, A. 2007. Application of high-power ultrasound for dehydration of vegetables: processes and devices. *Drying Technology: An International Journal*, 25, 1893–901.

Gallego-Juárez, J. A., Riera, E. and Acosta-Aparicio, V. M. 2008. Modal interactions in high-power ultrasonic processing transducers. *AIP Conference Proceedings*, 1022, 595–604.

Gallego-Juárez, J. A., Riera, E., Acosta, V., Rodríguez, G. and Blanco, A. 2010. Ultrasonic system for continuous washing of textiles in liquid layers. *Ultrasonics Sonochemistry*, 17, 234–8.

Gallego-Juárez, J. A., Rodriguez, G., Acosta, V. and Riera, E. 2010. Power ultrasonic transducers with extensive radiators for industrial processing. *Ultrasonics Sonochemistry*, 17, 953–64.

Ghildyal, N. P., Lonsane, B. K. and Karanth, N. G. 1980. Foam control in submerged fermentation: state of art. *Advances in Applied Microbiology*, 33, 173–222.

Gonzalez-Gomez, I., Rodriguez, J., Garmendia, I. and Gallego-Juárez, J. A. 2006. Application of high-intensity air-borne ultrasound for debubbling liquid films. *Ultrasonics*, 44, Suppl. 1, e529–32.

González, I., Hoffmann, T. L. and Gallego-Juárez, J. A. 2002. Visualization of hydrodynamic particle interaction: validation of a numerical model. *Acustica/Acta Acustica*, 88, 19–26.

Hoffmann, T. L. and Koopmann, G. H. 1994. A new technique for visualization of acoustic particle agglomeration. *Review of Scientific Instruments*, 65, 1527–36.

Hu, A.-J., Zhao, S., Liang, H., Qiu, T.-Q. and Chen, G. 2007. Ultrasound assisted supercritical fluid extraction of oil and coixenolide from adlay seed. *Ultrasonics Sonochemistry*, 14, 219–24.

Kordikowski, A., Robertson, D. G., Aguiar-Ricardo, A. I., Popov, V. K., Howdle, S. M. and Poliakoff, M. 1996. Probing vapor/liquid equilibria of near-critical binary gas mixtures by acoustic measurements. *The Journal of Physical Chemistry*, 100, 9522–6.

Langevin, P. 1918. *Procedes et appareils demission et de réception des ondes elastiques sous-marines a laide des proprietes piezo-electriques du quartz*. French patent application 505,703.

Mednikov, E. P. 1965. *Acoustic Coagulation and Precipitation of Aerosols*. New York: Consultants Bureau.

Moussatov, A., Granger, C. and Dubus, B. 2005. Ultrasonic cavitation in thin liquid layers. *Ultrasonics Sonochemistry*, 12, 415–22.

Nayfeh, S. A. and Nayfeh, A. H. 1994. Energy transfer from high-to low-frequency modes in a flexible structure via modulation. *Journal of Vibration and Acoustics*, 116, 203–7.

Neppiras, E. A. 1973. The prestressed piezoelectric sandwich transducer. In: *Ultrasonics International Conf. Proc.*, pp. 295–302.

Riehle, C. 1997. Chapter 3. In: Parker, K. R. (ed.) *Basic and Theoretical Operation of ESPs*. London: Blackie Academic & Professional.

Riera, E., Gallego-Juárez, J. A., Montoya-Vitini, F., Blanco-Blanco, A., Mulet, A., Benedito, J. J., Peña, R., Golás, Y., Berna, A., Subirats, S., Blasco, M. and Reverter, J. G. 2003. *Separation or extraction method using supercritical fluids assisted by high-intensity ultrasound*. International patent application PCT/ES03/00398.

Riera, E., Golás, Y., Blanco, A., Gallego, J. A., Blasco, M. and Mulet, A. 2004a. Mass transfer enhancement in supercritical fluids extraction by means of power ultrasound. *Ultrasonics Sonochemistry*, 11, 241–4.

Riera, E., Rodríguez, G., Vázquez, F., de-la-Fuente, S., Campos, C., Gallego-Juárez, J. A. and Mulet, A. 2004b. Development of a fluidized-bed dryer system assisted by power ultrasound. In: *9th Meeting of the European Society of Sonochemistry*, Badajoz (Spain). pp. 79–80 (OC-20).

Riera, E., Blanco, A., García, J., Benedito, J., Mulet, A., Gallego-Juárez, J. A. and Blasco, M. 2010. High-power ultrasonic system for the enhancement of mass transfer in supercritical CO_2 extraction processes. *Ultrasonics*, 50, 306–9.

Rodríguez, G., Gallego-Juárez, J. A., Vázquez, F., Campos, C., Riera, E. and Acosta, V. M. 2001. *Vibrating plate macrosonic emitter with reflectors and separators for obtaining directional radiation in fluids*. Spanish patent 200102610.

Seya, K. 1970. Macrosonic drying. In: *First International Symposium on High-power Ultrasonics*. Guildford, UK: IPC Science and Technology Press Ltd, pp. 136–40.

Soria, A. C., Corzo-Martínez, M., Montilla, A., Riera, E., Gamboa-Santos, J. and Villamiel, M. 2010. Chemical and physicochemical quality parameters in carrots dehydrated by power ultrasound. *Journal of Agricultural and Food Chemistry*, 58, 7715–22.

Tiwary, R. and Reethof, G. 1986. Hydrodynamic interaction of spherical aerosol particles in a high intensity acoustic field. *Journal of Sound and Vibration*, 108, 33–49.

Vinatoru, M. 2001. An overview of the ultrasonically assisted extraction of bioactive principles from herbs. *Ultrasonics Sonochemistry*, 8, 303–13.

Wood, E. W. and Loomis, A. L. 1927. XXXVIII. The physical and biological effects of high-frequency sound-waves of great intensity. *Philosophical Magazine Series 7*, 4, 417–36.

16

Nonlinear acoustics and its application to biomedical ultrasonics

P. A. LEWIN, Drexel University, USA and
A. NOWICKI, Polish Academy of Sciences, Poland

Abstract: Nonlinear acoustics and its application to biomedical ultrasonics are reviewed. Values of the nonlinear tissue parameter B/A are given and there is a discussion of a semi-empirical finite-amplitude method of B/A determination. The calibration of hydrophone probes in the whole imaging frequency range is described. Tissue harmonic imaging and multitone nonlinear coding are outlined. Multitone nonlinear coding enhances the signal-to-noise ratio of images compared with pulse inversion. Specific requirements for minimally invasive surgery using high-intensity focused ultrasound transducers are described. Clinically introduced procedures are reviewed. There is a discussion on shock wave use. Nonlinear acoustics is important for theragnostics.

Key words: nonlinear acoustics, nonlinear B/A parameter, ultrasound harmonic imaging, multitone nonlinear coding, piezoelectric composites, diagnostic and therapeutic ultrasound, ultrasound metrology, polyvinylidene di(fluoride) (PVDF) and fiber-optic hydrophones.

16.1 Introduction

The primary objective of this chapter was to review nonlinear acoustic (NLA) applications in biomedical ultrasonics; however, the selection was limited to include only relatively new developments. These include measurements of, and advances in, the determination of the nonlinear tissue parameter B/A, ultrasound metrology, visualization methods and theragnostics, which combines ultrasonically induced therapeutic and diagnostic procedures.

First, the basic principles of nonlinear acoustics are presented, with an emphasis on the physical interpretation of the interaction of ultrasound energy and tissue and its relevance to clinical applications, including diagnostic (imaging) and therapeutic (minimally invasive tissue modification) uses. The nonlinear parameter B/A is introduced and reviewed: it governs the development of a wave distortion as it propagates through a medium. In addition to the two widely used B/A measurement methods (finite amplitude and thermodynamic), an alternative, semi-empirical finite-amplitude method of B/A determination is described. The application of NLA in ultrasound metrology, especially the calibration of hydrophone probes in the conventional imaging frequency range, 1–20 MHz, and at frequencies exceeding 20 MHz, is described. The need for high-frequency calibration (>20 MHz) is explained with reference to the growing number of applications for intraluminal or catheter-based imaging, such as the characterization of vulnerable plaque and the network of capillaries in the vicinity of blood vessels and skin and ophthalmic imaging. The two critical parameters, namely the bandwidth of the probe and its finite aperture, which are required for a faithful reproduction of the pressure-time (p-t) waveform, are examined. The NLA calibration approach, which allows spatial averaging error correction and gives the complex (that is amplitude and phase) voltage sensitivity (V/Pa) versus frequency, is demonstrated. The diagnostic visualization of tissues using NLA is briefly summarized. This visualization includes tissue harmonic imaging (THI), which is widely used in clinical practice and enhances the quality of grayscale images, particularly in the examination and diagnosis of 'technically challenging patients', and a new ultrasound imaging method termed multitone nonlinear coding (MNC). MNC enhances the signal-to-noise ratio of images compared with pulse inversion (PI), which is another NLA imaging method. A section on NLA-based therapy describes specific requirements for minimally invasive surgery or interventions performed using high-intensity (up to 10 kW.cm^{-2}) focused ultrasound (HIFU) transducers. It reviews clinically introduced procedures, such as the treatment of liver tumors, prostate cancer and fibroids. There is a brief discussion on the use of shock waves in lithotripsy, pain management, drug-resistant-bacteria abatement and in the cosmetics industry. The chapter concludes with a summary and future development section, which stresses the importance of nonlinear acoustics in theragnostic, i.e. combined therapeutic and diagnostic, applications.

16.2 Basic aspects of nonlinear acoustic wave propagation and associated phenomena

This section gives a brief review of the principles of nonlinear acoustics, emphasizing the physical interpretation. For a rigorous analytical treatment of the fundamental equations of nonlinear ultrasonics, which are derived from the well-known equations of fluid mechanics, namely the equations of continuity, motion and energy, the reader is referred to specialty publications, textbooks or book chapters on the topic (Carstensen *et al.*, 1980; Muir and Carstensen, 1980; Haran and Cook, 1983; Beyer, 1984; Bjørnø and Lewin, 1986; Hamilton and Blackstock, 1998; Naugol'nykh and Ostrovskii, 1998; Szabo, 2004; Engflo *et al.*, 2008). Although there is a plethora of publications discussing different aspects of nonlinear acoustics, the publications listed above distinguish themselves in that they provide a comprehensive interpretation of the nonlinear propagation phenomenon and examine the generation and accretion of harmonics as an acoustic wave travels through the medium, allowing for intensity-dependent absorption.

The development of temporal distortion of a high-intensity (typically >1 W.cm^{-2}) or finite-amplitude (about 200 kPa) ultrasound wave is explained based on the dissipation arising from viscosity, heat conductivity and relaxation processes in the medium (here biological tissue or water), and the formation of higher harmonics to the fundamental frequency of the wave produced by the source. These two effects counteract, which explains why even a fully shocked wave eventually returns to a quasi-monochromatic frequency spectrum.

The physical interpretation of the nonlinearity parameter B/A as an indicator of a medium's susceptibility to generate harmonics is given in terms of density and specific entropy. The dimensionless material constant parameter B/A is a measure of the first-order deviation of the pressure–density relation from a linear dependence. The value of B/A determines the distortion level of the sound wave propagating through the nonlinear attenuating medium due to the generation of (native) harmonic frequencies. For most liquids, values of B/A range from about 4 to 11 (Bjørnø and Lewin, 1986). It may be shown that for B/A >2 (liquids) the waveform distortion mostly depends upon the nonlinearity of the equation of state, whereas for B/A <2 (gases) the convective contribution, given by the equation of state, prevails. Knowledge of the B/A parameter is necessary for predicting the behavior of nonlinear pressure fields in soft tissues in order to improve image quality using tissue harmonic imaging (THI) techniques (Averkiou, 2001; Szabo, 2004) and to assess the safety of modern ultrasound medical equipment. Verma *et al.* (2005a, b) showed that the use of the three-dimensional THI technique in obstetrics could produce harmonic-rich nonlinear waveform distortion. As the harmonic frequencies are generated in the nonlinear acoustic beam penetrating soft tissues whose attenuation coefficient increases with increasing frequency, this can lead to undesirable temperature elevation (Verma *et al.*, 2005b). Therapeutic ultrasound techniques, such as high-intensity focused ultrasound (HIFU, often referred to as high-intensity therapeutic ultrasound or HITU) and extracorporeal shock waves (ESWs or lithotripsy) produce a nonlinear waveform distortion, which is rich in harmonics, leading to enhanced local heating and thermal ablation of tissues in the focal region (Chavrier *et al.*, 2006; Curra *et al.*, 2007).

16.3 Measurements of and advances in the determination of B/A

Methods for the measurement of the nonlinear acoustic parameter in tissue were given in Bjørnø and Lewin (1986) and included the finite-amplitude (FA) and thermodynamic (TD) procedures along with real-time nonlinear tomography (RTT) (Ichida *et al.*, 1984).

The real-time tomography method was implemented using a 5-MHz continuous probing wave and a 500-kHz pumping wave, both applied at an intensity level of 0.01 W.cm^{-2} (spatial average, temporal average). Almost two decades later, a similar method was reported in Zhang *et al.* (2001). The tomography approach attempted to alleviate the inherent disadvantages of using FA or TD procedures for the clinical determination of B/A; both the FA and TD procedures are performed in vitro and at the best exhibit uncertainty of the order of 10%. However, whereas the RTT method may be capable of providing tomographic B/A related images in vivo, it was not immediately able to deliver the numerical values.

In the thermodynamic method, the parameter B/A is determined by measuring changes in the sound velocity caused by variations in the pressure for constant temperature, and variations in the temperature for constant pressure, applied to the tissue sample. The finite-amplitude method measures the second-harmonic pressure amplitude of an acoustic wave distorted during propagation through the medium tested. Both methods are based on simplified mathematical models, which assume propagation of a plane continuous acoustic wave in a lossless fluid. As already noted, the B/A values determined using these methods are seldom better than ±5% for liquids and ±10% for soft tissues (Bjørnø and Lewin, 1986). In Bjørnø and Lewin (1986), the biologically relevant B/A data were extracted from the literature to 1986. In the following, an attempt is made to succinctly summarize the B/A values published in the past quarter of a century and to present amendments to the measurement techniques that augment the overall confidence in the available values of the B/A parameter.

As mentioned above, the finite-amplitude and thermodynamic methods are widely used in the experimental determination of B/A. A modification of the FA method, in which the measurements were combined with results predicted using an iterative theoretical model, was proposed in Chavrier *et al.* (2006). Using an ultrasound source operating at 0.72 MHz to produce a wave traveling through a parallel structure comprising a 5-cm layer of water and a 15-cm layer of 1,3-butanediol, the rise times of the pressure-time waveforms recorded with a hydrophone probe were measured and subsequently compared with the ones calculated by the KZK model (Kuznetsov, 1971), by assuming that the unknown value of B/A for 1,3-butanediol ranged from 5 to 11. As expected, the results of modeling using successive iterations indicated that the nonlinear parameter for 1,3-butanediol is 11.05 ± 0.25. In other words, the hybrid semi-empirical approach enhanced confidence in the values obtained for a given medium by comparing experimentally determined data with those predicted by the model using an iterative procedure.

Another semi-empirical modified approach was proposed in Kujawska *et al.* (2009). The thickness of the examined or tested layer of an unknown medium was varied, a higher frequency source of 2 MHz was used and the waveforms recorded were compared not in time, but in the frequency domain. In contrast to the KZK model, which utilizes a parabolic approximation, a semi-empirical model (often referred to as the JW model for the initials of its developer) was used to predict the near-and far-field distributions by using a hyperbolic propagation operator (Radulescu *et al.*, 2003b). The JW model accounts for the effects of absorption, diffraction, and nonlinear interaction of the harmonics as well as for reflection and transmission at the media interfaces or boundaries. The boundary condition parameters, namely the acoustic source pressure amplitude and the pressure-time waveform, the insonifying aperture apodization function as well as the tested material density, sound velocity and frequency-dependent attenuation law are determined by preliminary measurements and are the input data to the model. The propagation of a finite-amplitude wave in a dissipative medium, including focusing and nonlinear and diffraction effects, is most widely described using the KZK equation (Kuznetsov, 1971), which assumes a cylindrical, well-collimated ultrasonic beam and is valid in the immediate vicinity of the acoustic axis of a symmetrical source. The JW model is somewhat more universal: it uses an experimentally determined distribution of the pressure amplitude measured at the transducer surface as one of the input parameters to predict the temporal and spatial field distribution of differently shaped sources at an arbitrary point in the field. In both Chavrier *et al.* (2006) and Kujawska *et al.* (2009), water was selected as the reference medium because its B/A value (5.3) has been determined numerous times and verified by several independent laboratories (Bjørnø and Lewin, 1986).

Comparison plots between the axial distributions of the measured pressure amplitudes and those predicted by the JW model are shown in Fig. 16.1 for the fundamental (2.25 MHz), second and third harmonics and exhibit an agreement to within ±3%, corroborating the validity of the (JW) nonlinear propagation model used.

B/A values, along with the corresponding values of density, sound velocity, the attenuation coefficient and the power law for a few materials, tested initially using the approach described above (Radulescu *et al.*, 2003; Kujawska *et al.*, 2009), are listed in Table 16.1. These values are to within 5% of the values given in the literature, which are shown in the column denoted 'B/A nominal'. The overall uncertainty of the semi-empirical FA method depends on the uncertainty of measurements of the boundary condition parameters used as input data to the numerical model and was estimated to be ±10%.

Table 16.1 Comparison of B/A and acoustic properties of a few liquids and biological media tested at a temperature of 25°C

Material	Density (kg/m^3)	Sound velocity (m/s)	Attenuation coefficient (N.pm^{-1}.Hz^b)	B/A (nominal)*	B/A using hybrid approach†	Attenuation, power law *b*
Distilled degassed water	997	1497	2.8×10^{-14}	5.3	5.3	2
Corn oil	920	1470	70×10^{-14}	10.5	10.0	2
Glycerol	1260	1890	570×10^{-14}	9.4	9.0	2
Pig blood	1080	1600	16×10^{-7}	6.2	6.0	1.1
Homogenized pig liver	1060	1550	78×10^{-7}	6.6	7.0	1

* B/A literature data: Beyer (1984), Chavrier *et al.* (2006), Cobb (1993) and Errabolu *et al.* (1987).

† This work: B/A results determined using the semi-empirical finite amplitude approach.

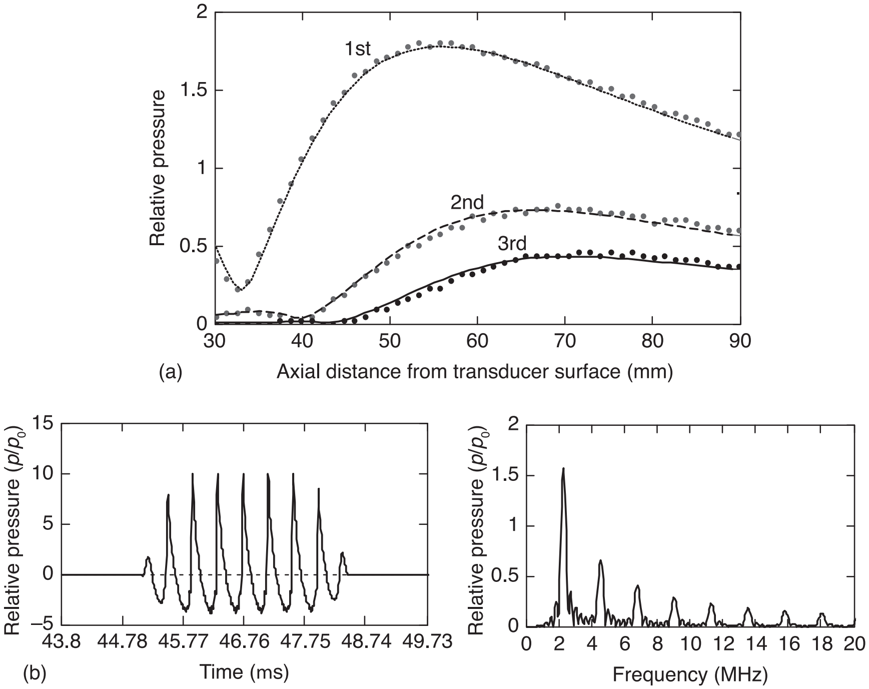

16.1 (a) Axial distributions of the fundamental (first), second and third harmonics obtained using a piezoelectric-focused source in water. The fundamental frequency of the source was 2.25 MHz with 8-cycles tone burst, the source pressure amplitude was 0.4 MPa, the effective radius 10 mm and the (linear) focal length 80 mm. Solid lines, predicted by JW model; dots, experimental data. (b) Pressure-time waveform recorded at 80 mm focal length (left) and the corresponding spectrum (right). Vertical axes represent normalized pressure amplitudes (p/p_0), where p_0=0.4 MPa. The waveform was generated by 2.25 MHz, 10 mm diameter, acoustic source having surface pressure p_0=0.4 MPa.

For convenience, additional B/A values of selected liquids and biological materials obtained at the ambient pressure using the FA and TD procedures are listed in Tables 16.2 and 16.3, respectively. These values were extracted from a comprehensive literature search including the data collected in Beyer (1984) and Bjørnø and Lewin (1986) and publications reported since 1986 (Law *et al.*, 1981; Cobb, 1983; Law *et al.*, 1983; Zhu *et al.*, 1983; Seghal *et al.*, 1984; Law *et al.*, 1985; Bjørnø, 1986; Seghal *et al.*, 1986; Errabolu *et al.*, 1987; Gong *et al.*, 1989; Dong *et al.*, 1999; Rielly, 2000; Grelowska, 2001).

The next section considers applications of nonlinear tissue properties in diagnostic ultrasound imaging.

Table 16.2 B/A values for different liquids obtained at the ambient pressure using the finite amplitude and thermodynamic methods

Medium	Temp. (°C)	B/A (finite amplitude)	B/A (thermo-dynamic)	Literature
Water, distilled	20	4.98		Bjorno and Lewin (1986); Cobb (1983)
Water, distilled	25		5.11 ± 0.2	Zhu *et al*. (1983)
Water, distilled	30	5.3	5.31	Bjorno and Lewin (1986); Law *et al*. (1983)
Water, distilled	30	5.5 ± 0.3	5.31	Bjorno and Lewin (1986); Law *et al*. (1985)
Sea water	30		5.47	Beyer (1984)
Ocean water	10		4.7	Grelowska (2001)
Methanol	20	9.6		Errabolu *et al*. (1987)
Ethanol	20	10.5		Errabolu *et al*. (1987)
n-Propanol	20	10.7		Beyer (1984)
n-Butanol	20	10.7		Beyer (1984)
Ethyl glycol	30		9.64	Bjorno and Lewin (1986); Law *et al*. (1985)
Ethyl glycol	30	9.93		Bjorno and Lewin (1986); Law *et al*. (1985)
Glycerine	30		9.08	Seghal *et al*. (1986)
Glycerine	30	8.96		Bjorno and Lewin (1986)
Glycerine	30	9.4		Bjorno and Lewin (1986); Law *et al*. (1985)
Corn oil	20	10.5		Errabolu *et al*. (1987)
Corn oil	22	10.6 ± 0.3		Dong *et al*. (1999)

16.4 Advances in tissue harmonic imaging

This section focuses on diagnostic imaging applications using tissue harmonic imaging (THI), which are widely used in clinical practice and provide an enhanced quality of grayscale images. In particular, the principles and advantages of a new ultrasound imaging method termed multitone nonlinear coding (MNC) (Nowicki *et al.*, 2007) are given. Its advantages compared with another nonlinear imaging-based method, the pulse inversion (PI) technique (Simpson *et al.*, 1999), are discussed.

It is instructive to briefly clarify the apparent ambiguity of the term ‘harmonic imaging’. In present clinical applications, two harmonic imaging modes can be identified: in contrast agent harmonic imaging higher harmonic frequencies are generated by reflection and scattering from microbubbles, whereas in tissue or grayscale harmonic imaging the harmonic frequency energy is generated gradually as an ultrasound wave propagates through the tissue. A discussion of

Table 16.3 B/A values for different biological materials obtained at the ambient pressure using the finite amplitude and thermodynamic methods

Medium	Concentration	Temp: (°C)	B/A (finite amplitude)	B/A (thermo-dynamics)	Literature
BSA (bovine serum albumin)	20 g/100 cm^3	25		6.23 ± 0.25	Zhu *et al*. (1983)
BSA	22 g/100 cm^3	30	6.45 ± 0.3		Bjorno and Lewin (1986); Law *et al*. (1981)
BSA	38.9 g/100 cm^3	30		6.68 ± 0.2	Bjorno and Lewin (1986); Law *et al*. (1983)
Hemoglobin	50%	30	7.6		Law *et al*. (1981)
Pork blood		26	5.8	6.3	Gong *et al*. (1989)
Pork blood		30	6.2 ± 0.25		Bjorno and Lewin (1986); Law *et al*. (1981)
Human blood		26	6.1	6.0	Gong *et al*. (1989)
Bovine liver (homogenized)		23	6.8 ± 0.4	7.0; 6.53	Bjorno and Lewin (1986); Law *et al*. (1985)
Bovine liver		30	6.42		Bjorno and Lewin (1986); Law *et al*. (1983)
Bovine liver		30	7.7 ± 0.9	7.23	Bjorno and Lewin (1986); Law *et al*. (1983)
Pork liver		25	6.7 ± 1.5		Bjorno (1986)
Pork liver		26	7.1	6.9	Gong *et al*. (1989)
Human liver (normal)		30	7.6 ± 0.8		Bjorno and Lewin (1986); Cobb (1983)
Human liver (congested)		30	7.2 ± 0.7		Bjorno and Lewin (1986); Cobb (1983)
Pork fat		26	10.8	10.9	Gong *et al*. (1989)
Pork fat		30	11–11.3		Seghal *et al*. (1984)
Breast fat tissue		30		9.91	Seghal *et al*. (1984)
Breast fat tissue		37		9.63	Seghal *et al*. (1984)
Tissue mimicking fluid		22	6.1		Rielly (2000)

the harmonic images produced by the nonlinear vibrations of the minute (typically less than 5 μm in diameter) contrast agents or microbubbles is beyond the scope of this chapter, and in the following only (native) tissue imaging is considered.

The ultrasound imaging modality referred to as tissue harmonic imaging (THI) was first described in Averkiou *et al.* (1997) and Averkiou (2001). This technique is routinely used in ultrasound imaging, providing an enhanced quality of grayscale images, especially in the examination and diagnosis of clinically ‘difficult or technically challenging patients’ (Becher *et al.*, 1998; Tranquart *et al.*, 1999). In comparison with conventional imaging, which uses the fundamental frequency only, THI has an enhanced (approximately twice) resolution and contrast-to-noise ratio, and uses scanheads (transducers) with a bandwidth capable of transmitting the fundamental or probing frequency and receiving (native) harmonic waves generated due to tissue nonlinearity. The implementation of these wideband transducers is discussed further in Section 16.5 of this chapter.

The higher the fundamental frequency, the better the spatial resolution; for instance, a 2.25-MHz probing frequency would collect echoes at 4.5 MHz, doubling the resolution. However, there is a trade-off associated with the penetration depth, because attenuation of the pressure amplitude increases with increasing frequency.

As discussed in Averkiou *et al.* (1997), the THI detection scheme is not optimal because only half of the transducer bandwidth available is used for image formation, i.e. the lower half during transmission and the upper half during reception. Image reconstruction also suffers from the reduced dynamic range and penetration depth. This is because images are formed with the first harmonic only and the pressure amplitude of the harmonic signal is approximately 20 dB lower than that of the fundamental or probing wave. By using a nonlinear imaging method, termed pulse inversion (PI), these disadvantages can be partly assuaged, giving an improved resolution and contrast-to-noise ratio. In contrast to conventional THI, the entire frequency spectrum of the scanhead can be used during reception. In this method, alternate pulses, π radians out of phase, are transmitted along the same scan line (Simpson *et al.*, 1999). The echoes received from the pair of transmitted signals are then summed to build the final image line. The advantage of the PI method is that it removes the requirement to transmit in a narrowband for harmonic signal extraction, and, even when transmitting in a broadband where fundamental and harmonic components overlap, it allows the harmonic component to be extracted.

A couple of examples showing an improvement in image quality are given in Fig. 16.2 and 16.3, where ultrasound images obtained using the fundamental frequency are compared side-by-side with images acquired using THI.

The multitone nonlinear coding (MNC) method is a further improvement in nonlinear imaging and it augments ultrasound image resolution (and hence quality). The signal-to-noise ratio of the mechanical index (MI, discussed in more detail below) (Szabo, 2004) is approximately 40% lower in comparison with the MI needed to obtain an image of identical quality using the pulse-inversion mode.

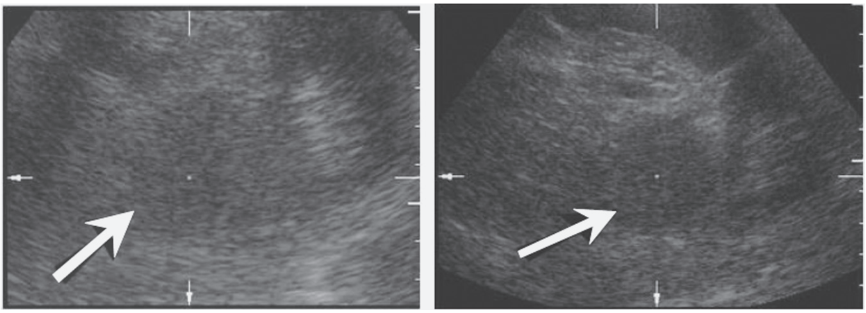

(a) (b)

16.2 Pheochromocytoma (a tumor mass) of the left adrenal gland (arrow). (a) Conventional 2.5-MHz (3.5-MHz center frequency) convex array (Antares, Siemens) image using the fundamental frequency only. (b) Tissue harmonic (TH) image obtained using 5-MHz reception. In panel (b), the borders of the adrenal mass are better delineated and more clearly visible. Contrast between the tumor and surrounding retroperitoneal tissues has increased.

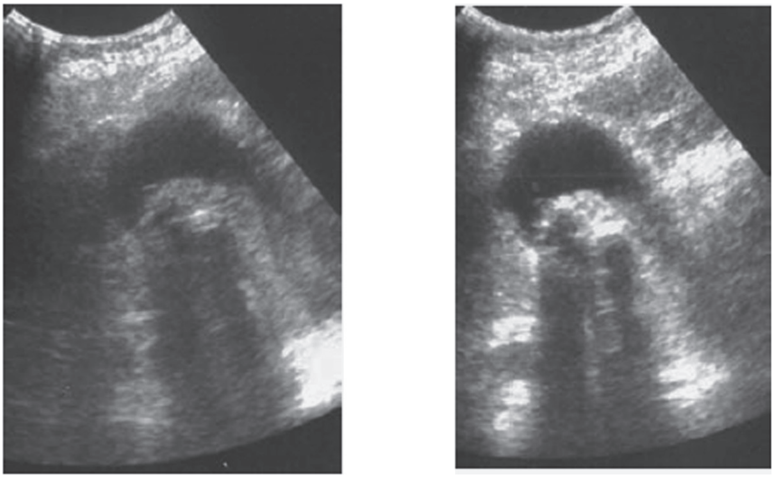

(a) (b)

16.3 Cholelithiasis (gallstones) of the gall-bladder. (a) Convex 2.5-MHz (3.5-MHz center frequency) array (Antares, Siemens) using the fundamental frequency only. (b) Tissue harmonic imaging. In panel (b) the gallstones are more clearly visible. The visibility of the characteristic acoustic shadow along with details of ultrasound features of the stones is also improved.

The MNC method was experimentally verified by scanning incident pulses propagating in soft tissue (Nowicki *et al.*, 2007) and also by scanning a thread phantom immersed in water. The method is outlined below.

Equation 16.1 describes how four different pulses are encoded through the choice of polarization of two individual tones:

$$P_{\mathrm{NC}}(t,\mathbf{x}) \equiv \left\{ \begin{array}{ll} +1 & +1 \\ or \cdot \sin(\omega_1 t) + & or \cdot \sin(\omega_2 t - \varphi) \\ -1 & -1 \end{array} \right\} \cdot \mathrm{Env}(t) \Rightarrow \left\{ \begin{array}{l} P_{pp}(t,\mathbf{x}) \\ P_{pm}(t,\mathbf{x}) \\ P_{mp}(t,\mathbf{x}) \\ P_{mm}(t,\mathbf{x}) \end{array} \right. , \ \mathbf{x} \in S(\mathbf{x}) \quad [16.1]$$

where $\omega_2 = 2\omega_1$, φ is the relative phase, here $\varphi = 0$, and Env(t) is a rectangular gating function.

Figure 16.4(a) is a graphic representation of the four MNC pulses encoded using Eq. 16.1 for fundamental and harmonic frequencies equal to 2.2 MHz and 4.4 MHz, respectively. The fundamental frequency of 2.2 MHz was selected as representative for cardiac and liver imaging. The corresponding pairs of the moduli of the Fourier spectra are shown in Fig. 16.4(b). The first contributing tone has a fundamental pulsation frequency equal to f_1 and the frequency of the second one is doubled. Hence, the transmitted pulses initially contain two frequencies: the fundamental f_1 and harmonic $f_2 \equiv 2f_1$. Also, each of the tones has its own polarization.

Although the moduli of the spectra of the transmitted pulses are pairwise identical – see Fig. 16.3(b) – the polarizations of the individual tones (i.e. their phases) are different within each pair. Even if $P_{pp} = -P_{mm}$ and $P_{pm} = -P_{mp}$, and their corresponding spectra are, respectively, $F_{pp} = -F_{mm}$ and $F_{pm} = -F_{mp}$ at the source plane, x∈ S(x), then, under the condition of nonlinear propagation in tissue, four different sets of pulses $P_{pp} \neq -P_{mm}$, $P_{pm} \neq -P_{mp}$ and $F_{pp} \neq -F_{mm}$, $F_{pm} \neq -F_{mp}$ are obtained. This is shown in Fig. 16.5, where the moduli of the Fourier spectra are

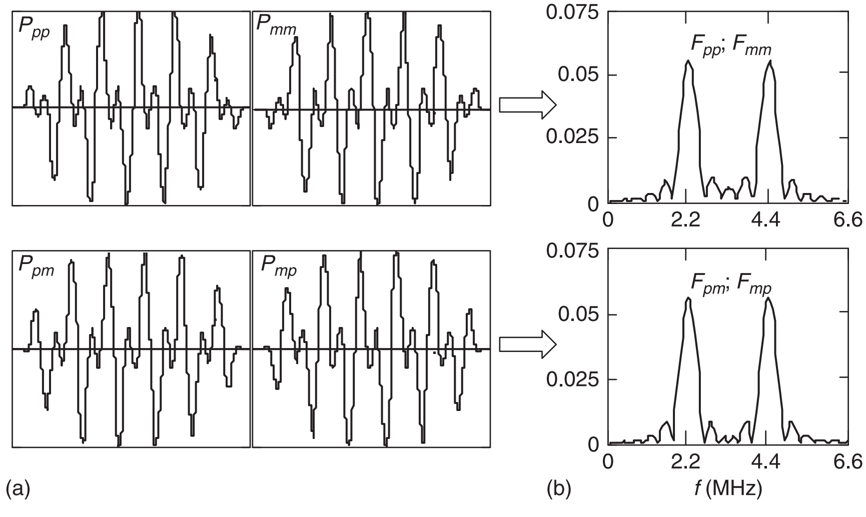

16.4 (a) Examples of four MNC pulses encoded using Eq. 16.1. Vertical axis is normalized to 1. (b) Corresponding pairs of the moduli of the Fourier spectra for the initial pulses shown in (a).

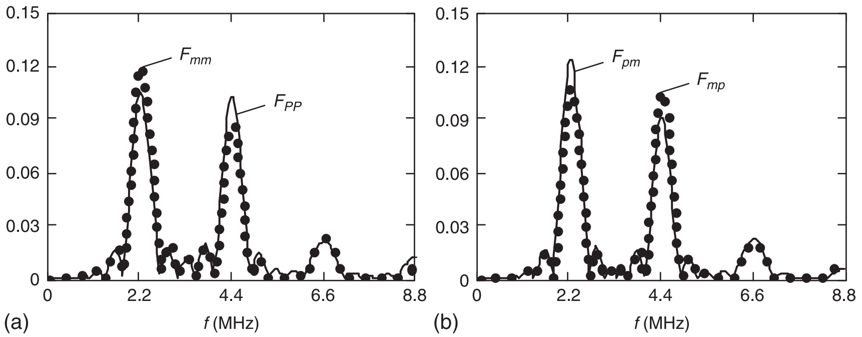

16.5 Moduli of Fourier spectra for nonlinear propagation near a physical focus of the 2.2-MHz source used for simulation: (a) for pulses P_{pp} and P_{mm}, (b) for pulses P_{pm} and P_{mp}.

plotted for pulses denoted as P_{pp}, P_{mm}, P_{pm} and P_{mp}. These simulations were performed for two tone bursts propagating in a tissue-like, lossy medium having an absorption of 7 Np.m^{-1}.MHz or about 0.6 dB.cm^{-1}.MHz^{-1}.

16.4.1 Pulse construction for MNC

Image construction requires an appropriate combination of the received echoes. In harmonic imaging, the received signals or echoes should be combined in such a way that the nonlinear propagation effects are amplified within the bandwidth of the harmonic frequency with the concurrent discrimination of the bandwidth of the original probing wave, i.e. the fundamental frequency. In conventional pulse inversion (Simpson *et al.*, 1999), only one pair of pulses and only one interrelation between the polarizations of the pulses within the pair (the pulses are of opposite phase) need to be considered. This limits the detection scheme to the one based on the summation of the detected echoes, only. However, by applying the above rule to the multitone nonlinear coding method, with the restriction that only two pulses can be combined, four basic pulses can be obtained, giving six pairs of pulses: [P_{pp}, P_{mm}], [P_{pm}, P_{mp}], [P_{pp}, P_{mp}], [P_{pm}, P_{mm}], [P_{pp}, P_{pm}] and [P_{mm}, P_{mp}]. For each of the pairs, the detection of the scattered or echo signals, with the subsequent addition or subtraction of the two echo signals, yields the combined signal. The nonlinear effects are amplified in the frequency bins corresponding to higher harmonics, i.e. $2f_1$ and $3f_1$. With respect to incident and scattered fields as well as the signals that are detected by the receiver, the combination of pulses within the relevant pairs can be expressed as:

$$\begin{aligned} P_{ppmm} &\equiv P_{pp} + P_{mm}, \quad & P_{pmmp} &\equiv P_{pm} + P_{mp}, \\ P_{ppmp} &\equiv P_{pp} + P_{mp}, \quad & P_{pmmm} &\equiv P_{pm} + P_{mm}, \\ P_{pppm} &\equiv P_{pp} - P_{pm}, \quad & P_{mmmp} &\equiv P_{mm} - P_{mp}. \end{aligned} \tag{16.2}$$

These equations are valid for transducer (or ultrasound source) excitation waveforms, probing waves and received echo pulses. The corresponding spectra of the incident MNC pulses for different combinations are shown in Fig. 16.6.

The two uppermost pairs of pulses of Eq. 16.2 produce combinations P_{ppmm} and P_{pmmp} (F_{ppmm} F_{pmmp}) and comprise pulses with opposite polarization (i.e. they have opposite polarizations of component tones with respect to the polarization of tones in the second pulse within the pair). These two special cases of

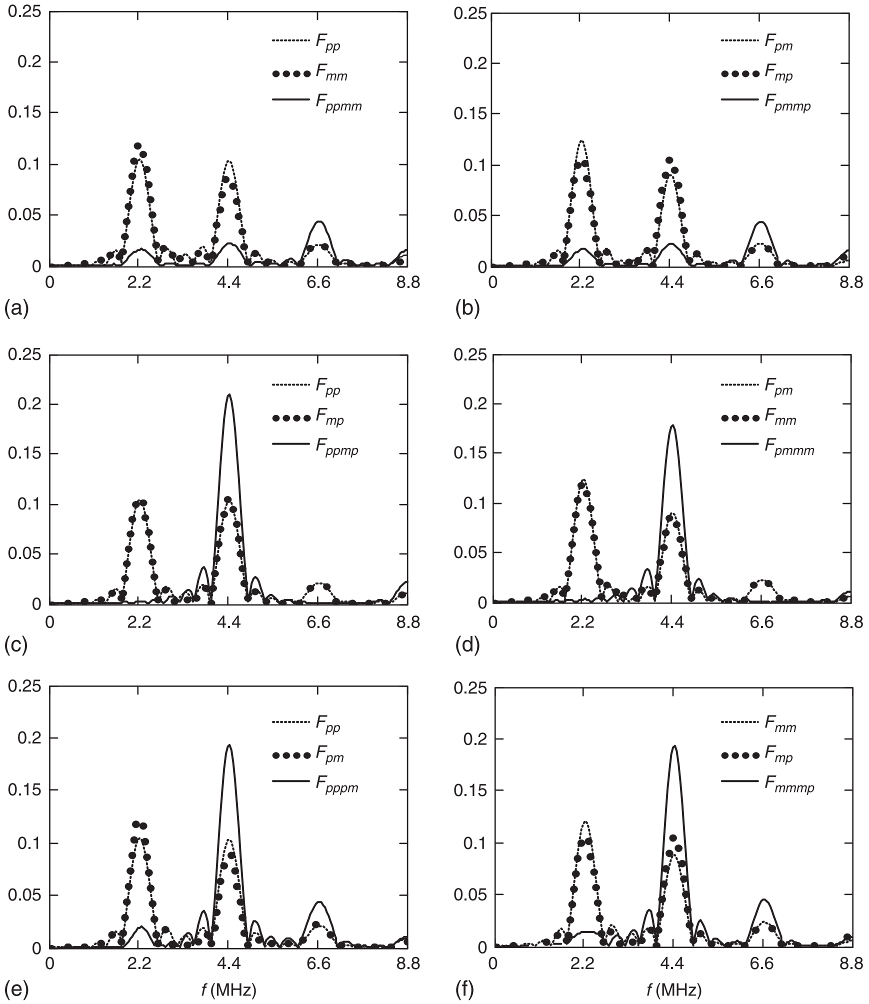

16.6 Moduli of Fourier spectra for different combinations of incident pulses (see Eq. 16.2).

the MNC method are referred to as multitone pulse inversion (MPI). In these two cases, as well as in the cases (e) and (f) shown in Fig. 16.5, in addition to the second harmonic, the third harmonic $3f_1$ is generated. Under specific conditions (sufficiently broadband scanhead and receiver), the third harmonic frequency can also be detected and processed for construction of the final image. A detailed description of the MNC imaging method can be found in Nowicki *et al.* (2007), where it is further demonstrated that, compared with conventional pulse inversion, in which the second harmonic is used to construct the image, MNC can be (as already pointed out) implemented without sacrificing image quality, with a mechanical index that is approximately 40% lower.

It is beyond the scope of this chapter to discuss the MI in detail; however, a few succinct comments are appropriate. Briefly, MI (Szabo, 2004) is widely accepted as an indicator of the likelihood of acoustically induced bioeffects that are associated with acoustic cavitation or streaming. Cavitation can be described as the mechanical response of cavities (gaseous voids or bodies) when subjected to mechanical stress exerted by an acoustic wave. There are two types of cavitation: stable (noninertial) and inertial (transient). Whereas inertial cavitation leads to implosion of the gaseous body accompanied by the local generation of high temperatures (of the order of 5000 K) and shock waves with pressure amplitudes close to 100 MPa, stable cavitation does not exhibit such violent behavior and is primarily associated with microstreaming in the fluid in which the cavity is immersed. MI is estimated in situ using the derating (attenuating) factor of $0.3\,\mathrm{dB.cm^{-1}.MHz}$, valid for soft (muscle) tissue, and is calculated from the ratio of the peak rarefactional (negative) pressure amplitude (MPa) and the square root of the acoustic frequency (MHz):

$$MI = \frac{p_{r,\alpha}(Z_{\mathrm{pii},\alpha})\ f_{\mathrm{awf}}^{-1/2}}{C_{\mathrm{MI}}}$$

where $C_{\mathrm{MI}} = 1\,\mathrm{MPa.MHz^{-1/2}}$, $p_{r,\alpha}(z_{\mathrm{pii},\alpha})$ is the attenuated peak rarefactional acoustic pressure measured at the so-called ‘global maximum’ distance and f_{awf} is the acoustic working frequency.

MNC can considerably reduce (by 40%) the value of the MI. That means that the rarefactional pressure amplitude of the probing wave is only 60% of the one needed for PI imaging, which lowers the likelihood of inertial cavitation. Preliminary testing of the method in vitro indicates that MNC has 10–30% better lateral resolution. In addition, which is most encouraging, the signal gain obtained using MNC can be up to eight times (18 dB) higher than that achievable with PI.

The next section focuses on the utilization of nonlinear wave propagation in water for the calibration of hydrophone probes in the wide, 100-MHz range and discusses ways of minimizing spatial averaging effects due to the finite aperture of the probes.

16.5 Nonlinear acoustics in ultrasound metrology

In order to fully appreciate the impact of NLA in stimulating advances in ultrasound metrology at the megahertz range of frequencies relevant for medical imaging, the background that prompted the development of the currently used hydrophone probes and their calibration using the nonlinear approach will be discussed.

Although the use of high frequency ultrasound, 15 MHz, was proposed as early as 1952 (Wild and Reid, 1952, 1957) for the detection of the histologic structure of living intact human breast tissue, it took over five decades before commercial imaging probes began to operate in the vicinity of this frequency. After the publication of Wild and Reid (1952, 1957), it was another decade or so before ultrasound imaging machines began to be commercially available, and the common wisdom at that time strongly supported the use of pulse-echo scanheads (imaging transducers) that operated at a resonance frequency of 2.25 MHz. The use of higher frequencies was initially dismissed due to the concern that frequency-dependent attenuation in tissue would cause the reflecting echoes to have inadequate amplitudes for forming clinically useful images. The scanheads were made of solid lead zirconate titanate (PZT) and had a relatively narrow fractional bandwidth (typically 30–35%). The basic characterization of a transducer's imaging performance was performed in pulse-echo mode by bouncing waves in water off a perfect reflector, small sphere or a sub-millimeter thick wire. This type of characterization was not able to provide any evidence of the finite-amplitude effects discussed in the previous subsection, because the recorded wave, displayed on an oscilloscope, was filtered twice: once on transmit and once on receive by the PZT transducer, which acted as a narrowband (bandpass) filter. This double filtering resulted in probing waves being displayed as a single tone, with a purely sinusoidal signal having an almost perfect Gaussian envelope. An alternative characterization of pulse-echo transducers was made in transmission mode using a relatively small (approximately 1 mm in diameter) ultrasound hydrophone probe as a receiver. However, the probes that were then available for characterization of the fields were also made of a solid, PZT ceramic. When carefully designed, PZT hydrophones have a relatively flat frequency response (Lewin and Chivers, 1982). However, probes using PZT disks suffered from a nonuniform frequency response and a sensitivity (in terms of V/Pa) that varied severely (of the order of 10 dB) as a function of frequency. This nonuniform response was caused by intrinsic mechanical resonances associated with both the fundamental and radial modes of vibration of the 1-mm-diameter PZT disk, which acted as a sensitive element. As a result, the observed pressure-time wave distortions measured by PZT hydrophones were ascribed to the imperfections of the transmitting circuitry and the imaging probe, and the poor frequency response of the hydrophone probe itself. During the early days of ultrasound medical imaging, hydrophones were calibrated at discrete frequencies only, often at coarse intervals of 1 MHz, and the calibration was seldom performed beyond 5 MHz.

In 1980, seminal papers by Carstensen *et al.* (1980) and Muir and Carstensen (1980) presented an analysis that indicated the possibility of nonlinear propagation of an ultrasound wave in tissue. At approximately the same time, the advent of the piezoelectric polymer polyvinylidene (di)fluoride (PVDF) allowed a new generation of ultrasound hydrophone probes to be designed (Lewin, 1981a; Harris *et al.*, 2000). This new generation of PVDF probes provided convincing experimental evidence for nonlinear acoustic wave propagation in tissue (Starrit *et al.*, 1985). The initial design of a miniature PVDF ultrasound hydrophone showed that it was possible to obtain a probe with a close to uniform frequency response (to within the overall uncertainty of calibration, typically ±10%) up to 10 MHz (Lewin, 1981a). In this context, it is appropriate to reiterate that at that time the interest in calibration of the probes beyond 10 MHz was limited because the imaging equipment operated primarily well below 5 MHz. Ultrasound hydrophone probes made of PVDF were not only able to confirm Muir and Carstensen's (1980) and Carstensen *et al.*'s (1980) analyses that nonlinear propagation could take place in the megahertz range (Starrit *et al.*, 1985) but also enabled the characterization of imaging transducers in terms of their directivity patterns and field distribution in the focal region at both fundamental and harmonic frequencies (Bjørnø and Lewin, 1982). As anticipated, these experiments confirmed that the lateral resolution (which is usually more limiting than the axial resolution, associated with the probing wave's pulse duration) achievable by using harmonic frequencies was enhanced by a factor of two, and hence this finding opened the possibility for improving image quality.

The impact that the advent of PVDF probes made in the field of biomedical ultrasonics can be appreciated even further by considering the outcome of yet another independent research initiative from the early 1980s. This research initiative was focused on improving ultrasound image quality by using minute spherical gas voids (of the order of a few microns) as contrast agents injected into the blood. The research into contrast agents spurred improvements of the fundamental model describing the dynamics of microbubbles and led to the experimentally verified conclusion that it was the harmonic and not the fundamental resonance frequency of a bubble that provided optimum image enhancement. It is this very finding that prompted efforts to design new imaging transducers capable of operating at both fundamental and harmonic frequencies. The imaging transducers used at that time were made of a solid piezoelectric ceramic with a rather narrow fractional bandwidth (30%), and consequently were not capable of processing frequencies higher than the fundamental one. The issue of the limited frequency bandwidth was resolved with the invention of a new class of piezoelectric materials, termed piezocomposites (Newnham *et al.*, 1980). These materials remarkably broadened the fractional bandwidth of imaging ultrasound transducers. Very briefly, piezocomposites are fabricated from a solid ceramic material diced in an appropriate manner (Fig. 16.7). The removed solid material is replaced by an epoxy filler. In a nutshell, this technology improved the pulse-echo sensitivity of

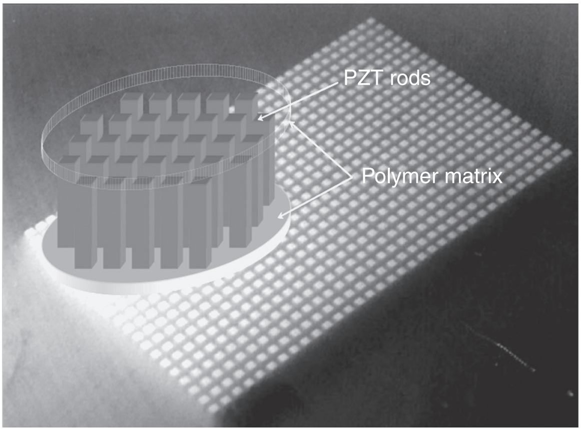

16.7 An example of an early design of a composite transducer: a solid PZT slab segmented into rods.

imaging transducers, allowed the acoustic impedance of a transducer to be controlled by the volume ratio of the soft filler and solid PZT ceramic, and also lowered the mechanical quality factor. As a result, a transducer's efficiency is substantially improved and its bandwidth almost doubles. More specifically, in comparison with solid PZT ceramics, the piezoelectric coupling coefficient, which controls electro-acoustic transducer efficiency, for this type of composite material increased by almost 100% (from about 0.25 to 0.5). The composite also has a lower quality factor, Q, which effectively doubles the fractional bandwidth from approximately 30–35% for solid ceramics to 60–70% for piezoelectric composites. The hybrid, piezoelectric material (usually PZT-5) and epoxy architecture means the acoustic impedance is adjustable, and it was reduced in practice from approximately 30 Mrayl down to 12–15 Mrayl. This, in turn, facilitated the optimization of the trade-off between image resolution and penetration depth (de facto the holy grail of ultrasound imaging). Figure 16.7 shows an example of an early design of a composite transducer and demonstrates the hybrid approach. The lengths of the solid PZT rods determine the fundamental mode of vibration. The space cut between them, called a kerf, will be embedded in an epoxy material (a polymer matrix). Both circular and rectangular geometries are easily implemented.

Closer testing of piezocomposite transducers led to the serendipitous discovery that echoes returning from the interrogated tissue volume contained both fundamental and harmonic frequencies. Apparently, some physicians misunderstood a manufacturer's request for them to test an experimental scanner designed to detect a second harmonic reflected from a contrast agent and, instead, used it without the contrast agent. Everyone was amazed by the picture quality obtained using the harmonic frequency. The harmonic-frequency image had a degree of detail which clearly surpassed anything available with conventional, fundamental-frequency grayscale imaging. The piezocomposite materials allowed the development of the now ubiquitously used wideband 1.5 D array scanners, which led to harmonic imaging. This imaging mode improved the quality of images and markedly boosted the diagnostic power of ultrasound.

To recap, wideband PVDF hydrophone probes were used to confirm the nonlinear propagation of ultrasound in biological tissue and facilitated the development and testing of a new generation of enhanced-bandwidth imaging transducers made of piezocomposite materials. This new generation of wideband, sensitive, multi-element transducers have highly improved image resolution, which was further enhanced by the introduction of digital technology, including digital beam formers with a high-dynamic range (exceeding 100 dB) and electronically controlled multi-focal zones. Concurrent advances in the associated electronic circuitry, along with advanced signal processing, improved the signal-to-noise ratio and made possible further improvements in image quality by enhancing the fundamental operating frequency.

As an aside – so this chapter is as up to date as possible – composite transducers are being gradually replaced by single crystal technology (Philips, 2004–2011), which gives a further enhancement of the fractional bandwidth and coupling coefficient. At the time of writing (May 2011) yet another, capacitive microfabricated ultrasound transducer (CMUT) technology awaits commercialization (Oralkan *et al.*, 2002). CMUT transducers made from cost-effective silicon (integrated circuits) lend themselves to mass-production using the same techniques as in electronic chip manufacturing. Their arrival will undoubtedly revolutionize both diagnostic and therapeutic ultrasound applications (Wong *et al.*, 2010). This technology means the front-end, the acoustic scanhead and associated electronics, including an analog-to-digital (A/D) converter, will be available as a self-contained assembly. This will considerably reduce the cost of transducer probes, whose current replacement price is close to 10–15% of the price of a top-of-the-line imaging system. With an individual transducer element of the order of 100 μm or less and a fractional bandwidth in excess of 100%, CMUTs can be fabricated in arbitrarily shaped patterns from fully populated two-dimensional arrays to switchable phased arrays using the annular array principle for maximizing the resolution at the edges of the deflected beam.

In the following, a succinct review of selected high-frequency clinical applications (>20 MHz) is given to underscore the need for truly wideband ultrasound hydrophone probes. With this background, the use of nonlinear wave propagation for the calibration of these probes is reviewed.

16.6 Nonlinear wave propagation in hydrophone probe calibration

Modern ultrasound diagnostic systems routinely use harmonic imaging and operate at center frequencies close to 15 MHz. The existing AIUM/NEMA standards (1998a, 1998b) and FDA guidelines (Patton *et al.*, 1994; FDA, 2008) require acoustic output characterization using hydrophone probes calibrated to eight times the center frequency of the imaging transducer. Thus, the ultrasound field generated by imaging arrays in the 12–15 MHz range should be measured by a calibrated hydrophone probe having a bandwidth of the order of 100 MHz (FDA, 2008).

In the last decade, the importance of measurements in the frequency range above 20 MHz increased substantially. Catheter-based systems often use frequencies beyond 20 MHz (Fleischer, 2000). Also, the characterization of vulnerable plaque and the network of capillaries in the vicinity of blood vessels is conducted using catheters operating in the frequency range 20–60 MHz (Goertz *et al.*, 2004). Likewise, ophthalmic examinations routinely use transducers operating beyond 20 MHz, and a frequency of 80 MHz is being tested to see if it can distinguish between epithelial and posterior corneal boundaries during a corneal scan. Monitoring of the blood flow in retinal vessels is also of interest; it increases the diagnostic power during routine eye examination and is also desirable during ocular occlusion-removal surgery. As blood velocity in retinal vessels is of the order of 10 mm/s or less, it is anticipated that Doppler systems operating at frequencies above 40 MHz will be needed to successfully detect and monitor blood flow (Lewin, nd). Skin imagers operating at 20 MHz are already fully accepted in clinical diagnostic practice, and can provide axial and lateral resolution of the order of 40 μm and 210 μm, respectively (Vogt *et al.*, 2007). However, this frequency is inadequate for the diagnosis of skin lesions in the epidermis; visualization of the epidermis is essential in an assessment of wound healing. Successful imaging of the dermis and epidermis can be obtained by using a 100-MHz imaging system as described in Vogt and Emert (2005). The system can also be used to diagnose skin tumors and differentiate between benign and malignant tissue based on the mechanical behavior of human skin. In addition to diagnostic applications, the imaging of skin is of interest to the cosmetic industry, as it allows monitoring of the effects of cosmetics on (ageing) skin.

The review presented above indicates a growing need for quantitative measurements of ultrasound fields in a frequency range that exceeds 20 MHz. However, in order to develop an appropriate measurement tool and to achieve this goal, two major challenges had to be overcome. The first was the finite aperture of ultrasound hydrophone probes and their frequency response and the second was calibration practice. The typical diameter of probes is of the order of several hundred (up to 500) microns and this leads to spatial averaging errors at frequencies below 10 MHz. The immediate consequence of the finite aperture and limited frequency response, which is usually insufficient to cover a wide, 100-MHz bandwidth (Beard *et al.*, 2000; Wilkens, 2003; Lewin *et al.*, 2005), is the inability of a hydrophone to reproduce the pressure-time waveform faithfully. Spatial averaging errors can be estimated using proven, experimentally verified models (Radulescu *et al.*, 2003a, 2003b). Alternatively, to eliminate the need for spatial averaging correction at 100 MHz, the effective diameter of the probe should be of the order of 7 μm. Such probes can be considered to be operating as point receivers at 100 MHz, but they require a fiber optic cable as a sensitive element (Lewin *et al.*, 2005). Hydrophone probes using fiber optics are an alternative to the currently used PVDF polymer probes, if small physical dimensions and the elimination of spatial averaging errors are of immediate concern for field measurements. However, PVDF probes are in general easier to operate and appropriate signal processing can provide spatial averaging error correction (Radulescu *et al.*, 2003a, 2003b).

The second challenge arose because at frequencies exceeding 10 MHz the calibration method using the reciprocity principle is difficult to implement. Although optic-based interferometric methods can be used, they require a fairly complex measurement arrangement (Esward and Robinson, 1999; Koch and Molkenstruck, 1999; Wilkens and Koch, 2004). To overcome this problem, calibration techniques taking advantage of nonlinear wave propagation have been recently developed (Radulescu *et al.*, 2003a, 2003b). Briefly, the techniques make use of a carefully developed semi-empirical nonlinear propagation model (Radulescu *et al.*, 2003a, 2003b; Umchid *et al.*, 2008), which can predict the field generated by an arbitrarily shaped source in terms of the pressure-time waveform of known amplitude. The model also takes into account the influence of the finite aperture of the probes immersed in the field at a selected distance (usually the focal plane). The same model was used in determining the B/A values given earlier. The absolute model-calculated pressure amplitude and the voltage measured across the hydrophone probe's terminals can be used to determine the absolute sensitivity of the probe (in terms of V/Pa) for a given frequency. The source transducer generates harmonics of the fundamental, and during calibration several sources operating at different fundamental frequencies are used. Several sources are needed to cover a wide, 100-MHz frequency range. The lower the operating frequency of the finite-amplitude source, the shorter the interval between harmonics and, consequently, the more accurate the extrapolation of the sensitivity values. A detailed description of the nonlinear calibration technique and the results obtained can be found in Radulescu *et al.* (2003a) and Umchid *et al.* (2008). Briefly, the voltage sensitivity of the fiber-optic (FO) sensors versus frequency is initially determined using the nonlinear calibration technique. As this technique yields the calibration at discrete frequencies only, additional calibration must be performed; to obtain a complete calibration up to 100 MHz, three acoustic methods are combined to determine the frequency-dependent sensitivity and the frequency response (Lewin *et al.*, 2008; Minasamudram *et al.*, 2009). These methods are time delay spectrometry (TDS) (Lewin, 1981b; Pedersen *et al.*, 1988), time-gated frequency analysis (TGFA) (Radulescu *et al.*, 2003a) and the semi-empirical nonlinear propagation model (Radulescu *et al.*, 2003b; Umchid *et al.*, 2008). The results of a calibration using this approach were verified by an independent national laboratory, which performed an optic calibration: it was found that both data were in close agreement (Fig. 16.8).

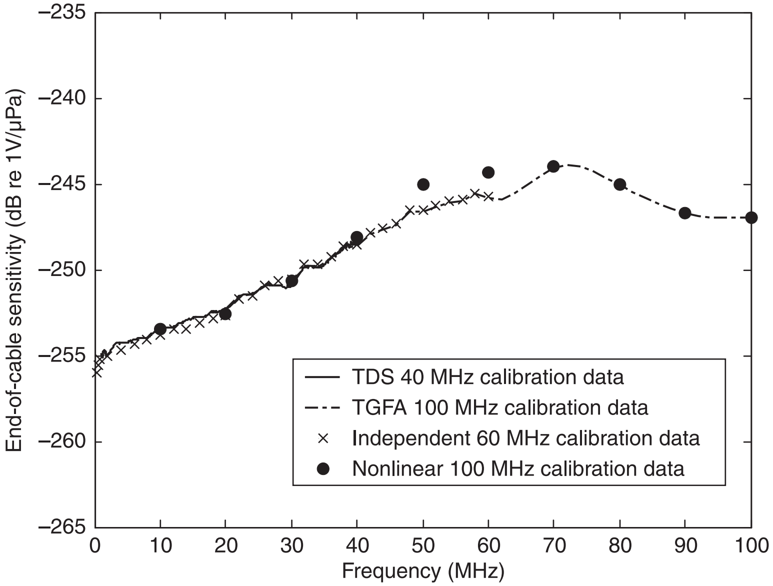

16.8 End-of-cable sensitivity of a 400-μm diameter bilaminar membrane hydrophone probe calibrated to 40 MHz using TDS and to 100 MHz using both TGFA and the nonlinear technique. Overall uncertainty: 1–40 MHz, ±1 dB; 40–60 MHz, ±1.5 dB; beyond 60 MHz, ±2 dB.

The application of TDS and TGFA to hydrophone calibration was independently reported in Koch and Molkenstruck (1999), Wilkens and Koch (2004) and Koch and Wilkens (2004). TDS and TGFA were selected because they allow a hydrophone's sensitivity to be obtained as a quasi-continuous function of frequency. The final calibration results shown in Fig. 16.8 were obtained by employing TDS from 1 to 40 MHz, TGFA from 20 to 100 MHz and the nonlinear model (Umchid *et al.*, 2008) from 10 to 100 MHz. This overlapping of the frequency ranges allowed verification of the developed calibration approach and has minimized the overall uncertainty.

Recently, phase measurements have been studied because a plot of phase versus frequency, when combined with the appropriate data processing of the measured pressure-time waveform, can be used to account for the complex phase relation induced by the finite aperture of a piezopolymer hydrophone (Koch and Wilkens, 2004; Cooling and Humphrey, 2008; Ghandi *et al.*, nd). In other words, there is an alternative to the point-receiver fiber-optic hydrophone, which exhibits zero phase shift in the relevant frequency range (100 MHz). Measurements of phase are not trivial (Koch and Wilkens, 2004; Cooling and Humphrey, 2008), but it should be noted that the semi-empirical nonlinear propagation model (Koch and Wilkens,

2004) has been used successfully to determine the phase versus frequency characteristic of a membrane hydrophone.

In the next section, nonlinear wave propagation in therapeutic applications is discussed.

16.7 Nonlinear acoustics in therapeutic applications

In addition to the nonlinear applications discussed above, a few other applications deserve some comment. These include therapeutic applications, drug-resistant-bacteria abatement and the increasing use of finite-amplitude waves in the cosmetics industry. All of these applications require the careful characterization of high-intensity focused ultrasound (HIFU) fields of up to 10 kW.cm^{-2} (Szabo, 2004). The detailed characterization of HIFU-produced fields, which are highly nonlinear, is crucial for optimizing tissue ablation and minimizing collateral damage. The measurement of these fields is difficult as widely used piezoelectric hydrophone probes cannot withstand the temperatures or cavitation effects produced by HIFU transducers in the focal region (Garcia-Murray *et al.*, 2006; Parsons *et al.*, 2006; Zhou *et al.*, 2006). Fiber-optic sensors have been shown to be well suited for HITU (HIFU) field measurements (Parsons *et al.*, 2006; Zhou *et al.*, 2006).

Whereas high-intensity therapeutic ultrasound (HITU) is primarily used for (malignant, such as tumor) tissue ablation using (extracorporeal) highly focused transducers producing several cycles or a quasi-continuous wave intensity of the order of 10 000 W.cm^{-2} in the focal plane or volume, devices capable of generating acoustic shock waves are used in therapeutic applications for the treatment of urethral, kidney or gall bladder stones. Shock-wave (also extracorporeally applied) devices are optimized to generate brief, microsecond-duration pulses with a peak compressional pressure amplitude of the order of 100 MPa and a rarefactional pressure amplitude of approximately 20 MPa in the focal plane or volume. Such peak pressures are used in ultrasound lithotripters and are capable of comminuting a kidney or urethral stone within 20 minutes or so of treatment during which the shock wave is delivered at the pulse repetition frequency of approximately 1 s. The pressure amplitudes generated in the focal planes of lithotripters are as high as hundreds of megapascals. Focused pressure amplitudes have been considered for pain relief, including the treatment of plantar fasciitis, patellar tendinitis (jumper's knee), lateral epicondylitis (tennis elbow), and medial and shoulder tendinitis or bursitis. There are too many publications on specific treatments to cite them here, but a relatively comprehensive review of the possible treatment of medical conditions can be found in Ogden and Warlick (2002). Although the specific mechanisms of action are not yet fully understood, it is believed that acoustic shock waves cause micro-disruptions, increased vascularization and the circulation and activation of growth factors that induce or accelerate the body's natural healing processes. More recently, acoustic shock waves have been proposed for the treatment of chronic wounds such as a diabetic foot ulcer or a pressure sore

(Ogden *et al.*, 2007). It has been suggested that the bacteria colonizing chronic wounds exist as persistent polymicrobial penicillin-resistant biofilm communities (Garth *et al.*, 2008). It is conceivable that this chemically impenetrable film could be shattered by a shock wave, after which an appropriate drug treatment could defeat the bacteria.

In the cosmetics industry, the adjusted-parameters extracorporeal shock wave (ESW) treatment has been proposed as a noninvasive cellulite therapy and for the redistribution and reduction of adipose tissue within the body (Kuhn *et al.*, 2008). This noninvasive reduction technique requires a highly focused ultrasound applicator to cause thermo-coagulation of adipocytes. The procedure is being explored as an alternative to invasive, and hence less desirable, liposuction procedures (Cimino, 2006).

16.8 Conclusions

In this chapter, selected applications of nonlinear ultrasonics in biomedical ultrasonics were discussed, including a semi-empirical approach for the determination of B/A, enhanced-resolution harmonic imaging schemes that, if successful, will allow imaging to be performed using the third harmonic, and advances in ultrasound metrology. The fusion of the nonlinear and TDS (also known as the swept frequency calibration) approaches gives the sensitivity versus frequency response of miniature hydrophone probes in a frequency range up to 100 MHz. Probes calibrated in such a wide frequency range will be indispensable for the further development of ultrasound imaging performed at frequencies that will produce images comparable with those achievable using magnetic resonance imaging (MRI). The diagnostic power of ultrasound and its clinical importance critically depend on image quality. If ultrasound can provide image quality comparable to MRI, there will be important societal effects, including the potential to contain or reduce the staggering healthcare expenses (a global priority at the time of writing), real-time image availability and advantages over alternative imaging such as computerized tomography (CT) and positron emission tomography (PET). MRI is irreplaceable for brain visualization and CT and PET are widely employed in all other diagnostic imaging applications; however, modern ultrasound probes, save for the brain and the limitations associated with air-rich tissues, offer equally acceptable tissue probing. In addition, the cost of noninvasive, nonionizing ultrasound in diagnostic applications compares favorably with the costs of using ionizing radiation devices (CT and PET) or MRI scanners. In conclusion, only selected *thera*peutic and dia*gnostic* ultrasound applications have been discussed. These can soon be expected to be combined into theragnostic feedback treatment, a term coined to describe a relatively new symbiosis field, where the diagnosis obtained through ultrasound imaging is followed by minimally invasive ultrasound therapy implemented through focused thermal ablation of malignant tissue and constant monitoring at diagnostic ultrasound exposure levels. In short, ultrasound will play a dual role: as a tissue modifying agent and as a powerful treatment monitoring tool.

16.9 Acknowledgements

The authors would like to express their sincere thanks to Dr T. Kujawska and Dr J. Wojcik of the Polish Academy of Sciences, Institute of Fundamental Technical Problems, for their insightful comments on the early draft of this chapter. Rafal Slapa, MD, Warsaw Medical University, Department of Radiology, Warsaw, Poland, is also thanked for the images shown in Fig. 16.2.

16.10 References

AIUM/NEMA (1998a) *Standard for Real-Time Display of Thermal and Mechanical Acoustic Output Indices on Diagnostic Ultrasound Equipment*, Rev. 1, American Institute of Ultrasound in Medicine (AIUM), Laurel, MD and National Electrical Manufacturers Association (NEMA), Rosslyn, VA.

AIUM/NEMA (1998b) *Acoustic Output Measurement Standard for Diagnostic Ultrasound Equipment*, American Institute of Ultrasound in Medicine (AIUM), Laurel, MD and National Electrical Manufacturers Association (NEMA), Rosslyn, VA.

Averkiou, M.A. (2001) *Tissue Harmonic Ultrasonic Imaging*, C. R. Acad. Sci., Paris, t. 2, Série IV (Applied Physics, Biophysics), 1139–51.

Averkiou, M.A., Roundhill, D.R. and Powers, J.E. (1997) A new imaging technique based on the nonlinear properties of tissues, *Proc. IEEE Ultrason. Symp.*, 2, 1561–6.

Beard, P.C., Hurrell, A.M. and Mills, T.N. (2000) Characterization of polymer film optical fiber hydrophones for use in the range 1 to 20 MHz: A comparison with PVDF needle and membrane hydrophones, *IEEE Trans. UFFC*, 47(1), 256–64.

Becher, H., Tiemann, K., Pohl, C., Nanda, N.C., Averkiou, M.A., Powers, J.E. and Luderitz, B. (1998) Improvement in endocardial border delineation using tissue harmonic imaging, *Echocardiography*, 15, 511–17.

Beyer, R.T. (1984) *Nonlinear Acoustics in Fluids*, Van Nostrand Reinhold, New York.

Bjørnø, L. (1986) Characterization of biological media by means of their nonlinearity, *Ultrasonics*, 24, 254–9.

Bjørnø, L. and Lewin, P.A. (1982) Nonlinear focusing effects in ultrasonic imaging, *Proc. of IEEE Ultrasonics Symposium*, San Diego, pp. 659–62.

Bjørnø, L. and Lewin, P.A. (1986) Measurement of nonlinear acoustic parameters in tissue, in *Tissue Characterization with Ultrasound*, Greenleaf, J.F., ed., CRC Press, Chapter 6, pp. 141–63.

Carstensen, E.L., Law, W.K., McKay, N.D. and Muir, T.G. (1980) Demonstration on nonlinear acoustical effects at biomedical frequencies and intensities, *Ultrasound Med. Biol.*, 6, 359–68.

Chavrier, F., Lafon, C., Birer, A., Barriere, C., Jacob, X. and Cathignol, D. (2006) Determination of the nonlinear parameter by propagating and modeling finite amplitude plane waves, *J. Acoust. Soc. Am.*, 119(5), 2639–44.

Cimino, W.W. (2006) VASER-assisted lipoplasty: Technology and technique, in *Liposuction: Principles and Practice*, Shiffman, M.A. and Giuseppe, A.D., eds, Springer, New York, NY, Berlin, Heidelberg, pp. 239–44.

Cobb, W.N. (1983) Finite amplitude method for the determination of the acoustic nonlinearity parameter B/A, *J. Acoust. Soc. Am.*, 73(5), 1525–31.

Cooling, M.P. and Humphrey, V.F. (2008) A nonlinear propagation model-based phase calibration technique for membrane hydrophones, *IEEE Trans. UFFC*, 55(1), 84–93.

Curra, F.P., Mourad, P.D., Khokhlova, V.A., Cleveland, R.O. and Crum, L.A. (2007) Numerical simulations of heating patterns and tissue temperature response due to high-intensity focused ultrasound, *IEEE Trans. UFFC*, 47, 1077–89.

Dong, F., Madsen, E.L., McDonald, M.C. and Zagzebski, J.A. (1999) Nonlinearity parameter for tissue-mimicking materials, *Ultrasound Med. Biol.*, 25(5), 831–8.

Engflo, B.O., Hedberg, C.M. and Kari, L., eds (2008) Nonlinear acoustics: Fundamentals and applications, *18th International Symposium on Nonlinear Acoustics (ISNA18)*, Stockholm, Sweden, 7–10 July, American Institute of Physics, ISBN: 9780735405448, 0735405441.

Errabolu, R.L., Seghal, C.M. and Greenleaf, J.F. (1987) Dependence of ultrasonic nonlinear parameter B/A on fat, *Ultrasonic Imaging*, 9, 180–94.

Esward, T.J. and Robinson, S.P. (1999) Extending the frequency range of the National Physical Laboratory primary standard laser interferometer for hydrophone calibrations to 60 MHz, *IEEE UFFC*, 46(3), 737–44.

FDA (2008) Revised FDA 510(k): *Information for Manufacturers Seeking Marketing Clearance of Diagnostic Ultrasound Systems and Transducers*, US Food and Drug Administration.

Fleischer, A.C. (2000) Sonographic depiction of tumor vascularity and flow: From in vivo models to clinical applications, *J. Ultrasound Med.*, 19(1), 55–61.

Garcia-Murray, E., Oscar, A., Rivas, K., Stecco, D.C. and Kuntz, L. (2006) Evaluation of acute and chronic systemic and metabolic effects from the use of HIFU for adipose tissue removal and non-invasive body sculpting, *Annual Society of Plastic Surgeons Meeting*, San Francisco, CA, 6–7 October, poster presentation.

Garth, A.J., Swagger, E., Wolcott, R., Pulcini, E., Secor, P., Sestrich, J., Costerton, J., and Philip, P.S., *et al.* (2008) Biofilms in chronic wounds, *Wound Rep. Reg.*, 160, 37–44.

Ghandi, G., Lewin, P.A. and Bloomfield, P.E. (nd) Nonlinear acoustics determination of phase characteristics of PVDF membrane hydrophones, *J. Physics (E)*, accepted for publication.

Goertz, D.E., Frijlink, M.E., de Jongand, N. and van der Steen, A.W. (2004) High frequency nonlinear scattering and imaging of submicron contrast agent, *Proc. IEEE Ultrasonics Symposium*, pp. 986–9.

Gong, X., Zhu, Z., Shi, T. and Huang, J. (1989) Determination of the acoustic nonlinearity parameter in biological media using FAIS and ITD methods, *J. Acoust. Soc. Am.*, 86(1), 1–5.

Grelowska, G. (2001) Fale sprężyste o dużym natężeniu w wodzie, Zeszyty Naukowe AMW, 146A, Gdynia (in Polish).

Hamilton, M.F. and Blackstock, D.T. (1998) *Nonlinear Acoustics*, Academic Press, San Diego, ISBN: 0123218608 9780123218605.

Haran, M.E. and Cook, B.D. (1983) Distortion of finite amplitude ultrasound in lossy media, *J. Acoust. Soc. Am.*, 73, 774–80.

Harris, G.R., Preston, R.C. and DeReggi, A.S. (2000) The impact of piezoelectric PVDF on medical ultrasound exposure measurements, standards and regulations, *IEEE Trans. UFFC*, 47(6), 1321–35.

Ichida, N., Sato, T., Miwa, H. and Kurukami, K. (1984) Real-time nonlinear parameter tomography using impulsive pumping waves, *IEEE Trans. UFFC (SU)*, 319(6), 635.

Koch, C. and Molkenstruck, W. (1999) Primary calibration of hydrophones with extended frequency range 1 to 70 MHz using optical interferometry, *IEEE Trans. UFFC*, 46(5), 1303–14.

Koch, C. and Wilkens, V. (2004) Phase calibration of hydrophones; heterodyne time-delay spectrometry and broadband pulse technique using an optical reference hydrophone, *J. Physics, Conference Series*, 1, 14–19.

Kuhn, C., Angehrn, F., Sonnabend, O. and Voss, A. (2008) Impact of extracorporeal shock waves on the human skin with cellulite: a case study, *Clinical Interv. Aging*, 3(1), 201–10.

Kujawska, T., Wojcik, J. and Nowicki, A. (2009) Determination of B/A of biological media by measuring and modeling nonlinear distortion of pulsed acoustic wave in two layer system of media, *Proc. of 2009 Acoustic Imaging Symposium*, Monterey, pp. 209–18.

Kuznetsov, V.P. (1971) Equations of nonlinear acoustics, *Sov. Phys. Acoust.*, 16, 467–70.

Law, W.K., Frizzell, L.A. and Dunn, F. (1981) Ultrasonic determination of the nonlinearity parameter B/A for biological media, *J. Acoust. Soc. Am.*, 69, 1210–12.

Law, W.K., Frizzell, L.A. and Dunn, F. (1983) Comparison of thermodynamic and finite amplitude methods of B/A determination in biological materials, *J. Acoust. Soc. Am.*, 74, 1295–7.

Law, W.K., Frizzell, L.A. and Dunn, F. (1985) Determination of the nonlinearity parameter B/A of biological media, *Ultrasound Med. Biol.*, 11(2), 307–18.

Lewin, P.A. (1981a) Miniature piezoelectric polymer ultrasonic hydrophone probes, *Ultrasonics*, 19, 213–20.

Lewin, P.A. (1981b) Calibration and performance evaluation of miniature ultrasonic hydrophones using time delay spectrometry, *Proc. IEEE Ultrasonics Symposium*, 660–4.

Lewin, P.A. (nd) High Frequency Biomedical and Industrial Ultrasound Applications, available at http://papers.icultrasonics.org/1796_lewin_plenary.pdf.

Lewin, P.A. and Chivers, R.C. (1982) Two miniature ceramic ultrasonic hydrophone probes, *Phys. E. Sci. Instrum.*, 14, 1420–4.

Lewin, P.A. and Schafer, M.E. (1986) Ultrasonic probes in measurement practice, *Med. Device Diagn. Ind.*, 8(5), 40–8.

Lewin, P.A., Mu, C., Umchid, S., Daryoush, A. and El-Sherif, M.A. (2005) Acousto-optic, point receiver hydrophone probe for operation up to 100 MHz, *Ultrasonics*, 43(10), 815–21.

Lewin, P.A., Gopinath, R., Umchid, S., Daryoush, A.S., Srinivasan, K., Bansal, L. and El-Sherif, M. (2008) Acousto-optic sensor for characterization of ultrasound fields up to 100 MHz, *Proceedings IEEE Sensors Conference*, Lecce, 27–31 October, Lecce, Italy, pp. 193–6.

Minasamudram, R.G., Arora, P., Gandhi, G., Daryoush, A.S., El-Sherif, M.A. and Lewin, P.A. (2009) Thin film metal coated fiber optic hydrophone probe, *Applied Optics*, 48, G77–82, PubMed # 19881652, NIHMSID # 179400, PMC # 2836494.

Muir, T.G. and Carstensen, E.L. (1980) Prediction of nonlinear acoustic effects at biological frequencies and intensities, *Ultrasound Med. Biol.*, 6, 345–59.

Naugol'nykh, K.A. and Ostrovskii, L.A. (1998) *Nonlinear Wave Processes in Acoustics*, Cambridge University Press, New York, ISBN: 052139080X 9780521390804 052139984X 9780521399845.

Newnham, R.E., Bowen, L.J., Klicker, K.A. and Cross, L.E. (1980) Composite piezoelectric transducers, *Materials in Engineering*, 2, 93–106.

Nowicki, A., Wójcik, J. and Secomski, W. (2007) Harmonic imaging using multitone nonlinear coding, 11, *Ultrasound Med. Biol.*, 33(7), 1112–22.

Ogden, J.A. and Warlick, J.F. (2002) Method for using acoustic shock waves in the treatment of medical conditions. United States Patent 6390995.

Ogden, J.A., Brown, R.S. and Wheelock, A. (2007) Method for using acoustic shock waves in the treatment of a diabetic foot ulcer or a pressure sore. United States Patent 7189209.

Oralkan, O., Ergun, A.S., Johnson, J.A., Karaman, M., Demirci, U., Kaviani, K., Lee, T.H. and Khuri-Yakub, B.T. (2002), Capacitive micromachined ultrasound transducer: Next generation arrays for acoustic imaging?, *IEEE Trans UFFC*, 49(11), 1596–610.

Parsons, J.E., Cain, C.A. and Fowlkes, J.B. (2006) Cost-effective assembly of a basic fiber-optic hydrophone for measurement of high-amplitude therapeutic ultrasound fields, *J. Acoust. Soc. Am.*, 119(3), 1432–40.

Patton, C., Harris, G.R. and Philips, R.A. (1994) Output levels and bioeffects indices from diagnostic ultrasound exposure data reports of the FDA, *IEEE Trans. UFFC*, 41(3), 353–9.

Pedersen, P.C., Lewin, P.A. and Bjørnø, L. (1988) Application of time-delay spectrometry for calibration of ultrasonic transducers, *IEEE Trans. UFFC*, 35(2), 185–205.

Philips (2004–2011) Pure Wave Transducer Technology. Available at: http://www.healthcare.philips.com/main/products/ultrasound/technologies/purewave.wpd.

Radulescu, E.G., Lewin, P.A., Wojcik, J. and Nowicki, A. (2003a) Calibration of ultrasonic hydrophone probes up to 100 MHz using time gating frequency analysis and finite amplitude waves, *Ultrasonics*, 41(4), 247–54.

Radulescu, E.G., Wojcik, J., Lewin, P.A. and Nowicki, A. (2003b) Nonlinear propagation model for ultrasound hydrophones calibration in the frequency range up to 100 MHz, *Ultrasonics*, 41(4), 239–45.

Rielly, M. (2000) A theoretical and experimental investigation of nonlinear ultrasound propagation through tissue mimicking fluids, *Proceedings of the 2000 IEEE Ultrasonics Symposium*, 1355–8.

Seghal, C.M., Bahn, R.C. and Greenleaf, J.F. (1984) Measurements of the acoustic nonlinearity parameter B/A in human tissues by a thermodynamic method, *J. Acoust. Soc. Am.*, 76(4), 1023–9.

Seghal, C.M., Porter, B.R. and Greenleaf, J.F. (1986) Ultrasonic nonlinear parameters and sound speed of alcohol-water mixtures, *J. Acoust. Soc. Am.*, 79(2), 566–70.

Simpson, H.D., Chin, C.T. and Burns, P.N. (1999) Pulse inversion Doppler: A new method for detecting nonlinear echoes from microbubble contrast agents, *IEEE Trans. UFFC*, 46(2), 372–82.

Starrit, H.C., Perkins, M.A., Duck, F.A. and Humphrey, V.F. (1985) Evidence for ultrasonic finite amplitude distortion in muscle using medical equipment, *J. Acoust. Soc. Am.*, 77, 302–12.

Szabo, T.L. (2004) *Diagnostic Ultrasonic Imaging Inside Out*, Elsevier, ISBN 0-12-680145-2, pp. 500–1, p. 508 (for MI).

Tranquart, F., Grenier, N., Eder, V. and Pourcelot, L. (1999) Clinical use of ultrasound tissue harmonic imaging, *Ultrasound Med. Biol.*, 25(6), 889–94.

Umchid, S., Gopinath, R., Srinivasan, K., Lewin, P.A., Daryoush, A.S., Bansal L. and El-Sherif, M. (2008) Development of calibration techniques for ultrasonic hydrophone probes in the frequency range from 1 to 100 MHz, *Ultrasonics*, 49(3), 306–11.

Verma, P.K., Humphrey, V.F. and Duck, F.A. (2005a) Broadband measurements of the frequency dependence of attenuation coefficient and velocity in amniotic fluid, urine and human serum albumin solutions, *Ultrasound Med. Biol.*, 31(10), 1375–81.

Verma, P.K., Humphrey, V.F. and Duck, F.A. (2005b) Broadband attenuation and nonlinear propagation in biological fluids: An experimental facility and measurements, *Ultrasound Med. Biol.*, 31(12), 1723–33.

Vogt, D. and Emert, H. (2005) Development and evaluation of a high frequency-ultrasound-based system for in vivo strain imaging of the skin, *IEEE Trans. UFFC*, 52(3), 375–85.

Vogt, M., Scharenberg, R., Moussa, G., Sand, M., Altmeyer, P. and Ermert, H. (2007) High Frequency Skin Imaging System, in *Acoustical Imaging*, Andre, P., ed., Springer, pp. 137–44.

Wild, J.J. and Reid, J.M. (1957) Progress in the techniques of soft tissue examination by 15 Mc (MHz) pulsed ultrasound, in *Ultrasound in Biology and Medicine*, Kelly, E., ed., AIBS, Washington, pp. 30–45.

Wild, J.J. and Reid, J.M. (1952) Application of echo ranging techniques to the determination of structure of biological tissues, *Science*, 115, 226–30.

Wilkens, V. (2003) Characterization of an optical multilayer hydrophone with constant frequency response in the range from 1–75 MHz, *J. Acoust. Soc. Am.*, 113, 1431–8.

Wilkens, V. and Koch, C. (2004) Amplitude and phase calibration of hydrophones up to 70 MHz using broadband pulse excitation and an optical reference hydrophone, *J. Acoust. Soc. Am.*, 115(6), 2892–903.

Wong, S.H., Kupnik, M., Watkins, R.D., Butts-Pauly, K. and Khuri-Yakub, B.T. (2010) Capacitive micromachined ultrasonic transducers for therapeutic ultrasound applications, *IEEE Trans. Biomed. Eng.*, 57(1), 114–23.

Zhang, D., Xiu-Fen, G. and Chen, X. (2001) Experimental imaging of the acoustic nonlinearity parameter B/A for biological tissue via a parametric array, *Ultrasound Med. Biol.*, 27(10), 1359–65.

Zhou, Y., Zhai, L., Simmons, R. and Zhonga, P. (2006) Measurement of high intensity focused ultrasound fields by a fiber optic probe hydrophone, *J. Acoust. Soc. Am.*, 120(2), 676–85.

Zhu, Z., Ross, M.S., Cobb, W.N. and Jensen, K. (1983) Determination of the acoustic nonlinearity parameter B/A from phase measurements, *J. Acoust. Soc. Am.*, 74(5), 1518–21.

17

Therapeutic ultrasound with an emphasis on applications to the brain

P. D. MOURAD, University of Washington, USA

Abstract: Diagnostic and therapeutic ultrasound have their roots in studies targeting applications to the brain from the 1920s and 1930s, with a heyday in the 1950s. There has been a significant resurgence over recent decades in applications of diagnostic and therapeutic ultrasound to the central nervous system. This chapter provides a review of how ultrasound interacts with tissue, followed by diagnostic ultrasound highlighting issues relevant to therapeutic applications, then a summary imaging the peripheral nervous system and brain. Therapeutic ultrasound is discussed: concepts, extensions or enhancements of concepts useful for diagnostic ultrasound, followed by a summary of recent advances, with a review of recent work, on neuromodulation with ultrasound.

Key words: ultrasound, diagnostic ultrasound, therapeutic ultrasound, central nervous system, tumors, blood clots, drug delivery, neuromodulation.

17.1 Introduction and summary

Here, I review diagnostic and therapeutic ultrasound, discussing examples that target applications of ultrasound to the central and peripheral nervous systems. I make liberal use (paraphrases, quotes, concepts) of the existing general review literature on diagnostic and/or therapeutic ultrasound, for example, O'Brien (2007), Leighton (1994), ter Haar and Coussios (2007), and Mourad (1999), among others. I will also directly cite specialized literature. Frankly, given the on-line resources these days, any interested reader can dig quite quickly through a number of dedicated websites and find relevant materials. My goal here, therefore, is to walk the reader through the concepts with a minimum of distractions rather than exhaustively review the literature. I will therefore cite, primarily, a mix of classic papers and books and recent review articles.

I first offer a general summary of ultrasound's interaction with tissue, starting with a description of its propagation, absorption and scattering.

Important phenomena involved in acoustic propagation include the fundamental non-linearity of this process, which produces down-stream effects from the ultrasound source that form the basis of a number of important diagnostic and therapeutic phenomena. In particular, ultrasound absorbs as it propagates in proportion to the local intensity of ultrasound, intrinsic properties at the molecular level of the medium supporting the propagation, among other factors. Such absorption adds heat and momentum to the tissue. That heat increases the tissue's temperature; the associated strain pushes the tissue. Ultrasound will induce heat both as it propagates, and especially at its focus, of concern for diagnostic ultrasound, generally desired for therapeutic applications. If the tissue has low enough internal coherence, or is instead a fluid, ultrasound's absorption will cause local flow known as 'acoustic streaming.' That heat and/or local strain can also cause 'cavitation,' that is the generation and/or stimulation of gas-filled voids within the material, described generically as bubbles, where stimulation causes the bubbles to grow and shrink and sometimes to break up or collapse. Cavitation can, in turn, produce local strains in the tissue and fluid that are close to the bubbles. (For example, local fluid flow around a bubble is called 'acoustic microstreaming.') Oscillating bubbles generate more ultrasound focally, at the carrier frequency of the incident ultrasound as well as at higher frequencies. (Lower-period motions can also occur, at fractional subharmonics of the incident wave.) Monitoring of these acoustic emissions forms the basis for some novel imaging practices. Their production also tends to cause an increase in the energy absorbed from the incident sound field, thereby producing more cavitation as well as more momentum and heat. Local cavitation generally also increases the subsequent scatter of ultrasound. The biological effects of ultrasound have their therapeutic effect in these thermal, mechanical, and chemical processes.

Typical applications of ultrasound for diagnostic purposes use short pulses (generally one to a few acoustic cycles) of intense (up to 5 MPa of instantaneous pressure, with instantaneous, spatially focal intensities of up to a few W.cm^{-2}) ultrasound spaced fairly far apart in time (typically of the order of a millisecond) at frequencies (generally 1 to 10 MHz) high enough to resolve, via the generation and measurement of acoustic backscatter, fine-scale biological structure (with length scales of fractions of a millimeter and larger). The specific choices of these parameters balance the need to maximize the backscattered signal strength and imaging resolution, by increasing the intensity and frequency of the sound, with the need to avoid harmful biological effects, achieved by decreasing the length and increasing the spacing of the pulses to help minimize the production of heat and mechanical forces within the imaged tissue.

With regard to diagnostic ultrasound, much research has been devoted to learning how to avoid altering tissue while using it, through what is known as study of ultrasound 'bioeffects'.

However, as in many things, a *desired* bioeffect can produce a desired therapeutic effect, and therapeutic ultrasound has as its guiding principle the study of its possible benefits, that is, its ability to treat disease with ultrasound, rather than to simply diagnose. Therapeutic ultrasound, especially for the brain, remains a research tool, one with significant promise that I will highlight here.

As summarized for diagnostic ultrasound, therapeutic ultrasound generates beneficial bioeffects by using a wider range of frequencies (0.02 to 10 MHz), focal pressures (1–50 MPa) and instantaneous, spatially focal intensities (10–10 000 W.cm^{-2}) applied either in pulsed mode as compared with diagnostic ultrasound, often with greater pulse lengths and more pulses per second than in diagnostic ultrasound, or with ‘continuous waves,’ where there is no break in the application of ultrasound from the time it is first turned on until it is finally turned off.

To understand its promise for therapy, I will first review the fundamentals of ultrasound’s interaction with tissue, then highlight its diagnostic usefulness before turning directly to its applications for therapy.

17.2 Fundamentals of propagation and absorption of ultrasound

Almost all basic texts on ultrasound start by considering ultrasound waves as strictly and invariably periodic disturbances to the local density, pressure, location and velocity. Examples include Kinsler *et al.* (1982) as well as Kremkau (1998).

When sound propagates in fluids it creates local, periodic perturbations in that fluid’s density, pressure, and temperature as well as inducing within the fluid small-scale displacements in the direction of wave propagation. When sound propagates in a simple solid, it generally does so both via ‘longitudinal’ pressure waves, just described, and via ‘shear’ waves, where the displacements and changes in pressure occur transverse to the direction of wave propagation. In the majority of biomedical applications the longitudinal waves dominate, and I restrict my discussion to this mode for this chapter. An important exception is sonoelastic imaging, as I discuss below.

While sound propagation is always in principle a ‘non-linear’ process (e.g., Blackstock and Hamilton, 1997), that is, the qualities of the sound as it propagates vary as a complex function of its amplitude, in many practical applications the properties of the sound vary linearly with amplitude, so that doubling the amplitude of the ultrasound wave doubles the associated variations in pressure, density, displacement and particle velocity. Under those circumstances, simple and useful formulae exist which relate the sound’s frequency, amplitude, intensity, particle displacement, etc., assuming that the pressure wave varies sinusoidally in space and time (again, Kinsler *et al.*, 1982). However, those formulae and the sinusoidal concept on which they rest break down when the amplitude of the sound increases sufficiently and/or the wave propagates sufficiently far (Christopher and Carstensen, 1996). For example, in an unbounded medium the initial ‘sine wave’ form of the acoustic wave will evolve into a sharpened saw-tooth structure through the processes of diffraction, absorption, and focusing. A useful example comes from the field of lithotripsy (Sapozhnikov *et al.*, 2007). There the application of high-intensity pulses of focused ultrasound breaks up calcified stones within the kidney and gallbladder, and standard applications create a short acoustic wave train whose shape is far from sinusoidal, with peak positive pressures of up to 50 MPa that come and go within a few nanoseconds, and peak negative pressures of up to 1 MPa that last a few microseconds. One can represent these non-linear waves via a Fourier series as a sum of sinusoids of increasing frequency relative to the frequency of the initial sinusoid. Within this description, one can say that

that the acoustic wave becomes non-linear via the generation of harmonics of the fundamental wave as the latter propagates and/or grows.

17.3 Acoustic attenuation as absorption plus scattering

As unfocused sound propagates through a medium, its amplitude decreases. It does so in part because the medium absorbs the sound and in part because the acoustic energy is scattered in a direction away from the propagation direction (Dunn *et al.*, 1969). The relative amount of absorption versus attenuation in biological tissue depends significantly on the type of tissue. To appreciate why tissue attenuates sound, we start with quantifying how much sound tissue attenuates. The attenuation coefficient of ultrasound measures how much the amplitude of a propagating wave decreases as it propagates over a standard distance. For example, if a medium has an attenuation coefficient of 1 Np.cm^{-1} (Np = Neper), this means that as the sound propagates 1 cm its pressure amplitude has shrunk to 1/e of its original value. The book by Duck (1990) organizes many fundamental constants describing ultrasound properties such as the attenuation coefficient, and is a required reference book for anyone working in ultrasound.

At 1 MHz the attenuation coefficient in water at room temperature is 0.00025 Np.cm^{-1}, a negligible amount in the laboratory and significant only over kilometers in the ocean. In pure water, attenuation occurs through thermal relaxation of the water molecule, with a few additional molecular relaxation mechanisms that correspond to each of the typical chemicals in salt water. However, attenuation in biological tissue at 1 MHz is significantly higher, partly due to increased absorption and also to increased scattering. For example, the attenuation coefficient for whole blood is 0.024 Np.cm^{-1} while for plasma (whole blood minus red and white cells and platelets) it is 0.008 Np.cm^{1}. The different attenuation values for plasma and whole blood at the same frequency arise mostly because of scattering of the sound by the cells in whole blood, an attenuation mechanism missing from plasma. The different attenuation coefficients for plasma and water at the same frequency arise because the individual proteins in the plasma absorb sound more efficiently than water, since proteins have many more degrees of freedom available than water molecules. However, although the levels of attenuation at 1 MHz differ as described, ultrasound attenuates more quickly in water as a function of increasing frequency than in biological tissue: attenuation increases as the square of the frequency in water but as only a little more than the first power of frequency in most tissue. (This means that the generation of higher and higher harmonics of a propagating ultrasound wave described above will eventually curtail due to the increase in attenuation of the higher frequency waves.) At 1 MHz, liver has an attenuation coefficient of 0.08 Np.cm^{-1}, larger than that of plasma, because liver has a greater concentration of proteins. Interestingly, pureed liver has a comparable attenuation coefficient to that of whole liver, thus showing that it is absorption on the molecular scale rather than at the scale of tissue structure that causes acoustic attenuation (Pauly and Schwan, 1971). The majority of papers on physical mechanisms of attenuation speak about multiscale springs within tissue responding in different, but coordinated, ways as an ultrasound wave propagates through the tissue. (A particularly pleasing example of this is offered by Kelly and McGough (2009), who consider a fractal distribution of springs.)

Note, however, that scattering from discrete structures in tissue decreases the net transmission of ultrasound waves to a given point of interest, contributing to an effective increase in attenuation above the molecular mechanisms I have just discussed. Collagen is the common protein in biological tissue, and its concentration in tissue correlates well with acoustic attenuation due to absorption. For example, at 2.2 MHz and body temperature, white matter in the brain has an attenuation coefficient of 0.121 Np.cm^{1}, while gray matter has an attenuation coefficient of 0.072 Np.cm^{-1}, and white matter absorbs more sound than gray matter. Finally, human lung tissue has an attenuation coefficient of 3.5 Np.cm^{1} at 1 MHz, owed almost entirely to the scattering of sound rather than to absorption, while bone at 1.0 MHz has an attenuation coefficient of 2.5 Np.cm^{1}, almost entirely owed to absorption rather than to scattering.

Absorption of sound in tissue can produce physical and chemical effects in biological media. These include the generation of heat, the addition of momentum and the production of bubbles, the latter known as ‘acoustic cavitation’. I will now discuss these phenomena.

17.4 Physical and chemical processes engendered by medical ultrasound

17.4.1 Heat generation and thermal index

Sound absorbed by tissue generates heat at the site of absorption in a process described mathematically by the negative gradient of the energy flux vector of the sound field (Jain, 1983; ter Haar and Coussios, 2007). When the acoustic waves are linear or weakly non-linear, that heat-generation term reduces to a quantity proportional to the intensity of the signal and absorption (not attenuation) coefficient of the tissue, although for most applications the attenuation coefficient replaces the absorption coefficient, primarily because the attenuation coefficient is easier to measure than the absorption coefficient. The ‘bio-heat’ equation describes the various processes that affect the translation of heat generated by ultrasound into increases in the temperature of tissue. It does so by codifying the net effect of tissue diffusion, heat capacity, and density along with the spatially integrated action of capillary beds, which can ‘perfuse’ heat away from the acoustic source of heat as long as the tissue remains undamaged. Arteries or veins conduct heat away from a site also, and their presence within real and modeled tissue severely alters the temperature effects induced by ultrasound. Under therapeutic conditions, the temperature can approach 100°C in a fraction of a second (ter Haar and Coussios, 2007). This rapid temperature rise can denature tissue, useful for 'cooking' cancer cells as a way to kill them, or even vaporize tissue, useful for ablation-based therapies for killing cancer, or for re-opening passages within the body, for example. (We discuss these applications in the section on therapeutic ultrasound.) However, such effects are to be avoided when applying ultrasound diagnostically. The thermal index gives a measure of the temperature rise induced in tissue under diagnostic conditions (Kremkau, 1998). It is based on conservative estimates of the average heat generated within tissue and takes into account transducer characteristics that govern the intensity of sound at the site of acoustic heat generation as well as attenuation as the wave propagates through intervening tissue.

17.4.2 Acoustic radiation pressure

Sound absorbed by tissue and fluids not only adds heat but also adds momentum to those tissues and fluids via a force known as the 'acoustic radiation force,' created by the negative of the gradient of 'radiation pressure' induced by acoustic waves (fun references include Rudenko *et al.*, 1996; Sarvazyan, 2010). When an acoustic wave with constant properties (intensity, frequency well-defined over a single pulse, etc.) deposits momentum in a substance away from boundaries, the sound effectively pushes the substance in a time-independent way in the direction of acoustic-wave propagation. In water, this process shows up as a steady current moving away from the transducer known as 'acoustic streaming.' Within tissue, this process strains the tissue by attempting to move it away from the acoustic source. Nightingale and colleagues (e.g., Palmeri and Nightingale, 2011) have developed sophisticated means of generating and analyzing the resulting tissue deformation (see Fig. 17.1 for an example of their technique, here applied transcranially to living rat brain). Myers (2006) gives a way of calculating the maximum displacement of tissue generated by this force. Finally, the presence of a bubble or any large impedance mismatch increases the acoustic radiation force generated by the absorption of ultrasound.

If two (or more) confocal transducers apply at their mutual focus ultrasound with slightly different frequencies, the resulting momentum will deposit with a 'beat' frequency such that the tissue will move at that frequency, in a field now known as vibroacoustography. Analysis of the resulting acoustic emissions gives information about the properties of the material at the focus, such as its stiffness. Greenleaf and colleagues developed this original idea (Fatemi and Greenleaf, 1999), generating interesting images of arterial plaque, defects in industrially derived materials and other relevant examples where variations in stiffness can be expected. One may find a detailed study of the physics of vibroacoustography in Silva and Mitri (2011).

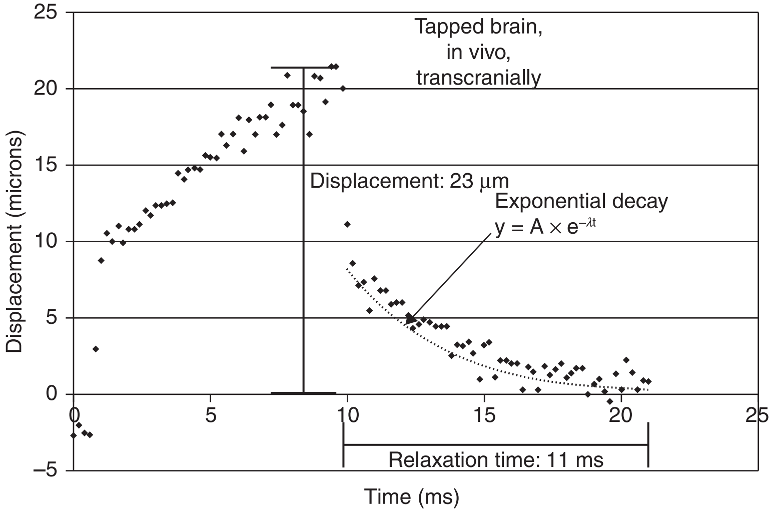

17.1 An example displacement of living rat brain, where a single pulse of focused ultrasound was applied through the skull of a rat for 10 ms in duration, with a comparable relaxation time. The maximum displacement measures less than the radius of a typical human hair.

17.4.3 Acoustic cavitation

Excellent surveys of cavitation review bubble formation and growth; bubble dynamics (the properties and behavior of isolated or communities of bubbles when stimulated by ultrasound, including bubble scattering and emission); mechanical effects of bubbles, including microstreaming; hydrodynamic jet and shock formation; and sonochemistry. Here, I would include classics such as Leighton (1994), Brennen (1995) and Young (1989) with recent review articles focusing on cavitation and contrast agents (discussed in the following), such as Wu and Nyborg (2008 – early pioneers of ultrasound in its many forms) as well as Ferrarra's recent article (Caskey *et al.*, 2011), among many. All these physical and chemical processes can occur in vivo with generally profound biological consequences. Given the existence of survey articles and books focused on cavitation, I shall highlight only essentials here before moving on to their applications. This general discussion of cavitation will focus on acoustic and bubble behavior in solutions, sometimes adjacent to (tissue) boundaries where current understanding has its firmest underpinnings. Exciting observations in vivo (e.g. Chen *et al.*, 2011) support the utility of this approach.

17.5 Bubble formation and growth

In practice water will cavitate at low ultrasonic frequencies at pressure amplitudes of a few tenths of a megapascal. However, in theory the threshold for cavitation of water should be a hundred times this pressure, based on the tensile strength of pure water. A significant reason for this disparity is the presence of impurities within water (Crum and Fowlkes, 1986). Examples include dust, which can trap minute quantities of gas within cracks on its surface, or microbubbles within the fluid stabilized by a skin of surfactant. (Electromagnetic radiation in the form of gamma rays represents another source of cavitation nuclei, independent of the purity of the liquid.) These are nascent bubbles, or ‘cavitation nuclei’. The amplitude necessary to form a bubble from these sources, known as the ‘cavitation threshold’, increases with increasing frequency and surface tension, for example, among a host of other parameters.

Once created, the oscillating sound field will cause the bubble’s size to oscillate within an acoustic cycle. Continued acoustic stimulation of a free bubble will cause that bubble to grow, at least initially, via a process known as ‘rectified diffusion.’ Rectified diffusion (Crum, 1984) describes the net effect on bubble size over a few to many acoustic cycles of changes in both the concentration gradient of diffusing gases near the bubble’s surface (generally of prime importance) and the surface area of the bubble (generally of secondary importance) within an individual acoustic cycle. Briefly, as a bubble expands the bubble’s surface area grows, as does the concentration gradient of the gas adjacent to the bubble’s surface within the liquid. At the same time, the concentration gradient of the gas inside the bubble adjacent to the bubble surface decreases. All these factors increase the flux of gas from the outside of the bubble to its inside. When the bubble’s size decreases, the surface area decreases and the changes in gas concentration gradient adjacent to the bubble’s surface reverse. The net result is an increase in the flux of gas from the inside to the outside of the bubble. However, because of asymmetry in this process (the surface area of the bubble is larger when the bubble is big compared with when it is small), the bubble grows minutely with each acoustic cycle and significantly over many acoustic cycles.

17.5.1 Bubble dynamics

Bubbles, like springs, have a primary resonant frequency. For bubbles, this frequency varies inversely with the bubble’s radius and also strongly depends on gas content and surface tension, among other factors. (Leighton, 1994, offers a masterful text on this and other processes involved in cavitation.) Newly formed bubbles within relatively weak acoustic fields often have a resonant frequency that is different from the applied frequency, making their temporal variations in volume both within an acoustic cycle and over many acoustic cycles initially small and sinusoidal. (‘Stable’ or non-inertial cavitation refers to bubbles undergoing such relatively simple volumetric changes where factors in addition to or instead of the inertia in the surrounding fluid govern the bubble behavior.) Under these circumstances the bubbles both scatter sound (because of their geometric properties and their impedance mismatch with the surrounding fluid) and emit sound (via the compression and rarefaction of the liquid surrounding the bubble) at the frequency of the applied signal. Generally the emitted sound has a larger amplitude than the scattered sound. As the bubbles grow toward their resonant frequency (which can happen in only a few cycles), or as the applied sound field increases, the volumetric changes in the bubble evolve to more complex functions of time within an acoustic cycle, as do the acoustic emissions, whether or not those changes remain radially symmetric. As a function of growing bubble amplitude, those emissions first include the superharmonics of the applied signal. Eventually, the once stably oscillating bubble collapses violently and/or becomes asymmetric. The individual 'mother' bubble may break down at this point into a small cloud of microbubbles – known as 'daughter' bubbles. With continued acoustic stimulation, the process of bubble growth and eventual destruction will re-commence. Without continued acoustic stimulation the bubbles will eventually decay or float away. With an appropriately timed re-start of the applied sound, as in pulsed applications of ultrasound, these daughters may be optimally configured for acoustically driven growth or violent collapse, as desired. Before the finish of possible daughter production, but requiring continued acoustic stimulation, will be larger-amplitude, broad-band acoustic emissions over a greater range of frequencies and the eventual emission of multiples of the subharmonic of the applied signal. The detection of these emissions via a hydrophone (e.g., various papers by Ron Roy such as his early paper, Roy *et al.*, 1990) offers a means of remotely assessing the level of cavitation activity within insonified material and often correlates with a variety of mechanical and chemical effects associated with cavitation, to which we now turn.

17.5.2 Microstreaming

Pulsating bubbles generate vorticity and hence a viscous boundary layer within the liquid adjacent to their surface. The shear in this layer will stress any material in the solute close to the bubble. Also, the oscillations of the bubble help bring material from afar into the vicinity of the bubble via the induction of a generally steady flow in the fluid known as acoustic microstreaming (e.g., Nyborg, 1965; Leighton, 1994).

There exist a number of studies whose central scientific principle is the use of an isolated bubble (mounted on the end of a minute tube, for example, or induced by a vibrating wire) or a collection of isolated bubbles (formed by hydrophobic membranes containing gas-filled micropores) to allow controlled study of the stable-cavitation process. Rooney (1970) used a 250-mm diameter bubble suspended at the end of a small tube within a vial of red blood cells stimulated by a 20-kHz sound source to measure the shear stresses necessary to create hemolysis. This value – about 450 Pa – was consistent with those determined experimentally with a standard viscometer, validating the supporting theory. Miller *et al.* (1979) show platelet aggregation created by a stably cavitating bubble. A much more recent example developed more analytical detail and documented analytically and in video the powerful shear forces around cavitating bubbles and their effect on cells (Marmottant and Hilgenfeldt, 2003). Also, Coakley and Nyborg (1978) make an instructive calculation of the strength and reach of microstreaming for a microbubble with a resting radius of 3.3 mm that is resonant at 1 MHz. For a weak, driving pressure of 5000 Pa, the bubble's amplitude variation will be a tenth of its resting radius. Platelets in saline drawn to the bubble's surface will arrive there with a velocity of about 1.3 $m.s^{-1}$, while platelets two resting radii away from the center of the bubble will approach with a velocity of 0.0004 $m.s^{1}$, which gives a sense of the reach of the streaming field. Nonetheless, these velocities are significant: they calculate that it would take about 0.003 s to clear the space around the vibrating bubble out to two resting radii from the center of the bubble.

Bubbles are not ordinarily present within the fluid within human beings, but can and have been introduced to enhance imaging and to disrupt the blood-brain barrier, as we discuss below. (Tanter's group has performed an interesting study searching for cavitation in sheep's brain – Gateau *et al.*, 2011.) This means that, without their introduction, for medical ultrasound to be dangerous in vivo it must initiate as well as stimulate acoustic bubbles. This generally requires the production of 'inertial cavitation,' to which we now turn.

17.6 Inertial cavitation and associated material stresses

A bubble may collapse asymmetrically because its amplitude becomes large enough that only inertial forces govern the collapse (during the process of 'inertial' cavitation) or because it is near an interface such as that formed by a container, blood vessel or another bubble. The result will be irregular and aperiodic microstreaming and hydrodynamic jet formation. This microstreaming has been recently documented using in vivo and ex vivo videography to stretch, deform and tear at blood vessels within reach of the bubble (again, Chen *et al.*, 2011), a desirable process for therapeutic effects such as facilitating drug delivery, a dangerous process in the context of most diagnostic applications of ultrasound.

The inertial collapse of a bubble can occur within a single acoustic cycle, and therefore the potential for inertial cavitation cannot be eliminated even for very short pulses of ultrasound. This fact forms the basis of the analysis behind the creation of the 'mechanical index' (by Apfel and colleagues – Holland and Apfel, 1989; Apfel and Holland, 1991), an index used in diagnostic ultrasound machines to avoid the possibility of inertial cavitation in vivo, to which we turn now.

17.7 Mechanical index

For diagnostic purposes, cavitation poses an obvious danger when one considers the mechanical, thermal, and chemical effects associated with it. Apfel and

Holland, noted previously, developed a conservative measure for the onset of inertial cavitation of a pre-existing bubble subjected to one cycle of applied acoustic pressure, called the 'mechanical index'. They chose inertial cavitation because associated with it are the potentially deleterious processes one can expect due to cavitation in the human body, where stable cavitation is quite unlikely. This measure is proportional to the peak negative pressure amplitude and inversely proportional to the square root of the frequency of the applied sound. Its governing assumptions include isothermal growth of an optimally sized bubble, the neglect of gas diffusion into the bubble, and that the fluid surrounding the bubble is incompressible. (All these assumptions produce the most violent bubble collapse, making the mechanical index as conservative as possible.) Their theory predicts the value of the mechanical index associated with the circumstances under which their theoretical bubble produces internal temperatures of 5000°C, which they argue diagnostic ultrasound machines should not exceed. Their basic approach has been accepted, and diagnostic ultrasound machines display a measure of the mechanical index that varies from application to application based on extensions of the original work of Apfel and Holland.

Hynynen (1991) measured the cavitation threshold in muscle. It remains the definitive experimentally determined reference on the subject. Interestingly, cavitation in tissue may explain observations of significant (around 10°C) increases in temperature generated within tissue or in vitro, because of simultaneous measurements of strong, broadband acoustic emissions and hyper-echogenicity within the tissue (e.g., Holt and Roy, 2001). This points to the presence and therefore possible thermal significance of bubbles in the same area as the temperature rise of a size too large to be explained by standard, bubble-free absorption of ultrasound by the tissue. This represents an area of ongoing research; the current consensus is that focal generation by cavitating bubbles of a large range of harmonics of the incident ultrasound energy causes rapid generation of heat local to the bubble due to the absorption of those harmonics, and hence a rapid temperature rise in the tissue (Holt and Roy, 2005).

17.8 Diagnostic ultrasound

17.8.1 Standard diagnostic imaging

There exist a multitude of useful and practical overviews of diagnostic ultrasound. A classic text is Kremkau (1998). The basic concept of diagnostic ultrasound resides in the notion that sound is backscattered from tissue as a function of the acoustic impedance and position of that tissue, and that the acoustic impedance and position tell you something fundamental about the tissue. In standard applications, that 'something fundamental' is the structure and hence identity of the tissue. So-called A-mode ultrasound produces a simple, one-dimensional trace of backscattered echoes. This modality is useful for applications of diagnostic ultrasound to the eye, for example, where capturing structure in more than one dimension is not the issue. In B-mode imaging, a series of A-mode scans at different angles from the diagnostic source are collected together to form two-dimensional maps of the backscatter values as functions of distance and angle relative to the acoustic source/receiver. In M-mode imaging, an A-mode scan is followed in time, producing a time–distance trace that finds particular use in imaging the heart with its periodic motion. Besides imaging stationary or moving structure, one can measure the speed and direction of moving tissue and fluids (blood is by far most analyzed in this fashion) via ‘Doppler imaging’. Doppler imaging takes advantage of the fact that blood moves relative to the direction of acoustic wave propagation to create images based on the strength and direction of the Doppler shift in the backscattered signal.

Important clinical examples of Doppler for the brain include monitoring for vasospasm (the constriction of cerebral blood vessels, producing ischemic damage downstream of the blood vessel), and emboli entering the brain, which can occlude blood vessels through the formation of blood clots, again producing ischemic effects (e.g., Tsivgoulis *et al.*, 2009).The practical details of these existing imaging methods, the avoidance of bioeffects, and the search for new imaging modalities make diagnostic ultrasound a challenge. As an example of an imaging detail, diagnostic ultrasound based on acoustic backscatter requires the careful interleaving of transmitted and received acoustic energy with the assumptions that one can translate time of flight into distance using a standard speed of sound. Artifacts in acoustic images can arise when these assumptions break down. Also, acoustic shadows form within tissue due to the strong absorption of sound by one tissue type that lies between the acoustic source and another tissue type.

However, when successful, diagnostic ultrasound can create spectacular images, useful for diagnostics of peripheral and central nervous system disorders. For example, a paper by Kermarrec *et al.* (2010) demonstrated the surprising anatomical detail afforded by recent diagnostic ultrasound machines for imaging peripheral nerves and their associated diseases in a manner that compares favorably with MRI. Peripheral nerves consist of axons, Schwann cells, and connective tissue sheaths. The endoneurium is a connective tissue sheath consisting of loose vascular connective tissue and extracellular fluid. A peripheral nerve is held together by the epineurium and consists of one or more nerve fascicles, which in turn are made up of bundles of endoneurium and nerve fibers. Currently, ultrasound provides the greatest resolution for peripheral nerves, and is non-invasive and low cost. It also provides dynamic imaging and is capable of being moved to image the entire length of a peripheral nerve. Some recent major improvements to ultrasound that make it even more useful for imaging peripheral nerves include high frequency high-resolution broadband transducers, artifact reduction software, and real-time spatial compound ultrasound. Ultrasound’s high resolution allows clinicians to detect lesions on nerve fascicles and differentiate them from lesions of the interfascicular epineurium. Extended field-of-view techniques allow clinicians to more easily depict neurogenic tumors, as the technique displays the abnormal structure and the adjacent structures as a whole, making it possible to measure large lesions and tumors. MR, in contrast to ultrasound, does not have a high enough resolution to image small distal nerves. Ultrasound is also advantageous in that it is cheaper than an MRI machine, has a higher spatial resolution, can travel along a nerve, and has dynamic imaging capabilities. Disadvantages to the use of ultrasound for diagnostic imaging of peripheral nerves include operator dependency, especially a steep learning curve, and the inability of high-frequency ultrasound to resolve deep nerves due to its high attenuation by the intervening tissues.

17.8.2 Sonoelastic imaging

A physician's palpation of tissue – essentially, a low-frequency interrogation of the elastic properties of tissue – gives them information on tissue not contained within standard diagnostic images. Sonoelastic imaging works on the principle behind palpation by taking advantage of the fact that differences in elasticity between tissue types may range over several orders of magnitude, whereas differences in acoustic impedance (the sound velocity times the density of the material) vary by less than an order of magnitude. To perform sonoelastic imaging one first creates a standard B-mode image of the tissue in question. One then displaces the tissue, and collects another B-mode image. Direct comparisons of the two images – specifically, direct comparison of highlights in local ultrasound speckle patterns – highlight regions with different elastic properties. This is because softer tissue will move more for a given push than stiffer tissue from one B-mode image to another.

For example, consider Scholz *et al.* (2007), who used 'exogenous' imaging to image tumors in patients with brain lesions. They achieved this exogenous imaging by vibrating the brain tissue directly using an ultrasound scan head. Selbekk *et al.* (2005) has shown that elastographic imaging can be done intra-operatively through 'endogenous' imaging, using the natural pulsatility of the brain from the pulsatile arterial blood to generate tissue displacements and measure the stiffness of the brain tissue. These measurements of strain were used to aid in tumor interpretation based on spatial variations in the pattern of strain, images with larger dynamic range, hence greater contrast, than B-mode images, with their basis in differences in tissue density and bulk compressibility.

Kucewicz *et al.* (2007; 2008) created images of endogenous brain tissue displacement in healthy humans, images whose average amplitude varied with arterial CO_2 blood gas concentration, a known determinant of brain tissue pulsatility, and with brain use: in essence an ultrasound-based functional brain mapping technique. With that technique we have imaged traumatic brain injury in preliminary studies (Fig. 17.2).

Another ultrasound technique (Tanter *et al.*, 2008) tracks shear waves propagating through tissue to create quantitative estimates of the shear modulus

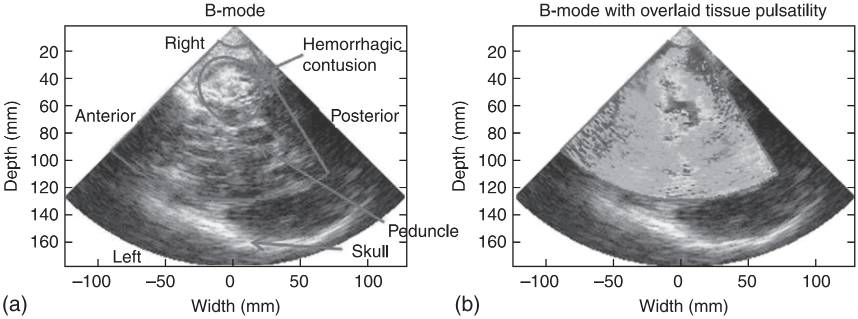

17.2 B-mode, transcranial image of human brain after traumatic brain injury (a) with simultaneously measured endogenous tissue pulsatility image (b). The hemorrhagic contusion preferentially scatters diagnostic ultrasound back to the scan head (B-mode imaging) and elevates the local pulsatility of the tissue.

of tissue. Here, specialized sequencing of a conventional US diagnostic probe generates a series of impulsive pushes of tissue via the acoustic radiation force associated with focused diagnostic ultrasound, thereby creating transient, propagating and non-destructive shear waves. While the shear waves propagate the device rapidly switches its ultrasound protocol to an ultrafast diagnostic image acquisition (of the order of thousands of B-images per second) to image the propagating shear wave. Local measurement of shear-wave propagation yields a direct estimate of the local shear modulus of the tissue through which the shear wave propagated.

We used a diagnostic ultrasound machine produced by SuperSonic Imagine, Inc. (SSI) to image variations in stiffness associated with ischemic stroke within the brains of mice. A difference in stiffness values can be seen between ischemic brain and normal brain, as seen in Fig. 17.3. Tanter's group currently leads this effort, producing beautifully detailed images of rat brains using a commercial machine based on tracking propagating shear waves.

17.8.3 Contrast agents

The previous discussion of cavitation has laid the groundwork for this section, in which I focus on exogenous acoustic contrast agents. Here we define 'acoustic contrast agent' as an artificial bubble of the order of one micron in radius placed within the bloodstream for the purpose of increasing the usefulness of an ultrasonic diagnostic process by virtue of the difference in acoustic properties between the agent and the biological tissue or fluid. One can attach a variety of substances to contrast agents – DNA, drugs, antibodies – to facilitate their targeting for specific imaging purposes, or to create a therapeutic effect (reviewed in Caskey *et al.*, 2011).

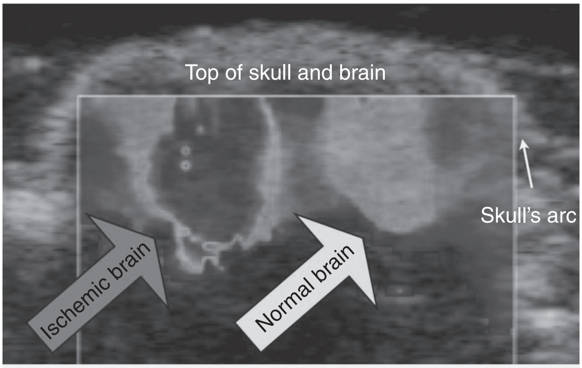

17.3 Coronal image of perfusion-fixed mouse brain after stroke taken with a research version of the commercial SuperSonic Imagine device, originally in color. The ischemic tissue has taken up more fixative than normal tissue, producing stiffer brain tissue on imaging.

As stated previously, manufactured acoustic contrast agents are typically micron-sized artificial bubbles placed within the bloodstream for the purpose of increasing the brightness of (desirable parts of) images created with diagnostic ultrasound. Contrast agents are typically brighter than the tissue in which they reside, most importantly because the contrast agents are acoustically active bubbles that ultrasound stimulates to emit sound more than the surrounding tissue can backscatter sound. In addition, contrast agents, like regular bubbles, oscillate in the presence of ultrasound, thereby emitting ultrasound at the incident frequency in addition to harmonics of that applied frequency. Monitoring those acoustic emissions with a diagnostic ultrasound machine lies at the foundation of 'harmonic imaging'. Specifically, one applies ultrasound at a given frequency to tissue perfused with contrast agents and then listens for the emission by the contrast agents of sound at generally twice that frequency. Since those harmonic emissions have much larger amplitude – by a factor of 1000 – than that scattered by tissue, the regions carrying the contrast agents stand out significantly in images made using the harmonic emissions, thus facilitating the imaging of fine structure within the tissue.

Assaying the quality of the local vasculature represents a clinically useful application of contrast agents for imaging. The first step requires achievement of steady-state perfusion of tissue by contrast agents under ultrasound imaging, followed by application of a relatively intense burst of ultrasound within a volume of tissue of interest. This burst destroys the contrast agents at the focus, changing that region's ultrasound backscatter signature from bright to relatively dark. The user then tracks the temporal evolution of the re-entry of contrast into the region of interest by tracking the rate of return of high-ultrasound backscatter within that region. Relative to control tissue – either from a cohort of healthy volunteers or from contralateral tissue – this gives a measure of the vascular health of local tissue. Meairs and colleagues (Meairs *et al.*, 2000) produced a lovely early example of a clinical application of this approach, whereby they imaged two hemispheres of the brain of a patient who had had an ischemic stroke. The hemisphere ipsilateral to the stroke took much longer to reperfuse than the contralateral hemisphere, consistent with the reduced blood flow one would expect to find distal to a major stroke.

It is possible to target acoustic contrast agents to tissues of interest to the clinicians by placing on the bubbles ligands that bind the bubbles to that tissue. Where there exist unique and fairly common cell markers – often for peripheral tumors – acoustic contrast agents have found utility, enhancing the ability of ultrasound to create clinically useful images. This remains very much an area of early investigation for brain, where unique and widespread cell-surface markers for primary brain tumors remain largely unidentified.

Imaging fine structure and blood flow within a fetus in utero represents another exciting (and potentially perilous) application of contrast agents with ultrasound for diagnostic purposes. A particularly fascinating study (Denbow *et al.*, 1997) showed that contrast agents injected into one of a pair of fetal twins in utero eventually appeared in the other twin, thus confirming the diagnosis that the circulation system of each twin communicated with the other through their connection with the mother. The researchers reported no adverse side effects. Concern for fetal harm makes such applications the exception rather than a rule.

Diagnostic ultrasound's safety has been extensively studied, as reviewed numerous times (Abramowicz, 1997; ISUOGEC, 2007). A recent paper raises interesting questions about large doses of diagnostic ultrasound, such as one might encounter during pregnancies that result from in vitro fertilization, where monthly monitoring, or more, is the norm. In this paper (Ang *et al.*, 2006) they insonified pregnant mice in 15 minute sessions for a range of total insonification times from 15 to 60 minutes. They found disturbed neuronal migration into the cortex of the mice for total insonification times between 30 and 60 minutes relative to sham-treated controls. This is a topic worth watching. In the meantime, by all means use diagnostic ultrasound to assay the health of the fetus following the usual rules: use just enough to get the data you need for the assay, and stop. These are the guidelines in place now – worth following.

17.9 Therapeutic ultrasound

The excellent book by Williams (1983) offers an extensive classic survey of the desired and undesired bioeffects of ultrasound as found in the literature prior to 1983. Readers interested in the roots of many aspects of therapeutic ultrasound should turn to this book. For a more recent survey, Jagannathan *et al.* (2009) highlight the history of therapeutic ultrasound applied to the brain. This represents a quite important summary worthy of detailed study. Especially interesting to this reader is that the earliest applications of ultrasound to the brain date to the time of the Great Depression, with serious and efficacious human trials in the 1950s led by the very famous Fry Brothers, whose publications remain a source of inspiration and teaching, many decades later (Fry, 1958).

Therapeutic ultrasound acts via the physical, chemical and thermal forces that it can generate, with its efficacy often affected in very specific ways by the biological disease, and the biological tissue to which it is applied. In this section I first discuss general issues involving therapeutic ultrasound, then highlight several interesting applications specific to the brain.

17.9.1 Rapid heating with ultrasound for therapeutic effect

Cancer cells die when sufficiently warmed sooner than normal cells under the same conditions. This has been covered in the classic paper by Dewey and Sapareto (1984). Put briefly, for every 1°C increase in temperature above 43°C, at which it takes approximately an hour to kill cells, the time necessary to kill cells via denaturation of proteins (this is what happens to the proteins in eggs when cooked for breakfast, for example) decreases by a factor of two. As an example, when cells are warmed to 50°C it takes approximately two minutes to kill them. Early work using ultrasound to create such modest increases in tissue temperature failed in practice because active and responsive perfusion by blood vessels at the capillary level (primarily) fought against the externally generated hyperthermia, which made it difficult for researchers to maintain the appropriate temperature for the desired length of time. Thanks to new transducer technology, the current approach is to rapidly raise the temperature of tissue focally with high-intensity focused ultrasound (HIFU), thereby creating a therapeutic effect before significant perfusion and diffusion can bring the tissue temperature back down out of the therapeutic range.

From the beginning, ter Haar and colleagues have been among the world leaders in this field, with an emphasis on liver and prostate (ter Haar and Coussios, 2007). Since liver surgery often produces dangerous amounts of bleeding, the ability of this methodology to cauterize tissue around the edges of where it kills tissue is particularly attractive. Another attractive feature of acoustic surgery is its extracorporeal application, particularly compelling for treating prostate cancer, where damage to local neuronal tissue through standard surgery causes all kinds of issues for the patient.

Problems remain with this therapy, however. A particularly interesting issue is the unwanted generation of cavitation within the tissue of interest. Cavitation in the context of HIFU can cause the distortion of the intended acoustic lesion. In particular, the lesion tends to grow towards the transducer by pre-focal heating apparently created by the backscatter properties of the bubbles formed at the initial site of cavitation. This creates volumes of tissue destruction that may encompass tissue that the clinician would like to spare. At the very least, cavitation within a given lesion tends to shield tissue beyond the site of cavitation, due to the large increase in acoustic impedance at the site of cavitation.

Regardless of the kind of therapeutic effect one may wish to create within a given portion of the brain – heating, cavitation, or a combination thereof – particularly problematic for using HIFU to treat the brain is the presence of the skull. As discussed above, bone severely attenuates propagating ultrasound. It also distorts that propagation, rendering what would be a tight focus of HIFU with the size and aspect ratio of a grain of rice into one or several smears of ultrasound application. Clinical devices such as those of Insightec use magnetic resonance imaging (MRI) to guide HIFU emitted transcranially from a hemispheric distribution of hundreds of individual transducers (O'Reilly and Hynynen, 2012). To paint a therapeutic volume of HIFU with a desired shape, users generate asynchronous emissions of HIFU from those transducers – a pre-distortion, if you will – such that after the sound crosses into the brain the sound propagates synchronously to create the desired HIFU shape and intensity at the target of interest. Design of the initial pattern of HIFU emission often requires knowledge of the propagation path the HIFU will encounter, derivable from CT images of the patient's head. A more recent approach focuses HIFU experimentally, by MRI-based monitoring then modulation of the shape and position of the HIFU focus through monitoring of the shape and position of displaced brain generated by the acoustic radiation force (again, see the very recent review article by O'Reilly and Hynynen, 2012).

Quite exciting work summarized in the review article by the Fry brothers dealt with the treatment of tremors in patients with Parkinson's disease (Fry, 1958; see the extensive review of the early literature – Jagannathan *et al.*, 2009). The researchers report that they were able to repeatedly create within a given human patient (they successfully treated 18 different patients in this fashion) the reversible alleviation of tremors, which they eventually removed permanently by a larger dose of ultrasound than that required to create the transient effects. Apparently side effects of this procedure were minimal.

This original work required neurosurgical procedures to expose the brain to facilitate HIFU delivery. Very recently, Jeanmonod and colleagues (Martin *et al.*, 2009) revisited this clinical problem, with modern, MRI-guided HIFU capable of generating therapeutic lesions in the central lateral thalamic nucleus of the brains of patients experiencing chronic pain. The patients remained awake throughout the procedure, did not require any neurosurgical intervention to facilitate delivery of HIFU, suffered no adverse events, and months after the procedure a majority reported reduction of their pain.

17.9.2 Thrombolysis

Breaking up unwanted blood clots is a difficult process and often an invasive one. Studies over 20 years (reviewed in Balucani and Alexandrov, 2010) indicate that

1 MHz ultrasound at intensities of 1–8 W.cm^{-2} accelerates the enzymatic reactions in thrombolysis rather than causing irreversible mechanical fragmentation, via a process known as ultrasound-enhanced thrombolysis. Ultrasound seems to do so by enhancing the transport of reactants, since experiments in vitro demonstrate that ultrasound increases transport of plasminogen activators both into and within thrombi. This is important because transport of reactants into and within thrombi is a rate-limiting step in fibrinolysis in vitro and therapeutically. The physical mechanism or mechanisms responsible for enhancement of fibrinolysis are unknown, but bulk heating alone is not a sufficient explanation. Cavitation could be important in systems exposed to air, for example, most in vitro experimental systems, or in animal models that include surgical exposure of the vessel. However, ultrasound also accelerates the destruction of blood clots in deep vessels within animal models under circumstances where cavitation is not likely to occur. One example is in animal models of small vessel injury. Another is electrically induced thrombosis, in which the method of vessel injury does not include introduction of gas. Moreover, seminal in vitro work designed to assess the relative importance of cavitation versus other nonthermal acoustic mechanisms (acoustic streaming, for example) has found that only 50% of ultrasound-enhanced thrombolysis in vitro can be explained by cavitation (Everbach *et al.*, 1997).

Despite uncertainty in the mechanisms by which ultrasound facilitates clot destruction, clinical work using ultrasound alone (CLOTBUST – Alexandrov *et al.*, 2004) or with acoustic contrast agents (TUSCON – Molina *et al.*, 2009) has shown exciting results, with some reason for caution from TUSCON given the increased risk of too rapid reperfusion of the ischemic tissue and possibility of intracerebral hemorrhage.

17.10 Ultrasound-facilitated delivery of drugs and antibodies into the brain

One of the more important and exciting applications of therapeutic ultrasound is to facilitate the delivery of therapeutic agents beyond the blood-brain barrier (BBB) into brain parenchyma to achieve a variety of therapeutic effects for big-time diseases such as tumors and any of the distressingly large number of neurodegenerative diseases. The BBB consists of specialized capillaries that form the lining of the blood vessels within the brain, a thick basement membrane, astrocytic endfeet and pericytes that restrict movement of chemicals that make it past or through the endothelial cells. The specialized endothelial cells restrict the diffusion of microscopic objects and large molecules into brain tissue in part by having unusually snug connections between adjacent endothelial cells (called tight junctions) as well as deploying an extensive array of pumps that pump back into the bloodstream most chemicals that make it into the endothelial cells themselves. One class of approach to getting drugs past the blood-brain barrier includes implantation of drug pumps where they can place chemicals into cerebral spinal fluid. Another approach consists of intra-hemispheric delivery of 'osmotic' agents (mannitol and the like) that disrupt the blood-brain barrier for 15–30 minutes. Another class of approach connects therapeutic drugs to peptides that are known to pass through the blood-brain barrier – a kind of Trojan horse approach. Like anything in life, these approaches have limitations, such as requiring a neurosurgical procedure, or exposing too much of the brain to the chemicals in the blood that can harm brain tissue, or delivering an insufficiency of drug.

There are hints of ultrasound's ability to disrupt the BBB in the 1950s and 1960s, always in the context of studying HIFU-induced lesions in brain. There was important new work in the field in the 1990s and early 2000s. Since then the technique has been honed extensively, primarily by the 'Harvard' group and their disciples, ably reviewed recently in O'Reilly and Hynynen (2012).

HIFU has been explored as a way to increase BBB permeability to drugs, to treat tumors (Mourad and Silbergeld, 2005; Tempany *et al.*, 2011) and movement disorders, Alzheimer's, etc. (Hynynen, 2010; O'Reilly and Hynynen, 2012). HIFU has many advantages in that it can noninvasively deliver a focused beam to a discrete region of the brain with minimal effects in adjacent tissue fields. Originally, HIFU could only effectively be delivered through a cranial window (a hole in the skull). Original studies delivered so much energy that the HIFU produced not only BBB disruption, but also necrosis of the surrounding brain tissue. Later studies by Ballantine reduced energy levels that produced BBB disruption without tissue necrosis, although there were still hemorrhagic areas (Ballantine *et al.*, 1960). These results led to the conclusion that further adjustment to HIFU parameters could produce BBB disruption without any damage, including hemorrhage, something we showed using HIFU delivered via cranial window (Mesiwala *et al.*, 2002). Moreover, electron microscopy showed that this method of ultrasound disrupted the tight junctions between the endothelial cells, which are responsible for the impermeability of the BBB.

Follow-on work reported by Mourad and Silbergeld (2005) and at conferences made use of an intra-operative device working at comparable ultrasound parameters to disrupt the BBB at and near the surface of the brain (Fig. 17.4) with dye flux volumes that were, on average, three times larger than the volume of damaged tissue. Parallel studies done with the same ultrasound system and tritiated chemotherapeutic agents relevant to the treatment of brain tumors demonstrated enhanced flux of those drugs from the bloodstream and into the same brain tissue that had enhanced dye flux. In this case, verapamil, a calcium channel blocker, was required to facilitate *net* drug flux, while dye always crossed the BBB.

A major advancement since this work has been the introduction of intravenously administered, gas-filled microbubbles known as acoustic contrast agents (ACAs). These microbubbles allow cavitation energy to be transferred specifically to endothelial cells both through an intact skull and at lower levels of energy than necessary without the use of ACAs. Moreover, damage to adjacent brain tissues

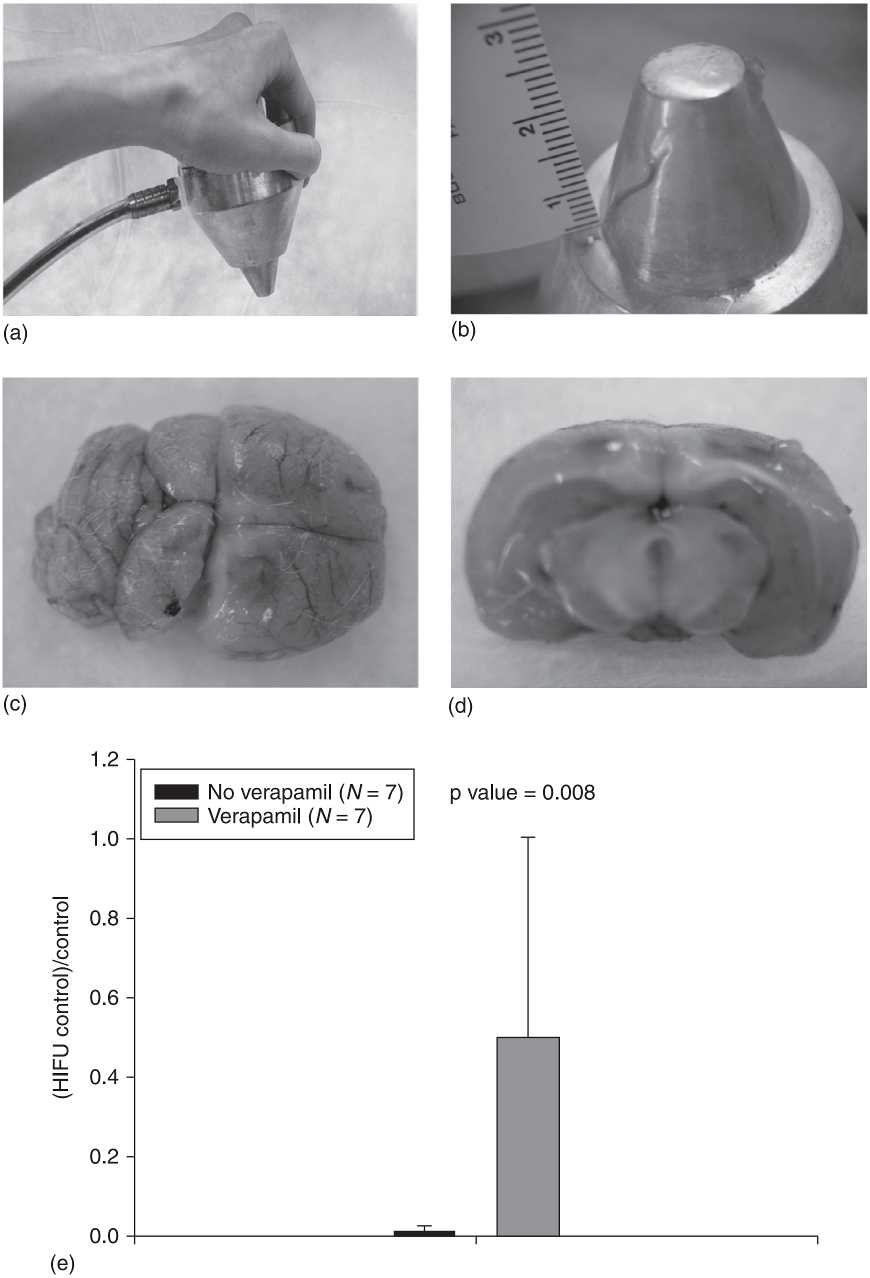
(a)
(b)
3
2
1
(c)
(d)
1.2
1.0
0.8
0.6
0.4
0.2
0.0
(HIFU control)/control
■ No verapamil (N = 7)
▨ Verapamil (N = 7)
p value = 0.008
(e)

17.4 (a) Solid cone HIFU device for opening the blood-brain barrier intra-operatively. (b) From below. (c, d) When applied to the exposed cortex of rats, it reliably produced BBB opening to Evans blue. (e) This same procedure, with the addition of verapamil, facilitated *net* drug flux into brain tissue.

does not occur. The microbubbles translate the HIFU energy into microscale mechanical (and possibly thermal – Hynynen *et al.*, 2001; Mesiwala *et al.*, 2002; Klotz *et al.*, 2010) stresses applied to the BBB that decrease cell membrane integrity. Specifically, several studies that use HIFU plus ACA for BBB disruption show that three ultrastructural characteristics that account for the BBB are reversed; that is, HIFU enhances pinocytosis, induces fenestrae, and opens tight junctions (e.g., Sheikov *et al.*, 2008; Deng *et al.*, 2012).

Important papers demonstrating drug flux into the brain facilitated by ultrasound, including the earliest to do so, include Treat *et al.* (2007) and Raymond *et al.* (2008). These and other studies of BBB disruption using ultrasound have not required calcium channel blockade for the delivery of drugs or antibodies to brain tissue, consistent with observations that there exist a variety of mechanisms by which HIFU can facilitate drug delivery across the BBB, tied in part to the physics behind the particular mechanism (among others, Hynynen, 2010; McDannold *et al.*, 2008).

A particularly interesting set of papers includes Choi *et al.* (2011) and Samiotaki *et al.* (2011), who have explored the minimum ultrasound, by several measures, necessary to produce BBB disruption via the combined effect of HIFU and ACA. They and others explored a range of low pressure (0.13–0.51 MPa), pulse length (typically 1–10 cycles), pulse repetition frequency (10 Hz through 100 kHz) and duration (single session of 60 s, or sets of 1000 pulses applied every 0.1 through 10 times per second for many minutes) with several ACAs (Definitity, Sonovue, etc.).

Choi *et al.* (2011) in particular sought to use the minimum amount of ultrasound to achieve spatially uniform and reliable BBB disruption through balance of several parameters that minimally stimulate ACA in situ while also facilitating their focal replenishment via blood flow from outside the region of HIFU application. They assayed for BBB disruption through quantification of dye flux into brain tissue. They successfully disrupted the BBB and minimized heterogeneity, which remained, however, pointing perhaps to a fundamental limitation of this technique, if clinical applications require homogeneous drug flux, that is.

17.11 Neuromodulation by ultrasound

The Fry brothers have been involved in much of the groundbreaking research in the application of therapeutic ultrasound to the brain. In one extensive review article, William Fry (1958) notes, among other things, that ultrasound applied to the visual cortex of cats' brains can repeatedly suppress in a transient manner various phases of cortical potentials normally evoked by flashing light into the cat's eye. This alteration of brain function by ultrasound has been the subject of recent work by Jamie Tyler, which I summarize here through attention to his latest articles.

Tyler and colleagues (e.g. Tufail *et al.*, 2010) have investigated the influence of low-intensity, low-frequency ultrasound (LILFU) on neuronal activity by transmitting ultrasound waveforms through hippocampal slice cultures and within intact mice. They determined that LILFU can remotely and noninvasively excite neurons and network activity through activating voltage-gated sodium and calcium channels. For their work on mice they used single ultrasound pulses containing between 80 and 225 acoustic cycles per pulse for pulse durations lasting 0.16–0.57 ms and they were repeated at pulse repetition frequencies ranging from 1.2 to 3.0 kHz to produce spatial-peak temporal-average intensities of 21–163 mW.cm^{-2} for total stimulus duration ranging between 26 and 333 ms. They studied the influence of these pulsed ultrasound protocols on intact motor cortex by measuring the electrophysiological and behavioral effects of brain activation. The results provide strong evidence that pulsed ultrasound can be used to directly stimulate neuronal activity and action potentials in intact brain circuits. For example, they observed motor circuit responses to ultrasound stimulation by acquiring simultaneous fine-wire EMG and videos of muscle contractions. The ultrasound stimulation method shows high specificity, as they were able to map the spatial distribution of neuronal activation triggered by transcranial pulsed ultrasound.

To assess the safety of transcranial ultrasound brain stimulation in mice, they first examined how pulsed ultrasound influenced blood-brain barrier (BBB) integrity and observed no evidence that ultrasound produced damage to the BBB. Next they probed the cellular-level consequences of pulsed ultrasound on brain tissues using antibodies against cleaved caspase-3 to monitor cell death, and no differences were found between the control mice and the mice that had undergone ultrasound stimulation. Indeed, in all the results they presented, none showed significant differences in the structure of the BBB, cerebrovasculature, cell death or brain ultrastructure between the control mice and the mice undergoing ultrasound stimulation. Hence, they concluded that it is possible to stimulate mouse cortex with their ultrasound protocols in a safe manner.

17.12 Conclusion

Study of the fundamental physics of ultrasound's interaction with tissue leads directly to an understanding of both diagnostic and therapeutic ultrasound. At its heart, ultrasound consists of a physical phenomenon whose reflection from tissue is sensitive to the relative variations in density and compressibility of tissue in a manner that can be enhanced through the introduction of microbubbles into the vasculature. This forms the basis of diagnostic ultrasound imaging, while those same factors can curtail the effective propagation of ultrasound to deep tissues. The passage of an ultrasound wave through tissue leaves residual amounts of heat and momentum, minimized for diagnostic purposes, maximized, in ways that depend upon the ultimate application, for therapeutic purposes. When applied to the brain, the specifics of neuroanatomy, down to the molecular scale for drug delivery, must be taken into account to achieve ultimate clinical success. This makes applications of therapeutic ultrasound for the treatment of brain disorders a particularly challenging field, and an important one, given the general intractability of many therapeutic modalities for such fearsome diseases as Alzheimer's and Parkinson's disease as well as brain tumors.

17.13 References

Abramowicz, J.S. (1997) Ultrasound contrast media and their use in obstetrics and gynecology. *Ultrasound Med. Biol.*, 23, 1287–98.

Alexandrov, A.V., Molina, C.A., Grotta, J.C., Garami, Z., Ford, S.R., Alvarez-Sabin, J. *et al.*, CLOTBUST Investigators (2004) Ultrasound-enhanced systemic thrombolysis for acute ischemic stroke. *N. Engl. J. Med.*, 351(21), 2170–8.

Ang, E.S.B.C., Gluncic, V., Duque, A., Schafter, M.E. and Rakic, P. (2006) Prenatal exposure to ultrasound waves impacts neuronal migration in mice. *Proc. Natl. Acad. Sci.*, 103(34), 12903–10.

Apfel, R.E. and Holland, C.K. (1991) Gauging the likelihood of cavitation from short-pulse, low-duty cycle diagnostic ultrasound. *Ultrasound Med. Biol.*, 17(2), 179–85.

Ballantine Jr, H.T., Bell, E. and Manlapaz, J. (1960) Progress and problems in the neurological applications of focused ultrasound. *J. Neurosurg.*, 17, 858–76.

Balucani, C. and Alexandrov, A.V. (2010) Ultrasound- and microspheres-enhanced thrombolysis for stroke treatment: State of the art. *Curr. Cardiol. Rep.*, 12(1), 34–41.

Blackstock, D.T. and Hamilton, M.F. (eds) (1997) *Nonlinear Acoustics*. New York: John Wiley & Sons, Inc.

Brennen, C.E. (1995) *Cavitation and Bubble Dynamics*. New York: Oxford University Press.

Caskey, C.F., Hu, X. and Ferrara, K.W. (2011) Leveraging the power of ultrasound for therapeutic designs and optimization. *J. Controlled Release*, 156(3), 297–306.

Chen, H., Kreider, W., Brayman, A.A., Bailey, M.R. and Matula, T.J. (2011) Blood vessel deformations on microsecond time scales by ultrasonic cavitation. *Phys. Rev. Lett.*, 106(3), 034301.

Choi, J.J., Selert, K., Vlachos, F., Wong, A. and Konofagou, E.E. (2011) Noninvasive and localized neuronal delivery using short ultrasonic pulses and microbubbles. *PNAS*, 108(40), 16359–544.

Christopher, T. and Carstensen, E. L. (1996) Finite amplitude distortion and its relationship to linear derating formulae for diagnostic ultrasound systems. *Ultrasound Med. Biol.*, 22, 1103–16.

Coakley, W.T. and Nyborg, W.L. (1978) Cavitation: Dynamics of gas bubbles; Applications. In F.J. Fry (ed.), *Ultrasound: Its Application in Medicine and Biology*. New York: Elsevier, Chap. 6, pp. 77–159.

Crum, L.A. (1984) Acoustic cavitation series: Part Five, Rectified diffusion. *Ultrasonics*, September, 22, 215–23.

Crum, L.A. and Fowlkes, J.B. (1986) Acoustic cavitation generated by microsecond pulses of ultrasound. *Nature*, 319, 52–4.

Denbow, M.L., Blomley, M.J.K., Cosgrove, D.O. and Fisk, N.M. (1997) Ultrasound microbubble contrast angiography in monochorionic twin fetuses. *Lancet*, 349, 773–9.

Deng, J., Huang, Q., Wang, F., Liu, Y., Wang, Z., Wang, Z., Zhang, Q., Lei, B. and Cheng, Y. (2012) The role of Caveolin-1 in blood-brain barrier disruption induced by focused ultrasound combined with microbubbles. *J. Mol. Neurosci.*, 46(3), 677–87.

Dewey, W.C. and Sapareto, S.A. (1984) Thermal dose determination in cancer therapy. *J. Radiat. Oncol. Biol. Phys.*, 10, 787–800.

Duck, F.A. (1990) *Physical Properties of Tissue: A Comprehensive Reference Book*. London: Academic Press.

Dunn, F., Edmonds, P.D. and Fry, W.J. (1969) Absorption and dispersion of ultrasound in biological media. In H.P. Schwan (ed.), *Biological Engineering*. Philadelphia: McGraw-Hill.

Everbach, E.C., White, J. and Francis, C.W. (1997) Overpressure reduces acceleration of thrombolysis due to ultrasound. *J. Acoust. Soc. Am.*, 102(5), 3154.

Fatemi, M. and Greenleaf, J.F. (1999) Vibro-acoustography: An imaging modality based on ultrasound-stimulated acoustic emission. *Proc. Natl Acad. Sci. USA*, 96(12), 6603–8.

Fry, W.J. (1958) Intense ultrasound in investigations of the central nervous system. In C.A. Tobias and J.H. Lawrence (eds), *Advances in Biological and Medical Physics*. New York: Academic, pp. 281–348.

Gateau, J., Aubry, J.-F., Chauvet, D., Boch, A.-L., Fink, M and Tanter, M. (2011) In vivo bubble nucleation probability in sheep brain tissue. *Phys. Med. Biol.*, 56, 7001–15.

Holland, C.K. and Apfel, R.E. (1989) An improved theory for the prediction of microcavitation thresholds. *IEEE Transactions on Ultrasonics, Ferroelectrics, and Frequency Control*, 36(2), 204–8.

Holt, R.G. and Roy, R.A. (2001) Measurements of bubble-enhanced heating from focused, MHz-frequency ultrasound in a tissue-mimicking material. *Ultrasound Med. Biol.*, 27(10), 1399–412.

Holt, R.G. and Roy, R.A. (2005) Bubble dynamics in therapeutic ultrasound. In *Bubble and Particle Dynamics in Acoustic Fields – Modern Trends and applications*, A.A. Doinikov (ed.). Research Signpost, Kerala, India.

Hynynen, K. (1991) The threshold for thermally significant cavitation in dog's thigh muscle *in vivo*. *Ultrasound Med. Biol.*, 17(2), 157–69.

Hynynen, K. (2010) MRI-guided focused ultrasound treatments. *Ultrasonics*, 50(2), 221–9.

Hynynen, K., McDannold, N., Vykhodtseva, N. and Jolesz, F.A. (2001) Noninvasive MR imaging-guided focal opening of the blood-brain barrier in rabbits. *Radiology*, 220(3), 640–6.

ISUOGEC – International Society of Ultrasound in Obstetrics & Gynecology Education Committee (2007) Sonographic examination of the fetal central nervous system: guidelines for performing the 'basic examination' and the 'fetal neurosonogram.' *Ultrasound Obstet. Gynecol.*, 29(1), 109–16.

Jagannathan, J., Sanghvi, N.T., Crum, L.A., Yen, C.P., Medel, R. *et al.* (2009) High-intensity focused ultrasound surgery of the brain: Part 1 – A historical perspective with modern applications. *Neurosurgery*, 64(2), 201–10.

Jain, R.K. (1983) Chapter 2: Bioheat transfer: Mathematical models of thermal systems. In *Hyperthermia in Cancer Therapy*, F.K. Storm (ed.). Boston: G.K. Hall & Co.

Kelly, J.F. and McGough, R.J. (2009) Fractal ladder models and power law wave equations. *J. Acoust. Soc. Am.*, 126(4), 2072–81.

Kermarrec, E., Demondion, X., Khalil, C., Le Thuc, V., Boutry, N. *et al.* (2010) Ultrasound and magnetic resonance imaging of the peripheral nerves: Current techniques, promising directions, and open issues. *Semin. Musculoskelet. Radiol.*, 14(5), 463–72.

Klotz, A.R., Lindvere, L., Stefanovic, B. and Hynynen, K. (2010) Temperature change near microbubbles within a capillary network during focused ultrasound. *Phys. Med. Biol.*, 55(6), 1549–61.

Kinsler, L.E., Frey, A.R., Coppens, A.B. and Sanders, J.V. (1982) *Fundamentals of Acoustics*. New York: John Wiley & Sons, Inc.

Kremkau, F.W. (1998) *Diagnostic Ultrasound: Principles and Instruments*. 5th ed., Philadelphia, PA: W.B. Saunders.

Kucewicz, J.C., Dunmire, B., Leotta, D.F., Panagiotides, H., Paun, M. *et al.* (2007) Functional tissue pulsatility imaging of the brain during visual stimulation. *Ultrasound Med. Biol.*, 33(5), 681–90.

Kucewicz, J.C., Dunmire, B., Giardino, N.D., Leotta, D.F., Paun, M. *et al.* (2008) Tissue pulsatility imaging of cerebral vasoreactivity during hyperventilation. *Ultrasound Med. Biol.*, 34(8), 1200–8.

Leighton, T.G. (1994) *The Acoustic Bubble*. New York: Academic Press.

Marmottant, P. and Hilgenfeldt, S. (2003) Controlled vesicle deformation and lysis by single oscillating bubbles. *Nature*, 423, 153–5.

Martin, E., Jeanmonod, D., Morel, A., Zadicario, E. and Werner, B. (2009) High-intensity focused ultrasound for noninvasive functional neurosurgery. *Ann. Neurol.*, 66(6), 858–61.

McDannold, N., Vykhodtseva, N. and Hynynen, K. (2008) Blood-brain barrier disruption induced by focused ultrasound and circulating preformed microbubbles appears to be characterized by the mechanical index. *Ultrasound Med. Biol.*, 34(5), 834–40.

Meairs, S., Daffertshofer, M., Neff, W., Eschenfelder, C. and Hennerici, M. (2000) Pulse-inversion contrast harmonic imaging: Ultrasonographic assessment of cerebral perfusion. *Lancet*, 355(9203), 550–1.

Mesiwala, A.H., Farrell, L., Wenzel, H.J., Crum, L.A., Silbergeld, D.L. *et al.* (2002) High intensity focused ultrasound selectively disrupts the blood-brain barrier *in vivo*. *Ultrasound Med. Biol.*, 28(1), 389–400.

Miller, D.L., Nyborg, W.L. and Whitcomb, C.C. (1979) Platelet aggregation induced by ultrasound under specialized conditions in vitro. *Science*, 205, 505–7.

Molina, C.A., Barreto, A.D., Tsivgoulis, G., Sierzenski, P., Malkoff, M.D. *et al.* (2009) Transcranial ultrasound in clinical sonothrombolysis (TUCSON) trial. *Ann. Neurol.*, 66(1), 28–38.

Mourad, P.D. (1999) Biological effects of ultrasound. In *Encyclopedia of Electronics and Electrical Engineering*, J.L. Webster (ed.). Philadelphia: John Wiley & Sons, Vol. 2, pp. 368–86.

Mourad, P.D. and Silbergeld, D.L. (2005) Breaking the blood-brain barrier: Using high-intensity focused ultrasound to treat malignant brain tumors. *RT-Image*, V18(32), 28–32.

Myers, M.R. (2006) Tissue deformation induced by radiation force from Gaussian transducers. *J. Acoust. Soc. Am.*, 119(5), 3147–52.

Nyborg, W.L. (1965) Acoustic streaming. In *Physical Acoustics*, W.P. Mason (ed.), Vol. 2, Part B. New York: Academic Press, Chap. 11, pp. 265–85.

O'Brien, W.D. (2007) Ultrasound-biophysics mechanisms. *Progress in Biophysics and Molecular Biology*, 93, 212–55.

O'Reilly, M. and Hynynen, K. (2012) Ultrasound enhanced drug delivery to the brain and central nervous system. *International Journal of Hyperthermia*. In press.

Palmeri, M.L. and Nightingale, K.R. (2011) What challenges must be overcome before ultrasound elasticity imaging is ready for the clinic? *Imaging Med.*, 3(4), 433–44.

Pauly, H. and Schwan, H.P. (1971) Mechanisms of absorption of ultrasound in liver tissue. *J. Acoust. Soc. Am.*, 50, 692–9.

Raymond, S.B., Treat, L.H., Dewey, J.D., McDannold, N.J., Hynynen, K. *et al.* (2008) Ultrasound enhanced delivery of molecular imaging and therapeutic agents in Alzheimer's disease mouse models. *PLoS One*. 14 May, 3(5), e2175.

Rooney, J.A. (1970) Hemolysis near an ultrasonically pulsating gas bubble. *Science*, 169, 869–71.

Roy, R.A., Madanshetty, S.I. and Apfel, R.E. (1990) An acoustic backscattering technique for the detection of transient cavitation produced by microsecond pulses of ultrasound. *J. Acoust. Soc. Am.*, 87(6), 2451–8.

Rudenko, O.V., Sarvazyan, A.P. and Emelianov, S.Y. (1996) Acoustic radiation force and streaming induced by focused nonlinear ultrasound in a dissipative medium. *J. Acoust. Soc. Am.*, 99, 2791–8.

Samiotaki, G., Vlachos, F., Tung, Y.S. and Konofagou, E.E. (2011) A quantitative pressure and microbubble-size dependence study of focused ultrasound-induced blood-brain barrier opening reversibility in vivo using MRI. *Magnetic Resonance in Medicine*. doi: 10.1002/mrm.23063.

Sapozhnikov, O.A., Maxwell, A.D., MacConaghy, B. and Bailey, M.R. (2007) A mechanistic analysis of stone fracture in lithotripsy. *J. Acoust. Soc. Am.*, 121, 1190–202.

Sarvazyan, A. (2010) Diversity of biomedical applications of acoustic radiation force. *Ultrasonics*, 50, 230–4.

Scholz, M., Lorenz, A., Pesavento, A., Brendel, B., Khaled, W. *et al.* (2007) Current status of intraoperative real-time vibrography in neurosurgery. *Ultraschall. Med.*, October, 28(5), 493–7.

Selbekk, T., Bang, J. and Unsgaard, G. (2005) Strain processing of intraoperative ultrasound images of brain tumours: Initial results. *Ultrasound Med. Biol.* January, 31(1), 45–51.

Sheikov, N., McDannold, N., Sharma, S. and Hynynen, K. (2008) Effect of focused ultrasound applied with an ultrasound contrast agent on the tight junctional integrity of the brain microvascular endothelium. *Ultrasound Med. Biol.*, 34(7), 1093–104.

Silva, G.T. and Mitri, F.G. (2011) Difference-frequency generation in vibro-acoustography. *Phys. Med. Biol.*, 56, 5985–93.

Tanter, M., Bercoff, J., Athanasiou, A., Deffieux, T., Gennisson, J.L. *et al.* (2008) Quantitative assessment of breast lesion viscoelasticity: Initial clinical results using supersonic shear imaging. *Ultrasound Med. Biol.*, September, 34(9), 1373–86.

Tempany, C.M., McDannold, N.J., Hynynen, K. and Jolesz, F.A. (2011) Focused ultrasound surgery in oncology: Overview and principles. *Radiology*, 259(1), 39–56.

ter Haar, G.R. and Coussios, C. (2007) High intensity focused ultrasound: Physical principles and devices. *Int. J. Hyperthermia*, 23, 89–104.

Treat, L.H., McDannold, N., Vykhodtseva, N., Zhang, Y., Tam, K. and Hynynen, K. (2007) Targeted delivery of doxorubicin to the rat brain at therapeutic levels using MRI-guided focused ultrasound. *Int. J. Cancer*, 15:121(4), 901–7.

Tsivgoulis, G., Alexandrov, A.V. and Sloan, M.A. (2009) Advances in transcranial Doppler ultrasonography. *Neurol. Neurosci. Rep.*, 9(1), 46–54.

Tufail, Y., Matyushov, A., Baldwin, N., Tauchmann, M.L., Georges, J. *et al.* (2010) Transcranial pulsed ultrasound stimulates intact brain circuits. *Neuron*, 10 June, 66(5), 681–94.

Tung, Y.S., Vlachos, F., Choi, J.J., Defflieux, T., Selert, K. *et al.* (2011) *In vivo* transcranial cavitation threshold detection during ultrasound-induced blood-brain barrier opening in mice. *Phys. Med. Biol.*, 55, 6141–55.

Williams, A.R. (1983) *Ultrasound: Biological Effects and Potential Hazards*. New York: Academic Press.

Wu, J. and Nyborg, W.L. (2008) Ultrasound, cavitation bubbles and their interaction with cells. *Advanced Drug Delivery Reviews*, 60, 1103–16.

Young, F.R. (1989) *Cavitation*. New York: McGraw Hill.

18

Microscale ultrasonic sensors and actuators

A. RAMKUMAR and A. LAL, Cornell University, USA

Abstract: This chapter presents research efforts towards the use of ultrasonic silicon-based micro-electromechanical systems (MEMS) for biomedical applications. Microfabricated silicon-horn-based surgical microprobes and their use in reducing penetration force into biological tissue are described. The chapter describes sensors integrated on the silicon horn, namely, platinum electrodes and piezoresistive polysilicon strain gauges. The chapter includes research studies detailing the use of these sensors in ex vivo cardiac signal recording, and in testicular tubule-size surgery for identifying fertile sperm in the testis.

Key words: micro-electromechanical systems, ultrasonic silicon horn, penetration force reduction, cardiac action potential, testicular sperm extraction surgery.

18.1 Introduction: ultrasonic horn actuators

Ultrasound is a form of stored mechanical energy and its application to matter, under the right circumstances, can result in permanent physical changes. Ultrasound refers to sound with frequency above the audible range (> 20 kHz). Depending upon the ultrasound amplitude, its uses can be divided into two principal categories (Table 18.1): high-intensity (> 1 W.cm^2) and low-intensity ultrasound (< 0.1 W.cm^2). Low-intensity ultrasound is used for diagnostics in applications such as medical ultrasonic imaging and non-destructive testing. High-intensity ultrasound is used in industry today for drilling and cutting ceramics, welding plastics and sonochemical processing (Table 18.1; Suslick, 1988). In medicine, high-intensity ultrasound is used to break up unwanted tissue, as in lithotripsy. The intensity range for these applications is usually greater than 1 W. cm^2 and can be as high as thousands of W. cm^2. For ultrasonic surgery, power outputs of 10–20 W and power intensities of 200–400 W. cm^2 are required to break the tissue. Table 18.1 also shows fuel injection and transdermal drug delivery (Mitragotri *et al.*, 1995; Bommanan, 1992) as applications that might be particularly suitable for the silicon-based transducers.

The ultrasonic hand piece used in phacoemulsification is the state-of-the-art in power ultrasonic transducer technology. It is also known as the bolted Langevin transducer, named after the physicist who first used it for sonar applications. The basic tool is shown in Fig. 18.1. The cutting tip vibrates longitudinally at amplitudes of ≈100 μm_{pp}, at frequencies in the range 40–60 kHz. The structure is machined from high-strength titanium alloy, one of the strongest known metals. Piezoelectric PZT (lead zirconate titanate) washers are held between a front and a back titanium section. The PZT washers expand or contract periodically when a

Table 18.1 Applications of ultrasound

High-intensity ultrasound	Low-intensity ultrasound
Ultrasound surgery: eye, ear, dental, cancer	Non-destructive testing
Ultrasonic welding: plastics, metals	Ultrasound imaging
Ultrasonic machining: cutting and drilling	Flow meters and control devices
Ultrasonic wire bonding	Surface acoustic wave devices
Sonochemistry	
Atomization	
Sonar	
Fuel injection	
Transdermal drug delivery	

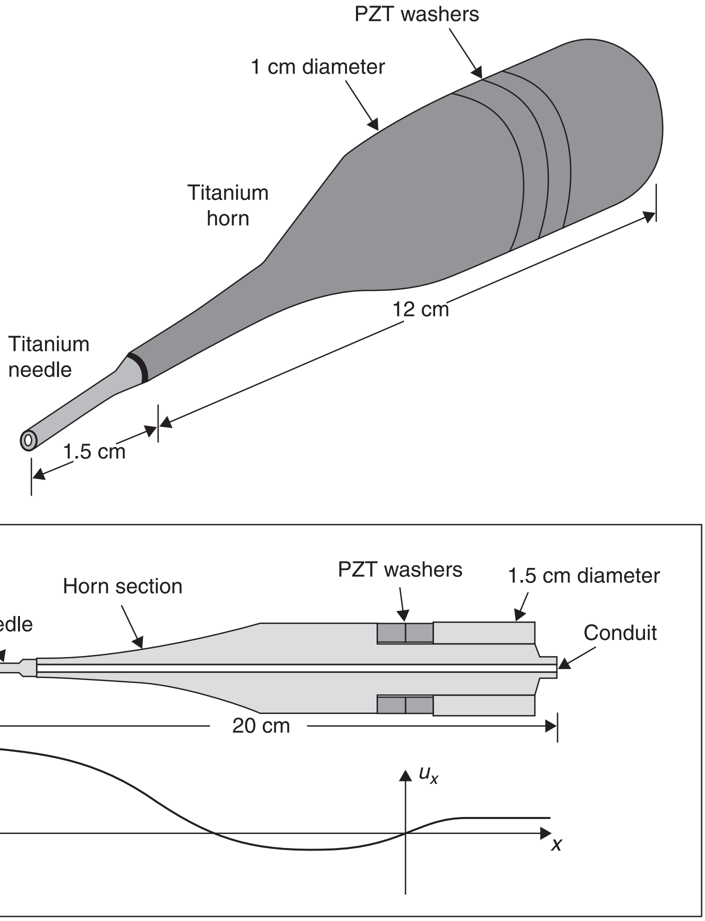
PZT washers
1 cm diameter
Titanium horn
Titanium needle
12 cm
1.5 cm
Horn section
PZT washers
1.5 cm diameter
Needle
Conduit
20 cm
u_x
x

18.1 Bolted Langevin transducer.

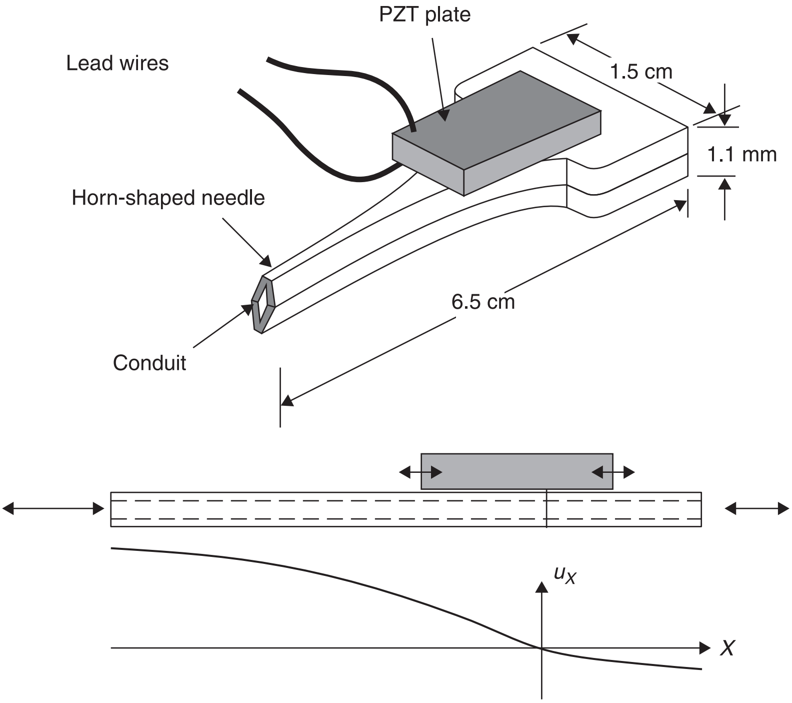

18.2 The silicon ultrasonic tool developed by Lal (1996).

sinusoidal drive voltage is put across them. These expansions and contractions are transmitted to the metal structure. When the structure is driven at its resonance frequency, the forces needed to strain the titanium cancel out the inertial forces, resulting in large displacements. Furthermore, the horn section magnifies this motion even more to reach necessary ultrasonic intensities.

The silicon-based ultrasonic tool is shown in Fig. 18.2. Micromachining is used to etch two halves of a needle structure out of a silicon wafer. The needle structure is formed by bonding these two structures. PZT plates are then bonded onto the needle to excite it in its longitudinal resonance via the d_{31} piezoelectric coefficient. The PZT plates, as in the titanium hand piece, couple mechanical energy into the silicon structure. By driving the PZT at the resonance frequency of the composite structure, high ultrasonic displacements and intensities can be achieved.

18.2 Advantages of silicon-based technology

The silicon-based technology provides solutions to the many shortcomings of the titanium-based technology. These advantages fall into two categories. They are material property-based advantages and micromachining-based advantages.

18.2.1 Material-based advantages

The material-based advantages stem from silicon's high strength, low internal loss and high thermal conductivity with respect to its use in power ultrasonic applications. In this section, performance values such as maximum output power density and ultrasonic particle velocity will be derived from basic material properties such as strength, Young's modulus and density.

Maximum output power density

In order to compare the titanium and silicon ultrasonic transducers, some terms have to be defined. First, the quality factor of a resonant transducer is defined as the ratio of the energy stored to the energy lost per cycle, or

$$Q = \frac{E_s}{\Delta E} \qquad [18.1]$$

where E_s is the stored energy and ΔE is the energy lost per cycle. The output power of this transducer is the energy lost per cycle times the frequency of the resonator,

$$P_{out} = \frac{fE_s}{Q} \qquad [18.2]$$

The energy stored in the resonator is equal to the integrated energy density along the length of the resonator,

$$E_s = \int_{length} YA(x)\left(\frac{\partial u}{\partial x}\right)^2 dx = kYS_m^2 Volume \qquad [18.3]$$

In Eq. 18.3, Y is the Young's modulus and $A(x)$ is the cross-sectional area along the length of the resonator, S_m is the maximum strain and k is a constant of proportionality of order unity. Using Eq. 18.3 in Eq. 18.2, one obtains

$$P_{out} = \frac{fE_s}{Q} = k\frac{fYS_m^2 Volume}{Q} \qquad [18.4]$$

which can also be written as

$$\frac{P_{out}}{Volume} = k\frac{fS_m^2 Y}{Q} \qquad [18.5]$$

Here, the power density has been expressed in terms of resonator material parameters, the frequency, f, and quality factor, Q. It is reasonable to assume that two transducers should be compared for the same f and Q. By this criterion, the quantity $S_m^2 Y$ becomes a figure of merit for a transducer material. Using the values given in Table 18.2, the value of $S_m^2 Y$ for silicon is $2.6\times108\,\mathrm{N.m}^2$, while for titanium it is $7.4\times106\,\mathrm{N.m}^2$. The value of S_m is calculated as the ratio of the

Table 18.2 Material properties of various relevant materials

Material	Y (GPa)	Strength (GPa)	Density (kg.m^{-3})	$S_m c$ (m.s^{-1})	Hardness (kg.mm^2)	Toughness (MPa.m$^{1/2}$)	Acoustic loss (1/Q)	Thermal conductance (W.m^{-1}.K)
Silicon	190	7	2300	335	850	1	$\approx 10^{-5}$	130
Diamond	1035	53	3500	881	7000	2.5	$\approx 10^{-5}$	600
Si_3N_4	385	14	3100	405	3486	5	$\approx 10^{-5}$	10–20
SiO_2	73	8.4	2500	622	820	0.6	$\approx 10^{-5}$	1–2
SiC	700	21	3200	444	2480	4	$\approx 10^{-5}$	70–80
Titanium alloy (C-120-AV)	110	0.9	4430	41	390	50	$\approx 3 \times 10^{-4}$	7–10
Carbon steel	200	2.1	7900	53	660	100	$\approx 10^{-4}$	60–70
PZT-4	85	0.024	7600	0.93	–	–	$\approx 2.5 \times 10^{-3}$	–
PZT-5H	67.5	0.0276	7700	1.21	–	–	$\approx 1.54 \times 10^{-2}$	–

strength to the Young's modulus. The high strength of 7 GPa was measured for silicon samples that were chemically etched and then oxidized (Ericson, 1990). Using this value for silicon strength, the ratio of $S_m^2 Y$ for silicon to titanium is 35, indicating that the maximum allowable power density for silicon is 35 times that of titanium. Alternatively, this means that a silicon transducer 35 times smaller than a titanium transducer can generate the same power.

Maximum particle velocity

The ultrasonic stroke of a resonant transducer is limited by two material properties: the maximum achievable particle velocity in a material $S_m c$ and the internal loss. The maximum tip velocity that an ultrasonic resonator can sustain is proportional to $S_m c$, where S_m is the maximum strain the material can sustain without failure. This value for $S_m c$ is tabulated in the second column of Table 18.2 for some of the relevant materials. Titanium alloys have $S_m c$ of 45 m.s^{-1}. With the typical stroke of 50 mm at 40 kHz, the current hand pieces operate at tip velocities of approximately 13 m.s^{-1}, or 1/3 of their maximum value. This is an adequate safety margin. Since titanium is a ductile metal with high dislocation density, its strength decreases with high-frequency operation due to fatigue. Hence, at higher frequencies, the value of $S_m c$ for titanium will probably decrease, although no experimental data for this have been reported.

Table 18.2 lists $S_m c$ for silicon as 335 m.s^{-1}, a value eight times that of titanium. This means that silicon can be driven to much higher tip velocities than titanium before the transducer fails. Silicon horn transducers, discussed in this chapter, have demonstrated displacements of 100 μm$_{pp}$ at a frequency of 72 kHz, resulting in the tip velocity of 23 m.s^{-1}. This is almost twice the velocity that titanium hand pieces generate to perform surgery. Since most ultrasonic processes depend either linearly or quadratically on the ultrasonic amplitude, much faster ultrasonic processing would be possible with silicon-based tools.

Table 18.2 also shows that the diamond and silicon nitride have higher $S_m c$ than silicon. However, there are no cost-effective micromachining technologies for these materials so far. Furthermore, there is a huge infrastructure for integrating sensors and circuits on silicon that allows inexpensive batch-processed devices to be made. Such technology does not exist for the other stronger materials.

Heat generation

Another major problem with titanium tools is heating due to internal friction. There are two sources of frictional heating. Titanium, like all other metals, has internal dislocations that rub against each other when it is strained ultrasonically. This source of friction produces heat, which raises the temperature of the cutting tip and damages the tissue if the irrigation system fails for any reason. This heating can also cause damage to the plastic parts used for packaging the transducer.

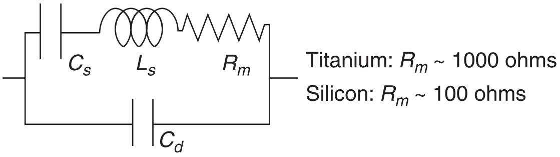

18.3 Electrical model of a piezoelectric resonator.

The electrical model of a piezoelectric resonator consists of a capacitor in parallel with a series-resonant Resistance, Inductance, Capacitance (RLC) circuit (Fig. 18.3). The titanium resonators, due to high internal losses in the material, friction between threaded parts and low electromechanical coupling, tend to have a large series resistance, $R_m > 1000\,\Omega$. Hence, for a drive current of 100 mA, 10 W of power is produced as heat in various parts of the resonator. This is of the same order of magnitude as the power needed to cut the tissue.

The internal losses in silicon are an order of magnitude lower than those of titanium. This is mainly because a silicon wafer produced today has almost no dislocations, as a result of the huge effort over the past 30 years to make silicon wafers dislocation free, a condition necessary for making useful electronic circuits. The prototype silicon resonators made already have series resistances of only $100\,\Omega$. Hence, silicon transducers should produce at least 10 times lower heat than the titanium tool.

Silicon's thermal conductivity (Table 18.2) is an order of magnitude higher than that of titanium alloys. Hence, even if heat is generated in some part of the silicon device, it can be carried away to a heat sink kept at a lower temperature. The temperature at the interface of the object being cut and the cutting tip can get quite high due to friction between the two surfaces. The higher thermal conductivity of silicon will allow it to carry that heat away faster than titanium and reduce any heat-related damage.

18.2.2 Micromachining-based advantages

The silicon transducers presented in this work are made using bulk silicon micromachining techniques. This manufacturing technology has been used primarily for making pressure sensors and accelerometers (Peterson, 1982). It is shown below that this technology will allow several performance-increasing features in high-intensity ultrasonic transducers.

Small devices

Bulk micro machining usually means etching of silicon parts out of silicon wafers that can range from 5 to 30 cm in diameter and are 1.5–1 mm in thickness. This technology enables fabrication of small transducers while maintaining tight tolerances over dimensions using optical lithography. The smaller devices allow two advantages.

Firstly, the resonance frequency of a longitudinal mode resonator is proportional to the ratio of speed of sound to the length of the resonator. The resonance frequency of a smaller silicon device, with speed of sound almost twice that of titanium, will therefore be much higher. The higher-frequency operation could minimize acoustic cavitation, a process for which the threshold power increases rapidly with increasing frequency. Secondly, the smaller size allows the possibility of making a compact array of transducers for high-power beam forming, and the inclusion of sensors and actuators for control functions.

Integration of sensors

Micromachining allows the integration of pressure and strain sensors using standard IC fabrication techniques of doping and diffusion of impurities into silicon. By integrating sensors with the driver, many open-loop variables in an ultrasonic process can be put under closed-loop control. For example, in ultrasonic surgery it would be a great advantage to be able to sense the hardness of the tissue being cut and to monitor the delivered ultrasonic power.

Lower cost and disposable transducers

The price of each titanium hand piece ranges from \$2000 to \$3000. The high price is due to the high cost of high-strength titanium alloys themselves and the great care taken to machine each transducer. Each hand piece is individually machined and packaged. The existing micromachining technology can be used to batch-process silicon tools so that the final cost is low enough to justify a disposable transducer. This will eliminate the problem of device reliability: one can throw away a device before it fails.

Lower actuation voltages

Very high actuation voltages ($\approx 1200\,V_{pp}$) are needed in current titanium transducers for two reasons. First, the PZT plates used are thick and hence large voltages are needed to generate sufficient electric field. Secondly, a large portion of the drive voltage is divided across the series resistor that was discussed in the above section. In the silicon structure, the piezoelectric plates are thinner (0.25–0.5 mm versus 1–3 mm). Furthermore, as mentioned previously, the series resistance can be an order of magnitude lower for silicon than for titanium. With a prototype silicon ultrasonic needle, a $100\,\mu m_{pp}$ displacement was achieved at a frequency of 72 kHz with a drive voltage of as low as $250\,V_{pp}$. This is in contrast to the high voltage ($1200\,V_{pp}$) needed for titanium-based actuators to achieve similar tip velocities.

Curved actuators

There are many applications where a curved transducer can be useful. For example, in ultrasonic cataract surgery the surgeon would like to use a needle that is curved so that it can naturally enter the eye. However, machining a curved titanium part reduces the metal's strength. With silicon micromachining, a curved silicon needle can easily be made using lithography and the strength of the needle is not sacrificed.

18.3 Silicon ultrasonic horns

In order to have higher ultrasonic particle velocities, velocity transforming waveguides (horns) are needed. The word 'horn' is prevalent in the literature because velocity transformers were first studied in the context of trumpets and musical horns. The basic principle of a velocity transforming waveguide is to concentrate energy from a region of large cross-sectional area into a region of smaller cross-sectional area. In a half-wavelength longitudinal-mode ultrasonic resonator, mechanical energy travels between the two free ends at the speed of sound in the material. In a structure with constant cross-sectional area, the energy density and displacements are equal on the two sides of the displacement node. By making the cross-sectional area on one side smaller, the energy density and hence the velocities can be made larger. Generally speaking, the low amplitude side is connected to a transducer that produces low velocities. The smaller end with the higher energy density and velocity is used to perform work on a load. Furthermore, several half-wavelength horns can be cascaded to produce higher velocities as long as each horn is connected to the other at its stress anti-node (Heuter, 1955).

The horn material has to have a high $S_m c$ so that it can withstand the higher ultrasonic particle velocities. In this chapter, the analytical and experimental data on silicon ($S_m c = 335\,\text{m.s}^{-1}$) ultrasonic horns will be presented. Conventional ultrasonic horns are made of high-strength metal alloys whose $S_m c$ is typically less than $45\,\text{m.s}^{-1}$. Hence, silicon horns should permit generating much higher ultrasonic amplitudes than is possible with metal-based horns. For example, using silicon horns one ought to be able to break the sound-barrier ($c_{\text{sound}} = 320\,\text{m.s}^{-1}$) and generate shock waves. This ability could be used to remotely radiate objects with high-intensity ultrasound.

In 1950, Mason extensively used solid horns to generate high-power ultrasound. He attached these horns to Langevin bolted PZT/metal transducers to increase ultrasonic displacement amplitudes. Mason's technique is currently used in most power-ultrasound applications such as ultrasonic welding, sonochemistry and bonding (Heuter, 1955; Neppiras, 1960). Mason had used a 'forward' method of horn design: he started from a horn with a taper described by an analytical function, and obtained a displacement profile along the horn by solving the Webster's horn equation (derived later). Eisner (1967) later developed a 'reverse' method where a certain strain profile along the waveguide was assumed and a horn shape capable of producing the profile was generated. In this chapter, only the forward method was used to design different horns. A brief account of the Webster's horn equation is presented below subject to the following conditions: (1) a condition of plane stress exists along the length of the waveguide; and (2) the lateral vibration in the x and y directions, due to Poisson coupling, are considered negligible. Both of these assumptions are true as long as the beam width and height are much less than the wavelength of sound at the resonance frequency. This is true of the silicon horns presented here because their thicknesses (≈ 1 mm) and maximum widths (≈ 10 mm) are much less than the wavelength (≈ 60 mm).

When a differential element from a rod with a variable cross-section is considered, under the assumptions of uniform stress distribution, material homogeneity and negligible lateral inertia, the equation of motion is given by (Chen, 2006):

$$-\sigma A + \left(\sigma + \frac{\partial \sigma}{\partial x} dx\right)\left(A + \frac{\partial A}{\partial x} dx\right) = \frac{1}{2}\rho\left(A + \left(A + \frac{\partial A}{\partial x} dx\right) dx \frac{\partial^2 u}{\partial t^2}\right) \quad [18.6]$$

where σ is the stress acting on the cross-section of the element, $A(x)$ is the variable cross-section as a function of the distance along the axis of the rod x, ρ is the density and $u(x)$ is the displacement along the x-direction. Ignoring the second-order partial differential terms, Eq. 18.6 can be reduced to

$$\frac{1}{A}\frac{\partial}{\partial x}(\sigma A) = \rho \frac{\partial^2 u}{\partial t^2} \quad [18.7]$$

Substituting stress with $\sigma = E\frac{\partial u}{\partial x}$ results in:

$$\frac{\partial}{\partial x}\left(EA\frac{\partial u}{\partial x}\right) = \rho A \frac{\partial^2 u}{\partial t^2} \quad [18.8]$$

Assuming uniform E and ρ,

$$\frac{1}{A}\frac{\partial}{\partial x}\left(A\frac{\partial u}{\partial x}\right) = \frac{1}{c_0^2}\frac{\partial^2 u}{\partial t^2} \quad [18.9]$$

or

$$\frac{\partial^2 u}{\partial x^2} + \left(\frac{\partial u}{\partial x}\right)\frac{\partial}{\partial x}(\ln(A(x))) = \frac{1}{c_0^2}\frac{\partial^2 u}{\partial t^2} \quad [18.10]$$

where $c_0 = \sqrt{E/\rho}$ is the speed of sound and E is the Young's modulus of the rod. Equation 18.10 is the Webster horn equation, used often in the field of acoustics. This is a second-order non-linear differential equation. Also notice that, if $A(x)$ is a constant, then the equation becomes the standard longitudinal wave equation for thin bars. In the 'forward' design of horns, first an analytical form of $A(x)$ is chosen and then the equation is solved either analytically or numerically by applying appropriate boundary conditions to obtain a *u(x)*. For example, in the case of free-free boundary conditions, the boundary condition of $\frac{\partial u_x}{\partial x} = 0$ has to be applied at the free boundaries.

Table 18.3 shows the analytical form of *A(x)* for exponential, catenary, linear and stepped horns. It also shows the parameters that are need to compute *A(x)*. A_0 (or A_i for initial area) and A_l (or A_f for final area) are the cross-sectional areas at the large and the small ends respectively. The parameter *l* is the resonant length of the horn for which stress-free boundary condition is satisfied for a given wavelength and frequency. For a uniform waveguide, this length is simply one-half wavelength. However, due to the extra non-linear term in the Webster's horn equation, this length is different from $\lambda/2$. The numerically calculated displacement profiles for the horn shapes are shown in Fig. 18.4. From these displacement profiles, a number of horn performance criteria can be calculated.

Magnification, *M*, of an ultrasonic horn is the ratio of the particle velocity at the small cross-section to that of large cross-section. Since $x(0) = 1$ was assumed, the displacement at $x = l$ in Fig. 18.4 can be read directly as the magnification of the horn. One usually wants the highest possible magnification for a given A_i/A_f. Figure 18.5 shows the magnification for different horns plotted against the area ratio A_i/A_f. The magnification for some horn shapes can be written as

Table 18.3 Horn shapes and parameters

Horn	A(x): $A_0 = A(0)$ = large cross-section $A_1 = A(1)$ = small cross-section **l** = $\lambda/2$ resonant length	Parameter definitions
Exponential 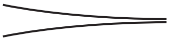	$A(x) = A_0 \exp(-2\alpha x)$	$\alpha = \dfrac{2\log\left(\dfrac{A_0}{A_1}\right)}{l}$
Catenary 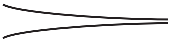	$A(x) = A_1\,(\cosh(\alpha(l-x)))^2$	$\alpha = \dfrac{a\cosh\sqrt{\left(\dfrac{A_0}{A_1}\right)}}{l}$
Linear 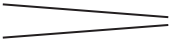	$A(x) = A_0\dfrac{(l-x)}{\beta} + A_1$	$\beta = \dfrac{A_0 l}{(A_0 - A_1)}$
Stepped 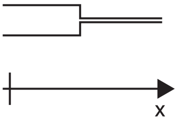 x	$A(x) = \begin{bmatrix} A_0 \\ A_1 \end{bmatrix}\begin{bmatrix} If\left(x < \dfrac{1}{2}\right) \\ If\left(x > \dfrac{1}{2}\right)\end{bmatrix}$ $\approx \dfrac{(A_0 - A_1)}{2}\left(1 - \tanh\left(\alpha\left(x - \dfrac{l}{2}\right)\right)\right) + A_1$	$\alpha = \dfrac{50}{l}$, 50 is chosen by trial and error to produce a sufficiently sharp step function.

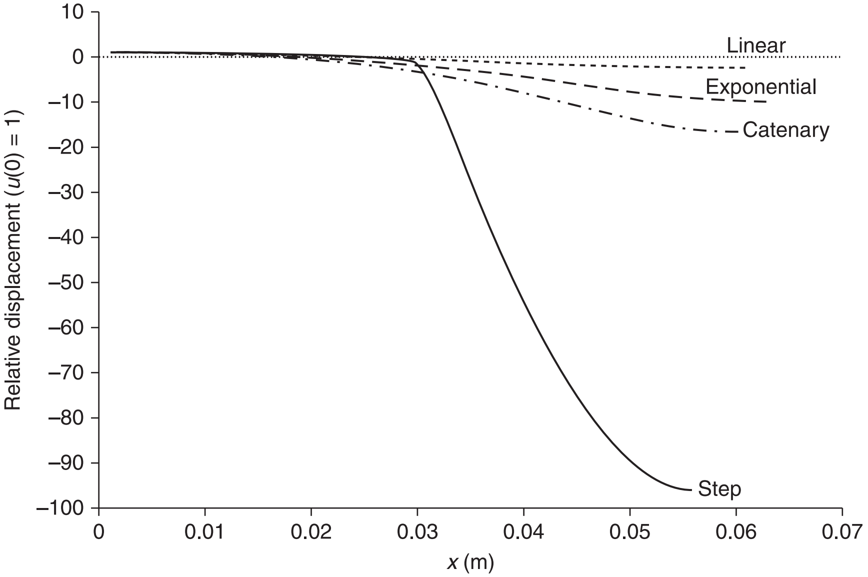

18.4 Numerically calculated displacement profiles for the horn shapes.

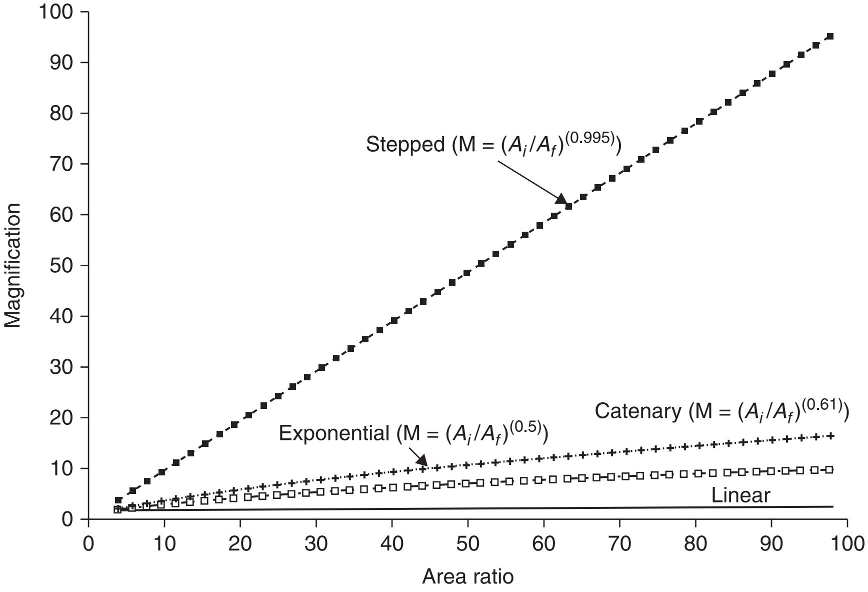

18.5 Magnification for different horns vs. area ratio.

$$M = \left(\frac{A_i}{A_f} \right)^n \qquad [18.11]$$

where n is a value ranging from 0 to 1. Magnification for the stepped horn is the largest for any given area ratio A_i/A_f with $n = 0.995–1.000$. The catenary horn has the next highest M with $n = 0.61$. Magnification for the exponential horn is smaller than that of the catenary, with $n = 0.5$. The linear horn has the smallest M and its dependence on A_i/A_f did not fit Eq. 18.11. Its maximum calculated gain was 2.4, which does not change much for values of A_i/A_f above 12.

18.4 Sensor integration and fabrication of silicon horns

Silicon-based power ultrasonic transducers were introduced by Lal (1996), suggesting silicon's high output power density, larger stroke velocity, lower internal loss and heat generation as compared with transducers made with traditional metal materials. During the past decade, silicon power ultrasonics has seen developments in the fields of microsurgery (Son and Lal, 2000), material characterization (Lee, 2001), ultrasonic nebulizers (Tsai *et al.*, 2004), etc. By integrating microprobes to the tip of the silicon ultrasonic horn actuators tissue-penetration force reduction has been demonstrated (Lal, 1996). Integration of silicon-based sensors on the microprobes has allowed interrogation of biological tissue for histology and surgical applications. In this section, we will concentrate on two types of microscale sensors integrated on the silicon horn actuator, namely, planar metal electrode array and piezoresistive strain gauges.

Silicon ultrasonic horns were fabricated by bulk micromachining from silicon wafers as shown in Fig. 18.6 (Chen, 2006). First a 6000 Å LPCVD (low-pressure chemical vapor deposition) silicon nitride was deposited on 4″ <100> silicon wafers to act as electrical insulation and wet KOH-etch mask layer. A 3000 Å platinum (Pt) and 300 Å chromium (Cr) layer was evaporated and patterned to form the electrode arrays, interconnects and bonding pads. A 1 μm PECVD (plasma-enhanced chemical vapor deposition) silicon nitride insulation layer was deposited on top of the metal layer. A second layer of Pt was evaporated and patterned to form a ground layer covering all the metal traces, except at the recording sites and the bonding pads, to reduce cross-talk between channels. A 1 μm PECVD silicon nitride passivation layer was deposited and openings were etched for the electrode recording sites and bonding pads. A DRIE etch on the front side of the wafer was done to define the shape and depth of the two microprobes at the tip of the ultrasonic horn. Finally, backside-only KOH etching releases the silicon horn from the wafer, with the thin-beam microprobes at the high-velocity end (the smaller tip) of the horn. The width of the microprobes is 200 μm and the thickness is 140 μm. The tip of the microprobe is triangular

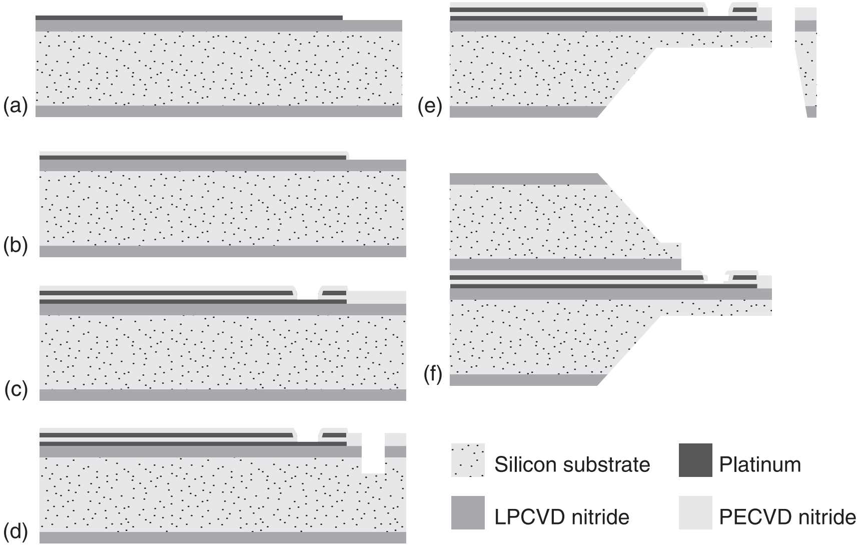

18.6 Steps in the bulk micromachining of a silicon ultrasonic microprobe with planar electrodes.

with 45° tip angle. There are five 40 × 40 μm Pt electrodes on each of the two microprobes, forming a 2 × 5 electrode array. The inter-electrode distance is 2 mm along the 10 mm microprobes. The microprobes are of much smaller dimensions, so they act as a small mass load and do not significantly affect the primary longitudinal resonance mode of the ultrasonic horn. The microprobes can be independently viewed as clamped-free cantilevers with the clamped end excited at ultrasonic frequency in the longitudinal direction. To reduce the excitation force in bending mode, another silicon horn with the same shape and dimension, but without the two microprobes, is bonded to the horn with microprobes to achieve symmetry in the thickness direction. The bonding between the two horns is achieved by silk printing with epoxy (Epoxy Technology, 360T).

Finally, two piezoelectric PZT-4 plates (EBL-1, Staveley Sensors Inc.) with matching resonance with the silicon ultrasonic horn are bonded to both sides of the horn at the half-wavelength displacement node. The horn is then clamped to a custom made PC board, also at the location of the displacement node. The Pt pads on the probe are wire-bonded to the PC board and then connected to an external circuit through a ribbon cable. Figure 18.7 is a photograph of the assembled device. The inset in Fig. 18.7 is a close-up view of the two microprobes showing the tip profile and the Pt electrode for electrical potential recording.

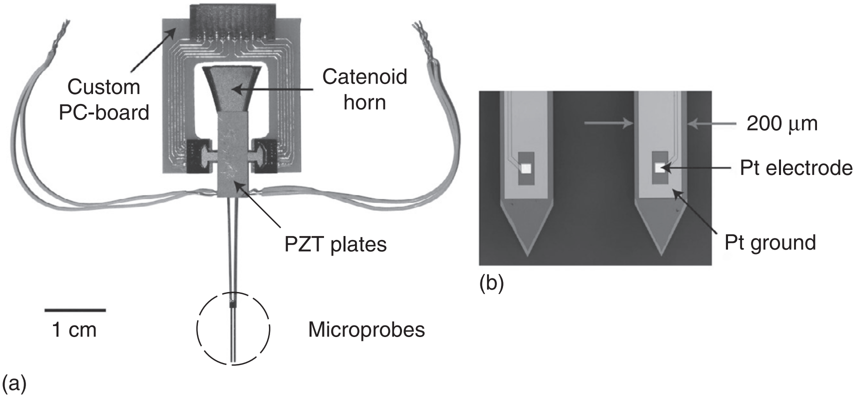

18.7 (a) Photograph of a silicon ultrasonic horn. (b) Microprobes.

18.5 Planar electrode characterization

Metal-based electrodes as a transducer for measuring bioelectric signals such as action potentials (cardiac and neural), electromyograms (EMG), etc. and stimulation of excitable tissues (neuron, muscle, etc.) have been widely used since the early 1800s (Geddes, 1997). In the physiologic environment, the bioelectric signals are carried in the electrolytic media in the form of ionic currents. The purpose of the metal-based electrodes is to transduce these signals to and from electronic signals. Thus the electrical characteristics (impedance) of the electrode–electrolyte interface are of utmost importance during electrophysiological studies. Experimental results have shown that the impedance of the interface has both reactive and resistive components which vary with frequency and current density. In this section, the theoretical origins of the different components of the electrode–electrolyte interface are discussed. Figure 18.8 shows the equivalent circuit comprising a constant phase angle impedance Z_{CPA} that represents the interfacial capacitance. The capacitance is further shunted by the charge transfer resistance R_{ct}, Warburg capacitance C_w and Warburg resistance R_w, together in series with the spreading resistance R_s (Kovacs, 1988; McAdams and Jossinet, 1994; Grahame, 1952).

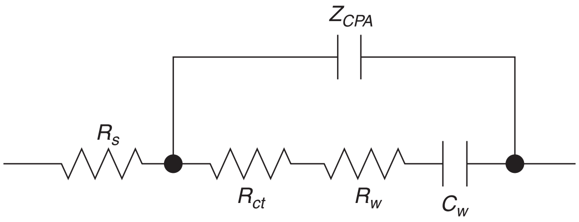

18.8 Equivalent circuit of a planar electrode–electrolyte interface.

18.5.1 Interfacial capacitance

A metal introduced into an ionic solution undergoes chemical reactions at the interface and builds up a space charge layer. These reactions, being thermodynamically favorable, proceed spontaneously, and result in the dissolution of metal (oxidation) in solution to form metal ions, leaving behind free electrons, which repel each other and accumulate at the interface. The excess electrons on the surface of the electrode and the metal ions dissolve in the solution for a space charge layer, as shown in Fig. 18.9. The electric potential developed by the space charge layer in turn lowers the barrier for the reverse electrochemical reaction (reduction of metal ions). This process eventually reaches equilibrium when a sufficient charge separation is achieved, wherein the forward and reverse reaction rates are equal, resulting in a zero net current across the interface. In terms of an electrical circuit element, this space charge layer represents a capacitance. The constant phase angle impedance Z_{CPA} models the capacitive characteristics of the electrode–electrolyte interface. A theoretical derivation of the interface capacitance C_I (i.e. $Z_{\mathrm{CPA}} = j\omega C_I$) is given by the Gouy–Chapman–Stern model (GCS) (Bard, 2001). The interface capacitance is

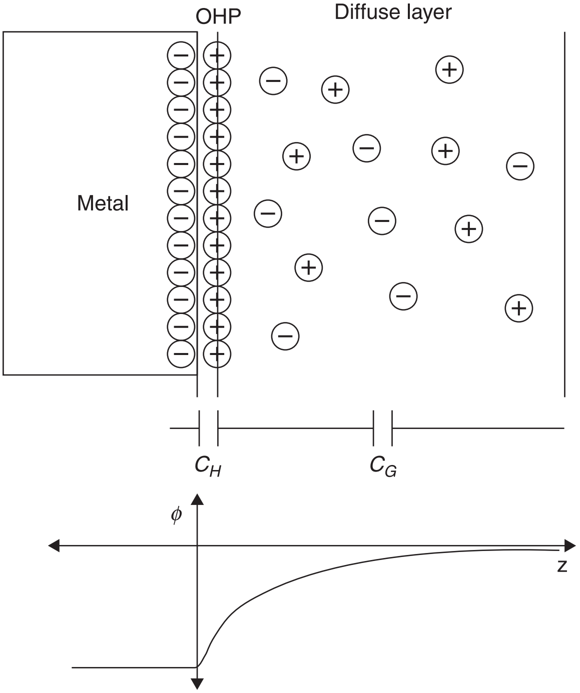

18.9 Interfacial capacitance.

taken to be the series combination of the double-layer (Helmholtz) capacitance C_H and the diffuse layer (Gouy–Chapman) capacitance C_G –

$$\frac{1}{C_I} = \frac{1}{C_H} + \frac{1}{C_H} \tag{18.12}$$

The Helmholtz capacitance C_H assumes that the charges in the solution are concentrated in a plane, the outer Helmholtz plane (OHP), parallel to the metal surface, and the capacitance can be described as that of a parallel plate capacitor in the Helmholtz–Perin model,

$$C_H = \frac{\varepsilon_0 \varepsilon_r A}{d_{OHP}} \tag{18.13}$$

where ε_0 is the dielectric permittivity of free space ($\varepsilon_0 = 8.854 \times 10^{-12}$ F.m^{-1}), ε_r is the relative dielectric permittivity of the medium between the plates of the capacitor, A is the surface area and d_{OHP} is the distance between the outer Helmholtz plane and the metal surface. In aqueous solutions, the medium between the outer Helmholtz plane and the metal surface is a layer of oriented water molecules with relative dielectric permittivity of ≈ 6 (Bockris and Reddy, 1970).

The actual space charge region extends from the interface into the solution, with charge density decreasing from a maximum value at the interface to its bulk concentration in the solution. As the potential applied to the electrode is increased, the ions tend to closely pack near the metal surface, reducing the thickness of the space charge region, and therefore increasing the interfacial capacitance. The potential dependant capacitance of the diffuse charge region described by the Gouy–Chapman model, C_G, is given by

$$C_G = \frac{\varepsilon_0 \varepsilon_r \cosh\left(\dfrac{z\varphi_0}{2V_t}\right)}{L_D} \tag{18.14}$$

where $V_t = kT/q$ is the thermal voltage (≈ 26 mV at 25 °C), z is the charge of the ions in question and ψ_0 is the applied electrode potential. The Debye length, L_D, is given by

$$L_D = \frac{\varepsilon_0 \varepsilon_r V_t}{2n^0 z^2 q} \tag{18.15}$$

where n^0 is the bulk number concentration of the ion and q is the charge of the electron (1.602×10^{-19} C). For physiological saline (0.9% w/v NaCl) at 25 °C, $\varepsilon_r \approx 78.54$ and $L_D = 7.8 \times 10^{-10}$ m. Therefore the interfacial capacitance C_I is given by

$$\frac{1}{C_I} = \frac{d_{OHP}}{\varepsilon_0 \varepsilon_r A} + \frac{L_D}{\varepsilon_0 \varepsilon_r \cosh\left(\dfrac{z\varphi_0}{2V_t}\right)} \tag{18.16}$$

Adding the Helmholtz and the Gouy–Chapman capacitances in series satisfactorily describes the behavior of the interface capacitance at DC. The

Gouy–Chapman capacitance dominates at lower applied electrode potentials, and as the potential is increased the Gouy–Chapman capacitance increases and the total capacitance approaches the Helmholtz capacitance. For physiological saline solutions, the total interface capacitance increases from 0.099 F.m^2 at zero applied potential to about 0.11 F.m^2 for potentials of 0.2 V and above (Bockris and Reddy, 1970). This corresponds to approximately 158–176 pF for the 35 × 35 μm platinum electrode surface used in the ultrasonic silicon microprobes.

18.5.2 Charge transfer resistance (R_{ct})

The DC current path across the electrode–electrolyte interface is represented by a non-linear resistive element in parallel with the interfacial capacitance (Fig. 18.8). This resistive element takes into account several mechanisms – charge transfer processes at the electrode, chemical reactions, and diffusion of reactants to and from the electrode surface and crystallization processes. During electrophysiological recordings using metal electrodes, crystallization processes and chemical reactions should not occur at the electrode and hence can be ignored. The resistive element is mainly due to charge transfer through the electrode double layer, which is necessary for any steady-state current flow. The movement of charge into or out of an electrode requires a shift in potential from its equilibrium value called the overpotential η.

In the state of equilibrium, the current due to the oxidation and reduction reactions is equal in magnitude since the reactions take place at an equal rate. The absolute value of this current for a given surface area, referred to as the exchange current density, J_0 (Bockris and Reddy, 1970), is given by

$$J_0 = Fk_c c_A e^{\frac{\beta\Delta\varphi_0}{V_t}} \qquad [18.17]$$

where $V_t = kT/q$ is the thermal voltage (≈26 mV at 25 °C), k_c is the reduction reaction rate constant, c_A is the concentration of electron-acceptor ions, A in solution plane of the interface, β is the symmetry factor and $\Delta\psi_0$ is the equilibrium potential. The value of J_0 is a property of the electrode material and the reactions taking place. In the presence of non-zero overpotential (η), the additional current through the electrode will be determined by the magnitude of J_0. The value of the overpotential can be related to the current density by the Butler–Volmer equation (Bard, 2001); exchange current density, J_0, is given by

$$J = J_0\left[e^{\frac{(1-\beta)z\eta}{V_t}} - e^{\frac{-\beta z\eta}{V_t}}\right] \qquad [18.18]$$

where z is the charge of the ion in question. The charge transfer resistance R_{ct} can be derived from Eq. 18.18,

$$R_{ct} = \left(\frac{V_t}{J_0 z}\right)\frac{1}{\cosh\left(\frac{z\eta}{2V_t}\right)} \qquad [18.19]$$

with $R_{ct} \approx \frac{V_t}{J_0 z} \forall \frac{z\eta}{2V_t} << 1$ and $R_{ct} \approx \frac{2V_t}{J_0 z} e^{\frac{z\eta}{2V_t}} \forall \frac{z\eta}{2V_t} >> 1$

R_{ct} is linear with η for low field and exponentially decaying at large η. Therefore R_{ct} can be electrically modeled as a pair of semiconductor diodes connected in reverse parallel.

18.5.3 Warburg capacitance (C_W) and resistance (R_W)

Warburg proposed the dependence of the spatial concentration gradient near the electrode–electrolyte interface on the frequency of a sinusoidal forcing function $-|Z_D| = k/\sqrt{f}$, where k is a constant determined by the electrochemistry and mobilities of the reactant species involved and f is the frequency in Hertz. The Warburg impedance is often expressed as a series combination of a resistance (R_w) and a capacitance (C_w),

$$Z_w = R_w + \frac{1}{j2\pi C_w}; \quad R_w = \frac{1}{2\pi C_w} \qquad [18.20]$$

Therefore Z_W has a constant phase of −45°. Experimental studies and models in the literature (Geddes, 1997) have shown that the resistance and reactance both vary as $1/f_m$, with m varying between 0.15 and 0.86 for different metals and at different temperatures.

18.5.4 Spreading resistance (R_s)

The final element to be considered in the theoretical model of the electrode–electrolyte interface is the net resistance encountered by the current spreading out from an electrode into a conductive solution, referred to as *spreading resistance* (R_s). The magnitude of the resistance is determined by the geometric surface area of the electrode and is expressed as

$$R_s = \int_{x=0}^{x=\infty} dR_s \qquad [18.21]$$

where x is the distance normal to the surface. For a planar rectangular electrode, it can be shown that the spreading resistance amounts to

$$R_s = \frac{\rho \ln\left(\frac{4l}{\omega}\right)}{\pi l} \qquad [18.22]$$

where l and w are the length and width of the rectangular surface, ρ is the resistivity of the solution (72 Ω.cm^{-1} for physiological saline). For the 35 × 35 µm platinum electrodes used in the ultrasonic silicon microprobes, the spreading resistance $R_s \approx 9.08\,\text{k}\Omega$.

In order to empirically estimate the electrode–electrolyte interfacial parameters, electrode impedance spectroscopy (EIS) and cyclic voltammetry (CV) measurements need to be performed. The equivalent circuit for EIS measurements of the silicon microprobe, using the potentiostat, is shown in Fig. 18.10. Figure 18.11(a) shows the results from the cyclic voltammetry experiments performed using the lower-most electrode at the tip of the silicon microprobe. The equilibrium exchange current density J_0 and the charge transfer resistance R_{ct} are calculated to be $38.99 \pm 2.06 \times 10^{-8}$ Å.cm^2 and 5.38 GΩ respectively, with an OCP of 201.7 mV. The modulus of impedance and phase of the electrode (area exposed is 1.23×10^{-5} cm^2, OCP = 142.6 ± 12.2 mV) and the corresponding fit to the model are shown in Fig. 18.11(b), and the empirical fit-based and predicted values of the

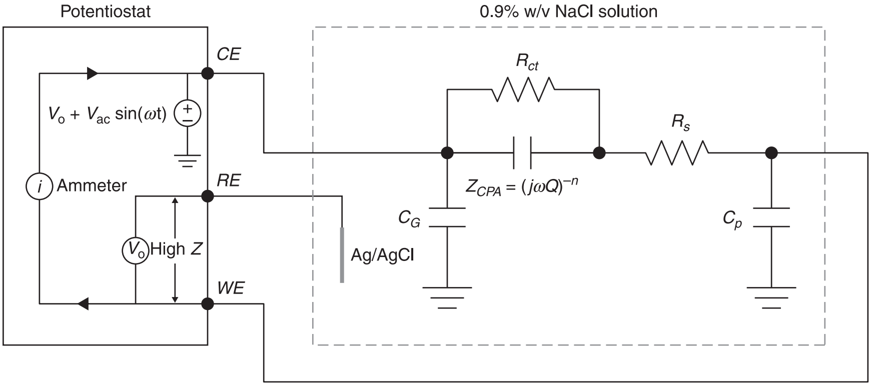

18.10 Equivalent circuit for EIS measurements of a silicon microprobe.

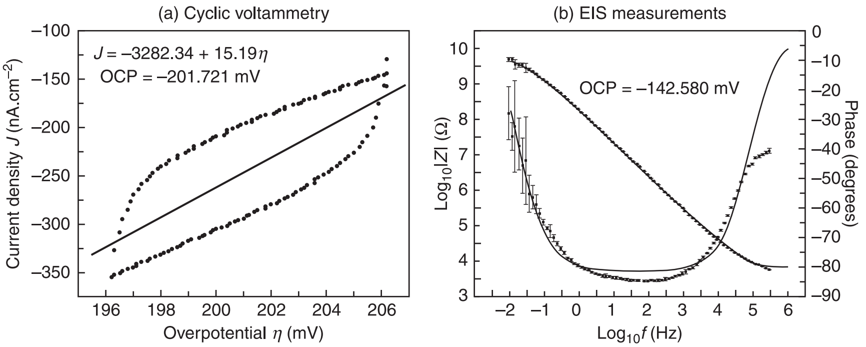

18.11 (a) Results from cyclic voltammetry experiments. (b) Modulus of impedance and phase of the electrode and the corresponding fit to the model.

Table 18.4 Table of parameters for equivalent circuit

	n	R_{ct} (GΩ)	R_s (kΩ)	$1/Q_n$ (GΩ.s)
Empirical	0.90	5.79	7.76	0.97
Theoretical	1.00	5.38	9.08	6.23

parameters of the equivalent circuit are shown in Table 18.4. The surface of the evaporated platinum electrode being prone to contamination leads to variation in the interfacial conditions, which results in drift in the magnitude of R_{ct}. This explains the large error bars in the phase data at low frequencies. The poor fit of the model to the phase data can be attributed to the presence of parasitics in the microprobe and the potentiostat experimental arrangement, which are not accounted for in the model.

18.6 Piezoresistive strain gauges

Minimally invasive medical procedures such as percutaneous liver biopsy and endoscopic surgery reduce tissue damage and patient discomfort but also pose great challenges to the surgeon due to reduced direct sensory feedback. Research efforts to improve the success rate of these procedures have been focused on experimental characterization and numerical modeling of the tissue–surgical tool interaction (Sacudean, 2002; Okamura, 2004). Force measurement during the tissue–tool interaction is important for building a realistic model based on which haptic interface and robotic assistance can be developed to help the surgeons regain tactile information during surgery. Furthermore, ability to distinguish tissue stiffness at microscale will allow for more accurate feedback and precise control of robotic minimally invasive systems. MEMS (micro-electro-mechanical-systems) devices are expected to play an increasingly important role in this field, e.g. measurement of mechanical properties of tiny tissue samples has been performed by a Lithographie, Galvanoformung and Abformung (LIGA)-fabricated microgripper (Menciassi *et al.*, 2001). Thin-beam silicon microprobes (Naja *et al.* 1985; Najafi, 1986; Ensell *et al.*, 1996; Kewley *et al.*, 1997; Yoon *et al.*, 2000) provide high spatial resolution, reduced tissue damage and easy integration with micro-electronics. Silicon microprobes for tissue characterization in robotic surgery are especially favorable due to the potential of integrating a variety of sensors for monitoring different parameters such as insertion/cutting force, tissue viscosity and temperature, etc.

In this section, the silicon ultrasonic horn actuator with microprobes integrated with piezoresistive strain gauges is described. The device fabrication and mechanical characterization are discussed in detail.

18.6.1 Fabrication process flow

The design and fabrication of the microprobe are similar to the ultrasonic microprobes discussed in the previous section. The catenoid horn is 4 cm long with shank-to-tip area ratio 10:1 and a longitudinal $\lambda/2$ resonance at 110 kHz, with two silicon microprobes 5 mm long, 100 µm wide and 140 µm thick projecting outwards at the tip of the horn. A further modification to the silicon microprobe is the addition of a set of four polysilicon resistors forming a Wheatstone bridge arrangement for each of the two tips (Fig. 18.12). The polysilicon strain gauges (≈10 kΩ), the resistance of which changes with the strain experienced by them, are positioned on both the microprobes – two reference polysilicon resistors are positioned on the bulk silicon part of the horn so their resistance remains nearly constant with respect to strain on the microprobe, and the other two piezoresistive polysilicon resistors are positioned on the microprobe near its clamped edge where the strain is expected to be high (Fig. 18.13). The polysilicon resistors on the microprobe forming a Wheatstone bridge are connected in a constant current configuration, with the current supplied by an operational amplifier (Fig. 18.14). The bias voltage (V_{bias}) is set at 4 V and the circuit is driven at $V_s = \pm$ 8V. The Wheatstone bridge output voltage is amplified by a factor of 100 using an instrumentation amplifier (AD524, Analog Devices, Inc.). Depending on the application, the circuit can be modified in order to achieve the appropriate strain sensitivity.

18.6.2 Strain gauge mechanical characterization

The microprobe assembly was clamped to a micromanipulator (MP-285, Sutter Instruments, Inc.), and placed across a force gauge sensitive up to 1 mN (DFGS

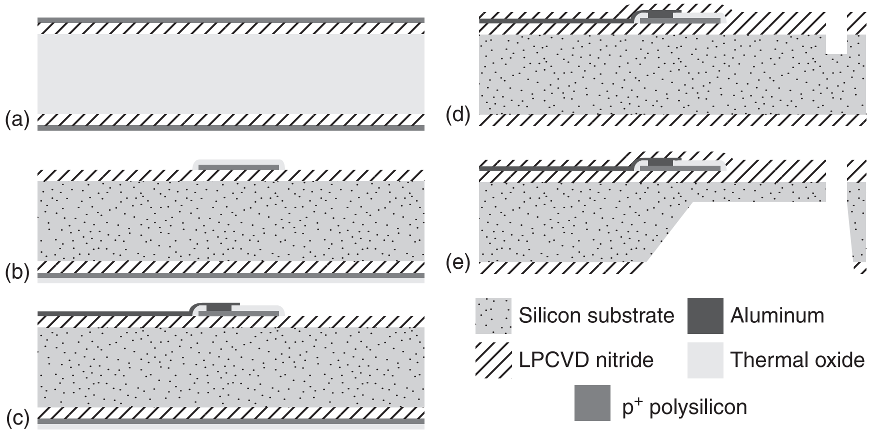

18.12 Steps in the bulk micromachining of a silicon ultrasonic microprobe with strain gauges.

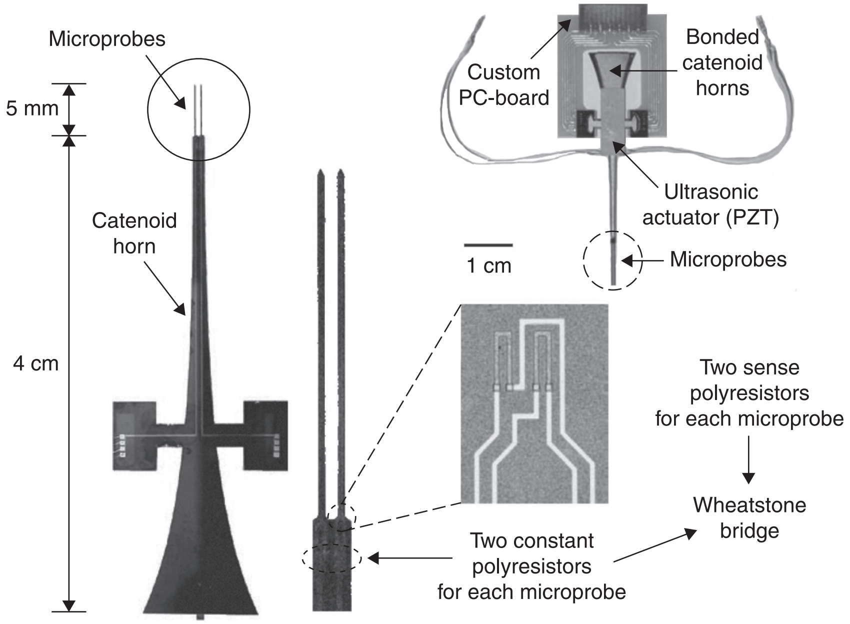
Microprobes
5 mm
4 cm
Catenoid horn
Custom PC-board
Bonded catenoid horns
Ultrasonic actuator (PZT)
1 cm
Microprobes
Two sense polyresistors for each microprobe
Wheatstone bridge
Two constant polyresistors for each microprobe

18.13 Silicon ultrasonic horn actuator with microprobes integrated with piezoresistive strain gauges.

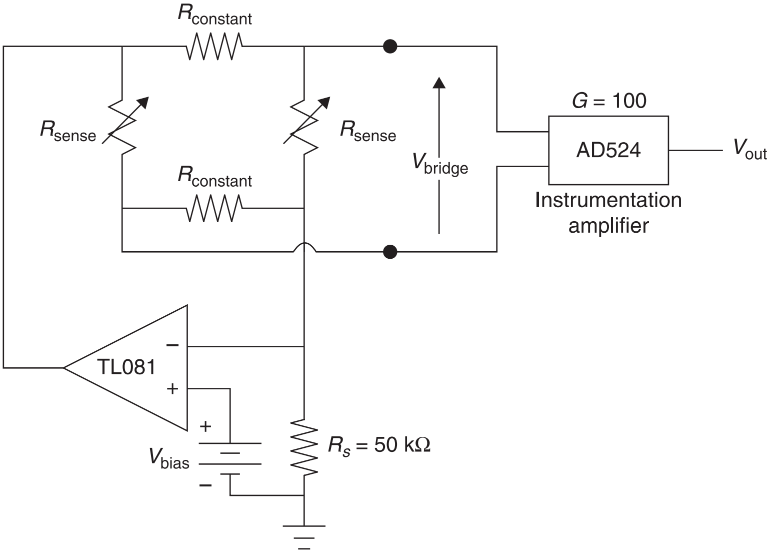
$R_{constant}$
R_{sense}
R_{sense}
$R_{constant}$
V_{bridge}
$G = 100$
AD524
V_{out}
Instrumentation amplifier
TL081
−
+
+
V_{bias}
−
$R_s = 50\ k\Omega$

18.14 Electronic circuit for a piezoresistive strain gauge.

series digital force gauge, Chatillon, Inc.), which is clamped to a stage such that the microprobes are perpendicular to the surface of the force gauge. The force calibration tests were carried out below this threshold load for elastic buckling, so that the microprobes can be assumed to be under uniform compressive load. The assumption in this testing was that the force experienced by each microprobe is identical, i.e. the force recorded by the force gauge is twice the force experienced by a single microprobe. The microprobes were pressed against the force gauge at steps of 20 mN from 0 to 300 mN, and the Wheatstone bridge voltage was recorded. The variation of the bridge voltage with the force applied was fitted to a second degree polynomial (Fig. 18.15). The second degree variation is because of imperfect alignment of the probe perpendicular to the force gauge. From this longitudinal force characterization curve, it is clear that the polysilicon resistors are sensitive to minute changes in strain experienced by the microprobe, with a sensitivity of $-0.41\,\text{V.N}^{-1}$ after electronic amplification by a factor of 100. Finite-element analysis (using ANSYS) of the microprobes was performed to estimate the strain induced on the polysilicon resistors due to forces experienced at the tip of the microprobes. Longitudinal and transverse gauge factors of 28 and −8 were used to estimate the resistance change corresponding to the expected longitudinal and transverse strains (Obermier *et al.*, 1986). The longitudinal force

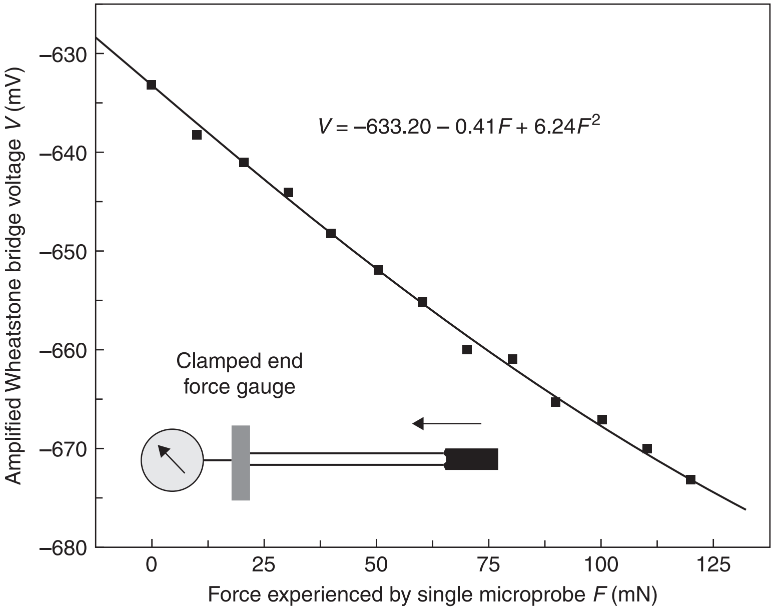

18.15 Wheatstone bridge voltage vs. axially applied force for a microprobe.

sensitivity was estimated to be $-0.43\,\mathrm{V.N}^{-1}$, which is close to the experimentally measured value.

The force sensitivity of the polyresistors to bending of the microprobes is characterized by positioning the microprobes with their longitudinal axes perpendicular to that of the strain gauge. The polyresistors experience tensile strain when the force is applied to the front of the microprobes (on the side of the polyresistors) and compressive strain when the force is applied to the back of the microprobes. The assumption in this testing is that the force experienced by each microprobe is identical, i.e. the force recorded by the force gauge is twice the force experienced by a single microprobe. The face of the microprobes was pressed against the force gauge at steps of 5 mN from 0 to 30 mN, and the Wheatstone bridge voltage was recorded. The variation of the bridge voltage with the force applied is fitted to a second degree polynomial (Fig. 18.16). The second degree variation is because of imperfect alignment of the probe parallel to the force gauge surface. From this characterization curve it is clear that the polysilicon resistors are sensitive to minute changes in bending-based strain experienced by the microprobe, with a sensitivity of $51.01\,\mathrm{V.N}^{-1}$ for transverse compressive strain and $36.13\,\mathrm{V.N}^{-1}$ for transverse tensile strain after electronic amplification by a factor of 100.

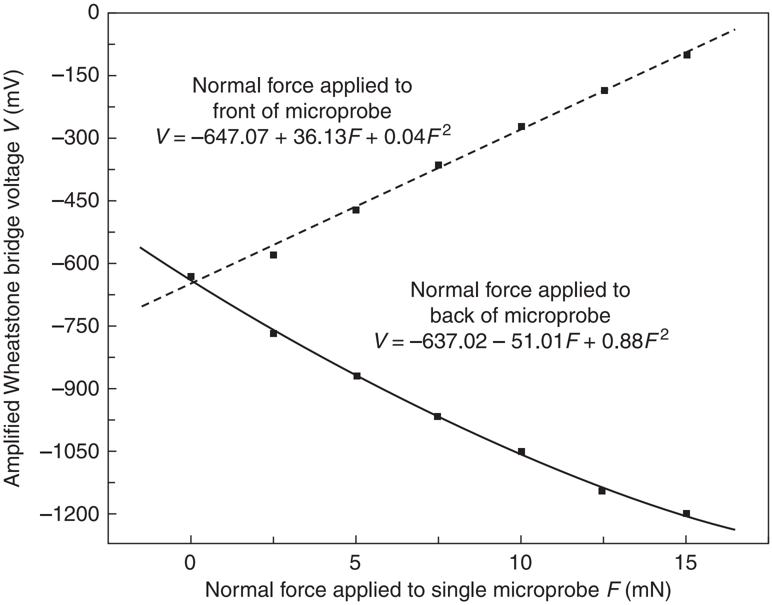

18.16 Wheatstone bridge voltage vs. transversely applied force for front and back of microprobe.

18.7 Applications: tissue penetration force reduction

There are two types of ultrasonic tissue cutting modalities: the focused ultrasound mode and the direct or impact mode. The actuator developed in this work was designed for direct contact surgery. Hence, most of this section concerns direct cutting.

18.7.1 Focused ultrasound

In this mode of cutting, an ultrasonic field focused on the unwanted tissue is induced into the body. Most water-containing tissues absorb high-frequency ultrasound (1–20 MHz) (Suslick, 1988), becoming heated to destructively high temperatures. The ultrasonic waves and high temperature also generate microbubbles, which implode causing cavitation, which can play a large role in tissue destruction. This form of tissue cutting is performed by an array of transducers placed outside the body, with their focus inside the body. This modality has been effectively used for gallstone and cancer removal (Frizell, 1996).

18.7.2 Impact mode

In this mode of surgery, the ultrasonic transducer is placed in direct contact with the tissue to be cut. The transducer surface impacts the tissue, transferring kinetic energy. The impact energy results in break-up of the tissue. Usually the tool impacting is a needle attached to an ultrasonic transducer (Fig. 18.17).

The main advantage of the ultrasonic impact mode of cutting is that the direct force applied by the doctor is considerably reduced. Part of the cutting force is shared by the vibrating tool, thus reducing the amount of direct force required. If one tries to slowly cut a free object with a steady force, the force is distributed quickly

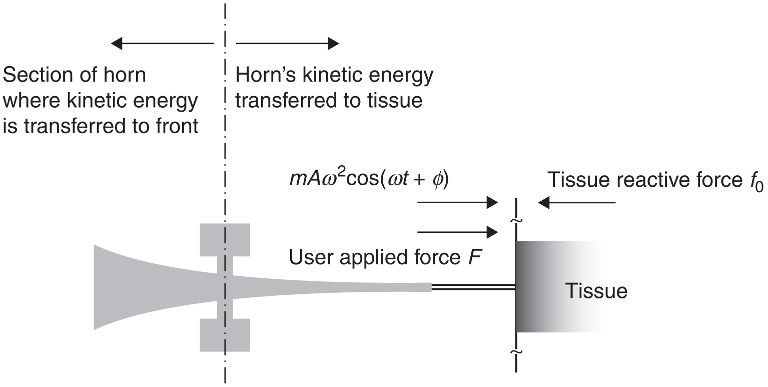
Section of horn where kinetic energy is transferred to front
Horn's kinetic energy transferred to tissue
$mA\omega^2\cos(\omega t + \phi)$
Tissue reactive force f_0
User applied force F
Tissue

18.17 Ultrasonic cutting of tissue during surgery.

to the center of mass of the object and causes it to move. However, if the force is applied in the form of an impulse and the mass of the body is large, the inertial forces oppose steady motion, causing the object to stay in place. Instead, the impact energy is absorbed by the surface, where tissue destruction takes place. This effect is often called inertia stiffening of a soft material. It has been discovered that this principle is used by leaf-eating ants (Tautz *et al.*, 1995) that vibrate their blades at 300 Hz to cut the leaves. The same principle is also used in a vibratome to cut very thin slices of tissue for biological tissue histology. In this section, the application of silicon ultrasonic horn actuators with integrated microprobes for tissue-penetration force reduction (ex vivo cardiac ventricular preparation) is discussed. The vibration modes of the microprobes are flexural modes excited by longitudinal periodic actuation of the silicon horn. The results indicate that the possible mechanism of ultrasound-induced penetration force reduction is the high-frequency stress in the tissue resulting from the vibration of the microprobe.

A successful model for the ultrasonic cutting of soft tissues by an ultrasonic chisel has been presented by Nabibekov and Plyushchenkov (1980a; 1980b). Their fundamental assumption was that the force required to penetrate tissue is a constant threshold. Frictional forces in fluid and tissue are assumed negligible. Furthermore, effects of cavitation and microstreaming are not considered. The goal of Nabibekov and Plyushchenkov was to determine the cutting velocity, or the rate at which an ultrasonic chisel can progress through a tissue. The user applies a steady force, F, to the complete surgical unit containing the transducer, which also acts against the tissue being cut. The force, F, and the force generated by the vibrating transducer act against the reaction force of the tissue (Fig. 18.17). Summing the forces, the differential equation of motion for the surgical unit is:

$$M\frac{d^2x}{dt^2} = F - mA\omega^2\sin(\omega t + \varphi) - f_0 \qquad [18.23]$$

The first term is the inertial force of the entire mass of the surgical unit. The force F is applied by the user and f_0 is the constant force of reaction of the tissue. The third term is the force generated by the section of the transducer that is cutting the tissue. It is the product of the acceleration $\omega^2 A$ (ω is the radian frequency, A is the transducer tip displacement amplitude) and an effective mass m. In the case of a resonator (silicon horn) half-wavelength long, m will be the effective mass of the section (see Figure 18.17) from the cutting tip to the first displacement node (the front $\lambda/4$ section), such that

$$mv_{tip}^2 = \int_{Node}^{Tip} \rho A(x)(v(x))^2 \; dx \qquad [18.24]$$

where $A(x)$ is the cross-sectional area, $v(x)$ is the longitudinal velocity along the transducer and $v_{Tip} = A\omega$ is the transducer tip velocity. During each cutting cycle, there will be an active cutting phase and an inactive cutting phase, where the tip is thrusting toward uncut tissue and withdrawing from cut tissue. For a particular range of constant forces $0 < F < f_0$ applied by the user, there exists a stationary cutting mode wherein the movement of the instrument in the tissue over some time occurs with a constant, stabilized velocity. Assuming the tissue reaction force $f_0 << mA\omega^2$, the use of high-frequency ultrasound and low-amplitude ultrasonic waves, and neglecting the friction and the first and second order terms of reaction force of tissue, Eq. 18.23 can be solved to determine the cutting velocity, V (defining $\xi = F/f_0$):

$$V = v_{Tip}\frac{m}{M}\frac{\sin^2 \pi\xi}{\pi\sqrt{\left(1-\xi+\frac{\sin 2\pi\xi}{2\pi}\right)+\frac{\sin^4 \pi\xi}{\pi^2}}} \qquad [18.25]$$

$$\xi = \frac{1}{\pi}\arcsin\sqrt{\left(\sqrt{\frac{\pi^2+4\left[\left(\frac{v_{Tip}}{V}\right)^2-1\right]\left[\pi^2(1-\xi)+\frac{\pi}{2}\right]-\pi}{2\left[\left(\frac{v_{Tip}}{V}\right)^2-1\right]}}\right)} \qquad [18.26]$$

When the microprobes attached to the silicon horn are inserted into tissue, there are three kinds of forces applied on the tissue by the microprobes. First, the DC force in longitudinal direction applied by the inserting mechanism; second, the back and forth (AC) longitudinal motion generated directly by the longitudinal resonance of the ultrasonic horn; lastly, the transverse force at ultrasonic frequency by exciting flexural modes of the microprobes. It has been reported previously (Chen, 2006) that, for a constant velocity of insertion of the microprobes into the tissue, the DC force (applied by user, F) required to penetrate biological tissue (left ventricle) is reduced as the PZTs are driven at higher voltages. By neglecting the transverse force due to the flexural modes of the microprobes, from Eq. 18.25 we can say that, assuming a constant insertion velocity of the microprobes, the force F applied by the user increases instantaneously at contact with the tissue and settles at a constant value before penetrating the tissue ($0 < \tau << T_{break}$). The value of ξ was numerically solved for a given value of v_{Tip} using Eq. 18.26. By solving the Webster's horn equation of motion (Lal, 1996) for a silicon horn of length 4 mm with 10 : 1 end-to-tip ratio and a resonance frequency ≈110 kHz, the ratio of the effective mass m/M was estimated to be 9.45%. The horn tip displacement A was taken to be 0.37 μm/Vpp (Chen, 2006).

Figure 18.18 shows the estimated decrease in the user applied force, F, at different insertion velocities, with increasing values of PZT drive voltage, V_{pp}, since f_0 corresponds to the constant force required by the user to puncture a given tissue without ultrasound. Figure 18.19 shows the estimated increase in ξ with increasing values of insertion velocity at PZT drive voltages of 1, 5 and 10 V_{pp}.

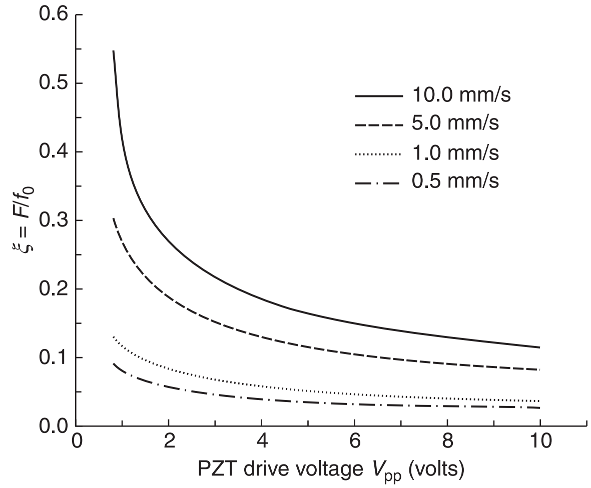

18.18 Estimated decrease in the user applied force for different insertion velocities vs. PZT drive voltage.

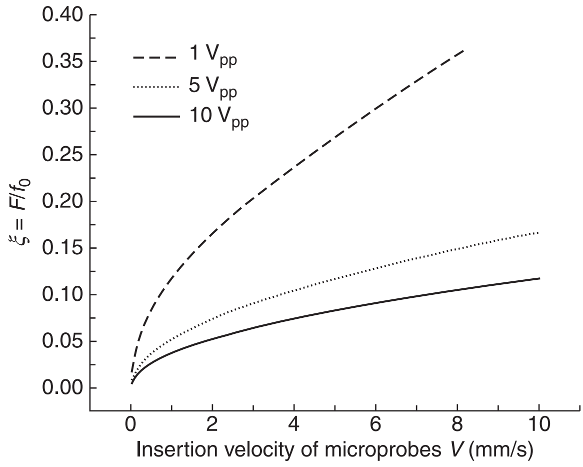

18.19 Estimated increase in ξ for different PZT drive voltages vs. insertion velocity.

From Eq. 18.26 we can say that, by optimizing the insertion velocity, V, and the tip displacement velocity, v_{Tip}, one can ideally minimize the force required by the user, F. In order to assume stationary cutting mode for the case of the silicon ultrasonic microprobes inserted at constant insertion velocities, the elasticity of the tissue is ignored (no buckling). The above model is valid for insertion velocities $V << v_{Tip}$. Since v_{Tip} is known to increase with PZT drive voltage, at higher drive voltages the working range with respect to insertion velocities is larger.

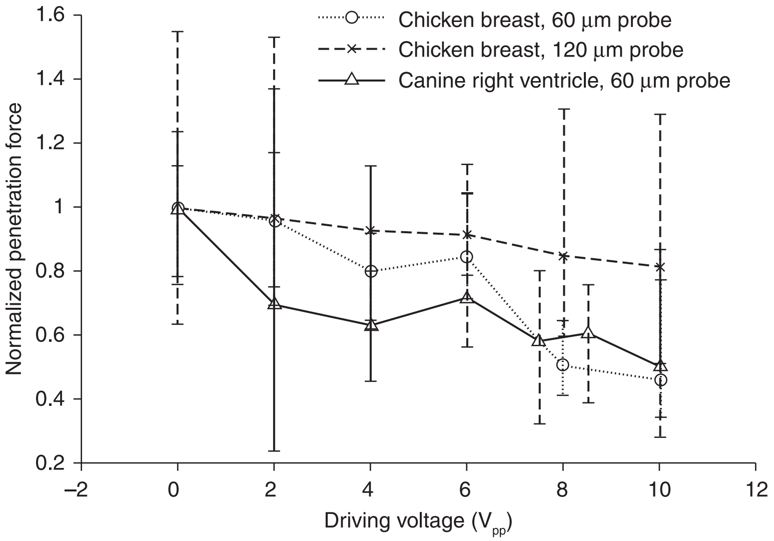

18.20 Penetration force vs. ultrasonic driving voltage (Chen, 2006).

Figure 18.20 shows the penetration force versus ultrasonic driving voltage curves for the right ventricular wall of excised canine heart and for chicken breast muscle. Longer silicon horn devices (6 mm long, 15 mm to 1 mm end-to-tip area ratio) with a single microprobe tip were fabricated for the force measurement. For devices with two or more tips the force is expected to be proportional to the number of tips. The mean and the standard deviation of the penetration forces without ultrasound were 0.056 ± 0.009 N for the 60 μm thick probes on chicken breast, 0.058 ± 0.019 N for the 120 μm thick probes on chicken breast and 0.046 ± 0.009 N for the 60 μm thick probes on canine right ventricle. These results are listed in Table 18.5. The absolute values of the penetration force depend on the tissue type, the sample freshness and condition, as well as the microprobe dimensions. Therefore the forces are normalized against their mean value at no ultrasonic actuation to illustrate the effect of ultrasound on the relative change of penetration force. All three curves show a trend of decreasing force with increasing ultrasonic driving voltage. For the 60 μm thick microprobe, the rates of force

Table 18.5 Penetration force without ultrasound

	Canine right ventricle	Chicken breast	Chicken breast
Probe thickness	60 μm	60 μm	120 μm
Penetration force	46 ± 9 mN	56 ± 9 mN	58 ± 19 mN

reduction by ultrasonic actuation on cardiac muscle and chicken breast muscle seem similar from Figure 18.20, with approximately 50% overall reduction at 10 V_{pp} from the values at 0 V_{pp} (no ultrasound). On chicken breast samples, the force reduction curve for the 60 μm microprobe has a larger slope than that for the 120 μm microprobe, possibly due to the fact that in thinner microprobes the ultrasonic actuation is coupled into flexural vibration of the microprobe more effectively. The flexural vibration results in lateral force by the microprobe tip on the surface of the tissue, acting like drilling motion to help break apart the surface tissue layer and achieve penetration.

18.8 Applications: cardiac electrophysiological measurement

Sudden cardiac death – likely to be caused by ventricular fibrillation (VF) – is the leading cause of mortality in the industrialized world (AHA, 2005). The mechanism of VF remains unclear, but it has been widely accepted that electrophysiological potential structures with characteristic spatial and temporal order – named 'rotors' in the cardiology community – underlie ventricular fibrillation. The two-dimensional form of rotors has been reported as rotating spiral waves observed on both epicardial and endocardial surfaces of mammalian hearts, during in vitro experiments where the reentrant spiral waves led to tachycardia (Allessie *et al.*, 1973; Davidenko *et al.*, 1992; Efimov *et al.*, 1999) and fibrillation (Bonometti *et al.*, 1995; Witkowski *et al.*, 1998; Chen *et al.*, 2000; Bitkashev *et al.*, 1999). The two-dimensional mapping of electrical activation on the heart has been performed with either potential sensitive dye imaging (Davidenko *et al.*, 1992; Efimov *et al.*, 1999; Witkowski *et al.*, 1998; Chen *et al.*, 2000; Bitkashev *et al.*, 1999) or plaque type electrode arrays (Allessie *et al.*, 1973; Davidenko *et al.*, 1992) to measure the electrical activity of the surface cells. However, the heart is a three-dimensional structure and experiments revealed that quite often surface spiral waves are not seen or are only seen transiently during fibrillation, indicating that the rotors could be masked by the three-dimensional nature of the heart wall (Bitkashev *et al.*, 1999). On the other hand, truly two-dimensional cardiac tissue samples, i.e. thin slices of epicardium, were found to be able to sustain rotors indefinitely but would not develop more complex electrical patterns and fibrillate (Winfree, 1994). The transition from reentrant waves to fibrillation may be inherently three-dimensional and it is, therefore, necessary to obtain three-dimensional mapping data to accurately study electrical wave propagation within the tissue.

Due to the size limitations of the traditional metal wire and glass micropipette electrodes used in cardiac electrophysiology studies, there have been relatively few experimental observations of three-dimensional reentrant waves (or scroll waves) compared with the two-dimensional case. One remarkable and representative example is (Chen *et al.*, 1988), where the authors assembled 40 21-gauge needles into five columns and eight rows with 5 mm space between needles. Each needle had three bipolar electrode pairs inserted to appropriate depths, 2 mm apart, to record potentials across the heart wall. The array of needles was inserted into the myocardium of canine right ventricles and persistence of a rotor generating scroll waves spanning the 7 mm thickness of the right ventricle was observed. The authors reported interstitial hemorrhage throughout much of the endocardium caused by the intrusion of the needle arrays, and commented that the 5 mm inter-electrode distance may be inadequate to map the interaction between Purkinje fibers and ventricular myocytes, which may be important in the maintenance of reentry after the onset of VF.

Recording electrical potentials using silicon microprobes within the ventricular wall of the heart poses new challenges. Although the three meninges (dura, anachrod and pia) surrounding the brain or spinal cord have higher tensile strength than the cardiac muscle tissue (Yamada and Evans, 1970), the underlying neural tissues are much softer than the cardiac muscle comprising most of the heart walls. Therefore, the microprobes will encounter a large force during insertion into cardiac tissues. In addition, to reach across the thickness of the ventricular wall the microprobes need to be longer than the typical length of the neural probes (e.g. 5–10 mm for canine ventricle). The thickness of the microprobe needs to increase significantly for higher buckling-load and mechanical strength. Thicker probes provide greater rigidity, but will cause more damage to the tissue being investigated and may affect their electrophysiological activity. As discussed in the previous section, ultrasonic silicon-horn based microprobes have proven to reduce penetration force in cardiac tissue. Platinum-based planar electrodes integrated along the length of the microprobes allows electrophysiological signal recording from cardiac cells in the ventricular wall. In this section, we will provide a brief account of the signals recorded using the microprobes in the canine left-ventricular preparation ex vivo.

Electrical recordings were obtained from isolated perfused sections of canine left and right ventricles. The hearts were excised from deeply anesthetized dogs and the region of the heart supplied by the left anterior descending coronary artery or the right coronary artery was isolated. The coronary artery was cannulated and perfused with oxygenated Tyrode solution maintained at 37.5°C. The preparations were allowed to beat spontaneously or were paced at a constant cycle length using a bipolar stimulating electrode placed on the epicardial surface. Detailed description of the experimental procedure is given in (Chen, 2006). The ultrasonic horn with microprobes is actuated at the $\lambda/2$ longitudinal resonance frequency of the horn and the microprobes were inserted using a manual positioning stage. A driving signal of 5–10 V_{pp} is used to ensure insertion of the microprobes without significant buckling. Microprobes, 10 mm in length and 140 μm in thickness, were successfully inserted into the ventricular wall. The ultrasonic actuation was turned off once the microprobes were fully inserted to reduce RF coupling noise from the PZT electrodes. The signals from multiple recording sites on the microprobe were amplified in unipolar configuration and recorded at a 1 kHz sampling rate with a National Instrument DAQ system (DAQCard™-6024E for PCMCIA).

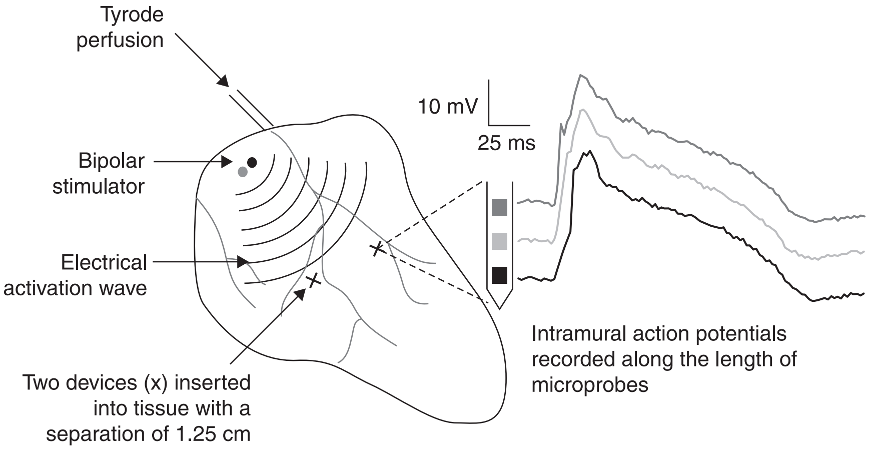
Tyrode perfusion
Bipolar stimulator
Electrical activation wave
Two devices (x) inserted into tissue with a separation of 1.25 cm
10 mV
25 ms
Intramural action potentials recorded along the length of microprobes

18.21 Multichannel recording from an isolated perfused canine left ventricle.

Figure 18.21 is a multichannel recording from the isolated perfused canine left ventricle, paced at a 700 ms cycle length by the surface stimulator. In this recording the action potentials have a MAP-like shape – the action potentials have peaks of only one polarity relative to the resting potentials – with subtle morphology difference and time delays between different electrodes, indicating the action potentials were propagated from the same stimulating source. The surface stimulating electrode was located a few centimeters away from the microprobe; therefore the shape and direction of the wave-front are indeterminate in this case due to the inhomogeneity of the heart. If the surface stimulating electrode was placed very close to the inserting location of the microprobe, or if the bottom-most microelectrode was used as the stimulating electrode, the conduction speed across the heart wall can be estimated from the inter-electrode distance and time delays between channels.

The activation time is identified as the moment of the maximum negative time derivative of the intrinsic detection in the cardiac signals (Caldwell, 2005). Taking the activation time in the uppermost channel (closest to the epicardial stimulator in this experiment) as baseline, the activation time delay progressively increases as the location of the electrodes moves downward, indicating the spread of activation from the epicardial pacing site across the thickness of the ventricular wall. The mean time delay between the third and fourth, and the fourth and fifth, channel from the epicardial surface is $\Delta\tau_a \approx 4$ ms. The conduction velocity can be estimated to be ≈ 0.5 m s^{-1}, which is typical for ventricular myocardium (Pressler *et al.*, 1995).

The cardiac MAP (cMAP) signal morphology was observed to change with length of time of the microprobes inserted into the tissue. The amplitude of the Na^+ spike in the extracellular cMAP signal is seen to be ≈ 18 mV as opposed to the intracellular microelectrode cMAP signal of ≈ 25 mV (Fig. 18.22a). The amplitude of the signal peak is observed to drop with time, reducing to ≈ 7 mV in 2 hours. Also the sharpness of the MAP peak is seen to deteriorate, with an increase in Na^+ peak rise-time from 2 ms in the ideal signal to ≈ 20 ms. The signal is seen to have peaks of both polarities relative to the resting potential. In Fig. 18.22a the recorded cMAP is seen to have a partial bipolar nature at $t = 0$ because of the circuitry having a high-pass filter cut-off of ≈ 0.225 Hz. At $t = 2$ hours the signal morphology is seen to be highly bipolar. This change in signal morphology is likely to be caused by the electrochemical changes (with time) taking place on the surface of the electrode, as opposed to physiological reasons. The shape of the cardiac MAP signal depends on the low- and high-pass cut-off frequency of the system. The bipolar nature of the signal can be explained by the increase in the high-pass cut-off frequency, $f_{HPF} \approx (2\pi(R_{ct}//R_L)Q^n)^{-1/n}$, which can be attributed to a decrease in interfacial capacitance, Q^n. Similarly, the sharpness of the peak can be explained by a decrease in the low-pass cut-off frequency, $f_{LPF} \approx (2\pi R_s C_L)^{-1}$, which can be a result of an increase in the spreading resistance, R_s, because of the presence of cardiac tissue all around the platinum electrodes.

Cardiac arrhythmias were also recorded by the ultrasonic microprobes by pacing the heart sample at progressively shorter cycle lengths until fibrillation was seen. Prior to VF, the electrical activity in each of the different channels was

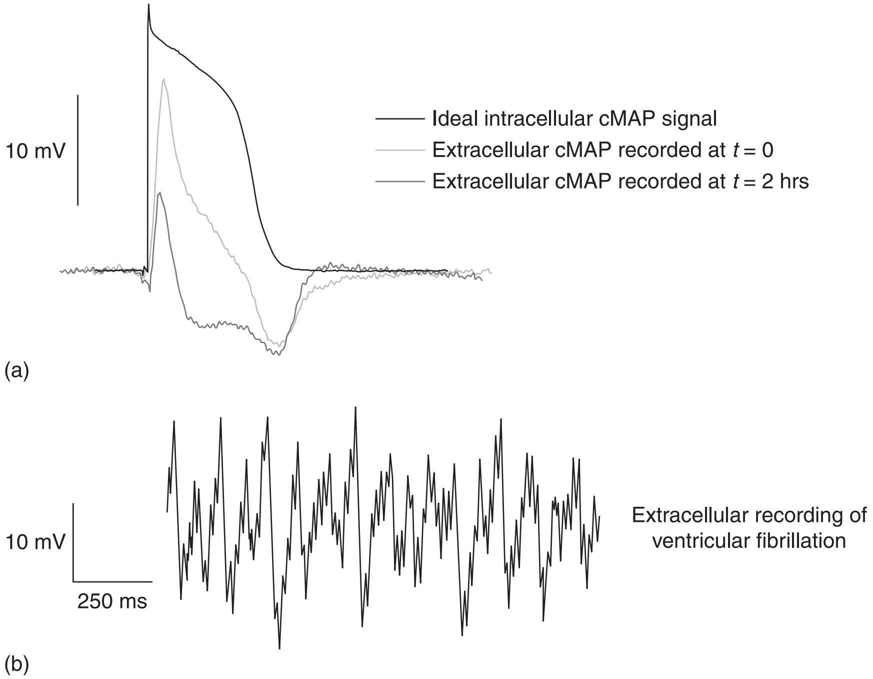

18.22 (a) cMAP signals. (b) Ventricular fibrillation.

regular and coordinated. When externally paced at higher than normal heart rate, ventricular tachycardia was observed exhibiting period-doubling bifurcations with alternans (alternating high-low-high action potential durations) and eventually leading to ventricular fibrillation (Luo and Rudy, 1991; Fig. 18.22b). After fibrillation has set in, higher-frequency components (compared with the pacing frequency) and multiple peaks are developed in the frequency spectrum. The difference in frequency characteristics could be used as a detection method to distinguish ventricular fibrillation from tachycardias.

18.9 Applications: microscale tissue metrology in testicular sperm extraction (TESE) surgery

Testicular failure affects approximately 1% of the male population and 10% of men who seek fertility evaluation. Men with testicular failure (non-obstructive azoospermia) show signs of severely impaired to non-existent sperm production (Silber, 2000; Foundation, 2010). Until recently, it was assumed that men with non-obstructive azoospermia were untreatable, and the only options offered to these couples to have children were the use of donor spermatozoa or adoption. Several clinically relevant findings have spotted the existence of sperm in men with non-obstructive azoospermia by direct evaluation of testis biopsy specimens. Testicular sperm extraction surgery and intracytoplasmic sperm injection (ICSI), as part of the in vitro fertilization (IVF) cycle, were first introduced in 1995 for the treatment of non-obstructive azoospermic men (Devroey *et al.*, 1995; Silber *et al.*, 1995b; Silber *et al.*, 1995a). The theoretical basis for attempting to retrieve spermatozoa for ICSI from the testes of men with apparent absence of spermatogenesis was based on early quantitative histological studies from testicle biopsies in fertile and infertile men (Zuckerman *et al.*, 1978; Silber and Rodriguez-Rigau, 1981) (Fig. 18.23). The technique of TESE-based ICSI was found to be successful in azoospermia in 60% of cases using only mature spermatids and spermatozoa (Silber *et al.*, 1995b; Silber *et al.*, 1996; Silber *et al.*, 1997). The spermatogenesis in such cases is seen to be diffuse rather than regional, thus resulting in a great deal of testicular damage, and sometimes even limiting successful patients to only one attempt (Schlegel *et al.*, 1997). Damage is sometimes minimized by using needle rather than open biopsy to obtain spermatozoa for ICSI (Craft *et al.*, 1997). However, control studies have shown that for difficult cases of non-obstructive azoospermia, where spermatogenesis is very meager, needle biopsy is much less likely to find the rare foci of spermatogenesis for ICSI than open biopsy (Friedler *et al.*, 1997). So far, there has been little effort to spatially map spermatogenesis in the testis of azoospermic men, despite large amounts of testicular tissue being often removed during biopsy (Silber *et al.*, 1996).

In order to reduce the amount of testicular tissue removed during TESE surgery, Schlegel (1999) performed microdissection TESE surgery, where the scarce foci of normal spermatogenesis could often be detected directly under the operating

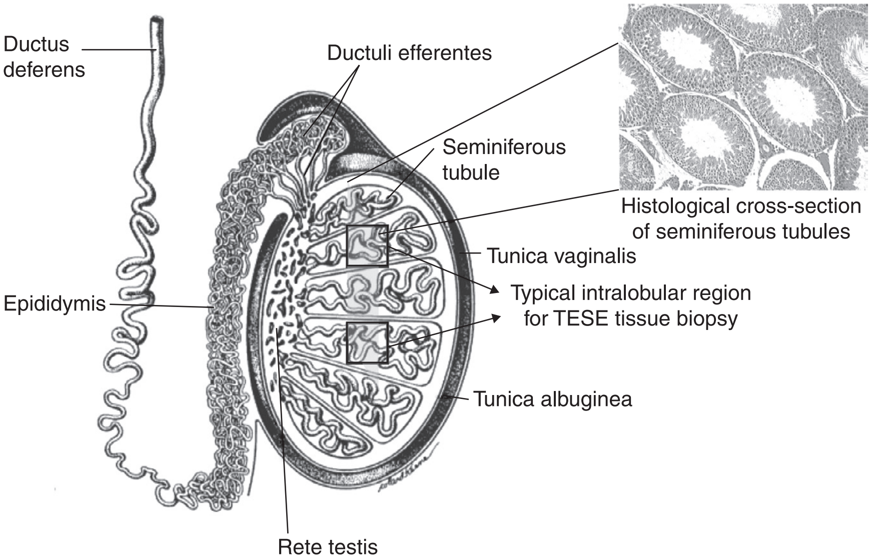
Ductus deferens
Ductuli efferentes
Seminiferous tubule
Histological cross-section of seminiferous tubules
Tunica vaginalis
Epididymis
Typical intralobular region for TESE tissue biopsy
Tunica albuginea
Rete testis

18.23 Anatomical sketch of a human testicle.

microscope and thereby, in some cases, only tiny portions of testicle needs to be removed. This highly invasive surgical procedure involves identifying seminiferous tubules carrying spermatozoa by visual examination of the infertile testis under a microscope, and biopsy of the region of interest is performed (Fig. 18.24). Tubules with low spermatogenesis have thinner walls and smaller diameter (≈100 µm) as compared with healthy tubules (≈ 200 µm). It has been observed that the larger sperm-producing tubules occupy only a fraction of the volume of the three-dimensional mass of tubules in the testis of an infertile male. Hence, dissection within the testis is necessary to search for healthy tubules embedded deep within the testis (Schlegel, 1999). A minimally invasive tool for identification of regions of interest below the two-dimensional field of view of the microscope during microdissection TESE surgery will help reduce the loss of a significant amount of tissue and can be used as a means to avoid vasculature in the testes. Information about the diameter and stiffness of the tubules in the depth direction without biopsy will help the surgeon make an informed decision about excision of tissue from a particular location with a high probability of locating tubules carrying spermatozoa.

In this section, tubule dimension measurement in rat testis tissue in vitro is presented, by insertion of silicon microprobes with integrated Wheatstone bridges formed by polysilicon strain gauges. By using the ultrasonic modality of the microprobe (Chen, 2006), the TESE surgery can be truly noninvasive by probing the organ from the outer surface, thus avoiding a large incision with a scalpel to examine the tissue. By way of modeling, expected tubule size measured by the microprobe is numerically simulated using the Monte Carlo method and

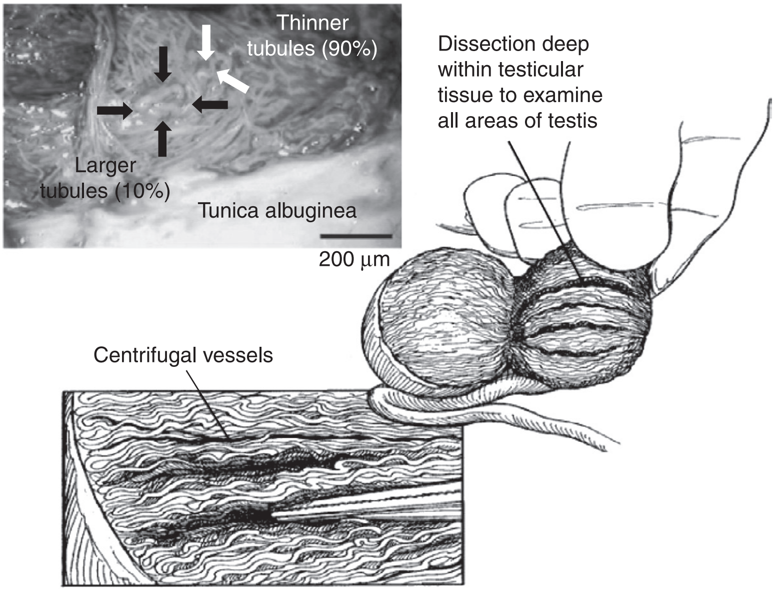

18.24 Microdissection TESE surgery showing the deep dissection of testicular tissue. Courtesy of Dr Peter N. Schlegel, Weill Cornell Medical College, New York, NY.

an analytical closed-form expression is derived for fitting the distribution of measured sizes.

18.9.1 Working principle

The silicon microprobes used are 4 mm long, 100 μm wide and 140 μm thick projecting outwards at the tip of the horn (Fig. 18.13). To monitor the force sensed by the microprobes when puncturing the walls of the tubules, a set of four polysilicon resistors forming a Wheatstone bridge incorporated on both the microprobes was used. The tip of the microprobe has two sharp blade-like edges – a V-shaped edge on the top formed by the LPCVD nitride film and one at the bottom formed by silicon due to the anisotropic backside-only KOH etch (Fig. 18.25). When the top blade (silicon nitride) on the microprobe encounters the tubules, the strain experienced by the sense polysilicon resistors positioned on the microprobe near its clamped edge is due to a combination of pure-axial and bending-based compression of the microprobe. This compressive puncture force experienced by the top blade is recorded in the Wheatstone bridge voltage as voltage spikes (Fig. 18.26). The bottom blade (silicon) when encountering tubules results in bending of the microprobe and, thus, in translating axial and tensile strain to the polysilicon resistors located on top of the device. From finite-element analysis, the force sensitivity of the bottom blade observed in the amplified

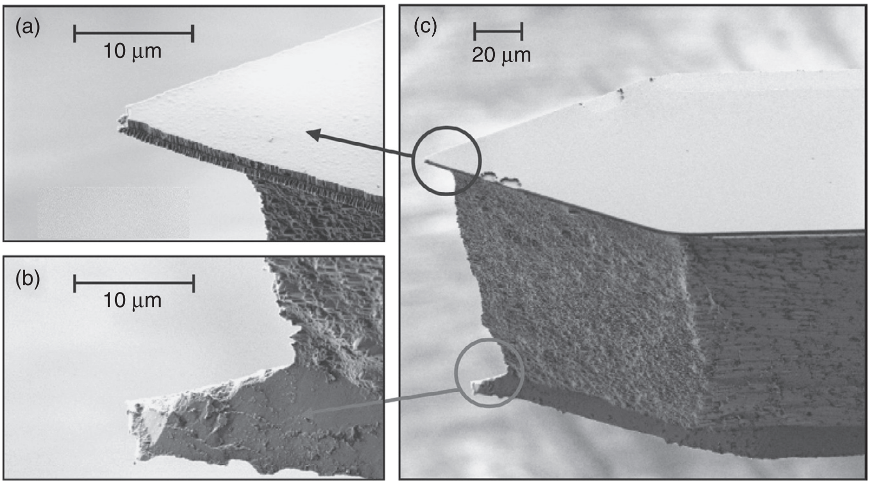
(a)
10 μm
(b)
10 μm
(c)
20 μm

18.25 SEM of a microprobe (c) showing sharp blade-like edges at the top (a) and bottom (b).

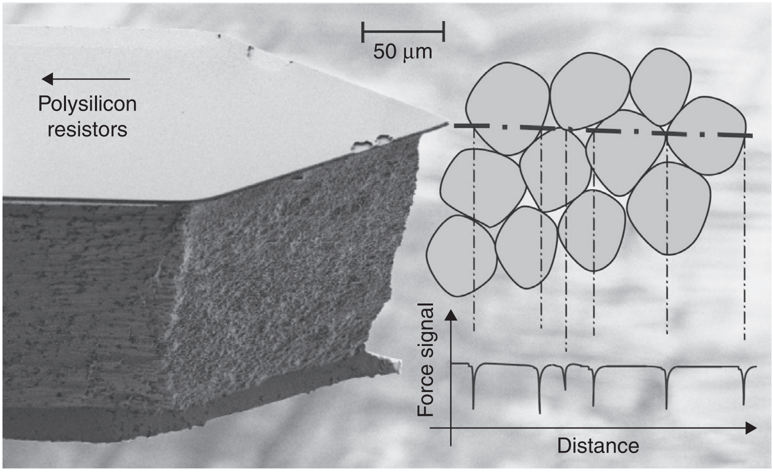
50 μm
Polysilicon resistors
Force signal
Distance

18.26 Compressive puncture force experienced by the top blade.

Wheatstone bridge voltage was estimated to be 0.81 V/N. The microprobes are inserted into the tissue using a micromanipulator with 0.2 μm precision (MP-285, Sutter Instruments, Inc.). The amplified Wheatstone bridge voltage is monitored, which gives an estimate of the forces encountered by the microprobes using the force sensitivity of the microprobes.

18.9.2 In vitro penetration experiments

The two microprobes were inserted in vitro to a depth of 2 mm into tissue excised from a healthy rat testis containing only seminiferous tubules at a velocity of 100 µm.s^{-1}. The bulk portion of the microprobe is intended to be thicker in order to be stiff enough to be used for penetrating the outer testicular muscle and connective tissue, and eventually reaching the seminiferous tubules. In addition, the thickness of the microprobe (140 µm) is chosen to be much larger than the diameter of the tubules in the tissue (≈ 50 µm) so that the top and bottom blades encounter different tubules, thus increasing the number of tubules sampled per microprobe. Once inside the tissue, the blades on the microprobe puncture the tubules, and the puncture signature in the force signal is observed to be a negative spike (compression) for the top nitride blade and a positive spike (tension) for the bottom silicon blade (Fig. 18.27). The puncture force can be calculated by measuring the magnitude of the spike due to the top nitride blade and dividing it by the estimated top-blade force sensitivity of the microprobe (−1.63 V/N). The range of voltage spike magnitudes in the Wheatstone bridge voltage suggests different kinds of punctures through tubules varying from maximum force when puncturing along the diameter of the tubule to minimum force when separating attached tubules.

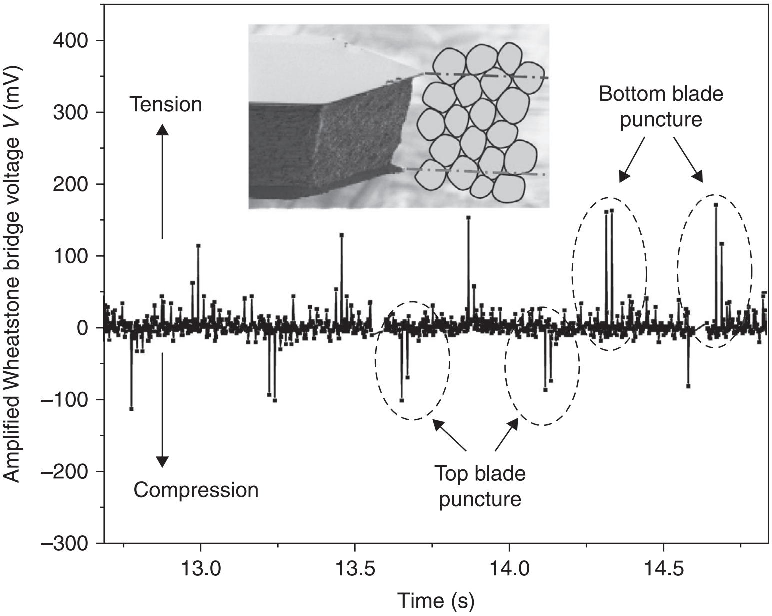

18.27 Puncture force for blades inside tissue measured by a strain gauge.

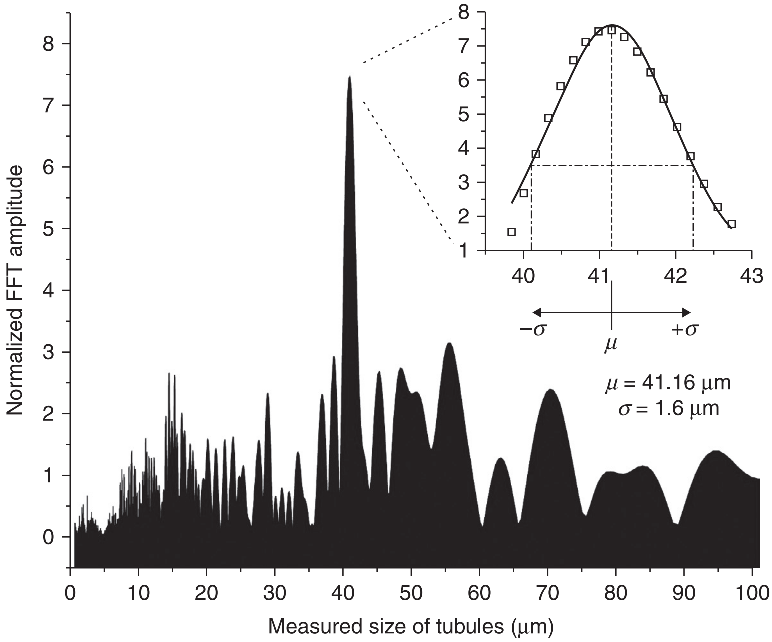

18.28 Normalized FFT amplitude vs. tubule size.

Since the orientation and position of the tubular axis with respect to the path of puncture are random, the size measured by the microprobes can vary from a fraction to more than twice the diameter of the tubule. This measured size is calculated by multiplying the speed of puncture (100 μm.s^{-1}) and the measured time between two consecutive puncture artifacts corresponding to the top nitride blade, since the tubules are densely packed wall-to-wall in the tissue. From the FFT (fast Fourier transform) of the positive and negative spike data, we observe the maximum occurrence of a size measured corresponding to 41.1 ± 1.6 μm (Fig. 18.28). This was close to the visually measured average tubule diameter (≈ 50 μm) in the tissue being probed. In order to detect the presence of tubules of two different diameters with different density of occurrence, it is crucial that we understand the distribution of sizes measured by the microprobe. Also, an analytical closed-form expression of the distribution of sizes (discussed in the next section) would help determine whether statistically significant sizes are measured corresponding to the two different diameters, thus checking for false positives.

18.9.3 Expected distribution of sizes measured using microprobe

Spermatogenesis occurs within a collection of U-shaped seminiferous tubules in the testis. The tubules are compartmentalized by connective tissue lobules in the testicular parenchyma. The tubules in each lobule are highly convoluted, closely packed, and start and end at the rete testis (Fig. 18.23), which serves as the reservoir for spermatozoa during ejaculation. If a constant volume of tissue is excised from the intralobular region at different locations of the testis (as in TESE surgery), the orientation of the tubules found in the excised tissue is expected to be completely random. When the microprobe is inserted into a volume of testicular tissue containing only seminiferous tubules at a constant velocity and a fixed direction, the penetration of tubules by the blades on the microprobes will be in a uniformly random orientation with respect to the local axis of the tubule and at a uniformly random distance away from the axis. Assuming constant velocity of insertion and high sample set of sizes measured, the distribution of frequency of occurrence of path lengths traversed by the blade inside the tubules (the sizes measured by the microprobe) is derived. Knowledge of the probability distribution of sizes measured by the microprobe when inserted into tissue is necessary to discern the existence of multiple populations of tubules with different diameters (in our case, thin and large diameters) in the testicular tissue being probed. The analytical expression for the probability distribution for a measured size, σ, and fixed tubular diameter, d, (Abhishek, 2010) is given by

$$f(\sigma)=\int_{\theta_0}^{\frac{\pi}{2}}\left(\sin\theta\cos\theta\left(\frac{8\sigma}{\pi d^2}\int_{\varphi_0}^{\frac{\pi}{2}}\sqrt{\frac{\left(1-(\sin\theta\sin\varphi)^2\right)^2}{1-\left(\frac{\sigma}{2}\right)^2\left(1-(\sin\theta\sin\varphi)^2\right)}}\cdot d\varphi\right)\right)\cdot d\theta \qquad [18.27]$$

$$\theta_0=0;\ \varphi_0=0 \quad \forall\sigma\le d;\ \theta_0=\arccos\left(\frac{2b}{\sigma}\right);\ \varphi_0=\arcsin\left(\frac{\sqrt{\sigma^2-(2b)^2}}{\sigma\sin\theta}\right) \quad \forall\sigma>d$$

where, assuming the tubule to be a randomly oriented right-circular cylinder, θ is defined as the angle made by the axis of the cylinder with the z-axis and φ is the angle made by the major axis of the cylinder's elliptical projection on the x-y plane. Monte Carlo simulations of sizes measured using the microprobe were done in MATLAB™ by assuming random orientation of tubules of diameter $d = 100\,\mu\text{m}$ and measuring the chord lengths made by the path of puncture of the microprobe. The generated chord lengths (σ) are binned, and a histogram predicting the frequency of occurrence of varied sizes measured is plotted (Fig. 18.29). The maximum frequency of occurrence was seen to be at $\sigma = d$, diameter of the tubules. The histogram is essentially a non-normalized version of the probability density function (PDF) of the chord length σ. The probability density function $f(\sigma)$ from Eq. 18.27 when scaled and plotted along with the histogram proved to be a good fit (Figure 18.29).

In the practical scenario, the surgeon needs to be able to detect the presence of larger diameter tubules embedded within a mass of thinner diameter tubules.

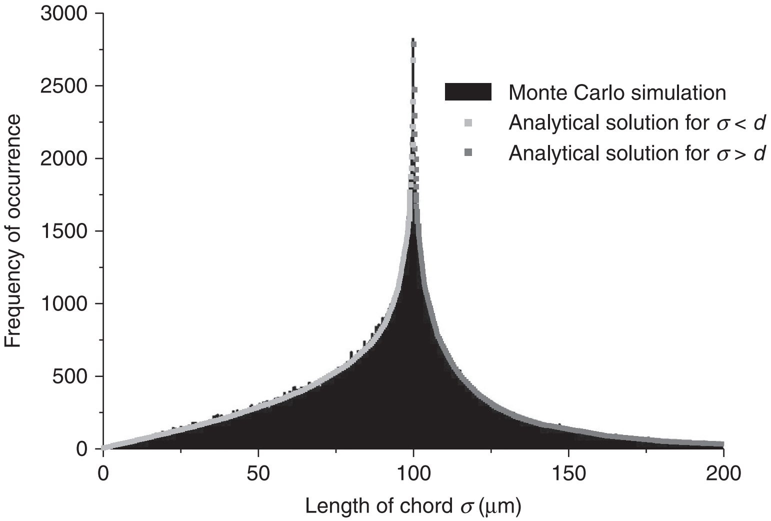

18.29 Monte Carlo simulation and analytical solutions of chord lengths for random orientation of tubules of diameter $d = 100\,\mu\text{m}$.

Knowledge about the probability distribution of measured sizes assuming an average diameter of tubules in the region of interest will help the surgeon detect the presence of larger fertile tubules embedded in the mass of thinner infertile tubules. Assuming a large set of sizes measured by probing multiple locations in a region of interest, if the tissue contains few larger tubules embedded in a mass of thinner tubules, then two peaks corresponding to the diameter of the thinner and larger tubules are expected when the measured sizes are binned. The peak for the thinner tubules is higher in magnitude than that of the larger tubules because of fewer large tubules. Two Monte Carlo simulations were performed with two different diameters, $d_S = 100$ and $d_L = 200\,\mu\text{m}$, and the resulting chord lengths were plotted in a single histogram in Fig. 18.30. The frequency of occurrence of size equal to $d_L = 200\,\text{m}$ was intentionally adjusted to be only a fraction of that of $d_S = 100\,\mu\text{m}$ for purely illustrational purposes. If the observed frequency of occurrence at measured size equal to the larger tubule diameter (i.e. $\sigma = d_L$) is greater than the value calculated by using the scaled analytical expression of the probability distribution function in Eq. 18.27 corresponding to the thinner tubule diameter (i.e. $f(d_S, \sigma = d_L)$), then the presence of larger tubules in the tissue is confirmed (Fig. 18.30). Thus, by sufficient sampling of tubules by the microprobe in a given region of interest, the surgeon can identify the presence of healthy tubules by using the analytical expression for the probability density of occurrence of measured sizes. To further validate the presence of larger tubules, the analytical expression in Eq. 18.27 for probability distribution of measured sizes corresponding to thinner and larger tubules (i.e. $f(d_S, \sigma) + f(d_L, \sigma)$) can be used to fit the frequency of occurrence of measured sizes.

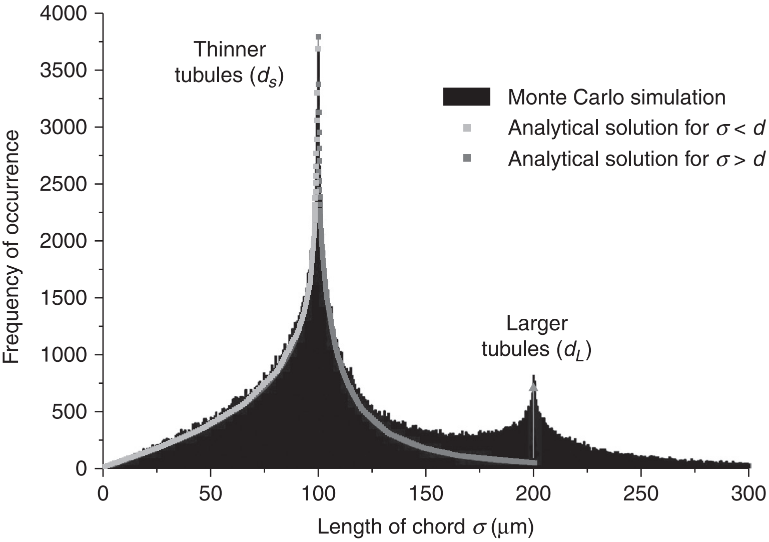

18.30 Monte Carlo simulations and analytical solutions of chord lengths for $d_S = 100$ and $d_L = 200\,\mu\text{m}$.

18.10 Conclusions

Silicon's high power output density, S_mc, low acoustic loss, and high thermal conductivity make it an ideal material for power silicon ultrasonic actuators. Also, its micromachinability allows various shapes to be formed, allowing complex designs with high efficiency. Batch processing and low material cost open doors for inexpensive power ultrasonic actuators. Silicon ultrasonic horn-shaped actuators help concentrate energy at the tip of the transducer, achieving high amplitude and efficiency due to silicon's superior material and mechanical properties. Microfabricated silicon horn-based surgical microprobes have been developed to reduce penetration force into biological tissues by actuating the surgical tool at its ultrasonic resonance. Silicon serves as an ideal platform for integration of a variety of microfabricated sensors on the surgical tools to monitor tissue activity. In this chapter, two sensors integrated on the microprobes were discussed, namely platinum electrodes and piezoresistive polysilicon strain gauge sensors. The use of these microprobes in biomedical applications was explored including ultrasonically actuated microprobes with platinum electrodes for cardiac signal recording, and ultrasonically actuated microprobes with strain sensors for a testicular tubule-size assay. These microprobes with platinum electrodes can potentially help provide a 3D map of the electrophysiological activity (wave propagation) in the heart, which may lead to the understanding of cardiac arrhythmias, as well as the prevention and cure of the disease. A testicular tubule-size assay is also demonstrated by monitoring the strain signal output recorded during insertion of the microprobe in rat testis tissue to estimate the average diameter of the seminiferous tubules. This information is important for the surgeon to distinguish between tubules with (larger diameter) and without (smaller diameter) fertile sperm during microdissection TESE surgery, thus enabling a microprobe-based assay for sperm viability. This technique is effectively a new biomedical imaging technique that can be used to image physical characteristics of tissue non-invasively. This can prove to be an invaluable tool during surgery for intelligent tissue biopsy by identifying specific regions of the tissue that exhibit detectable physical characteristics (stiffness, temperature, etc.).

18.11 References

Abhishek, R. (2010) *Micromachined Ultrasonic Silicon Horn Actuators for Biomedical Applications: Surgical tools, Cardiac Electrophysiological Recordings, Testicular Tubule-size Detection and Fluid Viscosity Measurement*. PhD, Cornell University.

AHA (2005) *Heart disease and stroke statistics* [Online]. Available: http://www.americanheart.org/presenter.jhtml?identifier=3000090.

Allessie, M.A., Bonke, F.I.M. and Schopman, F.J.C. (1973) Circus movement in a rabbit atrial muscle as a mechanism of tachycardia. *Circulation Research*, 33, 54–77.

Bitkashev, V.N., Holden, A.V., Mironov, S.F., Pertsov, A.M. and Zaitsev, A.V. (1999) Three-dimensional aspects of re-entry in experimental and numerical models of ventricular fibrillation. *International Journal of Bifurcation and Chaos*, 9, 695–704.

Bard, A.J. and Faulkner, L.R. (2001) *Electrochemical Methods*, New York, NY, John Wiley & Sons, Inc.

Bockris, J.O. and Reddy, A.K.N. (1970) *Modern Electrochemistry*, New York, NY, Plenum.

Bommanan, D. (1992) *Enhancement of Transdermal Drug Delivery: Mechanisms and Methodologies*. PhD, University of California Berkeley.

Bonometti, C., C. H., Hough, D., Lee, J.J., Fishbein, M.C., Karagueuzian, H.S., Chen, P.S. (1995) Interaction between strong electrical stimulation and re-entrant wavefronts in canine ventricular fibrillation. *Circulation Research*, 77, 407–16.

Bower, J.M. and Kovacs, G.T.A. (1997) Plasma-etched neural probes. *Sensors and Actuators A: Physical*, 58, 27–35.

Caldwell, B.J., B. S. H., Legrice, I.J., Hooks, D.A., Tai, D.C.S., Pullan, A.J. and Smaill, B. (2005) Intramural measurement of transmembrane potential in the isolated pig heart: validation of a novel technique. *Journal of Cardiovascular Electrophysiology*, 16, 1001–10.

Chen, J., Mandapati, R., Berefeld, O., Skanes, A.C. and Jalife, J. (2000) High-frequency periodic sources underlie ventricular fibrillation in the isolated rabbit heart. *Circulation Research*, 86, 86–93.

Chen, P.S., Wolf, P.D., Dixon, E.G., Danieley, N.D., Smith, D.W. and Idker, R.E. (1988) Mechanism of ventricular vulnerability to single premature stimuli in open chest dogs. *Circulation Research*, 62, 1191–209.

Chen, X. (2006) *Micromachined Ultrasonic Actuators for Biomedical Applications: Surgical Tools, Cardiac Microprobes, and Microfluidic Actuation*. PhD, Cornell University.

Chen, X., Lal, A., Riccio, R.F. and Gilmour, J.R. (2006) Ultrasonically actuated silicon microprobes for cardiac signal recording. *IEEE Transactions on Biomedical Engineering*, 53, 1665–71.

Craft, I., Tsirigotis, M., Courtauld, E. and Farrer-Brown, G. (1997) Testicular needle aspiration as an alternative to biopsy for the assessment of spermatogenesis. *Human Reproduction*, 12, 1483–7.

Davidenko, J.M., Pertsov, A.M., Salomonsz, R., Baxter, W. and Jalife, J. (1992) Stationary and drifting spiral waves of excitation in isolated cardiac muscle. *Nature*, 355, 349–51.

Devroey, P., Silber, S.J. and Nagy, Z. (1995) Ongoing pregnancies and birth after intracytoplasmic sperm injection (ICSI) with frozen-thawed epididymal spermatozoa. *Human Reproduction*, 10, 903–6.

Dimaio, S.P. and Sacudean, S.E. (2002) Needle insertion modelling and simulation. *IEEE International Conference on Robotics and Automation*, 2098–105.

Efimov, I.R., Sidorov, V., Cheng, Y. and Wollenzier, B. (1999) Evidence of 3d scroll waves with ribbon-shaped filament as a mechanism of ventricular tachycardia in the isolated rabbit heart. *Journal of Cardiovascular Electrophysiology*, 10, 1452–62.

Eisner, E. (1967) Complete solutions of the Webster horn equation. *Journal of Acoustic Society of America*, 32, 1126–46.

Ensell, G., Banks, D., Ewins, D., Balachandran, W. and Richards, P. (1996) Silicon-based microelectrodes for neurophysiology fabricated using a gold metallization/nitride passivation system. *IEEE Journal of Micromechanical Systems*, 5, 117–21.

Ericson, F. (1990) Micromechanical fracture strength of silicon. *Journal of Applied Physics*, 68, 5840–4.

Foundation, J.B.B. (2010) *Male infertility: Sperm retrieval techniques* [Online]. Department of Urology, Cornell Weill Medical College. Available: http://www.cornellurology.com/infertility/srt/azoospermia.shtml.

Friedler, S., Razid, A. and Strassburger, D. (1997) Testicular sperm retrieval by percutaneous ve needle sperm aspiration compared with testicular sperm extraction by open biopsy in men with non-obstructive azoospermia. *Human Reproduction*, 12, 1488–91.

Frizell, L. (1996) *Therapeutic Ultrasound*. Short course at the IEEE Ultrasonic Symposium, San Antonio, USA.

Geddes, L.A. (1997) Historical evolution of circuit models for the electrode-electrolyte interface. *Annals of Biomedical Engineering*, 25, 1–14.

Grahame, D.C. (1952) Mathematical theory of the faradaic admittance. *Journal of Electrochemical Society*, 99, 370C–85C.

Heuter, T.F. and Bolt, R.H. (1955) *Sonics: Techniques for the Use of Sound and Ultrasound in Engineering and Science*, New York, NY, John Wiley & Sons, Inc.

Kewley, D.T., Hills, M.D., Borkholder, D.A., Opris, I.E., Maluf, N.I., Stormemnt, C.W. and Kovacs, G.T.A. (1988) *Enabling technologies for cultured neural networks*, London, Academic Press.

Lal, A. (1996) *Micromachined Silicon Ultrasonic Longitudinal-Mode Actuators: Theory and Applications to Surgery, Pumping, and Atomization*. PhD, University of California Berkeley.

Lee, C.A.L. (2001) Silicon ultrasonic horns for thin film accelerated stress testing. *IEEE Ultrasonic Symposium*, pp. 867–70.

Luo, C.H. and Rudy, Y. (1991) A model of the ventricular cardiac action potential, depolarization, repolarization, and their interaction. *Circulation Research*, 68, 1501–26.

McAdams, E.T. and Jossinet, J. (1994) Physical interpretation of Schwan's limit voltage of linearity. *Medical and Biological Engineering and Computing*, 32, 126–30.

Menciassi, A., Eisinberg, A., Scalari, G., Anticoli, C., Carrozza, M.C. and Dario, P. (2001) Force feedback-based microinstrument for measuring tissue properties and pulse in microsurgery. *IEEE International Conference on Robotics and Automation*, 2001 Seoul, Korea 626–31.

Mitragotri, S., Blankschtein, D. and Langer, R. (1995) Ultrasound-mediated transdermal protein delivery. *Science*, 269, 850–3.

Nabibekov, M.K., Plyushchenkov, B.D. and Sarikisov, I.Y.U. (1980a) Study of ultrasonic cutting of soft biotissues. *Mekhanika Komozitnykh Materialov (Mechanics of Composite Materials)*, 3, 519–24.

Nabibekov, M.K., Plyushchenkov, B.D. and Sarkisov, I.Y.U. (1980b) Methods for raising the efficiency of the ultrasonic cutting of soft biological tissues. *Mechanics of Composite Materials*, 16, 488–91.

Naja, K., Wise, K.D. and Mochizuki, T. (1985) A high-yield ic-compatible multi-channel recording array. *IEEE Transactions on Electron Devices*, 32, 1206–11.

Najafi, K. and Wise, K.D. (1986) A high-yield ic-compatible multi-channel recording array. *IEEE Journal of Solid-State Circuits*, 21, 1035–44.

Neppiras, E.A. (1960) Very high energy ultrasonics. *British Journal of Applied Physics*, 11, 143–50.

Obermier, E., Kopystynski, P. and Niebl, R. (1986) Characteristics of polysilicon layers and their application in sensors. *IEEE Solid-State Sensors Workshop*, 19–35.

Okamura, A.M., Simone, C., and O'Leary M.D. (2004) Force modeling for needle insertion into soft tissue. *IEEE Transactions on Biomedical Engineering*, 51, 1707–16.

Peterson, K. (1982) Silicon as a mechanical material. *Proceedings of the IEEE*, 70, 420–57.

Pressler, M.L., Munster, P.N. and Huang, X.D. (1995) *Gap Junction Distribution in the Heart: Functional Relevance*, Philadelphia, PA, W.B. Saunders Company.

Schlegel, P.N. (1999) Testicular sperm extraction: microdissection improves sperm yield with minimal tissue excision. *Human Reproduction*, 14, 131–5.

Schlegel, P.N., Palermo, G.D. and Goldstein, M. (1997) Testicular sperm extraction with intracytoplasmic sperm injection for non-obstructive azoospermia. *Urology*, 49, 435–40.

Silber, S.J. and Rodriguez-Rigau, L.J. (1981) Quantitative analysis of testicle biopsy: determination of partial obstruction and prediction of sperm count after surgery for obstruction. *Fertility and Sterility*, 36, 480–5.

Silber, S.J. (2000) Microsurgical TESE and the distribution of spermatogenesis in non-obstructive azoospermia. *Human Reproduction*, 15, 2278–84.

Silber, S.J. Van Steirteghem, A.C. and Devroey, P. (1995a) Sertoli cell only revisited. *Human Reproduction*, 10, 1031–2.

Silber, S.J., Nagy, Z. and Devroey, P. (1997) Distribution of spermatogenesis in the testicles of azoospermic men: The presence or absence of spermatids in the testes of men with germinal failure. *Human Reproduction*, 12, 2422–8.

Silber, S.J. Nagy, Z.P. and Liu, J. (1995b) The use of epididymal and testicular spermatozoa for intracytoplasmic sperm injection: The genetic implications for male infertility. *Human Reproduction*, 10, 2031–43.

Silber, S.J., Liu, J. and Steirteghem, A.C.V. (1996) Normal pregnancies resulting from testicular sperm extraction and intracytoplasmic sperm injection for azoospermia due to maturation arrest. *Fertility and Sterility*, 66, 110–17.

Son, I.S. and Lal, A. (2000) *A multifunctional silicon-based micro scale surgical system*. Solid-State Sensor, Actuator and Microsystems Workshop, Hilton Head, South Carolina, USA.

Suslick, K.S. (1988) *Ultrasound – Its Chemical, Physical and Biological Effects*, New York, NY, VCH Publishers.

Tautz, J., Roces, F. and Holldobler, B. (1995) Use of a sound-based vibratome by leaf-cutting ants. *Science*, 267, 84–7.

Tsai, S., Song, Y., Tseng, T., Chou, Y., Chen, W. and Tsai, C. (2004) High-frequency, silicon-based ultrasonic nozzles using multiple Fourier horns. *IEEE Transactions on Ultrasonics, Ferroelectricity and Frequency Control*, 51, 277–85.

Winfree, A.T. (1994) Electrical turbulence in three-dimensional heart muscle. *Science*, 266, 1003–6.

Witkowski, F.X., Leon, L.J., Penkoske, P.A., Giles, W.R., Spano, M.L., Ditto, W.L. and Winfree, A.T. (1998) Spatiotemporal evolution of ventricular fibrillation. *Nature*, 392, 78–82.

Yamada, H. and Evans, F.G. (1970) *Strength of Biological Materials*, Baltimore, MD, The Williams and Wilkins Company.

Yoon, T.H., Hwang, E.J., Shin, D.Y., Park, S.I., Oh, S.J. and Jung, S.C. (2000) A micromachined silicon depth probe for multichannel neural recording. *IEEE Transactions on Biomedical Engineering*, 47, 1082–7.

Zuckerman, Z., Rodriguez-Rigau, L.J. and Weiss, D.B. (1978) Quantitative analysis of the seminiferous epithelium in human testicle biopsies and the relation of spermatogenesis to sperm density. *Fertility and Sterility*, 30, 448–55.

19

Piezoelectric and fibre-optic hydrophones

A. HURRELL, Precision Acoustics Ltd, UK and P. BEARD,
University College London, UK

Abstract: This chapter considers the many different types of hydrophone – both piezoelectric and fibre-optic. It begins with a presentation of the functional qualities common to all device types. As each design of hydrophone is introduced, its performance in terms of these general characteristics is assessed. Although the organisation of the chapter introduces piezoelectric hydrophones separately from their fibre-optic counterparts, there are many similarities between the two classes, and these are identified and considered throughout. Whilst piezoelectric hydrophones have been available for decades and have thus gained widespread acceptance in ultrasound metrology, fibre-optic hydrophones are a relatively recent development. Consequently, the consideration of such devices is given specific emphasis in order to shed further light on this rapidly developing field of study.

Key words: ultrasound, metrology, hydrophone, piezoelectric, fibre-optic.

19.1 Introduction

The word hydrophone derives from 'hydro' – of, or pertaining to, water – and 'phone' – of, or pertaining to, sound. As such, a hydrophone is simply a device for measuring sound in water – an underwater microphone. In ultrasonics the term 'hydrophone' is commonly used to describe a device that is purely a receiver of ultrasound. Compare this with the more general term 'transducer', which implies that a device has some transmit capability, be that as a pure transmitter or in a transmit/receive application. Hydrophones fall into two broad categories: piezoelectric and fibre-optic.

Piezoelectric hydrophones have been available for a number of decades. In fact, ultrasonic metrology has become sufficiently established that a range of international standards (IEC, 2007a, 2007b, 2007c) define the properties, calibration and measurement application of hydrophones. In comparison, fibre-optic hydrophones have only become widely available within the last decade. These devices have some unique and fascinating properties that provide an expanded range of measurement opportunities, above and beyond their piezoelectric counterparts. Fortunately, the similarities between the two device types ensure that ultrasonic measurement methods developed for piezoelectric hydrophones are often equally applicable for fibre-optic devices. In fact, at an initial level, piezoelectric and fibre-optic are entirely interchangeable, and it thus comes down to secondary considerations as to which device type is preferable in any given measurement scenario.

This chapter begins with a description of properties and characteristics that are common to both hydrophone types. Then an outline of common piezoelectric hydrophone types, along with an overview of the characteristics of each type, is presented. It should be noted that the vast majority of hydrophones in use worldwide are piezoelectric in nature. Consequently the literature related to the construction, characterisation and application of piezoelectric hydrophones is extensive (Harris, 1988, 2005; Harris and Shombert, 2005; IEC, 2007a; NEMA, 2004; Robinson *et al.*, 2000). For this reason their description within this chapter is kept deliberately brief to avoid repetition. In contrast, fibre-optic hydrophone use is currently much less widespread. As a result, the behaviour of these devices is less widely known, and in some cases misunderstood. The third part of this chapter seeks to provide an extensive and comprehensive review of fibre-optic hydrophone technology, containing a detailed examination of many of the intrinsic and extrinsic sensing methodologies.

19.2 General hydrophone considerations

The fundamental concern of anyone undertaking hydrophone measurements is 'Will I be able to measure anything?' Only once this question has a positive response can the researcher proceed to the more complex issue of 'Is my hydrophone signal a faithful representation of the acoustic pressure wave that is present?' This section gives a general overview of the issues that need to be considered when answering these two questions.

19.2.1 Sensitivity and dynamic range

The relationship between a hydrophone's voltage response, V, and the acoustic pressure it experiences, p, is called the hydrophone sensitivity, M, given by

$$E = -gT + \frac{D}{\varepsilon^T} \qquad \text{and} \qquad S = s^D T + gD \qquad [19.1]$$

Note that all three terms within Eq. 19.1 may be functions of other variables (to be discussed later). The hydrophone sensitivity is routinely determined via the process of hydrophone calibration. Generally (although not for some fibre-optic devices), hydrophone sensitivity is proportional to the area of the active element; however, a larger hydrophone will have a more directional response and cause more spatial averaging.

Minimum (noise equivalent) acoustic signal

All electrical systems have some level of inherent noise. The noise figure for any given hydrophone system could be expressed in terms of an electrical noise measurement. However, a hydrophone system is providing an acousto-electrical transduction and thus the minimum acoustic signal that can be measured is of more relevance. This can be conveniently achieved by considering the noise equivalent pressure (NEP), which is the acoustic pressure that provides an SNR of unity. This quantity is insensitive to the details of the transduction method (i.e. piezoelectric or fibre-optic) and has the added advantage of implicitly incorporating any gain/attenuation included within the system.

NEP is inherently related to sensitivity of a hydrophone, as well as the noise floor of the data acquisition (DAQ) system used to record the hydrophone's output signal. Consider an idealised hydrophone with a uniform sensitivity of 100 mV/MPa at all frequencies. Furthermore, let the bandwidth of the measurement system be 100 MHz and let the noise level of the hydrophone system be 50 μV rms over this bandwidth. The system thus has an NEP of

$$\frac{50\ \mu\text{V}}{100\ \text{mV/MPa}} = 0.5 \times 10^{-3}\,\text{MPa} = 500\ \text{Pa rms.}$$

Two slight complications arise from this initial, simplistic example. Firstly, the majority of DAQ systems currently in use are unable to quantify signals much smaller than 0.5 mV. Consequently the practical NEP of a hydrophone system connected to such a DAQ device would be at least an order of magnitude worse due to the inherent noise floor. As such, it is important for a hydrophone user to consider the difference between theoretically and practically achievable NEP, given the limitations of the DAQ they may be using.

Secondly, the example above assumed hydrophone sensitivity was independent of frequency. As will be discussed in some detail within Section 19.2.2 and elsewhere within this chapter, hydrophones have a frequency-dependent sensitivity. Ideally a spectral method of noise assessment capable of incorporating this frequency dependence should be used when assessing NEP. However, for many practical applications this added complexity is avoided by assuming a nominal hydrophone sensitivity across the bandwidth of interest.

Maximum acoustic signal

Dynamic range maxima commonly comprise two separate limits: the signal level at which there is no longer a linear relationship between voltage and acoustic pressure, and the signal level at which the hydrophone undergoes some form of damage mechanism. Linearity limits often arise from overload conditions at the input of stages of (pre)amplifiers or detectors (e.g. photodiodes) within the hydrophone system. The precise nature of the limit is likely to be system specific. In the case of an input signal's amplitude exceeding the supply voltage for an amplifier, this will probably manifest itself as 'hard' clipping with a flattening of the waveform at the maximum and/or minimum voltage excursions. In contrast, detector overloads often exhibit 'soft' clipping where there is a progressive deviation from linearity between input and output as signal magnitude increases.

Whilst these limitations compromise measurement integrity, they can often be addressed by addition of some suitable attenuation to the system, and are unlikely to result in irreversible degradation of the hydrophone system.

Damage thresholds need more careful consideration due to the possibility of permanent and irreversible impairment of a hydrophone's performance. Furthermore, damage thresholds may also be acoustic quantity specific. To illustrate this, consider therapeutic ultrasound, a specialism that contains many examples of acoustic fields that are specifically designed to be destructive. Lithotripsy uses very high pressure amplitude, short duration pulses to break down stones within the body (e.g. kidney, liver, gall stones). These waveforms contain a long rarefactional phase that could 'pull' the hydrophone active element away from the rest of the device. Additionally, any gas emboli within the liquid could cavitate near the active element of the hydrophone, thereby damaging it. These cases illustrate mechanical damage mechanisms, and maximum compressional and tensional pressures require consideration.

High Intensity Focussed Ultrasound (HIFU) and High Intensity Therapeutic Ultrasound (HITU) exploit much lower acoustic pressures than lithotripsy, but with often quasi-continuous signals. These fields can result in significant deposition of heat (potentially accompanied by cavitation). Here, a thermal mechanism could easily deform or damage the hydrophone active element (for example, thermal depolarisation of piezoelectric devices). Consequently an acoustic intensity threshold for damage should be considered alongside the potential for cavitation damage.

19.2.2 Frequency response

As described by Eq. 19.1, a hydrophone provides an output voltage in response to an incident acoustic pressure wave. For a simple harmonic oscillation, this sensitivity can be determined by placing a hydrophone in a known amplitude acoustic pressure field and recording its voltage. Fourier analysis techniques show that any waveform can be decomposed into a series of different frequency sinusoids, each of which has its own magnitude and phase. A temporally localised acoustic signal may therefore contain a wide range of frequencies and it then becomes important to consider whether the hydrophone's sensitivity is frequency dependent.

The first refinement of Eq. 19.1 is to allow all variables to be a function of frequency, f, thus

$$M(f) = \frac{V(f)}{p(f)}. \qquad [19.2]$$

This alteration raises the issue of how the frequency dependent sensitivity data can be incorporated into the voltage-to-pressure conversion. IEC (2007a) recommends two possible approaches. If the bandwidth of the acoustic signal is narrow, or the hydrophone exhibits minimal sensitivity variation about the acoustic working frequency (f_{awf}), then it can be assumed that the sensitivity is constant. Therefore the narrowband approximation of acoustic pressure is

$$p(t) = \frac{V(t)}{M(f_{awf})}. \qquad [19.3]$$

If this narrowband approximation is inappropriate, then a frequency domain deconvolution can be used to conduct the voltage-to-pressure conversion, thus

$$p(t) = \Im^{-1}\left\{\frac{\Im\{V(t)\}}{M(f)}\right\} \qquad [19.4]$$

where $\Im$ and $\Im^{-1}$ denote the Fourier and Inverse Fourier transforms respectively, and $M(f)$ is the frequency dependent hydrophone sensitivity. Commonly $M(f)$ is available as magnitude only data, and thus it may not be possible to correct for frequency dependent phase changes introduced by the hydrophone.

Phase variations do not alter the energy contained within a waveform; they merely change the waveform shape by time shifting the arrival of the various Fourier components. Consequently a magnitude only deconvolution will yield an accurate estimate of acoustic intensity parameters (which are phase insensitive). Acoustic output parameters that are based upon temporal waveform shape will be no worse an approximation with Eq. 19.4 than they are with Eq. 19.3. However, if the hydrophone has been calibrated in a phase-sensitive manner then the complex-valued sensitivity data should be used to ensure an accurate temporal representation of the acoustic signal.

19.2.3 Directional response

Hydrophone sensitivity is also a function of the angle of orientation between the acoustic axis of the hydrophone and the direction of propagation of the incident ultrasonic wave. Therefore Eq. 19.2 becomes

$$M(f,\theta) = \frac{V(f,\theta)}{p(f,\theta)} \qquad [19.5]$$

where θ is the angle of incidence. It is immediately obvious from Eq. 19.5 that hydrophone response could be represented as a surface in frequency-angle space. This dependence was deliberately exploited by Harris and Shombert (1985) in their method to characterise the directional response of hydrophones. A 3D graphical representation of a hydrophone response surface is shown in Fig. 19.1. Ideally the frequency dependent directional response should be measured for every hydrophone. In the absence of directly measured data, an analytic expression for directivity may be an acceptable alternative. Hydrophone active elements are commonly assumed to be represented by the well-known 'circular plane piston in a rigid baffle' model. A single integral formulation of this model is provided by

Archer-Hall and Gee (1980). In the far field of a circular plane piston the directional variation of the pressure field, $D(\theta)$, can be approximated as

$$D(\theta)=\frac{2J_1(ka\sin(\theta))}{ka\sin(\theta)} \qquad [19.6]$$

where k is the wavenumber and a is the radius of the circular piston.

It is important to state that the derivation of Eq. 19.6 is based upon a number of assumptions that may be irrelevant, or in some cases erroneous, in the context of a specific hydrophone. The most troubling aspect is the assumption of the circular element being in a rigid baffle of infinite extent. As will be seen later, many hydrophones are deliberately small to minimise their scattering cross-section, and this rigid baffle assumption (particularly at lower frequencies where wavelength is long) looks open to challenge. Some early work by Shombert *et al.* (1982) measured the directional response of a number of different hydrophones, and found that other analytical models involving soft- or un-baffled circular elements may be equally as valid. For certain types of hydrophones (e.g. membrane hydrophones – see Section 19.3.3) there may also be well-understood constructional reasons for which Eq. 19.6 is inappropriate. For this reason, care should be taken when comparing experimental directivities with Eq. 19.6.

The importance of considering directivity before undertaking hydrophone measurements is clearly displayed in Fig. 19.1. At low frequencies (< 3 MHz), a hydrophone placed perpendicular to the incident waveform would experience at most a 6–8 dB reduction in signal relative to a perfectly aligned device. However, multiple, well-defined minima appear in the directional response as frequency

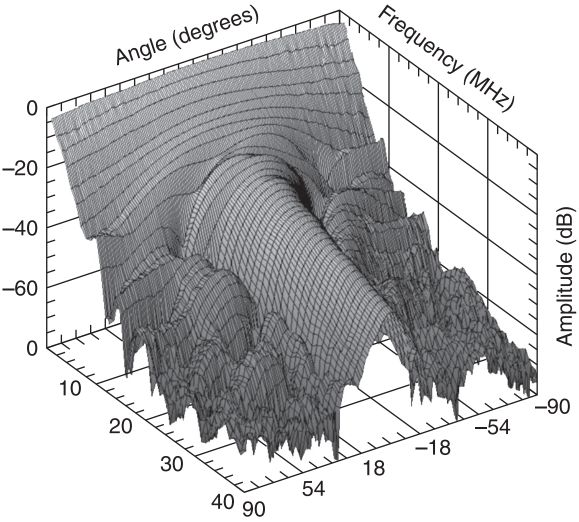

19.1 3D graphical representation of a hydrophone response surface.

increases. At 15 MHz a misalignment of only 15° coincides with a minimum and very little signal would be recorded by the hydrophone.

19.2.4 Spatial averaging

When a hydrophone is scanned through an acoustic field, the measured beam profile will be the convolution of the true acoustic pressure distribution with the hydrophone aperture. If the hydrophone is large relative to the spatial variation of the acoustic field, the spatial peak will be inaccurately resolved and its peak amplitude will be underestimated whilst beam-width becomes overestimated. This effect, known as spatial averaging, is illustrated in Fig. 19.2.

Note that this graph represents a one-dimensional problem only, whereas hydrophone spatial averaging is a two-dimensional effect. Moreover, the convolutional nature of spatial averaging means that changes to shape/dimension of the aperture of the sensor and/or the source distribution will yield different results. Thus, whilst the results displayed in Fig. 19.2 provide an indication of overall trends, they are not generally applicable to any specific measurement geometry.

For all three configurations shown in Fig. 19.2, the integrated signal amplitude is the same. The smallest sensor provides a reasonable estimation of the source distribution with error in both peak amplitude and full width at half maximum (FWHM) being approximately 10%. However, the pressure profile derived from the largest sensor contains gross errors, with the peak amplitude being less than half of its true value and the FWHM being more than double that of the source

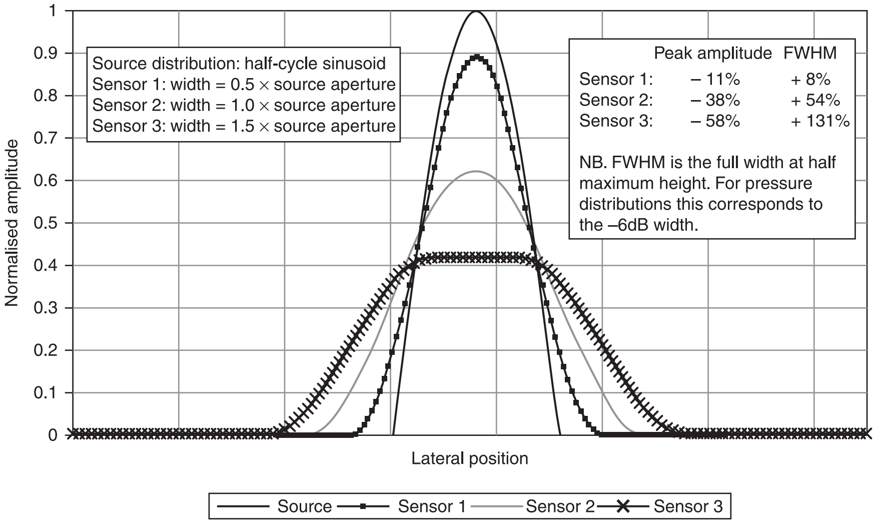

19.2 The effect of spatial averaging on measured beam profile.

distribution. In this case, the user may be oblivious to the spatial averaging, since the erroneously large FWHM would imply the field much broader than the sensor used to measure it.

One simple method of resolving this impasse is to apply a spatial equivalent of the Nyquist–Shannon sampling. By requiring that a sensor's dimension is no greater than half the smallest wavelength present in the field, spatial averaging should be avoided for most cases. A more rigorous approach has been proposed by Radulescu *et al.* (2004), who used a mathematical model to simulate the hydrophone's spatial response and thus derive the necessary spatial averaging corrections. These authors then applied their correction algorithm to clinically relevant acoustic fields measured with a range of hydrophones. They successfully demonstrated the validity of their method and were able to correct for spatial averaging to achieve consistent results with all hydrophones. These problems become even more complicated when attempting to quantify high amplitude acoustic waveforms. Once ultrasonic propagation becomes non-linear there will be significant harmonic generation. As such, the spectrum of the acoustic signal at some distance away from the source may contain much higher frequency (and hence shorter wavelength) features than it did when it was generated. Cooling *et al.* (2011) proposed a method based upon a numerical solution of the non-linear KZK equation to quantify the spatial averaging factor as a function of frequency, hydrophone diameter and pressure amplitude.

19.3 Piezoelectric hydrophones

Piezoelectricity, first discovered by the Curie brothers in 1880, is the property of a material that enables it to develop an electrical potential across its surfaces in response to an applied mechanical stress. This phenomenon is exploited by the active element of a piezoelectric hydrophone. As an incident acoustic wave impinges on the hydrophone it applies a stress to the active element, and a voltage is generated.

Many piezoelectric devices are good voltage sources, but may be relatively poor at sourcing current. As such, these sensors are relatively poor at driving the transmission line (cable) between hydrophone and oscilloscope (or other data acquisition device). A simple hydrophone comprising only a piezoelement and a cable must be calibrated with great care; the electrical impedance of both the hydrophone and the load into which it is operating must be carefully recorded. Any deviation from these conditions (e.g. additional lengths of cable, changes in terminating impedance) will result in additional cable loading. This will introduce frequency dependent perturbation that needs to be corrected for using Eq. 19.7

$$M_L = M_C \sqrt{\frac{\{\mathrm{Re}(Z_L)\}^2 + \{\mathrm{Im}(Z_L)\}^2}{\{\mathrm{Re}(Z_L) + \mathrm{Re}(Z)\}^2 + \{\mathrm{Im}(Z_L) + \mathrm{Im}(Z)\}^2}} \qquad [19.7]$$

where M_L is the loaded sensitivity, M_C is the hydrophone sensitivity determined during calibration, Z_L is the electrical impedance of the load and Z is the output impedance of the hydrophone. Note that all the terms in Eq. 19.7 are frequency dependent.

The application of cable loading corrections such as those of Eq. 19.7 can be an arduous and complicated procedure. An alternative approach is to incorporate a preamplifier immediately next to the active element of the hydrophone. Typically preamplifiers have three functions:

1. an impedance buffer, to convert the output impedance of the hydrophone to a more convenient level,
2. a gain stage, to provide some level of amplification to the signal,
3. a line driver, to ensure that the signal can be transmitted along a transmission line in a manner that preserves signal integrity.

As long as the preamplifier's output impedance is matched to both the input impedance of the DAQ device and the cable used to connect the two, there will be complete power flow from one device to another. Under these conditions, any length of cable can be used without introducing additional cable loading artefacts, and thus affecting the calibration. For this reason, preamplified hydrophone systems are normally preferable to unbuffered hydrophone systems that require cable loading corrections.

19.3.1 Piezopolymer versus piezoceramic

The vast majority of piezoelectric hydrophones are either piezoceramic or piezopolymer. Single crystal and piezocomposite devices do exist, but their use in hydrophone production is less common, and will not be discussed further in this chapter.

Piezoceramic devices tend to have well-defined resonance modes that are intrinsically related to their geometry; thickness mode, radial mode, length expander and width expander modes are typical examples. At resonance, piezoceramic devices tend to exhibit high piezoelectric sensitivity, but often have a high mechanical Q and thus a much smaller response off-resonance. Piezoceramics have high acoustic impedances (typically > 17 MRayl and often > 30 MRayl). There will thus be a significant reflection at a ceramic/water interface, and acoustic energy incident upon the hydrophone cannot easily propagate in to the active element. There is limited possibility for internal loss mechanisms due to crystal structural deformation within piezoceramics and thus they are very efficient at converting an applied electrical voltage into displacement/pressure. Consequently piezoceramics have high piezoelectric strain coefficients (d-coefficients) and are excellent materials for the generation of ultrasonic signals. However, these same properties mean that a high stress is required to achieve a given voltage response and thus piezoceramics have lower piezoelectric voltage coefficients (*g*-coefficients) and are a less common choice for receive-only devices.

Compared with ceramics, piezopolymers are much lower acoustic impedance (typically 3–4 MRayl). This means that much more of the incident energy propagates into the hydrophone active element and is thus available to generate an electrical response. Furthermore, piezopolymers are inherently low Q materials and consequently have a broad bandwidth. The compliant nature of polymers means that they are easy to compress, and this contributes to their high *g*-coefficient but low *d*-coefficient behaviour. Therefore, although piezopolymers make relatively low efficiency ultrasonic sources, they are excellent materials for broadband, high-sensitivity hydrophones.

19.3.2 Needle (probe) hydrophones

Needle hydrophones are good general purpose measurement devices and are constructed from a small disc of a piezoelectric material (commonly a piezopolymer such as PVDF) mounted on the end of a co-axial conductor. As a general rule, needle hydrophones incorporating a piezoceramic active element have a narrower bandwidth and exhibit a more noticeable resonant peak than their PVDF counterparts. However, piezoceramic needle probes tend to be more rugged and can be more tolerant of hostile acoustic environments. Needle hydrophones are commercially available in a wide range of sizes as small as 40 µm, as can be seen in Fig. 19.3. These hydrophones have greater sensitivity and lower cost than

19.3 Needle hydrophones.

comparably sized membrane sensors. They are also physically small and can thus be inserted into cavities within tissue to allow direct measurement of *in vitro* acoustic signals.

Highly resonant ultrasonic sources (e.g. therapeutic transducers) are often very susceptible to changes in the mechanical load they experience. Back reflections from objects placed in front of the transducer may load the source to such an extent that its radiation efficiency is altered and transducer output is reduced. For this reason, needle hydrophones are advantageous since they have a small cross-sectional area and thus the wave that is back-scattered from a probe tends to be small.

Linearity: as discussed previously, NEP is strongly dependent on the sensitivity of a hydrophone, and for a piezoelectric needle hydrophone this in turn involves a dependence on the diameter of the active element. This is illustrated by the data in Table 19.1. The upper limit of dynamic range for these hydrophones has two separate limits. Firstly, the linearity threshold, beyond which clipping may occur, is limited by the maximum signal that the preamplifier can tolerate at its input. Clearly a more sensitive hydrophone will present a larger signal to the preamplifier, and thus the upper limit of linearity is also hydrophone active area dependent.

Several commercially available hydrophone systems have either a switchable gain or an attenuator that can be inserted in between the hydrophone and the input stage of the preamplifier. This serves to extend the upper limit of linearity by reducing the amplitude of the signal presented at the preamplifier input. However, as was seen in the sample calculation in Section 19.2.1, a reduction of hydrophone sensitivity (through the addition of an attenuator) will reduce NEP. Therefore it could be considered that hydrophone systems have a fixed dynamic range (difference between maximum linear signal and NEP) and attenuators and/or input stage gain switching simply offset that range on a scale of absolute pressure. In practice, if an acoustic signal is sufficiently large that preamplifier overload is of concern then an NEP is unlikely to be encountered.

Needle hydrophone systems typically have damage thresholds in the 15–20 MPa range. At this pressure level, acoustic non-linearity will almost certainly be present and well-formed shock waves with significant waveform asymmetry are likely. Assuming the ratio peak compression to peak tension pressures to be 4:1

Table 19.1 Typical dynamic range limits for the range of hydrophones shown in Fig. 19.4. Preamplifier noise level of 60 μV rms over a 100 MHz bandwidth

Active diameter (mm)	Nominal sensitivity (mV/MPa)	NEP of system (Pa)	NEP into DAQ with 1 mV noise floor (kPa)	Maximum measurable linear signal (MPa)
1.0	850	7	1.17	0.8
0.5	300	200	3.3	2.7
0.2	55	1090	18.2	12.4
0.075	10	6000	100	68

(typical for non-linear waveforms) for a 15 MPa peak-to-peak field implies 12 MPa compression and 3 MPa tension.

Bandwidth and frequency response: The frequency response of any probe hydrophone may be influenced by the wave modes that are generated as an incident wave diffracts around the needle tip. A finite difference model (AFiDS, AMH Consulting, Poole, Dorset, UK) was used to simulate this behaviour. An axi-symmetric, radial cross-section of acoustic pressure is shown in Fig. 19.4.

Of particular interest are the circularly radiating, diffractive wave components, since these will propagate across the active element of the needle hydrophone. As diffracted components from opposite edges interact with each other, there will be an interference pattern generated at the surface of the hydrophone active element. The precise nature of this interference will be a function both of the dimensions of the hydrophone and of wavelength (and hence frequency). Thus, for any particular design of needle hydrophone there will be peaks and troughs in its low-frequency response arising from interference effects. This was first predicted analytically by Fay *et al.* (1994). It has also been shown by Hurrell (2002; 2004a) that modifying the tip geometry of a needle hydrophone can significantly reduce these diffraction effects. For this reason the magnitude of the diffractive influenced effects shown in Fig. 19.5 for a modified tip geometry is less than ±2 dB around the baseline

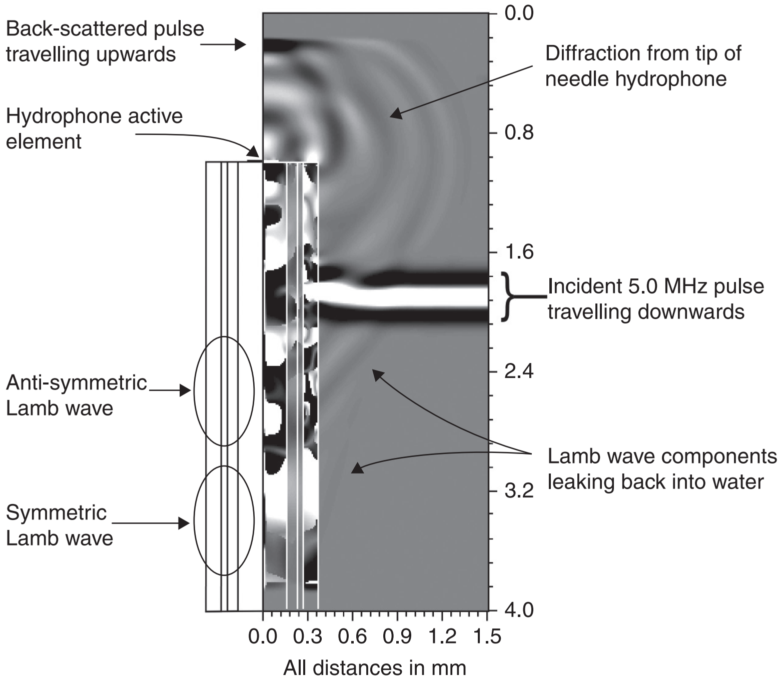

19.4 Axi-symmetric, radial cross-section of acoustic pressure shown in greyscale.

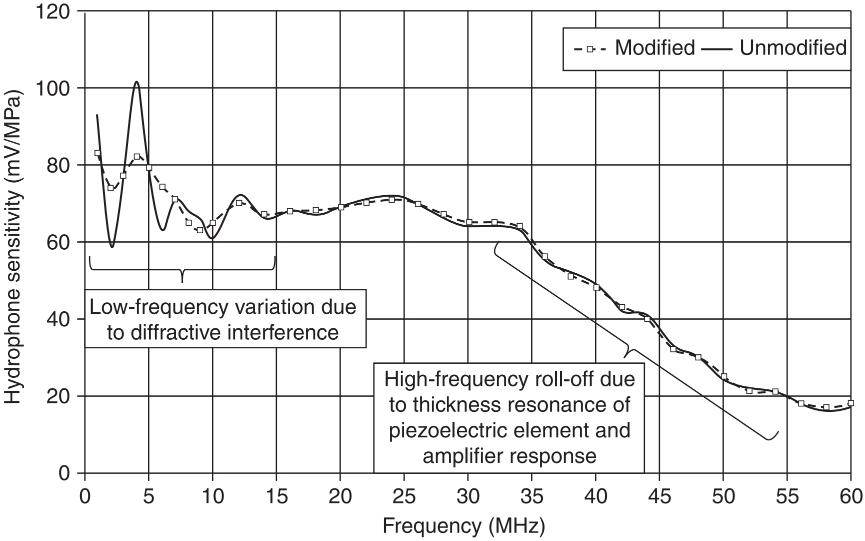

19.5 The effect of a modified tip geometry on the frequency response of a 0.2 mm needle hydrophone using 9 μm PVDF film.

sensitivity in the < 25 MHz region. In contrast, an unmodified geometry could be expected to show variations of at least ±5 dB.

Fay *et al.* (1994) also predicted a reduction of response at higher frequencies due to thickness resonance effects of the PVDF active element. Preamplifiers (or other associated electronics that form part of a hydrophone system) also tend to have a gain profile that decreases as frequency increases, and this too may contribute to higher frequency response roll-off.

Despite the non-smooth frequency response, needle hydrophones have been shown by both Hurrell (2004b) and Wilkens and Koch (2004) to yield an accurate representation of broadband acoustic signals if the whole frequency response is used to calculate the pressure waveform using a method such as that provided by Eq. 19.4. Clearly for continuous wave (CW) or long toneburst signals, the spectral variation is minimal and thus the narrowband approximation of Eq. 19.3 is nearly always sufficient.

Clearly, there are number of factors that can influence the frequency response of any given needle hydrophone, and thus the details of probe hydrophone design can greatly affect its bandwidth. To provide an indication of the typical frequency ranges it should be noted that the largest hydrophone type shown in Fig. 19.3 has been calibrated to national standards at frequencies as low as 10 kHz and up to 10 MHz. The smallest hydrophone design shown in the same figure is routinely calibrated from 1 MHz up to 60 MHz.

Directivity: The directional response of needle hydrophones at higher frequencies often conforms to that of the 'circular plane piston in a rigid baffle' model as described in Section 19.2.3. At lower frequencies, and thus long wavelengths, the validity of the 'rigid baffle of infinite extent assumption' that is inherent in this model becomes increasingly questionable. For this reason there can be a noticeable difference between theoretical predictions and measured responses. The data shown in Fig. 19.1 are for a 0.5 mm diameter needle hydrophone. For convenience, the directional response at 1, 5 and 15 MHz contained within Fig. 19.1 have been extracted and plotted in Fig. 19.6. A theoretical directional response according to Eq. 19.6 has also been included in the same figure for comparison. For this device there is good agreement between theoretical and experimental data (at least within the range of 30° either side of zero).

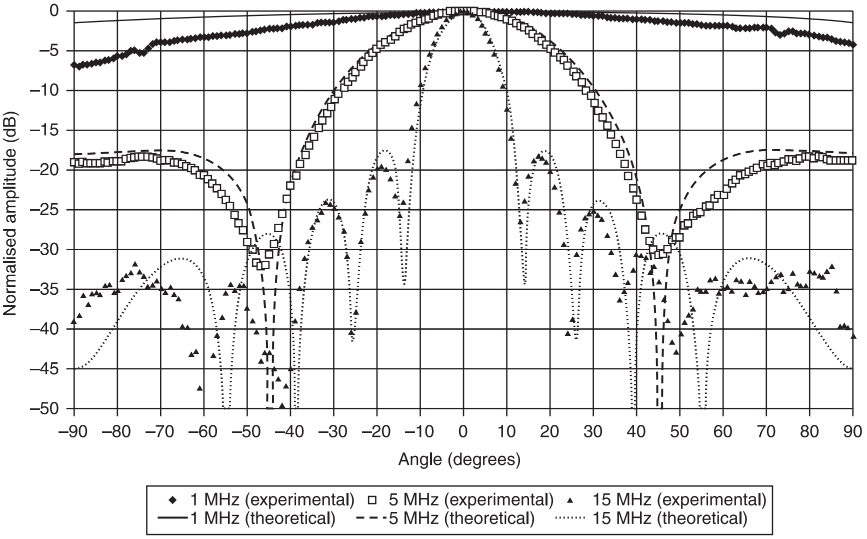

19.6 Comparison of experimental and theoretical directivity patterns for a 0.5 mm diameter needle hydrophone.

19.3.3 Membrane hydrophones

Membrane hydrophones are constructed from one or more very thin layers of the piezopolymer PVDF stretched taut within a frame. The PVDF (or its co-polymers) has to be carefully prepared so that only a small region (typically < 1 mm diameter) in the middle of the film is piezoelectrically active. An example of this kind of hydrophone is shown in Fig. 19.7. These hydrophones are considered the 'gold-standard' hydrophone due to their smoothly varying frequency response over a very broad frequency range. This response has been accurately modelled by Gélat *et al.* (2005) with the dominant feature being a peak due to the thickness resonance of the membrane.

Power
Supply

19.7 Membrane hydrophone.

Linearity: It is worth noting that membrane hydrophones are always of lower sensitivity than comparably sized needle hydrophones when subject to the same amplification. This arises from the fact that probe hydrophones usually have a rigid termination to the piezoelectric element. The wave reflected from this termination then passes back through the piezoelectric element where it is 're-measured'. In contrast, the thin membrane has an identical impedance on both its surfaces. Moreover, it has been designed to be acoustically transparent, to reduce field perturbation. Consequently, the active element does not experience the reflected wave present in needle hydrophones. As a result of experiencing the wave once only, the effective sensitivity of a membrane hydrophone is a factor of two smaller than a comparable needle-type sensor. Typical dynamic range limits for the hydrophone shown in Fig. 19.7 are given in Table 19.2.

As with needle hydrophones, maximum linear pressure range is related to hydrophone sensitivity and the linear input range of any preamplifier, and calculations presented in Section 19.3.2 apply here. Needle hydrophone damage thresholds are equally appropriate too.

Table 19.2 Typical dynamic range limits for the hydrophone shown in Fig. 19.7. Preamplifier noise level of 60 μV rms over a 100 MHz bandwidth

Active diameter (mm)	Nominal sensitivity (mV/MPa)	NEP of system (kPa)	NEP into DAQ with 1 mV noise floor (kPa)	Maximum measurable linear signal (MPa)
0.4	35	1.7	28.6	19.3
0.2	15	4	66.7	45

Bandwidth and frequency response: Membrane hydrophones are excellent for characterising the broadband short pulses that are produced by ultrasonic imaging systems due to their smoothly varying frequency response. Experimental frequency response curves for two configurations of membrane film and active element size are shown in Fig. 19.8. In each case the frequency response increases monotonically to the peak and then decreases monotonically beyond it. In keeping with the Gélat model, the principal resonance frequency of a membrane hydrophone is inversely proportional to the thickness of the film. This was further illustrated by Lum *et al.* (1996), who produced a membrane hydrophone on 4 μm film with a bandwidth well in excess of 150 MHz. More typically, commercially available hydrophones are based upon PVDF films within the thickness range 9–20 μm, leading to typical peak frequencies in the 35–60 MHz range dependent on the construction of the device (discussed in the following).

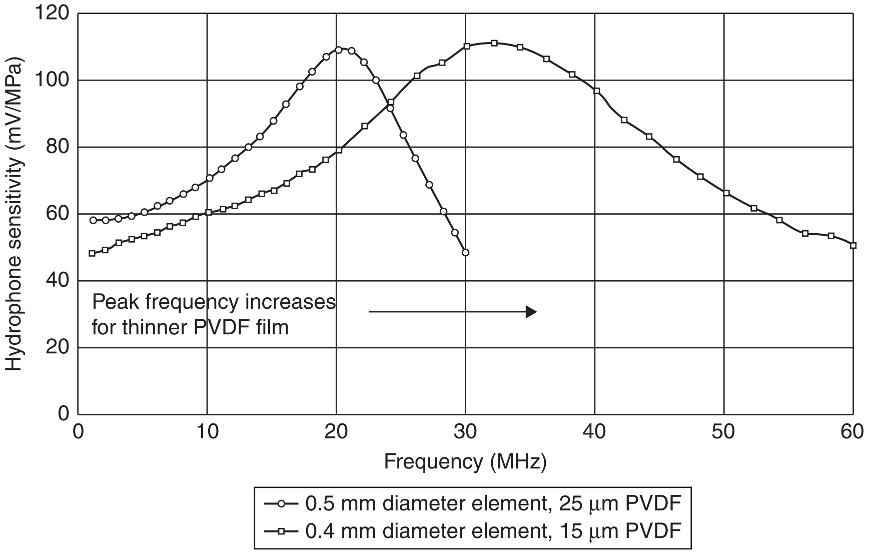

19.8 Frequency response of two types of bi-laminar membrane hydrophone.

Two sub-types of membrane hydrophone, distinguished by their electrode configuration, are common: co-planar shielded and bi-laminar shielded. A co-planar shielded membrane hydrophone is a single piece of film that has the live electrode on one surface whilst the return electrode is on the other side. There may be additional ground shielding electrodes on either side which may, or may not, be electrically connected to the return electrode. A bi-laminar shielded hydrophone is actually a laminate of two layers of film. The outer surfaces of the laminated stack contain the return/ground electrodes, whilst the live electrode is between the two inner surfaces of the laminate.

Since co-planar hydrophones have only a single layer film, their thickness resonance occurs at double the frequency of a comparable bi-laminar membrane made from the same thickness film. This means that co-planar hydrophones have twice the bandwidth of a comparable bi-laminar device. However, since both the return and live electrodes are exposed to the water within the measurement tank, co-planar devices can be prone to pick up of waterborne EM noise. Bi-laminar hydrophones were designed to address this deficiency by ensuring the live electrode is isolated from the water due to its position in the middle of the laminate. This offers benefits in terms of reduced susceptibility to EMI, but comes at the cost of reduced bandwidth, due to increased thickness of the two layers of film.

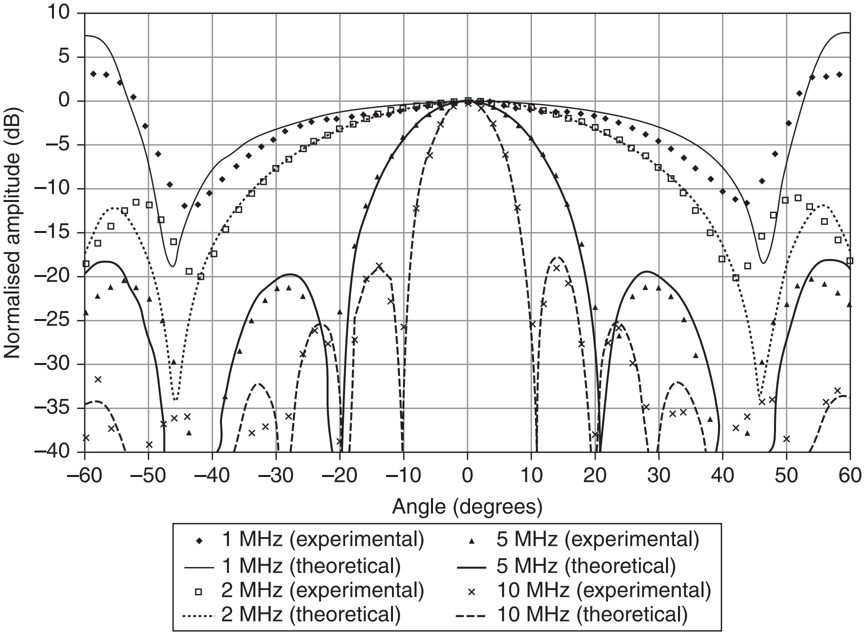

19.9 Comparison of experimental and theoretical directivity patterns for a 1.0 mm bi-laminar shielded membrane hydrophone (adapted, with permission, from Robinson *et al.*, 2000).

Membrane hydrophones are less suited to the measurement of CW signals due to the possibility of flexural standing waves modes developing on the membrane. Furthermore, although the amplitude of back-scattered reflection from the membrane is much lower than that from a needle hydrophone, the back-scattering area is much larger, and transducer loading effects may need careful consideration. Their large physical dimensions also preclude their use in space-restricted measurement configurations. Membrane hydrophones also carry a significant price premium compared with their needle probe counterparts.

Directivity: The directional response of a membrane hydrophone often shows a large side-lobe at lower frequencies and large angles. Bacon (1982) conducted a theoretical examination of the issue and concluded that the presence of Lamb waves on the membrane was responsible for this effect. Within the same paper, Bacon also experimentally confirmed the presence of these Lamb modes on the membrane. This directivity pattern is illustrated in Fig. 19.9.

19.3.4 Underwater low-frequency hydrophones

The majority of underwater low-frequency hydrophones operate at frequencies below 500 kHz. Moreover, devices of this type are routinely used in open ocean conditions at depths exceeding 100 m and thus need to be of a robust construction to withstand the hydrostatic pressure of the sea. Consequently piezoceramic elements (with their much higher rigidity) are common in these types of hydrophone. Furthermore, cylindrical and ball (spherical) geometries are frequently used for these hydrophones due to their preferable directional characteristics (discussed in more detail later within this section). Due to their lower frequency of operation, cylindrical and ball hydrophones can often be 10–25 mm in diameter and still be small compared with the wavelength in water.

Linearity: Low-frequency hydrophones are frequently used without preamplification or impedance buffering. As such, there are no electronic circuits introducing noise, and NEP is therefore limited by the combination of the sensitivity of the device and the noise floor of the DAQ device used to acquire the hydrophone signal. Similarly, the maximum measurable pressure is also not limited by preamplifier dynamic range, and is limited only by the value derived from the combination of hydrophone sensitivity and the maximum measurable signal of the DAQ. However, it is rare to encounter an oceanic acoustic signal > 1 MPa, and acoustic signals < 100 kPa are much more likely.

A common practice in underwater acoustics is to specify hydrophone sensitivity in dB re: 1 V/μPa, rather than the simpler linear units of mV/MPa used at higher frequencies. Conversion from one form to the other is simple and it can be easily shown that −240 dB re: 1 V/μPa is equivalent to 1V/MPa. It should be noted that, due to the much larger sensing elements of lower-frequency hydrophones, they are much more sensitive than needle and membrane counterparts. From Fig. 19.10, it can be seen that sensitivities of –220 and –200 dB re: 1 V/μPa are easily achievable and these correspond to 10 V and 100 V per MPa respectively. As before, the noise floor of a DAQ system will be assumed to be 1 mV. A hydrophone with sensitivity of 10 V/MPa (–220 dB re: 1 V/μPa) would therefore have an NEP of 100 Pa, whilst the –200 dB re: 1 V/μPa sensitivity would have an NEP of 10 Pa.

Bandwidth and frequency response: Both cylindrical and spherical resonators radiate in a radial mode, and thus their frequency response curves often feature a resonant peak governed by the dimensions of the piezoceramic. Given the hydrostatic pressures encountered underwater, a void/air filled piezoceramic shell would be likely to collapse. To counter this, the cylindrical/spherical shells are commonly filled with a material that is rigid enough to prevent collapse under pressure, whilst also providing some damping to broaden the resonance of the piezoceramic element. Protection for the active element from corrosion, impact damage and marine growth is routinely achieved by encapsulating the entire hydrophone in a polyurethane rubber. However, as with all visco-elastic media, the attenuation introduced by this latter increases with frequency, and thus the fall-off in sensitivity above resonance may be more rapid than would be seen with a single resonant mode system (such as membrane hydrophone). All of these features can be seen in Fig. 19.10, which plots the frequency response curves for several underwater hydrophones. Further information on the constructional details of these devices can be found in Table 19.3.

The lack of a preamplifier discussed previously means that the calibration data for many low-frequency hydrophones are supplied as 'end-of-cable' values. Consequently, unless the calibration conditions are replicated in use, the cable

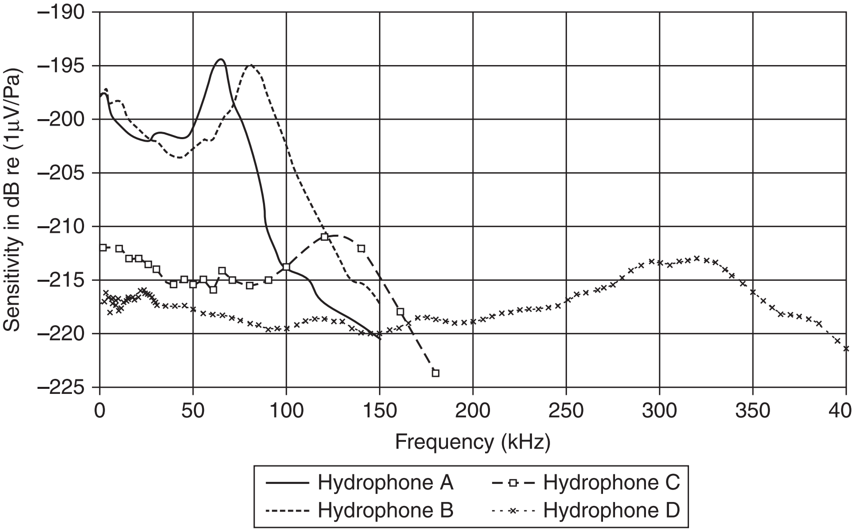

19.10 Frequency response of various low-frequency cylindrical and spherical hydrophones (courtesy of Neptune Sonar Ltd, Kelk, UK).

Table 19.3 Cylindrical and ball hydrophone construction parameters for the hydrophones used in Fig. 19.11

Hydrophone ID	Type	Diameter (mm)	Length (mm)
A	Ball	42	n/a
B	Ball	34	n/a
C	Cylinder	9	24.5
D	Cylinder	9	24.5

loading corrections of Eq. 19.7 are required. This can be particularly problematic in sea-borne trials since any damage to the cable (not uncommon aboard boat) would mean that the hydrophone should be immediately re-calibrated.

Directivity: Experiments conducted in an oceanic environment rarely provide the same level of positional control of measurement equipment that is available in laboratory based experiments. Consequently, a hydrophone exhibiting a highly directional response is likely to be misaligned, for the majority of measurements spherical (ball) hydrophones have a radiation pattern that is close to omnidirectional in 4π steradians. The directional response at resonance (60 kHz) of the ball hydrophones shown in Fig. 19.11 varies by less than 1 dB for rotation in any direction. Cylindrical hydrophones have a directional response that is omnidirectional when rotated about the axis of the cylinder, but may have a definite main lobe for rotations about the perpendicular to the cylinder's axis. The precise nature of this elevation directional response will be a function of hydrophone dimensions and frequency, but, as with all other hydrophone types, the response becomes broader when hydrophone dimensions are small compared with the wavelength of the received signal.

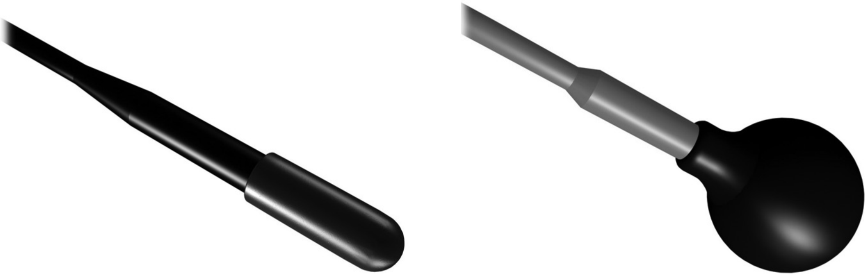

19.11 Ball hydrophones.

19.3.5 Passive cavitation detectors (PCDs)

Unlike most other hydrophone applications, PCDs are used to monitor the secondary effects of an acoustic field, rather than to measure the field directly.

Whenever high amplitude acoustic fields are present, cavitation phenomena may occur. The reader is referred to the excellent treatise by Leighton (1997) for a thorough discussion of acoustic bubble behaviour, including cavitation. In summary, a bubble undergoing stable cavitation due to an external field may emit sound at sub- and super-harmonics. If the external field amplitude increases to a level at which inertial cavitation occurs, then there will be additional broadband acoustic emissions from the bubble. These acoustic signatures are of considerable use to researchers in the field of high amplitude acoustics, since they provide a means of identifying when and where cavitation is occurring. A PCD is thus a specific type of hydrophone optimised to detect the acoustic emissions arising from cavitation events. To illustrate their application, Leighton *et al.* (2008) combined two orthogonally aligned PCDs with an external high pass filter to monitor clinical lithotripsy treatments. They clearly demonstrated how the acoustic emissions could be used to assist in the classification of the degree of stone fragmentation.

Linearity: PCDs typically have high sensitivity with an NEP below 500 Pa. This allows them to detect the low amplitude signals from the cavitating bubbles, but therefore runs the risk that these low amplitude signals are masked by the high amplitude source signal that has initiated the cavitation. To counter this, PCDs often have a frequency response that has been filtered to reduce sensitivity to the source signal. As with underwater low-frequency hydrophones, PCDs are often used without preamplification, and thus the upper limit of dynamic range is that of the maximum input signal to the DAQ or the threshold of damage.

Bandwidth and frequency response: The filtration required to exclude signal from the high amplitude source is commonly supplied by exploiting the inherent frequency response of the piezoelectric element used to make the PCD. Researchers in HIFU commonly use a source transducer whose centre frequency is 3 MHz or less (and often close to 1 MHz). Therefore a PCD whose centre frequency is some multiple (e.g. 3–5 times) of source would have a much reduced sensitivity at the fundamental frequency. Clearly, though, there is no generic frequency response for PCDs and it is usual to optimise the response of the PCD to complement the operating frequency of the source transducer. An example can be seen in Fig. 19.12. This PCD was optimised for use with a 3 MHz HIFU source, and thus the peak in its frequency response curve is approximately 10.5 MHz. The rapid fall-off in response below resonance can also be seen, and thus the sensitivity at the source frequency of 3 MHz is only 10% of its peak response.

Directivity: Given the need to identify not only when, but where, cavitation occurs, PCDs are often focussed so that they only interrogate one small region of the acoustic field. The PCD can then be mechanically scanned to produce a spatial map of cavitation activity. This is precisely the technique that has been employed by Kyriakou *et al.* (2011). Some HIFU transducers have an aperture through the middle of the active element to permit co-axial PCDs to be inserted through. For this scenario, the PCD is often designed to have the same focal length as the HIFU

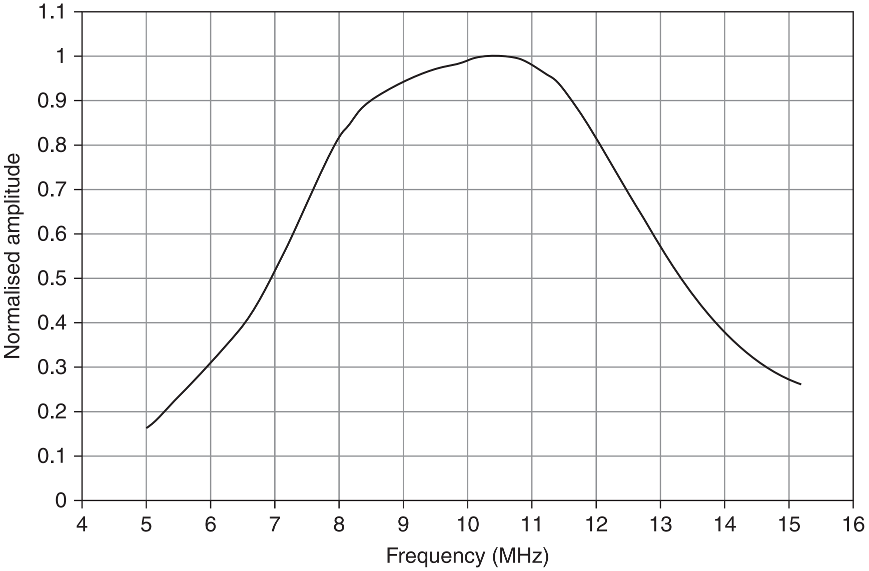

19.12 Frequency response of a 15 mm diameter PCD with focal distance 70 mm. PCD optimised for use with a 3 MHz HIFU source.

source. However, due to the much smaller diameter of the PCD relative to the source transducer, the focal depth of field may be considerably larger. This means that the PCD may be sensitive to acoustic emissions originating from a larger focal volume than that of the generating transducer. Consequently it would not be possible to distinguish cavitation signals emanating in a pre- or post-focal hot-spot from those at focus.

An alternative configuration is to arrange the PCD such that its acoustic axis is orthogonal to that of the HIFU source but with the focal zones of the two devices overlapping. This is often termed a con-focal configuration. A con-focal measurement requires more care and attention during the experimental setup to ensure the focal regions of both devices are aligned. However, the benefits of this configuration can be seen once the data of Fig. 19.13 are considered. The PCD can be seen to have a FWHM of less than 2 mm in the transverse direction, but more than 80 mm along its acoustic axis. If aligned co-axially it would be very difficult to isolate where (within the 80 mm axial focal zone) an acoustic cavitation event had occurred. Contrast this with a con-focal arrangement where the transverse profile of the PCD is parallel to, and aligned with, the acoustic axis of the HIFU source. In this case the PCD will be sensitive only to acoustic events that have occurred within its focal region; this effectively disregards all signals that have not originated from a 2 mm wide region along the acoustic axis of the HIFU source. The PCD can then be translated along the acoustic axis of the HIFU source and regions of significant cavitation activity can be identified.

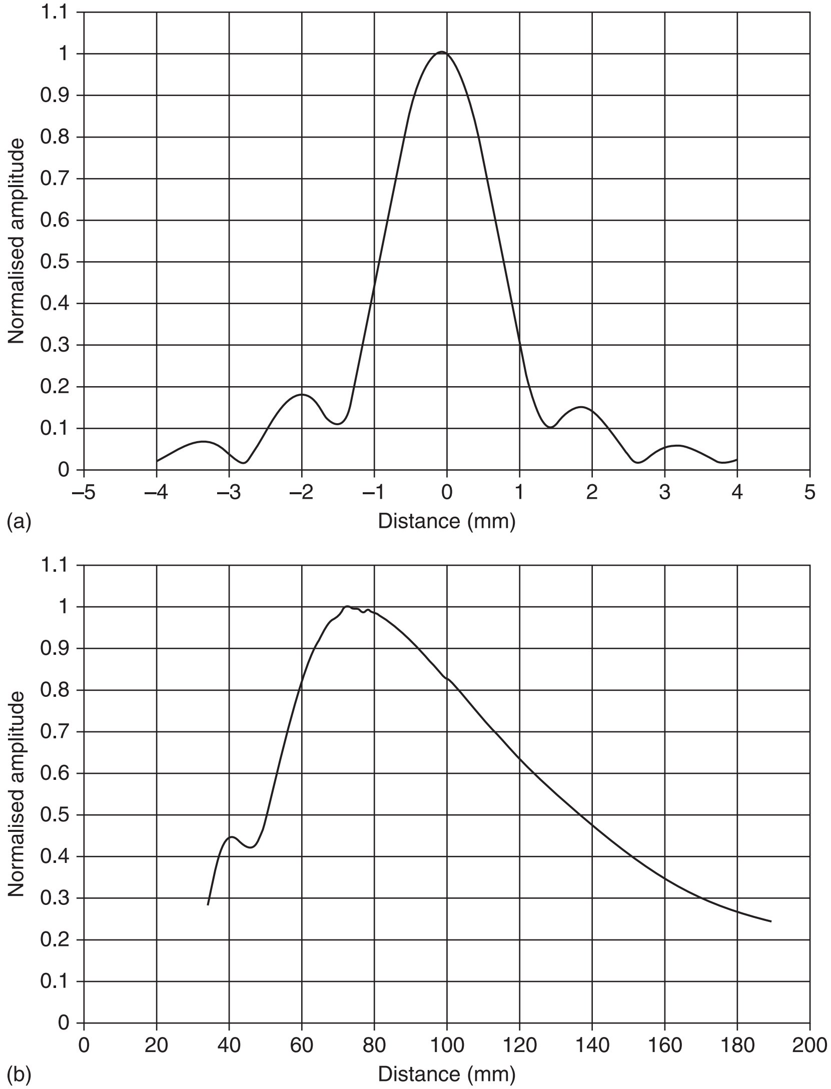

19.13 Beam profiles of a 15 mm diameter PCD: (a) in a transverse profile across the acoustic axis, (b) along the acoustic axis.

19.4 Fibre-optic hydrophones

Although piezoelectric hydrophones are the most widely used measurement devices in industrial and medical ultrasound metrology, fibre-optic hydrophones (FOH) are beginning to find application in a number of specific areas. A key point in relation to any discussion of FOHs, and one that is often unrecognised, is that it is difficult to generalise about their performance and utility. Unlike piezoelectric hydrophones, FOHs exploit a variety of different transduction mechanisms which yield a broad spectrum of device-specific acoustic characteristics. Hence the route to identifying the potential applications of a specific FOH is best achieved via a discussion of its transduction mechanism, which in turn defines its performance. This is the approach adopted in this section, in which the operating principles and performance characteristics of those FOHs that are either in current usage in ultrasound metrology, or have significant potential to be, are described.

19.4.1 Introduction

As discussed in the previous section, piezoelectric hydrophones can meet the requirements of many ultrasound measurement applications. However, there are certain limitations associated with the piezoelectric transduction mechanism that may preclude their use in some circumstances which FOHs can overcome. The sensing mechanism of FOHs is based upon the detection of acoustically induced changes in the intensity, phase or polarisation of light either guided within an optical fibre or interacting with an optical sensor located at the distal end of the fibre. In the former case, in which the acoustic field modifies the properties of the light guided within the optical fibre, the fibre itself acts as the acoustically sensitive element and the device is termed an intrinsic FOH. In the latter case the optical fibre merely acts as a conduit for delivering light to and from the sensing element at the tip of the fibre and is termed an extrinsic FOH.

Whilst the acoustic performance and utility of a FOH depend very much on the specific transduction mechanism employed, there are some practical features common to the majority of FOHs. Firstly, the optical nature of the sensing mechanism means that FOHs are inherently insensitive to electromagnetic interference (EMI). Although rarely a major issue when making pulsed measurements, it can be problematic when characterising CW or quasi CW fields. Secondly, FOHs can be better suited to characterising high amplitude or high power ultrasound fields which can damage expensive piezoelectric hydrophones. In some cases this is because the FOH is intrinsically more robust and less susceptible to mechanical and thermal damage than piezoelectric devices. In others it is because the optical sensing element (either the fibre itself or an external optical element) is of low unit cost and can be inexpensively replaced if damaged. Thirdly, the small size and flexibility of an optical fibre often permit a miniature probe type device to be fabricated for limited access applications, for example, for making measurements in biological tissues. Fourthly, unlike piezoelectric devices, some FOHs are sensitive to temperature as well as pressure, offering the prospect of making measurements of ultrasound-induced heating, such as that produced in HIFU therapy.

Although useful, the above mentioned attributes are rarely sufficiently compelling by themselves to warrant using a FOH in place of a piezoelectric hydrophone. To provide a truly competitive advantage, the acoustic performance needs to be comparable to, or preferably exceed, that of piezoelectric devices in at least some respects. Although it is difficult to generalise about FOH performance due to the diversity of transduction mechanisms employed, one attribute common to almost all extrinsic FOHs is the potential to provide smaller element sizes and thus a less directional response than piezoelectric devices. This is because the acoustically sensitive area is defined, to a first approximation, by the core diameter of the optical fibre, which can be as small as a few microns. By contrast, fabricating piezoelectric elements on this scale with adequate detection sensitivity is problematic because sensitivity decreases with element area. This inevitably implies that for a FOH to have a meaningful advantage in this respect it must also provide a higher detection sensitivity than an equivalently sized piezoelectric element. Interferometric based extrinsic FOHs can generally fulfil this criterion and thus have a role to play in high-frequency ultrasound metrology. By contrast, intensity based FOHs tend to exhibit much lower sensitivity and so do not generally provide a sensitivity-element size advantage over piezoelectric devices. However, they can provide other benefits, such as a high upper limit of detection and robustness, which lends them to high amplitude/power applications.

Other considerations relate to complexity, practical utility and availability. Again, these depend on the type of FOH. Some are complex high performance research tools, confined to the optics laboratory, and require personnel with specialist knowledge of their operating principles. Others can be readily constructed by practitioners with only a rudimentary knowledge of practical optics or have been engineered into robust commercially available instruments that are as straightforward to use as piezoelectric hydrophones.

In this section the operating principles, performance and applications of FOHs are described. The focus is on those extrinsic devices which have acoustic performance characteristics best suited to US measurement. With this in mind, the four types of FOH that are either the most commonly used or have the potential to find application as practical ultrasound measurement tools are reviewed in detail in Sections 19.4.2–19.4.5. Specific emphasis is placed on eliciting the underlying signal transduction mechanisms and their relationship to the key acoustic performance characteristics in terms of sensitivity, linearity, bandwidth and directional response. In Section 19.4.6 a brief overview of several intrinsic FOHs is provided. Finally, in Section 19.4.7 a comparison of the performance characteristics and practical utility of the different FOHs as well as the applications they lend themselves to is provided.

19.4.2 Eisenmenger fibre-optic hydrophone

The Eisenmenger type fibre-optic hydrophone (Staudenraus and Eisenmenger, 1993) was one of the first fibre-optic acoustic sensing devices to find application in ultrasound metrology. It has now been adopted by a number of research groups for characterising the output of shockwave sources (Huber *et al.*, 1994; Wang *et al.*, 1999) and HIFU transducers (Zhou *et al.*, 2006; Canney *et al.*, 2008) and is produced commercially by two companies, RP Acoustics and Onda Corp. Conceptually, and in terms of its practical implementation, it is perhaps the simplest of all FOH systems. Figure 19.14 shows a schematic of such a system. It comprises an optical fibre downlead, the distal end of which is cleaved and immersed in the medium in which the ultrasound field is propagating, usually water. Light from a laser is launched into the core of the fibre. A small fraction of the light is reflected from the fibre tip due to the mismatch between the refractive indices of the fused silica of the fibre core and the water that is in contact with it. The reflected light returns back along the fibre and is directed on to a photodiode-transimpedance amplifier unit (P_d) via a fused fibre coupler. A second photodiode unit (P_R) is sometimes incorporated in order to monitor and correct for fluctuations in the laser output power or allow common mode rejection of the relative intensity noise of the laser to improve SNR. The time-varying pressure due to an incident acoustic wave modulates both the density of the water adjacent to the fibre tip and that of the fused silica fibre itself. This produces a corresponding modulation of the refractive index mismatch between the fibre and the water, resulting in a variation in the reflected optical power detected by the photodiode.

The advantage of this approach is simplicity of implementation and operation, low component cost, very wide bandwidth and a high upper limit of linear detection. Furthermore, by using single mode optical fibres which have sub-10 µm core diameters, acoustically small element sizes and thus low directional sensitivity can, in principle, be achieved. The tip of the fibre also has a high mechanical damage threshold, significantly in excess of piezoelectric hydrophones, and should damage occur it can readily be repaired by re-cleaving. These attributes

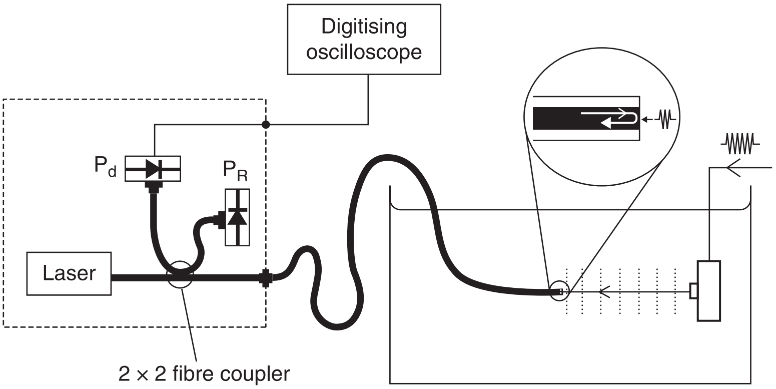

19.14 Schematic of Eisenmenger fibre-optic hydrophone. The transduction mechanism is based upon the detection of pressure induced changes in the refractive index mismatch between the tip of a fused silica optical fibre and water. Pd: signal photodiode unit, PR: reference photodiode unit.

lend it to the characterisation of high amplitude fields such as those produced by shockwave sources. Other advantages include the potential for self-calibration and the measurement of temperature as well as pressure. A significant limitation, however, is its low detection sensitivity, which is a consequence of the weak pressure dependence of the refractive indices of fused silica and water. The broadband noise-equivalent-pressure (NEP) without signal averaging has variously been reported to lie in the range 0.5–1 MPa (Staudenraus and Eisenmenger, 1993; RP Acoustics, 2002; Onda, nd), a detection sensitivity that is at least an order of magnitude lower than that provided by commercially available piezoelectric PVDF needle and membrane hydrophones. As a consequence, the application of this type of FOH is limited largely to the measurement of high amplitude ultrasound fields produced by shockwave sources such as lithotripters or in some cases, HIFU transducers. It is rarely suitable for the measurement of the much lower amplitude ultrasound fields produced by diagnostic medical ultrasound devices or general transducer characterisation applications. Sensitivity is also dependent upon the refractive index of the medium in contact with the tip of the fibre. This can lead to additional complexity in calibrating the hydrophone when making measurements in a medium other than water, such as tissue or a tissue mimicking phantom. A further limitation is that, in order to achieve even the modest NEPs referred to above, laser powers of several hundred milliwatts are required. Since the tip of the fibre is exposed this represents a significant ocular safety hazard. In many operating environments, this requires the system to be housed in a designated laser laboratory equipped with appropriate laser safety features such as door interlocks and the use of user to wear laser safety glasses during the operation of the system.

Transduction mechanism: The pressure p due to an incident acoustic wave produces a change in the density and thus the refractive index of both the fused silica fibre tip and the fluid adjacent to it. As a consequence, the refractive index mismatch at the fibre–fluid boundary is modulated. This produces a corresponding change in the Fresnel reflection coefficient *R(p)* and thus the optical power reflected back along the fibre. The pressure dependent Fresnel intensity reflection coefficient is given by

$$R(p) = \left(\frac{n_f(p) - n_w(p)}{n_f(p) + n_w(p)} \right)^2 \qquad [19.8]$$

where $n_f(p)$ is the refractive index of the fused silica fibre core and $n_w(p)$ is the refractive index of the fluid adjacent to the fibre tip, usually water. Thus, to fully describe the transduction mechanism requires consideration of (i) the relation between density and pressure and (ii) the relationship between density and refractive index. In the original description by Staudenraus and Eisenmenger (1993) the former relationship was described by the isentropic Tait equation of state;

$$\frac{P_0 + p + Q}{\rho(p)^{\gamma}} = const. = \frac{P_0 + Q}{\rho_0^{\gamma}} \qquad [19.9]$$

where P_0 is the static pressure and p the acoustic pressure. $\rho(p)$ is the density and is a function of acoustic pressure and ρ_0 is the density when $p = 0$. Q and γ are constants obtained by fitting Eq. 19.9 to experimental data. For $P_0 = 0.1$ MPa, and at a temperature of 20°C, $Q = 295.5$ MPa and $\gamma = 7.44$ (Staudenraus and Eisenmenger, 1993). Re-arranging Eq. 19.9 provides the relationship between density and pressure

$$\frac{\rho(p)}{\rho_0} = \left(\frac{P_0 + p + Q}{P_0 + Q}\right)^{1/\gamma} \qquad [19.10]$$

The relationship between refractive index and density for water is given by the empirical Gladstone-Dale relationship (also used in Staudenraus and Eisenmenger, 1993),

$$\frac{n_w(p) - 1}{\rho(p)} = const. = \frac{n_{0w} - 1}{\rho_0} \qquad [19.11]$$

where n_{0w} is the refractive index when $p = 0$. Rearranging Eq. 19.11 and substituting for $\rho(p)$ from Eq. 19.10 gives

$$n_w(p) = 1 + (n_{0w} - 1)\left(\frac{P_0 + p + Q}{P_0 + Q}\right)^{1/\gamma} \qquad [19.12]$$

Using $n_{0w} = 1.329$, $Q = 295.5$ MPa and $\gamma = 7.44$ in Eq. 19.12, the relation between $n_w(p)$ and acoustic pressure p is approximately linear for $0 < p < 100$ MPa. Over this pressure range, Eq. 19.12 gives a value of the piezo-optic constant $\Delta n_w(p)/\Delta p \sim 1.31 \times 10^{-4}\text{MPa}^{-1}$. In Staudenraus and Eisenmenger (1993) the pressure dependent change in the refractive index of fused silica fibre core was neglected on account of its piezo-optic constant being approximately two orders of magnitude lower than that of water. Using this assumption and substituting Eq. 19.12 into Eq. 19.8 provides the Fresnel reflection coefficient as a function of pressure. Figure 19.15 illustrates this relation. Although not strictly linear (a consequence of neither $n_w(p)$ being linear with p nor R being linear with $n_w(p)$) for most practical applications the non-linearity is very small and can be neglected over the range 0–100 MPa. With this assumption, the pressure dependence of the Fresnel reflection coefficient over this pressure range is calculated to be $\Delta R/\Delta p \sim 4.2 \times 10^{-6}\ \text{MPa}^{-1}$.

The above treatment is based largely upon the original simplified approach taken by Staudenraus and Eisenmenger (1993). Since then several more refined formulations have been proposed. These are aimed at providing a more accurate description of the transduction mechanism. This is achieved by explicitly accounting for the acoustically induced change in the refractive index of the fused

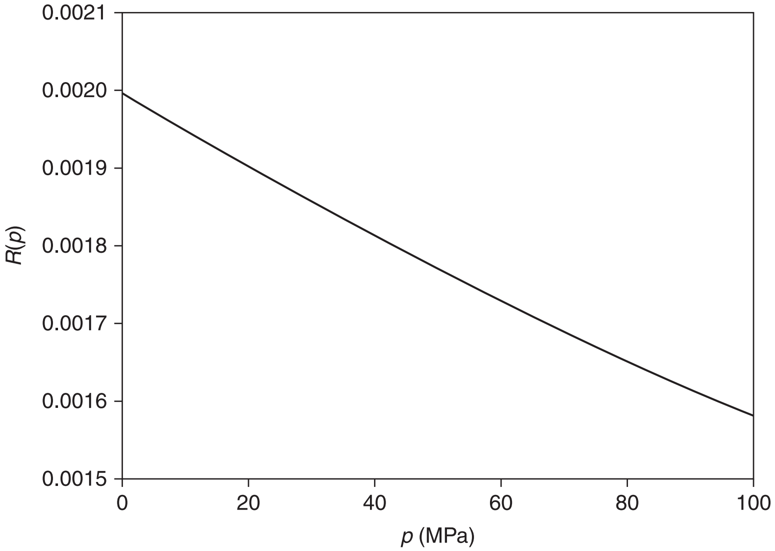

19.15 Relationship between Fresnel reflection coefficient and pressure using Eqs. 19.12 and 19.8.

silica fibre and avoiding the Tait and Gladstone-Dale relations, which are of questionable validity at high negative pressures (Arvengas *et al.*, 2011). These alternative descriptions are more satisfying and have implications for the self-calibration of the hydrophone but otherwise have little impact on measurement accuracy for most applications.

Acoustic detection sensitivity: The value of $\Delta R/\Delta p$~4.2 x 10^{-6} MPa^{-1} derived in the previous section provides some insight into the relatively low sensitivity of this type of hydrophone. Using a modest laser power of 1 mW (the output power of a typical laser pointer), the change in optical power reflected from the fused silica–water interface due to an incident acoustic wave of peak pressure 1 MPa would be just 4.2 nW. This is significantly below the shot noise limited detection sensitivity of a typical photodiode-transimpedance amplifier detector configuration assuming a measurement bandwidth of the order of several tens of megahertz. Much higher laser powers, typically several hundred mW, are therefore required to achieve useful detection sensitivities. Even then, the minimum detectable acoustic pressure or noise-equivalent-pressure (NEP) is limited to approximately 0.5 MPa for a measurement bandwidth of several tens of MHz – significantly higher than that of piezoelectric hydrophones. A combination of a balanced photodetector pair to mitigate the effect of the relative intensity noise of the laser source and increasing the laser power could be employed to reduce the NEP. However, even with such measures the NEP is unlikely to approach that of piezoelectric devices. Gopinath Minasamudram *et al.* (2009) make the claim for a more sensitive variant of the Eisenmenger type FOH in which a thin gold coating is deposited on to the tip of the fibre. It is claimed that the sensitivity is increased by 29 dB compared with that of an uncoated fibre. However, neither the absolute NEP nor an explanation for the apparent increase in sensitivity is provided.

Linearity: Although the pressure dependence of the Fresnel reflection coefficient is not strictly linear (as Fig. 19.15 shows), the non-linearity is within 5% over the range 0–100 MPa. For most measurement applications, it can therefore be regarded as negligible.

Bandwidth and frequency response: The bandwidth is ultimately limited by the distance to which the optical evanescent field penetrates beyond the tip of the fibre and is approximately one optical wavelength. For light at a wavelength of 800 nm, this means the evanescent field limited acoustic bandwidth is in excess of 1 GHz and thus for almost all practical purposes is effectively unlimited. In practice, however, the bandwidth is usually limited to a few hundred megahertz by the photodiode-transimpedance amplifier unit. The frequency response characteristics are determined by the interaction between the incident wave (which is assumed to be planar), its reflection from the fibre tip and the phase-inverted diffracted wave that originates from the edge of the fibre. Assuming the fibre is perfectly rigid, the frequency response can be simulated by summing the incident plane wave with the acoustic field radiated by a piston in an infinite rigid baffle, the latter being calculated using the Rayleigh Sommerfield integral (Krücker *et al.*, 2000).

Figure 19.16 shows the frequency responses for optical fibres of different core and outer diameters obtained using this model. For a single mode fibre of core diameter 10 μm and outer diameter 125 μm, the response is strongly oscillatory with minima occurring at frequencies that correspond to $\lambda_a = r/m$ where λ_a is the acoustic wavelength in water, r is radius of the fibre and m is an integer. Under these conditions, the diffracted edge wave propagates across the tip of the fibre and arrives at the core (the diameter of which defines the acoustically sensitive region) at the same time as the next incident plane wavefront impinges on the fibre tip. Since the edge wave is inverted with respect to the plane wavefront, the two interfere destructively, thus producing a minimum. Similar reasoning can be applied to explain the maxima which occur for $\lambda_a = r/(m + 0.5)$. The gradual decay in the amplitude of the oscillations with increasing frequency evident in Fig. 19.16 is due to the spatial averaging of the edge wave component over the fibre core diameter d. As the acoustic wavelength approaches d, the edge wave contribution to the sensor output decreases – and therefore so too does the oscillatory behaviour – eventually diminishing to zero at approximately 150 MHz when $\lambda_a = d$. Note that most practical embodiments of the concept use multimode fibres with a core diameter of 100 μm and an outer diameter of 140 μm rather than single mode fibres. As Fig. 19.16 shows, an optical fibre of these dimensions exhibits a flatter response with a much weaker oscillatory behaviour due to the greater degree of spatial averaging of the edge waves due to the larger core diameter. Although the frequency response beyond approximately 20 MHz is more uniform than that obtained with the 10 μm core diameter fibre, the larger

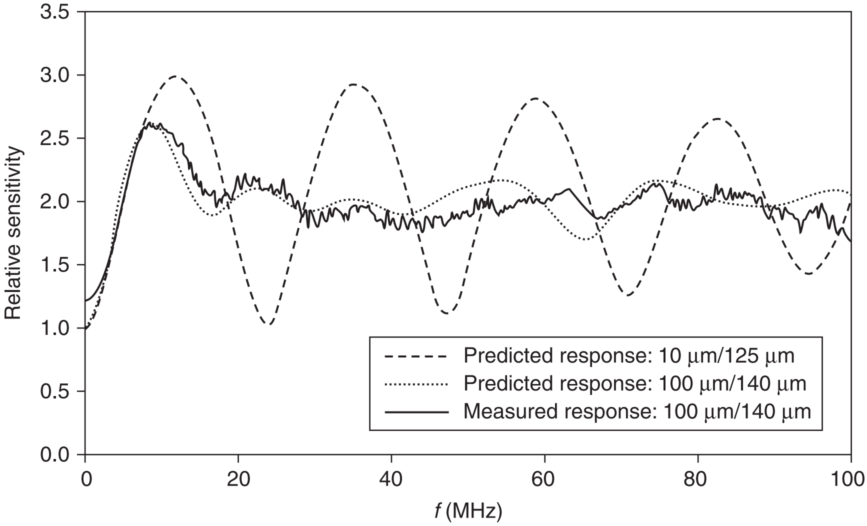

19.16 Frequency response of the Eisenmenger FOH for optical fibres of different core/outer diameters: 10 µm/125 µm (predicted), 100 µm/140 µm (predicted and measured). Measured data supplied by Dr Rainer Pecha of RP Acoustics (personal communication). The predicted responses were obtained using the model described in Krücker *et al.* (2000).

acoustically sensitive area produces a more directional response. Thus spatial averaging in this context is advantageous in the sense that it suppresses the edge waves which are responsible for the non-uniformities in the frequency response but disadvantageous in that it increases directional sensitivity.

As with any probe type hydrophone, the fibre tip geometry, as well as its dimensions, has a significant impact on the frequency response. By tapering the fibre so that the outer diameter at the tip is reduced, the frequency of the first maximum can, in principle, be shifted beyond the maximum frequency of interest, thus providing a more uniform response. Lewin *et al.* (2005) explore this approach using chemical etching to reduce a 125 µm outer diameter fibre to 7 µm at its tip.

Directivity: At first sight, it may seem reasonable to expect that the response to an incoming acoustic wave at a particular angle is given solely by the spatial average[1] of the incident wavefront over the lateral dimensions of the illuminated region defined by the fibre core diameter. However, as discussed in Section 19.3.2, in common with other probe type hydrophones this expectation is not borne out in practice. Although spatial averaging of the incident wave plays a role, the angle dependence of the edge wave interactions referred to above and the spatial averaging of these interactions over the fibre core diameter must also be considered (Krücker *et al.*, 2000). These additional interactions mean that the directional response does not in general follow the first order Bessel function that describes the directivity of an ideal receiver (Eq. 19.6), which is determined solely by the spatial average of the incident wavefront over its sensitive area. As a consequence, estimates of the effective radius obtained by fitting Eq. 19.6 to the measured directional response generally differ from the physical dimensions of the fibre core diameter. The discrepancy is particularly evident at low frequencies where the effective radius tends to be significantly larger than the fibre core radius. This has been studied in Krücker *et al.* (2000), in which the same model used to simulate the frequency response described in the previous section was employed to simulate the directivity. Figure 19.17 shows the measured directional response at three different frequencies for an optical fibre of 100 µm core diameter and 140 µm outer diameter. The response is almost omnidirectional at 2 MHz, becoming increasingly directional with increasing frequency. No directivity data are available for a single mode fibre, however, which would be expected to exhibit lower directional sensitivity.

---

[1] In this context, 'spatial averaging' refers to the spatial integral of the incident field over the fibre core diameter. This is distinct from the specific use of the term 'spatial averaging' in Section 2.4 which refers to the blurring of a measured acoustic field distribution due to the finite aperture of the hydrophone.

Temperature sensitivity: Since the refractive indices of water and glass are temperature dependent, it should be possible to measure ultrasound induced

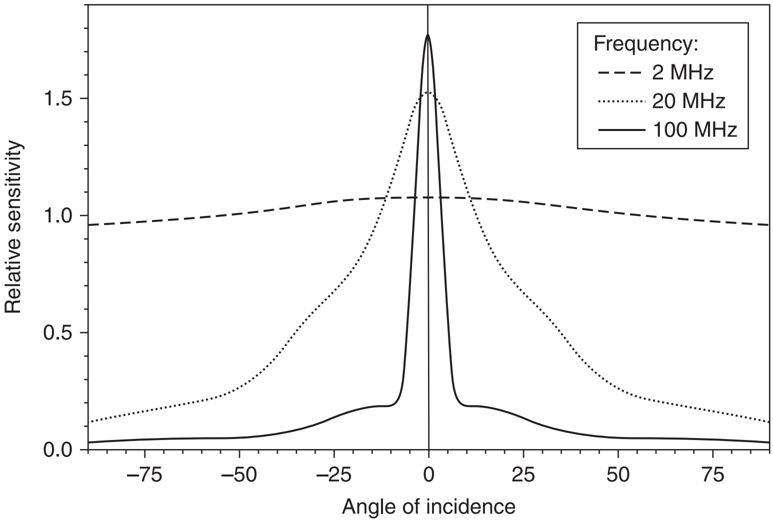

19.17 Measured directional response of an Eisenmenger type FOH for an optical fibre of 100 µm core diameter and 140 µm outer diameter. Measured data supplied by Dr Rainer Pecha of RP Acoustics (personal communication).

temperature changes. However, no reports of this capability have appeared in the scientific literature to date.

19.4.3 Fabry Perot polymer film fibre-optic hydrophone

The Fabry Perot polymer film hydrophone is based upon the interferometric detection of acoustically induced changes in the optical thicknesses of a thin-film sensing structure (Beard and Mills, 1997; Yasuto and Nakamura, 1999; Beard *et al.*, 2000; Morris *et al.*, 2009). The latter is a Fabry Perot interferometer (FPI) comprising a polymer film spacer sandwiched between a pair of mirrors. In one embodiment (Morris *et al.*, 2009) the FPI is deposited on to the tip of a single mode optical fibre as follows. First, a thin (~20 nm) partially reflective gold coating is evaporated on to the cleaved tip of the fibre. A Parylene C polymer film layer, approximately 10 µm thick, is deposited under vacuum directly from the gas phase on to the gold coating. A second gold coating that is fully reflective is then deposited on top of the spacer. Light emerging from the core of the optical fibre is incident on the FPI and multiply reflected back and forth between the two mirrors as shown in Fig. 19.18(a). An incident acoustic wave produces a strain which alters the physical thickness and refractive index of the polymer film spacer. The optical path-length taken by the reflected optical fields, and thus the phase difference between them, is therefore modulated, producing a corresponding variation in the total optical power reflected from the FPI which is transmitted back down the fibre for detection by a photodiode.

The optical system required to interrogate the sensor is conceptually similar to that depicted in Fig. 19.14. It comprises a laser source and an optical fibre coupler

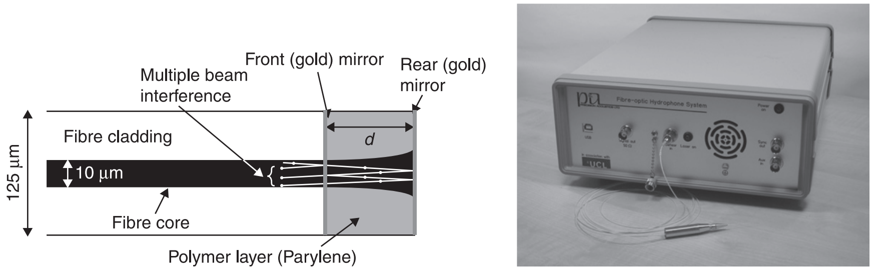

(a) (b)

19.18 Fabry Perot polymer film hydrophone. (a) Schematic of FPI sensing structure deposited on to the tip of a single mode optical fibre. Reproduced with permission from Morris *et al*. (2009). (b) Photograph of optical interrogation unit into which connectorised optical fibre downleads are inserted. (Photograph courtesy of Precision Acoustics Ltd, Dorchester, UK.)

to deliver the laser light to the tip of the fibre and re-direct the light reflected from the FPI on to a photodiode-transimpedance detector unit. However, unlike the Eisenmenger FOH, a tunable laser source and active control system are required in order to optimally bias the FPI, as discussed in the following section. The acoustic performance characteristics also differ significantly from the Eisenmenger FOH. The interferometric nature of the transduction mechanism provides a detection sensitivity that is at least an order of magnitude higher, albeit with a lower upper limit of detection. Broadband kilopascal NEPs are readily achievable, comparable to those of small aperture piezoelectric PVDF hydrophones. This significantly extends the range of measurement applications to include the characterisation of diagnostic as well as therapeutic medical ultrasound fields, measurements of ultrasonic NDT devices and general piezoelectric transducer characterisation. The bandwidth, however, is somewhat lower due to the larger dimensions of the sensing region, which is defined by the thickness of the Parylene spacer and the 10 μm fibre core diameter. For a 10 μm spacer, the bandwidth extends to approximately 60 MHz (–3 dB). Since no light is transmitted through the FPI and modest laser powers of a few mW are sufficient, the safety issues of the Eisenmenger FOH are avoided. A further advantage of this type of FOH is that it can measure temperature with high sensitivity (<0.1 K resolution) as well as acoustic pressure. The sensor fabrication process is more complex compared with the Eisenmenger FOH, which can simply be re-cleaved if damaged. However, the use of vacuum deposition methods permits batch fabrication of the sensors, enabling low unit cost to be achieved, allowing inexpensive replacement in the event of damage. The system hardware is not excessively complex and has been engineered as a practicable field usable instrument which is commercially available through Precision Acoustics Ltd.

Transduction mechanism: The variation in the optical power P_r reflected from the FPI as a function of phase ϕ is termed the phase interferometer transfer function (ITF). For an ideal FPI illuminated by a collimated beam this is given by the Airy function and comprises a periodic series of reflectance minima, one of which is depicted in Fig. 19.19. The phase shift ϕ between successively interfering optical fields is given by

$$\phi = \frac{4\pi nl}{\lambda} \qquad [19.13]$$

where n and l are the refractive index and thickness of the polymer film spacer respectively and λ is the optical wavelength. In order to make an acoustic measurement, the laser wavelength is adjusted so that $\phi = \phi_b$, where ϕ_b is the phase corresponding to the maximum value of the derivative of the ITF. At this wavelength, the sensitivity and linearity are at a maximum and the FPI is said to be optimally biased. Under these conditions, a small acoustically induced phase shift $d\phi_b$ can be regarded as being linearly converted to a corresponding change in the reflected optical power, dP_r, as illustrated in Fig. 19.19.

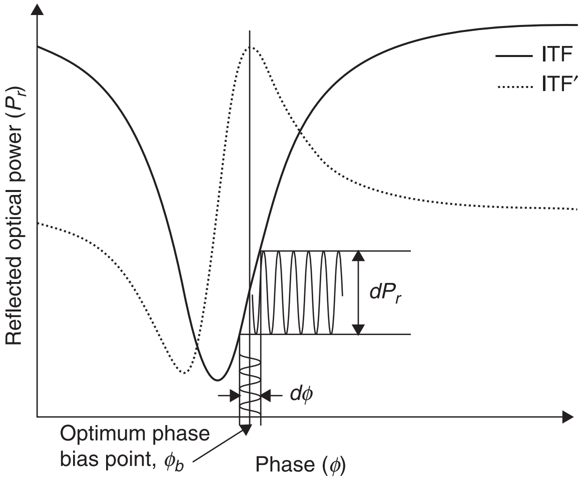
Reflected optical power (P_r)
ITF
ITF′
dP_r
$d\phi$
Optimum phase bias point, ϕ_b
Phase (ϕ)

19.19 Fabry Perot polymer film hydrophone transduction mechanism. The phase interferometer transfer function (ITF) and its first derivative ITF′ are shown. For the linear detection of a small acoustically induced phase modulation $d\phi$, the FPI is biased at the peak value of ITF′, ϕ_b, by tuning the laser wavelength. Reproduced with permission from Morris *et al.* (2009).

The sensitivity, the reflected optical power modulation per unit acoustic pressure, at ϕ_b is given by

$$\frac{dP_r}{dp} = \frac{dP_r}{d\phi}\frac{d\phi}{dp} \qquad [19.14]$$

where p is the acoustic pressure. $dP_r/d\phi$ is the derivative of the ITF at ϕ_b and is termed the optical phase sensitivity. It is dependent on the incident optical power and the finesse of the FPI, which provides a measure of the width of the reflectance minimum in Fig. 19.19. The finesse is in turn defined by the mirror reflectivities and the phase dispersion due to the divergence of the incident beam and non-uniformities in the spacer thickness. $d\phi/dp$ is termed the acoustic phase sensitivity and represents the magnitude of the optical phase shift produced per unit pressure. The optical phase shift arises from a change in the optical thickness of the spacer and may be caused by two mechanisms, a change in physical thickness dl or a change in refractive index dn. In general, the acoustic phase sensitivity can therefore be written as

$$\frac{d\phi}{dp} = \frac{4\pi}{\lambda}\left(n_0\frac{dl}{dp} + l\frac{dn}{dp}\right)P_l(k) \qquad [19.15]$$

where n_0 is the refractive index in the absence of an incident acoustic field and $P_l(k)$ is a frequency dependent modifying term that represents the normalised frequency response and depends on the geometry, structure and material properties of the fibre tip. For Parylene C, the change in refractive index *dn* can be neglected (Cox and Beard, 2007) so Eq. 19.15 reduces to

$$\frac{d\phi}{dp} = \frac{4\pi n_0}{\lambda}\frac{l}{E}P_l(k) \qquad [19.16]$$

where E is the Young's modulus of the spacer. Thus the lower the Young's modulus (and hence the more compliant the spacer) the higher the sensitivity. Sensitivity is also proportional to spacer thickness providing $\lambda_a >> l$.

As well as measuring pressure, the sensor can detect temperature changes. When subjected to a change in temperature, the optical thickness of the FPI spacer will change due to thermal expansion and the change in refractive index. In principle, the resulting phase shift could be recovered by optimally biasing the FPI and measuring the reflected optical power modulation as described above. However, for a polymer spacer, even a relatively small temperature change of only a few degrees will induce a phase shift that exceeds the phase range over which the ITF is linear around the optimum bias point ϕ_b. As well as compromising the linearity of the temperature measurement, a phase shift of this magnitude will shift the bias point to the extent that it no longer corresponds to the peak derivative of the ITF, thus reducing the acoustic sensitivity. To avoid these difficulties an alternative interrogation scheme which relies on tracking the optimum bias wavelength as the temperature varies is employed (Morris *et al.*, 2009). This requires initially tuning the laser output to the optimum bias wavelength and thereafter continuously monitoring the reflected optical power P_r. As soon as P_r changes due to a temperature-induced phase shift, the laser wavelength is immediately re-tuned so as to return P_r to its initial value. The amount the laser wavelength has to be retuned is proportional to the thermally induced optical thickness change and therefore provides a direct measure of the temperature change. By continually re-adjusting the laser wavelength to maintain a constant P_r, the thermally induced shift in the optimum bias wavelength, and therefore the temperature change, can thus be tracked over time. Providing the laser wavelength is rapidly re-tuned before the thermally induced phase shift becomes appreciable, the system will always be operating at, or close to, ϕ_b, thus allowing an acoustic measurement to be made. In this way ultrasound waveforms can be acquired at the same time that the temperature is being monitored.

The temperature sensitivity is dependent on several factors: the thickness of the Parylene spacer and its thermo-mechanical and thermo-optic properties. The phase change, $d\phi$, induced by a temperature change, dT, can be written as

$$\frac{d\phi}{dT} = \frac{4\pi l}{\lambda}\left(n_0\alpha + \frac{dn}{dT}\right), \qquad [19.17]$$

where α is the coefficient of thermal expansion and n_0 is the refractive index in the absence of dT. Unlike the acoustic phase sensitivity, the change in refractive index cannot be neglected as it produces a phase shift that is comparable to that produced by the change in physical thickness. The optical phase sensitivity $dP_r/d\phi$ also influences the thermal sensitivity since it defines the minimum detectable reflected power variation, which is used to determine when it is necessary to re-tune the laser to maintain a constant P_r.

Acoustic detection sensitivity: As discussed above, the detection sensitivity is a function of the elastic and elasto-optic properties of the spacer – the more compliant the spacer, the greater the acoustically induced phase shift. In addition, the slope of the phase ITF, a function of the mirror reflectivities, the beam divergence and the uniformity of the spacer, plays a critical role in defining sensitivity – the higher the ITF slope at ϕ_b the greater the sensitivity. Other factors include the relative intensity and phase noise characteristics of the interrogation laser and the photodiode-transimpedance amplifier noise characteristics. An NEP (rms) of 5 kPa over a 20 MHz measurement bandwidth,[2] limited by the phase noise of the interrogation laser, has been reported (Morris *et al.*, 2009). This is comparable to the NEP of PVDF piezoelectric needle and membrane hydrophones (see Sections 19.3.2 and 19.3.3). Furthermore, by using low noise external cavity tunable lasers to interrogate the sensor and dielectric mirrors to form the FPI, which exhibit significantly lower optical absorption than gold mirrors, there is the potential to achieve even higher sensitivities – sub-kilopascal NEPs have been demonstrated with free space illuminated FPIs fabricated in this way (Zhang *et al.*, 2008).

Linearity: Assuming the elastic limits of the polymer spacer are not exceeded, the upper limit of linear acoustic detection is determined by the shape of the ITF around the bias point ϕ_b. If the acoustically induced phase shift is sufficiently large that the gradient of the ITF can no longer be considered constant, the FPI output will not be linear. Linearity is thus defined as the phase range over which the gradient of the ITF at the bias point is constant within specified limits, 5% or 10% typically. The typical linear pressure range (to within 10%) is –6 MPa to 10 MPa (Morris *et al.*, 2009) – the limits are not the same for positive and negative pressures because the ITF is not symmetrical about the bias point. Although adequate for the measurement of most diagnostic medical ultrasound fields, this pressure range is insufficient for the characterisation of very high amplitude fields such as those produced by shockwave sources. However, there is considerable flexibility in the design of the FPI that allows the linear range of detection to be extended, albeit at the cost of reduced detection sensitivity. One approach is to reduce the reflection coefficients of the mirrors in order to lower the FPI finesse and thus increase the linear phase range. Another is to reduce the magnitude of the acoustically induced phase shift by decreasing the spacer thickness or using a less compliant material to increase the upper limit of detection.

---

[2] Note that in Morris *et al.* 2009a the peak rather than rms NEP value is quoted. This is because the peak NEP provides a more realistic indication of the smallest signal that can be detected when measuring broadband signals in the time domain – for example, when using an oscilloscope. However, the quoted NEPs of most other FOHs in the literature appear to be rms values which are approximately a factor of 3 lower than the peak NEP. Thus to facilitate comparison between different FOHs, rms NEP values are quoted throughout in this chapter.

Bandwidth and frequency response: Figure 19.20 shows examples of the measured frequency responses of two FP polymer film FOHs with different fibre tip geometries. One is a standard cleaved flat fibre tip on to which the FPI is deposited. The other is one in which the edges of the fibre tip are rounded to provide a hemispherical geometry. The bandwidth in both cases extends beyond 50 MHz, limited ultimately by the spatial averaging imposed by the dimensions of the illuminated volume of the FPI. As Fig. 19.20 shows, the frequency response of the flat fibre tip is non-uniform with several irregularly spaced features. These features are a consequence of a variety of acoustic interactions which have been investigated by Morris (2008) using a finite difference elastic wave model (AFiDS, AMH Consulting, Poole, UK) to simulate the frequency response. In common with the Eisenmenger type FOH, the nature of the frequency response is a consequence of the interaction of the incident plane wave, its reflection from the fibre tip and the diffracted edge waves propagating across the fibre endface. However, unlike the Eisenmenger FOH, in which the only edge wave component that significantly contributes to the sensor output is that propagating in the water adjacent to the fibre tip, edge waves propagating in both the polymer film spacer and the fibre have to be considered as well. In addition, since these waves are propagating in solid media, both shear and longitudinal edge wave components are produced. Furthermore, Rayleigh waves are produced at the FPI–water and FPI–fibre interfaces. These different wave components propagate across the fibre tip at different wave speeds and arrive at the core where they interfere with each other, the incident plane wave and its reflection from the fibre tip. The frequency response is therefore composed of the superposition of a number of damped oscillations, at least one for each edge wave–plane wave interaction and one for each interaction between different edge wave components. As Fig. 19.20 illustrates, this results in a complicated aperiodic response that is rather less amenable to intuitive interpretation than the frequency response of the Eisenmenger FOH. The maximum at 22 MHz has, however, been identified as being most likely a resonance associated with the Rayleigh wave propagating along the FPI–water interface (Morris, 2008). Note that, although the frequency response of the flat tipped sensor in Fig. 19.20 appears to be less uniform than that of the 100 μm core diameter fibre FOH shown in Fig. 19.16, this is a consequence of the differing core diameters – 10 μm versus 100 μm. The increased spatial averaging due to the larger core diameter of the Eisenmenger FOH bandlimits the edge waves, thus suppressing the diffraction related features and producing a more uniform response. Although at first sight this appears to be desirable, the larger core

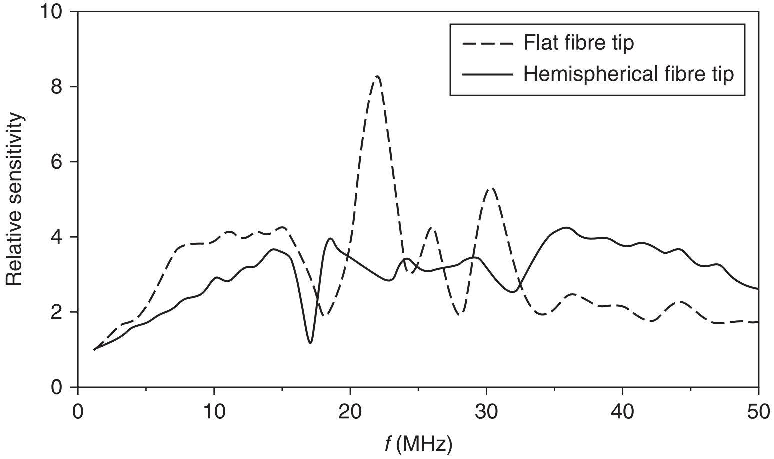

19.20 Measured frequency response of the Fabry Perot polymer film fibre-optic hydrophone for flat and hemispherical fibre tip geometries.

diameter has the disadvantage of increasing directional sensitivity. As Fig. 19.16 shows, if the core diameter is reduced to 10 µm the Eisenmenger FOH produces a response that is comparable in terms of non-uniformity to that of the flat fibre tip polymer film FOH shown in Fig. 19.20.

To achieve a more uniform frequency response requires a fibre tip geometry which either suppresses the edge wave components or shifts their influence outside the frequency range of interest. The latter is achievable by reducing the outer diameter of the fibre whilst the former approach has been demonstrated using a fibre in which the tip is rounded to produce a hemispherical geometry (Morris, 2008). The frequency response of this design is shown in Fig. 19.20. Compared with the conventional flat tip FOH, it is evident that it exhibits a significantly more uniform response.

Directivity: The 10 µm core diameter of the optical fibre represents, to a first approximation, the lateral dimension of the acoustically sensitive region. This suggests that, for frequencies in the tens of MHz range, spatial averaging will be minimal, thus providing a near omnidirectional response. However, in common with the Eisenmenger FOH, this expectation is not borne out in practice because the directional response is not defined solely by spatial averaging over the illuminated region of the FPI. This is in part because the sensor output depends on the differential displacement of the two gold mirrors. At the critical angles for shear and longitudinal wave transmission into the polymer spacer, the wavefronts propagate horizontally within the spacer (Cox and Beard, 2007). At these angles of incidence, there is zero displacement of the mirrors and the response falls to a minimum irrespective of spatial averaging considerations. In addition, the directional response is influenced by the interaction of the multiple edge wave components discussed in the previous section. These influences, combined with spatial averaging, result in complex frequency dependent features in the directional response. As a consequence, estimates of the effective radius obtained by fitting Eq. 19.6 to the measured directional response do not in general equal the dimensions of the illuminated region. This is particularly so at low frequencies when spatial averaging is negligible and critical angle and edge wave effects dominate. At higher frequencies spatial averaging can lead to the response decreasing to zero before other influences become significant, resulting in reasonable parity between the lateral dimensions of the illuminated region and the effective radius.

Figure 19.21 shows the measured directional response up to a frequency of 20 MHz. For frequencies up to 10 MHz, the response is well behaved with the sensitivity decreasing with increasing angle and the variation across the angular range increasing with increasing frequency. At 10 MHz, the sensitivity drops by approximately 6 dB for a 90° angle of incidence. Above 10 MHz the behaviour changes significantly as a consequence of the above mentioned edge wave and critical angle effects. The measurement at 13 MHz shows that the maximum sensitivity is no longer obtained at normal incidence, but at approximately ±45°. At 15 MHz, the sensitivity appears to oscillate as a function of angle, but with a maximum drop in sensitivity of just 1.8 dB across the full 180° range. As the

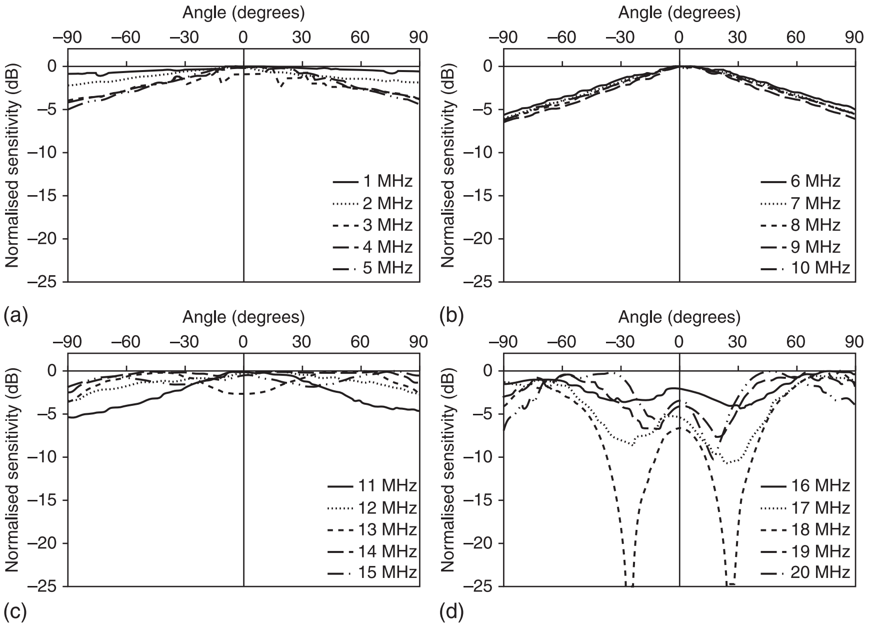

19.21 Measured directional response of Fabry Perot polymer film fibre-optic hydrophone at (a) 1–5 MHz, (b) 6–10 MHz, (c) 11–15 MHz, and (d) 16–20 MHz. Reproduced with permission from Morris *et al.* (2009).

frequency is increased to 18 MHz, two large drops in sensitivity of greater than 25 dB appear in the response at approximately ±30°. At 20 MHz, the nulls are reduced in magnitude but occur closer to normal incidence. Nevertheless, these results show that, for frequencies less than 15 MHz, a well behaved angular response with a lower directional sensitivity than most piezoelectric hydrophones is obtained.

Thermal characteristics: The temperature measurement resolution or noise equivalent temperature change is approximately 0.1°C. The upper limit of linear detection is 70 °C and is limited by the glass transition temperature of Parylene C beyond which irreversible changes take place. The intrinsic thermal response time is governed by the time it takes for heat to diffuse across the Parylene C spacer and is approximately 1ms, although in practice the acquisition electronics and the laser tuning speed limit the maximum measurable rate of temperature change to approximately 600 °C.s^{-1}. Figure 19.22 shows measurements of the time course of the temperature changes produced by embedding the FOH in a tissue mimicking phantom based on an oil–gelatin emulsion and ensonifying with the output of an HIFU transducer at different intensities. To provide a reference, a thin-film thermocouple (TFT) was also embedded within the phantom. Good agreement between the outputs of both devices is evident. This suggests that the FOH does not suffer from viscous self-heating measurement errors since the TFT is immune to these. This is in contrast to probe type thermocouples which are commonly used in studies of HIFU heating.

The arrangement shown in Fig. 19.22(a) was also used to demonstrate the ability of the system to conduct simultaneous acoustic and thermal measurements.

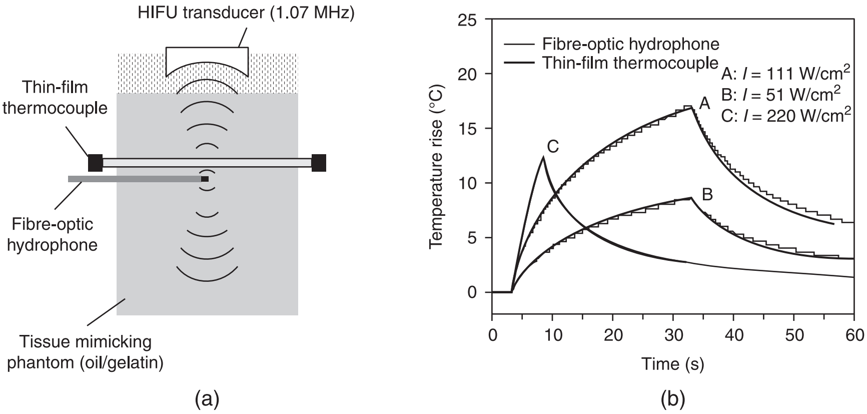

19.22 Measurements of heating induced by a HIFU field. (a) Experimental setup showing relative locations of thin-film thermocouple and fibre-optic hydrophone embedded in tissue mimicking phantom. (b) Comparisons of temperature time courses measured by thin-film thermocouple and FOH for three different HIFU intensities.

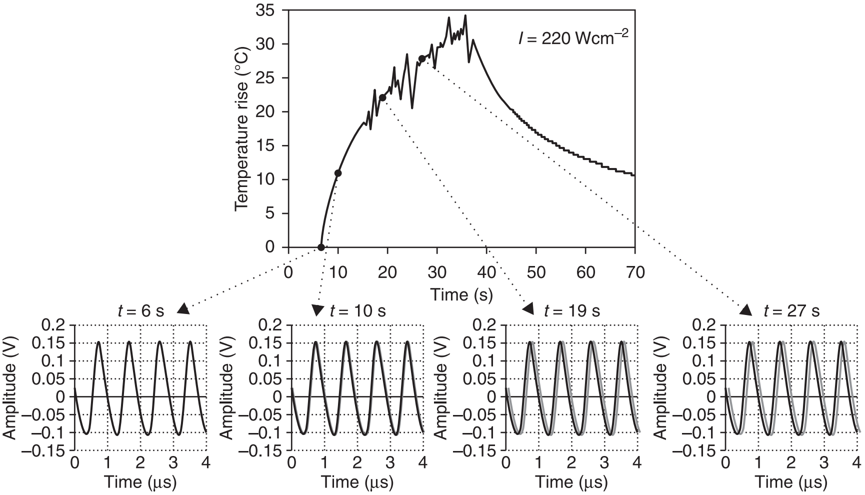

19.23 Simultaneous acquisition of a temperature–time curve (top) and acoustic waveforms (lower row) captured at four different times during a 30 s insonation period. For the acoustic waveforms obtained at $t = 10$, 19, and 27 s, the waveform captured at $t = 6$ s (grey line) is also shown in order to illustrate the phase shift due to the thermally-induced change in sound speed. Reproduced with permission from Morris *et al.* (2009).

The results can be seen in Fig. 19.23, which shows a temperature–time curve for a 30 s insonation with an acoustic intensity (I_{spta} – spatial peak, temporal average intensity) of 220 W.cm^{-2} and several acoustic waveforms taken at different times during the insonation period.

19.4.4 Multilayer dielectric fibre-optic hydrophone

The multilayer dielectric fibre-optic hydrophone is based upon the interferometric detection of acoustically induced changes in the optical thickness of a thin-film multilayer structure (Koch, 1996; Wilkens and Koch, 1999; Weise *et al.*, 2002). The sensing structure, shown in its most general form in Fig. 19.24, is composed of a series of thin dielectric films of alternating high and low refractive indices sputtered on to the tip of a single mode fibre. Acoustically induced changes in the optical thickness of each layer modulate the light reflected from each layer interface, producing a change in the total optical power reflected from the structure. The interferometric nature of the transduction mechanism means that this type of sensor has many similarities to the FP polymer film FOH.

An important difference, however, lies in the physical properties of the materials used to form the sensing layers. Instead of a relatively thick (~10 μm) highly compliant polymer spacer sandwiched between a pair of infinitesimally thin

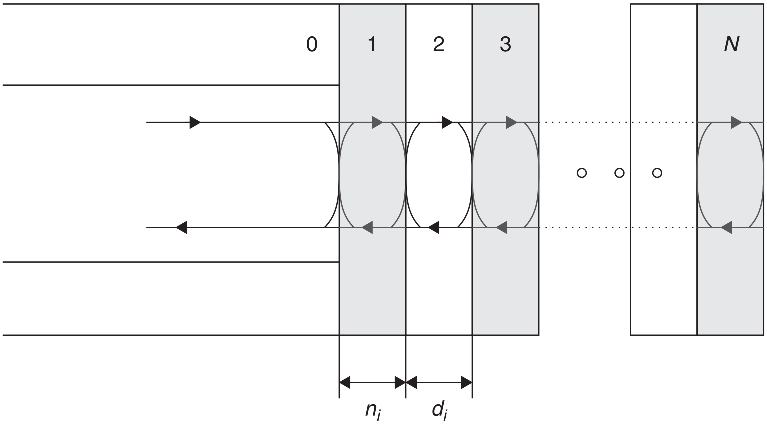

19.24 Schematic of sensing structure of multilayer dielectric fibre-optic hydrophone in its most general form. Multiple layers of alternating high and low refractive indices form the sensing structure. Figure reproduced with permission from Wilkens and Koch (1999).

metallic mirrors, a number of thin (<100 nm) alternating layers of a pair of hard dielectric materials of different refractive indices n such as silicon dioxide (SiO_2, $n = 1.48$) or niobium pentoxide (Nb_2O_5, $n = 2.3$) form the sensing structure. As well as being composed of materials of significantly different physical properties, the total thickness of the sensing structure is typically around 2 µm and thus significantly less than that of the FP polymer film FOH. The combination of the lower compliance of the structure and its smaller interaction length results in a smaller acoustically induced phase shift for a given acoustic pressure compared with that produced in the FP polymer film FOH. This leads to lower sensitivity but a higher upper limit of linear detection. Secondly, the smaller thickness and the higher sound speed of the dielectric materials used compared with polymers results in wider bandwidths, typically several hundred MHz. In common with the FP-FOH, measurements of temperature change can be made (Wilkens, 1999) although the measurement of ultrasound-induced heating has not been demonstrated. Also in common with the FP polymer film FOH, the use of vacuum deposition techniques enables the sensors to be batch fabricated at low unit cost. The optical architecture required to interrogate the sensor is essentially that depicted in Fig. 19.14. A tunable interrogation laser source can be used to bias the sensor, as with the FP-FOH, and offers the greatest flexibility, although, as discussed in the next section, a fixed wavelength laser can also be used in some circumstances.

Transduction mechanism: As illustrated in Fig. 19.24, the sensing structure is composed of a number of alternate layers of high and low refractive index. Light incident on the structure is multiply reflected from the two sides of each layer due to the refractive index mismatch at each interface. An incident acoustic wave produces a strain which alters the physical thickness and refractive index of each layer. This modifies the optical pathlength taken by the optical fields reflected from each interface and hence the total optical power reflected from the entire structure. A variety of designs utilising different layer thicknesses and numbers of layers have been explored. The simplest comprises a single Nb_2O_5 layer approximately 100 nm thick sputtered on to the tip of a single mode fibre (Koch, 1996). In essence, this layer acts as a low finesse FPI with the refractive index mismatches on either side of it forming the mirrors of the FPI. It thus operates in much the same way as the FP polymer film FOH except that, being of low finesse, the ITF is cosinusoidal rather than a series of sharp reflectance minima. Higher sensitivity can be obtained by creating a high finesse FPI. In this case, the structure comprises a central spacer sandwiched between a pair of stacks composed of alternating high and low refractive index layers. These stacks act as highly reflective mirrors, thus making the entire structure functionally equivalent to an FPI. The ITF, an example of which is shown in Fig. 19.25 for a 15-layer system, is characterised by a sharp reflectance minimum, the peak derivative of which defines the optimum bias point ϕ_b. The FPI can be biased at ϕ_b by tuning the laser wavelength as described in Section 19.4.3. Alternatively, sputtering techniques can provide sufficiently accurate thickness control of the dielectric layers that the optimum bias wavelength can be set to coincide with that of a fixed wavelength laser source, thereby avoiding the need for a tunable laser system. The success of this is inevitably contingent on the accuracy of the deposition process. It also requires that the temperature and static pressure remain constant during operation so that the optimum bias wavelength and hence the sensitivity does not change.

Another design comprises a series of alternating high and low index layers, each of the same optical thickness. This produces a rather different ITF shape

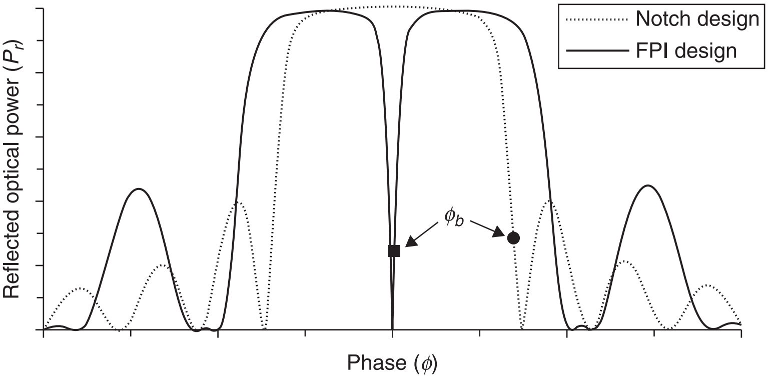

19.25 Multilayer dielectric fibre-optic hydrophone transfer functions for 15 layer notch and FPI designs (adapted from Wilkens and Koch, 1999). ϕ is the phase shift due to the optical thickness ($n_i d_i$) of each constituent layer. In the case of the FPI design the spacer thickness is $2n_i d_i$. ϕ_b is the bias point for each design. Reproduced with permission from Wilkens and Koch (1999).

from that of FPI design, comprising a broad notch shaped central maximum as shown in Fig. 19.25. The peak derivative and thus the bias point ϕ_b now lies on the edge of the notch. It has, however, been shown that for the same number of layers this design is not as sensitive as the FPI design and requires a smaller manufacturing tolerance in the optical thickness of each layer (Wilkens and Koch, 1999). For these reasons, the FPI configuration tends to be the most commonly used design.

Whilst the transduction mechanism is conceptually similar to that of the FP polymer film FOH, there is a significant difference between the two types. With the FP polymer film FOH, only acoustically induced changes in the physical thickness of the spacer contribute significantly to the output and any change in refractive index can be neglected. This is not the case with the multilayer dielectric type FOH and the second term in the bracket in Eq. 19.15 must be considered. The change in refractive index dn_i of the i_{th} layer is given by (Weise *et al.*, 2002)

$$dn_i = -\frac{1}{2}n_i^3\left(p_{12i}\left(\frac{dw}{dz}\right)_i + (p_{11i} + p_{12i})\left(\frac{du}{dr}\right)_i\right) \qquad [19.18]$$

where p_{12} and p_{11} are the strain-optic coefficients and w and u are the axial and radial strains. Note that, unlike the FP polymer film FOH, the need to consider *dn* requires that radial as well as axial strain components have to be accounted for (Weise *et al.*, 2002). This in turn impacts on the frequency response, as discussed below. Another difference, albeit one that does not significantly influence performance, is that, for the multilayer FPI design, the optical thickness change of the layers that form the mirrors as well as the central spacer contributes to the acoustically induced phase shift. This can be equivalently described by a system comprising two infinitesimally thin mirrors separated by a slightly thicker spacer – the extra spacer thickness representing the phase shift due to the optical thickness change of the mirror layers (Wilkens, 2001). By contrast, for the FP polymer film FOH, only the change in the thickness of the spacer need be considered.

Acoustic detection sensitivity: The factors that define sensitivity are broadly those that affect the FP polymer film FOH with the exception that elasto-optic properties of the dielectric layers also play a role. In general, the acoustically induced optical thickness change and hence phase shift is significantly smaller than observed with the FP polymer film FOH. This is due to the order of magnitude higher elastic modulus of hard dielectric materials such as SiO_2 and Nb_2O_5 compared with polymers such as Parylene C. However, for the preferred FPI multilayer dielectric design, the overall sensitivity is not proportionately lower because a higher finesse, and thus a higher ITF peak derivative, can be achieved – i.e. the reduced conversion of acoustic pressure to strain is partially compensated for by the higher conversion of optical thickness change to reflected optical power modulation.

An NEP of 50kPa over a measurement bandwidth of 50 MHz has been reported (Klann and Koch, 2005a) in contrast to the 5 kPa of the FP polymer film FOH

(Morris *et al.*, 2009). In general the FP polymer film FOH is always likely to have a higher sensitivity than the multilayer dielectric type. In principle, the finesse of the latter can be increased to compensate for the lower compliance of the hard dielectric spacer – there is scope to do this because the thickness uniformity of sputtered dielectric materials is better than that of Parylene C, enabling a higher quality FPI to be fabricated. However, there is a practical limit as to how much the finesse can be increased before the phase noise due to the finite linewidth of the laser limits the achievable NEP. In addition, an arbitrarily high finesse cannot be achieved due to limitations associated with the deposition of the dielectric layers.

Linearity: As discussed in Section 19.4.3, this is determined in part by the phase range over which the ITF is linear and the acoustic phase sensitivity (the phase shift produced in response to unit pressure). Given that the finesse of the FPI design is higher than that of the FP polymer film FOH, the maximum linear phase range is correspondingly lower. However, because the acoustic phase sensitivity is around an order of magnitude lower due to the higher Young's modulus of hard dielectric materials and the smaller thickness of the sensing structure, the upper limit of linear acoustic detection is significantly higher, typically approximately 50 MPa (Wilkens, 2003a).

Bandwidth and frequency response: Bandwidth is limited by the dimensions of the acoustically sensitive region, which is defined by the fibre core diameter and the thickness of the sensing structure. Given that the latter is typically less than 2 μm and the sound speed in hard dielectrics is of the order of 5000 m s^{-1}, bandwidths extending to several hundred MHz can readily be achieved. As with the FP polymer film FOH, the frequency response is defined by the interaction of the incident plane wave, its reflection from fibre endface and the diffracted edge wave components originating from the perimeter of the dielectric sensing structure. However, the number of the interactions is lower than that of the FP polymer film FOH. This is because the acoustic properties of the dielectric layers that form the sensing structure are similar to those of the fused silica of the fibre. Thus, there is only one rather than two diffracting boundaries and only one Rayleigh wave is generated – that propagating at the sensor–water interface. The frequency response is therefore more uniform and exhibits fewer features than the FP polymer film FOH. This can be seen in Fig. 19.26, which shows a comparison between the measured frequency response and that predicted by a FEM simulation for the FPI design (Weise *et al.*, 2002). Most notable is the peak at 23 MHz, which is attributed to the above mentioned Rayleigh wave. This wave is generated at the interface between the top surface of the dielectric structure and the surrounding water and reflected back and forth across the fibre endface. That it is so pronounced arises in part from the contribution of the elasto-optic effect. The Rayleigh wave-induced radial strain component which contributes to the change in the refractive index is of opposite sign to the longitudinal strain, so the thickness modulation and elasto-optic effect reinforce each other. The relative contribution of the two effects on the 23 MHz peak depends on the values of the strain optic coefficients

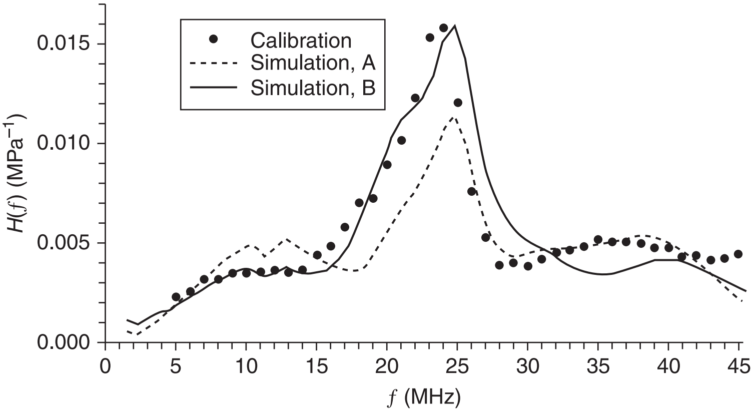

19.26 Measured and simulated frequency response of multilayer dielectric fibre-optic hydrophone compriwsing 19 alternating layers of SiO_2 and Nb_2O_5. Simulation A: $p_{11i} = 0.121$, $p_{12i} = 0.270$ (SiO_2), $p_{11i} = 4.73 \times 10^{-3}$, $p_{12i} = 1.28 \times 10^{-2}$ (Nb_2O_5). Simulation B: $p_{11i} = 0.121$, $p_{12i} = 0.270$ (SiO_2), $p_{11i} = 0.121$, $p_{12i} = 0.270$ (Nb_2O_5). Figure from Weise *et al.* (2002a).

used. This is illustrated in Fig. 19.26, which shows the simulated frequency response for two different values of p_{11i} and p_{12i}.

Directivity: Neither experimental measurements nor numerical simulations of the directional response of the multilayer dielectric FOH have been reported to date. However, in common with the FP polymer film FOH, the influence of edge waves and the differential displacement nature of the transduction mechanism suggest that it will not correspond to that of a purely spatial averaging receiver. Estimates of the effective radius are therefore unlikely to match that of the fibre core radius. The directional response of a free-space planar version of this type of sensor (in which the multilayer structure is deposited on to a glass plate) has been reported (Wilkens, 2003b). However, this arrangement is not representative of the FOH as the large lateral dimensions of the plate mean that edge waves are not produced.

Thermal characteristics: In principle, temperature measurements can be made by the detection of thermally induced changes in the optical thicknesses of the multilayer dielectric layers in much the same way as they are with the FP polymer film FOH. Although measurements of ultrasound-induced heating have not been reported, the characterisation of laser-induced thermal transients has been studied (Wilkens, 1999). The measurement was made by optimally biasing the FPI and measuring the reflected optical power modulation rather than the bias point tracking method described in Section 19.4.3. The reported temperature resolution was 0.4 °C.

19.4.5 Interferometric displacement fibre-optic hydrophone

Interferometry can also be used to detect acoustically induced displacements of the tip of an optical fibre. In this approach, the fibre downlead forms one arm of a receiving interferometer and the change in its length is detected interferometrically. Several approaches have been explored, the simplest being a scheme that employs a Michelson homodyne receiving interferometer (Koch *et al.*, 1997), shown schematically in Fig. 19.27. This provides a measurement proportional to the fibre tip displacement which is then differentiated to obtain the pressure. Another approach employs a more sophisticated heterodyne receiving interferometer to obtain a measurement of the velocity of the fibre tip which is then taken to be proportional to the pressure (Koch, 1999). Note that in both cases the conversion of the measurand (displacement or velocity) to pressure requires the far field assumption of a plane wave, which may not always apply, particularly in highly heterogeneous field distributions.

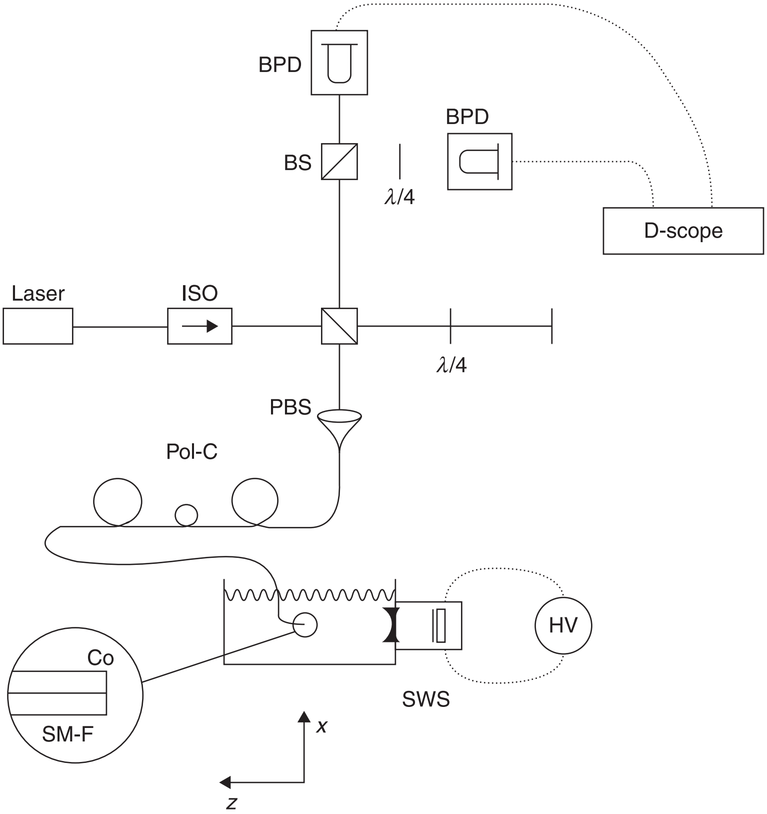

19.27 Interferometric displacement fibre-optic hydrophone. PBS, polarising beamsplitter; ISO, optical isolator; BS, beam splitter; BPD, balanced photodetector; D-scope, digitising oscilloscope; λ/4, quarter waveplate; Pol-C, polarisation controller; SWS, shockwave source; Co, metallic coating; SM-F, single mode fibre; HV, high voltage supply. Reproduced from Koch *et al.* (1997) with permission.

This type of hydrophone provides high acoustic detection sensitivity (1 kPa over a 20 MHz measurement bandwidth; Koch and Jenderka, 2008), bandwidths in excess of 50 MHz (Koch *et al.*, 1998) and a frequency response that is similar to that of the multilayer dielectric FOH shown in Fig. 19.26 (Koch *et al.*, 1998). The directional response, however, has not been reported. Neither has the upper limit of linear detection, although measurements of a shockwave with a peak pressure in excess of 70 MPa have been reported (Koch *et al.*, 1998). Despite offering a high level of acoustic performance, this type of FOH is not currently commercially available, a consequence perhaps of its greater technical complexity compared with other FOH systems.

19.4.6 Intrinsic fibre-optic hydrophones

A variety of so-called intrinsic fibre-optic sensors in which a length of the optical fibre itself is used as the transducing element have been explored for ultrasound sensing applications. Interferometric sensors of this type rely on the detection of acoustically induced strains that change the length and refractive index of the fibre and hence the phase of the light guided within it (De Paula *et al.*, 1983). The practical implementation of such an approach requires making the sensing fibre form one arm of a fibre interferometer in order to convert the acoustically induced phase shifts to an intensity modulation. Polarimetric devices rely on exploiting acoustically induced birefringence to modify the state of polarisation of the light guided within the fibre (De Paula *et al.*, 1982; Wang *et al.*, 2011). To detect the change in polarisation, the light emerging from the distal end of the fibre is passed through some form of polarisation, sensitive component (De Paula, 1982). This approach has been used to measure the output of hyperthermia transducers (Chan *et al.*, 1989). Another type of intrinsic sensor employs fibre Bragg grating (FBG) technology. An FBG is a periodic spatial modulation of the refractive index of the fibre core over a short length of fibre, typically ~1 mm in length. Light incident on the grating is reflected over a narrow range of wavelengths. The wavelength of maximum reflectivity is called the Bragg wavelength and depends on the spatial period of the grating. An acoustically induced modulation of the grating period produces a corresponding modulation of the Bragg wavelength. This can be detected by illuminating the grating with light of a wavelength that coincides with the edge of the reflectance peak and monitoring the reflected intensity modulation (Fisher *et al.*, 1997; Fomitchov and Krishnaswamy, 2002). Another approach that employs FBG technology is one in which a fibre laser is formed by writing a pair of identical Bragg gratings separated by a centimetre or so into the core of a doped fibre (Lau *et al.*, 2008). Because an optical fibre is birefringent, light can propagate in two orthogonal polarisation modes, resulting in a beat frequency when the two modes are aligned using a polariser. An incident acoustic wave modulates the birefringence of the fibre and thus the beat frequency, which can be detected using an RF spectrum analyser.

Some of the above intrinsic fibre sensing devices can provide reasonable sensitivity and a moderately broad bandwidth, albeit with a somewhat non-uniform frequency response due to the large acoustic impedance mismatch between fused silica and water. However, all possess a fundamental drawback which severely limits their practical utility as ultrasound measurement tools, namely, their long interaction length. For the interferometric and polarimetric fibre sensors, the interaction length is the length of fibre that intercepts the field and is typically several centimetres. As a consequence, the measurement is not a point measurement but the line integral of pressure or some related quantity over the length of the fibre. For the FBG sensors, the interaction length is smaller but still of the order of several millimetres. In principle, this limitation can be overcome by making measurements at different angles and using a computed tomography approach to reconstructing the pressure amplitude at a point. However, the inconvenience and time consuming nature of this procedure strongly limits practical utility. Thus, whilst these intrinsic fibre-optic sensors may find a role in ultrasound detection and monitoring (e.g. in acoustic emission sensing or industrial ultrasonic structural health monitoring), their practical application in quantitative ultrasound metrology is limited.

19.4.7 The role of fibre-optic hydrophones in ultrasound metrology

In order to define the role of FOHs in ultrasound metrology, we start by identifying the applications that are currently inadequately served by existing piezoelectric hydrophone technology and then examine whether FOHs could fill this application space. As intrinsic FOHs have limited application in ultrasound metrology, only the four extrinsic FOHs described in Sections 19.4.2–19.4.5 are considered. Table 19.4 provides a summary of their characteristics.

For characterising piezoelectric transducers that produce relatively low power or low amplitude fields such as those used in diagnostic medical ultrasound, the key acoustic performance requirements are adequate sensitivity, a bandwidth that coincides with that of the source output and an element size that is small compared with the acoustic wavelength. Very wide bandwidth and linear operating range, extreme robustness, small physical size and immunity to EMI are not usually essential requirements. The precise requirements obviously depend on application, but an NEP in the kilopascals range, a linearity extending to several megapascals and a bandwidth of 0.5–50 MHz can be taken as a typical working specification. PVDF piezoelectric hydrophones can readily fulfil the sensitivity and bandwidth requirements. However, to obtain a near omnidirectional response at the upper end of this frequency range requires element sizes on a scale of tens of microns. It is difficult to achieve this with adequate detection sensitivity using piezoelectric devices because their sensitivity decreases with element area. The E-FOH can, in principle, provide small enough element sizes but is

Table 19.4 Comparison of different fibre-optic hydrophones

	NEP*	Linear operating limits†	Bandwidth	Element diameter‡ (μm)	Temperature sensing/resolution	Commercial availability (suppliers)
Eisenmenger FOH (E-FOH)	0.5 MPa[1]	±100 MPa[5]	➢ 1 GHz[7]	100	Yes/unknown[10]	Yes (RP Acoustics, Germany & Onda Corp, USA)
Fabry polymer film FOH (FP-FOH)	5 kPa[2]	−6 to 10 MPa[2]	60 MHz[2]	10	Yes/0.1°C[2]	Yes (Precision Acoustics Ltd, UK)
Multilayer dielectric FOH (MD-FOH)	30 kPa[3]	+50 MPa[6]	>1 GHz[8]	5	Yes/0.4°C[11]	No
Interferometric displacement FOH (ID-FOH)	1 kPa[4]	>50 MPa[4]	50 MHz[9]	5	No	No

* To facilitate comparison, all NEPs are rms values assuming no signal averaging and normalised to a measurement bandwidth of 20MHz.

† The linear operating limits are defined as the positive and negative pressures that produce an output that differs by 10% from the true pressure.

‡ Element diameter is defined as the core diameter of the fibre. Values are those of systems reported in the literature.

[1] Staudenraus and Eisenmenger (1993).

[2] Morris *et al.* (2009).

[3] Klann and Koch (2005b). The NEP provided is for a multilayer dielectric sensor illuminated by a free-space laser beam, not the output of a single mode optical fibre.

[4] Koch *et al.* (1998a).

[5] Theoretical estimate based on Eq. 19.12.

[6] Wilkens (2003a). Calculated positive pressure that results in a departure of 10% from true pressure.

[7] Theoretical bandwidth limited by depth of evanescent field. In practice, the photodiode/transimpedance amplifier unit typically limits bandwidths to a few hundred MHz.

[8] Estimate based on 5 μm thick multilayer sensing structure. In practice, the photodiode/transimpedance amplifier unit typically limits the bandwidth to a few hundred MHz.

[9] Koch *et al.* (1998b).

[10] Temperature measurements have not been reported in the literature although the data sheet by one manufacturer (Onda) claims a temperature measurement ability.

[11] Wilkensless *et al.* (1999).

insufficiently sensitive. By contrast, the FP-FOH, MD-FOH and ID-FOH can provide element sizes of these dimensions with adequate sensitivity. The FP-FOH and MD-FOH have several advantages over the ID-FOH. They provide a measurement of pressure, rather than displacement, which requires the assumption of plane waves to convert to pressure, as well as reduced complexity and cost of implementation.

The requirements for high power and high amplitude measurement applications are somewhat different. Pressure amplitudes are usually large (typically > 500 kPa) so high detection sensitivity is not critical. However, in some cases a high upper limit of linear detection can be required, extending to tens or even hundreds of megapascals. The bandwidth requirements for characterising high power sources such as those used in HIFU therapy and ultrasonic cleaning tend to be modest, requiring a response in the low megahertz range, which in turn reduces the element size requirements. The bandwidth requirements for high amplitude fields such as those produced by shockwave sources can be more stringent, extending to 100 MHz. In general, these acoustic performance requirements can, with some exceptions, be met by piezoelectric hydrophones. The greater challenge, however, lies in withstanding the hostile environment produced by high amplitude or high intensity ultrasound beams. In the former case mechanical damage induced by large negative pressures can cause structural failure of a piezoelectric hydrophone, whilst in the latter case cavitational activity and temperature rises are the dominant damage mechanisms. In this respect, the E-FOH has an advantage, offering significantly greater robustness than piezoelectric devices, and even if the fibre tip is damaged it can be inexpensively renewed by re-cleaving the fibre. Furthermore, as discussed in Section 19.4.2, it has an extremely large linear range and very wide bandwidth. These attributes make it well suited to characterising the high amplitude wideband output of shockwave sources where its low sensitivity is not a significant limitation. The robustness of the E-FOH is also useful for high power measurement applications such as the characterisation of HIFU fields, although their lower amplitude can present difficulties in achieving adequate SNR. The more sensitive FP-FOH has been demonstrated to be capable of characterising HIFU fields at intensities approaching those used clinically (Morris *et al.*, 2009). Moreover, unlike other FOHs, it can measure the temperature rises produced by HIFU fields whilst simultaneously acquiring acoustic waveforms. It thus has application as a tool for investigating the relationship between acoustic field parameters and local temperature rise which could be used, for example, to study the role that cavitation plays in enhancing heating in HIFU therapy. The relatively limited linear operating range of the FP-FOH makes it less suited to characterising very high amplitude fields, although there is scope to increase the upper limit of detection, as described in Section 19.4.3. Although the use of the MD-FOH for shockwave and high power measurements has not been reported, its performance would appear to be adequate for these. The ID-FOH is clearly suitable for both, having been evaluated for characterising the output of lithotripters and ultrasonic cleaning baths. The limited number of studies exploring the use of FP-FOH, MD-FOH and ID-FOH for high amplitude/power applications makes it difficult to assess their long term robustness – however, in all cases the optical fibre sensor downleads can be fabricated at low unit cost so can be inexpensively replaced if damaged.

In summary, FOHs can be regarded as being complementary to piezoelectric hydrophones with a niche in ultrasound metrology that occupies two specific application areas: the measurement of (i) high-frequency ultrasound and (ii) high amplitude/power ultrasound. The FP-FOH and MD-FOH are best suited to (i) on account of their high sensitivity and ability to provide a more favourable element size–sensitivity compromise than piezoelectric hydrophones at high frequencies. Applications include the characterisation of high-frequency diagnostic medical ultrasound fields produced by high resolution skin, ocular and intravascular scanners, general high-frequency transducer characterisation and the measurement of laser generated ultrasound waves. The high upper limit of linear detection, robustness and low cost of the E-FOH make it suitable for characterising high amplitude fields such as those produced by lithotripters. Similarly, the MD-FOH and ID-FOH can be used to characterise shockwaves and provide higher sensitivity, noting that the former provides a reduced upper limit of detection compared with the E-FOH and the latter is significantly more complex and expensive to implement. For high power measurement applications such as HIFU field characterisation, the greater robustness and/or lower unit cost of FOHs compared with piezoelectric hydrophones is advantageous. The FP-FOH, MD-FOH and ID-FOH lend themselves to applications in this area, for example for characterising HIFU and industrial processes like ultrasonic cleaning and emulsifying. For HIFU studies the demonstrated ability to measure ultrasound induced temperature changes as well as acoustic pressure provides the FP-FOH with a significant advantage over piezoelectric hydrophones.

19.5 Summary

In summary, there is a wide variety of different hydrophone types that are used for ultrasonic and acoustic measurements. The majority of hydrophones in use are piezoelectric in nature; however, recent developments have seen the emergence of FOHs as a viable alternative. All hydrophone types have their own idiosyncrasies, and these should be studied and understood before embarking upon experimental investigation. As a general rule, smaller hydrophones have a less directional response, but often a lower overall sensitivity (particularly for piezoelectric devices); furthermore, all hydrophones will have an inherent frequency response that will often need to be accounted for when converting the hydrophone output voltage into pressure.

Of the available piezoelectric hydrophone types, membrane devices offer excellent characterisation of broadband, short pulse, ultrasonic signals. These types of signals are commonly produced by diagnostic ultrasound equipment. Moreover, the high drive amplitude used in diagnostic machines can result in non-linear acoustic propagation and subsequent higher harmonic generation. As such, this further extends the bandwidth requirements of a hydrophone – and membrane hydrophones are often the only devices that can meet this bandwidth challenge. However, the membrane itself is less well suited to the quantification of CW signals and can experience, or be the cause of, standing wave modes either on the membrane itself or between the hydrophone and the transducer. Needle hydrophones provide a much more cost effective measurement solution than membrane hydrophones. They do exhibit a more variable frequency response and this needs to be carefully accounted for when measuring broadband signal. However, use of a voltage-to-pressure method that uses all the available frequency response data (such as hydrophone deconvolution) can lead to results that are very comparable with those from membrane hydrophones. Moreover, their smaller physical dimensions ensure they cause minimal back reflections and are thus suitable for CW measurements (where their variable frequency response is also much less of a concern). Similarly, needle hydrophones can also be used in space restricted environments, such as *in vitro* measurements where the active element needs to be inserted into tissue.

Piezoelectric needle and membrane hydrophones find widespread use in all branches of ultrasound metrology. In medical ultrasound they are used extensively for characterising the output of diagnostic ultrasound scanners to ensure compliance with regulatory standards, device development and basic research in ultrasound–tissue interactions in order to assess bioeffects or improve imaging performance. Industrial applications include characterising transducers used for ultrasonic non-destructive testing of engineering materials, general transducer testing during development and production, and characterisation of ultrasonic induced cavitation (e.g. within cleaning baths). Academic institutions also use these hydrophone types for under- and post-graduate training, as well as for many wide and varied research purposes, including quantification of non-linear propagation parameters of liquids, analysis of the equations of state of liquids, determination of the conditions necessary for sono-luminescence and assessment of ultrasound bio effects.

Despite their ubiquity, however, there are some applications for which piezoelectric hydrophones are not ideally suited. Achieving acoustically small element sizes with adequate sensitivity in the tens of MHz regime where high resolution medical scanners operate, for example, can be challenging. Fragility and expense make them unsuitable for measuring very high amplitude and power fields encountered in the increasingly important areas of therapeutic ultrasound and industrial ultrasonic processing. Sensitivity to EMI can be a further limitation in the electrically noisy environment that often accompanies high power CW fields. As discussed in Section 19.4.7, FOHs can provide a solution that overcomes these limitations and are now beginning to emerge as viable alternatives, particularly in the high-frequency and high amplitude/power arenas in medical and industrial ultrasound metrology. Furthermore, the ability of some FOHs to simultaneously measure temperature and pressure offers a major advancement to researchers in the field of ultrasonic exposimetry.

It is clear that new devices are becoming available to meet the demands of new applications of ultrasound, but there remain a number of significant measurement challenges ahead. The increasing popularity of therapeutic ultrasound methods requires ever more robust sensors capable of withstanding extremes of ultrasonic pressure and intensity as well as the associated cavitation events and thermal rises. Ultrasonic therapies may also be turning increasingly to hydrophone technologies to enhance targeting, and thereby reduce patient collateral damage or exposure time. Significant advances in multi-element sensors are also anticipated; certainly the integration of piezoelectric and flexible circuit technologies has produced some fine examples of hydrophone arrays, and growth in this area should be expected. The micro-machining techniques developed initially for the processing of semiconductor materials are also starting to see application in all forms of ultrasonic receiver development. Although most FOHs have thus far been single element devices, these too will be enhanced to consider the spatial variation of ultrasonic field, whether by arrays of sensors or via optically scanned large area receivers. Hydrophones have always played an integral role in the determination of what are safe and appropriate levels of ultrasound exposure. As new technologies are developed and incorporated into hydrophone designs, this function seems set to flourish.

19.6 References

Archer-Hall, J. and Gee, D. (1980) A single integral computer method for axisymmetric transducers with various boundary conditions. *NDT International*, 13(3), pp. 95–101.

Arvengas, A., Davitt, K. and Caupin, F. (2011) Fiber optic probe hydrophone for the study of acoustic cavitation in water. *Review of Scientific Instruments*, 82(3), p. 034904.

Bacon, D.R. (1982) Characteristics of a PVDF membrane hydrophone for use in the range 1–100 MHz. *IEEE Transactions on Sonics and Ultrasonics*, SU-29, pp. 18–25.

Beard, P.C. and Mills, T. (1997) Miniature optical fibre ultrasonic hydrophone using a Fabry-Perot polymer film interferometer. *Electronics Letters*, 33(9), pp. 801–3.

Beard, P.C., Hurrell, A.M. and Mills, T.N. (2000). Characterization of a polymer film optical fiber hydrophone for use in the range 1 to 20 MHz: a comparison with PVDF needle and membrane hydrophones. *IEEE Transactions on Ultrasonics, Ferroelectrics, and Frequency Control*, 47(1), pp. 256–64.

Canney, M.S., Bailey, M.R. and Crum, L.A. (2008). Acoustic characterization of high intensity focused ultrasound fields: A combined measurement and modeling approach. *The Journal of the Acoustical Society of America*, 124, p. 2406.

Chan, H.L., Chiang, K.S., Price, D.C., Gardner, J.L. and Brinch, J. (1989) Use of a fibre-optic hydrophone in measuring acoustic parameters of high power hyperthermia transducers. *Physics in Medicine and Biology*, 34(11), pp. 1609–22.

Cooling, M.P., Humphrey, V.F. and Wilkens, V. (2011) Hydrophone area-averaging correction factors in nonlinearly generated ultrasonic beams. *Journal of Physics: Conference Series*, 279, 012002.

Cox, B.T. and Beard, P.C. (2007) The frequency-dependent directivity of a planar Fabry-Perot polymer film ultrasound sensor. *IEEE Transactions on Ultrasonics, Ferroelectrics, and Frequency Control*, 54(2), pp. 394–404.

Fay, B., Ludwig, G., Lankjaer, C. and Lewin, P.A. (1994) Frequency response of pvdf needle-type hydrophones. *Ultrasound in Medicine and Biology*, 20, pp. 361–6.

Fisher, N. *et al.* (1997) In-fibre Bragg gratings for ultrasonic medical applications. *Measurement Science and Technology*, 8, pp. 1050–4.

Fomitchov, P. and Krishnaswamy, S. (2002) Fiber Bragg grating ultrasound sensor for process monitoring and NDE applications. *Review of Quantitative Nondestructive Evaluation*, 21, pp. 937–44.

Gélat, P., Preston, R. and Hurrell, A. (2005) A theoretical model describing the transfer characteristics of a membrane hydrophone and validation. *Ultrasonics*, 43, pp. 331–41.

Gopinath Minasamudram, R. *et al.* (2009) Thin film metal coated fiber optic hydrophone probe. *Applied Optics*, 48(31), pp. G77–82.

Harris, G.R. (1988) Hydrophone measurements in diagnostic ultrasound fields. *IEEE Transactions on Ultrasonics, Ferroelectrics, and Frequency Control*, 35(2), pp. 87–101.

Harris, G.R. (2005) Progress in medical ultrasound exposimetry. *IEEE Transactions on Ultrasonics, Ferroelectrics, and Frequency Control*, 52(5), pp. 717–36.

Harris, G.R. and Shombert, D.G. (1985) A pulsed near-field technique for measuring the directional characteristics of acoustic receivers. *IEEE Transactions on Sonics and Ultrasonics*, SU-32, pp. 802–8.

Huber, P. *et al.* (1994) In vivo detection of ultrasonically induced cavitation by a fibre-optic technique. *Ultrasound in Medicine and Biology*, 20(8), pp. 811–25.

Hurrell, A.M. (2002) Finite difference modelling of acoustic propagation and its application in underwater acoustics. PhD Thesis, University of Bath, UK.

Hurrell, A.M. (2004a) Geophysical modelling techniques and their benefit to ultrasonic measurement tools. *Journal of Physics Conference Series*, 1, pp. 44–9.

Hurrell, A.M. (2004b) Voltage to Pressure Conversion: Are You Getting 'Phased' by the problem? *Journal of Physics Conference Series*, 1, pp. 57–62.

IEC (2007a) 62127-1:2007 Part 1 – Measurement and characterisation of medical ultrasonic fields up to 40 MHz, Geneva, International Electro-technical Commission.

IEC (2007b) 62127-2:2007 – Part 2 – Calibration for ultrasonic fields up to 40 MHz, 2007, Geneva, International Electro-technical Commission.

IEC (2007c) 62127-3:2007 – Part 3 – Properties of hydrophones for ultrasonic fields up to 40 MHz, 2007, Geneva, International Electro-technical Commission.

Koch, C. (1996) Coated fiber-optic hydrophone for ultrasonic measurement. *Ultrasonics*, 34(6), pp. 687–9.

Koch, C. (1999) Measurement of ultrasonic pressure by heterodyne interferometry with a fiber-tip sensor. *Applied Optics*, 38(13), pp.2812–19.

Koch, C. and Jenderka, K.-V. (2008) Measurement of sound field in cavitating media by an optical fibre-tip hydrophone. *Ultrasonics Sonochemistry*, 15, pp. 502–9.

Koch, C., Molkenstruck, W. and Reibold, R. (1997) Shock-wave measurement using a calibrated interferometric fiber-tip sensor. *Ultrasound in Medicine and Biology*, 23(8), pp. 1259–66.

Koch, C., Ludwig, G. and Molkenstruck, W. (1998) Calibration of a fiber tip ultrasonic sensor up to 50 MHz and the application to shock wave measurement. *Ultrasonics*, 36, pp. 721–5.

Krücker, J.F., Eisinberg, A., Krix, M., Lötsch, R., Pessel, M. and Trier, H.G. (2000) Rigid piston approximation for computing the transfer function and angular response of a fiber-optic hydrophone. *The Journal of the Acoustical Society of America*, 107(4), pp. 1994–2003.

Kyriakou, Z., Corral-Baques, M., Amat, A. and Coussios, C. (2011) Hifu-induced cavitation and heating in ex vivo porcine subcutaneous fat. *Ultrasound in Medicine and Biology*, 37(4), pp. 568–79.

Lau, S., Lau, S.T., Shao, LY, Chan HL, Tam HY, Hu CH, Kim HH, Liu R, Zhou Q, and Shung KK. (2008) Characterization of a 40-MHz focused transducer with a fiber grating laser hydrophone. *IEEE Transactions*, pp. 1–14.

Leighton, T.G. (1997) *The Acoustic Bubble*, Academic Press, London.

Leighton, T.G., Fedele, F., Coleman, A.J., McCarthy, C., Ryves, S., Hurrell, A.M., De Stefano, A. and White, P.R. (2008) A passive acoustic device for real-time monitoring of the efficacy of shockwave lithotripsy treatment. *Ultrasound in Medicine and Biology*, 34(10), pp. 1651–65.

Lewin, P.A., Mu, C., Umchid, S., Daryoush, A. and El-Sherif, M. (2005) Acousto-optic, point receiver hydrophone probe for operation up to 100 MHz. *Ultrasonics*, 43(10), pp. 815–21.

Lum, P., Greenstein, M., Grossman, C. and Szabo, T.L. (1996) High-Frequency Membrane Hydrophone. *IEEE Transactions on Ultrasonics, Ferroelectrics and Frequency Control*, 43, pp. 536–44.

Morris, P. (2008) A Fabry-Perot fibre-optic hydrophone for the characterisation of ultrasound fields. PhD Thesis, University of London.

Morris, P., Hurrell, A., Shaw, A., Zhang, E. and Beard, P. (2009) A Fabry-Perot fiber-optic ultrasonic hydrophone for the simultaneous measurement of temperature and acoustic pressure. *The Journal of the Acoustical Society of America*, 125(6), pp. 3611–22.

NEMA (2004) *Acoustic Output Measurement Standard for Diagnostic Ultrasound Equipment, Rev. 3*, Amer. Inst. Ultrasound in Med., Laurel, MD; Nat. Electr. Manu. Assoc., Rosslyn, VA, NEMA Publication UD 2.

Onda *Fiber Optic Hydrophone System HFO-660 with Optical Probes*, data sheet, Onda Corporation.

De Paula, R., Flax, L., Cole, J. and Bucaro, J. (1982) Single-mode fiber ultrasonic sensor. *IEEE Journal of Quantum Electronics*, 18(4), pp. 680–3.

De Paula, R., Cole, J. and Bucaro, J. (1983) Broad-band ultrasonic sensor based on induced optical phase shifts in single-mode fibers. *Journal of Lightwave Technology*, 1(2), pp. 390–3.

Radulescu, E.G., Lewin, P.A., Wojcik, J. and Nowicki, A. (2004) Probing acoustic fields of clinically relevant transducers: The effect of hydrophone probes with finite apertures and bandwidths. *IEEE Transactions on Ultrasonics, Ferroelectrics and Frequency Control*, 51, pp. 1262–70.

Robinson, S., Preston, R., Smith, M. and Millar, C. (2000) PVDF reference hydrophone development in the UK—From fabrication and lamination to use as secondary standards. *IEEE Transactions on Ultrasonics, Ferroelectrics and Frequency Control*, 47(6), pp. 1336–44.

RP Acoustics (2002) *Fiber Optic Probe Hydrophone FOPH 2000*, data sheet, RP Acoustics.

Shombert, D.G., Smith, S.W. and Harris, G.R. (1982) Angular response of miniature ultrasonic hydrophones. *Medical Physics*, 9(4), pp. 484–92.

Staudenraus, J. and Eisenmenger, W. (1993) Fibre-optic probe hydrophone for ultrasonic and shock-wave measurements in water. *Ultrasonics*, 31(4), pp. 267–73.

Wang, H.-wei *et al.* (2011) Vibrational Photoacoustic Microscopy for Depth-resolved Bond-selective Imaging of Tissues and Organisms. In CLEO 2011. p. JTuG3.pdf.

Wang, Z.Q. *et al.* (1999) Impulse response of a fiber optic probe hydrophone determined with shock waves in water. *Journal of Applied Physics*, 85(5), p. 2514.

Weise, W., Wilkens, V. and Koch, C. (2002) Frequency response of fiber-optic multilayer hydrophones: experimental investigation and finite element simulation. *IEEE Transactions on Ultrasonics, Ferroelectrics and Frequency Control*, 49(7), pp. 937–46.

Wilkens, V., Wiemann, C., Koch, Ch., Foth, H.-J. (1999) Fiber-optic dielectric multilayer temperature sensor: in situ measurement in vitreous during Er:YAG laser irradiation. *Optics & Laser Technology*, 31(8), pp. 593–9.

Wilkens, V. (2001) Dielektrische optische Interferenzschichthydrophone zur zeitlich und räumlich hochauflösenden Messung von Ultraschallfeldern, Dissertation Universität Oldenburg, PTB-Bericht, PTB-MA-67, 2001.

Wilkens, V. (2003a) Characterization of an optical multilayer hydrophone with constant frequency response in the range from 1 to 75 MHz. *The Journal of the Acoustical Society of America*, 113(3), p. 1431.

Wilkens, V. (2003b) Characterization of an optical multilayer hydrophone with constant frequency response in the range from 1 to 75 MHz. *The Journal of the Acoustical Society of America*, 113(3), p. 1431.

Wilkens, V. and Koch, C. (1999) Fiber-optic multilayer hydrophone for ultrasonic measurement. *Ultrasonics*, 37(1), pp. 45–9.

Wilkens, V. and Koch, C. (2004) Improvement of hydrophone measurements on diagnostic ultrasound machines using broadband complex-valued calibration data. *Journal of Physics: Conference Series*, 1, pp. 50–5.

Yasuto, U. and Nakamura, K. (1999) Pressure sensitivity of a fiber-optic microprobe for high-frequency ultrasonic field. *Japanese Journal of Applied Physics*, 38(5), pp. 3120–3.

Zhang, E., Laufer, J. and Beard, P. (2008) Backward-mode multiwavelength photoacoustic scanner using a planar Fabry–Perot polymer film ultrasound sensor for high-resolution three-dimensional imaging of biological tissues. *Applied Optics*, 47(4), pp. 561–77.

Zhou, Y. *et al.* (2006) Measurement of high intensity focused ultrasound fields by a fiber optic probe hydrophone. *The Journal of the Acoustical Society of America*, 120(2), p. 676.

20

Ultrasonic motors

K. NAKAMURA, Tokyo Institute of Technology, Japan

Abstract: An ultrasonic motor is a piezoelectric device which produces rotary or linear motion from ultrasonic vibrations via friction. Ultrasonic motors produce a much larger torque/force than conventional electromagnetic motors. Several basic principles are introduced for rotary and linear motors. Two orthogonal vibration components are essential for constructing an ultrasonic motor: one normal to the contact interface between the vibrator and the rotor/slider while the other is parallel to the interface. Two standing waves or a traveling wave are used, to give a standing-wave ultrasonic motor or a traveling-wave ultrasonic motor. Fundamental concepts for realizing these methods are explained and their performance is considered.

Key words: ultrasonic motor, rotary motor, linear motor, friction, actuator.

20.1 Introduction

Hybrid systems composed of electronic circuitry, actuators and sensors are of increasing importance in the modern world. This is illustrated, for example, with the recent rapid development of robotics. In comparison with the explosive growth of the capabilities of digital computing, both in speed and in data size, and the communications revolution propelled by the internet and related technologies, progress in actuating devices has been slow. There has been, of course, a steady improvement in the performance of conventional electromagnetic motors through the introduction of novel materials and numerical simulation techniques. On the other hand, the possibilities for new actuators have been studied by many researchers. The ultrasonic motor is one of these new actuators. An ultrasonic motor can produce rotary or linear motion from piezoelectric vibrations at an ultrasonic frequency via friction. In the 1970s, several ideas were proposed for actuators driven by piezoelectric vibrations. However, the main advances in the working principles were made in the 1980s. Details of this history can be found in the book by Ueha and Tomikawa (1993) and in other works.

The high-energy density of piezoelectric transducers was attractive to those who were interested in developing ultrasonic motors in the early days. Lightweight motors are very useful in many fields, especially robotics. Assuming high-amplitude vibration near the fatigue limit of a piezoelectric ceramic, 40 MPa in stress and 1.7 m/s at the peak vibration velocity, the kinetic energy stored in a piezoelectric transducer can reach 60 W/cm^3 at 20 kHz. In actual operation, the maximum vibration amplitude is lower than the estimated value since the temperature rises because of mechanical and dielectric losses due to the high-amplitude operation. But the energy density of a piezoelectric transducer at high frequencies is still expected to be excellent. On the other hand, the output force of a piezoelectric element is so large that the torque/thrust when acting as a motor will be high. This means that, in an ultrasonic motor, low speed and high torque can be realized without reduction gearing. The elimination of gears means quiet operation and high rigidity. The use of friction means there is a large holding force without an external braking system or energy consumption. Hence, ultrasonic motors are suitable for actuators in precise positioning systems. The very low emission of electromagnetic flux might also be an important feature of ultrasonic motors, and is useful in applications requiring the absence of a magnetic field.

To transform vibratory motion to unidirectional rotary or linear actuation via friction requires another vibration component. These two essential vibration components should be orthogonal to each other in both time and space. Elliptical motion is fundamental for a ultrasonic motor and can be practically achieved by a combination of two standing waves or a traveling wave. The basic concepts for realizing standing-wave ultrasonic motors and traveling-wave ultrasonic motors are explained in this chapter. The performance of ultrasonic motors is compared and considered in the final part of the chapter.

20.2 Standing-wave ultrasonic motors

20.2.1 Rotary motor

Figure 20.1 shows a typical configuration for rotary motion, combining two standing-wave vibrations. This type of motor is sometimes referred to as a hybrid transducer ultrasonic motor (Kurosawa and Ueha, 1991). A set of torsional and longitudinal PZT (lead zirconate titanate) elements are tightly clamped between the metal head and the bottom block with a bolt. Torsional and longitudinal vibration can be excited independently, since the torsional piezoelectric unit and the longitudinal one each have an isolated electrode. The torsional PZT disk is polarized in the circumferential direction to induce shearing strain with the piezoelectric constant of d_{15}, while the longitudinal one is in the thickness direction to generate axial strain with the constant d_{33}, as shown in Fig. 20.2. In order to have a circular polarization, the torsional PZT disk is composed of small wedge-shaped elements (Fig. 20.3). Each wedge-shaped element is poled using a temporary electrode plated on both sides. These temporary electrodes are removed after poling. The pieces are bonded together into an annular shape. This mosaic method of fabrication makes the torsional PZT element much more expensive than the longitudinal one. A rotor is pressed on to the top surface of the transducer with a spring and a ball bearing. The pressing force is referred to as ‘preload,’ and produces a sufficient frictional force. Appropriate friction materials or a surface coating are used in the interface between the rotor and the transducer.

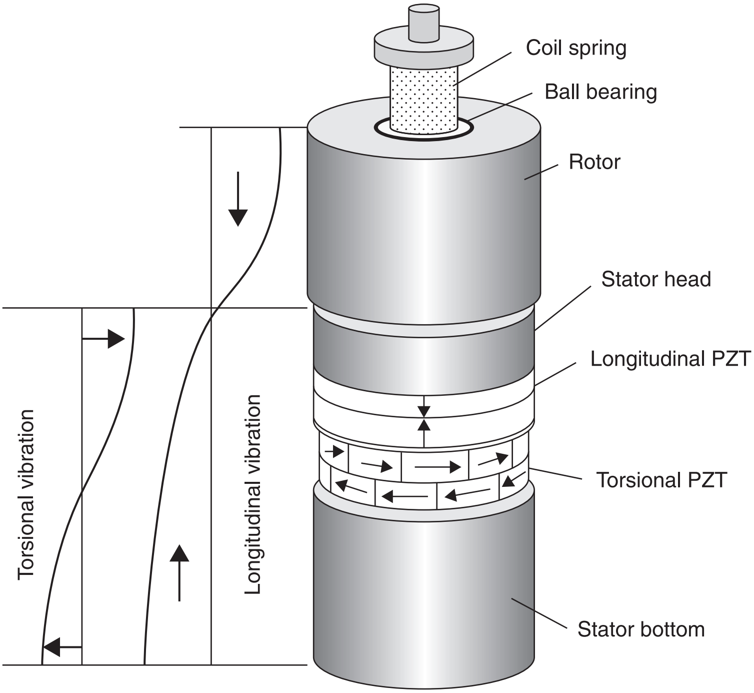

20.1 Two-mode standing-wave ultrasonic motor.

The operation of the motor is illustrated in Fig. 20.4, where one vibration cycle is divided into four phases. The longitudinal vibration is synchronized with the torsional one so that the transducer extends in the axial direction to make contact with the rotor when the torsional vibration velocity is at its maximum. The rotational force is transmitted to the rotor through friction during this phase. When the torsional vibration velocity is in the opposite direction to the rotor's rotation, the transducer shrinks and is not in contact with the rotor. In this way, the torsional vibration is rectified into the rotor's rotational motion with the help of the longitudinal vibration. In other words, the longitudinal vibration modulates the friction force so that the torsional vibration is selectively transmitted to the rotor for only half of the cycle. If the phase relation between the two vibrations is changed by 180°, the rotation direction of the rotor reverses. The rotation speed is almost proportional to the torsional vibration velocity. The waveform of the dynamic preload f_c acting vertically at the contact surface between the transducer and the rotor is displayed at the top of Fig. 20.5. The rotor is in contact with the transducer only for the angle ϕ_c. The time average of the dynamic preload should be equal to the static preload F_c applied to the rotor with the spring. The waveform shown here is a conceptual one, and the actual waveform may have a more complicated shape. The transmission of the torsional force is intermittent, but the

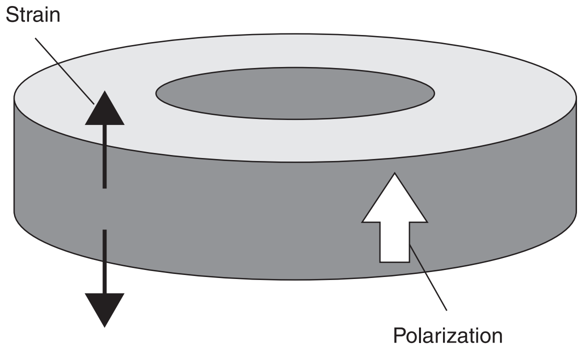

Longitudinal PZT

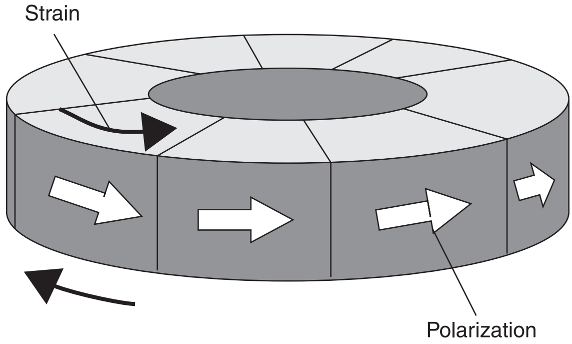

Torsional PZT

20.2 Piezoelectric elements used in the motor shown in Fig. 20.1.

torsional vibration waveform is almost sinusoidal because the motor is driven at the torsional resonance frequency of the transducer. In contrast, the rotor speed is approximately constant due to the large moment of inertia of the rotor. The instantaneous torque acting at the contact surface changes according to the sign of the difference of the angular velocities of the transducer and the rotor and the friction force determined by the dynamic preload. The torque is positive during the period when the torsional vibration velocity is larger than the rotor speed, while the torque is negative when the torsional vibration velocity is smaller than the rotor speed. We can obtain the output torque as an averaged value of the instantaneous torque over the period of vibration. Though, ideally, the contact angle should be less than 180° for efficiency, it is almost 360° in many real cases and the efficiency is under 50%.

Typical speed-load characteristics of a hybrid transducer ultrasonic motor are sketched in Fig. 20.6. If the voltage to the torsional PZT elements increases while the voltage to the longitudinal PZT elements is fixed, the no-load speed increases

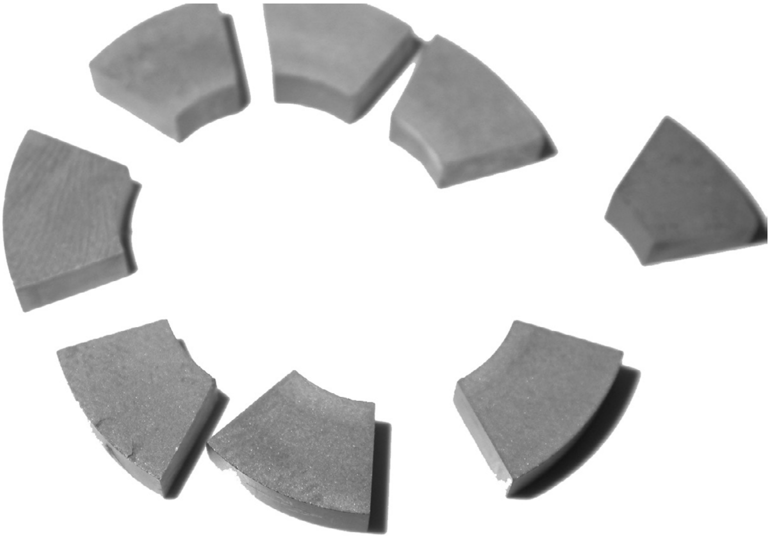

20.3 Wedge-shaped pieces of the torsional PZT unit.

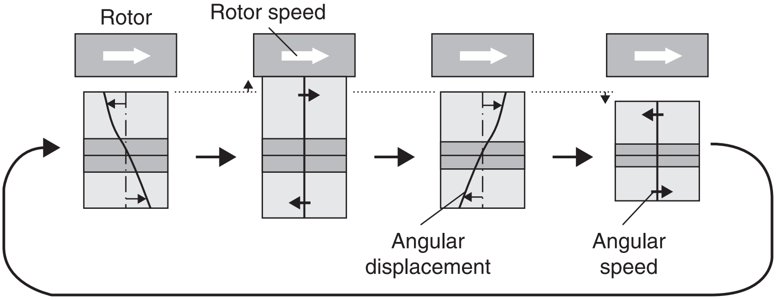

20.4 Operation of a hybrid transducer ultrasonic motor.

almost linearly. The torque also increases, but it becomes saturated at a certain value. The maximum torque never exceeds the torque determined by the friction $\mu F_c R$, where μ is the friction coefficient and R is the average radius of the contact surface. To increase the maximum torque, the static preload F_c must be increased. At the same time, a stronger longitudinal vibration is required to balance the larger static preload.

20.2.2 Linear motor

To realize linear motion, there are several possible combinations of the two vibrations as described below. First, two examples using multilayer piezoelectric

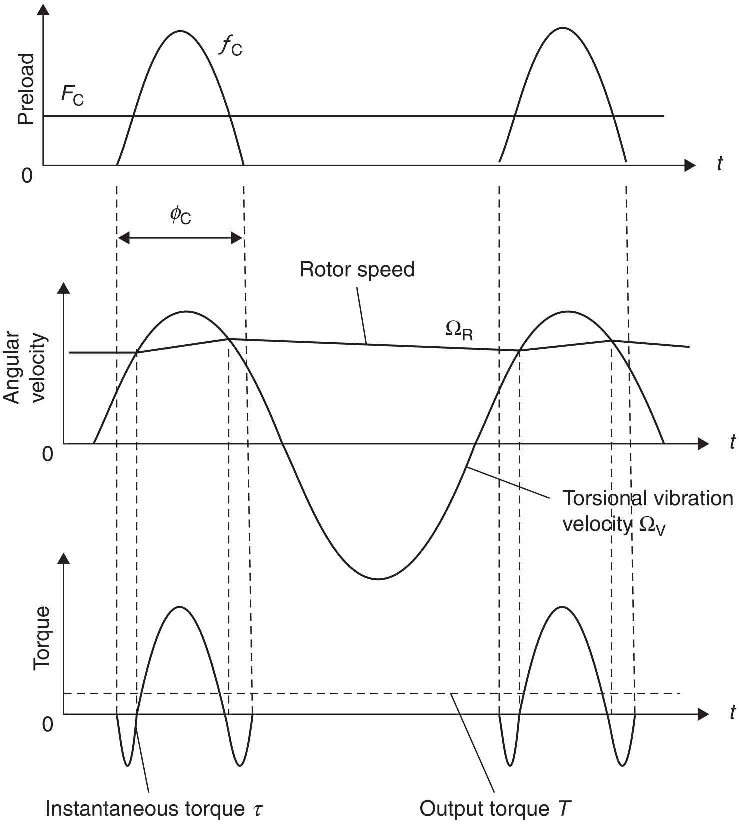

20.5 Waveforms for the preload, the angular velocities and the torque.

elements are shown in Fig. 20.7 and Fig. 20.8. In the structure shown in Fig. 20.7, a longitudinal Langevin transducer of half-wavelength is used to generate the thrust force, while two multilayer PZT elements are attached to both ends of the Langevin transducer to control the friction force (Kurosawa *et al.*, 1989a). In the Langevin transducer, a pair of piezoelectric ceramic disks is sandwiched between aluminum cylinders with a bolt, in order to excite strong longitudinal vibrations. This motor is operated at the fundamental longitudinal resonance frequency of the Langevin transducer. Each multilayer PZT element provides sufficient friction control even when not driven at resonance, by taking advantage of the multilayer structure. If the phase of the vibrations of the multilayer elements is chosen correctly, the longitudinal vibration will be transformed to unidirectional linear motion. When the longitudinal velocity at the end of the Langevin transducer

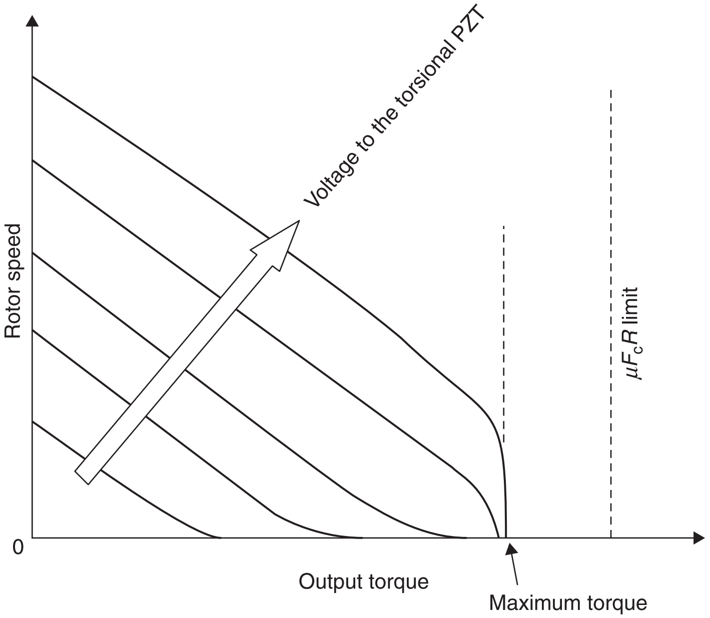

20.6 Typical speed-load characteristics of a hybrid transducer motor.

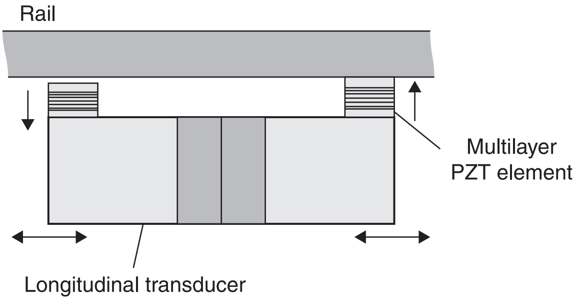

20.7 Linear motor using a combination of a longitudinal transducer and multilayer piezoelectric elements.

is at its maximum, one of the multilayer elements extends to make strong contact with the rail. At the same time, the multilayer element at the other end shrinks to minimize friction with the rail, since the longitudinal vibration velocity is in the opposite direction. The direction of motion can be reversed by changing the phase relation between the longitudinal vibration and the multilayer elements by 180°. A maximum thrust of 5 N and a no-load speed of 0.5 m/s were obtained using a prototype with a diameter of 20 mm.

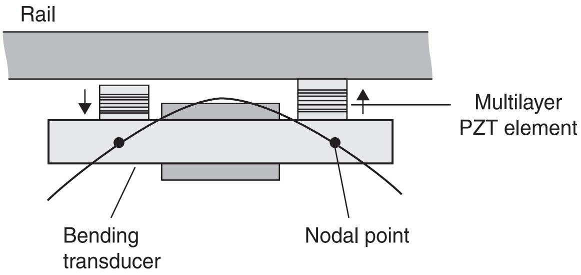

20.8 Linear motor using a bending vibrator and two multilayer piezoelectric elements.

In a modified version illustrated in Fig. 20.8, the longitudinal transducer is replaced by a bending transducer for downsizing (Kurosawa *et al.*, 1991). Two PZT plates polarized in the thickness direction sandwich a rectangular metal bar. The polarization directions and the polarity of the applied voltages are chosen so that the top PZT plate extends in the lateral direction while the bottom one shrinks, and vice versa. The fundamental bending vibration is excited in this way using the sandwich structure. Two multilayer piezoelectric elements are attached at the nodal points of the bending vibration on the metal bar where rotational motion is generated. The top of the multilayer elements has horizontal vibration components due to the rotational motion at the bottom. The horizontal vibration is converted into linear motion with the help of the vertical vibration of the multilayer piezoelectric elements. The transducer should be pressed to the rail stably with an appropriate vertical force to have sufficient friction at the contact surfaces, for both motors shown in the figures.

One of the most popular combinations of two vibrations for a linear motor is the degenerated modes of the first-longitudinal and the second-bending (L1-B2) vibrations. These modes in a rectangular body are shown in Fig. 20.9. The dimensions of the body are determined so that the resonance frequency of the longitudinal mode is close to that of the bending one. The speed of sound for the bending vibration is lower than for the longitudinal vibration in general. Consequently, it is difficult to tune the resonance of the first bending mode to the first longitudinal one. This is why the combination L1-B2 is often used for this type of motor. The longitudinal resonance frequency should be close to the bending one, as stated before; however, there should be an appropriate separation between the two resonance frequencies to avoid coupling between the two modes and thus to give independent control of the two orthogonal vibration components. Special care should be taken in the design of the resonance frequencies of this type of motor.

The two vibrations can be excited in a single plate of a piezoelectric material using divided electrodes as described below. A friction tip is attached at the end of the plate, and makes contact with a rail or a slider. The bending vibration is in a direction horizontal to the rail, while the longitudinal vibration is vertical. The former works as the driving force, the latter modulates the preload to control

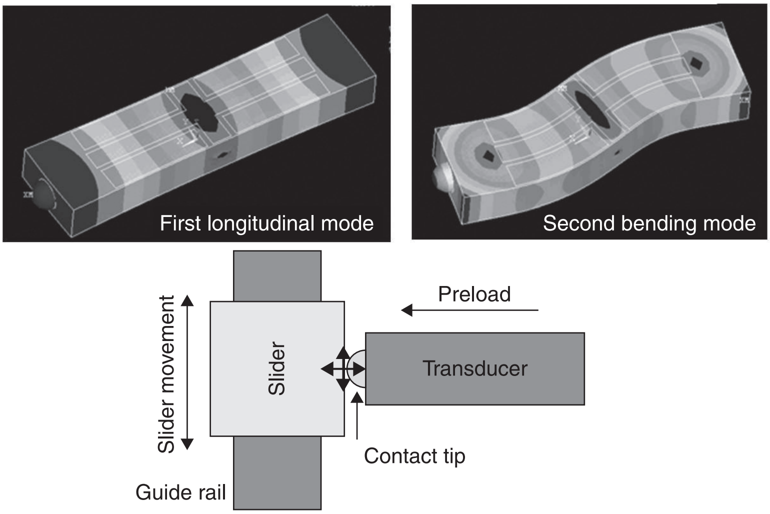

20.9 Linear motor using the L1-B2 mode of a rectangular PZT element.

friction. In other words, elliptical motion is formed at the contact point through the combination of the two orthogonal vibrations, which are out of phase by 90°. Many papers and textbooks on ultrasonic motors explain that elliptical vibratory motion is essential for ultrasonic motors. For smooth control of the motor speed, the amplitudes of the two vibrations should be controlled independently. To reduce the motor speed to near zero, the vibration parallel to the direction of motion should be lowered while the vertical vibration amplitude should be kept constant. This is illustrated in Fig. 20.10. If both vibrations are lowered simultaneously, since the contact surface has finite roughness, friction control using the vertical vibration in the small amplitude region does not work. This makes a difference to controllability, as shown in Fig. 20.11, where the speed of the motor is plotted as a function of the applied voltage. The function is linear when there is independent control of the two vibration components, as indicated by curve (1). In contrast, there is a dead region if the two orthogonal components are changed simultaneously, as shown by curve (2). It is often thought that controlling an ultrasonic motor is difficult because of the dead region in the speed-voltage characteristic. A structure has been proposed to give independent control of the two components, as shown in Fig. 20.12 (Takano *et al.*, 2011). A multilayer configuration, adapted for a low voltage operation, has different electrode patterns for the L1 mode and the B2 mode to give independent excitation of the two modes. One electrode is designed for longitudinal vibration and the other for bending. The shapes of the electrodes are optimized to give a high efficiency of the transformation of input electrical power to the output mechanical power.

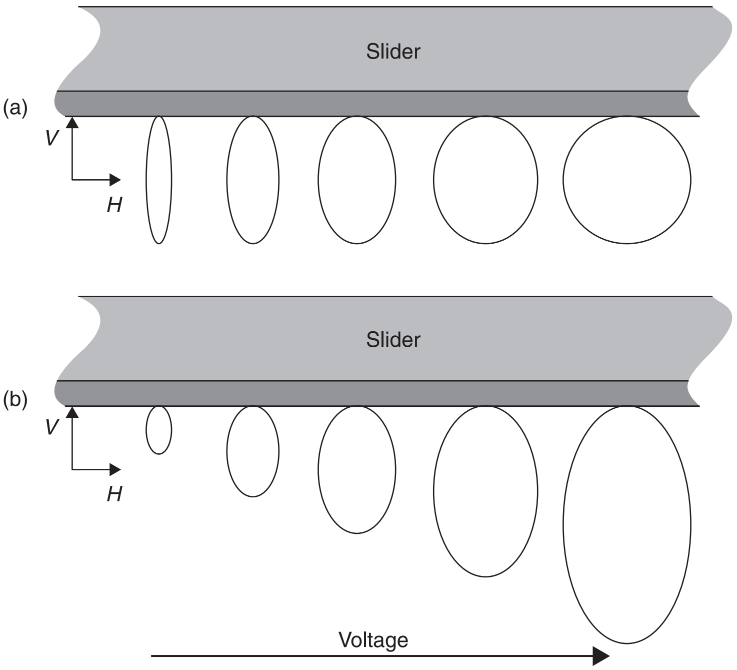

20.10 Control of the elliptical shape of the vibration trajectory: (a) independent control of the vertical *V* and horizontal *H* components, (b) simultaneous control of the vertical and horizontal components.

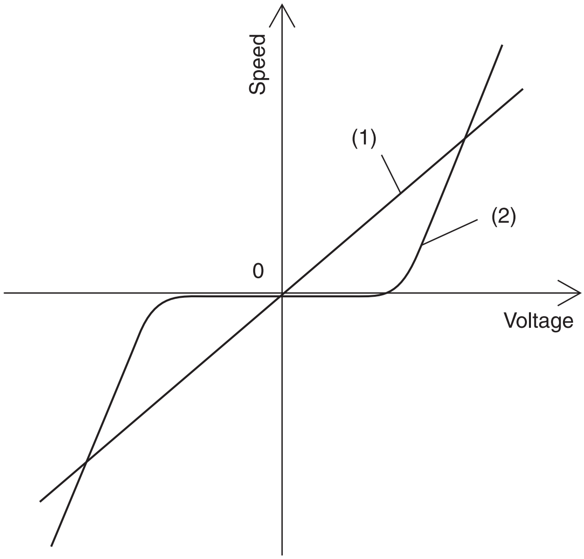

20.11 Motor speed as function of voltage: (1) independent excitation of the two modes, (2) simultaneous excitation of the two modes.

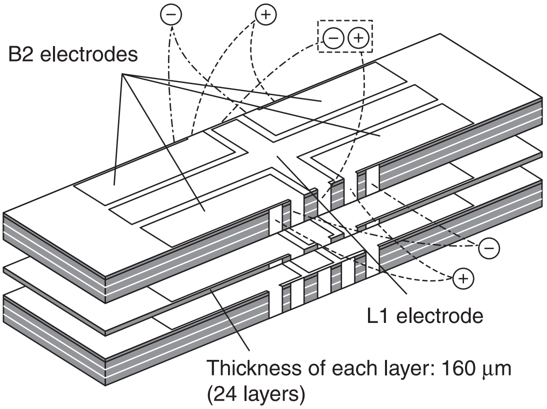

20.12 Electrode pattern for the first longitudinal and the second bending modes.

Actual results of using a L1-B2 transducer, 30 mm in length, of the type shown in Fig. 20.12, are given in Fig. 20.13. There is good linearity using the method proposed above, though there is no slider movement at low voltages around zero if the voltage for the longitudinal vibration is changed at the same time as the voltage for bending. The maximum thrust and no-load speed were measured as 12 N and 0.4 m/s, respectively. The resonance frequency was 52–54 kHz.

Careful consideration must be given to the shape and materials used for the contact tip bonded at the end of the transducer. The wear property of the material should be good, of course. In addition, the contact area should be unchanged even after long use, since the longitudinal resonance frequency is significantly affected by the contact area and the preload between the transducer head and the rail. For practical applications, nonlinear leaf springs are used to keep the preload constant

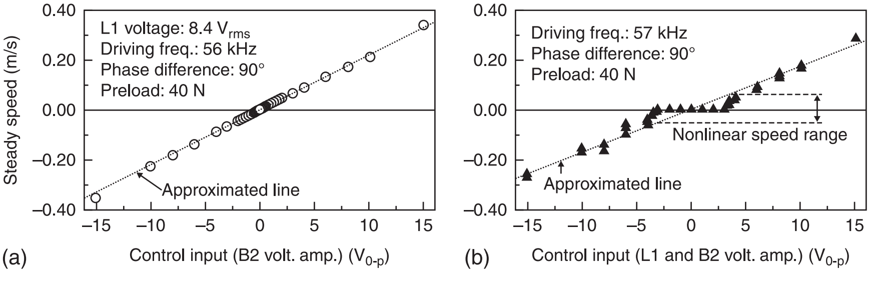

20.13 Slider speed: (a) only the voltage for the B2-mode is changed with that for the L1-mode constant; (b) the voltages for the L1-mode and the B2-mode are varied simultaneously.

even after long operation and abrasion of the friction material. The transducer is supported by four leaf springs, as shown in Fig. 20.14, where the springs are bonded onto the sides of the transducer and connected to a rectangular frame. The springs have nonlinear characteristics, as shown in Fig. 20.15. The load-displacement

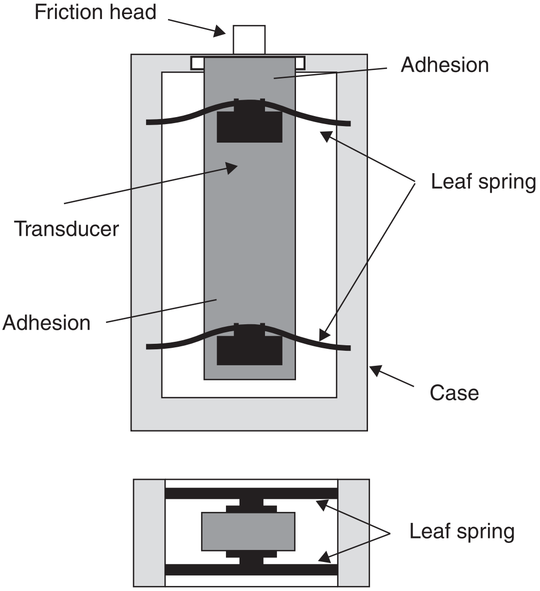
Friction head
Adhesion
Leaf spring
Transducer
Adhesion
Case
Leaf spring

20.14 Support mechanism of an L1-B2 transducer using nonlinear leaf springs.

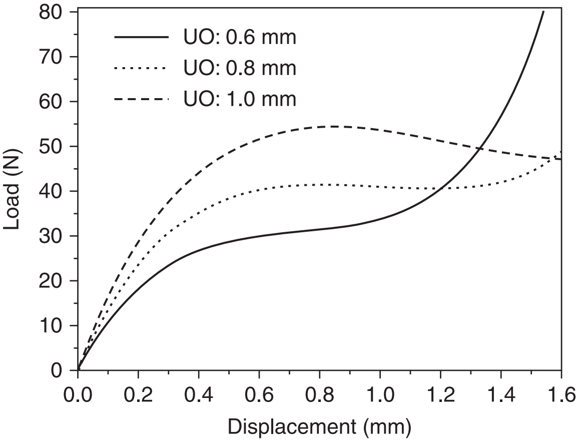

20.15 Load-displacement characteristics of nonlinear leaf springs with different arm offsets UO.

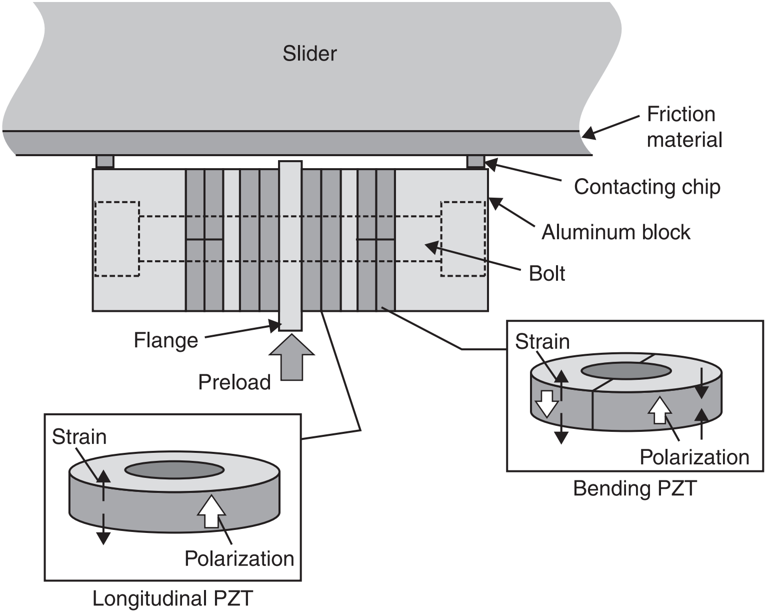

20.16 High-output bolt-clamped linear motor.

curve changes with the arm offset. The arm offset characterizes the shape of the leaf spring, and is defined as the vertical distance between the center and the edge of a leaf. For an arm offset of 0.8 mm, the generating load is constant, at around 40 N, in the displacement region from 0.6 mm to 0.8 mm. Because of the nonlinear characteristics of a spring, the preload remains stable for a long time.

A more powerful linear motor can be realized using a structure clamped with a bolt, as shown in Fig. 20.16 (Yun *et al.*, 2001). Two different types of PZT disks are sandwiched between aluminum blocks and clamped together with a bolt. Uniformly polarized PZT disks are used for exciting the longitudinal vibration. Another set of PZT disks have complex polarization: each disk is divided into two along a diameter. The polarization polarities are in opposite directions to stimulate a bending force: with a uniform electric field, one half of the PZT disk increases in thickness, while the other half shrinks. Using these PZT elements, the first longitudinal (L1) mode and the second bending (B2) mode can be excited independently with a two-phase driver circuit. The longitudinal and bending modes are shown in Fig. 20.17. Though the L1-B2 combination is again used, the roles of the longitudinal and bending modes are different from those in the previous motor: in this configuration the longitudinal vibration is used as the driving force and the bending vibration as the friction control. The slider surface is covered with an alumina ceramic as a friction material. The contact chips attached to both ends of the transducer are also made of an alumina ceramic. The

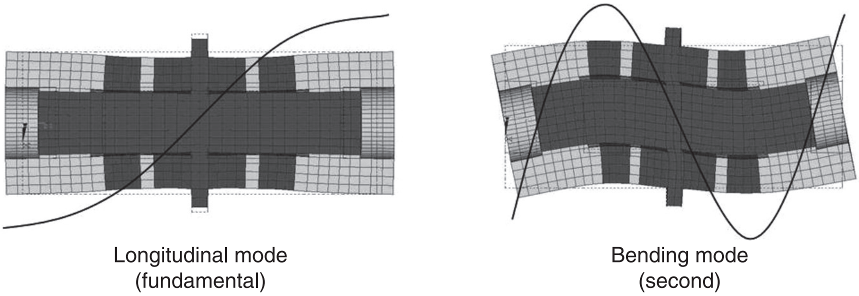
Longitudinal mode
(fundamental)
Bending mode
(second)

20.17 Vibration modes used in the linear motor of Fig. 20.16.

two vibrations with a phase difference of 90° or −90° result in a circular locus at the top of the contact chips.

The circular vibrations generate a driving thrust at the contact interface in the same manner as in other types of ultrasonic motor. Four phases of one cycle are shown in Fig. 20.18. The resonance frequency of the L1 mode should be tuned to that of the B2 mode for efficiency. Since the dependence of the longitudinal resonance frequency on the bolt length is different from that of the bending resonance frequency, the two resonance frequencies can be set close to each other for an appropriate bolt length, as shown in Fig. 20.19. In practice, the resonance frequencies can be reduced after assembling the transducer by shortening the bolt through machining.

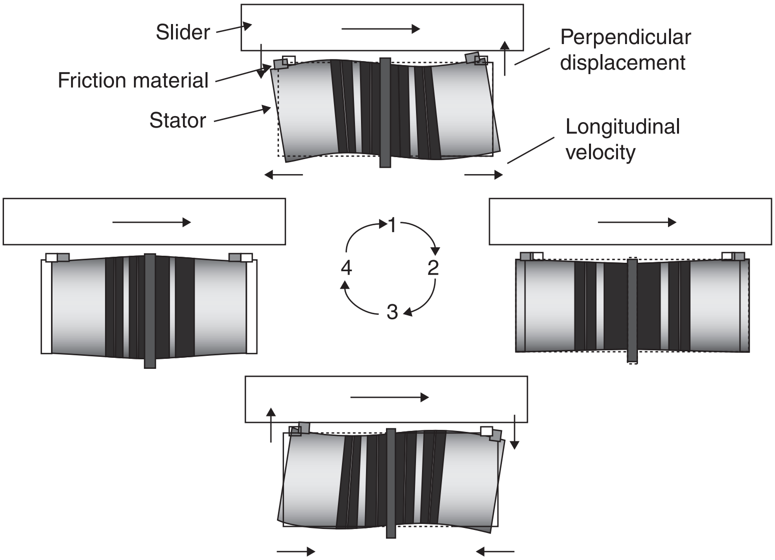
Slider
Friction material
Stator
Perpendicular displacement
Longitudinal velocity
1
2
3
4

20.18 Four phases of one cycle for a high-power linear motor.

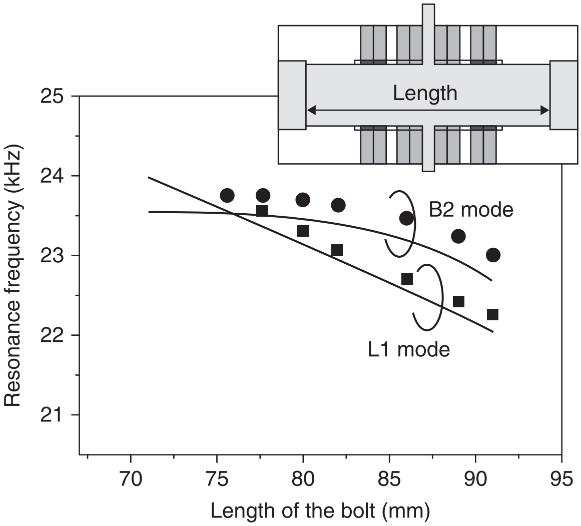

20.19 Adjustment of the resonance frequencies for the L1 and B2 modes through changing the bolt length. Continuous curves indicate numerical results while black circles and squares represent experimental ones.

Figure 20.20 shows slider speed plotted for a prototype motor as a function of the phase difference between the voltages applied for the longitudinal PZT elements and the bending elements. As can be seen from the figure, the maximum speed is obtained at −110° and 70°, which are 20° away from the theoretically expected values of −90° and 90°, and the curve is distorted from a pure sinusoidal

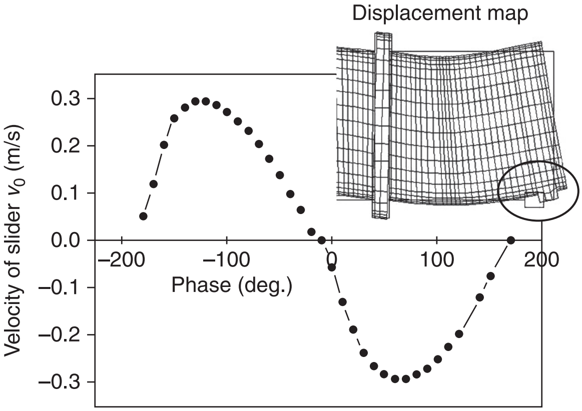

20.20 Slider speed as a function of the phase difference between the voltages for the longitudinal and bending electrodes. Upper right: displacement map.

shape. The reason for this discrepancy can be attributed to the geometrical structure of the contact part. Though the purpose of the bending vibration in this motor is to generate the vertical component, it also produces horizontal components, as shown in the displacement map in Fig. 20.20, estimated numerically, since the contact point is not located on the center line of the transducer. The contact point is circled on the map. The horizontal component is the addition of the longitudinal vibration and the bending vibration with 90° phase difference.

Figure 20.21 shows the slider speed measured as a function of the load for different voltages applied to the longitudinal PZT elements, where the voltage to the bending PZT elements and the preload are constant. The speed linearly decreases with an increase in the mechanical load. The maximum friction force is 36 N since the friction coefficient for the material used is 0.3 and the preload is 120 N. The maximum output force never exceeds the friction force given by the static preload even when the voltage is increased to generate a larger vibratory force, as explained for Fig. 20.6. Figure 20.22 shows the speed-load characteristics for a higher preload and higher voltages. The maximum thrust of approximately 100 N and the no-load speed of 500 mm/s were measured using a prototype with a diameter of 40 mm. The maximum efficiency, which is defined as the mechanical output power to the electrical input power to the longitudinal PZT elements, was 20%. A high static preload of around 400 N was needed to obtain a large friction force. Stronger bending vibration is needed for higher efficiency. The mechanism to hold the motor should be carefully designed for practical use so that the

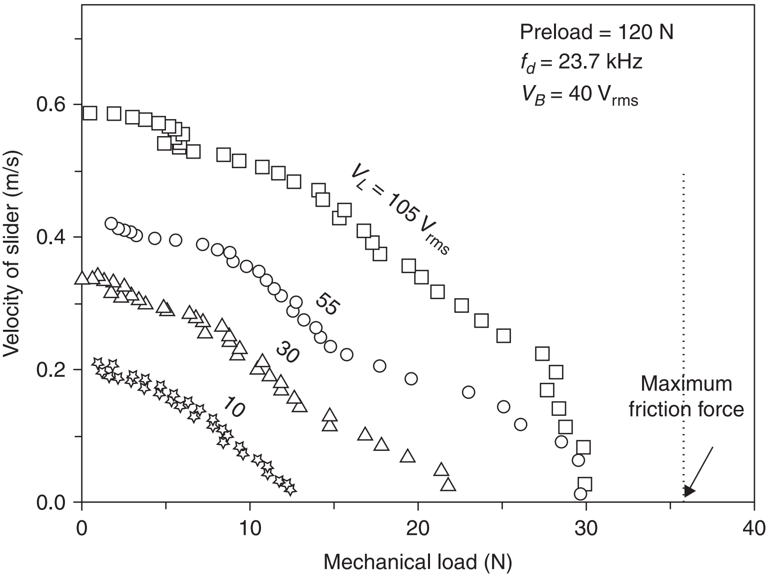

20.21 Speed-load characteristics for different voltages applied to the longitudinal PZT elements.

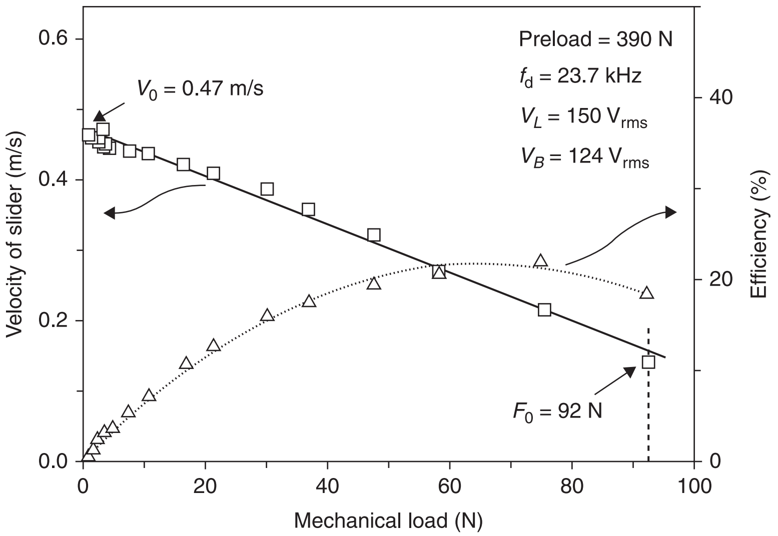

20.22 High-power performance of the motor.

transducer is held firmly and bears a large external force or an inertial force acting on the transducer during its transient operation. Positioning performance also depends on the holding method. Figure 20.23 shows the transient responses of the slider's speed for rise and fall states when the weight of the slider is 10 kg.

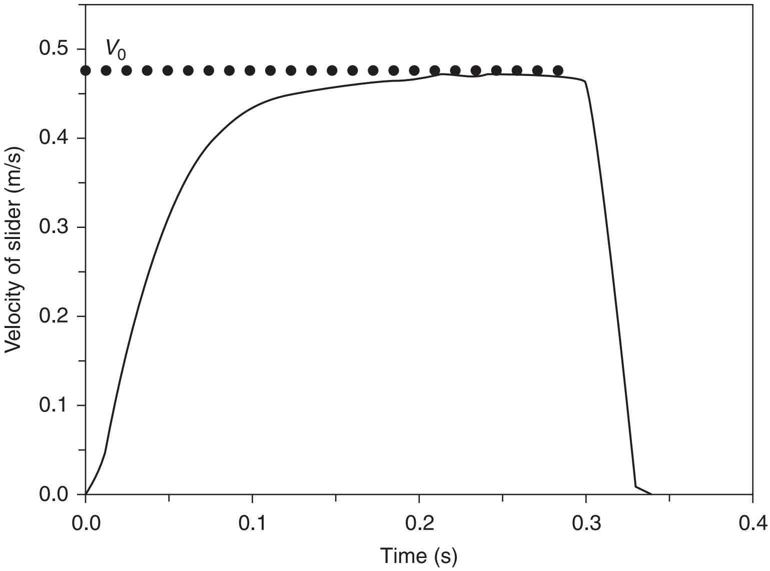

20.23 Start-stop transient responses for a 10-kg slider.

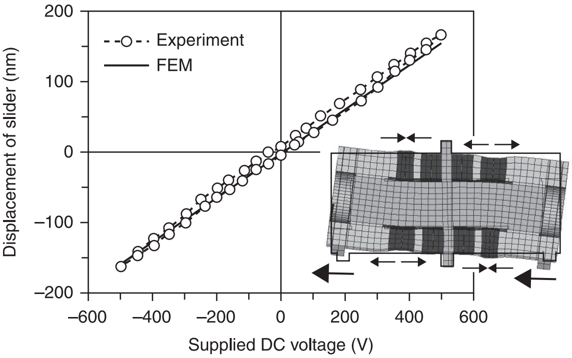

20.24 Fine positioning characteristics with static deformation.

The rise curve has a first-order delay characteristic, where the time constant is simply determined by the maximum thrust, the no-load speed and the weight of the slider. The fall state shows a constant negative acceleration due to the friction force. The settling time is sufficiently short with small residual vibrations. This excellent transient performance is useful for the high-speed control of the position of a table. In order to achieve nanometer-order positioning, static deformation is utilized by applying a high DC voltage to the bending PZT elements in addition to the action of the ultrasonic motor. A horizontal displacement of up to 200 nm is possible, as shown in Fig. 20.24. The slider position is adjusted by changing the DC voltage after the slider is roughly positioned through the motor's operation. A positioning error of less than 4 nm was achieved using a classical feedback control method. The error corresponded to the resolution of the linear position encoder used in the experiments.

20.3 Traveling-wave ultrasonic motors

Many ultrasonic motors produce elliptic motion at the surface, as mentioned in the previous section, which discussed the synthesis of elliptic motion using two orthogonal vibrations with a phase difference of 90°. In this section, another typical method of using elliptic motion is described. If traveling waves from any kind of elastic vibration propagate along the circumference of a ring or disk, or along a straight bar, particle motion at the surface will be, in general, elliptic. Techniques to construct a traveling-wave ultrasonic motor for both rotary and linear motion will be given below.

20.3.1 Rotary motor

Consider a standing wave of flexural vibration of the *n*th mode excited along an elastic ring. In practice, the ring will usually be composed of a metal body and a

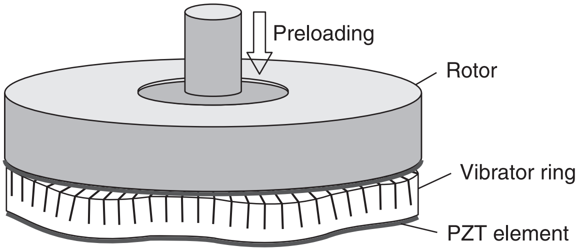

20.25 Basic configuration for a traveling-wave rotary motor.

thin piezoelectric ceramic disk bonded onto the bottom of the body, as shown in Fig. 20.25. A rotor disk is pressed against the vibrating body. The out-of-plane displacement of the standing wave is

$$u_C(\theta, t) = A\cos n\theta\cos\omega t. \tag{20.1}$$

Here, θ denotes the angular position and ω is the angular frequency of the vibration. The integer n is the order of the vibration mode. Another standing wave of the same order but shifted by 90° both in space and time is

$$u_S(\theta, t) = A\sin n\theta\sin\omega t. \tag{20.2}$$

The superposition of these two degenerate modes produces a progressive wave in the circumferential direction:

$$u_Z(\theta, t) = A\cos n\theta\cos\omega t + A\sin n\theta\sin\omega t = A\cos(n\theta - \omega t). \tag{20.3}$$

The electrode on the outer surface of the piezoelectric ceramic ring is divided into an appropriate number of sections to excite the two standing waves, as illustrated in Fig. 20.26. A two-phase power source ($V\cos\omega t$, $V\sin\omega t$) or a four-phase source ($V\cos\omega t$, $V\sin\omega t$, $-V\cos\omega t$, $-V\sin\omega t$) is used as a driver. Figure 20.26 shows an

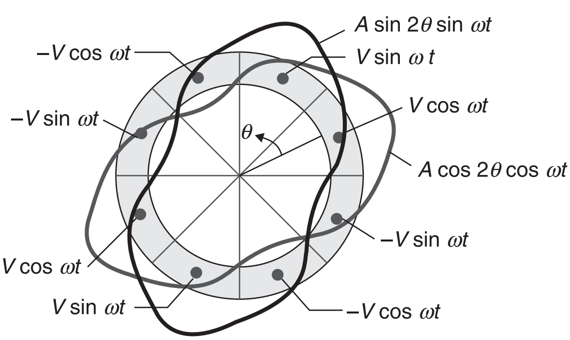

20.26 Voltage application for generating traveling waves along a ring vibrator.

example of the second order ($n = 2$) vibration and four-phase balanced feeding. For unbalanced two-phase excitation, a different electrode pattern with a ground port would be used.

If the vibrating ring has a thickness b, as shown in Fig. 20.27, the in-plane vibration displacement can be found from the gradient of the out-of-plane displacement:

$$u_\theta(\theta,t) = -\frac{b}{2}\frac{du_z}{d\theta} = \frac{bnA}{2}\sin(n\theta - \omega t), \tag{20.4}$$

as a thin-beam approximation for flexural waves. From Eqs 20.3 and 20.4, we can see that every point on the surface has elliptical motion. The rotation direction of the elliptical motion depends on the nature of the vibration mode used. The shape of the elliptic motion, the ratio of the in-plane component to the out-of-plane component, is determined by the thickness of the body. The rotation speed is proportional to the in-plane vibration component, while contact between the vibrator surface and the rotor is controlled by the out-of-plane component. The shape of the elliptical motion is important for traveling-wave ultrasonic motors. In practice, teeth are added to the contact surface of the metal body to amplify the in-plane vibration amplitude. The tooth-structure also acts as a mechanical transformer to give better matching between the transducer and the motor load. Both the in-plane and out-of-plane displacement amplitudes reduce together when the voltages are lowered for slow-speed operation. Slow-speed operation sometimes becomes unstable or a dead region may appear near zero for this type of motor.

In an ultrasonic motor, it is possible to have an annular structure with a large cavity inside the body, which cannot be realized easily with a conventional electromagnetic motor. Optical engineers have adapted this type of structure for the auto-focusing mechanism of commercial cameras. No reduction gear is

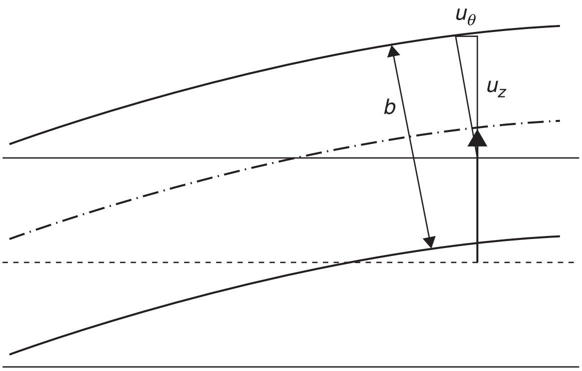

20.27 Out-of-plane and in-plane displacements in flexural vibration.

required since, in an ultrasonic motor, the torque is large and the speed is low, which results in quiet operation: low noise is one of the advantages of an ultrasonic motor over an electromagnetic motor with gears. Once the vibration is turned off, the rotor is locked by the friction force and does not need an additional brake. As a control system, total power consumption may be lower than a system with an electromagnetic motor and active brake. For precision and high-speed positioning applications, it is possible to realize a system with high rigidity using an ultrasonic motor, since reduction gears are not required.

A disk-shaped vibrator can also be used in a rotary motor instead of a ring-shaped one. The flexural mode having a nodal circle is useful for firmly supporting the vibrator in a disk vibrator; in a ring vibrator, it is not possible to theoretically find a clamping position. In practice, a ring vibrator is supported using soft material or a spring. Ideally, the supporting mechanism should be rigid in the rotation direction for precise positioning, but should be soft enough not to block vibrations. The design of the support mechanism to fulfill these two contradictory requirements is key to the practical implementation of ultrasonic motors.

A bar-shaped configuration, as shown in Fig. 20.28, can be constructed with a bolt-clamped structure (Kurosawa *et al.*, 1989b). Two orthogonal bending vibrations of the fundamental mode are driven with a phase difference of 90°, producing elliptical motion at the end of the bar. A rotor is pressed against one end of the bar or two rotors sandwich the bar. Two sets of bending PZTs are used for this type of transducer, where each set is rotated by 90° to excite the two orthogonal modes. Alternatively, PZT disks with uniform polarization are driven with four independent electrodes using a four-phase power source. This type of structure is usually considered to be a traveling-wave motor. There has been much research to make a miniature or ultra-miniature ultrasonic motor based on this principle. A

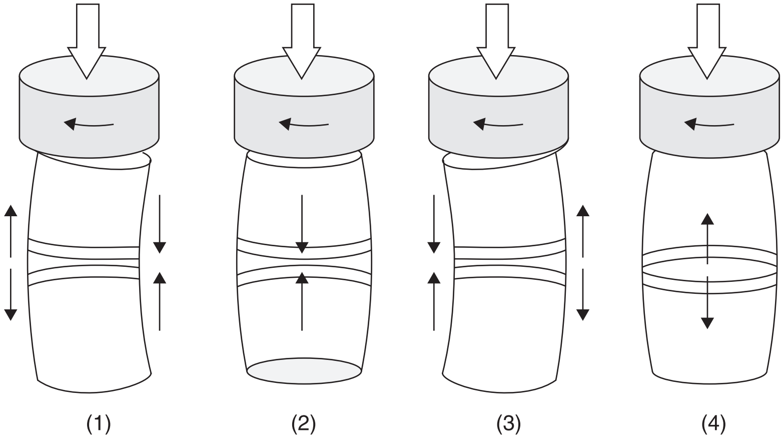

20.28 Bar-shaped motor with rotation due to the bending mode. One cycle of the vibration is divided into four phases: (1) 0; (2) 90; (3) 180; (4) 270 degrees.

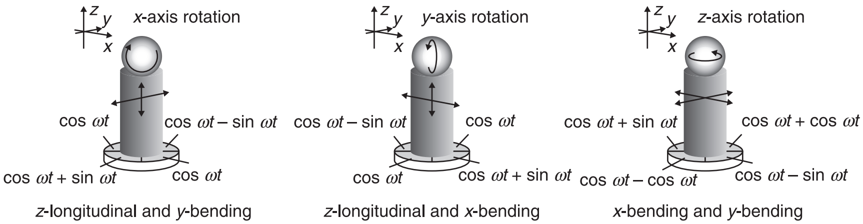
z
y
x
x-axis rotation
cos ωt
cos ωt − sin ωt
cos ωt + sin ωt
cos ωt
z-longitudinal and y-bending
z
y
x
y-axis rotation
cos ωt − sin ωt
cos ωt
cos ωt
cos ωt + sin ωt
z-longitudinal and x-bending
z
y
x
z-axis rotation
cos ωt + sin ωt
cos ωt + cos ωt
cos ωt − cos ωt
cos ωt − sin ωt
x-bending and y-bending

20.29 Three-degree-of-freedom motor fabricated on a substrate surface.

motor with three-degree-of-freedom motion is possible if longitudinal PZT disks are added to the transducer and a ball rotor is used. Two orthogonal bending vibrations and a longitudinal vibration can be independently excited on the bar. Elliptical vibrations parallel to any plane can be created if an appropriate combination of the three vibrations is used, and the ball rotor can be made to rotate around any axis. This type of motor would be useful for the joints in the arms or fingers of a robot because complex movement can be realized with a single actuator. A small multi-degree-of-freedom motor can be fabricated on the surface of a substrate using only one PZT disk with an electrode divided into four, if the applied voltage is systematically considered, as shown in Fig. 20.29 (Goda *et al.*, 2009). This type of structure is suitable for integrating with micro-electrical-mechanical systems.

20.3.2 Linear motor

A traveling wave can be excited along a bar to realize a linear motor. Figure 20.30 illustrates a basic setup for a flexural-wave linear motor (Kuribayashi *et al.*, 1985).

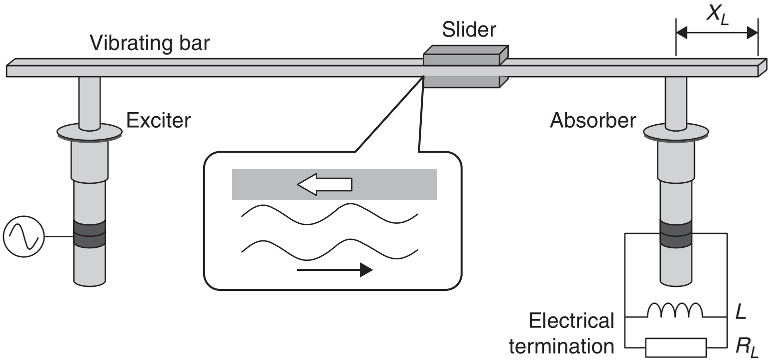
Vibrating bar
Slider
X_L
Exciter
Absorber
Electrical termination
L
R_L

20.30 Traveling-wave linear motor.

Two transducers of the same design are attached to the ends of the bar at right angles: one is driven by an electrical source to excite flexural waves, the other is used as a terminator to absorb the elastic waves. The absorbed mechanical energy is transformed to electrical energy through piezoelectricity, and consumed with a resistor connected at the electrical terminal of the transducer. An inductor is often used in parallel to cancel the capacitance of the transducer. When the flexural traveling wave propagates along the bar, every point on the surface moves elliptically. The rotation direction of the elliptical motion is opposite to the direction of propagation of the flexural waves. If an object is pressed against the vibrating surface, it experiences a thrust force from the elliptical motion through friction. The object moves from the sink of the wave to the source. We can change the direction of the linear motion by swapping the source and the sink. In designing a traveling-wave linear motor, the electrical load resistor R_L and the tail length x_L of the bar should be chosen to suppress standing waves.

From experiments, only a few percent of the mechanical energy transmitted by the bar was obtained as the motor output: the rest of the power supplied to the source transducer was received by the sink transducer. Consequently, in this type of motor, we should reuse the energy absorbed by the sink to drive the source for higher efficiency. This circulation of energy is automatically accomplished in rotary motors using traveling waves, as explained in the previous section.

A traveling-wave ultrasonic motor can be realized using surface acoustic waves (SAWs) with a very high frequency, in the tens of megahertz (Kurosawa *et al.*, 1996). Since the vibration displacement of SAWs is very small due to the high frequency, a special slider design is required. A high-power output was successfully reported using a $LiNO_3$ substrate and a silicone slider with small dots on the surface. Figure 20.31 is a photograph of a SAW motor.

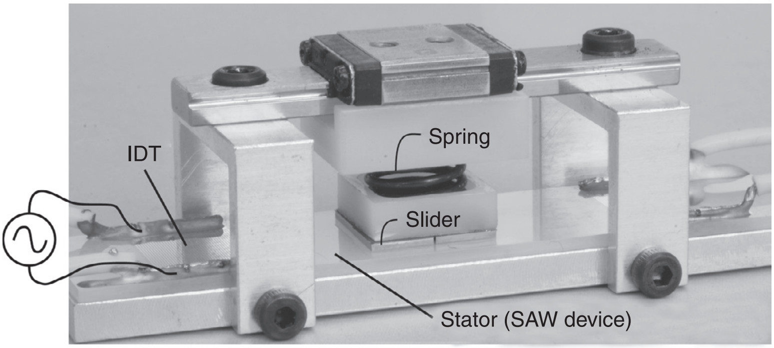

20.31 Surface acoustic wave ultrasonic motor. IDT: inter-digital transducer.

20.4 Ultrasonic motor performance

In this section, we will compare the performance of ultrasonic motors with conventional electromagnetic motors. Figures 20.32 and 20.33 show the maximum

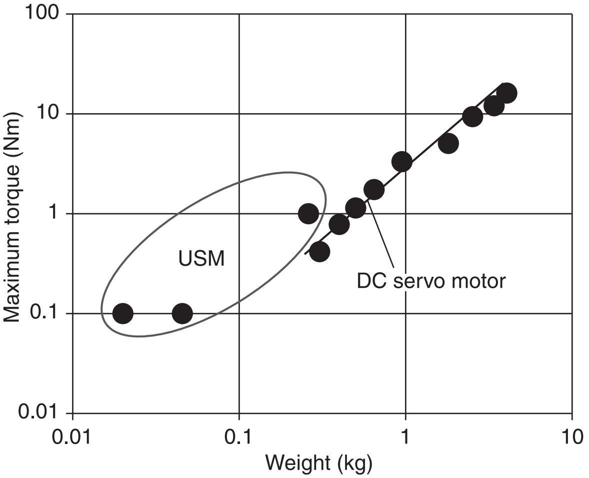

20.32 Maximum torque vs. motor weight. USM: ultrasonic motor.

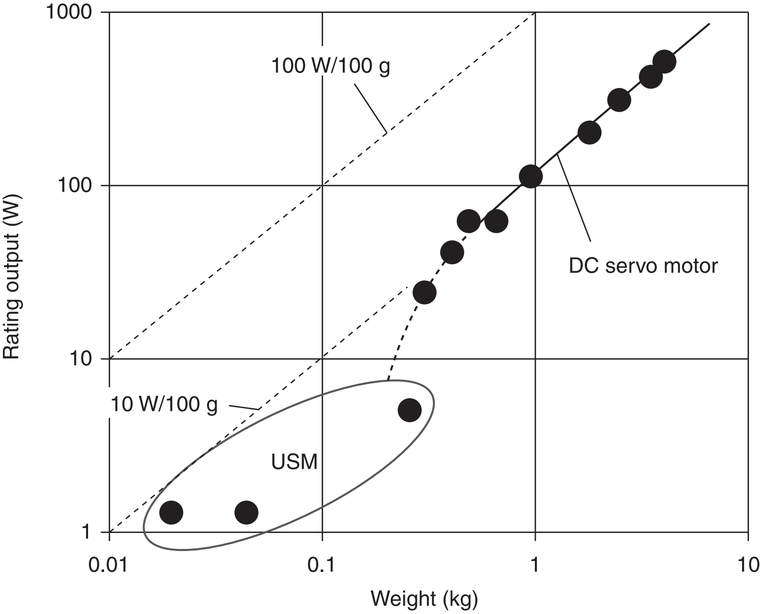

20.33 Output power vs. motor weight. USM: ultrasonic motor.

torque and the mechanical output power plotted against motor weight, respectively. Measurements were made using commercially available rotary ultrasonic motors with brass disk vibrators. Ultrasonic motors have a higher torque than DC servo motors with the same weight. The output power per unit weight is constant around 10 W/100 g for larger DC servo motors; however, the output drops rapidly for smaller motors. The efficiency of conventional electromagnetic motors is too low to be used practically when they are under 10 mm in diameter. However, the output power and efficiency of small ultrasonic motors are moderate. This is one of the reasons why ultrasonic motors are attractive as micro-actuators. The energy density of a piezoelectric transducer, in general, is much higher. Better performance is expected if sophisticated designs to transform the vibration to the actuator motion can be developed.

The output torque for various kinds of ultrasonic motor is plotted as a function of the diameter in Fig. 20.34. The output torque is approximately proportional to the cube of the diameter. The hybrid transducer motor described in Section 20.2.1 has the largest torque. A photograph of prototype motors from 5 mm to 80 mm in diameter is shown in Fig. 20.35. A rod-shaped traveling-wave ultrasonic motor

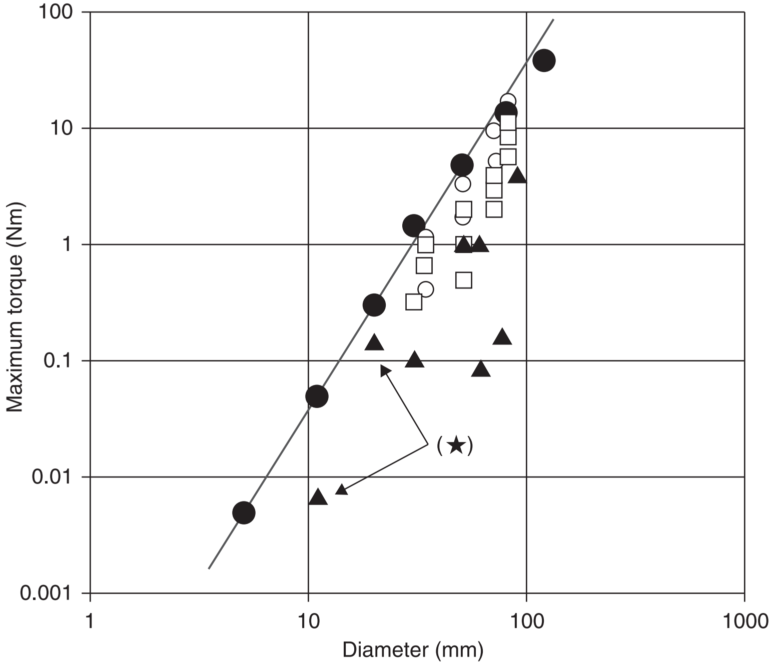

20.34 Maximum torque for various kinds of ultrasonic motor. Black circles: hybrid transducer motor (Fig. 20.1); black triangles: traveling-wave motor (Fig. 20.25); black star: rod-shaped traveling-wave motor (Fig. 20.28); open circles: DC servo motor; open squares: AC servo motor.

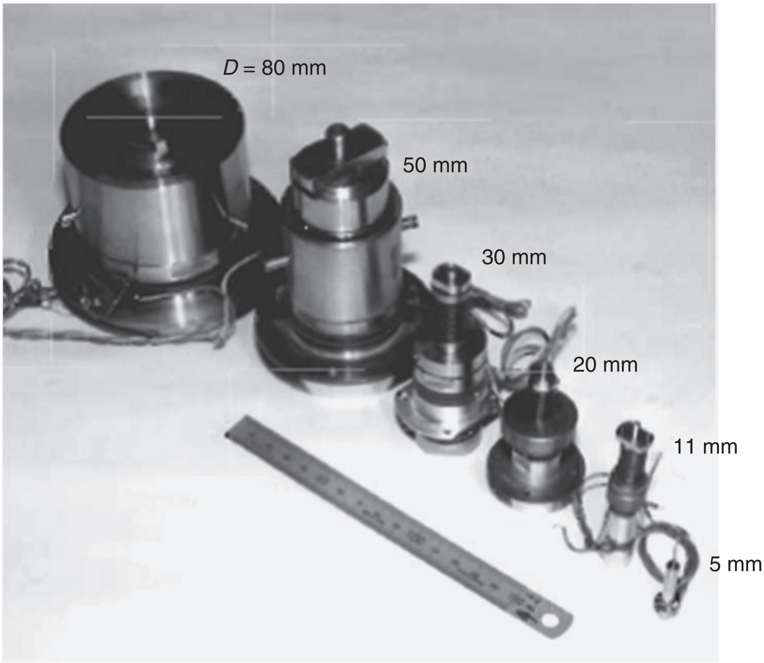

20.35 Hybrid transducer rotary motors from 5 mm to 80 mm in diameter.

also has a high torque and a small diameter. The torques of other traveling-wave ultrasonic motors are lower than conventional electromagnetic motors when they are compared by diameter, since traveling-wave motors have a thin disk shape. Revolution speed is smaller in larger motors in inverse proportion to the diameter, since the maximum vibration velocity at the circumference of a vibrator cannot exceed around 1 m/s because of the limitation in the vibration velocity produced by a transducer. Ultrasonic motors generally have low-speed and high-torque characteristics.

20.5 Summary and future trends

Several fundamental methods of realizing ultrasonic motors for both rotary and linear motion were given in this chapter. The motors can be categorized as of the standing-wave type or the traveling-wave type, in general. For standing-wave motors, various combinations of vibration modes with many different shapes have been developed to create adequate elliptical motion. The knowledge accumulated from developing mechanical filters for communications has been useful when designing effective combinations of modes for motors. Small linear motors based on the L1-B2 mode have been successfully used for the positioning of optical components or in cameras. Rotary motors with torsional and longitudinal modes are in limited use because of the high cost of the torsional PZT element, although they are powerful small motors. Traveling-wave rotary motors are widely used in consumer cameras for auto-focusing. Linear traveling-wave motors have not found application yet due to their bulky structure and low efficiency. SAW motors are attracting interest in several fields. The high energy density of $LiNO_3$ crystal substrates creates a high-output motor with a compact structure. Energy circulation circuits can be incorporated in the driving electronics to achieve higher total efficiency.

For the practical use of ultrasonic motors, the selection of the friction material is one of the most important issues to be considered. The vibrator body of a traveling-wave motor is made of an aluminum alloy or brass. A thin sheet of engineering plastic or hard polymer is sometimes used as a friction layer on the rotor surface. Plating or other surface treatment applied to the vibrating body and the rotor surface strengthen the friction characteristics. In addition to metals and polymers, fine ceramics are promising candidates as friction materials in ultrasonic motors. In some commercial ultrasonic motors, a lifetime of 1000–5000 hours has been stably achieved so far, and a 10 000-hour lifetime has been reported. But the lifetime depends significantly on the operating conditions, such as the load, the number of start-stop actions, the ambient humidity, etc. Further research on the friction interface from a wider point of view and with detailed analysis is required for broader application of ultrasonic motors.

The output force/torque of ultrasonic motors is already superior to conventional motors with the same weight. On the other hand, the efficiency is around 50% or less in most commercially available ultrasonic motors. This value is lower than conventional motors, especially for larger versions. However, in the practical use of ultrasonic motors, total energy consumption may be lower than for electromagnetic motors because the required output torque can be achieved without reduction gears and no energy is used to brake the rotor or to maintain its position.

The potential energy density and efficiency of piezoelectric transducers, in general, is much higher than achieved with ultrasonic motors so far. This gap can be attributed to the friction loss generated in the contact interface between the vibrator and the rotor/slider. According to numerical simulations, the friction loss can be theoretically reduced if the contact duration is shortened to a quarter period/wavelength of the ultrasonic vibrations. Sophisticated designs to minimize the gap will be used in the next generation of ultrasonic motors. At the same time, the driving circuits and control methods can be enhanced using modern inverter technology and low-cost microcomputer chips.

20.6 References

Goda Y, Koyama D and Nakamura K (2009), Design of multi-degree-of-freedom ultrasonic micromotors, *Jpn J Appl Phys*, 48, 07GM06-1-4.

Kuribayashi M, Ueha S and Mori E (1985), Excitation conditions of flexural traveling waves for reversible ultrasonic linear motor, *J Acoust Soc Am*, 77, 1431–5.

Kurosawa M and Ueha S (1991), Hybrid transducer type ultrasonic motor, *IEEE Trans Ultrason Ferroelec Freq Cont*, 38, 89–92.

Kurosawa M, Yamada H and Ueha S (1989a), Hybrid transducer type ultrasonic linear motor, *Jpn J Appl Phys*, 28, 158–60.

Kurosawa M, Nakamura K, Okamoto K and Ueha S (1989b), An ultrasonic motor using bending vibration of a short cylinder, *IEEE Trans Ultrason Ferroelec Freq Contr*, 36, 517–21.

Kurosawa M, Nishita K, Koike Y and Ueha S (1991), Hybrid transducer type ultrasonic linear motor using flexural vibrator, *Jpn J Appl Phys*, 30, 209–11.

Kurosawa M, Takahashi M and Higuchi T (1996), Ultrasonic linear motor using surface acoustic wave, *IEEE Trans Ultrason Ferroelec Freq Contr*, 43, 901–6.

Takano M, Takimoto M and Nakamura K (2011), Electrode design of multilayered piezoelectric transducers for longitudinal-bending ultrasonic actuators, *Acoust Sci & Tech*, 32, 100–8.

Ueha S and Tomikawa Y (1993), *Ultrasonic Motors, Theory and Applications*, New York, Oxford University Press.

Yun C, Ishii T, Nakamura K, Ueha S and Akashi K (2001), A high power ultrasonic linear motor using a longitudinal and bending hybrid bolt-clamped Langevin type transducer, *Jpn J App Phys*, 40, 3773–6.

Index

A-mode ultrasound, 555–6
absorption, 375
acoustic agglomeration, 502
acoustic contrast agent, 558, 564
acoustic field
  optical visualisation, 314–27
    Fresnel visualisation method, 320–2
    photoelastic visualisation method, 323–7
    Schlieren visualisation technique, 314–19
acoustic impedance, 92
acoustic microstreaming, 546
acoustic radiation force, 550
acoustic streaming, 546, 550
acoustic wave equation, 221–4
  diagonalisation, 233–4
AD524, 593
admittance loop, 268
AFiDS, 630
air-cleaning, 502–5
air-coupled non-destructive evaluation (NDE), 392–5
airborne ultrasound transducers, 374–403
  air-coupled non-destructive evaluation, 392–5
    carbon-fibre plate with impact damage, 394
    solid chocolate sample and chocolate sample containing nuts, 395
    square defect in a carbon-fibre plate produced by through-transmission system, 394
    through-transmission system for NDE, 393
  airborne transducer arrays, 390–2
    possible electrode geometry for line array of capacitance, 391
    scans in air by transducer array where the beam is focussed off-axis, 415
    scans in air by transducer array where the beam is focussed on-axis, 391
  applications, 392–402
  basic design principles, 375–81
    absorption coefficient as function of frequency for air, 377
    acoustic mismatch problem, 378–9
    acoustical properties of some piezoelectric materials, 379
    chirp signal, 380
    possible solutions to this problem, 379–81
    signal buried in noise, 380–1
    ultrasonic properties of air, 375–8
  curved devices, 386, 388
    curved capacitive transducers and their focal regions, 388
  flow and temperature measurement in gases, 398–402
    hot gas jet flow velocity measured experimentally, 399
    hot gas jet temperature measured experimentally, 399
    transmitting useful signals through flames, 400
    ultrasonic frequency spectra measured using simulated Martian atmosphere, 402
  future trends, 402–3
  gas-jet transducers, 396–8
    beam emitted from gas-jet transducer, 398
    illustration, 397
    watermark on banknote and banknote image using focused air-coupled ultrasound, 396
  planar devices, 385–6, 387
    radiated field amplitude for single air-coupled device, 386
    radiated field amplitude for single air-coupled device under tone-burst operation, 387
  radiated fields in air, 385–92
  thin materials imaging, 396
  transducer designs for use in air, 381–5
    capacitive membrane devices, 382–5
    capacitive transducer with etched pits in the backplate, 385
    membrane and backplate of capacitive transducer, 383
    piezoelectric transducers, 381–2

- use of external mirrors, 387–90
  - British ten-pence coin surface made by scanning in air, 390
  - capacitive transducer with external mirror, 389
- aluminium nitride (AlN), 16
- amplitude enhancement, 139
  - driving an ultrasonic micro-scalpel from both sides, 140
  - vibration velocity *vs.* driving voltage for an ultrasonic micro-scalpel, 140
- angle beam probes, 45–58, 61–6
  - non-segmented transducers, 46–52, 61–5
  - segmented transducers, 52–8, 65–6
- anti-resonance frequency, 268, 270
- aperture, 332
- apodisation, 351
- application programming interface (API), 466
- average detector, 460

- backing layers, 24–6
- barium titanate ($BaTiO_3$), 4–6, 7, 73–4
  - permittivity of tita-con doped with BaO, 74
- bi-directional loss, 352
- bi-laminar shielded membrane hydrophone, 635
- bias field *see* horizontal magnetic field
- bio-heat equation, 549
- biomedical ultrasonics
  - non-linear acoustics and its application, 517–40
    - advances in tissue harmonic imaging, 523, 525–30
    - basic aspects of wave propagation and associated phenomena, 518–19
    - measurements of and advances in B/A determination, 519–23, 524
    - non-linear wave propagation in hydrophone probe calibration, 534–8
    - therapeutic applications, 538–9
    - ultrasound metrology, 531–4
- birefringence, 323
- bismuth titanate (BIT), 413
- Blackman-Harris window, 355
- Blackman window, 355
- blocked capacitance, 266
- bolted Langevin transducer, 572
- booster, 294–5
- boundary element method
  - determining asymptotic expansion terms proposed method, 252–8
  - determining asymptotic expansion terms for $\eta \rightarrow 0$, 250–8
    - direct approach, 250–2
  - micro-acoustic devices, 220–60
    - acoustic wave equation, 221–4
    - construction of infinite-domain Green's functions, 224–39
    - future trends, 258–60
    - near-field analysis, 239–49
    - normalisation of field variables, 249–50
- Bragg reflection, 316–17
  - illustration, 317
- brain
  - acoustic attenuation as absorption plus scattering, 548–9
  - bubble formation and growth, 551–4
    - bubble dynamics, 552–3
    - microstreaming, 553–4
  - diagnostic ultrasound, 555–60
    - B-mode, transcranial image of human brain, 558
    - contrast agents, 558–
    - coronal image of perfusion-fixed mouse brain after stroke, 559
    - sonoelastic imaging, 557–8
    - standard diagnostic imaging, 555–7
  - fundamentals of ultrasound propagation and absorption, 547–8
  - inertial cavitation and associated material stresses, 554
  - mechanical index, 554–5
  - neuromodulation by ultrasound, 566–7
  - physical and chemical processes engendered by medical ultrasound, 549–51
    - acoustic cavitation, 551
    - acoustic radiation pressure, 550–1
    - displacement of living rat brain, 551
    - heat generation and thermal index, 549–50
  - therapeutic ultrasound, 560–3
    - applications, 545–68
    - rapid heating with ultrasound for therapeutic effect, 561–2
    - thrombolysis, 562–3
  - ultrasound-facilitated delivery of drugs and antibodies, 563–6
    - solid cone HIFU device for opening the BBB intra-operatively, 565
- Bridgman method
  - single crystals growth, 165–75
    - electrical property of PIMNT 16/51/33, 168–70
    - electrical property of PIMNT 24/42/34, 171–4
    - piezoelectric constants as a function of Curie temperature, 175
    - PIMNT 16/51/33, 165–8
    - PIMNT 24/42/34, 170–1
    - PSC of PIMNT, 174–5, 176
- buffer rod, 411, 416–18
  - ultrasonic performance of PZT/PZT IUT fabricated onto a clad buffer rod, 417
- Butler–Volmer equation, 589

- capacitive microfabricated ultrasound transducer technology, 534
- capacitive micromachined ultrasonic transducers (CMUT), 384, 402

cardiac electrophysiological measurement, 602–6
  cMAP signals and ventricular fibrillation, 605
  multichannel recording from isolated perfused canine left ventricle, 604
cavitation, 530
cavitation nuclei, 552
chirp signal, 378
Choi–Williams (CW) distribution, 473
Clevite Corporation, 75–6
CLOTBUST, 563
clutter, 445
Commission Directive 2008/50/EC, 502
converse piezoelectric effect, 70
coplanar shielded membrane hydrophone, 635
couplant, 410–11
coupling-of-modes (COM) theory, 331, 342–50
cutting test, 139–40
cyclic voltammetry (CV), 591
cylindrical bending vibrator
  ultrasonic micro-motor, 127–31
    amplitude *vs.* frequency, 130
    cross section, 129
    deformation and rotation, 129
    illustration, 128
    output torque *vs.* pre-load, 130
    revolution speed *vs.* input voltage, 131

damped capacitance, 266–7
Debye length, 588
delay line, 411
diagnostic ultrasound, 555–60
  B-mode, transcranial image of human brain, 558
  contrast agents, 558–
  coronal image of perfusion-fixed mouse brain after stroke, 559
  sonoelastic imaging, 557–8
  standard diagnostic imaging, 555–7
Dirac delta function, 222, 224, 241
direct piezoelectric effect, 70
displacement transducers, 77–8
distributed acoustic reflection transducer (DART), 342
Doppler imaging, 556
double refraction *see* birefringence
dual-element transducer, 27–8
  configuration, 28

Eddy current, 36, 40
Eigensystem, 234–6
Eisenmenger fibre-optic hydrophone, 643–51
  frequency response, 649
  measured directional response, 650
  relationship between Fresnel reflection coefficient and pressure, 647
  schematic, 644
elasto-electric matrix, 11
electric displacement, 8
electrical frequency response, 336
electrical measurements, 267–71
  admittance loop around the resonance frequency, 268
  frequency responses of the electrical admittance, 267
  simplified equivalent circuit model, 269
electrical polarisation, 8
electrode impedance spectroscopy (EIS), 591
electromagnetic acoustic transducers (EMAT), 36–66
  conventional ultrasonic transducer, 37
  magnetostriction-type, 60–66
  physical principles, 36–41
    excitation by Lorentz forces, 40
    excitation by magnetic forces, 40–1
    excitation by magnetostriction, 41
    parallel electromagnetic ultrasonic conversion with horizontal magnetisation, 39
    perpendicular electromagnetic ultrasonic conversion with horizontal magnetisation, 38, 39
  tubes and rods, 41–59, 58–9
    angle beam probes, 45–58
    EMAT for tube waves, 59
    normal probes, 41–5
    transmitter and receiver coil for tube waves, 59
electromechanical coupling coefficient, 11, 12, 18
electromechanical coupling factor, 89, 93–4
  piezoelectric resonators, 94
electrostatic precipitators (ESP), 502, 504
energy transmission coefficient, 90–1
engineering notation, 10
environmental processes
  power ultrasonics, 501–7
    acousto-electrostatic filter, 504
    air-cleaning, 502–5
    comparison of rotary vacuum filtration with and without ultrasound, 507
    multifrequency acoustic agglomerator with stepped-plate generators, 503
    reduction in particle emissions for two different frequencies, 505
    rotary vacuum filtration aided by rectangular grooved-plate transducer, 507
    sludge filtration, 506–7
epitaxial film, 150–1
epoxy resin ultrasonic probe, 147–50
  c-mode image of a coin produced by titanium wire-backed hydrophone, 150
  frequency spectrum by titanium wire-backed hydrophone, 149
  illustration, 148
  PZT film deposited on a titanium substrate, 148
  signal received by titanium wire-backed hydrophone, 149

equivalent electrical circuit, 265–7, 270
  equivalent electrical circuit with lumped constants, 266
  longitudinal transducer composed of piezoelectric ceramic plate, 265
  models, 195–202
    historical background, 195–6
    KLM model, 200–2
    Mason's model, 196–200
exchange current density, 589
extensive radiating area transducers, 479
extracorporeal shock waves (ESW), 519, 539

Fabry Perot interferometer (FPI), 651
Fabry Perot polymer film fibre-optic hydrophone, 651–60
  illustration, 651
  measured directional response, 658
  measured frequency response, 657
  measurements of heating induced by HIFU field, 659
  temperature-time curve and acoustic waveforms, 660
  transduction mechanism, 653
ferroelectricity, 4–6
  crystalline unit cell of $BaTiO_3$, 4
  polarisation loops for $BaTiO_3$, 6
  polarisation of $BaTiO_3$, 5
fibre Bragg grafting (FBG), 667
fibre-optic hydrophones (FOH), 619, 641–71
  comparison of different fibre-optic hydrophones, 669
  Eisenmenger fibre-optic hydrophone, 643–51
  Fabry Perot polymer film fibre-optic hydrophone, 651–60
  interferometric displacement fibre-optic hydrophone, 666–7
  intrinsic fibre-optic hydrophones, 667–8
  multilayer dielectric fibre-optic hydrophone, 660–6
  role in an ultrasound metrology, 668, 670–1
field analysis
  1D Fourier transform, 229–39
    diagonalisation of the acoustic equation, 233–4
    Eigensystem for shear horizontally polarised waves, 234–6
    Green function, 236–9
    preparatory considerations, 229–33
  2D Fourier transform, 224–8
    frequency independent formulation, 225–6
    material independent formulation, 226–8
field-programmable gate array (FPGA)-based hardware platform, 444
field variables, 249–50
flat-plate transducer with reflector, 487–9, 490
  directivity diagrams, 490
  illustration, 488
  prototype for operating in air, 489
flaw-to-clutter ratio (FCR), 446
flexible ultrasonic transducer (FUT), 421–2
  precise pipe thickness measurement at 200 °C, 430–2
    PZT/PZT FUT glued onto a steel pipe, 431
    ultrasonic signals in the frequency domain, 432
    ultrasonic signals in the time domain, 432
  pulse echo measurements at various temperatures, 422
floating-point unit (FPU), 470
fluid processing
  new technologies and applications of power ultrasonics, 476–514
    application, 490–513
flux method
  PIMNT single crystals growth, 163–5
    dielectric constant and dissipation factor of a PSC, 165
    illustration, 164
focused buffer-rod IUT
  ultrasonic imaging in 200 °C silicone oil, 425–9
    BIT/PZT buffer-rod IUT, 425
    experimental set-up for imaging hot silicone oil, 426
    ultrasonic front-surface image of US one cent coin, 427, 428
    ultrasonic subsurface image of a US one cent coin, 428, 429
food processing, 491–501
  supercritical fluid extraction assisted by ultrasound, 498–501
    pilot plant for extracting almond oil, 500
    results of extracting almond oil, 501
  ultrasonic defoaming, 491–3, 494
    rotary ultrasonic defoamer in a reactor, 494
    static ultrasonic defoamer in canning line, 493
    ultrasonic defoamer system, 492
  ultrasonic dehydration, 493–8, 499, 500
    fluidised-bed dryer with cylindrical-radiator transducer, 497
    system for food dehydration using a stepped-plate ultrasonic generator and forced air, 496
    system using high-intensity ultrasonic vibration, 499
  vegetable moisture content
    dried with cylindrical-radiator transducer, 498
    dried with forced air, 497
    high-intensity ultrasonic vibration, 500
forces, 193–5, 267
free motional admittance, 269
frequency agility, 445

frequency-diverse ultrasonic flaw-detection systems
  analysis and synthesis using order statistics and neural network processors, 444–74
  flaw-detection performance evaluation, 460–4
  future trends, 472–3
  neural network detection processor, 456–60
    back-propagation learning process, 458–9
    neural network architecture, 456–7
    neural network model for SSP post-processing, 457–8
    neural network software implementation, 459–60
  system-on-a-chip implementation, 465–72
    application software, 466–7
    execution time, 470
    hardware realisation, 465–6
    hardware/software co-design, 467–8
    resource usage, 470–2
    software and hardware performance evaluation for SSP, 468–70
  ultrasonic flaw-detection techniques, 445–56
    order-statistic (OS) processors, 452–6
    split-spectrum processing, 447–8
    ultrasonic signals frequency analysis, 448–52
Fresnel visualisation method, 320–2
  Fresnel diffraction, 320
  visualisation systems and images, 320–2
    sequence of ultrasonic pulses, 322
    ultrasonic pulse travelling in water, 321
    ultrasonic tone-burst waves propagating in water, 322

Gabor transform (GT), 473
gas-jet transducers, 396–8
Gauss's law, 190
Gélat model, 634
geometric-mean detector, 460
Gladstone–Dale relationship, 646
Gouy–Chapman capacitance, 588–9
Gouy–Chapman–Stern model (GCS), 587
Green's function, 224–39
  field analysis using a 1D Fourier transform, 229–39
    construction of Green's function, 236–9
    diagonalisation of the acoustic equation, 233–4
    Eigensystem for shear horizontally polarised waves, 234–6
    preparatory considerations, 229–33
  field analysis using a 2D Fourier transform, 224–8
    frequency independent formulation, 225–6
    material independent formulation, 226–8

Hamming function, 353, 355
Hankel function, 228
harmonic imaging, 523
Helmholtz capacitance, 588
Helmholtz model, 384
Helmholtz–Perin model, 588
heterodyne detection techniques, 280–4
  interferometer with the Bragg cell, 281
high-intensity airborne ultrasound, 510
high-intensity focused ultrasound (HIFU), 519, 538, 622
high-intensity therapeutic ultrasound (HITU), 519, 538, 622
high-intensity ultrasound, 572
high-intensity vibrator
  ultrasonic micro-scalpel, 135–40
    amplitude enhancement, 139
    cutting test, 139–40
    diagram and amplifier circuit, 137
    illustration, 136
    pickup voltage, 138–9
    vibration velocity and amplitude, 138
high-power transducers, 29–31
  Langevin transducer, 30
high-temperature non-destructive evaluation, 408–41
  process-monitoring demonstration, 433–40
    amplitude of the ultrasonic signals propagating through the parts during moulding, 436
    cross section of a mould with IUTs, 435
    injection moulding process optimisation for micro-fluidic device, 436–40
    inner surface of the mould showing the probe ends, 434
    IUT with and without electrical connection, 434
    maximum variation of surface profile of line pattern of moulded parts, 439
    monitoring of complete filling in injection moulding, 433–6
    moulded parts, 435
    outer surface of the mould showing four IUTs, 433
    steel buffer-rod IUT, 437
    test moulded part, 438
    ultrasonic probe with holder and electric cable, 438
    ultrasonic velocity during one cycle of moulding, 439
  sol-gel composite ultrasonic transducers, 411–22
    BIT/PZT ultrasonic performance, 414
    buffer-rod IUT, 416–18
    flexible ultrasonic transducer (FUT), 421
    general fabrication process, 412
    illustration of wedge IUT, 419
    integrated ultrasonic transducer (IUT), 415–16
    lithium niobate/PZT ultrasonic performance, 415
    longitudinal wave and shear wave generation by mode conversion, 418

    PZT/PZT ultrasonic performance, 413
    signal strength vs temperature, 415
    SNR vs temperature, 416
    sol-gel composite material, 411–14
    ultrasonic performance of PZT/PZT IUT fabricated onto a clad buffer rod, 417
    ultrasonic transducers made with sol-gel composites, 414–22
    wedge IUT, 418–21
  structural-health monitoring demonstration, 422–32
    barrel wear and screw wear monitoring of micro-moulding machine by IUT, 422–4
    BIT/PZT buffer-rod IUT, 425
    buffer-rod IUT probing end, 425
    experimental set-up for imaging hot silicone oil, 426
    line-defect detection on stainless steel plate by wedge IUT, 429–30
    precise pipe thickness measurement at 200 °C by FUT, 430–2
    pulse-echo measurements for the bare stainless steel plate, 430
    pulse-echo measurements for the painted stainless steel plate, 431
    PZT/PZT FUT glued onto a steel pipe, 431
    seven IUTs fabricated onto the micro-moulding machine barrel, 423
    signals acquired from UT6 in the barrel heating zone, 424
    stainless steel plate with line defect and the wedge IUT, 430
    ultrasonic front-surface image of US one cent coin, 427, 428
    ultrasonic imaging in 200 °C silicone oil by focused buffer-rod IUT, 425–9
    ultrasonic signals in the frequency domain, 432
    ultrasonic signals in the time domain, 432
    ultrasonic subsurface image of a US one cent coin, 428, 429
    ultrasonic wave propagation in pulse-echo mode, 424
higher-order transverse mode resonances, 364
homodyne detection techniques, 280–4
Hooke's law, 190
horizontal magnetic field, 41
hybrid transducer ultrasonic motor, 678
hydrodynamic effect, 502
hydrophones, 619
  fibre-optic hydrophones (FOH), 641–71
    comparison of different fibre-optic hydrophones, 669
    Eisenmenger fibre-optic hydrophone, 643–51
    Fabry Perot polymer film fibre-optic hydrophone, 651–60
    interferometric displacement fibre-optic hydrophone, 666–7
    intrinsic fibre-optic hydrophones, 667–8
    multilayer dielectric fibre-optic hydrophone, 660–6
    role in ultrasound metrology, 668, 670–1
  general considerations, 620–6
    3D graphical representation of hydrophone response surface, 624
    directional response, 623–5
    effect of spatial averaging on measured beam profile, 625
    frequency response, 622–3
    maximum acoustic signal, 621–2
    minimum (noise equivalent) acoustic signal, 620–1
    sensitivity and dynamic range, 620–2
    spatial averaging, 625–6
  piezoelectric and fibre-optic, 619–73
  piezoelectric hydrophones, 626–41
    membrane hydrophones, 632–5
    needle (probe) hydrophones, 628–32
    passive cavitation detectors (PCD), 638–41
    piezopolymer vs piezoceramic, 627–8
    underwater low-frequency hydrophones, 636–8
hydrothermal process, 118–27
  deposited film, 118–23
    autoclave for hydrothermal deposition, 120
    cross section of PZT film, 123
    film characteristics, 122–3
    film surface with crystal growth process, 123
    nucleation and crystal growth process, 121
    polycrystalline film deposited on titanium, 119
    solution preparation, 122
    weight and thickness change of a bimorph element, 121
    X-ray diffraction measurements of fabricated PZT films, 122
  material evaluation, 124–5
    bimorph element displacement, 125
    bimorph element used to measure the piezoelectric constant, 124
    longitudinal vibrator used to measure piezoelectric factor e_{31}, 125
  vibration velocity characteristics at resonance, 126–7
hydrothermal PZT film
  TiO_2 powder, 140–1
    large autoclave, 141, 142

implementation, 195
in-plane vibrometer, 308–11
  in-plane movement of small piezo-motor, 311

- measurement using an in-plane vibrometer, 310
- optical design, 309

inertial cavitation, 530

injection moulding
- monitoring of complete filling, 433–6
  - cross section of a mould with IUTs, 435
  - inner surface of the mould showing the probe ends, 434
  - IUT with and without electrical connection, 434
  - moulded parts, 435
  - outer surface of the mould showing four IUTs, 433
  - ultrasonic signals amplitude propagating through the parts during moulding, 436
- process optimisation for micro-fluidic device, 436–40
  - maximum variation of surface profile of line pattern of moulded parts, 439
  - steel buffer-rod IUT, 437
  - test moulded part, 438
  - ultrasonic probe with holder and electric cable, 438
  - ultrasonic velocity during one cycle of moulding, 439

integrated ultrasonic transducer (IUT), 415–16
- barrel wear and screw wear monitoring of micro-moulding machine, 422–4
  - seven IUTs fabricated onto the micro-moulding machine barrel, 423
  - signals acquired from UT6 in the barrel heating zone, 424
  - ultrasonic wave propagation in pulse-echo mode, 424

interdigital transducer (IDT), 331, 332–50
- coupling-of-modes theory, 342–50
  - change in frequency dependence, 347
  - frequency dependence, 346, 347, 348
  - frequency response, 349
  - IDT conductance variation with μ, 348
  - IDT directivity variation with μ, 349
  - three-port black box for an IDT, 343
- delta-function model, 332–9
  - electrical frequency response, 336
  - frequency response, 334
  - frequency response of input admittance, 339
  - impulse response, 333
  - impulse response of the transmission between two IDTs, 334
  - regenerated signal impulse response at first IDT, 335
  - SAW substrate materials in practical use, 338
- double-electrode IDTs, 339
- unidirectional transducers, 340–2
  - distributed acoustic reflection transducer, 341
  - double-electrode-type IDT with two different finger thickness, 341
  - group-type UDT, 341
  - multiphase UDTs, 340

interferometer, 279

interferometric displacement fibre-optic hydrophone, 666–7
- schematic, 666

International Technology Roadmap for Semiconductors (ITRS), 473

intracytoplasmic sperm injection (ICSI), 606

intrinsic fibre-optic hydrophones, 667–8

isentropic Tait equation of state, 645–6

JW model, 521

kerf, 533

KLM model, 200–2
- equivalent circuit, 201

KZK equation, 521

Langevin, 476

Langevin transducer, 30–1, 682

Laplace transform methods, 190

laser Doppler vibrometry (LDV)
- characterisation and optimisation of ultrasonic tools, 286–303
  - applications of LDV studies, 287–90
  - verification and optimisation in industrial production, 290–301
  - visualisation of transducer sound pressure, 301–3
- enhanced LDV designs for special measurements, 303–11
  - displacement profile of the device, 306
  - high-frequency and high-velocity transducers, 303–7
  - in-plane measurement of ultrasonic waves, 308–11
  - modified SLDV for micro-structures and small transducers, 307–8
  - optical arrangement of an ultra-high-frequency interferometer, 304
  - power SAW with asymmetrically excited transducer, 306
  - spectrum of a SAW filter with a resonance at 262MHz, 305
- non-contact vibration measurements, 278–86
  - principles of scanning laser Doppler vibrometer, 284–6
  - realisation of a single-point laser Doppler vibrometer, 279–84
  - theory and measurement principle, 279
- vibration measurement in ultrasonic transducers, 277–312

lead-free piezoceramics, 82

lead-free piezoelectrics, 82
  papers and patents, 83
  strain curves for oriented and unoriented ceramics, 84
lead zirconate titanate (PZT), 7, 74–5, 82, 412
  bending and longitudinal vibration of the d_{31} effect, 127–40
    cylindrical bending vibrator used for an ultrasonic micro-motor, 127–31
    high-intensity vibrator for an ultrasonic micro-scalpel, 135–40
    touch-probe sensor for precise surface texture measurement, 131–5
  epitaxial film, 150–1
  phase diagram of the $Pb(Zr,Ti)O_3$ solid-solution system, 75
  PZT deposition using hydrothermal process, 117–27
  thickness mode vibration, 140–50
  ultrasonic transducers, 117–51
Legendre function, 336
linear phase, 353
linear systems models, 202–5
  model, 202–5
    piezoelectric plate, 204
  overview, 202
lithium niobate, 16, 77, 413
lithium tantalate, 77
Lithographie, Galvanoformung and Abformung (LIGA)-fabricated microgripper, 592
lithotripsy, 519
load test, 274–5
  transducer load test, 275
longitudinal vibration mode, 95–8
  impedance of rod-shaped samples, 99
  longitudinal mechanical vibration of a piezo-ceramic plate, 95
  strain amplitude for a piezo-ceramic plate, 97
Lorentz forces, 36–8, 40
  electromagnetic ultrasonic conversion with perpendicular magnetisation, 40
low-intensity ultrasound, 572

Mach-Zehnder interferometer, 279–80
  compact set-up, 282
  set-up, 280
  typical measurement parameters, 282
magnetic forces, 40–1
magnetoelectric composites, 83–5
  unidirectionally solidified rod of a material with an excess of TiO_2 and magnetic field effect, 85
magnetostriction, 37, 38, 41
magnetostriction-type transducers, 60–66
  angle beam probes, 61–6
  normal probes, 60
Mason's model, 196–200
  final form for piezoelectric plate, 200
  general form of Mason's equivalent circuit, 198
matching layers, 24–6
mathematical analysis, 189–95
  equivalence between multiple layers and simplified form of external circuitry, 192
  forces, 193–5
  voltage, 191–3
mechanical damping, 24–6
mechanical index, 554–5
mechanical quality factor, 91–2
median detector, 460
membrane hydrophones, 632–5
  dynamic range limits, 634
  frequency response of two types of bi-laminar membrane hydrophone, 634
  illustration, 633
micro-acoustic devices
  boundary element method, 220–60
    acoustic wave equation, 221–4
    construction of infinite-domain Green's functions, 224–39
    determining asymptotic expansion terms for $\eta \to 0$, 250–8
    future trends, 258–60
    near-field analysis, 239–49
    normalisation of field variables, 249–50
micro-stereolithography (MSL), 402
MicroBlaze processor, 467
microelectromechanical system (MEMS)
  micromachining process used to fabricate a PZT micropump, 108
  micropump for testing blood, 108
microscale tissue metrology
  testicular sperm extraction surgery, 606–14
    compressive puncture force experienced by top blade, 609
    expected distribution of sizes measured using microprobe, 611–14
    human testicle anatomical sketch, 607
    in vitro penetration experiments, 610–11
    microdissection TESE surgery, 608
    Monte Carlo simulations and analytical solutions of chord lengths, 613, 614
    normalised FFT amplitude vs tubule size, 611
    puncture force for blades inside tissue measured by strain gauge, 610
    sharp blade-like edges at the top and bottom of microprobe, 609
    working principle, 608–9
microscale ultrasonic sensors and actuators, 572–615
  advantages of silicon-based technology, 574–80
    material-based advantages, 575–8
    material properties of various relevant materials, 576
    micromachining-based advantages, 578–80
    piezoelectric resonator electrical model, 578
  applications, 597–614

  cardiac electrophysiological measurement, 602–6
    cMAP signals and ventricular fibrillation, 605
    multichannel recording from isolated perfused canine left ventricle, 604
  microscale tissue metrology in testicular sperm extraction surgery, 606–14
    compressive puncture force experienced by top blade, 609
    expected distribution of sizes measured using microprobe, 611–14
    human testicle anatomical sketch, 607
    in vitro penetration experiments, 610–11
    microdissection TESE surgery, 608
    Monte Carlo simulations and analytical solutions of chord lengths, 613, 614
    normalised FFT amplitude vs tubule size, 611
    puncture force for blades inside tissue measured by strain gauge, 610
    sharp blade-like edges at the top and bottom of microprobe, 609
    working principle, 608–9
  piezoresistive strain gauges, 592–6
    electronic circuit for piezoresistive strain gauge, 594
    fabrication process flow, 593
    silicon ultrasonic horn actuator with microprobes with piezoresistive strain gauges, 594
    steps in bulk micromachining of silicon ultrasonic microprobe with strain gauges, 593
    strain gauge mechanical characterisation, 593–6
    Wheatstone bridge voltage vs axially applied force for a microprobe, 595
    Wheatstone bridge voltage vs transversely applied force for front and back of microprobe, 596
  planar electrode characterisation, 586–92
    charge transfer resistance, 589–90
    equivalent circuit for silicon probe EIS measurements, 591
    equivalent circuit of planar electrode–electrolyte interface, 586
    interfacial capacitance, 587–9
    results from cyclic voltammetry experiments, 591
    spreading resistance, 590–2
    table of parameters for equivalent circuit, 592
    Warburg capacitance and resistance, 590
  silicon ultrasonic horns, 580–4
    horn shapes and parameters, 582
    magnification for different horns vs area ratio, 583
    numerically calculated displacement profiles for the horn shapes, 583
    sensor integration and fabrication, 584–6
    steps in bulk micromachining of silicon ultrasonic microprobe with planar electrodes, 585
  tissue penetration force reduction, 597–602
    estimated decrease in user applied force for different insertion velocities vs PZT drive voltage, 600
    estimated increase in ξ for different PZT drive voltages vs insertion velocity, 600
    focused ultrasound, 597
    impact mode, 597–602
    penetration force vs ultrasonic driving voltage, 601
    penetration force without ultrasound, 601
    ultrasonic cutting of tissue during surgery, 597
  ultrasonic horn actuators, 572–4
    bolted Langevin transducer, 573
    silicon ultrasonic tool developed by Lal, 574
    ultrasound applications, 573
microstructure scattering transfer function, 450
minimum detector, 460
monomorphs, 87–8
motional current, 267
MP-285, 593
multilayer dielectric fibre-optic hydrophone, 660–6
  measured and simulated frequency response, 665
  sensing structure schematic, 661
  transfer functions, 662
multitone non-linear coding (MNC), 518, 523
multitone pulse inversion (MPI), 530
Murata Manufacturing Company, 76

Nallatech XtremeDSP development kit, 465
nascent bubbles, 552
naturally unidirectionality, 342
near-field analysis, 239–49
  asymptotic expansions for eigenvector-eigenvalue hybridised vectors, 247–9
  near-field asymptotic expansion of G_{22}, 239–43
  near-field expansion of G_{22} based on the asymptotic expansions of eigenpairs, 243–7
needle hydrophones, 628–32
  axi-symmetric, radial cross-section of acoustic pressure, 630
  dynamic range limits, 629
  effect of modified tip geometry on frequency response, 631
  experimental and theoretical activity patterns for 0.5mm diameter needle hydrophone, 632
  illustration, 628

neural network detection processor, 456–60
  architecture, 456–7
  back-propagation learning process, 458–9
  model for SSP post-processing, 457–8
    neural nodes model, 456
    three-layer feedforward neural network for SSP, 457
  software implementation, 459–60
    detection results using neural network-based SSP, 460
    experimental data in the time domain, frequency domain and SSP filters frequency bands, 462
    FCR enhancement of various ultrasonic target detectors, 462
    results from detectors applied to SSP channels covering full-frequency spectrum, 464
    results from detectors applied to SSP channels covering low-frequency region, 463
    training data and desired output data, 459
neural networks, 444
Newton's second law, 189
noise equivalent pressure, 621
non-linear acoustics
  advances in tissue harmonic imaging, 523, 525–30
    cholelithiasis of the gallbladder, 526
    Fourier spectra moduli for different combinations of incident pulses, 529
    graphic representation of four MNC pulses, 527
    MNC pulse construction, 528–30y
    moduli of Fourier spectra for non-linear propagation, 528
    pheochromocytoma of the left adrenal gland, 526
  application to biomedical ultrasonics, 517–40
  basic aspects of wave propagation and associated phenomena, 518–19
  measurements of and advances in B/A determination, 519–23, 524
    axial distributions of measured pressure amplitudes and those predicted by JW model, 521
    B/A acoustic properties of few liquids and biological media, 521
    B/A values obtained at ambient pressure using FA and TD procedures, 523, 524
  non-linear wave propagation in hydrophone probe calibration, 534–8
    end-of-cable sensitivity of bilaminar membrane hydrophone probe, 537
  therapeutic applications, 538–9
  ultrasound metrology, 531–4
    early design of composite transducer, 533
non-segmented transducers, 46–52, 61–5
  arrangement of magnets and RF coil in an EMAT probe, 65
  beam angle as a function of the frequency of the transducer, 48
  characteristic directivity pattern of an EMAT angle beam probe for SH waves, 52
  directivity patterns in the plane of incidence of an SH-wave, 63
  EMAT angle beam probe for SH waves, 50
  EMAT angle beam probe for SV waves, 46
  EMAT angle beam probes with metallic coil bodies, 49
  EMAT probe for SH wave, 62, 64
  EMAT probe for SV and Rayleigh waves, 61
  laboratory prototype EMAT, 65
  RF coils, 48
  superposition of elementary waves forming wave fronts and beam angle (SH wave), 51
  superposition of elementary waves forming wave fronts and beam angle (SV wave), 47
normal probes, 41–5, 60
  EMAT producing linearly polarised shear waves, 60
  linearly polarised shear waves, 42, 43
  longitudinal waves, 45
  radially polarised shear waves, 43, 44
Nyquist–Shannon sampling, 626

objective function, 456, 458
Olympus NDT, 411
one-dimensional transducer arrays, 28–9
  illustration, 29
operational deflection shapes, 278
optical visualisation
  acoustic field, 314–27
    Fresnel visualisation method, 320–2
    photoelastic visualisation method, 323–7
    Schlieren visualisation technique, 314–19
order-statistic, 444
order-statistic processors, 452–6
  inverse distribution functions
    chi-distributed target-plus-clutter and Weibull-distributed clutter, 454
    Rayleigh-distributed target-plus-cluster and Rayleigh-distributed clutter, 455
outer Helmholtz plane (OHP), 588
overpotential, 589

passive cavitation detectors (PCD), 638–41
  beam profiles of 15mm diameter PCD, 641
  frequency response of 15mm diameter PCD with focal distance 70mm, 640

$Pb(In_{1/2}Nb_{1/2})O_3$ –$Pb(Mg_{1/3}Nb_{2/3})O_3$ –$PbTiO_3$ (PIMNT)
  applications, 175–7
  ceramics, 157–63
  future trends, 177–9
  high-Curie-temperature piezoelectric single crystals, 154–80
  overview, 154–7
    PZNT and PMNT phase diagrams near the MPB, 156
    relaxor materials high T_c materials and their MPBs with lead titanate, 155
  single crystals grown by Bridgman method, 165–75
  single crystals grown by flux method, 163–5
$Pb[(Mg_{1/3}Nb_{2/3})_{0.68}Ti_{0.32}]O_3$ (PMNT), 156–7
$Pb(Sc_{1/2}Nb_{1/2})O_3$–$Pb(Mg_{1/3}Nb_{2/3})O_3$–$PbTiO_3$ (PSMNT), 157
$Pb(Sc_{1/2}Nb_{1/2})O_3$–$PbTiO_3$ (PSNT), 175–7
$Pb[(Zn_{1/3}Nb_{2/3})_{0.91}Ti_{0.09}]O_3$ (PZNT), 156–7
phased-array transducers *see* segmented transducers
photoelastic visualisation method, 323–7
  photoelasticity, 323–4
    illustration, 324
  visualisation system and image, 324–7
    stroboscopic photoelastic visualisation, 325
    tone-burst plane ultrasonic wave incident on glass block, 325
    tone-burst plane ultrasonic wave incident on glass boundary, 326
    ultrasonic tone-burst and Rayleigh wave propagating near the glass surface, 326
    visualised distribution of normal stress, 327
    visualised distribution of the S2 mode of Lamb waves, 327
photostrictive materials, 86–7
  two bimorph legs fixed to a plastic board, 87
pickup voltage, 138–9
  vibration velocity *vs.* frequency for ultrasonic micro-scalpel, 138
piezoceramic, 13–15, 627–8
  coefficients in the elasto-electric matrices, 15
  piezoelectric materials, 88–113
    overview, 98–105
    piezoelectric figures of merit, 88–92
    piezoelectric properties, 99
    piezoelectric resonance, 92–8
    piezoelectric transducer designs, 112–13
    surface acoustic wave materials, 105–9, 109–12
    thin films, 105–9
  piezoelectric transducers, 70–113
  piezoelectrics history, 70–88
  properties of selected piezoelectric materials, 14
piezoceramic plate, 205–12
  electric impedance of plate using a 1D model, 207
  electrical impedance, 209, 211
  properties of selected materials, 206
  time-domain and frequency-domain representation, 208, 210, 212
piezocomposites, 17–20, 82–6, 105
  coefficients and parameters, 19
  composite effects, 82–3
    output, 85
  magnetoelectric composites, 83–5
  material structures, 17
  piezoelectric dampers, 85–6
piezocrystals, 16
piezoelectric dampers, 85–6
  composite of a polymer and a piezo-ceramic powder, 86
piezoelectric effect, 4–12
  ferroelectricity, 4–6
piezoelectric equations, 92–3
piezoelectric hydrophones, 619, 626–41
  membrane hydrophones, 632–5
  needle (probe) hydrophones, 628–32
  passive cavitation detectors (PCD), 638–41
  piezopolymer vs piezoceramic, 627–8
  underwater low-frequency hydrophones, 636–8
piezoelectric resonance, 92–8
piezoelectric single crystals (PSC)
  $Pb(In_{1/2}Nb_{1/2})O_3$–$Pb(Mg_{1/3}Nb_{2/3})O_3$–$PbTiO_3$ (PIMNT) ternary system, 154–80
    applications, 175–7
    Bridgman method, 165–75
    ceramics, 157–63
    flux method, 163–5
    future trends, 177–9
    overview, 154–7
piezoelectric stiffness constant, 18
piezoelectric strain constant, 88
piezoelectric stress constant, 8
piezoelectric transducers, 20–31
  basic configurations and piezoelectricity, 3–33
    future trends, 31–3
    piezoelectric effect, 4–12
    piezoelectric materials, 13–20
  characterisation under high-power operation, 271–4
    force factor *vs.* vibration velocity, 273
    quality factor *vs.* vibration velocity, 273
    transient method for measuring high amplitude characteristics, 271
    waveforms observed in transient method, 272
  configurations, 27–31
  designs, 112–13
    3D positioning actuator a stacked structure, 113
    piezoelectric actuators, 112

- electrical evaluation, 264–76
    - electrical measurements, 267–71
    - equivalent electrical circuit, 265–7
    - load test, 274–5
  - piezoceramics, 70–113
    - piezoelectric materials, 88–113
    - piezoelectrics history, 70–88
  - single-element, 21–7

piezoelectric ultrasonic transducers
  - examples, 205–15
    - electrical impedance magnitudes of bar and impedance phase characteristics, 214
    - electrical impedance magnitudes of plate, plank and bar, 213
    - time-domain and frequency-domain representation, 215
  - one-dimensional models, 187–217
    - basic physical configuration, 189
    - equivalent electrical circuit models, 195–202
    - examples, 205–15
    - future trends, 216–17
    - linear systems models, 202–5
    - performance expressed through wave equation, 188–95

piezoelectric voltage constant, 88

piezoelectricity, 6–12, 31–2, 409, 626
  - direct and converse piezoelectric effect, 7
  - future trends, 31–3
  - piezoelectric effect, 4–12
  - piezoelectric materials, 13–20
    - piezoceramics, 13–15
    - piezocomposites, 17–20
    - piezocrystals, 16
    - piezopolymers, 15–16
  - piezoelectric transducers, 3–33, 20–31
  - variables and coefficients in the piezoelectric constitutive equations, 9

piezoelectrics
  - history, 70–88
    - barium titanate discovery, 73–4
    - ceramics and single crystals, 77–81
    - composites, 82–6
    - lithium niobate/tantalate, 77
    - Pb-free, 82
    - PVDF, 81–2
    - PZT discovery, 74–6
    - related materials, 86–8
    - underwater acoustic devices with quartz and Rochelle salt, 71–3

piezopolymer, 15–16, 104–5, 627–8
  - polyvinylidene difluoride, 104

pigment dispersion, 511

PIMNT 0/68/32, 157–8, 161–2

PIMNT 16/51/33, 161, 163, 165, 171, 173–5
  - crystal growth, 165–8
    - EPMA results for PSC wafers, 168
    - EPMA results of three wafers cut from a PSC of PIMNT, 168
    - wafer obtained from a PSC of PIMNT, 167
  - electrical property, 168–70
    - three wafers cut from PIMNT 24/42/34 PSC, 169

PIMNT 23/41/36, 158, 161–2

PIMNT 24/42/34, 161–2, 163, 174–5
  - crystal growth, 170–1
    - solution produced by Bridgman process, 170
  - electrical property, 171–4
    - dielectric properties of PSCs of PIMNT 16/51/33, 171
    - ideal PSCs for medical array transducers, 172
    - temperature dependence, 173

PIMNT 24/44/32, 176

PIMNT 25/43/32, 158

PIMNT 28–32/34–42/30–34, 176

PIMNT 63/0/37, 157–8, 161–2

PIMNT ceramics, 157–63
  - Curie temperature of the PIN-PMN-PT ternary ceramic system, 160
  - dielectric and piezoelectric properties across and along MPB, 162
  - dielectric constant *vs.* temperature for the PIN-PMN-PT ternary ceramic system, 160
  - electromechanical coupling factor of PIN-PMN-PT ternary ceramic system, 161
  - PIN-PMN-PT ternary system, 158
  - X-ray diffraction of the PIN-PMN-PT ternary ceramic system, 159

PMNT 70/30, 178

polarity detector, 461

polycrystalline materials, 100–2
  - composition *vs.* piezoelectric *d* constants, 102
  - piezoelectric, dielectric and elastic properties of typical PZTs, 103
  - PZT system, 101

poly(methyl methacrylate) (PMMA), 420

polyvinylidene difluoride, 81–2, 532

polyvinylidene fluoride, 15–16

potassium sodium niobate (KNN), 32

power ultrasonics, 476–514
  - application of the new technology to processing, 490–513
  - characteristics of power transducers with extensive radiators, 479–90
  - environmental processes, 501–7
    - acousto-electrostatic filter, 504
    - air-cleaning, 502–5
    - comparison of rotary vacuum filtration with and without ultrasound, 507
    - multifrequency acoustic agglomerator with stepped-plate generators, 503
    - reduction in particle emissions for two different frequencies, 505

  rotary vacuum filtration aided by rectangular grooved-plate transducer, 507
  sludge filtration, 506–7
flat-plate transducer with reflector, 487–9, 490
  directivity diagrams, 490
  illustration, 488
  prototype for operating in air, 489
food processing, 491–501
  fluidised-bed dryer with cylindrical-radiator transducer, 497
  pilot plant for extracting almond oil with SFE assisted by ultrasound, 500
  rotary ultrasonic defoamer in a reactor, 494
  static ultrasonic defoamer in canning line, 493
  supercritical fluid extraction assisted by ultrasound, 498–501
  system for food dehydration using a stepped-plate ultrasonic generator and forced air, 496
  system for ultrasonic dehydration using high-intensity ultrasonic vibration, 499
  ultrasonic defoaming, 491–3
  ultrasonic dehydration, 493–501
manufacturing, 508–13
  debubbling efficiency for solvent-based coating liquid, 512
  debubbling efficiency for water-based coating liquid, 512
  semi-industrial implementation of ultrasonic textile washing, 510
  semi-industrial reactor for pigment dispersal in paints, pastes and inks, 513
  semi-submerged bubbles with coating layer, 511
  textiles washing assisted by ultrasonic energy, 509
  ultrasonic debubbling of liquid coating layers, 510–11
  ultrasonic enhancement of pigment dispersion in paint manufacture, 511–13
  ultrasonic washing in textile manufacturing, 508–10
  ultrasonic washing vs conventional domestic washing, 509
new technologies for fluids and multiphase media, 478–90
stepped-grooved-plate transducer, 487
stepped-plate transducer, 480–6
  acoustic field of focusing circular-plate transducer, 484
  directional rectangular stepped-plate transducers characteristics, 485
  directivity diagrams for a flat-plate and stepped-plate radiator, 481
  directivity pattern for stepped-plate transducer with a directional stepped profile, 481
  directivity patterns of rectangular stepped-plate transducers, 486
  procedure used to design focusing radiators, 482
  prototypes circular stepped-plate directional and focusing, 482
  radiation pattern of directional circular stepped-plate transducer, 483
  rectangular stepped-plate transducers prototype, 485
 transducer with cylindrical radiator, 489–90
  simulation of vibration using finite element analysis, 490
Precision Acoustics Ltd, 652
preload, 678
pulse inversion (PI), 518, 523, 525
PUSONICS, 493
PZNT 91/9, 156, 163, 165, 173, 174, 178
PZT5H, 177–8

quartz, 71–3
quasi-static magnetic field, 36, 40

Radix-2, 470
Radix-4, 470
Raman-Nath effect, 315–16
  diffraction, 316
Rayleigh wave *see* surface acoustic wave (SAW)
rectified diffusion, 552
relaxor ferroelectrics, 77–81, 102–4
  electromechanical coupling factors, 80
  intuitive model of piezoelectricity, 81
  PZN-PT, 79
  strain level *vs.* electric field, 78
  ultrasound images created with different probe, 104
Remez exchange algorithm, 355
resonant SPUDT filters, 360–2
  designed weighting functions for excitation and reflection, 362
  optimisation result when amplitude flatness is specified, 361
  optimisation result when flatness for both the amplitude and group delay is specified, 361
RF coil, 42
Rochelle salt, 71–3
rotational absorption, 376

sandwich transducer *see* Langevin transducer
scanning laser Doppler vibrometry (SLDV), 278–9

  micro-structures and small transducers, 307–8
    schematic of a microscope laser scanning set-up, 308
  principles, 284–6
  simplified optical scheme of a measurement head, 284
  visualisation of the transducer sound pressure, 301–3
    arrangement proposed by Zipser and Franke, 302
    visualisation of the sound pressure distribution, 303
Schlieren visualisation technique, 314–19
  Bragg reflection, 316–17
    illustration, 317
  Raman-Nath effect, 315–16
    diffraction, 316
  visualisation systems and images, 317–19
    immersion focused transducer, 319
    rectangular pulse of plane waves, 319
    Schlieren system, 318
    short pulse of plane waves, 318
segmented transducers, 52–8, 65–6
  angle beam probe for SV waves with segmented RF coil, 53
  beam angles and optimised time delays for an SH-wave phased-array EMAT, 58
  directivity patterns of an SH-wave angle beam probe, 57
  EMAT phased-array probe for SH waves, 55
  RF coils, 53
  segmentation of an EMAT SH-wave angle beam transducer, 54
  variation of beam angle for a segmented EMAT, 56
self-coupling coefficient, 344
semi-empirical non-linear propagation model, 536
signal-to-noise ratio (SNR), 409
silicon-based technology
  advantages, 574–80
  material-based advantages, 575–8
    heat generation, 577–8
    maximum output power density, 575–7
    maximum particle velocity, 577
  micromachining-based advantages, 578–80
    curved actuators, 580
    lower actuation voltages, 579
    lower cost and disposable transducers, 579
    sensors integration, 579
    small devices, 578–9
silicon ultrasonic horns, 580–4
  actuator with microprobes with piezoresistive strain gauges, 594
  horn shapes and parameters, 582
  magnification for different horns vs area ratio, 583
  numerically calculated displacement profiles for the horn shapes, 583
  sensor integration and fabrication, 584–6
  steps in bulk micromachining of silicon ultrasonic microprobe with planar electrodes, 585
single crystal materials, 99–100
single-electrode IDT, 332
single-element transducer, 21–7
  ancillary components, 26–7
  mechanical damping material and matching layers, 24–6
  piezoelectric material, 22–4
  ultrasound medium and couplant, 21–2
single-phase unidirectional transducer (SPUDT), 340
  filters, 359–60
    frequency response, 359, 360
single-point laser Doppler vibrometer, 279–84
  3D LDV in a single-point design, 283
  2D model of a 3D LDV, 283
sludge filtration, 506–7
Snell’s law, 419
sodium potassium tartrate, 72
sol-gel composite ultrasonic transducers, 411–22
  buffer-rod IUT, 416–18
    ultrasonic performance of PZT/PZT IUT fabricated onto a clad buffer rod, 417
  flexible ultrasonic transducer (FUT), 421–2
    pulse echo measurements at various temperatures, 422
  general fabrication process, 412
  integrated ultrasonic transducer (IUT), 415–16
  sol-gel composite material, 411–14, 415, 416
    BIT/PZT ultrasonic performance, 414
    lithium niobate/PZT ultrasonic performance, 415
    PZT/PZT ultrasonic performance, 413
    signal strength vs temperature, 415
    SNR vs temperature, 416
  ultrasonic transducers made with sol-gel composites, 414–22
  wedge IUT, 418–21
    illustration, 419
    longitudinal wave and shear wave generation by mode conversion, 418
    measurements of transmission mode at 200 °C, 421
    reflected echo of longitudinal wave, 420
    reflected echo of SH wave, 420
    two PZT/PZT wedge IUTs set onto a stainless steel plate, 421
solid state crystal growth (SSCG), 177, 178
sonotrode, 287, 295
spatial averaging, 649
split-spectrum processing (SSP) technique, 444, 447–8, 449
  channels with flaw-echo information and null-observation channels, 449

  frequency bands, 447
  illustration, 447
spreading resistance, 590
squared-error function, 456, 458
stable cavitation, 530
standing-wave ultrasonic motors, 678–94
  linear motor, 681–94
    control of the elliptical shape of vibration trajectory, 686
    electrode pattern for the first longitudinal and second bending modes, 687
    fine positioning characteristics with static deformation, 694
    four phases of one cycle for high-power linear motor, 690
    high-output bolt-clamped linear motor, 689
    high-power performance of the motor, 693
    load-displacement characteristics of non-linear leaf springs with different arm offsets UO, 688
    motor speed as function of voltage, 686
    resonance frequencies adjustment for L1 and B2 modes, 690
    slider speed, 687
    slider speed as function of phase differences between voltages, 691
    speed-load characteristics for different voltages applied to longitudinal PZT elements, 692
    start-stop transient responses for 10-kg slider, 693
    support mechanism of L1-B2 transducer using non-linear leaf springs, 688
    using bending vibrator and two multilayer piezoelectric elements, 684
    using combination of longitudinal transducer and multilayer piezoelectric elements, 683
    using the L1-B2-mode of rectangular PZT element, 685
    vibration modes used in linear motor, 690
  rotary motor, 678–81, 682, 683
    hybrid transducer ultrasonic motor operation, 681
    piezoelectric elements used in the motor, 680
    speed-load characteristics of hybrid transducer motor, 683
    two-mode standing-wave ultrasonic motor, 679
    waveforms for preload, angular velocities and torque, 682
    wedge-shaped pieces of torsional PZT unit, 681
static magnetic field, 36, 40
stepped-grooved-plate transducer, 487
stepped-plate transducer, 480–6
  acoustic field of focusing circular-plate transducer, 484
  directional rectangular stepped-plate transducer characteristics, 485
  directivity diagrams for a flat-plate and stepped-plate radiator, 481
  directivity pattern for stepped-plate transducer with a directional stepped profile, 481
  directivity patterns of rectangular stepped-plate transducers, 486
  procedure used to design focusing radiators, 482
  prototypes, 482
  radiation pattern of directional circular stepped-plate transducer, 483
  rectangular stepped-plate transducers prototype, 485
Stokes–Kirchhoff loss, 376
supercritical fluid, 498
SuperSonic Imagine Inc (SSI), 558
surface acoustic wave (SAW), 699
  materials, 105–9
    bi-directional filter, 110
    properties, 111
surface acoustic wave (SAW) devices, 331–71
  interdigital transducers (IDT), 332–50
    coupling-of-modes theory, 342–50
    delta-function model, 332–9
    double-electrode IDTs, 339
    unidirectional transducers, 340–2
  resonators, 362–70
    beam diffraction and transverse modes, 364–5
    filters employing one-port resonators, 365–6
    multi-mode resonator filter, 367–70
    one-port SAW resonators, 362–4
    two-port SAW resonators and filters, 366–7
  transversal SAW filter, 351–62
    apodised IDTs, 351–6
    influence of peripheral circuits, 356–8
    resonant SPUDT filters, 360–2
    secondary effects, 358–9
    single-phase unidirectional transducer (SPUDT) filters, 359–60
surface acoustic wave (SAW) resonators, 362–70
  beam diffraction and transverse modes, 364–5
    SAW beam spreading due to diffraction, 365
    trapping the energy in wave guide structure, 365
  filters employing one-port resonators, 365–6
    frequency response of ladder-type filter, 366
    ladder-type filter basic configuration, 366

  multi-mode resonator filter, 367–70
    double-mode resonator filter frequency response, 369
    equivalent circuit for double-mode resonator filter, 369
    frequency response of multi-mode resonator filter, 370
    transversely coupled SAW resonator, 368
    with unbalanced-to-balanced and impedance conversion functions, 370
  one-port SAW resonators, 362–4
    electrical resonance characteristics, 363
    structure and equivalent electrical circuit, 362
  two-port SAW resonators and filters, 366–7, 368
    frequency response, 368
    structure and equivalent electrical circuit, 367
system-in-a-package (SiP) devices, 473
system-on-a-chip implementation, 465–72
  application software, 466–7
    software interface for ultrasonic flaw-detection system, 467
  execution time, 470, 471
    SSP algorithms processing time, 471
  hardware realisation, 465–6
    test system for processing real-time ultrasonic data using SSP algorithm, 465
  hardware/software co-design, 467–8
    illustration, 468
  resource usage, 470–2
    FPGA resource usage for implementing SSP, 472
  software and hardware performance evaluation for SSP, 468–70
    FCR improvement using different hardware and software co-design techniques, 469

ternary system, 76
testicular sperm extraction (TESE) surgery, 606–14
  compressive puncture force experienced by top blade, 609
  expected distribution of sizes measured using microprobe, 611–14
  in vitro penetration experiments, 610–11
  microdissection TESE surgery, 608
  Monte Carlo simulations and analytical solutions of chord lengths, 613, 614
  normalised FFT amplitude vs tubule size, 611
  puncture force for blades inside tissue measured by strain gauge, 610
therapeutic ultrasound, 560–3
  rapid heating with ultrasound for therapeutic effect, 561–2
  thrombolysis, 562–3
thermo-optic effect, 654
thickness mode vibration, 140–50
  applications, 144
  deposition process and film material, 141–4
    PZT films deposited on different TiO_2 powder, 143–4
    raw materials for the hydrothermal deposition of PZT, 142
  hydrothermal PZT film using TiO_2 powder, 140–1
  small-diameter ultrasonic probe, 144–50
thin films, 105–9
  constraints, 109
  MEMS applications, 108
  preparation techniques, 106–7
    magnetron sputtering, 106
    PZT films, 107
time delay spectrometry (TDS), 536
time-frequency algorithms, 473
time-gated frequency analysis (TGFA), 536
TiO_2 powder
  hydrothermal PZT film, 140–1
    large autoclave, 141, 142
tissue harmonic imaging (THI), 525
tissue penetration force reduction, 597–602
  estimated decrease in user applied force for different insertion velocities vs PZT drive voltage, 600
  estimated increase in ξ for different PZT drive voltages vs insertion velocity, 600
  focused ultrasound, 597
  impact mode, 597–602
  penetration force vs ultrasonic driving voltage, 601
  penetration force without ultrasound, 601
  ultrasonic cutting of tissue during surgery, 597
titanium wire ultrasonic probe, 145–7
  frequency spectrum for titanium wire-backed hydrophone, 147
  PZT film deposited onto the tip of a titanium wire, 145
  received waveform for titanium wire-backed hydrophone, 146
Tonpilz transducer, 30
top-seeded solution growth (TSSG), 178
touch-probe sensor
  precise surface texture measurement, 131–5
    amplifier circuit for a scanning probe sensor, 134
    amplitude *vs.* frequency for scanning probe sensor, 133
    pickup voltage *vs.* displacement for a scanning probe sensor, 134
    scanning probe sensor, 132
    surface of a glass grating measured using a scanning probe sensor, 135
transducers
  cylindrical radiator, 489–90

    - simulation of vibration using finite element analysis, 490
  - non-destructive evaluation at high temperatures, 408–41
    - process-monitoring demonstration, 433–40
    - sol-gel composite ultrasonic transducers, 411–22
    - structural-health monitoring demonstration, 422–32
- transient response method, 271
- transversal SAW filter, 351–62
  - apodised IDTs, 351–6
    - designed transversal filter frequency response, 356
    - designed weighting function, 355
    - electrode pattern and SAW pulse train, 351
    - Hamming function Fourier spectrum, 353
    - weighted and unweighted IDTs frequency response, 354, 355
  - frequency response, 354
  - illustration, 352
  - influence of peripheral circuits, 356–8
    - transversal SAW filter with peripheral circuits, 356
    - two-port SAW filter frequency response, 357
  - resonant SPUDT filters, 360–2
    - designed weighting functions for excitation and reflection, 362
    - optimisation result when amplitude flatness is specified, 361
    - optimisation result when flatness for both the amplitude and group delay is specified, 361
  - secondary effects, 358–9
  - single-phase unidirectional transducer (SPUDT) filters, 359–60
    - frequency response, 359, 360
- travelling-wave ultrasonic motors, 694–9
  - linear motor, 698–9
    - surface acoustic wave ultrasonic motor, 699
    - travelling-wave linear motor, 698
  - rotary motor, 694–8
    - bar-shaped motor with rotation due to bending mode, 697
    - basic configuration for travelling-wave rotary motor, 695
    - out-of-plane and in-plane displacements in flexural vibration, 696
    - three-degree-of-freedom motor fabricated on substrate surface, 698
    - voltage application for generating travelling waves along a ring vibrator, 695
- triple transit echo (TTE), 331, 358
- TUSCON, 563

- UE GROWTH-CRAFT-G1STCF-2002-50309, 513
- ultrasonic defoamer system (UDS), 491–3
- ultrasonic defoaming, 491–3
- ultrasonic dehydration, 493–8, 499, 500
- ultrasonic flaw-detection techniques, 445–56
  - order-statistic (OS) processors, 452–6
  - split-spectrum processing, 447–8, 449
    - channels with flaw-echo information and null-observation channels, 449
    - frequency bands, 447
    - illustration, 447
  - ultrasonic pulse-echo measurement set-up, 445
  - ultrasonic signal from a steel block with hole, 446
  - ultrasonic signals frequency analysis, 448–52
    - heuristic evaluation of relative spectrum ratio, 451
- ultrasonic horn actuators, 572–4
  - bolted Langevin transducer, 573
  - silicon ultrasonic tool developed by Lal, 574
  - ultrasound applications, 573
- ultrasonic micro-motor, 127–31
  - amplitude *vs.* frequency, 130
  - cross section, 129
  - deformation and rotation, 129
  - illustration, 128
  - output torque *vs.* pre-load, 130
  - revolution speed *vs.* input voltage, 131
- ultrasonic micro-scalpel, 135–40
  - diagram and amplifier circuit, 137
- ultrasonic motors, 677–703
  - future trends, 702–3
  - standing-wave ultrasonic motors, 678–94
    - hybrid transducer ultrasonic motor operation, 681
    - linear motor, 681–94
    - piezoelectric elements used in the motor, 680
    - rotary motor, 678–81, 682, 683
    - two-mode standing-wave ultrasonic motor, 679
    - wedge-shaped pieces of torsional PZT unit, 681
  - travelling-wave ultrasonic motors, 694–9
    - linear motor, 698–9
    - rotary motor, 694–8
    - surface acoustic wave ultrasonic motor, 699
  - ultrasonic motor performance, 700–2
    - hybrid transducer rotary motors from 5 mm to 80 mm in diameter, 702
    - maximum torque for various kinds of ultrasonic motor, 701
    - maximum torque vs motor weight, 700
    - output power vs motor weight, 700
- ultrasonic pulse compression (UPC), 393
- ultrasonic tools
  - applications of LDV for studies on ultrasonic transducers, 287–90
    - frequency spectrum using broadband chirp excitation, 288

    - magnitude of displacement, 290
    - more complex mode, 289
    - simple buzzer-type transducer, 288
    - transducer movement, 289
  - characterisation and optimisation, 286–303
  - verification and optimisation in industrial production, 290–301
    - capillary-type ultrasonic wire bonder, 293
    - capillary wire bonder, 291
    - deflection shapes for the sonotrode, 297
    - displacement distribution of a wire-bonding capillary for different materials, 292
    - droplet generation through ultrasonic mesh vibration, 299
    - excitation of an ultrasonic nebuliser mesh, 300
    - frequency spectrum (0Hz to 100kHz), 297
    - geometry of the sonotrode, 296
    - phases of rotation-symmetric bending mode of the actuator, 301
    - profile across the sonotrade front face, 298
    - rotation-symmetric deflection shape of the mesh at the operational frequency, 301
    - standard industrial ultrasonic transducer and sonotrode, 295
    - ultrasonic nebuliser with measurement grid on actuator, 300
    - ultrasonic welding, 294
    - uniform movement of the sonotrode front face, 298
- ultrasonic transducer
  - laser Doppler vibrometry for vibration measurement, 277–312
    - characterisation and optimisation of ultrasonic tools, 286–303
    - enhanced LDV designs for special measurement, 303–11
    - non-contact vibration measurements, 278–86
  - lead zirconate titanate (PZT) film, 117–51
    - bending and longitudinal vibration of the d_{31} effect, 127–40
    - epitaxial film, 150–1
    - PZT deposition using hydrothermal process, 117–27
    - thickness mode vibration, 140–50
- ultrasound, 572
  - applications, 573
  - bioeffects, 546
- ultrasound-enhanced thrombolysis, 563
- underwater acoustic device
  - quartz and Rochelle salt, 71–3
    - Langevin's transducer design, 71
- underwater low-frequency hydrophones, 636–8
  - ball hydrophones, 638
  - cylindrical and ball hydrophone construction parameters, 638
  - directivity patterns for bi-laminar shielded membrane hydrophone, 635
  - frequency response of various low-frequency cylindrical and spherical hydrophones, 637

- vibration velocity, 126–7, 138
  - pickup voltage *vs.* driving voltage for an ultrasonic micro-scalpel, 139
  - pickup voltage *vs.* frequency for an ultrasonic micro-scalpel, 127
- vibrational absorption, 376
- vibro-touch sensors, 131
- voltage, 191–3
  - equivalence between layers and external circuitry, 192

- Warburg impedance, 590
- wavelet transform (WT), 473
- Webster's horn equation, 581–2
- wedge IUT, 418–21
  - line-defect detection on stainless steel plate, 429–30, 431
    - pulse-echo measurements for the bare stainless steel plate, 430
    - pulse-echo measurements for the painted stainless steel plate, 431
    - stainless steel plate with line defect and the wedge IUT, 430
  - longitudinal wave and shear wave generation by mode conversion, 418
  - measurements of transmission mode at 200 °C, 421
  - reflected echo of longitudinal wave, 420
  - reflected echo of SH wave, 420
  - two PZT/PZT wedge IUTs set onto a stainless steel plate, 421
- Wigner–Ville distribution (WVD), 473

- Xilinx Embedded Development Kit (EDK), 467
- Xilinx Virtex-4 FPGA, 465, 470
- XtremeDSPunit, 465